NSEL Report Series
Report No. NSEL-025
September 2010

Large-Scale Cyclic and Hybrid Simulation Testing and Development of a Controlled-Rocking Steel Building System with Replaceable Fuses

Matthew R. Eatherton
and
Jerome F. Hajjar

NEWMARK STRUCTURAL ENGINEERING LABORATORY

Department of Civil and Environmental Engineering
University of Illinois at Urbana-Champaign

UILU-ENG-2010-1804

ISSN: 1940-9826

The Newmark Structural Engineering Laboratory (NSEL) of the Department of Civil and Environmental Engineering at the University of Illinois at Urbana-Champaign has a long history of excellence in research and education that has contributed greatly to the state-of-the-art in civil engineering. Completed in 1967 and extended in 1971, the structural testing area of the laboratory has a versatile strong-floor/wall and a three-story clear height that can be used to carry out a wide range of tests of building materials, models, and structural systems. The laboratory is named for Dr. Nathan M. Newmark, an internationally known educator and engineer, who was the Head of the Department of Civil Engineering at the University of Illinois [1956-73] and the Chair of the Digital Computing Laboratory [1947-57]. He developed simple, yet powerful and widely used, methods for analyzing complex structures and assemblages subjected to a variety of static, dynamic, blast, and earthquake loadings. Dr. Newmark received numerous honors and awards for his achievements, including the prestigious National Medal of Science awarded in 1968 by President Lyndon B. Johnson. He was also one of the founding members of the National Academy of Engineering.

Contact:
Prof. B.F. Spencer, Jr.
Director, Newmark Structural Engineering Laboratory
2213 NCEL, MC-250
205 North Mathews Ave.
Urbana, IL 61801
Telephone (217) 333-8630
E-mail: bfs@illinois.edu

The authors greatly appreciate the contributions to this research from our collaborators at Stanford University, Professors Gregory G. Deierlein, Helmut Krawinkler, and graduate student Xiang Ma. The contributions to this work from Professor Sarah Billington, graduate students Kerry Hall, Eric Borchers, and Alex Peña, Post-Doctoral Researcher Paul Cordova, and practicing structural engineers David Mar and Gregory Luth are appreciated. The authors also thank our Japanese collaborators for their contributions to this research, including Professor Toru Takeuchi, Professor Mitsumasa Midorikawa, Professor Kazuhiko Kasai, Professor Masayoshi Nakashima, Tsuyoshi Hikino, Ryota Matsui, Masaru Oobayashi, Yosuke Yamamoto, and Ryohei Yamazaki. This material is based upon work supported by the National Science Foundation under Grant No. (CMMI-0530756), the American Institute of Steel Construction, Stanford Univ., and the Univ. of Illinois at Urbana-Champaign. In-kind funding was provided by Tefft Bridge and Iron of Tefft, Indiana, MC Detailers of Merrillville, Indiana, Munster Steel Co. Inc. of Munster, Indiana, Infra-Metals of Marseilles, Indiana, and Textron/Flexalloy Inc. Fastener Systems Division of Indianapolis, Indiana. The LBCB Operations Manager and LBCB Plugin used in this research were developed by N. Nakata, O. S. Kwon, M. Bletzinger, S. J. Kim, C. Holub, and M. Eatherton with support from NEES@UIUC, Grant No. A6000 SBC NEES OMSA-2004, and the Mid-America Earthquake Center, NSF Grant No. EEC-9701785.

The cover photographs are used with permission. The Trans-Alaska Pipeline photograph was provided by Terra Galleria Photography (http://www.terragalleria.com/).

ABSTRACT

Current U.S. building codes and earthquake engineering practice utilize inelasticity in the seismic force resisting system to dissipate seismic energy and protect against collapse. Inelasticity in conventional structures can lead to structural damage distributed throughout the building and permanent drifts after the earthquake motion ceases which can make the structure difficult if not financially unreasonable to repair. A controlled rocking system has been developed that virtually eliminates residual drifts and concentrates the majority of structural damage in replaceable fuse elements. Portions of the development related to but not contained in this report include fuse testing, fuse analysis, large-scale shake table testing, development of a displacement based design procedure, and collapse modeling.

The controlled rocking system is investigated and developed through analytical, computational, and experimental means. A large-scale experimental program was conducted including quasi-static cyclic and hybrid simulation tests. Nine specimens were tested representing three-story frames at approximately half scale. These experiments validated the performance of the system, demonstrated system response when subjected to simulated ground motions, allowed the investigation of detailing and construction methods, provided information on frame member forces, and provided data to confirm and calibrate computational models.

Computational models were developed based on the experimental behavior and two computational studies were conducted. A single degree-of-freedom study consisting of over 25,000 analyses was performed to investigate system proportioning including defining the amount of restoring force that is necessary to provide reliable self-centering in the presence of ambient building resistance. A multi-degree-of-freedom study consisting of approximately 1500 analyses was performed to investigate the application of the controlled rocking system in different configurations. This study was also used to investigate the probabilities of reaching limit states for earthquake events with varying recurrence period.

The experimental and computational studies described in this report demonstrate that the controlled rocking system for steel-framed buildings can satisfy the performance goals of virtually eliminating residual drift and concentrating structural damage in replaceable fuses even during large earthquakes. The results of all phases of this work were synthesized into design recommendations which summarize the practical application of this system to building structures.

CONTENTS

INTRODUCTION

1.1 State of Practice in Earthquake Engineering

Since the inception of earthquake building code provisions in the United States, allowing inelasticity in structural elements has been a key component in the design of seismic lateral force resisting systems for large earthquake events. When referring to severe earthquake ground motions, John Blume and Nathan Newmark wrote:

> "To design for such earthquakes by requiring that the structure remain in the elastic range would be grossly uneconomical and would represent the payment of too great a cost to provide for the probability of such an occurrence." (Blume et al.1961)

It is in this spirit that the current U.S. building codes reduce the elastic seismic forces by the Response Modification Coefficient, *R* (ASCE 2005), which can be as large as a factor of 8, to determine the design level forces (ASCE 2005). The Structural Engineers Association of California (SEAOC) Blue Book, which up until 1999 provided a commentary for predominant U.S. earthquake building code provisions, summarizes this approach:

> "The specified design forces given herein are based on the assumption that a significant amount of inelastic behavior may take place in the structure subjected to significant ground shaking. As a result, these design forces and related elastic deformations are much lower than those that would be required if the structure were to remain elastic." (SEAOC 1996)

Detailing requirements are specified for each seismic force resisting system to provide adequate inelastic deformation capacity, and through those inelastic deformations, the seismic energy is dissipated. Moment frames rely primarily on plastic hinging in the beams, concentrically braced frames rely primarily on buckling of the braces, and eccentrically braced frames rely primarily on plastic deformation of the link beam, to list a few examples. This design approach considerably reduces construction costs compared to elastic design and if detailed properly prevents structural collapse. The design code is not intended, however, to limit the structural damage due to large earthquakes. The building code provisions are intended to safeguard against major failures and loss of life, not to limit damage, maintain function, or provide easy repair.

Based on this design approach it is reasonable to expect inelastic damage in structural elements distributed throughout the seismic force resisting system after a large earthquake. Virtually none of the seismic-force resisting systems currently available in the U.S. building codes are designed to allow easy repair of the damaged structural elements. Moreover, the inelastic deformations may also produce residual drifts such that

a structure is left with permanent story displacements after the ground motion ceases. Residual drifts and distributed structural damage can make a building designed to current U.S. building codes difficult if not financially unreasonable to repair following a large earthquake.

1.2 Role of Performance Based Design in the State of Earthquake Engineering Practice

Performance based design was developed for earthquake engineering in the 1990's primarily for the application of evaluating and retrofitting existing buildings. The discussion of performance criteria was a natural progression from evaluating the expected earthquake response of existing buildings. Since that time, performance based design has evolved through the work of several key groups and the publication of a number of documents:

- SEAOC Vision 2000, Performance Based Seismic Engineering of Buildings, Vols I and II: Conceptual Framework was published in 1995 (SEAOC 1995). This document laid out a framework for procedures that lead to the design of structures with predictable seismic performance. One of the most enduring parts of this work include a figure showing performance objectives for different design level earthquakes that has since been cited by many other documents.
- ATC 40 Seismic Evaluation and Retrofit of Concrete Buildings was published in 1996 (ATC 1996). This project was sponsored by the California Seismic Safety Commission in 1990 and was the first attempt to standardize the performance based design approach, although specifically directed towards existing concrete buildings.
- FEMA 273 NEHRP Guidelines for the Seismic Rehabilitation of Existing Buildings was built on ATC 40 and SEAOC Vision 2000 (FEMA 1997). This document was published in 1997 and was sponsored by the National Institute of Building Sciences (NIBS) and the Federal Emergency Management Agency (FEMA) in an effort to develop a set of nationally applicable guidelines for the seismic rehabilitation of existing structures.
- FEMA 356 Prestandard and Commentary for the Seismic Rehabilitation of Buildings further built on FEMA 273 largely by converting FEMA 273 to mandatory language (FEMA 2000). It was published in 2000 and was called a prestandard because it was intended to provide a basis for ASCE to ballot as a standard.
- ASCE/SEI 41-06 Seismic Rehabilitation of Existing Buildings is the first nationally recognized standard that incorporates performance based design for earthquake engineering (ASCE 2007). It was published in 2006 and is largely based on FEMA 356.
- ATC 58 Next-Generation Performance-Based Design Guidelines is expected to be the next major step in the development of performance based design for earthquake engineering (ATC 2007). In 2001, FEMA contracted with ATC for this project which is expected to require ten or more years to complete. The

stated objectives of this project include expanding performance based design guidelines to include new construction as well as quantifying risks in terms of loss of life, repair costs, and downtime that is probable for a given earthquake event or over the life of the building. This is a departure from previous documents which categorized performance levels into broad groups such as fully functional, immediate occupancy, life safety, or collapse prevention.

The evolution of performance based design for earthquake engineering shows a trend toward more detailed assessment of building performance during earthquakes and defining specific performance objectives by using quantified probable risks. This need is further reflected and possibly fueled by the wide use of the above listed documents by structural engineers as a basis for discussing performance objectives with building owners. As a result of the development of performance based design there has been considerable advances in the identification of the types of earthquake damage that contribute to earthquake risks such as repair costs and downtime.

Although nonstructural damage contributes a significant component of typical repair costs after a major seismic event, structural damage plays a key role in the overall repairability of a building. For example, residual drifts due to structural damage can severely increase the repair costs for a building or preclude the possibility of repair. Downtime is a function of whether the building is evaluated as structurally safe to occupy and whether repair activities or damage make it impractical to conduct normal building functions. Downtime is especially exacerbated by structural damage which can require intrusive repair or make a building unsafe to occupy following an earthquake.

1.3 Need for Higher Performance Seismic Systems

Performance based design for earthquake engineering has changed the way engineers, owners, and building officials discuss the structural design of buildings in seismic areas. It is a natural progression from the definition of performance criteria to the question of how to design structures that obtain higher performance levels. It is neither economical nor efficient to make traditional seismic force resisting systems stronger to satisfy performance goals related to repairability. It is therefore necessary to create new seismic force resisting systems that inherently satisfy higher performance goals.

Concentrating seismic structural damage in replaceable elements and limiting residual drifts to negligible magnitude are two criteria that together can significantly reduce repair costs and downtime due to earthquakes. The remaining repair costs and downtime will be largely due to damage of nonstructural elements which may someday also be designed in such a way as to limit their earthquake damage. None of the traditional seismic force resisting systems contained in current U.S. building codes, however, satisfy these two performance criteria with the possible exception of base isolation which can be cost prohibitive.

1.4 Description of the Controlled Rocking System

This research explores the development of a new, high-performance seismic force resisting system, referred to herein as the controlled rocking system. The controlled

rocking system is a seismic lateral resisting system for steel-framed buildings that has the ability to self-center after an earthquake and is configured to concentrate the majority of structural damage into replaceable elements. Figure 1.1 shows one possible configuration of the system, which employs the following main components:

1. Steel frames that remain essentially elastic and are allowed to rock about the column bases. As shown in Figure 1.1, the specially designed column base details permit column uplift and restrain horizontal motion by the use of bumpers or an armored foundation trough. The configuration in Figure 1.1 uses two side-by-side frames, though alternative configurations with single frames have also been investigated as part of this work.
2. Vertical post-tensioning strands provide active self-centering forces. The strands are initially stressed so as to permit additional elastic straining when the frames rock. The configuration in Figure 1.1 employs post-tensioning down the center of the frame; other configurations with strands located at the column lines are also feasible.
3. Replaceable energy dissipating elements act as structural fuses that yield, effectively limiting the forces imposed on the rest of the structure. In Figure 1.1, the fuses are configured as yielding shear elements between the two frames. Other configurations include fuses at the column bases or in inelastic vertical anchors.

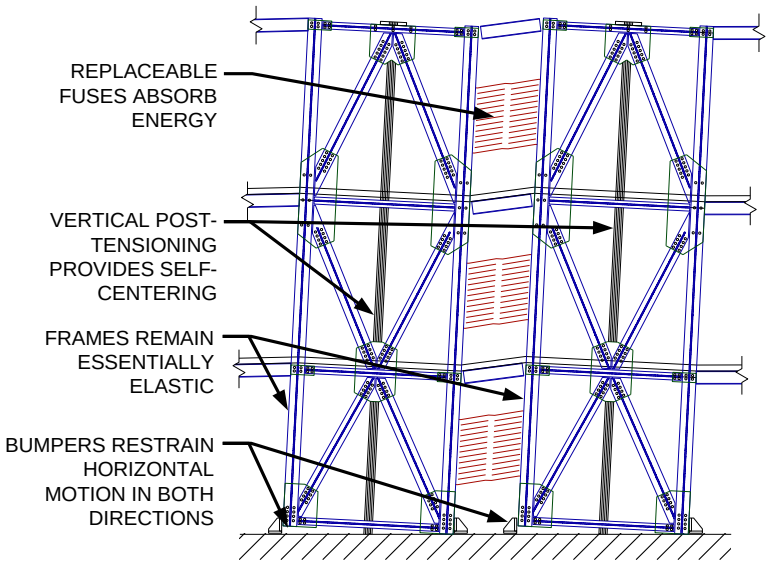

Figure 1.1 Schematic Representation of the Controlled Rocking Frame with Replaceable Energy-Dissipating Fuses

The objectives of this research project include the investigation of possible configurations and construction details for the controlled rocking system, the examination of the effects of system proportioning on seismic response and system demands, a large-scale testing program, evaluation of possible issues related to implementation, and the development of design recommendations. The large-scale testing was conducted to validate the system performance, investigate and improve construction details, and

examine force distributions in frame members. Using both the experimental and analytical studies, a proven basis is formed for reliable implementation of the controlled rocking system in practice.

1.5 Organization of this Report

This report describes some of the testing, analysis, and development of the controlled rocking system. It is organized as follows:

- Chapter 1 provides background including current U.S. earthquake engineering approaches, why higher performance systems are needed, and a brief description of the controlled-rocking system for steel-framed buildings.
- Chapter 2 presents a review of previous research into the development of self-centering seismic force resisting systems and structural fuses.
- Chapter 3 derives the expected response of the controlled rocking system, examines the resulting proportioning and design considerations, gives the objectives of this research, and gives an overview of all of the phases of this work including portions not part of this report.
- Chapter 4 presents the details of the large-scale experimental program including specimen design, test control, loading protocol, and instrumentation. Additional information about test setup can be found in Appendix A.
- Chapter 5 gives a summary of the cyclic test results. Raw data for all tests are located in Appendix B, data reduction calculations are included in Appendix C, and validation of the experimental data is presented in Appendix D.
- Chapter 6 outlines the computational models which were developed and compared to cyclic test results.
- Chapter 7 includes description of the hybrid simulation tests along with the associated results.
- Chapter 8 is a discussion of the test results which synthesizes the test data to compare and contrast the results from different configurations.
- Chapter 9 presents a single degree-of-freedom computational study which investigates the response of a wide range of self-centering hysteretic behavior in the presence of ambient building resistance.
- Chapter 10 presents a multi-degree-of-freedom computational study that was used to quantify the demands on different configurations of the controlled rocking system.
- Chapter 11 summarizes a capacity design methodology for sizing the frame members and examines its efficacy in the context of the MDOF study from the previous chapter.
- Chapter 12 provides a set of design recommendations that are built on the rest of the work included herein.

- Chapter 13 finishes with the conclusions from this research and suggestions for further work that is necessary.

LITERATURE REVIEW

There have been previous studies conducted on seismic rocking systems as well as other self-centering seismic systems. The literature review begins with a description of the residual drifts that can occur during earthquakes. General information on structural rocking is then presented specifically regarding impact at the base of rocking elements, and the 3D effect. Specific structural rocking systems are then examined followed by other specific self-centering systems such as horizontally post-tensioned moment frames, self-centering braces, and draped post-tensioned steel frames. Finally, information about the controlled rocking project parametric study and the fuse component tests conducted at Stanford University is presented.

2.1 Residual Drifts

Although there are examples of buildings that experience permanent drifts after earthquakes, concerted studies that quantify the residual drifts experienced in actual buildings after earthquakes are difficult to find. Computational predictions of residual drifts, however, are not uncommon and some of the key findings are presented below.

An analytical study of buckling restrained braced frames (BRBFs) showed that residual story drifts can exceed 1% drift under the design-level seismic input (Sabelli et al. 2003). Kiggins and Uang (2006) studied a BRBF-MRF dual system configuration with the intent of limiting residual drifts and found that although residual drift was approximately cut in half, it could not be eliminated.

Other computational studies have found that residual drifts are often less than the maximum possible residual drift, which is defined as the drift obtained when the load is slowly removed from the point of peak drift. MacRae and Kawashima (1997) identified a propensity for self-centering in elastic-plastic hardening systems with no explicit self-centering component. A strong correlation was drawn between residual drifts and the post-yield kinematic hardening stiffness of the hysteretic system. It was found that increasing the post-yield stiffness greatly reduces residual drifts, but reducing post-yield stiffness below zero can result in large residual drifts.

Similarly, a study by Ruiz-Garcia and Miranda (2006) examined the effect of ground motion parameters, system strength, and hysteretic shape on residual drifts. It was found that post-yield stiffness and unloading stiffness had significant effect on the residual drifts. Christopoulos et al. (2003) and Pettinga et al. (2007) also examined the fact that residual displacements in the presence of positive post-yield hardening are less than the maximum possible residual displacement. The relationship between residual displacements and maximum displacements is further examined and quantified for elastic-plastic, degrading hysteretic, and fully self-centering models in Christopolous and Pampanin (2004) and Christopolous et al. (2002) as a function of the post-yield stiffness.

In the past decade there have been several computational studies that have examined the response of self-centering SDOF systems (Christopoulos et al. 2002, Christopoulos et al. 2003, Pampanin et al. 2003, Seo and Sause 2005). These studies are

largely based on parametric SDOF analyses on bilinear elastic-plastic, idealized flag-shape, and sometimes stiffness degrading hysteretic response. Parameters pertaining to hysteretic shape are varied to examine their effect on response indices such as residual drift. As might be expected, the flag-shaped systems that preclude drifts when the lateral force is removed were found to eliminate residual drifts in dynamic analyses.

Although most studies neglect the resistance of the rest of the building, Pettinga et al. (2007) investigated the effect of considering the gravity system as a secondary seismic force resisting system to mitigate residual drifts. Non-self-centering systems were analyzed using MDOF models. The post-yield hardening stiffness of a building's lateral force resisting system was increased to account for the gravity system and reductions in the residual drifts were found. However, after undergoing inelastic deformations, the gravity system and other elements of the building will resist the ability of the restoring forces to eliminate residual drifts. This effect was not considered in the studies described here.

With some exceptions (e.g., fib 2003), the studies found in the literature also commonly treat flag-shaped hysteretic response as distinct from elastic-plastic response even though actual systems can be tuned to any combination of self-centering and energy dissipation. In addition, the ability of a structure to tend toward zero residual drift through probabilistic dynamic effects is neglected in the development of most self-centering systems outside of precast concrete (e.g., fib 2003).

2.2 Structural Rocking Behavior

2.2.1 General Rocking Behavior

Rocking, although not commonly used in seismic design, has been investigated by numerous researchers. Rocking of stone monuments, building foundations on soil, masonry wall piers, concrete walls, bridge piers, and steel braced frames has been studied in various forms. It has been shown by multiple studies described herein that rocking motion reduces seismic loading and ductility demands. There is also anecdotal evidence of seemingly unstable large elevated tanks that survived earthquakes by rocking while nearby more stable looking structures were destroyed (Priestley et al. 1978). Issues that have relevance to the current study include impact forces, the energy dissipated during impact, and the effect of three-dimensional behavior on rocking resistance.

Impact has three important effects on rocking behavior including: 1. exciting vertical mode shapes, 2. creating vertical accelerations which in turn causes increased member forces, and 3. dissipation of energy through inelastic action at the interface. The stiffness of the column support also has been found to have a noticeable effect on the fundamental frequency of the system.

Housner (1963) noted that as any element rocks, there is a certain amount of energy that is absorbed by impact as the uplifting side comes down during each half cycle. Without energy absorption, the rocking element would bounce upward. Housner calculated the amount of energy required to just preclude bouncing.

Clough and Huckleridge (1977) examined the effect of impact on the rocking response of a steel frame. It was found that the stiffness of the impact pads beneath the column bases had a pronounced effect on the fundamental frequency of vibration of the structure. The first mode period was computationally found to vary from 0.46 sec to 0.34

sec as the impact pad stiffness varied from 1.75 kN/mm to 87.6 kN/mm (10 k/in to 500 k/in) respectively. Stiffness values for the neoprene pads were calibrated in the computational model to match the experimental response resulting in values between 7.0 kN/mm to 70.1 kN/mm (40 k/in to 400 k/in).

Priestley et al. (1978) found that large vertical accelerations were induced during impact, and that placing rubber pads underneath the impacting legs to represent a flexible foundation decreased the vertical accelerations significantly. Aslam et al. (1980) carried out tests to determine the amount of energy lost on impact for specific concrete blocks and found that the angular velocity was reduced by a fairly constant value of 7.5% with each impact. Psycharis (1982) considered different methods to account for the soil radiation damping due to impact. Spring-dashpot and elastic-plastic spring systems were used to model the effect. Mander and Cheng (1997) developed a method for converting the energy lost on impact into equivalent viscous damping. Makris and Konstantinidis (2003) investigated impact of rocking elements and drew the parallel between energy loss during impact and damping. The minimum amount of energy loss that allows rocking without bouncing was found to be a function of the rocking elements slenderness, was calculated, and further used in their examples. Ajrab et al. (2004) includes impact damping in their model of a rocking concrete wall. They calculate equivalent viscous damping based on Housner, which equates to approximately 2% damping for a specific example.

Pollino and Bruneau (2004) found that impact excited the vertical modes of vibration which can increase the force demands on the members. Two vertical modes were considered, the axial compression of the column, and the vertical shear deformation of the frame. The effect of energy dissipation due to impact was neglected in their study because it was less significant than the energy dissipated by yielding steel elements, and ignoring it was conservative. Pollino and Bruneau (2004) developed a method for amplifying the base shear to account for dynamic effects. They then go on to calculate demand on the columns as the sum of the force due to the impact velocity plus gravity loads multiplied by a dynamic amplification factor plus the force from the energy dissipating element multiplied by a different dynamic amplification factor.

Lu (2005) investigated the behavior of a rocking reinforced concrete (RC) wall in conjunction with RC moment frames. He defines the 3D effect as the additional self-centering forces created by rotationally fixed beams that frame into the uplifting side of the wall. The beams coming from out-of-plane relative to the rocking wall also contribute to the 3D effect if they have rotational fixity. It was found that 3D effects reduced the vertical displacements by 50%, and plastic hinge rotation reduced by 30%.

2.2.2 Rocking of Concrete and Masonry Walls with Vertical Post-Tensioning

Ajrab et al. (2004) analytically investigated the rocking behavior of concrete shear walls with vertical and draped post-tensioned tendons. It was determined that draping the tendons to conform to the overturning moment diagram results in lower and more evenly distributed interstory drifts. The six-story prototype structure represented in Figure 2.1 was used to study the effect of different post-tension profiles as well as initial prestress level and wall width. Supplemental dampers were attached in series at the base of the post-tensioning tendons to provide a reliable source of damping.

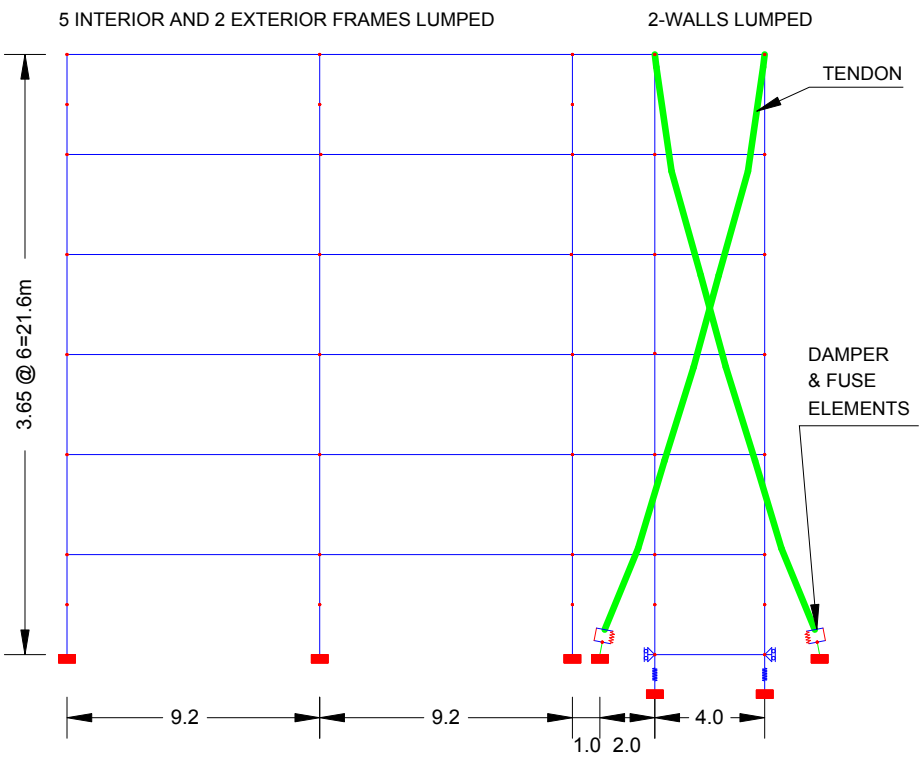

Figure 2.1 Computational Model of the Rocking RC Wall with Draped Post-Tensioning Tendons [after (Ajrab et al. 2004)]

Holden, Restrepo, and Mander (2003) tested two similar concrete walls, one with conventional ductile detailing, and the other a precast concrete wall with vertical carbon fiber post-tensioning strands and energy dissipating yielding bars. The test setup in Figure 2.2 shows the post-tensioned wall that has the energy dissipaters that consist of reinforcing bars that are milled down to a reduced diameter for a specified length. It was found that the post-tensioned precast wall exhibited virtually no residual drift or visible damage up to and exceeding 2.5% drift. This project is discussed further in Rahman and Restrepo (2000) and Restrepo and Rahman (2007). As part of the system design, it is desired to preclude yielding in the post-tensioning strands but there is no discussion of post-tension strand fracture.

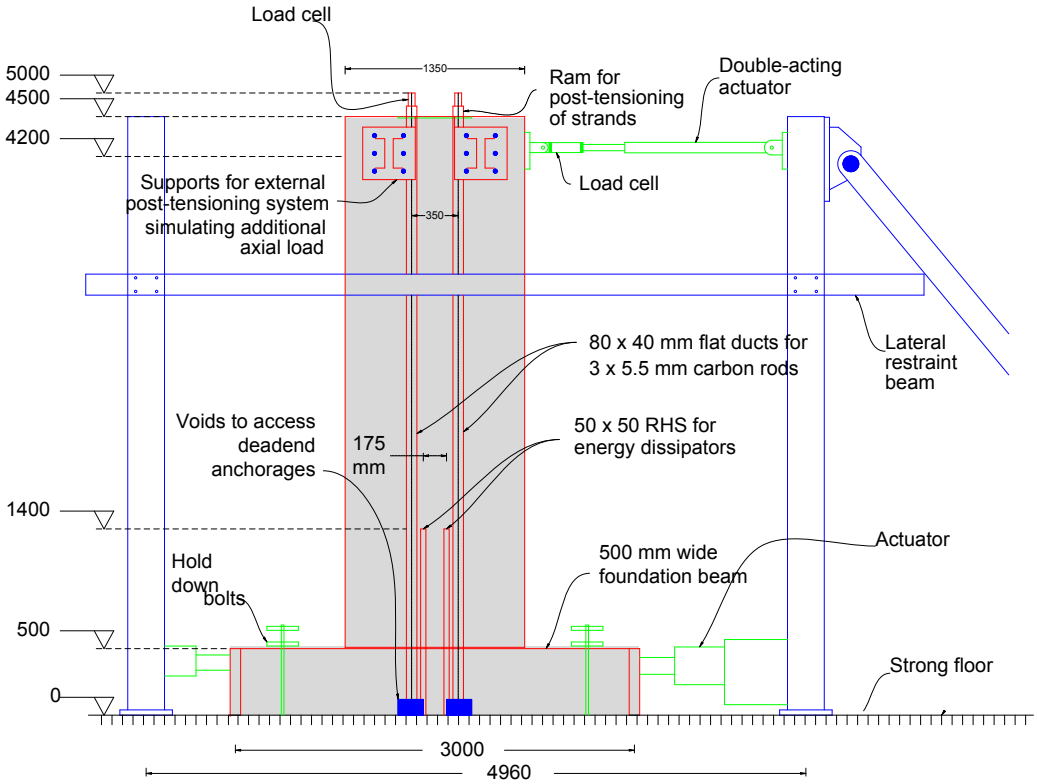

Figure 2.2 Post-Tensioned Rocking Wall Test Setup [after Holden et al. (2003)]

The study of a masonry wall with vertical post-tensioning shown in Figure 2.3 concentrated on finding analytical models that accurately represent the dynamic shake table response of the experimental specimen (Ma et al. 2006). It was postulated that the poor correlation of a detailed finite element model was due to the stress singularity at the rigid point of impact. The second method consisting of fiber based discrete beam-column elements also did not match the experimental results very well. Perez et al. (2007) details and further develops this method. The third computational model achieved the best results and consisted of an SDOF cantilevered mass with an elastic rotational spring at the base of the cantilever. The velocity was reduced as the spring went through the neutral position to model the impact radiation damping. It was determined that this method for accounting for radiation damping was considerably more accurate than the use of equivalent viscous damping.

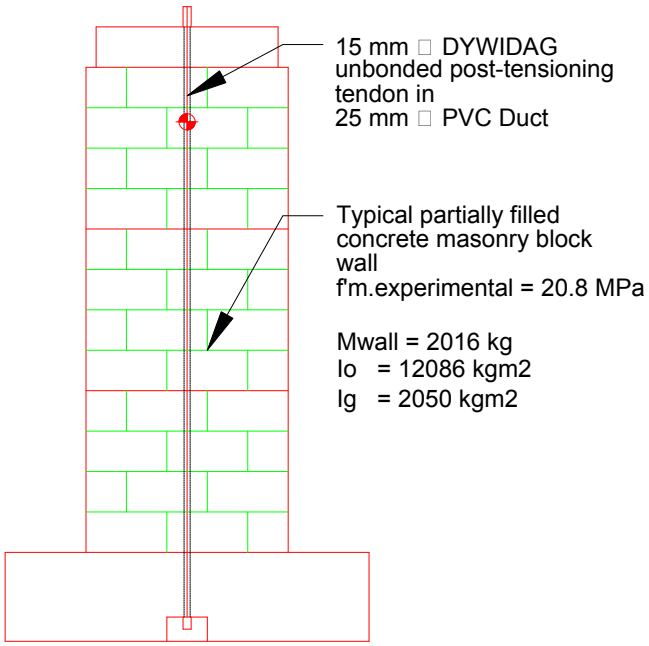

Figure 2.3 Rocking Masonry Wall with Vertical Post-Tensioning Strand [after (Ma et al. 2006)]

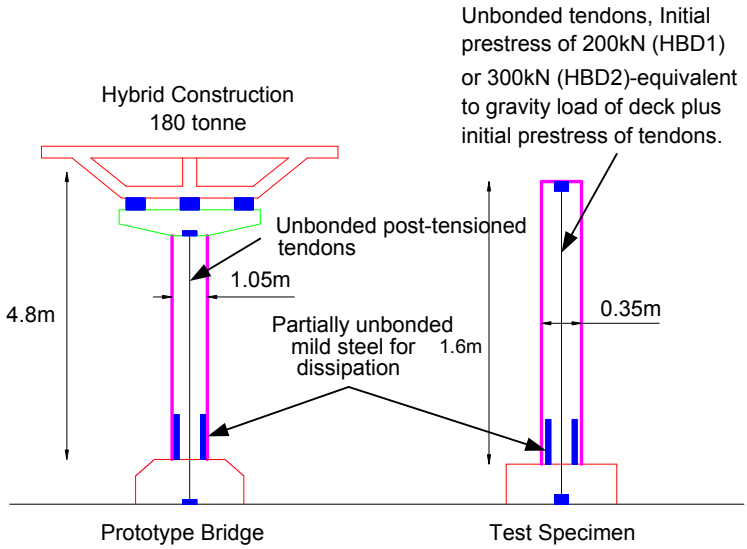

Figure 2.4 Vertically Post-Tensioned Bridge Pier Column [after (Palermo et al. 2007)]

Palermo et al. (2007) studied the seismic response of vertically post-tensioned concrete bridge columns allowed to rock as shown in Figure 2.4. It was found that 5 to 8 kN (1.1 kips to 1.8 kips) of prestressing load was lost due to relaxation of the anchorage. Tests were stopped at 3% to 3.5% drift to keep the post-tensioning strands from reaching yield. Excellent self-centering and low damage response was observed.

2.2.3 Rocking of Steel Frames

Perhaps the earliest tests on rocking steel frames were conducted by Clough and Hucklebridge (1977). The frame is shown in Figure 2.5. The base of the column framed into a block through a pin. The block was then allowed to move vertically using roller guides on each side. Directly beneath the column base was an impact pad made from neoprene and steel plates. Some tests were also carried out with the base of the columns not allowed to uplift. Tests without uplift exhibited less displacement, but larger accelerations and member forces. In some comparisons, the member forces were 1.5 times greater than the uplift case. The uplift was considered a "fuse effect" in the way it limited overturning moment. A companion study by Hucklebridge (1977) tested a one bay by three bay nine-story structure on a shake table. Similar to the previous study, the structure was tested with uplifting column bases and fixed column bases.

Kelley and Tsztoo (1977) used the same three-story uplifting frame to study the effect of adding energy dissipators to the uplifting structure. The energy dissipators utilized the uplifting displacement to apply torsion to steel bar.

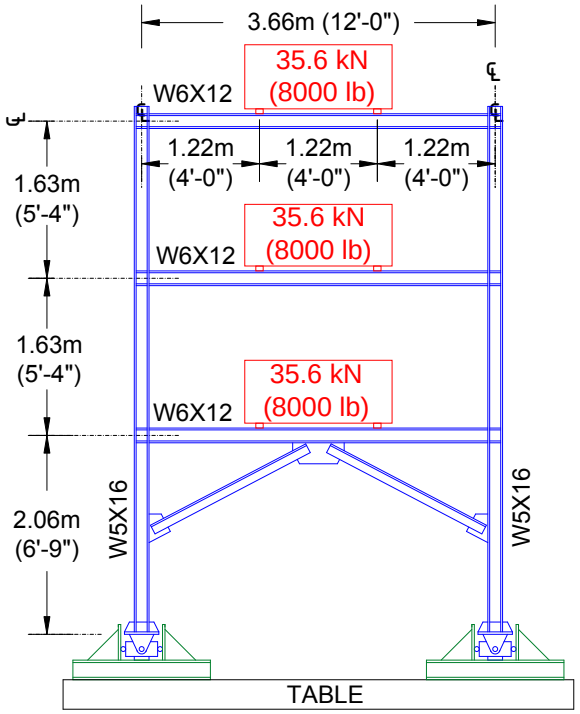

Figure 2.5 Rocking Frame [after (Clough and Huckleridge 1977)]

Researchers have also investigated self-centering column bases. Ikenaga et al. (2006) studied a column base incorporating vertical post-tensioned bars and yielding steel plate dampers. As the columns rotate relative to the rigid foundation, the post-tensioned bars shown on the left side of Figure 2.6 stretch, providing self-centering force while the dampers yield in tension and buckle in compression contributing energy dissipation. Alternatively, as shown on the right side of Figure 2.6, Takamatsu et al. (2006) has developed a column base with anchor bolts that are allowed to yield with spring loaded wedges that take up the slack on load reversal.

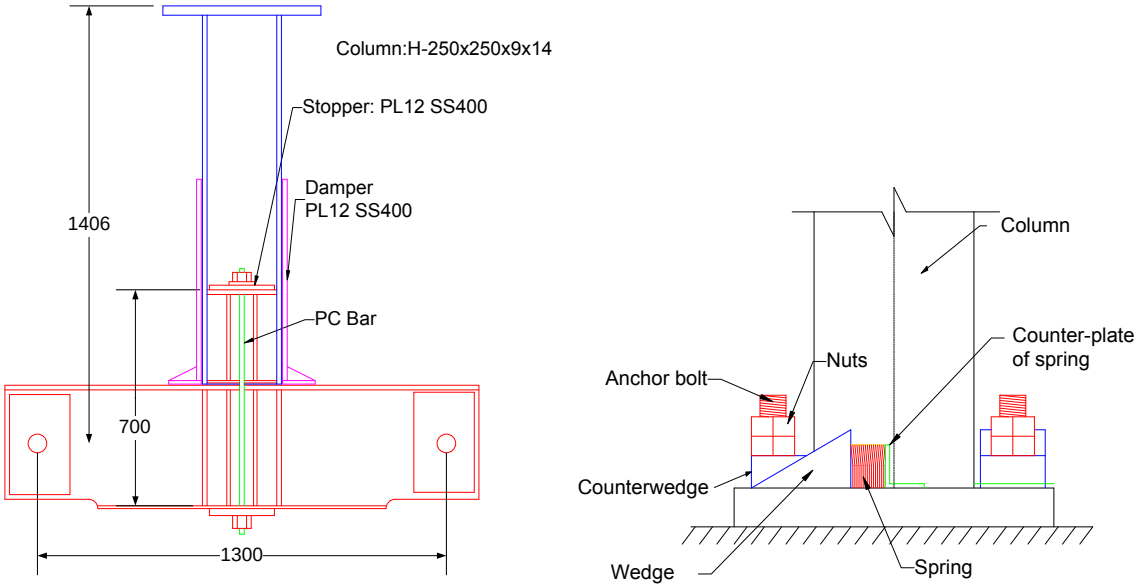

Figure 2.6 Rocking Bases [from (Ikenaga et al. 2006)] (left), and [after (Takamatsu et al. 2006)] (right).

Midorikawa et al. (2006) has studied base plates that allow rocking of a steel frame. The base plate yields providing energy dissipation, and it was shown that this reduces the response of moment frames and braced frames. An example of the yielding base plate is shown in Figure 2.7.

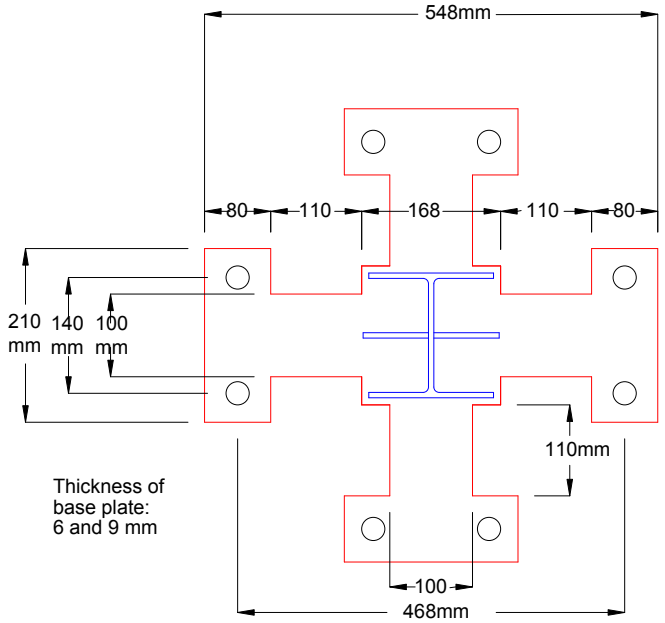

Figure 2.7 Plan View of Yielding Base Plates [after (Midorikawa 2006)]

Wada (2001) implemented similar limiting devices in columns of a tall braced frame. The limiting device consists of wide cap plates and base plates at column splices bolted together is such a way as to allow separation when subjected to enough tension while dissipating energy through yielding. It was found that the amount of seismic

energy input to the building was decreased by the limiting force imposed by the uplifting device.

Pollino and Bruneau (2008) have examined retrofit of existing low ductility bridge piers by allowing rocking. Buckling restrained braces were used to dissipate energy, and gravity loads alone provided enough self-centering force. Chen et al. (2006) studied a similar topic. It was determined that sliding and foot damage due to impact are issues that must be considered.

2.3 Horizontally Post-Tensioned Moment Frames

Shen and Kurama (Shen and Kurama 2002, Kurama et al. 2006) developed a self-centering coupling beam intended for use between concrete shear walls. As shown on the left of Figure 2.8, horizontal post-tensioning provides initial compression in the coupling beam. As the shear walls deflect and rotate relative to one another, gaps open at the beam-to-wall interfaces. Top angles and seat angles are used at the connection to create inelastic energy dissipation as the gaps open and close. The post-tensioning force provides a restoring force that closes the gaps and drives the walls and beams back toward their undisplaced position upon unloading. One advantage of the system is that it can be used to couple existing walls as part of a seismic retrofit.

A similar concept has been developed for concrete moment frames (Rahman and Sritharan 2007) (Priestley et al. 1999) (Nakaki et al. 1999). As shown on the right of Figure 2.8, unbonded post-tensioning strands are oriented horizontally in ducts near the mid-depth of the beams. Mild steel reinforcing bars at the top and bottom of the section are debonded over a short length near the interfaces to reduce their inelastic strain demands. A friction mechanism is relied upon for shear transfer across the precast connection interface. As the beam moment increases a gap will open up at the beam-to-column interface. The post-tensioning strands provide a restoring force to close the gap, and the mild steel reinforcing bars dissipate energy through inelastic deformations.

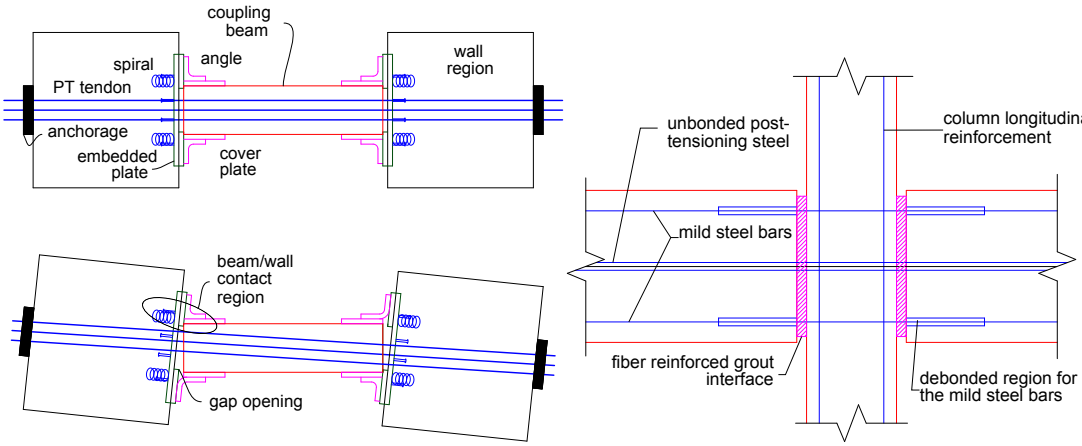

Figure 2.8 Coupling Beams with Post-Tensioning [after (Shen 2002)] (left) and Concrete Moment Frames [after (Rahman et al. 2007)] (right)

Ricles et al. (2001) as well as Christopoulos et al. (2002) have developed steel moment frames with self-centering capabilities shown in Figure 2.9. The post-tensioned

energy-dissipating (PTED) beam-to-column connections, as they are called in (Christopoulos et al. 2002) and Self-Centering Moment Resistant Frames (SC-MRF), as they are called in (Ricles et al. 2001, Garlock 2002, and Garlock et al. 2005, Wolski et al. 2006), consist of horizontally oriented post-tensioned bars or strands that hold a beam flush to a column. During a seismic event, the beam rotates relative to the column, opening a gap between the beam flange and the column. The self-centering force is provided by the post-tensioned bars or strands and energy dissipation is implemented using yielding seat angles, friction dampers, or energy dissipating bars confined in tubes.

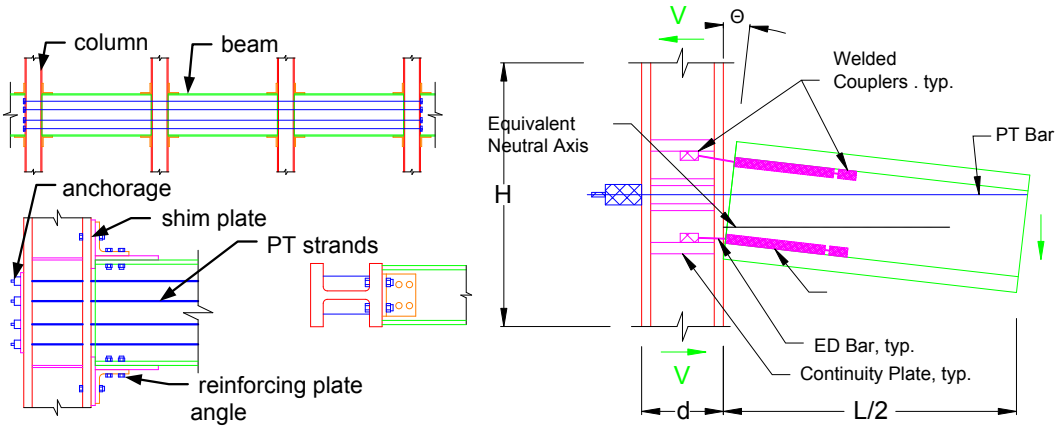

Figure 2.9 Post-Tensioned Steel Moment Frames [after (Garlock et al. 2007)] (left), and [after (Christopoulos et al. 2002)] (right)

2.4 Other Self-Centering Systems for Steel-Framed Buildings

A self centering brace was developed using post-tensioned high-strain-capacity aramid-fiber tendons to clamp the brace together (Christopoulos et. al. 2008). Inner and outer steel tubes are configured such that self-centering forces are produced when both tensile and compressive deformations are imposed on the brace. Energy dissipation is introduced using friction pads clamped together with pretensioned bolts. This brace configuration is shown in Figure 2.10.

Dolce and Cardone (2006) and Zhu and Zhang (2008) developed self-centering braces using shape memory alloy (SMA) elements. In the former study, the SMA wires were used to create the self-centering force and to dissipate energy, whereas in the latter study, the high strain capacity of SMA wires was used to create the self-centering force, but friction was used to introduce energy dissipation.

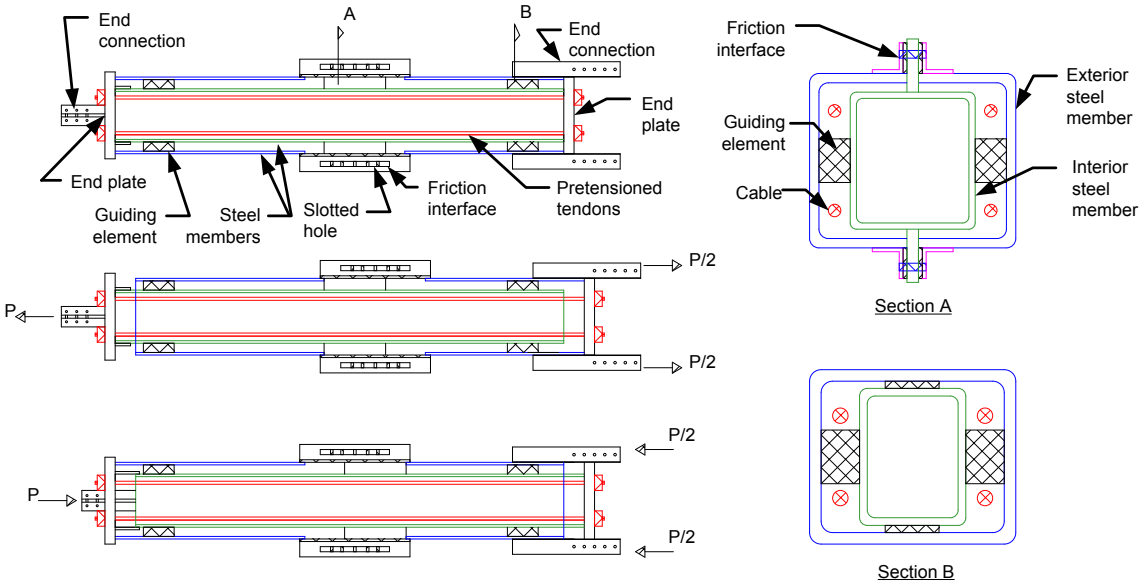

Figure 2.10 Self-Centering Energy Dissipating Brace [after (Christopoulos et al. 2008)]

Pekcan et al. (2000) studied a system with draped post-tensioned tendons with a non-rocking steel frame. The tendons spanned over multiple bays and multiple floors. Elastomeric spring dampers and fuse bars were used in series with the post-tensioned tendons to provide energy dissipation. This is similar to the draped post-tensioning for concrete shear wall buildings described previously.

2.5 Structural Fuses for Seismic Resistance

Structural fuses for seismic resistance in the broadest sense of the term can include any structural elements that absorb seismic energy and thus protect the surrounding structure. Vargas and Bruneau (2004) further define structural fuses as replaceable elements that are designed such that all structural damage is concentrated in this element, allowing the primary structure to remain elastic. Although there are several examples of structural fuses found in the literature, this section focuses on the added damping and stiffness (ADAS) and triangular-plate added damping and stiffness (TADAS) dampers as background for the fuses investigated as part of this work.

Added damping and stiffness (ADAS) dampers were developed in the 1980's and early 1990's as a ductile link to be used between braces extending from one floor level and the beam of an adjacent floor (Bergman and Goel 1987, Xia and Hanson 1992). The ADAS damper itself consists of a set of plates, sandwiched together with spacers between them, anchored into two end blocks and bent about their minor axis. The plates were designed in two patterns. One pattern referred to as X-shaped consists of plates that are wide at the ends and tapered to a reduced section at the center. The other pattern consists of triangular plates that are fixed at the wide end and pinned at the reduced width end. The tapered shape of the plates encourages a uniform distribution of inelastic curvature along the length of the plate. The X-shaped specimens showed full hysteretic energy

absorbing behavior while the V-shaped specimens showed some pinching hysteretic response due to slip in the pinned connections.

The ADAS dampers were found to be capable of producing stable hysteretic behavior for displacement amplitudes as large as 14 times the device yield displacement. The energy dissipation can be concentrated in the ADAS elements to protect the surrounding structural members. Furthermore, it was concluded that the yielding of ADAS dampers will not affect the gravity load carrying capacity of the system since they only participate in the lateral load resistance.

Since these dampers exhibit full hysteretic behavior, they can be approximated by relatively simple bilinear hysteretic models (Xia and Hanson 1992). Computational studies (Xia and Hanson 1992) demonstrate the success of the dampers in protecting the rest of the structural members from damage.

The triangular-plate added damping and stiffness (TADAS) dampers are similar to the triangular dampers tested by Bergman and Goel (1987), but improve upon the anchorage of the plates (Tsai et al. 1993). The wide end of the plates are welded into an anchorage block whereas the reduced portion ends in a pin that transfers lateral loads but is allowed to move up and down in a slotted hole. The anchorage of the TADAS damper reduces the sensitivity of the damper stiffness to the tightness of bolts as experienced with ADAS dampers. Also the use of pins in slotted holes removes axial force effects in the dampers making the mechanical properties of the TADAS dampers highly predictable. It was found that the stiffness of the TADAS dampers can be calculated based on flexural deformations only.

Cyclic tests were conducted up to 0.30 radians (Tsai et al. 1993) with full stable hysteretic behavior. A strain hardening factor of 1.5 was found at 0.20 radians. Large-scale pseudo-dynamic tests on a two-story frame were conducted with and without TADAS dampers to demonstrate the effectiveness of the dampers. The added stiffness reduced the first mode period of the frame from 0.881 sec to 0.573 sec through the use of TADAS dampers. The dampers also led to significant reductions in frame drifts without any instabilities occurring in the damper or brace assembly. It was suggested that because the system has such predictable properties, a moment frame with TADAS damper system might be designed without conducting time history analyses.

Steel beams with web perforations have also been investigated as yielding elements to protect the surrounding structure (Aschheim and Halterman 2002, Lepage Aschheim and Senescu 2004). A range of perforation geometries were tested including round holes, oval holes, and longitudinal slots in the web of a steel beam. The investigators identified two modes of deformation in these elements, one mode primarily due to flange deformation at the location of the web hole, and the other due to plastic shear deformations of the web. The test specimens were designed to experience particular modes of deformation and it was found that the tests achieved the intended mechanisms. It was concluded that the reduced web sections allowed the beam to column connection to remain elastic through interstory drifts as large as 6% to 11%. Out-of-plane buckling of the webs after yielding was observed along with an associated loss in lateral load carrying resistance. Post-buckling capacity strengths were maintained up to interstory drifts of 5% to 6%.

2.6 Prior Work on the Controlled Rocking System

As part of the controlled rocking project, some of the research objectives have been addressed by others. A parametric study was conducted by Hall et al. (2006) to determine the effect of system variables on the seismic response of the controlled rocking system, shear fuses were developed, analyzed, designed, and tested at Stanford University (Ma et al. 2010c), and large-scale shake table tests were conducted at E-Defense in Miki, Japan (Ma 2010).

Hall et al. (2006) subjected two-dimensional frame models created using the OpenSees Software to a suite of ground motions. Figure 2.11 shows a schematic representation of the analytical model. The fuses were represented by equivalent elastic-plastic diagonal truss elements. One of the primary purposes of the parametric study was to determine how design variables affect the hysteretic behavior and overall system response. The three design variables selected as the most significant were:

Geometric Parameter:

$$A/B\ Ratio = \frac{\text{Frame Width}}{\text{Fuse Width}} = \frac{A}{B} \tag{0.1}$$

Strength Parameter:

$$OT\ Ratio = \frac{\text{Overturning Resistance}}{\text{Design Overturning Moment}} = \frac{A\,F_{PT} + V_P\left(A+B\right)}{\sum F_i\,h_i} \tag{0.2}$$

Self-Centering Parameter:

$$SC\ Ratio = \frac{\text{Post-Tensioning Resistance}}{\text{Fuse Resistance}} = \frac{A\,F_{PT}}{V_P\left(A+B\right)} \tag{0.3}$$

Where: F_{PT} = Initial Tension Force in Post-Tensioning Strands
V_P = Total Yield Strength of the Fuses
F_i = Design Story Shear Based on ASCE 7-05 with a Response Modification Factor, R = 8
h_i = Story Height Above Rocking Interface

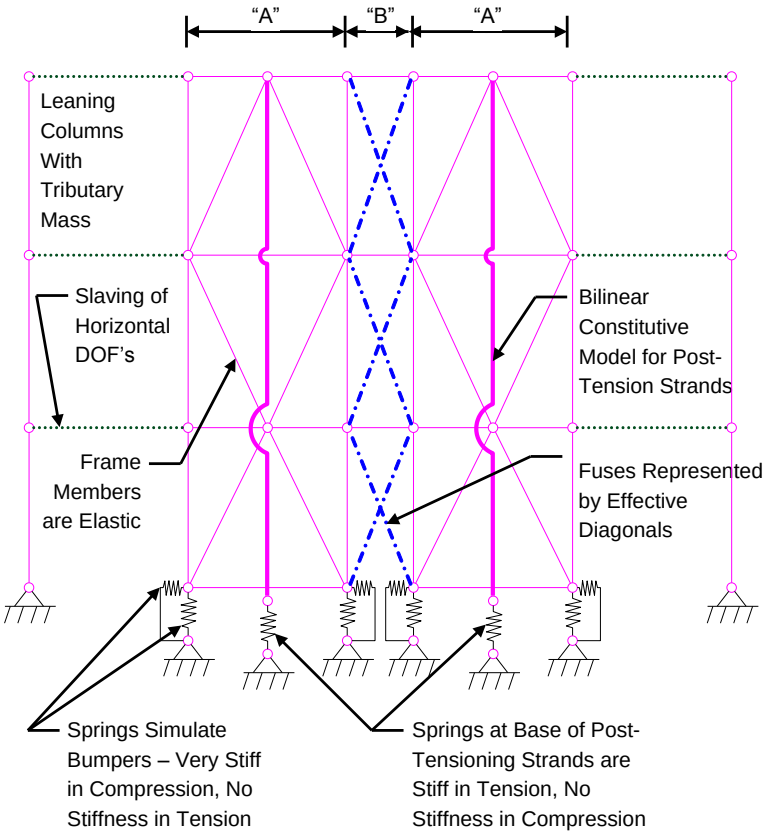

Figure 2.11 Computational Model Used for the Parametric Study [after (Hall et al. 2006)]

The two-dimensional frame model was subjected to twenty-three ground motions scaled to three earthquake hazard levels for a site in Los Angeles, CA: 50% probability of exceedance in 50 years, 10% in 50 years, and 2% in 50 years. Example results are shown in Figure 2.12 and Figure 2.13.

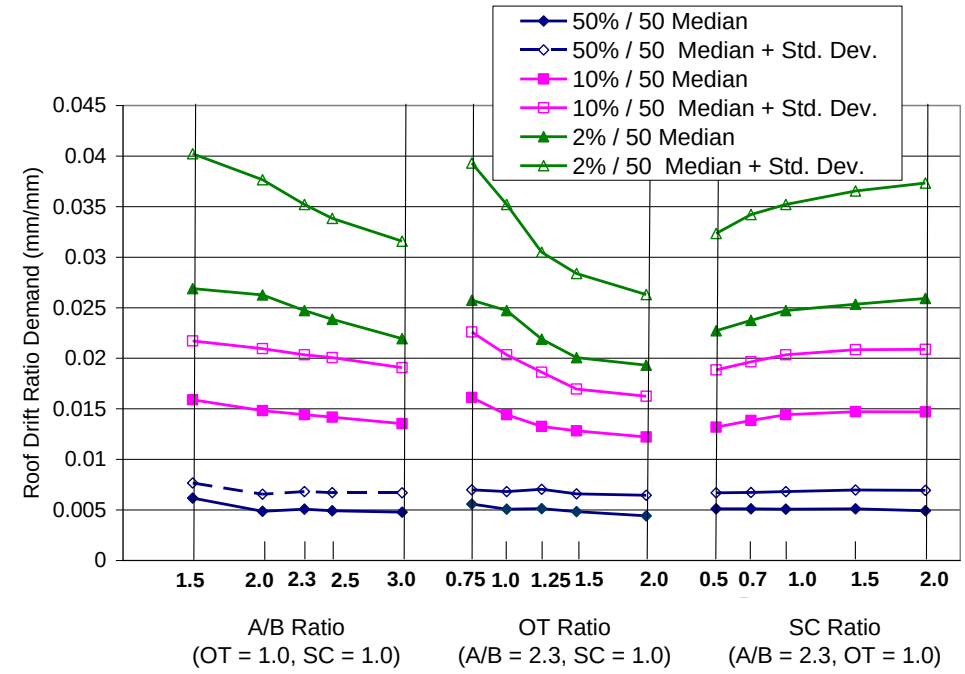

Figure 2.12 Roof Drift Demand Predicted by the Parametric Study [Adapted from (Hall et al. 2006)]

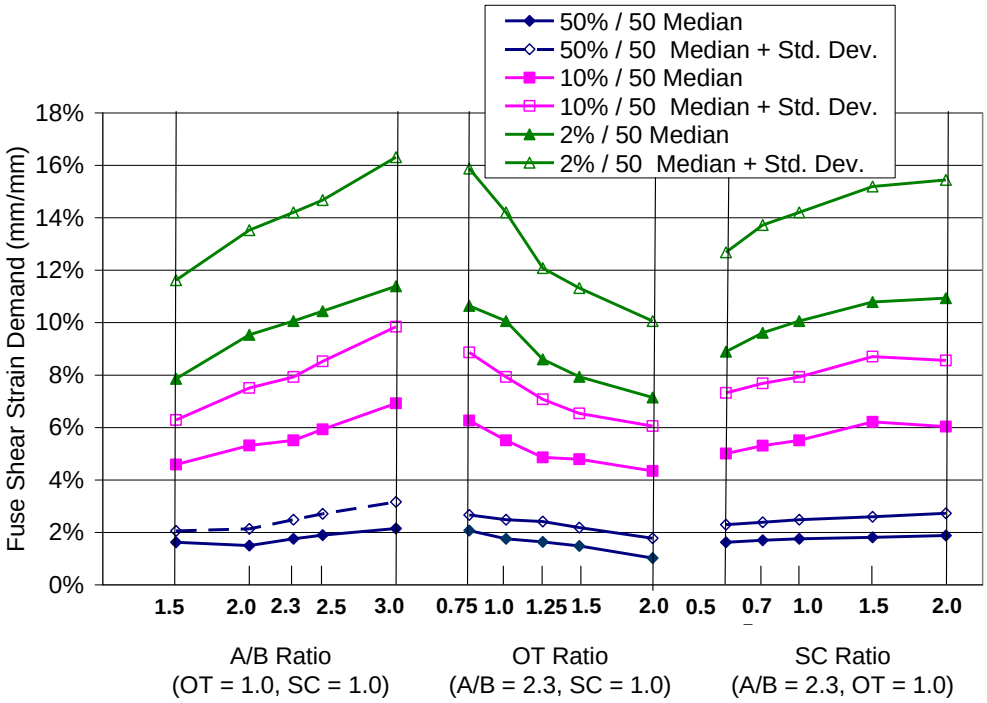

Figure 2.13 Fuse Shear Strain Demand Predicted by the Parametric Study [Adapted from (Hall et al. 2006)]

Based on the results of the parametric study, it was concluded in Hall et al. (2006) that:

- Increasing the geometric ratio (A/B) resulted in a significant increase in the peak fuse shear strains. Approximately 50% more peak fuse shear strain was found for A/B=3.0 as for A/B=1.5. This conclusion is based on the assumption that the fuse spans the entire width between frames, B.
- Increasing the geometric ratio (A/B) also resulted in larger drifts.
- Higher strength ratio (OT) results in stronger systems with increased stiffness and energy dissipation.
- Higher strength ratio (OT) factors , therefore, result in reduced displacement response, including residual displacements. Fuse shear strains are also reduced. Doubling the lateral strength of the system resulted in a 25% reduction in peak displacements and peak fuse shear strains.
- The benefits of higher strength ratio (OT) are tempered by the cost of larger forces that must be transmitted through the frame and foundation.
- It was found that self-centering (SC) values of 0.5 still resulted in excellent self-centering response.
- It was concluded that since the system self-centers well for all values of the self-centering (SC) ratio considered, that it is not necessary to use large values for SC to achieve self-centering performance.

As shown in Figure 2.13, it is crucial to have fuse elements capable of stable hysteretic behavior to large levels of shear strain. Fuses were designed and tested that employed steel plates with straight slits and steel plates with butterfly cut-outs (Deierlein et al. 2009, Ma et al. 2010b, Deierlein et al. 2010). Eleven tests, described in Table 2.1 and Figure 2.14 were conducted at Stanford University on fuses that represent approximately half-scale relative to the prototype building. The ID used in Table 2.1 starts with either the letter S to refer to slit steel panel fuses or the letter B to refer to butterfly steel plate. The first number is equal to the length of the link divided by the thickness, and the second number is the link end width divided by the thickness.

The test setup shown on the left of Figure 2.15, consisted of a top horizontal loading beam suspended by two pinned struts (hidden by the vertical columns), and braced against out-of-plane motion by bearing contact with the vertical columns on either side. The loading beam connected to the top of the fuse with two angles, and the fuses connected at their bottom to a fixed base.

The slit steel plate fuses were shown to exhibit a progression of behavior: yielding at the ends of the links, initiation of out-of-plane buckling, crack initiation at the link ends, tearing of the links, and full link fracture. The out-of-plane buckling of the fuse links coupled with large tension stresses at the extreme fibers caused crack initiation at the ends of the links at 5.6% to 10.0% shear strain across the link length. Significant strength loss due to fracture of the links caused the end of the tests at fuse link shear strains between 18.6% and 30%. The onset of tearing in the fuse links caused strength reduction, but did not eliminate the ability of the fuse to resist load. Fracture of one of the slit steel panels is shown on the right in Figure 2.15.

Table 2.1 Fuse Specimen Test Matrix (from [Ma et al. 2010c]) (See Figure 2.14 for Definition of Variables)

ID	L (mm)	b (mm)	t (mm)	a (mm)	n	b/t	L/t	a/b	w_s (mm)
S12-36	229	73	6	N/A	7	12	36	N/A	3
S10-40	254	60	6	N/A	13	10	40	N/A	3
S10-56	356	60	6	N/A	13	10	56	N/A	3
S10-36W	229	64	6	N/A	6	10	36	N/A	13
S10-56BR	356	60	6	N/A	13	10	56	N/A	3
B10-36	229	64	6	25	6	10	36	0.40	13
B09-56	356	57	6	19	7	9	56	0.33	13
B06-37	356	57	10	19	7	6	37	0.33	13
B02-14	356	57	25	19	3	2	14	0.33	13
B10-36W	229	64	6	25	6	10	36	0.40	13
B07-18W	229	89	13	30	3	7	18	0.34	13

ID notation: Beginning letters "S"/"B": Slit fuse/Butterfly fuse; two numbers: b/t and L/t ratios; ending letters "W"/"BR": Welded end connection/Buckling-Restrained.

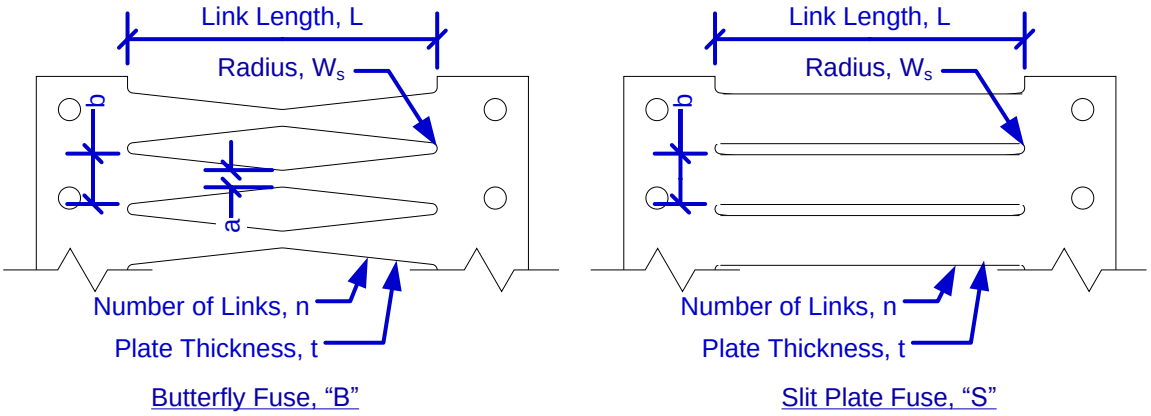

Figure 2.14 Nomenclature for Fuse Geometry

Figure 2.15 Fuse Test Setup (Left) and Fractured Slit Plate Fuse (Right) (from [Ma et al. 2010c])

Butterfly fuse plates on the other hand did not exhibit cracking or fracture in the links until late in the loading history. Fracture of the fuse links in the butterfly fuse specimens did not occur until between 30% and 46.5% shear strain across the fuse link length. Figure 2.16 shows fuse specimen B02-14, one of the more stocky fuses, before and during the test, along with the resulting load-deformation response. As demonstrated in the plot of the steel butterfly plate response, stable hysteresis loops can be obtained up to and exceeding link shear strains of 30%.

The geometry of the butterfly fuse plates was selected to cause the initiation of yield and the initiation of plastic hinging at the quarter point of the fuse link. Concentrating the yielding and maximum fiber stresses away from locations of discontinuity allows larger ductility and displacement capacity. For this reason, the butterfly fuses were shown to have the largest and most repeatable shear strain capacity of the different types of fuses tested at Stanford University.

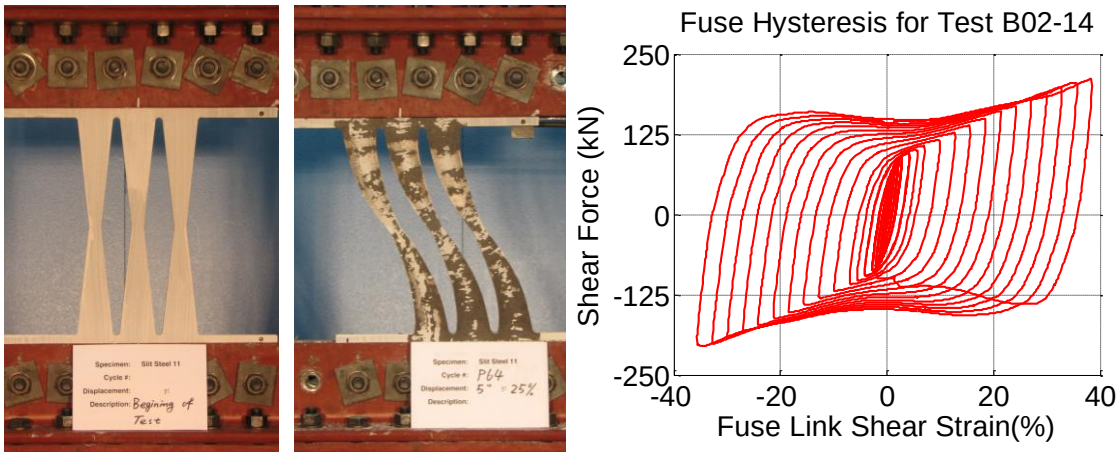

Figure 2.16 Butterfly Fuse B02-14 Before Test (Left), During Testing (Middle), and Hysteretic Response (Right) [from (Ma et al. 2010c)]

A picture of the thinnest of the butterfly fuse tests, at the completion of the loading history, is shown in Figure 2.17. It is clear from this picture that the thinner fuse links experienced visually significant lateral-torsional buckling whereas the thicker fuse

links shown in Figure 2.16 remained relatively planer. The experimental response of these same fuses are shown in Figure 2.16 and Figure 2.17.

Thinner fuse behavior is governed by several distinct modes of shear resistance. Initially, the fuse links act primarily in flexure. The fuse link geometry is widest at the ends and smallest at the middle by a ratio of 3 to 1. Since the section modulus is a function of the depth squared the moment capacity has a quadratic distribution along the link length. The ratio of end depth to middle depth of 1/3 coupled with a reversed moment caused by shear loading creates first yield at the quarter points of the fuse link. Similarly the plastic section modulus is quadratic with section depth and also encourages plastic hinging to form at the quarter points. Initiating inelasticity at the quarter points away from locations of discontinuity enhances the ductility and deformation capacity of these elements.

For thinner fuses, the link then experiences lateral-torsional buckling. During buckling, the flexural strength and stiffness are reduced significantly. The link then transitions to represent a pinned end truss element with length equal to the length between buckled ends. Further shear deformations cause tensile elongations in the effective truss element, whereas unloading creates compressive deformations that then cause compression buckling.

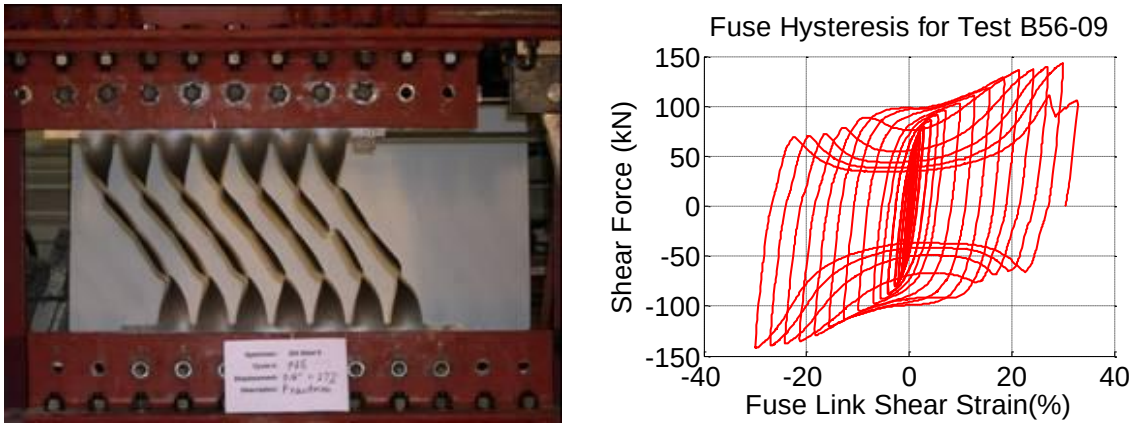

Figure 2.17 Picture of Stanford University Fuse Test B56-09 (left), and the Resulting Load-Deformation Response (right)

Butterfly fuse plates were found to possess exceptional strength, ductility, and deformation capacity while producing predictable stable behavior. For this reason, butterfly fuse plates were selected for use in the large-scale tests described later in this report.

DESCRIPTION OF THE CONTROLLED ROCKING SYSTEM

As described in Chapter 1, the controlled rocking system is a high-performance seismic lateral resisting system for steel-framed buildings that has the ability to self-center after an earthquake and is configured to concentrate the majority of structural damage into replaceable elements. The response of the system is derived and discussed in general terms in this section. First the expected load-deformation response is derived based on simple analysis of the components. Based on the expected response of the system, the following subsection describes the general system proportioning that results in desired response as well as specific system design considerations. Finally, the multi-institution controlled rocking research project is described for which this work is a subset.

3.1 Expected System Response

The expected response is derived based on the idealized frames shown in Figure 3.1. Investigating this expected response enables an exploration of the fundamental and relative contributions made to the system performance by the fuses, the post-tensioning, and the frames. Two configurations are presented: a dual frame configuration with fuses between the frames, and a single frame configuration with fuses at the base. Equations presented in this section are generalized for both configurations unless they are stated as specifically applying to one configuration or the other. All members are idealized as truss elements with pinned ends. The response is decomposed into the response of the rocking frames with post-tensioning and the response due to the fuses. These two components are then combined in a way analogous to springs in parallel to examine the combined system response.

The frame stiffness can be approximated as the sum of the shear deformations due to axial deformations of the braces:

$$\frac{1}{K_{fr}} = \sum_{i=1}^{N_{floors}} \frac{1}{\sum_{\#Braces} A_{br}E \Big/ L_{br}} \qquad \Rightarrow \qquad K_{fr} = \frac{N_{braces}A_{br}E}{N_{floors}L_{br}} \qquad (3.1)$$

Where:
K_{fr} = Approximate elastic stiffness of the braced frames
A_{br} = Area of one brace
E = Modulus of elasticity
N_{braces} = Number of braces per floor
N_{floors} = Number of floors
L_{br} = Length of one brace = $\sqrt{(A/2)^2 + H^2}$

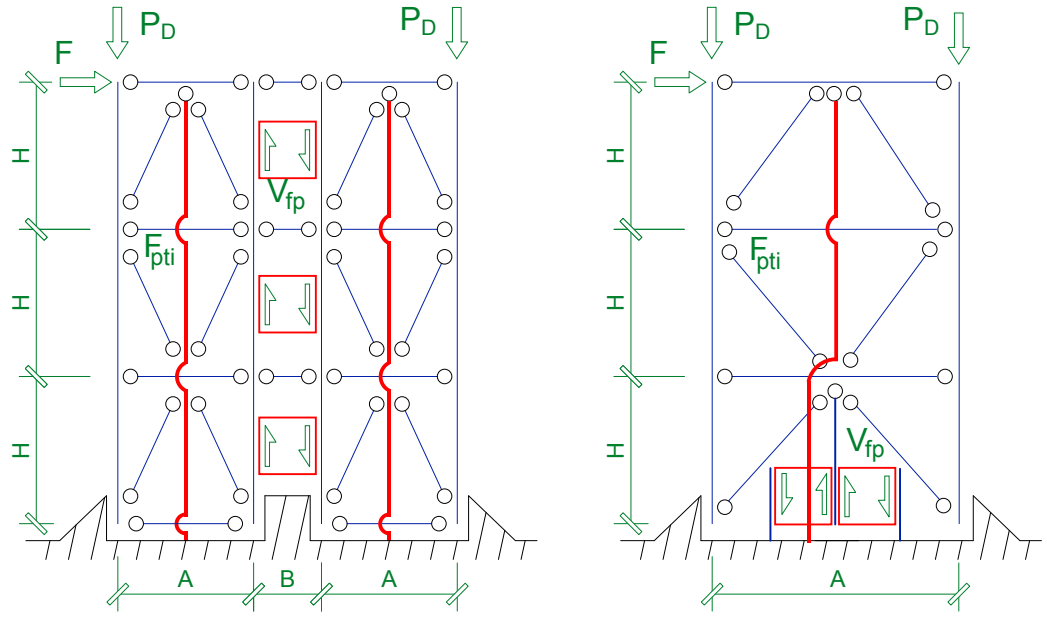

Figure 3.1 Idealized Controlled Rocking Frame in the Dual Frame Configuration (Left) and Single Frame Configuration (Right)

The force applied at the roof level that causes uplift, F_{up}, can be estimated by equating the moment due to externally applied force to the initial restoring force due to post-tensioning:

$$F_{up}(N_{floors}H) = F_{pti}\frac{A}{2}N_{frames} \qquad \Rightarrow \qquad F_{up} = \frac{F_{pti}AN_{frames}}{2N_{floors}H} \quad (3.2)$$

Where:
F_{pti} = Initial post-tensioning force
A, H = Dimensions shown in Figure 3.1
N_{frames} = Number of frames, 2 for dual frame configuration, 1 for single frame configuration

The displacement when uplift occurs can be estimated as the quotient of F_{up} / K_{fr}. After uplifting, the post-tensioning continues to elongate further, increasing the post-tensioning restoring force and thus resulting in a post uplift stiffness, K_{up}. Assuming negligible geometric nonlinearity, negligible frame deformations due to added post-tensioning force, and ignoring frame stiffness after uplift, the post uplift stiffness can be calculated by starting with similar triangles:

$$\frac{|\Delta\delta|}{N_{floors}H} = \frac{\Delta\delta_{pt}}{A/2} \quad (3.3)$$

Where:

$\Delta\delta$ = Increment in horizontal deflection at the roof level

$\Delta\delta_{pt}$ = Increment in the length of the post-tensioning

Rearranging for $\Delta\delta$ assuming positive displacement gives:

$$\Delta\delta = \frac{2\Delta\delta_{pt} N_{floors} H}{A} \tag{3.4}$$

Then, calculating the increment in post-tension force, ΔF_{pt}, based on the increment in the post-tension length, $\Delta\delta_{pt}$, gives:

$$\Delta F_{pt} = \left[\frac{\Delta\delta_{pt}}{N_{floors} H} E \right] A_{pt} \tag{3.5}$$

Equating the moment created by an increment in lateral force, ΔF, with the moment created by an increment in the post-tension force, ΔF_{pt} , results in:

$$N_{floors} H(\Delta F) = \Delta F_{pt} \frac{A}{2} N_{frames} \tag{3.6}$$

Rearranging equation (3.6) for ΔF , and substituting the value for ΔF_{pt} from equation (3.5) yields:

$$\Delta F = \frac{\Delta\delta_{pt} E A_{pt}}{\left(N_{floors} H\right)^2} \frac{A}{2} N_{frames} \tag{3.7}$$

Finally, defining the secondary stiffness, K_{up}, as the ratio of the increment in lateral force, ΔF, divided by the increment in lateral displacement, $\Delta\delta$ results in the following equation:

$$K_{up} = \frac{\Delta F}{\Delta\delta} = \frac{E A_{pt} A^2 N_{frames}}{4\left(N_{floors} H\right)^3} \tag{3.8}$$

The fuse behavior depends on the type of fuse, but for the purposes of examining the system response here, an elastic-perfectly plastic shear fuse is assumed. Figure 3.2 shows the idealized forces due to the fuse yielding assuming the frames have already uplifted.

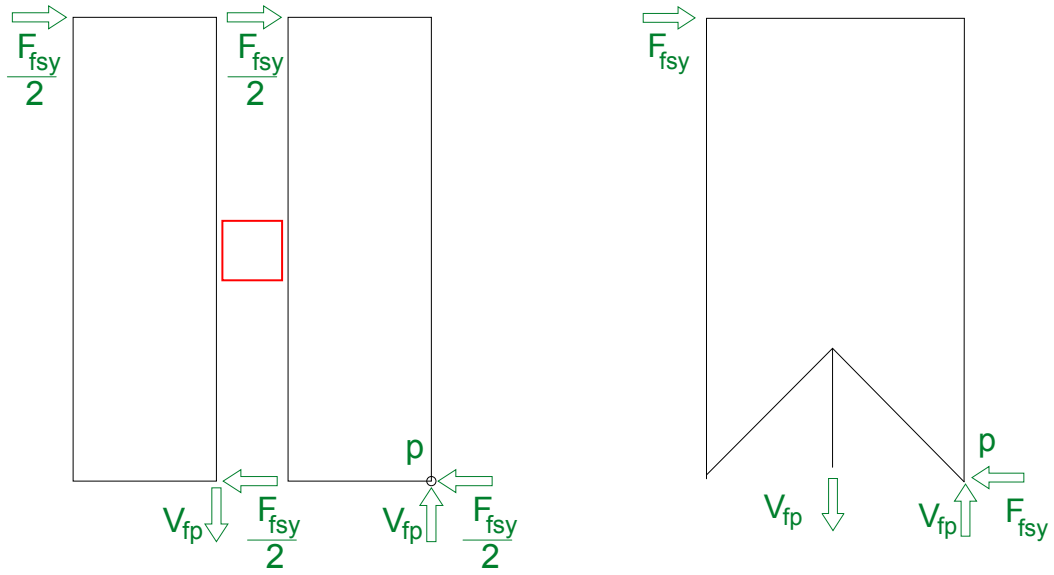

Figure 3.2 Idealized External Forces Due to Fuse Yielding for Dual Frame Configuration (left) and Single Frame Configuration (Right)

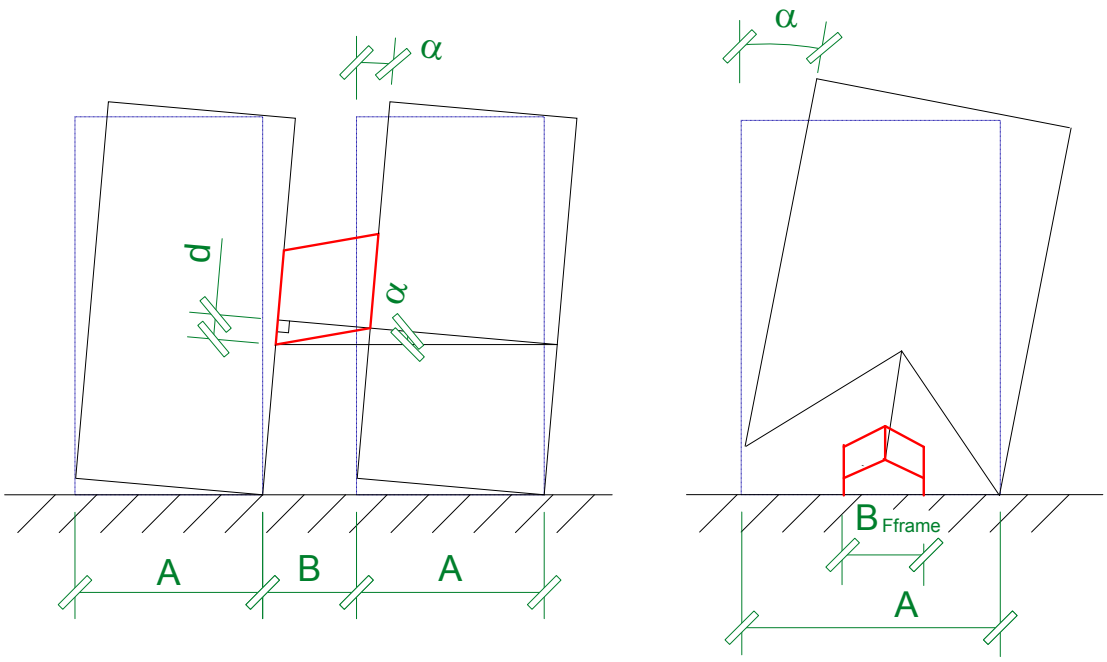

Figure 3.3 Idealized Fuse Shear Deformation for Dual Frame Configuration (left) and Single Frame Configuration (Right)

The force applied at the roof level required to yield the fuses, F_{fsy}, is calculated by summing the moments around point *p* as shown in Figure 3.2:

$$F_{fsy} = \frac{V_{fp}(A+B)}{N_{floors}H} \qquad \text{(DUAL FRAME)} \qquad (3.9)$$

$$F_{fsy} = \frac{V_{fp}\left(A/2\right)}{N_{floors}H} \qquad \text{(SINGLE FRAME)} \qquad (3.10)$$

Where:

V_{fp} = Yield force of the fuse in shear

It is demonstrated on the right side of Figure 3.2 that the shear deformation of the fuse is amplified relative to the shear deformation of the system as a whole. The right side of Figure 3.2 shows idealized rigid body rotation of the frames through some roof drift angle, α. Using the small angle assumption, the fuse shear strain angle, γ, can be calculated as a function of the roof drift angle, α, as follows:

$$d = \alpha\left(A+B\right) \qquad \text{(DUAL FRAME)} \qquad (3.11)$$

$$\gamma = \frac{d}{B} = \alpha\frac{A+B}{B} \qquad \text{(DUAL FRAME)} \qquad (3.12)$$

$$\gamma = \alpha\frac{A}{B_{Fframe}} \qquad \text{(SINGLE FRAME)} \qquad (3.13)$$

Where:

B_{Fframe} = Width of the Fuse Frame as Shown in Figure 3.3

Furthermore, if the shear strain across the fuse link length is desired, the relationship can be modified as:

$$\gamma_{link} = \alpha\frac{A+B}{L_{link}} \qquad \text{(DUAL FRAME)} \qquad (3.14)$$

$$\gamma_{link} = \alpha\frac{A}{2L_{link}} \qquad \text{(SINGLE FRAME)} \qquad (3.15)$$

The response of the rocking frames with post-tensioning as derived in this section is shown in Figure 3.4(a), and the response of rigid frames with fuses is shown in Figure 3.4(b). The combination of these two systems in parallel is given in the combined response shown in Figure 3.4(c). The flag shape of the combined response is characteristic of a self-centering system which is intuitive in that the displacement returns to near zero as the force is removed.

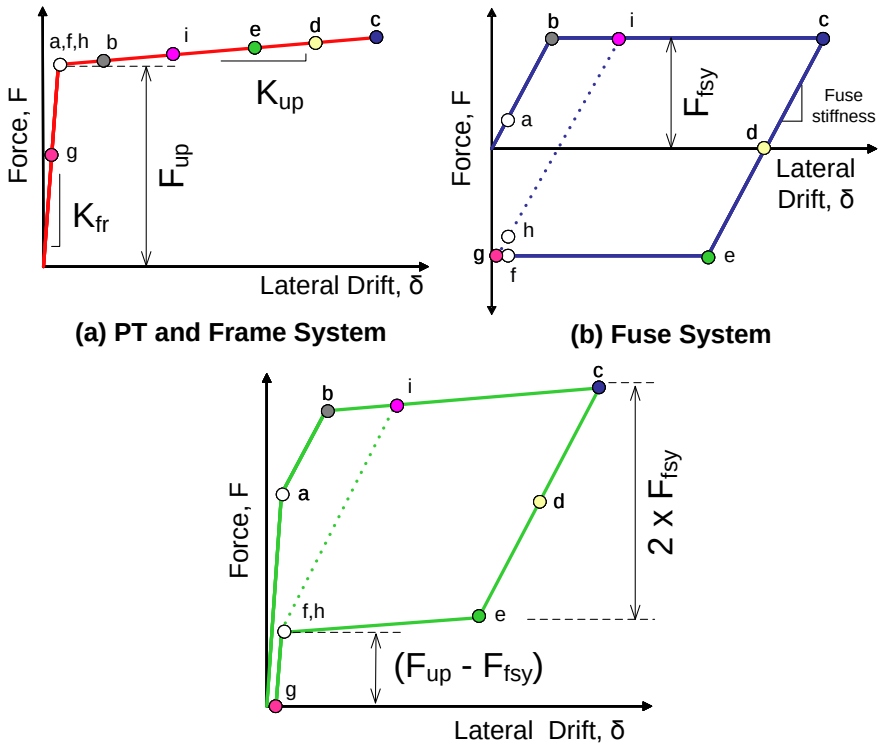

Figure 3.4 Response of Uplifting Frames with Post-Tensioning (a), System with Fuses Only (b), and Combined Response (c)

Some of the important aspects of the response are identified with letters in Figure 3.4(c). The response of the combined system is defined by the following stages:

a. Uplift of the frames
b. Yield of the fuse
c. Arbitrary point of load reversal
d. Fuse is at zero force and begins to load in the opposite direction
e. Fuse yields in the opposite direction
f. Frames set back down
g. At zero total force there is minor residual drift as the fuse is still at yield force and frame experiences elastic deformations due to this force.
h. The frames start to uplift as they are reloaded
i. The fuse starts to yield. Note that the path is different for the second cycle because the fuse starts the cycle with forces equal to negative yield.

3.2 System Proportioning and Design Considerations

General proportioning guidelines for this structural system have been derived to promote self-centering and mitigate negative limit states. These guidelines are presented in a general form in this section, applied specifically to a prototype structure in a subsequent section, and discussed again in the development of the sensitivity study and design recommendations.

3.2.1 Design of System Strength

Equivalent lateral forces can be calculated according to building codes such as ASCE 7-05. Using load combination 7 given in Section 2.3.2 of ASCE 7-05 (ASCE 2005) the overturning moment is found to be:

$$0.9\,D + 1.0\,E \tag{3.16}$$

$$M_{ovt} = \sum_{i=1}^{\#Floors} F_i H_i \tag{3.17}$$

Where:

F_i = Equivalent lateral force at level i
H_i = Height of level i

The resistance to overturning is calculated with an assumed resistance factor of 0.9 applied. The ability of the system to resist lateral forces is checked using Equation (3.18) which expands out to Equation (3.19) and Equation (3.20).

$$\phi M_{resist} \geq M_{ovt} \tag{3.18}$$

$$0.9\left[\left(F_{pti} + 0.9P_D\right)A + V_{fp}\left(A + B\right)\right] \geq M_{ovt} \quad \text{(DUAL FRAME)} \tag{3.19}$$

$$0.9\left[\left(F_{pti} + 1.8P_D + V_{fp}\right)\frac{A}{2}\right] \geq M_{ovt} \quad \text{(SINGLE FRAME)} \tag{3.20}$$

Where:

F_{pti} = Initial post-tension force
V_{fp} = shear yield capacity of all fuses
A, B = Dimensions Shown in Figure 3.1
P_D = Total dead load applied to one exterior uplifting column (it is assumed that significant gravity load is only applied to the exterior columns)

3.2.2 Proportioning Fuse Strength and Initial Post-Tension Force

To create a fully self-centering flag-shaped load-deformation response, the restoring moment must be greater than the moments that are resisting self-centering, namely the fuses. Equation (3.21) gives the general condition for full self-centering which is then expanded in Equation (3.22) and Equation (3.23).

$$M_{restore} \geq M_{fuse} \tag{3.21}$$

$$\left(F_{pti} + 0.9P_D\right)A \geq V_{fp}\left(A + B\right) \quad \text{(DUAL FRAME)} \tag{3.22}$$

$$F_{pti} + 1.8P_D \geq V_{fp} \quad \text{(SINGLE FRAME)} \tag{3.23}$$

Subtracting Equation (3.19) from Equation (3.22) or subtracting Equation (3.20) from Equation (3.23), causes the contribution of the P/T force and gravity load to drop out leaving an equation for proportioning the fuse strength based on the design overturning moment:

$$V_{fp} \geq \frac{M_{ovt}}{1.8(A+B)} \qquad \text{(DUAL FRAME)} \qquad (3.24)$$

$$V_{fp} \geq \frac{M_{ovt}}{0.9A} \qquad \text{(SINGLE FRAME)} \qquad (3.25)$$

After designing the fuse, the initial post-tension force required for full self-centering can be calculated by rearranging Equation (3.22) and Equation (3.23), which results in the following:

$$F_{pti} \geq V_{fp} \frac{(A+B)}{A} - 0.9P_D \qquad \text{(DUAL FRAME)} \qquad (3.26)$$

$$F_{pti} \geq V_{fp} - 1.8P_D \qquad \text{(SINGLE FRAME)} \qquad (3.27)$$

Equation (3.26) and Equation (3.27) demonstrate that the dead load and the initial post-tension force are essentially interchangeable. The dead load can be used, therefore, to offset the amount of post-tensioning required.

3.2.3 Global Uplift Design Check

If the fuses are too strong, the frames experience global uplift characterized by both legs of a frame lifting off the supports. In the dual frame configuration, this corresponds to the windward frame being lifted off the ground. In the single frame configuration global uplift corresponds to the frame sitting up in the air supported on the fuses. See Figure 3.5 for a schematic representation of global uplift for the dual frame configuration and the single frame configuration. To prevent the global uplift, the post-tensioning force has to be greater than the resisting force of the fuses.

$$F_{pti} > C_{sh} V_{fp} \qquad (3.28)$$

Where:
C_{sh} = Factor for Strain Hardening

Although the post-tensioning force is increased during rocking, it is necessary to use the initial post-tension force in this calculation to prevent global uplift even at low levels of roof drift. Furthermore, it may be desired to use a factor that accounts for strain hardening of the fuse, C_{sh}.

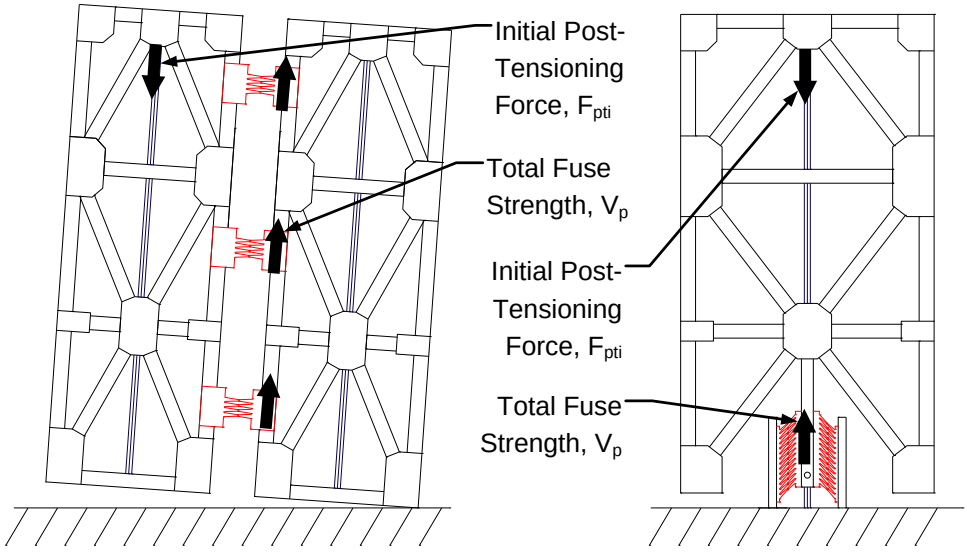

Figure 3.5 Global Uplift for the Dual Frame Configuration (Left) and the Single Frame Configuration (Right)

3.3 Overview of the Project Phases and Objectives

The conceptual design, development, and validation of the controlled rocking system was divided into several phases:

1. Schematic design to define feasible configurations and schematic construction details.
2. SDOF study to examine the characteristics of the flag-shaped hysteresis loop and study the proportioning of the system (Described in Chapter 3).
3. Initial parametric study using an MDOF model to identify key variables and their effect on the system response (Hall et al. 2006).
4. Fuse development through analysis and large-scale testing at Stanford University (Ma et al. 2010c).
5. Large-scale quasi-static cyclic and hybrid simulation tests of the rocking frame at the University of Illinois (Described in Chapters 4, 5, 7, and 8, and summarized in Eatherton et al. 2008, Eatherton et al. 2010a, Eatherton et al. 2010b, Hajjar et al. 2008, and Hajjar et al. 2010).
6. Large-scale shake table testing at E-Defense in Miki, Japan (Deierlein et al. 2010, Ma et al. 2010a, Ma et al. 2010b, Ma 2010).
7. Development of computational models to capture salient features of system response (Described in Chapter 6 and [Ma 2010]).
8. SDOF study to examine the residual drifts of self-centering systems in the presence of ambient building resistance (Described in Chapter 9).
9. MDOF Parametric studies to investigate the application of the controlled rocking system to a range of practical building situations (Described in Chapter 10 and 11).

10. Development of design recommendations to enable implementation in practice (Included in Chapter 12 and [Ma 2010]). Development of direct displacement based design methodology (Ma 2010).

This project was conducted in conjunction with Stanford University and many of the phases listed above were performed by the group. References to chapters of this report and other publications where information can be found on each phase are included in the list above. Testing was conducted at Stanford University (item 4), the UIUC MUST-SIM facility (item 5), and the E-Defense facility in Japan (item 6). This report describes the large-scale testing at UIUC, multiple analytical investigations, and some of the development of the controlled rocking system for implementation in practice. The research included in this report had several objectives which fit into the above listed phases including:

- Investigate the response of the controlled rocking system through conducting a series of half-scale quasi-static and hybrid simulation experiments with the following objectives:
    - Validate system performance by examining the ability of the system to self-center and concentrate the majority of damage in the fuse elements.
    - Provide data for use in developing the computational model.
    - Examine detailing of the system which uses components not typical to steel construction such as post-tensioning and column bases allowed to uplift.
    - Study fuse performance as it acts as part of the overall system as well as determining the forces imparted to the fuse during testing.
    - Define the distribution of member forces in this indeterminate system.
    - Investigate the performance of post-tensioning in this type of application, specifically examining post-tension force losses and tendon fracture.
- Develop a computational model that accurately represents the significant aspects of the experimental response.
- Conduct MDOF analyses using the developed computational model to:
    - Examine the response of the system as applied to buildings with different heights and frame geometry.
    - Investigate the occurrence of limit states.
    - Build on the work done by Hall et al. (2006) to further investigate system demands due to given seismic hazard levels.
- Conduct SDOF analyses to determine the amount of restoring force necessary to reliably self-center a building
    - Examine the range of self-centering from all restoring force (elastic-bilinear) to all energy dissipation (elastic-plastic).
    - Include the resistance of the rest of the building to determine its effect on self-centering.
- Develop design recommendations for implementation in practice:

- Develop a capacity design method for selecting framing members and verify this proposed method
- Create proportioning guidelines for design fuse strength, initial post-tensioning force, and post-tensioning area.
- Provide guidance for column base details that are allowed to uplift and post-tensioning details in steel frames subjected to cyclic loading.

EXPERIMENTAL PROGRAM

The large-scale quasi-static cyclic and hybrid testing program was conducted at the Multi-Axial Full-Scale Substructure Testing and Simulation (MUST-SIM) facility at the University of Illinois at Urbana-Champaign. A prototype three-story building is used to define realistic masses and forces tributary to a controlled rocking frame which are then scaled using similitude. The preliminary proportioning guidelines presented in the previous section are then applied and the design of the test specimen is described. Features of the construction are then explained including key connection details, the construction schedule, and material tests. The chapter then concludes with details of the testing program, including the test matrix, loading protocol, ground motions used for hybrid simulation, test control architecture, and instrumentation.

4.1 Prototype Building

The design resistance of the tested configurations is based on a prototype building that is one of the SAC configurations (Gupta and Krawinkler 1999). The building is three stories tall and has a 36.6m x 54.9m (120'x180') plan with typical floor and roof framing shown in Figure 4.1. The building is located in Los Angeles, California with site class D as defined in ASCE 7-05 (ASCE 2005). Floor weights and masses are summarized in Table 4.1.

The controlled rocking system has substantial ductility so it is therefore believed that the system will warrant a large response modification factor, similar to eccentrically braced frames. A value of $R = 8$ (ASCE 7-05) is assumed. Design spectral accelerations were calculated for an arbitrary location in Los Angeles, California to be:

$$S_{DS} = 1.00g \qquad S_{D1} = 0.60g \tag{4.1}$$

Table 4.1 Weights and Masses for the Prototype Building

Level	Seismic Mass kN-sec^2/m (kips-sec^2/ft)	Total Dead Load, kN (kips)	Reduced Total Live Load, kN (kips)	Total Gravity Load, kN (kips)
Roof	1033 (70.9)	10151 (2282)	1183 (266 for 12 psf)	11,334 (2548)
Third Floor	955.5 (65.5)	10373 (2332)	1975 (444 for 20 psf)	12,348 (2776)
Second Floor	955.5 (65.5)	10373 (2332)	1975 (444 for 20 psf)	12,348 (2776)

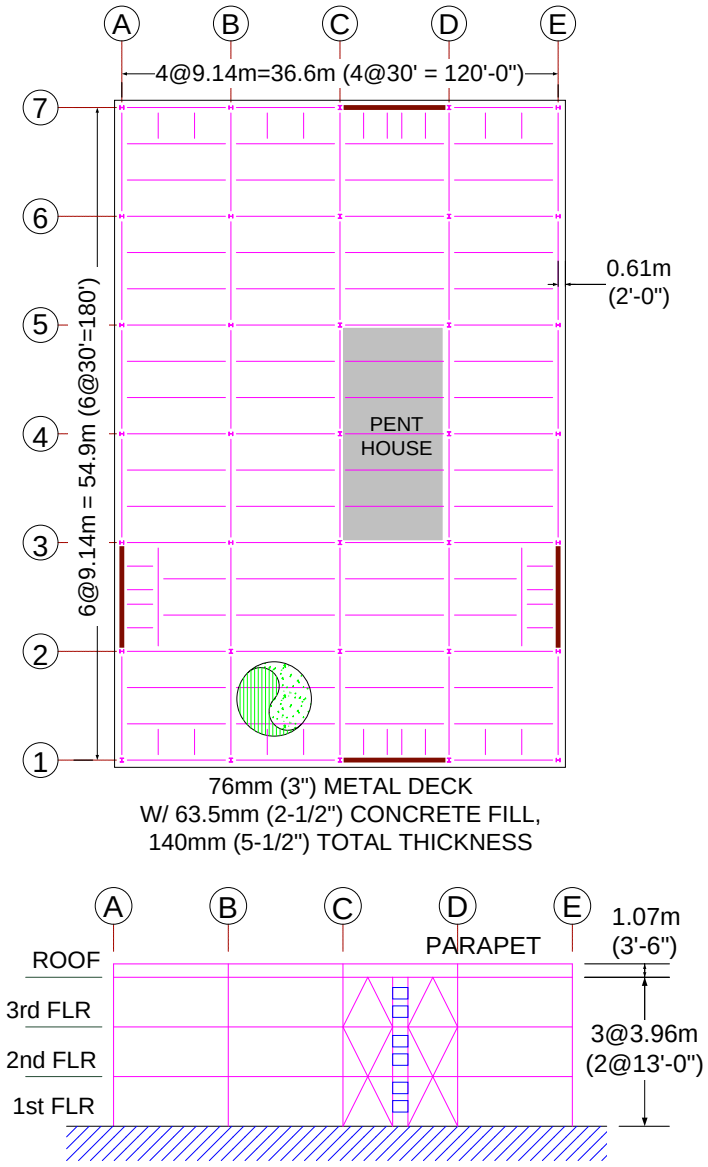

Figure 4.1 Prototype Building Typical Floor and Roof Framing Plan (top), and Elevation (bottom)

The approximate initial fundamental building period using was determined using Section 12.8.2.1 (ASCE 7-05) with $C_t = 0.02$ and $x = 0.75$ for a braced frame:

$$T_a = C_t h_n^{\,x} = 0.02 \times 39^{0.75} = 0.31 \text{ sec} \qquad (4.2)$$

The response coefficient and resulting design base shear was then calculated using Equations 12.8-1 through 12.8-6 (ASCE 7-05) to be:

$$C_s = \frac{S_{DS}}{\left(\frac{R}{I}\right)} = \frac{1.00}{\left(\frac{8.0}{1.0}\right)} = 0.125 \quad \leq \left[\frac{S_{D1}}{T\left(\frac{R}{I}\right)} = \frac{0.60}{0.31\left(\frac{8.0}{1.0}\right)} = 0.242 \right] \qquad (4.3)$$

$$C_s \geq 0.01 \quad and \quad C_s \geq \frac{0.5S_1}{\left(\frac{R}{I}\right)} = \frac{0.5 \times 0.60}{\left(\frac{8.0}{1.0}\right)} = 0.0375 \qquad (4.4)$$

$$V = C_s W = 0.125 \times 28922 = 3615 \text{ kN} \qquad (4.5)$$

The vertical distribution of the lateral forces is then calculated using Section 12.8.3 (ASCE 7-05) as shown in Table 4.2 using k = 1 since the period is less than 0.5 seconds.

Table 4.2 Vertical Distribution of Lateral Forces

Level	w_i kN (kips)	h_i m (ft)	$w_i h_i^k$ kN-m (k-ft)	C_{vx}	F_x kN (kips)
Roof	10151 (2282)	11.9 (39)	89,007 (65650)	0.52	1878 (422.3)
3rd	9386 (2110)	7.9 (26)	54,853 (40450)	0.32	1158 (260.3)
2nd	9386 (2110)	4.0 (13)	27,427 (20230)	0.16	579 (130.1)
Total	28922 (6502)		171,287 (126300)		3615 (812.7)

There are two bays of controlled rocking frames in each direction as shown in Figure 4.1. The loads applied to each controlled rocking frame and resulting overturning moments are summarized in Table 4.3. The lateral resisting elements are located such that the center of rigidity coincides with the center of gravity. For the purposes of these calculations, accidental torsion has been neglected.

Table 4.3 Design Lateral Loads Applied To Each Controlled Rocking Frame

Level	Story Shear, kN (kips)	Overturning Moment, kN-m (k-ft)
Roof	939.5 (211.2)	11168 (8237)
3rd	579.2 (130.2)	4589 (3385)
2nd	289.6 (65.1)	1147 (846)
Total	1808 (407)	16904 (12468)

All rocking frames are on the exterior of the building. The gravity load is only applied at the outside columns of the frame as shown in Figure 4.1. Dead load, P_D, and live load, P_L, at each exterior column and at each level are given by:

$$A_{trib} = 9.14m \bullet 4.57m = 41.8m^2 \quad (450\ \text{ft}^2) \tag{4.6}$$

$$P_D = 41.8\text{m}^2 \bullet 4.60\frac{\text{kN}}{\text{m}^2} = 192\text{kN} \quad (43.2\ \text{kips}) \tag{4.7}$$

$$P_L = 41.8\text{m}^2 \bullet 2.39\frac{\text{kN}}{\text{m}^2} = 100\text{kN} \quad (22.5\ \text{kips}) \tag{4.8}$$

4.2 Test Variables and Testing Matrix

The testing matrix was created to vary key design variables. The parametric study presented in Hall et al. (2006) defined three primary dimensionless design variables: a geometric ratio, a design strength ratio, and a self-centering ratio. Two of these design parameters were investigated experimentally along with several other design parameters. The variables that are investigated in the testing program include: 1) OT strength ratio, 2) SC self-centering ratio, 3) Fuse thickness, 4) Number and location of fuses, 5) dual frame configuration (series A) versus single frame configuration (series B), 6) Single width fuse for dual frame configuration (series A) versus double width fuses for single frame configuration (series B), 7) Single thickness fuses (Typical) versus double thickness fuses with a restraining plate between (B1 Right), 8) Initial stress level in post-tensioning strands, and 9) Quasi-static cyclic loading versus hybrid simulation.

Based on the variation of these parameters, the test matrix given in Table 4.4 was defined. The reasons for selecting specific ranges of values for the parameters are discussed in the following paragraphs.

The testing program was divided into two series. The first series, designated as series A, is a dual frame configuration including fuses and struts between the frames. The second series is designated as series B, in which the two frames act independently and the fuses are located at the base of the frames as shown in Figure 4.7. The two B series specimens were tested simultaneously.

The geometric ratio, (A/B), is the ratio of the frame width, A to the fuse width, B. Both dimensions are from centerline of column to centerline of column and are shown schematically in Figure 3.1. Due to the need to limit the number of specimen configurations it was not possible to vary the A/B ratio in the testing program, but the effects of this geometric ratio have been studied computationally as described in Chapter 10.

The overturning ratio (OT) is the ratio of the strength of the system to the effects of the equivalent lateral forces calculated using ASCE 7-05 (ASCE 2005). Since the design strength of the system consists primarily of vertical acting elements whereas the lateral forces are horizontal acting, the ratio is executed in the moment domain as the moment resistance divided by the design overturning moment. The ratio is obtained by dividing the left hand side of Equation 3.19 or Equation 3.20 by the right hand side as given in Equation (4.9) and Equation (4.10). Since gravity loads were not applied in the

experiments they were neglected in this calculation of the overturning ratio. The design overturning moment was found using ASCE 7-05 assuming a response modification factor, R = 8. A value of the OT ratio greater than one means, therefore, that the system has strength greater than that required by current U.S. building codes based on the prototype building configuration and R = 8.

$$OT = \frac{\varphi M_n}{M_{ovt}} = \frac{0.9\left[A\,F_{PT} + V_P\left(A+B\right)\right]}{M_{ovt}} \qquad \text{(DUAL FRAME)} \qquad (4.9)$$

$$OT = \frac{\varphi M_n}{M_{ovt}} = \frac{0.9\left[\left(F_{PT} + V_P\right)A/2\right]}{M_{ovt}} \qquad \text{(SINGLE FRAME)} \qquad (4.10)$$

Table 4.4 Matrix Defining the Testing Program

Spec-imen ID (Config)	OT Ratio	SC Ratio	Num. of 12.7 mm (0.5") P/T Strands	Initial P/T Stress and Force	Fuse Type and Fuse Strength	Fuse Configuration / Notes	Testing Protocol
A1 (Dual)	0.96 (R=8.3)	0.86	8	0.287 Fu 422 kN (94.8 kips)	8 Links 349 kN (78.4 kips)	Six – 6.4 mm (¼") thick fuses	Quasi-Static
A2 (Dual)	1.07 (R=7.5)	0.71	8	0.287 Fu 422 kN (94.8 kips)	10 Links 425 kN (95.5 kips)	Two – 15.9 mm (5/8") thick Fuses	Quasi-Static
A3 (Dual)	0.88 (R=9.1)	1.01	8	0.287 Fu 422 kN (94.8 kips)	7 Links 297 kN (66.8 kips)	Two – 15.9 mm (5/8") thick Fuses	Quasi-Static
A4 (Dual)	1.43 (R=5.6)	1.13	8	0.489 Fu 718 kN (161.5 kips)	7 Links 455 kN (102.2 kips)	Two – 25.4 mm (1") thick Fuses	Quasi-Static
A5 (Dual)	1.03 (R=7.8)	1.05	8	0.338 Fu 497 kN (111.8 kips)	8 links 340 kN (76.4 kips)	Two – 15.9 mm (5/8") thick Fuses	Hybrid Sim.
A6 (Dual)	1.04 (R=7.7)	1.02	8	0.338 Fu 497 kN (111.8 kips)	8 Links 349 kN (78.4 kips)	Six – 6.4 mm (¼") thick fuses	Hybrid Sim.
A7 (Dual)	1.04 (R=7.7)	1.02	8	0.338 Fu 497 kN (111.8 kips)	8 Links 349 kN (78.4 kips)	Six – 6.4 mm (¼") thick fuses no struts	Quasi-Static
B1 (Single)	1.09 for ten frames	1.84	4	0.454 Fu 334 kN (75.0 kips)	6 links total 181 kN (40.8 kips)	One 19.1 mm (3/4") thick with bar strut across the top	Quasi-Static
B2 (Single)	1.04 for ten frames	2.08	4	0.454 Fu 334 kN (75.0 kips)	20 links total 161 kN (36.1 kips)	Two 4.8 mm (3/16") thick plates with Plate In Between	

The range of the OT strength ratio selected to be tested was based on the parametric study by Hall et al. (2006). Higher OT factors could be used to satisfy higher performance requirements by limiting interstory drifts. As shown in Figure 2.12, the effectiveness of the OT factor in limiting drifts starts to plateau around a value of OT=1.5. Larger OT factors also require the frame to be designed for larger loads so it was decided to limit the OT factor to 1.5 for the specimen configurations. Conversely, lower OT factors require greater fuse shear strain capacity as shown in Figure 2.13. At the time that the test matrix was defined, it was thought that the fuses would not have large enough shear strain capacity to validate the use of OT less than 1.0. Furthermore, since OT less than 1.0 corresponds to R greater than 8 and ASCE 7-05 currently does not use R>8 for any systems (ASCE 2005), it was decided to set 1.0 as the lower limit for the specimen configurations.

The self-centering ratio (SC) is a measure of how well the system will return to its original position after unloading. Similar to the OT ratio, it is computed in the moment domain as the restoring moment divided by the resistance to self-centering. Similar to the OT ratio the SC ratio is computed neglecting gravity since there was no gravity load applied in the experiment. The SC ratio is found by dividing the left hand side of Equation (3.22) or Equation (3.23) by the right hand side as given in Equation (4.11) and Equation (4.12). An SC ratio value greater than 1 means that the initial post-tensioning force is capable of overcoming the fuse yield capacity and bring the system back to center upon unloading. For the purposes of the test specimen design, the resistance to self-centering that is associated with the rest of the building (simple beam-column connections, partitions, etc.) is neglected. However, the effects of the rest of the building on the self-centering performance of the system is investigated in Chapter 9.

$$SC = \frac{A\,F_{pti}}{V_{fp}(A+B)} \qquad \text{(DUAL FRAME)} \qquad (4.11)$$

$$SC = \frac{F_{pti}}{V_{fp}} \qquad \text{(SINGLE FRAME)} \qquad (4.12)$$

The preliminary parametric study found that the controlled rocking system exhibits almost no residual drift even when the SC ratio is less than 1.0 (Hall et al. 2006). SC values as low as 0.5 still resulted in negligible residual roof drift or residual uplift. This phenomenon is explored in Chapter 9. For this reason the test matrix was initially defined with SC = 0.8 for every specimen. After specimen A2, however, it was decided to increase the SC factor so that load-deformation plots of future specimens would demonstrate near zero drift when the load was removed.

The SC ratio needed to be larger for the single frame configurations to prevent global uplift. As discussed in Chapter 3 and given in Equation (3.28), the initial post-tensioning force, F_{pti}, must be greater than the hardened fuse shear capacity, $C_{sh}V_{fp}$ to prevent global uplift. For the dual frame configuration, an SC ratio less than 1.0 may still satisfy this requirement. For Specimen A1 and A2, the SC=0.8 resulted in an initial post-tensioning force that was larger than the fuse capacity because the moment arm for the fuse is larger than the moment arm for the post-tensioning. However, the single frame

configuration SC is calculated using Equation (4.12) which shows that the SC ratio cannot be less than 1.0 and still satisfy the global uplift requirement. For the nonbuckling fuses, a strain hardening factor, C_{sh}=1.5 was assumed based on previous tests which also includes hardening due to fuse axial forces. The single frame configuration specimens, B1 and B2, therefore, used SC greater than 1.5.

The dual frame configuration used for most of the specimens depends on a shear fuse with large shear strain capacity. The butterfly steel plate fuses are especially well suited for this application. The number of fuses was varied to represent different possible configurations such as one fuse location and multiple fuse locations, one at each of the three floors. Also, the fuse thickness was varied to be 4.8 mm (3/16"), 65.4 mm (1/4"), 15.9 mm (5/8"), 19.1 mm (3/4") and 25.4 mm (1") thick to examine the difference in behavior between thin fuses which exhibit lateral-torsional buckling and thick fuses that don't buckle.

As will be discussed in later chapters, selecting the proper initial PT stress is important for allowing adequate strain capacity to preclude yielding or strand fracture. Although it is advantageous in some cases to use the lowest possible initial PT stress in order to allow the most strain capacity, there may be a practical limit. A lower limit of approximately 0.3 F_u and an upper limit of approximately 0.5 F_u were selected. No issues were encountered with implementing these levels of initial post-tension force.

4.3 Specimen Design

4.3.1 Scaling

The specimen is scaled to be 0.43 times the dimensions of the full-scale prototype structure. The prototype structure has a center-to-center spacing of the columns, A=3.66m (12'-0"), and center-to-center spacing between the frames, B=1.46m (4' 9-7/16"), which yields a total bay width of 8.77m (28' 9-7/16") and an A/B ratio of 2.5. The specimen frame width, measured between the column centerlines, is A=0.43x3.66" = 1.57m (5.16'). Figure 4.2 shows key specimen dimensions relative to the prototype frame.

Table 4.5 gives the scale factors used to reduce prototype dimensions to specimen scale. To satisfy similitude, the design overturning moment calculated above is scaled down by the cube of the length. Since the scale of the specimen is 0.43 times the size of the prototype building frame, the design overturning moment is scaled by M_r = 0.43^3 = 0.0795 and for the specimen is:

$$M_u = M_r \, M_{ovt-prototype} = 0.0795x16,904 = 1344\text{kN-m} \qquad (4.13)$$

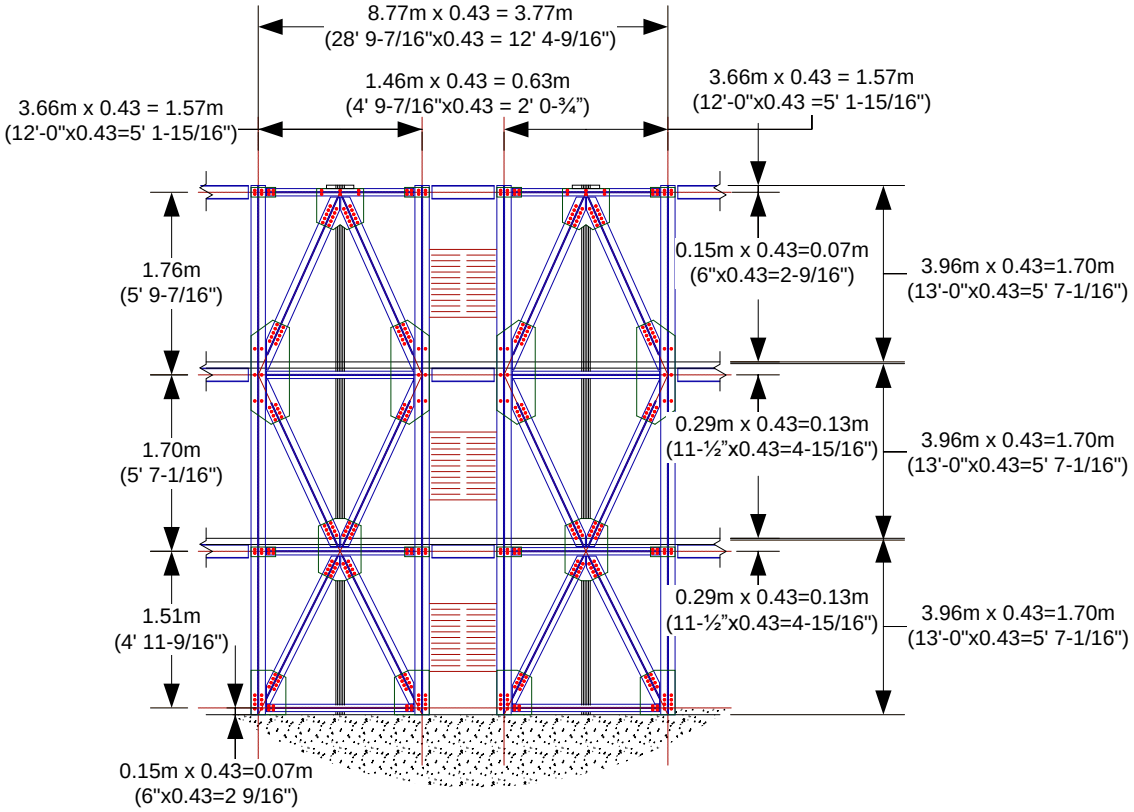

Figure 4.2 Scale of Specimen Compared to the Prototype

Table 4.5 Scale Factors to Satisfy Similitude

Scaling Parameters		Derivation	Values
Length	l_r	Decided by test design	0.43
Young's modulus	E_r	Decided by test design	1.0
Accel. of Gravity	g_r	Decided by test design	1.0
Displacement	δ_r	$= l_r$	0.43
Rotation	θ_r	Dimensionless	1.0
Force	F_r	$= E_r l_r^{\,2} = l_r^{\,2}$	0.185
Moment	M_r	$= F_r l_r = l_r^{\,3}$	0.0795
Acceleration	a_r	$= g_r$	1.0
Mass	m_r	$= \frac{E_r l_r^{\,2}}{a_r} = l_r^{\,2}$	0.185
Time	t_r	$= \sqrt{\frac{m_r}{E_r l_r}} = \sqrt{l_r}$	0.656
Period	T_r	$= t_r$	0.656

4.3.2 Experimental Test Setup

The experimental program was conducted at the Multi-axial Full-scale Substructure Testing and Simulation (MUST-SIM) facility at the University of Illinois at Urbana-Champaign, which is part of the National Science Foundation (NSF) George E. Brown, Jr. Network for Earthquake Engineering Simulation (NEES). Loading is applied using one of the Loading and Boundary Condition Boxes (LBCB), which contains six actuators making it possible to control all six DOFs at the top of the specimen. The stroke limits and force capacities for the LBCB are listed in Table 4.6. The actuators are single-sided pistons, so the force capacities when the actuators are in compression are greater than those listed in Table 4.6. The LBCB coordinate system is shown in Figure 4.3 and Figure 4.4.

Table 4.6 Stroke Limits and Force Capacities for the LBCB

Direction	Stroke, mm (in)	Capacity, kN (kips)
δ_x	± 250 (± 10)	1921 (432)
δ_y	± 125 (± 5)	960 (216)
δ_z	± 125 (± 5)	2882 (648)
Direction	**Stroke, degrees (rad)**	**Capacity, kN-m (k-in)**
Roll, ϑ_x	± 16° (0.279)	862 (636)
Pitch, ϑ_y	± 11.8° (0.206)	1152 (850)
Yaw, ϑ_z	± 16° (0.279)	862 (636)

As shown in Figure 4.3, the LBCB is bolted to the strong wall and the LBCB loading platform is bolted to a loading beam. The loading beam is connected to the specimen through two biaxial load cell pins that measure the vertical and horizontal load applied to each frame.

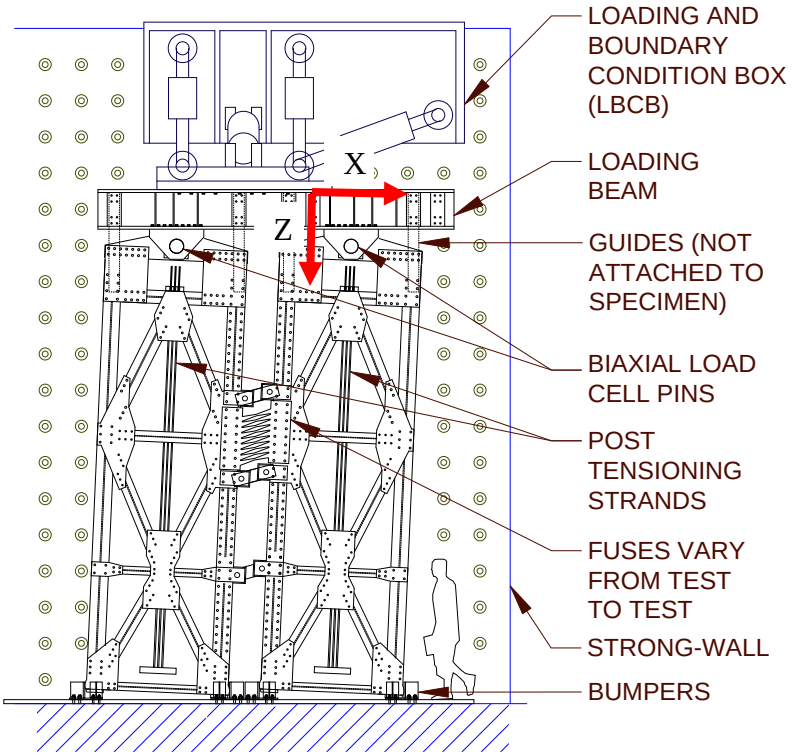

Figure 4.3 Test Setup at the MUST-SIM Facility

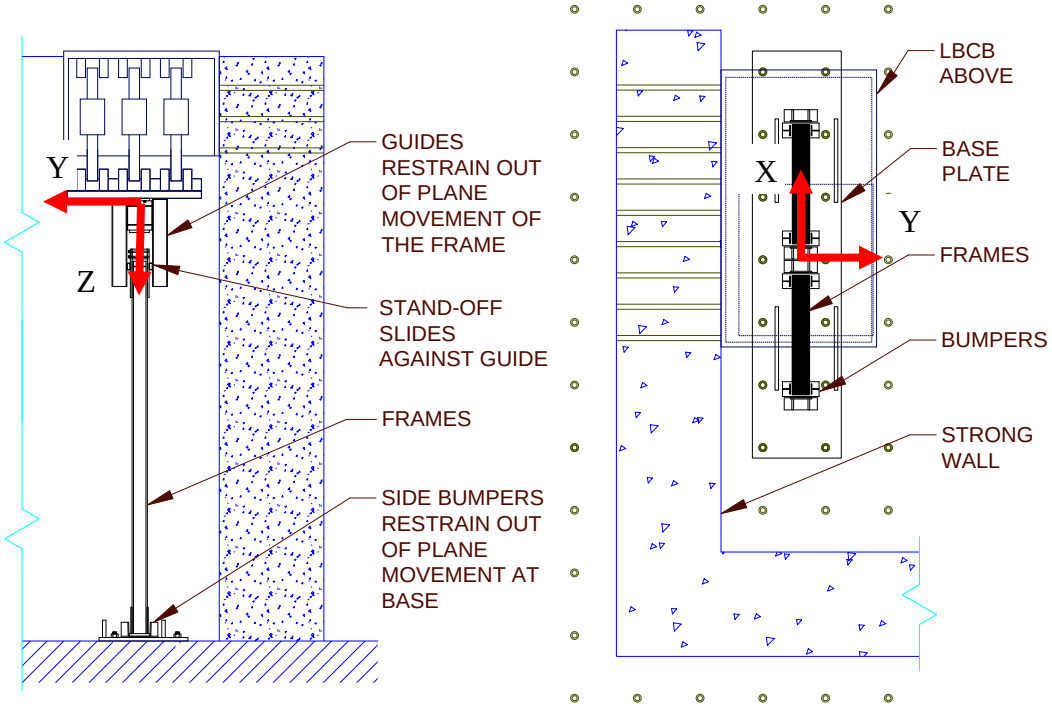

Figure 4.4 Side View (left) and Plan View (right) of the Test Setup

The frames are braced against out-of-plane movement as shown in Figure 4.4 by bumpers at the bottom and guides at the top. The guides are bolted to the loading beam,

but not to the frames. A stand-off piece at the top of the frame is designed to slide against the inside of the guides. It was found during the testing of the first few specimens that the guides were not being engaged and that the rotational resistance proved at the pin connections was sufficient to brace the frame from out of plane motion. The guides were removed after the testing of specimen A4. The LBCB loading platform is restrained by the test control not to move in the out-of-plane directions: $\delta_y = 0$, $\theta_x = 0$, and $\theta_z = 0$, which is discussed further in a later section on test control. A photograph of the test setup is shown in Figure 4.5.

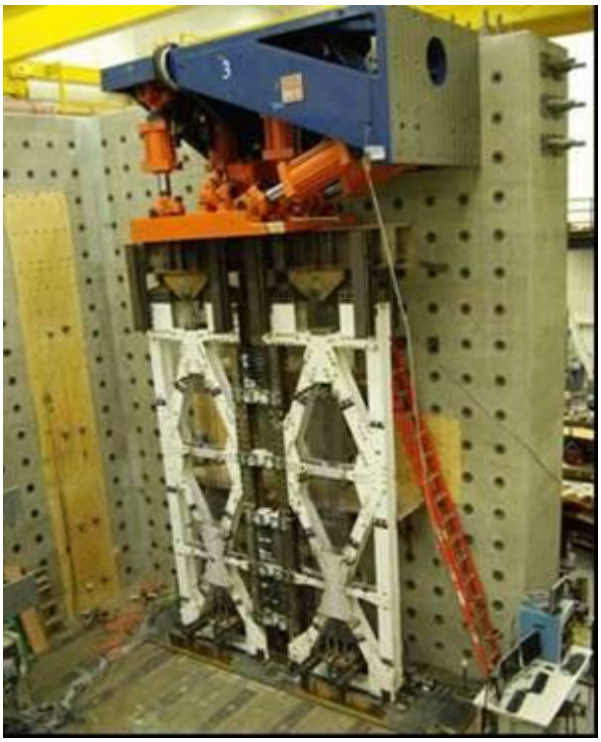

Figure 4.5 Photograph of the Test Setup

4.3.3 Member and Connection Design

The two specimen frames were designed for a range of possible fuse and post-tensioning combinations experiencing roof drift ratios greater than 4%. For this reason the frame sections and connections are designed for much more severe loading than would be required of the prototype frames which would be designed for a specific combination of post-tensioning strands, initial post-tensioning force, fuse location, and fuse strength. OpenSees analyses were conducted with models similar to that described in Chapter 8 for every combination of:

1. Three different fuse configurations: 6 fuses that are 6.4 mm (¼") thick, 2 fuses that are 15.9 mm (5/8") thick, or 2 fuses that are 25.4 mm (1") thick.
2. Two different fuse widths: B=628 mm (2.06') for A/B=2.5, B=933 mm (3.06') for A/B=1.69. However, the final testing program eliminated the A/B=1.69 configuration.
3. Two different OT ratios: OT = 1.0, and OT = 1.5.

The combination of the above listed parameters resulted in 12 different design configurations. In addition to these design configurations another configuration was considered which uses fuses at the base of the frames:

4. Two individual frames with fuses at the base of the frames (Series B).

OpenSees analysis was performed to predict the frame element forces as the model was subjected to the full extent of the LBCB stroke which is ±254 mm (±10”). The maximum forces were then used to check the adequacy of the braced frame members according to AISC 360-05 (2005) for: compression, tension, bending, shear, combined peak tension and flexure, combined peak compression and flexure, combined axial and peak moment for end 1, and combined axial and peak moment for end 2.

The adequacy of the gusset plate connections were calculated in a similar way using the same analyses results. The design calculations included assessment of edge distance limits, bolt shear, bolt bearing, block shear, Whitmore section yield, net section fracture, and slip critical strength of the bolts. The material used and nominal strength of each is provided in. Ancillary material tests are reported in Section 4.4.3. Wide flange member sizes and some other key design information are given in Figure 4.6. The single frame configuration used in the B series specimens is shown in Figure 4.7.

Table 4.7 Material Grades and Nominal Strengths Used for the Specimen

Item	ASTM Material Specification	Nominal Yield Strength	Nominal Ultimate Strength
½” Post-Tensioning Strand	A416	N/A	1862 MPa (270 ksi)
Wide Flange Shapes	A992 Grade 50	345MPa (50 ksi)	448 MPa (65 ksi)
Typical Bolts	A490	N/A	1034MPa (150 ksi)
Threaded Rod	A193 Grade B7	N/A	862MPa (125 ksi)
Gusset Plates	A572 Grade 50	345MPa (50 ksi)	448MPa (65 ksi)
Fuse Plates	A36	248MPa (36 ksi)	400MPa (58 ksi)

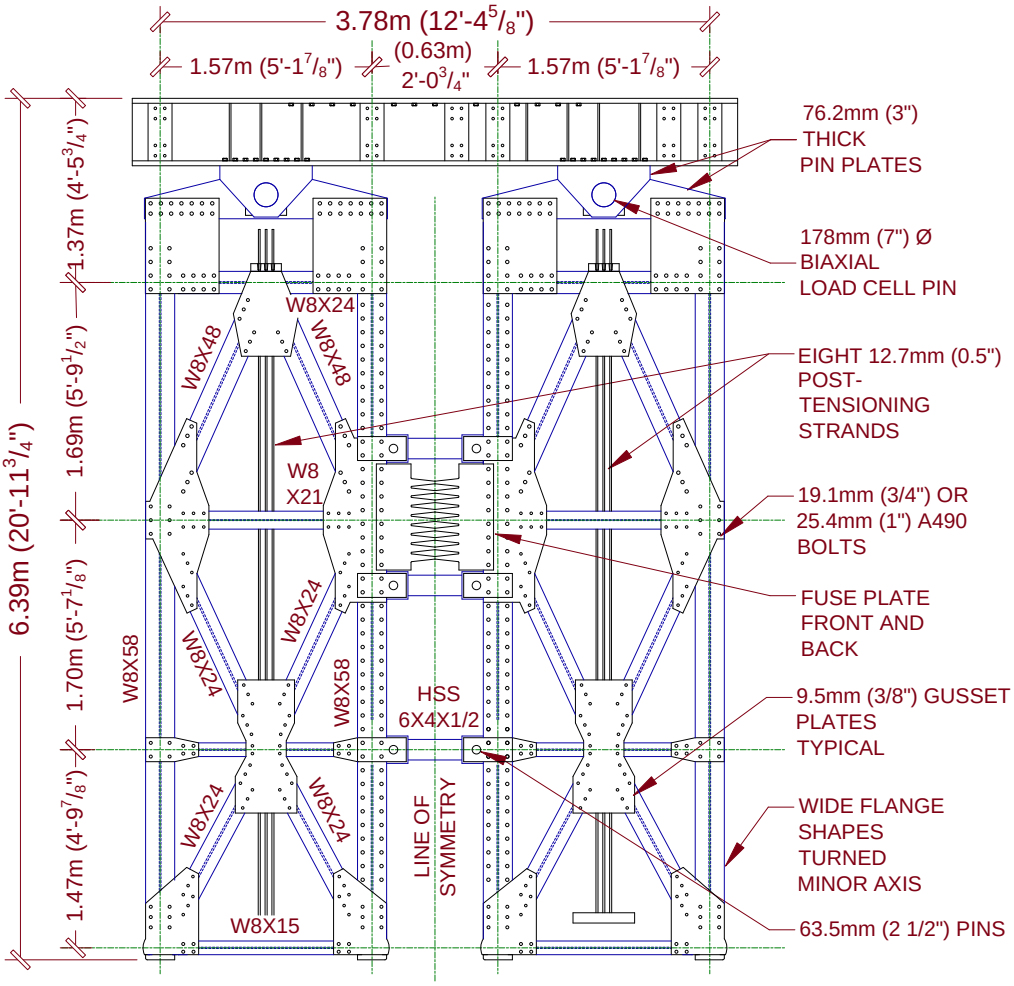

Figure 4.6 Specimen Design Information Including Member Sizes Showing the Series A Configuration

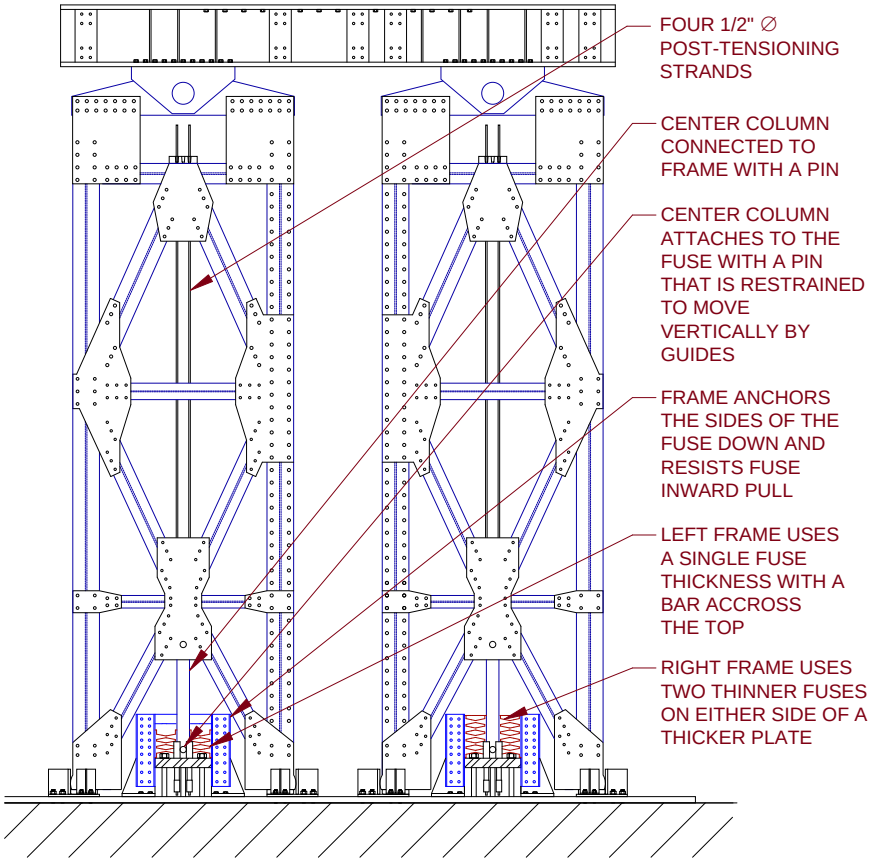

Figure 4.7 Single Frame Configuration Used in the B Series Specimens

4.3.4 Key Details of the Experimental Test Specimen

4.3.4.1 Post-Tensioning Anchorage

An important goal of the experimental program was to examine and improve details not typical in steel construction such as post-tensioning anchorage and uplifting column bases. The 12.7 mm (½") post-tensioning strands are anchored at the top of the specimen using two-part wedges that fit in conical shaped holes machined in a thick anchorage plate as shown in Figure 4.8. The wedges were obtained from Dywidag along with details for the shape of the wedge shaped holes. Machining the conical holes required the use of two specialized tapered reamers. The wedges before and after installation are shown on the right side of Figure 4.9. The top anchorage plate was welded to gusset plates which were welded to the beam and bolted to the braces. The post-tensioning strands passed through a large hole in the beams and connections as they extended down to the lower anchorage plate so as to allow sufficient clearance that the strands were not contacted along their length during the rocking motion.

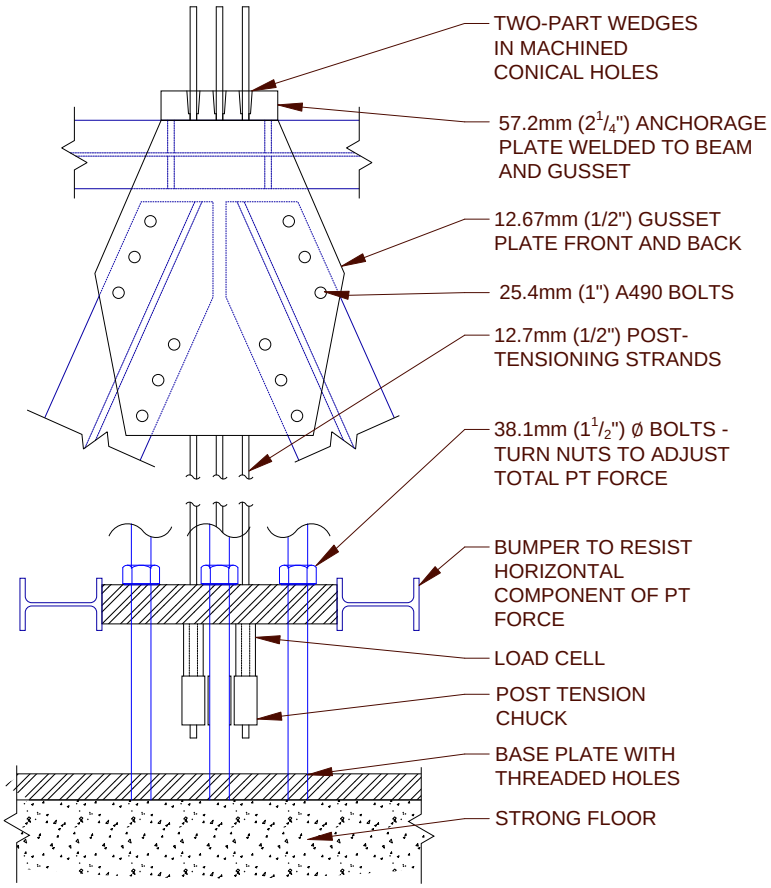

Figure 4.8 Details of the Post-Tensioning Anchorage

The strands pass through the anchorage plate to be anchored below by post-tension chucks. The post-tension chuck, as shown in the top left portion of Figure 4.9, consists of a cylindrical casing that has a conical shape on its interior, a three-part wedge held together by a rubber band, and a spring loaded cap that pushes the wedges down. Load cells were designed and built to measure the load in each post-tensioning strand and were placed between the chuck and the anchorage plate. The anchorage plate is held down by six 38.1 mm (1-1/2") threaded anchor rods. Each anchor rod was machined down to a smooth 31.8 mm (1-1/4") diameter for 152 mm (6") length at which location two strain gages were applied to provide a second measurement for the verification of post-tension force. This entire assembly is shown in the bottom left portion of Figure 4.9.

Figure 4.9 Post-Tension Chucks (top left), Wedges (top right), Installed Chucks (bottom left), and Installed Wedges (bottom right)

4.3.4.2 Column Base

The base connection is shown in Figure 4.10. The column, brace, and beam are bolted to a 25.4 mm (1") thick gusset plate that has a 127 mm (5") radius on the edge facing the stiffened bumper. The curved portion is machined and acts as the horizontal bearing surface between the frame and the bumper. A 38.1 mm (1-1/2") thick base plate is welded to the gusset plates and has a 12.7 mm (½") bull nose on three sides. As the frame rocks, the vertical bearing surface is the bull-nosed edge pivoting on the base plate below.

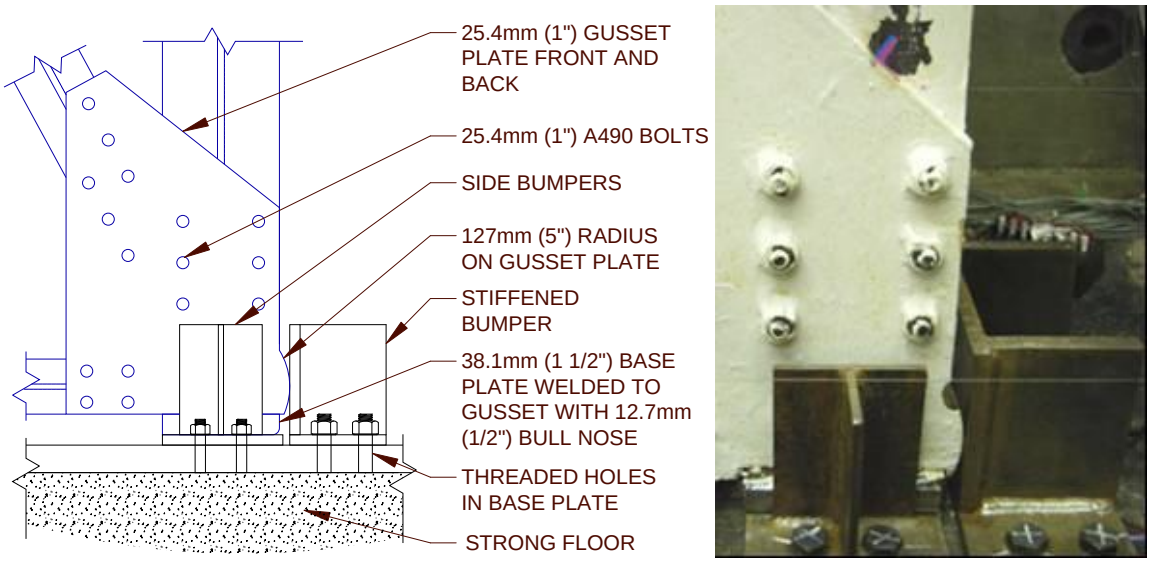

Figure 4.10 Column Base Detail Allowing Pivoting and Uplifting

4.3.4.3 Replaceable Fuse Plates

The fuses were designed based on the results of fuse component tests carried out at Stanford University. Stanford University conducted a testing program on a range of fuse materials and configurations (Ma et al. 2010c) as described in the literature review of Chapter 2. Fuse plates with diamond shaped cutouts exhibited outstanding plastic shear strain capacity and allowed adjustable shear force capacity. The shape of the cutouts, demonstrated in Figure 4.11, is designed to promote the initiation of inelastic action and plastic hinging at the quarter point away from areas of discontinuity. The reason for this is demonstrated in Figure 8.15.

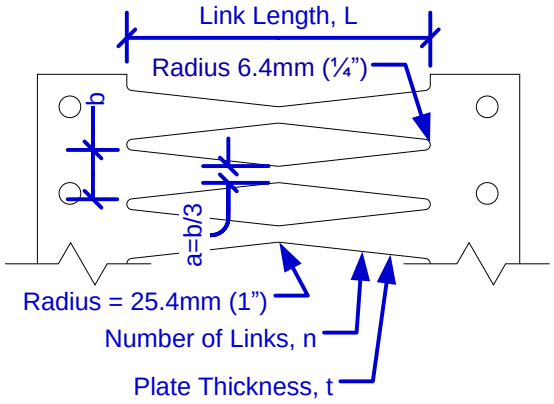

Figure 4.11 Fuse Geometry and Variable Definitions Used in Design

Since the plastic hinging is designed to occur at the quarter point of the fuse link, the shear capacity of the fuse is derived based on the plastic moment capacity at the quarter point of the fuse which is given in Equation (4.14) and simplified in Equation (4.15). The shear capacity of the fuse is calculated as given in Equation (4.16) and simplified in Equation (4.17). The definitions of the variables are given in Figure 4.11.

Fuses were designed using Equation (4.17) to have the total shear capacity for all fuses given in Table 4.4. The resulting fuse designs are given in Table 4.8. The fuse link geometry used for Specimen A1 through Specimen A7 was selected to match three of the Stanford fuse component tests, B09-56, B06-37, and B02-14, which performed well (Ma et al. 2010c). These three component test specimens, as well as the fuses for Specimens A1 through Specimen A7, use a link length, L=355.6 mm (14"), end depth, b=58.7 mm (2.31"), and middle depth, a=19.6 mm (0.77").

$$M_{p-qp} = \frac{\left[\frac{(b+b/3)}{2}\right]^2 t}{4} n\, F_{yp} \tag{4.14}$$

$$M_{p-qp} = \frac{1}{9} b^2 t n F_{yp} \tag{4.15}$$

$$V_{fp} = \frac{2M_{p-qp}}{L/2} \tag{4.16}$$

$$V_{fp} = \frac{4b^2 t}{9L} n F_{yp} \tag{4.17}$$

Table 4.8 Fuse Geometry and Design Shear Capacities

Specimen	Link Length, *L*, mm (in)	Depth at End, *b*, mm (in)	Depth at Middle, *a*, mm (in)	Thick-ness *t*, mm (in)	Number of Links *n*	Measured Yield Stress, F_{yp}, MPa (ksi)	Fuse Shear Capacity, $V_{fp\text{-}one}$, kN (kips)
A1	355.6 (14)	58.7 (2.31)	19.6 (0.77)	6.4 (0.25)	8	265 (38.5)	58.1 (13.1)
A2	355.6 (14)	58.7 (2.31)	19.6 (0.77)	15.9 (0.625)	10	310 (45)	212 (47.7)
A3	355.6 (14)	58.7 (2.31)	19.6 (0.77)	15.9 (0.625)	7	310 (45)	149 (33.4)
A4	355.6 (14)	58.7 (2.31)	19.6 (0.77)	25.4 (1.0)	7	296 (43)	227 (51.1)
A5	355.6 (14)	58.7 (2.31)	19.6 (0.77)	15.9 (0.625)	8	310 (45)	170 (38.2)
A6	355.6 (14)	58.7 (2.31)	19.6 (0.77)	6.4 (0.25)	8	265 (38.5)	58.1 (13.1)
A7	355.6 (14)	58.7 (2.31)	19.6 (0.77)	6.4 (0.25)	8	265 (38.5)	58.1 (13.1)
B1	152.4 (6)	42.9 (1.69)	14.3 (0.56)	19.1 (0.75)	3	296 (43)	90.8 (20.4)
B2	152.4 (6)	47.6 (1.87)	15.9 (0.63)	4.8 (0.188)	5	255 (37)	40.2 (9.0)

4.4 Specimen Construction

4.4.1 Frames

The frames were fabricated by Tefft Iron and Steel of Tefft, Indiana. The majority of the specimen was fabricated with methods and tolerances typical to steel construction. Portions that required machining such as the milled based plates, base gusset plates with machined 127 mm (5") radius, conical holes in the top post-tension anchorage plate, and high tolerance pin connections at the top were fabricated at the UIUC Civil and Environmental Engineering Machine Shop. Fuses were manufactured separately and are discussed in the next section.

4.4.2 Fuses

The fuses were manufactured by Wagner Machine Company of Champaign, Illinois using water cutting technology. Water cutting capabilities were found to be common in large machine shops and therefore not expensive, ranging in price from approximately $80 for the 6.4 mm (¼") thick specimen A1 fuses to as much as $500 for the 25.4 mm (1") thick specimen A4 fuses. The left side of Figure 4.12 shows the water cutting process. Different levels of water cutting quality are possible depending on the speed at which the water jet moves. Inelastic action during loading is primarily concentrated along the length of the butterfly link so all of the diamond shaped cutouts were cut with the highest waterjet cutting quality. The outside straight edges of the fuses were cut using a low quality setting. It was also required that the cutting not begin near the fuse links.

Figure 4.12 Photo of Water Cutting (Left) and Finished Fuse (Right)

4.4.3 Ancillary Tests

4.4.3.1 Post-Tension Strand Material Tests

Four ancillary tension coupons were cut from the same post-tensioning strand material that was used in the large-scale specimen. The material tests took place at the Newmark Structural Engineering Laboratory (NSEL) at the University of Illinois at Urbana-Champaign (UIUC) on December 20, 2007 using the 445kN (100 kip) capacity MTS machine. The tests were performed according to ASTM standard A370-07a Section A7 (ASTM 2007), which outlines the method for testing multi-wire strand for pre-stressed concrete. The monotonic loading rate started at 3.8 mm/min (0.15 in/min) and was raised incrementally to 10.2 mm/min (0.4 in/min) during each test. A 51 mm (2") gage length and a 610 mm (24") gage length extensometer were used to measure strain during the loading. Both are shown in Figure 4.13, and a representative force-strain relationship is shown in Figure 4.14. The results of the post-tensioning strand material tests are given in Table 4.9. Additional information about the ancillary tests on post-tensioning strand coupons is located in Tanamal et al. (2007).

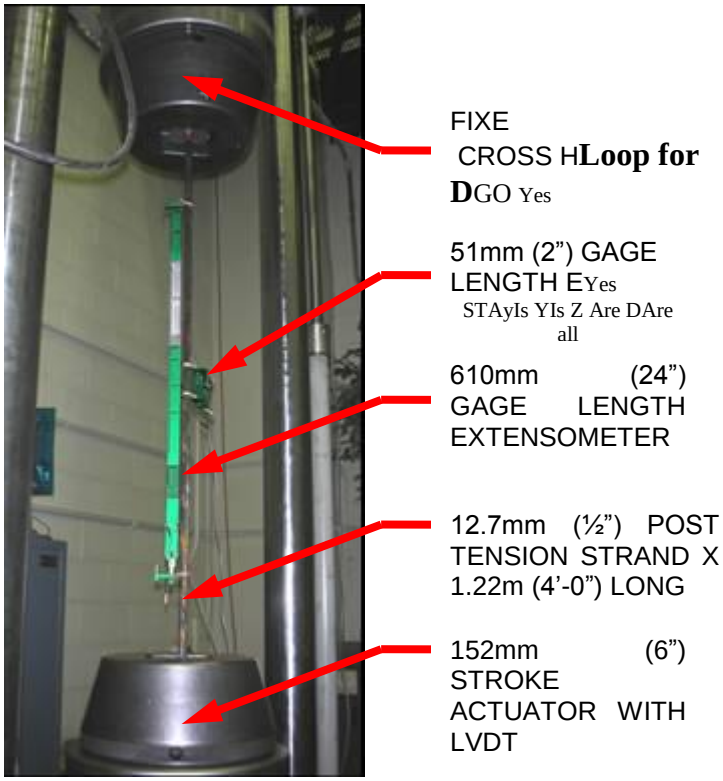

Figure 4.13 Post-Tension Strand Material Test Setup

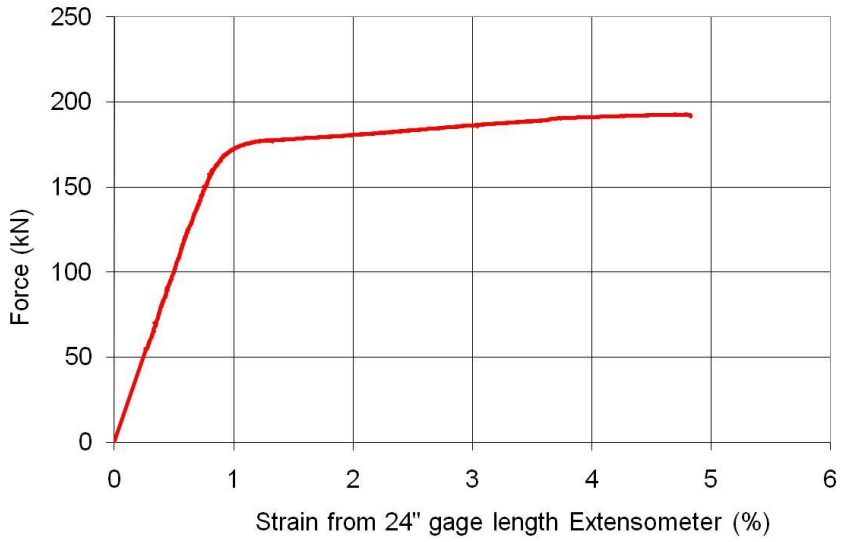

Figure 4.14 Representative Force-Strain Relationship from Post-Tension Strand Material Tests

Table 4.9 Summary of the Results of the Post-Tension Strand Material Tests

Test	Modulus of elasticity, GPa (ksi)	Max Load, kN (kips)	Yield Load, kN (kips)	Elongation (%)
1	200.6 (29,100)	191.7 (43.1)	173.5 (39.0)	-
2	199.3 (28,900)	192.6 (43.3)	171.7 (38.6)	4.73
3	206.8 (30,000)	194.4 (43.7)	174.8 (39.3)	4.82
4	202.0 (29,300)	193.5 (43.5)	173.9 (39.1)	4.78
Average	202.0 (29,300)	193.1 (43.4)	173.5 (39.0)	4.78

The minimum values for yield strength and elongation required to satisfy ASTM A416/A416M-06 (ASTM 2006) are 172.2 kN (37,710 lbs) and 3.5% respectively. All four tests exceeded these minimum values. Copper tubing was used to protect the grip ends during testing, but failure still occurred at the end of the grips.

These tests were intended to test the behavior of the material and not the behavior of the post-tensioning system which heavily depends on the type of anchorage used. During the large-scale testing program it was found that strand fracture can occur at elongations well below the elongations experienced in the material tests.

4.4.3.2 Fuse Plate Material Tests

Sixteen dogbone-shaped tension coupon tests were conducted on the fuse plate material. The tests took place at the Newmark Structural Engineering Laboratory (NSEL) at the University of Illinois at Urbana-Champaign (UIUC) in February, 2008. The 25.4 mm (1") thick coupons were tested using the 2669kN (600 kip) capacity MTS machine and the 445kN (100 kip) capacity MTS machine was used to test the 19.1 mm (3/4"), 15.9 mm

(5/8”), 6.4 mm (1/4”), and 4.8 mm (3/16”) thick coupons. ASTM standard A370-07a was used to define the geometry of the tensile coupons. Gage lengths for instruments, types of instrumentation, speed of testing, and procedures for computing pertinent values from the data were based on ASTM standard E8-01 (ASTM 2001). The Structural Stability Research Council (SSRC) Technical Memorandum Number 7 was used to determine static yield strength (Galambos, 1998). Additional information about the ancillary tests on fuse plate coupons is located in Tanamal et al. (2009).

Figure 4.15 shows the tension specimens. The specimens were cut using a waterjet cutting machine at Wagner Machine Company in Champaign, Illinois. Specimens were cut from the same material used for the fuses. The geometry of the reduced section was the same for all specimens, but the grip section was enlarged for the 25.4 mm (1”) thick plate to allow more gripping area for use in the 2669kN (600 kip) machine. Overall outside dimensions of the coupons were 584 mm x 76.2 mm (23”x3”) for the 6.4 mm (¼”) thick and 15.9 mm (5/8”) specimens and 787 mm x 102 mm (31”x4”) for the 25.4 mm (1”) thick specimens. The reduced section was 38.1 mm (1-1/2”) wide and 229 mm (9”) long between fillets.

Figure 4.15 Tension Coupons for 25.4 mm (1”) Thick (left), 15.9 mm (5/8”) Thick (middle), and 6.4 mm (¼”) Thick Fuses (right)

A 51 mm (2”) gage length extensometer and an 203 mm (8”) extensometer was used to measure strain as shown in Figure 4.16. The monotonic loading rate started at 1.3 mm/min (0.05 in/min) and was raised to 12.7 mm/min (0.5 in/min) after yielding. In accordance with the SSRC appendix (Galambos, 1998), loading was halted at multiple points during yielding to get static yield strength. The 15.9 mm (5/8”) thick plate did not exhibit a defined yield plateau, so the yield stress was calculated using the 0.2% offset method. The results of the ancillary tests are summarized in Table 4.11, Table 4.12, and Table 4.14. Necking and fracture occurred in the middle of the reduced section on all ten tension specimens.

Figure 4.16 Photograph of the Fuse Material Tension Test

Table 4.10 Summary of Results from 4.8 mm (3/16”) Thick Fuse Material Tests

4.8 mm (3/16") Test	Static yield strength, MPa (ksi)	Dynamic yield strength, MPa (ksi)	Ultimate strength, MPa (ksi)	% Elongation based on 8” Extensometer
1	245 (35.5)	255 (37.0)	360 (52.2)	30.2
2	261 (37.9)	272 (39.4)	363 (52.6)	30.6
3	245 (35.5)	255 (37.0)	360 (52.2)	31.1
average	250 (36.3)	261 (37.8)	361 (52.3)	30.6

Table 4.11 Summary of Results from 6.4 mm (1/4”) Thick Fuse Material Tests

6.4 mm (1/4") Test	Static yield strength, MPa (ksi)	Dynamic yield strength, MPa (ksi)	Ultimate strength, MPa (ksi)	Yield Point Elongation (%)	% Elongation based on 8” Exten-someter
1	257 (37.3)	269 (39.0)	420 (60.9)	0.56	27.8
2	263 (38.1)	277 (40.2)	429 (62.2)	0.43	28.4
3	260 (37.7)	274 (39.8)	423 (61.4)	0.45	28.9
4	261 (37.9)	276 (40.0)	424 (61.5)	0.47	29.0
average	261 (37.8)	274 (39.8)	424 (61.5)	0.48	28.5

Table 4.12 Summary of Results from 15.9mm (5/8”) Thick Fuse Material Tests

15.9 mm (5/8") Test	Static yield strength, MPa (ksi)	Dynamic yield strength, MPa (ksi)	Ultimate strength, MPa (ksi)	Yield Point Elongation (%)	% Elongation based on 8” Extensometer
1	303 (43.9)	313 (45.4)	403 (58.5)	0.44	28.2
2	309 (44.8)	319 (46.2)	411 (59.6)	0.39	24.6
3	308 (44.6)	319 (46.3)	410 (59.5)	0.41	24.9
average	306 (44.4)	317 (46.0)	408 (59.2)	0.41	25.9

Table 4.13 Summary of Results from 19.1 mm (3/4”) Thick Fuse Material Tests

19.1 mm (3/4") Test	Static yield strength, MPa (ksi)	Dynamic yield strength, MPa (ksi)	Ultimate strength, MPa (ksi)	Yield Point Elongation (%)	% Elongation based on 8” Extensometer
1	267 (38.7)	276 (40.0)	366 (53.1)	0.66	29.0
2	288 (41.8)	299 (43.3)	389 (56.4)	0.68	27.6
3	319 (46.2)	327 (47.4)	415 (60.2)	0.92	23.9
average	291 (42.2)	301 (43.6)	390 (56.6)	0.75	26.8

Table 4.14 Summary of Results from 25.4 mm (1”) Thick Fuse Material Tests

25.4 mm (1") Test	Static yield strength, MPa (ksi)	Dynamic yield strength, MPa (ksi)	Ultimate strength, MPa (ksi)	Yield Point Elongation (%)	% Elongation based on 8” Extensometer
1	-	297 (43.1)	495 (71.8)	1.25	29.4
2	293 (42.5)	304 (44.1)	495 (71.8)	1.47	28.3
3	-	301 (43.7)	498 (72.2)	1.32	28.7
average	293	301 (43.6)	496 (71.9)	1.35	28.8

4.4.4 Post-Tensioning Process During Specimen Construction

The post-tensioning strands in the specimen were stressed from above the top anchor plate as shown on the right of Figure 4.17. The post-tension jack, shown on the left of Figure 4.17, uses an automatic seating mechanism consisting of a half circle protrusion that shoots forward when the strand is released. As is common in post-tensioning, some force was lost as the wedges found traction on the strand and seated in the conical hole. The post-tension load cells were used to monitor the amount of load held in the strands and the force was increased in steps until the target load was acquired. A calibrated pressure gage on the post-tension pump was monitored and found to correlate well with the load cell reading.

Figure 4.17 Post-Tensioning Jack (left), and Post-Tensioning in Progress (right)

4.5 Timeline for Construction and Testing

The process for the procurement of materials, shop drawings, fabrication, and erection took place from August 2007 to July 2008. The tests were conducted between August 2008 and March 2009. The timeline of events was as follows:

- February 2007 – First set of design drawings was completed. Several refinements to the design were made in the subsequent months based on using one LBCB instead of two, more accurate computational modeling, and further investigation of design detailing.
- August 9, 2007 – The design drawings were sent to the fabricator.
- August to October, 2007 - Steel material was procured.
- November 28, 2007 - Final shop drawings were completed by M. C. Detailers.
- December to January - Fabrication was conducted at Tefft Bridge and Iron, Infra-Metals, and Munster Steel Co. Bolts, nuts and washers were obtained from Textron / Flexalloy Fastener Systems Division.
- February 6, and February 27, 2008 - Fabricated frames and materials were delivered to the University of Illinois.
- March to April, 2008 - Whitewashing was conducted and strain gages were applied.
- May 15, 2008 – The MUST-SIM strong wall and LBCB became available for this project.
- May to July, 2008 - The UIUC Civil and Environmental Engineering Machine Shop performed final fabrication, fit-up, and erection.
- July, 2008 – Test runs with the LBCB
- August 4, 2008 to August 6, 2008 – Testing Specimen A1
- August 25, 2008 to August 27, 2008 – Testing Specimen A2
- September 8, 2008 to September 12, 2008 – Testing Specimen A3

- October 1, 2008 to October 3, 2008 – Testing Specimen A4
- November 14, 2008 to November 17, 2008 – Testing Specimen A5
- December 19, 2008 to December 20, 2008 – Testing Specimen A6
- January 28, 2009 to January 30, 2009 – Testing Specimen A7
- March 9, 2009 to March 11, 2009 – Testing Specimens B1 and B2

4.6 Loading Protocol

Testing was conducted with quasi-static cyclic loading and hybrid simulation. The quasi-static loading protocol consists of cyclic displacement histories designed to approximate the cumulative inelastic fuse shear strain expected during design level earthquakes as described in the next section. Hybrid simulation testing was performed in which the experimental setup was linked to two computational components and computationally subjected to earthquake ground motions. The two computational models simulated the lateral forces due to the P-Δ effect and the lateral resistance of the rest of the building due to interior wall partitions and simple shear beam-to-column connections. These tests were conducted to examine and validate the self-centering performance of the controlled rocking system during real earthquake ground motions in the presence of ambient building resistance and destabilizing P-Δ effects.

4.6.1 Quasi-Static Cyclic Loading Protocol

For eccentrically braced frames (EBF), the cumulative link rotation demand has been found to be an important parameter in the testing of shear dominated links (Richards and Uang 2006). The fuses that are part of the proposed controlled rocking system have similarities to shear-dominated EBF links in function. Richards and Uang (2006) created a quasi-static loading protocol that simulates the cumulative inelastic fuse shear strain and total number of inelastic cycles as a 90^{th} percentile earthquake with a 10% chance of exceedance in 50 years. The primary purpose for this loading protocol is to ensure that tested shear links do not fail prematurely compared to the response that might be expected during earthquake ground motions. The loading sequence in Appendix S of the AISC Seismic Provisions (AISC 2005) is based on the work by Richards and Uang (2006).

The loading protocol consists of 38 cycles up to the target fuse shear strain, then continues loading in 2% increments of fuse shear strain with one cycle of loading at each step. Since the target EBF link rotation angle was based on the 90^{th} percentile ground motion with a 10% chance of exceedance in 50 years, a loading protocol target for the controlled rocking tests was selected based on similar criteria. The target fuse shear strain was determined to be 9% for a representative specimen configuration with A/B=2.5, OT=1.0, and SC=1.0 using Figure 2.13 to find the fuse shear strain demand that correlates to the median plus one standard deviation for the earthquake motion that has 10% probability of exceedance in 50 years. The target fuse shear strain in this case, is given as the shear strain between column centerlines. The resulting fuse shear strain loading protocol has 18 inelastic cycles with shear strain greater than 0.75% and a cumulative fuse shear strain of 110%. The displacement history and fuse shear strain

goals for specimen A1 are shown in Figure 4.18. The shear strain targets reported in Figure 4.18 are given as shear strain between the bolts connecting the fuse to the columns.

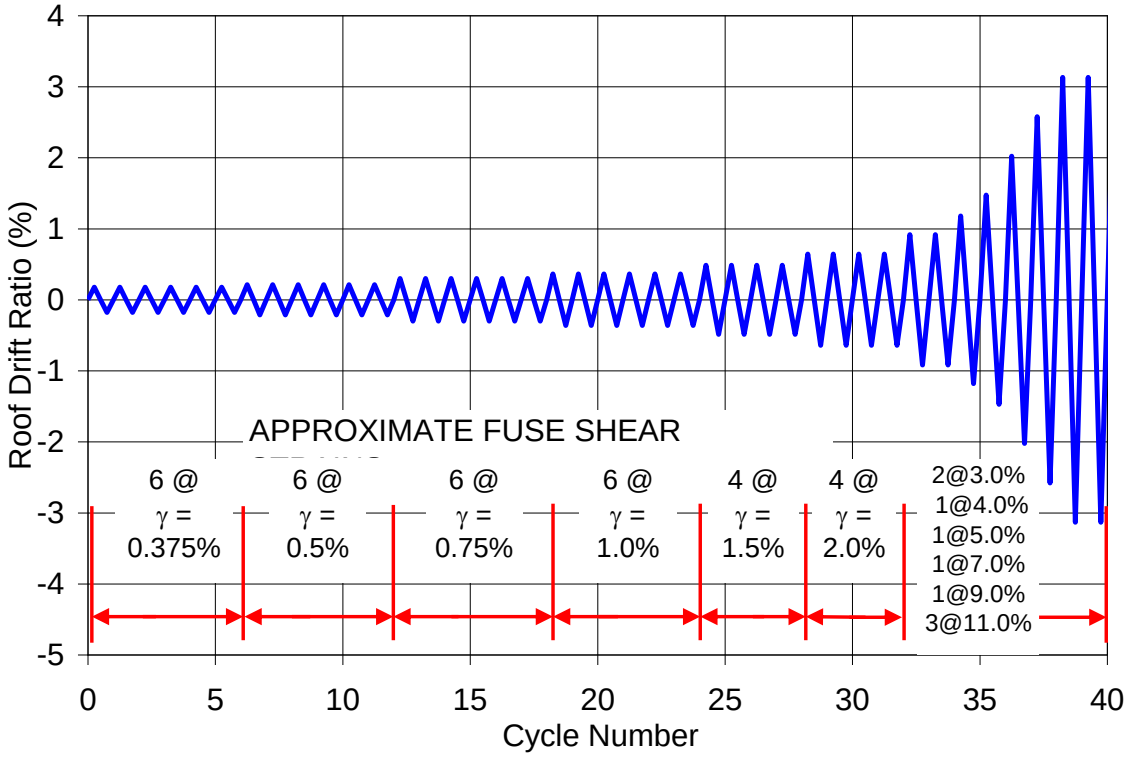

Figure 4.18 Loading Protocol for Specimen A1

4.6.2 Hybrid Simulation Test Setup for Specimen A5

Hybrid simulation testing was conducted using the UI-SIMCOR software (Kwon et al. 2007). A computational model of a leaning column was created in OpenSees to simulate the P-Δ effect. The leaning column model consisted of a single near-rigid element with a pinned-base and height equal to the height of the prototype structure. A single degree-of-freedom model was chosen over a leaning column with nodes at each floor to simplify the communications between OpenSees and UI-SIMCOR and to eliminate higher modes. Displacements were applied only at the top of the specimen so it was not possible to link the specimen horizontal degrees of freedom at the intermediate floors to the computational model.

The mass and gravity loads given in Table 4.1 and shown on the left of Figure 4.19 were converted to an equivalent SDOF system as shown on the right of Figure 4.19. The equivalent SDOF mass was found by applying an arbitrary ground acceleration, determining the moments about the base due to inertial loads, and setting them equal to the moments created by the SDOF system subjected to the same acceleration:

$$M_{3DOF} = \left(\sum m_i h_i\right) a = 11511\, a \ \text{kN-m} \tag{4.18}$$

$$M_{SDOF} = 11.89\, m\, a \quad \text{kN-m} \tag{4.19}$$

$$m = 968 \frac{\text{kN-sec}^2}{\text{m}} \quad = 68.15 \frac{\text{k-sec}^2}{\text{ft}} \tag{4.20}$$

The equivalent gravity loads were found by applying an arbitrary rotation of the column relative to vertical, *b*, determining the P-Δ moments about the base due to the gravity loads, and setting them equal to the P-Δ moments created by the SDOF system subjected to the same rotation angle.

$$M_{3DOF} = \sum F_i h_i \sin(b) = 140800 \sin(b) \quad \text{kN-m} \tag{4.21}$$

$$M_{SDOF} = 11.89 F \sin(b) \tag{4.22}$$

$$F = 11860\text{kN} \quad = 2662 \text{ kips}$$

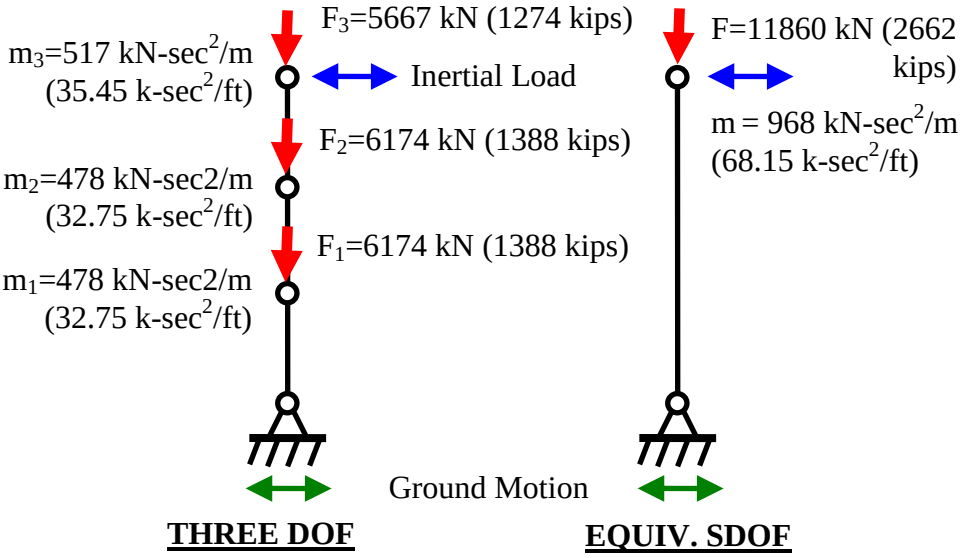

Figure 4.19 Converting Mass and Gravity to an Equivalent SDOF System

For specimen A5, UI-SIMCOR computationally linked the top of the OpenSees leaning column model to the roof drift of the experimental setup and assigns mass to this location which is called a control node in UI-SIMCOR. UI-SIMCOR uses the α-OS method (Combescure and Pegon 1997) for numerical integration. In this method, the displacement for the first step is computed without using the restoring force. This displacement is then imposed on the test specimen and an applied force is measured from the experiment. Similarly the displacement at the control node is applied to the computational model and the associated applied force is calculated. The displacement for the next step is computed using the total current applied force and the time step is incremented. The time step used for the hybrid simulation tests of Specimen A5 was set to 0.005 seconds which is equal to the time increment for the ground motion that is

described in a subsequent section. The maximum size of the displacement increment applied to the specimen in any given substep is discussed in a subsequent section.

To reduce the chances of errors in scaling the ground motion, periods used for damping, computational model geometry, and computational model gravity load, the time stepping algorithm and OpenSees models were both conducted at prototype scale. Similitude scaling was only required in the interaction between UI-SIMCOR and the test specimen. Target displacements computed for the control node were multiplied by the length scale factor, l_r, as given in Table 4.5 before being applied to the specimen. Similarly, the measured forces were divided by the force scale factor, F_r before being incorporated in the time-stepping calculations.

4.6.3 Hybrid Simulation Test Setup for Specimen A6

The hybrid simulation test setup for Specimen A6 incorporated the SDOF leaning column from the previous section along with a three-story one-bay model that simulated the lateral resistance of the rest of the building. As the elements of a building become inelastic, they then resist the ability of the restoring force to bring the building back to center. One of the purposes of the Specimen A6 hybrid simulation was to examine whether the resistance of the rest of the building would hamper the ability of the controlled rocking frame to self-center. The building resistance due to partition walls and simple shear beam-to-column connections was included in the model. The computational model is shown in Figure 4.20 and consists of diagonal braces representing the resistance of partitions tributary to one bay, and rotational springs which represent the resistance of the simple shear beam to column connections.

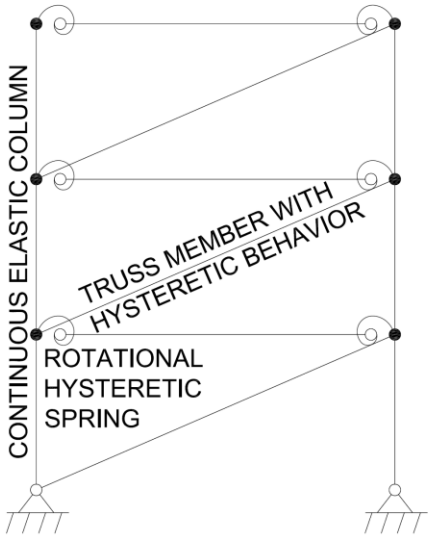

Figure 4.20 Computational Model Approximating the Building Resistance Used in the Hybrid Simulation Tests

The average density of partition walls in an office building was determined by examining the architectural floor plan for one floor of a high rise building in San

Francisco. On average there was approximately 9.14 lineal meters (30') of partition wall in each direction contained in a 9.14m x 9.14m (30' x 30') area which represents one bay of the prototype building used in this study. An experimental study that represents typical office partition construction with gypsum board over metal studs (Gad 1999) was used to calibrate the diagonal brace hysteretic response. The test used 2.44m x 2.44m (8'x8') panels. The pinching4 material was used in OpenSees with four points defined along the backbone curve, reloading stiffness degradation and unloading stiffness degradation. The calibrated response is shown in Figure 4.21 compared to the experimental response adapted from Gad (1999). The OpenSees pinching model had the following parameters:

- Backbone stresses are 7.08 kPa, 15.3 kPa, 25.1 kPa, and 21.8 kPa
- Corresponding backbone strains are 0.00015, 0.0012, 0.0039, and 0.0057 mm/mm.
- OpenSees parameters for the Pinching4 material, rdispp=0.6, rforcep=0.45, and uforcep=0.1

The partition was implemented as a truss element with an area equal to one square meter. The backbone was modified as described below to be input into the model shown in Figure 4.23.

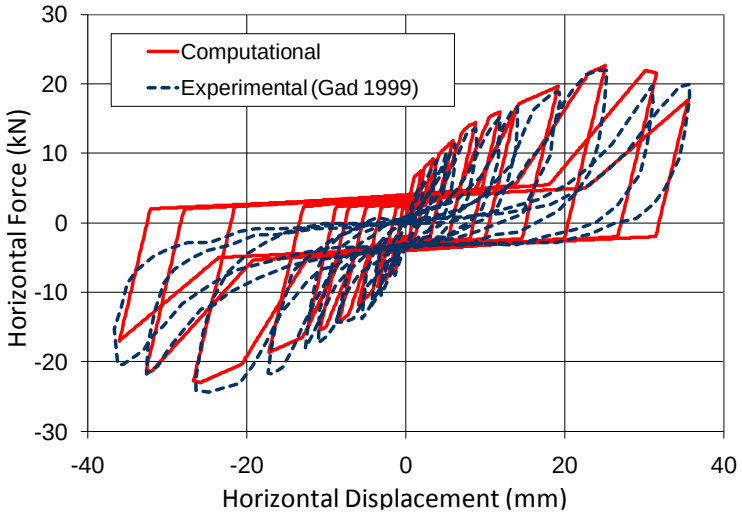

Figure 4.21 Calibration of the Partition Response to Experimental Curve

A study conducted by Liu and Astaneh (2000) provides experimental data for simple shear beam-to-column connections with and without floor slabs. The tests used a W18x35 beam with four 22 mm (7/8") diameter A325 bolts in a single shear plate connection to the minor axis of a W14x90 column. The slab consisted of 152 mm (6") lightweight concrete on metal deck. It was assumed that this configuration approximately represents the beam to column connections that might be used in the prototype building. The pinching4 material was used in OpenSees to calibrate the rotational spring with four points defined along the backbone curve. Reloading stiffness

degradation was incorporated for the case with slab, but not for the case without slab. The calibrated rotational spring responses are shown in Figure 4.22.

The opensees pinching model calibrated for the connection with slab had the following parameters:

- Backbone moments are 70 kN-m, 143 kN-m, 140 kN-m, 60 kN-m
- Corresponding backbone rotations are 0.005 rad, 0.023 rad, 0.035 rad, and 0.065 rad.
- Opensees parameters for the Pinching4 material, rdispp=0.6, rforcep=0.45, and uforcep=0.1

The opensees pinching model calibrated for the connection without slab had the following parameters:

- Backbone moments are 33 kN-m, 49 kN-m, 56 kN-m, 46 kN-m
- Corresponding backbone rotations are 0.006 rad, 0.03 rad, 0.06 rad, and 0.011 rad.
- Opensees parameters for the Pinching4 material, rdispp=0.6, rforcep=0. 5, and uforcep=0.3

The calibrated constitutive was modified as described below to be input into the model shown in Figure 4.23 as a rotational spring.

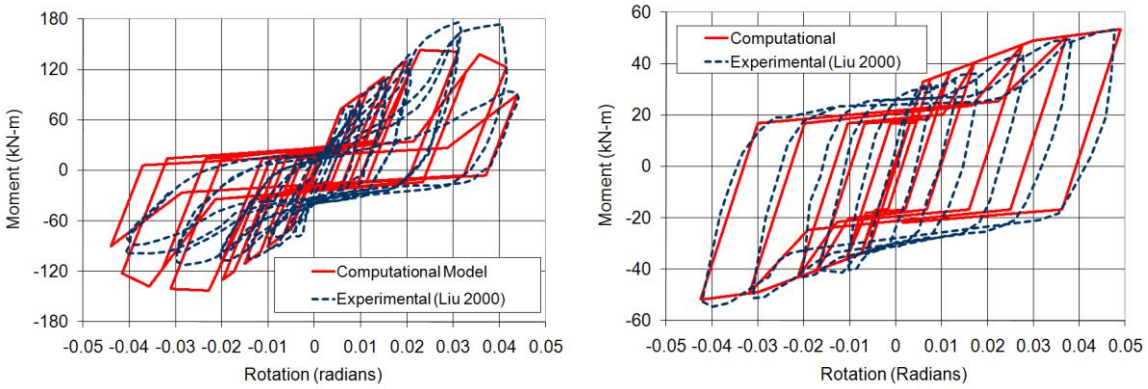

Figure 4.22 Calibration of the Beam-To-Column Connection Response With Slab (Left) and Without Slab (Right)

The experimental results for the case with the slab are unsymmetric because the moment capacity is greater when the slab is in compression. The computational model was made symmetric to represent the average of the positive and negative bending response. The experimental results for the case without slab were shifted on the moment axis by 23 kN-m because of applied gravity load. The experimental curve shown in Figure 4.22 has been shifted by this amount to facilitate the comparison to the analysis.

After calibration of the diagonal brace and rotational spring elements, the resistance of the 14 bays that are tributary to one controlled rocking frame, as shown in Figure 4.1, was lumped into the one bay model. The backbone forces for the diagonal brace that represent partition resistance were first multiplied by 9.14m / 2.44m (30'/8') to simulate 9.14m (30') of wall for one bay compared to the 2.44m (8') long test specimen. Then, assuming that all the partitions on the floor experience the same deformation

history, the backbone forces for multiple bays were also considered additive. The backbone forces for the diagonal brace representing one bay were therefore multiplied by 14 to represent all of the tributary bays of partition walls.

Similarly, the simple beam-to-column connections at a floor are assumed to experience the same rotation angle history so the backbone moments were multiplied by 14 to represent all of the tributary bays of beam-to-column connections. The parameters that govern degradation are unitless and therefore do not require scaling. The effectiveness of the lumping was validated by creating a separate two-dimensional model of the tributary prototype building frames, lined up one next to the other and linked together with multi-point constraints. An increasing cyclic roof displacement was applied and compared to the results from the lumped frame model and the two were found to produce identical results.

The hybrid test setup is shown schematically in Figure 4.23. The horizontal degrees of freedom associated with the top corner of the building resistance frame, the top of the leaning column, and the roof drift of the specimen were constrained using UI-SIMCOR to move together. This control node was subjected to ground motion accelerations. Since the time stepping algorithm was carried out at full-scale, scaling of the target displacements that are applied to the specimen as well as scaling of the force feedback was carried out as described in the previous subsection.

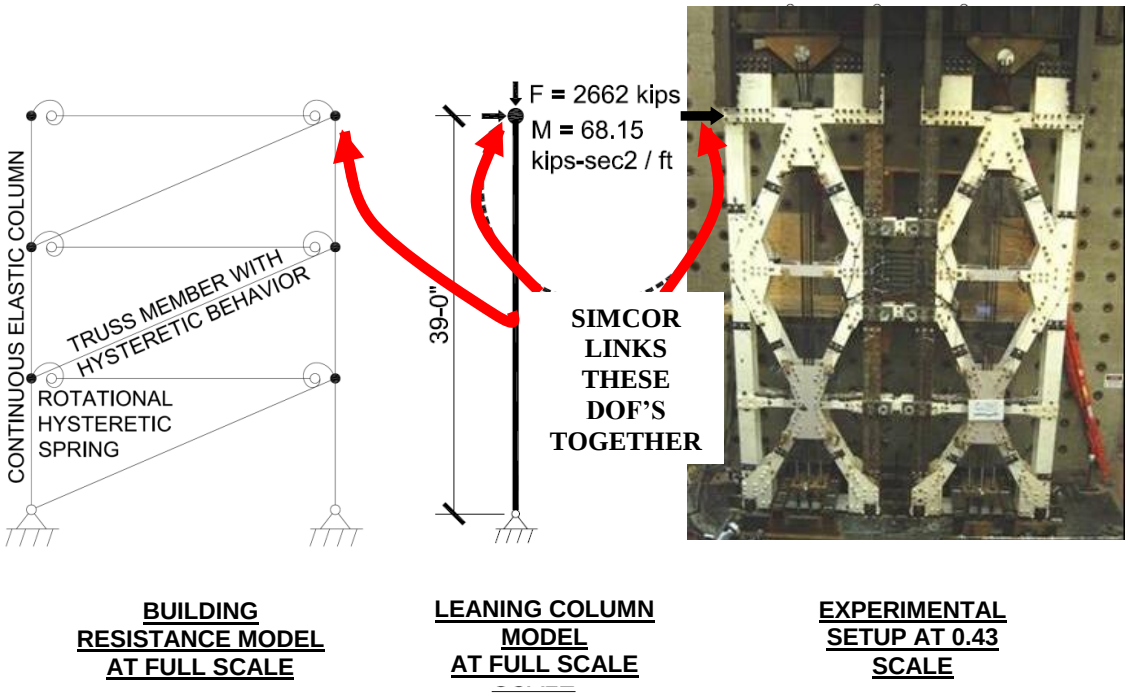

Figure 4.23 Schematic Representation of the Hybrid Simulation Setup Used for Specimen A6

4.6.4 Ground Motions for Hybrid Simulation Tests

The ground motion selected for the hybrid simulation testing was the JMA Kobe ground motion from the January 16, 1995 Kobe, Japan Earthquake. The primary reason for

selecting this ground motion was to match the ground motion that was used for the majority of the associated shake table tests conducted at E-Defense in Miki, Japan. The earthquake had a magnitude of M_w=6.8 and the JMA station is 18.27 km from the epicenter. The peak ground acceleration (PGA), peak ground velocity (PGV), and peak ground displacement (PGD) were 0.7105 g, 77.83 cm/sec, and 18.87 cm, respectively. The north-south component of the record, which is shown in Figure 4.24, was chosen because it has larger energy content in the period range of interest.

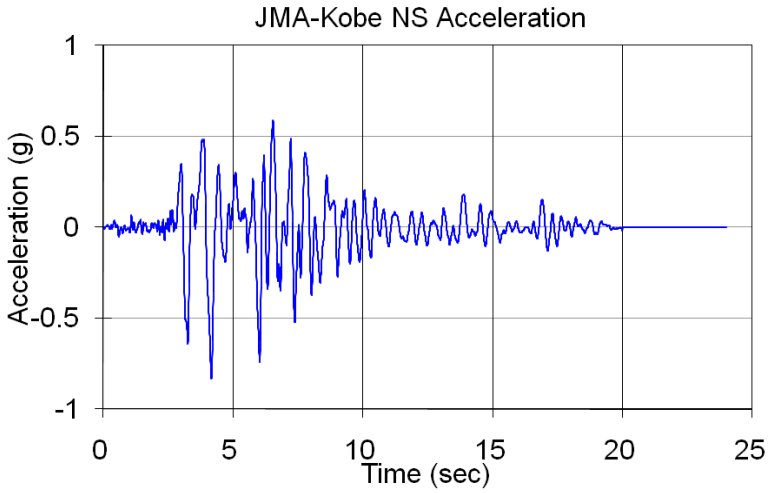

Figure 4.24 JMA Kobe Ground Motion Used in Pseudo-Dynamic and Hybrid Simulation Tests

The ground motion was scaled to best match the design spectrum over a range of periods. As the controlled rocking frames uplift, the stiffness and therefore the period of the system changes dramatically. The range of periods used the initial stiffness as a lower bound, and the secant stiffness at a roof displacement of 140 mm (5.5") as the upper bound. The displacement used in the upper bound was determined by subjecting the preliminary computational model of Specimen A5 to the largest scaling of the JMA Kobe ground motion that was to be used in the hybrid simulation test.

As shown in Figure 4.25, the initial stiffness of the analytical model of the specimen is 145 kN/mm (827 k/in). The secant stiffness at the upper bound displacement is 4.0 kN/mm (23 k/in). Using the above stiffnesses scaled to full scale and a full scale mass of 968 kN-sec^2/m (68.15 kip-sec^2/ft), the periods that this structure was found to experience ranged from 0.34 sec to 2.0 sec. The system acts as a single degree-of-freedom system, so an example of the calculation of natural period is as follows:

$$K = 145\frac{0.43}{0.43^2} = 337\ \frac{\text{kN}}{\text{mm}}$$

$$m = 968/1000 = 0.968\ \frac{\text{kN-sec}^2}{\text{mm}} \qquad (4.23)$$

$$\omega_n = \sqrt{\frac{k}{m}} = 18.4\ \frac{\text{rad}}{\text{sec}} \qquad T_n = \frac{2\pi}{\omega_n} = 0.34\ \text{sec}$$

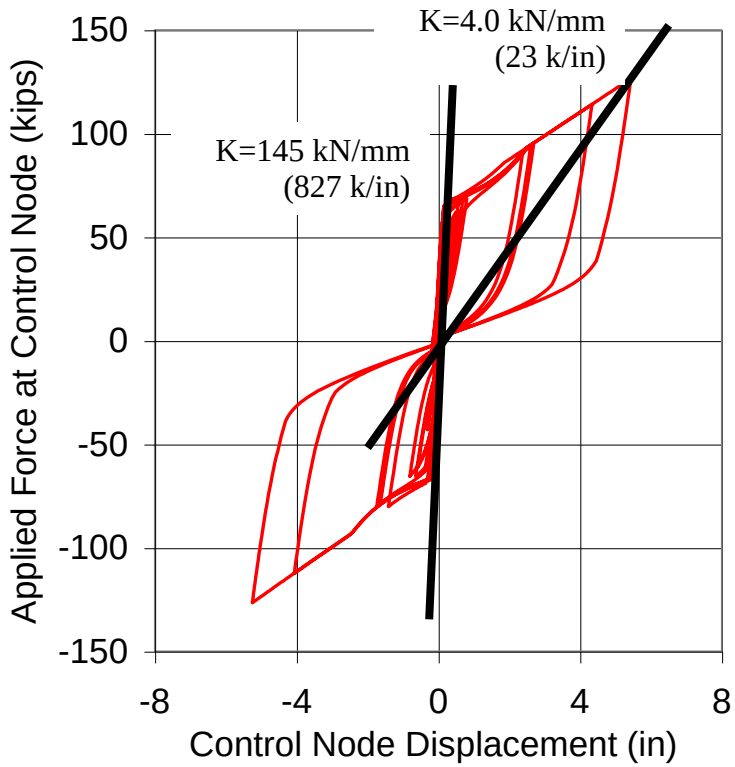

Figure 4.25 Initial Stiffness and Final Secant Stiffness for Simulated Response

A least squares method was used to find the scale factor that minimized the difference between the design spectrum and the scaled response spectrum. The scale factors for the hazards that have a 50% probability of exceedance in 50 years (50% in 50), 10% probability of exceedance in 50 years (10% in 50), and 2% probability of exceedance in 50 years (2% in 50), were found to be 0.200, 0.461, and 0.691 respectively, as shown in Figure 4.26. The least squares calculation took the following form:

$$MIN_F \left\{ \sum_{T=0.34\text{sec}}^{2.0\text{sec}} \left[\left(A_{DS}(t) - F\ A_{RS}(T) \right) \Delta T \right]^2 \right\} \qquad (4.24)$$

$A_{DS}(T)$ = Design Acceleration at Period T
F = Scale Factor
$A_{RS}(T)$ = Spectral Acceleration at Period T (5% Damping)
ΔT = Increment in the Period

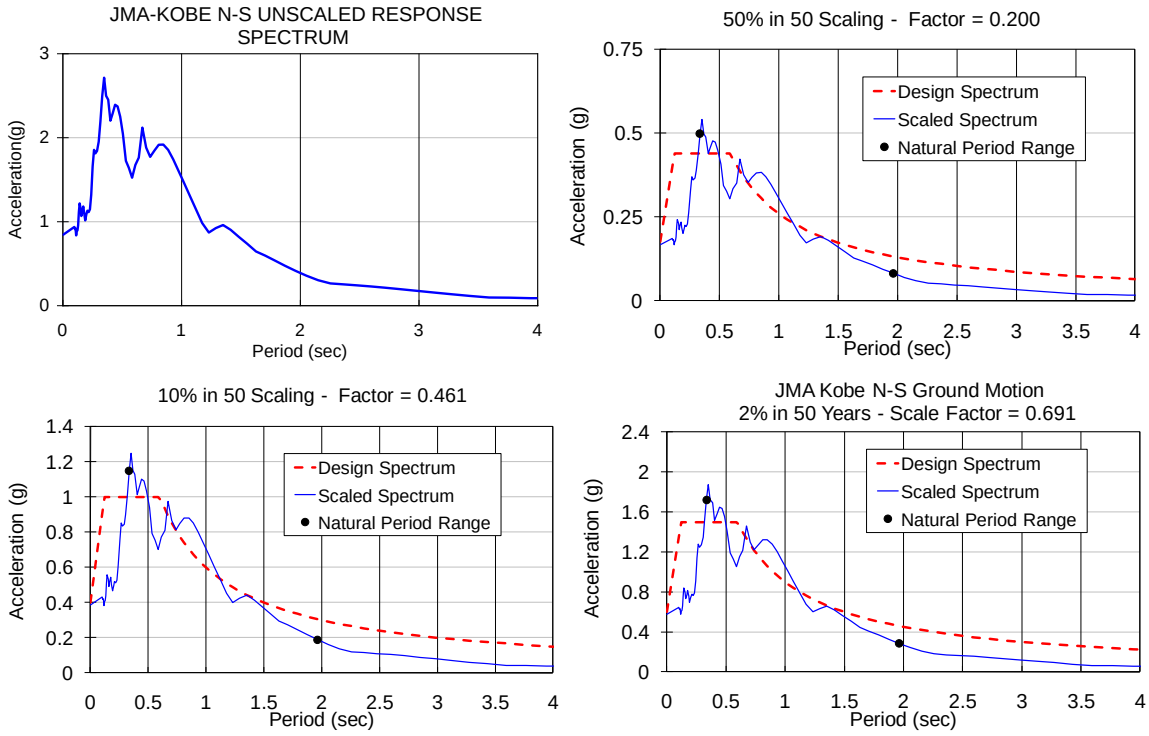

Figure 4.26 Unscaled 5% Damping Response Spectrum (upper left), 50% in 50 Years Scaling (upper right), 10% in 50 Years (lower left), and 2% in 50 Years (lower right)

4.7 Data Flow and Test Control

4.7.1 Data Flow

The large-scale test control was devised and implemented to synchronize as many components as possible. Figure 4.27 shows the data flow between computers, cameras, and instrumentation. The LBCB Plugin computer acted as the main test interface and was capable of sending commands to the LBCB Operations Manager software, triggers to take step data to the data acquisition (DAQ) computer, and triggers to take pictures to the camera control computers. Step data recorded by the DAQ software included measurements from the LBCB and control instrumentation that were acquired through a TCP / IP link with the Operations Manager Software. The typical large-scale test used 9 computers and the hybrid simulation tests used 10 computers:

- LBCB Plugin Computer
- LBCB Operations Manager Computer
- Shore Western DAQ Computer and Shore Western Control Computer
- Data Acquisition Computer
- Two Camera Control Computers
- Remote Data Viewer Computer which was also used to view webcam feeds through the internet
- Computer to run UI-SIMCOR (Only used during hybrid simulation tests)

- Krypton Computer

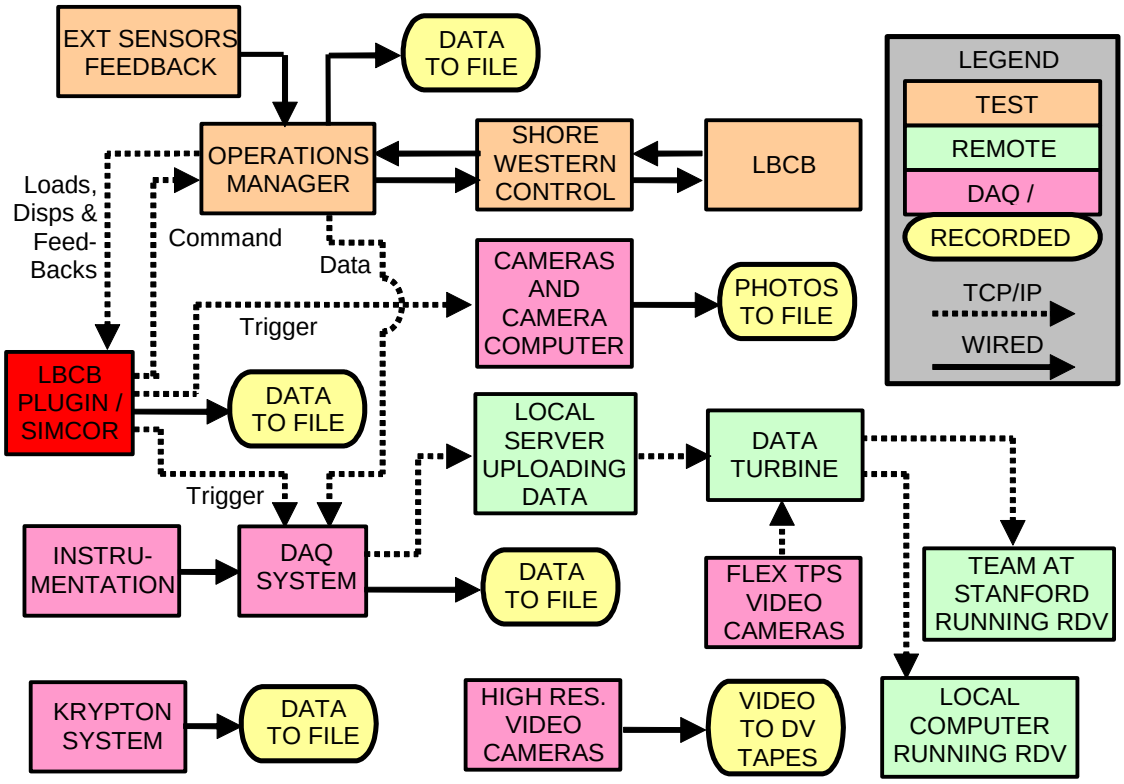

Figure 4.27 Data Flow Diagram for the Large-Scale Test

4.7.2 Test Control Architecture

The LBCB Plugin served as the main interface for running the large-scale tests, but it also carried out the mixed mode control using external feedbacks. The control scheme and mixed mode control algorithm used in the LBCB Plugin are discussed in this section.

The LBCB was only capable of applying force to the top of the specimen and it was not desirable to incorporate additional actuators at the floor levels. For this reason, the applied loads in the experiment do not exactly represent the loads that might be experienced in a building frame subjected to actual earthquake loading. However, since the controlled rocking system is designed to resist lateral loads through a global rocking mechanism rather than through energy dissipation mechanisms relying on interstory displacements, it was found that global overturning moment was a more important parameter than interstory shear. This point is supported by the fact that the frames were designed to remain elastic so the deformations of the frame were small relative to the rigid body rotation of the frame.

Also, since the lateral load is applied at a height above the roof of the specimen, the lateral load that corresponds to a given overturning moment will not equate to the lateral loads associated with the same overturning moment created by different loading patterns such as a lateral load at the roof level or inverted triangular loading. For these reasons, the results of the experiments are almost exclusively presented in the overturning moment domain to eliminate any ambiguity or load distribution dependence.

In an effort to better simulate the forces experienced in the frame members, it was desired to reduce the moments that are induced at the roof level of the specimen due to the eccentricity between the LBCB and the roof level. As shown in Figure 4.28, there is 1.36m (4'-5½") between the LBCB and the centerline of the roof beam with a true pin connection 0.71m (2'-4") below the LBCB. The pins make it impossible for the LBCB to create zero moments at the roof level while applying horizontal force, F_x. It is only possible, therefore, to eliminate the moment due to the eccentricity between the LBCB and the pins. This is accomplished by making one of the test control goals to maintain zero vertical force at the load cell pins (Fz1 = Fz2 = 0).

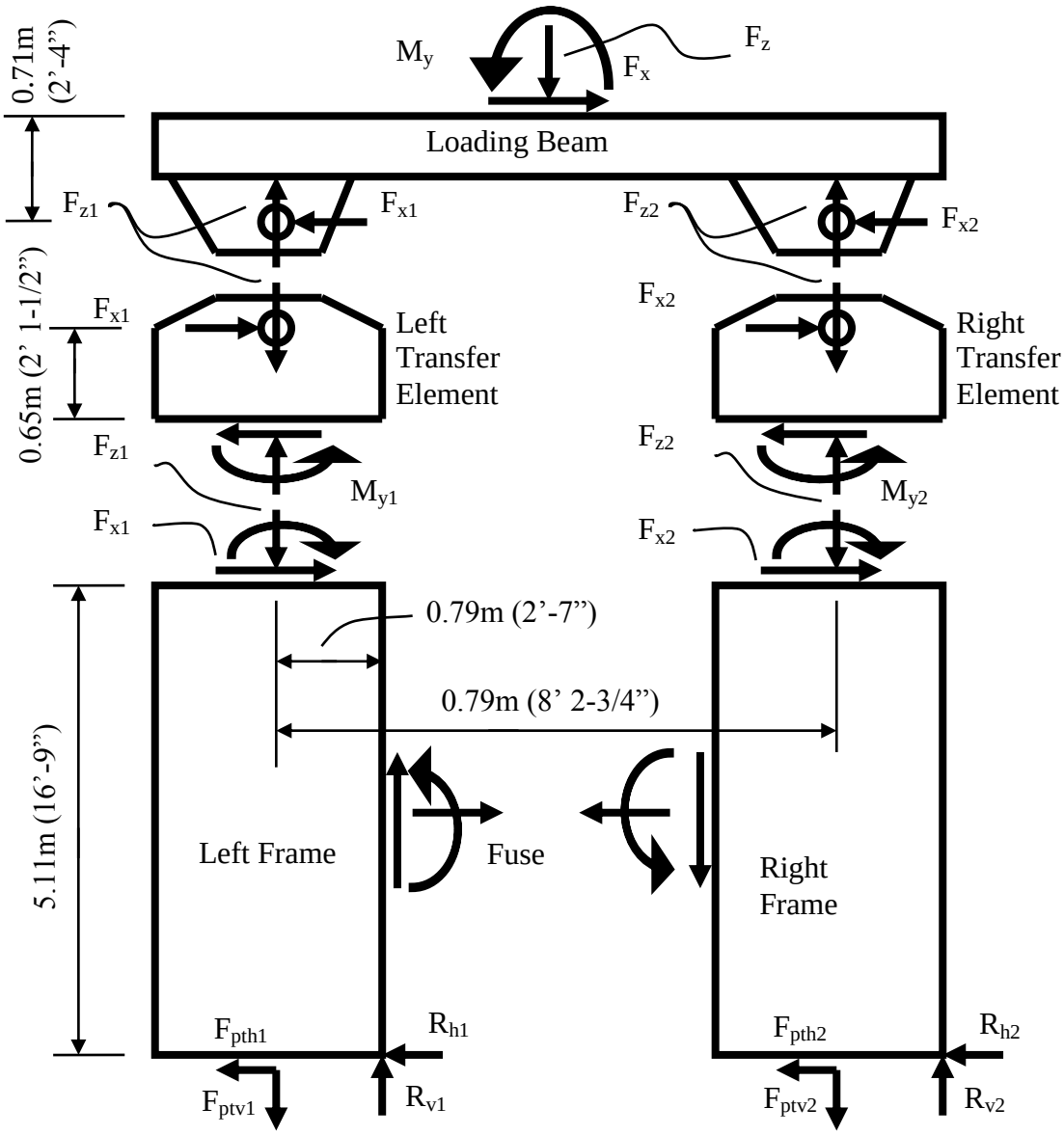

Figure 4.28 Free Body Diagram of the Large-Scale Test Specimen

It was shown in a previous section that gravity load accomplishes the same effect as post-tensioning force. Instead of applying constant vertical force equal to the gravity load during the tests, the gravity loads were neglected and considered to be incorporated into the post-tension force. The amount of post-tensioning required in the prototype building could therefore be reduced relative to the specimen based on the action of the gravity loads.

One of the test control goals is to iterate to get the vertical forces, F_{z1}, and F_{z2} to be zero. See Figure 4.29 for locations and abbreviations for the displacement and force feedbacks. The external feedbacks listed below and the goals for the controls on each degree-of-freedom are given in Table 4.15.

External Feedbacks Used in Control:

F_{x1}, F_{z1}, F_{x2}, F_{z2}, δ_{x3L}, and δ_{x3R}

Internal Feedbacks Used in Control:

δ_y, θ_x, and θ_z

Table 4.15 Control Goals for Each Degree-of-freedom

DOF	Control Goals	Notes
1	$\delta_{x3} = \frac{\delta_{x3R} + \delta_{x3L}}{2}$ = Applied Displacement History	External Displacement Feedback
2	$\delta_y = 0$	Internal Displacement Feedback
3	$F_z = F_{z1} + F_{z2} = 0$	External Force Feedback
4	$\theta_x = 0$	Internal Displacement Feedback
5	$M_y = \frac{F_{z1} - F_{z2}}{2L} = 0$	External Force Feedback
6	$\theta_z = 0$	Internal Displacement Feedback

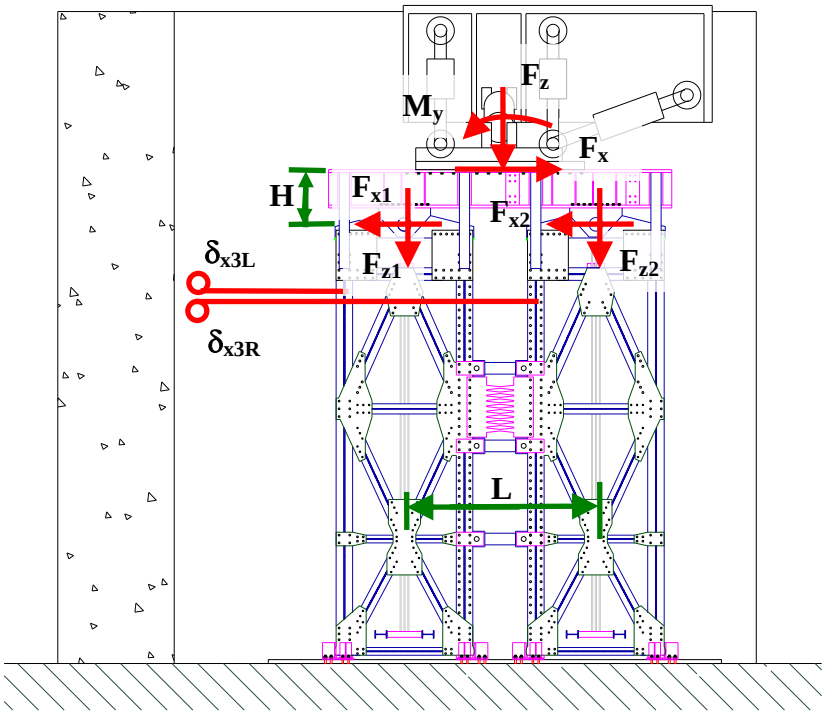

Figure 4.29 Displacement and Force Feedbacks

Figure 4.30 and Figure 4.31 show the flow charts that were the basis of the LBCB Plugin mixed mode control algorithm. The algorithm shown in Figure 4.30 and Figure 4.31 was chosen because of its inherent reliability in consistently converging. The process requires the vertical stiffness, $K_{\delta z}$, and the rotational stiffness, $K_{\theta y}$ to be input before the test. Since both stiffnesses depend primarily on the vertical stiffness of the frames, it is not expected that these values would change significantly even during rocking. A modified Newton-Raphson approach is therefore reasonable. In Figure 4.31, the calculation of the new command in the loop for force in the Z direction and the loop for moment in the theta Y direction consists of dividing the force residual by the initially input stiffness value.

In the control scheme, a step was defined by a peak roof displacement in either the positive or negative direction. For cyclic tests, the step targets were loaded from a file. For the hybrid simulation, the targets for each step corresponded to each time step. Each step was then split up into substeps with maximum X-Displacement of 0.69 mm (0.027”). The LBCB Operations Manager was set to execute each command with a ramp time of 0.25 seconds and a hold time of 0.15 seconds. The maximum substep size was calculated to not exceed the pump flow capacity when executed with the specified ramp time. Each substep consisted of multiple iterations of commands being executed by the LBCB to bring all degrees-of-freedom within tolerances as described in Figure 4.31.

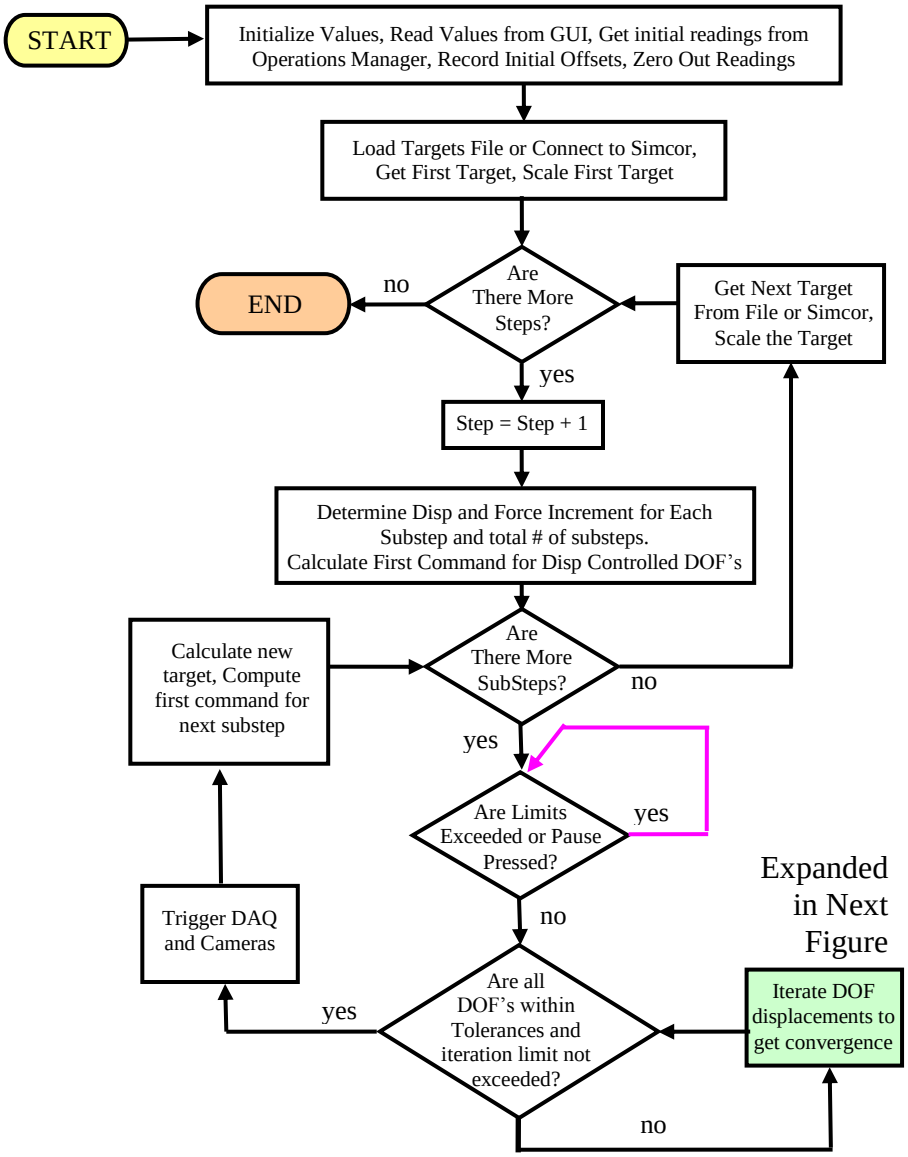

Figure 4.30 Flow Chart for the Main Body of the LBCB Plugin Programming

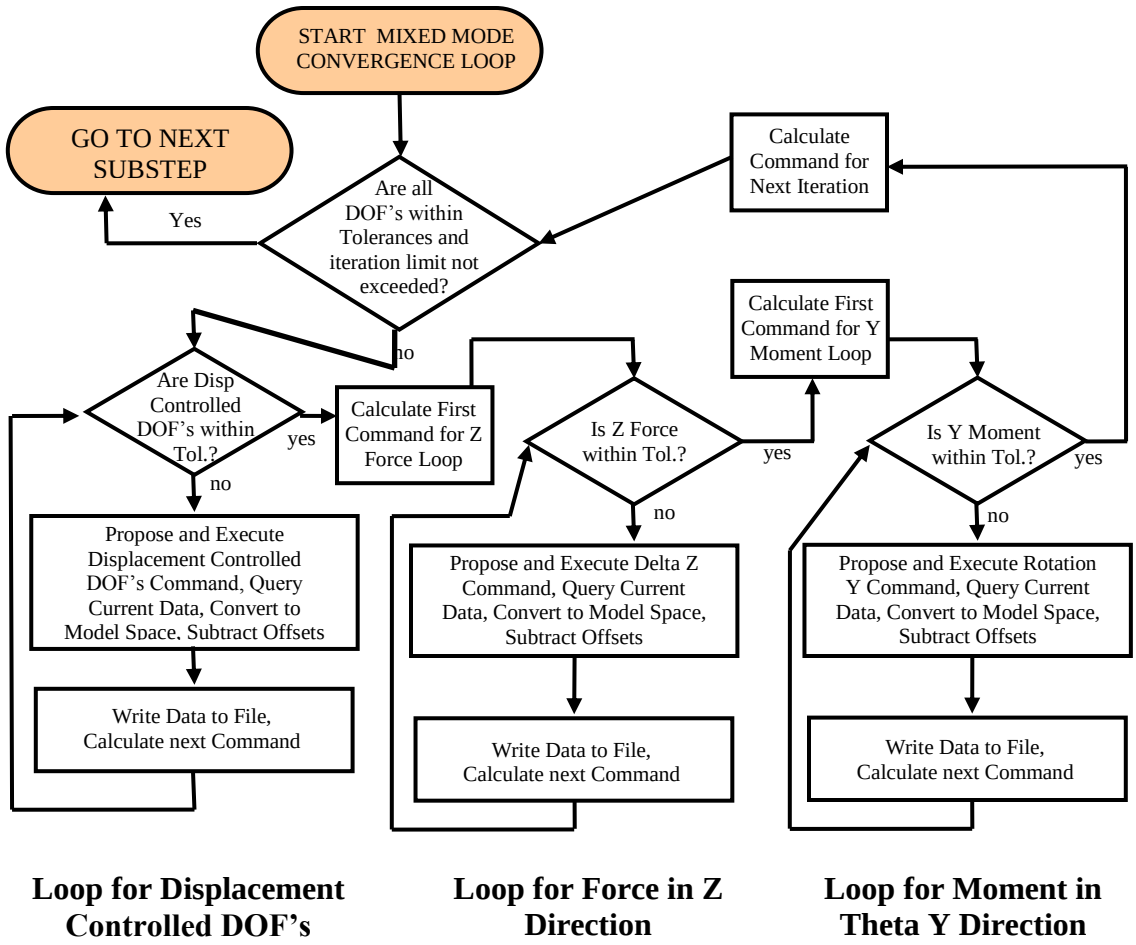

Figure 4.31 Flow Chart for the Mixed Mode Convergence Loop Programming

4.8 Instrumentation

Approximately 500 channels of data were recorded during each test. The types and typical number of gages used in one of the large-scale tests are contained in Table 4.16. The general instrumentation plan is shown in Figure 4.32 and Figure 4.33, and a detail of the strain gages that are applied to each wide flange shape at a strain-gaged section is shown in Figure 4.34. This section provides an overview of the instrumentation plan and objectives of the instrumentation. More detailed information on the instrumentation setup is included in Appendix B.

As shown in Figure 4.33, the strain gages on the frame members are grouped into three horizontal sections. Where the section crosses each wide flange member there are four strain gages and two strain gage rosettes applied to the member as shown in Figure 4.34. These measurements were used to calculate axial force, major axis moment, minor axis moment, and shear force for each wide flange member. The individual member forces can then be summed to calculate total resultant axial force, shear, and moments at the section as a whole.

The LBCB force feedbacks provide the resultant forces and moments input into the system at the top, and the load cell pins provide all of the in-plane forces at that level.

Between these two locations and the three strain-gaged sections, there are a total of five sections in which the resultant axial force, shear force, and in-plane moment were calculated. This redundancy allowed the verification of the data as well as calculation of the distribution of forces in the frame members.

High-strain, strain gage rosettes were applied at three locations on the trunk of every fuse. Although the strain fields in the fuse are complex, it was expected that these gages might give a general level of fuse shear force as the fuse trunk was expected to stay relatively elastic. However, these gages were placed within 25 mm (1") of the end of the links and inelasticity occurred at these locations.

Krypton LED's were applied at approximately 100 locations on and around one of the fuses of each specimen. There were many applications for this data including measurement of fuse shear strain, out-of-plane buckling of the fuse links, slip of the fuse or gusset plates relative to the columns, axial deformations of the fuse links, axial deformation of the struts, and more as described in Appendix D.

Two measurements allowed the calculation of post-tensioning force. Load cells were designed, manufactured, and calibrated to measure the force in each post-tensioning strand. Also, strain gages were installed on a reduced portion of the anchor rods that hold the lower post-tensioning anchorage plate down. These strain gages allow a calculation of the force in each anchor rod. The comparison of the total anchor rod force to the total post-tensioning strand force allowed validation of the data's accuracy.

Table 4.16 Summary of Instrumentation Used in a Typical Large-Scale Test

Type of Gage	Number of Sensors
Strain Gages	130
Strain Gage Rosettes	48 x 3 channels each
High Strain – Strain Gage Rosettes	18 x 3 channels each
Linear Potentiometers	15
String Potentiometers	16
Post-Tension Load Cells	16
LBCB Actuator Load Cells	6
LBCB Actuator LVDTs	6
Inclinometers	3
Pin Type Load Cells	2 x 2 channels
Krypton LEDs	100
Web-Based Video Cameras	4
Digital Still Cameras	5
High Resolution Video Cameras	2

String potentiometers were used to measure the movements of the system including horizontal drifts, uplift, out-of-plane movement, and post-tensioning elongation. Linear potentiometers were used to measure diagonal displacement across the fuses and elongation across the struts. Together these measurements allowed the calculation of the fuse shear strain.

Several digital still cameras were triggered in a synchronized way during the test so that time lapse video can be created from the images. High resolution video was taken during the largest cycles to provide more detailed record including sound. Web-based video cameras were also recorded to allow playback using NEES IT tools.

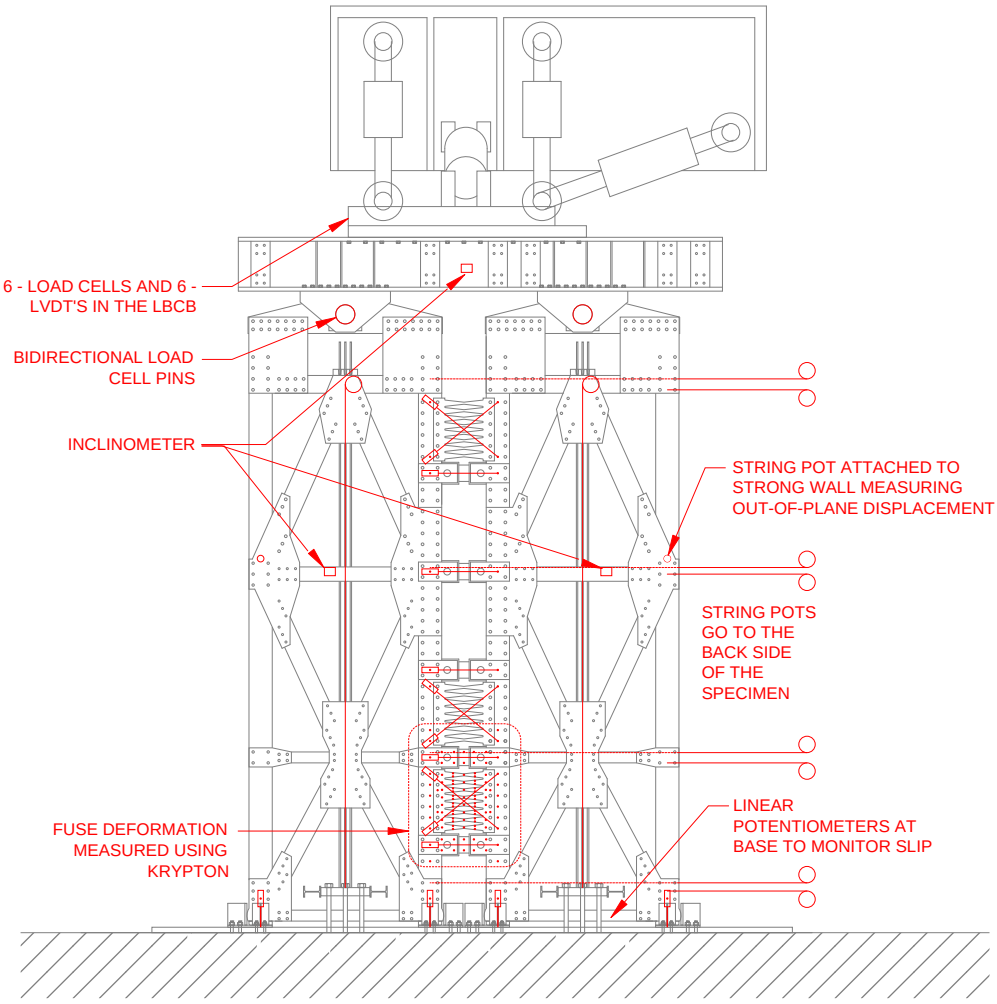

Figure 4.32 General Instrumentation Plan Excluding Strain Gages

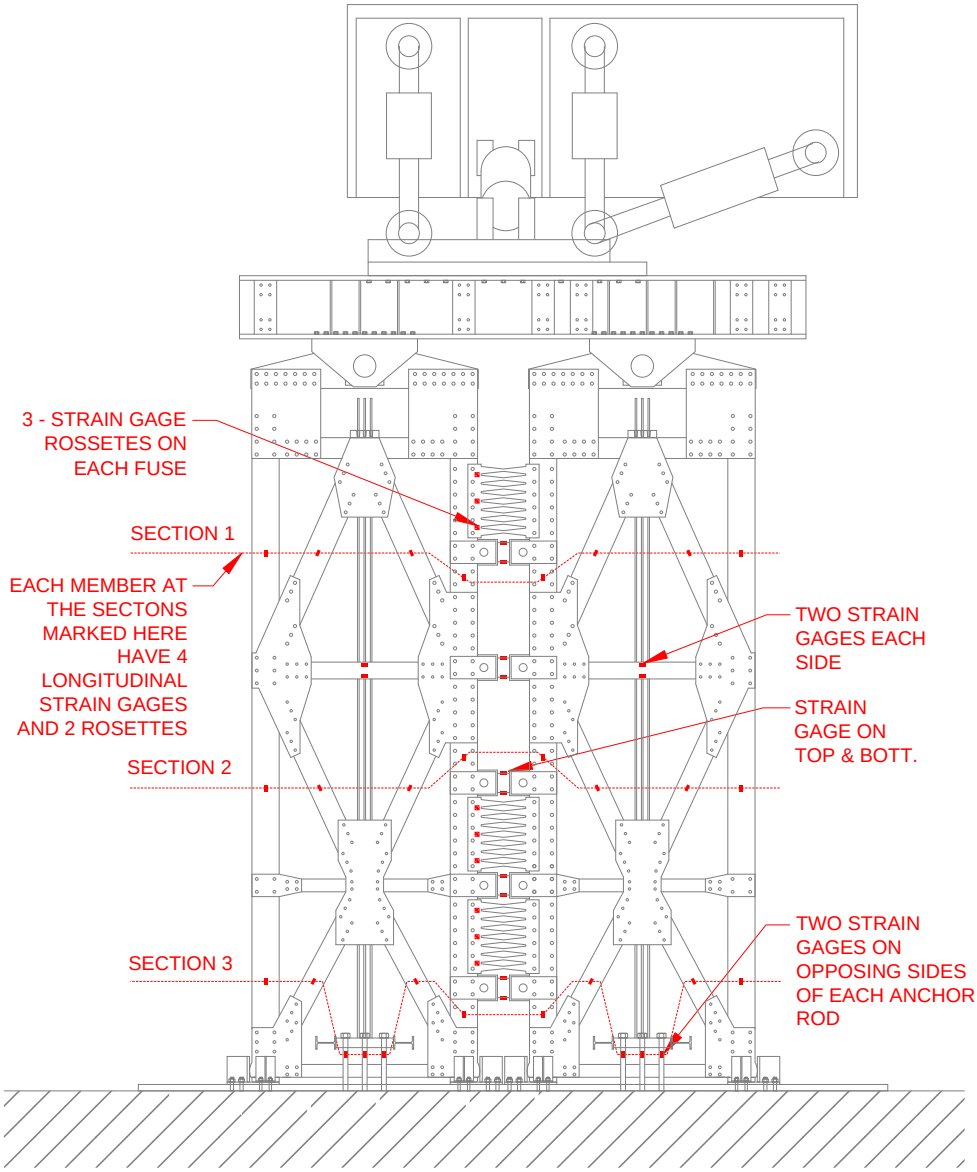

Figure 4.33 Strain Gage Instrumentation Plan

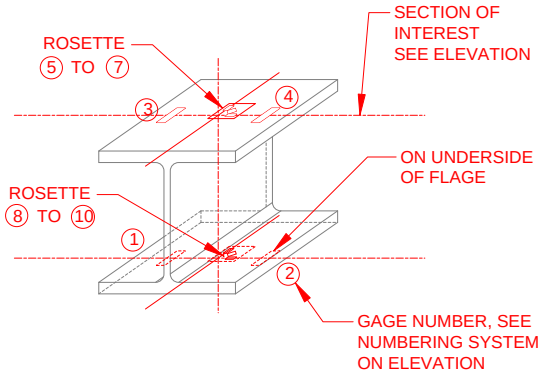

Figure 4.34 Diagram of Strain Gaged Section at Wide Flange Shape

QUASI-STATIC CYCLIC EXPERIMENTAL BEHAVIOR

With approximately 500 channels recorded for each specimen, the experimental program produced a large amount of data for investigating the local and global response of the controlled rocking system and for validating the accuracy of the data through analysis of redundant measurements. Only plots demonstrating salient features of the experimental behavior are included in this chapter. Plots showing all of the raw data are included in Appendix B, the calculations used to convert the measurements into other useful quantities are given in Appendix C, and plots showing the validation of the data and other details of the response are given in Appendix D.

This chapter discusses the quasi-static cyclic behavior of the controlled rocking system. There were seven quasi-static cyclic tests and the results from those tests are presented in this section in chronological order: Specimen A1, Specimen A2, Specimen A3, Specimen A4, Specimen A7, Specimen B1, and Specimen B2.

The load-deformation response of the specimens is generally shown in the overturning moment domain. As discussed in Chapter 3, the response of the controlled rocking specimen is governed primarily by first mode rigid body rotation of the frames. For this reason, the overturning moment is a more important quantity for examining response than base shear. For example, the overturning moment that causes yielding of the fuses will be relatively constant for different distributions of lateral loads even though the associated base shear will change. The lateral load in the experimental program is a point load above the roof level which will produce less base shear when the fuses yield than an inverted triangular load pattern, for example. Plotting the applied load as an overturning moment therefore gives more generalized information that is not as tied to a specific lateral load distribution.

The fuse shear force and overturning moment are normalized to calculated capacities. The shear capacity of the fuses, V_{fp}, is based on the plastic moment capacity at the quarter point which is given in Equation (5.1). The moment capacity of the system is based on the fuse capacity and the initial post-tension force as given in Equation (5.2) and Equation (5.3) for dual frame configuration and single frame configuration respectively.

$$V_{fp} = \frac{4}{9} N_{fuses} N_{links} \frac{b^2 t}{L} F_y \qquad (5.1)$$

Where:
N_{fuses} = number of fuses
N_{links} is the number of links per fuse
b is the link depth at the end
t is the thickness of the fuse
L is the length of the link
F_y is the measured yield strength of fuse plate

$$M_y = F_{pti}A + V_{fp}(A+B) \qquad \text{(DUAL FRAME)} \qquad (5.2)$$

$$M_y = \left(F_{pti} + V_{fp}\right)\frac{A}{2} \qquad \text{(SINGLE FRAME)} \qquad (5.3)$$

5.1 Specimen A1

Specimen A1 consisted of a dual frame configuration with six fuses between the frames. The fuses were, t=6.35 mm (¼") thick with 8 tapered links each that had a link length, L=356 mm (14"), a link depth at the ends, b=58.7 mm (2.3125"), and a link depth at the middle that was one-third the link depth at the end. The resulting design capacity for all the fuses was calculated to be V_{fp}=348.7 kN (78.4 kips). The post-tensioning consisted of eight 12.7 mm (½") diameter post-tensioning strands stressed to 29% of their ultimate strength or F_{pti}=421.7 kN (94.8 kips) total.

Using the equations defined in Chapter 3, the overturning ratio was found to be, OT=0.96, the self-centering ratio was SC=0.86, and the geometric ratio of frame width to fuse width was A/B=2.5.

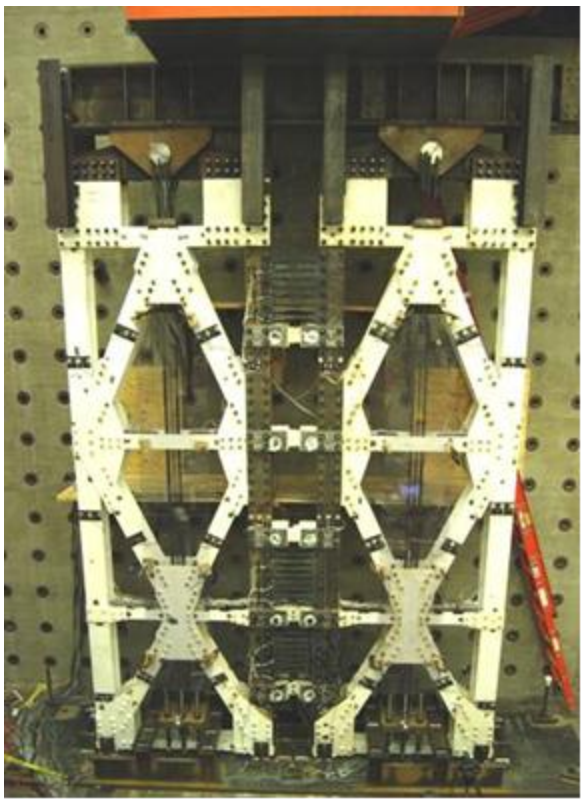

Figure 5.1 Photograph of Specimen A1

The load-deformation response for Specimen A1 is shown in Figure 5.2. As shown in Figure 5.3, the specimen was tested up to 3% roof drift ratio. The general behavior of specimen A1 was quite similar to the expected response. The flag-shaped hysteretic behavior described in Chapter 3 is evident in the experimental response which

corresponds to the ability of the assembly to return to its original position when the lateral load was removed.

Since the self-centering ratio is less than 1.0, it might be expected that that this configuration would not possess full self-centering capability. Examining the response for cycles at individual displacement levels as shown on the right in Figure 5.3 shows that the drift at zero load was increasing up to the 1.2% roof drift ratio displacement level. The fuses began to experience lateral-torsional buckling on the following displacement level effectively reducing the resistance against the restoring force. As a result, the roof drifts at zero force actually decreased after fuse buckling even though the associated roof displacement levels were increasing.

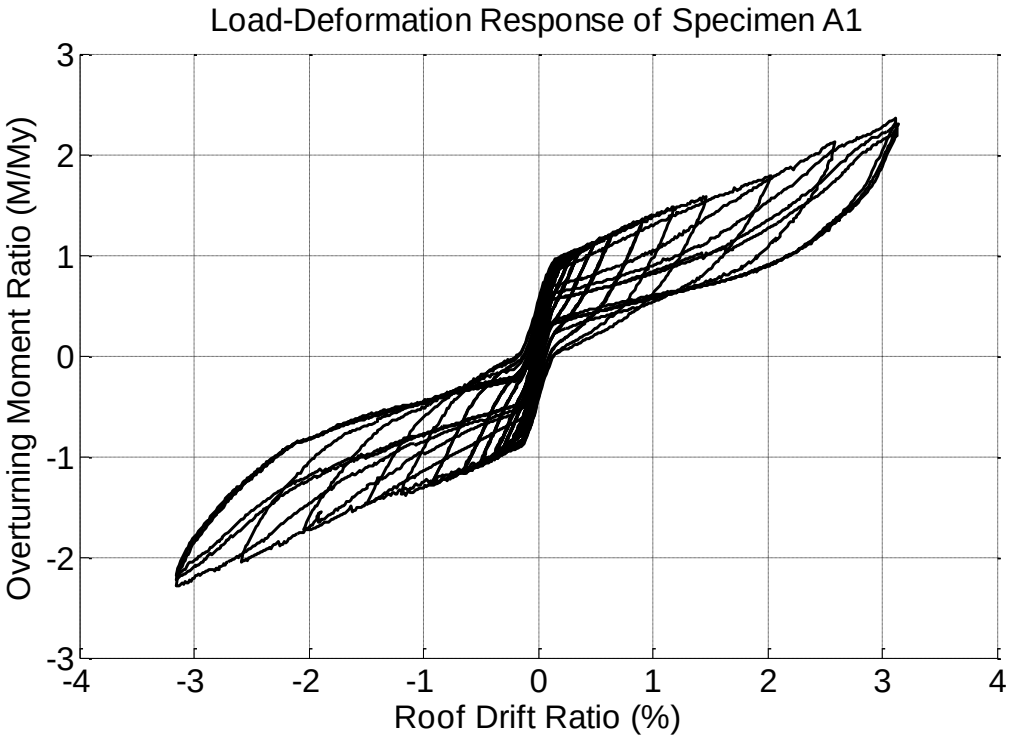

Figure 5.2 Load-Deformation Response for Specimen A1

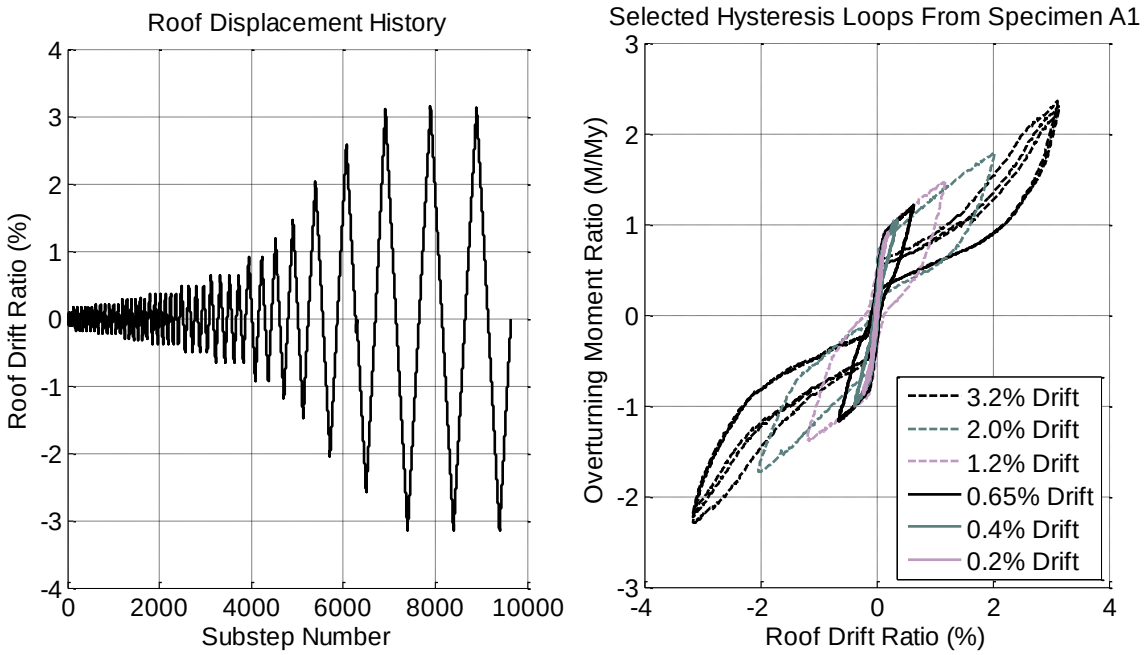

Figure 5.3 Roof Displacement History (Right) and Selected Hysteresis Loops (Left) for Specimen A1

Another effect of fuse buckling on system behavior is the reduced ability to absorb energy. The right side of Figure 5.3 demonstrates that at large drifts, such as the 3.2% roof drift ratio displacement level, the loading and unloading branches start to approach one another which represents a trend toward less area under the load-deformation curve and therefore reduced hysteretic energy.

An examination of the fuse hysteretic response given on the left of Figure 5.4 further demonstrates these points. The fuse response shows an evolution of behavior that begins with significant flexural inelasticity up to a shear strain of 8% across the fuse link length. The right side of Figure 5.4 shows almost half of the loading protocol was complete before the fuses began to buckle and degrade. During this initial pre-buckling portion of the response, the fuse exhibited shear loads during reloading that exceeded the shear loads of the loading regime. Since this increase in shear force appears to vanish as the fuse passes from positive to negative or negative to positive shear strain, this hump is attributed to a snap-through type of response related to axial compression and the geometric configuration. As shown on the left side of Figure 5.5, the fuse links are not moving out-of-plane significantly during this portion of response implying that the snap-through is occurring in the plane of the fuse.

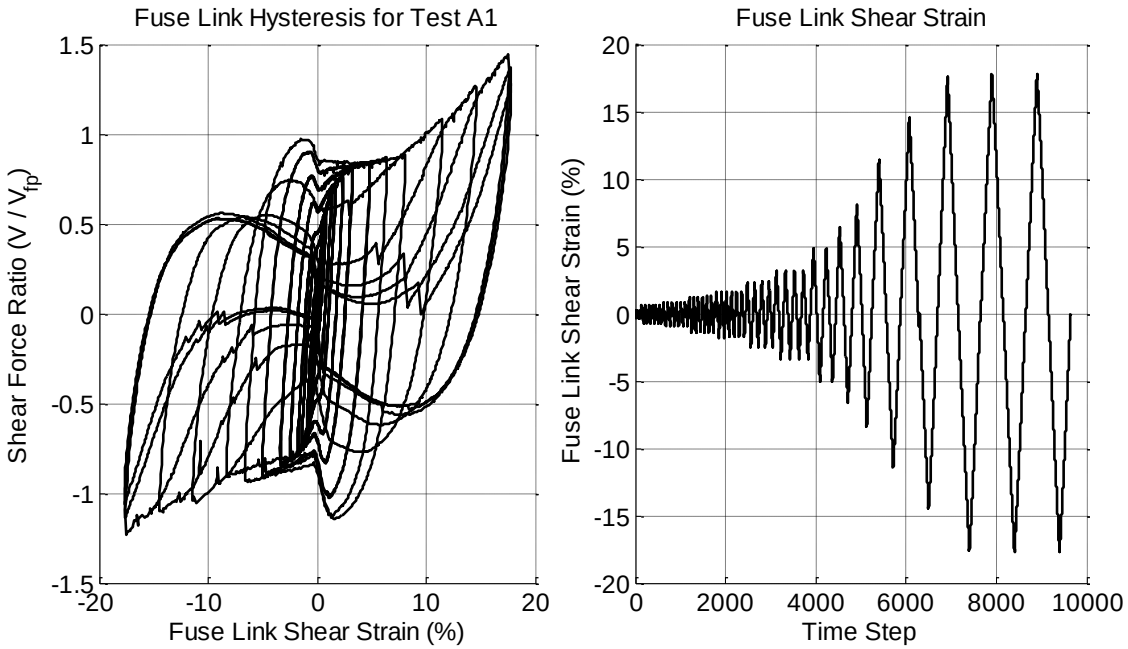

Figure 5.4 Fuse Hysteretic Behavior (Left) and Fuse Shear Strain History (Right) for Specimen A1

After a fuse link shear strain of approximately 8%, the fuses begin to experience lateral-torsional buckling. This is shown in the photograph included in Figure 5.6 and the plot on the left of Figure 5.5 which shows the out-of-plane location of four points on the top fuse link of the fuse that was instrumented with Krypton LED's. The four points are at the top and bottom of the fuse link at the quarter points of the link. The out-of-plane motion of these points demonstrates that lateral-torsional buckling occurs at approximately step 4900 in the displacement history. This plot also shows that after buckling the bottom of the fuse link moves inward toward the strong wall and the top of the fuse link moves outward away from the strong wall. Upon further cycling, the left side of the fuse link moves outward with negative fuse shear strain and the right side of the fuse link moves outward with positive fuse shear strain. This type of motion implies initial lateral-torsional buckling followed by both lateral-torsional deformations and second mode axial buckling deformations.

In fact the fuse behavior shown on the left of Figure 5.4 shows that as the fuse link shear strain cycles exceed 10%, the fuse links act primarily as axial members. During loading, the buckled fuses pick up load as they are engaged in tension. Upon reloading in the other direction, the fuse link compression dominates the response which reduces to very small shear resistance as the fuse passes through zero shear strain and begins loading in the opposite direction. The photographs in Figure 5.6 show the fuse at the beginning of the test, after lateral-torsional buckling, and at the end of the test. The photograph at the end of the test illustrates the significant amount of inelastic buckling experienced by the fuse links.

As discussed above, buckling reduces the fuse resistance against self-centering. The force that the fuse applies in resisting self-centering can be viewed as the fuse shear force at zero shear strain. For the purposes of the test program, other building elements are ignored and this is the fuse force that the post-tensioning needs to overcome to

completely close the gap at the base of the frames. As shown in Figure 5.4 the fuse shear force at zero shear strain reduces significantly after buckling. Similar to the examination of the system response, the ability of the fuse to absorb seismic energy is demonstrated by the area enclosed by the load-deformation response through a cycle. Figure 5.4 shows that the trade-off for improved self-centering is a loss in the ability of the fuse to dissipate seismic energy.

The axial forces in the fuse are primarily reacted by the pinned end struts between the frames in addition to the restraint provided at the top and bottom of the frames. The axial forces in the struts are shown on the right of Figure 5.5. The effectiveness of the struts in reacting the fuse axial forces was hampered by pin hole tolerances in the strut connections. Figure 5.5 shows the strut forces are near zero for large portions of the test. The strut forces are compressive and can be correlated to the time when the fuse is experiencing large tension forces during loading.

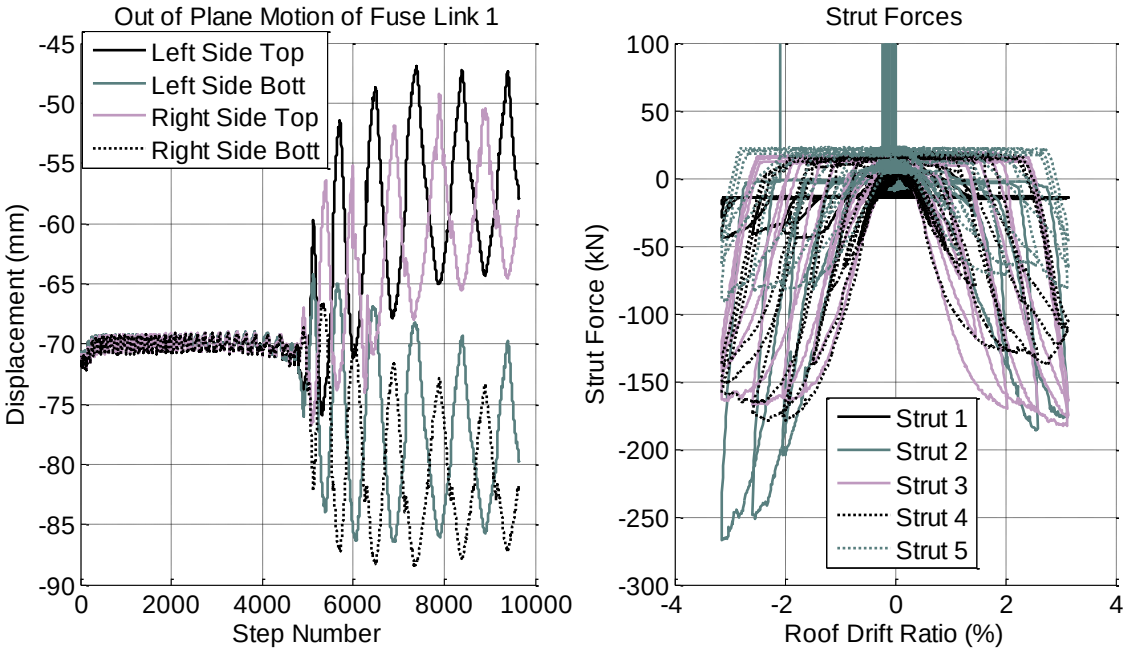

Figure 5.5 Out-of-Plane Movement of Fuse (Left) and Strut Forces (Right) for Specimen A1

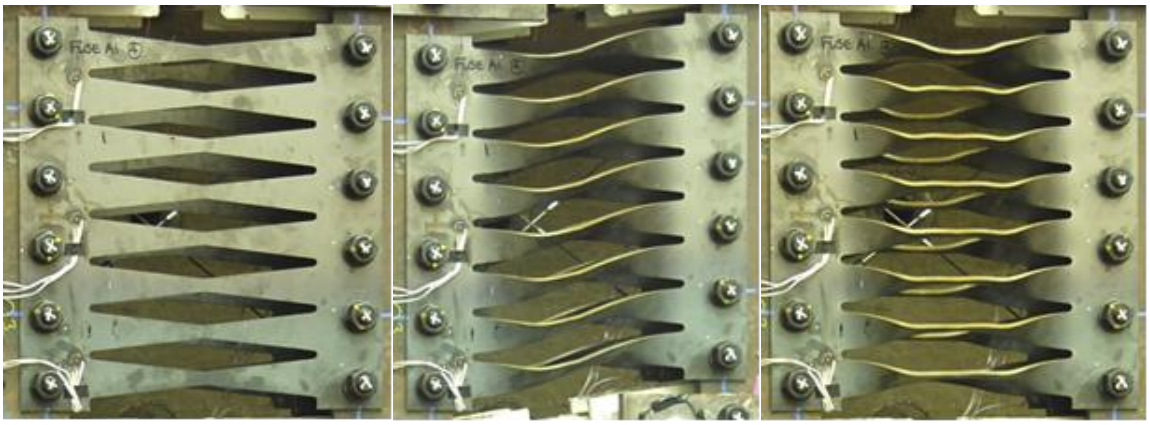

Figure 5.6 Photographs of the Specimen A1 Fuse at the Beginning of the Test (Left), After Lateral-torsional Buckling (Right), and at the End of the Test (Right)

After buckling, the effect of the fuse axial forces can be examined by comparing the response of Specimen A1 with a trial run conducted on the same configuration as Specimen A1 without fuses shown on the left of Figure 5.7. It is shown that at drift levels greater than 2% roof drift ratio, the Specimen A1 response starts to approach the response without fuses with the largest departure occurring during loading when the fuse links sustain tension forces. The two components of response are decoupled on the right side of Figure 5.7. The system force is essentially the sum of the forces from these two components at any given time step.

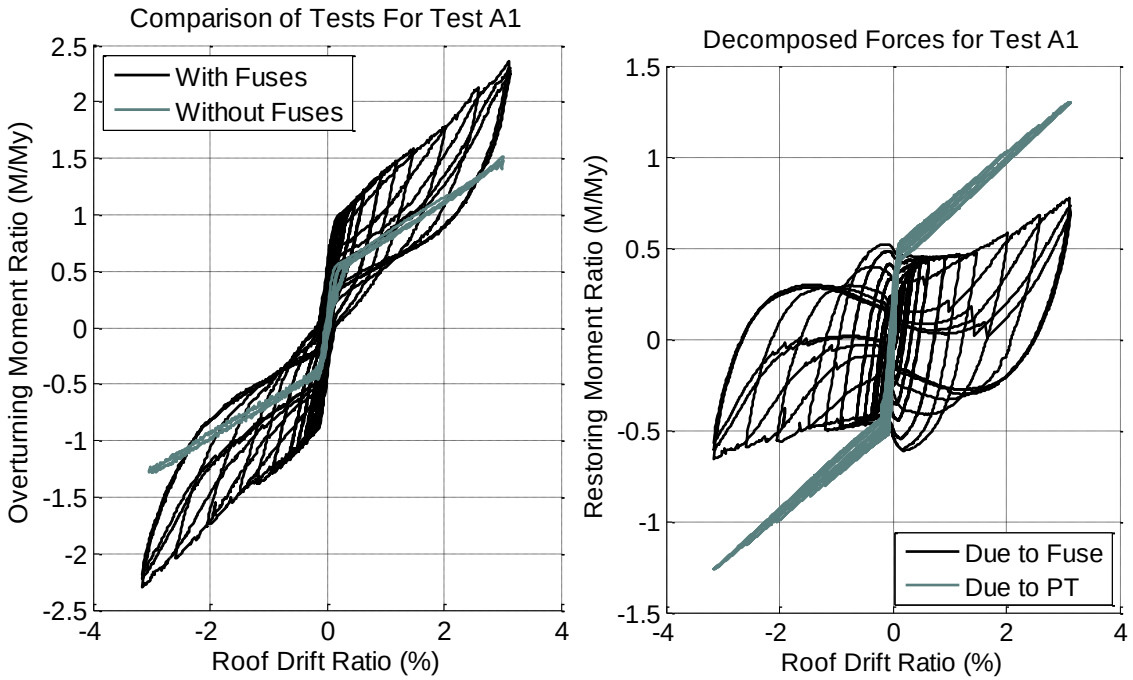

Figure 5.7 Comparison of Trial Run Without Fuses to Run With Fuses (Left) and Components of Response Due to Fuse and Post-Tensioning (Right) for Specimen A1

Although the load-deformation response of the trial run without fuses shown on the left of Figure 5.7 is quite similar to the response of the component of the system response due to the post-tensioned frame shown on the right of Figure 5.7, there are some differences. The post-tensioned frame component is shown to experience some loss in force as the test is conducted. The left side of Figure 5.8 shows the stress in a post-tensioning strand versus effective strain. The strain is measured using the change in distance between the anchorage plates. This strain, however, does not take into account the change in seating at the anchorage and is therefore labeled as effective strain. As the post-tensioning strand is stressed to a load higher than it has previously attained, the wedges in the anchorage are pulled a little deeper into the mating conical hole. This additional seating leads to a reduction in the post-tension force commonly referred to as post-tension seating losses. Figure 5.8 shows that this occurs at stress levels well below yield.

The occurrences of seating losses during the testing of Specimen A1 are quantified in the plot on the right side of Figure 5.8. As the post-tension strand forces were cycled up and down during the test, the amount of seating loss can be quantified as the change in the minimum post-tension strand force from one cycle to the next. The cause of the additional seating can be quantified as the amount that the post-tension strand force is increased above any previous peak or in other words the change in maximum post-tension strand force from one cycle to the next. This relationship is explored further in Chapter 8.

The effect of seating losses on the post-tension forces is illustrated in Figure 5.9. As discussed at the beginning of this section the post-tension forces started the test at 29% of ultimate. The seating losses accumulated during the test and the post-tension forces at the end of the test were 24% of ultimate and 22% of ultimate for the right frame and left frame respectively.

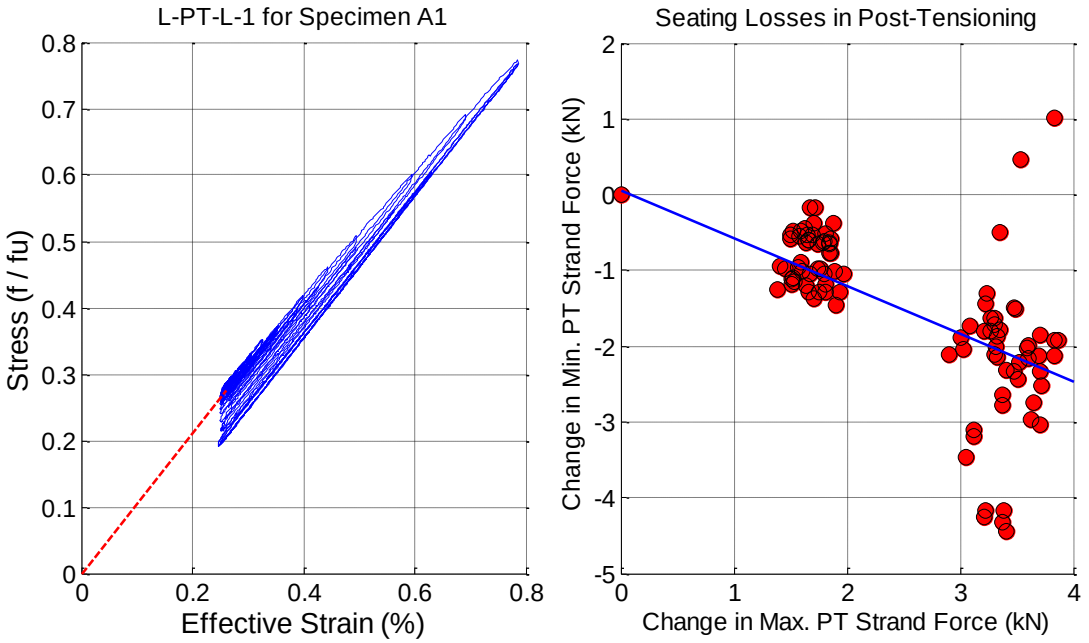

Figure 5.8 Example of Post-Tensioning Stress-Strain Response (Left) and Characterizing Post-Tension Seating Losses (Right) for Specimen A1

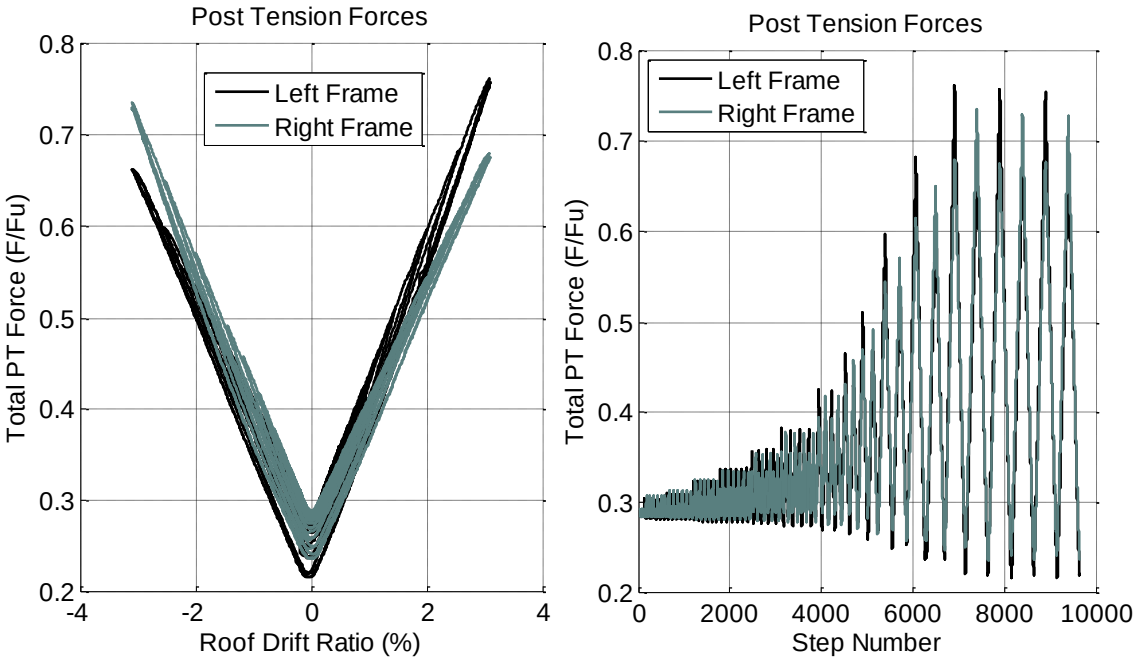

Figure 5.9 Post-Tensioning Response as Plotted Against Roof Drift (Left) and Step Number (Right) for Specimen A1

The motion of the frames was found to be near rigid body rotation as shown on the left of Figure 5.10. Because the interstory drift at all three levels is almost identical and equal to the roof drift, it is shown that the deformations of the system are dominated by rigid body rotation of the frames. Similarly, the uplift at the base of the columns on the right of Figure 5.10 demonstrates linear uplift behavior with roof drift implying rigid body rotation of the frames. The uplift of the four columns also shows that the two frames are tilting toward each other during rocking. During rocking motion to the right which is represented by positive roof drift ratio, the left frame experiences more uplift and therefore more rotation than the right frame. This also explains why the post-tension forces for the windward frame are greater than the leeward frame as shown in Figure 5.9.

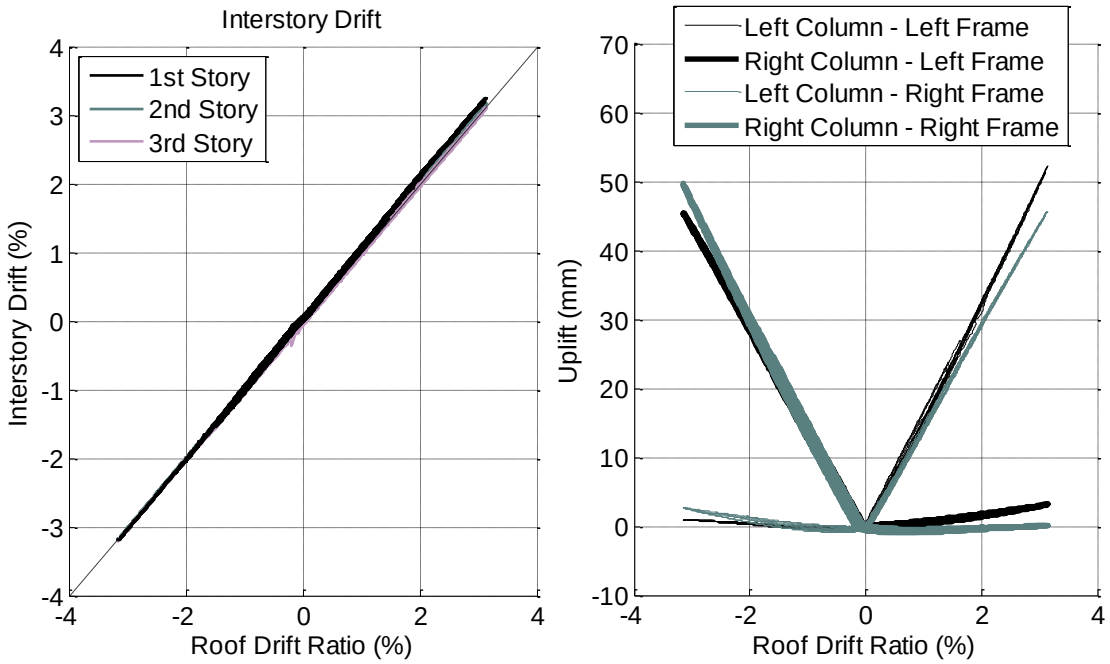

Figure 5.10 Interstory Drift (Left) and Column Uplift (Right) for Specimen A1

Finally, the post-tension strand forces during the stressing operation are presented in Figure 5.11. These plots show the process that was used during stressing and will be discussed further in the discussion of post-tension strand fracture for Specimen A4. All strands were stressed to a preliminary force level between 3 kN and 7 kN (0.7 kips to 1.6 kips) to take up the slack in the strands. Then the strands were stressed up to the desired loads sometimes through two additional pulls or three total pulls. As one strand was being stressed, the forces in the other strands of that frame are shown to reduce as the frames undergo elastic shortening. The stress in any one strand could be as much as 10% different from the target, but the sum of the post-tension forces for each frame was within 1% of the target.

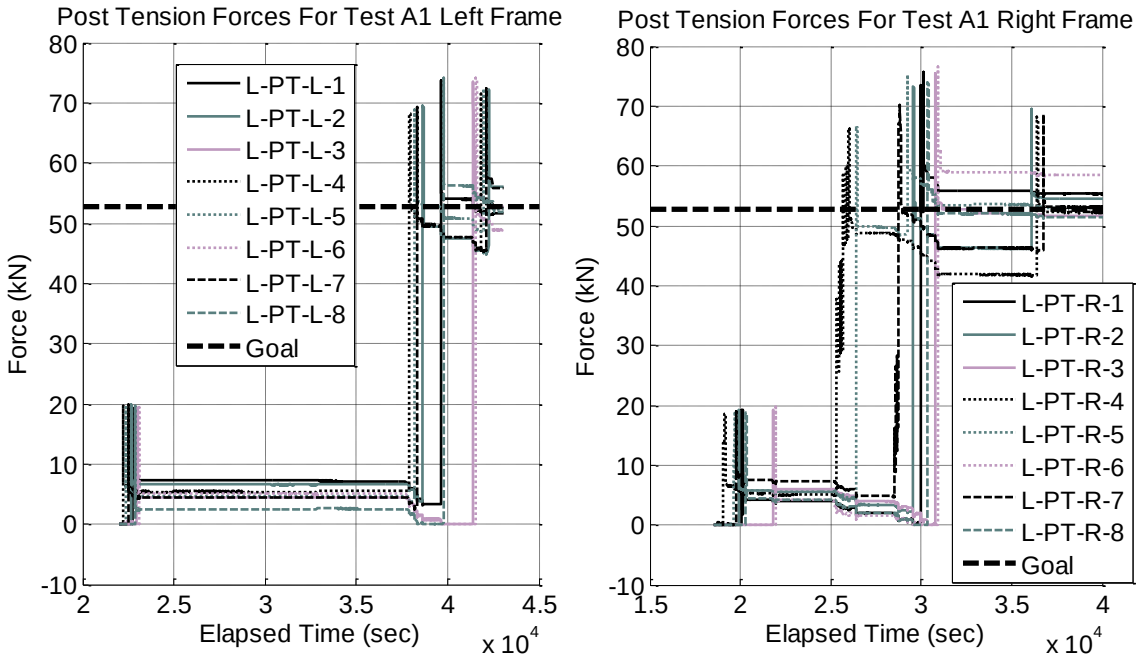

Figure 5.11 Post-Tension Strand Stressing for the Left Frame (Left) and Right Frame (Right) for Specimen A1

5.2 Specimen A2

Specimen A2 has similar proportioning as Specimen A1. The overturning ratio was, OT=1.07, the self-centering ratio was SC=0.71, and the geometric ratio of frame width to fuse width was A/B=2.5. The primary difference between Specimen A1 and Specimen A2 was the type and locations of the fuses.

Specimen A2 consisted of a dual frame configuration with two fuses between the frames concentrated at the second floor level. The fuses were, t=15.9 mm (5/8") thick with 10 tapered links each that had a link length, L=356 mm (14"), a link depth at the ends, b=58.7 mm (2.3125"), and a link depth at the middle that was one-third the link depth at the end. The resulting design capacity for all the fuses was calculated to be V_{fp}=424.8 kN (95.5 kips). The post-tensioning consisted of eight 12.7 mm (½") diameter post-tensioning strands stressed to 29% of their ultimate strength or F_{pti}=421.7 kN (94.8 kips) total.

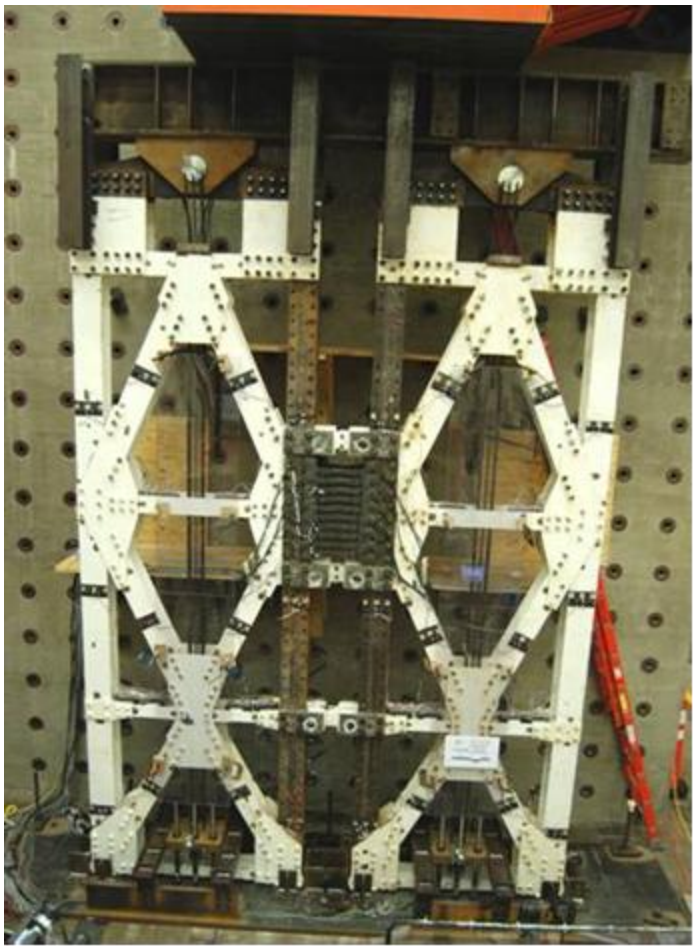

5.12 Photograph of Specimen A2

The load-deformation response for Specimen A2 is shown in Figure 5.13. The displacement history shown on the left of Figure 5.14 and the backbone curve are similar to Specimen A1, but the response at roof drift ratios greater than 1% is distinct in several ways. As shown on the right of Figure 5.14 the hysteretic response continues to absorb significant seismic energy through the entire displacement protocol but the drift at zero force continues to grow throughout the test. The drift at zero force ranges between -0.82% and 0.49% at the end of the test. It is not surprising that there is drift at zero force because the self-centering ratio is less than 1.0. The comparison between Specimen A1 and Specimen A2 demonstrates that fuse buckling improves the ability of the system to eliminate drift at zero force, but reduces the ability of the system to absorb seismic energy compared to systems with fuses that don't buckle.

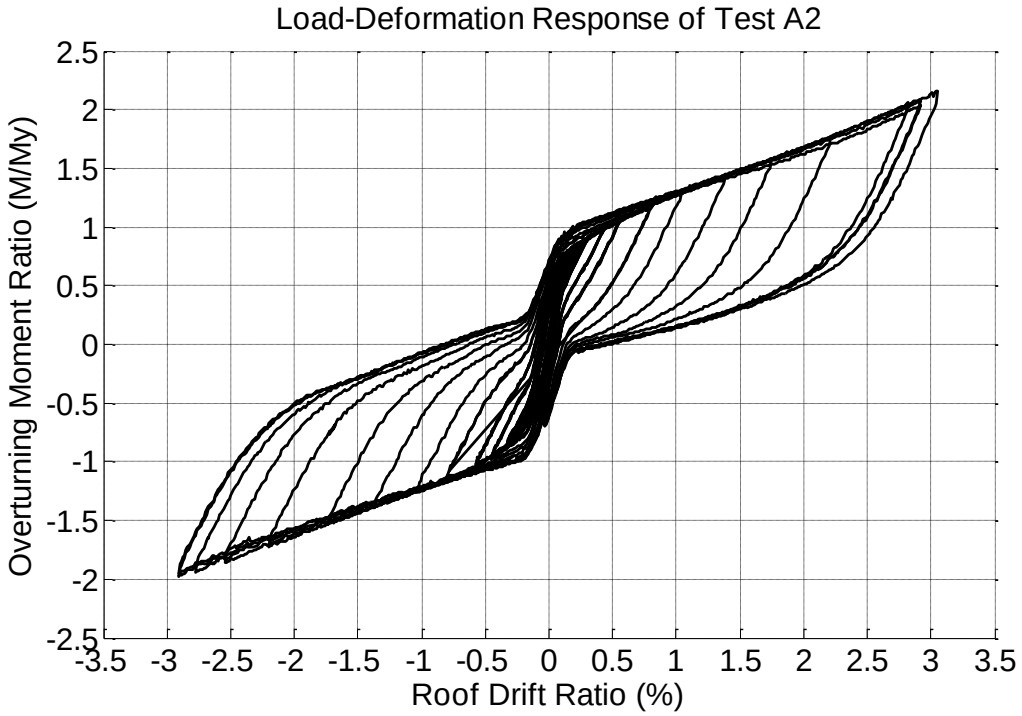

Figure 5.13 Load-Deformation Response for Specimen A2

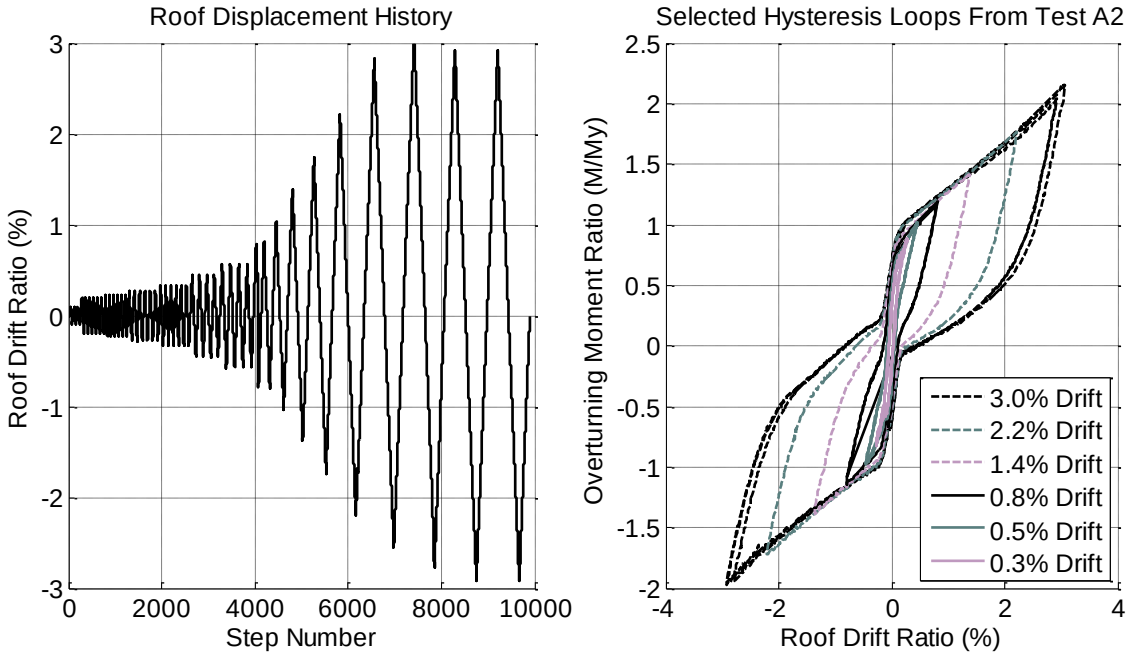

Figure 5.14 Roof Displacement History (Right) and Selected Hysteresis Loops (Left) for Specimen A2

The fuse response is shown on the left of Figure 5.15 to be a very full hysteretic behavior throughout the test which reached fuse shear strains across the link of 18%. Because the fuse did not buckle, two of the struts did not even become engaged during

the test as illustrated on the right of Figure 5.15 as the primarily flat lines. Strut 1, which is the lowest strut in the setup, picked up a nominal amount of axial load. The Specimen A2 fuse also did not exhibit any snap-through response as did Specimen A1. Both points imply that axial forces did not play as large a factor in the Specimen A2 response compared to Specimen A1. A photograph of the deformed fuse is included on the left of Figure 5.16.

The uplifting base is shown in a photograph on the right of Figure 5.16. The uplift history and interstory drift responses were similar to Specimen A1 so were not included here. The frames in this configuration were found to tilt toward one another as roof drift ratios increased as was demonstrated for Specimen A1 and as was found to occur for all of the dual frame configuration tests.

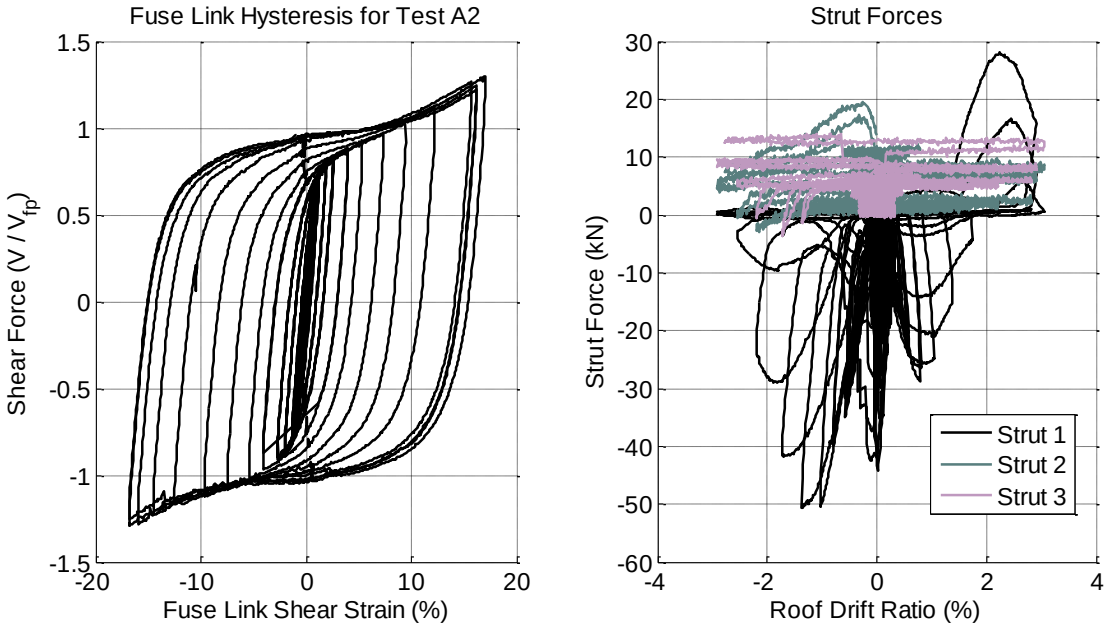

Figure 5.15 Fuse Hysteretic Behavior (Left) and Strut Forces (Right) for Specimen A2

Figure 5.16 Photograph of the Deformed Specimen A2 Fuse (Left) and Uplifted Column Base (Right)

Another difference between the Specimen A1 response and Specimen A2 related to post-tension seating losses. In the Specimen A1 test, the post-tension forces were increasing past their previous maximum during each displacement level. Since the post-tension strands were not removed between Specimen A1 and Specimen A2, the strands had already been stressed to approximately 75% of their ultimate force during the testing of Specimen A1. The post-tension strand forces were not, therefore, exceeding their previous maximum at any time during the Specimen A2 test. As expected, there were no seating losses observed in the post-tensioning response as demonstrated on the left of Figure 5.17. The total post-tension force shown on the right of Figure 5.17 also demonstrates that there were no losses in the total post-tension force during the testing of Specimen A2.

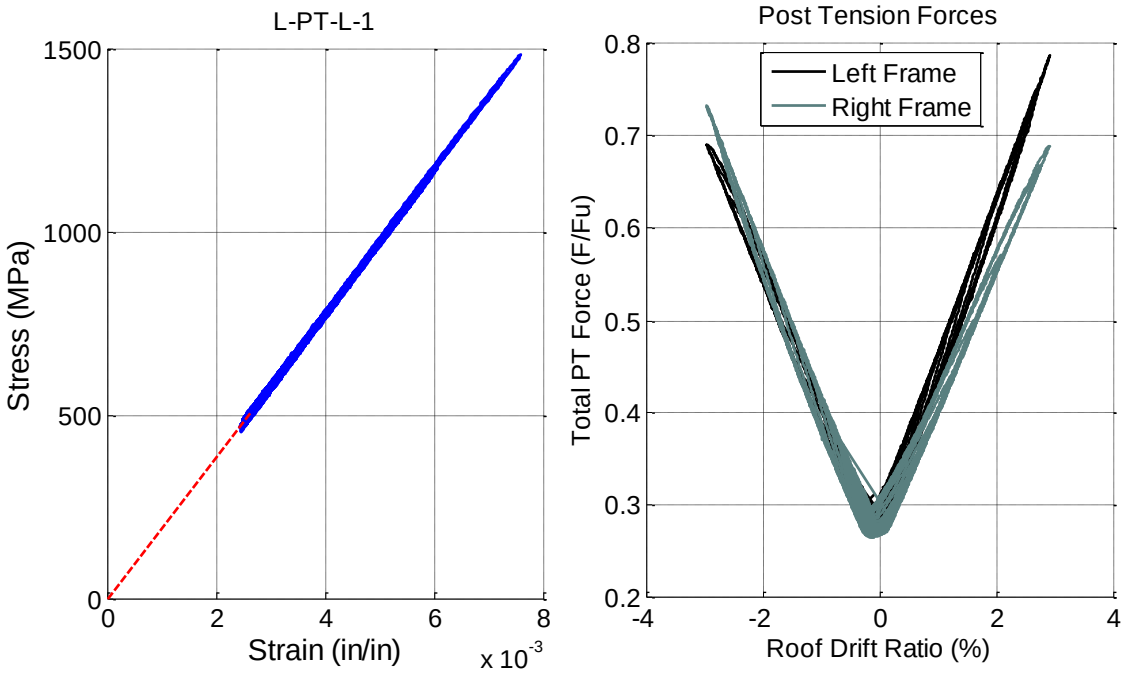

Figure 5.17 Example of Post-Tensioning Stress-Strain Response (Left) and Total Post-Tensioning Force (Right) for Specimen A2

5.3 Specimen A3

Specimen A3 was similar to Specimen A2 in configuration and fuse thickness, but utilized slightly different system proportioning. The overturning ratio was, OT=0.88, the self-centering ratio was SC=1.01, and the geometric ratio of frame width to fuse width was still A/B=2.5. This represents an increase in the SC ratio to near the limit for full self-centering, and a reduction in the overall system strength compared to Specimen A2.

Specimen A3 consisted of a dual frame configuration with two fuses between the frames. The fuses were, t = 15.9 mm (5/8") thick with 7 tapered links each that had a link length, L=356 mm (14"), a link depth at the ends, b=58.7 mm (2.3125"), and a link depth at the middle that was one-third the link depth at the end. The resulting design capacity for all the fuses was calculated to be V_{fp}=297.3 kN (66.8 kips). The post-tensioning consisted of eight 12.7 mm (½") diameter post-tensioning strands stressed to 29% of their ultimate strength or F_{pti}=421.7 kN (94.8 kips) total.

A photograph of the Specimen A3 configuration is included in Figure 5.18. The load deformation response for Specimen A3 is shown in Figure 5.19. The effect of adjusting the self-centering ratio from 0.71 to 1.01 can be seen by comparing the ability of Specimen A2 to self-center compared to Specimen A3. The drifts at zero force are reduced by half to a range between -0.42% and 0.09%. The selected hysteresis loops shown on the left of Figure 5.20 demonstrate that the drift at zero force is less than 0.2% up to the cycles at 2.2% roof drift ratio.

The decomposed system response included on the right of Figure 5.20 shows that the component due to the fuses has almost identical strength as the component due to

post-tensioning. The ratio of these two components at near zero roof drift is a graphical representation of the self-centering ratio which in this case is near 1.0. As shown in Figure 5.21, the fuses did not buckle and as such did not create enough axial force to engage the struts.

The post-tensioning response was extremely similar to Specimen A2 as shown in Figure 5.22. The post-tensioning strands did not experience any appreciable nonlinearity due to seating losses or inelasticity. As a result the post-tensioning forces returned to the same value at zero roof drift. The difference in the post-tensioning forces between the left and right frames as shown on the right of Figure 5.22, demonstrates that the fuses tilted toward one another with growing drift levels similar to the previous specimens.

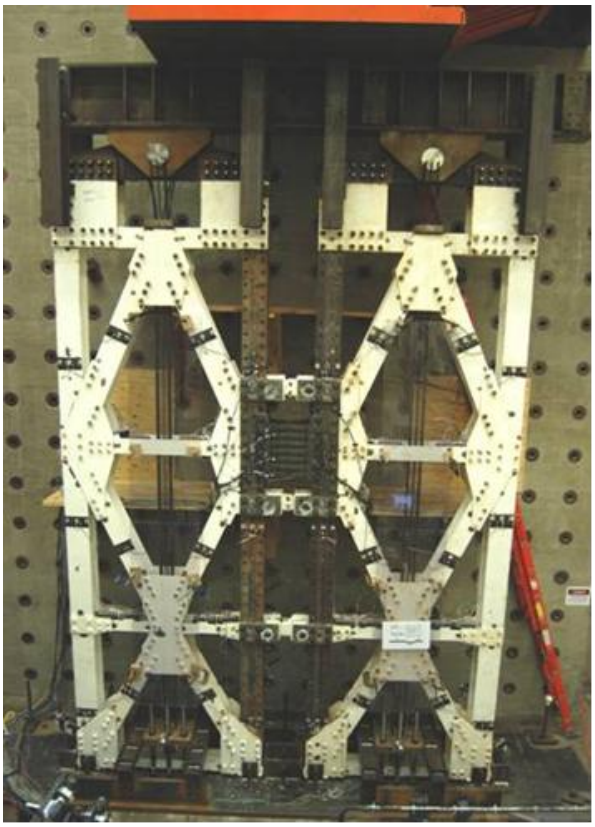

Figure 5.18 Photograph of Specimen A3

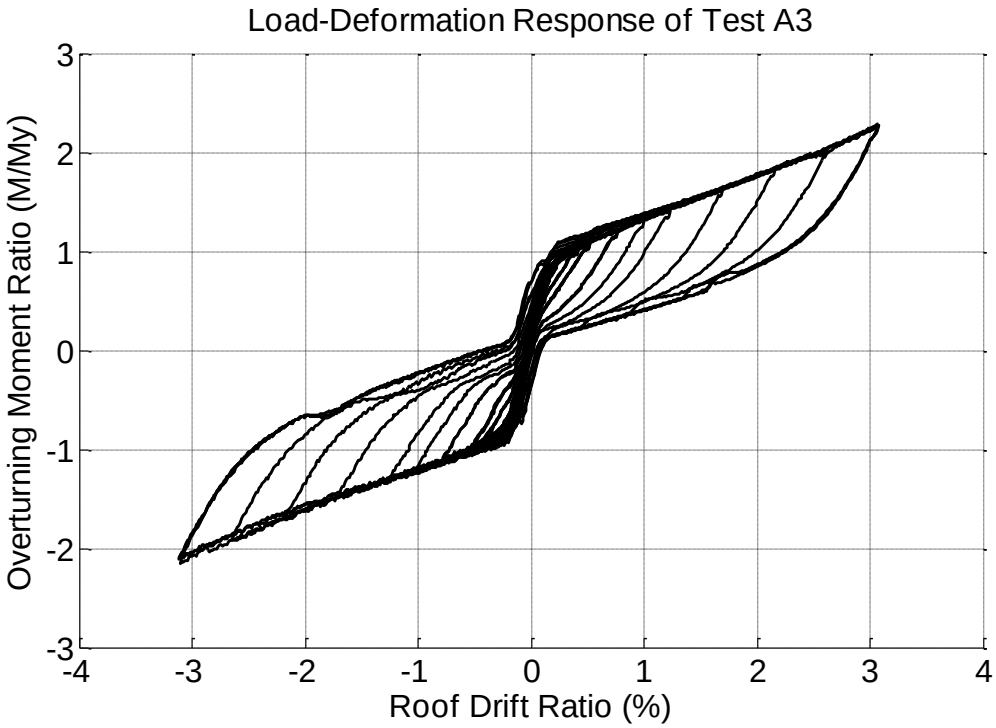

Figure 5.19 Load-Deformation Response for Specimen A3

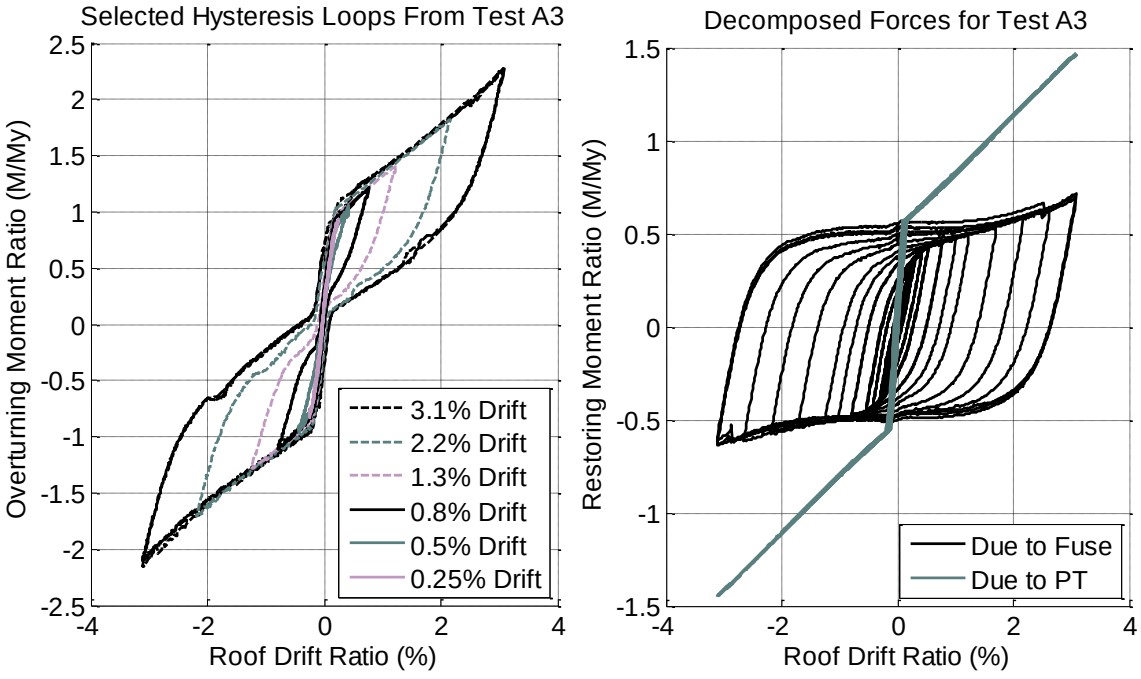

Figure 5.20 Selected Hysteresis Loops (Left) and Decomposed Component Response (Right) for Specimen A3

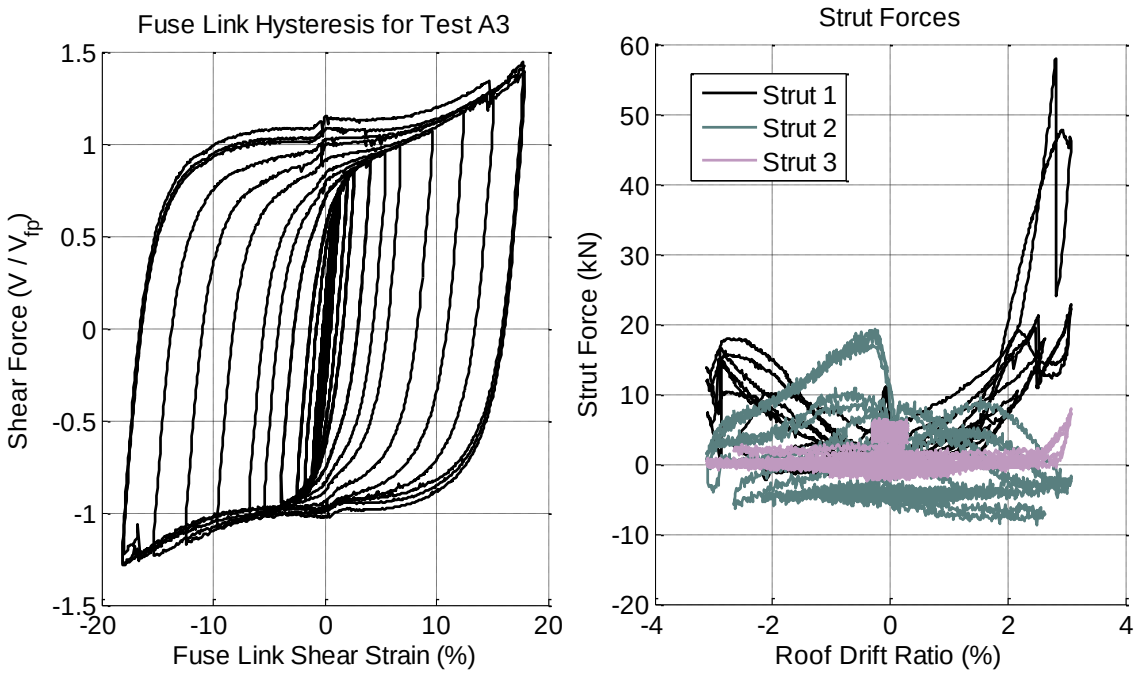

Figure 5.21 Fuse Hysteretic Behavior (Left) and Strut Forces (Right) for Specimen A3

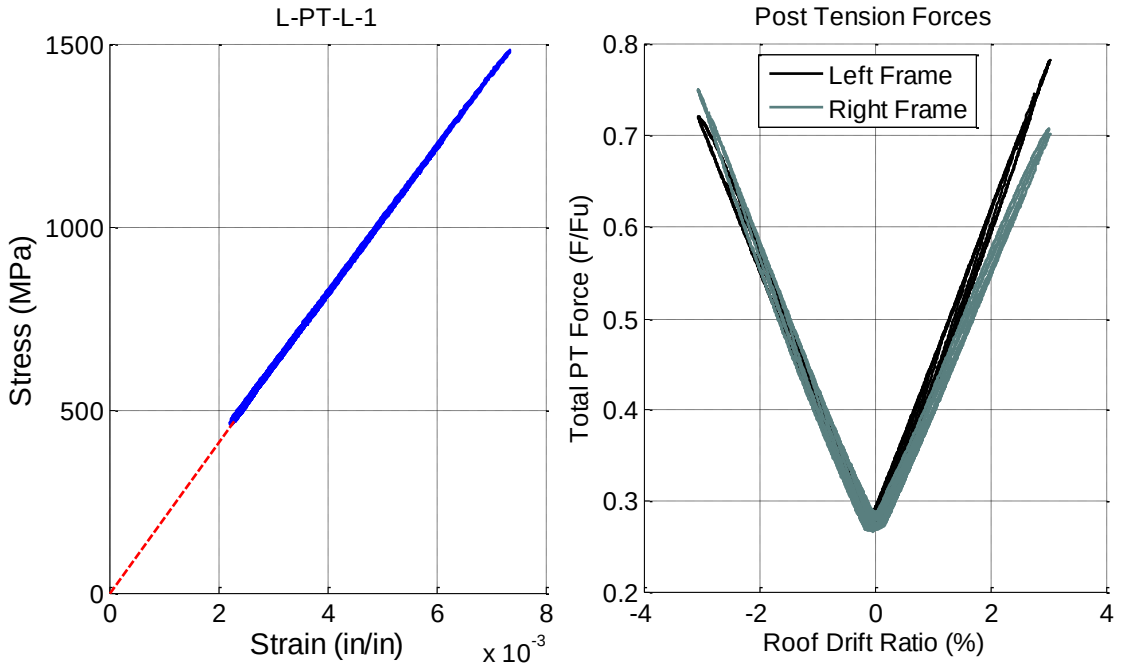

Figure 5.22 Example of Post-Tensioning Stress-Strain Response (Left) and Total Post-Tensioning Force (Right) for Specimen A3

5.4 Specimen A4

Specimen A4 was different from the previous tests in that it had higher resistance to overturning forces with an overturning ratio, OT=1.43, a higher capacity to self-center with a self-centering ratio, SC=1.13, and the highest initial post-tensioning stress of any of the specimens. The geometric ratio of frame width to fuse width was still constant at A/B=2.5. Specimen A4 also used thicker fuses than any other specimen in this testing program and this was the first specimen for which the post-tension strands were pushed past their yield strain.

Specimen A4 consisted of a dual frame configuration with two fuses between the frames. The fuses were, t = 25.4 mm (1") thick with 7 tapered links each that had a link length, L=356 mm (14"), a link depth at the ends, b=58.7 mm (2.3125"), and a link depth at the middle that was one-third the link depth at the end. The fuses were concentrated at the second floor level as shown in Figure 5.23. The resulting design capacity for all the fuses was calculated to be V_{fp}=454.6 kN (102.2 kips). The post-tensioning consisted of the same eight 12.7 mm (½") diameter post-tensioning strands as Specimens A1 through A3. The initial force in the post-tensioning strands was increased to 49% of their ultimate strength or F_{pti}=718.4 kN (161.5 kips) total by adjusting the lower anchorage plate downward. This was accomplished by turning the nuts that held the anchorage plate down.

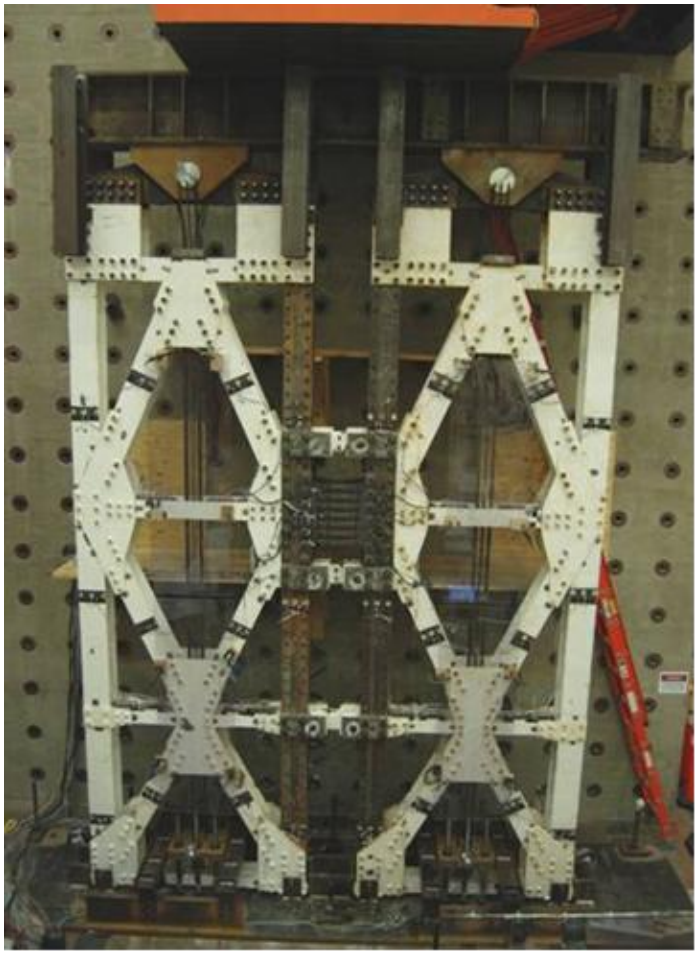

Figure 5.23 Photograph of Specimen A4

The load-deformation response included in Figure 5.24 demonstrates several distinct aspects of response compared to the previous specimens. It is shown that at drifts greater than 2.7% there is a loss in self-centering ability and degradation in the load-deformation backbone. This is due to post-tension strand yield and fracture. One of the purposes of this specimen was to examine the behavior of the post-tensioning strands when the yield strain was exceeded. Large post-tension strand strains were encouraged by starting with a large initial strain and then conducting this test to larger roof drifts than the previous specimens. Near the positive peak of the 2.7% roof drift ratio cycle one of the wires in one of the strands fractured. Each post-tensioning strand is made up of 7 individual wires twisted together. In total, six of the 112 wires that made up the 16 post-tensioning strands fractured as the strands were elongated to strains as high as 1.06%. The details of each fracture are summarized further in Chapter 7 including discussion about possible methods for mitigating post-tension wire fracture.

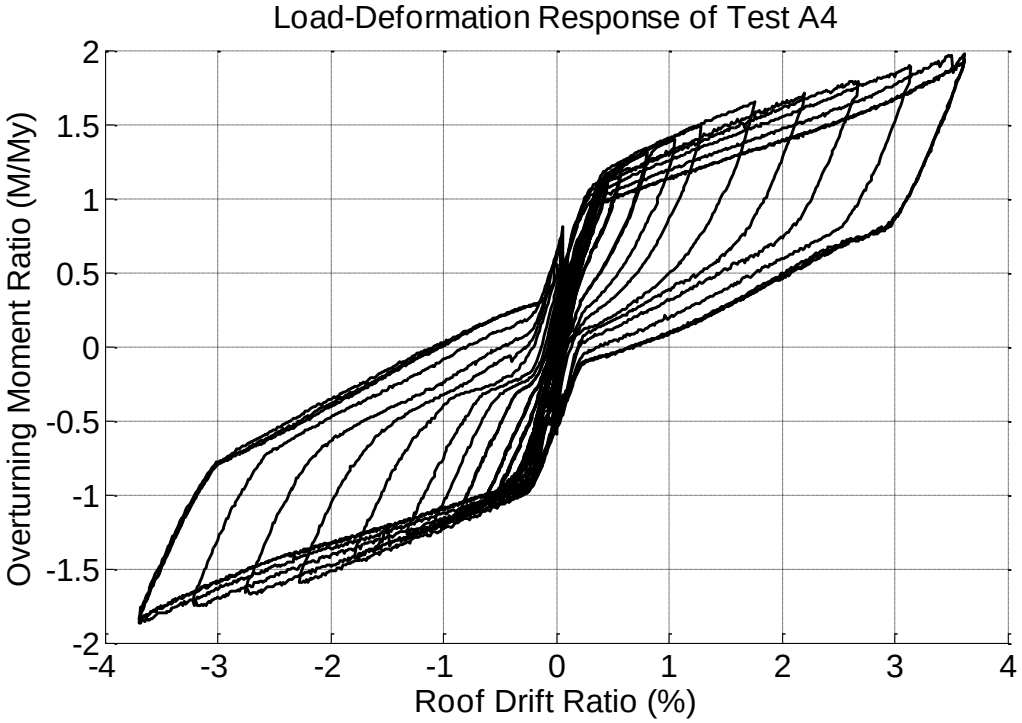

Figure 5.24 Load-Deformation Response for Specimen A4

Examining selected hysteresis loops as shown in Figure 5.25, reveals that the drift at zero force was small prior to the post-tensioning wire fractures, and even though it increases after the wire fractures, the zero-force drift remains small relative to the peak roof drift of 3.7%. It is also shown that the strength of the system continues to increase with increasing drift due to additional elongation of the post-tensioning strands and hardening in the fuses.

These points are demonstrated on the right side of Figure 5.25 in the decomposed component responses. At the beginning of the test, the post-tensioning force at uplift makes up almost 60% of the systems resistance to overturning whereas the fuses

comprise only 40% of the system strength. After cycles at roof drift ratios above 2.7% the secondary branch of the post-tensioning bilinear elastic response starts shifting downward as the strands yield and wires fracture. The fuses, on the other hand, continue to gain in strength through a combination of isotropic and kinematic hardening. At the end of the test, the post-tensioning force at uplift makes up only 40% of the systems resistance to overturning and the fuse makes up the other 60%. The overturning moment at uplift remains relatively constant, but the ability of the system to eliminate drifts when the load is removed is reduced.

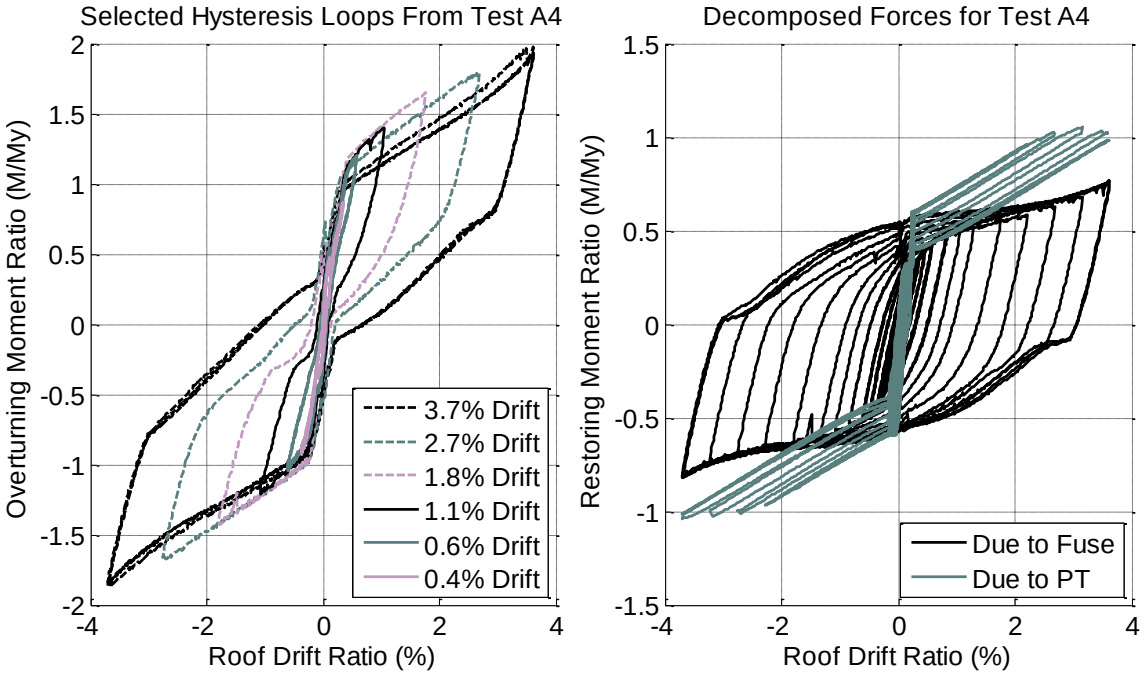

Figure 5.25 Selected Hysteresis Loops (Left) and Decomposed Component Response (Right) for Specimen A4

An example of a post-tensioning strand that experienced wire fracture and one that did not is included on the left of Figure 5.26. The strand that fractured, L-PT-L-1, experienced a sharp 25% drop in effective stress and related force. The vertical axis is labeled as effective stress because this is calculated based on the original area of the strand before fracture. The stiffness of the strand is shown to change after fracture because of the reduction in area. However, the strand that did not fracture, L-PT-L-4, experienced yielding. At the end of the test, strand L-PT-L-1 experienced a total loss of initial prestress of 59% whereas strand L-PT-L-4 experienced a total loss of 37% of its initial prestress.

The loss of post-tensioning force due to post-tension strand yield and wire fracture are further demonstrated on the right of Figure 5.26. At the beginning of the test, the post-tension force was approximately 49% of the strands ultimate strength. At the end of the test, the total post-tension forces were 30% and 26% of ultimate for the left and right frame respectively which represents a loss of 43% of the total post-tension force for both frames. In general, yielding of the post-tensioning strands and wire fracture

were found to reduce the post-tensioning force in a controlled gradual manner in this quasi-static displacement-controlled test.

As the wires fractured, the wire rebounded toward the opposite anchorage and was found to unravel from the rest of the strand. Figure 5.27 shows multiple unraveled wires at the bottom anchorage due to wire fractures at the top anchorage.

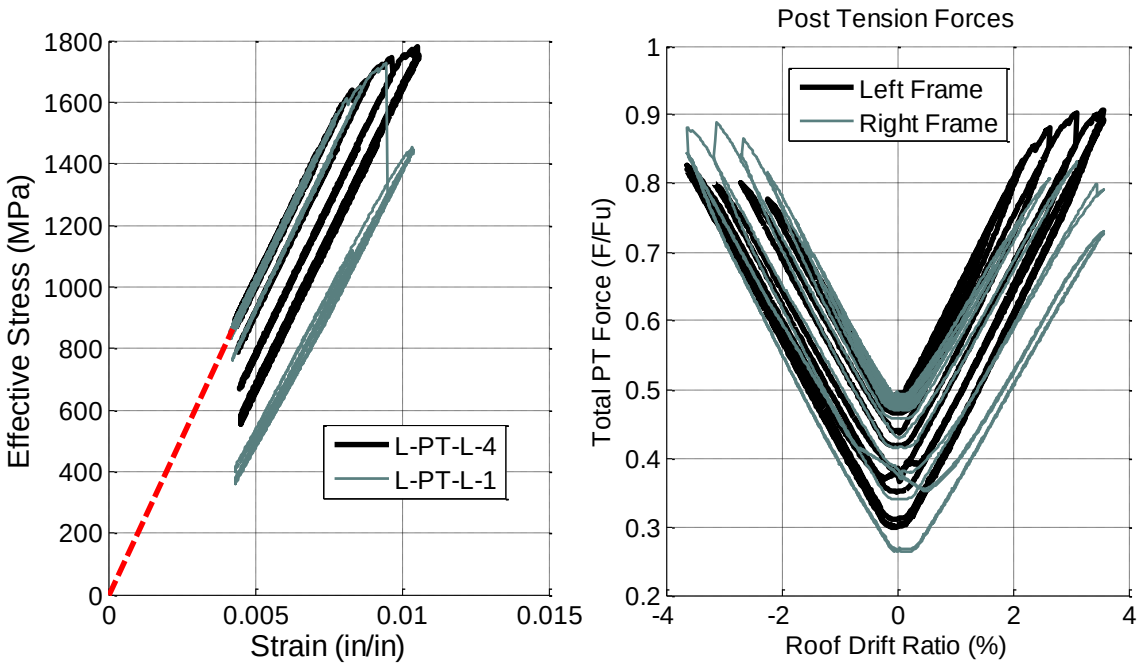

Figure 5.26 Example Stress-Strain Response (Left) and Total Post-Tension Force (Right) for Specimen A4

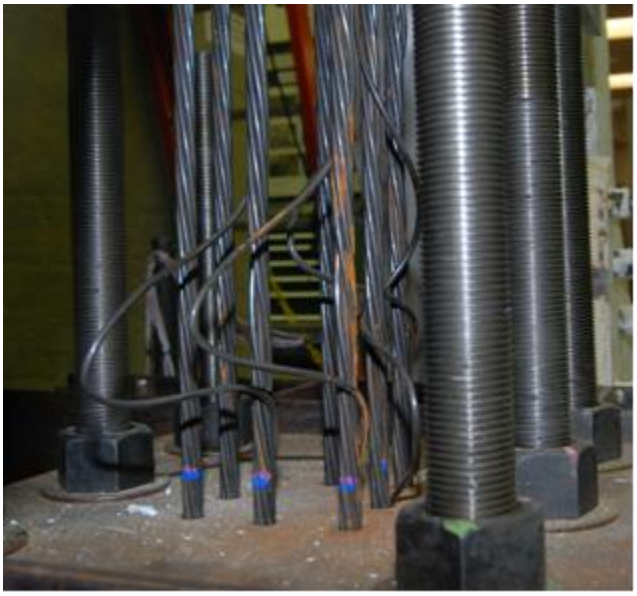

Figure 5.27 Photograph of Specimen A4 Unraveled Post-Tensioning Strands After Single Wire Fractures

Another difference in the load-deformation response shown in Figure 5.24 compared to previous specimens is a sharper change in stiffness on unloading from large displacements. This can be traced to the component of response due to the fuses as shown on the right of Figure 5.25 and then to the fuse hysteretic behavior shown on the left of Figure 5.28. The fuse response was significantly influenced by slipping of the fuse plate at its connections to the columns. The amount of slip was measured using the krypton measurements and is shown on the left of Figure 5.29 to be as much as 5 mm (0.2") in the direction parallel to the columns and 2.5 mm (0.1") in the direction perpendicular to the columns.

The prevalence of slip, and the amount of slip experienced by the fuses in Specimen A4 were dictated by several factors. Since the fuse was thicker and the number of bolts was more correlated to the number of fuse links than the fuse capacity, the bolted fuse connection had less strength relative to the fuse capacity than other specimens. Second, the frames were reused from one specimen to the next and deformations of the frame and displacements of the frames relative to one another caused alignment issues with the fuse bolts. To accommodate these dimensional changes, the standard size bolt holes in the fuse were drilled out to 38.1 mm (1.5") diameter holes and large washers were used between the nut and the fuse plate.

The fuse shear force at first slip was approximately 325 kN (73 kips) and the maximum shear force sustained by the fuse was 396 kN (89 kips). The slip critical strength of a 1" diameter A490 bolt is calculated to be 96.5 kN (21.7 kips) for class B surfaces including a resistance factor, ϕ=0.6 corresponding to long-slotted holes to be conservative (AISC 360-05). It is clear from these calculations, that the connection, if loaded in pure shear, should not have slipped. However, the fuse connection to the column acts as an eccentrically loaded bolt group. The eccentricity of the loading can be considered to be the distance from the quarter point of the fuse link to the bolt line which is 156 mm (6.13"). Using this eccentricity and a slip capacity of 96.5 kN (21.7 kips) per bolt, the connection should have had a shear capacity of 443 kN (99.5 kips) before slipping. It is expected that the reason for the difference was due to improper surface preparation to achieve class B slip resistance. The column surfaces were not sand-blasted between use, and the fuse plate surfaces were sand-blasted months prior to bolting. If the surfaces were more representative of class A surfaces, then the slip capacity of the bolts would correspond to 292 kN (65.7 kips) fuse shear force which relates to the approximate level of shear force in the fuse at the initiation of slip.

Despite the slippage of the fuse connections, the fuses still dissipated significant amounts of energy through inelastic deformations. The photograph included in Figure 5.30 shows the large zones of inelasticity as a slightly darker gray areas where the mill scale has flaked off. The photograph also shows the extent of slip that occurred as the dark area on the column next to the fuse.

Similar to previous tests, the forces in the struts remained relatively small as shown on the right of Figure 5.28. The struts only became engaged at large roof drifts after the fuses began to slip relative to the columns.

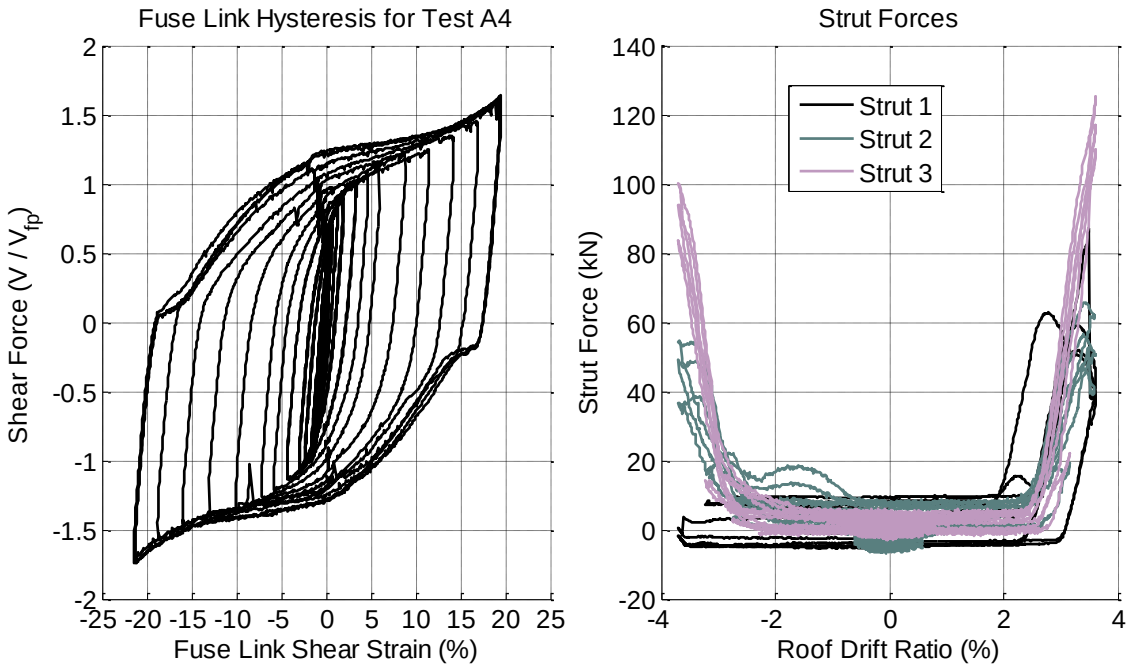

Figure 5.28 Fuse Hysteretic Behavior (Left) and Strut Forces (Right) for Specimen A4

The slipping of the fuse was not the only slip that was occurring in the specimen. All of the specimens experienced some amount of sliding at the base of the frames. The right side of Figure 5.29 shows the average displacement of the two frames at a height of 375 mm (14.75") above the bearing point. The lateral movement of this point shows a jump as the frames pass through zero roof drift ratio. This jump corresponded to the base of one or both frames sliding from one bumper to hit the other bumper. As shown in Figure 5.29, there was approximately 5 mm (0.2") of sliding occurring during this test. This amount of sliding correlates well with the amount of tolerance observed between the frames and the bumpers. Figure 5.31 shows photographs of both the pivoting and uplifting column bases when the frame was subjected to its second largest displacement cycle.

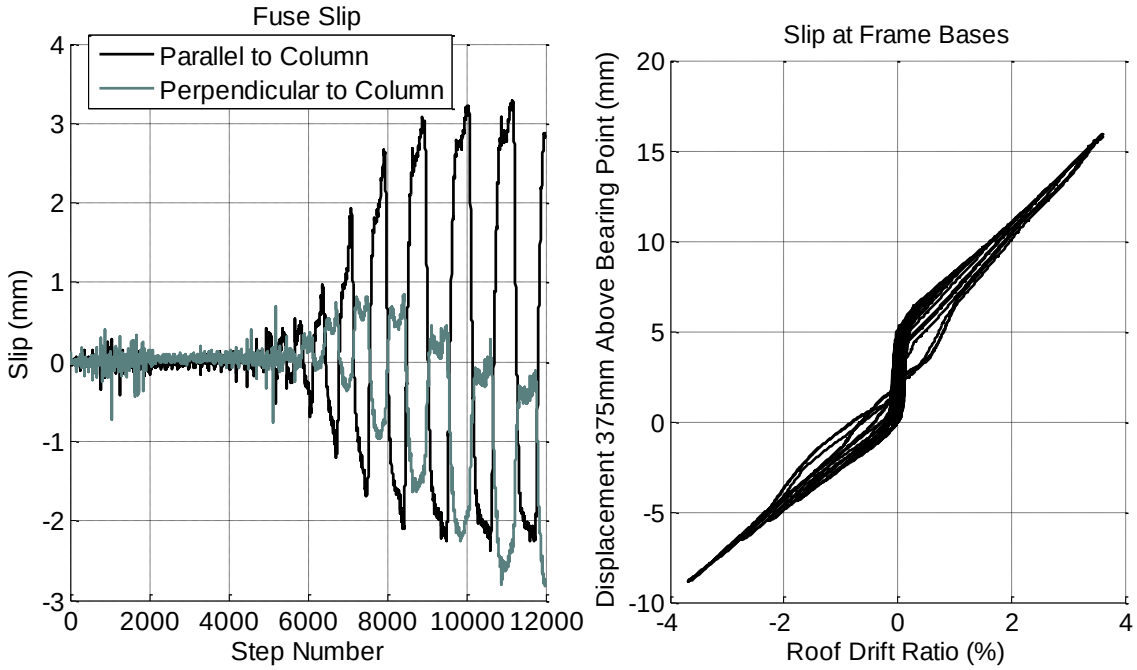

Figure 5.29 Fuse Slip Relative to the Column (Left) and Horizontal Displacement Near the Base Demonstrating Sliding (Right) for Specimen A4

Figure 5.30 Photograph of Fuse Showing Slip Relative to the Column and Yielding Along the Fuse Links for Specimen A4

Figure 5.31 Photograph of Pivoting Column Base (Left) and Uplifting Column Base (Right)

5.5 Specimen A7

Specimen A7 was a similar configuration as Specimen A1 except that it was the only dual-frame configuration that was tested without struts between the frames. Specimen A7 was also one of the three tests that were conducted to over 3.5% roof drift ratio allowing the post-tension strands to reach strains past yield. The self-centering ratio was slightly larger than Specimen A1 through a slightly larger initial post-tension force.

The fuses were, t = 6.35 mm (1/4") thick with 8 tapered links each that had a link length, L=356 mm (14"), a link depth at the ends, b=58.7 mm (2.3125"), and a link depth at the middle that was one-third the link depth at the end. The resulting design capacity for all the fuses was calculated to be V_{fp}=348.9 kN (78.4 kips). The post-tensioning consisted of eight 12.7 mm (½") diameter post-tensioning strands stressed to 34% of their ultimate strength or F_{pti}=497.3 kN (111.8 kips) total.

Using the equations defined in Chapter 3, the overturning ratio was found to be, OT=1.04, the self-centering ratio was SC=1.02, and the geometric ratio of frame width to fuse width was A/B=2.5. A photograph of the Specimen A7 configuration is provided in Figure 5.32.

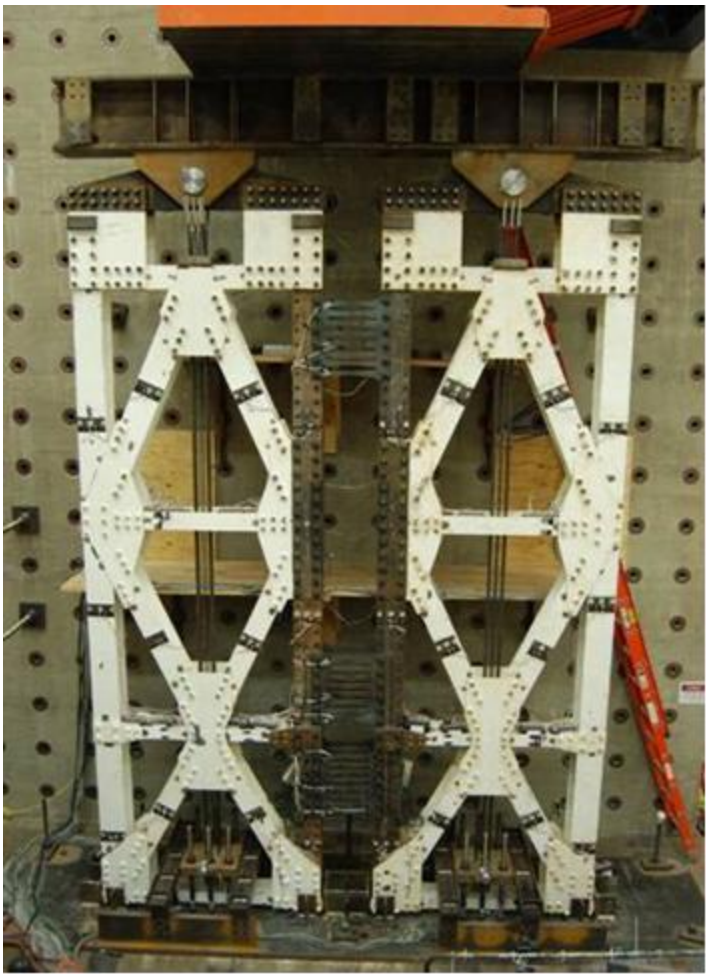

Figure 5.32 Photograph of Specimen A7

The system response as shown in Figure 5.33 is similar to the response of Specimen A1. The slightly larger self-centering ratio is evident in the reduction of drift at zero force compared to Specimen A1 and the height to the base of the flag in the hysteresis loops. Buckling of the fuses occurred in a manner similar to Specimen A1 and caused similar reduction in energy absorbing capability. As shown on the left of Figure 5.34, this test was conducted to approximately 4% roof drift ratio compared to the 3% peak roof drift ratio of Specimen A1. The effect of the buckled fuse as the system is pushed to 4% roof drift is shown on the right of Figure 5.34 to continue the trend noted for Specimen A1 in approaching the bilinear elastic response of the post-tension only system with additional resistance at large drifts due to tension in the fuses.

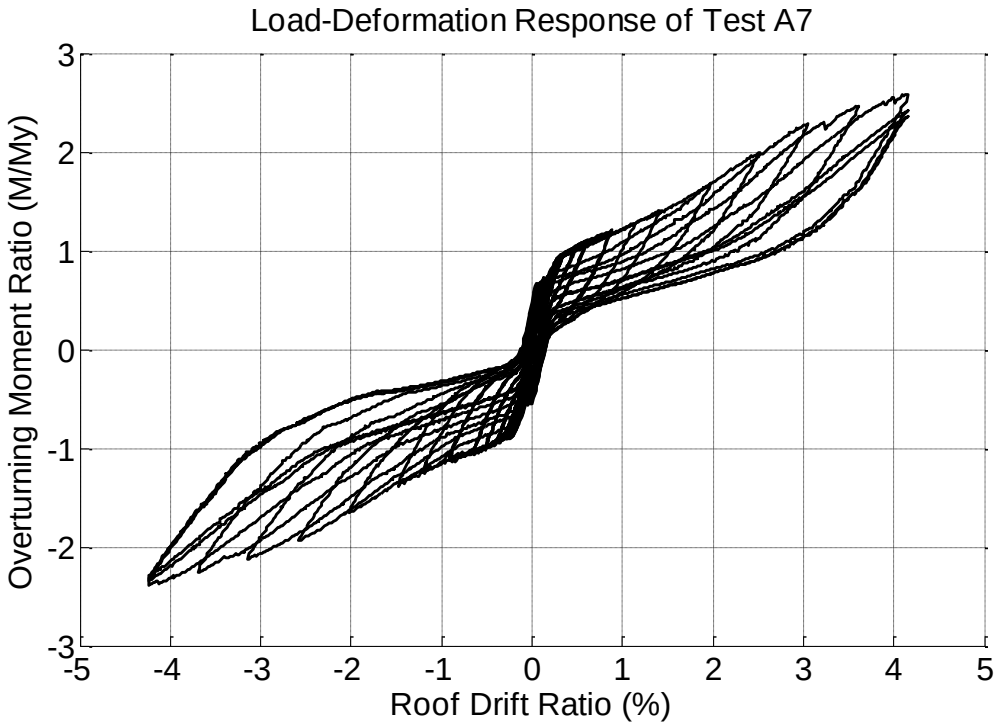

Figure 5.33 Load-Deformation Response for Specimen A7

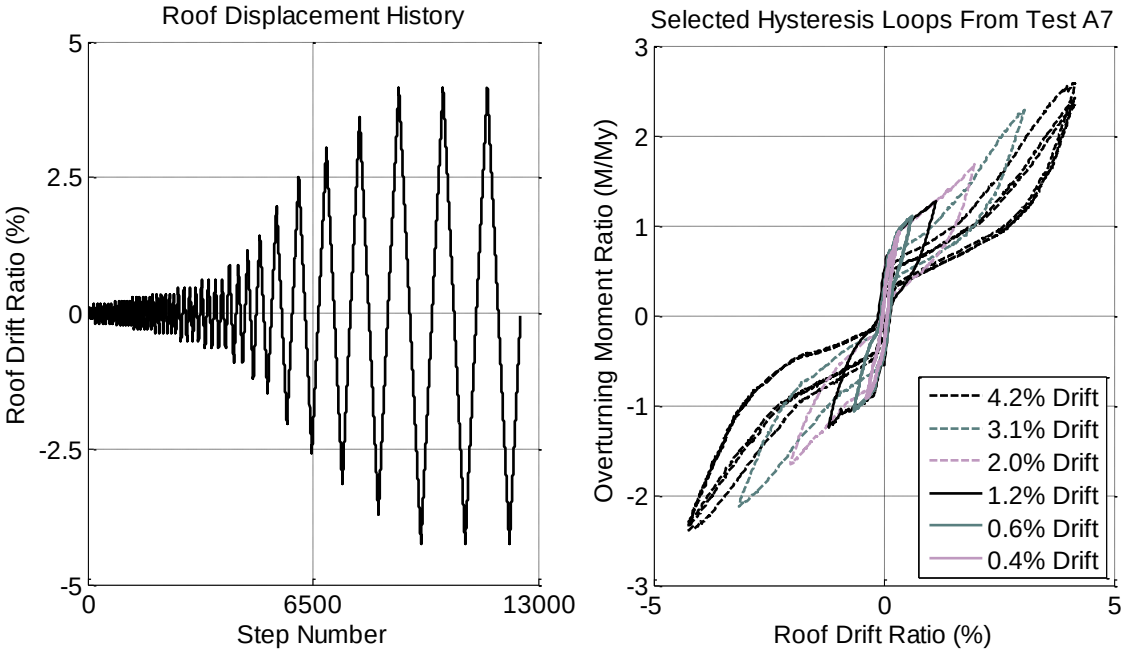

Figure 5.34 Roof Displacement History (Right) and Selected Hysteresis Loops (Left) for Specimen A7

The decomposed component behavior shown on the left Figure 5.35 further illuminates this point. After cycles at large roof drift, the fuse resistance is quite small through most of the cycle and then increases significantly as the fuse links engage in

tension at large drifts. As the fuse is stretched in a cycle and yields in tension, the amount of roof drift required to engage the fuse in tension for the next cycle is increased.

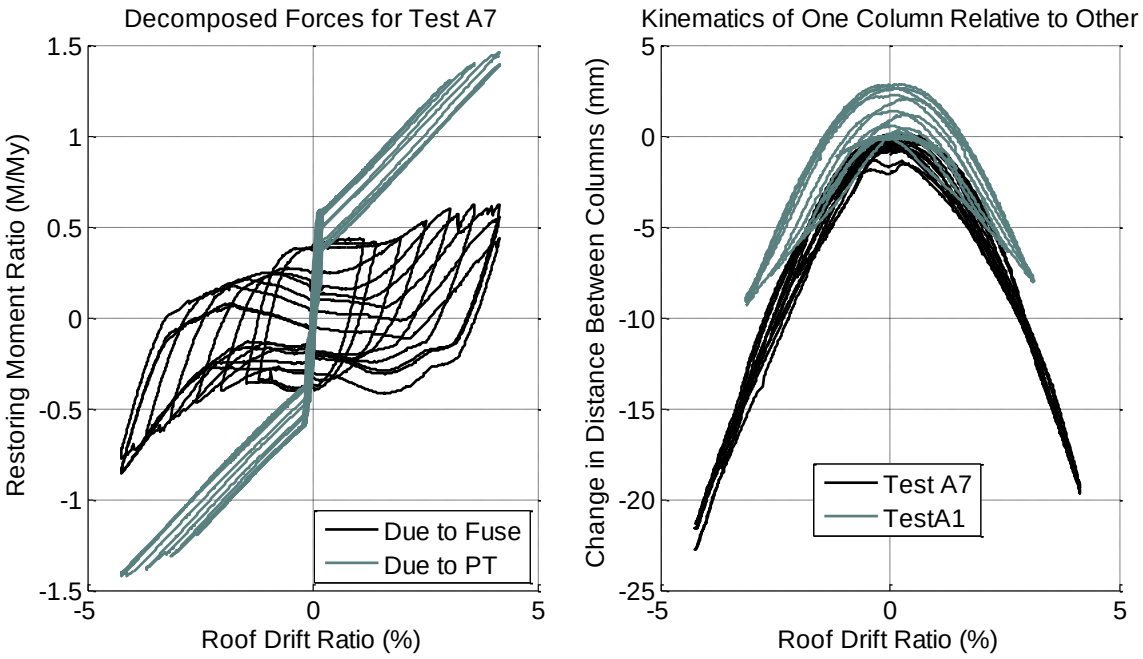

Figure 5.35 Decomposed Component Responses for Specimen A7 (Left) and Distance Between the Columns for Specimen A1 and A7 (Right)

It is noted that the fuse response shown in Figure 5.35 and Figure 5.36 does not include the first set of cycles up to 5% fuse shear strain which comprise the first 4550 steps. The beginning data is left out of the plots because the force measurements were erratic. Fuse shear forces are calculated as the difference in vertical force resultants in each frame above and below the fuse as calculated with all of the strain gages at the section just above and just below the fuse. At the start of the Specimen A7 test, approximately 20% of the strain gage wire connections to the junction boxes had become loose and were resulting in erratic strain measurements. After the problem was identified, the connections were fixed and the subsequent data was found to be stable and validated well between redundant measurements.

The hysteretic behavior of the fuses shown on the left of Figure 5.36, exhibits similar behavior as Specimen A1. The same initial elastic-plastic response is evident through the cycles at 8% fuse link shear strain at which point the response transitions into lateral-torsional buckling and then into axial tension and compression. The out-of-plane motion of the top fuse link as shown on the right of Figure 5.36 shows more dominance of the axial buckling mode than Specimen A1. This is shown by the amplitude of the second mode buckling deformations. After step number 6000, the left side of the fuse link is moving out-of-plane with a magnitude of approximately 25 mm (1") in a motion that is out of phase with the right side of the fuse link which is moving out-of-plane with an amplitude of 20 mm (0.79"). This implies a second mode axial buckling shape and the

deformations associated with this buckling are greater than those experienced in Specimen A1 which had struts between the frames.

The effect of struts on the dual frame configuration was measured in several ways. The effect of struts on frame member forces is investigated further in Chapter 11. The deformations and displacements of the frame are demonstrated by the fuse buckling described above and also by the distance between the columns shown on the right of Figure 5.35. The interior columns of the two rocking frames of a dual frame configuration get closer together during rocking due to the kinematics of rigid body rotation. It has been shown earlier in this section that the frames are also tilting toward each other as they rock. Figure 5.35 shows, however, that the columns of Specimen A7 were drawn closer together than for Specimen A1. This is due to less restraint between the columns because of the absence of the struts. The frames were still constrained against relative motion by bumpers at the bottom and the loading beam at the top. The axial forces in the fuses were transferred through the frames to the top and bottom constraint.

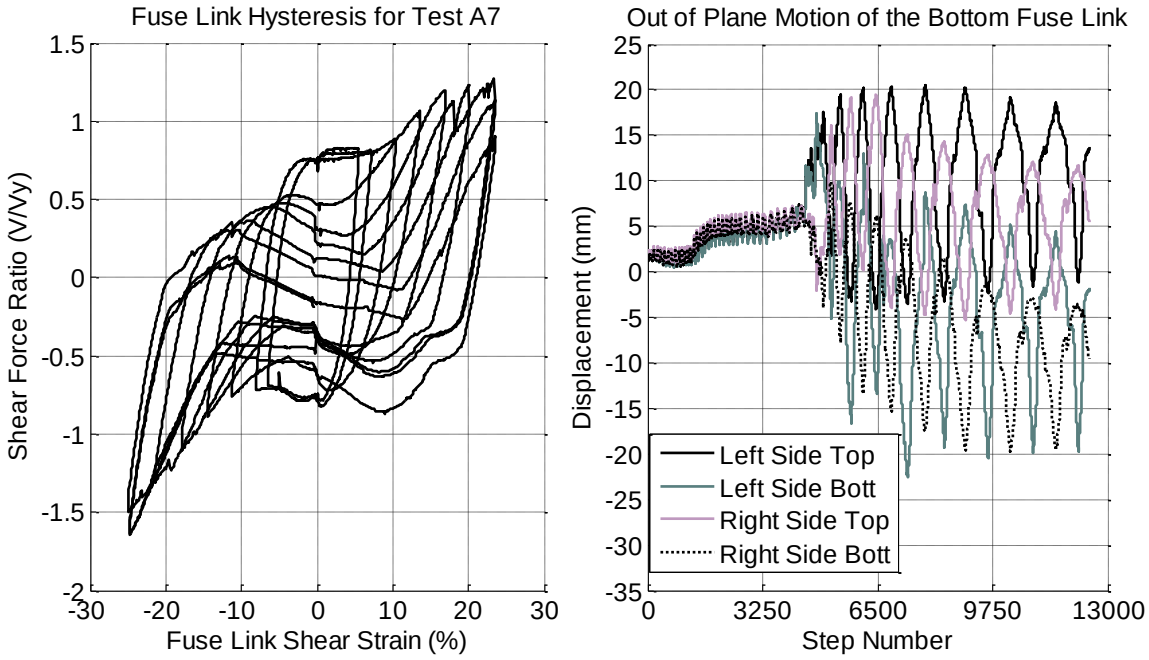

Figure 5.36 Fuse Hysteretic Behavior (Left) and Fuse Out-Of-Plane Displacements (Right) for Specimen A7

Two of the post-tensioning strand wires fractured in the right frame at drifts exceeding 3% roof drift ratio. Figure 5.37 shows a comparison of two strands that underwent similar strain histories but one fractured while the other did not. Similar to the discussion above for Specimen A4, only one wire of the seven wires fractured leading to a reduction in the initial prestress force and a slight reduction in stiffness. As shown in Figure 5.38, both frames experienced a loss of post-tension force during the test. The losses in post-tensioning force for the left frame were due exclusively to yielding of the post-tensioning strands, while the losses in post-tensioning force for the right frame were due to a combination of yielding and two wire fractures. Both frames lost 38% of their

initial post-tensioning force but the frames did not exhibit significant losses in system strength or self-centering ability for this configuration.

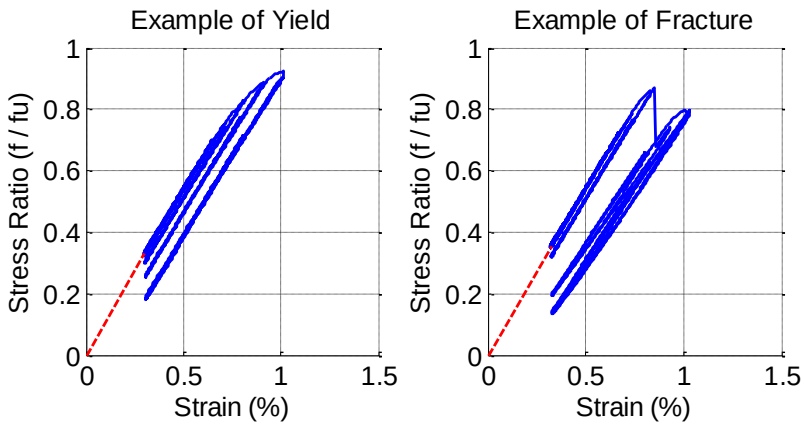

Figure 5.37 Examples of Stress-Strain Response for a Strand That Did Not Fracture (Left) and One that Did (Right)

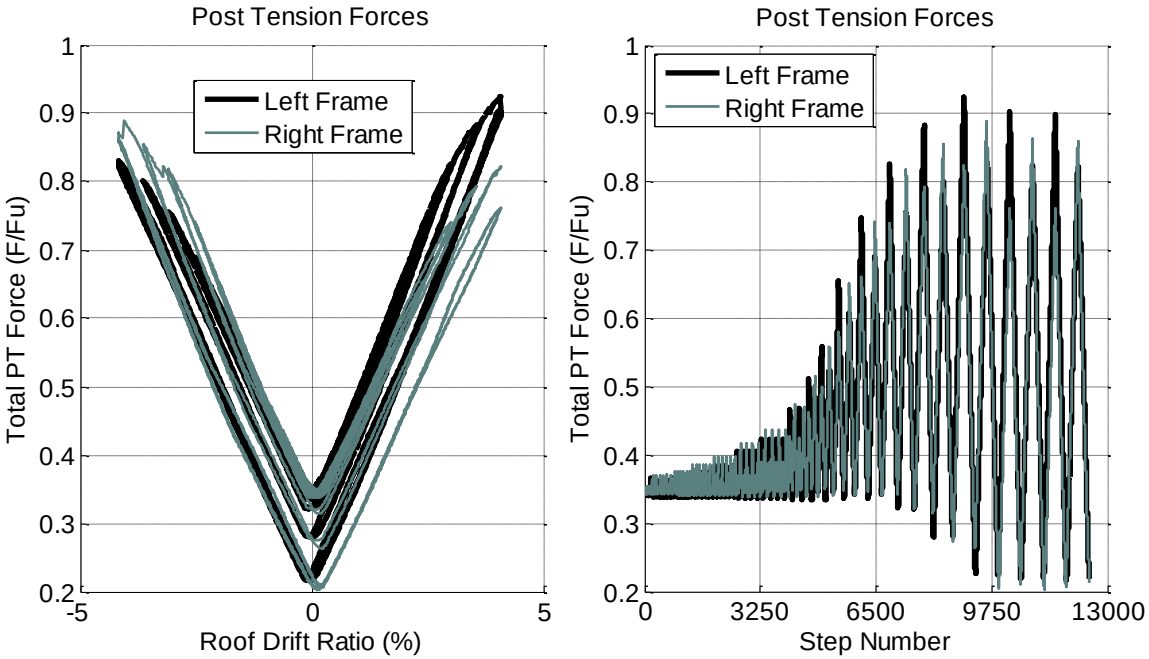

Figure 5.38 Total Post-Tension Force Versus Roof Drift Ratio (Left) and Versus Step Number (Right)

5.6 Specimen B1

Specimen B1 was one of the two single frame configuration specimens tested. The two single frame configurations had similar system proportioning and configuration but differed on the type of fuse. The fuse for Specimen B1 consisted of a single plate with fuse links on both sides of the central connection. The fuse was, t = 19.1 mm (3/4") thick with 3 tapered links on each side that had a link length, L=152.4 mm (6"), a link depth at

the ends, b=42.9 mm (1.6875”), and a link depth at the middle that was one-third the link depth at the end. The resulting design capacity for the fuse was calculated to be V_{fp}=181.6 kN (40.8 kips). The post-tensioning consisted of four 12.7 mm (½”) diameter post-tensioning strands stressed to 45% of their ultimate strength or F_{pti}=333.6 kN (75.0 kips) total. Using the equations defined in Chapter 3, the overturning ratio was found to be, OT=1.09, and the self-centering ratio was SC=1.84. The two single frame tests used higher self-centering ratios than the dual frame configurations because of the difference in the requirement to avoid global uplift.

A photograph of the setup for the Specimen B1 and Specimen B2 tests is shown on the left of Figure 5.39 and the fuse assembly is shown on the right of Figure 5.39. The fuse is anchored down on the two sides by double channels bolted onto the front and back of the fuse. The center of the fuse is attached to a center column through a pin connection and the other end of the center column is attached to the frame with a pin connection. As the frame rocks, the middle of the frame will uplift engaging the center column and through it, the fuse. The single frame configuration is described in more detail in Chapter 4.

Figure 5.39 shows the two specimens, B1 and B2 side by side. In fact the specimens were tested simultaneously using the same displacement history. Since there were no connections between the frame and the pin load cells at the top monitored the loads input into the frames separately, the two specimens did not interact during the test.

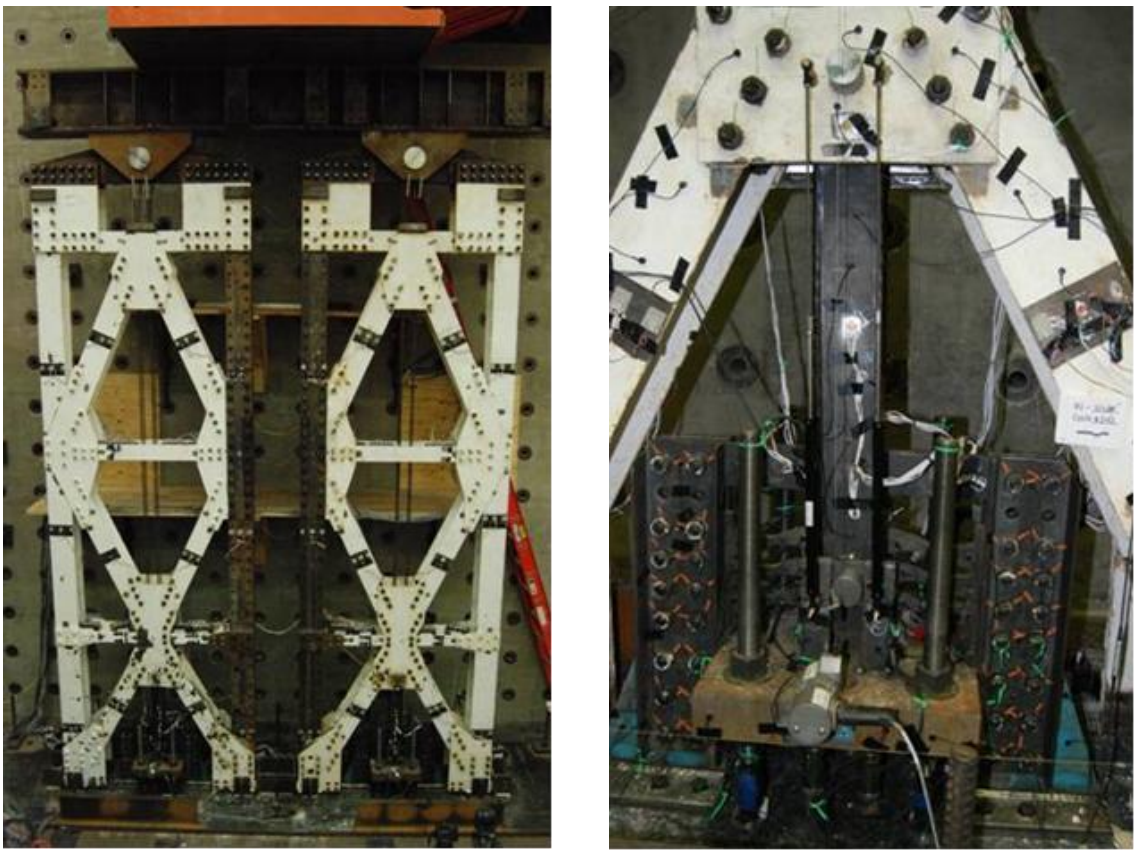

Figure 5.39 Photograph of Specimen B1 and B2 (Left) and Close-Up Photograph of the Specimen B1 Fuse Assembly (Right)

The load-deformation response for Specimen B1 is given in Figure 5.40. Although the general response is similar to the dual frame configurations, there are several distinct features. There are lags in the loading and unloading curves that indicate horizontal displacement of the frame without associated change in lateral load. These lags in the response are due to pin hole tolerance in the connection of the fuse to the frame. There are two pin connections, one from the fuse to the center strut and one from the center strut to the frame which both have pin hole tolerances in both the outer plies of plates and the inner plies. In total, the cumulative tolerances for four pin holes combine to create the amount of uplift that the middle of the frame must experience before the load in the fuse can change direction. The lags in response are therefore occurring when the fuse is at zero force.

Furthermore, even though the displacement history is similar to Specimen A7 as shown on the left of Figure 5.41, there is almost no energy dissipation until after the cycle at 0.6% roof drift ratio as shown on the right of Figure 5.41. The effect of the pin hole tolerance is further described by the response of the decomposed component responses shown on the left of Figure 5.42. The lag in fuse shear force upon load reversal is clear. However, the fuse hysteretic response shown on the right of Figure 5.47 demonstrates that the fuse response has no lags in behavior. Note that the issue of pin hole tolerances are addressed in Chapter 7 and methods for mitigating the problem are described and were successfully implemented in the single frame configuration shake table tests at E-Defense.

The fuse response as shown on the right of Figure 5.47 exhibits full hysteresis loops and near elastic-plastic behavior. It is shown that the fuse is only strained in the positive shear strain direction. This is because positive shear strain is defined as the middle of the fuse displacing upward which is the only direction in which the frame can apply displacements.

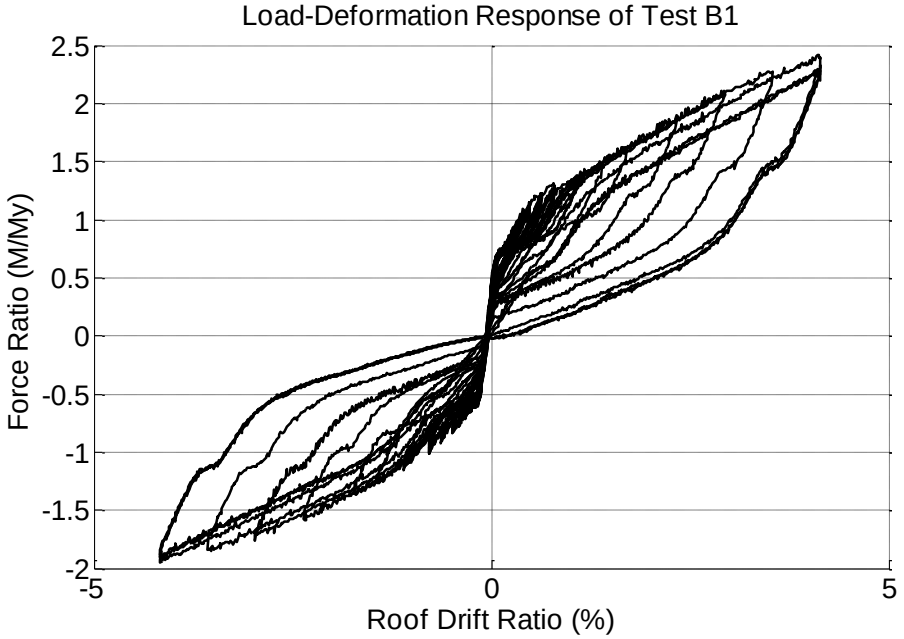

Figure 5.40 Load-Deformation Response for Specimen B1

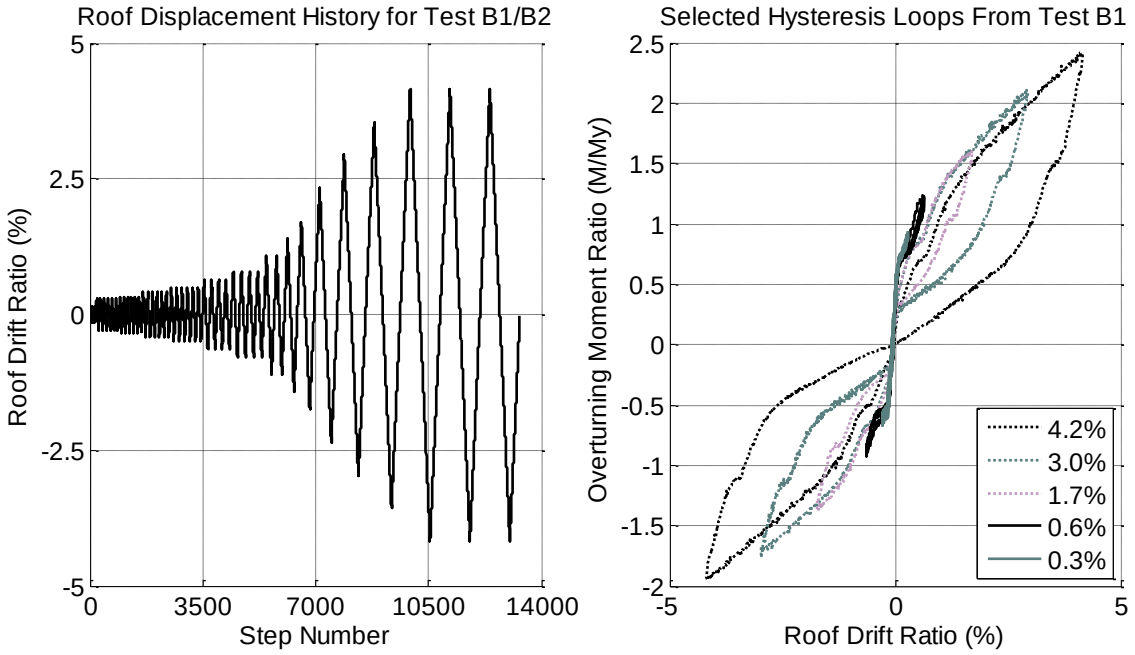

Figure 5.41 Roof Displacement History (Left) and Selected Hysteresis Loops (Right) for Specimen B1

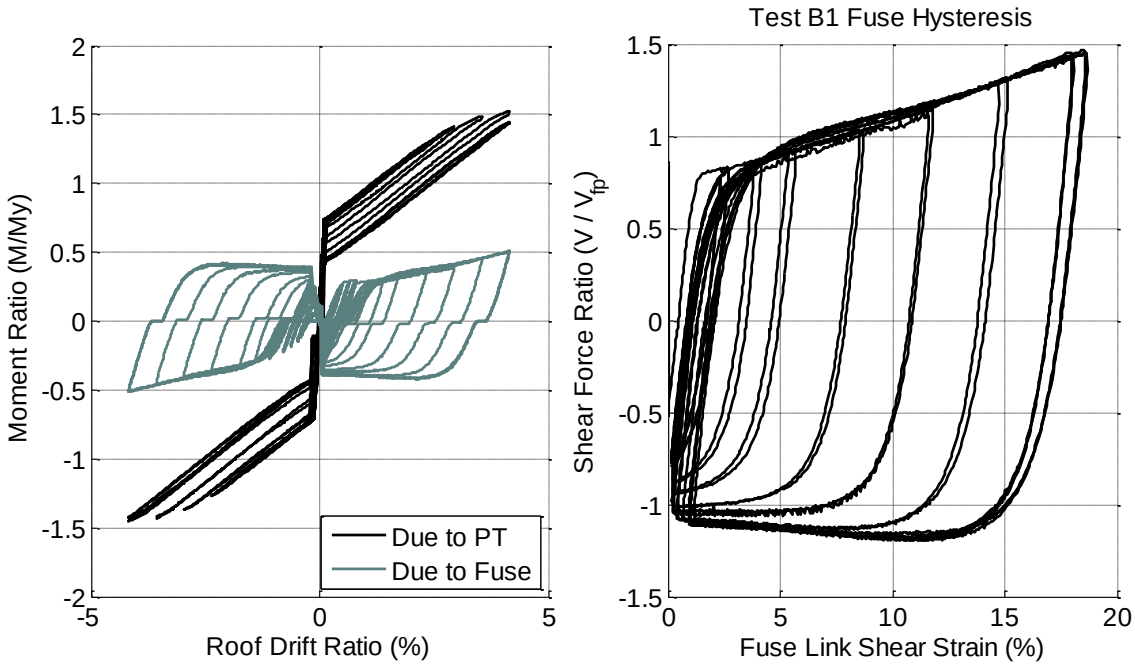

Figure 5.42 Decomposed Component Response (Left) and Fuse Hysteretic Behavior (Right) for Specimen B1

The post-tensioning behavior for Specimen B1 and Specimen B2 highlighted the uncertainty associated with post-tension wire fracture. As shown on the left of Figure 5.43, the post-tensioning forces in the Specimen B1 strands reached as high as 95% of

ultimate without fracturing. Instead, all four of the strands underwent significant yielding, reaching strains as large as 1.06%. On the right side of Figure 5.43, the post-tension forces for Specimen B1 are compared to Specimen B2. As discussed in the next section, the post-tension strands in Specimen B2 experienced multiple wire fractures.

Even with the loss in post-tension force experienced by the system, the overall system response still exhibited almost no drift at zero force as shown in Figure 5.40. This is in part due to the large self-centering ratio, but also due to the difference in configuration compared to the dual frame configuration. The dual frame configuration has fuses along the height of the frames. The fuses retain large loads when the lateral loads are removed which cause elastic deformations and displacements of the frames. The single frame configuration on the other hand has the fuses concentrated at the base where they can not cause any significant deformations in the frames.

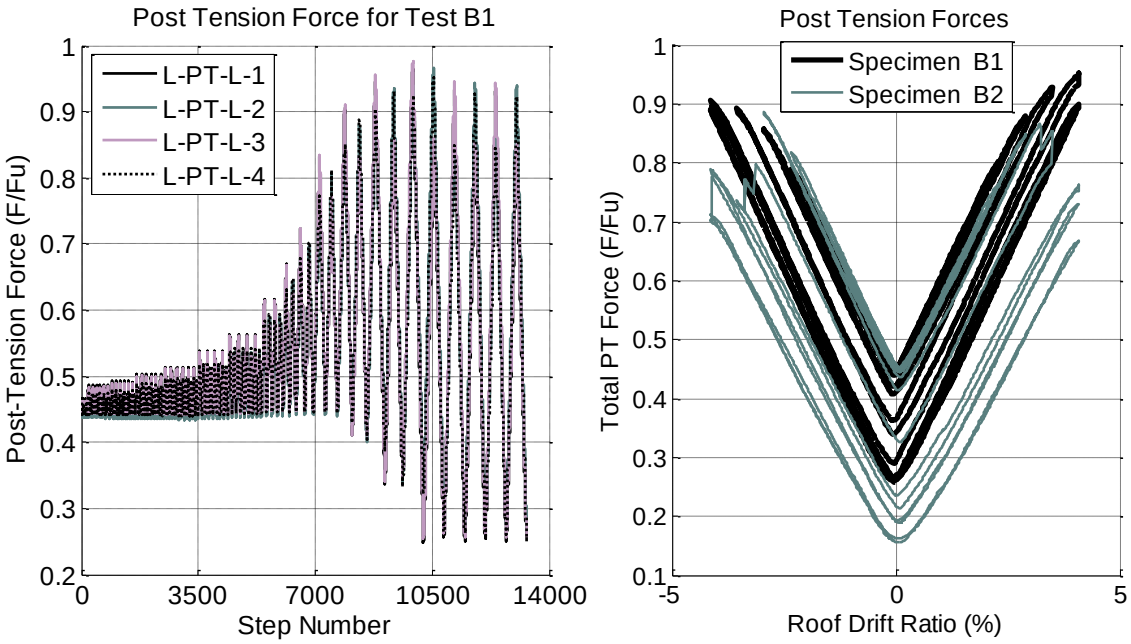

Figure 5.43 Post-Tension Strand Forces Throughout the Test for Specimen B1 (Left) and Comparison of Total Post-Tension Forces in Specimens B1 and B2 (Right)

5.7 Specimen B2

Specimen B2 was the other of the two single frame configuration specimens tested. The fuse consisted of two plates with a bracing plate in between, as shown in Figure 5.44. The central bracing plate was not connected to the center strut or pin and instead acted to brace the double channels on either side of the fuse against inward pull. The bracing plate also restricted the fuse link buckling to only occur away from the bracing plate.

The fuse was , t = 4.76 mm (3/16") thick with 5 tapered links on each side that had a link length, L=152.4 mm (6"), a link depth at the ends, b=47.6 mm (1.875"), and a link depth at the middle that was one-third the link depth at the end. The resulting design capacity for both fuses was calculated to be V_{fp}=160.7 kN (36.1 kips). The post-tensioning consisted of four 12.7 mm (½") diameter post-tensioning strands stressed to 45% of their ultimate strength or F_{pti}=333.6 kN (75.0 kips) total. Using the equations

defined in Chapter 3, the overturning ratio was found to be, OT=1.04, the self-centering ratio was SC=2.08.

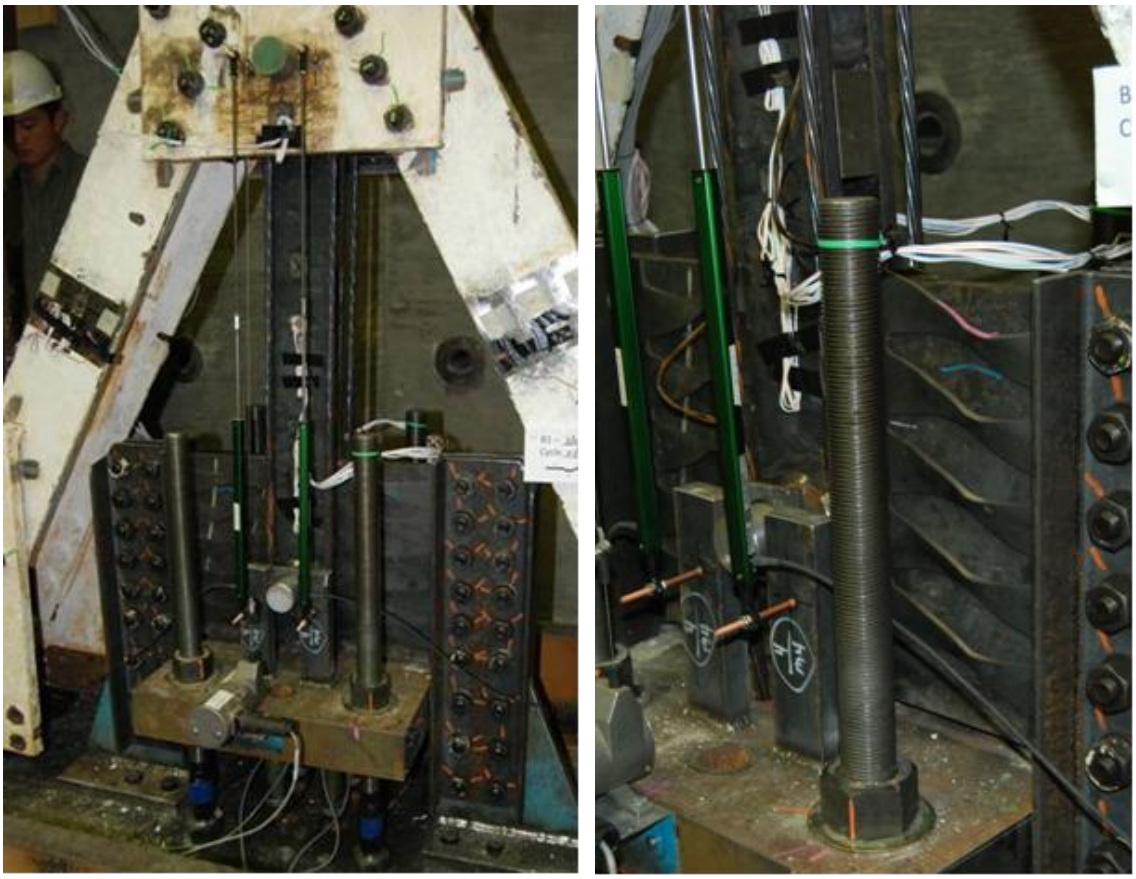

Figure 5.44 Photograph of the Specimen B2 Fuse Assembly (Left) and Photograph of the Deformed Fuse (Right)

The same lag in response due to pin hole tolerances is seen in Figure 5.45 as was demonstrated in Specimen B1. The lag was found to be even greater in Specimen B2 and is illustrated in both plots of Figure 5.46. The initial load-deformation response exhibits a sharp change in stiffness at uplift at approximately 60% or 70% of the system yield force. The response does not develop the full system yield force until a roof drift ratio 0.7% or 0.8%. As noted above for Specimen B1, however, the experimental program described here was successful in identifying this issue and methods for mitigating the lag have been devised and successfully implemented in the E-Defense shake table test specimen. These mitigation techniques are discussed in Chapter 7.

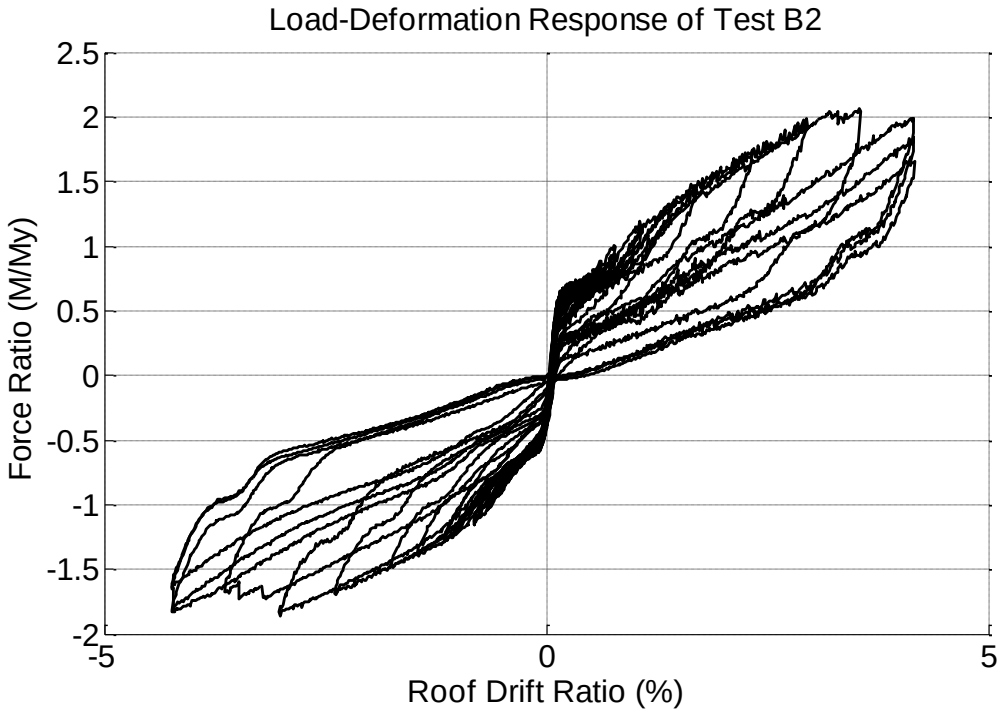

Figure 5.45 Load-Deformation Response for Specimen B2

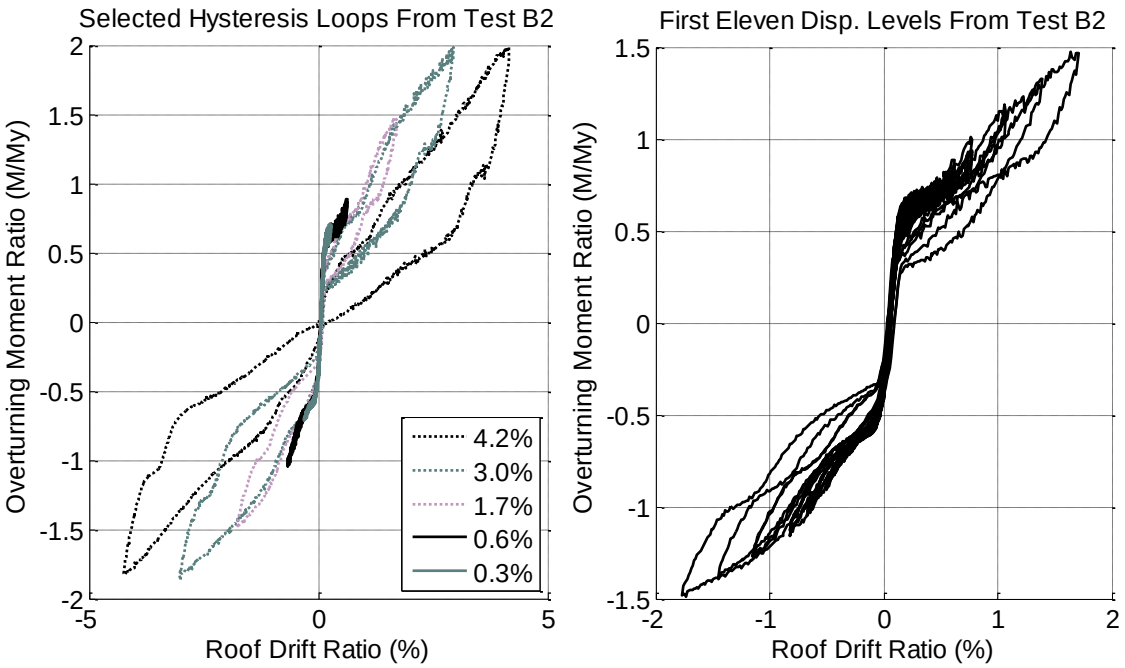

Figure 5.46 Selected Hysteresis Loops (Left) and Hysteresis Loops Up to 1.7% Roof Drift (Right) for Specimen B2

The fuses as shown in the photograph in Figure 5.44 were thin and buckled regardless of bracing on one side. The buckled fuse response is shown in Figure 5.47.

The backbone continues to increase after buckling and the reduction in energy dissipating capacity was not reduced as much as the Specimen A1 or A7 fuses.

As mentioned in the previous section, the post-tensioning behavior for Specimen B2 was significantly different than the post-tensioning response for Specimen B1. Both frames were fabricated using the same methods and processes, the post tension anchorage was nearly identical and the post-tensioning strand installation procedures were the same for both Specimens. However, of the 28 wires contained in the 4 strands of each Specimen, five fractured in Specimen B2 whereas none of the wires in Specimen B1 fractured. The strands in Specimen B2 reached slightly larger strains as high as 1.14%, but for the most part experienced similar displacement histories as Specimen B1. The effect of the strand fracture on the decomposed post-tension component response is shown on the left of Figure 5.47.

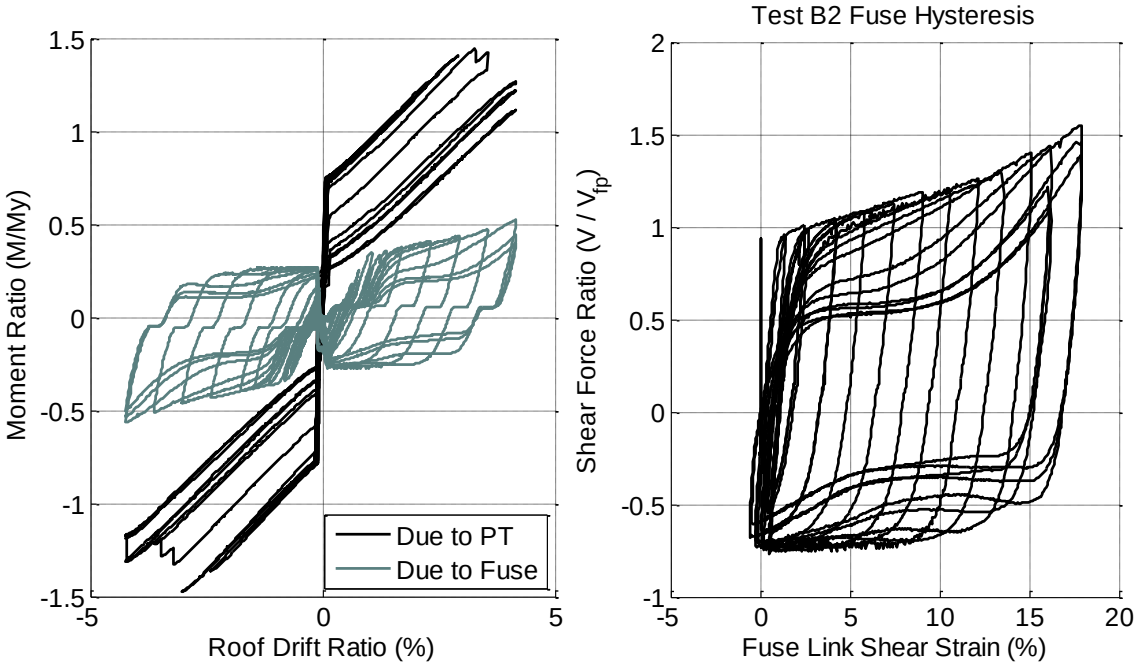

Figure 5.47 Decomposed Component Responses (Left) and Fuse Hysteretic Behavior (Right) for Specimen B2

The loss in force for each post-tension strand is shown on the left of Figure 5.48. Unlike the strands that don't fracture, the strands loose large portions of their prestress at distinct moments of the test. The right side of Figure 5.48 shows the one strand in any of the tests that experienced fracture of more than one wire. It is shown that the post-tension force in this strand is near zero by the end of the test. However, similar to Specimen A4 and Specimen A7, the fracture of individual post-tension wires did not propagate through to other wires or to other strands in this displacement controlled test. Also, for this specimen, the strand yielding and wire fracture did not cause a significant loss of system load carrying capacity or the ability of the system to eliminate drift when the loads are removed.

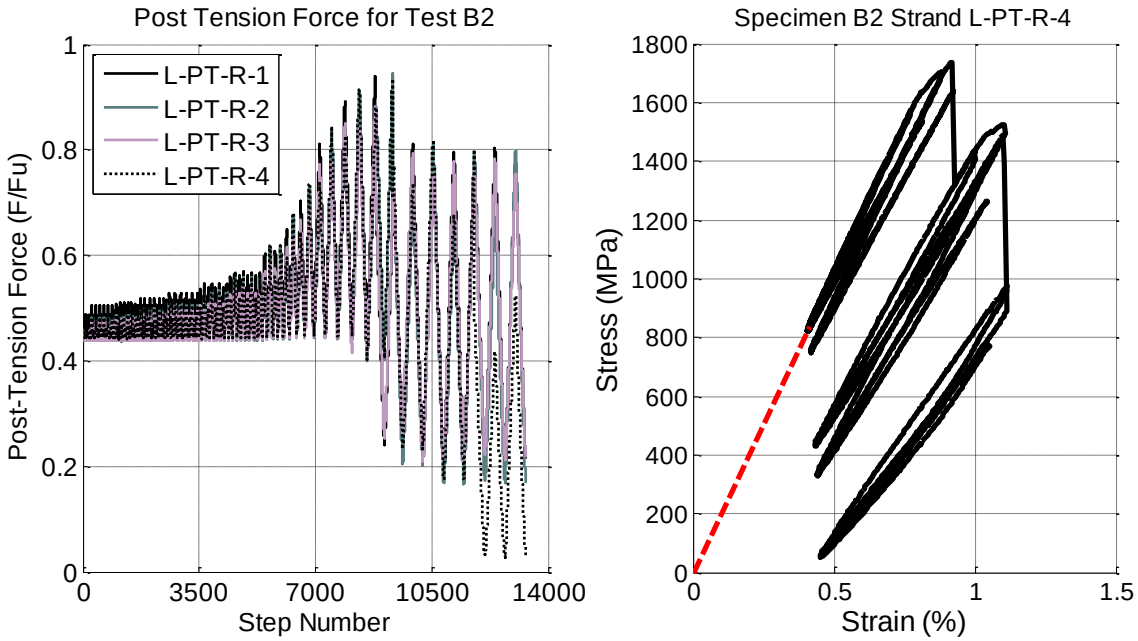

Figure 5.48 Post-Tension Forces for Each Strand in Specimen B2 (Left) and Stress-Strain Response for a Strand that Fractured Two Wires (Right)

5.8 Summary of the Cyclic Test Results

As described in Chapter 4, and at the beginning of this chapter, the large-scale cyclic tests produced a considerable amount of data for use in quantifying the performance of the individual components, validating the performance of the system, and developing computational models. The reader is directed to Appendix B for the raw data, Appendix C for the calculations performed on the data, and Appendix D for the validation of the data.

The controlled rocking system exhibited cyclic performance similar to the expected response described in Chapter 3. The global load-deformation response was a flag-shape which possessed near zero displacements when the forces were removed. The frames were reused for all the cyclic test specimens and did not experience any observed damage. The cyclic tests were successful in experimentally validating the expected system performance, identifying which connection details worked well, and identifying details and construction methods that could be improved. See chapter 8 for further conclusions and interpretation of the test results.

The cyclic tests included variations in several of the system parameters to allow their effect on component response and global behavior to be investigated. Observations about the response of each specimen tested cyclically were described in this chapter. Chapter 8 includes synthesis of all the test data obtained from the testing program to draw conclusions about the global system response, effectiveness of specimen detailing, post-tensioning behavior, fuse behavior, effect of struts in the dual frame configuration, and comparisons of the single frame and dual frame configurations.

COMPUTATIONAL MODEL DEVELOPMENT

6.1 Description of the Model

A two-dimensional computational model of the specimen was created using the OpenSees software (Mazzoni et al. 2009). The model primarily uses frame elements and includes a simplified phenomenological model for the fuses. The purpose of this model is to provide an experimentally verified, computationally inexpensive model that can be used to examine the application of the controlled rocking system to different configurations, to conduct the sensitivity study described in a later chapter, and to inform design procedures.

A corotational transformation is used to map local coordinates to global coordinates incorporating large displacements and large rotations. Since the tests were conducted to roof drift ratios exceeding 4% in some cases, capturing the geometric nonlinearity due to the associated displacements was found to have a significant effect. Geometric nonlinearity is most noticeable in the fuse response as the fuse experiences large axial deformations and forces which are not captured in a linear analysis. Fuse axial forces contribute to the global resistance of the system to horizontal loads and are an important consideration in frame design.

The model is built in stages to simulate actual construction sequencing. First the frames, spring supports, and post-tensioning are modeled. The initial post-tension force is applied as an initial strain in the material constitutive model. Ten analysis steps are run to allow the post-tension force to be applied to the frames. Some post-tension force is lost as the frames shorten, and iterations are performed, if necessary, to increase the initial strain in the post-tension strands until the target initial force is obtained. Subsequently, the fuses are added to the model and the ends of the fuses are secured to the frames using multi-point constraints through the use of the OpenSees command, equalDOF.

The geometry of the analytical model is defined to closely match the physical specimen as shown in Figure 6.1. The typical frame members were defined with the same area and moment of inertia as the wide flange shapes they represent and used an elastic beam column element. The ends of the frame members are allowed to transfer moment, except for the struts and the post-tensioning, as shown by open circles in Figure 6.1. Horizontal displacement is applied equally at the load cell pin locations to produce the target displacement. Since the test control is designed such that the vertical force at the load cell pins is zero, the application of horizontal load at the load cell pins simulates the effect of the test control.

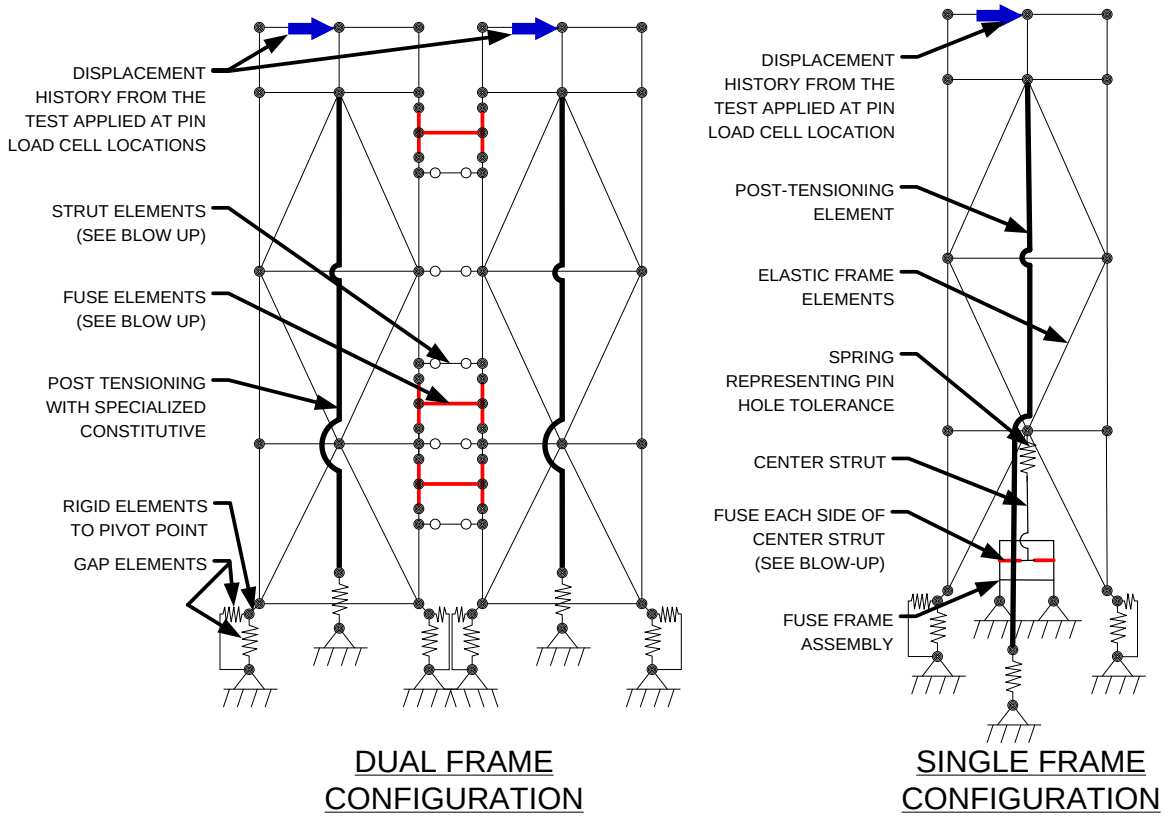

Figure 6.1 Computational Model for the Dual Frame Configuration (Left) and Single Frame Configuration (Right)

The frames sit on gap elements that are stiff in compression, but have no stiffness in tension. Conversely, the post-tensioning strand element connects at the bottom to a gap element that is stiff in tension, but has no stiffness in compression so that the post-tensioning strands which have negligible buckling capacity are not allowed to experience compression forces. The stiffness of both types of elements is 1751 kN/mm (10,000 kips/in) which is four times greater than the stiffness of the specimen frame columns.

The struts that connect the two frames utilize an elastic perfectly plastic constitutive relationship with 345 MPa (50 ksi) yield stress and modulus of elasticity of 200 MPa (29,000 ksi), but were not found to experience yielding in the computational simulations of the tests. As discussed in the previous chapter, one of the characteristics of the strut behavior observed from the tests was a lag in picking up force due to hole tolerances in the pin connections. The pin holes were machined to be approximately 1.6 mm (1/16") greater than the size of the pin. At the pin connections on both ends of the struts, there were holes in both parts being connected. The tolerances from all four holes were cumulative in creating the lag in engaging the struts. This totaled approximately 6.35 mm (0.25") of displacement to go from axial tension to axial compression or vice versa. This lag was modeled using a zero length spring that represented the pin hole tolerance. As shown schematically on the small inset load-deformation plot on Figure 6.2, the spring had a low stiffness of 0.88 kN/mm (5 k/in) and then at displacements of

±3.18 mm (±0.125”) the stiffness was increased to 880 kN/mm (5000 k/in). This type of bilinear elastic constitutive was implemented using the self-centering material in OpenSees with zero energy dissipation and properly set stiffness values.

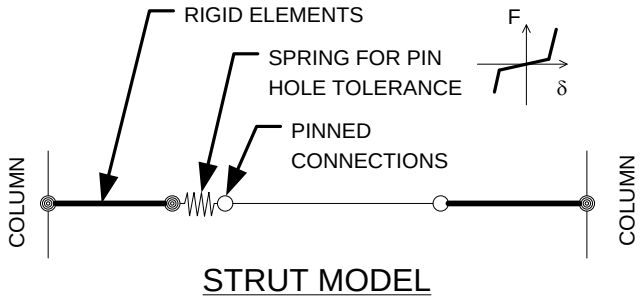

Figure 6.2 Computational Model for the Axial Struts

As discussed in Chapter 5, sliding at the base was another form of slip observed in the experimental behavior. Sliding at the base is also discussed further in Chapter 8. The frames were found to slide as much as 5.7 mm (0.22”) during the tests. Zero length springs similar to those described above for the strut connections were attempted at the base connections of the computational model, but were ultimately abandoned for four reasons. First, unlike the strut connections, sliding at the base experiences more friction between the two bearing surfaces. It was determined that the simple zero-length spring with bilinear elastic constitutive was not accurately capturing the friction aspect of behavior. Second, the computational model including base sliding had problems converging during slippage. Third, it was determined that sliding at the base is something that can be controlled in practical applications of the controlled rocking system. Lastly, the amount of tolerance between frames and bumpers is not expected to be larger for full scale buildings than those for the half-scale specimen. As a result, base sliding will have less effect on full scale building response. As described in Chapter 8, sliding at the base was virtually eliminated with the addition of shim plates between the bumpers and the frames. Adding shims is a quick and simple method for allowing tolerances during construction and eliminating any adverse affects of sliding.

The computational model for the single frame configuration consisted of the same components as the dual frame model. As shown on the right of Figure 6.1, there were two fuses, one on each side of the center strut. The center strut is connected to the frame with a zero-length spring that simulates the pin hole tolerances in the pin connections a the top and bottom of the center strut. This zero-length spring was implemented in an identical way as the zero-length spring representing pin hole tolerances for the struts described above. In this case, the hole tolerances were approximately 1.27 mm (0.050”) larger than the pin which were cumulative over the four sets of holes totaling the 5.1 mm (0.2”) of pin hole tolerance that was implemented in the model.

6.2 Post-Tensioning Model

The post-tensioning strands utilize a trilinear constitutive relationship as shown in Figure 6.3 to account for seating losses and yielding of the post-tensioning strands. As discussed in Chapter 5, the post-tensioning strands experience losses in force as the wedges at the anchorages get pulled farther into the anchorage. This occurs whenever the strand is stressed past its previous maximum force. Chapter 8 discusses methods for mitigating seating losses through some simple additional steps in the installation procedure, but seating losses are included in the computational model to facilitate the investigation of their effect in the later sensitivity study.

The post-tensioning strand element uses a trilinear constitutive relationship denoted in Figure 6.3 as Material 3 which is the combination of two other constitutive relationships in parallel. First, an elastic-perfectly plastic material, denoted Material 1 in Figure 6.3, is created with an initial stress, σ_0, equal to the target initial stress in the post-tensioning strands, modulus of elasticity, E_1, as given in Equation (6.3), and yield stress, σ_1, as given in Equation (6.5). The second component, denoted Material 2 in Figure 6.3 is a hardening material with stiffnesses, E_2 and E_3 as defined in Equation (6.1) and Equation (6.3) respectively and yield stress, σ_1, as given in Equation (6.6).

$$E_2 = \beta_1 E_{PT} \tag{6.1}$$

$$E_3 = \beta_2 E_{PT} \tag{6.2}$$

$$E_1 = E_{PT} - E_2 \tag{6.3}$$

$$\varepsilon_1 = \frac{\sigma_{prev} - \sigma_0}{E_{PT}} \tag{6.4}$$

$$\sigma_1 = \varepsilon_1 E_1 + \sigma_0 \tag{6.5}$$

$$\sigma_2 = \sigma_y - \sigma_1 \tag{6.6}$$

Where:

E_1, E_2, E_3, and ε_1 are Defined in Figure 6.3

E_{PT} is modulus of elasticity from material tests = 202 GPa (29,300 ksi)

β_1 is calibrated ratio for seating losses =0.90

β_2 is kinematic hardening ratio from material tests = 0.017

σ_{prev} is the previous maximum strand stress

σ_0 is the initial stress in the post-tension strand

σ_y is yield stress from material tests = 1750 MPa (253.8 ksi)

By combining Material 1 and Material 2 in parallel, a third constitutive relationship is created which is denoted Material 3 in Figure 6.3. This material approximates the behavior of the post tension strands. The initial stress, σ_0, is set to the initial pretension stress, and then elastic loading occurs with a modulus of elasticity equal to E_{PT}. At the previous maximum stress, σ_{prev}, the stiffness changes to a secondary slope, E_2, which is calibrated based on test results as described in Chapter 8. When the yield stress, σ_y is attained, the material starts to yield in a kinematic hardening regime. Upon

unloading from any point along the backbone, the unloading stiffness will follow the initial modulus of elasticity, E_{PT}. Figure 6.4 gives an example of the material constitutive with multiple unloading and reloading branches.

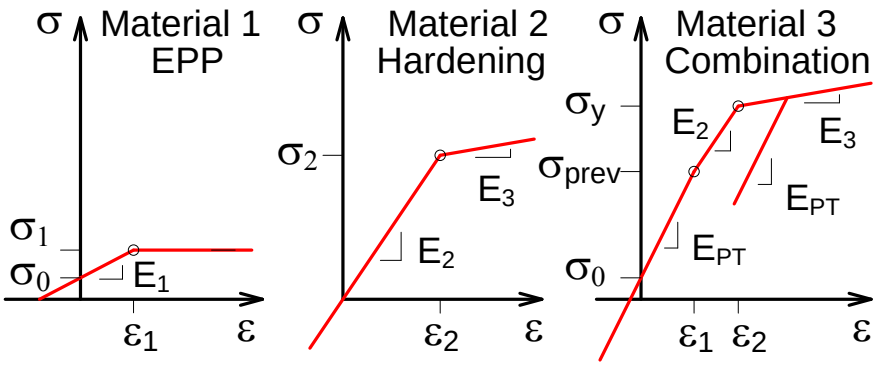

Figure 6.3 Creation of the Post-Tensioning Constitutive Relationship that Includes Initial Force and PT Seating Losses

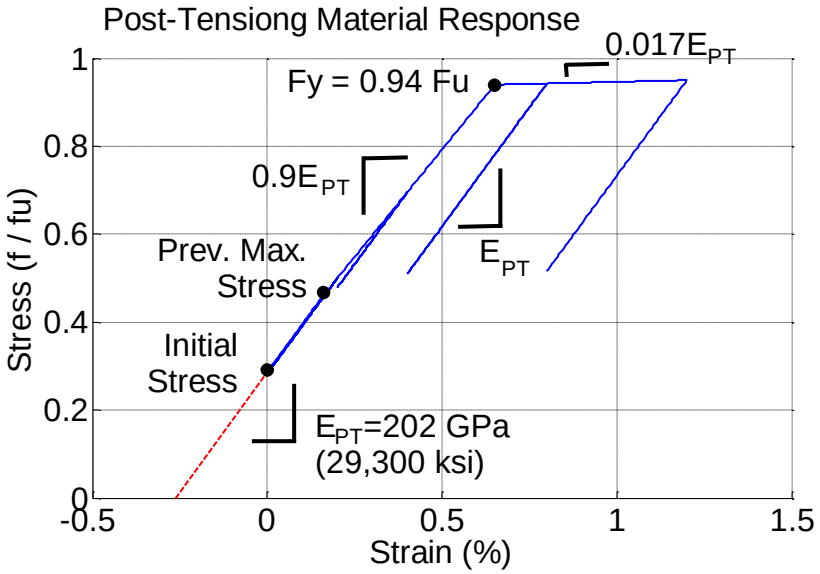

Figure 6.4 Example of the Post Tension Constitutive Relationship

Comparing the computational model results for the post-tensioning to the experimental response such as shown in Figure 6.10, demonstrates some error in modeling the stiffness of the experimental frame with post-tensioning. This difference was found to be due to the stiffness of lower anchorage. It was verified that the difference in PT stiffness was due to the anchorage by evaluating the modulus of elasticity obtained from the force and elongation measurements for the experimental post-tension response. The modulus of elasticity obtained using these measurements is given in Table 8.7 and was similar to the value obtained in the material. It was deduced that the discrepancy in stiffness must be occurring because not as much elongation was

being applied to the post-tensioning strands as compared to the computational model, and that the lower anchorage was the cause.

The anchorage at the bottom end of the post-tensioning strands consisted of a chuck on the bottom side of a 76 mm (3") thick anchorage plate. The anchorage plate was held approximately 305 mm (12") above the base plate and anchored down to the anchor plate using six 38 mm (1.5") diameter anchor rods. In the computational model this anchorage was modeled using a stiffness equal to 1751 kN/mm (10,000 k/in). However, it was found that a value closer to 70 kN/mm (400 k/in) was necessary to more accurately model the stiffness obtained from the experiment. Ultimately, the larger stiffness of 1751 kN/mm (10,000 k/in) was used for the computational models. Since the anchorage stiffness was an artifact of the experimental setup that might not represent an anchorage assembly to be used in practice, it was decided to neglect the reduction in stiffness. The computational model, therefore, represents post-tension anchorage that is nearly rigid.

6.3 Component Model of the Fuses

A phenomenological model was created to simulate the flexural, axial, and lateral-torsional buckling behavior of the fuse links. As shown in Figure 6.5, the fuse is modeled with twelve fiber section elements. The depth of the fiber section matches the average depth of the fuse link along that portion of its length. The thickness of the section is set equal to the thickness of the fuse plate multiplied by the number of links being represented. Since the model is two-dimensional, both the fuse on the front of the frames and the back of the frames is represented by this one modeled fuse link. This implicitly assumes that all fuse links are undergoing the same displacements and rotations which appeared to be a reasonable assumption based on observations from the tests.

One of the advantages of modeling the geometry of the link directly is the ability to simulate the behavior of different fuse geometries using a fairly standard steel material constitutive model. The left side of Figure 6.6 shows an example of the application of the fuse material constitutive relationship. The yield stress was obtained from the coupon tests performed on the fuse plate material. The Steel02 material was used in OpenSees with an isotropic hardening ratio of 0.005 and a kinematic hardening ratio of 0.0005. It was found that using kinematic hardening with the rotational spring configuration presented here best fit the experimental data for the thin fuses that were allowed to buckle. Conversely, the isotropic hardening was found to better represent the behavior of the thick fuses that did not buckle. The resulting compromise with a mix of both kinematic and isotropic hardening was found to best fit all seven of the quasi-static cyclic tests presented in the previous chapter.

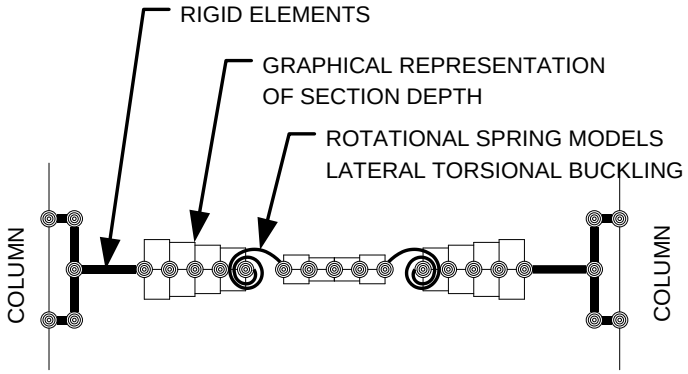

Figure 6.5 Phenomenological Model of the Fuse

At the third points of the fuse link, rotational springs are included to simulate lateral-torsional buckling. The rotational spring is a zero-length element with a behavior using the Pinching4 material in OpenSees. It has a steep initial stiffness up to a lateral-torsional buckling critical moment as shown on the right of Figure 6.6. The method used to calculate the critical moment is discussed in Chapter 8. Then the backbone curve exhibits a sharp reduction in moment capacity which simulates the reduced moment capacity after lateral-torsional buckling. The shape of the post-buckling backbone curve was calibrated based on the quasi-static cyclic test results, namely Specimens A1, A7, and B2. The final parameters for the rotational spring which are included in Table 6.1 were also based on values that produced relatively reliable convergence of the model.

Table 6.1 Parameters Used to Define the Fuse Rotational Spring in OpenSees

Backbone	Moment / M_{cr}	Rotation (rad)	Other Parameters
Coordinate 1	1.0	0.02	rDispP = 0.9
Coordinate 2	0.75	0.1	rForceP = 0.35
Coordinate 3	0.60	0.2	uForceP = 0.3
Coordinate 4	0.55	0.3	

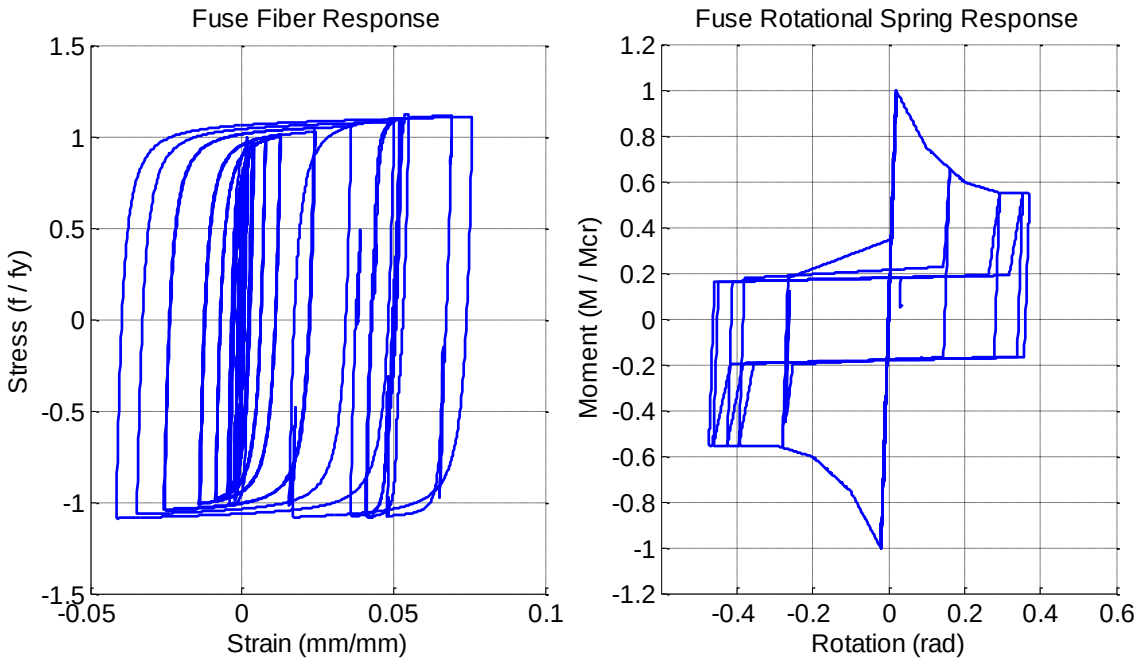

Figure 6.6 Examples of Fuse Fiber Constitutive Response (Left) and Fuse Rotational Spring Response that Simulates Lateral-Torsional Buckling (Right)

Two examples of computational model simulation compared to experimental behavior are provided here, and then comparisons for all of the quasi-static cyclic tests are presented in the next section. For thick fuses that did not buckle, the rotational springs remain elastic and do not contribute significantly to the fuse response. Figure 6.7 demonstrates the response of the fuse model compared to the hysteretic response of the Specimen A2 fuses. In this case, the computational simulation proves to be quite accurate in representing the fuse behavior using only the actual fuse geometry and representative steel constitutive. Since none of the parameters are calibrated to a specific configuration or set of tests, this model should be able to accurately model fuses with links of different sizes and geometries.

The second example comparison provided here shows the response of a thin fuse compared to the computational model. Figure 6.8 shows that the character of the hysteretic response of specimen A1 is generally captured by the computational model. The model undergoes elastic-plastic type of behavior up to a point at which buckling occurs. After buckling, the modeled fuse transitions into an axial dominated response as the rotational resistance is lost. The axial forces in the fuse are shown in Figure 6.8 compared to the computational simulation. Because of the isotropic hardening, there is a gain in axial strength with additional straining which results in larger axial forces than the experimental fuse experienced. This strength gain is shown in the fuse hysteretic response as increased strength after loading the fuse past 10% shear strain across the fuse link.

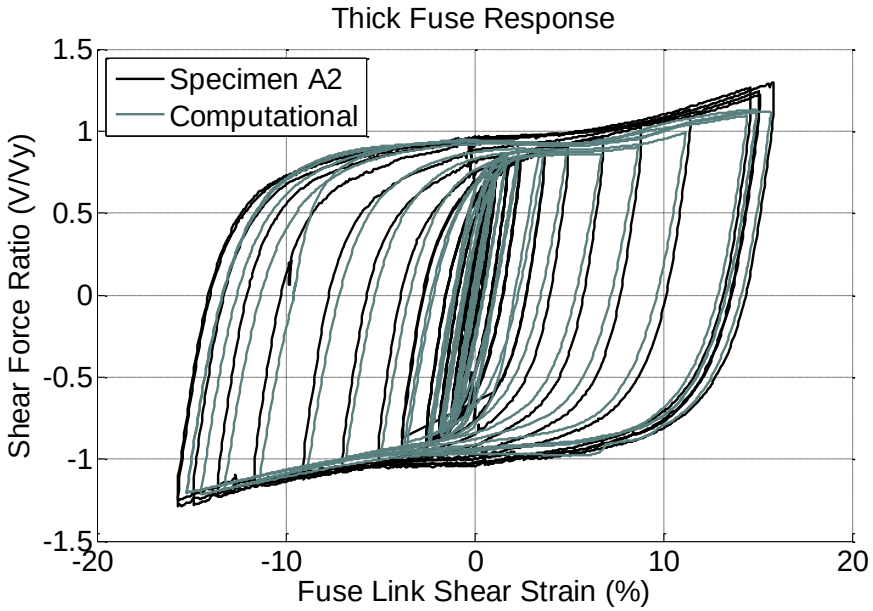

Figure 6.7 Example Computational Simulation Compared to Experimental Response for a Thick Fuse

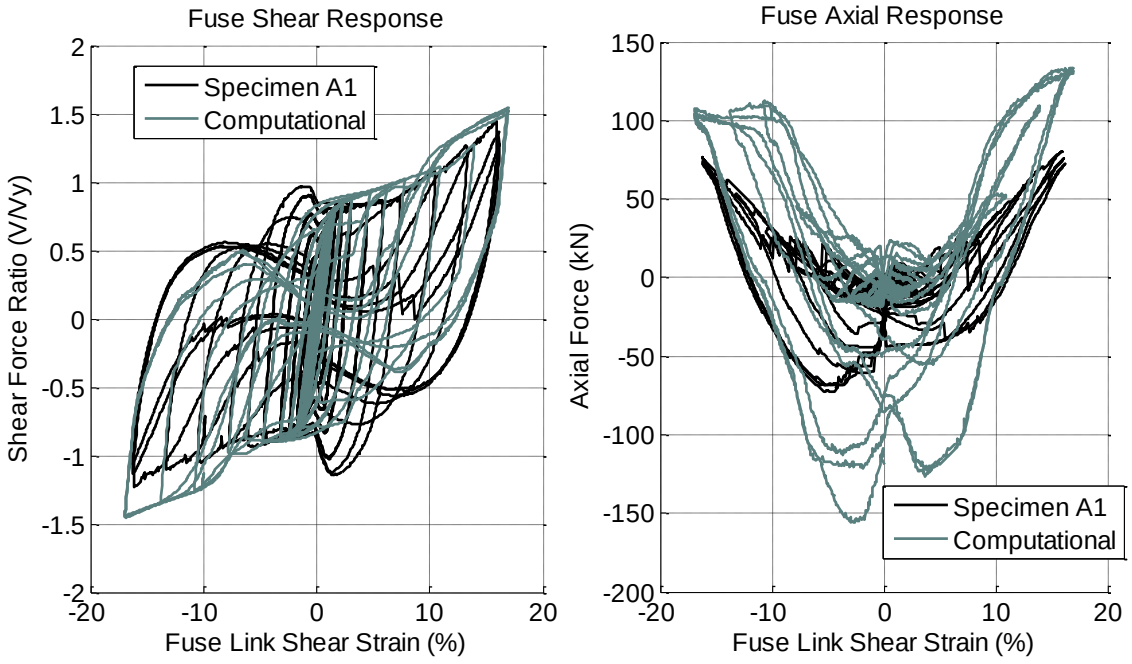

Figure 6.8 Example Computational Simulation Compared to Experiment for Fuse Hysteretic Response (Left) and Fuse Axial Forces (Right) for a Thin Fuse

6.4 Calibration and Validation of the Computational Model

There are two components of the computational model that are calibrated to the results of the experimental program. The secondary stiffness representing seating losses in the post-tensioning strand constitutive model was calibrated to the experiments. Several

parameters in the fuse model were calibrated, including the steel material hardening ratio, the buckling strength, and the variables governing post-buckling response of the rotational spring. The calibration of these parameters is discussed in Chapter 8 and was based on the quasi-static cyclic tests presented in the previous chapter and the fuse component tests conducted at Stanford University.

In this section, the ability of the computational model to simulate the response of the quasi-static cyclic tests is presented. Since these experiments were also used in the calibration of some of the parameters as listed above, additional verification of the computational model is presented in the next chapter as the computational simulations are compared to the hybrid simulation experimental response.

6.4.1 Specimen A1

The load-deformation response of the tested Specimen A1 is compared to the computational simulation in Figure 6.9. The backbone curve of the experiment is well captured as is the character of the post-buckled fuse response. It is noted that the critical buckling moment for the fuse rotational spring was adjusted by a factor 0.95 to account for the fact that the fuse buckled a little earlier than the characterization from Chapter 8 predicted.

The left side of Figure 6.10 demonstrates the strengths and weaknesses of the computational model of the post-tensioning. As shown, the loss of post-tensioning force due to seating losses is simulated well by the specialized constitutive described above. The right side of Figure 6.10 shows that the response of the post-tensioning element represents the stress-strain behavior with seating losses experienced by an individual strand, in this case strand L-PT-L-2 from Specimen A1. Specimen A1 is the only one of the experimental tests that experienced significant post-tensioning seating losses. The strands in the other specimens had all been previously stressed to high loads eliminating seating losses before the test began. However, additional data was obtained during trial runs of the frames without fuses in which seating losses were experienced.

The left side of Figure 6.10 also shows that the stiffness of the post-tensioning system was different from the experiment. The juxtaposition of the accuracy of the simulated stress-strain behavior with the inexactness of the post-tension stiffness illustrates that this error is not due to post-tension strand behavior, but instead due to the stiffness of the anchorage. As discussed above, it was decided not to consider anchorage flexibility in the computational model.

The fuse response for Specimen A1 was compared to the computational model in Figure 6.8 above. As discussed above, the computational model of the thin fuses captures the character of the pre- and post-buckled fuse behavior.

The uplift of the columns for Specimen A1 is shown in Figure 6.11. Since the column uplift is governed by rigid body rotation of relatively stiff elastic frames, it is not surprising that the computational model accurately simulates the uplift response of the column bases. It is shown that the apparent uplift at the pivoting column base is also matched reasonably well. Although the pivoting column base is not uplifting, the centerline experiences upward motion as the pivot point is at an eccentricity to the column centerline.

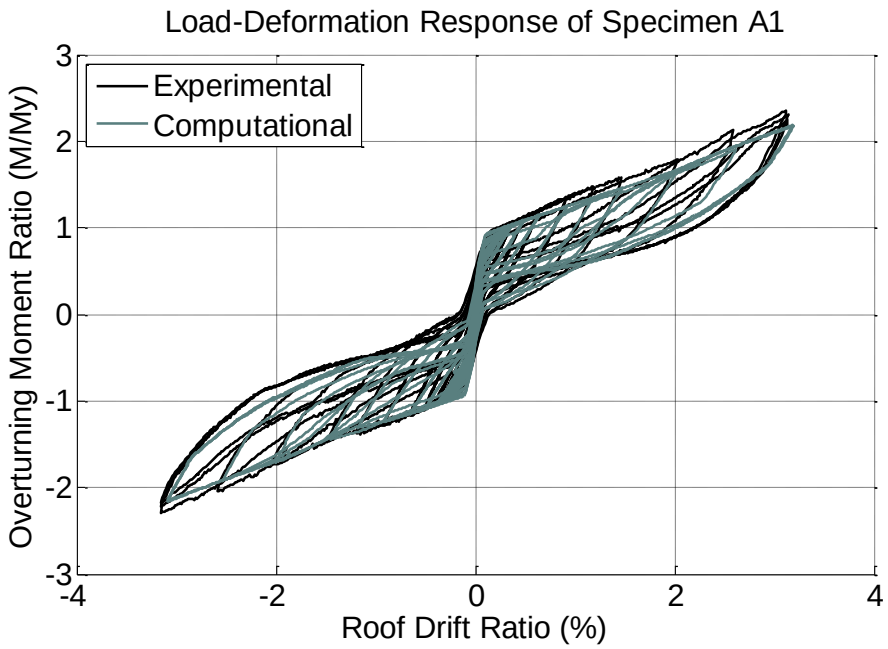

Figure 6.9 Load-Deformation Response for Specimen A1 Compared to the Computational Model

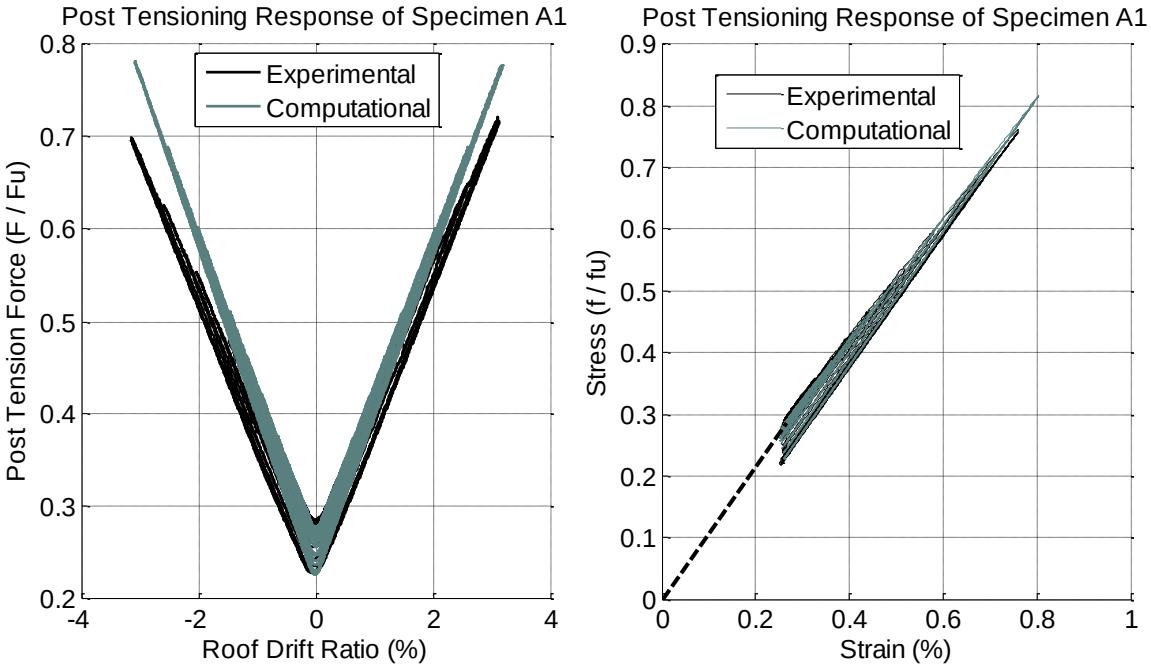

Figure 6.10 Post-Tensioning Response (Left) and Stress-Strain Response (Right) Compared to Experiment for Specimen A1

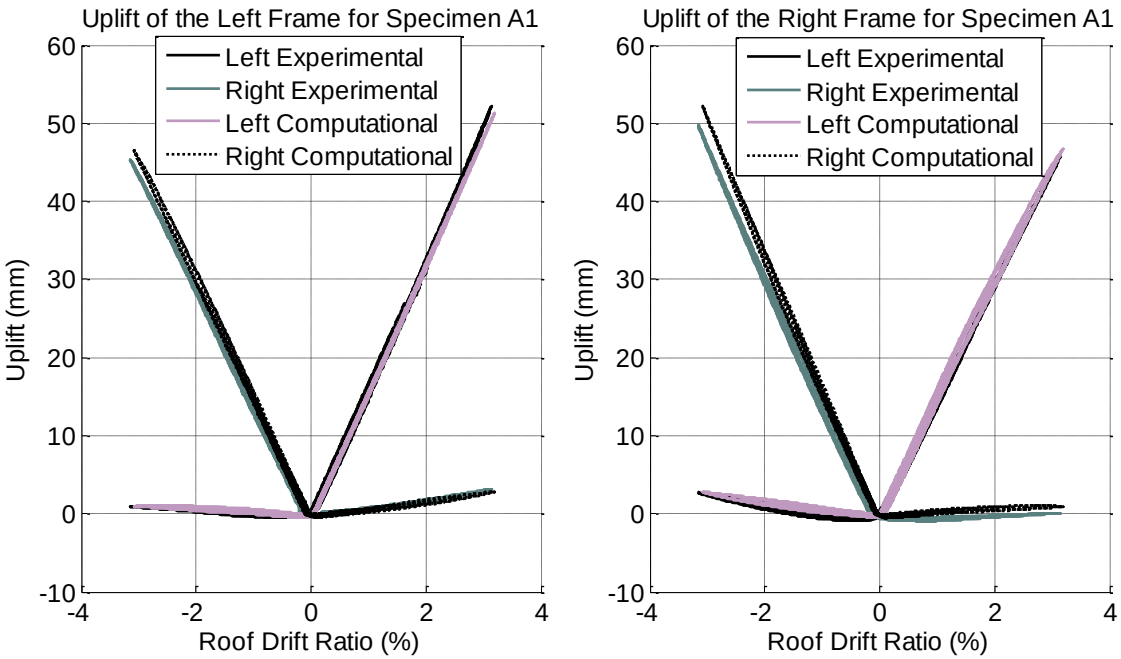

Figure 6.11 Uplift of the Left Frame (Left) and the Right Frame (Right) Compared to Experiment for Specimen A1

6.4.2 Specimen A2

The load-deformation response of Specimen A2 is compared to the computational simulation in Figure 6.12. It is shown that the backbone is matched well, but the unloading stiffness of the computational model is smaller than the experiments. A slight hardening in the system observed in the experimental response at drifts greater than 2% is not exhibited in the computational response. It is believed that this hardening is due to forces developed due to the constraint between the two frames which is difficult to model because of the actual tolerances and stiffnesses of these constraints are difficult to match exactly.

It is noted that the roof drift ratios for the computational model were shifted by -0.12% to match the starting location of the experiment. Since previous testing of the frames ended with the negative roof drift ratio portion of the loading cycle, the frames started the test all the way against the left bumpers (negative direction). It was therefore necessary to adjust the computational results to account for these initial conditions.

The fuse response and post-tensioning response are compared to the computational model in Figure 6.13. The lack of losses in post-tensioning force is evident in Figure 6.13 as is the difference in stiffness discussed above. The fuse behavior was found to be captured well by the fuse model.

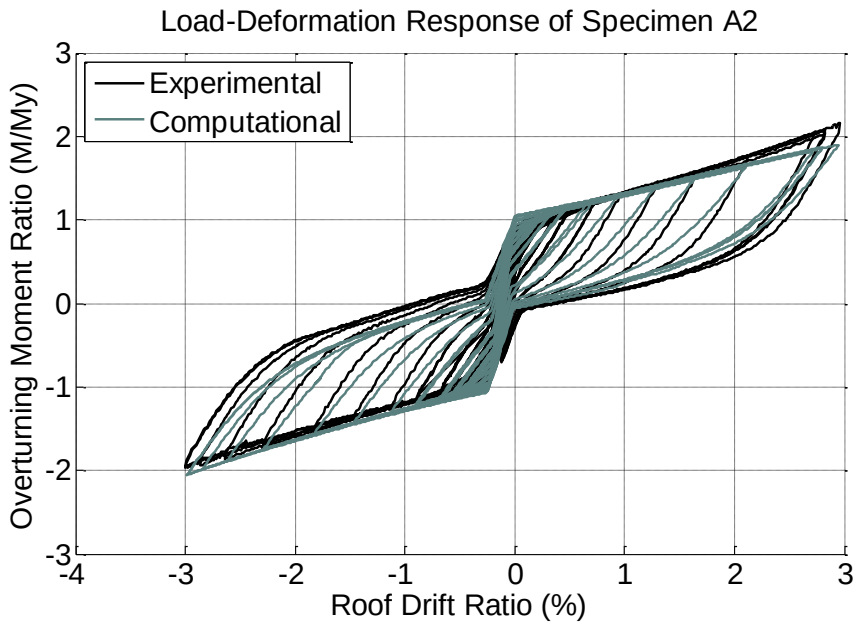

Figure 6.12 Load-Deformation Response of Specimen A2 Compared to Experiment

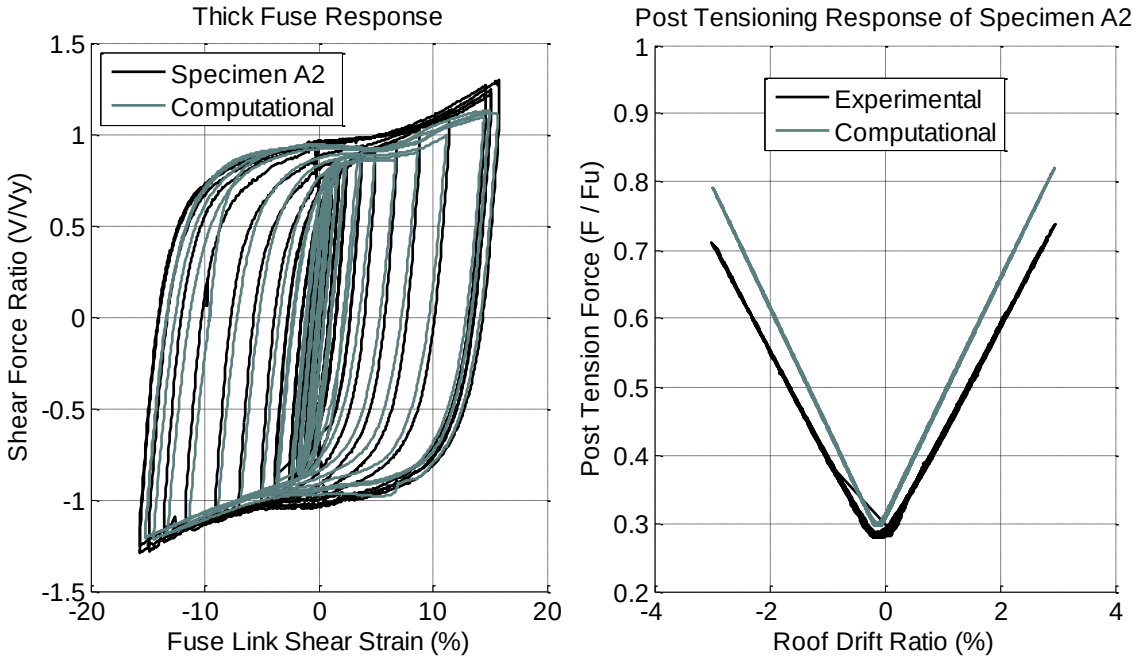

Figure 6.13 Fuse Response (Left) and Post-Tensioning Response (Right) Compared to Experiment for Specimen A2

6.4.3 Specimen A3

The comparison of experimental response of Specimen A3 is compared to the computational load-deformation response in Figure 6.14. As shown, the positive loading regime including backbone and unloading are well represented by the computational model. There is a slight hardening in the experimental system response that is not captured by the model similar to that observed to in Specimen A2 and discussed above.

The most dramatic difference in the computational and experimental response is the relative shift in the negative loading regime. It is believed that this shift could be due to several factors including sliding at the base, nonsymmetry in the fuse response due to hardening, forces between the frames due to constraint, and loads in the experiment that are erroneously transferred through the specimen in a way not modeled. In general, the computational model did not accurately represent the variation in tolerances and variation in the initial position of the moving parts within their tolerance of this experimental setup. Specific connections in question included the frame to bumper bearing, the strut pin connections, and the pin connection at the top of the specimen to the loading beam. These connections directly governed the amount of constraint between the two frames during rocking and the corresponding forces that were developed, but their exact configuration and variation are not modeled exactly thus creating error.

The experimental and computational fuse responses as shown in Figure 6.15 is not exactly anti-symmetric because of the axial forces developed by in the fuse due to constraint between the frames. The applied displacement history for the computational model was the displacements at the pin load cells as measured during the testing of Specimen A3. Because the actual displacements were applied, the model response is not as symmetric as would be expected from a perfectly symmetric displacement history. The post-tensioning response shown on the right of Figure 6.15 is similar to the response discussed above for Specimen A2.

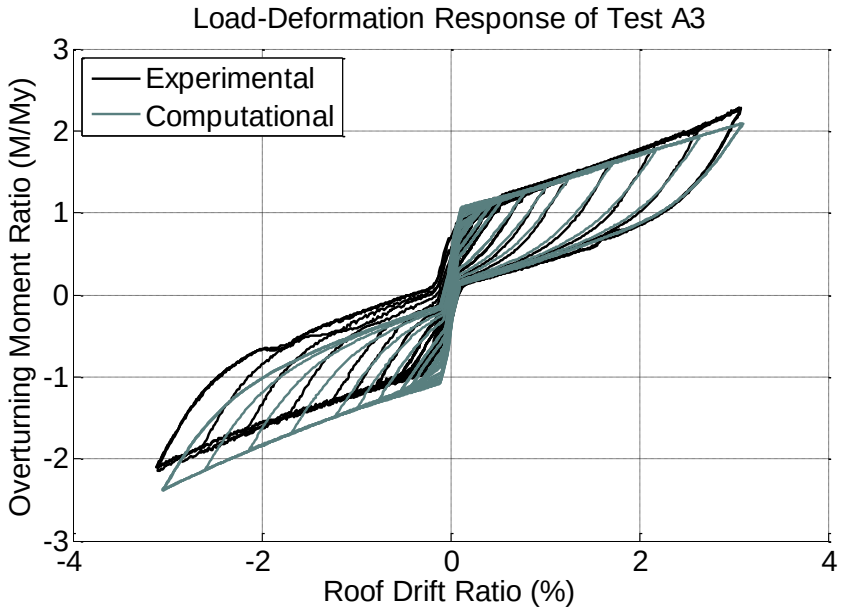

Figure 6.14 Load-Deformation Response of Specimen A3 Compared to Experiment

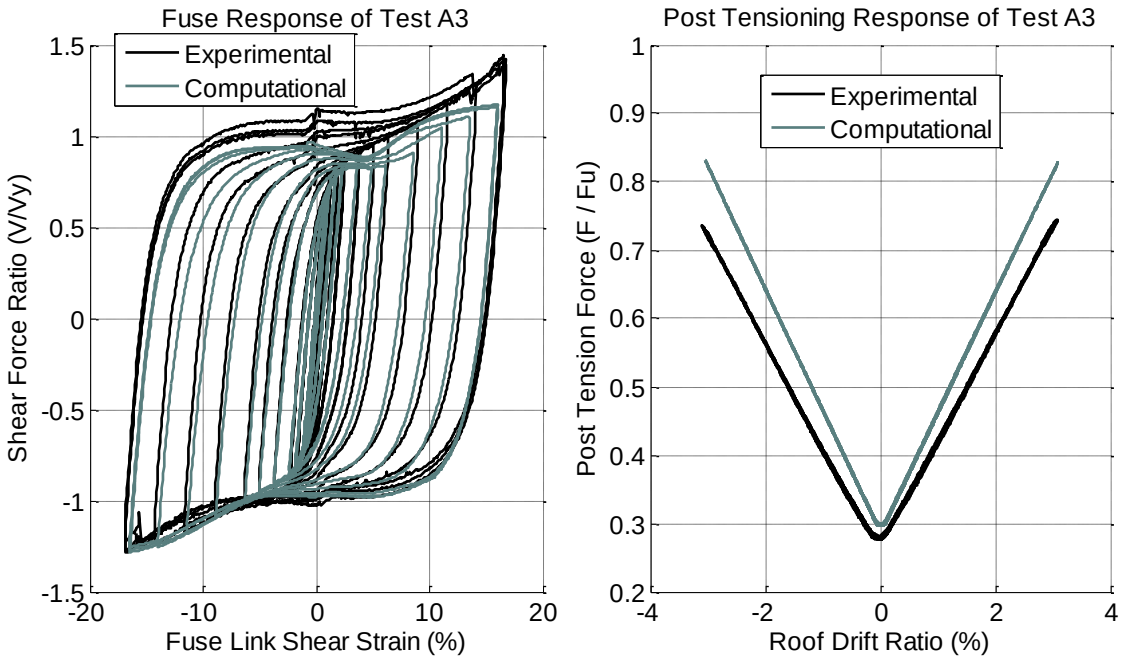

Figure 6.15 Fuse Response (Left) and Post-Tensioning Response (Right) Compared to Experiment for Specimen A3

6.4.4 Specimen A4

The experimental load-deformation behavior of Specimen A4 is compared to the computational simulation in Figure 6.16. The majority of the differences between the experimental response and the computational model response are attributed to not considering slip of the fuse relative to the columns, and the approximation of post-tensioning yielding response at large strains.

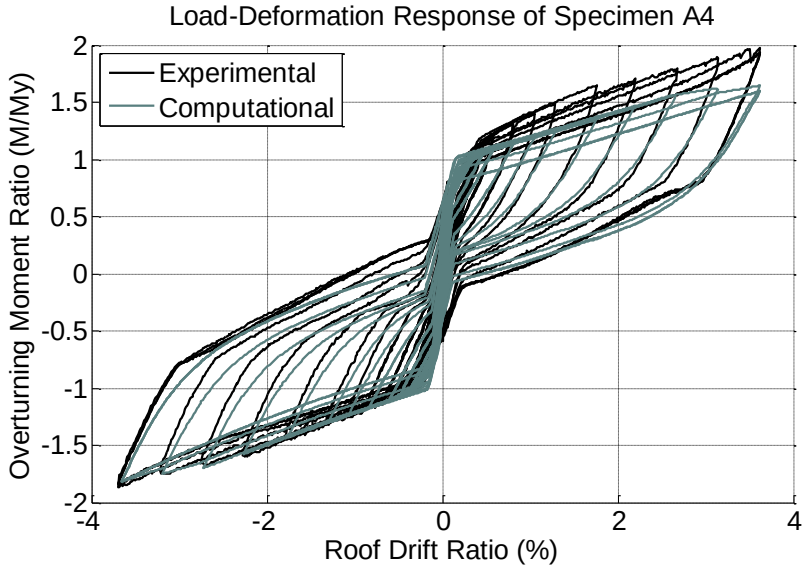

Figure 6.16 Load-Deformation Response of Specimen A4 Compared to Experiment

The fuse hysteretic behavior shown on the left of Figure 6.17 shows significant differences between the fuse model results and the experimental results. As discussed in the previous chapter, the fuses for Specimen A4 slipped relative to the column. Since the measurement of fuse shear strain is based on aggregated deformations from column to column as opposed to local fuse shear strain, the experimental fuse behavior shown includes the slip displacements. The effect of slip is shown to increase the secondary stiffness of the fuses. This is attributed to the fact that the fuses rotated as they slipped thus orienting themselves to resist more load through axial tension than if the fuse were stationary. As a result the effect of axial forces on the Specimen A4 fuses was found to be more significant.

The post-tensioning response shown on the right of Figure 6.17 demonstrates that although the yield force in the modeled post-tensioning strands was larger than the experiment, the amount of loss in post-tensioning force due to yielding is reasonable well represented.

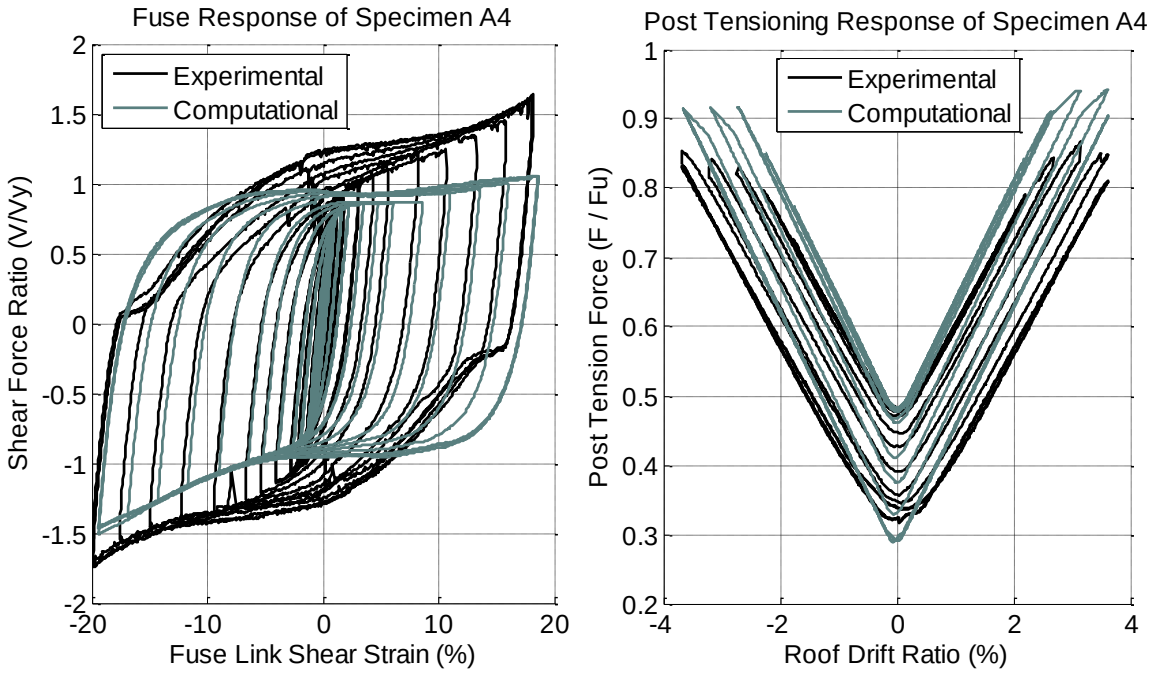

Figure 6.17 Fuse Response (Left) and Post-Tensioning Response (Right) Compared to Experiment for Specimen A4

6.4.5 Specimen A7

The experimental load-deformation response for Specimen A7 is compared to the computational simulation in Figure 6.18. Similar to Specimen A1, the character of the pre- and post-buckled responses are captured by the computational model. Similar to Specimen A2 and Specimen A3 discussed above, there was some hardening noted at roof drifts exceeding 2% that were not captured in the computational model.

The computational fuse response shown on the left of Figure 6.19 experiences some increases in shear strength after exceeding fuse link shear strains greater than 10%. This is due largely to the isotropic hardening used in the fuse material constitutive model. As discussed in the section on the fuse model, it was found that isotropic hardening

resulted in the best fit with experimental data for the thick non-buckling fuses whereas kinematic hardening resulted in more accurate models of the thin buckling fuses. The final computational model presented in this chapter represented a compromise to allow reasonable accuracy for the range of fuse thicknesses studied.

Similar to Specimen A4, the right side of Figure 6.19 shows that the post-tensioning response can simulate the forces during much of the loading regime, but results in larger yield forces, and slightly lower force at zero roof drift.

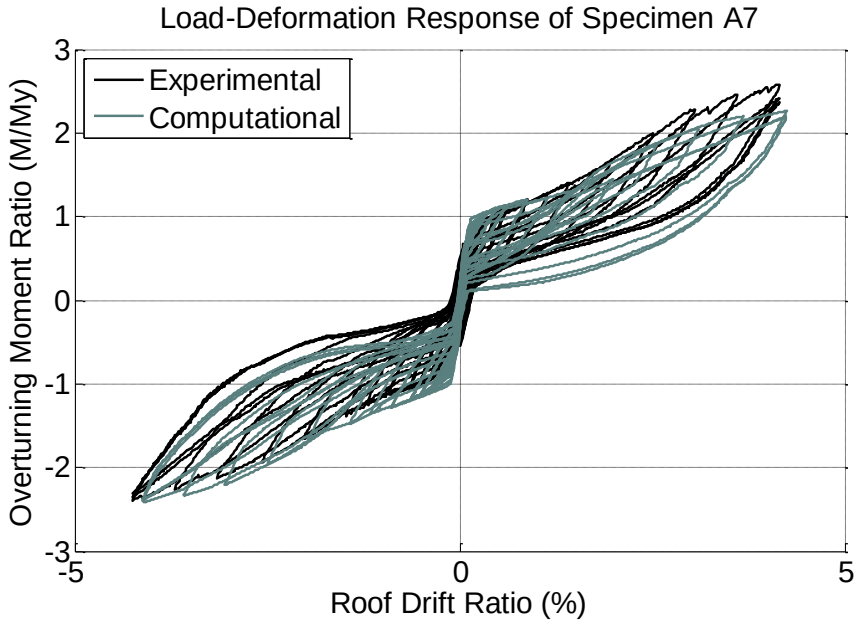

Figure 6.18 Load-Deformation Response of Specimen A7 Compared to Experiment

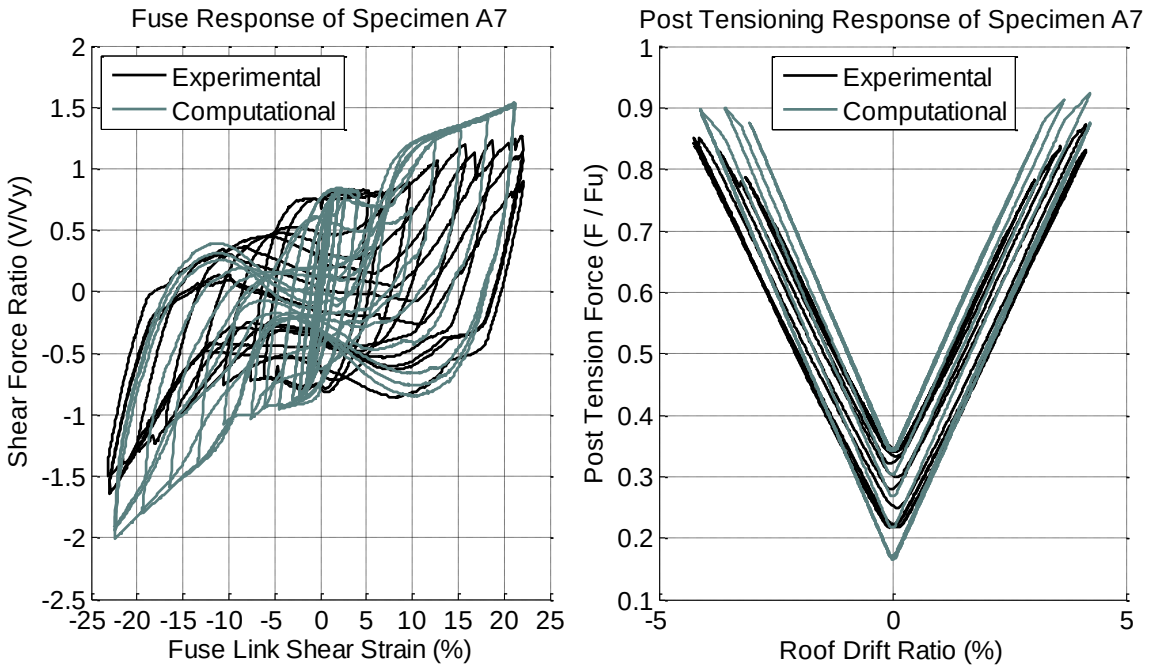

Figure 6.19 Fuse Response (Left) and Post-Tensioning Response (Right) Compared to Experiment for Specimen A7

6.4.6 Specimen B1

Figure 6.20 demonstrates the ability of the computational model to simulate the response of a single frame configuration. The lag in response due to pin hole tolerances in the center strut are captured through the use of the zero-length spring described above. The comparison between experimental system response and computational simulation as well as the comparison shown on the right of Figure 6.21 demonstrates that the computational model can simulate post-tension strand yielding better than post-tensioning strand wire fracture as was experienced in Specimen B2 and shown in Figure 6.22.

The fuse response shown on the left of Figure 6.21 exhibits some discrepancies in the fuse link shear strain history as the computational modeled fuse was not subjected to the exact same displacements as the experiment. The computational simulation was controlled by applying the same lateral displacement at the load cell pin as was experienced by the experiment. As a result of differences in frame deformations and displacements as well as differences in the center strut connections relative to the computational model, the fuse did not undergo the exact same displacements as the experiment.

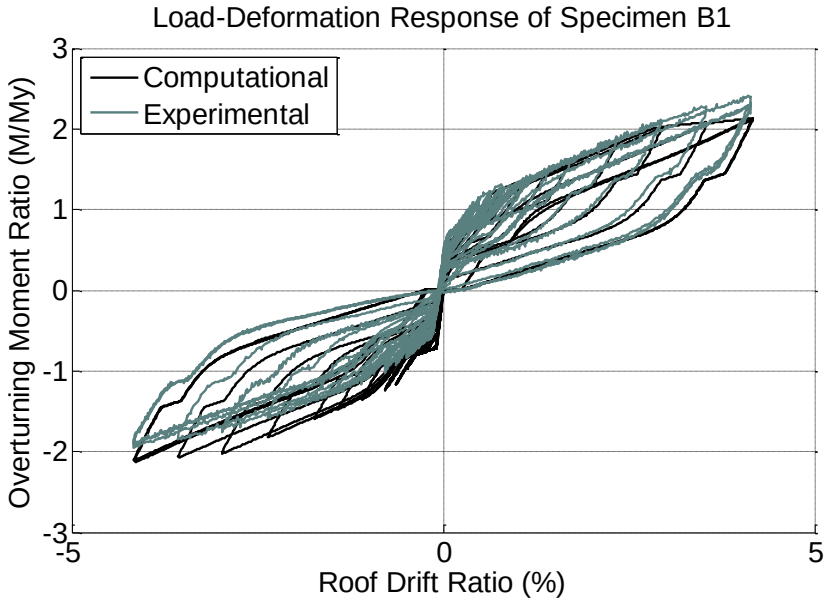

Figure 6.20 Load-Deformation Response of Specimen B1 Compared to Experiment

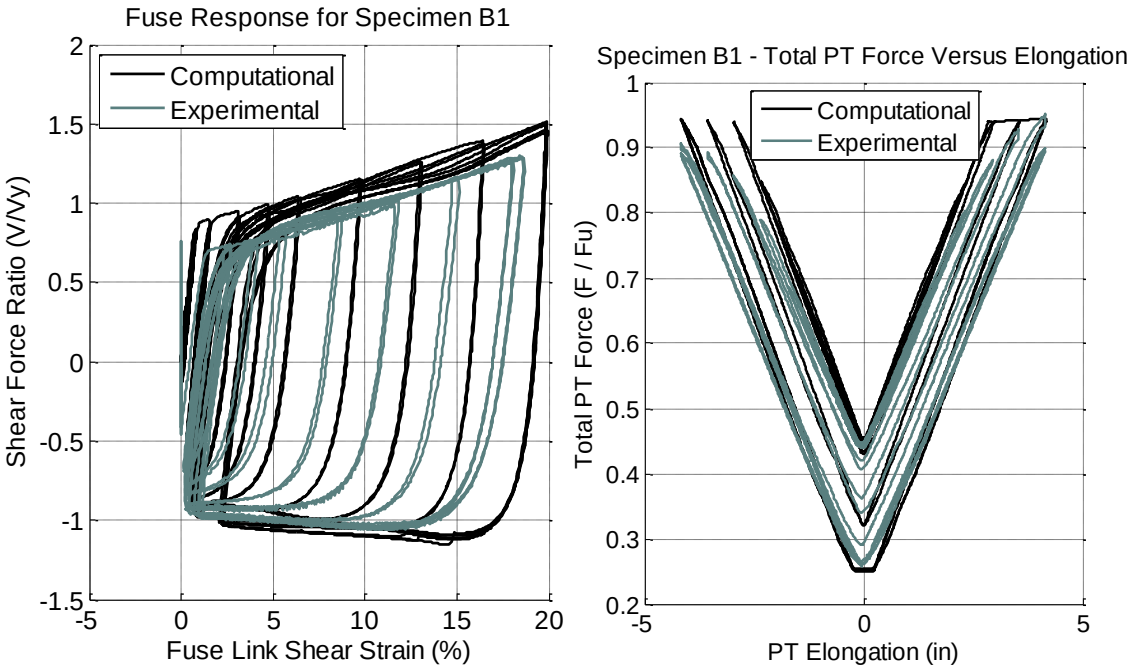

Figure 6.21 Fuse Response (Left) and Post-Tensioning Response (Right) Compared to Experiment for Specimen B1

6.4.7 Specimen B2

The computational simulation and experimental load-deformation response are compared in Figure 6.22. It is illustrated in the system response as well as in the post-tensioning response shown on the right of Figure 6.23 that the computational model does not capture the loss in post-tensioning stiffness and underestimates the loss in post-tensioning force when the post-tensioning strand wires fracture. An examination of the load-deformation

response reveals this to be more of an issue in predicting unloading stiffness and drifts during unloading than it is for representing the backbone response and strength of the system.

The experimental fuse shear strain history is different than the experiment similar to Specimen B1 discussed above. Similar to Specimen A1 and Specimen A7, the fuse hysteretic behavior as shown on the left of Figure 6.23 demonstrates that the computational model can capture the character of the pre- and post-buckled response.

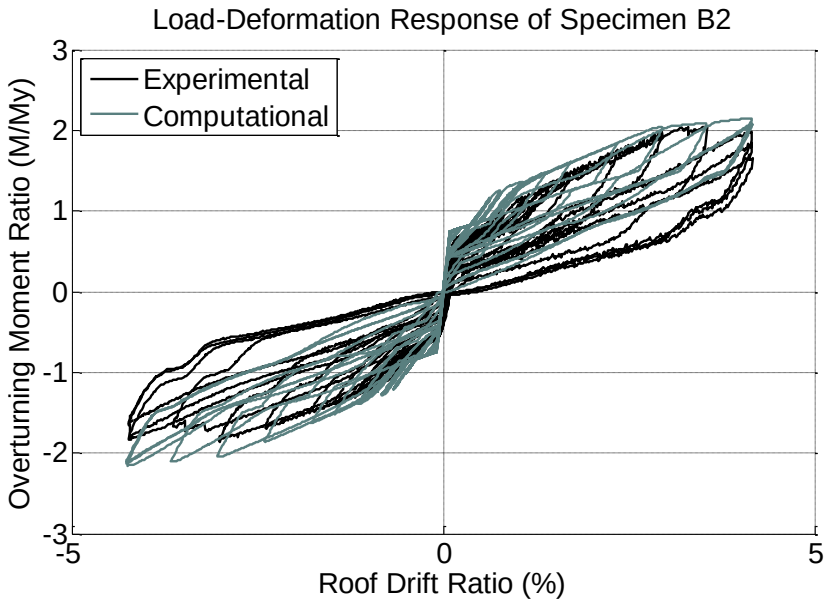

Figure 6.22 Load-Deformation Response of Specimen B2 Compared to Experiment

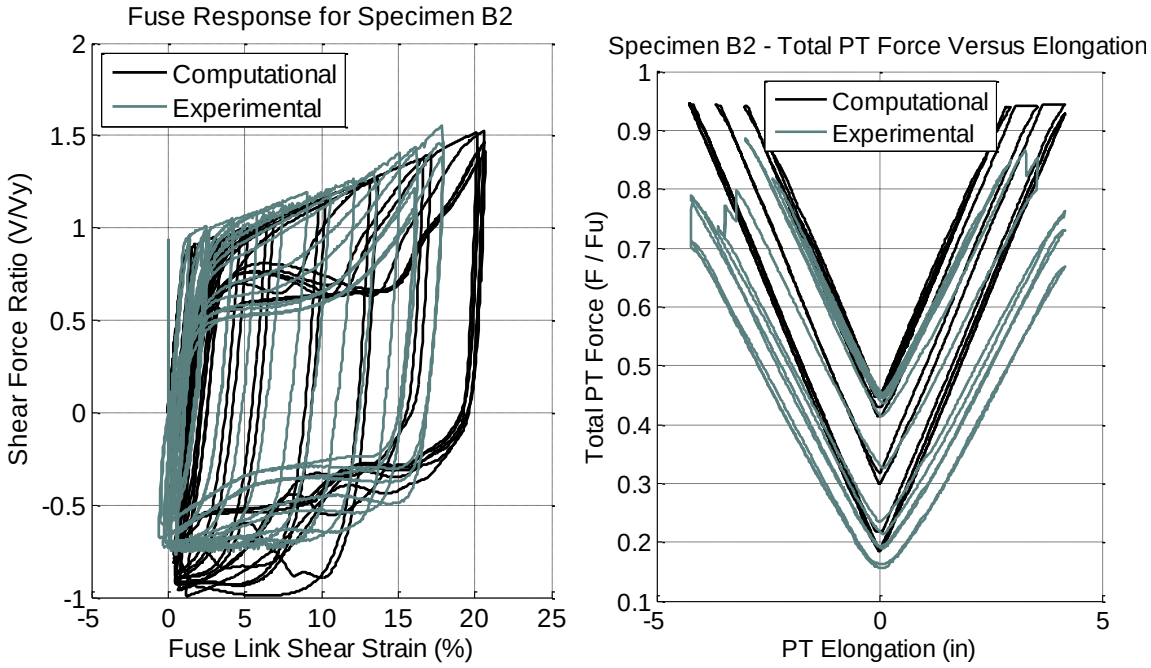

Figure 6.23 Fuse Response (Left) and Post-Tensioning Response (Right) Compared to Experiment for Specimen B2

6.5 Conclusions Regarding the Computational Model

A summary of the advantages and limitations of the computational model described in this chapter are presented here. Phenomena that the computational model does not capture include:

- Sliding of the frames relative to the base plate as they moved between bumpers was neglected for four reasons as listed above.
- The slip of the fuse relative to the column experienced during the testing of Specimen A4 was neglected. The testing of this specimen succeeded in highlighting fuse slip as a limit state, but this was ignored in the model because it is expected that slip would be avoided in practical designs.
- The computational stiffness of the post-tensioning anchorage is represented by a near rigid support. The experimental response indicates that the post-tensioning anchorage has a finite but stiff resistance. This was ignored in the computational model because it was specific to the test configuration and may not be applicable to practical full scale buildings.
- The reduction in post-tensioning element stiffness and loss in post-tensioning prestress force are not accurately represented when the post-tensioning stand wires fracture.

Advantages of the computational model described in this chapter include:

- The model presented here is a computationally compact 2D frame model that has been shown to capture the salient features of system and component behavior.
- No new formulations or specialized elements were required. Only elements and material constitutive models readily available in OpenSees were utilized allowing similar implementation in many nonlinear software packages.
- The range of behavior experienced by the thinner buckling fuses was captured through a phenomenological model including rotational springs that simulated the effects of lateral-torsional buckling.
- The response of thicker non-buckling fuses was shown to be well represented without calibrating any parameters to the experimental data.
- The constitutive model used for the post-tensioning can account for post-tensioning seating losses, yield, and initial pretension. Even though some aspects of post-tensioning wire fracture were not fully captured, it was shown that the backbone curve and strength of the computational model were not significantly inaccurate.

QUASI-STATIC HYBRID SIMULATION RESPONSE

There were several purposes for the hybrid simulation tests. One of the primary reasons for conducting hybrid simulation tests was to validate the performance of the controlled rocking system when subjected to earthquake ground motions. Second, the ability of the controlled rocking frames to eliminate residual drifts in the presence of destabilizing second-order gravity load effects and the resistance of the rest of the building was investigated. The resistance of the rest of the building is an important consideration when investigating self-centering because the components of the remainder of the building will counteract the restoring forces. After the components of the remainder of the building undergo inelastic action, it will require additional restoring forces to force these elements back to their original position. The effect of ambient building resistance and P-Δ forces were therefore considered to give a more accurate assessment of the system's ability to self-center a building.

Specimen A5 and Specimen A6 were tested using hybrid simulation as part of the testing program. This chapter provides a description of the hybrid simulation test setup and presents the results from these specimens.

7.1 Hybrid Simulation Setup

The hybrid simulation configuration consisted of the experimental component and computational components representing portions of the rest of the building. The computational model components were created using the OpenSees software (Mazzoni et. al 2009) to represent the second order effects of the gravity load, and the effect of ambient building resistance. These computational components were linked to the experimental setup using the UI-SIMCOR software (Kwon et al. 2007), as schematically demonstrated in Figure 7.1. Test A5 included only one computational component that represented second order gravity effects, whereas Test A6 also included a computational component representing ambient building resistance as shown in Figure 7.1.

The second-order gravity effects were modeled as a pinned-base leaning column with an effective gravity load lumped at the top. Chapter 4 contains the details of the leaning column model. The other model which was used with Specimen A6, simulated two of the largest contributors to ambient building resistance, namely wall partitions and simple shear beam-to-column connections. As shown in Figure 7.1, the simple shear beam-to-column connections were modeled as rotational springs between the beams and columns of a one bay frame. The rotational springs were calibrated to match experimental tests as described in Chapter 4 and amplified to represent all connections tributary to one controlled rocking frame. The partitions were represented by a nonlinear hysteretic truss element that were calibrated to match experimental tests and were similarly amplified to represent all of the partitions tributary to the controlled rocking frame. Additional details can be found in Chapter 4.

The JMA Kobe ground motion was selected to allow direct comparison with dynamic shake table tests performed at the E-Defense facility in Miki, Japan. The ground motion was scaled to best match the design spectrum using a least squares method over a period range of interest as described in Chapter 4. Multiple trials were conducted for both Specimen A5 and Specimen A6. Specimen A5 was tested at a scale level with a 2% probability of exceedance in 50 years, and then two trials with a scale factor of 1.10 applied to the JMA Kobe record. Specimen A6 was tested at a scale level with a 2% probability of exceedance in 50 years, the same scale level with out-of-plane motion also applied, and then with a scale factor of 1.20 times the JMA Kobe ground motion.

In the hybrid simulation process, a displacement, Δ, is applied to both computational components, and a displacement reduced by the length scale factor, r_L, is applied to the experimental setup. The resulting forces are measured and summed together. The displacement for the next time step is calculated using the α-OS time stepping method (Comberscure and Pegon 1997) using the measured force, F^i, computationally applied mass, M, computationally applied Rayleigh damping, ζ=0.02 at periods of 0.34 seconds and 1.0 seconds full scale, velocity, v^i, acceleration, a^i, an elastic stiffness, K_e, and the ground acceleration, $\ddot{x}_g$.

The computational simulations presented in this chapter were conducted using the UI SIMCOR software and the same process as described above for the experiment, except that the experimental module was replaced with a computational model of the system at specimen scale. Additional information about the computational model is located in Chapter 6.

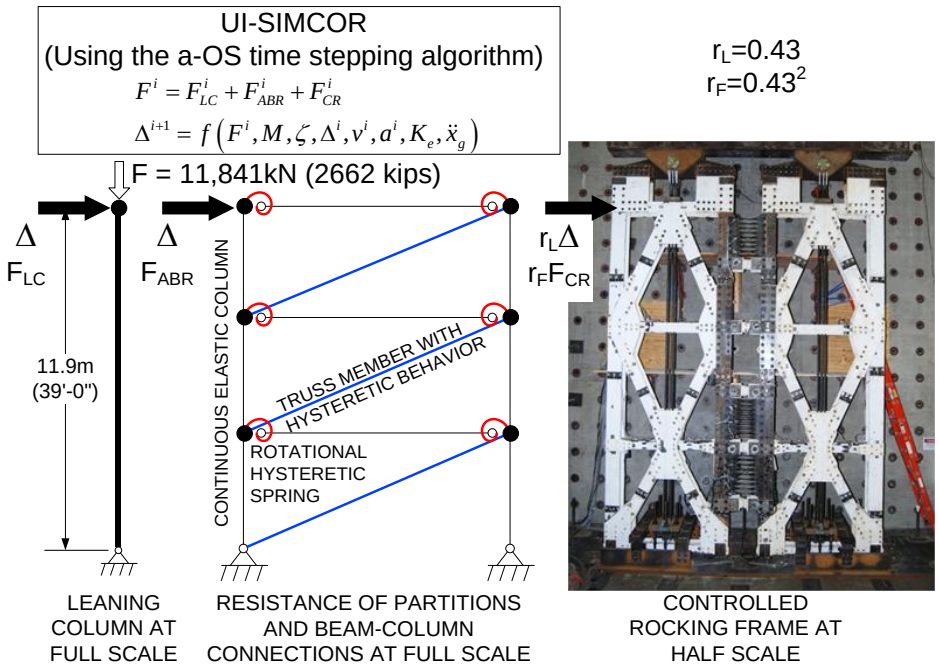

Figure 7.1 Schematic Representation of the Hybrid Simulation Setup

7.2 Specimen A5 Behavior

Specimen A5 consisted of a dual frame configuration with two fuses between the frames as shown in Figure 7.2. The fuses were, t=15.9 mm (5/8") thick with 8 tapered links each that had a link length, L=356 mm (14"), a link depth at the ends, b=58.7 mm (2.3125"), and a link depth at the middle that was one-third the link depth at the end. The resulting design capacity for all the fuses was calculated to be V_{fp}=348.7 kN (78.4 kips). The post-tensioning consisted of eight 12.7 mm (½") diameter post-tensioning strands stressed to 34% of their ultimate strength or F_{pti}=497.3 kN (111.8 kips) total. Using the equations defined in Chapter 3, the overturning ratio was found to be, OT=1.03, the self-centering ratio was SC=1.05, and the geometric ratio of frame width to fuse width was A/B=2.5.

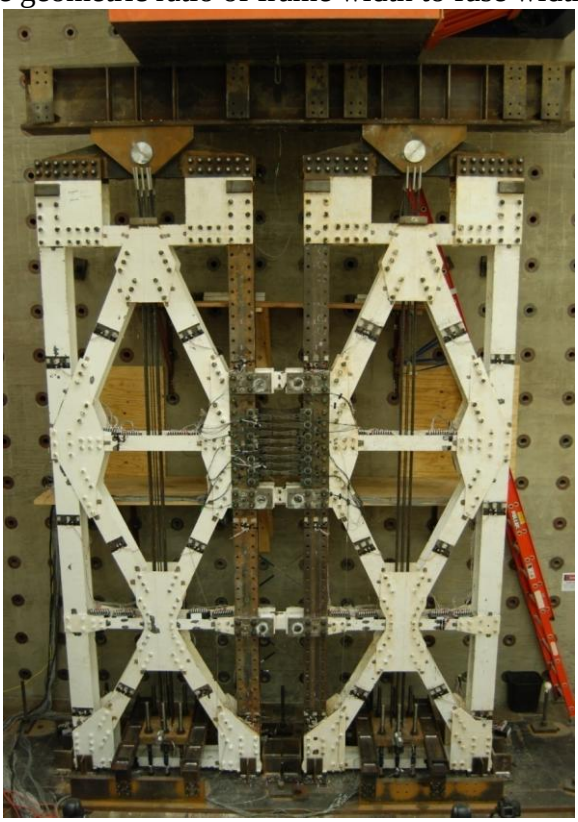

Figure 7.2 Photograph of Specimen A5

All of the hybrid simulation tests demonstrated the effectiveness of the controlled rocking system in satisfying the performance goals. All observed inelasticity was concentrated in the fuses and residual drifts were found to be negligible. Figure 7.3 and Figure 7.4 demonstrate the response of Specimen A5 when subjected to the JMA Kobe ground motion scaled to a level that has a 2% probability of exceedance in 50 years. A peak drift of 1.65% roof drift ratio was achieved 6.5 seconds into the ground motion.

The computational model displacement response is shown in Figure 7.3 to capture the frequency content of the response quite well. A summary of the ability of the computational model to predict the peak drift is included at the end of this chapter. The computational simulation was conducted with UI SIMCOR and the leaning column

computational component just like the hybrid simulation but with a computational model substituted for the experimental component. Details about the computational model of the specimen are included in Chapter 6. The system backbone, hysteretic shape, and fuse response are shown to be represented well by the computational model.

The column uplift for this ground motion and scaling was found to be 20 mm (0.79”). The peak roof drift, residual drift, and peak uplift were small enough to not trigger any negative limit states for this large magnitude earthquake ground motion.

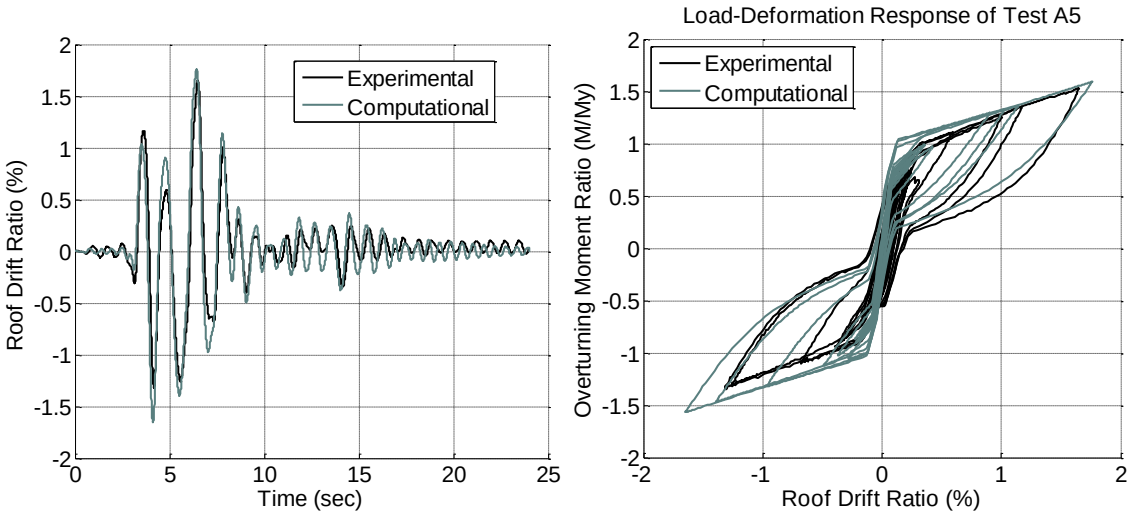

Figure 7.3 Displacement History (Left) and Load-Deformation Response (Right) for the Scale Level With 2% Probability of Exceedance in 50 Years

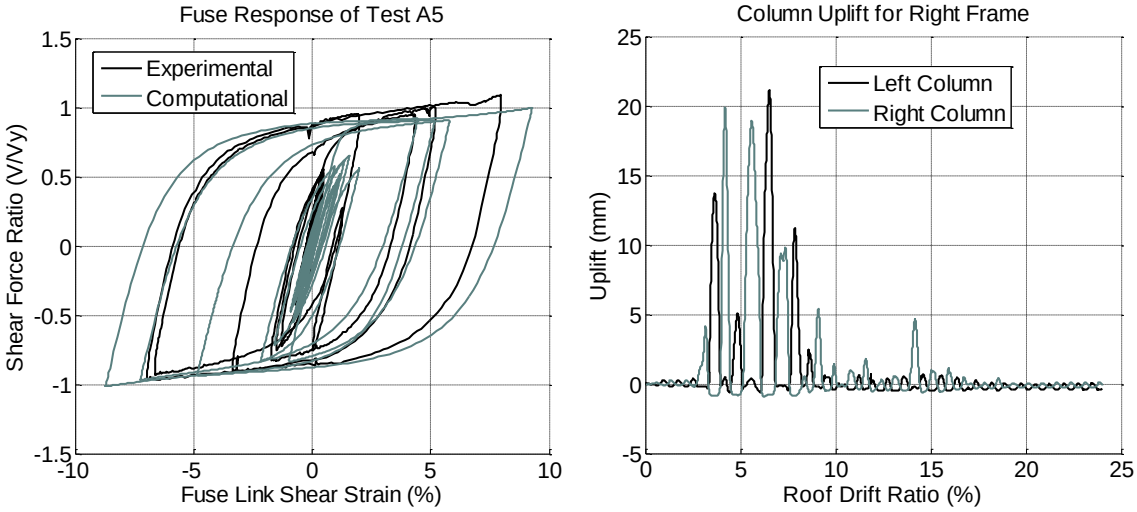

Figure 7.4 Fuse Hysteretic Response (Left) and Column Uplift History (Right) for the Scale Level With 2% Probability of Exceedance in 50 Years

Since the performance of the system when subjected to a ground motion with 2% probability of exceedance in 50 years was found to be more than satisfactory, two trials were performed at a larger scale level. The 2% in 50 scale level corresponded to a scale factor of 0.691 applied to the JMA Kobe ground motion. The second and third trials

were performed with a scale factor of 1.10 which represents a ground motion 69% larger than the 2% in 50 years event.

The response due to the first trial at the 1.10 scale factor level is shown in Figure 7.5, Figure 7.6, and Figure 7.7. A peak drift of 2.4% roof drift ratio was experienced at 6.55 seconds. The computational model response had a peak roof drift ratio of 2.78% at the same time.

The ability of the computational model to simulate the fuse and post-tensioning response was similar to that observed for Specimen A2 and specimen A3 which used similar configurations. The stiffness of the computationally simulated post-tensioning was found to be larger than the experiment, again because the anchorages were modeled as near rigid.

The leaning column simulating the destabilizing second order effects of gravity loads acting on a displaced configuration had a near linear negative stiffness as shown in Figure 7.7.

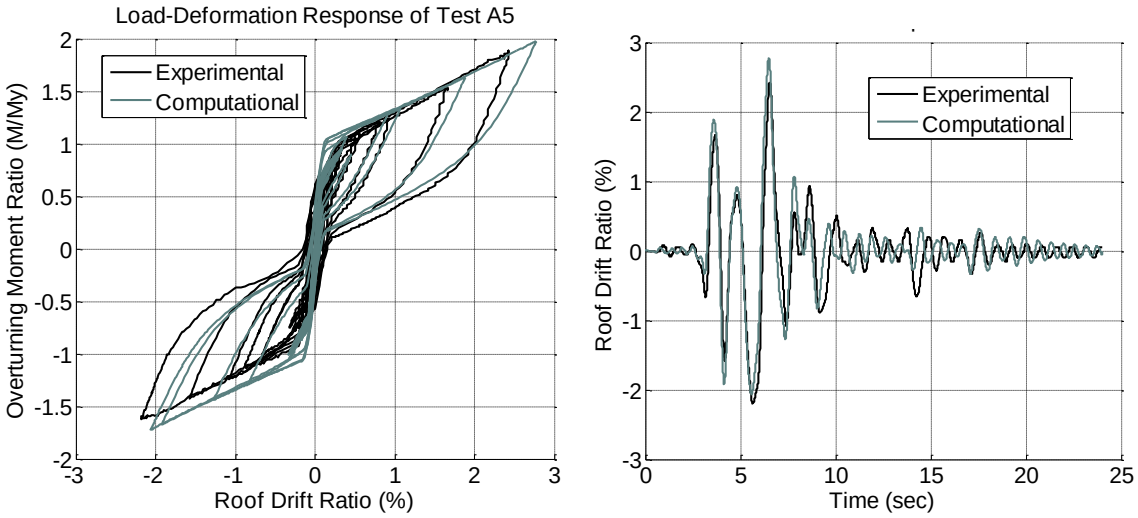

Figure 7.5 Displacement History (Left) and Load-Deformation Response (Right) for the First Trial at 1.10 Times JMA Kobe

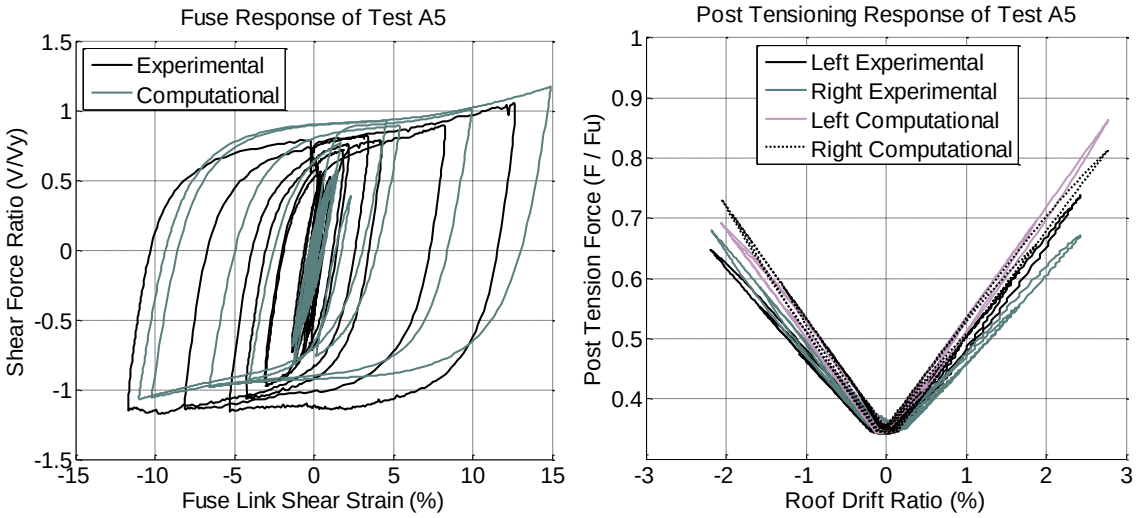

Figure 7.6 Fuse Hysteretic Behavior (Left) and Post-Tensioning Response (Right) for the First Trial at 1.10 Times JMA Kobe

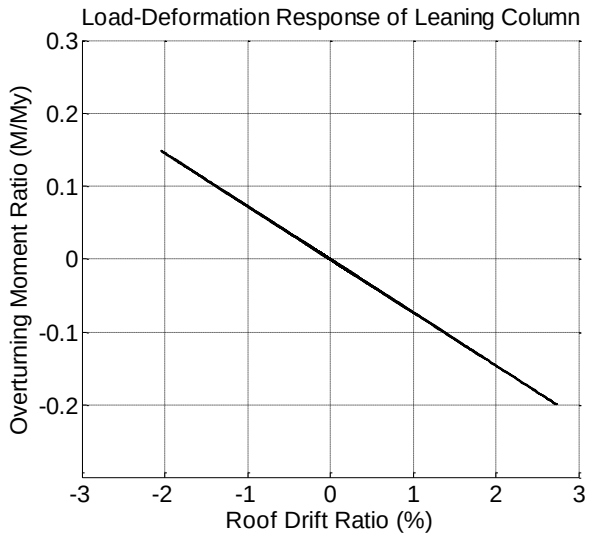

Figure 7.7 Computational Component Response for the First Trial at 1.10 Times JMA Kobe

Two trials were conducted at the scale level of 1.10 x JMA Kobe to investigate the amount of degradation in the system response. As shown in Figure 7.8, there was little degradation in the system response or fuse hysteretic behavior after being subjected to a ground motion that is 69% larger one that has a 2% probability of exceedance in 50 years. In other words, the specimen was subjected to a ground motion significantly larger than the 2% in 50 event and did not exhibit any degradation or damage outside of the fuse. Based on the performance demonstrated here, it could be concluded that this specimen could be subjected to multiple large earthquakes without requiring any repair.

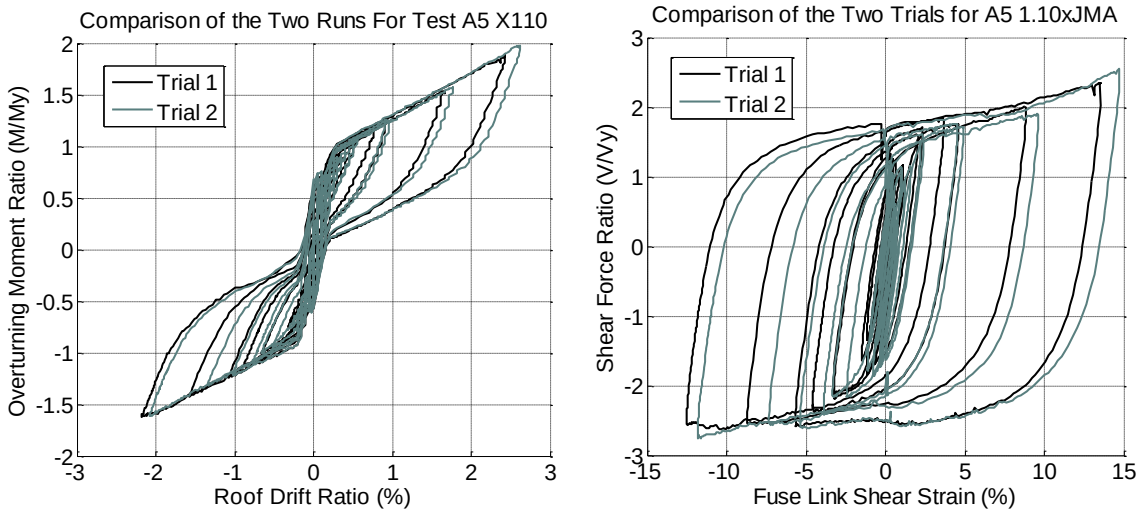

Figure 7.8 Load-Deformation Response (Left) and Fuse Hysteretic Behavior (Right) for Both Trials at 1.10 Times JMA Kobe

7.3 Specimen A6 Behavior

Specimen A6 as shown in Figure 7.9, consisted of a dual frame configuration with six fuses between the frames as shown . The fuses were, t=6.35 mm (¼") thick with 8 tapered links each that had a link length, L=356 mm (14"), a link depth at the ends, b=58.7 mm (2.3125"), and a link depth at the middle that was one-third the link depth at the end. The resulting design capacity for all the fuses was calculated to be V_{fp}=348.7 kN (78.4 kips). The post-tensioning consisted of eight 12.7 mm (½") diameter post-tensioning strands stressed to 34% of their ultimate strength or F_{pti}=497.3 kN (111.8 kips) total. Using the equations defined in Chapter 3, the overturning ratio was found to be, OT=1.04, the self-centering ratio was SC=1.02, and the geometric ratio of frame width to fuse width was A/B=2.5.

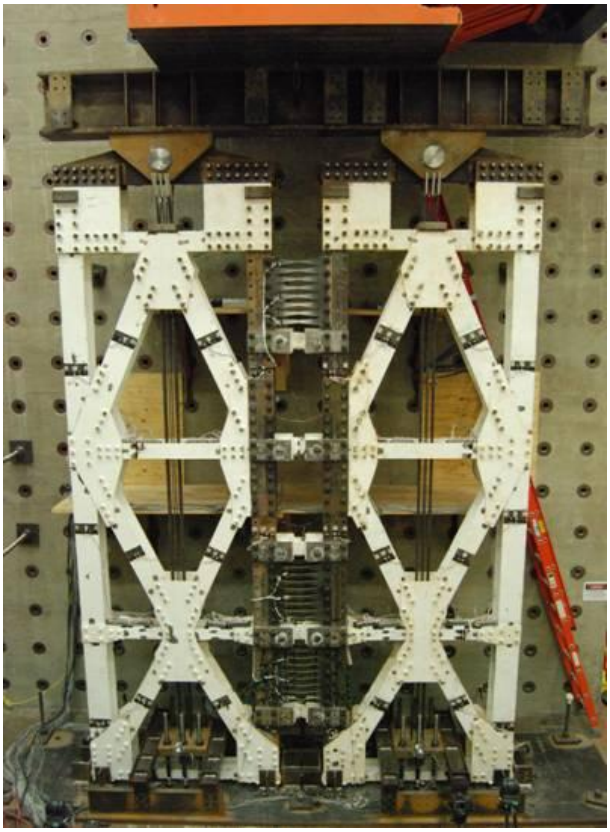

Figure 7.9 Photograph of Specimen A6

Test A6 also consisted of three trials, one at the MCE level (scale factor of 0.69), a second at the MCE level including out-of-plane motion, and a third at a scale factor of 1.20 applied to the JMA Kobe ground motion. Test A6 used 6.4 mm (¼") thick fuse plates that experienced significant lateral-torsional and axial buckling during the last trial, but not during the trials at ground motion scaling that has 2% probability of exceedance in 50 years.

As shown in Figure 7.10, the computational model predicted buckling during this trial, but the experiment did not experience buckling in the fuses. This is clear in the fuse hysteretic behavior shown on the left of Figure 7.11. Regardless of this shortcoming, the computational model accurately captures the frequency content as shown on the right of Figure 7.10. The additional energy dissipation exhibited by the experimental fuse may have contributed to the fact that the computational model over-predicted the peak roof drift.

The right side of Figure 7.11 shows the horizontal displacements at a point near the base of the frames and is presented here to highlight a trend that occurred during the progression of the testing program. During the course of the tests, the frames slide relative to the base plate and impact the bumpers. Over several tests, the bumpers were found to be slipping creating larger tolerances between the frames and the bumpers. Figure 7.11 shows that the frames are sliding approximately 5 mm (0.2") as they move from one bumper to the other.

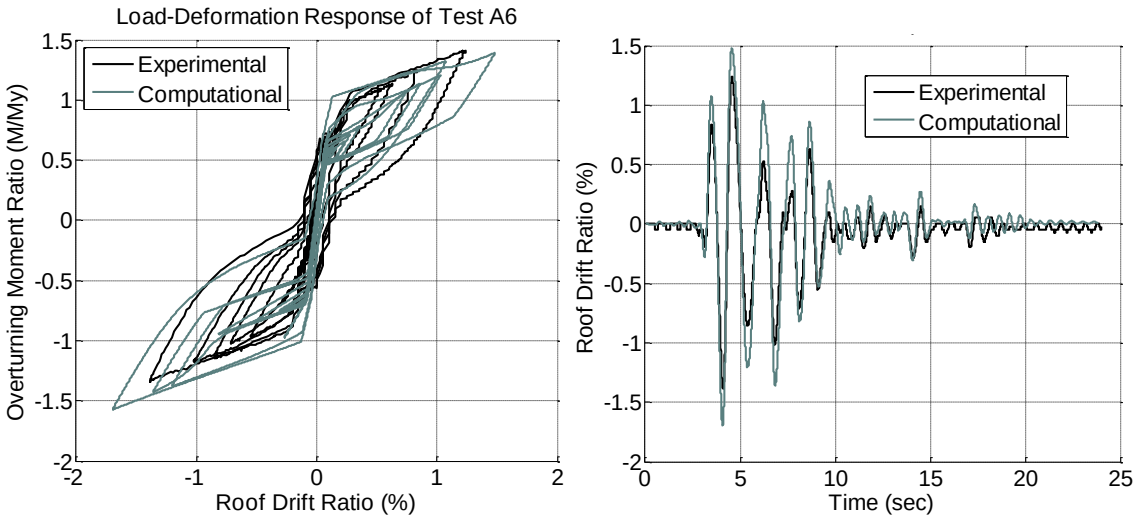

Figure 7.10 Load-Deformation Response (Left) and Displacement History (Right) for the Trial at Scaling that has 2% Probability of Exceedance in 50 Years

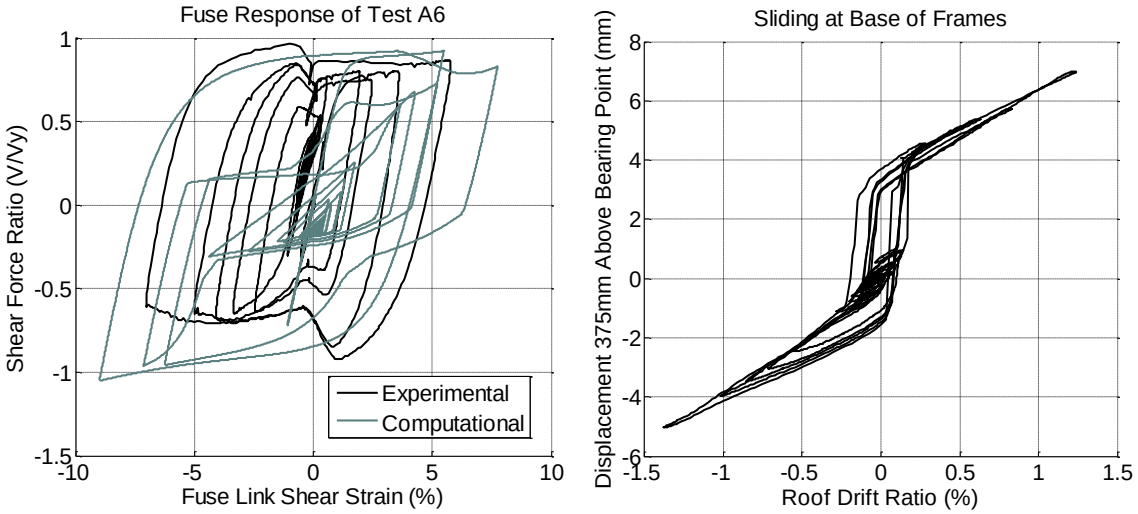

Figure 7.11 Fuse Hysteretic Behavior (Left) and Displacement Trace Near the Base (Right) for the Trial at Scaling that has 2% Probability of Exceedance in 50 Years

A trial was performed at the scale level that has 2% probability of exceedance in 50 years while applying out-of-plane motion in the proportion of 10% of the in-plane motion. This trial was performed in recognition that earthquake ground motions rarely occur in only one direction. The ability of the system to sustain out-of-plane displacements while resisting loads in plane was investigated. Figure 7.12 shows the displacement history and load-deformation response during this test. The out-of-plane drift ratio is also shown on the left of Figure 7.12. No damage or undesirable limit states were observed as a result of the out-of-plane motion. The pivoting column was found to bear on just one corner of the bearing plate. However, no local buckling or inelasticity was observed besides some almost imperceptible indentation in the bearing plate.

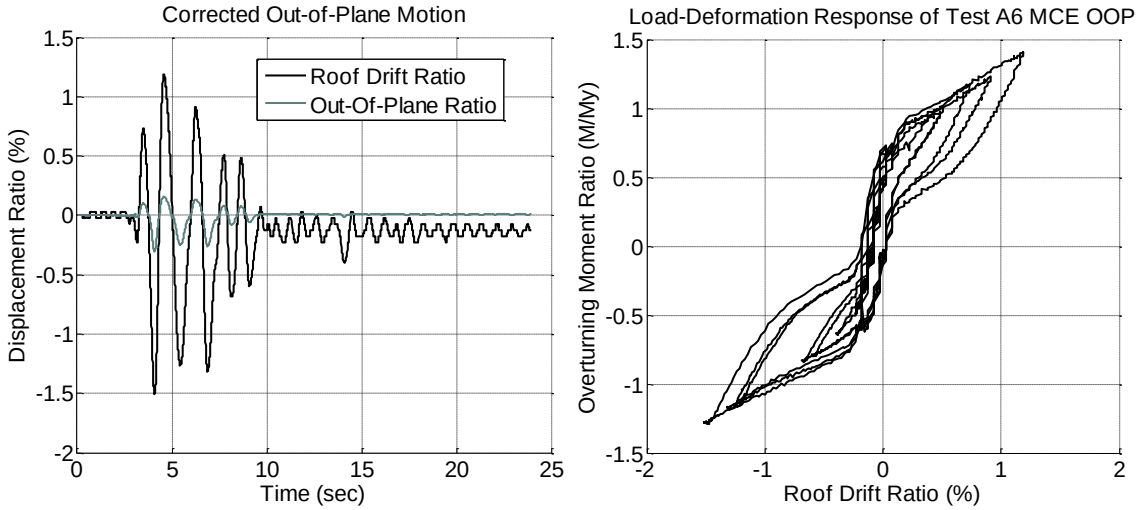

Figure 7.12 Displacement History (Left) and Load-Deformation Response (Right) for the 2% in 50 Scale Level With Out-Of-Plane Motion

The results from the last hybrid simulation trial are presented in Figure 7.13 and Figure 7.14. It is noted that from one experimental trial to the next, the resistance of the rest of the building was reset and started fresh with no previous degradation. However, in the computational simulation it was not possible to reset the resistance of one computational model while retaining the current state of the controlled rocking frame model. The computational model results shown in the following figures is obtained by running the 2% in 50 ground motion and the 1.20 x JMA Kobe ground motion both through the same model. This represents a basic difference in the ambient building resistance component between the experiment and the computational model.

As shown on the left of Figure 7.14 and the right of Figure 7.13, the fuse model captures the fact that the fuse has buckled, but does not accurately capture the post-buckling degradation for this case. The experimental results show a dominance of axial forces as demonstrated by the sharp rise in shear force at large deformations and corresponding compression snap-through type behavior upon loading in the opposite direction. The computational model also exhibits similar axial dominated post-buckling load-deformation response, but does not exhibit enough degradation in the shear strength especially for the large positive shear strain excursion. The main reason for the difference is that this comparison is for the third hybrid simulation test on the same specimen. The computational simulation was conducted for all three trials run sequentially without resetting the model. It might be concluded from the experimental response, that there is damage accumulating in the fuses that is affecting the fuse shear behavior. As described in Chapter 6, the computational model for the fuse does not consider the accumulation of damage. Implementing more advanced degradation related to quantities such as cumulative energy absorbed by the fuse, peak shear deformation, or cumulative shear deformations would likely improve the match with experimental results.

Regardless of the computational fuse response, the resulting computational system response exhibits similar strength and hysteretic shape as the experiment as shown on the right in Figure 7.13. The dominance of the post-tensioned frame component of the system after fuse buckling and degradation is evident.

The right side of Figure 7.14 shows the response of the leaning column and the ambient building resistance computational components. The ambient building resistance is shown to produce initial resistance as large as the yield strength of the lateral resisting system. The strength and stiffness of the ambient building resisting elements degrades significantly. The degradation is simulating phenomena such as crushing of the concrete in the composite simple beam-to-column connections and ovalization in gypsum board at the screw connections to the metal studs.

It is noted that the ambient building resistance response shown on the right of Figure 7.14 comes from the hybrid simulation test. The computational model, on the other hand, was run sequentially for all three trials without resetting the ambient building resistance model. It is not possible in the OpenSees software to reset the ambient building resistance model without also resetting the computational model of the specimen. As a result, the ambient building resistance computational models had already experienced two prior MCE level events along with the associated degradation in hysteretic behavior. This difference is likely to be part of the reason that the computational model experienced larger drifts than the experimental hybrid simulation test.

The Specimen A6 trials demonstrated that the controlled rocking system can self-center after very large earthquakes (74% larger than the scaling that has 2% probability of exceedance in 50 years) in the presence of destabilizing second order gravity effects and ambient building resistance.

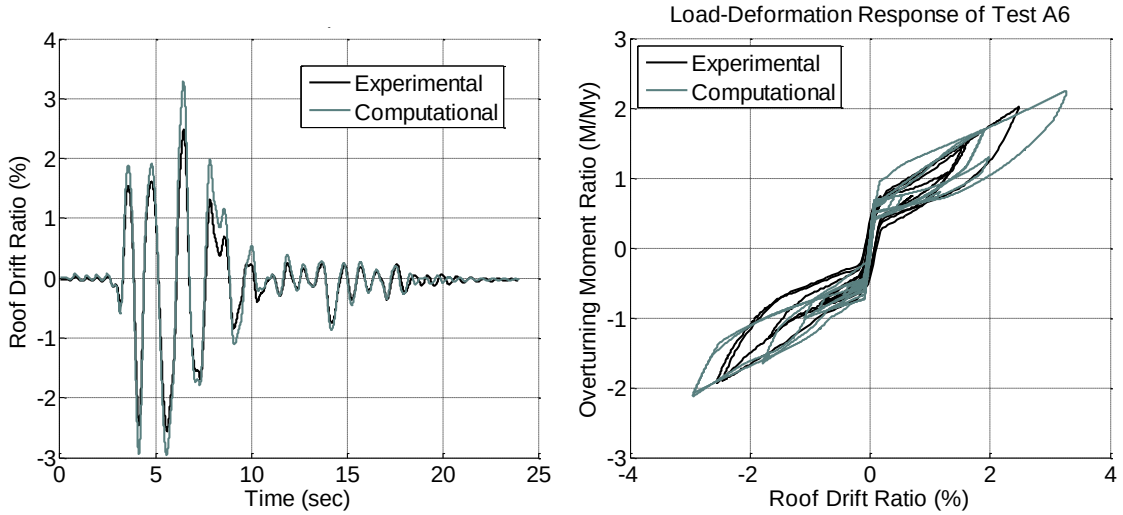

Figure 7.13 Displacement History (Left) and Load-Deformation Response (Right) for the 1.20xJMA Kobe Scale Level

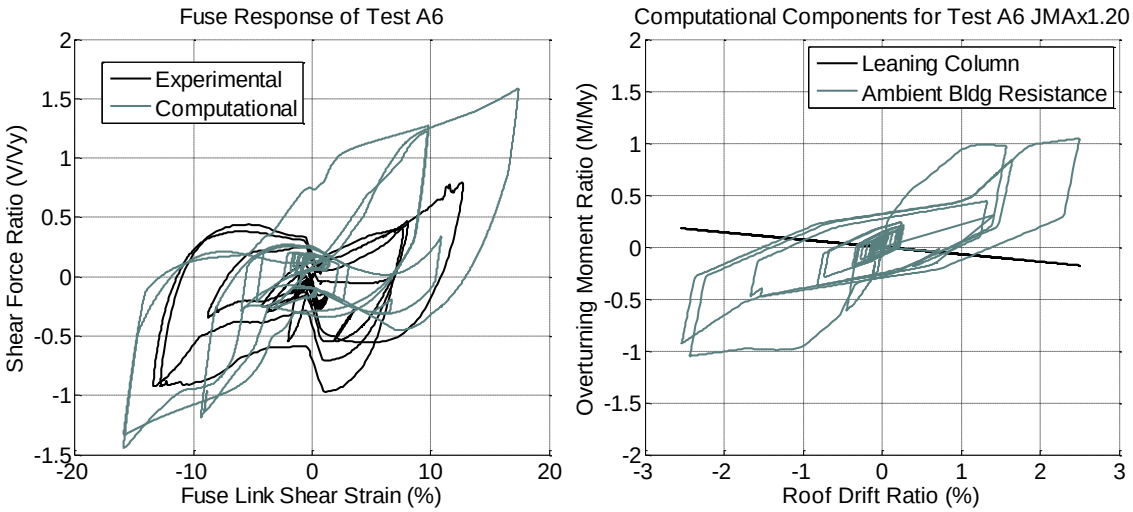

Figure 7.14 Fuse Hysteretic Behavior (Left) and Computational Component Responses (Right) for the 1.20xJMA Kobe Scale Level

7.4 Summary of Hybrid Simulation Response

As described at the beginning of this chapter, the hybrid simulation tests served several important purposes. The ability of the controlled rocking system to eliminate residual drifts and concentrate structural damage in the fuse elements was validated in all six of the hybrid simulation trials. The residual drifts are summarized in Table 7.1 and shown to be negligible for all trials even for trials including second order gravity effects and ambient building resistance. Furthermore, the thicker fuses that don't buckle such as those used in Specimen A5 were shown not to experience significant degradation even after multiple trials with an earthquake record s**c**aled to 69% larger than the motion that has 2% probability of exceedance in 50 years. This implies that thicker non-buckling fuses may not need to be replaced even after very large earthquakes.

The hybrid simulation tests also represented an opportunity to validate the computational model against a set of experiments not used to calibrate any of the model parameters. It was shown in this section that the computational model accurately captured the frequency content of the displacement response. Furthermore, the strength and stiffness of the thicker fuse configurations was accurately represented. Some limitations in the ability of the fuse model to capture accumulated damage from repeated testing were discussed, but overall system strength and self-centering were found to be well represented.

Table 7.1 Summary of Drifts During the Hybrid Simulation Tests

Spec-imen	Scale Level	Experiment Peak Roof Drift Ratio (%)	Time at Peak Roof Drift (sec)	Compu-tational Model Peak Roof Drift Ratio (%)	Time at Peak Roof Drift (sec)	Percent Difference in Peak Drift (%)	Experimental Residual Roof Drift (%)
A5	MCE	1.65%	6.49	1.76%	6.43	6.7%	0.04%
A5	1.10xKobe Trial 1	2.42%	6.55	2.78%	6.50	14.9%	-0.02%
A5	1.10xKobe Trial 2	2.62%	6.60	2.78%	6.50	6.1%	0.00%
A6	MCE	1.38%	4.10	1.70%	4.10	23.2%	-0.03%
A6	MCE w/ 10% OOP	1.51%	5.10	1.70%	4.10	12.6%	-0.13%
A6	1.20x JMA Kobe	2.54%	5.59	3.29%	6.47	29.5%	-0.02%

INTERPRETATION OF EXPERIMENTAL RESULTS

There were numerous aspects of global and local response of the controlled rocking system that were investigated as part of the experimental program. Additionally, the effects of varying parameters such as system proportioning, configuration type, fuse geometry, and inclusion of struts were studied. This chapter synthesizes the data from all of the specimens tested in the experimental program to allow conclusions to be made about the salient features of the experimental response as system parameters are varied. The flow of forces in the frame members is discussed in Chapter 11.

Behavior of the experimental specimens is divided up into global system response, post-tensioning response, fuse response, effect of struts, and comparison of the single frame versus dual frame configuration response.

8.1 Global System Response

This section on global system response starts with an investigation into the ability of the system to resist lateral loads including strength, stiffness, and energy dissipation. Then, the deformations and displacements experienced by the system as it resists lateral loads are examined. The section ends with a discussion about the effectiveness of the steel connections and details.

8.1.1 Strength, Stiffness and Energy Dissipation

As lateral loads are applied, the first response parameter of interest is the stiffness of the system. Table 8.1 gives the initial stiffness of each specimen. Comparisons between the initial stiffness obtained from the experiment and the initial stiffness of the computational models revealed that the experimental stiffness was generally less than half of the value predicted using a model with perfect geometry. The difference is demonstrated in Figure 8.1 which includes the experimental and computational results from the test of Specimen A3 without fuses attached.

However, computational simulations were also conducted in which the frames were pulled together before the simulation of the test began to simulate possible initial conditions in which fit-up of the specimen might have caused the frames to not bear uniformly on all four columns. This was implemented by applying an initial strain to elements between the frames as allowed with the elastic perfectly plastic material model in the Opensees software. Pulling the frames together causes one or both of the exterior columns to have an initial uplift. This initial condition, shown schematically on the right side of Figure 8.1, results in non-uniform bearing at the bases of the columns as well as uplift of the column bases that is not synchronized between the two frames. As shown on the left of Figure 8.1 the computational model with non-uniform bearing exhibits an initial stiffness similar to the experiment. The fact that all of the specimens had a smaller

initial stiffness relative to the computational model with perfect geometry means that it is likely that all of the specimens were affected by this phenomenon.

Table 8.1 Initial Stiffness, Roof Drift Ratio at Uplift, and Roof Drift Ratio at Fuse Yield for All Specimens

Spec-imen	Experiment Initial Stiffness, kN-m/% (K-ft/%)	Roof Drift Ratio at Uplift (%)	Roof Drift Ratio at Fuse Yield (%)
A1	10433 (7695)	0.12	0.48
A2	11555 (8523)	0.13	0.56
A3	9286 (6849)	0.20	0.51
A4	6536 (4821)	0.32	0.69
A5	8165 (6022)	0.23	0.68
A6	8164 (6021)	0.25	0.67
A7	9371 (6912)	0.24	0.70
	Mean for A Series =	0.21	0.61
B1	2279 (1681)	0.11	1.41
B2	2669 (1969)	0.11	1.50
	Mean for B Series =	0.11	1.46

The load-deformation response near zero drift for the computational model was found to change with the amount that the frames were pulled together. For small values of initial inward displacement, one column may be uplifted, and the other is partially decompressed resulting in a load-deformation response with the same initial larger stiffness as the perfect model which transitions to the lower stiffness prior to uplift. For large values of initial inward displacement, both exterior columns begin the simulation with uplift and the load-deformation response exhibits the lower initial stiffness, except that horizontal sliding at the base occurs at zero force causing a horizontal jog in the load-deformation response. Because of the sensitivity of the computational model to the amount of initial inward displacement and the unknown nature of the exact initial conditions of the specimen, this phenomenon was neglected in the computational model.

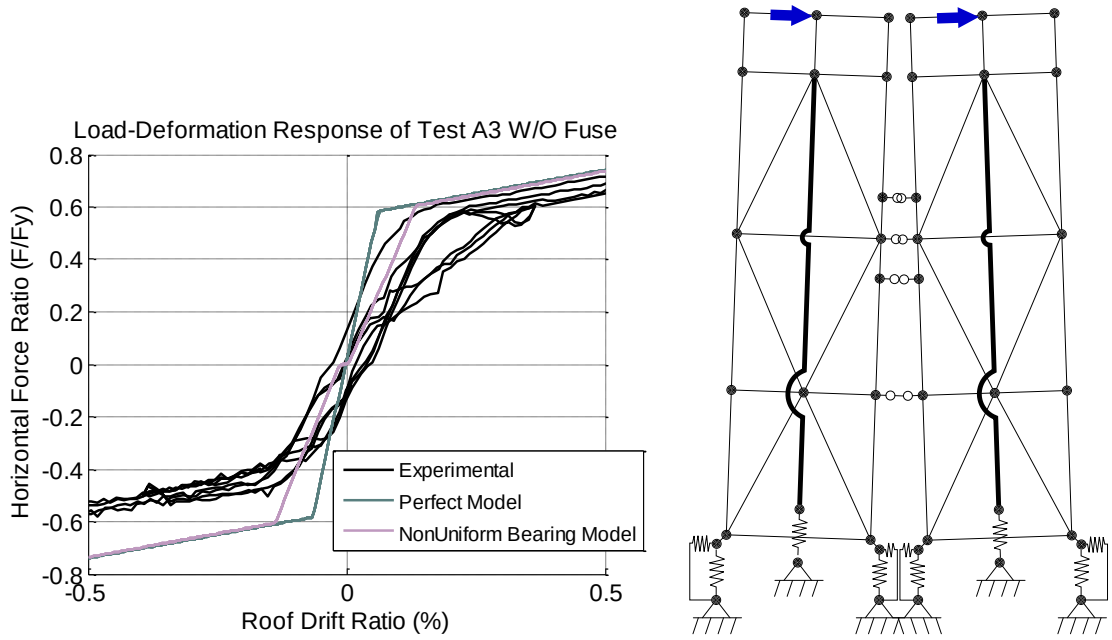

Figure 8.1 Effect of Non-Uniform Bearing on Initial Stiffness (Left) Schematic Drawing of Non-Uniform Bearing

The roof drift ratio at uplift is given in Table 8.1. These values were obtained as the point in the load-deformation response when significant nonlinearity occurs. Table 8.1 shows that the roof drift ratio at uplift was small for Specimen A1 and A2, but increased for Specimen A3 and A4. The roof drift ratio includes the drift due to sliding at the base of the frames. As discussed later in this chapter and given in Table 8.6, the sliding at the base of the frame accounted for 0.11% of the roof drift ratio for Specimen A4 but less for the other specimens.

The overturning moment applied to the specimen when the fuse yielded is included in Table 8.2. The definition of fuse yield is defined later in this chapter. The predicted overturning moment at yield was calculated with Equations 5.2 and Equation 5.3 using the initial post-tensioning force and the calculated fuse yield capacity based on measured material yield strength. As given in Table 8.2, the average ratio of actual moment at fuse yield to the predicted is 1.14 for the A series specimens and 1.43 for the B series specimens. The reason that the B series specimens exhibited larger overturning moment at fuse yield than the equations predict was because the average roof drift ratio at fuse yield was 1.46%. The post-tensioning provides additional resistance to overturning moment as the strands stretch due to uplift. The additional post-tensioning forces above the initial post-tensioning force account for the differences noted here.

Table 8.2 System Response Parameters

Specimen	Predicted Yield Moment, kN-m (k-ft)	Experiment Moment at Fuse Yield, kN-m (k-ft)	Ratio of Actual to Predicted Yield
A1	1432 (1057)	1589 (1172)	1.11
A2	1599 (1180)	1702 (1256)	1.06
A3	1319 (973)	1419 (1047)	1.08
A4	2132 (1573)	2705 (1995)	1.27
A5	1531 (1129)	1722 (1270)	1.12
A6	1551 (1144)	1834 (1353)	1.18
A7	1551 (1144)	1752 (1292)	1.13
		Mean for A Series =	1.14
B1	404 (298)	595 (439)	1.47
B2	389 (287)	540 (398)	1.39
		Mean for B Series =	1.43

As discussed in Chapter 5 and as discussed at the end of this chapter, the B series specimens had a lag in the fuse response due to pin hole tolerances in the connection of the frame to the fuses. This lag led to the larger drifts required to yield the fuse. Proven methods for mitigating the pin hole tolerances are presented at the end of this chapter.

To further illuminate the load-deformation behavior of the controlled rocking system, the equations derived in Chapter 3 for analytically predicting the SDOF response were applied to Specimen A3. The load-deformation response is presented in Figure 8.2 compared to the experimental response up to 1% roof drift ratio.

The difference in initial stiffness discussed above is noticeable in Figure 8.2. The analytical solution also predicts a change in stiffness when the frames uplift at an overturning moment ratio of approximately 0.6. With the possible exception of the B series specimens, the experimental response did not exhibit a sharp change in stiffness at the moment associated with fuse yield as the analytical response suggests. Instead the change in stiffness due to fuse yielding was gradual.

The roof drift ratio at fuse yield is given in Table 8.1 to be 0.5% for Specimen A3. Significant nonlinearity had occurred prior to this point, unlike the analytical solution which assumes that the fuse is elastic-perfectly plastic prior to fuse yield. The backbone of the analytical prediction overestimates the experimental response therefore. The overturning moment at fuse yield is given in Table 8.2 to be 8% larger than the calculated yield moment. Since this occurs at a roof drift ratio of 0.5%, the post-tensioning is supplying the system with additional resistance due to further elongation of the post-tensioning strands during uplift. Similarly this is the reason that the analytical response shows a change in stiffness associated with fuse yield that is above the yield moment of the system, M_y.

The post-yield stiffness is slightly underestimated because the hardening in the fuse is neglected in the analytical derivation. The unloading regime is shown in Figure

8.1 to be the most inaccurate aspect of the analytical prediction. The Bauschinger effect and associated delay in reaching the yield force in the opposite direction caused the discrepancy with the elastic-perfectly-plastic assumption used in the analytical derivation.

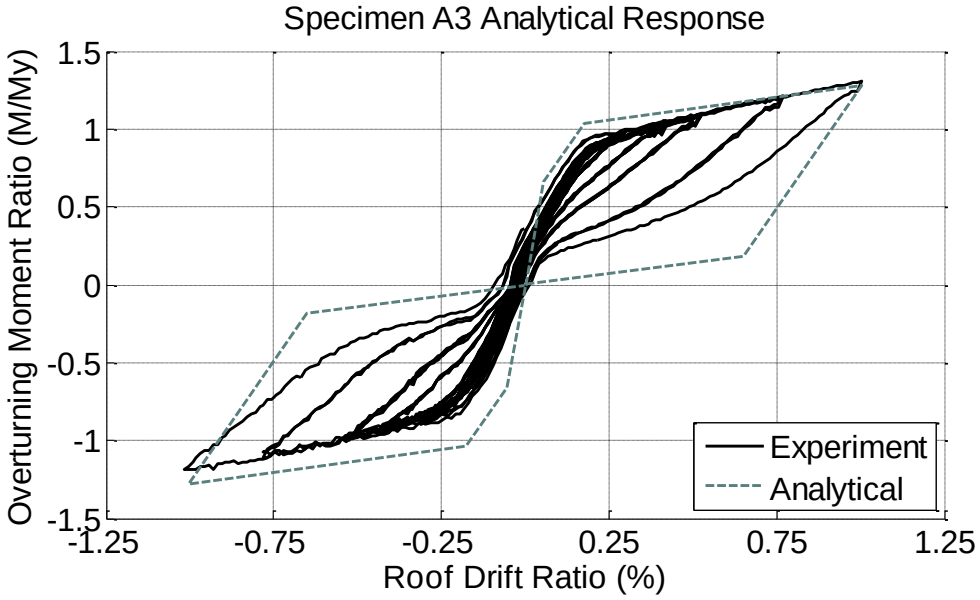

Figure 8.2 Comparison of Analytical Response to Experimental Response for a Portion of Specimen A3 Response

The peak drifts and the drifts at zero force are given in Table 8.3 and Table 8.4 for each specimen and are shown graphically in Figure 8.3. A significant difference is noted in the ability of the system to eliminate drifts when the load is removed between the Specimens with buckling fuses ant the specimens with non-buckling fuses. The drift at zero force for Specimen A1 as shown on the left of Figure 8.3 demonstrates the advantages the thin buckling fuses possess in promoting self-centering. The drift at zero force is shown to increase steeply up to a roof drift ratio of approximately 1.1%. At this point, the fuses buckled reducing their resistance to the post-tensioning's restoring force. After reaching a roof drift ratio of 3%, Specimen A1 only exhibited 0.04% roof drift ratio when the loads were removed.

On the other hand, Specimen A2 which has a similar self-centering ratio and overturning ratio as Specimen A1 (see Equation 4.9, Equation 4.10, Equation 4.11, and Equation 4.12 for the definition of these variables) shows a much different drift at zero force response as shown on the right of Figure 8.3. The residual roof drift ratio when the loads were removed was found to continue to increase up to a value greater than 0.5% at the end of the test. As expected, the ability to self-center is also adversely affected by post-tensioning strand yield and fracture as demonstrated by the drifts at zero force for Specimen A4 as the displacement history exceeded 2.7% roof drift ratio.

However, Specimen A2 had a self-centering ratio of , SC=0.71 which implies less than full self-centering ability, and Specimen A4 was specifically designed to investigate behavior when post-tensioning strand yield stress is exceeded. It is concluded from the results shown here that if the self-centering ratio is designed to be greater than 1.0 and the

post-tensioning is designed not to yield, that the roof drifts at zero force are limited to 0.2% after cycles at 2% roof drift ratio and 0.35% after cycles at 3% roof drift ratio.

Table 8.3 Summary of Peak Drifts and Drifts at Zero Force for Specimens A1 Through A4

Displace-ment Level	Specimen A1		Specimen A2		Specimen A3		Specimen A4	
	Peak Drift Ratio	Drift at Zero Force	Peak Drift Ratio	Drift at Zero Force	Peak Drift Ratio	Drift at Zero Force	Peak Drift Ratio	Drift at Zero Force
1	0.09%	0.01%	0.10%	0.10%	0.09%	0.01%	0.11%	0.03%
2	0.18%	0.01%	0.20%	0.12%	0.18%	0.03%	0.22%	0.02%
3	0.22%	0.01%	0.23%	0.10%	0.20%	0.03%	0.25%	0.02%
4	0.30%	0.03%	0.28%	0.10%	0.25%	0.03%	0.30%	0.02%
5	0.37%	0.03%	0.33%	0.11%	0.30%	0.03%	0.36%	0.02%
6	0.49%	0.05%	0.46%	0.11%	0.43%	0.03%	0.48%	0.04%
7	0.64%	0.07%	0.57%	0.11%	0.53%	0.03%	0.59%	0.05%
8	0.92%	0.11%	0.81%	0.13%	0.78%	0.03%	0.83%	0.07%
9	1.19%	0.16%	1.04%	0.17%	1.01%	0.05%	1.07%	0.09%
10	1.48%	0.16%	1.38%	0.26%	1.24%	0.07%	1.30%	0.11%
11	2.03%	0.08%	1.74%	0.24%	1.71%	0.10%	1.77%	0.17%
12	2.58%	0.05%	2.21%	0.46%	2.17%	0.13%	2.24%	0.23%
13	3.14%	0.04%	2.69%	0.56%	2.64%	0.24%	2.71%	0.35%
14	N/A	N/A	2.99%	0.52%	3.10%	0.29%	3.19%	0.59%
15	N/A	N/A	N/A	N/A	N/A	N/A	3.66%	0.82%

Table 8.4 Summary of Peak Drifts and Drifts at Zero Force for Specimens A7, B1, and B2

Displacement Level	Specimen A7		Specimen B1		Specimen B2	
	Peak Drift Ratio	Drift at Zero Force	Peak Drift Ratio	Drift at Zero Force	Peak Drift Ratio	Drift at Zero Force
1	0.09%	0.00%	0.29%	0.06%	0.29%	0.05%
2	0.18%	0.01%	0.33%	0.06%	0.33%	0.05%
3	0.22%	0.03%	0.41%	0.06%	0.41%	0.05%
4	0.29%	0.04%	0.48%	0.05%	0.49%	0.05%
5	0.36%	0.05%	0.64%	0.05%	0.64%	0.05%
6	0.49%	0.07%	0.79%	0.05%	0.80%	0.05%
7	0.63%	0.09%	1.10%	0.05%	1.11%	0.04%
8	0.90%	0.12%	1.41%	0.05%	1.42%	0.06%
9	1.17%	0.13%	1.72%	0.05%	1.74%	0.08%
10	1.45%	0.13%	2.35%	0.05%	2.37%	0.07%
11	2.00%	0.10%	2.96%	0.04%	2.99%	0.08%
12	2.55%	0.09%	3.56%	0.05%	3.60%	0.07%
13	3.10%	0.09%	4.16%	0.04%	4.20%	0.11%
14	3.65%	0.08%	N/A	N/A	N/A	N/A
15	4.20%	0.08%	N/A	N/A	N/A	N/A

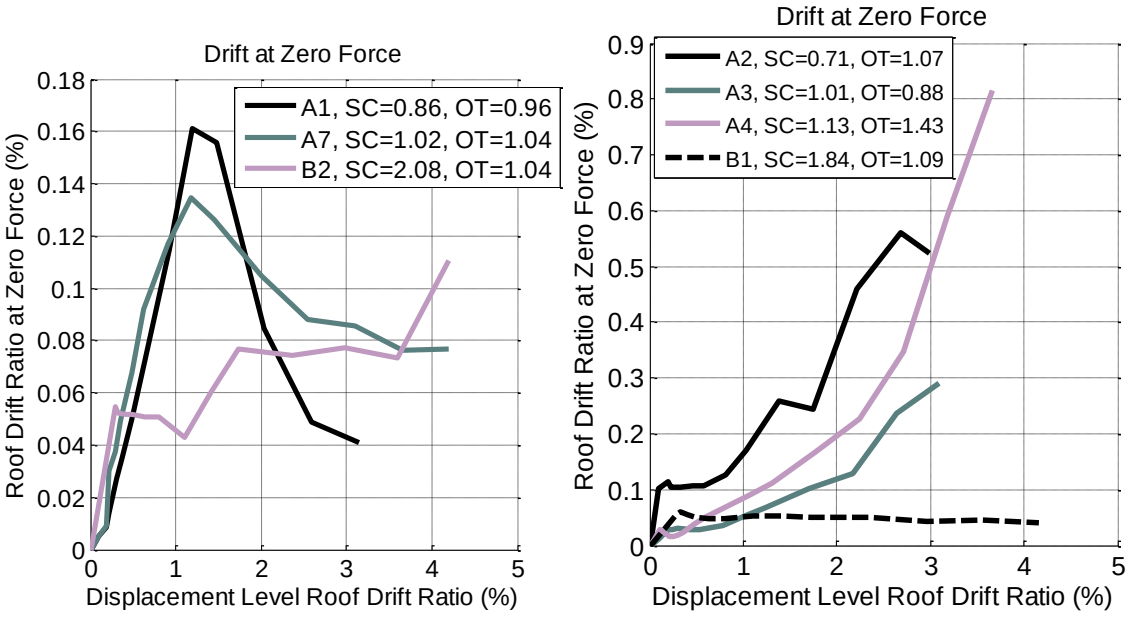

Figure 8.3 Drift at Zero Force for Specimens with Buckling Fuses (Left) and Non-Buckling Fuses (Right)

The hysteretic energy absorbed by the specimen is presented in Table 8.5 for each of the cyclically tested specimens. The energy was calculated as the amount of energy absorbed in that cycle as normalized by the energy dissipated by a corresponding elastic-plastic hardening system. As shown in Figure 8.4, the normalizing energy quantity represents the amount of energy absorbed by an elastic-perfectly plastic hardening system with the same initial stiffness and secondary stiffness as the controlled rocking specimen. If a self-centering hysteresis loop fully encloses the first and third quadrants of the load-deformation response, the absorbed energy would be 50% of the elastic perfectly plastic system. For a fully self-centering system, the maximum normalized energy absorption is therefore 50%.

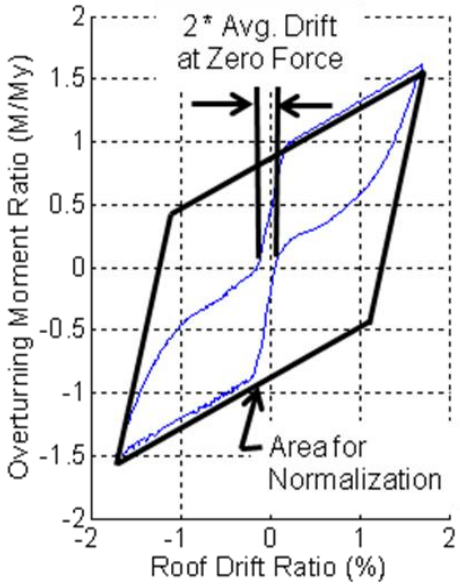

Figure 8.4 Definition of the Drift at Zero Force and Hysteretic Absorbed Energy

Table 8.5 Summary of Energy Absorbed Per Displacement Level

Displace-ment Level	A1 Norm-alized Energy	A2 Norm-alized Energy	A3 Norm-alized Energy	A4 Norm-alized Energy	A7 Norm-alized Energy	B1 Norm-alized Energy	B2 Norm-alized Energy
1	-1.9%	6.3%	2.2%	11.8%	-1.0%	12.9%	15.4%
2	15.1%	24.8%	-0.5%	35.5%	12.1%	5.2%	5.3%
3	15.1%	27.0%	-1.0%	11.9%	24.9%	4.4%	4.8%
4	19.8%	20.7%	3.0%	5.3%	19.5%	4.1%	4.4%
5	22.7%	20.6%	7.4%	8.1%	20.9%	3.0%	2.8%
6	27.9%	24.5%	8.7%	15.7%	25.0%	5.2%	5.0%
7	32.3%	29.1%	14.8%	23.0%	29.2%	4.6%	3.4%
8	38.5%	29.9%	23.1%	30.7%	33.0%	6.9%	5.8%
9	42.9%	40.1%	28.1%	35.7%	33.3%	17.5%	14.1%
10	42.3%	44.6%	31.7%	40.0%	33.9%	23.7%	20.8%
11	33.7%	48.5%	36.8%	45.0%	28.5%	28.0%	23.8%
12	27.6%	52.1%	40.4%	49.0%	24.2%	36.5%	36.1%
13	20.8%	55.3%	43.4%	51.3%	23.9%	40.4%	28.4%
14	N/A	54.4%	46.1%	54.4%	24.7%	24.2%	14.7%
15	N/A	N/A	N/A	53.1%	20.0%	N/A	N/A

The data included in Table 8.5 is also shown in Figure 8.5. The specimens with thinner fuses allowed to buckle, exhibited similar energy dissipating ability as the thicker fuse configurations up to 1% roof drift ratio. After this point, the fuses in Specimen A1 and Specimen A7 buckled causing a decline in the ability of the system to absorb energy. The systems with thicker fuses, however, continued to increase the amount of seismic energy that was being absorbed each cycle approaching 50%. The response of the single frame configurations had some additional aspects that will be discussed in a subsequent section.

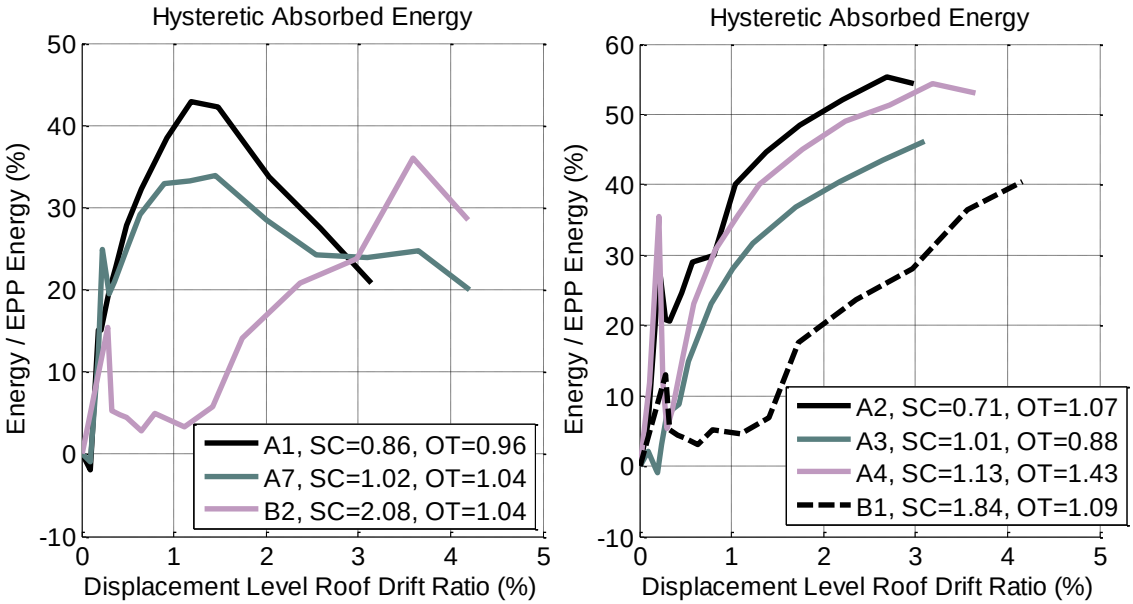

Figure 8.5 Hysteretic Absorbed Energy for Specimens with Buckling Fuses (Left) and Non-Buckling Fuses (Right)

8.1.2 System Displacements and Deformations

The displacements of the experimental specimen were shown to be governed largely by rigid body rotation of the frames. This was demonstrated by showing that the interstory drift for all three stories was equal to each other and equal to the roof drift ratio on the left of Figure 5.10. This was also demonstrated by the linearity of the uplift with increases in roof drift as shown on the right of Figure 5.10.

It was also shown in Chapter 5 that the two frames tilt toward each other as they rock. The post-tensioning forces demonstrate this point such as the right side of Figure 5.17 in that the post-tensioning forces in the windward frame are larger than the leeward frame. Similarly, the uplift as shown on the right of Figure 5.10 shows that the windward frame experiences more uplift than the leeward frame.

The reason that the frames tilt together stems from the fact that there are elements such as fuses and struts connecting points on the interior columns. As the frames undergo rigid body rocking, the points on the interior columns tend to get farther apart unless otherwise constrained. Figure 8.6 shows an initial configuration, denoted as configuration a, with an element at a height, *h*, between the frames with an initial length, *La*. Although the struts and fuses are actually connected at some eccentricity from the column centerline, this idealized connecting element is useful for examining the stretching effect. Similar derivations can be conducted for specific connecting element geometries. The frames have width, *A*, and a width between the frames, *B*. If it is assumed that both frames undergo the same roof drift angle, α, then the coordinates for the two ends of the connecting element can be derived based on geometry. Equation (8.1), Equation (8.2), Equation (8.3), and Equation (8.4) give the location of the two ends in configuration a and in configuration b. The length of the connecting element is calculated in Equation (8.5) and Equation (8.6).

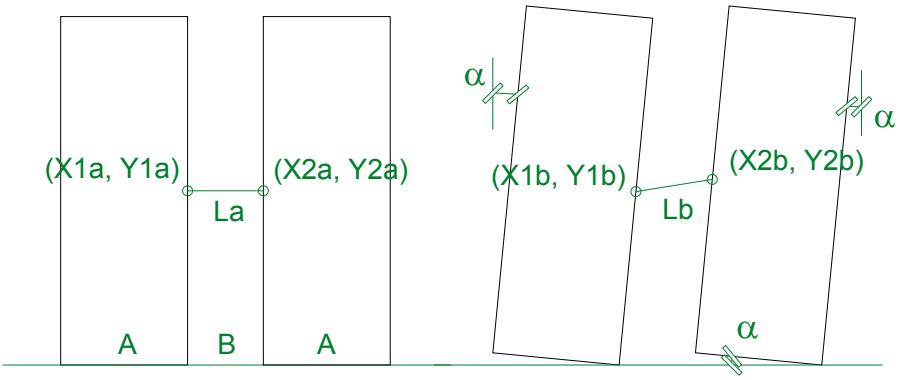

Figure 8.6 Derivation of the Distance Between Points on the Two Frames

$$\left[X_{1a}, Y_{1a}\right] = \left[\frac{-B}{2},\ h\right] \tag{8.1}$$

$$\left[X_{1b}, Y_{1b}\right] = \left[\frac{-B}{2} + h\sin(\alpha),\ h\cos(\alpha)\right] \tag{8.2}$$

$$\left[X_{2a}, Y_{2a}\right] = \left[\frac{B}{2},\ h\right] \tag{8.3}$$

$$\left[X_{2b}, Y_{2b}\right] = \left[\frac{B}{2} + A\sin(\alpha)\tan(\alpha) + h\sin(\alpha),\ h\cos(\alpha) + A\sin\alpha\right] \tag{8.4}$$

$$L_b = \sqrt{\left(X_{2b} - X_{1b}\right)^2 + \left(Y_{2b} - Y_{1b}\right)^2} \tag{8.5}$$

$$L_b = \sqrt{\left(B + A\sin(\alpha)\tan(\alpha)\right)^2 + \left(A\sin(\alpha)\right)^2} \tag{8.6}$$

The length of the connecting element is shown to grow as a nonlinear function of the roof drift angle, α. When plotted against the roof drift angle as shown in Figure 8.7, it is clear that the connecting element is undergoing tension as the frames rock in unison. The specimens had constraint at the bottom in the form of bumpers and at the top in the form of pin connections to the loading beam. Since the constraint at both the top and bottom had some tolerance, it was possible for the frames to not move in unison as assumed in the above derivation. However, the amount of constraint provided between the two frames is an important consideration. As discussed in an upcoming section, axial forces in the fuses due to the amount of constraint provided by the frames, is a significant aspect of the fuse response. Preliminary computational models that used perfect pins at the connection to the loading beam and struts along with zero tolerances between the frames and the bumpers at the base experienced significantly larger member forces due to the added constraint.

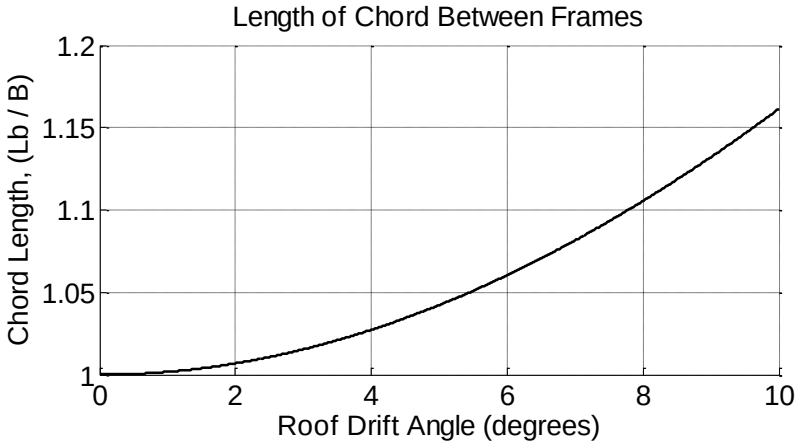

Figure 8.7 Plot of Derived Distance Between Frames Assuming A=1573 mm (61.92") and B=628 mm (24.72")

The member forces are discussed further in Chapter 11, but it is noted here that although minor yielding of extreme fibers may have occurred during some tests, the frame members, struts, and connections remained essentially elastic throughout the tests. No local buckling or global buckling was encountered. In fact, the same pair of frames was used for all nine specimens. The controlled rocking system succeeded in concentrating all structural damage in the fuse elements.

8.1.3 Effectiveness of System Detailing

One of the significant discoveries about detailing of the controlled rocking system as evidenced from the experimental program was the importance of understanding and controlling the tolerances used in connections with moving parts. The effect of the tolerances in the strut pin connections is examined in a subsequent section on struts. The effect of the tolerances in the pin connections between the frame and the fuse in the single frame configuration are discussed in a subsequent section on the single frame configuration. The tolerances between the frames and the bumpers are examined further here.

In the erection of the rocking frame on the base plate it was necessary to make the distance between bumpers larger than the width of the frames. It is not reasonable to attempt to assemble the system with zero tolerances. Figure 8.8 shows the effect of the sliding at the base of the frames on the displacement near the base. The example shown in Figure 8.8 demonstrates that Specimen A4 had a total tolerance between the frames and bumpers of approximately 5.7 mm (0.22"). The amount of slip experienced in the tests is summarized in Table 8.6.

The holes in the bumper assembly in its connection to the larger base plate below were oversized to allow some adjustment in the bumper location. At the beginning of the Specimen A1 test, the bumpers were pushed against the specimen and the bolts were pretensioned. As given in Table 8.6, the amount of sliding at the base increased in the testing of Specimen A4 as the bumpers slipped relative to the larger base plate below. Before the testing of Specimen A7, the bumpers were adjusted to reduce the tolerance

between the frames and bumpers, but as given in Table 8.6, the bumpers likely slipped again.

However, for the testing of Specimen B1 and Specimen B2, shims were added between the frames and the bumpers. The shims which consisted of 1.59 mm (1/16") thick plates were added at two the locations and were spot welded to the bumpers. Table 8.6 shows that the sliding at the base for Specimen B1 and Specimen B2 was negligible. Adding shims after erection was found to be an easy and effective way to eliminate sliding at the base.

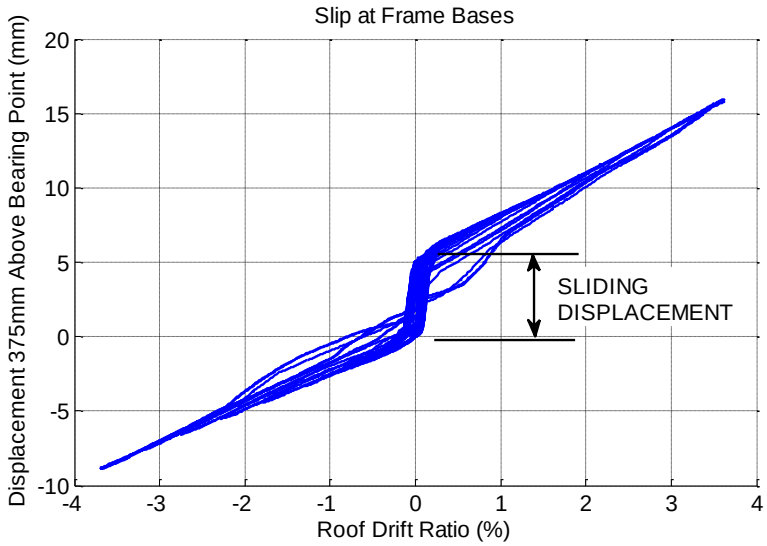

Figure 8.8 Example of Sliding From Specimen A4 Test

Table 8.6 Approximate Sliding Displacements at the Base of the Frames

Specimen	Sliding Displacement, mm (in)	Equivalent Roof Drift Ratio
A1	1.5 (0.06)	0.03%
A2	2.7 (0.11)	0.05%
A3	1.3 (0.05)	0.03%
A4	5.7 (0.22)	0.11%
A5	5.1 (0.20)	0.10%
A6	4.6 (0.18)	0.09%
A7	3.2 (0.13)	0.06%
B1	0.0 (0.00)	0.00%
B2	0.6 (0.02)	0.01%

The effectiveness of the detailing to allow efficient repair of the system after an earthquake was demonstrated several times. Disregarding the adjustment of post-tension force, the preparation between specimens often replicated the repair that might take place

in a real building after a large earthquake. The fuses were removed, and replaced with new ones. Since the fuses had been yielding, they often had large forces in them which made it difficult to unbolt and remove. However, if desired, the fuse links could easily be torch cut with portable equipment which would relieve any built-up internal forces.

The bearing connections at the base of the columns performed well in that they were subjected to nine sets of tests and did not exhibit significant signs of wear. Figure 8.9 shows the bottom of one of the column base plates after all of the testing was complete. At the right edge of the plate an almost imperceptible amount of angle between a straight edge and the base plate was noted at the last 12 mm (0.5") or so. The corresponding base plate shown in Figure 8.10 did not show any noticeable indentation where the frame was pivoting.

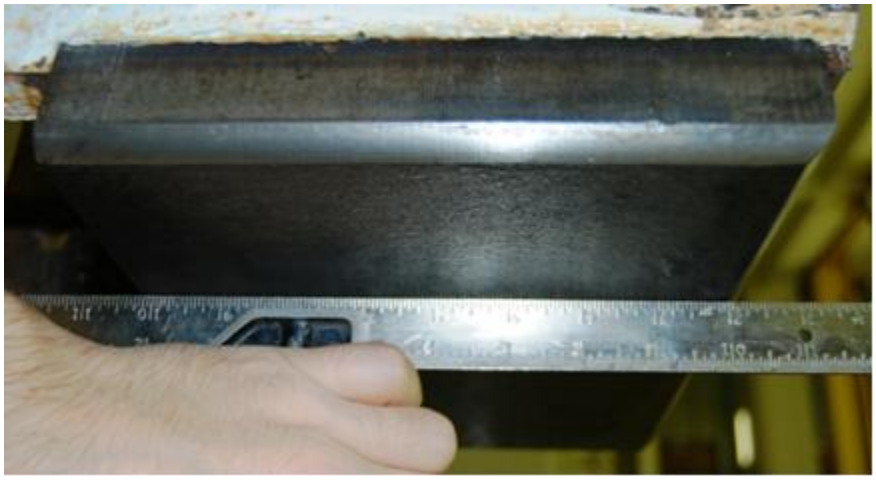

Figure 8.9 Photograph of the Bottom of a Column Base Plate After the Experimental Program Showing Lack of Damage

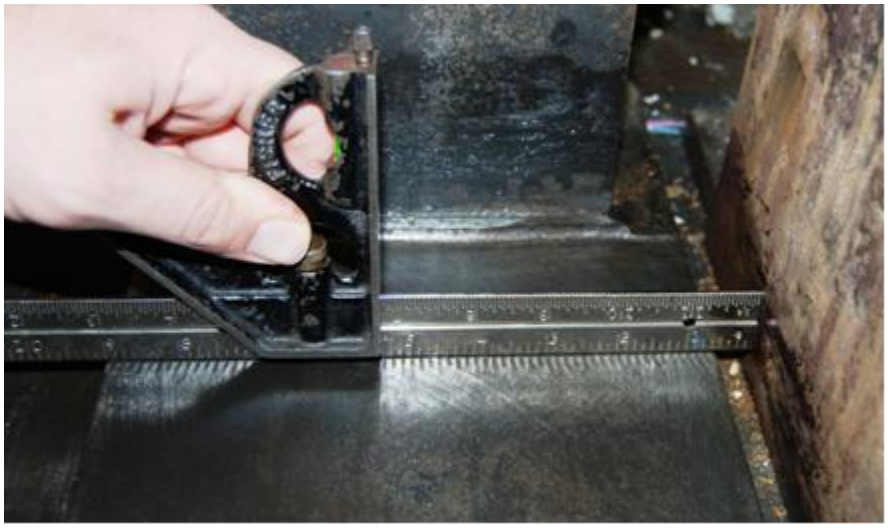

Figure 8.10 Photograph of the Base Plate Showing Lack of Indentation

In general the connections and details used for the specimen performed as intended without experiencing damage. The tolerances between pieces as discussed in

this section and others in this chapter were identified as an important aspect, but easy mitigation techniques have been devised and shown to be effective.

8.2 Post-Tensioning Behavior

8.2.1 Elastic and Yield Behavior

The post-tensioning strands were designed to remain elastic through the majority of the tests. Stress in the post-tensioning strands was calculated using the measurements from specially made load cells that were placed between the lower post-tensioning anchorage chuck and the anchorage plate. Strain in the post-tensioning strands was calculated using string potentiometers that measured the change in distance between the upper and lower anchorage plates. Using these measures for stress and strain, the modulus of elasticity was calculated for all of the strands in Specimen A2 and included in Table 8.7. As shown in Table 8.7, the values for the modulus of elasticity did not vary much with a mean of 197.2 GPa (28595 ksi) and a standard deviation of 2.7 GPa (396 ksi). Specimen A2, A3, and A4 did not undergo significant seating losses because the post-tensioning seating losses had already occurred for these strands during the testing of Specimen A1. The seating losses for specimens A5, A6, A7, B1, and B2 were exhausted by conducting cycles on the post-tensioned frame without the fuses attached prior to testing of the specimen.

The modulus of elasticity measured from the four ancillary tests on coupons from the same post-tension strand material was found to have more variation with a mean of 202 GPa (29300 ksi). It is shown in Figure 8.11, that the monotonic behavior from coupon test number 4 was quite similar to the backbone of the response of one of the strands in the Specimen A4 test.

It was noted in Chapter 6 that the lower anchorage of the post-tensioning was not rigid. The stiffness of the lower anchorage was found to reduce the amount of elongation and force in the post-tensioning compared to the computational model which assumed near rigid anchorage.

Table 8.7 Measured Modulus of Elasticity for Post-Tensioning Strands in Specimen A2

Specimen A2 Strand	Modulus of Elasticity	
	(GPa)	(ksi)
L-PT-L-1	194.8	28251
L-PT-L-2	194.6	28220
L-PT-L-3	197.9	28703
L-PT-L-4	193.2	28020
L-PT-L-5	197.1	28585
L-PT-L-6	198.5	28791
L-PT-L-7	198.6	28799
L-PT-L-8	198.6	28799
L-PT-R-1	199.6	28950
L-PT-R-2	195.8	28397
L-PT-R-3	203.5	29522
L-PT-R-4	200.6	29093
L-PT-R-5	194.2	28160
L-PT-R-6	196.2	28458
L-PT-R-7	196.9	28560
L-PT-R-8	194.5	28209
Mean =	197.2	28595
Std. Dev. =	2.7	396

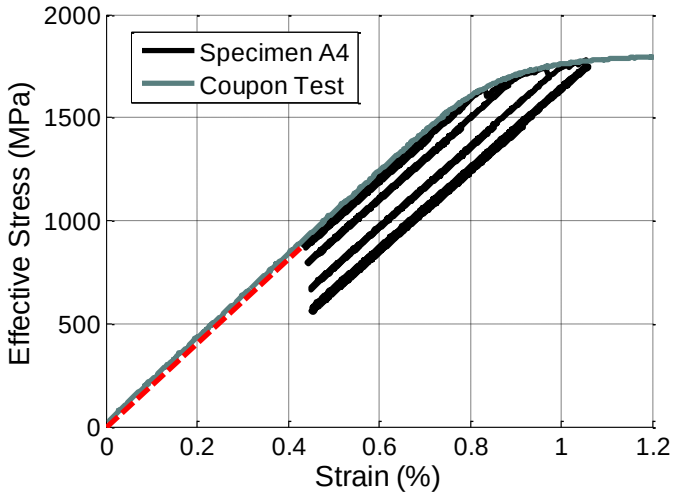

Figure 8.11 Comparison of the Post-Tensioning Behavior in Specimen A4 to the Monotonic Coupon Test

8.2.2 Post-Tensioning Seating Losses

As part of the examination of experimental behavior of Specimen A1 in Chapter 5 the phenomenon referred to as seating losses was demonstrated in the data and discussed. It was found that as the force in a post-tensioning strand exceeded its previous maximum force that the wedges at the anchorage were pulled incrementally further into the mating conical hole. The associated displacement results in a loss of post-tensioning strand force. The amount of loss is characterized in Figure 8.12 including data from Specimen A1, the trial run before Specimen A5 without fuses, and the trial run before Specimen B1/B2 without fuses. The cause of the seating losses is the change in the maximum post-tension force above its previous level. The amount of loss is quantified as the change in the post-tensioning force because of a cycle when the configuration returns to its original position. In other words, the loss is the change in the minimum post-tension force from one cycle to the next. A linear regression was performed to fit a trend line to the data. The resulting relationship is given by Equation (8.7).

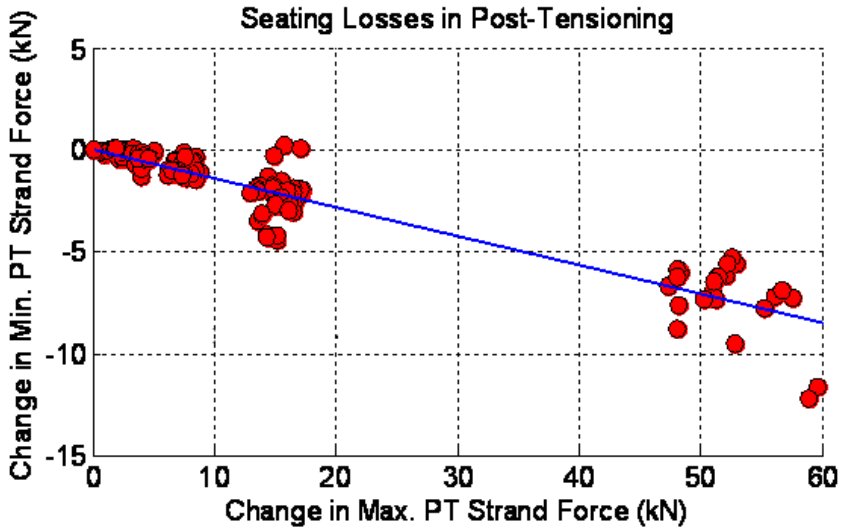

Figure 8.12 Characterization of Post-Tensioning Seating Losses

$$\Delta F_{\min} = -0.1422 \Delta F_{\max} \tag{8.7}$$

Chapter 6 describes the implementation of a constitutive model for the post-tensioning that captures the effect of seating losses. The constitutive model is shown in Figure 8.13 and includes a secondary slope with slope αE. The seating loss parameter, α, can be derived based on equal triangles to be as given in Equation (8.8). Using the slope of the seating losses trendline presented in Equation (8.7), the stiffness of the secondary seating loss slope is found to be α=0.88 times the elastic modulus.

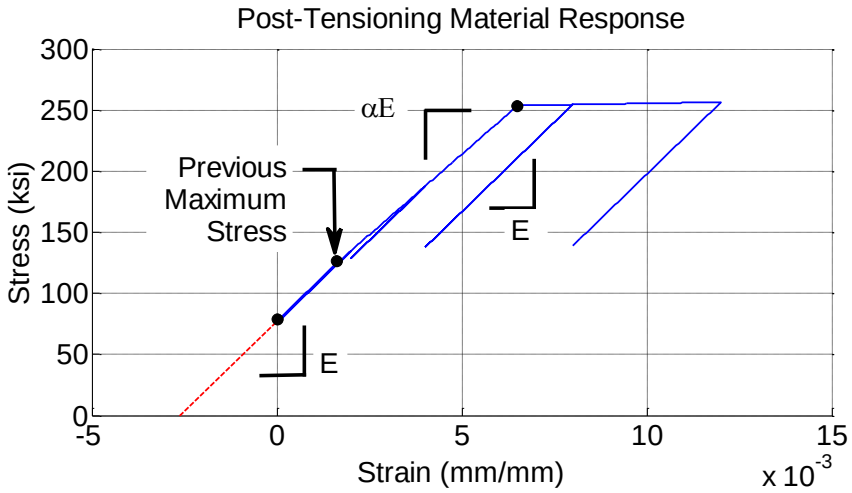

Figure 8.13 Applying Post-Tensioning Seating Losses in Material Constitutive

$$\alpha = \frac{1}{1 - \frac{\Delta F_{\min}}{\Delta F_{\max}}} = 0.88 \tag{8.8}$$

It is possible to eliminate seating losses, though. Techniques were devised as part of the E-Defense test specimen installation (Ma 2010) to mitigate seating losses. The method is described in Chapter 12.

8.2.3 Post-Tensioning Strand Wire Fracture

Four of the specimens (A4, A7, B1, and B2) were tested to displacement levels that caused the post-tensioning strand stress to exceed its yield stress. During these tests some of the individual wires in the post-tensioning strand fractured. Each post-tensioning strand consists of seven wires twisted together. In all cases of fracture, it was only one wire that fractured at a time and never did it propagate to the other wires or to the other strands. In one case (L-PT-R-4 for Specimen B2), the same strand experienced two wire fractures, but the fractures occurred during different cycles.

It the time a fracture occurred, a loud twang noise could be heard as the wire experienced elastic rebound toward the opposite anchorage. The wire unraveled from the rest of the strand for the last meter or so at the opposite anchorage. Photographs of the unraveled wire and plots of the stress-strain response of fractured strands are presented in Chapter 5.

Table 8.8 gives the stress and strain at fracture for all 13 strands that fractured in these four specimens. The lowest strain at wire fracture was 0.85% for strand L-PT-R-8 in Specimen A7. From the range of strains at wire fracture and the fact that 267 wires did not fracture during these tests it is concluded that there is considerable variability in the fracture strain. It is expected that conditions such as the type of anchorages used and installation procedures would have a considerable effect on post-tensioning strand wire fracture.

Table 8.8 Summary of Post-Tensioning Wire Fractures

Specimen	Strand ID	Stress at Wire Fracture (f/f_u)	Stress at Wire Fracture, MPa (ksi)	Strain at Wire Fracture (%)
A4	L-PT-R-8	0.871	1622 (235.3)	0.86
A4	L-PT-L-2	0.910	1695 (245.8)	0.88
A4	L-PT-R-7	0.885	1647 (238.8)	0.91
A4	L-PT-R-6	0.910	1695 (245.8)	0.93
A4	L-PT-L-1	0.928	1727 (250.4)	0.95
A4	L-PT-R-4	0.995	1852 (268.6)	1.05
A4	Other 106 Wires Exceeded 1% strain without Fracture			
A7	L-PT-R-8	0.871	1621 (235.2)	0.85
A7	L-PT-R-7	0.924	1720 (249.5)	0.98
A7	Other 110 Wires Exceeded 1% strain without Fracture			
B1	All of the 28 Wires Exceeded 1% strain without Fracture			
B2	L-PT-R-3	0.880	1637 (237.5)	0.87
B2	L-PT-R-4	0.934	1738 (252.1)	0.91
B2	L-PT-R-1	0.939	1747 (253.4)	0.94
B2	L-PT-R-2	0.944	1757 (254.9)	0.96
B2	L-PT-R-4	0.800	1490 (216.1)	1.10
B2	Other 23 Wires Exceeded 1% strain without Fracture			

A probability distribution for single wire fracture can be imagined for which the data in Table 8.8 represents the frequencies for fracture at the lower end of fracture strains. Although there is not enough data to fully define this probability distribution, some useful conclusions can be made about the probability of wire fracture. For instance, after loading to 1% post-tensioning strand strain, 11 of the 280 wires fractured. This implies that there is a 3.93% probability that any given wire will fracture when subjected to 1% strain. The cumulative distribution function for a binomial distribution can be used to calculate the probability of a certain number of wire fractures. Equation (8.9) gives the probability that the number of wire fractures will be less than or equal to a limiting number for a set of post-tensioning wires subjected to a limiting strain. The calculated probabilities are given in Table 8.8 for limiting post-tensioning strains of 0.9%, 0.95%, and 1.0%. The probabilities are calculated for different amount of wire fracture that might be allowed including 1%, 3%, 5%, 7%, and 10% of the wires.

$$\Pr\left(N_f \le X\right)_N = \sum_{i=0}^{X} \frac{N!}{i!(N-i)!} p^i \left(1-p\right)^{N-i} \tag{8.9}$$

Where: N_f = number of wire fractures

X = a limiting number of wire fractures for consideration

N = number of post-tensioning wires (7 per strand)

$\Pr\left(N_f \le X\right)_N$ = the probability that less than X wires will fracture in a set of N wires subjected to the limiting strain

p = the probability of a given wire fracturing when subjected to the given strain (given as the percent of wire fractures in Table 8.9)

Table 8.9 Probability that No More Than the Given Fraction of Wires Will Fracture If Post-Tensioning Strains Are Limited to the Given Values

Post-Tensioning Strain Limit (mm/mm)	Number of Fractured Wires Out of 280	Percent of Wires that Fractured	Fraction of Wires Allowed to Fracture				
			0.01	0.03	0.05	0.07	0.10
0.0090	4	1.43%	58%	94%	100%	100%	100%
0.0095	9	3.21%	17%	60%	90%	98%	100%
0.0100	11	3.93%	9%	44%	80%	96%	100%

For example, Specimen A4 had N=112 wires and if it is desired to limit the number of wire fractures to no more than 5% of the total wires or X=6, then it can be calculated using Equation (8.9) that there is an 80% probability of this occurring if the post-tensioning strain is limited to 1%. Using Table 8.9, a limit could be set on the post-tensioning strain to create a high likelihood of controlling the number of wire fractures. Since Specimen A4 retained its ability to resist lateral loads and its ability to eliminate drifts at zero force was impaired but not completely lost after fracturing 5% of the wires in the post-tensioning strands, it might be desirable to limit the number of acceptable wire fractures to 5% of the total number of wires. Using Table 8.9, it is shown that limiting the post-tensioning strand strain to 1% leads to an 80% probability that less than 5% of the post-tensioning wires will fracture. Allowing some post-tensioning wires to fracture during extreme events might be acceptable especially considering that in post-tensioned concrete bridge construction it is not unusual to allow 2% of the wires to fracture during installation (Corven and Moreton 2004).

The stress-strain behavior of a post-tensioning strand that experienced wire fracture is shown in Figure 8.14. The stress shown in this figure is engineering stress using the original strand area. A 25% loss of stress is experienced at the time of fracture. The slope of the stress-strain response reduces from the modulus of elasticity for this strand, 196.5 GPa (28,500 ksi), to an effective modulus of elasticity after wire fracture of 180.0 GPa (26,100 ksi) representing an 8% reduction. These reductions in force and stiffness were found to be fairly typical for the wire fractures. It was found that neither of these values equated to the reduction in area due to the removal of one of seven wires which is 14%.

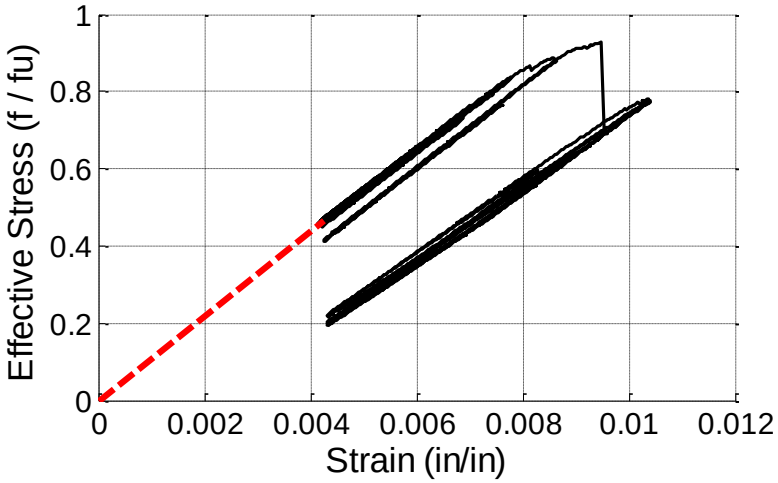

Figure 8.14 Typical Stress-Strain Behavior of a Post-Tensioning Strand that Experienced Wire Fracture

The installation of the post-tensioning strands was discussed in Chapter 4 and plots of post-tensioning force during stressing are given for Specimen A1 in Chapter 5. The strands were stressed to a preliminary force level between 3 kN and 7 kN (0.7 kips to 1.6 kips) to take up the slack in the strands. Subsequently, the strands were stressed up to the desired loads. For some strands an additional round of stressing was required as the forces in the strands was reduced as the frames underwent elastic shortening. In total, each strand was stressed between 2 and 4 times. References such as the FHWA Post-Tensioning Manual (Corven and Moreton 2004) discourages re-gripping a strand in a portion of the strand that was previously gripped by the anchorage wedges.

It is likely that re-gripping the post-tensioning strands by stressing multiple times contributed to some of the post-tensioning wire fractures experienced in the tests. An example of the performance of post-tensioning strands that were not re-gripped are the controlled rocking specimens tested dynamically at E-Defense (Ma 2010). The last test of the series of shake table tests used the Canoga Park ground motion record from the Northridge earthquake scaled by a factor of 1.75. The eight post-tensioning strands all exceeded 1.2% strain without fracturing a single wire.

8.3 Fuse Behavior

8.3.1 Fuse Hysteretic Behavior

The fuses demonstrated excellent ability to dissipate seismic energy without fracturing. As derived in Chapter 3, the amount of shear strain is amplified relative to the roof drift ratio based on a geometric ratio as given by Equation 3.14 and Equation 3.15. As a result the fuse links underwent shear strains as large as 25% across the link as the specimens were displaced to roof drifts as large as 4.2%. None of the fuses fractured during these tests.

The deformation capacity of the fuses is attributed to two things. The tapered geometry of the fuse links encourages first yield and plastic hinging at the quarter point

of the fuse link away from areas of discontinuity. This is demonstrated in Figure 8.15. The moment associated with first yield along the length of the fuse link is plotted as a quadratic curve. The yield moment is quadratic because the section modulus is a quadratic function of the fuse link depth and the fuse link depth is linearly varying along the length. Similarly, the plastic moment capacity of the fuse link along its length is plotted in Figure 8.15 and shown to be quadratic. The applied moment due to shear loading is also shown as the shear force is increased from zero to the plastic shear force, V_{fp}. It is shown that the moment demand contacts the yield moment distribution at the quarter point. This will be the location of first yield. The same location will also be the location of the plastic hinge as shown in Figure 8.15.

The large deformation capacity of the fuses is also attributed to the smooth cuts along the sides of the links. The fuse plates were cut using water jet cutting. This technology is becoming ubiquitous in machine shops and is capable of producing extremely smooth cut surfaces.

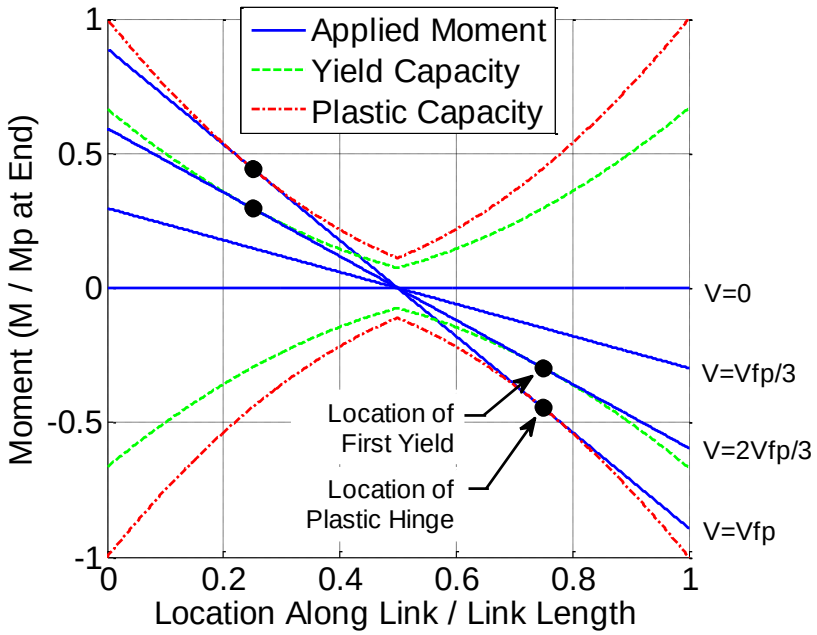

Figure 8.15 Moments Along the Length of the Link Showing Location of First Yield and Plastic Hinging

The zones of plasticity are clearly indicated in Figure 8.16 as the darker grey areas along the link lengths where the mill scale has flaked off. The plasticity is concentrated along the tapered portion of the link but is not as prevalent at the middle or end of the link where the plate develops stress concentrations.

Figure 8.16 Photograph of Specimen A4 Fuse Showing Plasticity in the Links

The progression of fuse behavior for the buckling fuses is demonstrated in Figure 8.17, Figure 8.18, Figure 8.19, Figure 8.20, and Figure 8.21 for the Specimen A1 fuse. Stage 1 of the fuse behavior is primarily flexural dominated with significant yielding along the link length similar to that experienced by the thick fuse shown in Figure 8.16. In stage 1 shown in Figure 8.17, the fuses are also resisting axial loads as the ends of the fuse move apart during large deformations. Stage 2 shown in Figure 8.18 demonstrates that upon reloading in the opposite direction the fuse develops a hump in the load-deformation response due to axial compression in addition to the flexural yielding. Figure 8.19 shows the first cycle in which lateral-torsional buckling occurs. After lateral-torsional buckling, the flexural resistance of the fuse links is reduced and instead shear forces due to axial elongation start to dominate as in Stage 4 shown in Figure 8.20. The Krypton measurements were used in Chapter 5 to show that soon after lateral-torsional buckling, second mode axial buckling takes over the deformations of the fuse link. Stage 5 shown in Figure 8.21 represents the portion of the fuse response when the fuse is undergoing axial buckling. The final fuse hysteretic response shown in Figure 8.22 includes the full response from flexural dominated, to lateral-torsional buckling, to axial buckling.

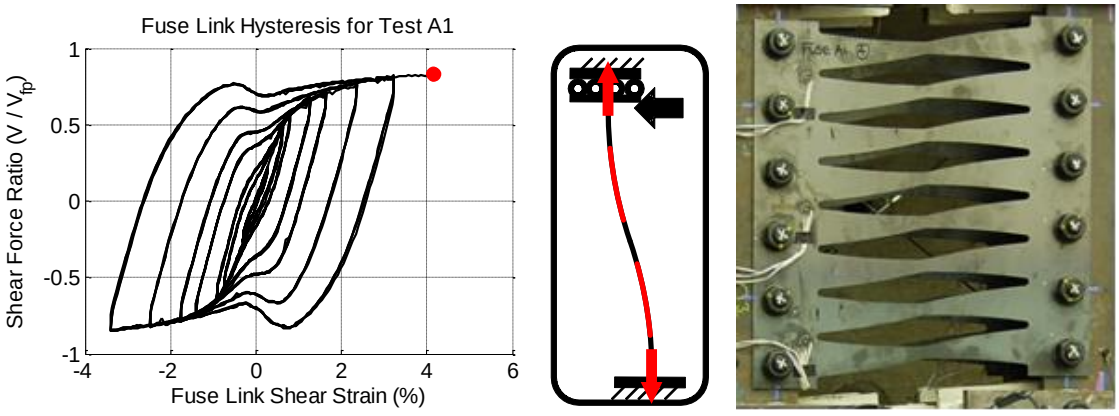

Figure 8.17 Stage 1 of Buckling Fuse Behavior – Flexural Inelasticity

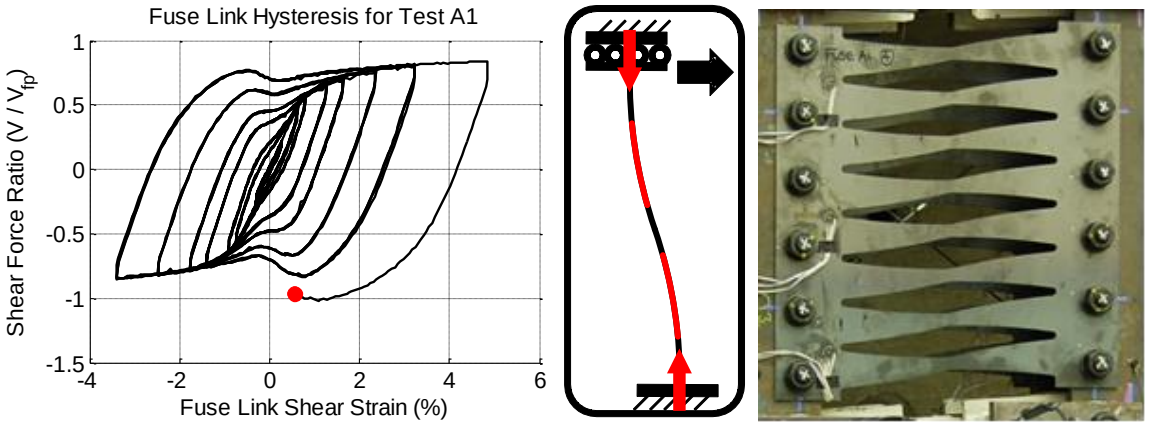

Figure 8.18 Stage 2 of Buckling Fuse Behavior – Compression on Load Reversal

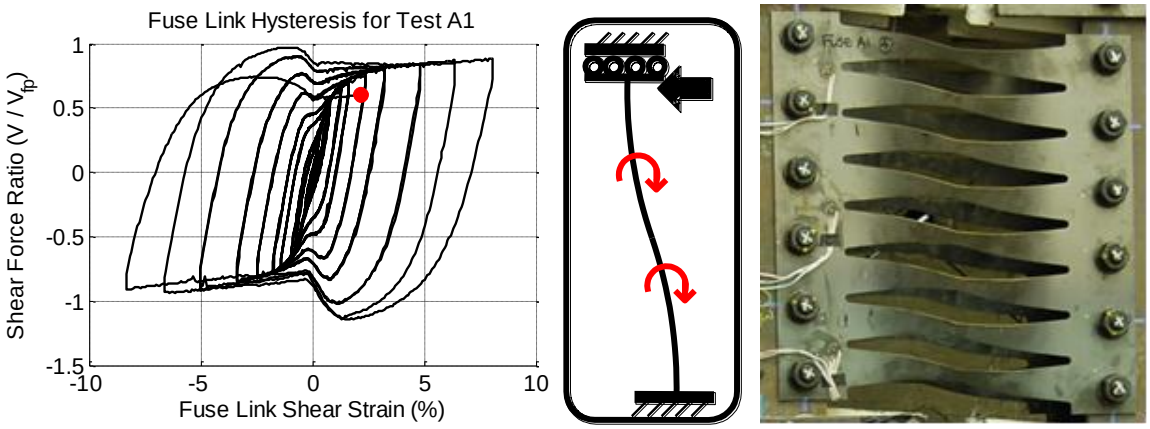

Figure 8.19 Stage 3 of Buckling Fuse Behavior – Lateral-Torsional Buckling

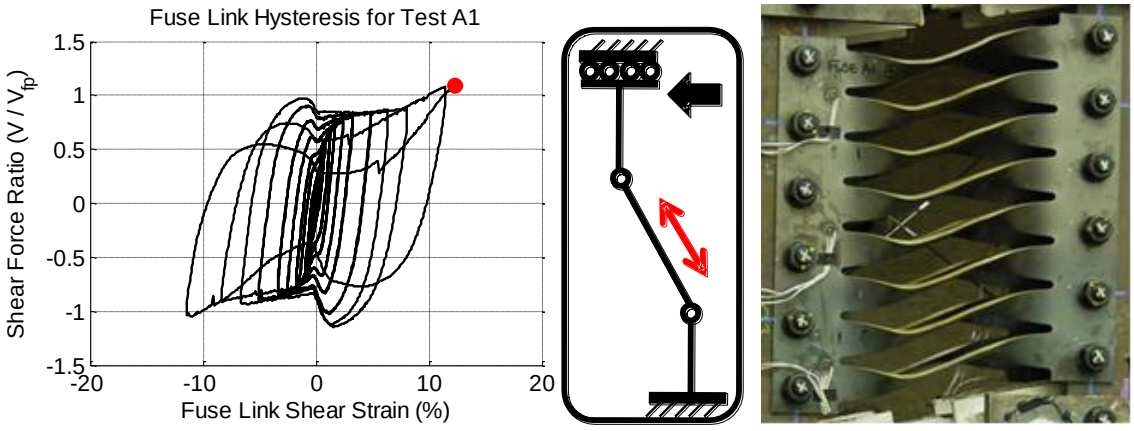

Figure 8.20 Stage 4 of Buckling Fuse Behavior – Axial Elongation

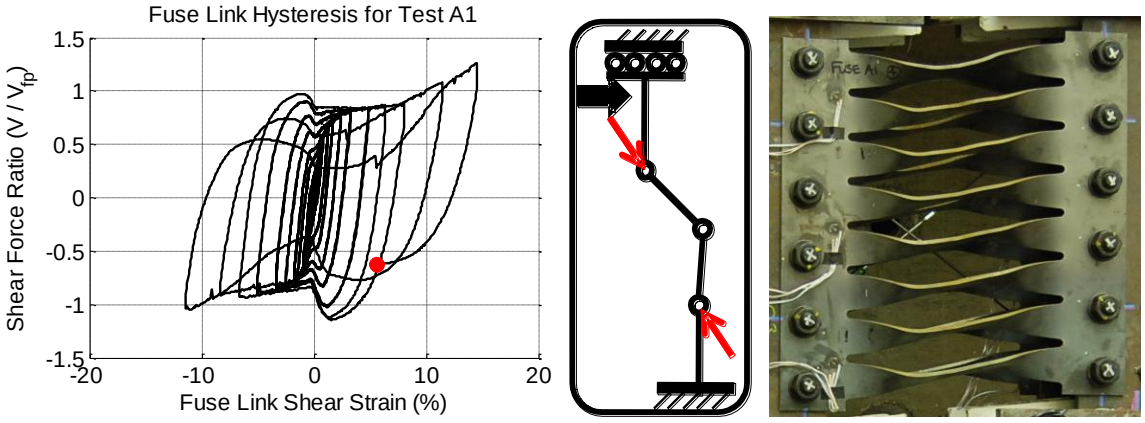

Figure 8.21 Stage 5 of Buckling Fuse Behavior – Compression Buckling

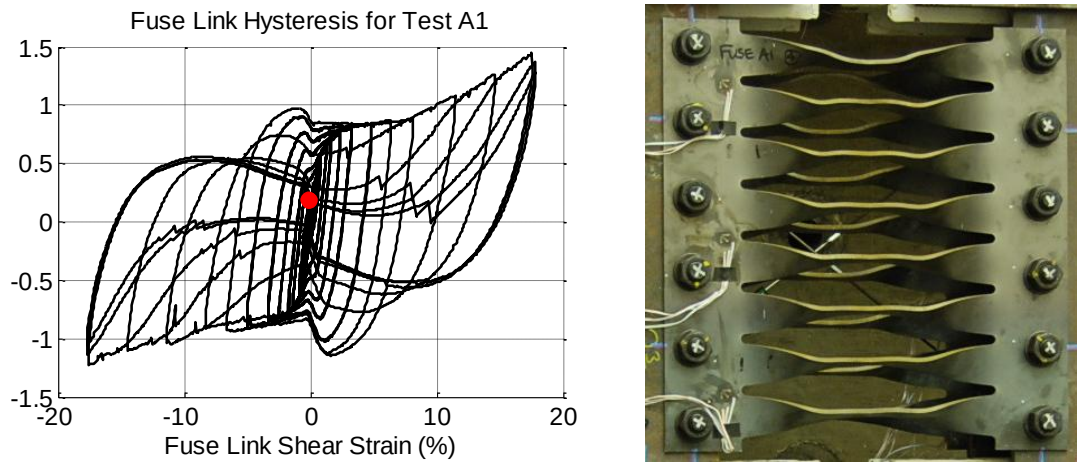

Figure 8.22 Fuse Hysteresis at End of Test (Left) and Photograph of Fuse After Testing (Right)

To compare computational and analytical predictions for the strength of the fuse to the experimental response, the shear yield strength of the fuses must be defined. Since the fuse response exhibits a gradual yielding as it transitions from elastic to a secondary post-yield stiffness, it is necessary to develop a consistent method for defining the shear yield strength of each fuse. A method similar to the 0.2% offset strain method for calculating yield stress in metals was adopted in which the shear yield strength, V_y, is defined by offsetting the initial stiffness by 1.5% fuse link shear strain, and finding the intersection with the experimental response. The value of 1.5% was obtained by plotting the intersection of lines fit to the initial stiffness and post-yielding secondary stiffness and determining the offset that produced similar force on average for the set of fuses tested. The calculation of the experimentally obtained fuse yield force is shown in Figure 8.23 for Specimen A1.

The buckling strength, V_b, is defined as the largest shear force experienced by the fuse prior to lateral-torsional buckling. Figure 8.23 shows the buckling strength and associated fuse link shear strain for Specimen A1.

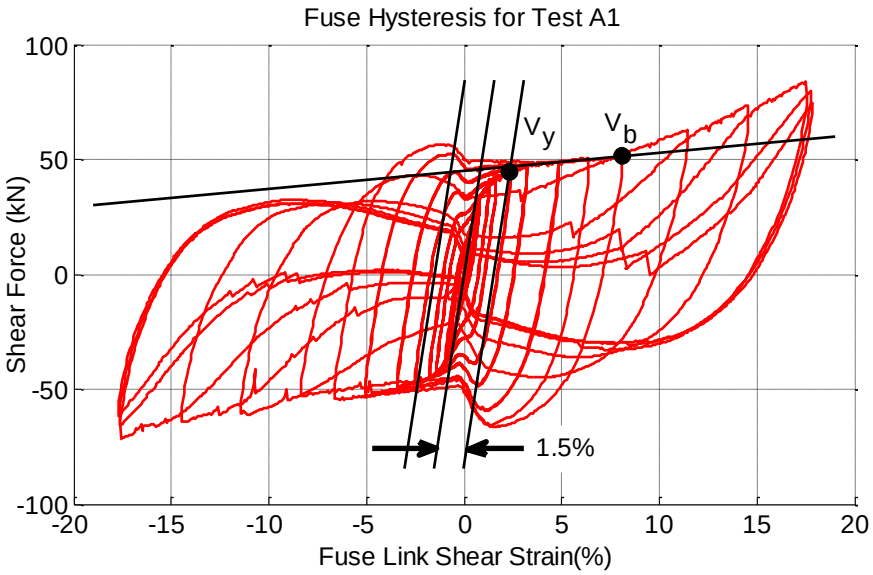

Figure 8.23 Calculation of the Fuse Yield Strength and Fuse Buckling Strength

The geometry of the fuses from all of the specimens along with four of the specimens tested as part of the testing program conducted at Stanford University (Deierlein et al. 2010) are included in Table 8.10. The experimentally obtained and predicted values for stiffnesses are given in Table 8.11, and the yield strength and buckling strengths are given in Table 8.12. The equation for stiffness is derived in Ma (2010) and given in Equation (8.10) based on a ratio of the depth at the middle to the depth at the ends of 1/3.

$$k = \frac{1}{1+2.40(b/L)^2} 0.47 N_{links} E\, t \left(\frac{b}{L}\right)^3 \tag{8.10}$$

It is shown in Table 8.11 that the equation for predicting fuse shear stiffness is most accurate for thicker non-buckling fuses. The stiffness is over-predicted for buckling fuses and found to significantly over-predict the stiffness of the fuses with short link lengths such as Specimen B1 and Specimen B2 fuses.

Table 8.10 Fuse Geometry for All Tests Including Four Tests From Stanford Testing Series (Deierlein et al. 2010)

Speci-men	Link Length, *L*, mm (in)	Depth at End, *b*, mm (in)	Depth at Middle, *a*, mm (in)	Thick-ness *t*, mm (in)	Number of Links	Slender-ness *L/t*	Ratio *b/t*
A1	355.6 (14)	58.7 (2.31)	19.6 (0.77)	6.4 (0.25)	8	56	9.25
A2	355.6 (14)	58.7 (2.31)	19.6 (0.77)	15.9 (0.625)	10	22.4	3.7
A3	355.6 (14)	58.7 (2.31)	19.6 (0.77)	15.9 (0.625)	7	22.4	3.7
A4	355.6 (14)	58.7 (2.31)	19.6 (0.77)	25.4 (1.0)	7	14	2.3125
A5	355.6 (14)	58.7 (2.31)	19.6 (0.77)	15.9 (0.625)	8	22.4	3.7
A6	355.6 (14)	58.7 (2.31)	19.6 (0.77)	6.4 (0.25)	8	56	9.25
A7	355.6 (14)	58.7 (2.31)	19.6 (0.77)	6.4 (0.25)	8	56	9.25
B1	152.4 (6)	42.9 (1.69)	14.3 (0.56)	19.1 (0.75)	3	8	2.25
B2	152.4 (6)	47.6 (1.87)	15.9 (0.63)	4.8 (0.188)	5	32	10
SS5	228.6 (9)	63.5 (2.5)	25.4 (1)	6.4 (0.25)	6	36	10
SS9	355.6 (14)	57.2 (2.25)	19.1 (0.75)	9.5 (0.375)	7	37	6
SS10	355.6 (14)	57.2 (2.25)	19.1 (0.75)	6.4 (0.25)	7	56	9
SS11	355.6 (14)	57.2 (2.25)	19.1 (0.75)	25.4 (1.0)	3	14	2.3

Table 8.11 Fuse Stiffnesses for All Tests Including Four Tests From Stanford Testing Series (Deierlein et al. 2010)

Specimen	Initial Stiffness, kN/mm (k/in)	Predicted Stiffness, kN/mm (k/in)	Secondary Stiffness kN/mm (k/in)	Secondary Stiffness Ratio
A1	15.3 (87.5)	13.5 (103.2)	0.22 (1.26)	0.0144
A2	47.4 (270.9)	11.0 (312.7)	1.63 (9.30)	0.0343
A3	36.6 (209.1)	11.0 (218.9)	0.93 (5.32)	0.0254
A4	64.6 (368.8)	22.6 (451.8)	1.86 (10.62)	0.0288
A5	35.7 (203.7)	11.0 (250.2)	1.24 (7.07)	0.0347
A6	9.0 (51.6)	13.5 (103.2)	0.42 (2.38)	0.0460
A7	8.2 (46.9)	13.5 (103.2)	0.07 (0.40)	0.0085
B1	49.0 (280.1)	211.9 (1210.1)	1.70 (9.69)	0.0346
B2	54.0 (308.6)	200.9 (1147.4)	1.29 (7.35)	0.0238
SS5	19.0 (108.3)	64.7 (369.7)	0.62 (3.56)	0.0328
SS9	12.7 (72.4)	24.5 9 (139.9)	0.20 (1.12)	0.0154
SS10	16.2 (92.6)	16.3 (93.2)	0.80 (4.56)	0.0492
SS11	19.1 (109.1)	28.0 (159.8)	1.01 (5.79)	0.0531

On average, the measured fuse yield strength was approximately 89% of the calculated fuse strength based on plastic hinging at the quarter point. This may be due in part to the axial forces that are present in the fuse but neglected in the calculation of the fuse shear strength.

Table 8.12 Fuse Response Parameters for All Tests Including Four Tests From Stanford Testing Series (Deierlein et al. 2010)

Speci-men	Measured Yield Force kN (kips)	Predicted Shear Capacity kN (kips)	Yield Strain (%)	Buckling Shear Force, kN (kips)	Link Strain at Buckling (%)
A1	44.8 (10.1)	58.1 (13.1)	2.32	54.7 (12.3)	8.07
A2	177.3 (39.9)	212.4 (47.7)	2.55	N/A	N/A
A3	126.2 (28.4)	148.7 (33.4)	2.47	N/A	N/A
A4	223.7 (50.3)	227.3 (51.1)	2.47	N/A	N/A
A5	153.2 (34.4)	169.9 (38.2)	2.71	N/A	N/A
A6	46.0 (10.4)	58.1 (13.1)	2.93	49.9 (11.2)	6.10
A7	48.0 (10.8)	58.1 (13.1)	3.15	51.7 (11.6)	10.40
B1	131.7 (29.6)	181.6 (40.8)	2.25	N/A	N/A
B2	80.6 (18.1)	80.4 (18.1)	2.34	112.7 (25.3)	15.10
SS5	106.2 (23.9)	98.8 (22.2)	3.08	121.6 (27.3)	8.73
SS9	53.4 (12.0)	90.1 (20.3)	2.68	60.1 (13.5)	9.90
SS10	82.1 (18.5)	60.1 (13.5)	2.92	129.5 (29.1)	18.52
SS11	90.3 (20.3)	102.9 (23.1)	2.83	N/A	N/A

8.3.2 Characterizing Fuse Buckling

The lateral-torsional buckling capacity of the fuse links was investigated. Two methods for approximating the lateral-torsional buckling strength are presented and a third method is discussed. The second method which correlates the lateral-torsional buckling shear force to the slenderness of the fuse link was implemented in the computational model.

The elastic lateral-torsional buckling strength of a tapered section was calculated using equations derived by Challamel et al. (2007). For the case when the depth at the middle of the fuse link is 1/3 of the depth at the ends, the critical shear force, V_{cr}, is given by Equation (8.11), where I_{yo} is the minor axis moment of inertia at the end of the link, and J_o is the torsional constant for the end of the link. The critical moment associated with this critical shear force is given by Equation (8.12).

$$V_{cr} = 3.112 \frac{\sqrt{EI_{yo}GJ_o}}{L^2} \tag{8.11}$$

$$M_{cr} = \frac{V_{cr}L}{2} \tag{8.12}$$

$$M_r = \left(F_y - F_r\right) S_{xqp} \quad \text{(Calculated at the Quarter Point)} \tag{8.13}$$

$$L_r = \frac{3.112}{2M_r}\sqrt{EI_{yo}GJ_o} \tag{8.14}$$

$$L_p = \frac{300r_y}{\sqrt{F_y}} \tag{8.15}$$

$$M_p = \frac{b^2 t F_y}{9} \quad \text{(Calculated at the Quarter Point)} \tag{8.16}$$

The first yield moment strength, M_r, is given in Equation (8.13). The residual stresses in the plate, F_r, are assumed to be 0.3 times the yield stress. Studies such as Leon-Salamanca (2005) and Bahadur et al. (2007) suggest that residual stresses in 19 mm (¾") thick and 63.5mm (2-1/2") thick hot rolled steel plates are as large as 100 Mpa. Assuming a yield stress of 345 MPa (50 ksi), the maximum residual stresses might be approximately 0.3 times the yield stress. By setting the elastic lateral-torsional moment strength, M_{cr}, equal to the first yield moment strength, M_r, the link length, L_r, that marks the transition from elastic to inelastic lateral-torsional buckling can be found. The length that allows the fuse link to become plastic, L_p, is found using equation(8.15), (Salmon and Johnson 2008). The inelastic lateral-torsional buckling regime is assumed to be a linear fit between these two points as shown in Figure 8.24.

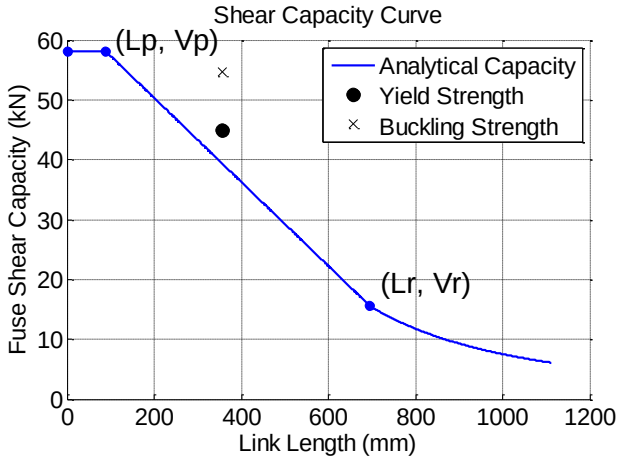

Figure 8.24 Sample Fuse Shear Capacity Curve for Specimen A1 with the Measured Yield Force

The shear yield force and the measured shear buckling strength for Specimen A1 are plotted compared to the analytical solution for the fuse shear capacity in Figure 8.24. The link length of Specimen A1 is shown to be well within the range associated with inelastic lateral-torsional buckling. The fuse links, however, buckled at a load well above the capacity curve. In fact, the fuse in Specimen A1 underwent significant plastic hinging before buckling occurred.

All of the tested fuses including the Stanford component tests are shown in Figure 8.25 for the inelastic LTB range. The axes are made to be dimensionless so different configurations can be compared. The range of tested fuse link lengths extends from near

the plastic range well into the inelastic lateral-torsional buckling regime. It is shown in Figure 8.25 that the capacity curve as derived above, while largely conservative, does not predict the shear load at which the fuse will buckle. One of the reasons for the discrepancy stems from the applied loads on the fuses. Axial forces and additional moments are present in the fuses during the test and are not considered in the equations derived above.

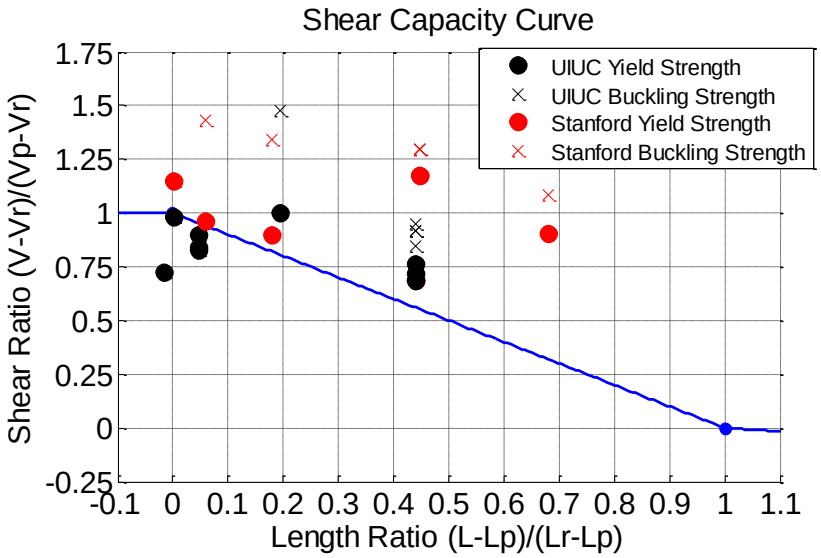

Figure 8.25 Fuse Shear Capacity for All Tests in the Inelastic Lateral-torsional Buckling Range

Figure 8.26 shows a second method for predicting the fuse buckling force. A linear regression was conducted on the available buckling strength data and the resulting relationship is given in Equation (8.17). This method has the advantage that the buckling strengths used in this calibration have the types of axial forces and moments experienced in the fuses applied to the controlled rocking system. This can also be considered a drawback of this method if it is desired to predict the buckling capacity of a fuse with different boundary conditions.

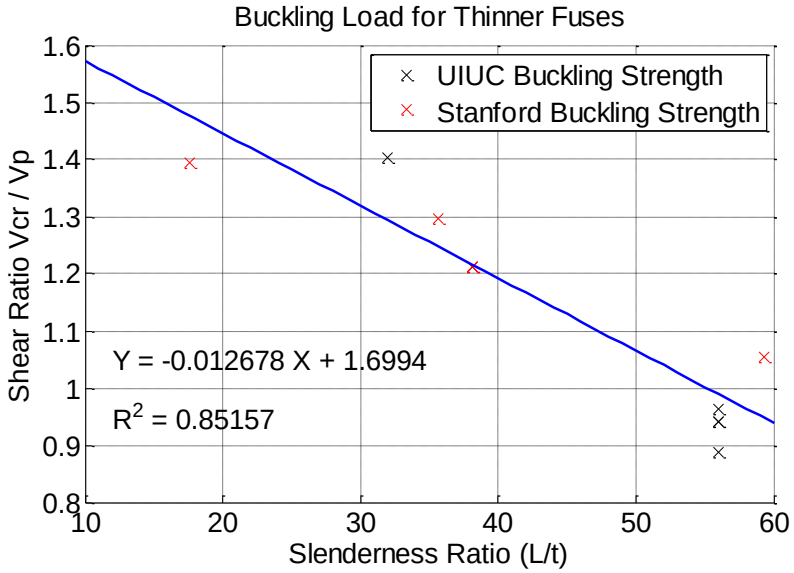

Figure 8.26 Characterizing Fuse Buckling Force Based on a Slenderness Parameter

$$\frac{V_{cr}}{V_p} = -0.0127\frac{L}{t} + 1.6994 \tag{8.17}$$

As mentioned in the beginning of this section, the relationship given in Equation (8.17) was used in the computational model to predict fuse buckling. The calculation of the critical moment to use in the lateral-torsional buckling rotational spring is given in Equation (8.18).

$$\begin{aligned} M_{cr} &= \frac{1}{2}\frac{L}{3}\left(V_{cr} \bullet 2 \text{ fuses}\right) \\ M_{cr} &= \frac{1}{3}LV_p\left(-0.0127\frac{L}{t} + 1.6994\right) \end{aligned} \tag{8.18}$$

A third method for predicting buckling of the fuses was not conducted but is discussed here as future research needs. Since the buckling strength of the fuses was found to be only marginally greater than the yield strength, it is believed that the mechanism for buckling may be more related to deformations than force. A multivariate regression analysis could be used to characterize fuse buckling as a function of variables such as shear strain, cumulative shear strain, and measures of energy. This type of relationship is expected to be more accurate in predicting buckling, but would also create complexities for implementation in computational models.

8.3.3 Kinematics of Fuse Deformation and Axial Forces

The kinematics of the fuse deformation were found to be an important factor in the forces that were developed in the fuses. The relative motion of the two sides of the fuse

included shear deformations, axial deformations, and in some cases slip relative to the columns.

Slip of the fuses relative to the columns was observed in a small degree in Specimen A2 and in a much more significant way in Specimen A4. The slip capacity of the connection was compared to the applied forces in the discussion of Specimen A4 in Chapter 5. It was determined that to provide adequate resistance to slip, it is necessary to consider the fuse to column bolts as an eccentrically loaded bolt group. A reasonable assumption is that the fuse shear force acts at an eccentricity equal to the distance to the fuse link quarter point.

The axial and shear deformations of the fuse were investigated by plotting the kinematics of the motion of one of the interior columns relative to the other as provided by the Krypton measurements. Figure 8.27 shows the relative motion of the interior columns for a specimen with a representative thick fuse (Specimen A4), and a specimen with a representative thin fuse (Specimen A1). As shown in this figure, the motion of the thick fuse specimen occurs along a path with a diameter of 628 mm (24.7") which corresponds to the distance between column center lines. The interior columns of the specimen with a thin fuse are shown to move relative to one another with a diameter of 178 mm (7.0") which corresponds to the distance between the quarter points of the fuse links.

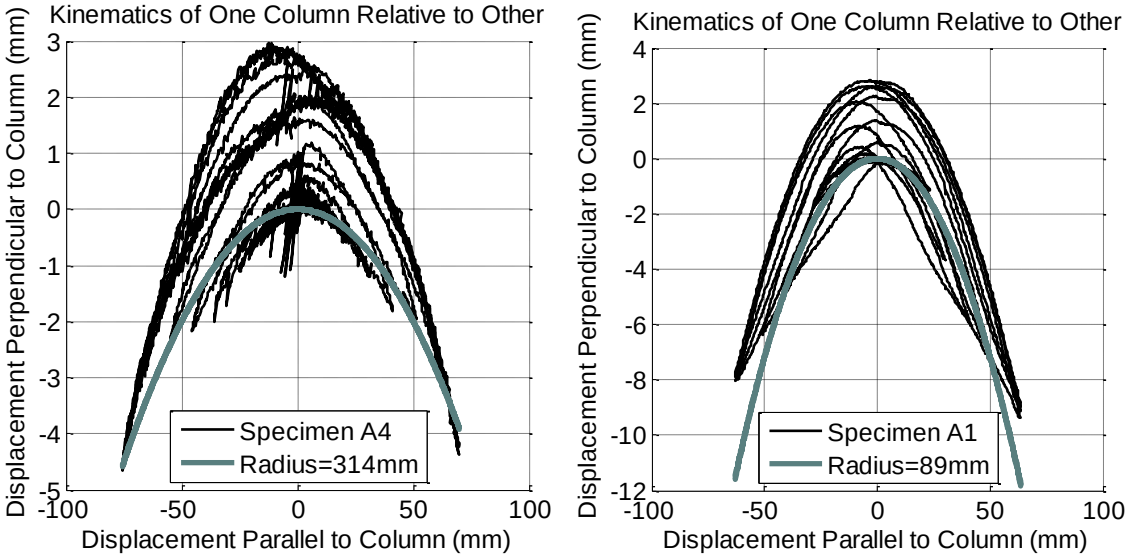

Figure 8.27 Relative Motion of Interior Columns for a Representative Specimen with a Thick Fuse (Left) and a Thin Fuse (Right)

The axial forces in the fuse are shown for all specimens in Figure 8.28 plotted against the moment. An axial force-moment interaction surface was created for the fuse link element based on the plastic strength of the critical sections and assuming reversed moments due to shear loading. The vertical and horizontal axes of this plot are the axial force and moment at the ends of the link as normalized to the plastic axial capacity and plastic moment capacity at the end of the fuse link respectively. The area of the middle of the link represents a limiting factor in the tension capacity of the fuse link. As such,

the axial force is capped at one third of the plastic capacity at the end of the link because that is the ratio of the areas. The moment capacity is controlled by the plastic capacity of the fuse link quarter point. The maximum moment at the end of the link is 8/9 times the plastic capacity at the end of the link due to the plastic hinging at the quarter point. The relationship between axial force and moment was derived by assuming an arbitrary plastic neutral axis at the quarter point. The interaction surface for a fuse link element with a ratio of middle depth to end depth of 1/3 is given in Equation (8.19) and shown in Figure 8.28.

$$\frac{T}{T_p} = \sqrt{\frac{4}{9} - \frac{1}{2}\frac{M}{M_p}} \qquad for \left|\frac{M}{M_p}\right| > \frac{2}{3}$$
$$\frac{T}{T_p} = \frac{1}{3} \qquad for \left|\frac{M}{M_p}\right| \le \frac{2}{3} \tag{8.19}$$

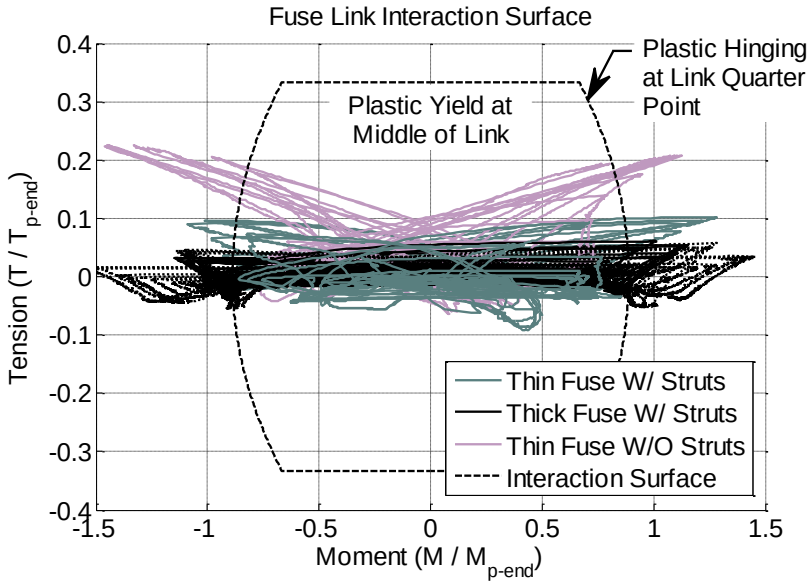

Figure 8.28 Axial Force and Moment Interaction for the Fuse Links

Figure 8.28 shows that the fuses, although exceeding the interaction surface in the moment domain because of strain hardening, did not reach their maximum axial forces based on the plastic capacity at the middle of the fuse. Furthermore, it is shown in Figure 8.28 that the axial forces divided by the plastic axial capacity at the end of the fuse links range between -0.1 to 0.1 for thin fuses with struts, -0.05 to 0.05 for thick fuses with struts and -0.1 to 0.2 for the thin fuse specimen without struts.

For the design of the frames in the dual frame controlled rocking system, it is necessary to consider the axial forces that develop in the fuses. If nonlinear time history analyses are not performed a method for predicting fuse forces is necessary. A capacity design method is presented in Chapter 11 that uses the maximum possible post-tensioning forces and fuse forces for frame design. However, designing for the maximum axial force the fuses can develop in conjunction with the maximum moment is overly

conservative as demonstrated above. Instead, the range of axial forces listed above, provide a basis for axial forces that might be experienced in a dual frame configuration. See Chapter 11 for more information about how this can be incorporated into a capacity design methodology.

8.4 Effect of Struts

The elimination of the struts was included in the testing program because it is considered a possible option for implementation in practice. It might be desired to eliminate the struts to simplify the erection and installation of the frames. Specimen A7 was a configuration that used thin fuses and no struts. However, the two frames still had constraints on their motion in the form of the top connection to the loading beam and the bumpers at the base.

To investigate the effect that the struts had on the system, data was examined regarding the motion of the columns relative to one another, the forces experienced by the struts, and the forces in the members. A further discussion of the member forces is included in Chapter 11.

The distance between the two interior columns is shown for both Specimen A1 and Specimen A7 in Figure 8.29. In the testing of Specimen A1, the distance between frames is found to increase at zero roof drift ratio after the fuses have elongated. Specimen A7, on the other hand, shows only negative displacements that are larger than those experienced by Specimen A1. The larger displacements were found to translate into larger frame forces and specifically interior column moments at the locations of the fuses. The amount of fuse tension force shown previously in Figure 8.28 also demonstrates the additional tension forces experienced in the fuses when the struts were not present to hold the columns apart.

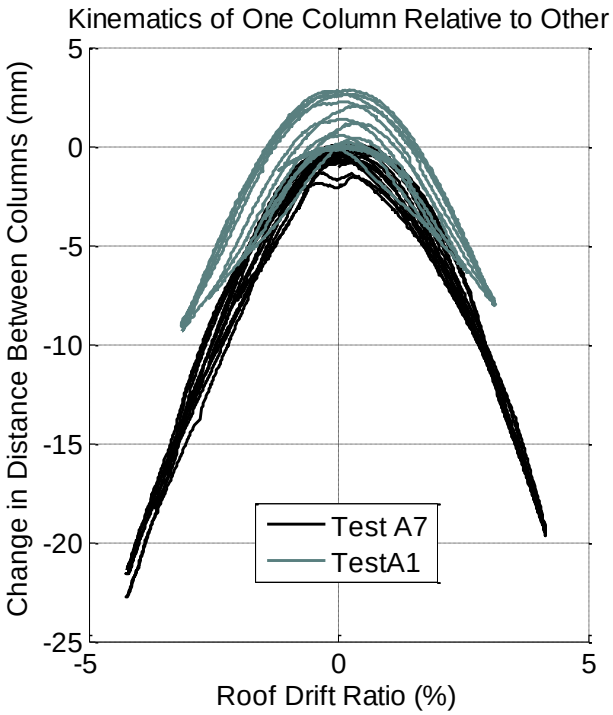

Figure 8.29 Distance Between Columns For a Specimen With struts (Specimen A1) and a Specimen Without Struts (Specimen A7)

The strut forces for a representative specimen with thin fuses (Specimen A1) and a representative specimen with thick fuses (Specimen A3), are shown in Figure 8.30. The axial forces in the struts are found to be larger for the specimens with thin fuses but still a small proportion of the fuse axial capacity. In fact, the struts were designed based on a computational model that did not consider pin hole tolerances in the strut connections. As a result, the amount of constraint between the frames was over-predicted relative to the actual specimen. The differences in the forces experienced by the thin fuse configuration and the thick fuse configuration are largely due to the pin hole tolerances. Large axial deformations are required to occur in the fuse before the struts become engaged. Thus, the struts in the thick fuse specimens hardly become engaged as shown in Figure 8.30 because the distance between interior columns is held more constant by the thick fuses.

It is concluded, therefore, that the struts were not necessary for use with thicker non-buckling fuses. This conclusion, however, is based on tests in which the frames still possessed significant relative restraint of the two frames at the top and bottom of the test setup. For specimens with thinner buckling fuses, the struts became engaged in compression and were effective in resisting the axial tension developed in the fuses. The frames of Specimen A7, although they did not use struts, were constrained relative to one another by a loading beam at the top and bumpers at the base. In this context, it was noted that the system performance was not significantly affected by the elimination of the struts. If there were no constraints between the two frames, it is expected that the frames

would tilt toward each other even more than what was experienced in the tests, and that the portion of the fuse shear response due to axial forces would be diminished.

In practice, however, it will be necessary to transfer collector forces through or around the controlled rocking frames and it will be necessary to transfer diaphragm shear to the controlled rocking system. If struts are not included, alternate means for collector load transfer and diaphragm shear transfer will be necessary which may introduce constraint between the two frames.

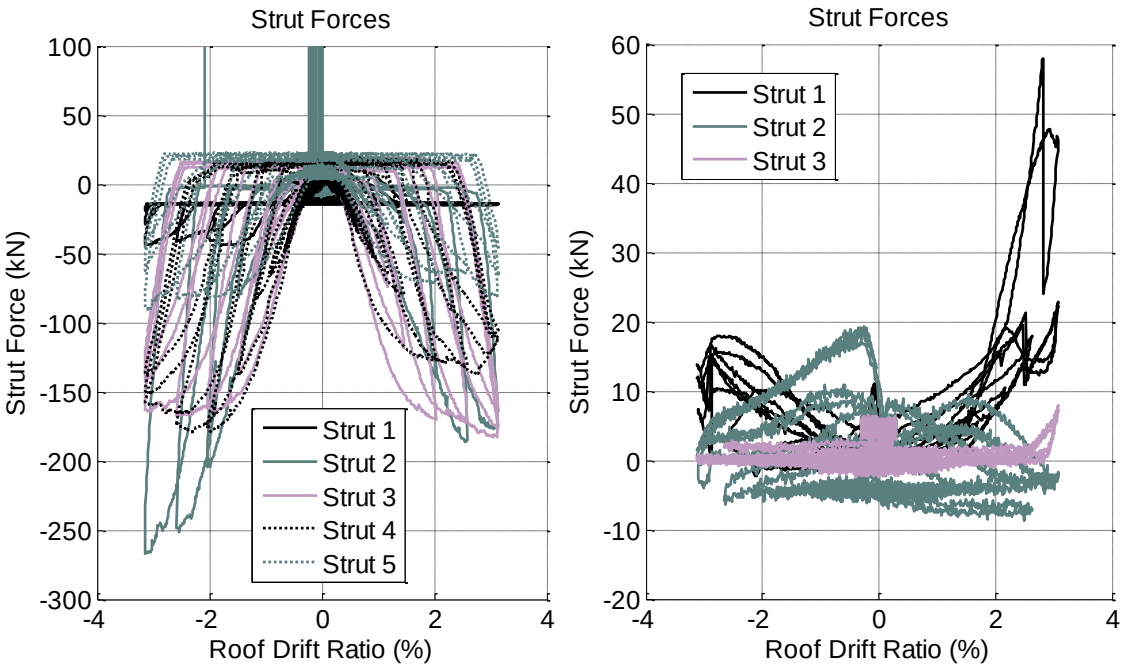

Figure 8.30 Strut Axial Forces for a Representative Specimen with Thin Fuses (Left) and a Representative Specimen with Thick Fuses.

8.5 Single Frame and Dual Frame Configuration

The single frame configuration and the dual frame configuration offer several advantages relative to each other for different applications. A comparison of the single frame and dual frame configurations is discussed in this section in the context of experimental behavior. A list of advantages of both systems is included in Chapter 12 including architectural, engineering, and construction considerations.

The two most significant aspects of the single frame configuration behavior not common to the dual frame configuration are the improved ability to eliminate drifts at zero force and the effect of pin connections between the frame and the fuses. There are residual drifts that remain in a dual frame configuration when the loads are removed due to the built-up forces in the fuses which cause elastic deformations in the frames. The single frame configuration is immune to this effect because the fuses are concentrated at the bottom of the frame instead of distributed along the height of the frames. The two single frame specimens exhibited near zero drift at zero force even after significant

yielding and fracture of the post-tensioning strands as demonstrated in Figure 8.3. This is also shown in the load-deformation behavior of the single frame configuration specimens included in Figure 5.40 and Figure 5.45.

The effects of the pin hole tolerance in the connection of the fuse to the frame through a center strut were found to cause delayed fuse yield and lack of energy absorbing capability early in the displacement history. The reduction in energy absorbing capacity is shown in Figure 8.5. The lag in engaging the fuse during fuse load reversal is shown in Figure 5.42 and Figure 5.47.

The testing program was successful in identifying pin hole tolerance as an important issue and the corresponding shake table tests performed at E-Defense utilized a modified detail that mitigated the effect (Ma 2010). The pin hole connection was eliminated at the top of the center strut and the pin hole tolerances were used in the connection of the center strut to the fuse. The associated details are discussed further in Chapter 12.

Chapter 9

SDOF INVESTIGATION OF SELF-CENTERING RESPONSE WITH AMBIENT BUILDING RESISTANCE

The development of the controlled rocking system has as one of its primary performance goals to virtually eliminate residual drifts after large earthquakes. The ability of the system to eliminate drifts when the load is removed has been quantified in Chapter 8, but as described in the Chapter 2, several studies have investigated the ability of systems to reduce residual drifts without eliminating static drifts when the forces are removed.

As discussed in Chapter 7, the elements of the building not included in the seismic force resisting system can resist the restoring forces after becoming inelastic. In effect, the restoring force has to pull the remainder of the building back to center in order to successfully achieve self-centering. On the other hand, there is a probabilistic mechanism that can lead to significant reductions in residual drifts compared to the maximum residual drifts which are the drifts obtained by removing the loads from the peak drift. In fact, it will be shown in this chapter that reliable control of residual drifts can be achieved even for lateral force resisting systems that do not return to zero displacement when the lateral loads are removed.

A parametric study is presented in this chapter, including approximately 25,000 SDOF nonlinear time history analyses representing four prototype buildings, to investigate the effect of several parameters on response indices such as residual drifts including the effects of ambient building resistance. The hysteretic response was built from components typical to all current self-centering systems, so system response is more accurately represented than can be achieved using an idealized flag shape. This study explores the full range of self-centering from none (elastic-plastic) to zero energy dissipation (bilinear elastic).

9.1 Characterizing the Self-Centering Hysteretic Response

The self-centering hysteretic behavior is established in the context of the controlled rocking system which can be decoupled into the two main components discussed in Chapter 3: the post-tensioned frame and the fuses. The general form of these two main system components which are a precompressed element that creates a restoring force and an energy-dissipating component, are universal to almost all of the self-centering systems found in the literature.

Figure 9.1a shows the bilinear elastic response of the restoring force element that deforms elastically with a stiffness, K_{rf}, until the gap opening force, F_{rf}, is attained, after which the reduced stiffness, αK_{rf}, of the system is attributed to effects such as the increase in post-tension force as the post-tensioning strands elongate. Figure 9.1b shows the idealized energy-dissipation component as a bilinear elastic-plastic hardening hysteretic response with initial stiffness, K_{ed}, up to a yield force of F_{ed}, after which there is a post-yield stiffness of αK_{ed}. For simplicity, the energy-dissipating element is assumed to exhibit kinematic hardening with the same hardening ratio as the ratio of the two elastic

stiffnesses for the restoring force element. Although this was found to approximately represent the experimental response of large-scale controlled rocking frames, this may not represent all self-centering systems.

The combined response, shown in Figure 9.1c, is the result of the two components acting in parallel. The combined hysteretic response is characterized by three stiffnesses, K_o, K_y, and K_2, a system yield force, F_y, and a self-centering coefficient, β, which describes the height of the flag shape relative to the yield force. The strength of the system and the self-centering coefficient are related to the component variables as given in Equation (9.1) through Equation (9.5). The correlation between the self-centering coefficient, β, and the self-centering ratio, SC, as defined and used in other chapters, is given in Equation (9.6).

$$K_o = K_{sc} + K_{ed} \tag{9.1}$$

$$K_2 = \alpha K_{sc} + K_{ed} \tag{9.2}$$

$$K_y = \alpha K_{sc} + \alpha K_{ed} \tag{9.3}$$

$$F_y = F_{rf} + F_{ed} \tag{9.4}$$

$$\beta = \frac{2F_{ed}}{F_y} \tag{9.5}$$

$$SC = \frac{F_{rf}}{F_{ed}} = \frac{2-\beta}{\beta} \tag{9.6}$$

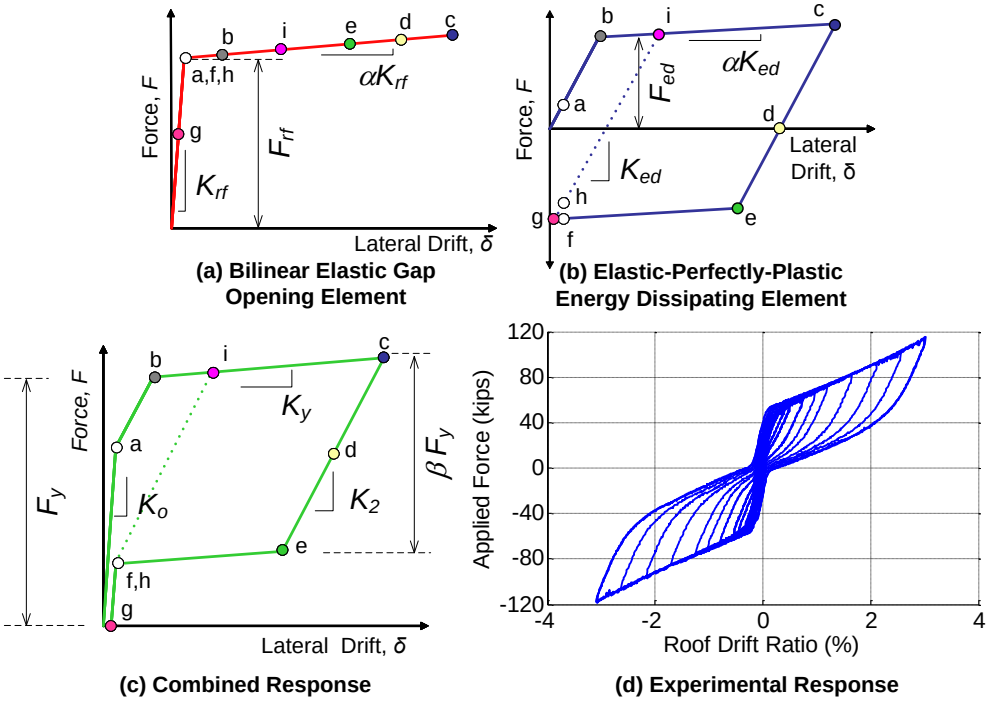

Figure 9.1 Response of a Typical Self-Centering System: (a) Gap Opening Element, (b) Energy-Dissipating Element; (c) Combined Gap Opening Element and Energy-Dissipating Element; (d) Compared to Experimental Response.

Although there are many examples of using the two components in parallel in the development of self-centering systems (e.g. Palermo 2007, fib 2003), the parametric studies found in the literature more commonly use an idealized flag-shape (e.g. Christopoulos et al. 2002, Christopoulos et al. 2003, Pampanin et al. 2003, Seo and Sause 2005). There are several advantages of using the flag-shaped hysteretic behavior built from components rather than using an idealized flag-shape. The combined response more accurately represents the changes in stiffness including the reduction in stiffness experienced in the second cycle due to the energy-dissipating element already being at yield force as represented in Figure 9.1b and Figure 9.1c by dotted lines. These changes in stiffness are demonstrated in the experimental system response shown in Figure 9.1d. Furthermore, the range of self-centering characterized by the coefficient β, can be varied between 0 and 2 to represent the entire range between bilinear elastic response (no energy dissipation component) to bilinear elastic-plastic (no self-centering component) as shown in Figure 9.2.

However, it is important to note that for some types of self-centering systems including this one, the configuration and method of implementing energy dissipation and restoring force may dictate the practical range of the self-centering coefficient, β. Limitations can occur if the action of the self-centering system depends on the restoring force element being stronger than the energy dissipating element. For instance, the particular configuration shown for the controlled rocking system in Figure 9.1 requires that initial post-tensioning force in each frame be larger than the yield capacity of the fuse elements to prevent a deformation mode in which the entire back frame uplifts. However, alternate configurations of this system that separate the two components can allow the full range of β.

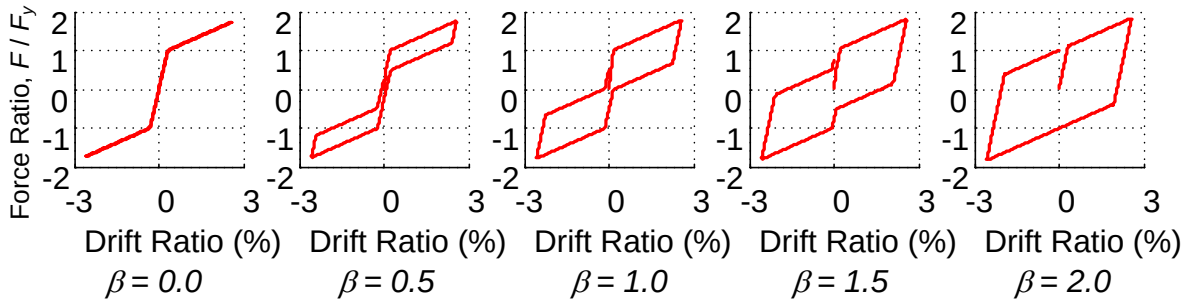

Figure 9.2 Shapes of Hysteretic Response for Different Values of β

9.2 Ambient Building Resistance

Ambient building resistance is used here to mean the lateral load-deformation response of portions of a building that are not typically included in the structural model. Although considered in damping, they are widely neglected in structural modeling because the added stiffness and strength are considered beneficial to seismic response and their effect is highly variable depending on the types of material, detailing, and construction. By the inclusion of these elements in the study described herein, it is not suggested that ambient

building resistance should be included explicitly in the design process. Instead, these elements are considered here to investigate the positive and negative effects that ambient building resistance has on residual drifts, as well as other response indices, to illuminate the proportioning of self-centering seismic force resisting systems that can reliably eliminate residual drifts. Although it may not be advisable to rely on the highly variable elements of ambient building resistance in cases where they reduce residual drifts, the negative impacts of these elements on residual drifts should be considered.

A non-inclusive list of building elements that contribute to ambient building resistance includes interior partitions, simple shear beam-to-column connections, stair stringers, hysteretic behavior of horizontal diaphragms including floor coverings and ceilings, mechanical systems, and exterior cladding such as precast concrete panels, stucco, brick, glass curtain walls or other material.

Masonry infill walls and stair stringers that are rigidly tied into the structure can significantly alter the seismic response of a building. To achieve expected seismic response, these elements can be detailed not to transfer lateral loads and therefore are not incorporated in this investigation. It is expected that the interior partitions and simple shear beam-to-column connections will dominate the ambient building response and are thus included in this study. Although future work will explicitly include exterior cladding, for simplicity, it is assumed that exterior cladding has a similar load-deformation response as the interior partitions. Since this study was developed in the context of steel-framed buildings, the beam-to-column connections considered are typical of steel framing and commercial partition construction is assumed, consisting of gypsum board over metal stud infill framing.

9.2.1 Interior Partitions

A review of experimental research reveals many factors that influence the shear resistance of interior partitions including wall geometry, gypsum wall panel thickness and orientation, construction quality and finishing, fastener spacing, uplift anchorage, and stud framing. However, four general types of partition construction were identified, and are listed in Table 9.1, which separate levels of shear wall action in the gypsum panels.

Table 9.1 General Categories of Interior Gypsum Board on Metal Stud Construction

	Gypsum Board Category Description
1	No connection between the gypsum board panels or the metal studs to the bottom track (Blume 1966, Blume 1968, Freeman 1971, Rihal 1980); the shear transfer is due solely to friction
2	The studs are attached to the track with either rivets or screws, but the gypsum board panels are not attached to top or bottom track (Blume 1966, Blume 1968, Freeman 1971); some amount of shear wall action is realized
3	The studs and gypsum board panels are attached to the top and bottom tracks (Adham 1988, Gad et al. 1999, Serrette and Ogunfunmi 1996, Serrette et al. 1997, Tarpy 1980, Tarpy 1984); the gypsum board has fasteners along the perimeter of each panel resulting in full shear wall response
4	Combination of gypsum board and diagonal steel straps (e.g., Adham 1988)

Although interior partitions found in practice demonstrate many variations, the objective here is to calibrate an SDOF oscillator to represent the resistance of typical interior partitions. Type 3 interior partitions were considered representative of typical construction and were used in this study. Test specimen 1 from Adham (1988) and Stage 2 EW Racking Test from Gad et al. (1999) were used for calibration. Both experimental specimens were approximately 2.4m x 2.4m (8'x 8') panels with two gypsum board faces attached with screws around the perimeter.

A calibration of the pinching4 material in OpenSees (Mazzoni et al. 2006) , which can reproduce a pinched hysteretic response with four points along the backbone curve, cyclic stiffness degradation, and strength degradation, was conducted by defining an average backbone curve with reloading rules to simulate the experimental strength and stiffness degradation. Strength and stiffness degradation due to screw hole elongation, resulting slip in the connections, and cracking of the gypsum wall panels are an important feature of interior partition response. The calibrated response is shown with the experimental response from Gad (1999) and Adham (1988) in Figure 9.3.

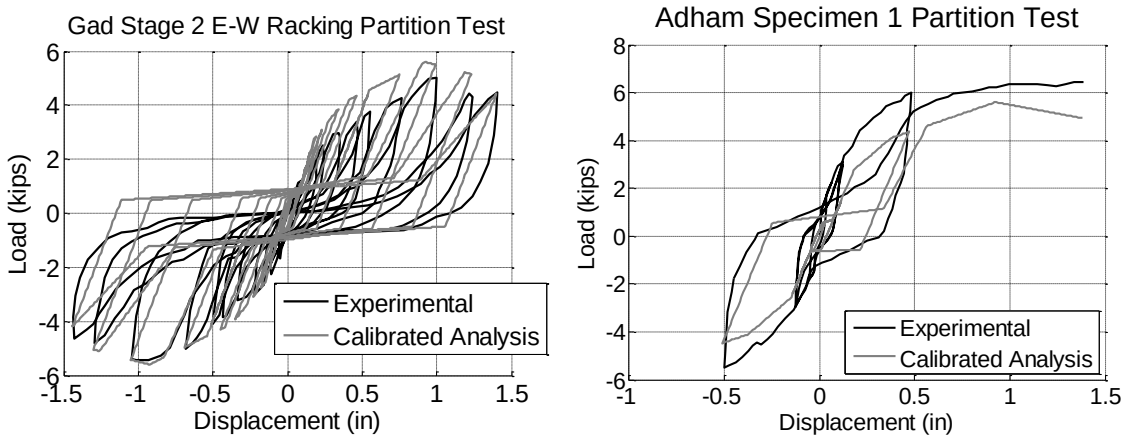

(a) (b)

Figure 9.3 (a) Calibrated Partition Response Shown with Experimental Response from Gad (1999); (b) Calibrated Partition Response Shown with Experimental Response from Adham (1988)

9.2.2 Simple Shear Beam-to-Column Connections

The type of building being examined in this study is intended to represent a typical steel-framed structure with concrete on metal deck floor system. Relatively limited data is available on the cyclic response of simple shear beam-to-column connections with concrete slabs. One of the most extensive testing programs on these types of connections was conducted by Liu and Astaneh (2000). The experimental curve from Liu and Astaneh (2000) shown in Figure 9.4 is the moment at the centerline of the column due to the connections on both sides. Thus the response is relatively symmetric and was assumed to be so in the calibration, since the connection on one side is in positive bending while the connection on the other side is in negative bending.

Test specimens 6A (lightweight concrete) and 6B (normal weight concrete) were used to calibrate a computational model representing W24x55 beams connected to a W14x90 column each using six 22 mm (7/8") diameter A325 bolts through 9.5 mm (3/8") thick shear tabs. Figure 9.4 shows the representative response of the rotational spring using the pinching4 material as defined in OpenSees compared to Specimen 6B of Liu and Astaneh (2000). The calibrated peak moment is within 5% of the peak moments from Specimen 6A and 6B. The experimental response is distinguished by a significant loss of moment capacity when the slab cracks and crushes, leading to complete loss of slab participation by 0.04 radians rotation. At larger rotations, the beam flange begins to bear on the column flange resulting in the increase in moment capacity shown in Figure 9.3(b) after 0.08 radians. As shown in Figure 9.4, the loss of slab participation is captured in the calibrated model, but flange bearing was neglected because the computational study did not produce such large rotations.

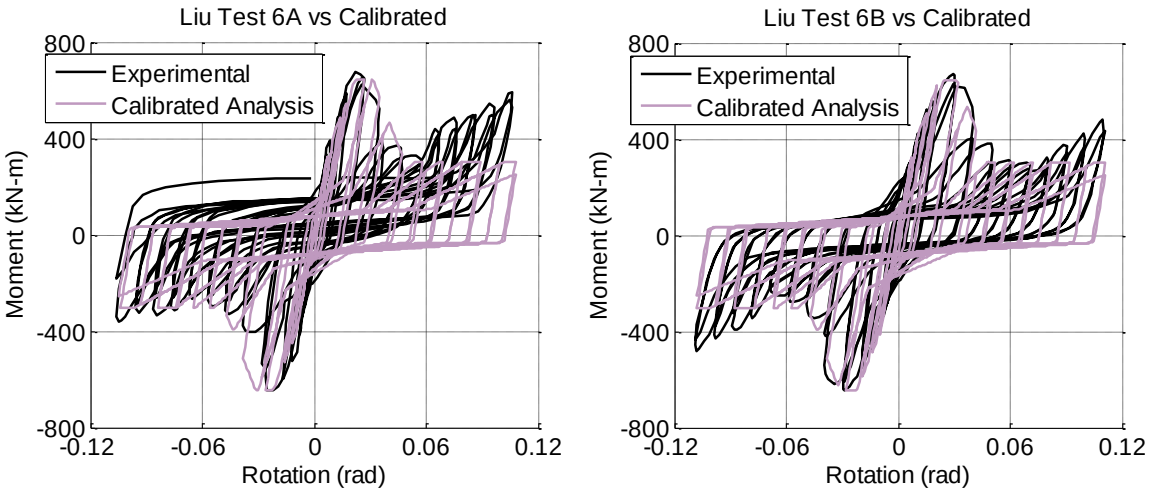

Figure 9.4 Calibrated Beam-to-Column Connection Response Shown with Experimental Response from Liu and Astaneh (2000)

The calibrated moment-rotation relationship was converted to a force-deformation response by assuming that the beams and columns are rigid relative to the rotational springs as shown in Figure 9.5. The resulting relationships are given in Equation (9.7) and Equation (9.8).

$$\delta = H \tan^{-1} \theta \tag{9.7}$$

$$F = \frac{M}{H} \tag{9.8}$$

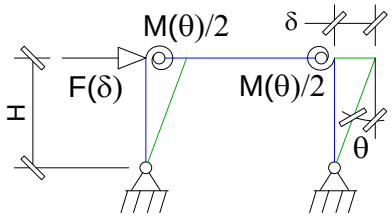

Figure 9.5 Conversion of Rotational Spring Moment-Rotation Relationship to Force-Deformation

9.3 Description of Analyses

This section describes how the calibrated computational elements representing ambient building resistance were amplified to represent the load-deformation response of complete prototype buildings and then simplified into an SDOF system. Time history analyses are then detailed; these were conducted using 17 ground motions and a range of parameters to examine their effect on system response.

9.3.1 Prototype buildings

In order to develop context for using the calibrated elements of ambient building resistance, four prototype buildings were chosen. The prototype buildings are shown in Figure 9.6 and include 3-story, 6-story, 9-story, and 12-story buildings. The buildings all have 3.96m (13') story heights, use the same floor plan, and have a seismic force resisting system along two portions of the perimeter in each coordinate direction, which leads to the tributary floor area and tributary floor mass shown in Figure 9.6 for a typical seismic force resisting system along the 36.6m (120') side.

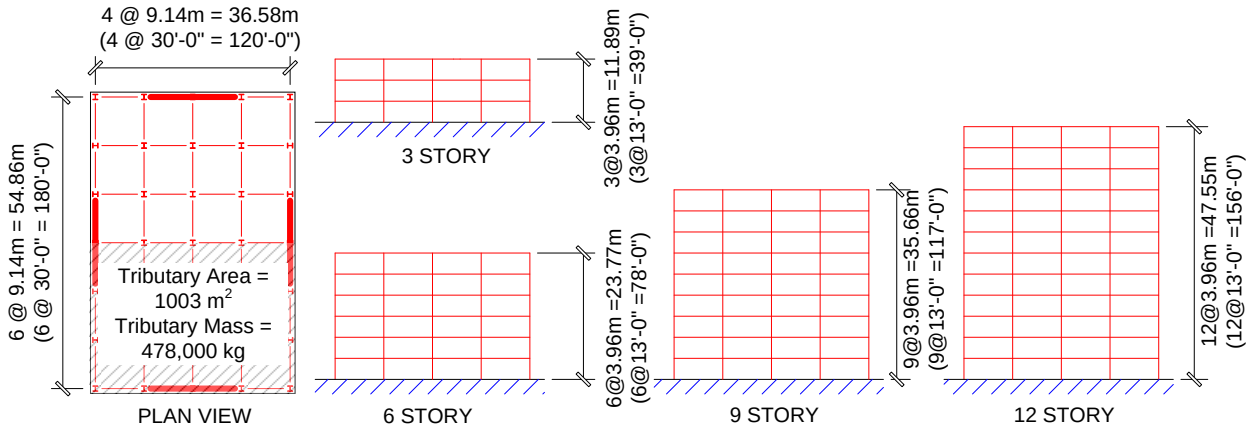

Figure 9.6 Plan and Elevation of Buildings Used in the Parametric Study

The seismic force-resisting system is proportioned using an equivalent lateral force type procedure (ASCE 7-05 2005). The yield force of the equivalent SDOF system, F_y, is set equal to the design spectral acceleration, S_a, multiplied by the seismic dead load, divided by the response modification factor, R, as given in Table 9.5. As described in a subsequent section, the design spectral acceleration is based on a location in Los Angeles, CA with site class D. The response modification factor, R, is varied between 10, 8, 6, and 4 in the parametric study and the ratio of restoring force to energy dissipation, β, is varied between 0 and 2.0. Only the restoring force component and the energy dissipating component are considered in the design resistance of the system.

The ratio of the energy dissipating components stiffness to the total stiffness of the lateral force resisting system, K_{ratio}, was varied between 0.25 to 0.9 as given in Table 9.5 and shown in Figure 9.1. The post-yield stiffness ratio, α, was varied between 0 and 0.05 as given in Table 9.5 and shown in Figure 9.1. P-Δ effects were not explicitly considered in this study. If desired, however, the post-yield stiffness ratio, α, can be reduced to approximate the destabilizing effect of P-Δ moments. The stiffness reduction can be approximated, for example, by multiplying the effective SDOF mass given in Table 9.2 by the acceleration of gravity and dividing by the effective height of the SDOF system. The reduction in the post-yield stiffness ratio calculated in this way was found to be between 0.002 and 0.008 for the range of prototype buildings from 3-story to 12-story.

The resistance of partitions and simple shear beam-column connections was extrapolated to represent the cumulative resistance for an entire floor in the prototype

building. The partition wall backbone curve was first adjusted to account for the difference between the prototype building floor height and test specimen height by multiplying the backbone curve displacements by the ratio of heights, 3.96m / 2.4m (13'/8'). This might represent a wall in which the gypsum board does not extend above the ceiling level, but there is still adequate shear transfer between the wall and the diaphragm above. To account for longer and multiple partition walls, the forces in the backbone curve were then amplified as given in Equation (9.9) to account for the parameter ρ_{wall}, which is the density of interior partition walls in units of length per floor area.

The calibrated response of the simple shear beam-to-column connection was converted to a lateral force vs. displacement relationship by assuming that the beams and columns are rigid relative to the connection. To account for multiple bays of connections, the forces in the backbone curve were then amplified as given in Equation (9.10) by the parameter N_{bc} which is the number of tributary bays of simple shear beam-to-column connections. This is demonstrated in Figure 9.7.

$$F_{ia-p} = \frac{\rho_{wall} A}{2.44} F_{i-p} \tag{9.9}$$

$$F_{ia-bc} = N_{bc} F_{i-bc} \tag{9.10}$$

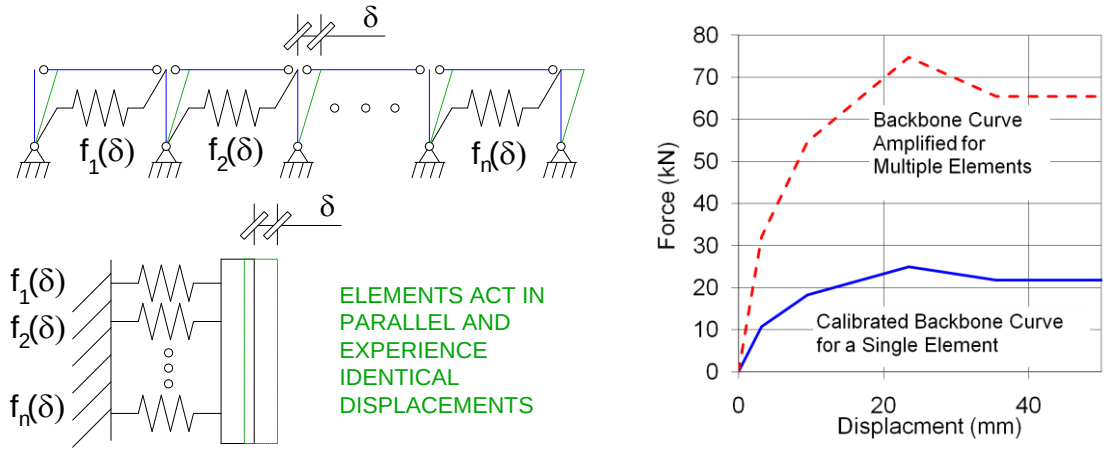

Figure 9.7 Amplifying the Response of One Element to Represent the Entire Floor

Equation (9.9) and Equation (9.10) use the terms F_{i-p} and F_{i-bc}, which are the i^{th} ordinate of force along the backbone for partion walls and beam-column connections, respectively. F_{ia-p} and F_{ia-bc} are the adjusted values to represent an entire floor and A is the tributary floor area given in Figure 9.6.

The resulting load-deformation responses for a single floor were then extrapolated to represent the entire multistory prototype buildings. To determine the appropriate scale factor, a base shear, V, was applied to a multistory simplified model in proportion to the first mode shape. Assuming that all stories have the same stiffness, K_{floor}, the resulting roof displacement was calculated as a coefficient, d_{top}, multiplied by the base shear, V, divided by K_{floor} as given in Equation (9.11). The values for d_{top} are summarized in Table 9.2.

$$\delta_{roof} = d_{top} \frac{V}{K_{floor}} \tag{9.11}$$

If it is assumed that each floor experiences approximately the same interstory displacement history such that the secant stiffness, K_{floor}, is the same for all floors and that all floors experience approximately the same force, V, Equation (9.11) can be converted into a relationship between the roof displacement and floor displacement as given in Equation (9.12). Figure 9.8 demonstrates this type of condition. Using Equation (9.12), the displacement coordinates on the backbone curves were amplified by the factor d_{top} to account for multiple stories.

$$\delta_{roof} \cong d_{top} \delta_{floor} \tag{9.12}$$

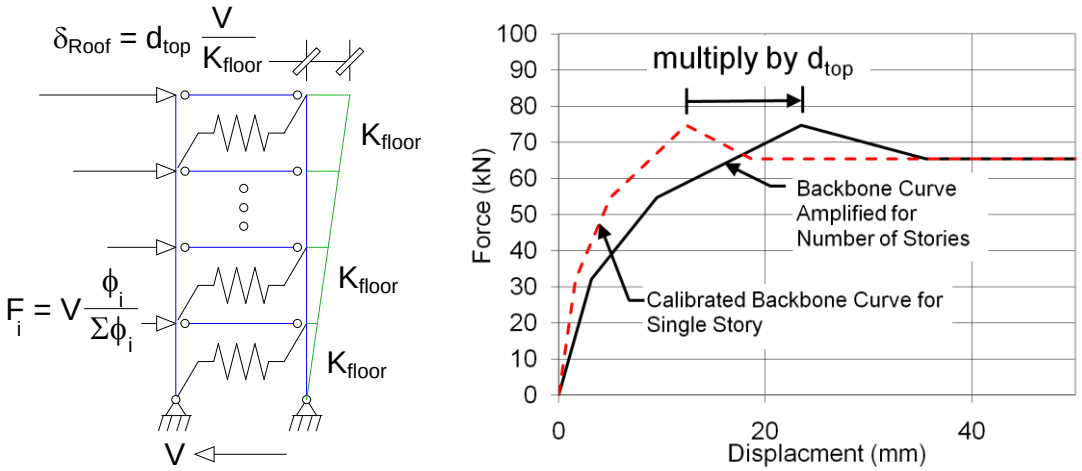

Figure 9.8 Amplifying the Response of One Floor to Represent Multiple Floors

9.3.2 Simplifying the System to SDOF

After extrapolating the response of individual partition wall and beam-to-column elements to represent the resistance of an entire building, the load-deformation response and related tributary mass of the prototype building were then converted into an equivalent SDOF system. It is noted, however, that there are inherent limitations in using an SDOF model to represent the nonlinear response of an MDOF system. The method used herein assumes that the distribution of deformations along the height of the structure is uniform. Although the rocking structures previously described are designed to have elastic frames and thus resist significant concentration of inelastic deformations or soft story mechanisms, this is not the case for all self-centering systems. Also, the derivation below is based on the first mode response. In structures that experience inelasticity that is not uniform along the height of the building, the first mode shape changes thus changing the effective height of the SDOF system. Varying the SDOF effective height is not included in this SDOF representation.

The MDOF system was simplified into an SDOF model by isolating the first mode response as is used in the capacity spectrum method (e.g., Fajfar 1999). The equation of motion of an MDOF system is given in Equation (9.13). The decoupled

equation of motion for the first mode is given in Equation (9.14) using the modal participation factor given in Equation (9.15) where q_1 is the 1st mode response, Γ_1 is the modal participation factor, and ϕ_1 is the 1st mode shape normalized to 1.0 at the roof.

$$\underset{\sim}{M}\ddot{\underset{\sim}{u}} + \underset{\sim}{C}\dot{\underset{\sim}{u}} + \underset{\sim}{K}\underset{\sim}{u} = -\underset{\sim}{M}\ \underset{\sim}{I}\ \ddot{u}_g \tag{9.13}$$

$$\ddot{q}_1 + 2\xi_1\omega_1\dot{q}_1 + \omega_1^2 q_1 = -\Gamma_1\ddot{u}_g \tag{9.14}$$

$$\Gamma_1 = \frac{\underset{\sim}{\phi_1}^T \underset{\sim}{M}\underset{\sim}{I}}{\underset{\sim}{\phi_1}^T \underset{\sim}{M}\underset{\sim}{\phi_1}} = \frac{\sum_j m_j\phi_{1j}}{\sum_j m_j\phi_{1j}^2} \tag{9.15}$$

The equivalent single degree of freedom (SDOF) system consists of an equivalent mass, m_{sdof}, given in Equation (9.16) and a set of equivalent load-deformation responses. The roof drift vs. base shear response is scaled to represent the first mode response using Equation (9.17) and Equation (9.17), and the response indices are inversely scaled after the analysis was completed. The resulting modal participation factors and SDOF masses are tabulated in Table 9.2.

$$m_{sdof} = \Gamma_1\sum_j m_j\phi_{1j} = \frac{\left(\sum_j m_j\phi_{1j}\right)^2}{\sum_j m_j\phi_{1j}^2} \tag{9.16}$$

$$\delta_{roof} = \Gamma_1\delta_{SDOF} \tag{9.17}$$

$$V_{base} = \Gamma_1 F_{SDOF} \tag{9.18}$$

Table 9.2 Summary of Masses, Periods, and Initial Stiffnesses

Number of Stories, n	d_{top}	Γ_1	M_{SDOF} kg (kip-sec2/in)	Assumed Initial Period, T_o	K_o kN/mm (k/in)
3	2.25	1.22	$1.08\text{x}10^6$ (6.14)	0.3 sec	648 (3700)
6	4.15	1.26	$1.98\text{x}10^6$ (11.33)	0.6	324 (1850)
9	6.05	1.27	$2.89\text{x}10^6$ (16.52)	0.9	216 (1233)
12	7.96	1.27	$3.81\text{x}10^6$ (21.73)	1.2	162 (925)

9.3.3 SDOF System and Analyses

The initial stiffness of the flag-shaped system, K_o, as shown in Figure 9.1c, was calculated so that the elastic natural period would be equal to *0.1n*, where n is the number of stories. The elastic period and initial stiffness are given in Table 9.2. The rest of the self-centering hysteretic response was parameterized using variables described in Figure 9.1 and Table 9.5.

Typical damping values used in time history analyses include consideration for nonstructural elements such as interior partitions and simple shear beam-to-column connections. Because those elements are modeled explicitly here, a reduced amount of damping is appropriate. Damping was implemented using Rayleigh damping to impose 1% damping at the fundamental period and at 3 times the fundamental period.

The resulting SDOF system used in the computational analyses has three nonlinear hysteretic springs that represent the simple shear beam-to-column connections, F_{bc}, the partition walls, F_p, and the self-centering system, F_{sc} which is the sum of the restoring force component, F_{rf}, and energy-dissipating, F_{ed} component. This configuration is shown schematically in Figure 9.9. The equation of motion given in Equations (9.19) and Equation (9.20) was solved using OpenSees with the Newmark-beta constant acceleration time integration method.

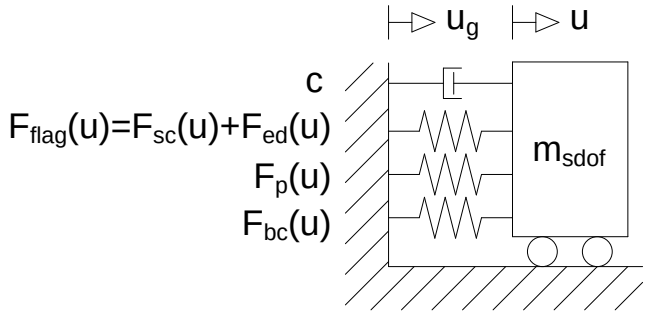

Figure 9.9 SDOF Computational Model Used in the Parametric Study

$$m\ddot{u} + c\dot{u} + F(u) = -m\ddot{u}_g \tag{9.19}$$

$$F(u) = F_{sc}(u) + F_p(u) + F_{bc}(u) \tag{9.20}$$

9.3.4 Ground Motions

Time history analyses were performed using ground motions that were taken from the large magnitude, short range (LMSR-N) group defined in Medina (2002). Scale factors were computed to match the spectral acceleration at one second for a design spectrum that was based on a site in Los Angeles, California with site class D. One second design spectral accelerations were 0.90g and 0.60g for the hazard level that has 2% probability of exceedance in 50 years and the 10% in 50 years event, respectively. Ground motions that required a scale factor greater than 4.0 for the 2% in 50 years event were discarded, leaving 17 ground motions. The resulting group of ground motions includes records with source distance between 13 km and 37 km and soil shear wave velocities between 192 m/s and 425 m/s. The design spectrum parameters are given in Table 9.3, and the list of

ground motions is included in Table 9.4. Response spectra for the set of ground motions are shown in Figure 9.10 as scaled for the hazard level with 2% probability of exceedance in 50 years.

Table 9.3 Parameters for Each of the Hazard Levels Considered

Parameter	2% / 50 Yrs	10% / 50 Yrs
Short Period Spectral Acceleration, S_S	1.5g	1.0g
One Second Period Spectral Acceleration, S_1	0.90g	0.60g

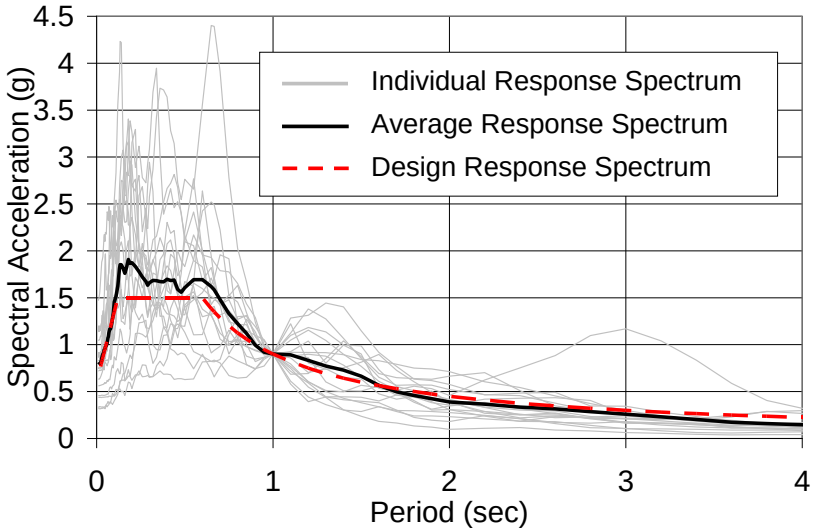

Figure 9.10 Ground Motion Spectra for the Hazard Level that Has 2% Probability of Exeedance in 50 Years

Table 9.4 Ground Motion Records Used in the SDOF Computational Study

Mat-lab #	Record	Event	Year	Station	Direction	R (km)	PGA (g)	Scale Factor for 10% in 50	Scale Factor for 2% in 50
1	IV79chi	Imperial Valley	1979	Chihuahua	012	28.7	0.270	2.13	3.20
2	IV79qkp	Imperial Valley	1979	Cucapah	085	23.6	0.309	1.78	2.68
3	LP89cap	Loma Prieta	1989	Capitola	090	14.5	0.443	2.14	3.22
4	LP89g03	Loma Prieta	1989	Gilroy Array #3	090	14.4	0.367	1.58	2.38
5	LP89g04	Loma Prieta	1989	Gilroy Array #4	090	16.1	0.212	1.76	2.64
6	LP89hch	Loma Prieta	1989	Hollister City Hall	090	28.2	0.247	1.18	1.77
7	LP89hda	Loma Prieta	1989	Hollister Differential Array	255	25.8	0.279	1.09	1.63
8	LP89svl	Loma Prieta	1989	Sunnyvale – Colton Ave	270	28.8	0.207	2.31	3.47
9	NR94cnp	Northridge	1994	Canoga Park – Topanga Can.	196	15.8	0.420	1.19	1.78
10	NR94hol	Northridge	1994	LA – Hollywood Stor FF	090	25.5	0.231	2.58	3.88
11	NR94stc	Northridge	1994	Northridge – 17645 Saticoy St.	090	13.3	0.368	2.07	3.10
12	SH87icc	Superstition Hills	1987	El Centro Imp. Co. Cent	000	13.9	0.358	1.94	2.91
13	SH87wsm	Superstition Hills	1987	Westmorland Fire Station	090	13.3	0.172	2.44	3.67
14	LP89slc	Loma Prieta	1989	Palo Alto – SLAC lab	270	36.3	0.194	1.08	1.63
15	NR94cen	Northridge	1994	LA – Centinela St.	245	30.9	0.322	1.75	2.63
16	NR94lh1	Northridge	1994	Lake Hughes #1	000	36.3	0.087	2.56	3.84
17	NR94stn	Northridge	1994	LA – Saturn St	020	30.0	0.474	1.64	2.46

9.3.5 Parameters and Response Indices

Eight parameters are varied as part of this study. The parameters, their range, and a description are provided in Table 9.5.

Table 9.5 Parameters Varied in the Computational Study

	Parameter	Name	Range of Values	Description / Comment
1	Response Modification Factor	R	10, 8, 6, 4	$R = \frac{S_a \; g \; m_{sdof}}{F_y}$ Higher R means Weaker Lateral Resisting System
2	Flag-Shape Height Ratio	β	0, 0.25, 0.5 0.75, 1.0, 1.25, 1.5, 1.75, 2.0	See Figure 9.1 — 0 means Elastic Bilinear, 1.0 means Full Flag Shape, 2.0 means Elastic Perfectly Plastic
3	Partition Wall Density	ρ_{wall}	0, 0.1, 0.16, 0.33	Units of m of wall / m^2 of floor area — Area = 1003 m^2 per floor
4	Number of Tributary Bays of Connections	N_{bc}	0, 14, 31, 48	Floor plan in Figure 9.6 with 9.14m bays has N_{bc}=14 — For column spacing of 4.57m in each direction, N_{bc}=48
5	Number of Stories	N_{flr}	3, 6, 9, 12	See Figure 9.6
6	Stiffness Ratio	K_{ratio}	0.25, 0.5, 0.75, 0.9	Ratio of Energy Dissipating Stiffness to Total Stiffness — See Figure 9.1, $K_{ratio} = K_{ed} / K_o$, $K_{rf} = (1-K_{ratio}) K_o$
7	Post-Yield Stiffness Ratio	α	0, 0.01, 0.025, 0.05	Ratio of Post Yield Stiffness to Initial Stiffness — See Figure 9.1
8	Ground Motion Intensity	I_{grnd}	10% in 50 years, 2% in 50 years	Mean and Mean + One Standard Deviation are Considered

Four response indices were examined in this study including residual roof drift ratio (the primary index of interest in this study), peak roof drift ratio, ductility demand, and hysteretic absorbed energy. As the oscillations had not fully damped out by the end of the ground motion, the time integration was carried out for an additional 30 to 120 seconds depending on the ground motion, with zero ground acceleration. The drift was averaged over this time and used as the residual drift. The ductility demand was calculated as the peak displacement divided by the displacement at which the energy-dissipating element yielded. Absorbed hysteretic energy was calculated as the cumulative area within the traced load-deformation response.

Acceptable residual drifts were determined using the out-of-plumb limits for new steel construction outlined in the AISC *Code of Standard Practice* (AISC 2005). The maximum out-of-plumbness of an individual element is the length over 500, or 0.2%. However, limits are also placed on the total out-of-plumbness to restrict cumulative tolerances. The maximum cumulative out-of-plumbness is 25 mm (1") toward the building line, and since the residual drift will always be toward a building line on one side of the building, the maximum limit of 25 mm (1") is used. The resulting proposed limits on residual roof drift ratios are 0.2%, 0.1%, 0.07%, and 0.05% for the 3-story, 6-story, 9-story, and 12-story buildings respectively. These limits are given in Table 9.6 and shown as thick dashed lines in Figure 9.14, Figure 9.15, and Figure 9.16 .

Table 9.6 Residual Drift Limits Based on the AISC Code of Standard Practice

Building	Height m (in)	L/500 mm (ft)	Out- of-Plumbness Limit mm (ft)	Effective Limit mm (ft)	Residual Drift Ratio Limit
3 Story	11.89 (468″)	23.9 (0.94″)	25.4 (1″)	23.9 (0.94″)	0.2%
6 Story	23.77 (936″)	47.5 (1.87″)	25.4 (1″)	25.4 (1″)	0.1%
9 Story	35.66 (1404″)	71.4 (2.81″)	25.4 (1″)	25.4 (1″)	0.07%
12 Story	47.55 (1872″)	95.0 (3.74″)	25.4 (1″)	25.4 (1″)	0.05%

9.4 Results and Discussions

Thousands of individual analyses were performed to examine trends in system response. Two samples of computational runs are described and then results for groups of analyses are presented thereafter.

9.4.1 Example Analyses

A sample of the analyses is shown in Figure 9.11, Figure 9.12, and Figure 9.13. A six-story structure is chosen with an interior partition density, ρ_{wall} = 0.33 m/m^2 (0.05 ft/ft^2), N_{bc} = 31 bays of simple shear beam-to-column connections, lateral resistance based on R = 8, stiffness ratio, K_{ratio} = 0.5, post-yield stiffness ratio, α = 0.01, and the 2% in 50 year hazard level scale factor applied to the 1989 Loma Prieta ground motion measured at the Hollister Differential Array. For the six-story building, a limit on residual drifts of 0.1% is considered as described in the previous section. Flag-shape height ratios of β = 0.5 and β = 1.5 were examined. The resulting hysteretic response of the lateral resisting system, the simple shear beam column connections, and the interior partitions are shown in Figure 9.11. The total response including ambient building resistance for both systems is shown in Figure 9.12, and the displacement histories are shown in Figure 9.13.

The difference in the self-centering hysteresis is pronounced as the flag-shape height ratio is changed from a system with reserve self-centering capacity, β = 0.5, to a system without full static self-centering capability, β = 1.5. As shown in Figure 9.11b, the self-centering lateral system with β = 1.5 does not pass near zero displacement when the force is removed from the peak displacement. This allows the possibility for significant residual drifts. On the other hand, the greater hysteretic energy dissipation of the more full hysteretic response causes reduced drifts in general.

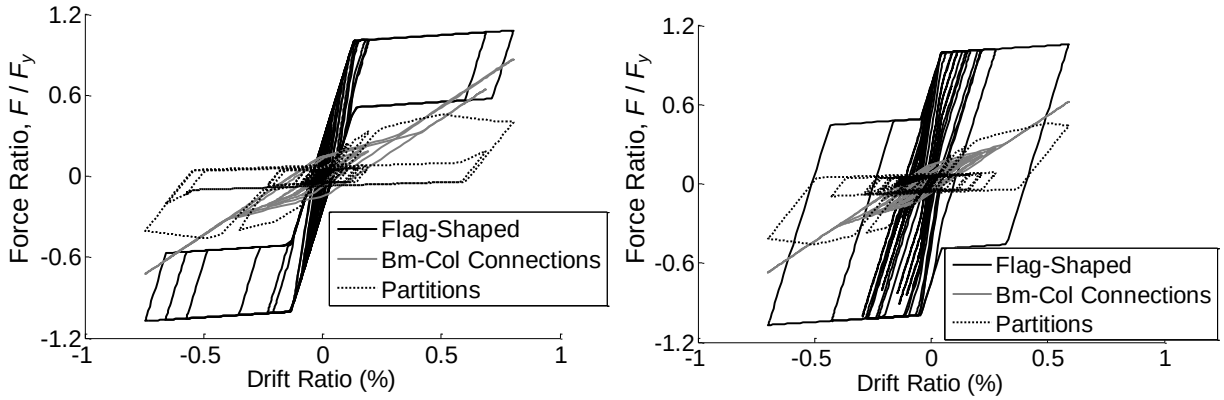

Figure 9.11 Comparison of Hysteretic Response for Each Element in the Analysis (a) Example Run with β = 0.5 (b) Example run with β = 1.5

As expected, the ambient building resistance causes an increase in lateral resistance. As shown in Figure 9.12a, a 25% additional force at yield and a 100% larger peak force were realized for this example when ambient building resistance was included. Also, as expected, the inclusion of partitions and beam-to-column connections increase hysteretic absorbed energy. In general, the added stiffness, strength, and absorbed energy associated with ambient building resistance results in reduced peak drifts.

However, after the ambient building resistance elements experience inelastic deformations, they also act to resist restoring forces. Partitions develop significant resistance, but strength degradation depletes the majority of the resistance after the initial large displacement excursions. Afterwards, the partitions behave similar to a weak friction damper. The simple shear beam-to-column connections experience little inelasticity at these small drift levels which are less than 1% for this ground motion.

One way to compare the efficacy of a self-centering system at eliminating residual drifts is to examine the range of possible residual drifts when the load is slowly removed from the points of maximum and minimum drifts. The flag-shaped system shown in Figure 9.11a allows a range of ±0.045% drift at zero force, whereas the system including ambient building resistance shown in Figure 9.12a allows a range of ±0.075% drift at zero force. This range is labeled as full self-centering on Figure 9.12a because the restoring force can overcome the other components, thus not allowing residual displacement outside of this range. Figure 9.13a shows that the final residual drift was found to be -0.01% drift for the sample system with β = 0.5.

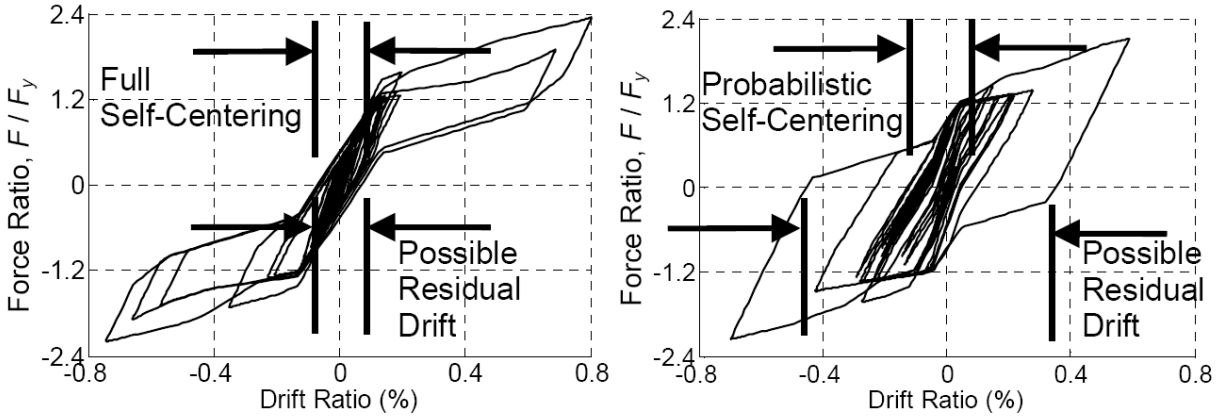

(a) $\beta = 0.5$ (b) $\beta = 1.5$

Figure 9.12 Comparison of Hysteretic Response Including Ambient Building Resistance (a) Example Run with β = 0.5 (b) Example run with β = 1.5

Unlike the fully self-centering system ($\beta \leq 1.0$), the β = 1.5 system shown in Figure 9.11b does not restrict residual drifts to a small range when the load is removed. Drift levels as great as 0.5% were experienced at zero load, implying that for this configuration and ground motion, the largest possible residual drift is 0.5%. However, the actual residual drift was found to be -0.085%. In fact, besides three large displacement excursions, the majority of the drifts experienced at zero force were found to land between ±0.1% which is within the proposed limit on residual drift for the six-story building. This range is labeled as probabilistic self-centering on Figure 9.12b because there is a propensity for the residual drifts to land in this range. The mechanism for this propensity to self-center is described in detail in a later section and is governed by an increased probability for the system to experience inelastic deformations in the direction toward zero displacement rather than away.

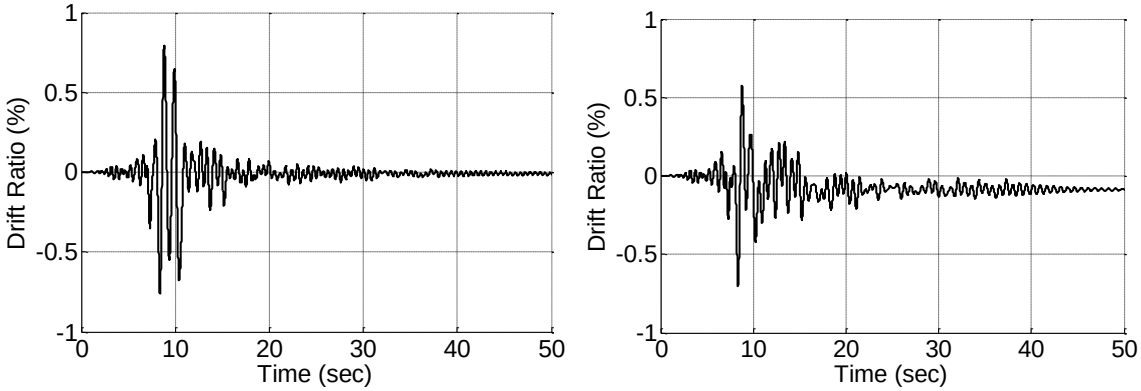

(a) $\beta = 0.5$ (b) $\beta = 1.5$

Figure 9.13 Comparison of Displacement Histories (a) Example Run with β = 0.5 (b) Example run with β = 1.5

9.4.2 Effect of Hazard Level and System Strength

The variables given in Table 9.5 were grouped into three parametric studies which are summarized in this section and the following two sections. All of the parametric studies consider four building heights and all nine flag-shape height ratios, β. The first study focuses on the hazard level and the strength of the system as given by the response modification factor, R. For this study, the partition wall density was, ρ_{wall} = 0.16 m/m^2 (0.03 ft / ft^2), there were N_{bc}=14 bays of simple shear beam-to-column connections tributary to the lateral resisting system, the self-centering element and the energy-dissipating element had equal stiffness, K_{ratio}=0.5, and the post-yield stiffness was α = 0.01 times the initial stiffness, K_o. Resulting peak drifts and residual drifts are shown in Figure 9.14 as a function of the amount of self-centering included in the system (β).

Figure 9.14 demonstrates that although the peak roof drifts increase significantly as the hazard level is increased from the 10% probability of exceedance in 50 years to the 2% probability of exceedance in 50 years, the residual drifts remain negligible for buildings with flag shape height equal to 1.5 or smaller ($\beta \leq 1.5$). For the 2% probability of exceedance in 50 years earthquake event, one standard deviation above the mean results in residual drifts that are below the proposed limit for values of the flag-shape height factor of 1.5 or less ($\beta \leq 1.5$).

Figure 9.14 also shows that the residual drifts are quite small compared to the peak drifts even for systems with no self-centering component (β = 2.0). This is in part due to the use of kinematic hardening with a positive post-yield stiffness as will be described in a subsequent section on the probabilistic mechanism for self-centering.

Other trends shown in Figure 9.14, include that taller buildings were found to experience smaller roof drift ratios, although the proposed limits on residual roof drifts are also smaller. For the three-story buildings, the lower system strength marked by higher response modification factors, R, exhibited slightly larger residual drifts for the structures with low self-centering capability, but generally did not have a pronounced affect on residual drift in other configurations. As expected, the response modification factor instead had more correlation with the ductility demands, which are not shown in the figure.

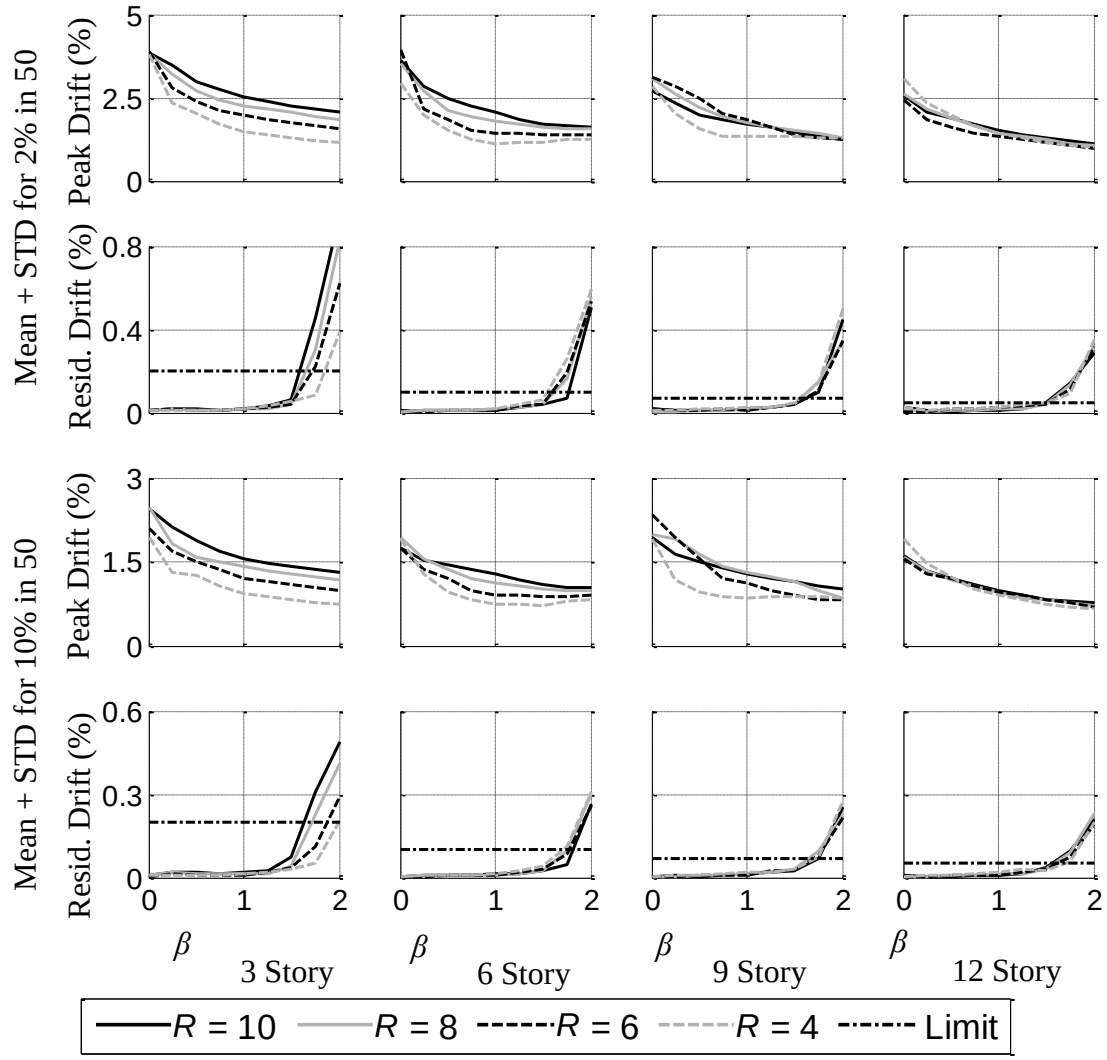

Figure 9.14 Peak Drift Ratios and Residual Drift Ratios for Parametric Study on Hazard Level and System Strength

The effect of source distance was also investigated as shown in Figure 9.15 using the same parameters with the hazard level with 2% probability of exceedance in 50 years. The set of 17 ground motions were divided into a group referred to as near-source records consisting of 7 motions with distance less than 17 km, and a group referred to here as medium range records consisting of the other 10 ground motions between 17 km and 37 km from the source. As shown in Figure 9.15, ground motions recorded at closer distance to the source produce larger residual drifts although the effect is reduced as the building height and period are increased. This is similar to the result found by Ruiz-Garcia and Miranda (2005). However, the trends in the residual drift for various levels of self-centering are similar for different source distances in that residual drifts are found to be below the proposed limit for values of $\beta \leq 1.5$.

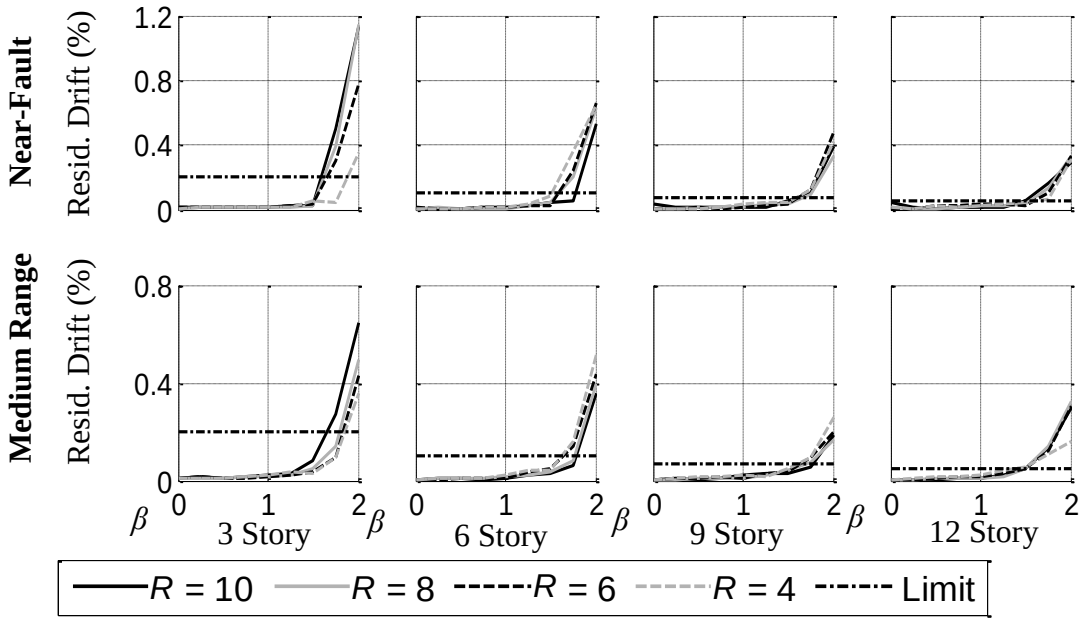

Figure 9.15 Residual Drift Ratios for Near Fault and Medium Range Ground Motion Records

As described above for the example analyses and expanded upon in the next section, the elements of the ambient building resistance reduce peak drifts, but degrade after large cycles. It is expected, therefore, that the sequence of large and small cycles will affect the way ambient building resistance effects residual drifts. This added variability in the way that ambient building resistance affects residual drifts reinforces that it may not be advisable to rely on these elements for self-centering. However, as stated previously, the possible negative effects of ambient building resistance should be considered.

9.4.3 Effect of Ambient Building Resistance

The second study focuses on the variation of the partition wall density and number of tributary simple shear beam-to-column connections. As in the previous study, the number of stories and the flag-shape height ratio are varied. The hazard level of the mean plus one standard deviation for the hazard level that has 10% probability of exceedance in 50 years is held constant as are the response modification factor of R=8, the ratio of energy-dissipating stiffness to total stiffness, K_{ratio}=0.5, and the post-yield stiffness ratio of α = 0.01.

Ambient building resistance was found to have two competing effects related to residual drifts. First, the strength and stiffness of the system can be significantly increased with the addition of partitions and shear beam-column connections which leads to reduced peak drifts. On the other hand, after becoming inelastic, these elements also resist the ability of the restoring forces to self-center the building.

A transition is shown in Figure 9.16 as β and the number of beam-column connections, N_{bc}, increase. At low values of β, more beam-column connections result in

larger residual drifts, but as β approaches 2, more beam-column connections cause a reduction in residual drifts. This transition implies that in systems with little or no restoring force component, ambient building resistance helps limit residual drifts, but that ambient building resistance actually causes larger residual drifts in systems with significant restoring force components.

By comparing the change in residual drifts with interior partition density (difference between the lines in Figure 9.16) to the change in residual drifts with beam-to-column connections (difference between rows in Figure 9.16), it is shown that the beam-column connections have more effect on self-centering than the interior partitions. This point is further demonstrated by Figure 9.17, which shows the residual drifts for the three-story building with $\beta = 1.5$. A clear increase in residual drifts with added beam-to-column connections is found, whereas no clear trend is noted with partition wall density.

In the example analyses results depicted in Figure 9.11, it is shown that the partitions present significant resistance on the first large excursion and then strength degradation depletes most of their resistance. Although simple shear beam-to-column connections also reduce peak drifts, they do not experience the same amount of strength degradation and for that reason are shown to have more effect on the ratio of residual drift to peak drift. The hysteretic absorbed energy shown in Figure 9.17 supports this point in that beam-to-column connections cause more significant increase in absorbed energy than interior partitions and therefore maintain a higher level of resistance to restoring forces.

The ratios of residual drift to peak drift shown in Figure 9.17 isolates the negative impact of ambient building resistance by showing that increasing the density of partitions and number of shear beam-column connections results in an increase in residual drifts relative to the peak drift for the configuration shown. However, the residual drifts shown in Figure 9.17 experience smaller increases and in some cases decreases in residual drift with increasing partition wall density. That is because the peak drifts, also shown in Figure 9.17, decrease with increased ambient building resistance which leads to less magnitude of residual drift.

It is shown that the prototype buildings still exhibited excellent self-centering capability even for large values of β. For example, the floor plan included in Figure 9.6 shows 14 bays of tributary beam-to-column connections, whereas the value of $N_{bc} = 48$ represents column spacing of 15 feet in both directions. Even with this large number of connections resisting the restoring forces, only the three-story buildings experienced residual drifts larger than the proposed limit when using $\beta \leq 1.5$, and all configurations satisfied the proposed limits on residual drift when using $\beta \leq 1.33$. A flag shape height factor of $\beta = 1.33$ means proportioning restoring forces to have at least one-half the capacity of the energy-dissipating element as calculated using Equation (9.5) and is shown to reliably control residual drifts for all configurations considered herein.

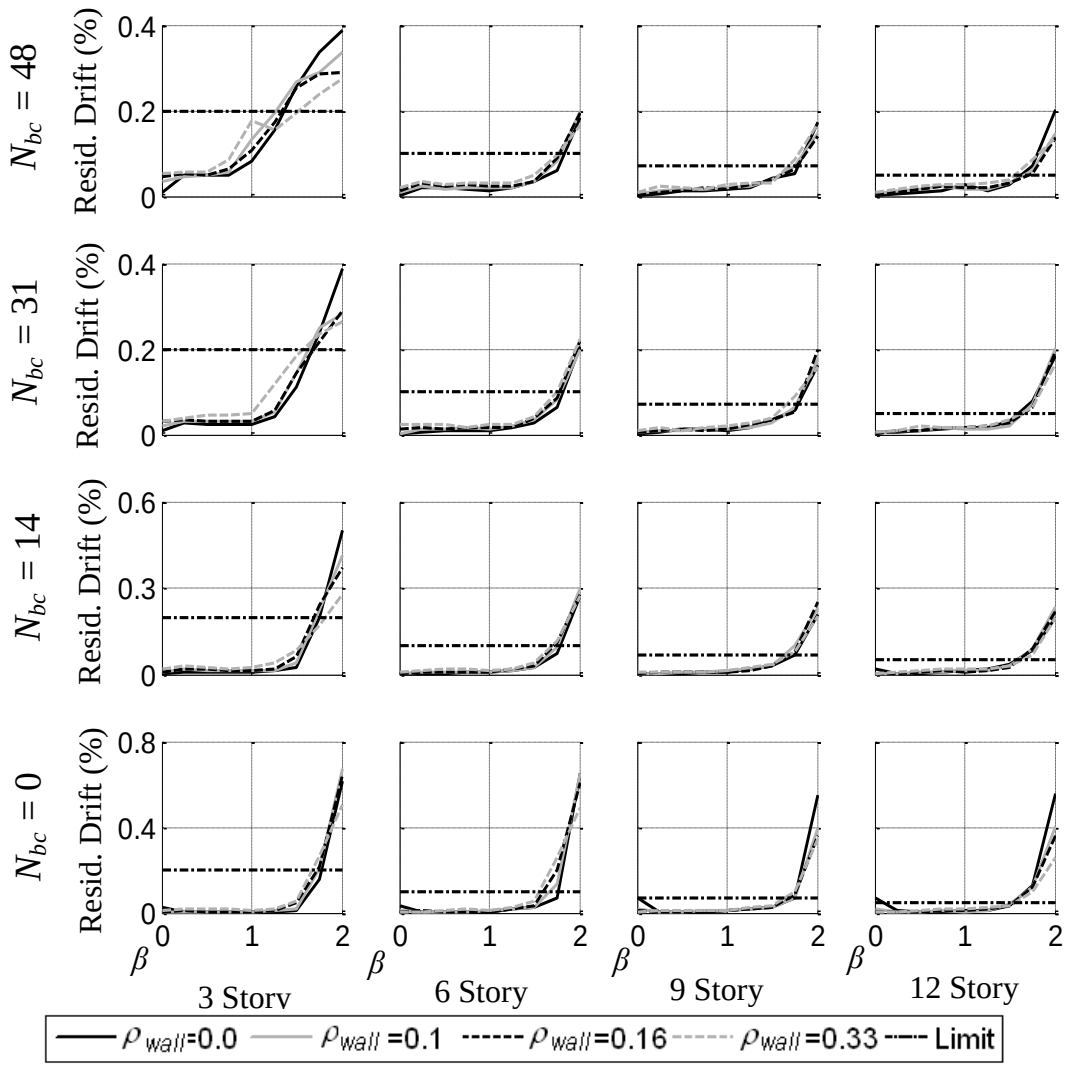

Figure 9.16 Residual Drift Ratios for Parametric Study on Ambient Building Resistance

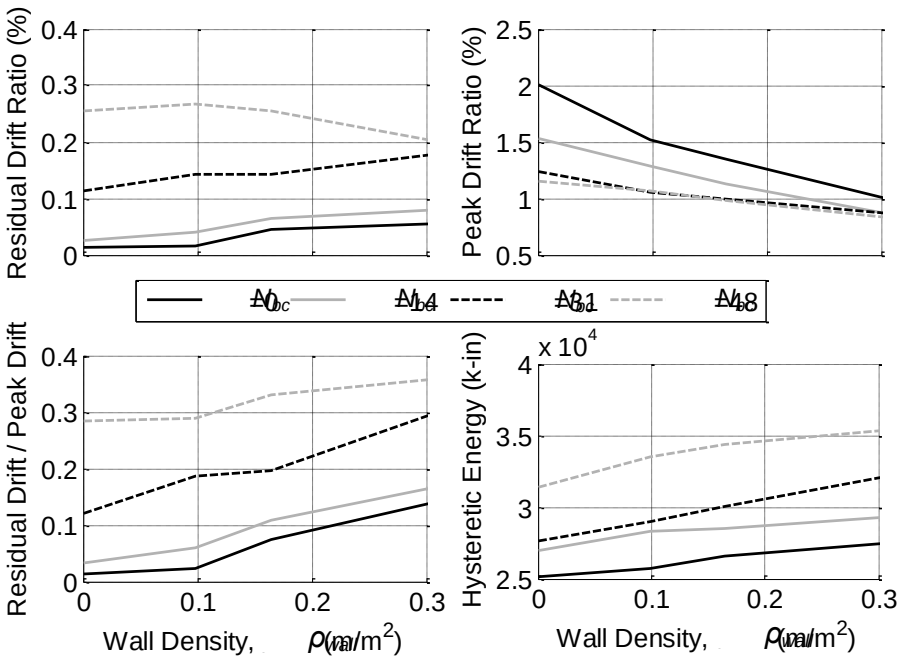

Figure 9.17 Residual Drift, Peak Drift, Ductility Demand, and Hysteretic Energy for the Three-Story Building with β = 1.5

9.4.4 Effect of Stiffness Variations

The third study focuses on the variation of the stiffnesses including the ratio of the energy-dissipating element stiffness to the total flag-shape stiffness, K_{ratio}, and the post-yield stiffness, α. As in the previous studies, the number of stories and the flag-shape height ratio are also varied. The hazard level of the mean plus one standard deviation for the 10% probability of exceedance in 50 years event is held constant as are the response modification factor of R=8, the partition wall density, ρ_{wall} = 0.16 m/m^2 (0.03 ft/ft^2), and number of tributary bays of simple shear beam-to-column connections, N_{bc}=14. Representative results for the stiffness study are shown in Figure 9.18 for the three-story building.

The residual drifts were found to be sensitive to the post-peak stiffness, α, when the flag-shape height ratio becomes large such as shown for β=2.0 in Figure 9.18a. This is due to the increase in probabilistic self-centering described in the following section. However, Figure 9.18a also shows that in the presence of a restoring force, β<2.0, the increase in post-yield stiffness does not have a significant effect on residual drift because they are already reduced to small amounts.

Increasing the ratio of energy-dissipating stiffness relative to the system stiffness, K_{ratio}, has the effect of increasing the residual drifts for all values of β as shown in Figure 9.18b. This effect is due to the change in shape of the hysteresis loops and the expansion of the range of possible residual drift even in fully self-centering systems. For all values of K_{ratio} and α considered, the residual drifts were found to be below the proposed limit for values of β less than or equal to 1.5.

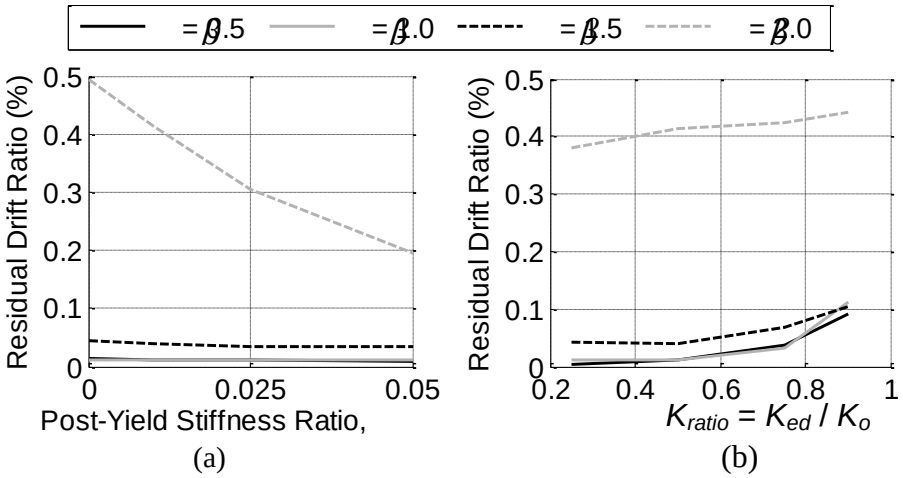

Figure 9.18 Effect of Varying Stiffness on the Residual Drifts for the Three-Story Building

9.4.5 Minimum Amount of Energy Dissipation Required

The computational studies in this chapter consider system proportioning with no energy dissipating component (β =0). The bilinear elastic force resisting system, as shown in Figure 9.2 does not possess the capacity to dissipate seismic energy. The peak drifts in systems without energy dissipation are larger than the peak drifts of systems with comparable strength and stiffness that have energy dissipating components.

Figure 9.19 and Figure 9.20 shows the peak roof drifts for the 3-story, 6-story, 9-story, and 12-story buildings as subjected to the hazard level with 10% probability of exceedance in 50 years. The models did not include ambient building resistance (partition wall density, ρ_{wall} = 0.0 m/m^2 and number of tributary bays of simple shear beam-to-column connections, N_{bc}=0), used a response modification factor, R=8.0, a ratio of energy-dissipating stiffness to total stiffness, K_{ratio}=0.5, and post-yield stiffness ratio of α = 0.01. The peak roof drifts from each ground motion are shown along with the median, one standard deviation above the median, and one standard deviation below the median. The standard deviation is calculated as the standard deviation of the log of the peak roof drifts, assuming a lognormal distribution. A dashed line is shown at 2% roof drift ratio which is the allowable story drift defined in ASCE 7-05 (2005) for general building structures not fitting particular requirements for building type or special occupancy categories.

Figure 9.19 and Figure 9.20 show that the peak roof drifts are not very sensitive to the flag-shape height ratio in the range of $1.0 < \beta < 2.0$. It was also shown that the shorter buildings experience larger peak roof drift ratios. The 3-story building exhibits median peak roof drift ratios that just start to exceed 2% for a value of the flag shape height ratio of β = 0.5. This means that for the systems included in this study, a flag shape height ratio of β >0.5 (SC<3.0) produced peak roof drifts below the 2% peak roof drift limit in most cases, and on average for the β =0.5 configurations.

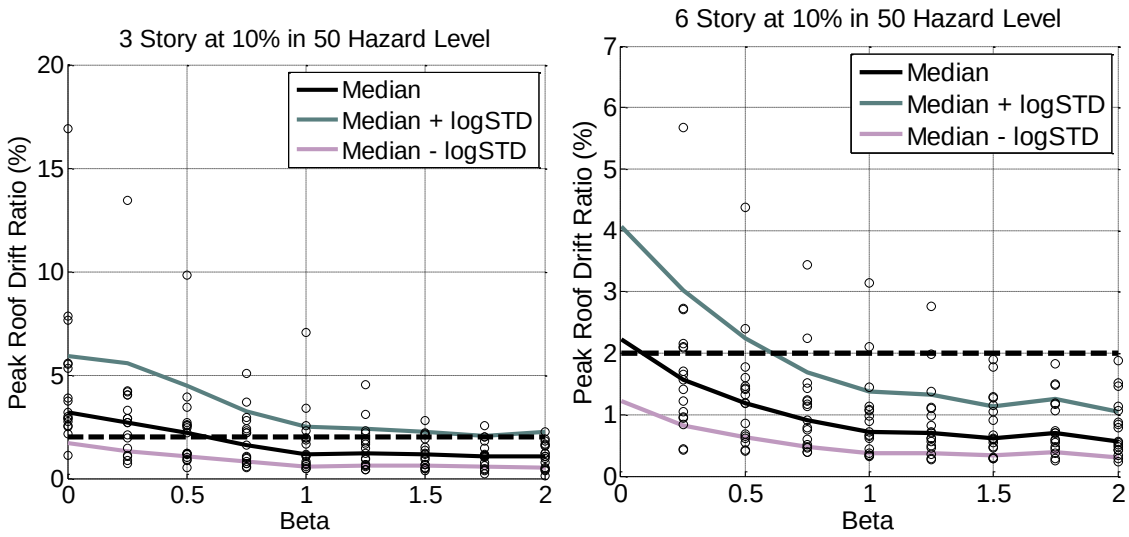

Figure 9.19 Peak Drift Ratios for 3-Story and 6-Story Buildings Subjected to the 10% in 50 Years Hazard Level with No Ambient Building Resistance

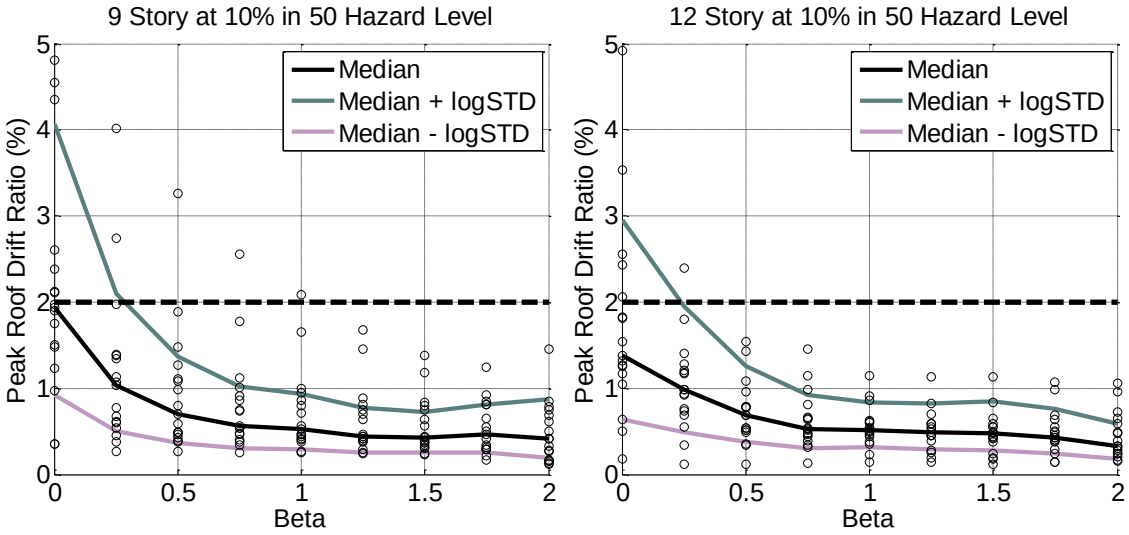

Figure 9.20 Peak Drift Ratios for 9-Story and 12-Story Buildings Subjected to the 10% in 50 Years Hazard Level with No Ambient Building Resistance

9.5 Mechanism of Probabilistic Self-Centering

The example analyses presented in Section 9.4.1 provide anecdotal evidence that residual drifts are often less than the maximum possible residual drift computed as the drift achieved after load is slowly removed from the point of peak drift. Furthermore, the parametric studies presented above show that systems with less than full self-centering, (β>1.0) can still reliably eliminate residual drifts. Systems with less than full self-centering do not prevent the possibility of residual drift by including enough restoring force to eliminate the drift at zero load. The mechanism for this type of self-centering is governed by an increased probability that the system will experience inelastic deformations in the direction *toward* zero displacement rather than *away* from zero

displacement. MacRae and Kawashima (1997) outlined this concept as applied to elastic-plastic hardening systems using the term dynamic stability. The phenomenon is found here to be especially effective when any restoring force is present. The concept and the reason for this increased effectiveness are described and quantified below.

Consider a self-centering system with restoring force that is less than the lateral force required to yield the energy-dissipating element. A sample time history response of such a system with β = 1.5 and post yield stiffness ratio, α = 0.025 is shown in Figure 9.21a. The load-deformation response does not prevent the possibility of residual drift and as such does not exhibit near zero displacement when the force is removed.

This system was subjected to all 17 ground motions scaled to the hazard level with 10% probability of exceedance in 50 years. The force at each time step was recorded and converted into a histogram which was then normalized into the probability distribution shown in Figure 9.21b. There are spikes in the probability distribution at flatter portions of the load-deformation response because the force occurrences are closer together on the force axis. Using this distribution, the probability that the force will be above or below a particular level can be calculated directly as the area above or below that value.

For example, at an initial value of drift ratio equal to 0.2%, it is shown in Figure 9.21a that the corresponding negative yield force F_{ny} and positive yield force F_{py} are -0.42 F_y and +1.12 F_y respectively. Figure 9.22a shows the corresponding probabilities that the force will be less than F_{ny}, $P(F<F_{ny})$ or greater than F_{py}, $P(F>F_{py})$, for any given time step are 34% and 14% respectively. These probabilities are shown as dots on Figure 9.22b along with the trends for these probabilities as they vary with initial drift ratio. As shown in Figure 9.22b, at zero displacement, the probability of yielding in the positive direction is equal to that in the negative direction at 15%. The probability of the force exceeding the positive yield force goes down with increasing drift ratio because the positive yield force becomes larger. Similarly, the probability of the force being below the negative yield force increases as the negative yield force increases. A sharp jump in the probability that the negative yield force will be exceeded is shown to occur at the drift at which the negative yield force experiences a sharp increase due to the restoring force contribution.

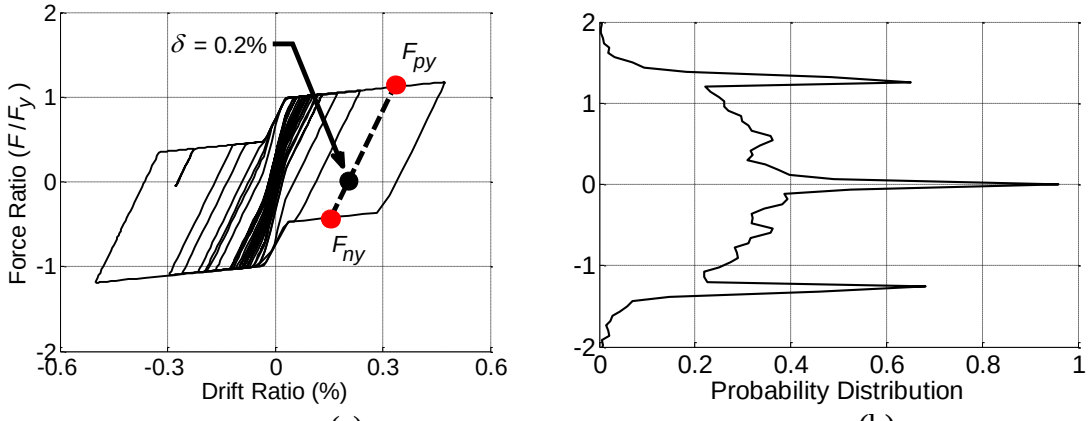

Figure 9.21 (a) Load Deformation Response of a Self Centering System with Description of Forces F_{py} and F_{ny} (b) Corresponding Force Probability Density Function

The probability that inelastic deformations will occur toward zero displacement rather than away can therefore be calculated using Equation (9.21). As shown in Figure 9.22b, this probability is 50% for zero displacement implying equal probability for inelastic deformations in each direction. For the example starting at a drift ratio of 0.2% it is shown that there is a 71% chance that inelastic deformations will be toward zero displacement which is marked on Figure 9.22b by a dot.

$$P(\delta_{in}\ toward\ zero) = \frac{P(F < F_{ny})}{P(F > F_{py}) + P(F < F_{ny})} \tag{9.21}$$

These probability plots provide a quick method for gauging the propensity of a system to self-center. Several trends are clear from the plot of five different systems that are compared in Figure 9.23. Systems with a restoring force (β <2.0) component exhibit a significant positive jump in probability of inelastic deformations toward zero. This jump occurs at the drift level in which the absolute value of the yield force in the direction of zero displacement decreases. These changes in yield forces are demonstrated in the system shown in Figure 9.21a.

Positive kinematic hardening also provides a propensity to self-center as the positive and negative yield forces transition uniformly due to the Bauschinger effect and the resulting retention of a constant elastic zone within the constitutive response. Isotropic hardening, on the other hand, has no effect on these probabilities, as the elastic zone expands such that neither the positive nor the negative yield forces are closer to zero. The trend that larger hardening slope causes a steeper rise in the probability that inelastic deformations will occur toward zero is clear in Figure 9.23. It is also shown in Figure 9.23 that an elastic-perfectly plastic system (β = 2.0, α = 0.0) exhibits no preference to self-center or diverge from zero displacement.

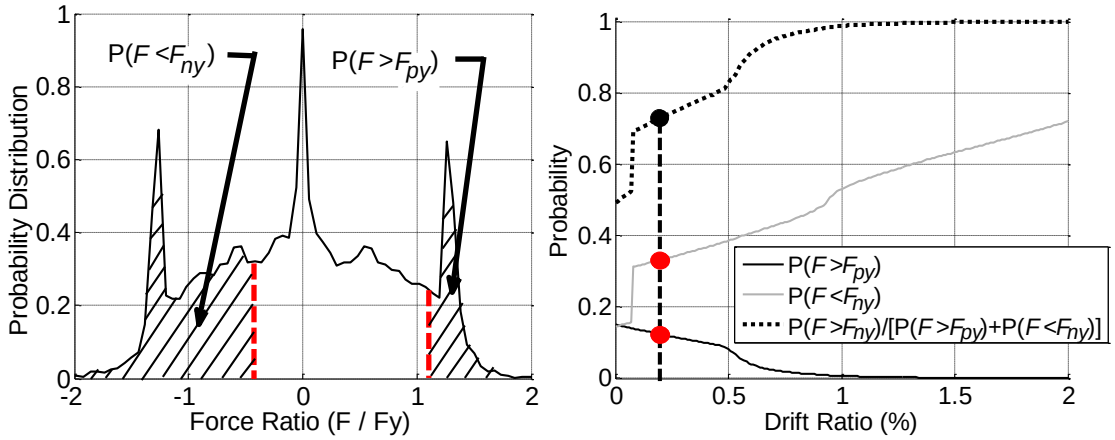

(a) (b)

Figure 9.22 (a) Calculating the Probabilities for Inelastic Deformations in the Positive and Negative Directions (b) Progression of the Probabilities with the Drift Ratio

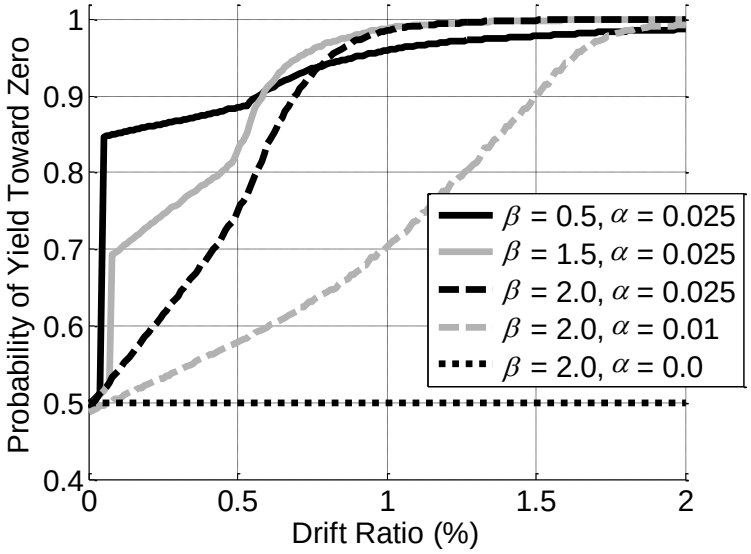

Figure 9.23 Probabilities that Inelastic Deformations will Occur Toward Zero Displacement for Different Systems

9.6 Conclusions From SDOF Investigation of Self-Centering Response

As self-centering systems have gained in popularity in the past two decades, a need has developed not only to quantify the ability of these systems to eliminate residual drifts in the presence of ambient building resistance, but also to determine how much restoring force is required to provide reliable self-centering. Time history analyses were conducted on four prototype buildings including the effects of ambient building resistance from partitions and beam-to-column shear connections within the steel gravity framing. The sensitivity of system response to a range of parameters was examined with a special focus on residual drifts.

Two modes of self-centering were discussed. Full self-centering, utilizes a load-deformation response that does not allow large displacements at zero force. The second mode, referred to here as probabilistic self-centering, occurs when the yield force in the direction towards returning to zero displacement is less than the yield force in the opposite direction, creating a propensity for inelastic deformations to occur in the direction towards zero displacement (self-centering). It was found that reliable self-centering performance can be accomplished even with systems that exhibit load-deformation response that allow large static displacements when load is removed.

This conclusion is based on the examination of typical steel framed buildings designed using response modification factors between R = 4 and R = 10, gypsum clad steel stud interior partition walls with wall length per floor area between $\rho_{wall} = 0$ and $\rho_{wall} = 0.33 m/m^2$ ($0.1 ft/ft^2$), considering between $N_{bc} = 0$ to $N_{bc} = 48$ bays of simple shear beam-to-column connections tributary to the lateral resisting system, building heights between 3 and 12 stories, ratios of energy dissipating stiffness to total stiffness between $K_{ratio} = 0.25$ and $K_{ratio} = 0.9$, and ratios of post-yield stiffness to initial stiffness between $\alpha = 0$ and $\alpha = 0.05$. The derivation of SDOF response was also based on the assumption

that deformations will not concentrate in a single story. Although experimental and computational studies have shown that deformations do not focus in single stories for the controlled rocking system, this may not be the case for all self-centering systems. It was also assumed that the kinematic hardening ratio for the energy dissipating element was equal to the ratio of the two elastic stiffnesses of the restoring force element. Although this approximates the experimental response of the controlled rocking system, this may not represent some self-centering systems.

This study showed that typical gypsum interior partitions, although opposing restoring forces, also reduce peak drift and experience strength degradation such that they do not dramatically affect residual drifts. Residual drift is more sensitive to simple shear beam-to-column connections because they do not experience as much cyclic strength degradation and thus retain their resistance to restoring forces. However, while ambient building resistance alters the total hysteretic response, it does not neutralize the ability of a system to self-center in part because of probabilistic self-centering.

Probabilistic self-centering, which is especially effective in the presence of even small amounts of restoring force, can significantly reduce residual drifts. Using proposed limits on residual drifts based on new steel construction tolerances, it was determined that flag-shaped height ratios of $\beta \leq 1.5$ (where β is the flag-shape height ratio (see Figure 9.2) can satisfy residual drift limits for most of the configurations considered herein when subjected to events scaled to the hazard level with 2% probability of exceedance in 50 years or smaller. Furthermore, $\beta \leq 1.33$ can reliably (with confidence of one standard deviation above the mean) satisfy residual drift limits for all configurations considered in this study when subjected to the hazard level with 10% probability of exceedance in 50 years. This means that proportioning restoring forces to have at least one half the capacity of the energy-dissipating element can reliably control residual drifts if the building configuration is within the range of parameters studied herein, which are characteristic of a wide range of multi-story steel structures.

MDOF SENSITIVITY STUDY

The experimental program validated that the controlled rocking system can satisfy the stated performance goals of eliminating residual drifts and concentrating structural damage in fuse elements. The experimental results were used to inform the development of a computational model which was then used to examine a much wider range of configurations. The development of the computational model was described in Chapter 6. This chapter presents a parametric study that investigates the behavior of the controlled rocking system as applied to a range of buildings with a range of input parameters.

10.1 Introduction

The sensitivity study consisted of seventeen configurations that included three different building heights. Nonlinear time history analyses were conducted on a 2D model of each configuration with twenty-two ground motions scaled to four different hazard levels. A total of 1496 analyses were executed. Nonlinear static analyses were also conducted on each configuration to obtain initial stiffnesses and associated periods. There were several objectives of the sensitivity study including:

- Further validate system performance by showing the ability to control residual drifts and concentrate structural damage in fuses for a range of configurations.
- Demonstrate the effect of rocking by comparing the response of a fixed base braced frame to the rocking frame.
- Investigate the effects of building height on system behavior (e.g., assessing dominance of the rocking mode as height increases).
- Investigate possible limits on building height. (e.g., shorter buildings have larger post-tensioning strain demand).
- Investigate the effect of higher modes of vibration on member force demands and system behavior (included in Chapter 11).
- Investigate the effect of the A/B ratio on system behavior and demands.
- Investigate the impact of eliminating post-tensioning seating losses on system demand.
- Investigate the ability of assumed design rules to create expected seismic performance.
- Compare the response for configurations with struts between the frames to configurations with diaphragm elements that connect the beams in the controlled rocking frames.

There are several things the sensitivity study is not intended to include. This study does not include the following:

- This study is not intended to fulfill the requirements of ATC 63 (FEMA P695 2009). The range of variables and configurations were not selected for this purpose, incremental dynamic analyses (IDA) were not performed, and the associated post-processing required to quantify seismic performance factors was not conducted.
- One set of design rules was used for determining required system resistance, proportioning of the system, and designing the individual elements and frame members. It was not the intent of this study to investigate different design strategies for this structural system.
- It was not the intent of this study to investigate the collapse behavior of the system. Although the inelastic response of key components is considered, behavior at fracture is not modeled.

10.2 Configurations Included in the Study

The configurations used in the sensitivity study are listed in Table 10.1. Three building heights were included: three, six, and nine-story buildings. The majority of the frames were dual frame configurations meaning they consisted of two rocking frames with fuses attached between them. The majority of the frames also used diaphragm elements, which means that there were elastic truss elements connecting the midspan of one frame to the mispsan of the other frame. This element simulates the constraint provided by a beam that is adjacent to the rocking frames that transfers diaphragm shear into the lateral force resisting system.

Table 10.1 Matrix Showing Configurations Included in the Sensitivity Study

Analysis Number	Number of Stories	Dual vs. Single Frame Configuration	A/B Ratio	Fuse Slenderness	SC	Eliminate Seating Losses	Strutural Configuration	Bay Width m (ft)
1	3	Dual	2.5	Thick (L/t=22.4)	1.1	Yes	Diaphragm Element	9.14 (30.0)
2	6	Dual	2.5	Thick (L/t=22.4)	1.1	Yes	Diaphragm Element	9.14 (30.0)
3	9	Dual	2.5	Thick (L/t=22.4)	1.1	Yes	Diaphragm Element	9.14 (30.0)
4	3	Dual	2.5	Thick (L/t=22.4)	1.5	Yes	Diaphragm Element	9.14 (30.0)
5	3	Single	N/A	Thick (L/t=9.1)	1.5	Yes	Diaphragm Element	6.10 (20.0)
6	6	Dual	2.5	Thick (L/t=22.4)	1.5	Yes	Diaphragm Element	9.14 (30.0)
7	6	Single	N/A	Thick (L/t=9.1)	1.5	Yes	Diaphragm Element	9.14 (30.0)
8	3	Dual	1.5	Thick (L/t=22.4)	1.1	Yes	Diaphragm Element	9.14 (30.0)
9	3	Dual	3.5	Thick (L/t=22.4)	1.1	Yes	Diaphragm Element	9.14 (30.0)
10	6	Dual	1.5	Thick (L/t=22.4)	1.1	Yes	Diaphragm Element	9.14 (30.0)
11	6	Dual	3.5	Thick (L/t=22.4)	1.1	Yes	Diaphragm Element	9.14 (30.0)
12 and 13 are omitted								
14	3	Dual	2.5	Thick (L/t=22.4)	0.75	Yes	Diaphragm Element	9.14 (30.0)
15	6	Dual	2.5	Thick (L/t=22.4)	0.75	Yes	Diaphragm Element	9.14 (30.0)
16	3	Single	N/A	Thick (L/t=22.4)	1.5	No	Diaphragm Element	6.10 (20.0)
17	6	Dual	2.5	Thick (L/t=22.4)	1.1	Yes	Strut With No Tolerances	9.14 (30.0)
18	6	Dual	2.5	Thick (L/t=22.4)	1.1	Yes	Strut With Tolerances	9.14 (30.0)
19	6	Dual	2.5	Thick (L/t=22.4)	1.1	Yes	Diaphragm Element	9.14 (30.0)

The configurations given in Table 10.1 were organized into eight studies that isolated one system variable for investigation. Table 10.2, Table 10.3, Table 10.4, and Table 10.5 describe the individual studies including information about the parameters that were held constant for all configurations in that study.

Table 10.2 Description of the Height Study and the Strut Study

Height Study		Strut Study	
Height (Config. No.)	**Fixed Parameters**	**Config. (Config. No.)**	**Fixed Parameters**
3-Story (1)	• Dual Frame • A/B = 2.5 • Thick Fuse (*L/t*=22.4) • SC=1.1 • Seating Losses are Eliminated • Diaphgram Element • 9.14m (30') Bay	Strut Without Pin Hole Tolerances (17)	• Six-Story • Dual Frame • A/B = 2.5 • Thick Fuse (*L/t*=22.4) • SC=1.1 • Seating Losses are Eliminated • 9.14m (30') Bay
6-Story (2)		Struts With Pin Hole Tolerances (18)	
9-Story (3)		Diaphragm Elements (2)	

Table 10.3 Description of the A/B Ratio Study and the SC Ratio Study

A/B Ratio Study		Self-Centering Ratio Study	
A/B Ratio, Height (Config. No.)	**Fixed Parameters**	**SC Ratio, Height (Config. No.)**	**Fixed Parameters**
A/B=1.5 3-Story (8)	• Dual Frame • Thick Fuse (*L/t*=22.4) • SC=1.1 • Seating Losses are Eliminated • Diaphgram Element • 9.14m (30') Bay	SC=0.75 3-Story (14)	• A/B = 2.5 • Thick Fuse (*L/t*=22.4) • Seating Losses are Eliminated • Diaphgram Element • 9.14m (30') Bay
A/B=2.5 3-Story (1)		SC =1.1 3-Story (1)	
A/B=3.5 3-Story (9)		SC =1.5 3-Story (4)	
A/B=1.5 6-Story (10)		SC =0.75 6-Story (15)	
A/B=2.5 6-Story (2)		SC =1.1 6-Story (2)	
A/B=3.5 6-Story (11)		SC =1.5 6-Story (6)	

Table 10.4 Description of the Single Frame vs. Dual Frame Study

Single Frame vs. Dual Frame Study	
Config. and Height (Config. No.)	**Fixed Parameters**
Dual Frame 3-Story (4) 9.14m (30') Bay Single Frame 3-Story (5) 6.10m (20') Bay Dual Frame 6-Story (6) 9.14m (30') Bay Single Frame 6-Story (7) 9.14m (30') Bay	• A/B = 2.5 where applicable • Thick Fuse (*L/t*=22.4) • SC=1.5 • Seating Losses are Eliminated • Diaphgram Element

Table 10.5 Description of the PT Seating Losses Study and the Rocking vs. Fixed Base Study

Eliminating PT Seating Losses Study		Rocking vs. Fixed Base Study	
PT Seating Losses (Config. No.)	**Fixed Parameters**	**Configuration (Config. No.)**	**Fixed Parameters**
Seating Losses Eliminated (5)	• Singe Frame Configuration • Three-Story • SC=1.1 • Thick Fuse (*L/t*=22.4) • Diaphgram Element • 6.10m (20') Bay	Uplifting Base (2)	• Six-Story • Dual Frame • A/B = 2.5 • Thick Fuse (*L/t*=22.4) • SC=1.1 • Seating Losses are Eliminated • Diaphgram Element
Seating Losses Not Eliminated (16)		Fixed Base (19)	

The buildings used were based on the floor plan of the three-story building from the SAC buildings as described in Gupta and Krawinkler (1999). The floor plan, shown in Figure 10.1 is 4 bays by 6 bays with 9.14 m (30') bay widths and 3.96 m (13') floor heights. The mass and gravity loads also match the three-story building from Gupta and Krawinkler (1999) and are given in Table 10.6. As shown in Figure 10.1, the three-story building has two controlled rocking elements in each direction whereas the six-story and nine-story buildings have four controlled rocking elements in each direction. Overturning moments were calculated according to ASCE 7 (ASCE 2005) using seismic design category D and an assumed value for the response modification factor, R=8.0. Design information including the design overturning moments is included in Table 10.7.

Table 10.6 Masses and Weights for the Floor and Roof

Level	Seismic Mass, kN-sec^2/m (kips-sec^2/ft)	Total Gravity Load, kN (kips)
Roof	1033 (70.9)	11,300 (2548)
Floor	955.5 (65.5)	12,350 (2776)

Table 10.7 Design Information for the Buildings

	3-Story	6-Story	9-Story
Number of Controlled Rocking Elements	2	4	4
Seismic Coefficient, Cs	0.125	0.125	0.106
Force Per Frame, kN (kips)	3615 (812.7)	7135 (1604)	9034 (2031)
Design Overturning Moment Per Frame, kN-m (k-ft)	16900 (12465)	30940 (22820)	57153 (42154)

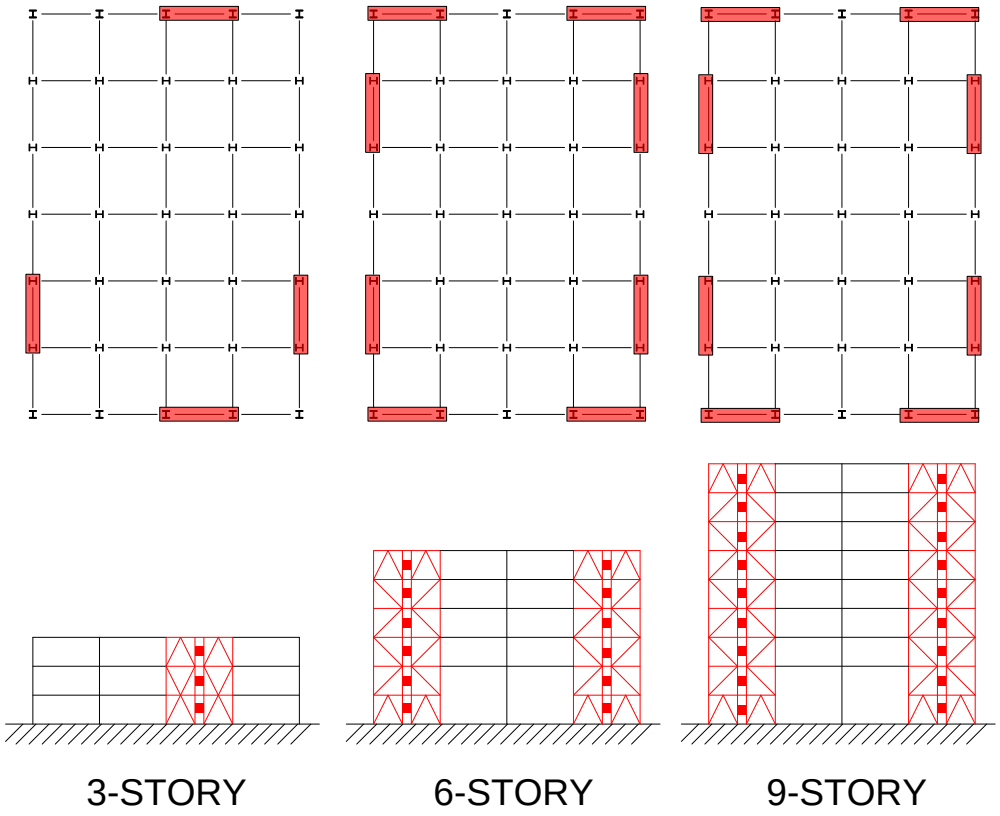

Figure 10.1 Building Plans and Elevations Used in the Sensitivity Study

10.3 Design of the Systems

The design rules given in this section were used to proportion the components and design the elements of the controlled rocking system. As part of the sensitivity study, these design rules were investigated for their ability to produce the expected performance. The design rules presented here were subsequently adjusted based on the results of the sensitivity study and the resulting design recommendations are presented in Chapter 12.

10.3.1 Proportioning the Initial Post-Tensioning Force and Fuse Capacity

The controlled rocking system is proportioned based on strength and self-centering. The factored design overturning moment per frame, M_{ovt}, was calculated in the previous section and presented in Table 10.7. The overturning resistance of the controlled rocking system comes from fuse yield capacity, V_{fp}, initial post-tensioning force, F_{pti}, and dead load, P_D, multiplied by their respective moment arms. The equation that governs the strength check is given in Equation (10.1), and includes a resistance factor assumed to be ϕ=0.9. The dead load, P_D, is the load applied to the exterior columns of the frames which is assumed to be a tributary area of 9.14m x 4.57m (30'x15') based on the assumed configuration shown in Figure 10.2.

$$\phi\left[\left(F_{pti}+0.9P_D\right)A+V_{fp}\left(A+B\right)\right]=M_{ovt} \qquad \text{(DUAL FRAME)} \qquad (10.1)$$

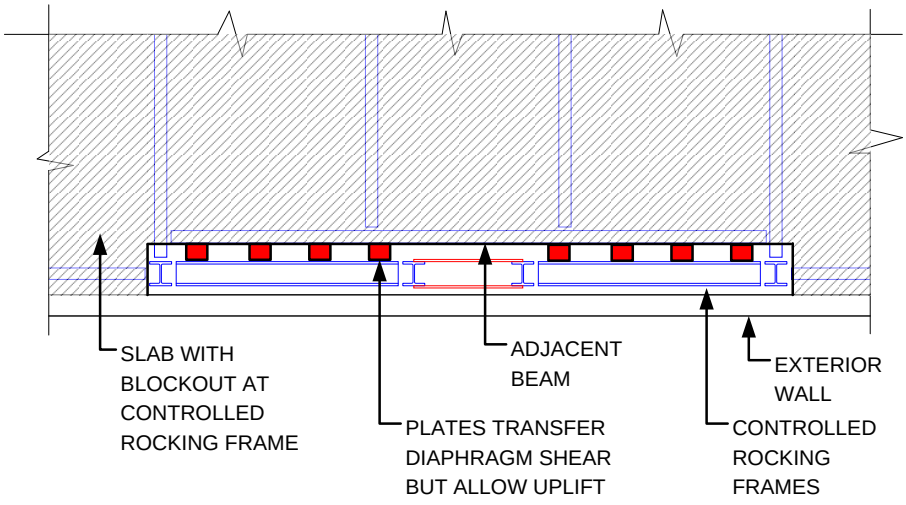

Figure 10.2 Plan View of Floor Connection to Controlled Rocking Frames Assumed in the Sensitivity Study

Proportioning the system for self-centering was one of the variables investigated as part of this study. The self-centering ratio, *SC*, is given in Equation (10.2) as the ratio of the restoring forces divided by the forces resisting self-centering motion. If the self-centering ratio is greater than one, the hysteretic response will exhibit small drifts when the forces are removed.

$$SC = \frac{\left(F_{pti} + 0.9P_D\right)A}{V_{fp}\left(A+B\right)} \qquad \text{(DUAL FRAME)} \qquad (10.2)$$

The two relationships given in Equation (10.1) and Equation (10.2) are then used to proportion the required fuse capacity and the initial post-tensioning force. Equation (10.3) gives the required fuse capacity based on the design overturning moment. The proportioning and design of the fuse is carried out first so that any overstrength built into the fuse design can be accounted for in the proportioning of the post-tensioning. Equation (10.4) was used to calculate the required initial post-tensioning force to satisfy the specified self-centering ratio, *SC*, considering the actual supplied fuse shear capacity, V_{fp}.

$$V_{fp} = \frac{M_{ovt}}{\phi\left(1-SC\right)\left(A+B\right)} \qquad \text{(DUAL FRAME)} \qquad (10.3)$$

$$F_{pti} = SC\frac{A+B}{A}V_{fp} - 0.9P_D \qquad \text{(DUAL FRAME)} \qquad (10.4)$$

10.3.2 Post-Tensioning Design

Once the initial post-tensioning force is calculated, the number of post-tensioning strands was selected. A lower bound on the initial post-tensioning stress was imposed at 20% of the nominal ultimate strength which is taken as 1862 MPa (270 ksi). The experimental program used initial stresses as low as 28% of ultimate without any related problems.

However it is advantageous to use the largest possible initial post-tensioning stress to reduce the number of strands required. An upper bound on initial post-tensioning strain was set to restrict the total post-tensioning strain to 0.85% when the frames undergo 2.5% roof drift ratio. The first post-tensioning strand wire fracture occurred at 0.85% strain in the experimental program. In this case, a simple closed form calculation was performed to assess the strain in the post-tensioning strands assuming rigid body rotation of the frames added to the initial strain. A limiting roof drift ratio of 2.5% was chosen because the parametric study discussed in the literature review (Hall et al. 2006) found a mean peak roof drift ratio of 2.5% when subjected to the hazard level that has 2% probability of exceedance in 50 years for most of configurations considered.

Equation (10.5) describes the general rule adopted for selecting the initial post-tensioning stress and Equation (10.6) includes the simplifying calculation of the post-tensioning strain at 2.5% roof drift ratio based on rigid body rotation of the frames. The number of 15 mm (0.6") diameter post-tensioning strands was calculated using Equation (10.7) with A_{Strand} = 140 mm^2 (0.217 in^2). The resulting post-tensioning design information is given in Table 10.8.

$$\sigma_{pt-init} = \left(0.0085 - \frac{\delta_{pt\,2.5\%}}{L_{pt}}\right)E_{pt} \quad \geq 0.2\sigma_u \qquad (10.5)$$

$$\sigma_{pt-init} = \left(0.0085 - \frac{0.025A}{2H_{flr}N_{flr}} \right) E_{pt} \quad \geq 0.2\sigma_u \tag{10.6}$$

$$N_{strands} = \frac{F_{pti}}{\sigma_{pt-init} A_{Strand}} \tag{10.7}$$

Table 10.8 Post-Tensioning Design Information for Each Configuration

Config-uration Number	Initial PT Force, F_{pti}, kN (kips)	Provided Number of 15 mm Strands	PT Area, mm^2 (in^2)	Initial PT Stress / Fu
1	2026 (455)	17	2380 (3.69)	0.46
2	3613 (812)	20	2800 (4.34)	0.69
3	7060 (1587)	36	5040 (7.81)	0.75
4	2409 (542)	20	2800 (4.34)	0.46
5	3139 (706)	54	7560 (11.72)	0.22
6	4292 (965)	24	3360 (5.21)	0.69
7	3394 (763)	33	4620 (7.16)	0.39
8	2317 (521)	17	2380 (3.69)	0.52
9	1906 (428)	16	2240 (3.47)	0.46
10	4129 (928)	23	3220 (4.99)	0.69
11	3378 (759)	19	2660 (4.12)	0.68
12 and 13 are omitted				
14	1550 (348)	13	1820 (2.82)	0.46
15	2744 (617)	16	2240 (3.47)	0.66
16	3147 (707)	54	7560 (11.72)	0.22
17	3613 (812)	20	2800 (4.34)	0.69
18	3613 (812)	20	2800 (4.34)	0.69
19	3613 (812)	20	2800 (4.34)	0.69

10.3.3 Fuse Design

The fuse design consists of selecting the thickness, *t*, link length, *L*, link depth, *b*, and number of links, N_{links}. It was assumed that there were two fuses at each floor so the number of fuses, N_{fuses}, is equal to two times the number of floors. The fuse yield force was assumed to be σ_{fy}=310MPa (45 ksi) for an A36 steel. It was demonstrated in the experimental program that the fuses with *L/t* ratios of 22.4 did not buckle as they were displaced up to 19% shear strain across the link. This ratio was used for most of the configurations. The fuse design information is included in Table 10.9.

$$V_{fp} = \frac{4}{9}\frac{b^2 t}{L}\sigma_{fy} N_{links} N_{fuses} \tag{10.8}$$

Table 10.9 Fuse Design Information for Each Configuration

Config-uration Number	Fuse Thickness, *t*, mm (in)	Fuse Link Length, *L*, mm (in)	Link Depth at Ends, *b*, mm (in)	Number of Links Per Fuse, N_{links}	V_{fp} Provided, kN (kips)
1	31.8 (1.25)	711 (28)	107 (4.2)	4	1681 (378)
2	31.8 (1.25)	711 (28)	102 (4.02)	4	3081 (693)
3	31.8 (1.25)	711 (28)	113 (4.46)	4	5688 (1279)
4	31.8 (1.25)	711 (28)	113 (4.45)	3	1416 (318)
5	44.5 (1.75)	406 (16)	76 (3.01)	14	2468 (555)
6	31.8 (1.25)	711 (28)	108 (4.25)	3	2583 (581)
7	44.5 (1.75)	406 (16)	77 (3.02)	17	3017 (678)
8	31.8 (1.25)	711 (28)	103 (4.06)	4	1571 (353)
9	31.8 (1.25)	711 (28)	109 (4.28)	4	1746 (393)
10	31.8 (1.25)	711 (28)	114 (4.48)	3	2870 (645)
11	31.8 (1.25)	711 (28)	104 (4.09)	4	3189 (717)
12 and 13 are omitted					
14	31.8 (1.25)	711 (28)	104 (4.11)	5	2013 (452)
15	31.8 (1.25)	711 (28)	112 (4.4)	4	3691 (830)
16	31.8 (1.25)	711 (28)	109 (4.28)	17	2474 (556)
17	31.8 (1.25)	711 (28)	102 (4.02)	4	3081 (693)
18	31.8 (1.25)	711 (28)	102 (4.02)	4	3081 (693)
19	31.8 (1.25)	711 (28)	102 (4.02)	4	3081 (693)

10.3.4 Designing Frame Members

The frame was designed using a capacity design approach described in the following chapter. As shown in Figure 11.34, the left frame in the dual frame configuration is designed and then the frame member sizes are mirrored for use in the right frame. The maximum forces for the fuses were applied to the frame as shown on the right of Figure 11.34. The post-tensioning is considered as an elastic element in the frame model and the lateral loads are calculated to produce the maximum post-tensioning force, F_{ptu}. The calculation of the lateral load factor, γ, is given in Equation (11.5) for and Equation (11.6) for the dual frame configuration and Equation (11.7) for the single frame configuration.

Three different lateral load distributions, shown in Figure 11.34 and Figure 11.35, were considered in an effort to capture the range of inertial load distributions that might control frame member design forces. The approach used for designing the frame members in the sensitivity study was to use the worst case effects of load case IT1 and IT2 for column design and the worst case effects of load cases UT1, UT2, RL1, and RL2 in brace and beam design. The resulting axial forces, shear forces, and moments were not

amplified. Member design checks for tension, compression, flexure, shear, and flexure-axial interaction were conducted for all frame members using AISC 360-05 (2005).

10.3.5 Resulting Designs for Each Configuration

Five representative examples of the frame design and system proportioning are presented here in figure form. Figure 10.3 shows the first three configurations which are three-story, six-story, and nine-story examples of the dual frame configuration. Figure 10.4 shows two single frame configurations for the three-story building, and the six-story building. The brace sizes for the single frame configuration are larger than those for the dual frame configuration because the post-tensioning force in the single frame is larger than the post-tensioning force in one of the dual frames. It is also shown that the brace forces for the three-story frames are larger than the six-story or nine-story frames. This is because the three-story building only used two frames in each direction, whereas the six-story and nine-story buildings were designed using four frames in each direction.

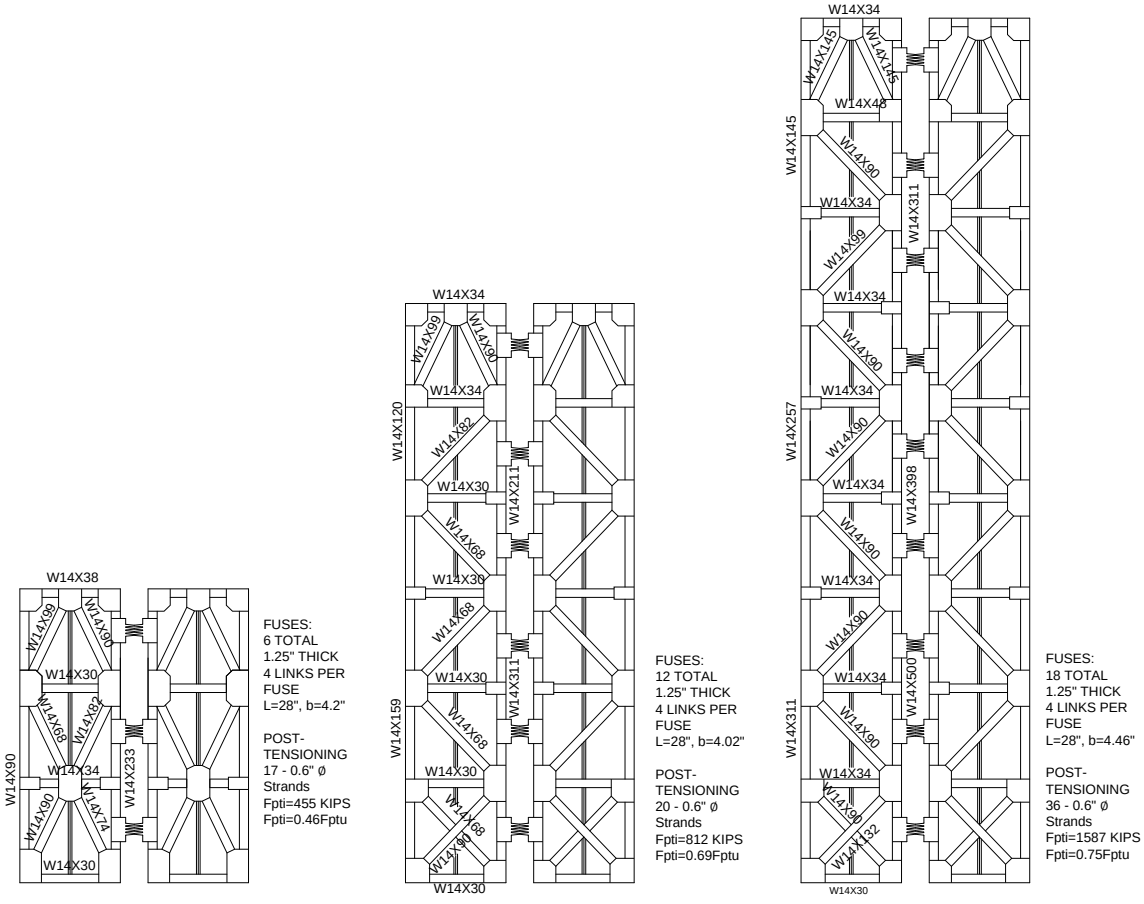

Figure 10.3 Frame Designs for Configuration 1 (Left) Configuration 2 (Middle) and Configuration 3 (Right)

The dual frame configurations shown in Figure 10.3 have the fuses located at the mid-height of each floor. In this case, the fuses apply significant forces to the interior frame columns and require larger interior column section sizes as compared to

configurations with the fuses located at the floor lines. However, depending on the floor construction, locating the fuses between the floors may allow easier replacement after larger earthquakes. If floor construction allows access to the fuses at the floor line, it is suggested to locate the fuses at the floor level to optimize the frame design.

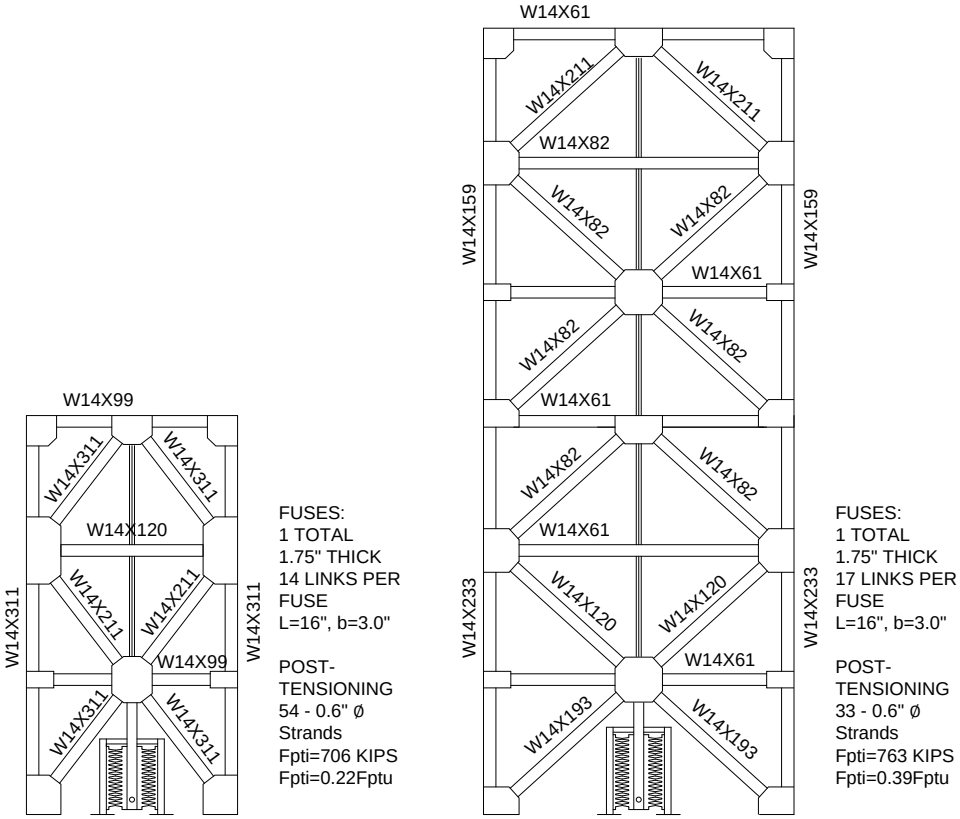

Figure 10.4 Frame Designs for Configuration 5 (Left) and Configuration 7 (Right)

10.4 Description of the Analyses

10.4.1 Computational Model

The computational model described in Chapter 6 was used for the sensitivity study with two modifications. First leaning columns were included in the model as shown in Figure 10.5. The gravity loads and mass tributary to the controlled rocking frames were applied to the leaning column nodes. Second, the majority of the analyses used a diaphragm element instead of struts. This condition, which is shown in plan view in Figure 10.2, represents a floor beam adjacent to the rocking frame that connects to the rocking frame bean through a connection that is stiff in shear, but allows uplifting motion.

The fuse model was the same as described in Chapter 6 and shown graphically in Figure 6.5. The base springs and post-tensioning are also the same as described in Chapter 6.

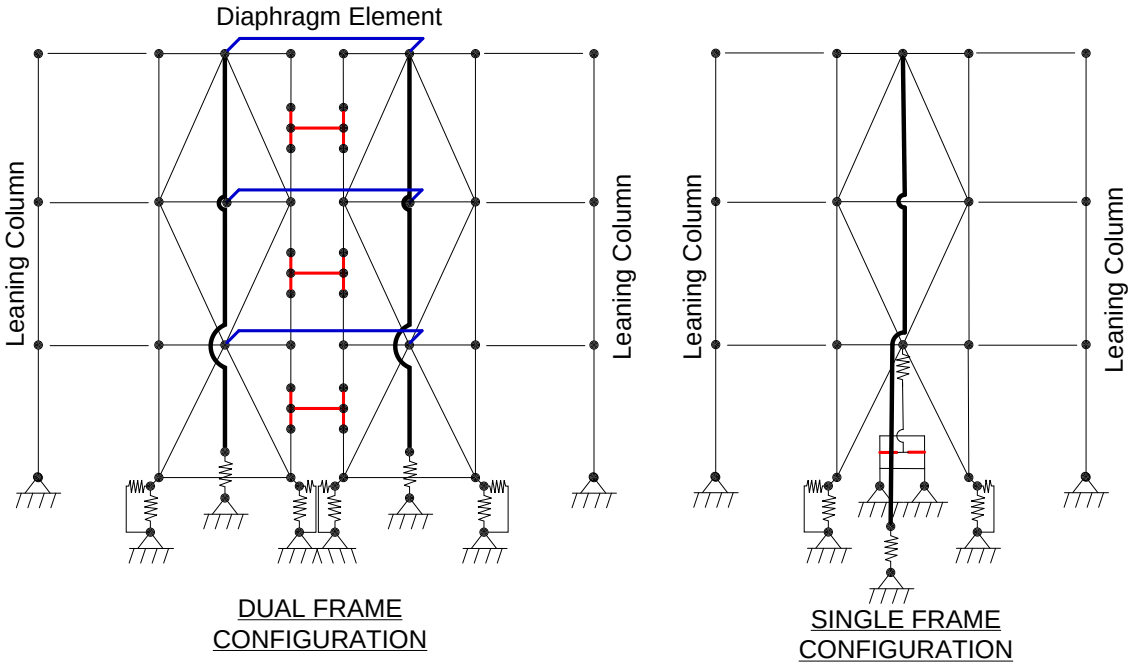

Figure 10.5 Drawings of the Computational Model Used for the Sensitivity Study

10.4.2 Ground Motions and Dynamic Analyses Parameters

A subset of the ground motions from the ATC 63 project were used (FEMA P695 2009). One component of each of the twenty-two ground motion records was selected from the far field set. The choice of which of the two horizontal components to use was made at random and the resulting set of ground motions is given in Table 10.10. Scaling of the ground motions was conducted using the method recommended in FEMA P695 (2009). Ground motions were first normalized based on peak ground velocity with factors that are included in Table A-4D of FEMA P695 (2009). Then, the median of the ground motion set was found by fitting a lognormal distribution to the spectral accelerations associated with each period. The medians of the lognormal distributions were assembled into a median spectral acceleration which is shown in Figure 10.6. Scale factors were calculated based on the ratio of the design spectral acceleration to this median spectral acceleration and the entire set of ground motions was scaled using the resulting scale factor.

Table 10.10 Ground Motion Information

ID	Earthquake			Recording Station Name	NEHRP Site Class	Distance Closest to Plane	Component Name Selected	Recorded PGAmax (g)	Normal-ization Factor
	M	Year	Name						
12011	6.7	1994	Northridge	Beverly Hills - Mulhol	D	17.2	NORTHR/ MUL279	0.52	0.65
12012	6.7	1994	Northridge	Canyon Country-WLC	D	12.4	NORTHR/ LOS000	0.48	0.83
12041	7.1	1999	Duzce, Turkey	Bolu	D	12	DUZCE/ BOL000	0.82	0.63
12052	7.1	1999	Hector Mine	Hector	C	11.7	HECTOR/ HEC090	0.34	1.09
12061	6.5	1979	Imperial Valley	Delta	D	22	IMPVALL/ H-DLT352	0.35	1.31
12062	6.5	1979	Imperial Valley	El Centro Array #11	D	12.5	IMPVALL/ H-E11230	0.38	1.01
12071	6.9	1995	Kobe, Japan	Nishi-Akashi	C	7.1	KOBE/ NIS000	0.51	1.03
12072	6.9	1995	Kobe, Japan	Shin-Osaka	D	19.2	KOBE/ SHI090	0.24	1.10
12081	7.5	1999	Kocaeli, Turkey	Duzce	D	15.4	KOCAELI/ DZC180	0.36	0.69
12082	7.5	1999	Kocaeli, Turkey	Arcelik	C	13.5	KOCAELI/ ARC000	0.22	1.36
12091	7.3	1992	Landers	Yermo Fire Station	D	23.6	LANDERS/ YER270	0.24	0.99
12092	7.3	1992	Landers	Coolwater	D	19.7	LANDERS/ CLW-LN	0.42	1.15
12101	6.9	1989	Loma Prieta	Capitola	D	15.2	LOMAP/ CAP090	0.53	1.09
12102	6.9	1989	Loma Prieta	Gilroy Array #3	D	12.8	LOMAP/ G03000	0.56	0.88
12111	7.4	1990	Manjil, Iran	Abbar	C	12.6	MANJIL/ ABBAR--T	0.51	0.79
12121	6.5	1987	Superstition Hills	El Centro Imp. Co.	D	18.2	SUPERST/ B-ICC000	0.36	0.87
12122	6.5	1987	Superstition Hills	Poe Road (temp)	D	11.2	SUPERST/ B-POE360	0.45	1.17
12132	7.0	1992	Cape Mendocino	Rio Dell Overpass	D	14.3	CAPEMEND/ RIO270	0.55	0.82
12141	7.6	1999	Chi-Chi, Taiwan	CHY101	D	10	CHICHI/ CHY101-N	0.44	0.41
12142	7.6	1999	Chi-Chi, Taiwan	TCU045	C	26	CHICHI/ TCU045-N	0.51	0.96
12151	6.6	1971	San Fernando	LA - Hollywood Stor	D	22.8	SFERN/ PEL180	0.21	2.10
12171	6.5	1976	Friuli, Italy	Tolmezzo	C	15.8	FRIULI/ A-TMZ000	0.35	1.44

Four scaling levels were selected: 50% probability of exceedance in 50 years, 10% in 50 years, 2% in 50 years, and 150% of the 2% in 50 years event. Scaling was based on the spectral acceleration at different periods depending on the height of the building. The three-story, six-story, and nine-story buildings were scaled based on the 1.0 second, 1.5 second, and 2.0 second spectral accelerations respectively. These periods were intended to represent the approximate dominant period of the inelastic system. The resulting scale factors are given in Table 10.11.

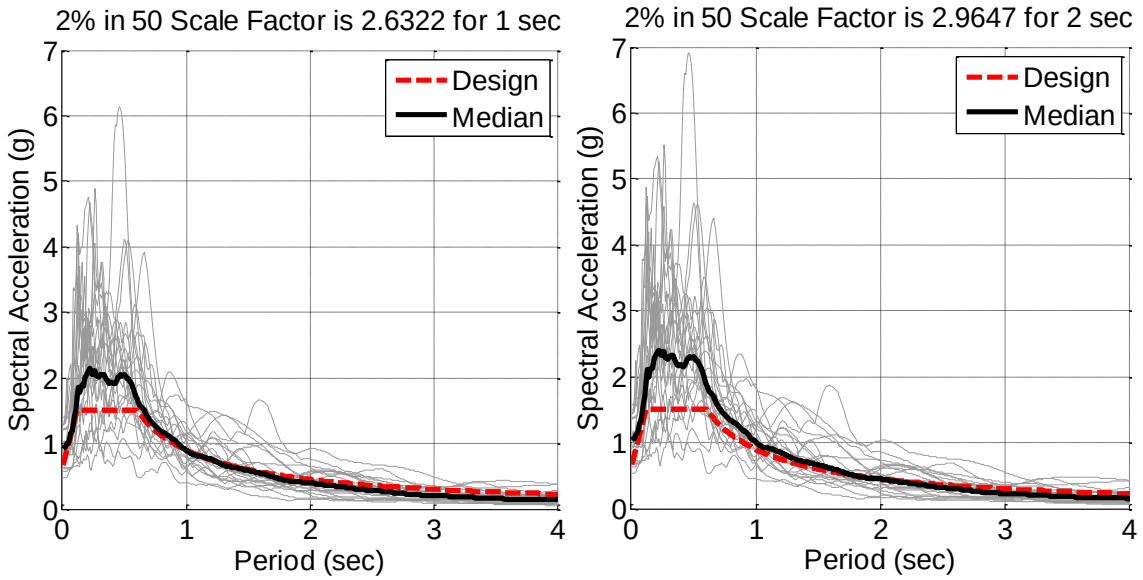

Figure 10.6 Example of Scaling for the Event with 2% Probability of Exccedance in 50 Years Based on 1 Second Period (Left) and 2 Second Period (Right)

Table 10.11 Summary of Scale Factors

Hazard Level	3 story Building Scaled Based on 1.0 second period	6 story Building Scaled Based on 1.5 second period	9 story Building Scaled Based on 2.0 second period
50% in 50 Years Event	0.76	0.78	0.86
10% in 50 Years Event	1.75	1.79	1.98
2% in 50 Years Event	2.63	2.68	2.96
1.5 x 2% in 50 Years	3.95	4.02	4.44

The sensitivity study analyses were conducted using the OpenSees software (Mazzoni et al. 2009). The tributary horizontal mass was assigned to the leaning column nodes. Vertical mass was assigned to the exterior frame columns to match the tributary area of 9.14m x 4.57m (30'x15'). Vertical mass consistent with the tributary frame weight was assigned to the nodes of the frame interior columns. Gravity load was applied to the leaning column nodes and the frame exterior column nodes based on their tributary area. Rayleigh damping was applied with 2% damping at a period equal to 0.1 times the number of stories (0.3 sec for 3 story, 0.6 sec for 6 story, and 0.9 sec for 9

story), and at a period that was three times this period (0.9 sec for 3 story, 1.8 sec for 6 story, and 2.7 sec for 9 story).

10.4.3 Response Indices

A number of response indices were examined to assist in achieving the objectives of the sensitivity study which include verifying expected performance of the controlled rocking system as designed for a range of applications. Median and standard deviation were calculated for each response index for the set of 22 ground motions at a given hazard level. Response measures include:

- Peak roof drift ratio and peak uplift ratio
- Initial elastic period, simple building code formula for period, secant period at 1% drift, secant period at 2% drift, dominant periods from FFT of the displacement histories.
- Peak base shear
- Peak vertical reactions and vertical accelerations
- Peak fuse shear strain
- Peak post-tensioning strain
- Residual roof drift, residual interstory drifts, and residual uplift
- Magnitude of global uplift defined as the lesser uplift experienced by the two columns in a frame.
- Total hysteretic absorbed energy
- Ratio of member axial force demand to design axial force (results are discussed in Chapter 11).

Values for residual quantities are calculated by taking the mean of the response over the last 5 seconds. The last 5 seconds of every input ground motion has zero acceleration.

10.5 Example Results for Configuration 1

10.5.1 Example Time History Analysis Results

An example of the time history results is presented for one of the analyses out of the 1496 computational simulations conducted. Configuration 1 was selected which is a three-story building with frame width divided by fuse width ratio, A/B=2.5, self-centering ratio, SC=1.1, bay width equal to 9.14m (30’), a diaphragm element connecting the midspan of the beams, and no post-tensioning seating losses. The hazard level with 2% probability of exceedance in 50 years was selected for the ground motion ID = 120121, which is the Northridge earthquake as measured at the Canyon Country – WLC recording station.

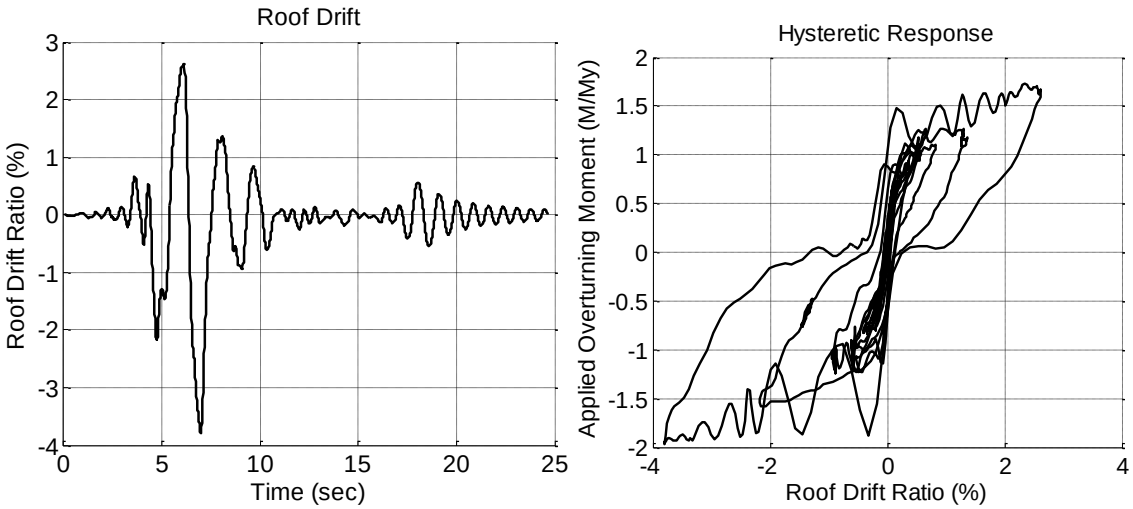

Figure 10.7 Roof Drift History (Left) and Hysteretic Response (Right) for the Example Analysis

Figure 10.7 shows the roof drift history and hysteretic response obtained from the example analysis. A peak roof drift of 3.8% was experienced at a time approximately equal to 7 seconds. The left side of Figure 10.7 demonstrates that the residual drift was zero as the roof drift oscillates around zero during the last 5 seconds of the simulation for which the ground acceleration is zero. The shape of the hysteresis loops matches the expected response with near full self-centering associated with SC=1.1 demonstrated as the drifts return to near zero when applied overturning moment is zero. After some of the large excursions the post-tensioning strands yielded as shown in Figure 10.8 causing the self-centering ability to reduce.

During the three largest cycles, the mean period was found to be 1.9 seconds. A discrete fast fourier transform of the displacement history identified 2.05 seconds as the dominant period which is the period of the largest cycle. The displacement history free vibration during the last 5 seconds of the ground motion was found to have a period of approximately 0.75 seconds. Higher frequency oscillations are also shown to occur in the overturning moment (Figure 10.7) and the first floor drift ratio (Figure 10.9). These higher frequency vibrations had a period of approximately 0.23 sec. The values for free vibration period, and higher frequency vibrations match the first mode and second mode eigenvalues calculated from the computational model which corresponded to periods of 0.68 sec and 0.21 sec.

The fuse hysteretic behavior shown in Figure 10.8 appears to exhibit degradation, but a closer examination of the response shows that the fuse is not representing a buckled state. After the large displacement cycles, the fuse response returns to full hysteretic behavior. The post-tensioning behavior shown on the right of Figure 10.8 demonstrates that the post-tensioning reached the yield force for this ground motion with 2% chance of exceedance in 50 years. The peak post-tensioning strain is 1.1%.

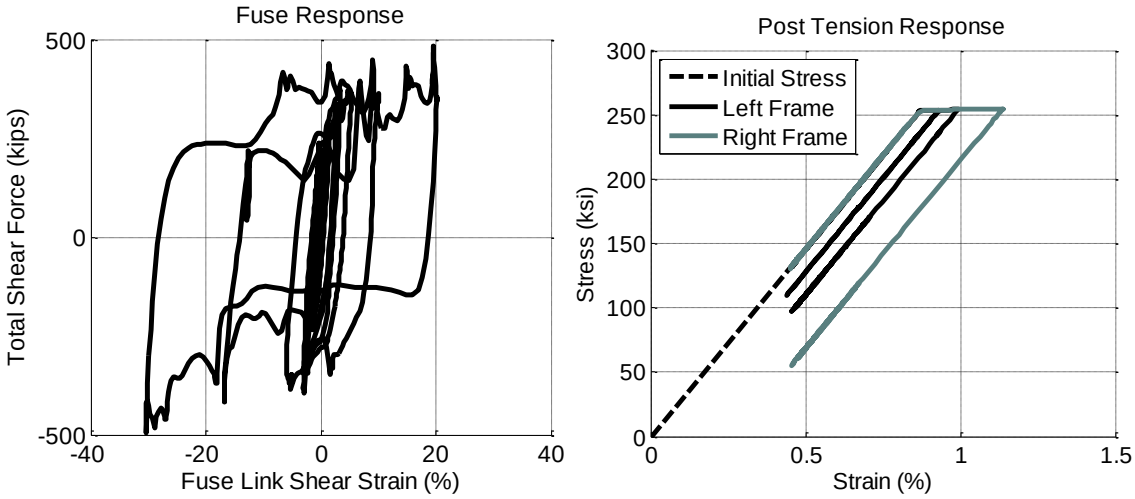

Figure 10.8 Fuse Hysteretic Response (Left) and Post-Tensioning Response for the Example Analysis

The total drift ratios for each floor relative to the ground are plotted against time and against the roof drift ratio in Figure 10.9. These two plots show the strong dominance of the first mode as the drifts of the floors are nearly identical through the simulation. The second mode is also clear in these plots as the oscillations of the 1st floor.

Global uplift is shown in Figure 10.10 and defined as the lesser uplift experienced by the two columns in a frame. If both columns are uplifted, this value will be greater than zero. The global uplift at given time steps may be larger than zero implying that one of the frames lifted off the ground. This occurs when the post-tensioning has yielded such that the post-tensioning force at zero drift is less than the fuse capacity.

It was found that the horizontal and vertical accelerations of the column nodes had frequency content that was too high to accurately investigate with the time step used in these analyses. The accelerations oscillated between large positive and large negative values at each time step.

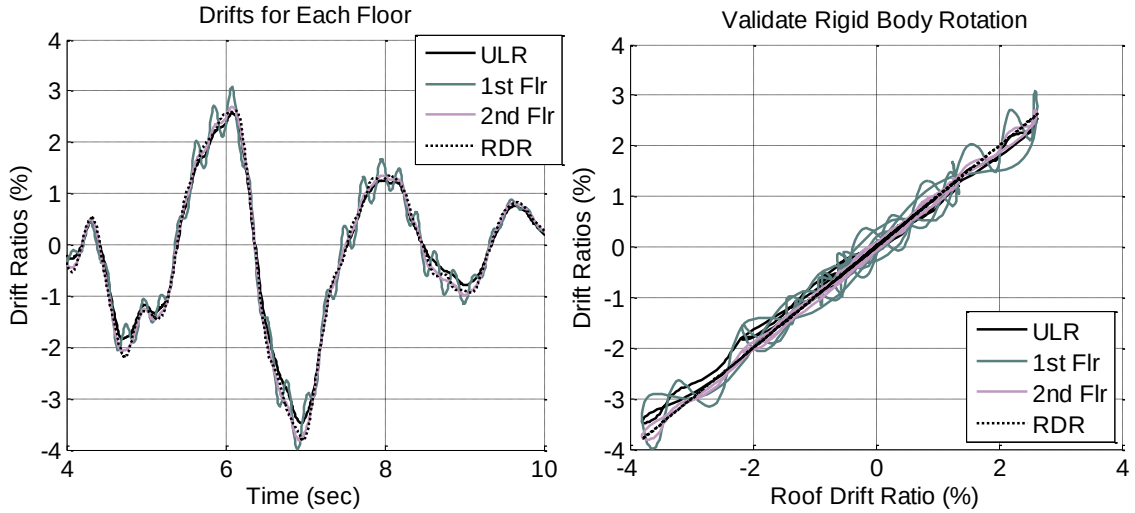

Figure 10.9 Excerpt of the Drift History for Each Floor (Left), and Comparison of Different Drift Ratios (Right) for the Example Analysis

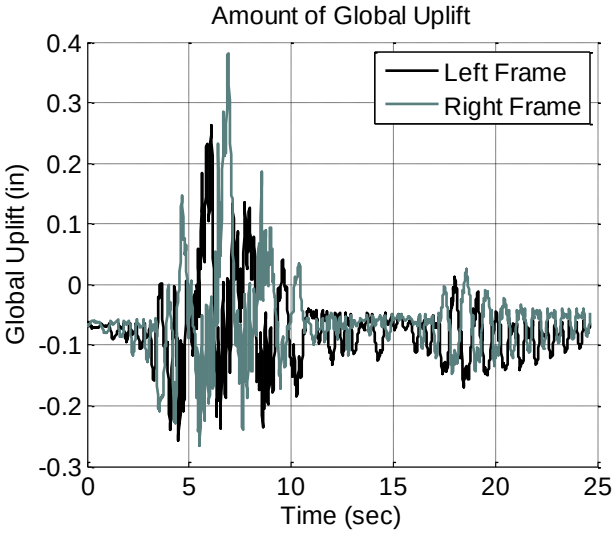

Figure 10.10 Global Uplift of Both Frames for the Example Analysis

10.5.2 Example Summary Results for Configuration 1

Example results for one configuration are shown in this section with plots that contain data points for every analysis conducted for this configuration. Lines showing the median and median plus one standard deviation of the data are also shown on each plot. In the following sections, only the median and median plus one standard deviation lines are shown to allow clear comparisons between configurations. The first configuration was chosen which is described at the beginning of the previous section. Figure 10.11 shows the peak roof drift ratios and peak uplift ratios for all 88 analyses run for this configuration. The vertical axis is spectral acceleration and shows increasing severity of the hazard level as the spectral acceleration increases.

As expected, the median uplift ratios and the median roof drift ratios are almost identical because the dominant mode of displacement is rigid body rotation of the frames. The median peak roof drift ratio is 0.69%, 1.71%, 2.91%, and 4.72% for the hazard levels with 50% probability of exceedance in 50 years, 10% in 50 years, 2% in 50 years, and 1.5 x 2% in 50 years respectively. The current building code which is based on the 10% in 50 years hazard level, imposes a limit on the drift equal to 2%. Using the median and standard deviation and assuming a lognormal distribution, it was calculated that there is a 34% probability that the roof drift ratio will exceed 2% for the 10% in 50 years event. This limit state and associated objectives are discussed in the following section.

The peak global uplift values shown in Figure 10.12, demonstrate that at the hazard level with 2% probability of exceedance in 50 years and above, global uplift starts to occur. This is related to the amount of yielding in the post-tensioning, but provides a targeted examination of the probability of this limit state being breached. The residual roof drift ratios shown on the right of Figure 10.12 demonstrates that this configuration is well proportioned to eliminate residual drifts up to the 2% in 50 years hazard level, but starts to allow residual drifts for larger events.

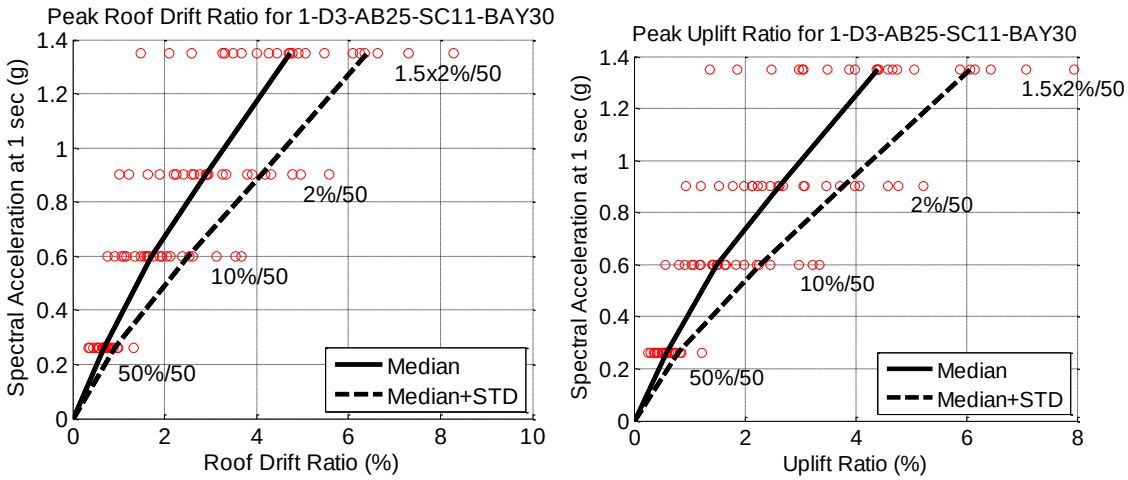

Figure 10.11 Peak Roof Drift Ratios (Left) and Peak Uplift Ratios (Right) for Example Configuration

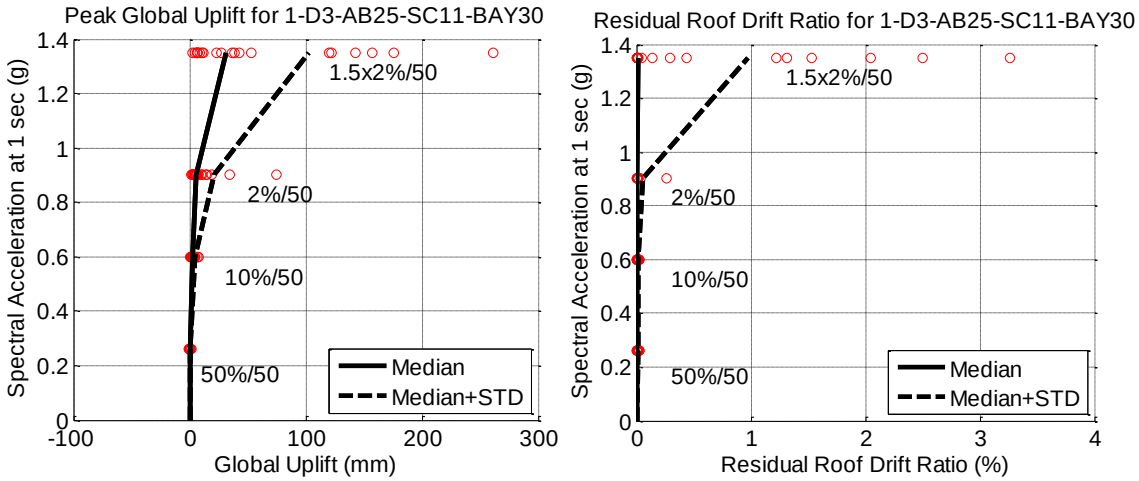

Figure 10.12 Peak Global Uplifts (Left) and Residual Roof Drifts (Right) for the Example Configuration

The roof drift ratio for the hazard level with 2% probability of exceedance in 50 years has a median of 2.91% which is larger than the roof drift ratio of 2.5% assumed for this hazard level in the calculation of the allowable initial post-tensioning strain. Regardless of this discrepancy, Figure 10.13 shows that the peak post-tensioning strain for the 2% in 50 years hazard level was found to have a median value of 0.89%. According to Table 8.9, if the post-tensioning strain is less than 0.9%, there is a 94% probability that less than 3% of the post-tensioning wires will fracture. It is expected, therefore, that the majority of ground motions scaled to the 2% in 50 years hazard level would cause less than 3% of the wires to fracture which can produce good system performance..

The median values for peak fuse shear strain were 3.5%, 12.4%, 22.4%, and 37.3% for the hazard levels with 50% probability of exceedance in 50 years, 10% in 50 years, 2% in 50 years, and 1.5 x 2% in 50 years respectively. Although the fuses did not

reach fracture in the testing program described in previous chapters, fracture of the fuses was achieved in the fuse component tests conducted at Stanford University. Fracture of the fuse links occurred at shear strains across the link between 30% and 46.5% with a mean value of 37.6% as discussed below. Using the median and standard deviation of the assumed lognormal distribution for peak fuse shear strain for the 2% in 50 years event, a 23.8% probability of reaching 30% fuse shear strain was calculated. This is a relatively small chance that the fuses would reach the levels of shear strain in which fractures occurred in component tests.

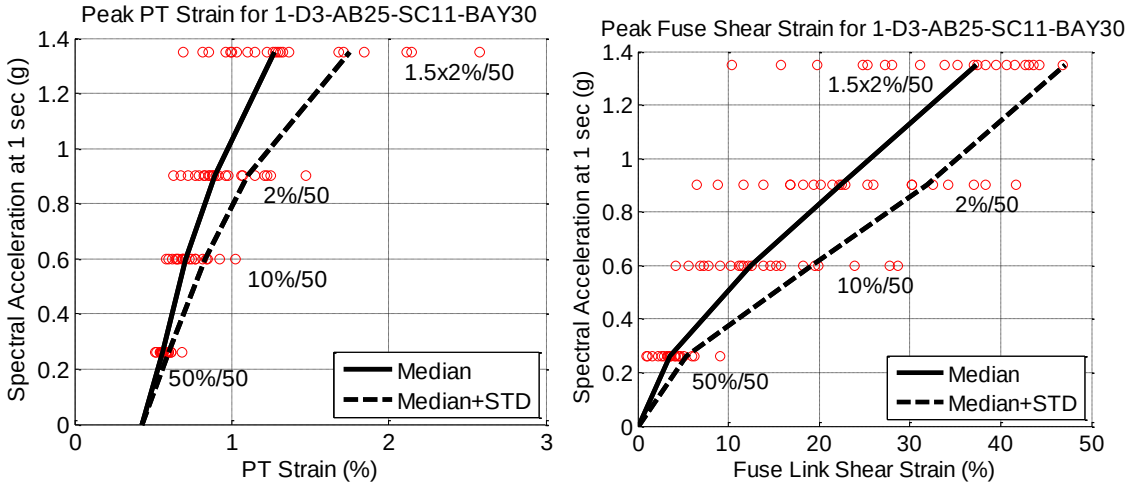

Figure 10.13 Peak Post-Tensioning Strains (Left) and Peak Fuse Shear Strains (Right) for the Example Configuration

The peak base shear and peak overturning moment shown in Figure 10.14 demonstrate the need for different design rules for columns and braces in the elastic braced frame. The peak overturning moments have medians that range from 1.4 to 2.3 times the moment associated with yield. This factor is consistent with the overstrength created by additional post-tensioning force above the initial force, and strain-hardening in the fuses. The peak base shears on the other hand demonstrate that the shear forces experienced by the frame are significantly larger than the yield base shear, which is calculated assuming an inverted triangular lateral load distribution. Since the lateral load distribution varies throughout the test, the peak story shears can be several times larger than the predicted yield base shear with inverted triangular lateral load distribution. The resulting member forces and recommendations are included in Chapter 11.

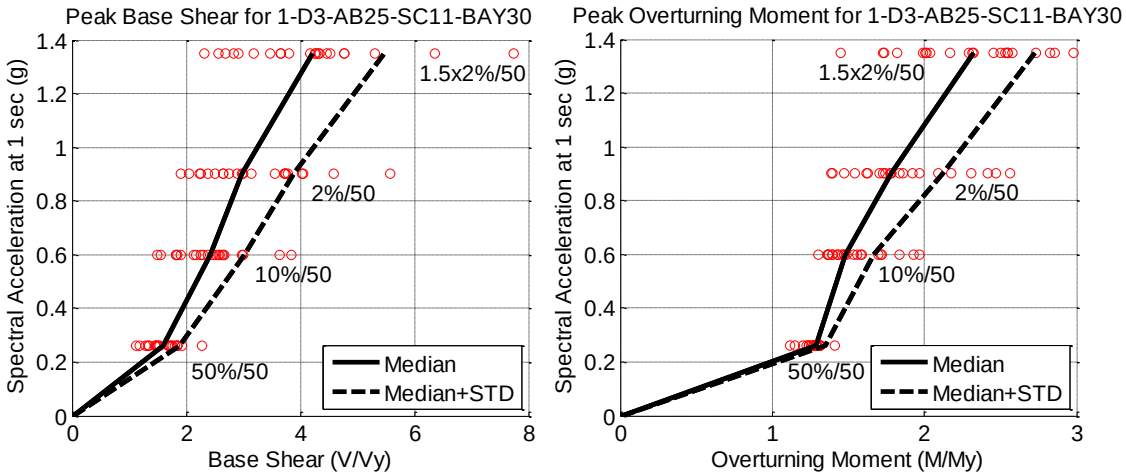

Figure 10.14 Peak Base Shears (Left) and Peak Overturning Moments (Right) for the Example Configuration

10.6 Interpretation of the Analyses Results

10.6.1 Assessing the Performance of the Designed Systems

To assess the performance of the configurations that were designed and proportioned using the design rules described earlier in this chapter, it is necessary to define the possible undesirable limit states along with targets for restricting these limit states for given hazard levels. A list of undesirable limit states includes:

- Fracture of the fuse links
- Yielding of the post-tensioning strands and fracture of post-tensioning wires
- Global uplift in which the frame as a whole lifts off the support
- Frame member reaches a strength limit state (discussed in following chapter)
- Connection reaches some limit state (related to frame member limit states discussed in the following chapter)

It is noted that the frame members and connections are assumed to be elastic in the computational model. Methods for reliably achieving elastic frame performance are discussed in the following chapter. For the purposes of examining system response, however, it is assumed that since the frame elements are modeled elastically, slight changes in the stiffness of these members will have negligible effect compared to the larger rigid body rotations of the frames, deformations in the post-tensioning, and inelasticity in the fuse elements. Therefore, if the designed member sizes in this section are inadequate and a slightly larger size is required, it is assumed that the difference in the section properties will have negligible impact on the response measures.

Fracture of the fuse links is an undesirable limit state that removes the major contributor to energy dissipation in the system. The experimental program described in previous chapters did not experience any fractures in the fuses. However, the fuse component tests conducted at Stanford University applied larger shear strains across the

fuse links and were able to produce fractures. Fractures in the fuses for SS5, SS9, SS10, and SS11 were experienced at 46.5%, 38.5%, 30.0%, 35.5% fuse link shear strain respectively. The mean fuse link shear strain at fracture was 37.6%. More information about these specimens is included in Chapter 8.

Since fuse fracture is a highly undesirable limit state, it is advantageous to have a low probability of reaching strains where fracture is likely. For the four butterfly fuse tests conducted at Stanford there is approximately a 50% chance of fuse link fracture occurring at a fuse link shear strain of 37.6%. The goal, therefore, was to have a low probability of exceeding 37.6% fuse link shear strain at the hazard level that has a 2% probability of exceedance in 50 years. Table 10.12 gives the probabilities that the fuses will reach this level of fuse link shear strain. As shown in Table 10.12, configuration 4 has the largest probability (16%) of reaching this limit state for the 2% in 50 years hazard level. This represents a probability of exceedance that is approximately the same as one standard deviation above the median for a normal distribution or 16%.

Table 10.12 Probabilities of Exceeding Fuse Shear Strain Limit

Model	50% in 50 $P(\gamma_{Fuse}>37.6\%)$	10% in 50 $P(\gamma_{Fuse}>37.6\%)$	2% in 50 $P(\gamma_{Fuse}>37.6\%)$	1.5x(2% in 50) $P(\gamma_{Fuse}>37.6\%)$
1	0.0%	1%	12%	33%
2	0.0%	2%	4%	13%
3	0.0%	1%	2%	9%
4	0.0%	1%	16%	45%
5	0.2%	1%	7%	34%
6	0.0%	2%	7%	22%
7	0.4%	6%	15%	42%
8	0.0%	2%	13%	36%
9	0.0%	1%	11%	32%
10	0.0%	2%	7%	19%
11	0.0%	2%	4%	16%
12 and 13 are omitted				
14	0.0%	1%	7%	15%
15	0.0%	1%	2%	11%
16	0.0%	0%	1%	8%
17	0.0%	2%	8%	22%
18	0.0%	2%	8%	22%
19	0.0%	0%	1%	9%

The post-tensioning strains at wire fracture are discussed in Chapter 8. Based on the types of anchorage and installation procedures used in the experimental program, it was found that limiting the post-tensioning strand strain to 1% leads to an 80% probability that fewer than 5% of the post-tensioning wires will fracture as given in Table 8.9. As shown in Chapter 5, Specimen A4 had 5% of the post-tensioning wires fracture

with minor effect on strength and self-centering. Depending on the self-centering ratio, wire fractures exceeding 5% of the total post-tensioning wires may start to deteriorate the ability of the post-tensioning to overcome the fuse yield strength, resulting in global uplift. Since this limit state is based on a lower probability of adverse effects compared to the fuse fracture, a more relaxed probability of exceedance is appropriate. A target of limiting the probability of exceeding 1% strain in the post-tensioning to 50% or the median value is adopted for the hazard level that has a 2% probability of exceedance in 50 years.

Table 10.13 shows that the designed configurations satisfy this limit. The largest probability of exceeding 1% strain are given for configuration 16 to be 47%.

Table 10.13 Probabilities of Exceeding Post-Tension Strain Limit

Model	50% in 50 $P(\varepsilon_{PT}>1.0\%)$	10% in 50 $P(\varepsilon_{PT}>1.0\%)$	2% in 50 $P(\varepsilon_{PT}>1.0\%)$	1.5x(2% in 50) $P(\varepsilon_{PT}>1.0\%)$
1	0%	3%	37%	77%
2	0%	1%	30%	62%
3	0%	0%	16%	46%
4	0%	2%	40%	79%
5	0%	4%	39%	78%
6	0%	1%	22%	58%
7	0%	4%	28%	63%
8	0%	2%	41%	79%
9	0%	4%	43%	81%
10	0%	0%	19%	56%
11	0%	1%	33%	62%
12 and 13 are omitted				
14	0%	3%	44%	80%
15	0%	0%	33%	63%
16	0%	6%	47%	81%
17	0%	0%	15%	53%
18	0%	0%	16%	53%
19	0%	0%	0%	0%

Goals for the roof drift ratio included limiting the roof drift ratio to 2% for the event that has 10% probability of exceedance in 50 yearsto be consistent with limits in the current U.S. building code (ASCE 2005). Goals for the peak roof drift ratios during the 50% in 50 years event and the 2% in 50 years event were assigned as 0.75% and 3.0%, respectively. Table 10.14 shows that the largest probability of exceeding the goal for the 10% in 50 years event is 51% and all others are below 50%.

Table 10.14 Probabilities of Exceeding Roof Drift Limits

Model	50% in 50 P(RDR>0.75%)	10% in 50 P(RDR>2.0%)	2% in 50 P(RDR>3.0%)
1	38%	34%	43%
2	36%	27%	26%
3	34%	20%	22%
4	34%	32%	44%
5	48%	44%	51%
6	34%	26%	26%
7	52%	42%	36%
8	52%	30%	43%
9	36%	36%	44%
10	35%	23%	21%
11	38%	29%	28%
12 and 13 are omitted			
14	46%	34%	43%
15	38%	23%	22%
16	47%	51%	58%
17	44%	31%	29%
18	45%	31%	29%
19	28%	16%	16%

Global uplift is defined above as the lesser uplift of the two columns in a frame and is equal to the height that a frame is lifted off the ground. Global uplift less than 25 mm (1") will not cause significant loss in energy dissipating capacity and thus is used as a limit state for the 25 in 50 hazard level. The probabilities of exceeding a global uplift limit state of 25 mm (1") are tabulated in Table 10.15. It is shown in Table 10.15 that the probability of exceeding this limit state is at most 28% for the hazard level with 2% probability of exceedance in 50 years.

Table 10.15 Probabilities of Exceeding Global Uplift Limits

Model	50% in 50 P(Up>25 mm)	10% in 50 P(Up>25 mm)	2% in 50 P(Up>25 mm)	1.5x(2% in 50) P(Up>25 mm)
1	0%	0%	7%	51%
2	0%	4%	12%	39%
3	0%	1%	10%	24%
4	0%	1%	11%	40%
5	0%	0%	10%	34%
6	0%	1%	10%	30%
7	0%	0%	8%	40%
8	0%	1%	7%	48%
9	0%	0%	10%	56%
10	0%	3%	12%	35%
11	0%	5%	13%	40%
12 and 13 are omitted				
14	0%	0%	26%	70%
15	0%	2%	28%	59%
16	0%	0%	13%	45%
17	0%	2%	7%	28%
18	0%	2%	7%	28%
19	0%	0%	0%	0%

The dispersion of the peak roof drifts were calculated as the standard deviation of the log of the peak roof drift ratios. The resulting dispersions are tabulated in Table 10.16 and provide a measure of the record-to-record variability in peak roof drifts. The dispersions are shown to increase as the hazard level increases with a maximum value of 0.78 for configuration 15.

Table 10.16 Dispersions of the Peak Roof Drifts

Model	50% in 50 $\sigma_{(LN\ Peak\ RDR)}$	10% in 50 $\sigma_{(LN\ Peak\ RDR)}$	2% in 50 $\sigma_{(LN\ Peak\ RDR)}$	1.5x(2% in 50) $\sigma_{(LN\ Peak\ RDR)}$
1	0.31	0.42	0.44	0.41
2	0.39	0.47	0.50	0.58
3	0.47	0.57	0.56	0.49
4	0.34	0.41	0.46	0.42
5	0.54	0.38	0.43	0.43
6	0.40	0.49	0.50	0.55
7	0.44	0.49	0.47	0.52
8	0.29	0.40	0.41	0.37
9	0.35	0.42	0.45	0.42
10	0.38	0.45	0.47	0.53
11	0.40	0.48	0.53	0.69
12 and 13 are omitted				
14	0.33	0.43	0.41	0.45
15	0.36	0.45	0.54	0.78
16	0.56	0.39	0.48	0.42
17	0.41	0.51	0.52	0.52
18	0.41	0.51	0.52	0.52
19	0.43	0.45	0.46	0.45

10.6.2 Building Height Study

Three building heights were examined, three-story, six-story, and nine-story. As described in Table 10.2, the configurations included in this study were all dual frame configurations with geometric ratio, A/B=2.5, thicker non-buckling fuses, self-centering ratio, SC=1.1, no seating losses, a diaphragm element connecting the centers of the two frames floor beams, and a 9.14m (30') bay width. The analyses configuration numbers included in this study were 1, 2, and 3 consisting of the three-story, six-story, and nine-story buildings respectively.

Figure 10.15 shows minor differences between the hysteretic response of the controlled rocking system with three different heights. The system experiences uplift at a smaller roof drift ratio as the building becomes shorter. The roof drift ratio at uplift was found to be 0.133%, 0.189%, and 0.255% for the three-story, six-story, and nine-story frames respectively. The taller frames are therefore experiencing larger roof drifts due to frame deformations. In particular, the taller frames experience global bending deformations that cause additional roof displacement not experienced by the shorter frames. The shorter frames also experience larger post-yield stiffness. This is due to the ratio of post-tensioning area between the different configurations. The shorter

configurations have larger post-tensioning strain demands for a given roof drift ratio because the length of the strands is shorter. The initial strains in the post-tensioning were proportioned accordingly, resulting in initial stresses in the strands equal to 46%, 69%, and 75% of the ultimate stress for the three-story, six-story, and nine-story buildings respectively. Using higher initial stresses in the taller frames allowed the use of fewer post-tensioning strands, and the area of strands in the six-story and nine-story buildings was 117% and 212% of that used in the three-story building. The fact that the increase in post-tensioning strand area was less than the increase in height from one configuration to the next leads to a reduction in the post-yield stiffness with height.

The peak roof drifts on the right of Figure 10.15, show that all three configurations had similar roof drift ratios through the event that has 10% probability of exceedance in 50 years which has a spectral acceleration of 0.6g. Above this level, the shorter structures experience larger peak roof drift ratios. The post-tensioning strains shown on the left of Figure 10.17 are in the elastic range for the smaller earthquake levels, but at the 2% in 50 years event (spectral acceleration of 0.9) and above, the post-tensioning was experiencing yield in almost half of the time histories. As shown in Figure 10.17, the peak post-tensioning strains are larger in the shorter buildings relative to the taller buildings for spectral accelerations at 2% in 50 years and above. For this reason, the strands are more likely to yield in the shorter buildings during large earthquake events, which leads to larger drifts.

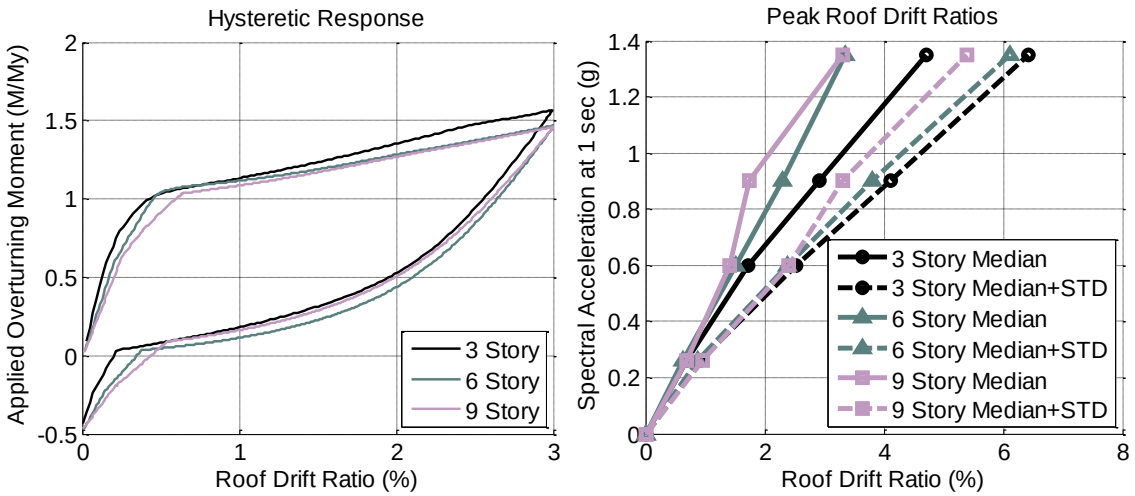

Figure 10.15 Hysteretic Behaviors (Left), and Peak Roof Drift Ratios (Right) for Varying Heights

Figure 10.16 shows that the median residual roof drift ratios were negligible for all three configurations at all considered spectral accelerations including 1.5 times the hazard level with 2% probability of exceedance in 50 years. The median plus one standard deviation values are relatively large at 1.5 times the 2% in 50 years event, but only the six-story building has appreciable residual roof drift at the 2% in 50 years event. The controlled rocking system successfully eliminated residual drifts up to the 2% in 50 years event with a less than 50% probability that the six-story building will experience some residual drift at this hazard level. The right side of Figure 10.16 shows that the

median response had only negligible peak global uplift up to the 2% in 50 years hazard level.

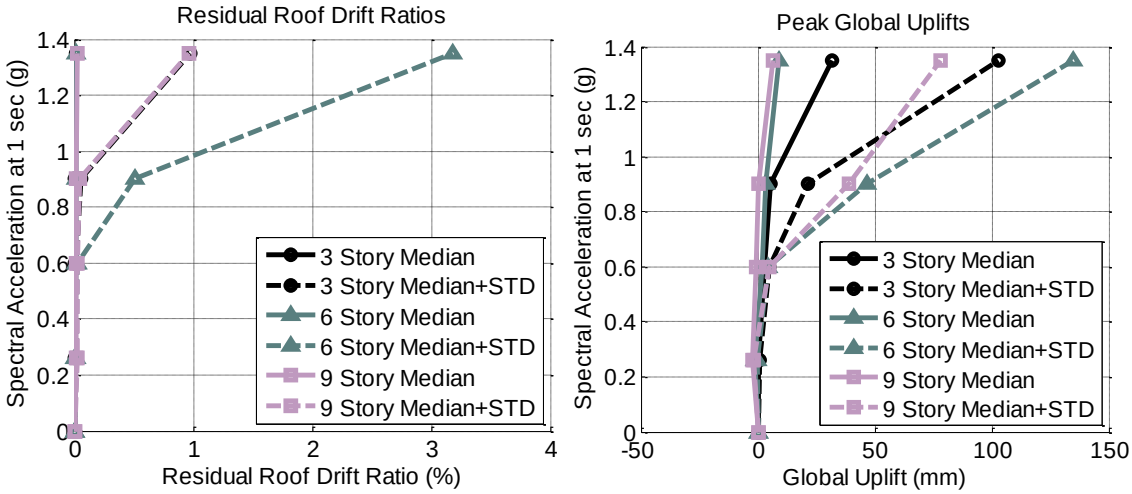

Figure 10.16 Residual Roof Drift Ratios (Left) and Peak Global Uplifts (Right) for Varying Heights

Figure 10.17 demonstrates that these three configurations adequately avoid the limit states outlined in the previous section for post-tensioning strand yield, post-tensioning strand wire fracture, and fuse link fracture. This is shown by the fact that all three configurations have a median post-tensioning strand strain less than 1% when subjected to ground motions with 2% probability of exceedance in 50 years (S_a=0.9), which implies that there is a low probability that more than 5% of the post-tensioning wires will fracture, and that the median plus one standard deviation fuse link shear strain is less than 37.6%, indicating a low probability that the fuse links will fracture.

The effect of increasing building height on post-tensioning strain appears as an increase in the slope of the spectral acceleration vs. peak post-tensioning strain relationship. For a given uplift ratio at the base of the frames, the amount of strain in the strands is inversely proportional to the length of the strands. The initial post-tensioning strain was adjusted for this fact with the intent that the peak post-tensioning strains would be approximately equal at the 2% in 50 years hazard level.

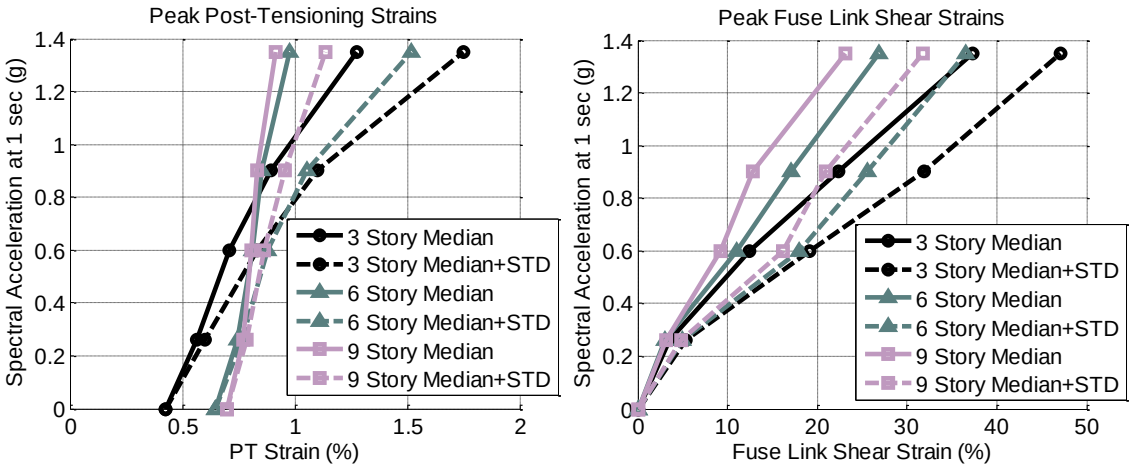

Figure 10.17 Peak Post-Tensioning Strains (Left) and Peak Fuse Link Shear Strains (Right) for Varying Heights

The peak base shear and peak overturning moment shown in Figure 10.18, give some indication on the effect of building height on frame design. The peak base shear relates to the peak force in the first floor braces, and is shown to increase well above the yield base shear with increasing building height and hazard level. The overturning moment is related to column axial forces and is shown to be much more consistent as the hazard level increases and across the different heights.

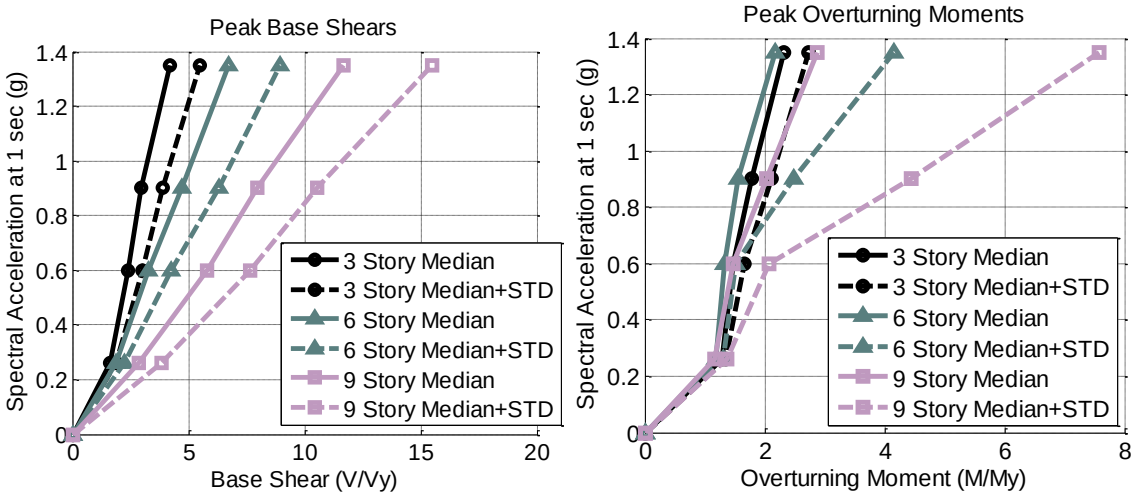

Figure 10.18 Peak Base Shears (Left) and Peak Overturning Moments (Right) for Varying Heights

10.6.3 Single Frame vs. Dual Frame Configuration

Both single frame and dual frame configurations were investigated in the experimental program. The differences in their dynamic response are discussed in this section. As described in Table 10.4, the dual frame configurations included in this study had a geometric ratio, A/B=2.5. All configurations used thicker non-buckling fuses, self-centering ratio, SC=1.5, no seating losses, and a diaphragm element connecting the centers of the two frames floor beams. All configurations used 9.14m (30') bay width

except for the three-story single frame configuration which used 20’ bay width to reduce the post-tension strain demand so that the initial post-tensioning stress was greater than 0.2 times the ultimate stress. The analyses configuration numbers included in this study were 4, 5, 6, and 7 consisting of the three-story dual frame, three-story single frame, six-story dual frame, and six-story single frame respectively.

The hysteretic response on the left of Figure 10.19 shows several differences in the load-deformation response of the different configurations. The stiffnesses of the single frame configurations were larger than the dual frame configurations. The three-story single frame single frame configuration was especially stiff after uplift and yielding compared to the other configurations. The post-yield stiffness is controlled by the post-tensioning component and is sensitive to the total area of post-tensioning strands and the length of the post-tensioning strands. The three-story single frame configuration had the largest area of post-tensioning for all configurations considered here with 54 strands and the shorter strand length compared to the six-story single frame configuration which had 33 strands. The three-story dual frame configuration had 40 total strands which is less than the 48 strands for the six-story dual frame configuration. The three-story dual frame configuration has a larger post-yield stiffness than the six-story dual frame due to shorter strand lengths.

Because the single frame configurations have post-tensioning components with greater stiffness, the overturning moment at fuse yield is slightly greater for single frame configurations compared to the dual frame configurations. The left side of Figure 10.19 also demonstrates that the single frame systems exhibit almost no drift when the forces are removed. In the dual frame configurations, the drifts that remain when the force is removed are related to elastic frame deformations due to yield level forces that remain in the fuses along the height of the frames. In the single frame configuration, the fuses are concentrated at the base of the frames which does not cause any residual elastic deformations in the frames.

The peak roof drift ratios shown on the right of Figure 10.19 and the peak uplift ratios shown on the left of Figure 10.20 are found to be more dependent on building heights than frame configuration. The peak global uplifts shown on the right of Figure 10.20 were small at the hazard level with 2% probability of exceedance in 50 years for all four configurations considered here.

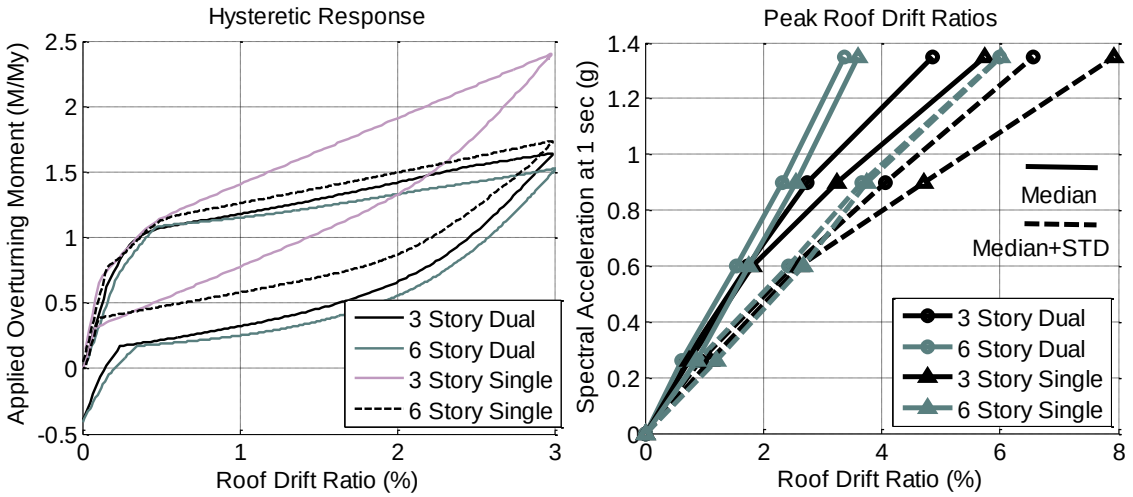

Figure 10.19 Hysteretic Behavior (Left) and Peak Roof Drift Ratios (Right) for Single and Dual Frame Configurations

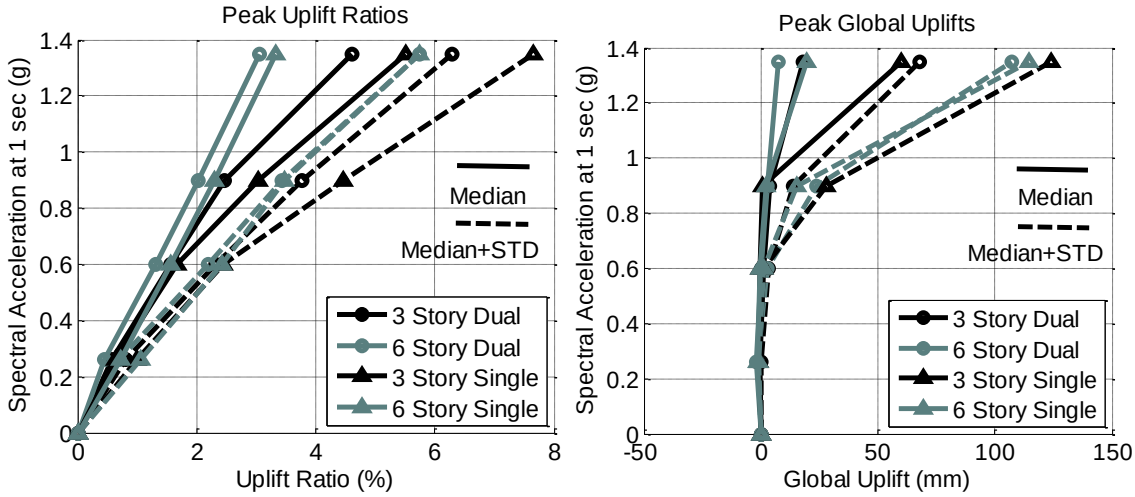

Figure 10.20 Peak Uplift Ratios (Left), and Peak Global Uplifts (Right) for Single and Dual Frame Configurations

Even though the monotonic loading of Figure 10.19 demonstrated that the roof drifts at zero force are smaller for the single frame configurations, there was not a similar clear trend in the residual roof drift ratios and residual uplift ratios shown in Figure 10.21. This implies that the residual deformations are more related to the amount of post-tensioning strand yielding than the load-deformation shape before post-tensioning yield.

The peak post-tensioning strains shown on the left of Figure 10.22 illustrate the effect of post-tensioning strand length and frame width. For a given uplift ratio, the amount of strain in the post-tensioning strands is proportional to frame width and inversely proportional to original strand length. Therefore shorter buildings and wider frames will experience more post-tensioning strain for a given uplift ratio. This is shown in Figure 10.22, by decreasing slope of the post-tensioning strain demand as the spectral acceleration increases. The initial strain was designed to create post-tensioning strain

demand around 0.85% at the hazard level with 2% probability of exceedance in 50 years. Figure 10.22 shows that the median post-tensioning strain demand at the 2% in 50 years hazard level is similar among the four configurations and less than 1%.

The peak fuse link shear strain demands shown on the right of Figure 10.22 show relatively little dependence on frame configuration. The peak base shears and peak overturning moments were found to be larger for the single frame configuration compared to the dual frame as shown in Figure 10.23.

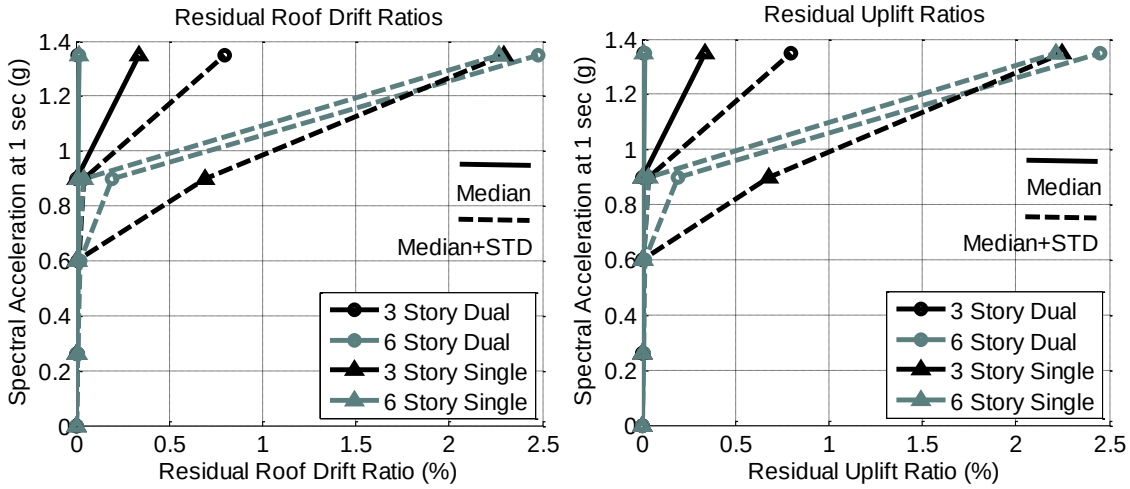

Figure 10.21 Residual Roof Drift Ratios (Left) and Residual Uplift Ratios (Right) for Single and Dual Frame Configurations

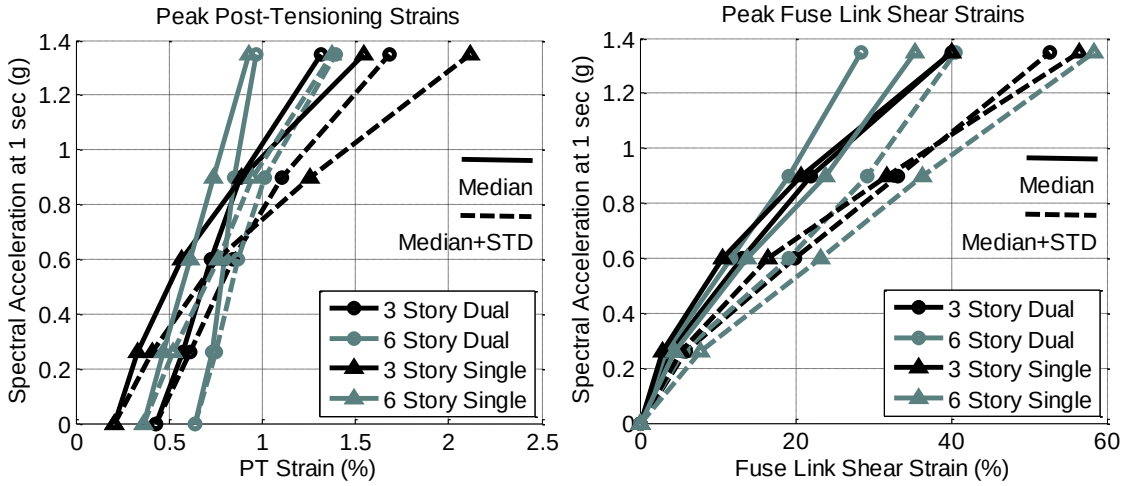

Figure 10.22 Peak Post-Tensioning Strains (Left) and Peak Fuse Link Shear Strains (Right) for Single and Dual Frame Configurations

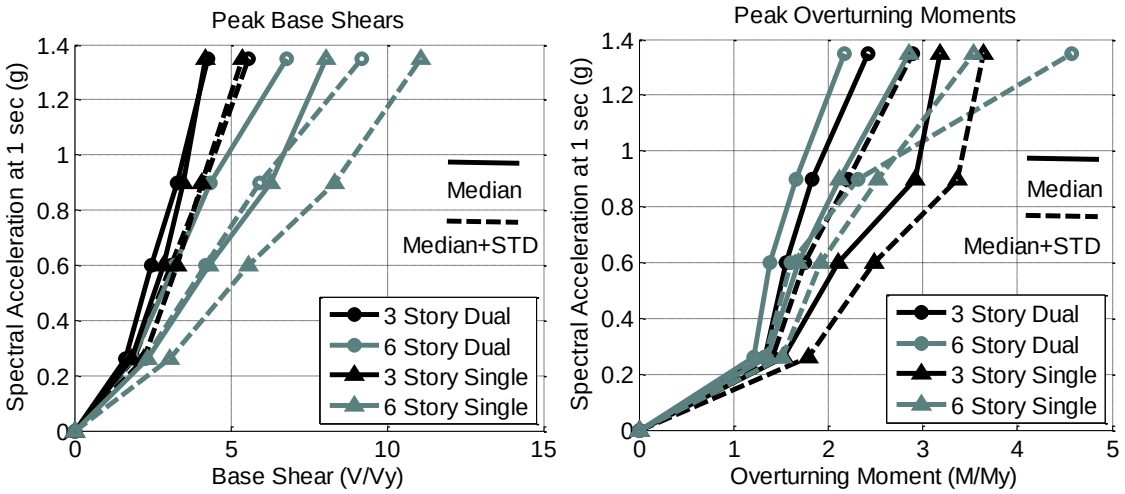

Figure 10.23 Peak Base Shears (Left) and Peak Overturning Moments (Right) for Single and Dual Frame Configurations

10.6.4 A/B Geometric Ratio Study

The ratio of the frame width, A, to the fuse width, B, was studied by varying the geometric ratio A/B between 1.5 and 3.5. Six configurations were considered, three that were three-story, and three that were six-story, with A/B ratios of 1.5, 2.5, and 3.5. As described in Table 10.3, the configurations included in this study were all dual frame configurations with thicker non-buckling fuses, self-centering ratio, SC=1.1, no seating losses, a diaphragm element connecting the centers of the two frames floor beams, and a 9.14m (30') bay width. The fuse link length was also held constant at 711 mm (28") as given in Table 10.9. The analyses configuration numbers included in this study were 8, 1, 9, 10, 2, and 11 for the three-story buildings with A/B=1.5, 2.5, and 3.5, and the six-story buildings with A/B=1.5, 2.5, and 3.5 respectively.

As shown on the left of Figure 10.24, the hysteretic shape does not change much with the varying A/B ratio. As a result, the peak roof drift ratios were also fairly independent of the A/B ratio as shown on the right of Figure 10.24. In fact, the median values for most of the response indices up to the 2% probability of exceedance in 50 years event were relatively unaffected by the A/B ratio as shown in Figure 10.24, Figure 10.25, Figure 10.26, and Figure 10.28.

The shear strain across the fuse link as derived in Equation (3.14) and Equation (3.15), is shown to be dependent only on the link length, L_{link}, and not on the width between the interior columns, B. Because the link length was constant through these analyses, the fuse shear response was similar in all runs. The median peak fuse shear strain for the three-story buildings subjected to the 2% in 50 years hazard level was found to be 15.3%, 17.0%, and 19.8% for A/B ratios of 1.5, 2.5, and 3.5 respectively. This trend in which the larger A/B ratios created slightly larger fuse link shear strains was also noted in the six-story buildings. It is expected that varying the link length may have a more pronounced effect on fuse response than varying the A/B ratio.

The peak post-tensioning strains show the trend that larger A/B ratios experience larger post-tensioning strains because the width of the frame is greater, leading to larger uplift for the same amount of roof drift.

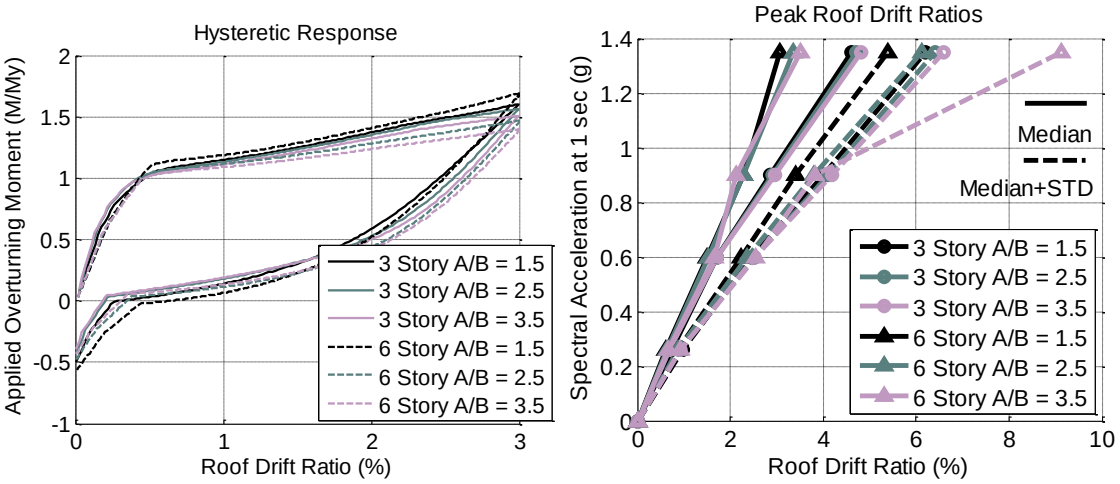

Figure 10.24 Hysteretic Response (Left) and Peak Roof Drift Ratios (Right) for Varying A/B Ratios

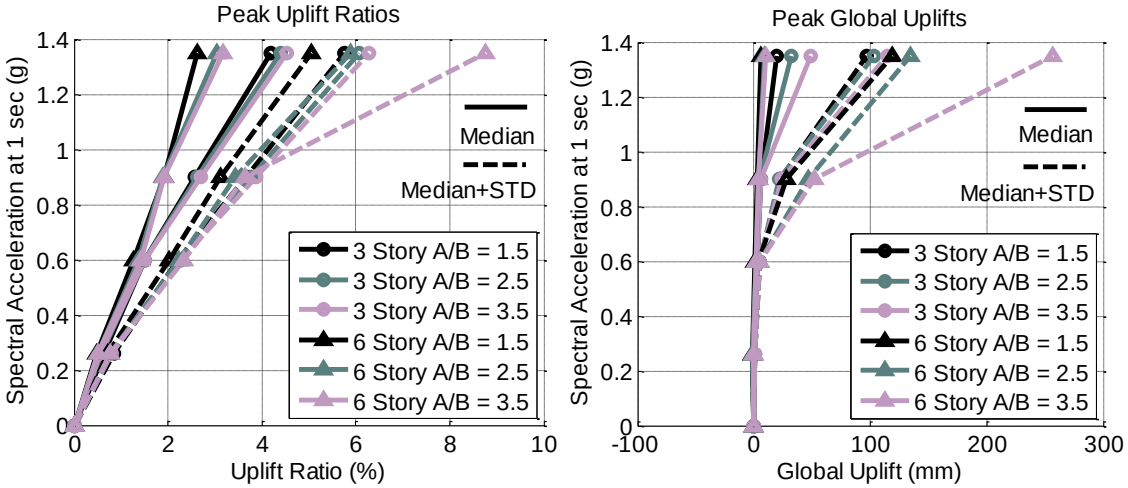

Figure 10.25 Peak Uplift Ratios (Left) and Peak Global Uplifts (Right) for Varying A/B Ratios

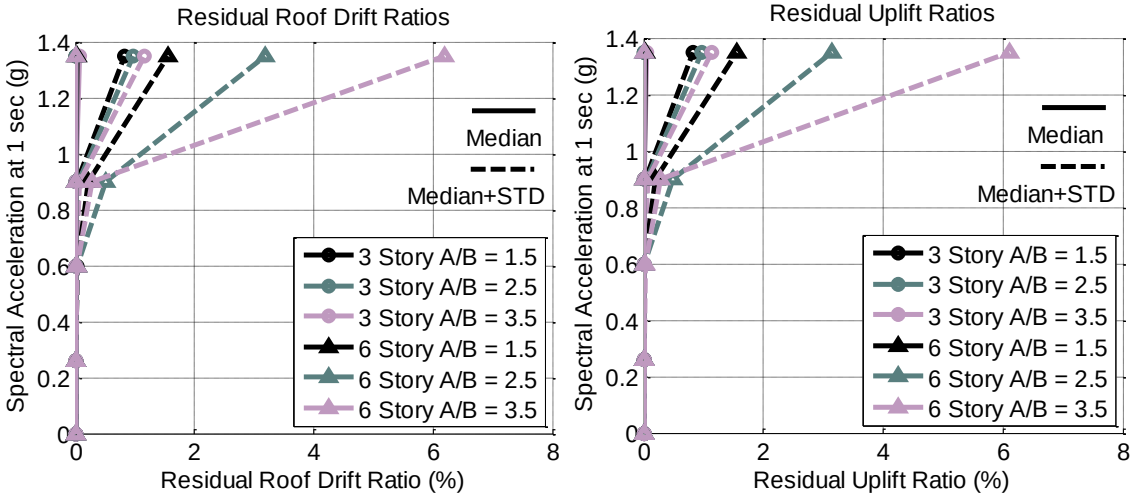

Figure 10.26 Residual Roof Drift Ratios (Left) and Residual Uplift Ratios (Right) for Varying A/B Ratios

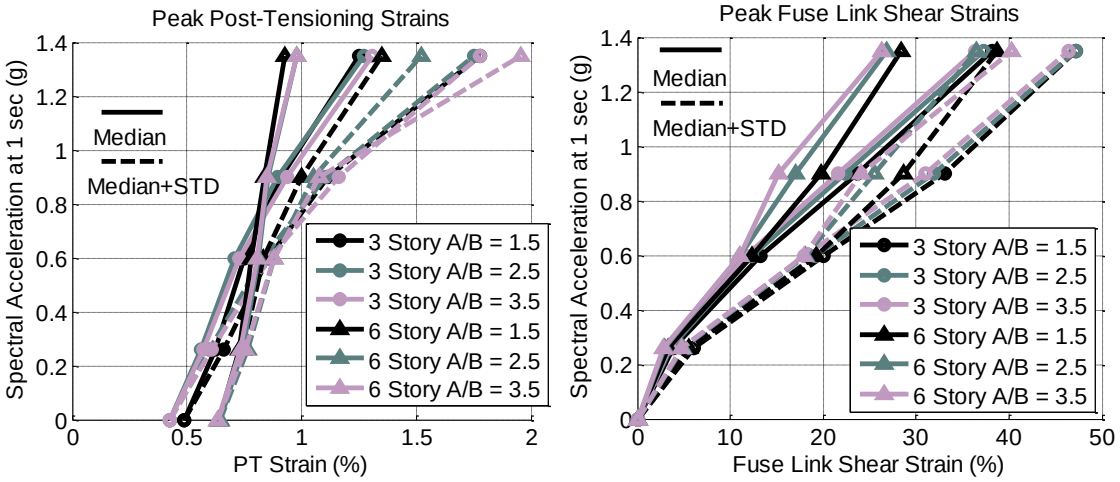

Figure 10.27 Peak Post-Tensioning Strains (Left) and Peak Fuse Link Shear Strains (Right) for Varying A/B Ratios

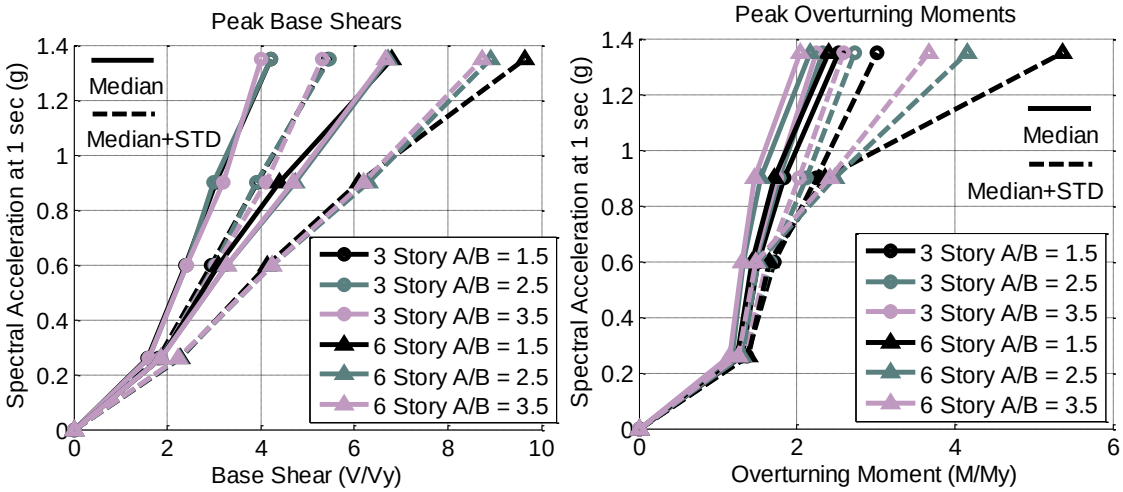

Figure 10.28 Peak Base Shears (Left) and Peak Overturning Moments (Right) for Varying A/B Ratios

10.6.5 Self-Centering Ratio Study

The relative proportioning of the fuse and initial post-tensioning force were investigated by varying the self-centering ratio between 0.75 and 1.5 for the three and six-story dual frame configurations. As described in Table 10.3, the configurations included in this study were all dual frame configurations with geometric ratio, A/B=2.5, thicker non-buckling fuses, no seating losses, a diaphragm element connecting the centers of the two frames floor beams, and a 9.14m (30') bay width. The analyses configuration numbers included in this study were 14, 1, 4, 15, 2, and 6 for the three-story buildings with SC=0.75, 1.1, and 1.5, and the six-story buildings with SC=0.75, 1.1, and 1.5 respectively.

The left side of Figure 10.29 shows the effect of varying the SC ratio on the hysteretic behavior of the controlled rocking system. The self-centering ratios greater than one have small drift at zero force whereas the three-story and six-story configurations that have SC=1.5 have flag-shaped behavior that dips below the horizontal

axis on load reversal. It is also shown that the systems with larger SC ratios have more post-tensioning and therefore the post-yield slope is greater.

It is shown on the right of Figure 10.29 and the left of Figure 10.30 that the changes in hysteretic behavior did not cause much change in peak roof drifts or peak uplifts. It is concluded that reducing the hysteretic absorbed energy in the range considered here, did not have significant effect on peak roof drifts. Furthermore, larger self-centering ratios may be possible without adversely affecting drift demands. The response of SDOF systems with no energy dissipating component was studied in Chapter 9.

The right side of Figure 10.31 shows that the lower SC ratios are more susceptible to the global uplift limit state. The self-centering ratio, SC=0.75, actually violates the global uplift check described in Chapter 3 in that the initial post-tensioning force is less than the fuse shear capacity for these two configurations. It is not surprising, then, that the global uplift for the 2% probability of exceedance in 50 years hazard level was 49 mm, and 74 mm for the three-story and six-story buildings at median plus one standard deviation. Because of strain hardening in the fuses, the configurations with SC=1.1 also experienced some global uplift for one standard deviation above the median.

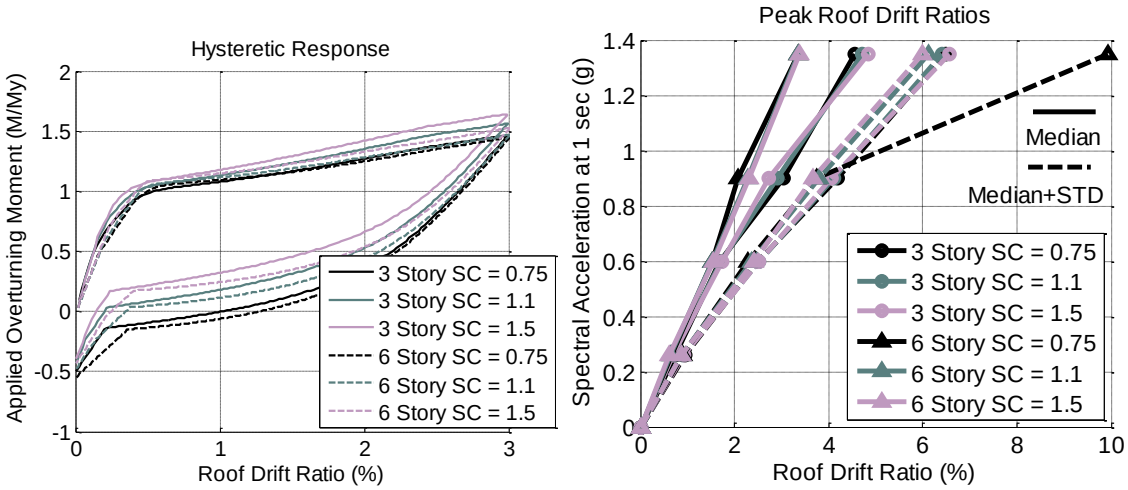

Figure 10.29 Hysteretic Response (Left) and Peak Roof Drift Ratios (Right) for Varying SC Ratios

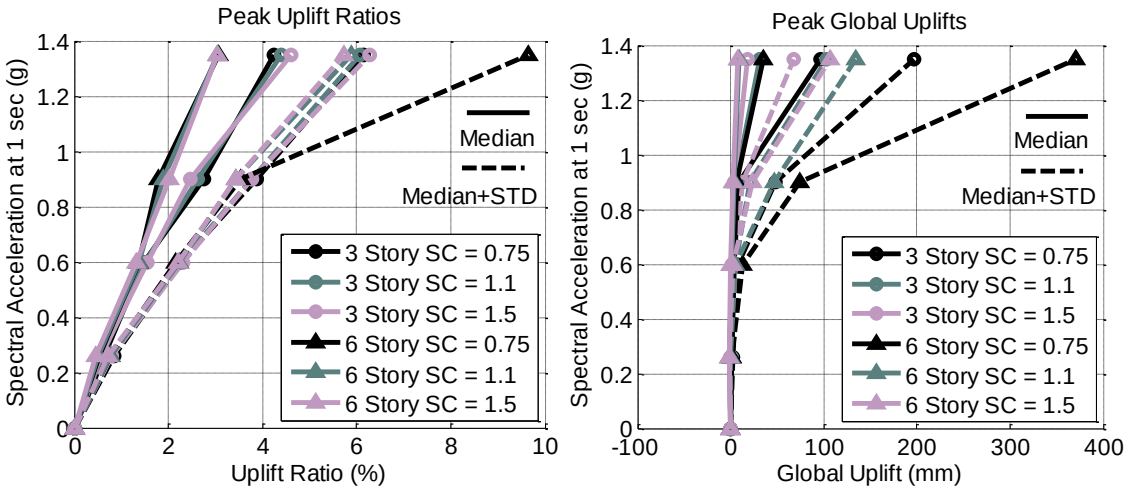

Figure 10.30 Peak Uplift Ratios (Left) and Peak Global Uplifts (Right) for Varying SC Ratios

The residual roof drifts and uplifts were found to be small up to the 2% probability of exceedance in 50 years hazard level even for the configurations with self-centering ratios less than 1.0. Chapter 9 discusses a probabilistic mechanism by which systems can self-center even if the monotonic hysteretic behavior has large drifts when the loads are removed.

The range of self-centering ratios considered here were not found to have a significant effect on median peak post-tensioning strains up to the 2% in 50 years hazard level. Although variation in the median fuse link shear strains was noted with varying self-centering ratio, all configurations considered here were found to have values at one standard deviation above the median for the 2% in 50 years hazard level that were below the mean fracture strain of 36.7%. The peak base shears and peak overturning moments were not found to vary significantly with the self-centering ratio.

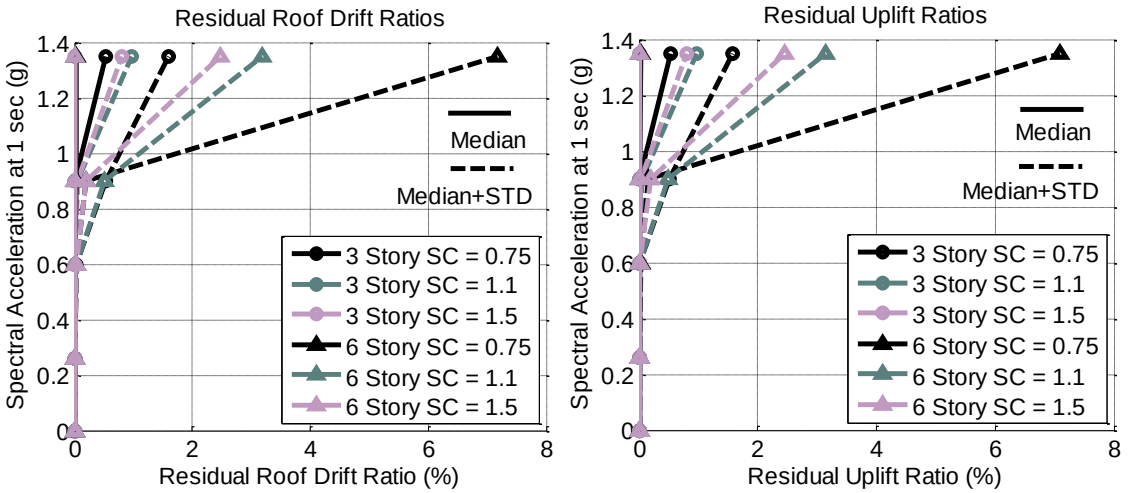

Figure 10.31 Peak Residual Roof Drift Ratios (Left) and Residual Uplift Ratios (Right) for Varying SC Ratios

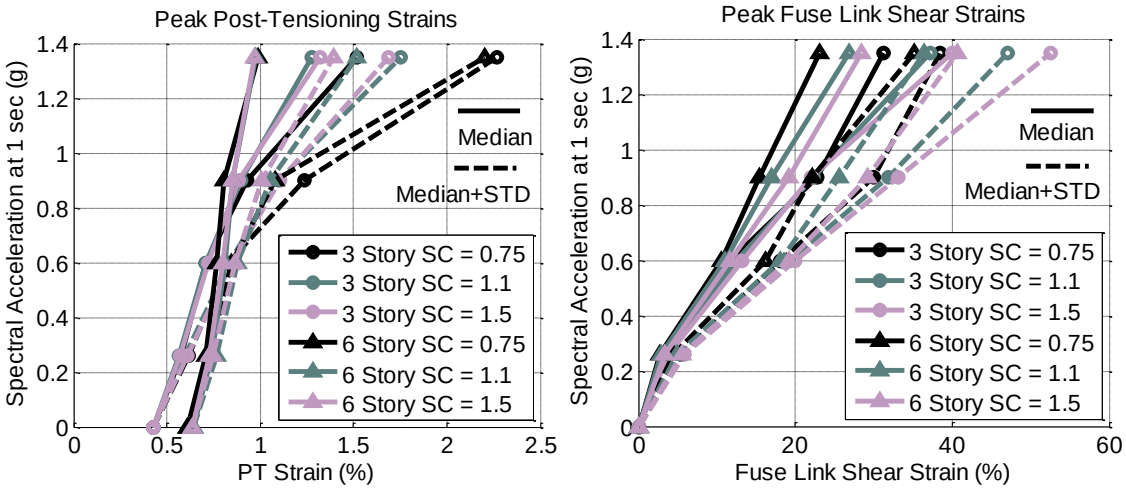

Figure 10.32 Peak Post-Tensioning Strains (Left) and Peak Fuse Link Shear Strains (Right) for Varying SC Ratios

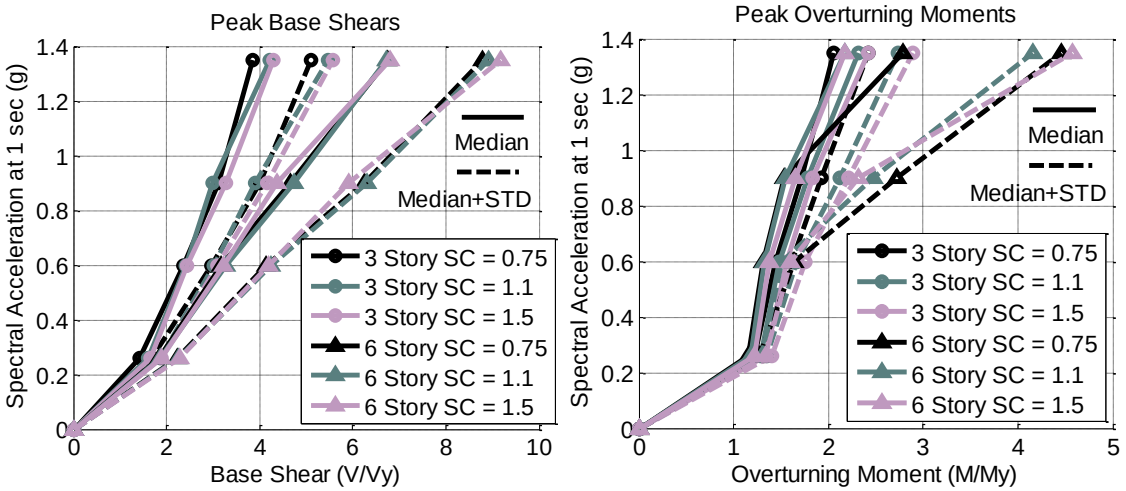

Figure 10.33 Peak Base Shears (Left) and Peak Overturning Moments (Right) for Varying SC Ratios

10.6.6 Effect of Eliminating Seating Losses

Two configurations were compared to investigate the effect of eliminating post-tensioning seating losses. A single frame configuration was selected in which the computational model for one configuration did not include seating losses in the post-tensioning constitutive model, and another configuration that did. The two configurations were analysis number 5, and 16 respectively. Post-tension seating losses are described and quantified in Chapter 8. These losses in the post-tension force are due to the wedges of the post-tensioning anchorage getting pulled farther into the anchorage as the strand is stressed to forces higher than previously obtained. Methods for eliminating post-tensioning seating losses have been devised and implemented (Ma 2010) and are discussed in more detail in Chapter 12. For the sake of this sensitivity study, it was assumed that post-tensioning seating losses were eliminated for all configurations except for one. The effect that these seating losses have on system performance is discussed in this section. As described in Table 10.5, both configurations were three-

story buildings with single frame controlled rocking system. Both configurations used thicker non-buckling fuses, self-centering ratio, SC=1.1, and a 6.10m (20') bay width.

For the loading and unloading pushover analysis shown on the left of Figure 10.34, the effect of seating losses on the hysteretic response of the system is a reduction in post-uplift stiffness and a loss of post-tensioning force during large displacement excursions. During the monotonic excursion to 3% roof drift ratio and subsequent unloading, 19.5% of the post-tensioning force is lost as shown on the right of Figure 10.34 by the difference in stress at the beginning of the loading at the end of the loading.

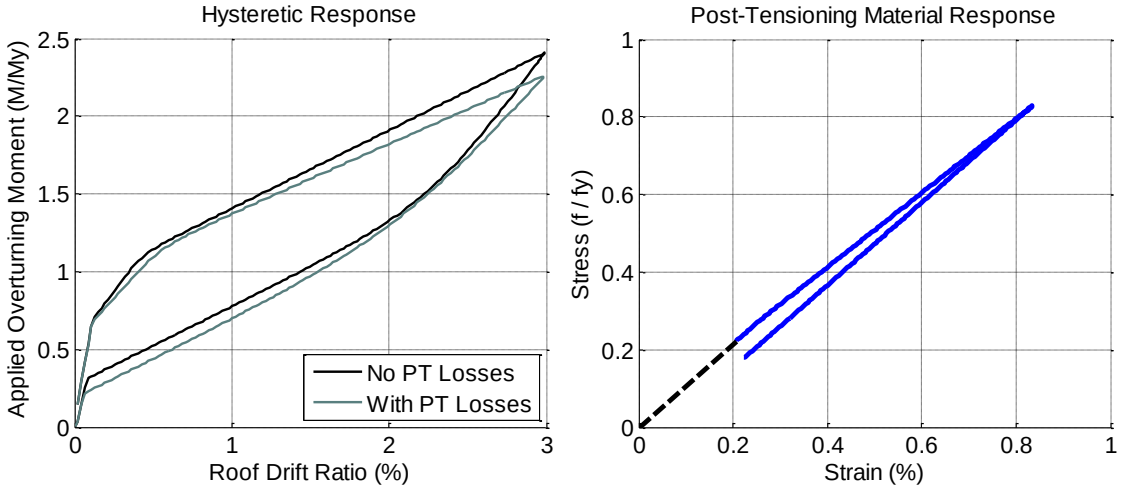

Figure 10.34 Hysteretic Response (Left) and Associated Post-Tensioning Response with Seating Losses (Right)

The difference in hysteretic response has some effects on several of the response parameters. The peak roof drifts shown on the left of Figure 10.35 are similar between the two configurations up to the hazard level that has 2% probability of exceedance in 50 years. Above this level, the post-tension force losses due to seating are compounded by yielding of the strands. The configuration with seating losses experiences slightly larger peak roof drifts and global uplift as shown in Figure 10.35 at the largest spectral acceleration investigated here. This same trend is noted in the residual roof drift ratios and residual uplifts shown in Figure 10.36.

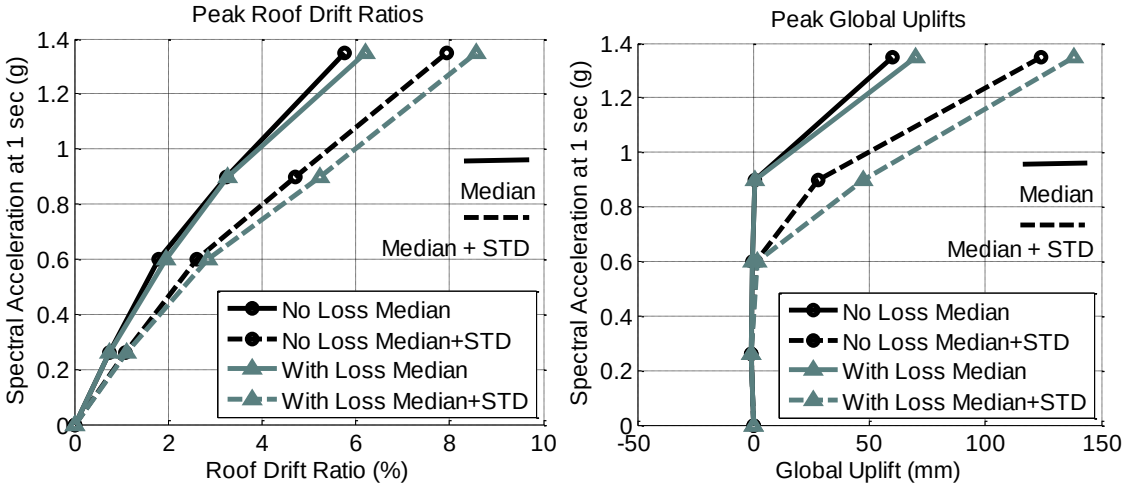

Figure 10.35 Peak Roof Drift Ratios (Left) and Peak Global Uplifts (Right) for Post-Tensioning Seating Loss Study

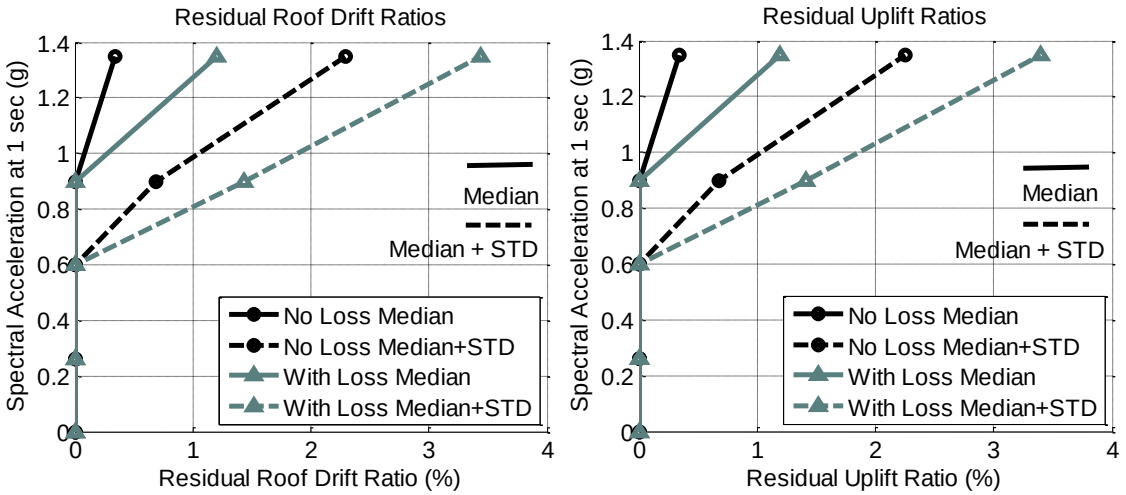

Figure 10.36 Residual Roof Drift Ratios (Left) and Residual Uplift Ratios (Right) for Post-Tensioning Seating Loss Study

Although the peak post-tensioning strains are similar up through the 2% in 50 years hazard level, the loss in post-tensioning force and the reduced stiffness of the system is experienced by the fuses as larger peak fuse link shear strains as shown in Figure 10.37. The peak base shear and peak overturning moments are not greatly affected, implying that frame member forces would not be greatly affected either.

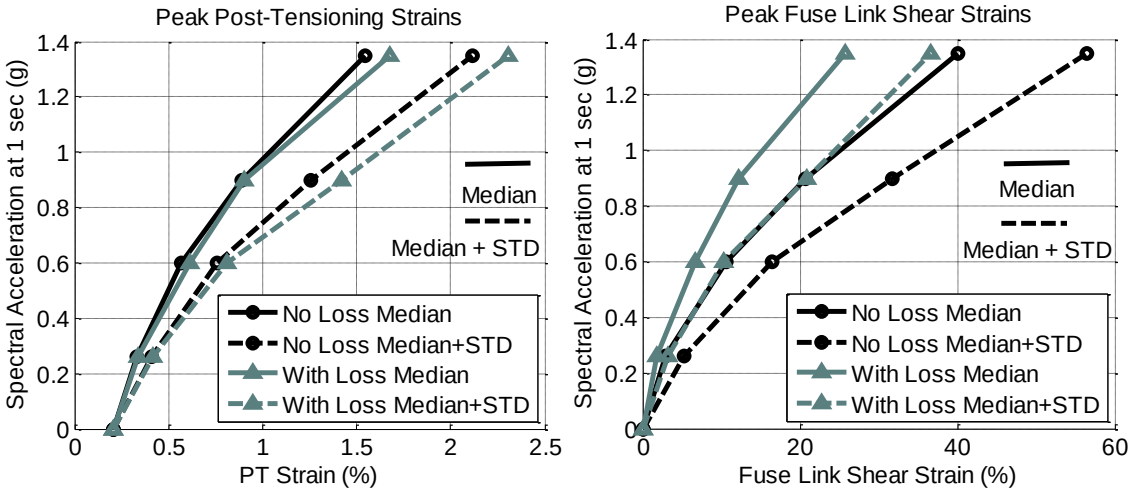

Figure 10.37 Peak Post-Tensioning Strains (Left) and Peak Fuse Link Shear Strains (Right) for Post-Tensioning Seating Loss Study

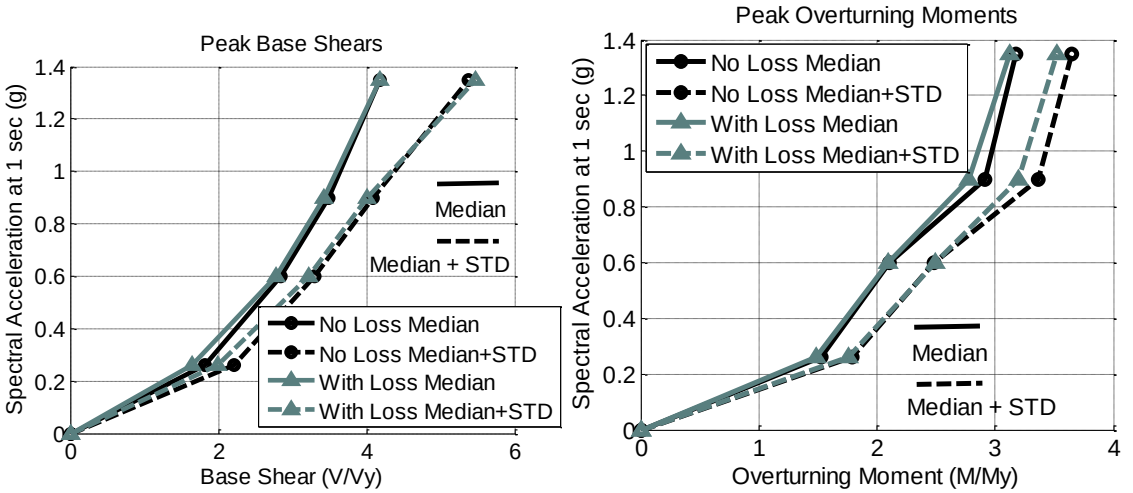

Figure 10.38 Peak Base Shears (Left) and Peak Overturning Moments (Right) for Post-Tensioning Seating Loss Study

10.6.7 Strut Study

The effect of using struts versus diaphragm elements was investigated by comparing the results of three configurations. The first configuration included struts between the frames that had pinned connections to the frame. The second configuration was identical except the pin connections included a zero length element representing pin hole tolerances. More information about this zerolength element is located in Chapter 6. The third configuration used beam elements that connect to points at the middle of the floor beam of both frames. These elements represent the stiffness of an adjacent floor beam and connection of the diaphragm to the lateral resisting system.

As described in Table 10.5, all three configurations were six-story dual frames with geometric ratio, A/B=2.5, thicker non-buckling fuses, self-centering ratio, SC=1.1, 9.14m (30') bay width, and no seating losses. The analyses configuration numbers

included in this study were 17, 18, and 2 for the struts with no pin hole tolerances, struts with tolerances, and diaphragm elements respectively.

As shown in Figure 10.39, Figure 10.41, Figure 10.42, Figure 10.43, and Figure 10.44, considering pin hole tolerances had almost no effect on the configuration with struts. Figure 10.40 is an example of the strut forces for these two configurations when subjected to the first ground motion scaled to the hazard level with 2% probability of exceedance in 50 years. The pin hole tolerances are shown to reduce the strut forces, but the roof drift response for these two examples is virtually identical.

The diaphragm element creates more constraint between the two frames than the strut elements as shown on the left of Figure 10.39 by larger stiffness. However, the diaphragm element did not have a large effect on the median response parameters compared to the configurations with struts as shown in Figure 10.41, Figure 10.42, Figure 10.43, and Figure 10.44. There was more noticeable difference at one standard deviation above the median for which the diaphragm configurations showed larger peak global uplift, residual displacements, post-tensioning strains and forces. The added degree of constraint associated with the diaphragm element caused larger variability in the response indices.

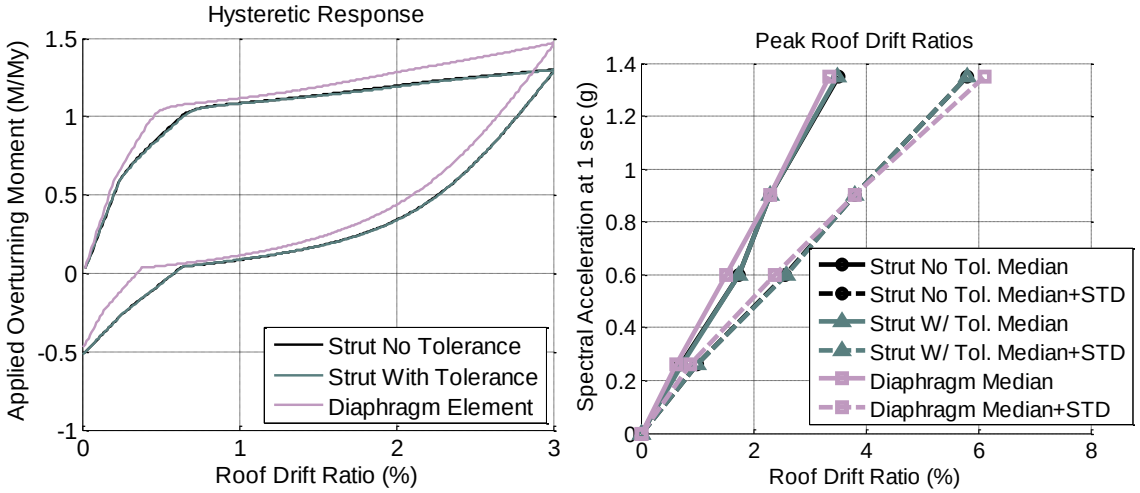

Figure 10.39 Hysteretic Response (Left) and Peak Roof Drift Ratios (Right) for the Strut Study

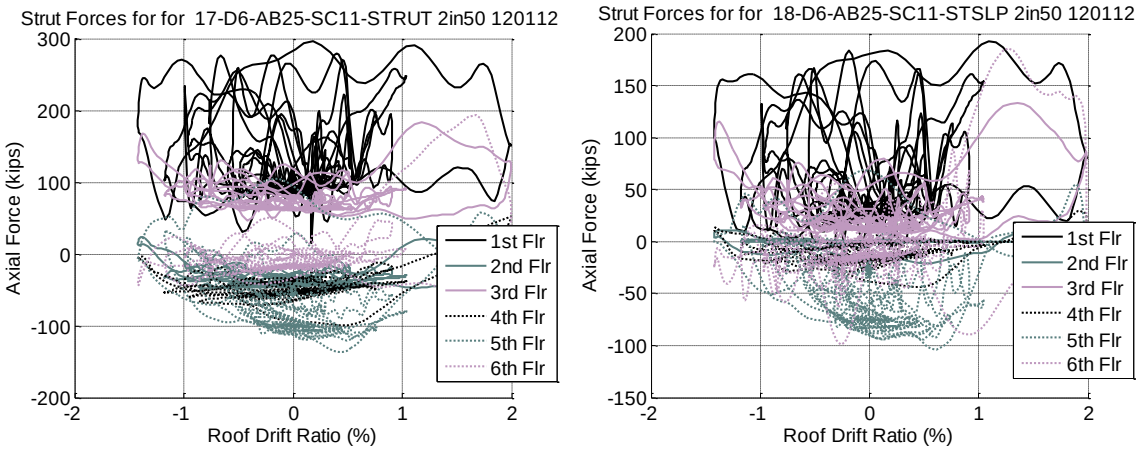

Figure 10.40 Example of the Strut Forces for the Configuration Without Pin Hole Tolerance (Left) and With Pin Hole Tolerance (Right)

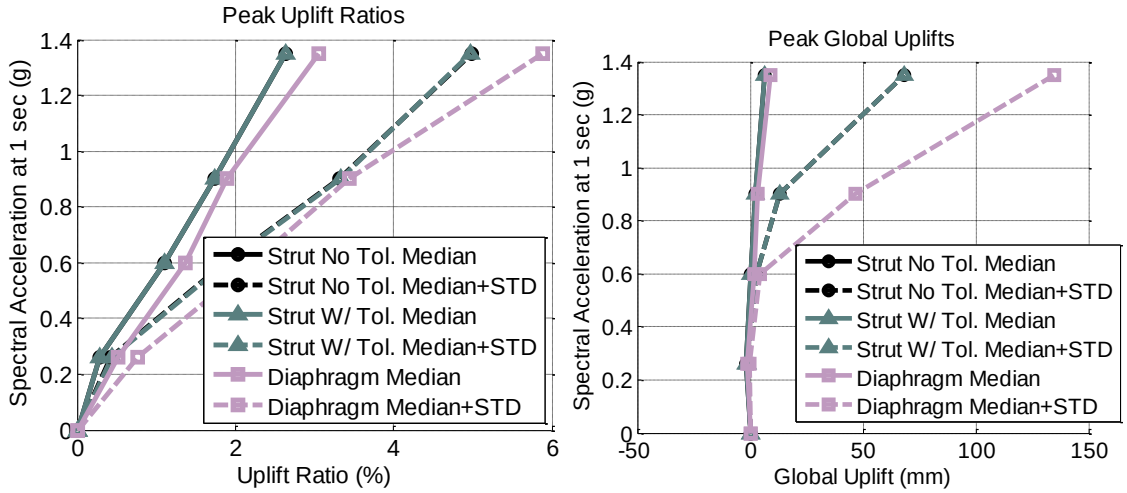

Figure 10.41 Peak Uplift Ratios (Left) and Peak Global Uplifts (Right) for the Strut Study

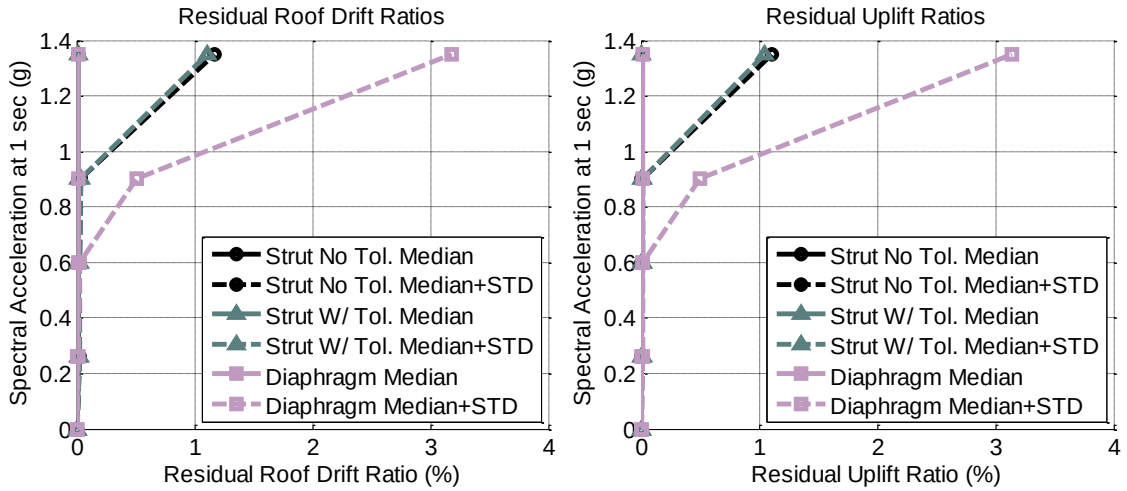

Figure 10.42 Residual Roof Drift Ratios (Left) and Residual Uplift Ratios (Right) for the Strut Study

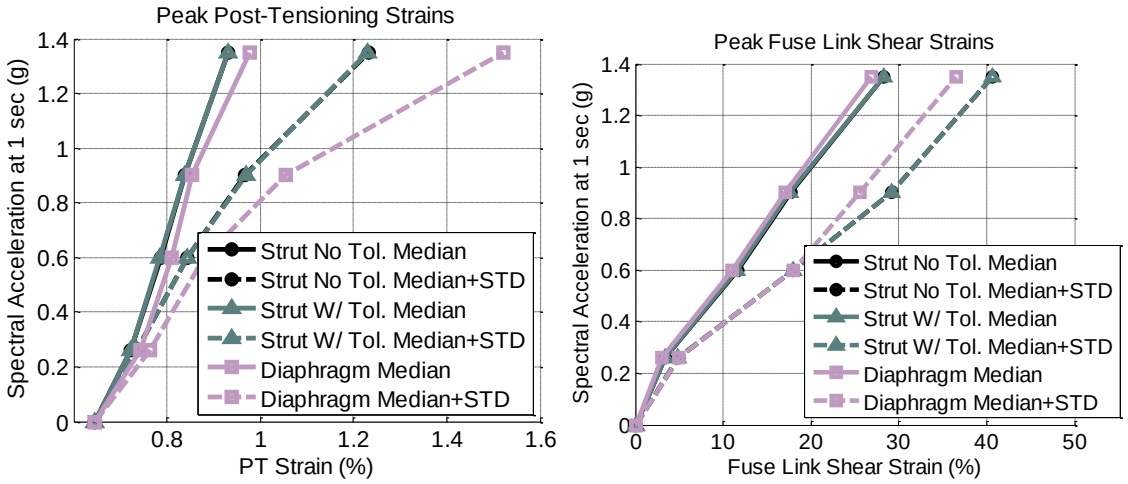

Figure 10.43 Peak Post-Tensioning Strains (Left) and Peak Fuse Shear Strains (Right) for the Strut Study

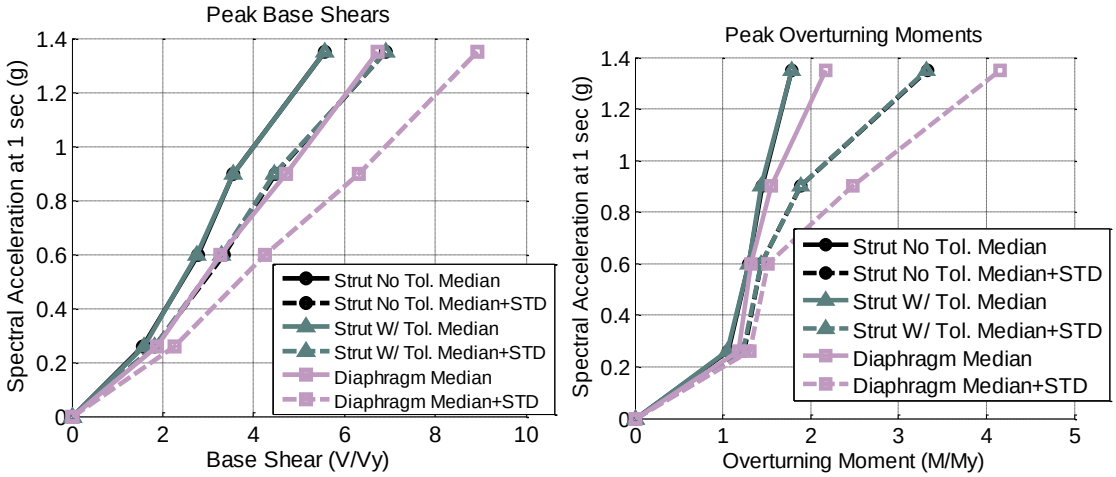

Figure 10.44 Peak Base Shears (Left) and Peak Overturning Moments (Right) for the Strut Study

10.6.8 Rocking Base vs. Fixed Base Comparison

A comparison is made between the controlled rocking system and an identical configuration with fixed bases. The fixed base model is intended to highlight the comparison of response parameters given different base constraints. Neither model captures inelasticity or buckling of the frame members, but providing an elastic frame may not represent a practical design for the fixed base braced frame. Conversely, the uplifting frame members are expected to respond elastically.

The two configurations compared in this section are analysis number 2 and analysis number 19, which simulate the uplifting base and fixed base respectively. As described in Table 10.5, both configurations were six-story dual frame systems with geometric ratio, A/B=2.5, thicker non-buckling fuses, self-centering ratio, SC=1.1, no seating losses, 9.14m (30') bay width, and diaphragm elements between the two frames.

The left side of Figure 10.45 shows that the fixed base frame experiences some nonlinearity as the fuses yield. Although the bases of the columns are fixed, the elastic deformations of the frame are large enough to cause yielding of the fuses. This point is further demonstrated by the area enclosed by the load-deformation response representing hysteretic absorbed energy. The rocking frame, on the other hand, experiences uplift in addition to fuse yield. Allowing uplift acts to limit the forces applied to the system. Figure 10.49 shows that the base shear and overturning moments are limited when the bases are allowed to uplift. In the controlled rocking system this effect is used to protect the frame members from experiencing inelasticity and damage. The peak roof drift is shown to be larger for the uplifting frame as given in Figure 10.45. At the 50% probability of exceedance in 50 years hazard level, the median roof drift ratio are 0.56% and 0.63% for the fixed base and uplifting frames respectively. At the 2% in 50 years hazard level, the median roof drift ratios are 1.81% and 2.30%.

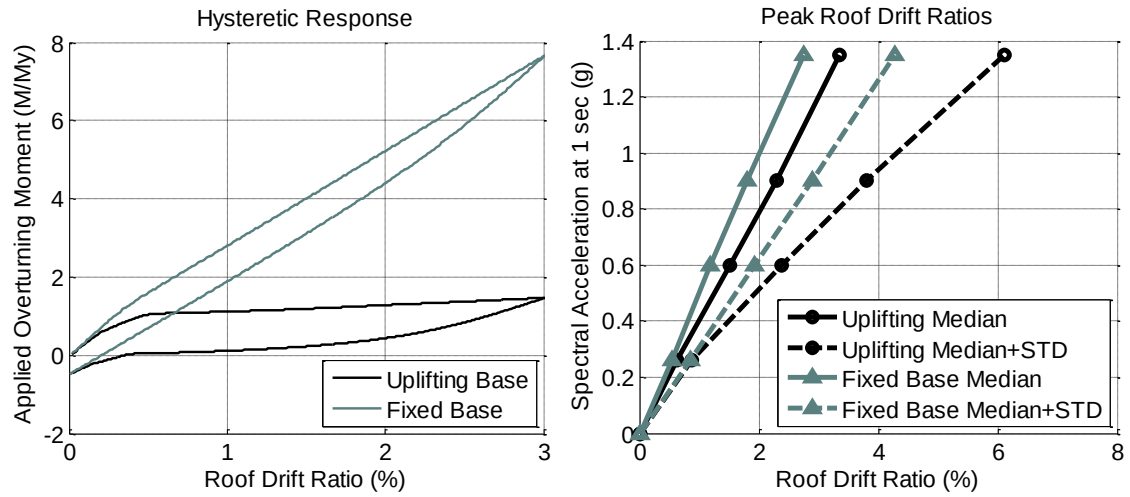

Figure 10.45 Hysteretic Response (Left) and Peak Roof Drift Ratios (Right) for Uplifting and Fixed Base Frames

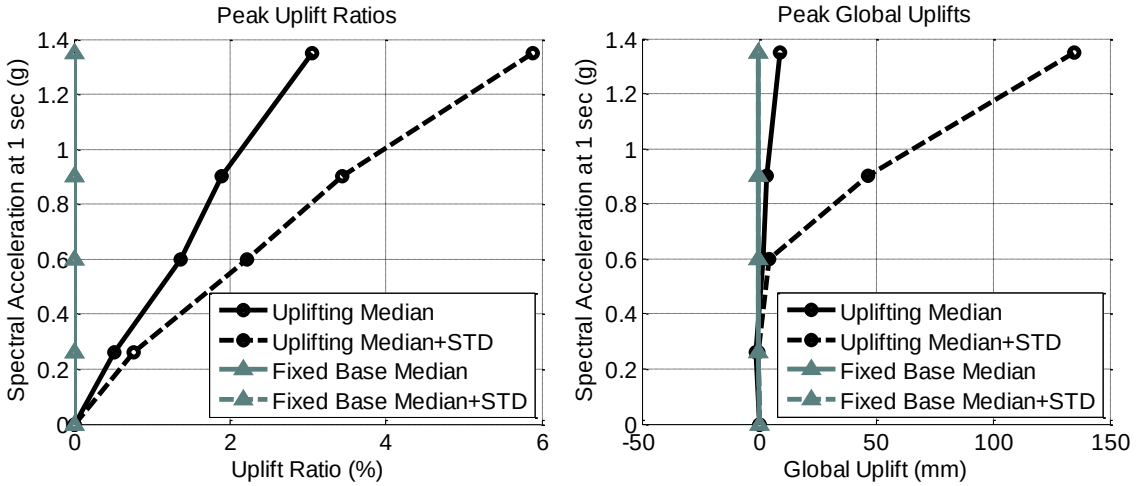

Figure 10.46 Peak Uplift Ratios (Left) and Peak Global Uplift (Right) for Uplifting and Fixed Base Frames

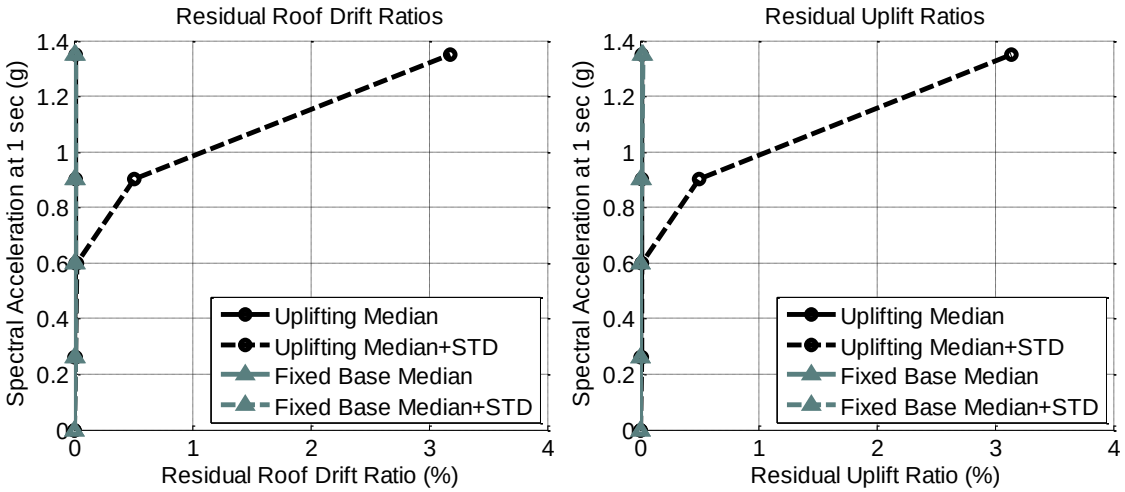

Figure 10.47 Residual Roof Drift Ratios (Left) and Residual Uplift Ratios (Right) for Uplifting and Fixed Base Frames

The peak post-tensioning strains and peak fuse link shear strains are shown in Figure 10.48. The uplifting frame undergoes more deflections than the fixed base frame, but as discussed in a previous section, the post-tensioning strains and fuse link shear strains are within a range that has a low probability of triggering negative limit states.

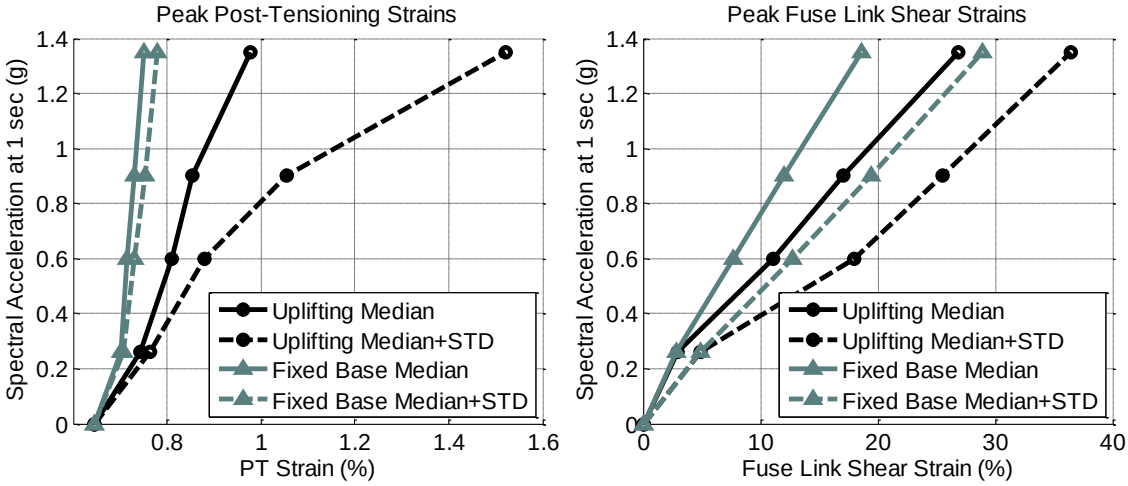

Figure 10.48 Peak Post-Tensioning Strains (Left) and Peak Fuse Shear Strains (Right) for Uplifting and Fixed Base Frames

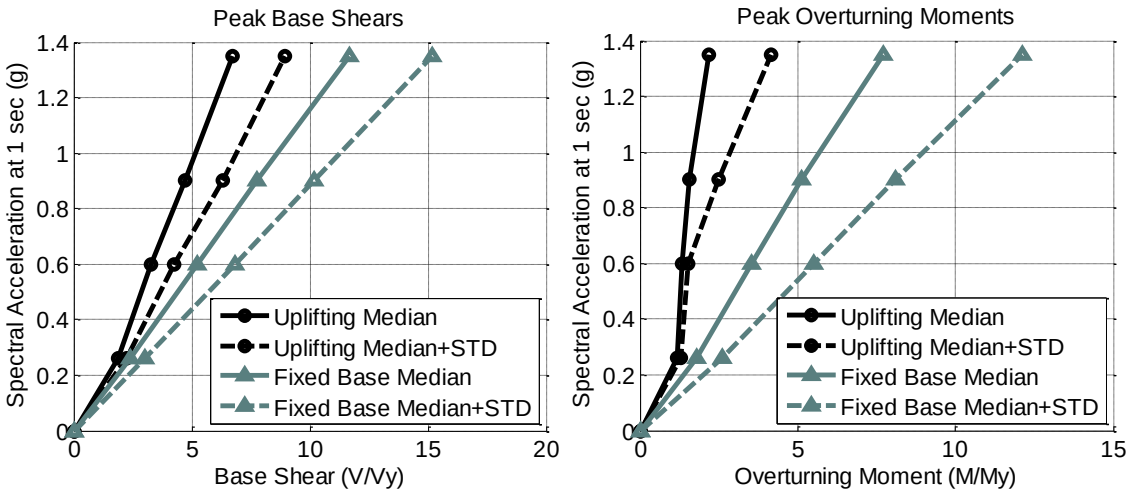

Figure 10.49 Peak Base Shears (Left) and Peak Overturning Moments (Right) for Uplifting and Fixed Base Frames

FRAME MEMBER FORCE DISTRIBUTIONS AND FRAME MEMBER DESIGN

This chapter includes discussion of the forces experienced by the frame members in the controlled rocking system and a proposed capacity design procedure. First, the resultant forces and moments calculated from measured strains in the testing program are presented and compared to computational simulation. This comparison is shown to validate the use of the computational model for predicting force distributions. Next, a general-purpose capacity design approach is defined for the design of the controlled rocking system that allows flexibility in the target hazard level at which the design is assessed and in the lateral load distribution utilized to the obtain force distribution. The capacity design approach was used to compute axial force demands for the range of configurations described in the previous chapter. The resulting design force distributions are compared to force demands determined from the suite of time history analyses described in the previous section, which enables the derivation of amplification factors for use in design to produce specific probabilities of exceedance for different hazard levels.

11.1 Experiment and Computational Model Force Distributions

In order to validate the use of the computational model in predicting frame member forces in the controlled rocking system, the experimentally obtained resultant force envelopes are compared to forces obtained from computational models exposed to the same displacement histories. The experimental specimens are described in Chapter 4, and the computational models are described in Chapter 6. Observations are also made in this section about the level of strains and forces experienced by the frame members during the tests.

There are several assumptions used in the development of the force distribution plots shown in this section. These assumptions include:

1. Forces and moments due to post-tensioning strand initial force are calculated based on the initial stressing operation and do not consider intermediate tests, test runs without fuses, or adjusting of the lower anchorage to attain the same initial post tension force level.
2. The forces are shown to go from centerline to centerline, but in actuality the forces and moments change at the gussets plates. Gusset plate dimensions are ignored.
3. On the interior columns, there are both fuses and struts attached. The envelope is shown in a lighter color in these regions because these forces and moments do not show the change in forces and moments at these attachment locations.

4. Beam strains were recorded for some specimens, but they are not included here to allow easier comparison between all specimens.
5. Moment envelopes are shown by connecting the maximum and minimum moments at the two ends of a member with a line. Since the maximum and minimum values at the two ends do not occur at the same time, the moment envelope along the length of a member may not be accurately represented; these plots are thus more useful to gain a relative sense of the maximum values that occur along the length.

11.1.1 Resultant Forces From Post-Tensioning Stressing

Strain gage data was recorded during all post-tensioning strand stressing operations. Resultant axial forces, shear forces, and moments were calculated based on strain gage data using equations given in Appendix C.

Initial post-tensioning forces were set to the same level for groups of the specimens. Specimen A1, A2, and A3 had the same initial post-tensioning force. Specimen A4 had a larger initial post-tensioning force. Specimens A5, A6, and A7 used the same initial post-tensioning force which was then changed for Specimens B1 and B2. Therefore, there were four unique levels of initial post-tensioning force for which plots are included below. These plots are presented because the associated data was added to the resultant forces and moments for the specimen tests presented in the next section where they are then compared to computational predictions.

The left sides of Figure 11.1, Figure 11.3, Figure 11.5, and Figure 11.7 show the resultant axial forces due to the initial post-tensioning forces. The left side of Figure 11.1 shows that the axial forces associated with post-tensioning strand stressing were fairly uniform throughout the columns in some cases. On the other hand, Figure 11.5 shows a case where the axial forces in the columns were not uniformly distributed. The bases of the columns were likely not in uniform bearing when the stressing operation began for Specimen A5 causing the non-uniform distribution of column axial forces. Figure 11.1 through Figure 11.8 show that the shears and moments experienced were small relative to the axial forces.

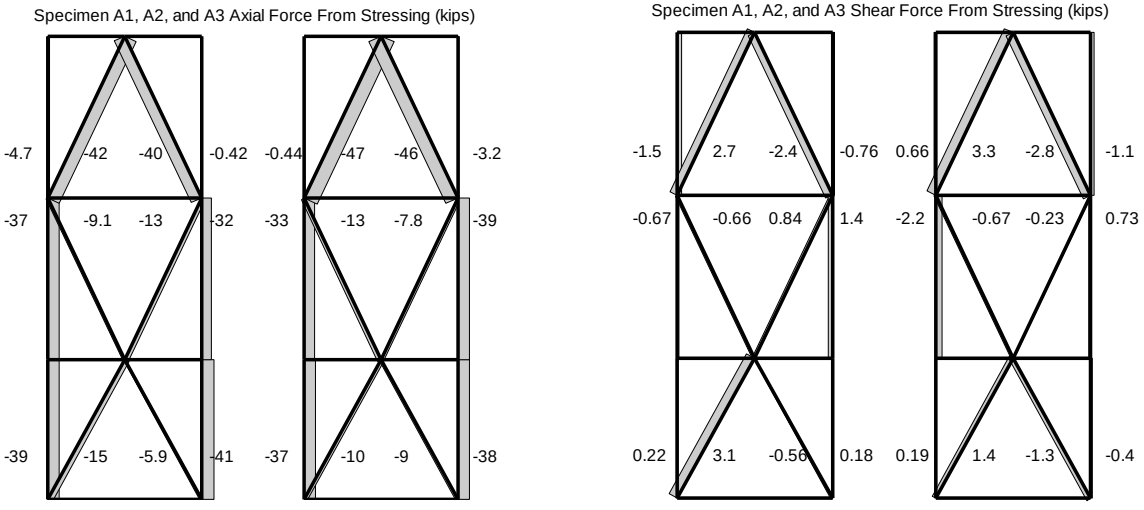

Figure 11.1 Resultant Axial Forces (Left) and Shear Forces (Right) Due to Post-Tensioning Strand Initial Stress for Specimens A1, A2, and A3

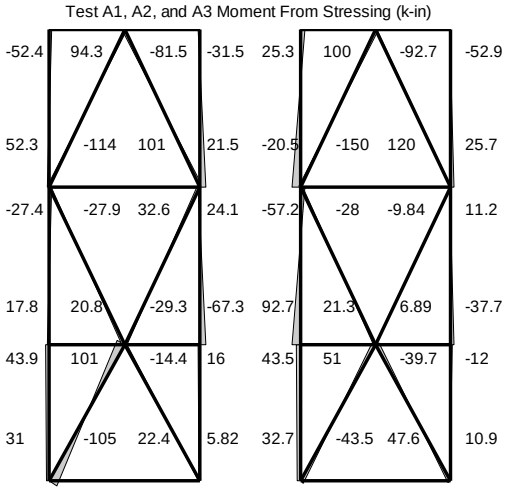

Figure 11.2 Resultant Moments Due to Post-Tensioning Strand Initial Stress for Specimens A1, A2, and A3

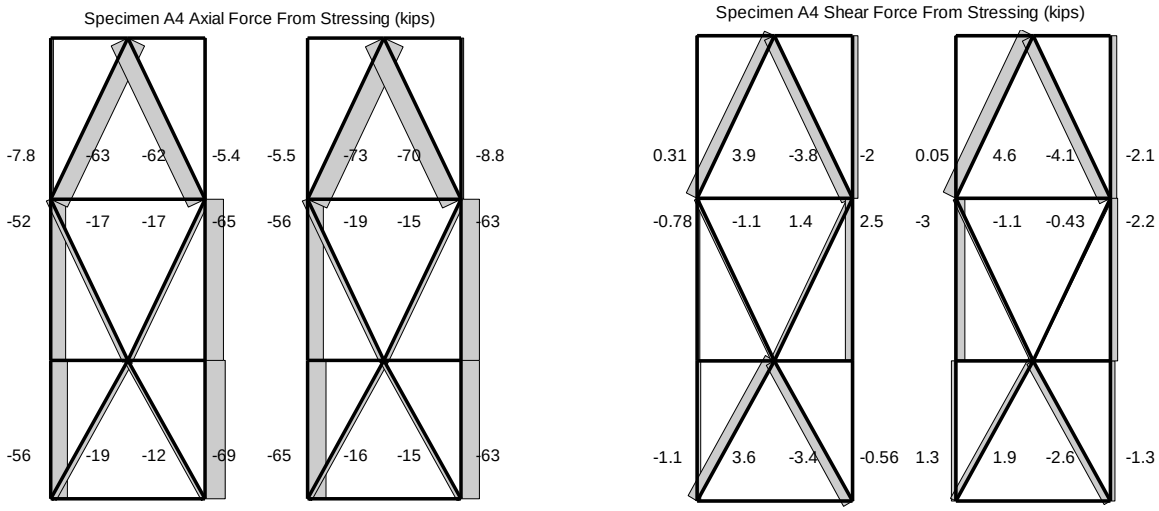

Figure 11.3 Resultant Axial Forces (Left) and Shear Forces (Right) Due to Post-Tensioning Strand Initial Stress for Specimen A4

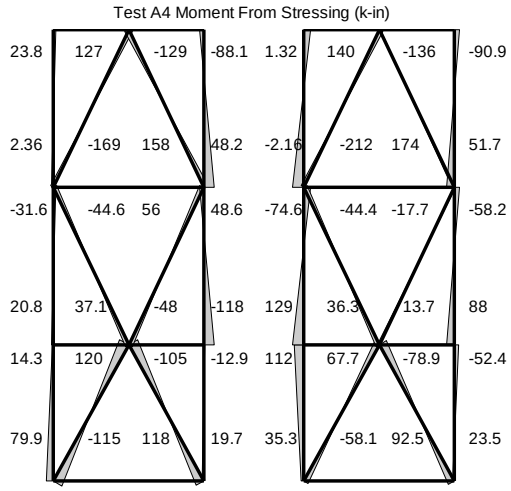

Figure 11.4 Resultant Moments Due to Post-Tensioning Strand Initial Stress for Specimen A4

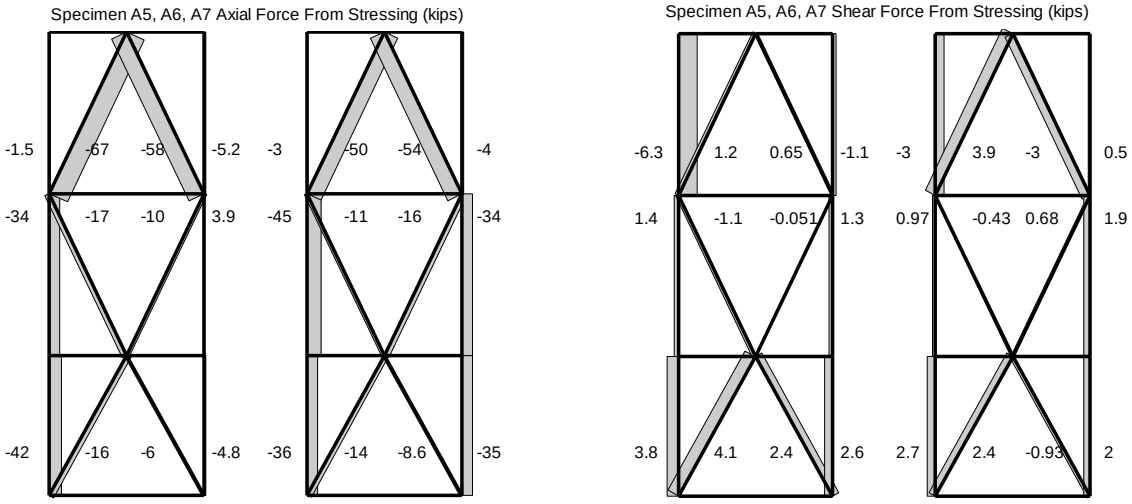

Figure 11.5 Resultant Axial Forces (Left) and Shear Forces (Right) Due to Post-Tensioning Strand Initial Stress for Specimens A5, A6, and A7

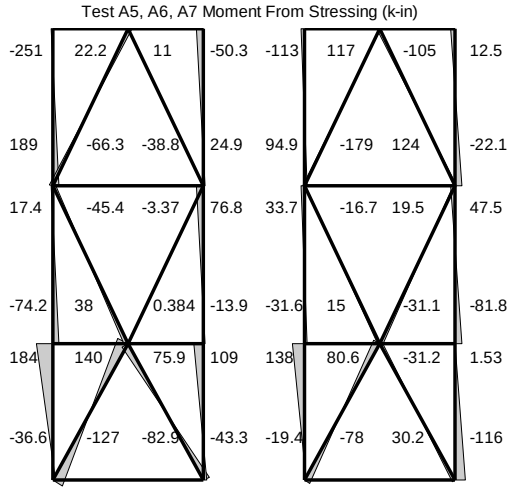

Figure 11.6 Resultant Moments Due to Post-Tensioning Strand Initial Stress for Specimens A5, A6, and A7

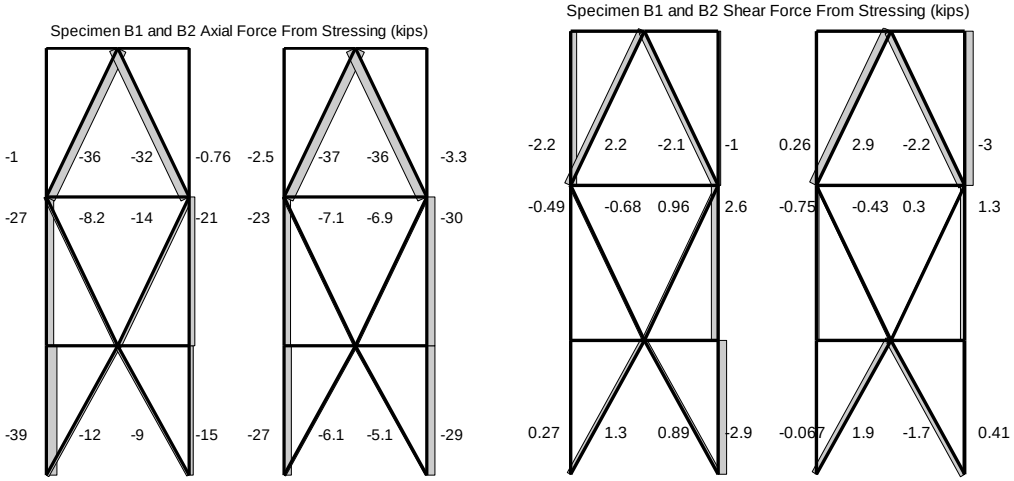

Figure 11.7 Resultant Axial Forces (Left) and Shear Forces (Right) Due to Post-Tensioning Strand Initial Stress for Specimens B1 and B2

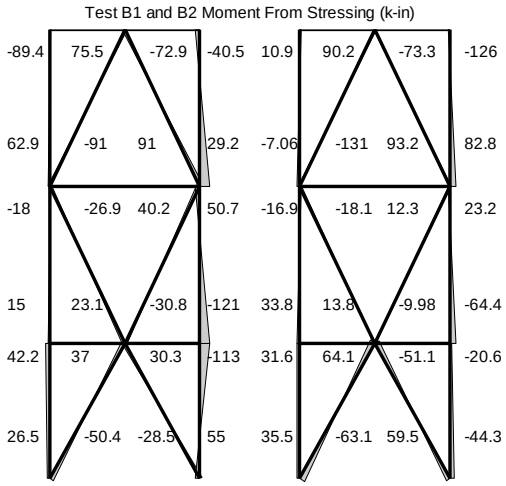

Figure 11.8 Resultant Moments Due to Post-Tensioning Strand Initial Stress for Specimens B1 and B2

11.1.2 Resultant Forces for Specimen A1

In this section, the envelopes of resultant axial forces, shear forces, and moments are presented for the testing of specimen A1 and compared to the force envelopes produced by computational simulation. As shown in Figure 11.9, the column axial forces are generally well approximated by the computational simulation with average errors being conservative relative to the experiment by 18%, 22%, and 16% for the first, second, and third floors respectively. The computationally obtained brace axial forces were less consistent with average errors of 14%, -13%, and 33% relative to the experiment for the first, second, and third floors respectively. The interior braces at the second floor were one of the few locations where the experimental axial forces were larger than the computational model.

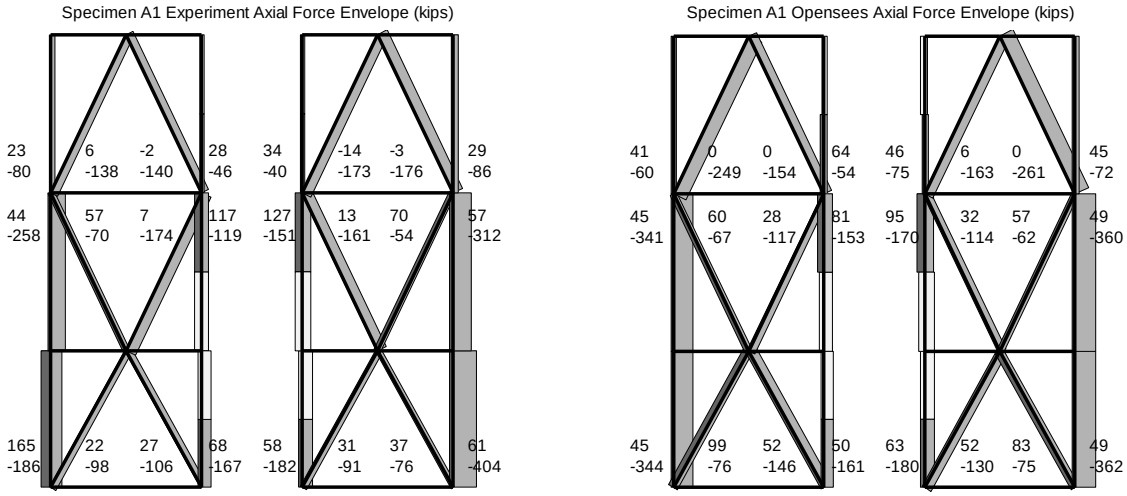

Figure 11.9 Axial Force (kips) Envelope Comparison Between Experiment (Left) and Computational Simulation (Right) for Specimen A1

The shear forces shown in Figure 11.10 are small compared to the axial forces. The shear forces are relatively similar between the experiment and the computational model except for the interior columns in the areas shown with unfilled rectangles (e.g., the top of the first floor interior columns). As explained at the beginning of this section, there were fuses and struts connecting to the columns along this portion of the interior columns. The distribution of shear forces and moments are not represented exactly by the unfilled envelope rectangles shown in these regions.

Only four strain gages experienced maximum strains larger than 1000 με during the testing of Specimen A1 (not including strains due to initial post-tensioning force). See Appendix B for raw strain gage data. The maximum strains in the frame were experienced by the four outer gages applied to the base of the exterior columns. The largest strains occurred in the base of the exterior columns because of the moments related to the eccentricity of axial bearing relative to the column centerline when the frame is pivoting on that column. These four strain gages experienced a maximum strain of 1634 με not including the strains due to post-tensioning and 1718 με including forces due to post-tensioning. This is just nine percent less than the yield strain associated with the material certification reported yield strength of 55 ksi which is equal to 1897 με. Considering that the strain-gaged section was not at the location of maximum moment, strains due to initial post-tensioning were not included in the figure cited above, and the gages were not applied at the extreme fiber of the flange tip (they were applied 0.75" from the flange tip), it is possible that the flange tips at the outside edge of the exterior columns reached the material yield stress. However, no yielding or local buckling was observed in the inspection of Specimen A1 after testing.

The resultant axial forces and moments shown in Figure 11.9 and Figure 11.11 respectively are misleading in that the forces shown near the joint are not being resisted by the frame member alone. Large gusset plates at the ends of members participate in the moment resistance at locations such as the base of the exterior columns. The maximum moment, M=1010 k-in, and maximum axial force, P=404 kips, at the base of the right exterior column suggests that the maximum stress at the flange tips might be as large 79 ksi, but this does not consider that the maximum axial force and maximum moment might not occur at the same time, nor that there are 1" thick gusset plates on the front and back of the specimen at this location contributing to moment resistance.

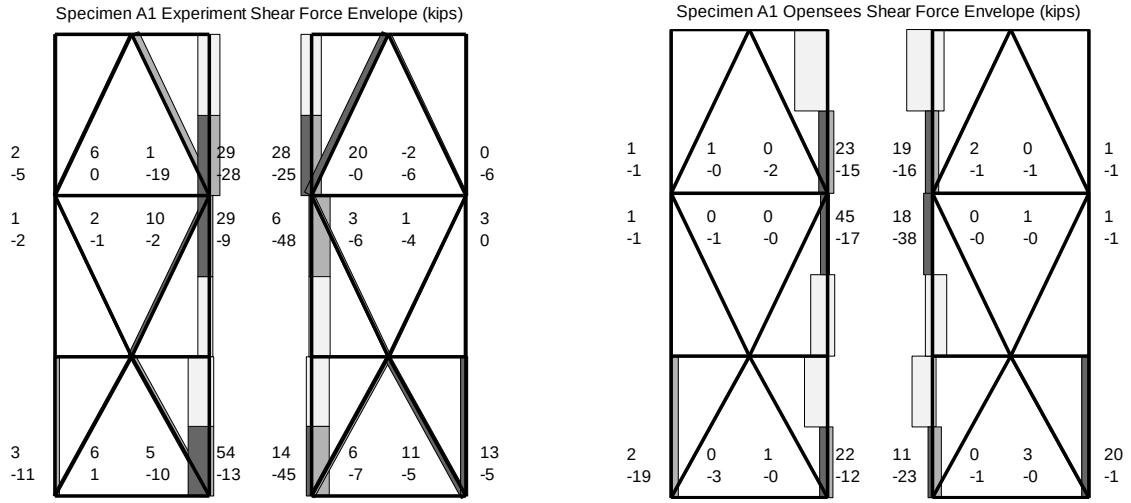

Figure 11.10 Shear Force (kips) Envelope Comparison Between Experiment (Left) and Computational Simulation (Right) for Specimen A1

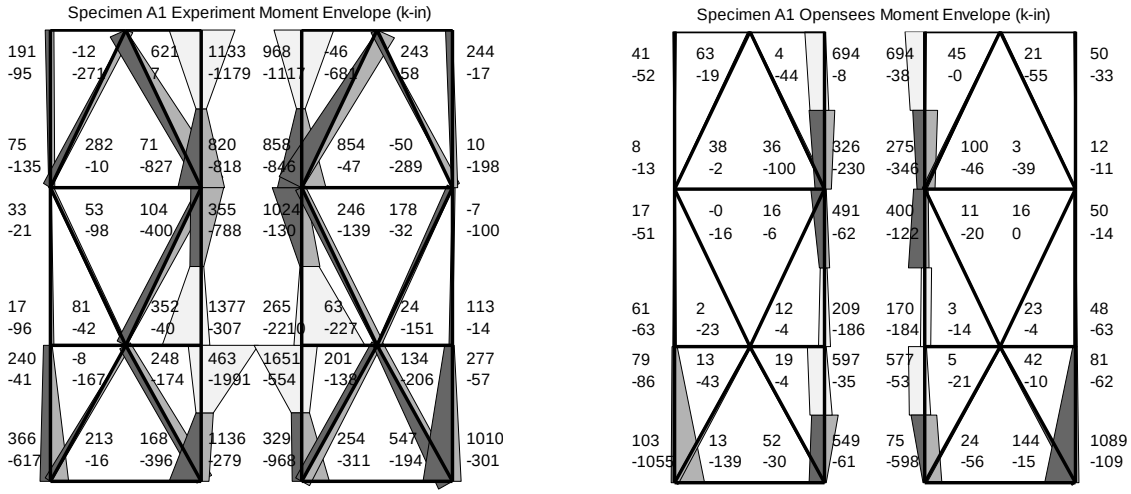

Figure 11.11 Moment (k-in) Envelope Comparison Between Experiment (Left) and Computational Simulation (Right) for Specimen A1

11.1.3 Resultant Forces for Specimen A2

In this section, the envelopes of resultant axial forces, shear forces, and moments are presented for the experimental response of Specimen A2 and compared to the force envelopes produced by computational simulation. Since most of the results are similar to Specimen A1, only the differences are highlighted here.

Similar to Specimen A1, the maximum strains were experienced at the outside flange tips of the exterior columns. The raw strain data from Appendix B shows that the maximum strain in the four gages at the outside flange tips of the exterior column was 1450 με not including strains due to initial post-tensioning forces. The maximum strain of any of the other gages was 900 με. In general, the resultant forces were less for Specimen A2 relative to Specimen A1. The buckled fuse configurations are expected to

apply larger loads to the frames because of the larger axial loads present in buckled fuses. See Chapter 8 for a discussion of axial forces in the fuses.

The forces and moments obtained using the computational model were similar to those obtained through the testing of Specimen A2 as shown in Figure 11.12, Figure 11.13, and Figure 11.14.

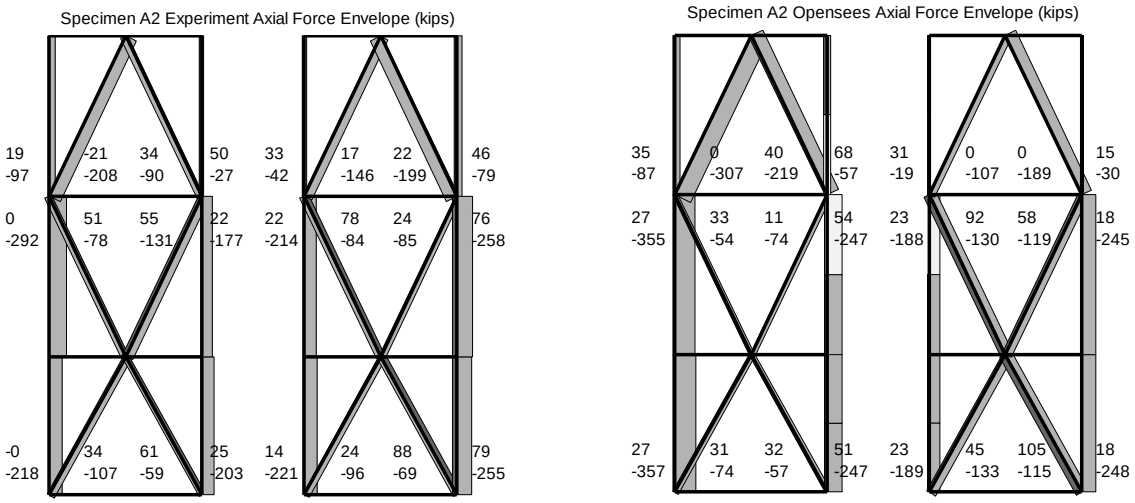

Figure 11.12 Axial Force (kips) Envelope Comparison Between Experiment (Left) and Computational Simulation (Right) for Specimen A2

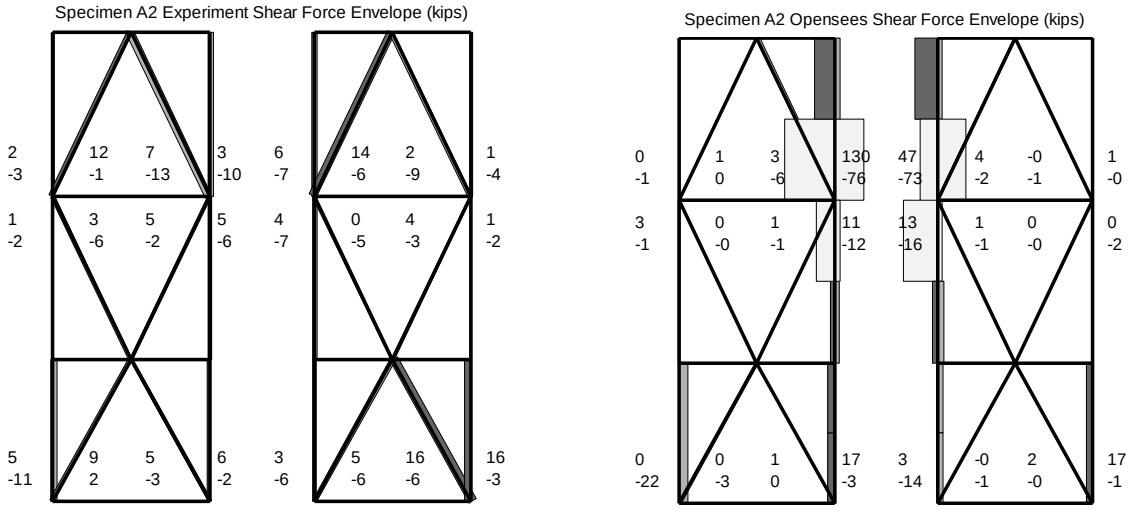

Figure 11.13 Shear Force (kips) Envelope Comparison Between Experiment (Left) and Computational Simulation (Right) for Specimen A2

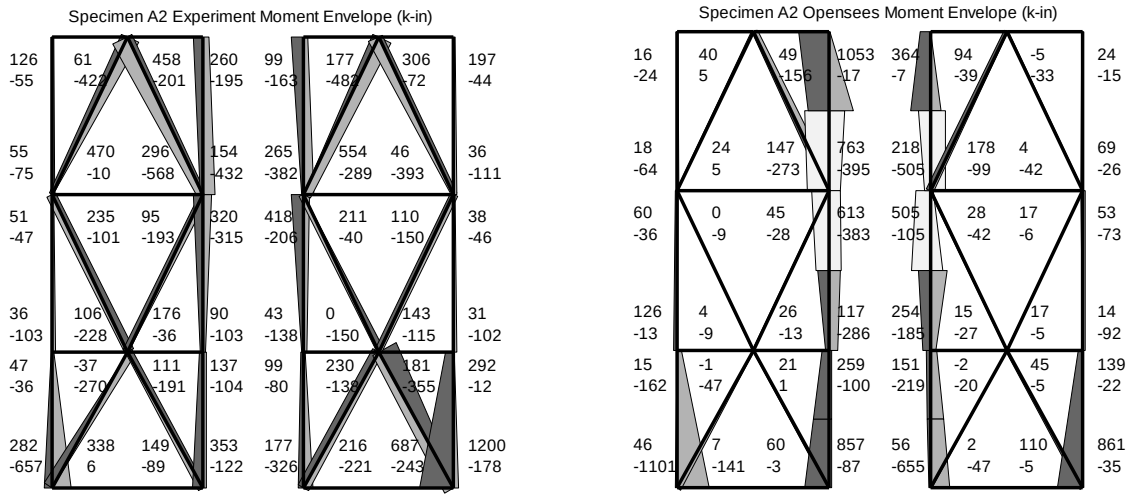

Figure 11.14 Moment (k-in) Envelope Comparison Between Experiment (Left) and Computational Simulation (Right) for Specimen A2

11.1.4 Resultant Forces for Specimen A3

In this section, the envelopes of resultant axial forces, shear forces, and moments are presented for the experimental response of Specimen A3 and compared to the force envelopes produced by computational simulation. As shown in Figure 11.15, Figure 11.16, and Figure 11.17, similar trends can be observed for Specimen A3 as were discussed in the previous section for Specimen A2.

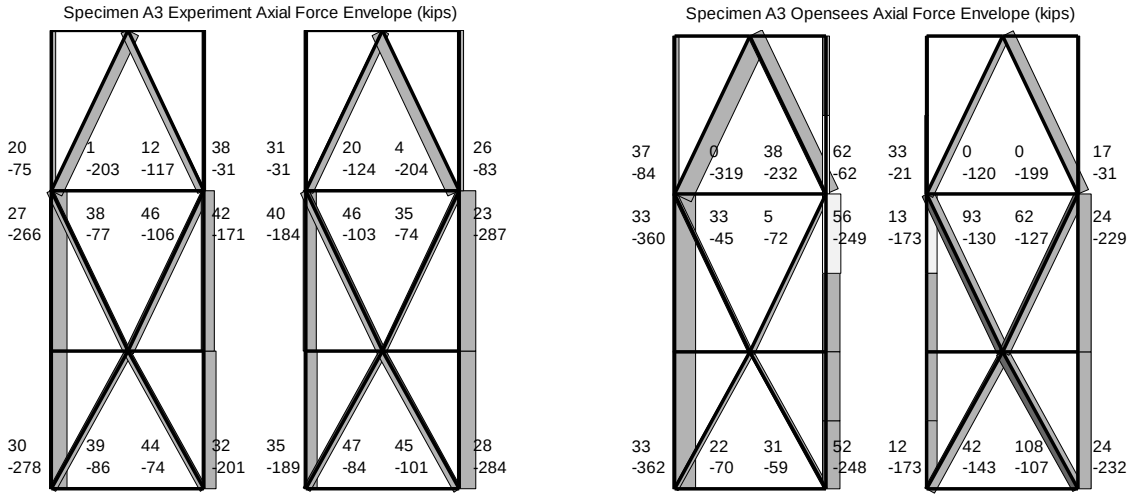

Figure 11.15 Axial Force (kips) Envelope Comparison Between Experiment (Left) and Computational Simulation (Right) for Specimen A3

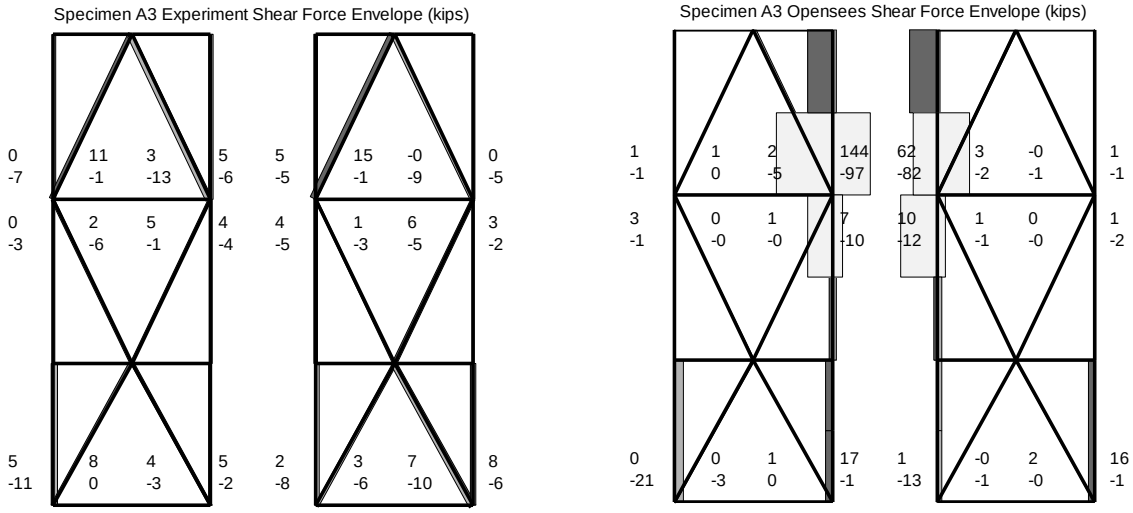

Figure 11.16 Shear Force (kips) Envelope Comparison Between Experiment (Left) and Computational Simulation (Right) for Specimen A3

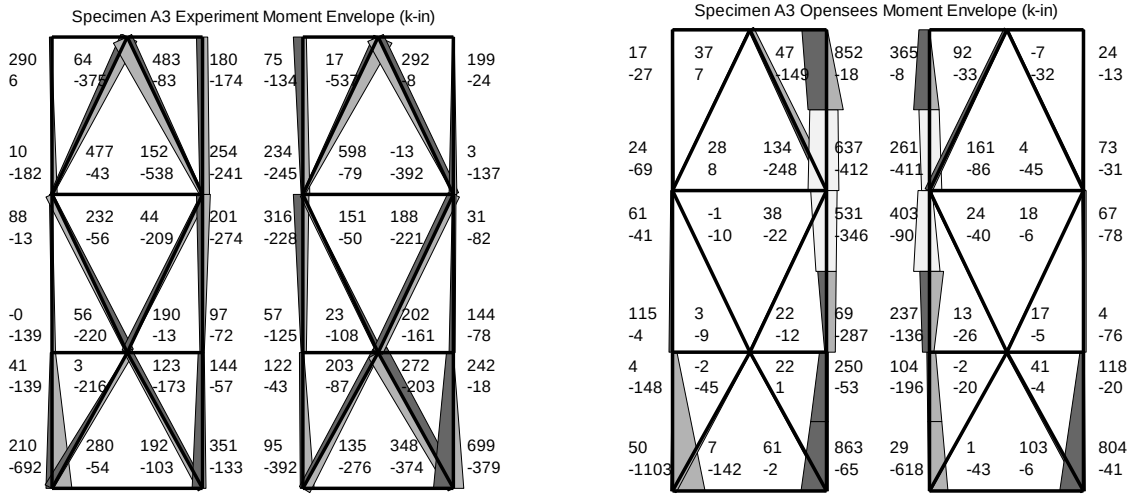

Figure 11.17 Moment (k-in) Envelope Comparison Between Experiment (Left) and Computational Simulation (Right) for Specimen A3

11.1.5 Resultant Forces for Specimen A4

In this section, the envelopes of resultant axial forces, shear forces, and moments are presented for the experimental response of Specimen A4 and compared to the force envelopes produced by computational simulation. The comparison of axial forces shown in Figure 11.18 between the braces in the experiment and the computational simulation highlights a trend observed in most of the specimens. The braces going from the interior columns at the second floor to the exterior columns at the base of the frames have axial force that is consistently under-predicted by the computational simulation by an average of 35%. In this case, the computational model predicted that the vertical forces would be transferred more through the exterior columns than the braces which may have resulted

from the way the fuse attached to the frame in the computational model. Other member axial forces are generally slightly overpredicted by the computational simulation.

The maximum strains experienced at the outside flange tips of the exterior columns was 1650 με not including strains due to initial post-tensioning forces and 1670 με including the forces due to post-tensioning. The maximum strain of any of the other gages was 1260 με. This range of strain is similar to Specimen A1 meaning that there may have been local yielding of extreme fibers at the base of the exterior columns, but no visible damage was noticed in the inspection.

Figure 11.19 and Figure 11.20 show that the shear forces are generally small and Figure 11.20 shows that the moment distributions in the base of the columns are similar in the computational model as the experiment even if the moments experienced in the tests were generally larger than the near zero moments predicted by the computational simulation. As explained at the beginning of this chapter, the large shear forces shown on the right of Figure 11.19 are in a region of the interior columns where the fuses and struts attach. The shear forces shown do not accurately consider how the fuses transmit forces to the column along their height and also stiffen the column.

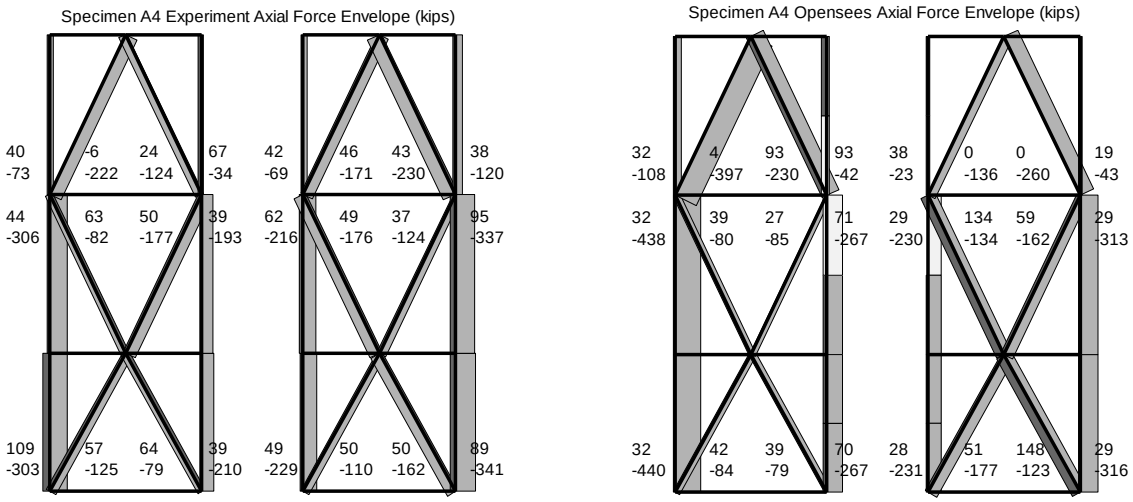

Figure 11.18 Axial Force (kips) Envelope Comparison Between Experiment (Left) and Computational Simulation (Right) for Specimen A4

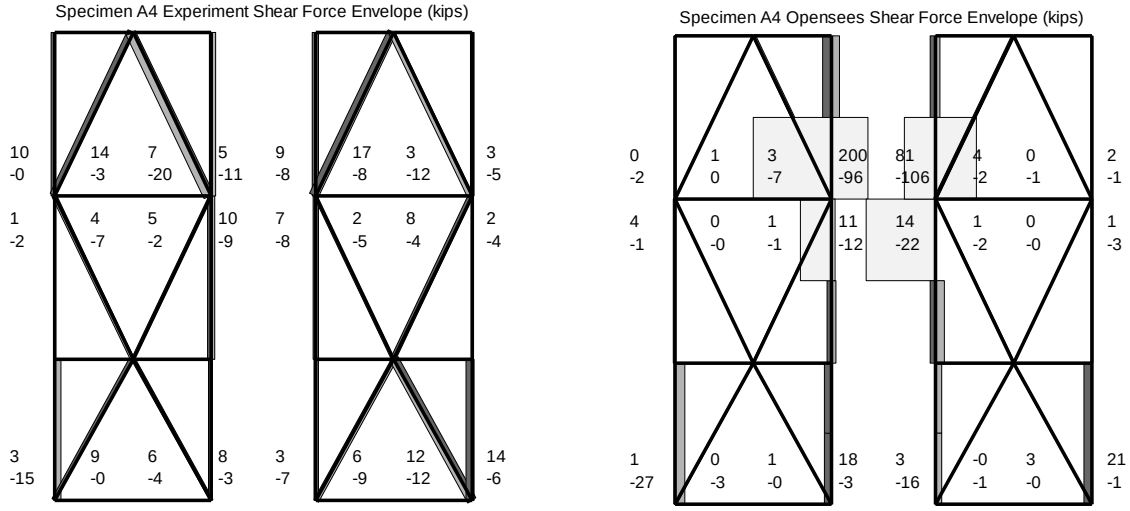

Figure 11.19 Shear Force (kips) Envelope Comparison Between Experiment (Left) and Computational Simulation (Right) for Specimen A4

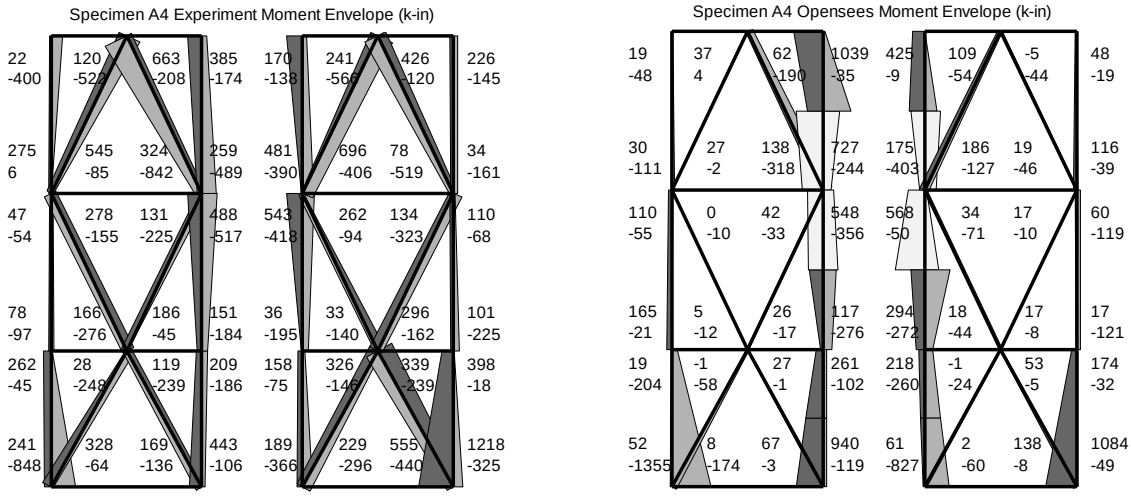

Figure 11.20 Moment (k-in) Envelope Comparison Between Experiment (Left) and Computational Simulation (Right) for Specimen A4

11.1.6 Resultant Forces for Specimen A5

Specimen A5 and A6 were tested as hybrid simulations. The peak roof drift ratio for Specimen A5 was 2.5% whereas Specimen A4 was tested to 3.7% roof drift ratio. The forces in the members are therefore smaller than that of the previous specimen. Three hybrid simulation tests were conducted at the hazard level with 2% probability of exceedance in 50 years, and twice at a level 60% larger than the 2% in 50 years hazard level. The enveloped forces and moments shown in Figure 11.21, Figure 11.22, and Figure 11.23, are for all three runs. The resultant forces and moments did not cause yielding in any members.

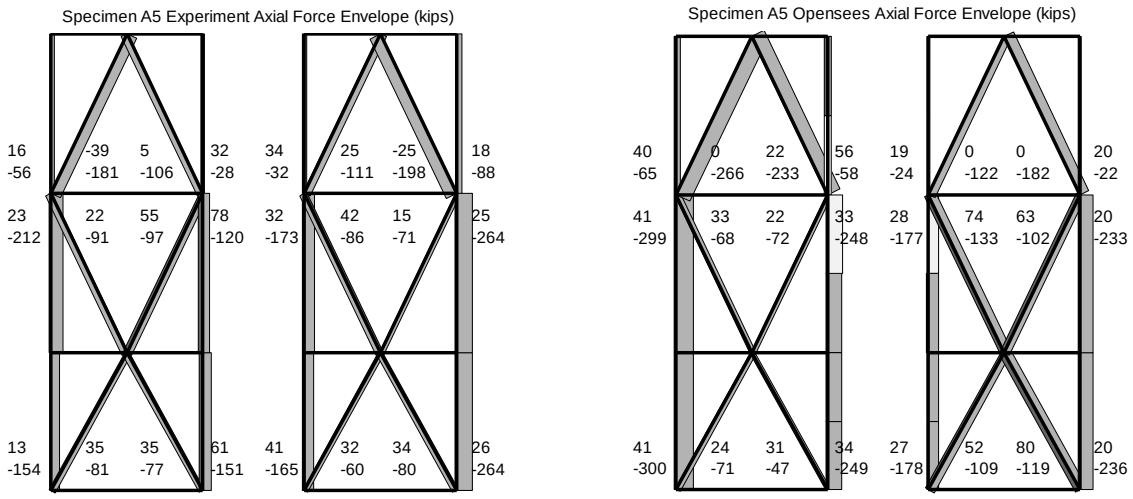

Figure 11.21 Axial Force (kips) Envelope Comparison Between Experiment (Left) and Computational Simulation (Right) for Specimen A5

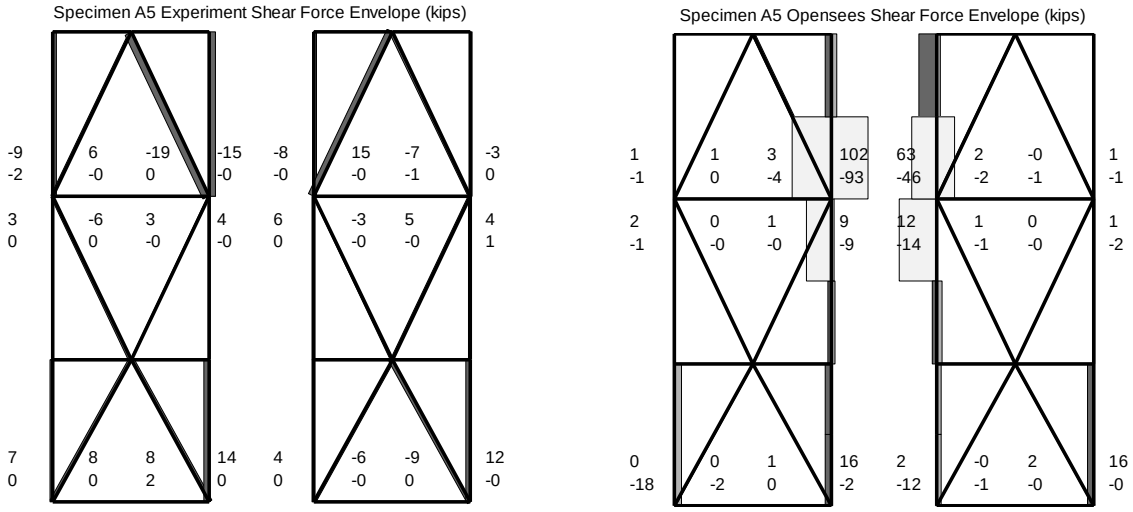

Figure 11.22 Shear Force (kips) Envelope Comparison Between Experiment (Left) and Computational Simulation (Right) for Specimen A5

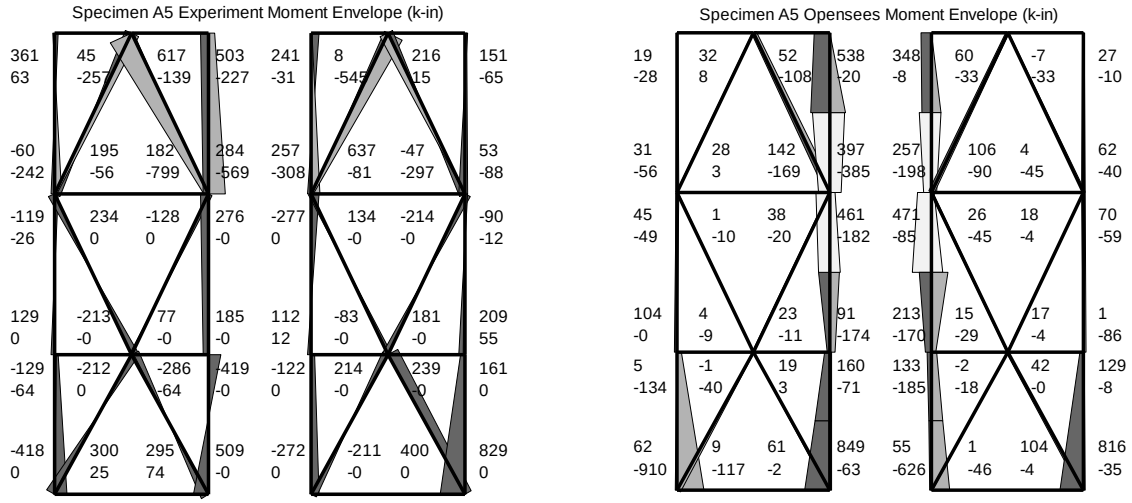

Figure 11.23 Moment (k-in) Envelope Comparison Between Experiment (Left) and Computational Simulation (Right) for Specimen A5

11.1.7 Resultant Forces for Specimen A6

In this section, the envelopes of resultant axial forces, shear forces, and moments are presented for the experimental response of Specimen A6 and compared to the force envelopes produced by computational simulation. Three runs were conducted, one at the hazard level that has 2% probability of exceedance in 50 years, a second at the 2% in 50 years hazard level with out-of-plane motion applied concurrently, and a third at a level 74% larger than the 2% in 50 years hazard. The trial with out-of-plane motion was conducted to investigate the performance of the rocking system in conditions representing earthquake excitation in multiple directions. As given in Appendix B, the maximum strains in the exterior columns during this run was 850 με compared to 745 με measured during the test with no out-of-plane motion. The maximum strains in the interior columns were 575 με with out-of-plane motion and 600 με without.

The trends in axial force, shear force, and moment resultants shown in Figure 11.24, Figure 11.25, and Figure 11.26 were found to be similar to those noted for Specimen A5.

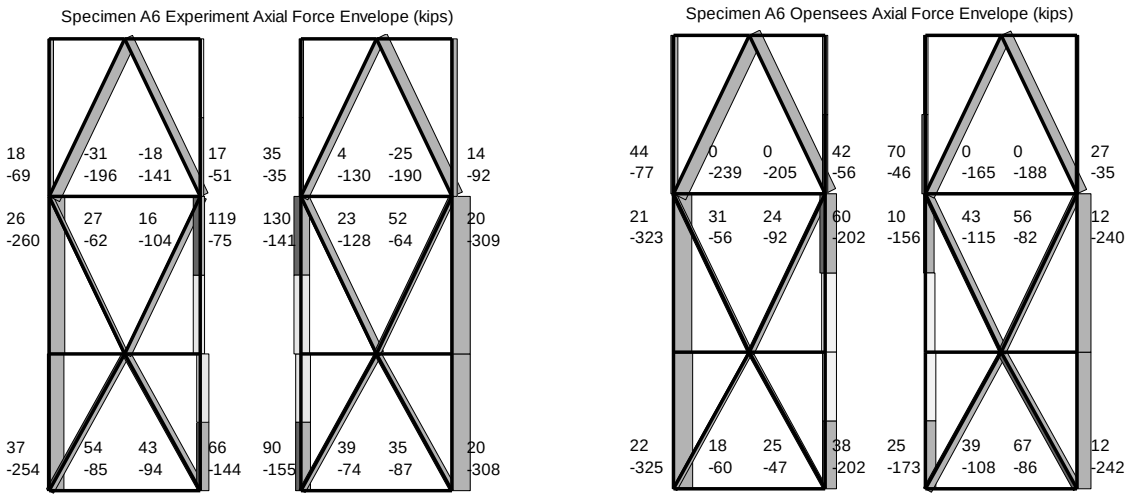

Figure 11.24 Axial Force (kips) Envelope Comparison Between Experiment (Left) and Computational Simulation (Right) for Specimen A6

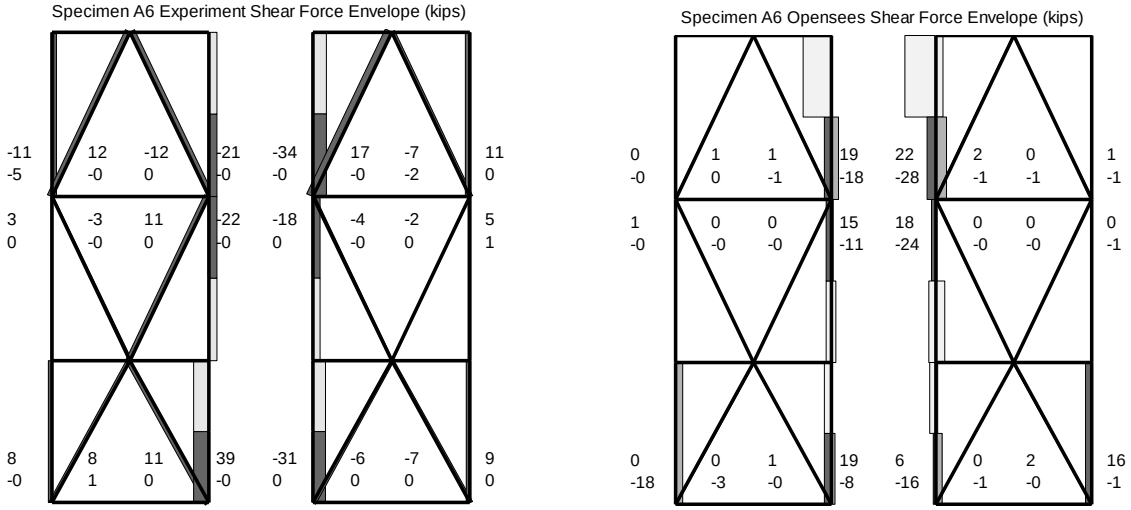

Figure 11.25 Shear Force (kips) Envelope Comparison Between Experiment (Left) and Computational Simulation (Right) for Specimen A6

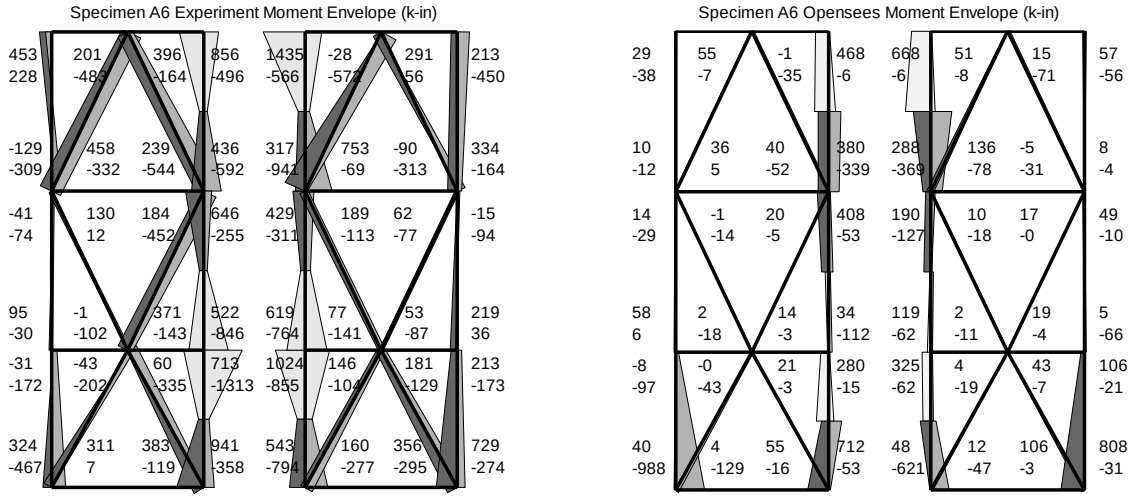

Figure 11.26 Moment (k-in) Envelope Comparison Between Experiment (Left) and Computational Simulation (Right) for Specimen A6

11.1.8 Resultant Forces for Specimen A7

The resultant axial force, shear force, and moment envelopes for Specimen A7 are presented in this section and compared to the force and moment envelopes calculated using the computational model. The forces and moments experienced by Specimen A7 are also compared to Specimen A1 to illuminate the effect of struts on the frame member force distributions.

It is shown in Figure 11.27 that the axial force is better predicted for Specimen A7 than for most of the other specimens. The amount of pin hole tolerance, and the starting location of the pin and connected plies is highly variable throughout the specimens. Minor differences can cause changes in the force distribution. Eliminating the struts and associated pin hole tolerances increased the accuracy of the computational model in matching the experimental resultant forces.

The experimental shear forces and moments shown in Figure 11.28 and Figure 11.29 for the interior columns are larger than those experienced by Specimen A1 and shown in Figure 11.10 and Figure 11.11. The frames in Specimen A7 are still constrained in their movement by the top loading beam and at the bottom by the bumpers, but eliminating the five struts between the frames increased the maximum shear from 54 kips in Specimen A1 to 75 kips in Specimen A7. The experimental moments in the interior columns were similar for Specimen A7 compared to Specimen A1at the first and second floors, but doubled for the bottom of the third floor interior column relative to Specimen A1. There was not a clear trend in axial forces for Specimen A7 compared to Specimen A1. In general, the axial forces did not change significantly with the elimination of the struts, while the shear forces and moments experienced an increase in some members and little change in the majority of members.

As discussed in Chapter 8, the fuses act to pull the frames together as they rock. The forces that develop in the frames related to forces between the two frames is dependent on the fuse thickness, fuse location, amount of constraint between the frames, and location of constraint between the frames. These considerations can be important in frame design.

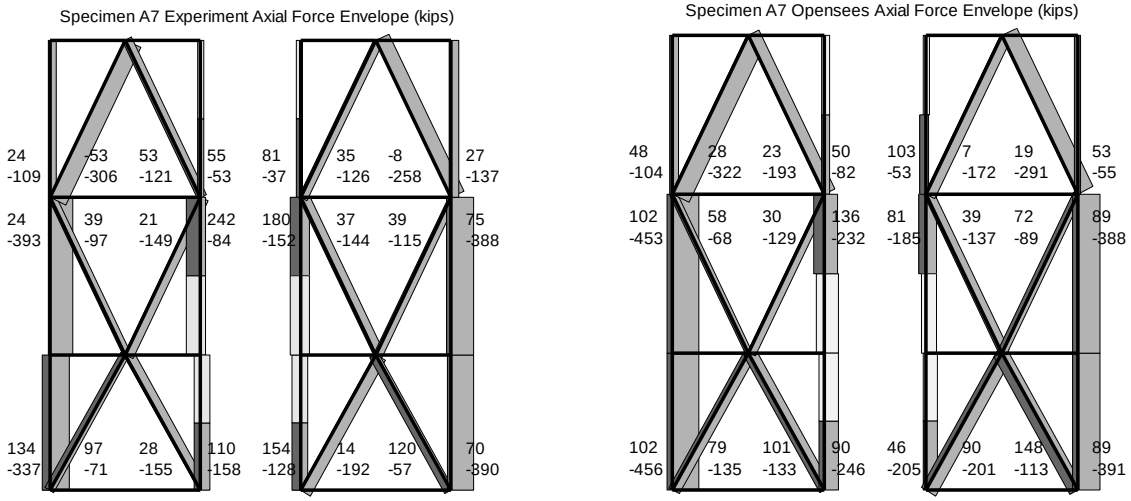

Figure 11.27 Axial Force (kips) Envelope Comparison Between Experiment (Left) and Computational Simulation (Right) for Specimen A7

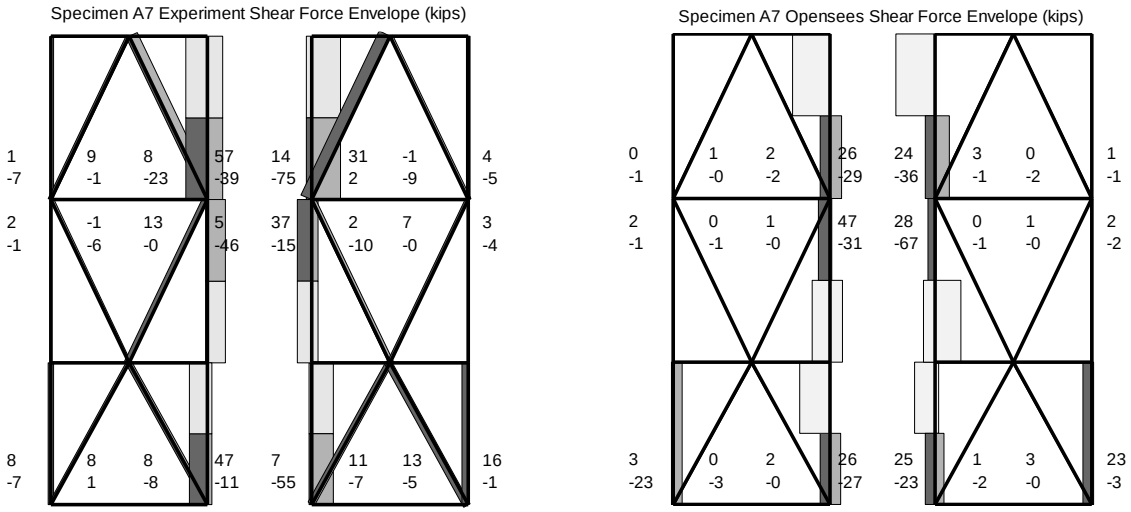

Figure 11.28 Shear Force (kips) Envelope Comparison Between Experiment (Left) and Computational Simulation (Right) for Specimen A7

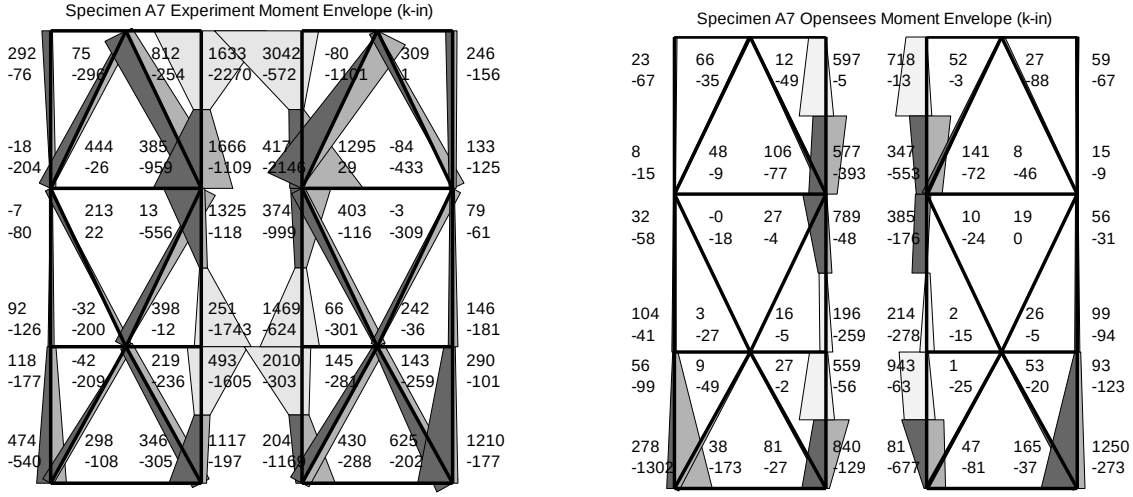

Figure 11.29 Moment (k-in) Envelope Comparison Between Experiment (Left) and Computational Simulation (Right) for Specimen A7

11.1.9 Resultant Forces for Specimen B1 and B2

The force and moment envelopes for Specimen B1 and Specimen B2 demonstrate the behavior of a single frame configuration that has less degrees of indeterminacy than the dual frame configuration. The axial force envelopes shown in Figure 11.30 demonstrate that the computational model is more accurate in matching the experimental forces. This improved accuracy also applies to the shear and moment distributions shown in Figure 11.31 and Figure 11.32.

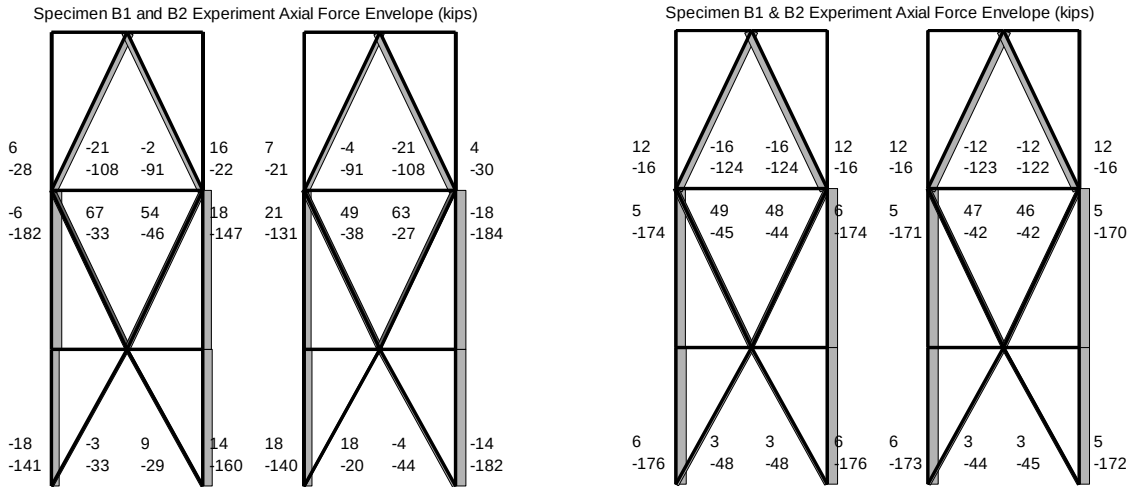

Figure 11.30 Axial Force (kips) Envelope Comparison Between Experiment (Left) and Computational Simulation (Right) for Specimens B1 and B2

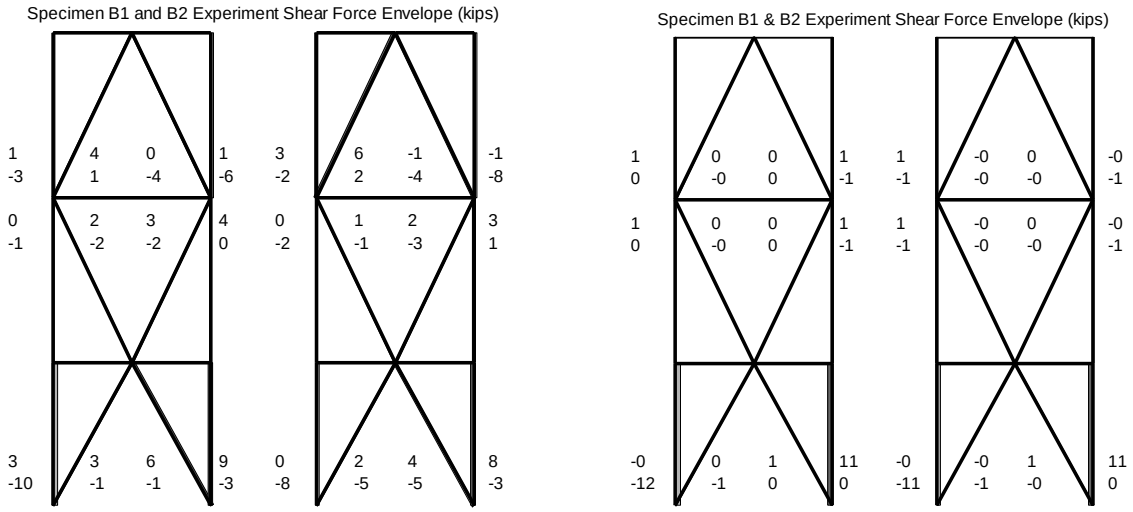

Figure 11.31 Shear Force (kips) Envelope Comparison Between Experiment (Left) and Computational Simulation (Right) for Specimens B1 and B2

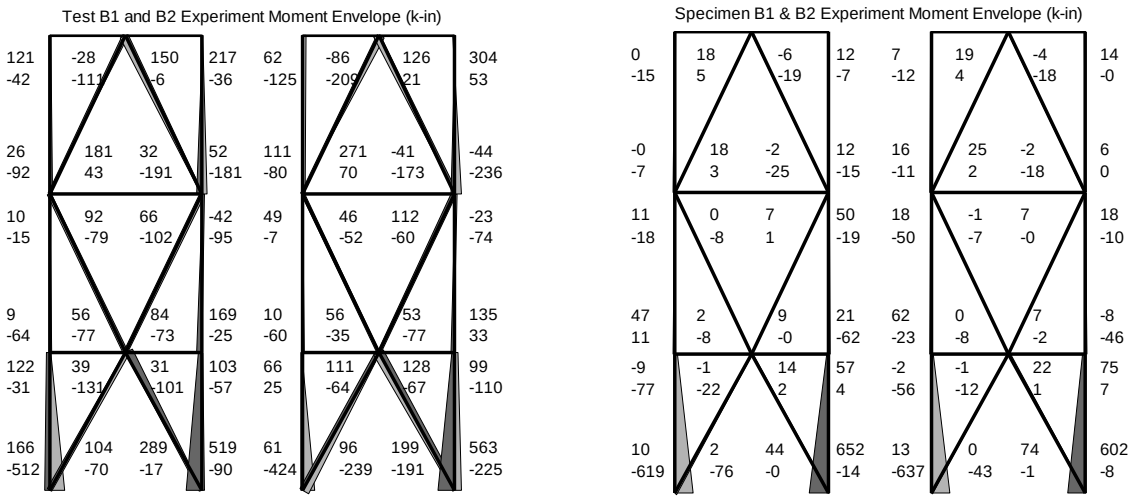

Figure 11.32 Moment (k-in) Envelope Comparison Between Experiment (Left) and Computational Simulation (Right) for Specimens B1 and B2

11.2 Capacity Design Approach and Lateral Load Distributions Considered

A capacity design approach is investigated in this chapter wherein the maximum forces that the fuses and post-tensioning can sustain are applied to the frame. A linear elastic frame analysis is performed based on the loads described in this section. The resulting frame member forces and moments would then be amplified to account for dynamic effects and higher modes. Also, it may be desired to use the worst case loads from multiple load cases.

The maximum post-tensioning force is the area of the post-tensioning, A_{pt}, multiplied by the post-tensioning ultimate stress, σ_u, as given in Equation (11.2). The maximum shear force in the fuses, V_{fp}, is given by Equation (11.1). The moment associated with the fuse shear force, M_{fp}, is given in Equation (11.3) as the fuse shear force multiplied by the distance from column centerline to the fuse link quarter point. The axial force in the fuse was calculated based on the maximum fuse axial forces realized in the experimental program which is shown in Figure 8.28 and described mathematically in Equation (11.4). The equations given here assume an accurate estimate of the yield stress of the fuse plate, σ_{fy}. If nominal stresses are used, appropriate amplification factors, R_y, such as those given in the AISC Seismic Provisions (AISC 2005) should be applied to the yield stress in the following equations.

$$V_{pf} = \frac{4}{9}\frac{b^2 t}{L}\sigma_{fy} N_{links} N_{fuses} \tag{11.1}$$

$$F_{ptu} = \sigma_u A_{pt} \tag{11.2}$$

$$M_{fp} = V_{fp}\frac{B - L_{link}}{2} \tag{11.3}$$

$$P_f = b\, t\, \sigma_{fy}\, 2N_{links} C_{axial} \tag{11.4}$$

Where: C_{axial} = 0.05 for non buckling fuses
C_{axial} = 0.1 for buckling fuses with struts
C_{axial} = 0.2 for buckling fuses without struts

As shown in Figure 11.34, the left frame in the dual frame configuration is designed and then the frame member sizes are mirrored for use in the right frame. The maximum forces for the fuses were applied to the frame as shown on the right of Figure 11.34. The post-tensioning is considered as an elastic element in the frame model and the lateral loads are calculated to produce the maximum post-tensioning force, F_{ptu}. The calculation of the lateral load factor, γ, is given in Equation (11.5) for and Equation (11.6) for the dual frame configuration and Equation (11.7) for the single frame configuration.

$$\gamma_1 = \frac{N_{flrs} T_{fp}\frac{N_{flrs} h_{flr}}{2} - M_{fp} N_{flrs} + P_D A + F_{ptu}\frac{A}{2}}{\sum c_i h_i} \qquad \text{Dual Frame} \tag{11.5}$$

$$\gamma_2 = \frac{N_{flrs} T_{fp}\frac{N_{flrs} h_{flr}}{2} + M_{fp} N_{flrs} + V_{fp} A N_{flrs} + F_{ptu}\frac{A}{2}}{\sum c_i h_i} \qquad \text{Dual Frame} \tag{11.6}$$

$$\gamma_1 = \frac{P_D A + F_{ptu}\frac{A}{2} + V_{fp}\frac{A}{2}}{\sum c_i h_i} \qquad \text{Single Frame} \tag{11.7}$$

Where γ_1 and γ_2 are the load factors applied to the lateral loads as shown in

Figure 11.34 and Figure 11.35

c_i = coefficient for the lateral load given in Figure 11.34 and Figure 11.35
h_i = height of the lateral load

There are two different loading states considered and three different lateral load distributions, totaling six load cases for the dual frame configuration. The single frame configuration only uses one loading state and three load cases. The capacity design methodology proposed here would use the forces for each member found to be the worst from all of the load cases for use in design. The two loading states are shown graphically by the middle two configurations shown in Figure 11.33. As discussed below, the left frame will be designed and the resulting frame sections will be mirrored for use with the right frame. In Load State 1 shown in Figure 11.33, the frames are unloading after an excursion to the right. The fuse is exerting a downward force on the left frame and the left frame is pivoting on its right column. Load State 2 shows loading to the left in which case the fuse shear is still acting downward, but the frame is pivoting on its left column. These two conditions were found to control member forces over the other two possible loading states shown in Figure 11.33.

Three different lateral load distributions were considered in order to capture a range of inertial load distributions that might control frame member design forces. Other seismic force resisting systems typically include elements at each floor that are capable of inelastic action when a critical interstory shear is achieved. Inelasticity can therefore be activated due to higher mode actions, and it is not an issue if interstory shears exceed the design shear capacity of a given floor. Conversely, it is a performance target for the controlled rocking frames that they remain essentially elastic during earthquakes as large as the hazard level with 2% probability of exceedance in 50 years. Inertial load distributions associated with higher modes create interstory shears that are larger than those associated with first mode rocking and must be considered in frame design.

The inverted triangular load cases, IT1 and IT2 shown in Figure 11.34, were intended to create an accurate distribution of column axial forces. The upward triangular load cases, UT1 and UT2, were intended to predict the story shears in lower floors, whereas the reversed linear distributions, RL1 and RL2, were meant to predict the peak story shears in the upper floors. The efficacy of these lateral load distributions are examined in the following sections by comparing the resulting design axial forces to those obtained from nonlinear time history analyses.

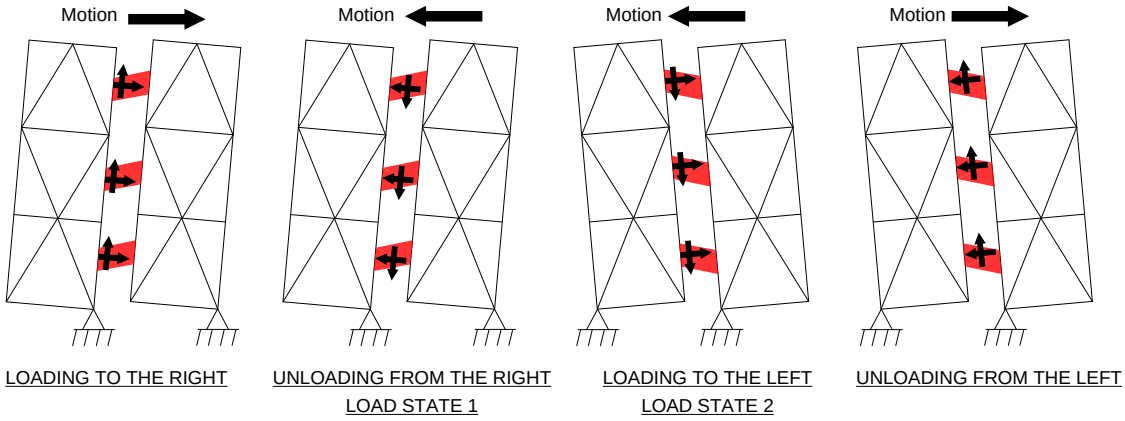

Figure 11.33 Loading States During a Typical Cycle Used to Define Worst Case Loading Conditions for the Left Frame

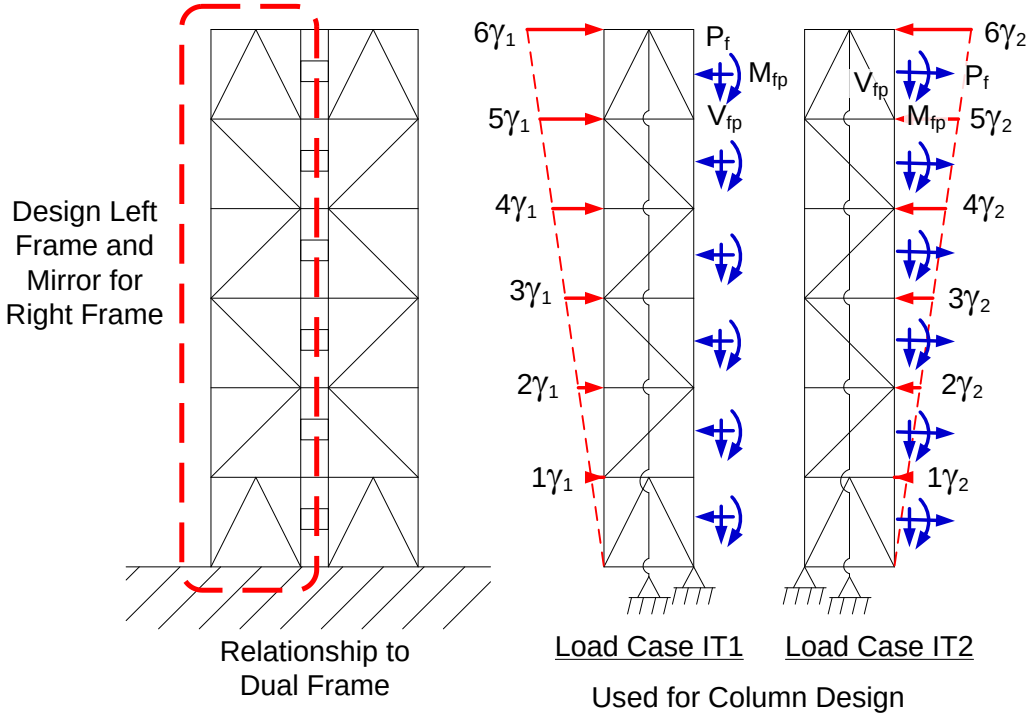

Figure 11.34 Schematic Drawing of Frame Being Designed (Left) and Load Cases IT1 and IT2 (Right)

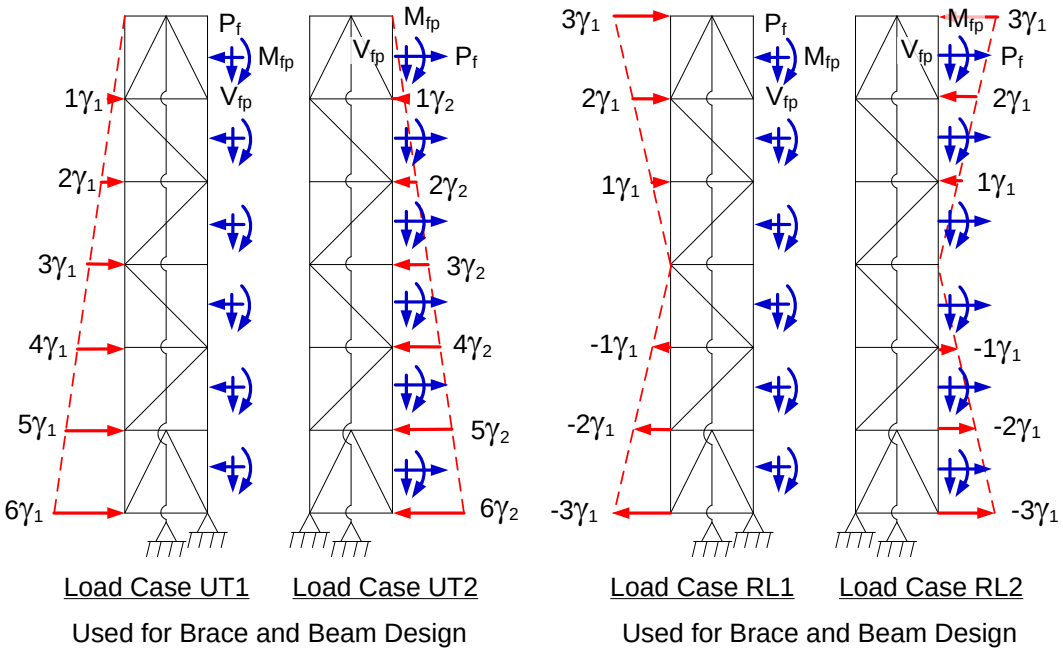

Figure 11.35 Load Cases UT1 and UT2 (Left) and Load Cases RL1 and RL2 (Right)

There are several assumptions implicit in the capacity design method proposed here. These assumptions include:

1. The struts and diaphragm elements between the frames are neglected in the capacity design. The constraint provided by the strut and diaphragm elements would change the lateral load distributions and result in interstory shears that are less severe. It is therefore conservative to neglect them in the capacity design process.
2. Nonlinear time history analyses reflect the additional forces due to vertical modes because vertical mass was included in the sensitivity study computational model. However, the effect of impact and radiation damping during impact are neglected. It is expected, however, that the additional forces due to impact will not be significant for member design because the impact occurs when the column first sets down and the axial load is small.
3. Strain hardening and buckling of the fuses are ignored.
4. The frame member sections used in the sensitivity study were designed based on the method described in Chapter 10. It is assumed that since the frame elements are elastic, that small changes in the section sizes due to different design methods will not significantly change the resulting response.

11.3 Validation of the Capacity Design Approach

All six load cases described in the previous section were applied to all 17 configurations considered in the sensitivity study discussed in the preceding chapter. Linear elastic frame analyses were performed using SAP 2000 software (CSI 2010). The design axial forces predicted for the frame members are compared to those obtained through nonlinear time history analyses of the same configurations with 22 ground motions at varying hazard level. See Chapter 10 for more information about the configurations and ground motions. Chapter 6 contains details about the computational model.

This section starts by showing an example of the comparisons for one configuration subjected to one load case compared to the nonlinear time history analysis results. The comparisons focus on axial forces and are divided into exterior columns, interior columns, and braces. The following subsection shows examples for five of the configurations. Finally, results from all 17 configurations are combined and the ability of the different lateral load distributions to predict the axial forces in the frame members is quantified.

11.3.1 Example Results for Configuration 2 with Inverted Triangular Load Distribution

This section includes the results for one example configuration. The plots presented in this section show the results from each individual analysis run. Since so much data was produced as part of this study, it would not be useful to include similar plots for all of the configurations. The plots in the following section show the results for five representative configurations with only the median and median plus one standard deviation for the data set. The subsequent section shows the results from all configurations combined.

Figure 11.36 shows the ratio of axial demand to design axial force for the interior columns, exterior columns, and braces of Configuration 2 described in Chapter 10. The axial demand is calculated as the peak member force experienced when subjected to the suite of ground motions scaled to the hazard level with 10% probability of exceedance in 50 years. The design axial forces were calculated using the worst case of the two inverted triangular load cases. Figure 11.37 shows similar plots using the demand related to the 2% in 50 years hazard level.

It is shown in Figure 11.36 and Figure 11.37 that the axial forces in the columns were as much as 5 times larger than the design axial forces for the 10% in 50 years hazard level and 7 times larger than the design axial forces for the 2% in 50 years hazard level. The expected brace forces were even larger relative to design axial forces with ratios of 12 and 19 for the 10% in 50 years and 2% in 50 years hazard levels respectively. The median axial force ratios and one standard deviation above the median axial force ratios are also plotted in these figures and shown to be larger than 1.0 in almost all cases.

It is also shown that the axial force demand to design axial ratios are largest at the upper floors whereas the largest ratios for the braces occurs a the lower floors. The difference in axial force ratios suggests that it might be worthwhile to use different methods to obtain design forces for the columns and braces.

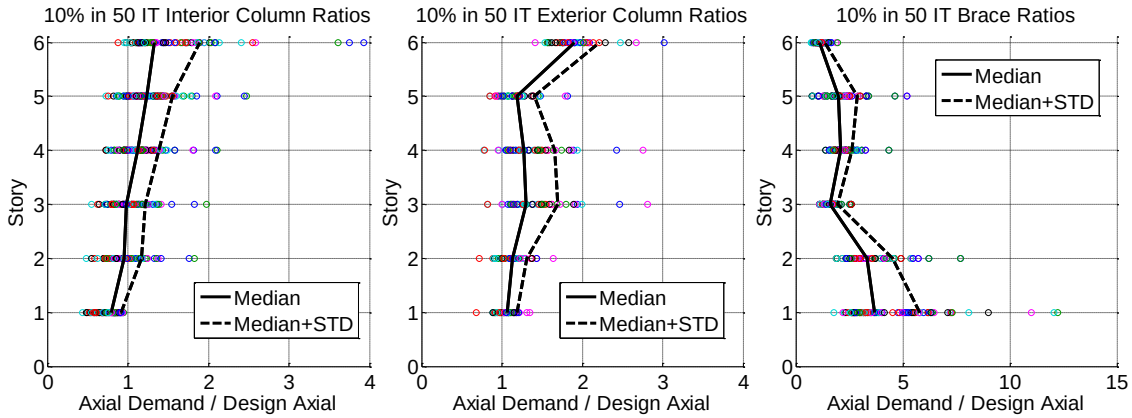

Figure 11.36 Axial Force Demand to Design Ratios for Configuration 2 Using the Inverted Triangular Load Patterns Compared to the 10% in 50 Years Hazard Level

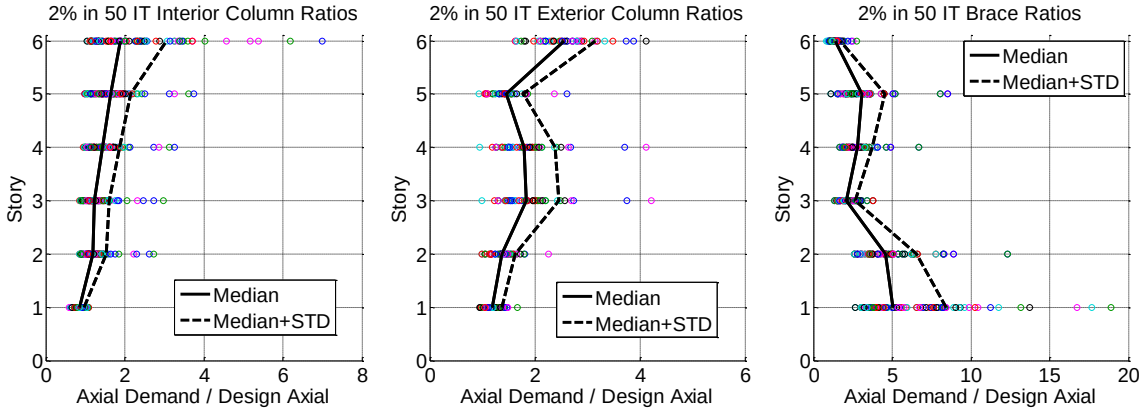

Figure 11.37 Axial Force Demand to Design Ratios for Configuration 2 Using the Inverted Triangular Load Patterns Compared to the 2% in 50 Years Hazard Level

11.3.2 Resulting Axial Force Ratios for Five Configurations

The sensitivity study described in Chapter 10, consisted of almost 1500 analyses. Each of the dots in Figure 11.36 and Figure 11.37 represent the axial demand to design axial ratio for each floor due to one analysis. Instead of presenting plots showing the results of every computational simulation, a representative group of five configurations are presented with the median axial force ratio and one standard deviation above the median. Figure 11.38 shows the axial demand to design axial force ratios for Configuration 1 which was a three-story dual frame configuration. The design axial forces used for Figure 11.38 were computed as the worst case axial forces for each member due to the two inverted triangular load patterns.

It is seen that the columns at the first and second floor exhibit axial force demand close to the design axial force. The columns at the third floor, on the other hand, experience axial forces that are larger than the design force using the inverted triangular load pattern. The design axial forces for the third floor columns are quite small because there is little load applied to them. The nonlinear dynamic time history analyses predict larger forces in these members because vertical accelerations are exciting the mass at the roof level. Although this also occurs at the first and second floor columns, the force

associated with vertical accelerations is small relative to the column axial force. It is also important to note that the consequences of failure of the top floor column are typically not as significant as the consequences of the lower floor columns failing.

The ratios of axial demand to design axial for the braces shown in Figure 11.38 shows the opposite trend in that it is the lower floor braces that exhibit axial force ratios that are significantly larger than 1.0. In conventional seismic force resisting systems, there are typically yielding elements at each floor that limit the amount of force exerted on the steel frame. Since the controlled rocking frame is intended to remain elastic during most ground motions, the distribution of member forces for large earthquake motions is different than conventional systems. The frame not only must resist the forces associated with the first mode, but also the maximum interstory shear forces associated with higher modes.

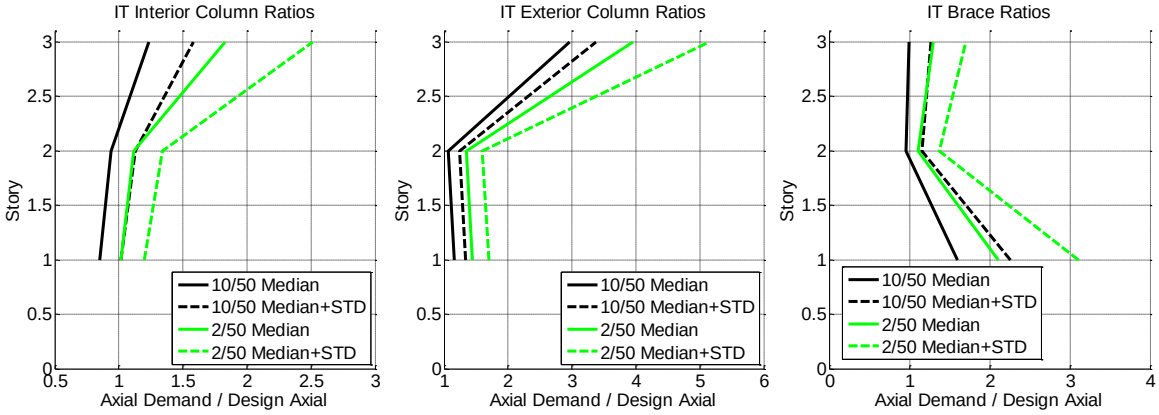

Figure 11.38 Axial Force Demand to Design Ratios for Configuration 1 Using the Inverted Triangular Load Patterns

Figure 11.39 and Figure 11.40 demonstrate how these trends shift as the building is made taller. Figure 11.39 shows the axial force ratios for Configuration 2 which is a six-story structure and Figure 11.40 shows the axial force ratios for Configuration 3 which is a nine-story structure. The largest axial force ratios for the columns occur in the top floor for the same reasons described above for the three-story building. The magnitude of the column axial ratios remains in the same range as the building height increases, but the magnitude of the brace axial ratios increases as the building is made taller. This relationship highlights the fact that maximum brace forces are related to peak interstory shears which are sensitive to higher dynamic modes. The columns on the other hand are more related to cumulative frame shears which are not as sensitive to higher modes.

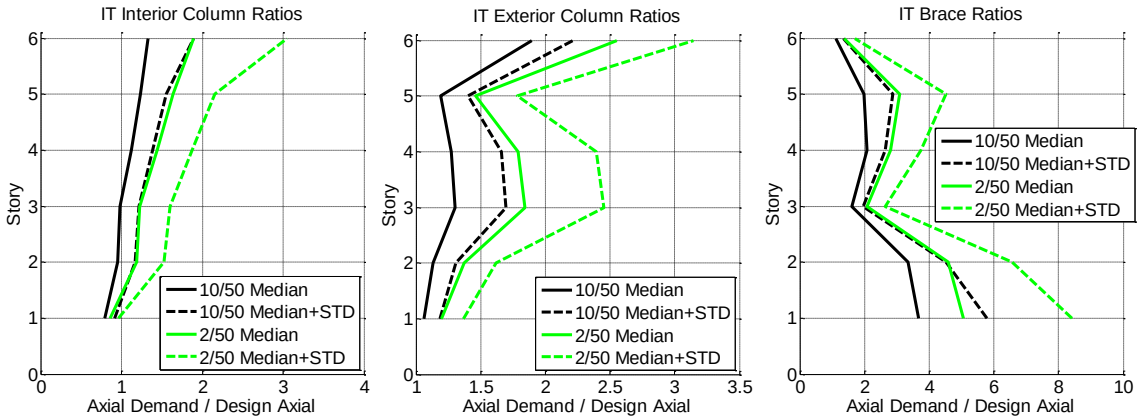

Figure 11.39 Axial Force Demand to Design Ratios for Configuration 2 Using the Inverted Triangular Load Patterns

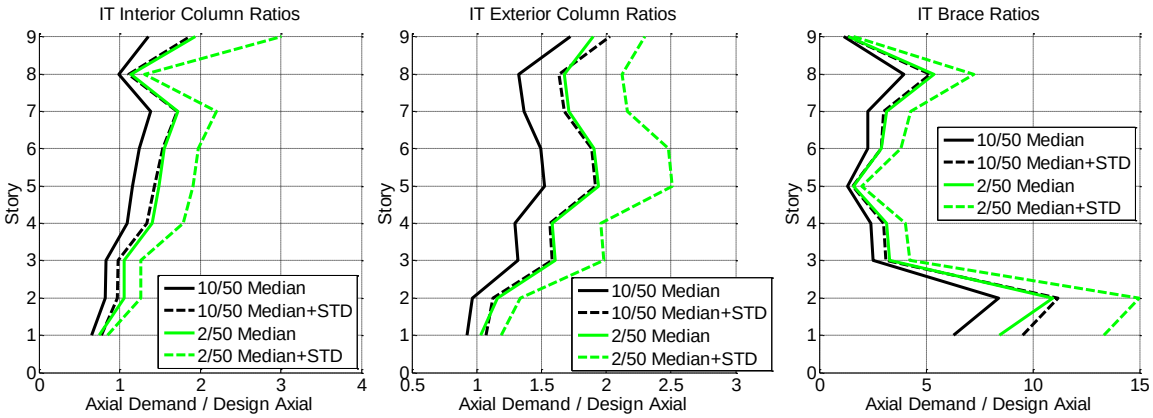

Figure 11.40 Axial Force Demand to Design Ratios for Configuration 3 Using the Inverted Triangular Load Patterns

Figure 11.41 and Figure 11.42 show the axial demand to design axial force ratios for two single frame configurations including a three-story and six-story structure respectively. Comparing these figures to Figure 11.39 and Figure 11.40 reveals that the axial force ratios and in particular the brace axial force ratios are smaller for the single-frame configuration. The exception is the column axial force ratio at the top floor for which the effect of vertical accelerations is found to be worse than the dual frame configuration.

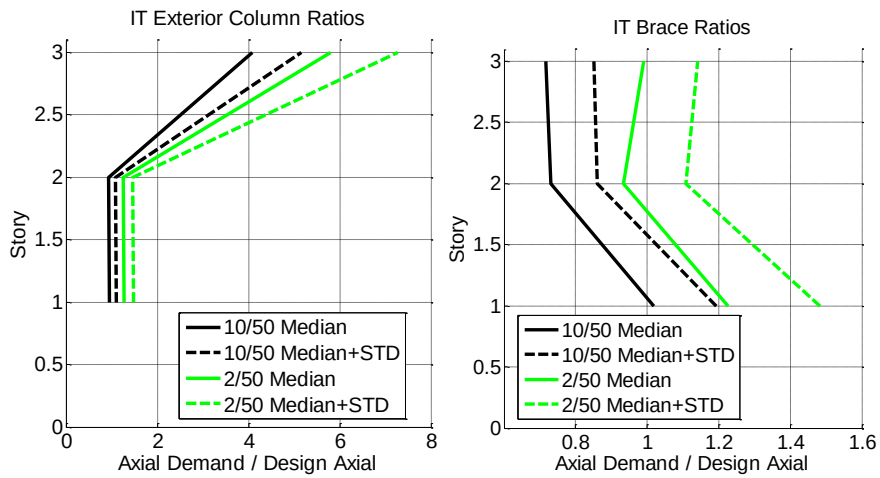

Figure 11.41 Axial Force Demand to Design Ratios for Configuration 5 Using the Inverted Triangular Load Patterns

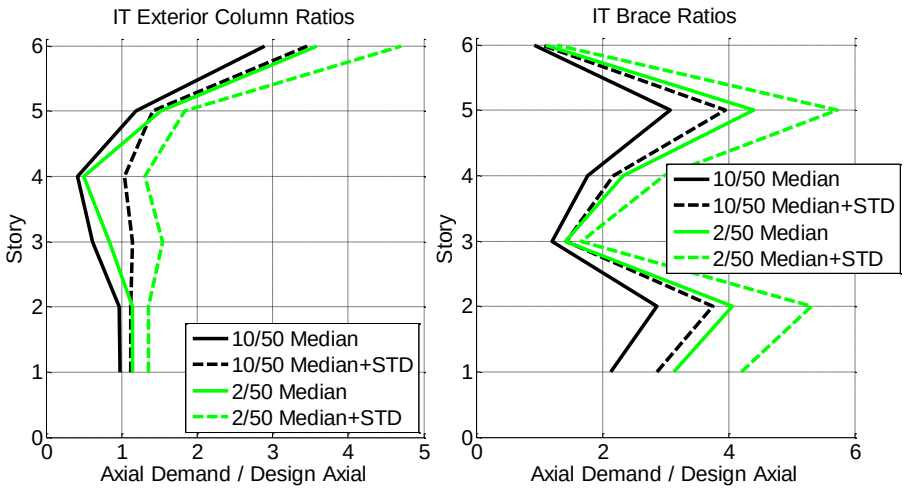

Figure 11.42 Axial Force Demand to Design Ratios for Configuration 7 Using the Inverted Triangular Load Patterns

11.3.3 Axial Force Ratios for all Configurations Combined

The examples provided in the previous section all used the inverted triangular lateral load pattern. In this section the results from all configurations are combined to investigate the effect of using different lateral load patterns and how these methods might be reliably be used to design controlled rocking frame members. Each plot in this section represents the result of 374 nonlinear time history analyses.

Figure 11.43 and Figure 11.44 present the axial demand to design axial force ratios for the hazard level with 10% probability of exceedance in 50 years and 2% in 50 years hazard level respectively. The maximum column axial force ratio occurs at the top floor as described in previous sections. Since the consequences of top column axial failure are less severe than failure of the lower columns, it is instructive to look at the maximum axial force ratio not at the top level. For the median response to the 10% in 50 years hazard level, the maximum interior column axial force ratio (not including the top

floor) occurs near 80% of the building height and is equal to 1.39. If it is desired to limit the interior column's median 10% in 50 years axial demand to be less than the design axial force obtained using the inverted triangular lateral load distribution, the design axial forces should therefore be multiplied by 1.39. This maximum axial force ratio can be used as an amplification factor to account for dynamic effects and higher modes.

All of the maximum axial force ratios are summarized in Table 11.1. The maximum axial force ratios for the interior columns and braces are 1.53 and 8.40 for the same conditions described above. It is clear that while the inverted triangular load distribution approximates the axial load effects on the columns, it does not capture the significant effect of higher modes on the brace design.

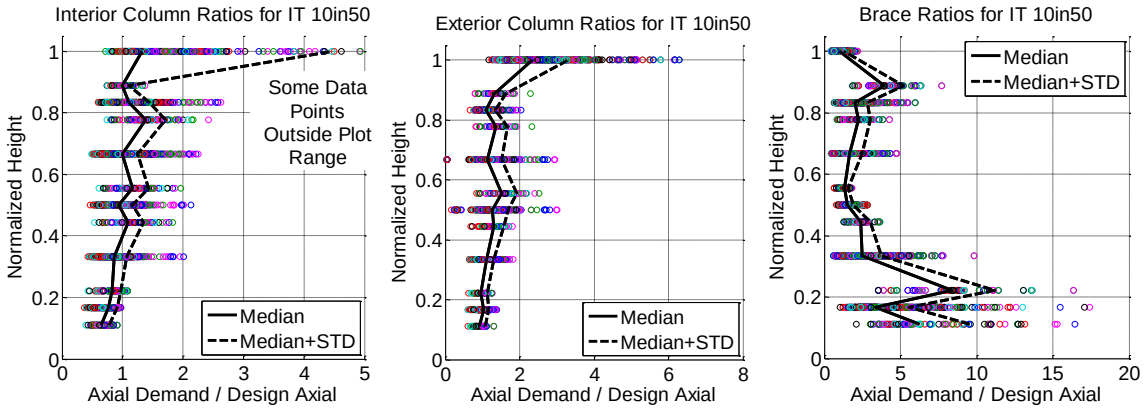

Figure 11.43 Ratios of Axial Force Demand Based on the 10% in 50 Years Hazard Level to Design Axial Forces Calculated Using the Inverted Triangular Load Pattern for All Configurations

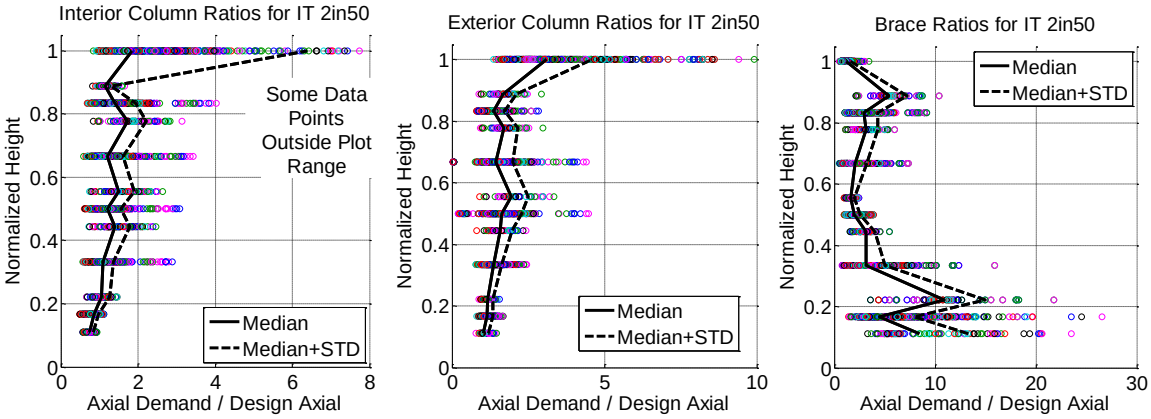

Figure 11.44 Ratios of Axial Force Demand Based on the 2% in 50 Years Hazard Level to Design Axial Forces Calculated Using the Inverted Triangular Load Pattern for All Configurations

As described in a previous section, alternate lateral load distributions were considered in an attempt to simulate some of the forces associated with higher modes. Figure 11.45 and Figure 11.46 show the results of using an upward triangular load distribution, shown in Figure 11.35, to compute the design axial forces. It is shown that the brace axial forces in the lower half of the structure are more accurately predicted with

the design forces associated with the upper triangular load distribution. However, as given in Table 11.1, the brace axial forces are under-represented by a factor between 22 and 52 compared to the median 10% in 50 years axial forces and the median plus one standard deviation for the 2% in 50 years hazard level respectively.

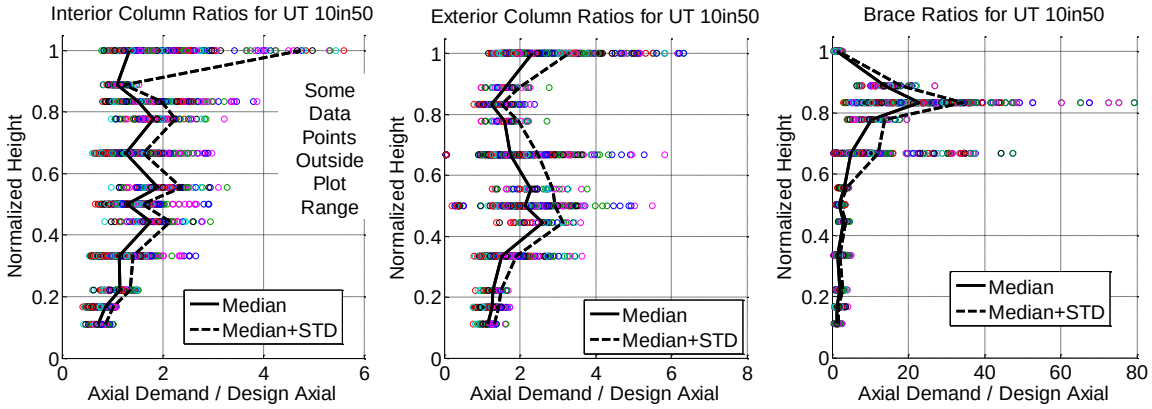

Figure 11.45 Ratios of Axial Force Demand Based on the 10% in 50 Hazard Level to Design Axial Forces Calculated Using the Upward Triangular Load Pattern for All Configurations

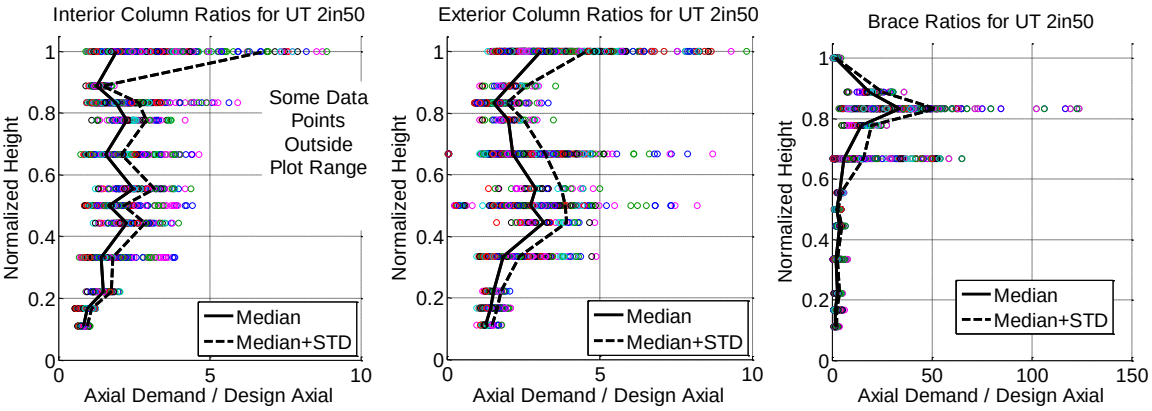

Figure 11.46 Ratios of Axial Force Demand Based on the 2% in 50 Hazard Level to Design Axial Forces Calculated Using the Upward Triangular Load Pattern for All Configurations

Similarly, a reverse linear lateral load distribution, shown on the right of Figure 11.35 was used to calculate design axial forces which led to the axial force ratios given in Figure 11.47 and Figure 11.48. This lateral load distribution is shown to more accurately predict the brace axial forces in the upper half of the building. The brace axial forces in the lower floors are considerable underestimated however.

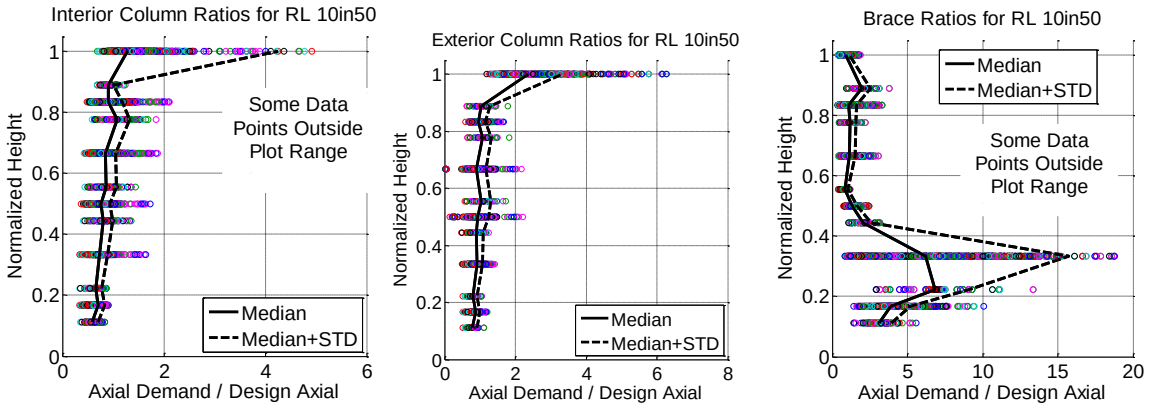

Figure 11.47 Ratios of Axial Force Demand Based on the 10% in 50 Hazard Level to Design Axial Forces Calculated Using the Reversed Linear Load Pattern for All Configurations

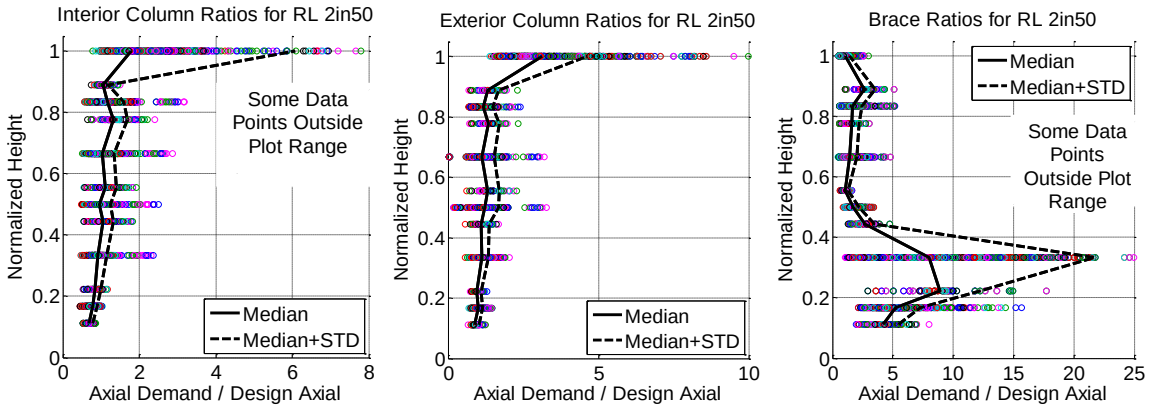

Figure 11.48 Ratios of Axial Force Demand Based on the 2% in 50 Hazard Level to Design Axial Forces Calculated Using the Reversed Linear Load Pattern for All Configurations

Clearly, both the upward triangular lateral load distribution and the reversed linear lateral load distribution are not efficient on their own in simulating the brace forces experienced in the nonlinear time history analyses. These lateral load distributions were instead intended to be used together to simulate worst case load combinations. Figure 11.49 and Figure 11.50 show the axial demand to design axial force ratios in which the design axial forces for each member are taken to be the larger of the axial forces resulting from the upward triangular and reversed linear lateral load distributions. As shown in Figure 11.49, the maximum brace axial force ratios were 2.06 for the median response to motions with 10% probability of exceedance in 50 years and 2.74 for the median plus one standard deviation response to the 10% in 50 years motions. The axial demand to design axial force ratios are smaller and more consistent for the braces using this method for calculating design axial forces.

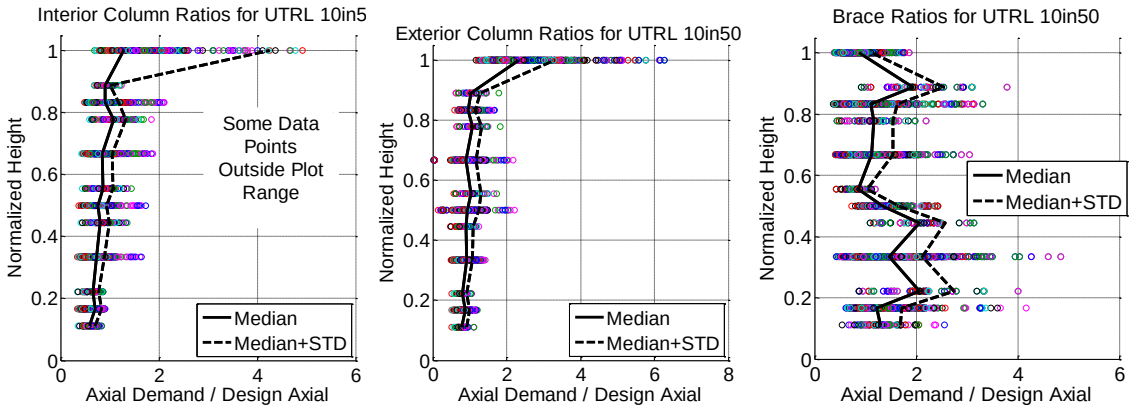

Figure 11.49 Ratios of Axial Force Demand Based on the 10% in 50 Hazard Level to Design Axial Forces Calculated Using the Worst of the Upward Triangular and Reversed Linear Load Pattern for All Configurations

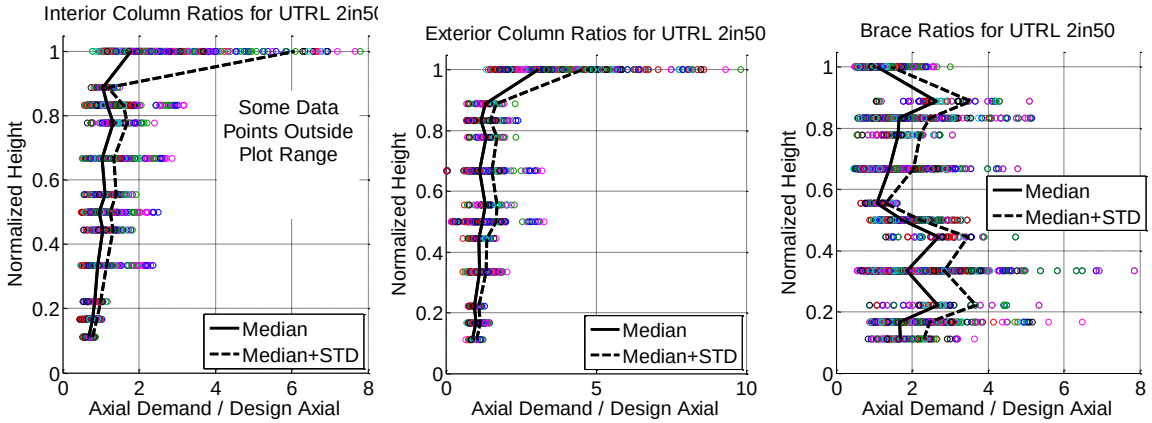

Figure 11.50 Ratios of Axial Force Demand Based on the 2% in 50 Hazard Level to Design Axial Forces Calculated Using the Worst of the Upward Triangular and Reversed Linear Load Pattern for All Configurations

The maximum axial force ratios for all of the lateral load distributions considered are given in Table 11.1. These maximum axial force ratios can be used as amplification factors to be applied to the design axial forces to account for dynamic effects and higher modes. Different levels of exceedance probability and hazard level can be considered in design by choosing the amplification factor that corresponds to either the hazard level with 10% probability of exceedance in 50 years or the 2% in 50 years hazard level and the probability of exceeding the design forces (e.g., 50% probability of exceedance for the median value and 84% probability of exceedance for the median plus one standard deviation value). Other probabilities of exceedance are possible by assuming a lognormal distribution with the given median and standard deviation.

Table 11.1 Maximum Demand to Design Ratios* for Different Capacity Design Lateral Load Distributions and Different Hazard Levels (Amplification Factors)

			Exterior Column	Interior Column	Braces
Inverted Triangular Load Distribution	10% / 50	Median	1.53	1.39	8.40
		Med + STD	1.92	1.71	11.18
	2% / 50	Median	1.94	1.72	10.94
		Med + STD	2.51	2.20	14.98
Upward Triangular Load Distribution	10% / 50	Median	2.60	1.90	22.82
		Med + STD	3.14	2.36	34.24
	2% / 50	Median	3.18	2.48	34.00
		Med + STD	3.93	3.18	52.09
Reversed Linear Load Distribution	10% / 50	Median	1.07	1.07	6.84
		Med + STD	1.31	1.32	15.74
	2% / 50	Median	1.34	1.32	8.92
		Med + STD	1.71	1.69	21.71
Worst of UT and RL Load Distributions	10% / 50	Median	1.07	1.07	2.06
		Med + STD	1.31	1.33	2.74
	2% / 50	Median	1.34	1.32	2.70
		Med + STD	1.71	1.69	3.67

* Maximum demand to design ratios do not include the top floor columns

An example of how this table might be used is as follows. For a given controlled rocking frame it is decided that the frame member axial forces should not have more than a 50% probability of exceedance when subjected to an earthquake at that has a 2% probability of exceedance in 50 years. A linear elastic frame analysis model is created with four load cases including the upward triangular lateral load pattern and the reversed linear lateral load pattern shown in Figure 11.35. The amplification factors of 1.34 and 2.70 are obtained from Table 11.1 (after further research, these may be rounded to values appropriate for more general design) for the column and braces respectively. The worst case axial forces from the four load cases are multiplied by these amplification factors and used to design the members.

The FEMA document used to calculate building seismic performance factors (FEMA P695 2009), provides context for the choice of hazard level. The acceptability of seismic performance factors is based on a margin of safety against collapse at the hazard level with 2% probability of exceedance in 50 years as defined using the median of the set of ground motions. Also, as discussed in Chapter 12, it is desirable to prevent inelasticity in the frame members for the majority of ground motions that have a 2% probability of exceedance in 50 years.

Using the median 2% in 50 years values from Table 11.1 for the design of the controlled rocking frame is expected to produce frames that satisfy these performance goals although the current study did not investigate flexure-axial interaction or

probabilities of collapse. Further investigation is needed to determine whether the proposed capacity design method satisfies FEMA P695 or the goal that the frame members stay elastic for the average 2% in 50 years ground motion.

11.4 Summary of Frame Member Forces

Peak resultant axial forces, shear forces, and moments from the experimental program were presented and discussed in conjunction with some maximum strains recorded for individual strain gages. The largest resultant forces, moments, and strains occur at the base of the exterior columns. Based on the available data, it is likely that the outside flange tips at the base of the exterior columns experienced localized inelastic strains during some of the specimen tests. However, no yielding or buckling was observed in the post-test inspections of the specimens.

In general, the computational simulations were shown to produce axial forces, shear forces, and moments similar to those experienced in the experimental program. The computational model was therefore considered adequate for predicting member force demands using nonlinear time history analyses for comparison with design forces.

A capacity design methodology was presented in which a linear elastic frame model is used to calculate force demands based on multiple load cases. The worst case member forces are then multiplied by an amplification factor to account for dynamic effects and higher modes. The amplification factors were calculated as the maximum ratio of axial force obtained using nonlinear time history analyses on a range of buildings to the design axial force. Although amplification factors are presented for different hazard levels, it is the goal of the capacity design methodology that the frame members remain elastic for the majority of ground motions that have a 2% probability of exceedance in 50 years.

It is important to note that there are limitations to the capacity design method presented here and needs for future research:

- The assessment of the capacity design method only considered axial forces. A more thorough assessment of the methodology is warranted considering shear, moment, and flexure-axial force interaction.
- The effect of vertical modes was included in the computational model, but other dynamic effects such as radiation damping due to impact were neglected. However, it is conservative to neglect the effect of radiation damping.
- The assessment of the capacity design method included in this chapter does not represent a full reliability study. A more comprehensive reliability study would also consider the statistical distribution of member resistance to investigate probabilities of member failure.
- A more comprehensive reliability study should also consider the consequences of member failure. The proposed method presented in this chapter uses the maximum ratio across the height of the building of axial force demand (for either median or median plus one standard deviation) to design axial force as the factor to amplify the design forces. This does not take into account the fact that the failure of some members has more severe consequences than others.

Finally, it is noted that the capacity design method presented in this chapter is intended to be easy to conduct. However, there are more advanced and accurate methods for conducting frame design for the controlled rocking system. Three tiers of frame design are identified and include:

1. A capacity design method based on elastic frame analysis such as the method presented in this chapter.
2. Modal combination approaches, such as those described in Roke et al. (2009).
3. Nonlinear time history analyses.

RECOMMENDED DESIGN STRATEGY

12.1 Introduction

The purpose of this chapter is to synthesize the results, observations, and conclusions from all of the previous chapters as they pertain to the practical design of the controlled rocking system. As such, some information is repeated and in other cases reference is made to previous chapters. A summary list of recommended design steps is included in Chapter 13.

The limit states for the controlled rocking system are given in Table 12.1. The target performance when subjected to different hazard levels is described. Methods for preventing the listed limit states are discussed in this chapter.

Table 12.1 Goals for Preventing Limit States for Different Hazard Levels

Limit State	50% in 30 Years	10% in 50 Years	2% in 50 Years
Uplift	Small	Allowed	Allowed
Fuse Yield	Small	Allowed	Allowed
Post-Tension Yield	Not Allowed	Not Allowed	Limit to Low Probability
Post-Tension Wire Fracture	Not Allowed	Not Allowed	Limit to Small Percentage of Wires if Any
Fuse Fracture	Not Allowed	Not Allowed	Limit to Low Probability
Inelasticity in Frames or Frame Connections	Not Allowed	Not Allowed	Limit to Low Probability
Global Uplift	Not Allowed	Not Allowed	Not Allowed
Fracture of all Post-Tensioning Strands	Not Allowed	Not Allowed	Not Allowed

There are a variety of structural configurations that may use a controlled rocking approach with energy-dissipating fuses. This research investigated both single frame and dual frame configurations. As a first step to design, it is necessary to select the structural configuration; in the context of this research either a dual frame configuration or a single frame configuration would be selected to initiate design. Considerations for this decision are given in Table 12.2.

Table 12.2 Summary of the Advantages of the Dual Frame and Single Frame Configurations

Advantages of the Dual Frame Configuration	Advantages of the Single Frame Configuration
• Fuses along the height of the frames can dissipate energy due to higher mode deformations • Less congested detailing because fuse is away from the post-tensioning • No need for pin connections between the fuse and the frame eliminating issues with pin hole tolerances • No additional fuse frame assembly is necessary as is needed for single frame. • Post-tensioning is split into two bundles which may be easier to detail • Ability to use smaller self-centering ratios	• Fuses do not apply forces along the height of the frames and thus do not cause residual elastic frame deformations • One frame can be applied to shorter bay widths than two frames • Flow of forces in the frame is simpler • No issues related to relative motion of two frames such as constraint or forces between the dual frames • Only one fuse location for each frame translates into less cost for replacement • Less fit-up issues in the field with only one frame

12.2 System Proportioning

The design process then begins with the calculation of design earthquake forces. Based on strength requirements, self-centering goals, and the prevention of global uplift, the desired fuse capacity and initial post-tensioning force are calculated, as discussed below. Alternative methods for proportioning the fuse capacity and initial post-tensioning force may have advantages, such as direct displacement-based design (Ma 2010).

12.2.1 Proportioning for Strength

Equivalent lateral forces can be calculated according to building codes such as ASCE 7-05 (ASCE 2005). A response modification factor of R=8.0 has been assumed in this work based on the large ductility of the system and the performance of the sensitivity study configurations. The configurations designed as part of the sensitivity were shown to have between 15.9% and 51.1% probability of exceeding a roof drift ratio of 2.0% for the hazard level with 10% probability of exceedance in 50 years and between 15.9% and 58.3% probability of exceeding a roof drift ratio of 3.0% for the 2% in 50 years hazard

level. Probabilities of exceeding fuse and post-tensioning limit states were found to be low and are discussed in the following sections. Although the probability of adverse limit states or large drifts was found to be relatively low using a response modification factor of R=8.0, the sensitivity study was not conducted to meet the requirements of an ATC 63 investigation (FEMA P695 2009).

The load combination for use in designing the system is given in Equation (12.1) which is load combination 7 from Section 2.3.2 of ASCE 7-05 (ASCE 2005). The design overturning moment, M_{ovt}, is given as the sum of the equivalent lateral forces multiplied by their respective heights as given in Equation (12.2) and shown schematically in Figure 12.1 for an example three-story structure.

$$0.9\,D + 1.0\,E \tag{12.1}$$

$$M_{ovt} = \sum_{i=1}^{\#Floors} F_i H_i \tag{12.2}$$

Where:

F_i = Equivalent lateral force at level i
H_i = Height of level i

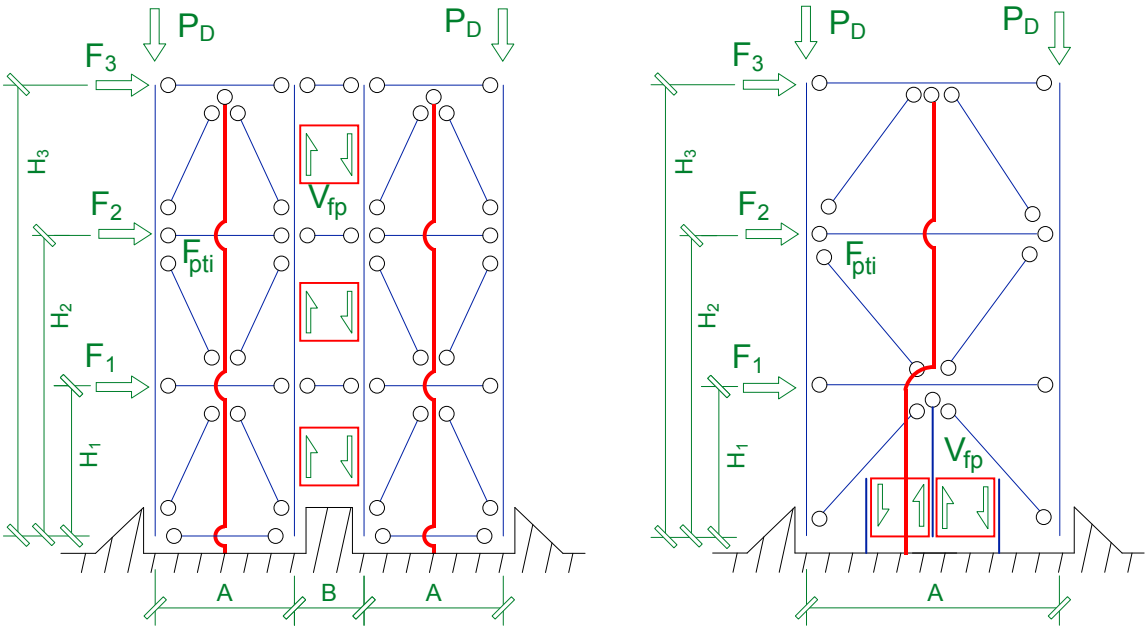

Figure 12.1 Idealized Controlled Rocking Frame in the Dual Frame Configuration (Left) and Single Frame Configuration (Right)

The resistance to overturning is calculated in Equation (12.3), (12.4), and (12.5). A resistance factor of 0.9 was applied to the overturning moment. As shown in Figure 12.1, the overturning moments are resisted by the initial post-tensioning force, F_{pti}, the total fuse shear capacity, V_{fp}, and the tributary dead load P_D. The dead load is assumed to act only on the exterior columns for the sake of these equations, but application of dead

load in different patterns can be considered by adjusting the dead load term to account for the horizontal eccentricity of the dead load relative to the pivot points.

The ability of the system to resist lateral forces results in the first design relationship given in Equation (12.3) which expands out to Equation (12.4) and (12.5). This relationship is combined with the self-centering goals in the next section to solve for the required fuse capacity and initial post-tensioning force.

$$\phi M_{resist} = M_{ovt} \tag{12.3}$$

$$0.9\left[\left(F_{pti} + 0.9P_D\right)A + V_{fp}\left(A + B\right)\right] = M_{ovt} \qquad \text{(DUAL FRAME)} \tag{12.4}$$

$$0.9\left[\left(F_{pti} + 1.8P_D + V_{fp}\right)\frac{A}{2}\right] = M_{ovt} \qquad \text{(SINGLE FRAME)} \tag{12.5}$$

Where:
F_{pti} = Initial post-tension force
V_{fp} = shear yield capacity of all fuses
A, B = Dimensions Shown in Figure 12.1
P_D = Total dead load applied to one exterior uplifting column

12.2.2 Proportioning for Self-Centering

To proportion the fuse capacity and initial post-tensioning force, it is necessary to define the desired level of self centering. To create a fully self-centering flag-shaped load-deformation response, the self-centering ratio presented in chapter 3 will be equal to or larger than 1.0. However, it was demonstrated through a parametric study presented in Chapter 9 that probabilistic self-centering can reliably eliminate residual drifts with self-centering ratios as low as 0.5. To utilize self-centering ratios significantly less than 1.0 will require the use of different configurations that are not susceptible to global uplift, as discussed in the following section.

The restoring moment is set equal to the moments that are resisting self-centering multiplied by the self-centering ratio. Equation (12.6) gives the general condition which is then expanded in Equation (12.7) and (12.8) for dual frame configurations and single frame configurations respectively.

$$M_{restore} = SC\, M_{fuse} \tag{12.6}$$

$$\left(F_{pti} + 0.9P_D\right)A = SC\, V_{fp}\left(A + B\right) \qquad \text{(DUAL FRAME)} \tag{12.7}$$

$$F_{pti} + 1.8P_D = SC\, V_{fp} \qquad \text{(SINGLE FRAME)} \tag{12.8}$$

Subtracting Equation (12.4) from Equation (12.7) or subtracting Equation (12.5) from Equation (12.8), causes the contribution of the P/T force and gravity load to drop out leaving an equation for proportioning the fuse strength based on the design overturning moment given in Equation (12.9) and (12.10).

$$V_{fp} = \frac{M_{ovt}}{0.9(1+SC)(A+B)} \qquad \text{(DUAL FRAME)} \qquad (12.9)$$

$$V_{fp} = \frac{2M_{ovt}}{0.9(1+SC)A} \qquad \text{(SINGLE FRAME)} \qquad (12.10)$$

After designing the fuse, the initial post-tension force required to satisfy the specified self-centering ratio can be calculated by rearranging Equation (12.7) and (12.8), which results in Equation (12.11) and (12.12).

$$F_{pti} = V_{fp}\frac{SC(A+B)}{A} - 0.9P_D \qquad \text{(DUAL FRAME)} \qquad (12.11)$$

$$F_{pti} = SC\,V_{fp} - 1.8P_D \qquad \text{(SINGLE FRAME)} \qquad (12.12)$$

12.2.3 Proportioning Against Global Uplift

It is necessary to prevent undesirable limit states and deformation modes. Global uplift is characterized by both legs of a frame lifting off the supports. In the dual frame configuration, this corresponds to the windward frame being lifted off the ground. In the single frame configuration global uplift corresponds to the frame not being supported by the column supports, but instead supported on the fuses. See Figure 3.5 for a schematic representation of global uplift for the dual frame configuration. To prevent global uplift, the post-tensioning force has to be greater than the resisting force of the fuses as given in Equation (12.13).

$$F_{pti} > C_{sh}V_{fp} \qquad (12.13)$$

Where:

C_{sh} = Factor for Strain Hardening

Alternative configurations are possible that are not susceptible to global uplift. For instance, the energy-dissipating elements might be separated from the rocking frame (e.g., a buckling restrained braced frame in a different bay than the rocking frame). If the energy-dissipating components and restoring force components are separated, the global uplift limit state would not apply.

12.3 Fuse Design and Considerations

The steel fuse plates can be designed based on plastic hinging at the quarter points of the fuse links. Equation (12.14) gives the plastic shear capacity of the fuses.

$$V_{fp} = \frac{4}{9}\frac{b^2 t}{L}\sigma_{fy} N_{links} N_{fuses} \quad (12.14)$$

Where b = link depth at the ends
t = fuse plate thickness
L = link length
σ_{fp} = fuse plate yield strength
N_{links} = Number of links per fuse
N_{fuses} = Number of fuses

The slenderness of the fuse should be set to produce either buckling or non-buckling response. Tested fuses with slenderness ratios between L/t=8 and L/t=22.4 did not exhibit buckling. Tested fuses with slenderness ratios of L/t=32 and larger experienced lateral-torsional buckling. Based on the experimental program and computational simulations, it is concluded that thicker non-buckling fuses offer several advantages over thin buckling fuses:

- It was found that buckling fuses experienced significantly larger axial forces after buckling than the non-buckling fuses.
- Larger fuse axial forces create larger frame column moments and shears
- Buckled fuses absorb less seismic energy
- Fuse link buckling occurs due to the combination of shear, moment, and axial forces. In this indeterminate system, the axial forces vary making it difficult to predict fuse buckling and making seismic performance less consistent.
- Thick fuses exhibit an elastic-plastic hardening response that is easy to simulate in a computational model.
- Based on the hybrid simulation tests of Specimen A5 and the other thick fuse specimens, it is concluded that thick fuses may not need to be replaced even after large earthquakes.

Another consideration in fuse design is preventing fuse link fracture. Although none of the large-scale system tests experienced fuse fracture, the fuse component tests conducted at Stanford University were conducted up to fuse fracture. The four steel butterfly plate fuses that were bolted to the supports experienced fracture between 30% and 46% shear strain across the fuse link. The large-scale cyclic system tests reached fuse shear strains of 25% without any fractures of the fuse links.

It is advisable therefore, to limit the expected fuse shear strain to 30% across the fuse link for the hazard level that has 2% probability of exceedance in 50 years. This would represent a low probability of fracturing the fuse in a long return period earthquake. This limit can be enforced by estimating the fuse link shear strain for a given level of roof drift ratio. The sensitivity study suggests that the controlled rocking system will have a 50% probability or less of exceeding 3% roof drift ratio under the 2% in 50 years event. Equation (12.15) and (12.16) give the fuse link shear strain, γ_{link} assuming rigid body motion of the frames.

$$\gamma_{link} = \alpha \frac{A+B}{L} \qquad \text{(DUAL FRAME)} \qquad (12.15)$$

$$\gamma_{link} = \alpha \frac{A}{2L} \qquad \text{(SINGLE FRAME)} \qquad (12.16)$$

Where α = Roof drift ratio

12.4 Post-Tensioning Design and Considerations

Designing the post-tensioning consists of selecting the number of post-tensioning strands and the initial post-tensioning stress to satisfy the required initial post-tensioning force. A minimum initial post-tensioning stress will be dictated by the lowest initial force that can be practically applied to a strand. The large-scale testing program utilized initial post-tensioning stress as low as 28.7% of ultimate. Use of lower initial post-tensioning stress may be possible, but should be verified.

A maximum initial post-tensioning stress is dictated by the amount of elastic strain capacity required for a given configuration. Table 8.9 gives the maximum post-tensioning strains required to limit the probability of fracturing post-tensioning wires to an acceptable level. For instance, since Specimen A4 did not experience significant loss of strength, stiffness, or self-centering abilities after 5% of the post-tensioning wires fractured, it might be deemed acceptable to allow a 50% probability of fracturing 5% of the post-tensioning wires during the earthquake event that has 2% probability of exceedance in 50 years. According to Table 8.9, if the post-tensioning strands are limited to 1% strain, then there will be a 78% probability that no more than 5% of the post-tensioning wires will fracture. According to Table 10.14, a roof drift ratio of 3.0% will approximately represent the median 2% in 50 years event. By estimating the amount of superimposed elastic strain in the post-tensioning strands due to this level of roof drift, and subtracting from the limit of 1% strain, a maximum initial post-tensioning strain can be calculated.

An initial post-tensioning stress that is between the minimum and maximum values described above is then selected. The required area of the post-tensioning strands can then be calculated as the required initial post-tensioning force divided by the initial post-tensioning strand stress. The exact area of post-tensioning will have to be selected based on the available sizes for strands such as 0.5" diameter strands (A=0.153 in^2) or 0.6" diameter strands (A=0.217 in^2). The initial post-tensioning stress should then be adjusted based on the actual area of strands used by dividing the required post-tensioning force by the area of post-tensioning strands.

Another consideration regarding the post-tensioning is the seating losses associated with the wedges getting pulled farther into the anchorage as the strand is stressed to forces larger than previously attained. If seating losses are not eliminated as described in the section on detailing below, it may be worthwhile to use a larger self-centering ratio that has additional post-tensioning. The effect of seating losses was studied as part of the sensitivity study and more details about the effects on response are included in Chapter 10.

12.5 Frame Design

Three tiers of frame member design were identified at the end of Chapter 11 and they include:

1. A capacity design method based on elastic frame analysis.
2. Modal combination approaches, such as those described in Roke et al. (2009).
3. Nonlinear time history analyses.

Chapter 11 presented a capacity design approach wherein the maximum forces that the fuse can produce are applied to an elastic frame analysis model that includes the post-tensioning as a truss element. The maximum fuse forces to be used with this method were given in Equation (11.1), (11.2), (11.3), and (11.4). One or more lateral load distributions are considered, such as the inverted triangular distribution shown in Figure 11.34, the upward triangular distribution shown in Figure 11.35, or the reversed linear distribution shown in Figure 11.35. The lateral load factor, γ, is calculated using Equation (11.5), (11.6), or (11.7) which will cause the post-tensioning element to reach the ultimate force of the post-tensioning strands.

The worst case member forces calculated from all the load cases considered is then multiplied by an amplification factor to account for dynamic effects and higher modes. The amplification factors are given in Table 11.1 for different hazard levels, probabilities of exceedance (e.g., median has a 50% probability of exceedance), and load cases.

12.6 Detailing and Construction Considerations

One of the goals of the large-scale tests conducted at the University of Illinois was to investigate and improve the performance of controlled rocking construction details not common in steel structures such as post-tensioning anchorage and column bases allowed to uplift and pivot. The key details are described in Chapter 4 and the design details are included in Appendix A. In this section, the experiences gained through the experimental program are used to define suggestions for detailing the controlled rocking specimen.

As discussed in Chapter 5, the testing of Specimen A1 illuminated the effects of post-tensioning strand seating losses. Since these losses in the post-tensioning force are due to the wedges being pulled down farther into the anchorage when the forces in the strands increase above previous maximum levels, it is recommended that the seating losses be eliminated by subjecting the strands to forces on the same order as what they might experience in an earthquake. Figure 12.2 shows pictures from the large-scale shake table testing of the controlled rocking system conducted at E-Defense in Japan (Ma 2010). On the left of Figure 12.2, there is a set of split washers wrapped in green tape immediately above the anchorage plate. The post-tensioning chucks were stressed against these temporary washers to a force level near the maximum expected to occur during the shake table testing. On the right of Figure 12.2, the procedure for jacking the strand against an open steel block is shown. Installers were careful not to disengage the post-tensioning chuck, pulling the strand up just high enough to remove the temporary

washers. Afterwards, the post-tensioning strand was released and the chuck came to bear directly on the anchorage plate. The thickness of the temporary washers was calculated such that the post-tensioning force after removal equaled the required initial post-tensioning force. This method was found to be effective in eliminating post-tensioning seating losses.

Figure 12.2 Method for Mitigating Seating Losses During Installation Including Installation of Temporary Washers (Left), and Removal of Temporary Washers (Right)

As described in Chapter 8 in the section on post-tensioning wire fracture, it is not recommended to regrip the post-tensioning strands on portions of the strand previously gripped. In the large scale tests conducted at the University of Illinois, the strands were re-jacked such that the strand was gripped more than once on the same portion of the strand. It is believed that this contributed to the post-tensioning wire fractures experienced in the experimental program. The post-tensioning strands in the E-Defense specimen were intentionally stressed only one time and the strands reached strains greater than 1.2% without fracturing any wires.

The connection of the fuses to the columns was examined in Chapter 6 as it pertained to slippage of the fuse in Specimen A4. Using the measured fuse forces and assumed values for the coefficient of friction, it was determined that the moment applied to this bolted connection caused significant increase in the shear force at each bolt. Based on these results, it is recommended that the fuse to column connection be designed for the moment associated with the fuse shear capacity acting at the quarter point of the fuse links.

Sliding of the frames between the base bumpers was observed during the testing and in the displacement data. The amount of sliding and the equivalent roof drift ratio

were reported in Table 8.6 for each specimen. Although tolerances are necessary to allow erection of the frames, it was determined that the sliding at the base could be mitigated. Before the testing of Specimen B1 and Specimen B2, the gap between the frames and bumpers were filled with thin shims that were then tack welded to the bumper. These shims were easy to install and eliminated sliding at the base of the frames.

The effect of tolerances was also found to be an issue in the single frame configuration where the center column connects to the frame and to the fuse. Standard pin hole tolerances in all plies added up to a lag in the fuse response when the fuse force changed directions. This effect was mitigated in the E-Defense specimen by eliminating the pin connection at the top of the center column as shown on the left of Figure 12.3. To further mitigate the effect of pin hole tolerance, the bottom of the center column, shown on the right of Figure 12.3, can be welded to the pin. Although this was not tested in the E-Defense specimen, the combination of these two approaches effectively eliminates the pin hole tolerances in three of the four plies reducing the associated lag in fuse response by 75%.

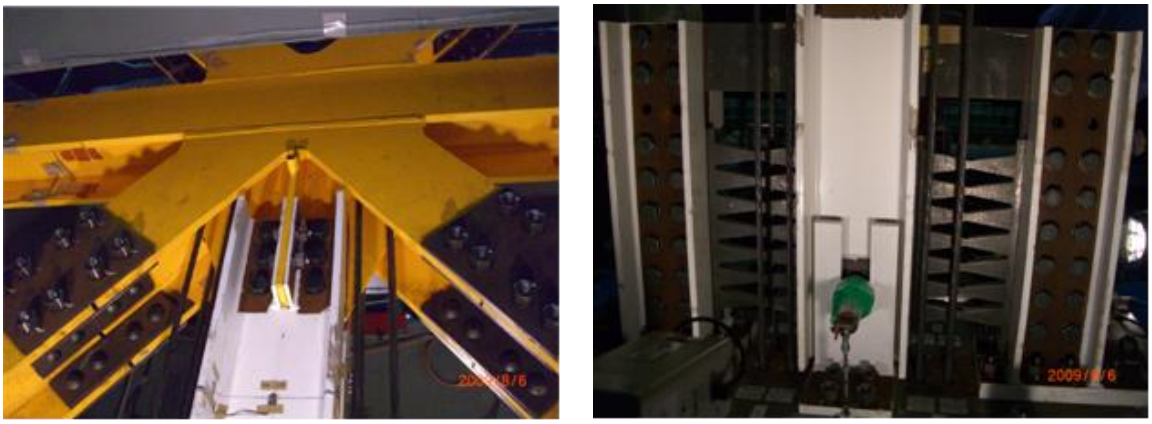

Figure 12.3 Mitigating Pin Hole Tolerances in the Single Frame Configuration at the Top of the Center Column (Left) and at the Bottom of the Center Column (Right)

The effect of out-of-plane motion on the in-plane rocking of the frames was investigated during Test A6 of the experimental program as described in Chapter 7. Out-of-plane motions equal to 10% of the in-plane motions were applied during an MCE level event. As described in Chapter 8 and Chapter 11, the effect of out-of-plane motions on system response and member forces was not found to be significant. The strains in the columns were slightly larger for the hybrid simulation test that included out-of-plane motion, but otherwise there was little effect on the system. This suggests that no additional detailing requirements to account for out-of-plane motion are likely to be necessary.

12.7 Connection with the Diaphragm and Collectors

Column uplift could cause local floor damage and creates challenges in connecting the floor diaphragm to the controlled rocking frames. A range of possible details have been

created and are presented in this section in schematic drawings. Possible options for connecting the diaphragm to the rocking frame include:

1. Typical connection of the diaphragm to the frame beam and from the collector beam to the end of the frames. Some localized damage is expected at the uplifting columns as shown in Figure 12.4.
2. The collectors are split around the rocking frame into adjacent beams. The adjacent beams would attach to the rocking frame through shear plates that allow the frame to uplift through flexure in the plate. As shown in Figure 12.5, the floor slab could be blocked out around the rocking frame. The resulting configuration would transfer shear to the controlled rocking frame but protect the floor slab from damage associated with uplifting elements.
3. Similar to the previous option, the collectors feed into adjacent beams. A roller attaches between the adjacent beams and bears on the side of the rocking frame. This type of yoke configuration transfers lateral loads only through compression. This option is shown in Figure 12.6. The large-scale shake table specimen tested at E-Defense used a similar attachment to the masses, using beams on either side of the specimen with a bolted connection on one end of the frame only.
4. The possible floor damage in dual frame configurations is exacerbated by the close proximity of the interior columns. As shown in Figure 12.7, an option for reducing floor damage involves blocking out the slab next to the rocking frames and adding an adjacent beam. This detail has the collectors connecting directly to the rocking frame similar to the first option.

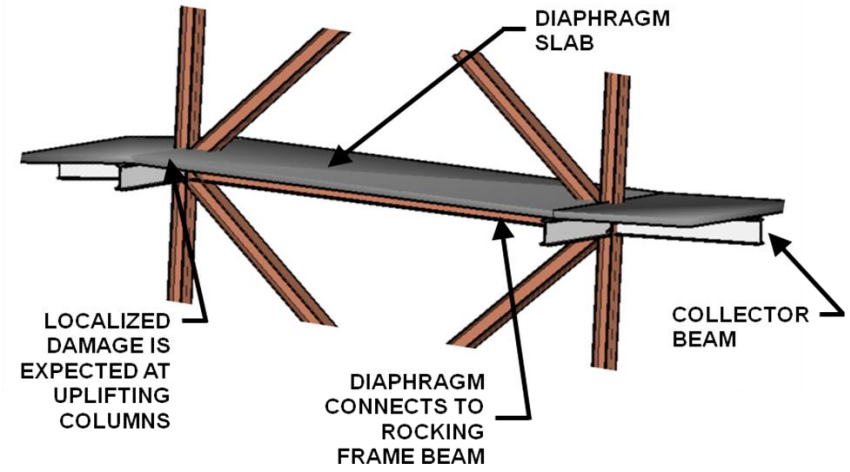

Figure 12.4 Isometric View of a Standard Diaphragm Connection

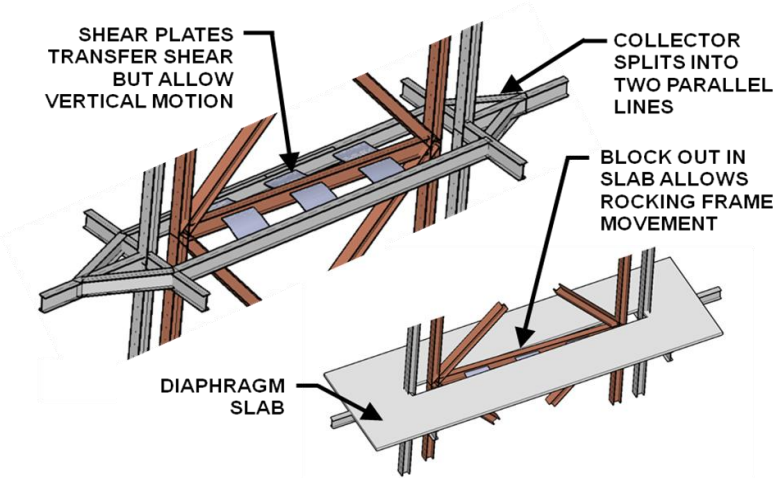

Figure 12.5 Isometric View of a Possible Diaphragm to Rocking Frame Connection that Allows Uplift Without Damage

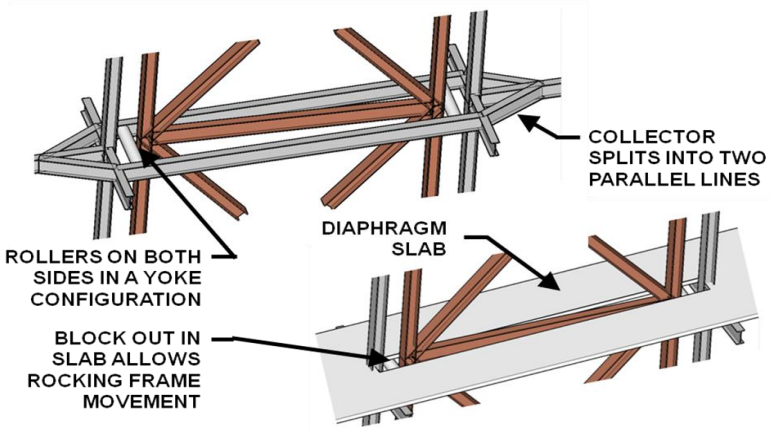

Figure 12.6 Isometric View of a Possible Diaphragm to Rocking Frame Connection Using a Yoke

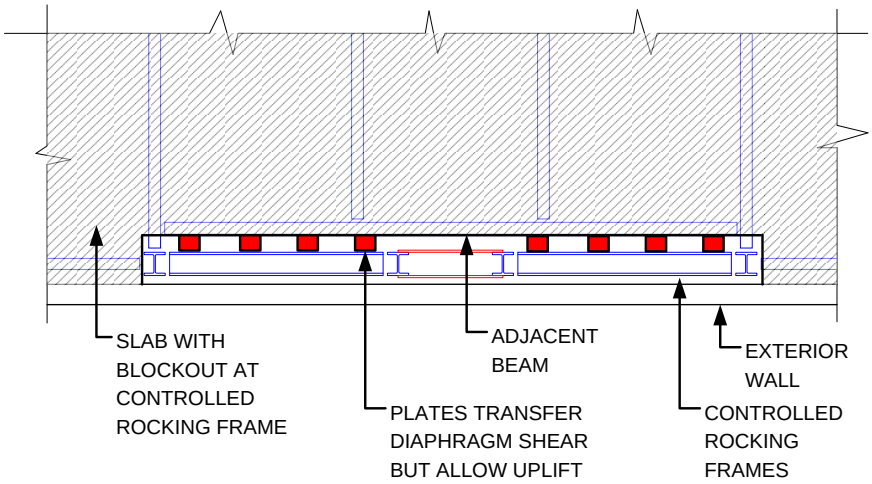

Figure 12.7 Plan View of a Possible Diaphragm to a Dual Frame Rocking System Connection that Reduces Damage

Chapter 13

CONCLUSIONS

Current seismic building codes use inelasticity in structural elements to protect buildings from collapse. As a result, conventional seismic force resisting systems subjected to large earthquakes can experience structural damage that is distributed throughout a building and permanent drifts after the earthquake motions cease. Distributed structural damage and residual drifts can make a building difficult if not economically unreasonable to repair.

To create a structure that has a high level of repairability after a large earthquake requires that the structural damage be concentrated in replaceable elements and the residual drifts be eliminated. Conventional seismic force resisting systems cannot satisfy these goals without strengthening them to near elastic behavior. It is necessary, therefore, to create innovative higher performance seismic resisting systems that inherently satisfy the stated performance goals related to repairability.

The controlled rocking seismic force resisting system for steel-framed buildings is a higher performance system that concentrates inelasticity in replaceable steel fuse components and eliminates residual drifts using vertical post-tensioning to close uplifting gaps at the base of rocking frames. The work described in this report is part of a multi-institution, international research project to investigate and develop the controlled rocking system for practical implementation.

Work that is associated with the larger research project but was not part of the research reported in this report includes fuse component tests and development, large-scale shake table testing at the E-Defense facility in Miki, Japan, parametric computational studies to investigate different configurations and building heights, and the development of a direct displacement based design methodology for system proportioning. Chapter 3 includes the references for these phases of the work.

This report describes several phases of the validation and development of the controlled rocking system including an experimental program and computational studies. The experimental program consisted of large-scale cyclic and hybrid simulation testing. Computational studies included a parametric study on SDOF systems to investigate the amount of restoring force necessary to control residual drifts in the presence of ambient building resistance, and an MDOF sensitivity study to examine the application of the controlled rocking system to a range of building configurations. Both the experimental program and the computational studies validated that the controlled rocking system is capable of eliminating residual drifts and concentrating virtually all of the structural damage in replaceable fuse elements. The results of the work described herein suggest that the controlled rocking system is a valid higher performance seismic force resisting system that can be implemented in practice to achieve significantly improved structural repairability after large earthquakes.

13.1 Description of the Controlled Rocking System

The controlled rocking system for steel-framed buildings employs the following three main components: (1) Steel frames that remain essentially elastic and are allowed to rock about the column bases. The column base detail permits column uplift but restrains horizontal motion using bumpers or an armored foundation trough. (2) Vertical post-tensioning strands provide active self-centering forces. The strands are initially stressed to less than half of their ultimate strength, so as to permit additional elastic straining when the frames rock. (3) Replaceable energy dissipating elements act as structural fuses that yield, effectively limiting the forces imposed on the rest of the structure. The fuses are configured as yielding shear elements between two frames in a dual frame configuration or at the base of the frame in a single frame configuration.

The controlled rocking system has a flag-shaped hysteretic response that is characteristic of self-centering systems. The post-tensioned frame creates a bilinear elastic response with an initial stiffness due to elastic deformations in the frame and a secondary stiffness due to additional elongation of the post-tensioning strands after uplift. The fuse, on the other hand, can have full hysteretic load-deformation behavior. The effect of combining the two components is a flag-shaped hystersis loop that returns to near zero displacement when the load is removed.

13.1 Summary of Experimental Program

The large-scale cyclic and hybrid simulation tests were conducted at the University of Illinois at Urbana-Champaign MUST-SIM facility, which is part of the George E. Brown, Jr. Network for Earthquake Engineering Simulation (NEES). The specimen was based on a three-story prototype building that is 36.6 m x 54.9 m (120’ x 180’) located in Los Angeles, California.

Nine specimens were tested consisting of seven dual frame configuration specimens (A series), in which the two frames are linked together with fuses, and two single frame configurations (B series), in which the fuses were concentrated at the base of the frame. The specimen design strength was calculated using an assumed response modification factor of R=8.0, four frames in each direction for the dual frame configuration, ten frames in each direction for the single frame configuration, and a scale factor of 0.43 relative to the prototype.

A three-story test specimen was constructed using W8 wide flange members turned minor axis and connected using gusset plates on both sides. Eight post-tensioning strands were used for the dual frame configuration and four post-tensioning strands were used for the single frame configuration. The post-tensioning consisted of 12.7 mm (½”) diameter strands anchored at the roof beam and to an anchorage plate at the base that was connected to the strong floor. Steel plates with diamond shaped cut-outs served as the energy dissipating fuses. The base of the frames were not attached to the base plate, instead a milled base plate with rounded bull nose edges was allowed to pivot and uplift between bumpers on all sides.

Load was applied to the specimen using a Load and Boundary Condition Box (LBCB) connected to a loading beam at the top of the specimen. The loading beam was connected to the specimen through two load cell pins that measured horizontal and

vertical forces input into the two frames. The vertical forces in the pins were maintained at zero force throughout the test. The displacement of the specimen was controlled using feedback from two horizontal string potentiometers at the roof level. Seven of the tests were conducted with cyclic displacement protocol and two of the dual-frame configuration tests, Specimen A5 and Specimen A6, were conducted as hybrid simulation tests.

The nine specimens were designed to vary several variables including 1) OT strength ratio, 2) SC self-centering ratio, 3) Fuse thickness, 4) Number and location of fuses, 5) Dual frame configuration (series A) versus single frame configuration (series B), 6) Single width fuse for dual frame configuration (series A) versus double width fuses for single frame configuration (series B), 7) Single thickness fuses (Typical) versus double thickness fuses with a restraining plate between (Specimen B2), and 8) Initial stress level in post-tensioning strands.

The frames were reused for all nine specimens with some modifications made to the frames for the single frame configuration specimens. In between specimen tests, the fuses were replaced and the post-tensioning strands were either adjusted or replaced. The same post-tensioning strands were used without de-stressing for Specimen A1 through Specimen A4 and were then replaced for use in Specimen A5 through Specimen A7. The strands were again replaced for Specimen B1 and Specimen B2.

13.2 Observations from the Experimental Program

13.2.1 Global System Behavior

The cyclic and hybrid simulation tests validated that the controlled rocking system satisfies the stated performance goals. The hysteretic behavior of the system was found to be predictable and several aspects of the system response such as strength can be computed with closed form equations.

Uplift of the frames occurred at roof drift ratios between 0.11% and 0.32%. The roof drift ratio at uplift was found to be sensitive to the amount of sliding allowed at the base of the frame relative to the foundation. The average roof drift ratio at fuse yield was approximately 0.6% for the dual frame configuration but almost 1.5% for single frame configuration. Accumulation of pin hole tolerances in the connections between the frame and the fuse caused a lag in engaging the fuses for the single frame configurations. As discussed below, this issue was mitigated for shake table tests conducted at E-Defense.

The cyclic tests were conducted to roof drift ratios between 3% and 4.2%. The permanent drift that remained after the force was removed was between 0.0% and 0.8%, although the majority of specimens exhibited 0.1% drift or less.

The displacements of the frames were shown to be almost entirely due to rigid body rotation of the stiff steel braced frames. For the dual frame configuration, it was shown that the frames tilt toward one another because equal drift of the two frames would cause significant axial elongation in elements that connect the two frames. The constraint between the two frames provided by the fuses acts to pull the frames together.

Large-scale testing of the dual frame configuration and the single frame configuration show that both are valid arrangements for the controlled rocking system. Comparisons of the hysteretic energy absorbed by the two configurations showed that the single frame configuration required larger displacements to absorb the same amount of

energy as the dual frame configuration. This was due to the pin hole tolerances in the center column that connected the frame to the fuse. Based on the results of this experimental program, the pin hole tolerances were successfully mitigated for the E-Defense tests by using a bolted connection at the top of the center column instead of a pin connection, and reducing the tolerances used for the lower pin connection.

Another difference between the dual frame and single frame configuration relates to the frame drifts that remain after the loads are removed. There are residual drifts that remain in a dual frame configuration when the loads are removed due to the built-up forces in the fuses which, because they are distributed along the height of the system, cause elastic deformations in the frames. The single frame configuration is immune to this effect because the fuses are concentrated at the bottom of the frame. The two single frame specimens exhibited almost no drift at zero force even after yielding of the post-tensioning strands and fracture of several post-tensioning wires. On the other hand, the single frame configuration requires larger self-centering ratios to prevent global uplift because the moment arm associated with the fuse force is shorter in the single frame configuration.

13.2.2 Post-Tensioning Behavior

The post-tensioning strands are intended to remain elastic in most earthquake events. To understand the possible limit states, the post-tensioning strands were elongated past the yield strain in the experimental program. The post-tensioning strand behavior was investigated including post-tensioning seating losses, strand yielding, and wire fracture.

It was found that as the force in a post-tensioning strand exceeded its previous maximum force, that the wedges at the anchorage were pulled incrementally further into the mating conical hole. Through the testing of specimen A1 up to a roof drift ratio of 3%, seating losses caused approximately 18% loss in the initial post-tensioning force. However, due to the testing of Specimen A1, the anchorages were well seated and the post-tensioning strands did not experience significant seating losses in the testing of Specimen A2, A3, or A4. Seating losses were eliminated before the testing of Specimen A5, A6, A7, B1, and B2, by conducting large displacement cycles after installing the post-tensioning strands but before installing the fuses. A method for eliminating seating losses in practical applications was developed for the E-Defense tests and consisted of including a removable shim between the post-tensioning chuck and anchorage plate, stressing the strand to a force greater than the design initial post-tensioning force, and then removing the shim.

A linear trendline was fit to the data to correlate the amount of force reduction due to seating losses to the increase in peak post-tension force above previous force levels. The relationship was then used to create a post-tensioning material constitutive relationship for use in the computational model that allowed the investigation of the effects of seating losses on system performance in the sensitivity study. The constitutive model uses the previous maximum force experienced by the post-tensioning strands as an input to define the force at which the seating losses would initiate.

At large strains, individual wires in the seven-wire post-tensioning strand fractured. In the four specimens that were subjected to post-tensioning strains greater than yield, 13 of 280 wires fractured. In all cases, the fractures did not propagate to other wires, nor did the fractures propagate to the other strands. Furthermore, the system

strength was not affected, and ability of the system to eliminate drifts at zero force was only slightly affected.

Based on the post-tensioning wire fractures experienced in the experimental program, the probability of fracturing a certain proportion of the strands in a controlled rocking frame was computed for several limits on post-tensioning strain. These results could be used in design to define a limit on post-tensioning strain that creates a desired probability of post-tensioning wire fracture.

13.2.3 Fuse Behavior

The fuses demonstrated excellent ability to dissipate seismic energy without fracturing. The shape of butterfly links was designed to cause initiation of first yield and plastic hinging at the quarter point of the fuse link away from locations of discontinuity. Because of this design feature and smooth cut surfaces, the fuses possessed large ductility and deformation capacity. In the experimental program, the fuses were deformed to as much as 25% shear strain across the fuse link and none fractured.

A range of fuse thicknesses were included in the experimental program. Thinner fuses were allowed to buckle and underwent a progression of behavior including flexural yielding, lateral-torsional buckling, axial elongation at large deformations, and compression buckling. Thicker fuses did not buckle and exhibited full hysteretic behavior. The buckling fuses were found to improve self-centering by exerting less resistance to oppose the post-tensioning restoring force, but also had reduced ability to absorb seismic energy compared to the non-buckling fuses. A linear relationship was fit to the data to relate the buckling shear load for thinner fuses to the fuse link slenderness defined as the link length divided by the fuse plate thickness. The relationship was then used to define the buckling load to be used in the computational model. Based on the results of the experimental program, the thicker non-buckling fuses were found to have several advantages over the buckling fuses:

- Buckling fuses experienced larger axial forces after buckling than the non-buckling fuses. Larger fuse axial forces create larger frame column moments and shears
- Buckled fuses absorb less seismic energy.
- Fuse link buckling occurs due to the combination of shear, moment, and axial forces. In this indeterminate system, the axial forces vary making it difficult to predict fuse buckling and making seismic performance less consistent.
- Thick fuses exhibit an elastic-plastic hardening shear force-shear deformation response that is easier to simulate in a computational model than the more complex pinched behavior of the thinner fuses.
- Based on the hybrid simulation tests of Specimen A5 and cyclic testing of other thick fuse specimens, it is concluded that thick fuses may not need to be replaced even after large earthquakes.

13.2.4 Frame Behavior and Detailing

Resultant forces and moments were calculated for the frame members using measurements from the strain-gaged sections. The largest resultant forces, moments, and

strains occur at the base of the exterior columns. Based on the data, it is likely that the outside flange tips at the base of the exterior columns experienced inelastic strains during some of the specimen tests. However, no yielding or buckling was observed in the post-test inspections of the specimens and the braced frames were largely undamaged as they were used for all nine specimens.

The construction tolerances used in several of the bearing details were found to have an effect on system behavior. Details for which the tolerances played a role included pin hole tolerances in dual frame strut connections, pin hole tolerances in the single frame center column connections, pin hole tolerances in the pin load cell connections and bumper to frame tolerances at the base. Sliding at the base of the frame was found to be as large as 6 mm for one of the specimen tests, but effective mitigation of base sliding was implemented for Specimen B1 and Specimen B2 by inserting shims between the frames and bumpers.

The effectiveness of the struts between the frames in a dual frame configuration was found to be governed by the amount of pin hole tolerance. Thicker fuse configurations hardly engaged the struts as the relative displacements were not large enough to engage the pin with all connecting plies.

Thinner, buckling fuse configurations engaged the struts because the buckled fuses developed larger axial forces and axial deformations. Specimen A7 which did not use struts exhibited larger moments and forces in the frame members than the comparable Specimen A1. It was determined that for the tested configurations, struts were not necessary for use with the thicker fuse specimens. For the thinner fuse specimens, the struts served a purpose in reducing the frame member forces, but the global performance was not affected by the removal of the struts. If the frames are designed accordingly, it was determined that struts may not be necessary for thinner fuse configurations.

However, it will still be necessary to transfer collector forces through or around the controlled rocking frames and it will be necessary to transfer diaphragm shear into the controlled rocking system. If struts are not included, alternate means for collector load transfer and diaphragm shear transfer will be necessary, which may introduce constraint between the two frames similar to the struts. The experimental and computational studies included in this report did not examine dual frame controlled rocking configurations that have no constraint between the frames.

The tests were also quite successful in identifying several details that could be improved for the subsequent large-scale shake table tests conducted at E-Defense. Construction details and processes that were improved include eliminating post-tensioning seating losses, mitigating pin hole tolerances in the singe frame configuration, and eliminating sliding at the base.

13.2.5 Observations from the Hybrid Simulation Testing

The ability of the controlled rocking system to eliminate residual drifts and concentrate structural damage in the fuse elements was validated in all six of the hybrid simulation trials. The residual drifts were shown to be negligible for all trials even for trials including second order gravity effects and ambient building resistance. Furthermore, the thicker fuses that don't buckle, such as those used in Specimen A5, did not to experience any significant degradation even after multiple trials with an earthquake record s**c**aled 69% larger than the event that has 2% probability of exceedance in years. This implies

that thicker non-buckling fuses may not need to be replaced even after very large earthquakes.

13.3 Conclusions from the Computational Investigations

13.3.1 Conclusions from the SDOF Study on Self-Centering

The first computational study consisted of a parametric SDOF study that was conducted using time-history analyses on several prototype buildings to quantify the effect of varying system parameters on structural response including residual drifts. Over 25,000 analyses were performed. SDOF elements that represented the resistance of the rest of the building were included to investigate the effect of ambient building resistance on self-centering ability. The full range of restoring force from none (all energy dissipation), to only restoring force (elastic bilinear) was considered to identify the required amount of restoring force.

After undergoing inelastic deformations, the gravity system and other elements of the building will resist the ability of the restoring forces to bring the building back to center. On the other hand, the added strength and stiffness provided by the rest of the building reduces peak drifts. To determine the amount of restoring force required to self-center an actual building, it is therefore necessary to consider ambient building resistance. The resistance of the rest of the building was represented by two SDOF elements which simulated interior partitions and beam to column connections. An SDOF model was calibrated to experimental test data from the literature for gypsum board on metal stud partitions walls, and for simple shear beam to column connections. The calibrated models were then extrapolated to represent the resistance of these types of elements for an entire building.

System parameters varied in the study included: response modification factor, height of the load-deformation flag shape, partition wall density, number of tributary shear beam to column connections, number of stories, ratio of energy dissipating stiffness to total stiffness, and ratio of post-yield stiffness to initial stiffness. Time history analyses were conducted for 17 ground motions scaled to two earthquake hazard levels. Response indices included residual roof drift, peak roof drift, ductility demand, and hysteretic absorbed energy.

This study showed that typical gypsum interior partitions, although opposing restoring forces, also reduce peak drift and experience strength degradation such that they do not dramatically affect residual drifts. Residual drift is more sensitive to simple shear beam-to-column connections because they do not experience as much cyclic strength degradation and thus retain their resistance to restoring forces.

The minimum amount of energy dissipation required to limit peak roof drifts was investigated for the hazard level that has a 10% probability of exceedance in 50 years. For the systems included in this study, a flag shape height ratio of β >0.5 (SC<3.0) produced peak roof drifts below a 2% limit in most cases, and on average for the worst case configuration (β =0.5 three-story) when subjected to the 10% in 50 years hazard level.

As part of this computational study, a probabilistic mechanism was identified that causes self-centering in systems with even small amounts of restoring force.

Probabilistic self-centering, which is especially effective in the presence of even small amounts of restoring force, can significantly reduce residual drifts. Using proposed limits on residual drifts based on new steel construction tolerances, it was determined that proportioning restoring forces to have at least one half the capacity of the energy-dissipating element can reliably control residual drifts (with confidence of one standard deviation above the mean for the event that has 10% probability of exceedance in 50 years).

13.3.2 Observations from the MDOF Sensitivity Study

The experimental results were used to inform the development of a computational model that can capture the salient features of controlled rocking system behavior. The 2D computational model was built using the OpenSees software and included geometric nonlinearity. A phenomenological component model was used to simulate lateral-torsional buckling of the thinner fuses. The behavior of the thicker fuses was captured without calibrating any parameters to the experimental data. A constitutive model was created for the post-tensioning that accounted for post-tensioning seating losses, yield, and initial pretension.

The computational model was used to investigate the application of the controlled rocking system to 17 different configurations. Nonlinear time history analyses were performed with twenty-two ground motions scaled to four different hazard levels. A total of 1496 analyses were conducted. The study was used to investigate the application of the controlled rocking system to different height structures, investigate higher mode effects, examine the effects of different frame geometries, evaluate proposed system proportioning concepts, and assess a proposed capacity design approach. Conclusions drawn from the MDOF sensitivity study include:

- The probabilities of exceeding limit states were calculated, including post-tensioning wire fracture, fuse link fracture, and drift limits. It was shown through the tabulation of these probabilities that the risk of exceeding negative limit states can be controlled.
- Varying the self-centering ratio between 0.75 and 1.5, which effectively varied the amount of hysteretic energy dissipation in the system, was not found to have a significant effect on peak roof drifts.
- The residual drifts were found to be negligible up to the hazard level with 2% probability of exceedance in 50 years for self-centering ratios as low as 0.75. However, for the configurations studied in this report, preventing the global uplift limit state does not allow the use of smaller self-centering ratios. Global uplift occurs when the fuse shear capacity is greater than the initial post-tensioning force and results in the entire frame being lifted off the support.
- The dual frame geometric ratio equal to the frame width divided by the fuse width was revealed to have little effect on the response indices if the fuse link length was held constant.
- The controlled rocking system was investigated for building heights from three stories to nine stories and all were shown to perform well, engage the rocking mechanism, and dissipate energy. Differences were noted such as

the roof drift ratio at uplift was larger for taller buildings because of elastic frame deformations.

- Seating losses were shown to cause increases in the response indices at and above the 2% in 50 years hazard level. The seating losses were found to exacerbate the loss of post-tensioning forces as they reached yield strains.
- The drifts experienced by the controlled rocking system were found to be similar to other traditional seismic force resisting systems. As such, it is expected that standard detailing for the rest of the structure would be reasonable. However, to facilitate effective reuse after self-centering is achieved, it is advantagaeous to use either repairable details or details that sustain minimal damage during the expected drifts.

13.4 Recommendations for Practical Application

The information collected from the experimental program and computational studies was condensed into a recommended design strategy. Within the limitations of the experimental and computational studies presented herein, it is believed that the controlled rocking system can be safely implemented in practice to achieve higher seismic performance.

Limit states were identified as frame uplift, fuse yield, post-tensioning strand yield, post-tensioning wire fracture, fuse link fracture, inelasticity in the frames or frame connections, global uplift, and fracture of all post-tensioning strands. Only uplift and fuse yield are allowed for hazard levels up to those with 10% probability of exceedance in 50 years. For the 2% in 50 years hazard level, the probability of post-tension strand yield, post-tensioning wire fracture, or frame inelasticity is limited to small values. The steps included in the recommended design strategy include:

1. Decide between a dual frame or single frame configuration. The advantages of each are given in Table 12.2. Define preliminary frame width, *A*, and width between the frames, *B*, for a dual frame configuration.
2. Calculate the design earthquake forces using a method such as the equivalent lateral force method. Calculate the design overturning moment due to these lateral forces.
3. Proportion the fuse shear capacity and initial post-tensioning force:
    a. Select a desired self-centering ratio.
    b. Calculate the required fuse capacity and initial post-tensioning force to satisfy strength requirements and the selected self-centering ratio. Equations based on the strength requirement and self-centering ratio were presented in Equations (12.9), (12.10), (12.11), and (12.12).
    c. Check that global uplift is prevented using Equation (12.13). Adjust the self-centering ratio, fuse capacity, and initial post-tensioning force as necessary to satisfy this requirement.
4. Design the butterfly fuse plates:
    a. Select a trial fuse link length. Compute the expected fuse link shear strain associated with 3% roof drift ratio (3% roof drift ratio is associated with

the hazard level with 2% probability of exceedance in 50 years according to the sensitivity study). Equations (12.15) and (12.16) provide an approximate method for calculating the fuse shear strain based on assumed rigid body rotation of the frames.

b. Adjust the fuse link length as necessary to limit the fuse link shear strain to 30% which was the smallest fuse shear strain that produced fracture in the Stanford fuse component tests. If necessary, adjust the frame geometry and start the design process over.
c. Select fuse plate thickness to prevent buckling. The tested fuses that did not experience buckling had slenderness ratios as large as L/t=22.4 where L is the fuse link length and t is the plate thickness.
d. Select the fuse link depth, number of links, and number of fuses to satisfy the fuse shear force computed in Step 3. Equation (12.14) gives the plastic shear capacity of the fuses.

5. Design the post-tensioning:
    a. Estimate the superimposed post-tensioning strain for a roof drift ratio of 3%, which, as stated above, is associated with the 2% in 50 years hazard level.
    b. Determine the post-tensioning strain limit to produce the desired level of reliability related to post-tensioning wire fracture using Table 8.9. For instance limiting the post-tensioning strain to 1.0% will result in a low probability that more than 5% of the wires will fracture.
    c. Subtract the superimposed strain from the limiting strain to get the allowable initial post-tensioning strain. Convert the initial strain to initial stress and determine the number of post-tensioning strands to satisfy initial post-tensioning force computed in Step 3.
    d. If necessary, adjust the frame geometry to reduce the amount of superimposed post-tensioning strain and begin the design process again.
6. Design the frame members:
    a. Conduct linear elastic frame analyses for a set of load cases. Six load cases are presented in Chapter 11 and shown in Figure 11.34 and Figure 11.35. These load cases are intended to represent a range of inertial load distributions.
    b. Identify the worst case forces for a given member and amplify these forces by a factor to approximate the forces that might be experienced in a dynamic event. Examples of the amplification factors based on axial forces are presented in Table 11.1.
    c. Design the frame members for the amplified forces.
7. Design and detail the frame and connections:
    a. Recommendations are provided in Chapter 12 for eliminating post-tensioning seating losses
    b. Recommendations are presented in Chapter 12 for mitigating motion due to pin hole tolerances and sliding at the base.
    c. A discussion is presented in Chapter 12 regarding the connection of the controlled rocking frame to the diaphragm and collectors.

d. Other parts of the structure may also need to be detailed to ensure minimal damage or a minimum level of repairability after the earthquake.

13.5 Further Research Needs

Additional research needs were identified throughout this report and are summarized in this section. The research needs are categorized into three groups: further characterization of component performance, further computational studies, and the development of other details and configurations.

Further characterization of component performance:

- Although post-tensioning strain wire fracture was investigated at lower levels of post-tensioning strains, it is necessary to characterize post-tensioning wire fracture and full strand fracture for different types of anchorage and different types of post-tensioning strands. This is necessary to ensure the desired level of reliability in preventing undesirable post-tensioning limit states.
- To ensure consistent system performance at any time during a buildings service life it will be necessary to investigate time dependent effects on the perpetually stressed frame, such as relaxation in the post-tensioning strands.
- Further characterization of butterfly fuse links is warranted. A linear regression was described in Chapter 6 that approximates the buckling shear load to a fuse link slenderness parameter. It is recommended that a multivariate regression analysis be performed to examine the dependence of fuse buckling on parameters such as an energy measure, peak shear strain, or cumulative shear strain. This would be useful for more accurately defining limits on fuse link slenderness for fuses that are not allowed to buckle and predicting the behavior of thinner buckling fuses.
- It would be beneficial to characterize the conditions that cause fuse link fracture. Only a limited number of tests were conducted at Stanford University up to fuse fracture, which does not provide a statistically large amount of data for characterizing fuse link fracture.
- The effect of impact and other dynamics on member forces requires further study. The data from the shake table tests conducted at E-Defense coupled with some additional computational simulations could be used to clarify these dynamic effects.

Further computational studies and simulations

- More advanced models for predicting the behavior of the thinner buckling fuses would allow more accurate simulation of a wider range of fuse geometries. A phenomenological model of the fuse was presented in Chapter 6 that predicts buckling based on the moment experienced in the fuse link. A method that predicts buckling based on an energy measure or fuse link shear strain may provide enhanced accuracy.

- The sensitivity study reported in Chapter 10 did not include any thin buckling fuse configurations. Nonlinear time history analyses of configurations with thinner buckling fuses are necessary to ensure expected dynamic response if those types of fuses are to be used.
- A larger reliability study should be conducted to validate the frame member design methodology. A reliability study could use the statistical distribution of demand coupled with the statistical distribution of member capacities to produce probabilities of member failure that consider axial, shear and moment. This type of reliability study would also take into account the consequences of member failure.
- Seismic design parameters such as the response modification factor were assumed based on the performance of the system in experimental and computational phases of this research. An ATC 63 (FEMA P695 2009) type of analysis could be performed to provide a solid basis for the seismic design parameters.
- The sensitivity study did not include any structures taller than nine stories. Although the structures up to nine stories were found to perform well, it is necessary to investigate taller buildings to determine the height at which the controlled rocking system is not viable.
- A lower limit on the amount of energy dissipation required in the system was investigated in several portions of this report, but more research is warranted. The self-centering ratio was varied between 0.75 and 1.5 in the MDOF sensitivity study without significant effect on peak roof drifts. The amount of energy dissipation was varied in the SDOF parametric study from no energy dissipation to energy dissipation without self-centering. The resulting peak roof drifts became large as the energy dissipation was eliminated. Further study is needed to define the minimum amount of energy dissipation required in a self-centering system to adequately limit peak drifts.

Development of other details and configurations.

- As discussed in Chapter 9, restoring forces less than the capacity of the energy dissipating component can still reliably self-center. To achieve proportioning with smaller restoring forces will require the investigation of configurations where the restoring force is separated from the energy dissipating component. This will allow the use of less restoring force without initiating negative limit states such as global uplift.
- The connection of the diaphragm and collectors to the rocking frame may require additional study. Schematic details were proposed in Chapter 12, but details utilizing nonstandard mechanisms should be verified.
- To ensure repairability after an earthquake, it is necessary to investigate the performance of other details throughout the building. It may be necessary to develop more repairable details for the rest of the structure to ensure that the whole structure is reusable after self-centering following an earthquake.

- To further limit downtime and repair costs, it is also necessary to reduce nonstructural damage. Improved detailing of nonstructural components to resist damage or allow repairability is necessary.

REFERENCES

Adham, S. A., (1988) *Shear Wall Resistance of Lightgage Steel Stud Wall Systems, Final Technical Report*, Agbabian Associates, El Segundo, California.

Ajrab, J. J., Pekcan, G., and Mander, J. B. (2004) "Rocking Wall-Frame Structures with Supplemental Tendon Systems" *ASCE Journal of Structural Engineering*, Vol. 130, No. 6.

American Institute of Steel Construction (2005) *AISC 303-05 Code of Standard Practice for Steel Buildings and Bridges*, American Institute of Steel Construction (AISC), Chicago, IL.

ANSI/AISC 360-05 (2005) *Specification for Structural Steel Buildings*, Published by the American Institute of Steel Construction (AISC).

ASCE / SEI 7-05 (2005) *Minimum Design Loads for Buildings and Other Structures* Published by the American Society of Civil Engineers (ASCE), Prepared by the Structural Engineering Institute of ASCE.

ASCE / SEI 41-06 (2007) *Seismic Rehabilitation of Existing Buildings* Published by the American Society of Civil Engineers (ASCE), Prepared by the Structural Engineering Institute of ASCE.

Aschheim, M., and Halterman, A. (2002). "Reduced Web Section Beams: Experimental Findings and Design Implications." *7th US National Conference on Earthquake Engineering*, Boston, July 21-25.

Aslam, M., Godden, W. G., and Scalise, D. T. (1980) "Earthquake Rocking Response of Rigid Bodies", *ASCE Journal of the Structural Division*, Vol 106, no. ST2.

ASTM Standard A370-07a (2007) "Standard Test Methods and Definitions for Mechanical Testing of Steel Products" Published by the American Standards for Testing and Materials International (ASTM), West Conshohocken, PA.

ASTM Standard A416/A416M-06 (2006) "Standard Specification for Steel Strand, Uncoated Seven-Wire for Prestressed Concrete" Published by the American Standards for Testing and Materials International (ASTM), West Conshohocken, PA.

ASTM standard E8-01 (2001) "Standard Test Methods for Tension Testing of Metallic Materials" Published by the American Standards for Testing and Materials International (ASTM), West Conshohocken, PA.

ATC 40 (1996) *Seismic Evaluation and Retrofit of Concrete Buildings, Volume 1* Published by the Applied Technology Council (ATC), funded by Seismic Safety Commision.

ATC 58 (2007) *Guidelines for Seismic Performance Assessment of Buildings 35% Draft* Published by the Applied Technology Council (ATC).

Bahadur, A., Mitra, A., Kumar, B., R., and Sagar, S., P. (2007) "Evaluation and Correlation of Residual Stress Measurement in Steel" *Journal of Nondestructive Evaluation*, Vol. 26, pp 47-55.

Bergman, D. M. and Goel, S. C. (1987) *Evaluation of Cyclic Testing of Steel-Plate Devices for Added Damping and Stiffness*, University of Michigan Report UMCE 87-10.

Blume, J. A., Newmark, N. M., and Corning, Leo H. (1961) *Design of Multistory Reinforced Concrete Buildings for Earthquake Motions* published by the Portland Cement Association, Chicago, Illinois.

John A. Blume and Associates, Research Division (Blume) (1966) *First Progress Report on Racking Tests of Wall Panels*, San Francisco, CA.

John A. Blume and Associates, Research Division (Blume) (1968) *Second Progress Report on Racking Tests of Wall Panels*, San Francisco, CA.

Challamel, N., Andrade, A., and Camotim, D. (2007) "An Analytical Study on the Lateral-Torsional Buckling of Linearly Tapered Cantilever Strip Beams" *International Journal of Structural Stability and Dynamics*, Vol. 7, No. 3, pp 441-456.

Chen, Y.-H., Liao, W.-H., Lee, C.-L., and Wang, Y.-P. (2006) "Seismic Isolation of Viaduct Piers by Means of a Rocking Mechanism" *Earthquake Engineering and Structural Dynamics*, Vol. 35 pp 713-736.

Christopoulos C., Filiatrault A., Uang C.-M., And Folz B. (2002) "Posstensioned Energy Dissipating Connections for Moment-Resisting Steel Frames," *ASCE Journal of Structural Engineering*, Vol. 128, No. 9, pp 1111-1120.

Christopoulos, C., Pampanin, S., and Priestley, M. J. N. (2003) "Performance-Based Seismic Response of Frame Structures Including Residual Deformations, Part I: Single-Degree of Freedom Systems", *Journal of Earthquake Engineering*, Vol. 7, No. 1, pp 97-118.

Christopoulos, C., and Pampanin, S. (2004) "Towards Performance-Based Seismic Design of MDOF Structures with Explicit Consideration of Residual Deformations", *ISET Journal of Earthquake Technology*, Paper No. 440, Vol. 41, No. 1, pp 53-73.

Christopoulos, C., Tremblay, R., Kim, H.-J., and Lacerte, M. (2008) "Self-Centering Energy Dissipative Bracing System for the Seismic Resistance of Structures: Development and Validation" *ASCE Journal of Structural Engineering*, Vol. 134, No. 1.

Clough, R.W., and Huckelbridge, A.A. (1977) *Preliminary Experimental Study of Seismic Uplift of a Steel Frame,* Earthquake Engineering Research Center (EERC) Report No. UCB/EERC-77-22.

Combescure, D. and Pegon, P. (1997) "α-Operator Splitting Time Integration Technique for Pseudodynamic Testing Error Propagation Analysis." *Soil Dynamics and Earthquake Engineering*, Vol. 16, pp 427-443.

CSI (2009) *CSI Analysis Reference Manual For SAP2000, ETABS, and SAFE*, Published by Computers & Structures, Inc.

Corven, J., and Moreton, A. (2004) *Post-Tensioning Tendon Installation and Grouting Manual* Published by the Federal Highway Adminstration (FHWA).

Deierlein, G., Hajjar, J, Eatherton, M., Billington, S., Krawinkler, H., and Ma, X. (2009) "Seismically Resilient Steel Braced Frame Systems with Controlled Rocking and Energy Dissipating Fuses" *NEES 7th Annual Meeting*, Honolulu, Hawaii, June 23-25.

Deierlein, G. G., Ma, X., Hajjar, J., Eatherton, M., Krawinkler, Hl, Takeuchi, T., Midorikawa, M., Hikino, T., and Kasai, K. (2010) "Seismic Resilience of Self-Centering Steel Braced Frames With Replaceable Energy-Dissipating Fuses – Part II: E-Defense Shake Table Test" *Joint Conference Proceedings, 7th International Conference on Urban Earthquake Engineering (7CUEE) and 5th International Conference on Earthquake Engineering (5ICEE),* Tokyo Institute of Technology, Tokyo, Japan, March 3-5.

Dolce, M., and Cardone, D. (2006) "Theoretical and Experimental Studies for the Application of Shape Memory Alloys in Civil Engineering" *ASME Journal of Engineering Materials and Technology*, Vol. 128.

Eatherton, M. R., Hajjar, J. F., Deierlein, G. G., Krawinkler, H., Billington, S., Ma, X. (2008) "Controlled Rocking of Steel-Framed Buildings with Replaceable Energy-Dissipating Fuses" *Proceedings of the 14th World Conference on Earthquake Engineering*, Beijing, China, October 12-17.

Eatherton, M., Hajjar, J., Ma, X., Krawinkler, H., and Deierlein, G. (2010a) "Seismic Design and Behavior of Steel Frames with Controlled Rocking – Part I: Concepts and Quasi-Static Subassembly Testing" *ASCE Structures Congress*, Orlando, Florida, May 12-15

Eatherton, M., Hajjar, J., Deierlein, G., Ma, X., and Krawinkler, H. (2010b) "Hybrid Simulation Testing of a Controlled Rocking Steel Braced Frame System" *9th National Conference of Earthquake Engineering*, Toronto, Canada, July 25-29.

Fajfar, P., (1999) Capacity Spectrum Method Based on Inelastic Demand Spectra, *Earthquake Engineering and Structural Dynamics*, Vol. 28, No. 9, pp 979-993.

FEMA 273 (1997) *NEHRP Guidelines for the Seismic Rehabilitation of Existing Buildings* Published by the Federal Emergency Management Agency.

FEMA 356 (2000) *Prestandard and Commentary for the Seismic Rehabilitation of Buildings* Published by the Federal Emergency Management Agency.

FEMA P695 (2009) *Quantification of Building Seismic Performance Factors*, Published by the Federal Emergency Management Agency.

Freeman, S. A., (1971) *Third Progress Report on Racking Tests of Wall Panels,* San Francisco, CA, John A. Blume and Associates, Research Division, San Francisco, CA.

International Federation for Structural Concrete (2003). *Seismic Design of Precast Concrete Building Structures State-of-Art Report Prepared by Task Group 7.3*, International Federation for Structural Concrete (fib), Report FIB No. 27.

Gad, E. F., Chandler, A. M., Duffield, C. F., and Stark, G. (1999) "Lateral Behavior of Plasterboard-clad Residential Steel Frames", *Journal of Structural Engineering,* Vol. 125, no. 1, pp 32-39.

Galambos, T. V. (1998) *Guide to Stability Design Criteria for Metal Structures,* 5th Edition, In Conjunction with the Structural Stability Research Council, Published by Wiley.

Garlock, M. (2002) *Design, analysis, and experimental behavior of seismic resistant post-tensioned steel moment resisting frames* PhD Dissertation, Lehigh University.

Garlock, M., Ricles, J. M., and Sause, R. (2005) "Experimental Studies of Full-Scale Posttensioned Steel Connections" *ASCE Journal of Structural Engineering,* Vol. 131, No. 3.

Garlock, M. M., Sause, R., and Ricles, J. M. (2007) "Behavior and Design of Posttensioned Steel Frame Systems" *ASCE Journal of Structural Engineering*, Vol. 133, No. 3.

Gupta, A., and Krawinkler, H. (1999) *Seismic Demands for Performance Evaluation of Steel Moment Resisting Frame Structures* John A. Blume Earthquake Engineering Center Report Number 132.

Hajjar, J. F., Eatherton, M., Deierlein, G. G., Ma, X., Pena, A., Krawinkler, H., and Billington, S. (2008). "Controlled Rocking of Steel Framed Buildings as a Sustainable New Technology for Seismic Resistance in Buildings," *Creating And Renewing Urban Structures*, Chicago, Illinois, International Association for Bridge and Structural Engineering (IABSE), Zurich, Switzerland, September 17-19.

Hajjar, J., Eatherton, M., Ma, X., Deierlein, G. G., and Krawinkler, H. (2010) "Seismic Resilience of Self-Centering Steel Braced Frames With Replaceable Energy-Dissipating Fuses – Part I: Large-Scale Cyclic Testing" *Joint Conference Proceedings, 7th International Conference on Urban Earthquake Engineering (7CUEE) and 5th International Conference on Earthquake Engineering (5ICEE)*, Tokyo Institute of Technology, Tokyo, Japan, March 3-5.

Hall, K. S., Eatherton, M., and Hajjar, J. F. (2006) *Nonlinear Behavior of Controlled Rocking Steel-Framed Building Systems with Replaceable Energy Dissipating Fuses* UIUC Report No. ST-06-01.

Holden, T., Restrepo, J., and Mander, J. B. (2003) "Seismic Performance of Precast Reinforced and Prestressed Concrete Walls" *ASCE Journal of Structural Engineering* Vol. 129, No. 3, pp 286-296.

Housner, G.W. (1963) "The Behavior of Inverted Pendulum Structures During Earthquake." *Bulletin of the Seismological Society of America*, Vol. 53, No. 2, pp 403-417.

Hucklebridge, A. A. (1977) *Earthquake Simulation Tests of a Nine Story Steel Frame with Columns Allowed to Uplift,* Earthquake Engineering Research Center (EERC) Report No. UCB/EERC 77-23.

Ikenaga, M.; Nagae, T., Nakashima, M., and Suita, K. (2006) "Development of Column Bases Having Self-Centering and Damping Capability" *Proceedings of the Fifth International Conference on Behaviour of Steel Structures in Seismic Areas STESSA 2006*, Yokohama, Japan, August 14-17.

Kelley, J. and Tsztoo, D. (1977) *Earthquake Simulation Testing of a Stepping Frame with Energy-Absorbing Devices,* Earthquake Engineering Research Center (EERC) Report No. EERC 77-17.

Kiggins, S., and Uang, C.-M. (2006) "Reducing Residual Drift of Buckling-Restrained Braced Frames as a Dual System" *Engineering Structures,* Vol. 28, pp 1525-1532.

Kurama, Y. C., Weldon, B. D., and Shen, Q. (2006) "Experimental Evaluation of Posttensioned Hybrid Coupled Wall Subassemblages" *ASCE Journal of Structural Engineering*, Vol. 132, No. 7.

Kwon, O.-S., Nakata, N., Park, K.-S., Elnashai, A., and Spencer, B. (2007) *UI-SIMCOR User Manual and Examples for UI-SIMCOR v2.6 and NEES-SAM v2.0* Available from NEES Forge website: http://neesforge.nees.org/.

Lepage, A., Aschheim, M., and Senescu, R. (2004) "Shear-Yielding Steel Outriggers for High-Rise Construction" *13th World Conference on Earthquake Engineering*, Vancouver, Canada, August 1-6.

Leon-Salamanca, T., and Bray, D. F. (1996) "Residual Stress Measurement in Steel Plates and Welds Using Critically Refracted Longitudinal (LCR) Waves" Journal of Nondestructive Evaluation, Vol. 7, pp 169-184.

Liu, J., and Astaneh-Asl, A. (2000) *Cyclic Tests on Simple Connections Including Effects of the Slab*, SAC Joint Venture Report No. SAC/BD-00/03.

Lu, Y. (2005) "Inelastic Behaviour of RC Wall-Frame With a Rocking Wall and its Analysis Incorporating 3-D Effect" *The Structural Design of Tall and Special Buildings*, Vol. 31, pp 79-97.

Ma, Q. T., Wight, G.D., Butterworth, J.W., and Ingham, J.M. (2006) "Assessment of Current Procedures for Predicting the In-Plane Behaviour of Controlled Rocking Walls" *Proceedings of the 8th U.S. National Conference on Earthquake Engineering*, San Francisco, CA, April 18-22, Paper No. 654.

Ma, X., Eatherton, M., Hajjar, J., Krawinkler, H., and Deierlein, G. (2010a) "Seismic Design and Behavior of Steel Frames with Controlled Rocking – Part II: Large Scale Shake Table Testing and System Collapse Analysis" *ASCE Structures Congress*, Orlando, Florida, May 12-15.

Ma, X., Deierlein, G. G., Eatherton, M., Krawinkler, H., Hajjar, J., Takeuchi, T., Kasai, K., Midorikawa, M., and Hikino, T. (2010b) "Large-Scale Shaking Table Test of Steel Braced Frame with Controlled Rocking and Energy Dissipating Fuses" *9th National Conference of Earthquake Engineering*, Toronto, Canada, July 25-29.

Ma, X., Borchers, E., Peña, A., Krawinkler, H., and Deierlein, G. (2010c) *Design and Behavior of Steel Shear Plates With Openings as Energy-Dissipating Fuses*, Internal Report, Blume Earthquake Engineering Center, Stanford University.

Ma, X. (2010) *Seismic Design and Behavior of Self-Centering Braced Frame with Controlled Rocking and Energy Dissipating Fuses*, Ph.D. Dissertation, Stanford University.

MacRae, G. A., and Kawashima, K., 1997. Post-earthquake Residual Displacements of Bilinear Oscillators, *Earthquake Engineering and Structural Dynamics*, Vol. 26, No. 7, pp 701-716.

Makris, N. and Konstantinidis (2003) "The Rocking Spectrum and the Limitations of Practical Design Methodologies" *Earthquake Engineering and Structural Dynamics* Vol. 32, pp 265-289.

Mander, J.B., and Cheng, C.T. (1997) *Seismic Resistance of bridge piers based on damage avoidance design.* Technical Report Number NCEER-97-0014.

Mazzoni, S., McKenna, F., Scott, M. H., and Fenves, G. L. (2009) *Open System for Earthquake Engineering Simulation User Command-Language Manual,* OpenSees Version 2.0.

Medina, R. A. (2002) *Seismic Demands for Nondeteriorating Frame Structures and Their Dependence on Ground Motions*, Ph.d. Dissertation, Department of Civil and Environmental Engineering, Stanford University, Stanford, CA.

Midorikawa, M., Azuhata, T., Ishihara, T., and Wada, A. (2006) "Shaking Table Tests on Seismic Response of Steel Braced Frames with Column Uplift" *Earthquake Engineering and Structural Dynamics*, No. 35, pp 1767-1785.

Nakaki, S., Stanton, J., and Sritharan, S. (1999) "An Overview of the PRESSS Five-Story Precast Test Building" *PCI Journal,* Vol. 33, No. 2, pp 26-39.

Palermo, A., Pampanin, S., Marriott, D. (2007) "Design, Modeling, and Experimental Response of Seismic Resistant Bridge Piers with Posttensioned Dissipating Connections" *ASCE Journal of Structural Engineering*, Vol. 133, No. 11, 2007, pp 1648-1661.

Pampanin, S., Christopoulos, C. and Priestley, M. J. N. (2003) "Performance-based Seismic Response of Frame Structures including Residual Deformations. Part II: Multi-degree of Freedom Systems", *Journal of Earthquake Engineering,* Vol. 7, No. 1, pp 119-147.

Pekcan, G., Mander, J.B., and Chen, S.S. (2000) "Balancing lateral loads using tendon-based supplemental damping system" *ASCE Journal of Structural Engineering*, Vol. 126, No. 8, pp 896-905

Perez, F. J., Sause, R., and Pessiki, S. (2007) "Analytical and Experimental Lateral Load Behavior of Unbonded Posttensioned Precast Concrete Walls" *ASCE Journal of Structural Engineering*, Vol. 133, No. 11.

Pettinga, D., Christopoulos, C., Pampanin, S., and Priestley, N. (2007) "Effectiveness of Simple Approaches in Mitigating Residual Deformations in Buildings", *Earthquake Engineering and Structural Dynamics,* Vol. 36, No. 12, pp 1763-1783.

Pollino, M., and Bruneau, M. (2004) *Seismic Retrofit of Bridge Steel Truss Piers Using a Controlled Rocking Approach,* Technical Report MCEER-04-0011.

Pollino, M., and Bruneau, M. (2008) *Analytical and Experimental Investigation of a Controlled Rocking Approach for Seismic Protection of Bridge Steel Truss Piers,* Technical Report MCEER-08-0003.

Priestley, M. J. N., Evison, R. J. and Carr, A. J. (1978). "Seismic Response of Structures Free to Rock on Their Foundations," *Bulletin of the New Zealand Society for Earthquake Engineering*, Vol. 11, No. 3, pp. 141-150.

Priestley, M. J. N., Sritharan, S., Conley, J. R., and Pampanin, S. (1999) "Preliminary Results and Conclusions From the PRESS Five-Story Precast Concrete Test Building" *PCI Journal*, Vol. 44, No. 6, pp 42-67.

Psycharis, I. (1982) *Dynamic Behavior of Rocking Structures Allowed to Uplift*, PhD Dissertation, California Institute of Technology, Pasadena, California.

Rahman, A. and Restrepo, J. (2000) *Earthquake Resistant Precast Concrete Buildings : Seismic Performance of Cantilever Walls Prestressed Using Unbonded Tendons*, University of Cantebury Research Report 2000-05.

Rahman, M. A., Sritharan, S. (2007) "Performance-Based Seismic Evaluation of Two Five-Story Precast Concrete Hybrid Frame Buildings" *Journal of Structural Engineering*, Vol. 133, No. 11, 2007, pp 1489-1500.

Restrepo, J., and Rahman, A. (2007) "Seismic Performance of Self-Centering Structural Walls Incorporating Energy Dissipators" *ASCE Journal of Structural Engineering*, Vol. 133, No. 11.

Rihal, S. S., (1980) *Racking Tests of Non-Structural Building Partitions*, Report ARCE R80-1, California Polytechnic State University, San Luis Obispo, CA.

Richards, P. W. and Uang, C.-M. (2006) "Testing Protocol for Short Links in Eccentrically Braced Frames" *ASCE Journal of Structural Engineering*, Vol. 132, No. 8, pp 1183-1191.

Ricles J., Sause R., Garlock M., and Zhao C. (2001) "Posttensioned Seismic-Resistant Connections for Steel Frames," *ASCE Journal of Structural Engineering*, Vol. 127, No. 2, pp. 113-121.

Roke, D., Sause, R., Ricles, J. M., and Gonner, N. (2009) "Damage-Free Seismic-Resistant Self-Centering Steel Concentrically-Braced Frames" *Behaviour of Steel Structures in Seismic Areas (STESSA)*, Philidelphia, Pennsylvania, August 16-20.

Ruiz-Garcia, J., and Miranda, E. (2006) "Residual Displacement Ratios for Assessment of Existing Structures", *Earthquake Engineering and Structural Dynamics*, Vol. 35, pp 315-336.

Sabelli, R., Mahin, S., and Chang, C. (2003) "Seismic Demands on Steel Braced Frame Buildings with Buckling Restrained Braces" *Engineering Structures*, Vol. 25, pp 655-666.

Salmon, C. G., and Johnson, J. E. (1997) *Steel Structures: Design and Behavior*, 4th Edition Published by HarperCollins.

Seo, C.-Y., and Sause, R. (2005) "Ductility Demands on Self-centering Systems under Earthquake Loading", *ACI Structural Journal,* Vol. 102, No. 2, pp 275-285.

Serrette, R., and Ogunfunmi, K., (1996) "Shear Resistance of Gypsum-sheathed Light-gauge Steel Stud Walls", *Journal of Structural Engineering,* Vol. 122, No. 4, pp 383-389.

Serrette, R. L., Encalada, J., Juadines, M., and Nguyen, H. (1997) "Static Racking Behavior of Plywood, OSB, Gypsum, and Fiberbond Walls with Metal Framing", *Journal of Structural Engineering,* Vol. 123, No. 8, pp 1079-1086.

Shen, Q., and Kurama, Y. C. (2002) "Nonlinear Behavior of Posttensioned Hybrid Coupled Wall Subassemblages" *ASCE Journal of Structural Engineering,* Vol. 128, No. 10.

Structural Engineers Association of California (1996) *SEAOC Blue Book Sixth Edition* Published by SEAOC.

Structural Engineers Association of California (1995) *SEAOC Vision 2000, Performance Based Seismic Engineering of Buildings, Vols I and II: Conceptual Framework* Published by the SEAOC.

Takamatsu, T., Tamai, H., Yamanishi, T., and Matsuo, A. (2006) "Self-Centering Performance of Non-Slip-Type Exposed Column Base" *Proceedings of the Fifth International Conference on Behaviour of Steel Structures in Seismic Areas (STESSA),* Yokohama, Japan, August 14-17.

Tanamal, A., Eatherton, M., and Hajjar, J.F. (2009) *Controlled Rocking of Steel-Framed Buildings With Energy Dissipating Fuses, Fuse Material Coupons – Tension Tests,* Internal Report, University of Illinois at Urbana-Champaign.

Tanamal, A., Eatherton, M., and Hajjar, J.F. (2007) *Controlled Rocking of Steel-Framed Buildings With Energy Dissipating Fuses, Post-Tensioning Strand Material Tests,* Internal Report, University of Illinois at Urbana-Champaign.

Tarpy, T. S. (1980) "Shear resistance of steel-stud wall panels", *Proceedings of the 5th International Specialty Conference on Cold-Formed Steel Structures,* St. Louis, Mo, pp 331–348.

Tarpy, T. S. (1984) "Shear Resistance of Steel Stud Wall Panels: A Summary Report", *Proceedings of the 7th International Specialty Conference on Cold-Formed Steel Structures,* University of Missouri–Rolla, Rolla, MO, pp 203–248.

Tsai, K.-C., Chen, H.-W., Hong, C.-P., and Su, Y.-F. (1993) "Design of Steel Triangular Plate Energy Absorbers for Seismic-Resistant Construction" *Earthquake Spectra*, Vol. 9, No. 3, pp 505-528.

Vargas, R. and Bruneau, M. (2006) "Seismic Response and Design of Buildings with Metallic Structural Fuses" *Proceedings of the Fifth International Conference on Behaviour of Steel Structures in Seismic Areas (STESSA)*, Yokohama, Japan, August 14-17.

Wada, A, Yamada, S., Fukuta, O., and Tanigawa, M. (2001) "Passive Controlled Slender Structures Having Special Devises at Column Connections" *7th International Seminar on Seismic Isolation, Passive Energy Dissipation and Active Control of Vibrations of Structures*, Assisi, Italy, October 2-5.

Wolski, M., Ricles, J.M., Sause, R. (2006) "Seismic Resistant Self-Centering Steel Moment Resisting Frames With Bottom Flange Friction Devices" *Proceedings of the Fifth International Conference on Behaviour of Steel Structures in Seismic Areas STESSA 2006*, Yokohama, Japan, August 14-17.

Xia, C., and Hanson, R. D., (1992) "Influence of ADAS Element Parameters on Building Seismic Response" *ASCE Journal of Structural Engineering*, Vol. 118, No. 7, pp 1903-1918.

Zhu, S., and Zhang, Y. (2008) "Seismic Analysis of Concentrically Braced Frame Systems with Self-Centering Friction Damping Braces" *ASCE Journal of Structural Engineering*, Vol. 134, No. 1.

SPECIMEN DRAWINGS, DISPLACEMENT PROTOCOLS, AND INSTRUMENTATION DETAILS

This appendix includes information about the experimental program including specimen design drawings, work plan drawings, erection drawings, design drawings for the single frame configuration tests, shop drawings, loading protocol for each specimen, data acquisition setup information, and lists of channels recorded for each specimen.

A.1 Specimen Design Drawings

The following drawings consist of a set of drawings labeled with "S" drawing identification labels, and a set of drawings with "F" drawing identification labels. The "S" set of drawings were drawings for pieces that were used for all tests. The "F" set of drawings showed pieces that would be specific to a test or specimen. The preliminary test plan included a B series of specimens that were a dual frame configuration with a distance between the two frame that was different from the value used in the A series. This set of tests was not conducted and does not correspond to the B series of tests used in the final test plan which refers to single frame configurations.

It is also important to note that the fuses and configurations for the A series of specimens changed from these design drawings. The drawings in the subsequent sections show many of these changes, and the configurations that were actually tested are summarized in Chapter 4.

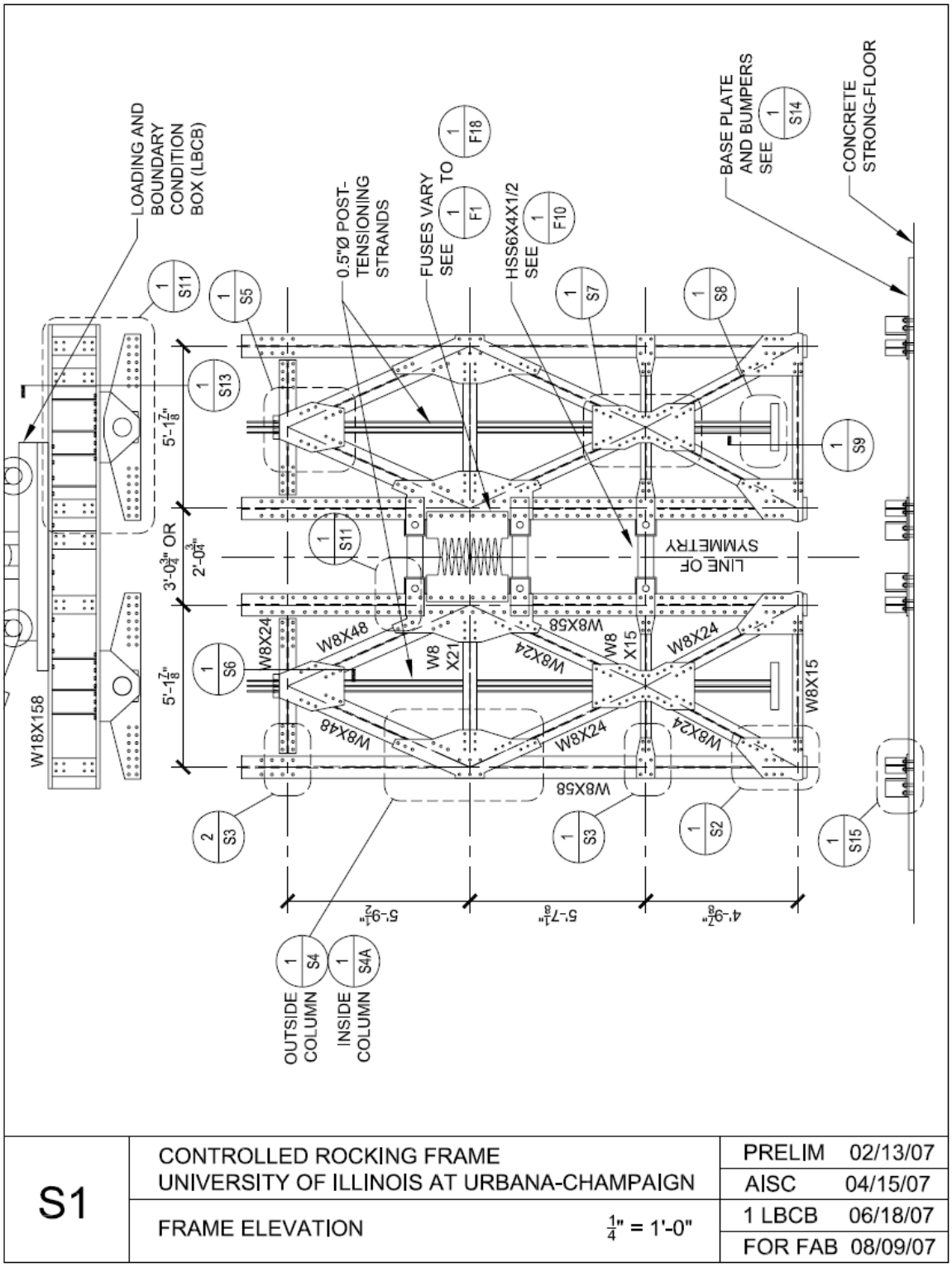

S1	CONTROLLED ROCKING FRAME UNIVERSITY OF ILLINOIS AT URBANA-CHAMPAIGN	PRELIM 02/13/07 AISC 04/15/07
	FRAME ELEVATION $\frac{1}{4}$" = 1'-0"	1 LBCB 06/18/07 FOR FAB 08/09/07

Figure A.1 Specimen Design Drawing – Frame Elevation

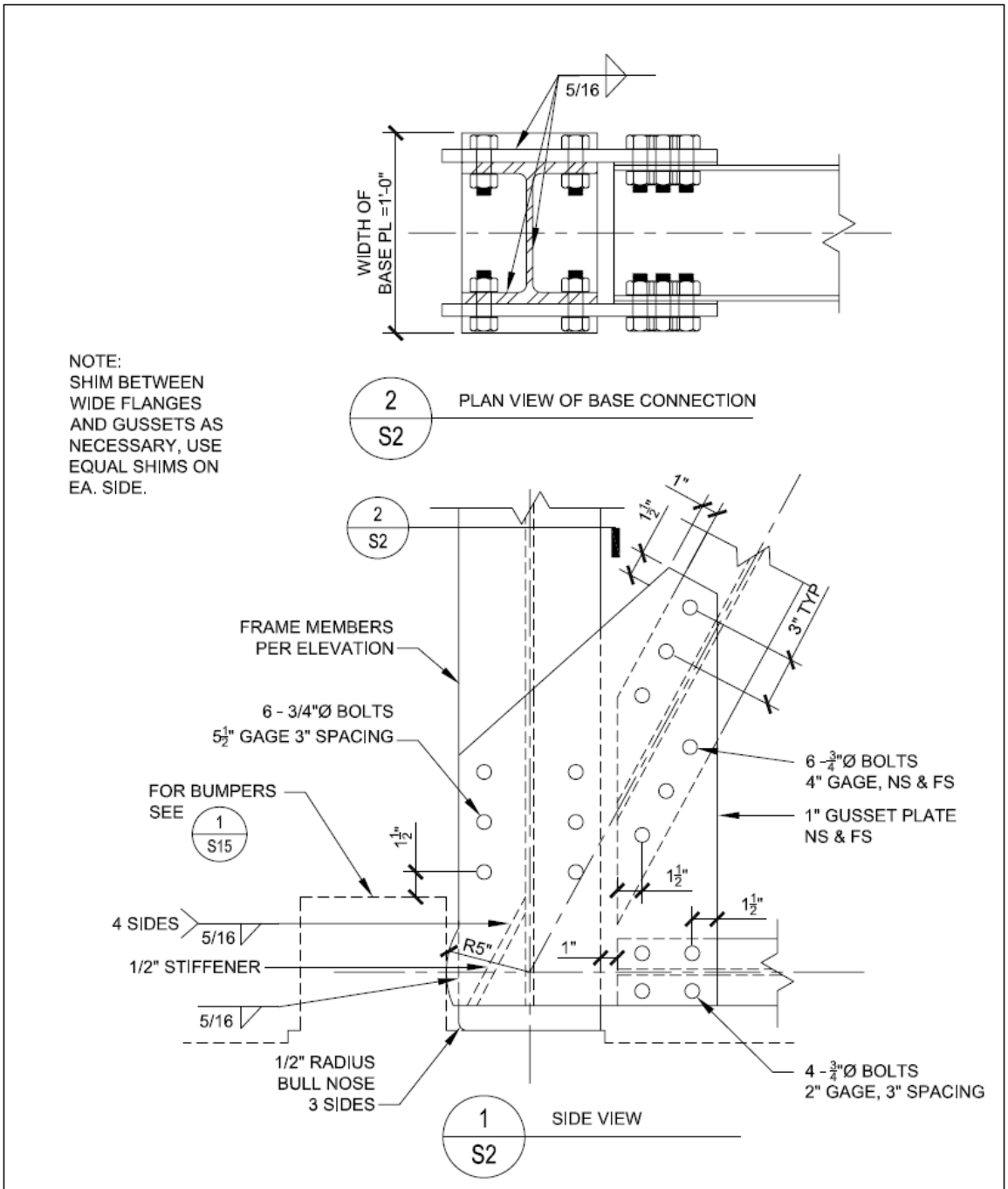

S2	CONTROLLED ROCKING FRAME UNIVERSITY OF ILLINOIS AT URBANA-CHAMPAIGN	PRELIM 02/13/07 AISC 04/15/07
	COLUMN BASE $1\frac{1}{2}$" = 1'-0"	1 LBCB 06/18/07 FOR FAB 08/09/07

Figure A.2 Specimen Design Drawing – Column Base

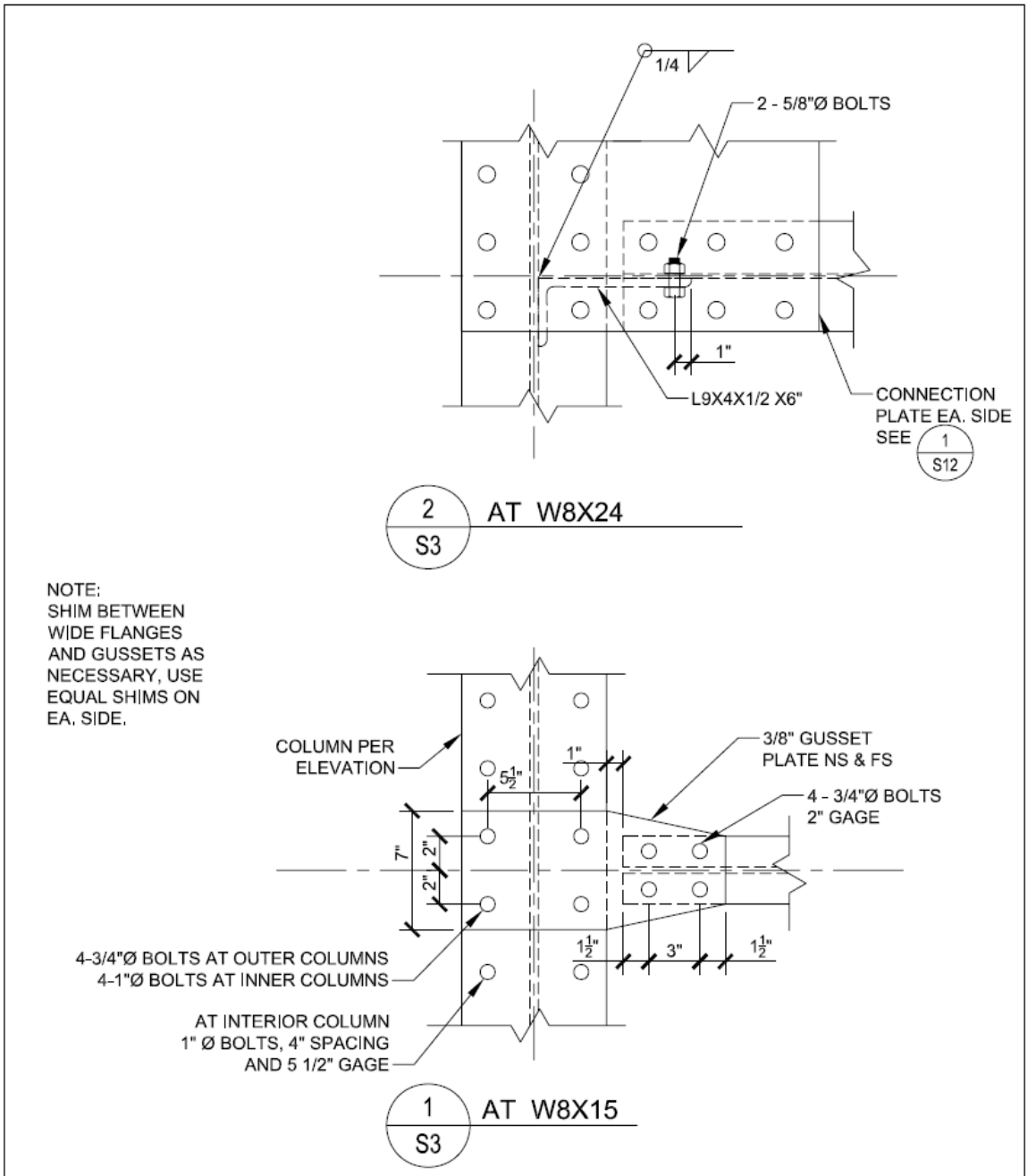

Figure A.3 Specimen Design Drawing – Beam-to-Column Connection

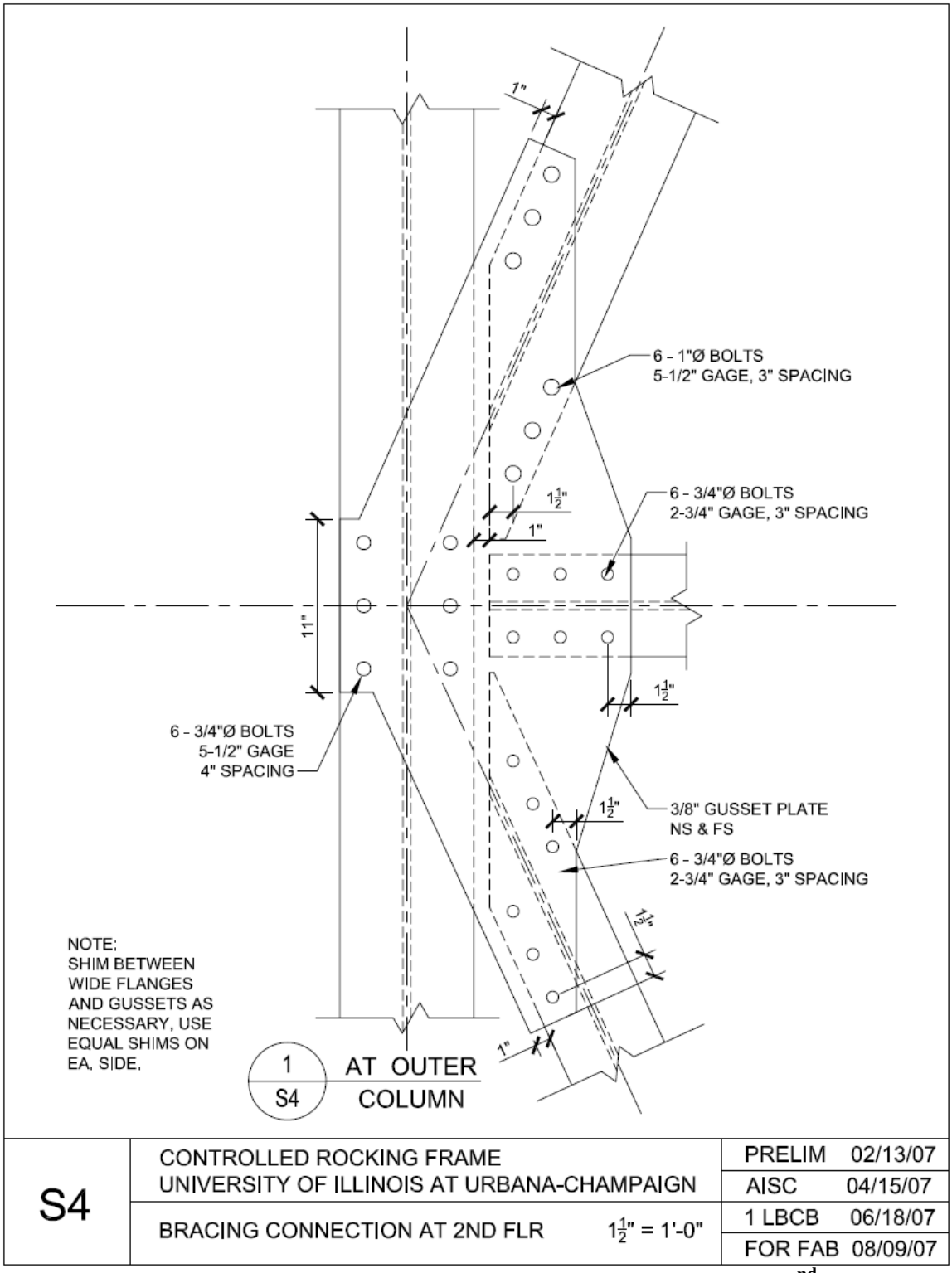

Figure A.4 Specimen Design Drawing – Bracing Connection at 2nd Floor

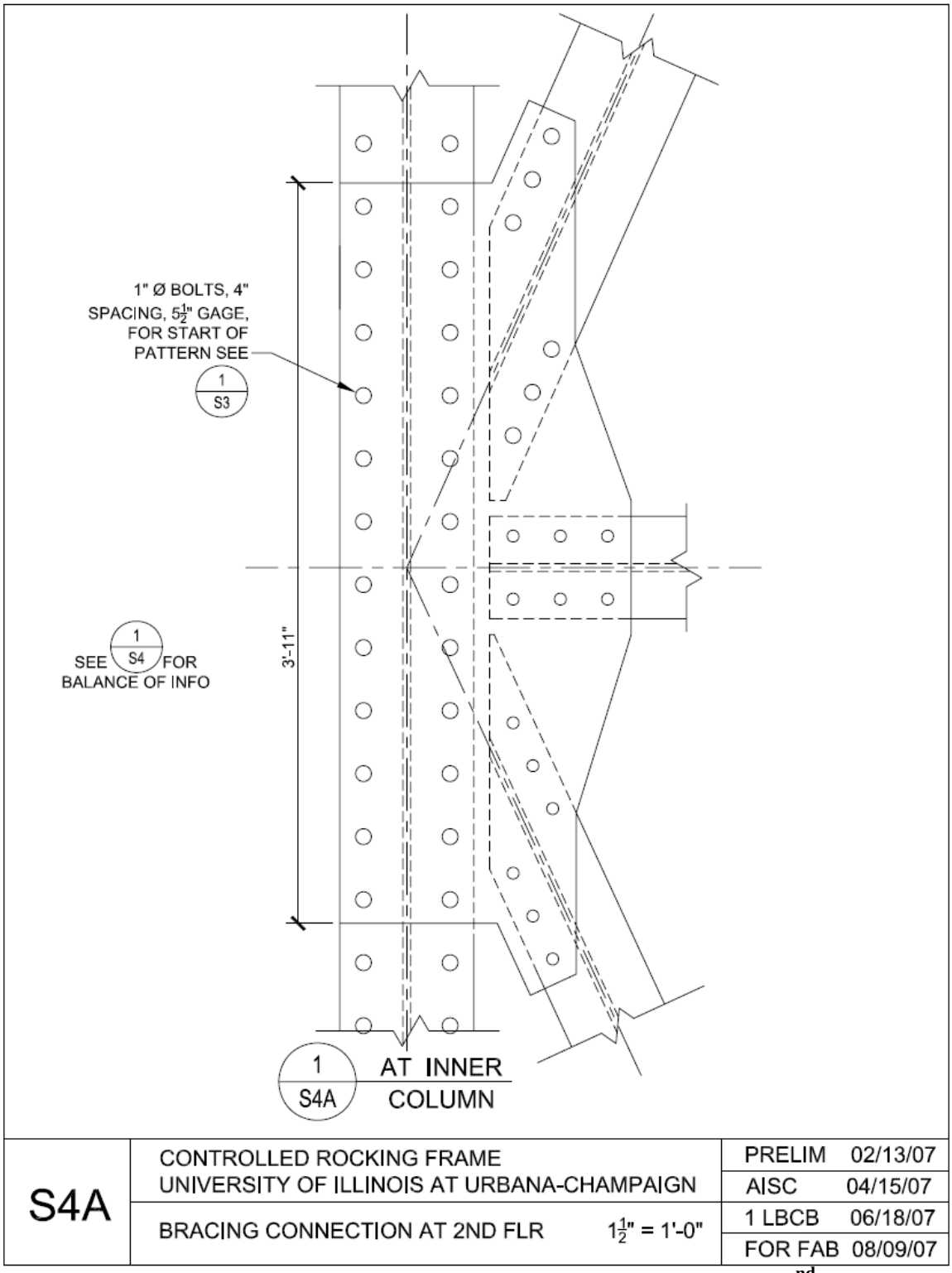

Figure A.5 Specimen Design Drawing – Bracing Connection at 2nd Floor

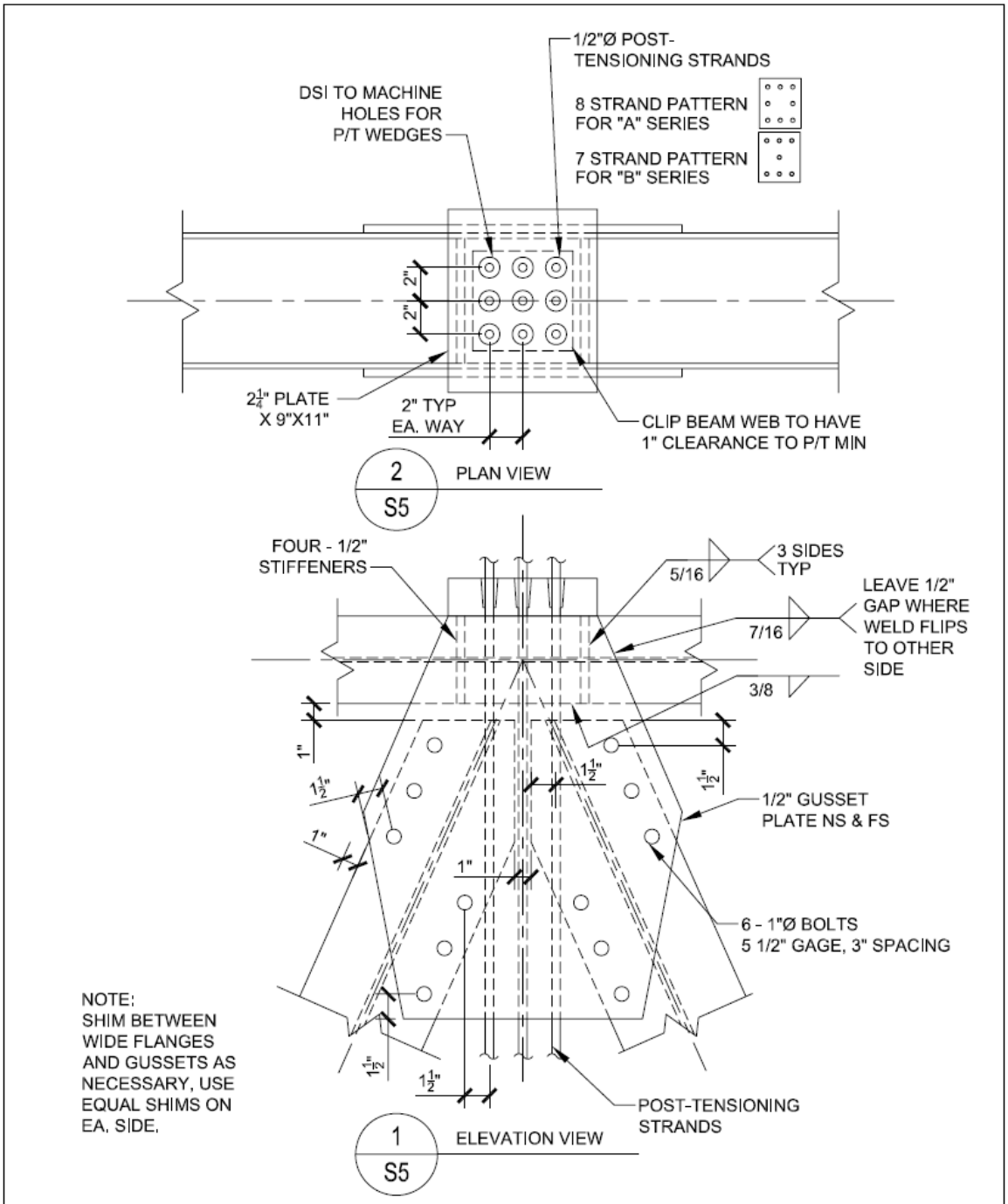

S5	CONTROLLED ROCKING FRAME UNIVERSITY OF ILLINOIS AT URBANA-CHAMPAIGN	PRELIM 02/13/07 AISC 04/15/07
	TOP P/T ANCHORAGE 1½" = 1'-0"	1 LBCB 06/18/07 FOR FAB 08/09/07

Figure A.6 Specimen Design Drawing – Top Post-Tensioning Anchorage

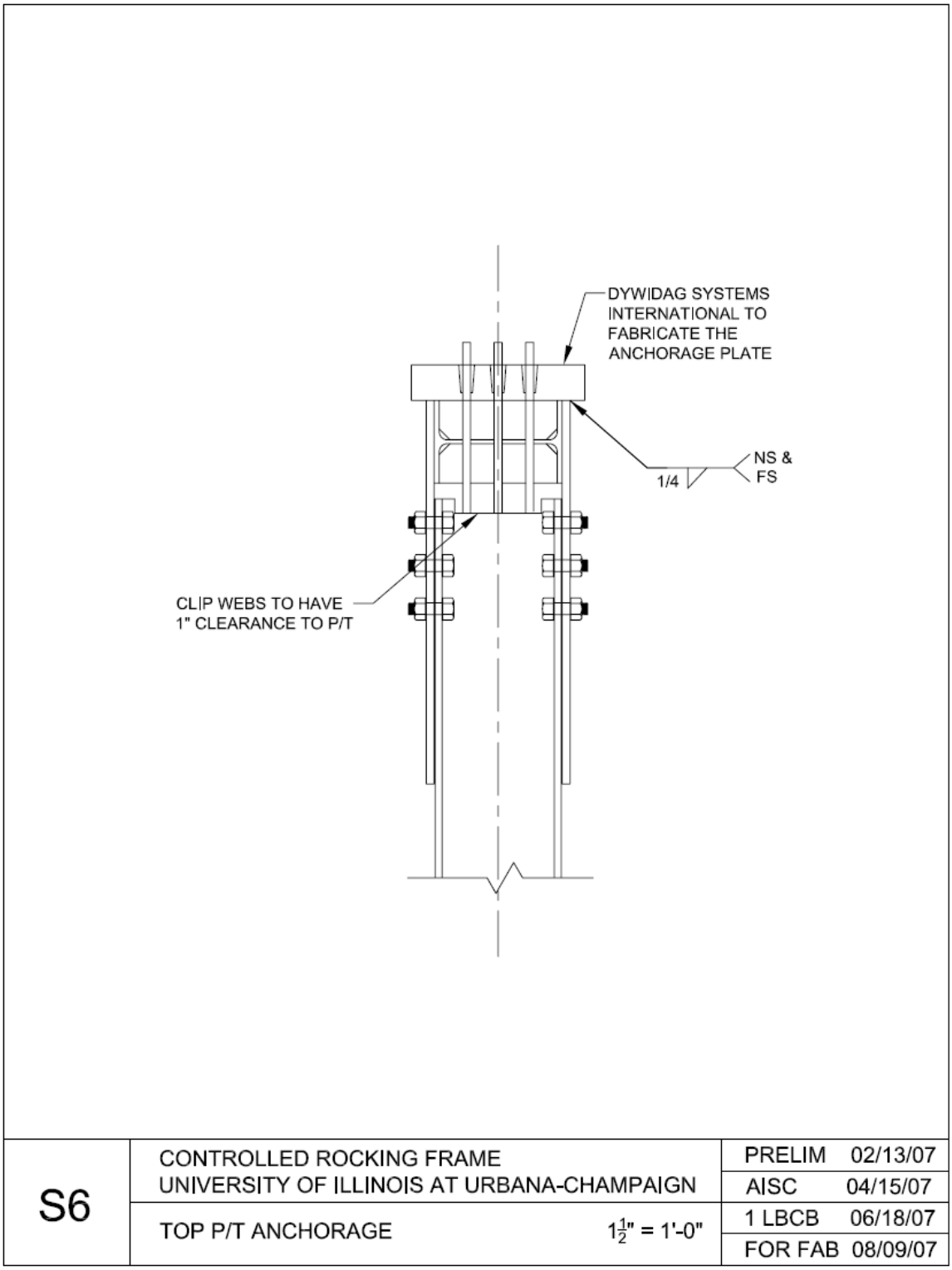

S6	CONTROLLED ROCKING FRAME UNIVERSITY OF ILLINOIS AT URBANA-CHAMPAIGN	PRELIM 02/13/07 AISC 04/15/07
	TOP P/T ANCHORAGE $1\frac{1}{2}$" = 1'-0"	1 LBCB 06/18/07 FOR FAB 08/09/07

Figure A.7 Specimen Design Drawing – Top Post-Tensioning Anchorage

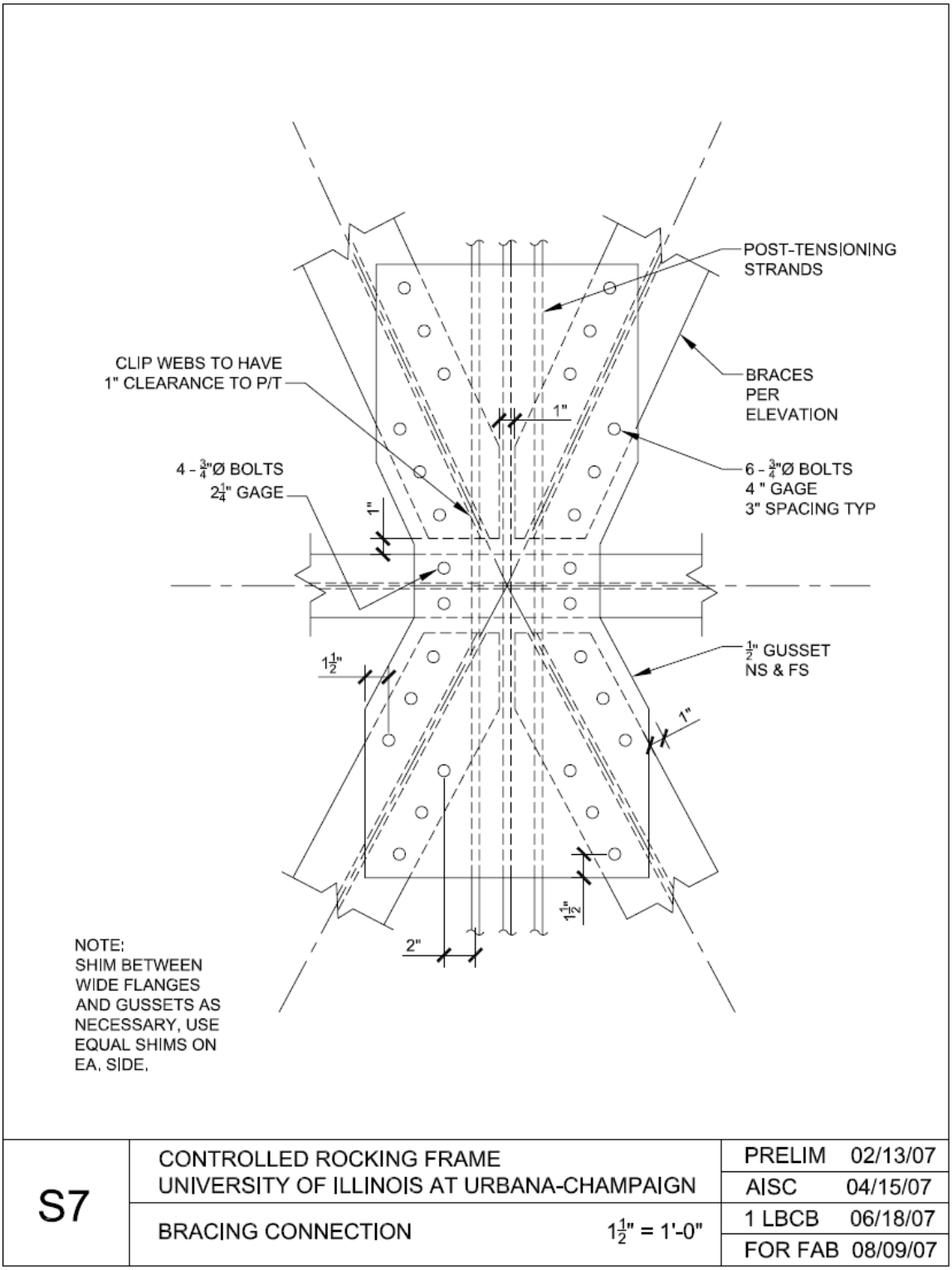

Figure A.8 Specimen Design Drawing – Bracing Connection

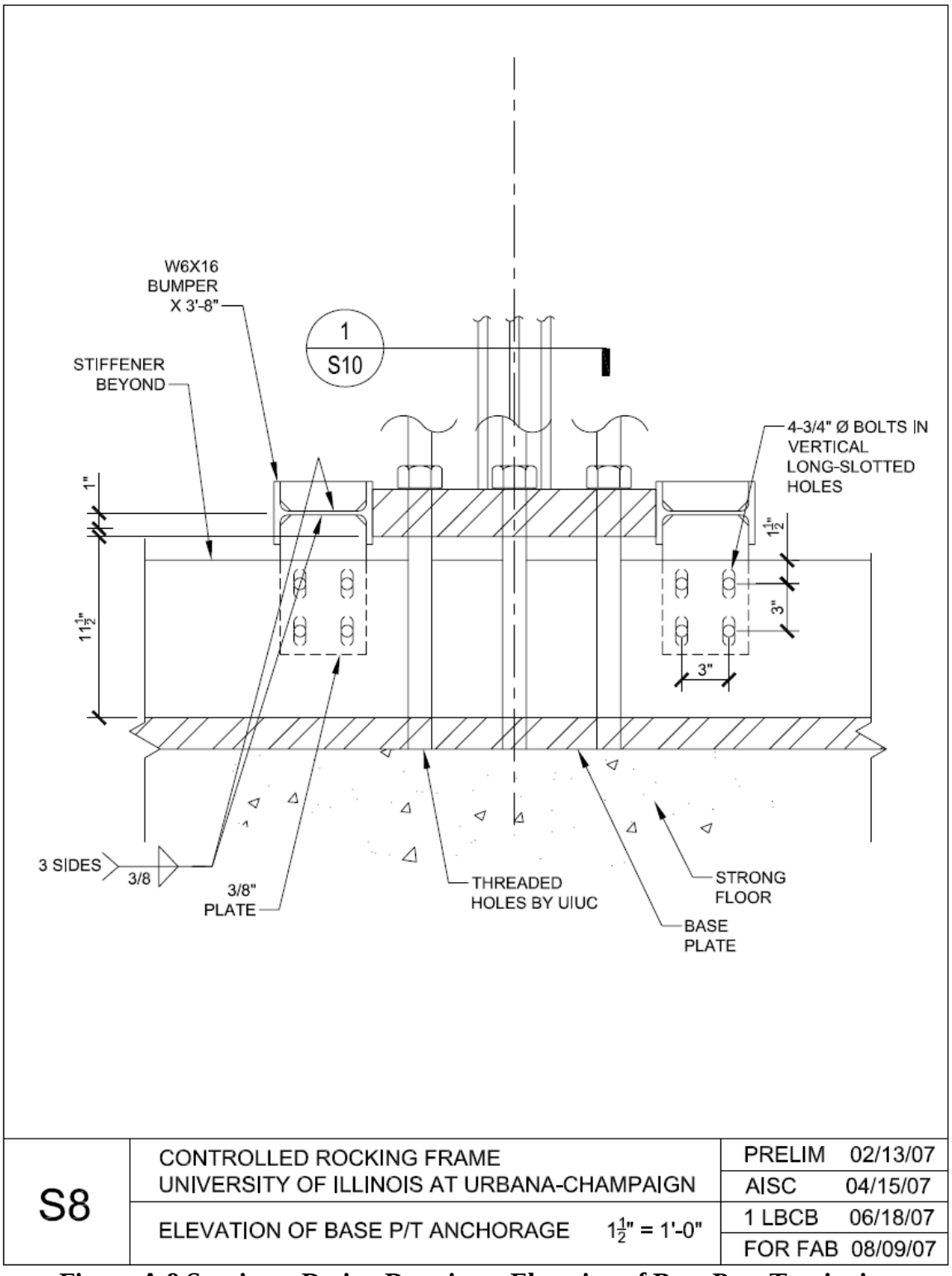

S8	CONTROLLED ROCKING FRAME UNIVERSITY OF ILLINOIS AT URBANA-CHAMPAIGN	PRELIM 02/13/07 AISC 04/15/07
	ELEVATION OF BASE P/T ANCHORAGE 1½" = 1'-0"	1 LBCB 06/18/07 FOR FAB 08/09/07

Figure A.9 Specimen Design Drawing – Elevation of Base Post-Tensioning Anchorage

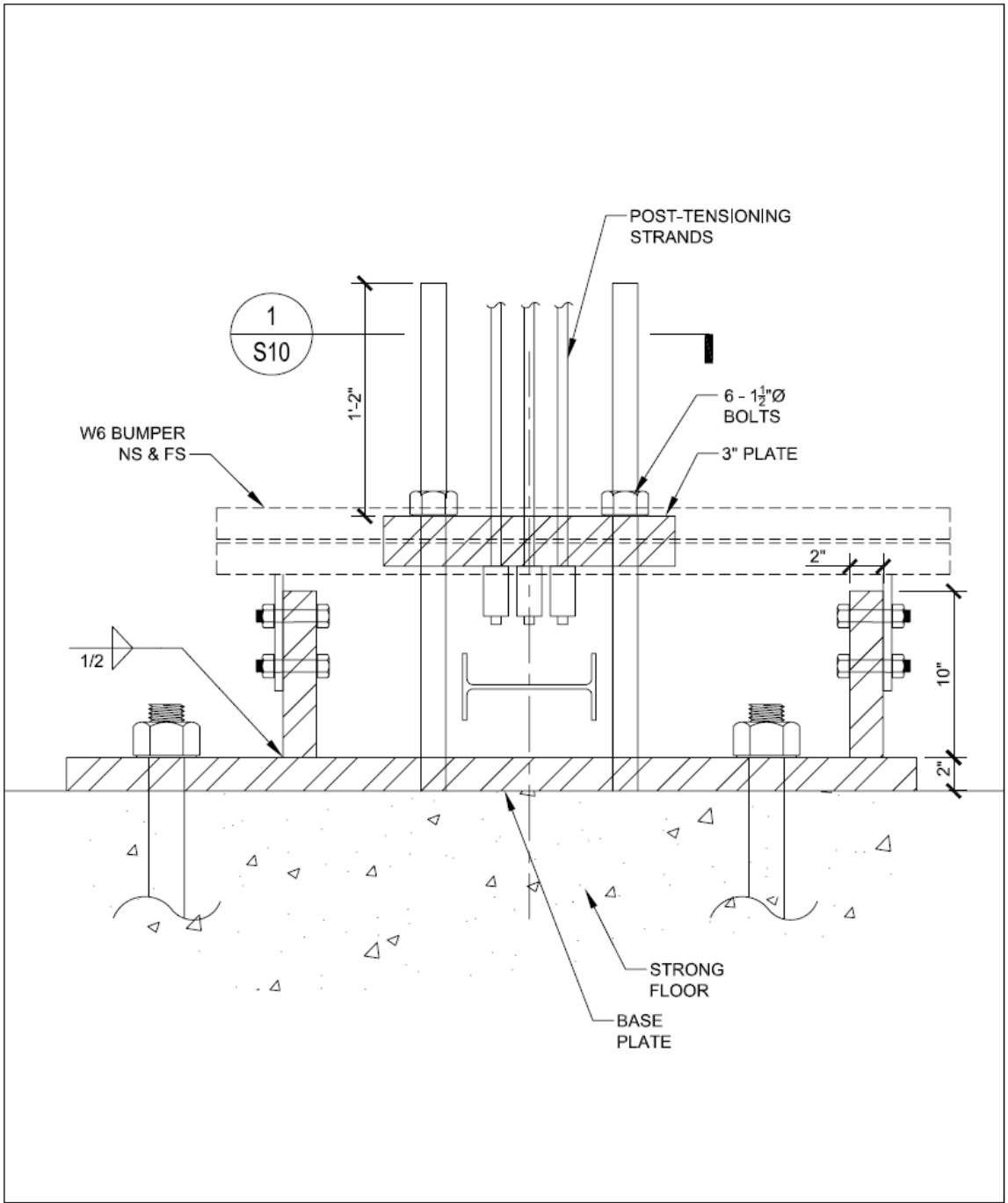

S9	CONTROLLED ROCKING FRAME UNIVERSITY OF ILLINOIS AT URBANA-CHAMPAIGN	PRELIM 02/13/07 AISC 04/15/07
	SECTION OF BASE P/T ANCHORAGE	1 LBCB 06/18/07 FOR FAB 08/09/07

Figure A.10 Specimen Design Drawing – Section of Base Post-Tensioning Anchorage

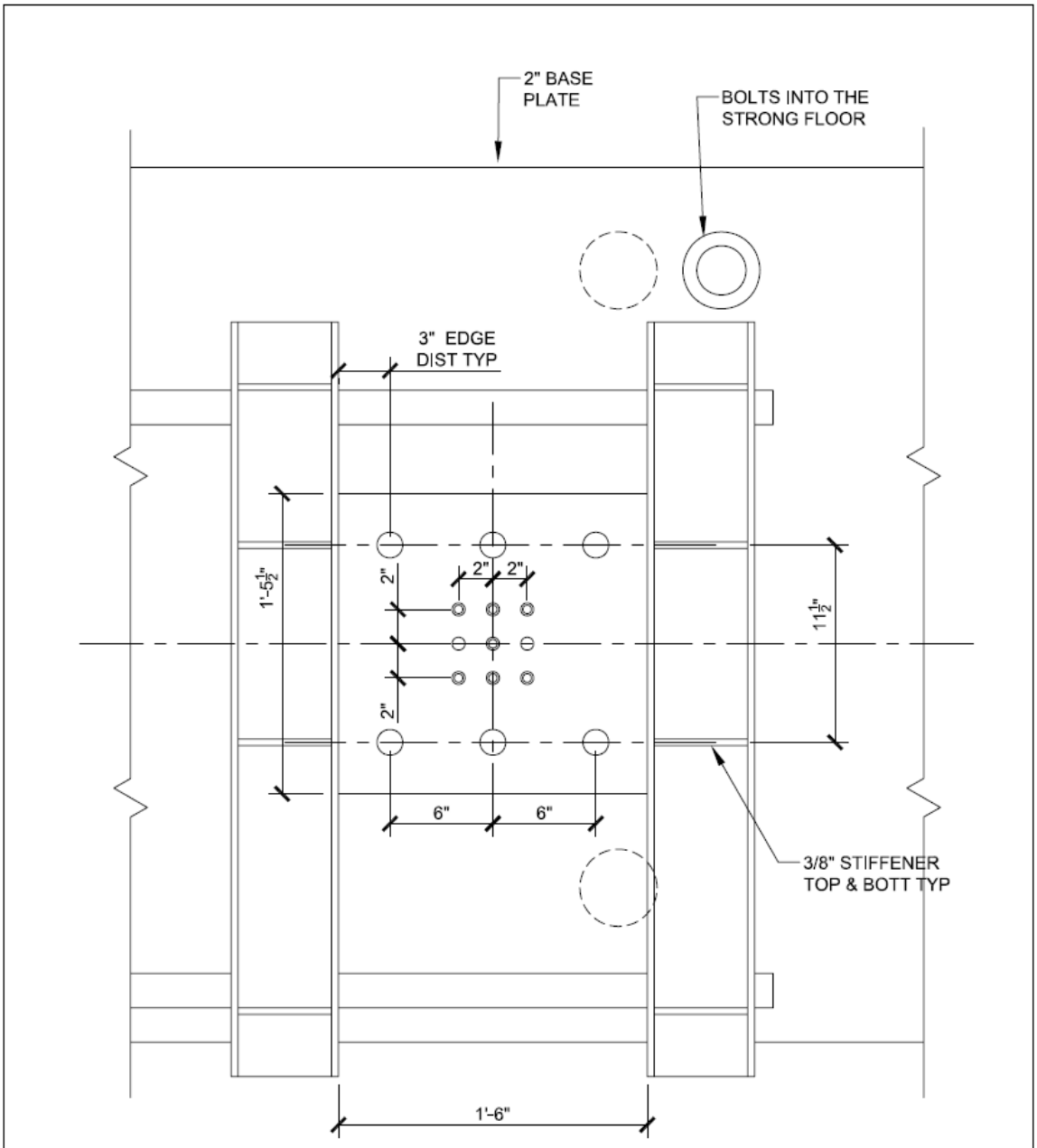

S10	CONTROLLED ROCKING FRAME UNIVERSITY OF ILLINOIS AT URBANA-CHAMPAIGN	PRELIM 02/13/07 AISC 04/15/07
	PLAN VIEW OF BASE P/T ANCHORAGE 1½" = 1'-0"	1 LBCB 06/18/07 FOR FAB 08/09/07

Figure A.11 Specimen Design Drawing – Plan View of Base Post-Tensioning Anchorage

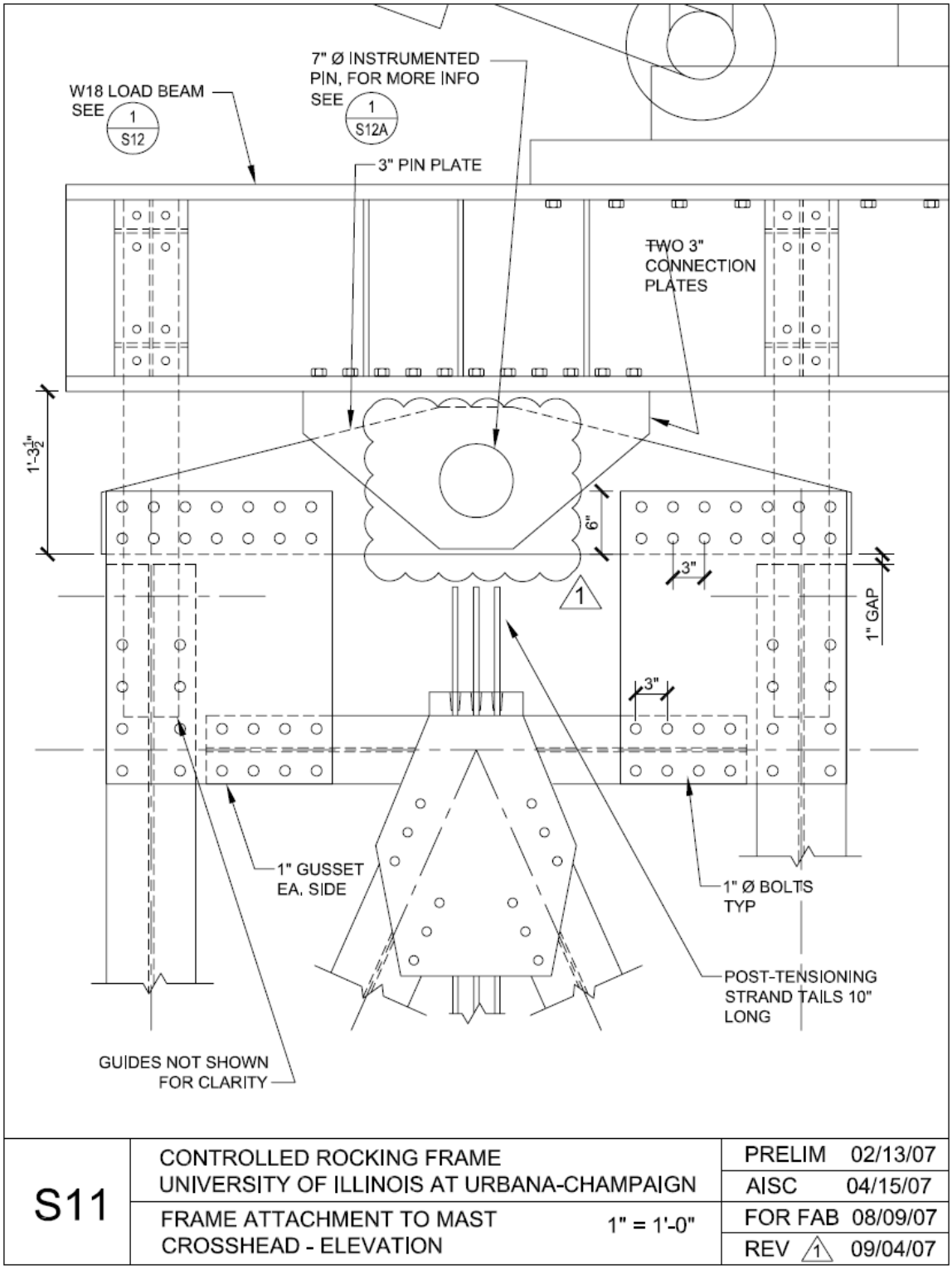

Figure A.12 Specimen Design Drawing – Frame Attachment at Top

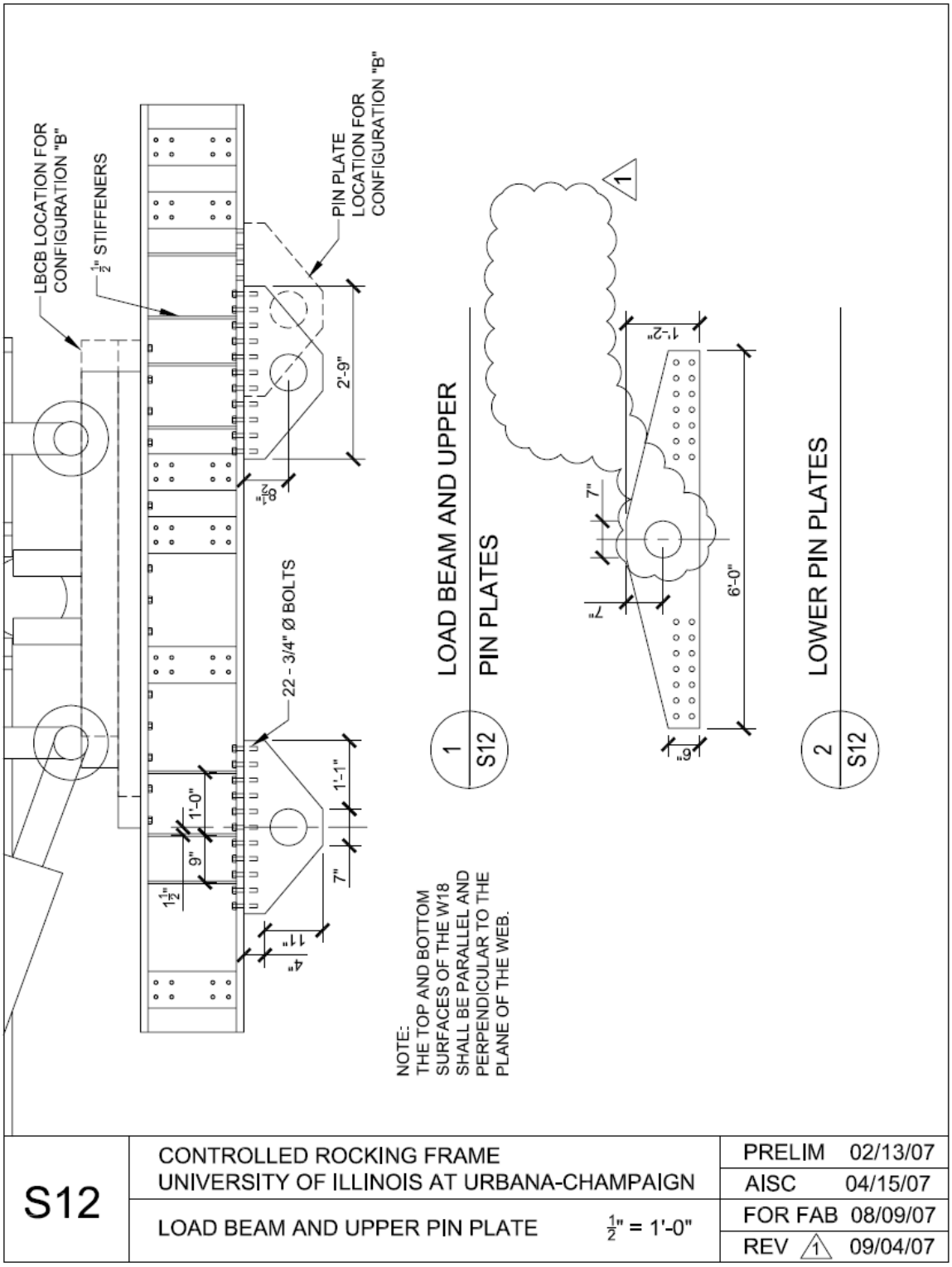

Figure A.13 Specimen Design Drawing – Load Beam and Upper Pin Plate

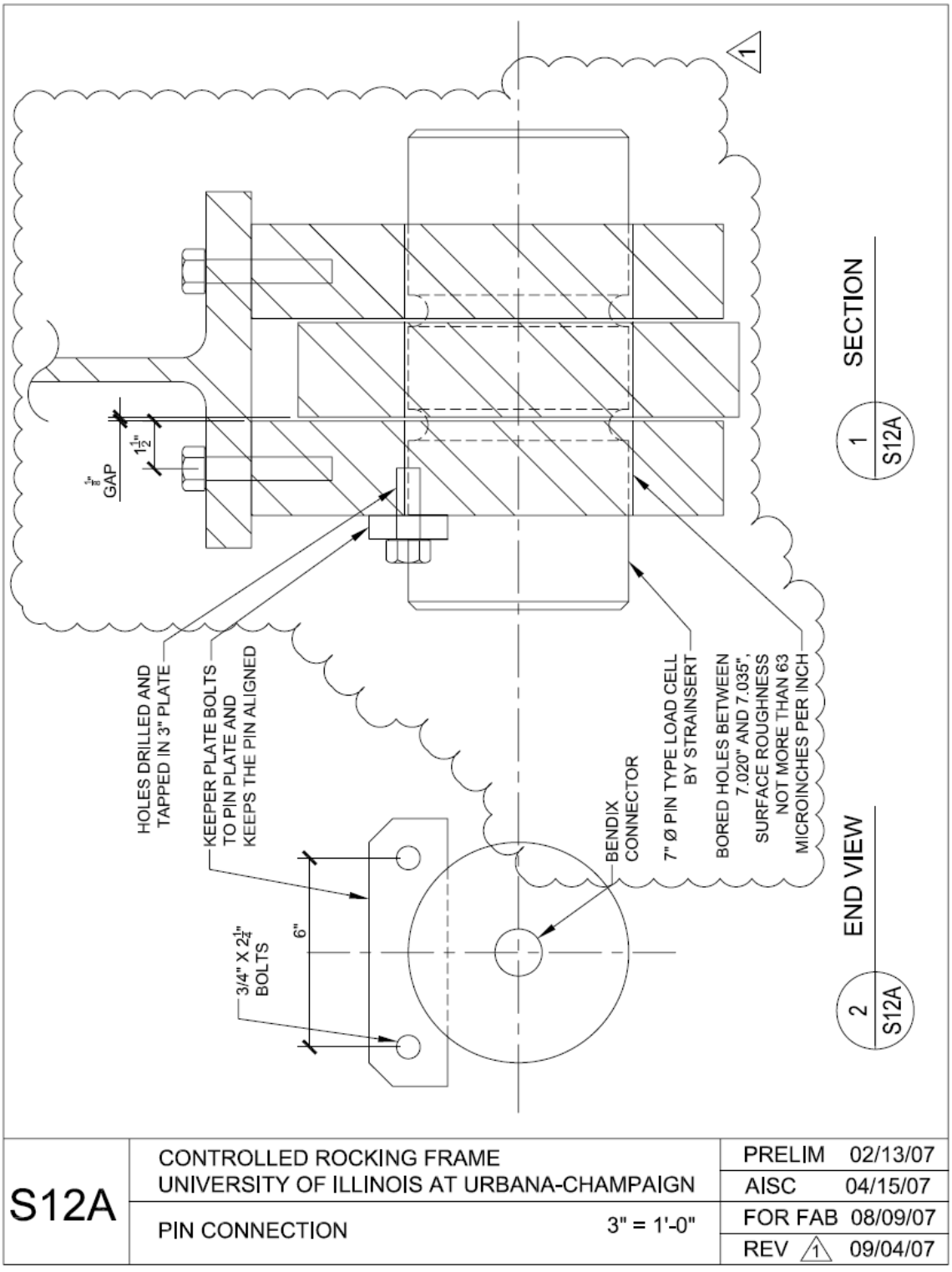

Figure A.14 Specimen Design Drawing – Pin Connection

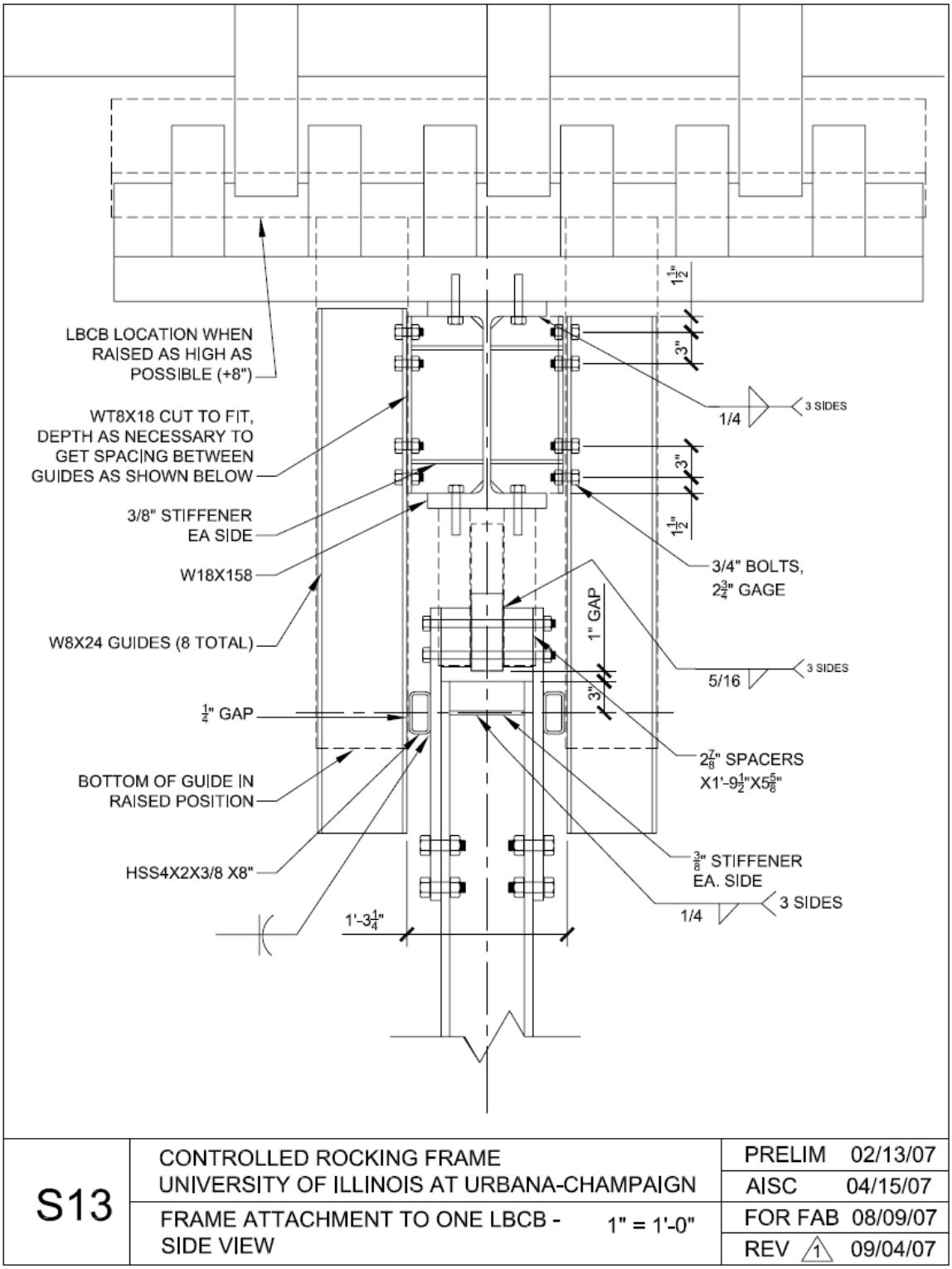

Figure A.15 Specimen Design Drawing – Frame Attachment to One LBCB – Side View

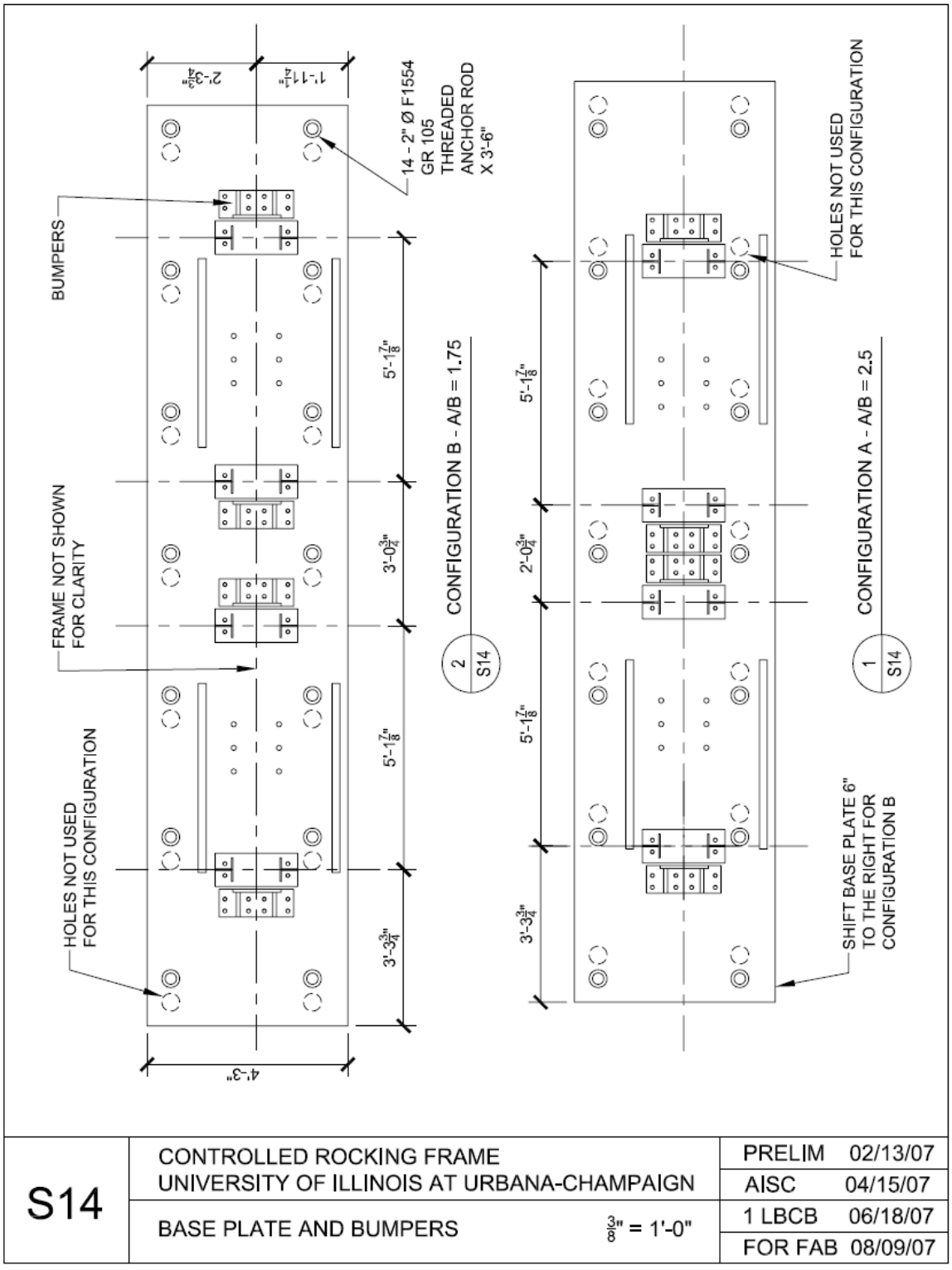

Figure A.16 Specimen Design Drawing – Base Plate and Bumpers

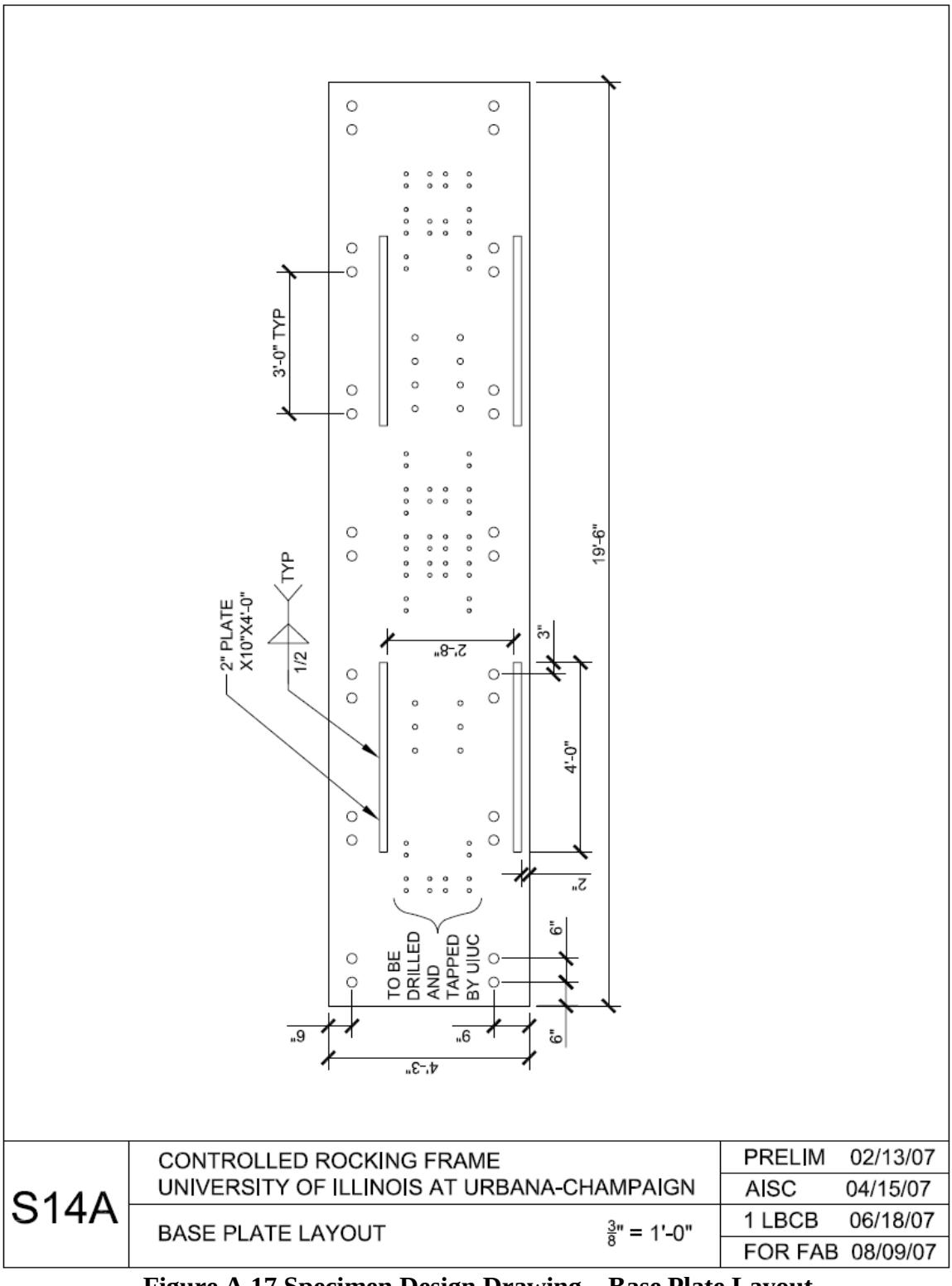

S14A	CONTROLLED ROCKING FRAME UNIVERSITY OF ILLINOIS AT URBANA-CHAMPAIGN	PRELIM 02/13/07 AISC 04/15/07
	BASE PLATE LAYOUT $\frac{3}{8}$" = 1'-0"	1 LBCB 06/18/07 FOR FAB 08/09/07

Figure A.17 Specimen Design Drawing – Base Plate Layout

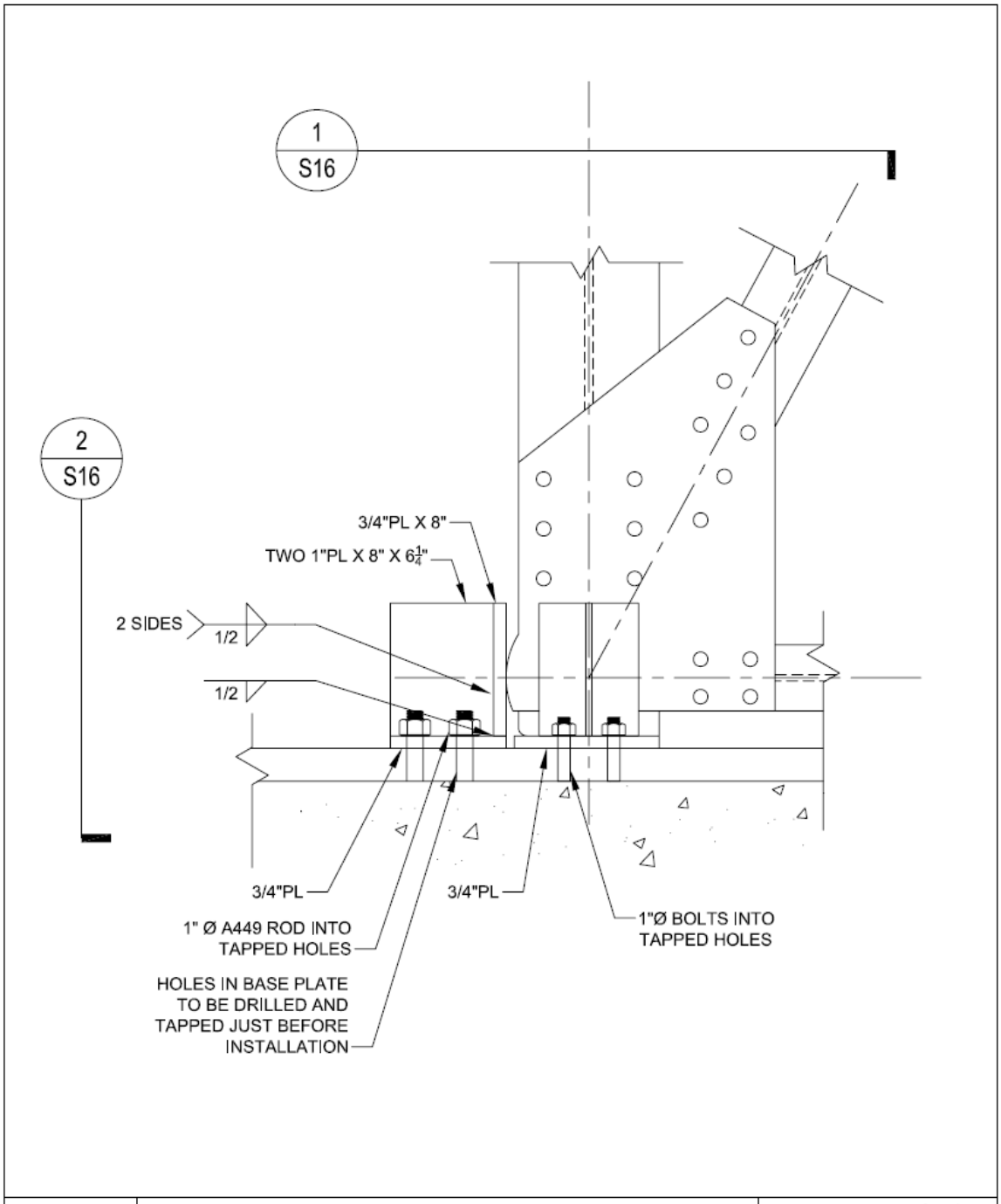

S15	CONTROLLED ROCKING FRAME UNIVERSITY OF ILLINOIS AT URBANA-CHAMPAIGN	PRELIM 02/13/07 AISC 04/15/07
	BUMPER DETAIL 1½" = 1'-0"	1 LBCB 06/18/07 FOR FAB 08/09/07

Figure A.18 Specimen Design Drawing – Bumper Detail

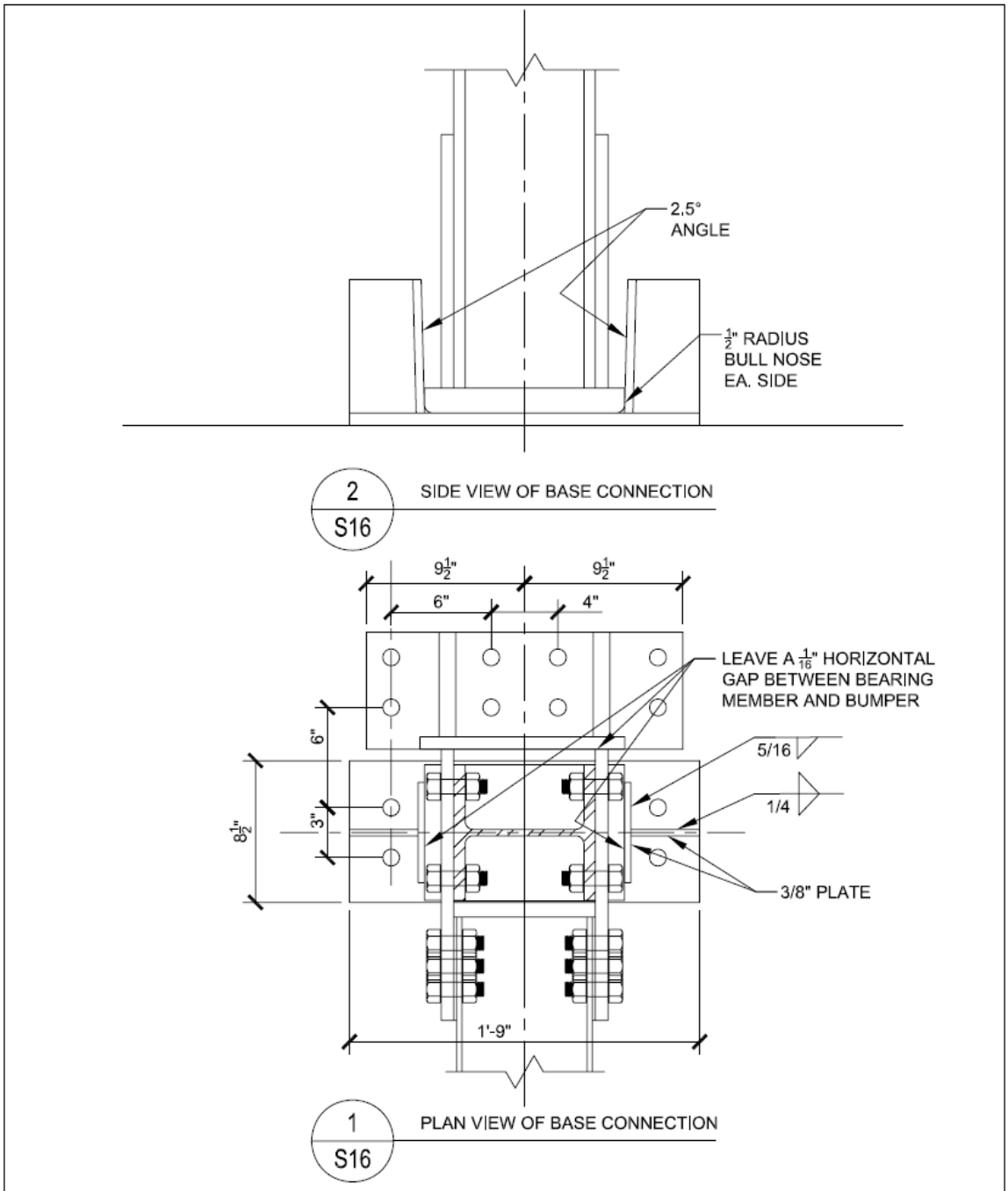

S16	CONTROLLED ROCKING FRAME UNIVERSITY OF ILLINOIS AT URBANA-CHAMPAIGN	PRELIM 02/13/07 AISC 04/15/07
	BUMPER DETAIL 1½" = 1'-0"	1 LBCB 06/18/07 FOR FAB 08/09/07

Figure A.19 Specimen Design Drawing – Bumper Detail

THE "F" SERIES OF DRAWINGS SHOWS THE ELEMENTS OF THE TEST SETUP THAT CHANGE WITH EVERY TEST

NOTES FOR FUSE MATERIAL AND FABRICATION:

1. FUSE MATERIAL IS A36.
2. FABRICATOR AND UIUC SHOULD DISCUSS THE CUTTING METHOD THAT WILL BE USED FOR THE FUSE PLATES.
3. CUTTING SHOULD NOT BEGIN NEAR THE CURVED PARTS OF THE LINKS.
4. MILL CERTS SHALL BE PROVIDED FOR ALL FUSE MATERIAL
5. ALL FUSES FOR A GIVEN TEST CONFIGURATION NEED TO COME FROM THE SAME HEAT.

	TEST ID	"B" DIMENSION	NUMBER OF P/T STRANDS	FUSE CONFIGURATION ID
A SERIES	A1	2' - 0 3/4"	8	3F-025-AB2,5-OT1,0
	A2	2' - 0 3/4"	8	1F-0625-AB2,5-OT1,0
	A3	2' - 0 3/4"	8	1F-0625-AB2.5-0T1.5
	A3 ALTERNATE	2' - 0 3/4"	8	1F-0625-AB2.5-0T1.5
	A4	2' - 0 3/4"	8	1F-1-AB2.5-OT1.5
B SERIES	B1	3' - 0 3/4"	7	3F-O25-AB1.69-OT1.0
	B2	3' - 0 3/4"	7	1F-0625-AN1.69-OT1,0
	B3	3' - 0 3/4"	7	3F-025-AB1,69-OT1,0
	B3 ALTERNATE	3' - 0 3/4"	7	1F-1-AB1,69-OT1,0
	B4	3' - 0 3/4"	7	1F-1-AB1.69-OT1.5

F1	CONTROLLED ROCKING FRAME UNIVERSITY OF ILLINOIS AT URBANA-CHAMPAIGN	PRELIM 02/13/07 AISC 04/15/07
	ADDITIONAL NOTES FOR STRUTS AND FUSES	1 LBCB 06/18/07 FOR FAB 08/09/07

Figure A.20 Specimen Design Drawing – Additional Notes for Struts and Fuses

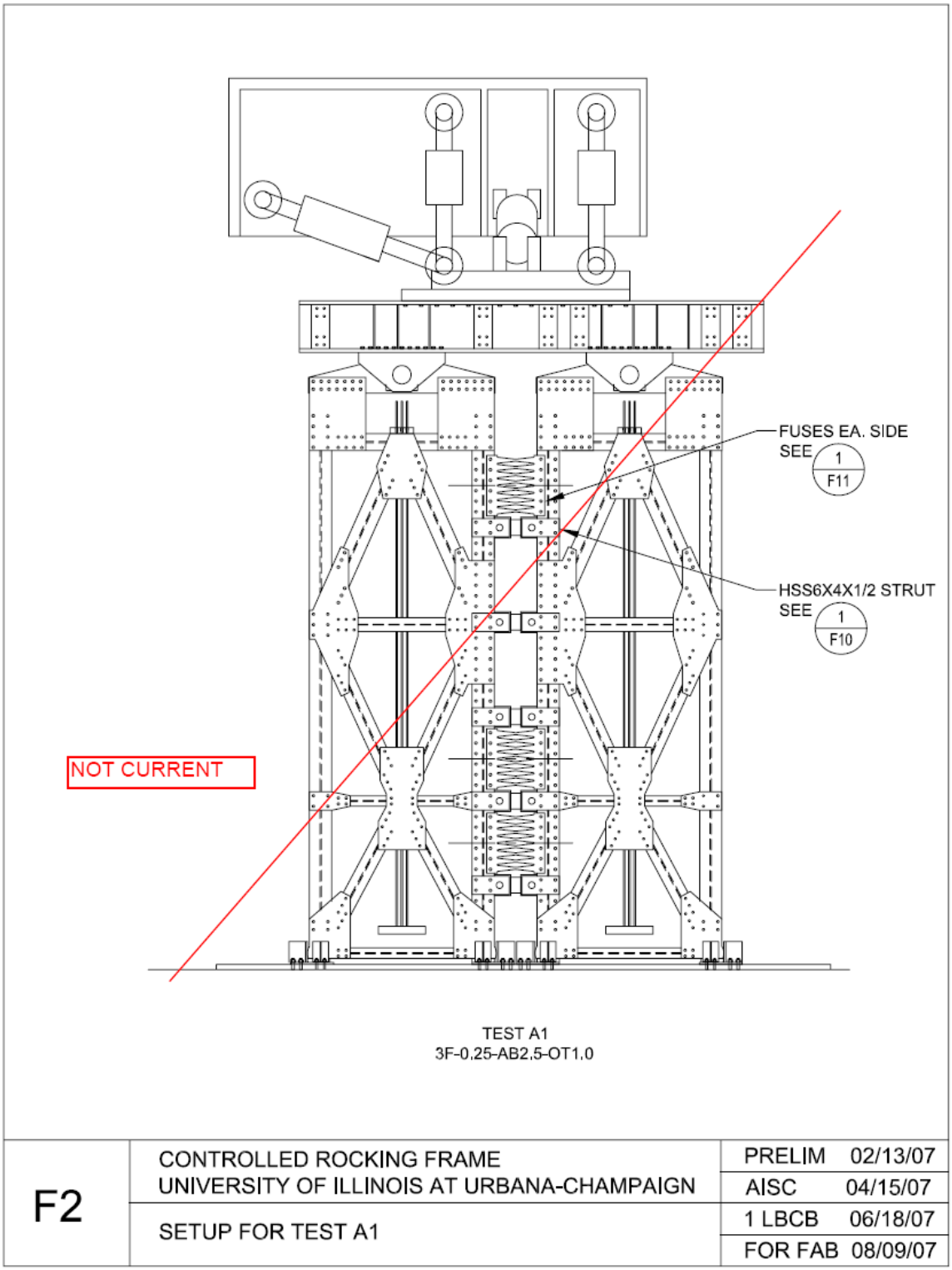

Figure A.21 Specimen Design Drawing – Setup for Test A1

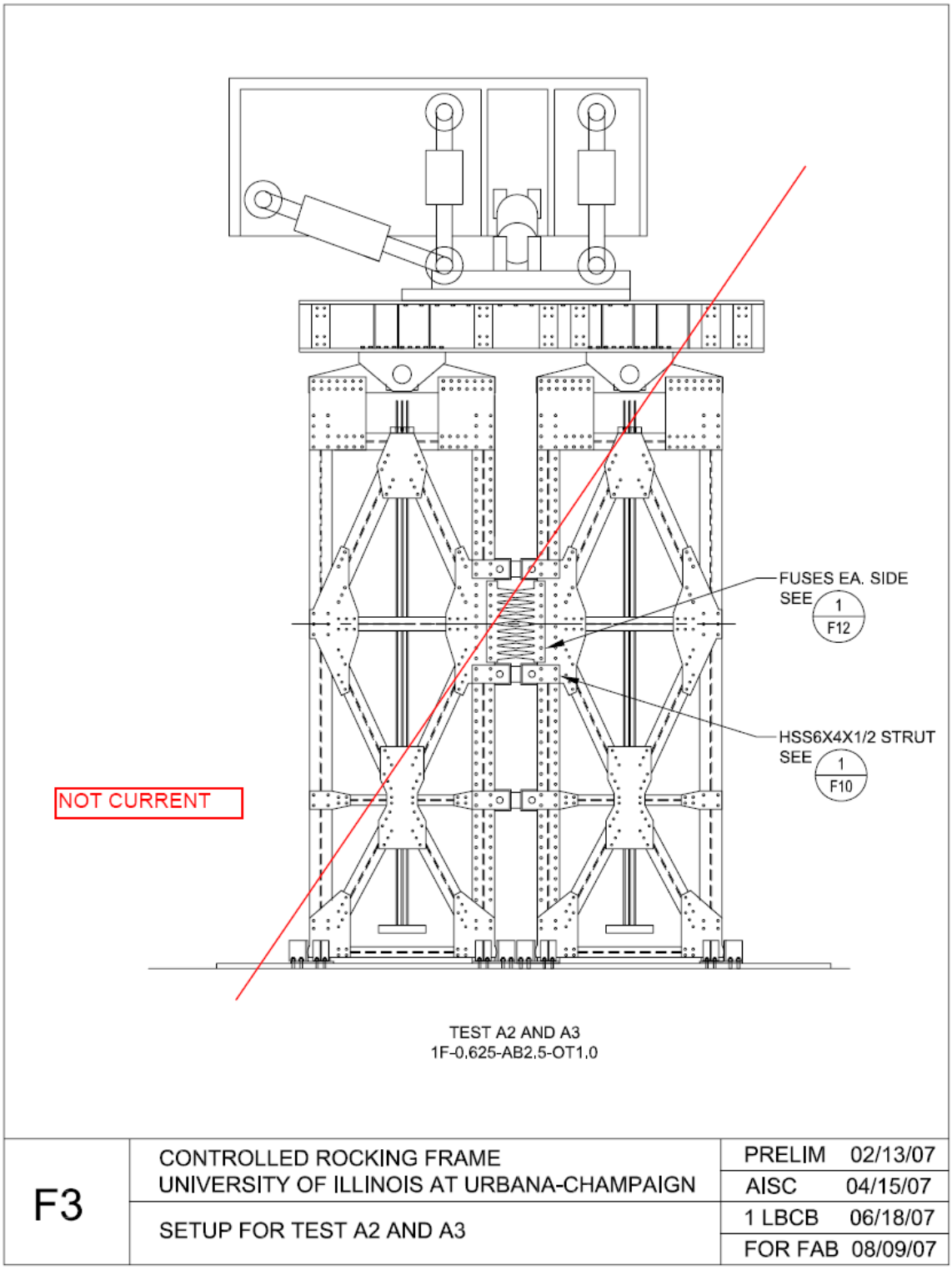

Figure A.22 Specimen Design Drawing – Setup for Test A2 and A3

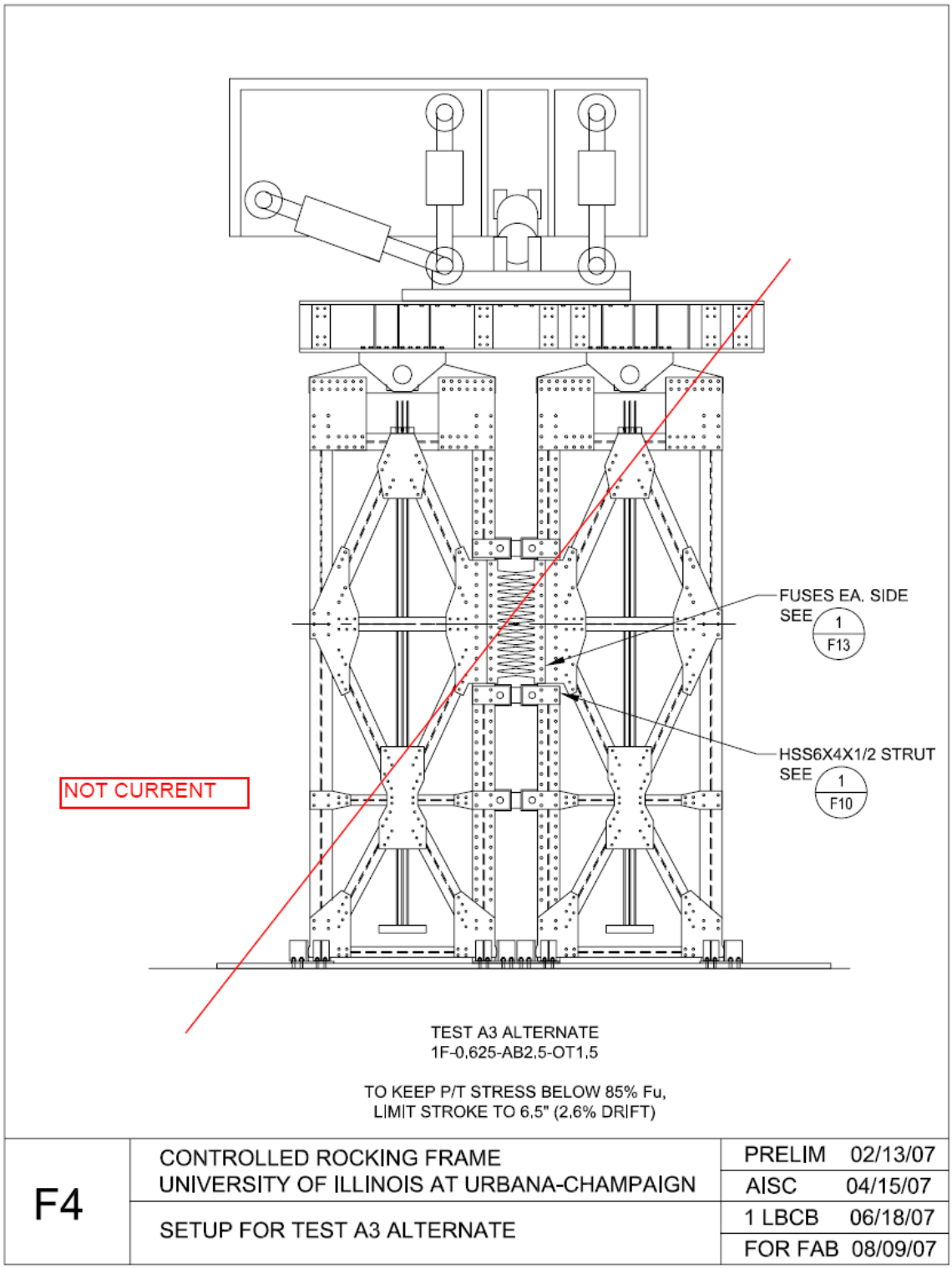

Figure A.23 Specimen Design Drawing – Setup for Test A3 Alternate

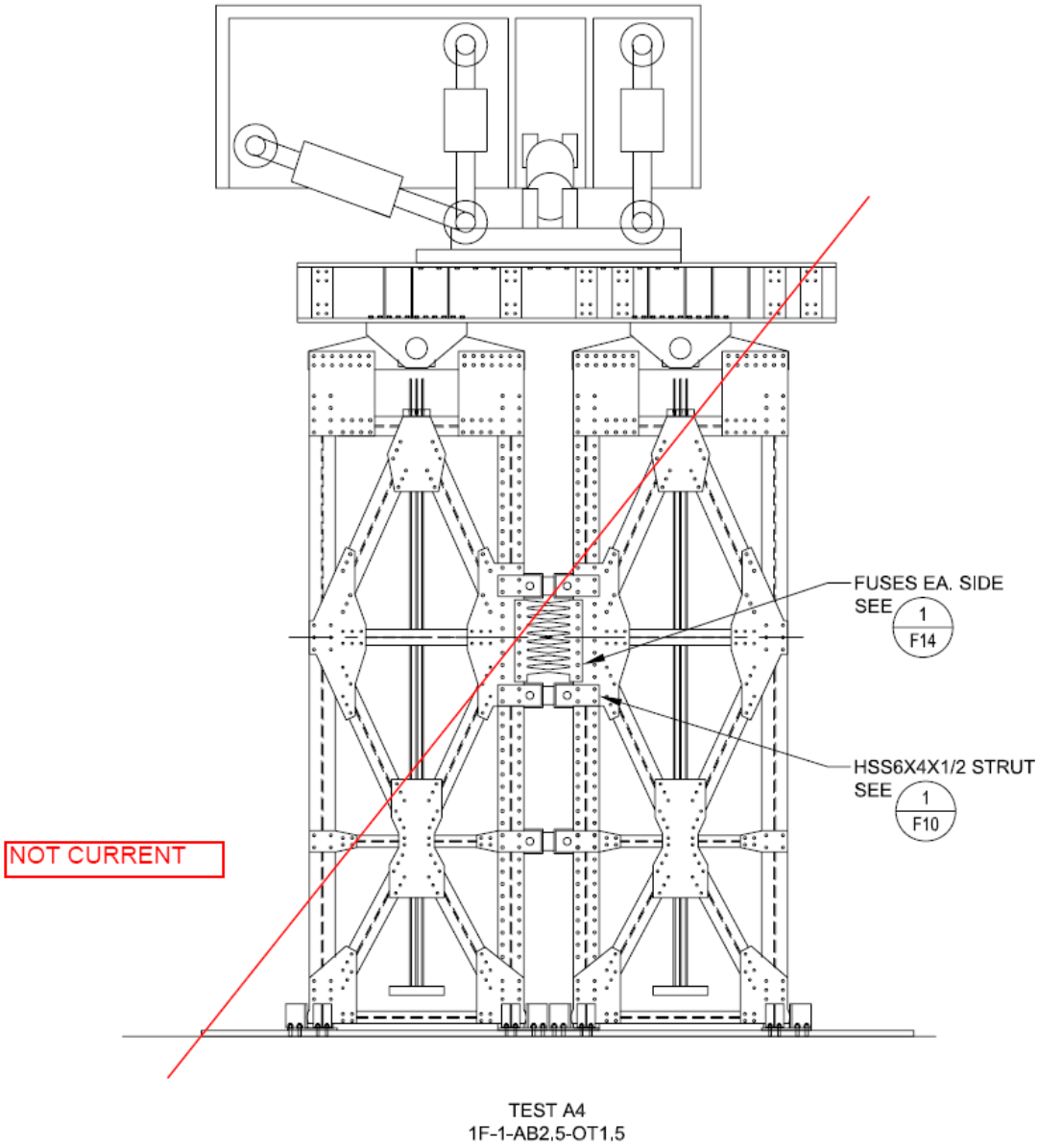

F5	CONTROLLED ROCKING FRAME UNIVERSITY OF ILLINOIS AT URBANA-CHAMPAIGN	PRELIM 02/13/07 AISC 04/15/07
	SETUP FOR TEST A4	1 LBCB 06/18/07 FOR FAB 08/09/07

Figure A.24 Specimen Design Drawing – Setup for Test A4

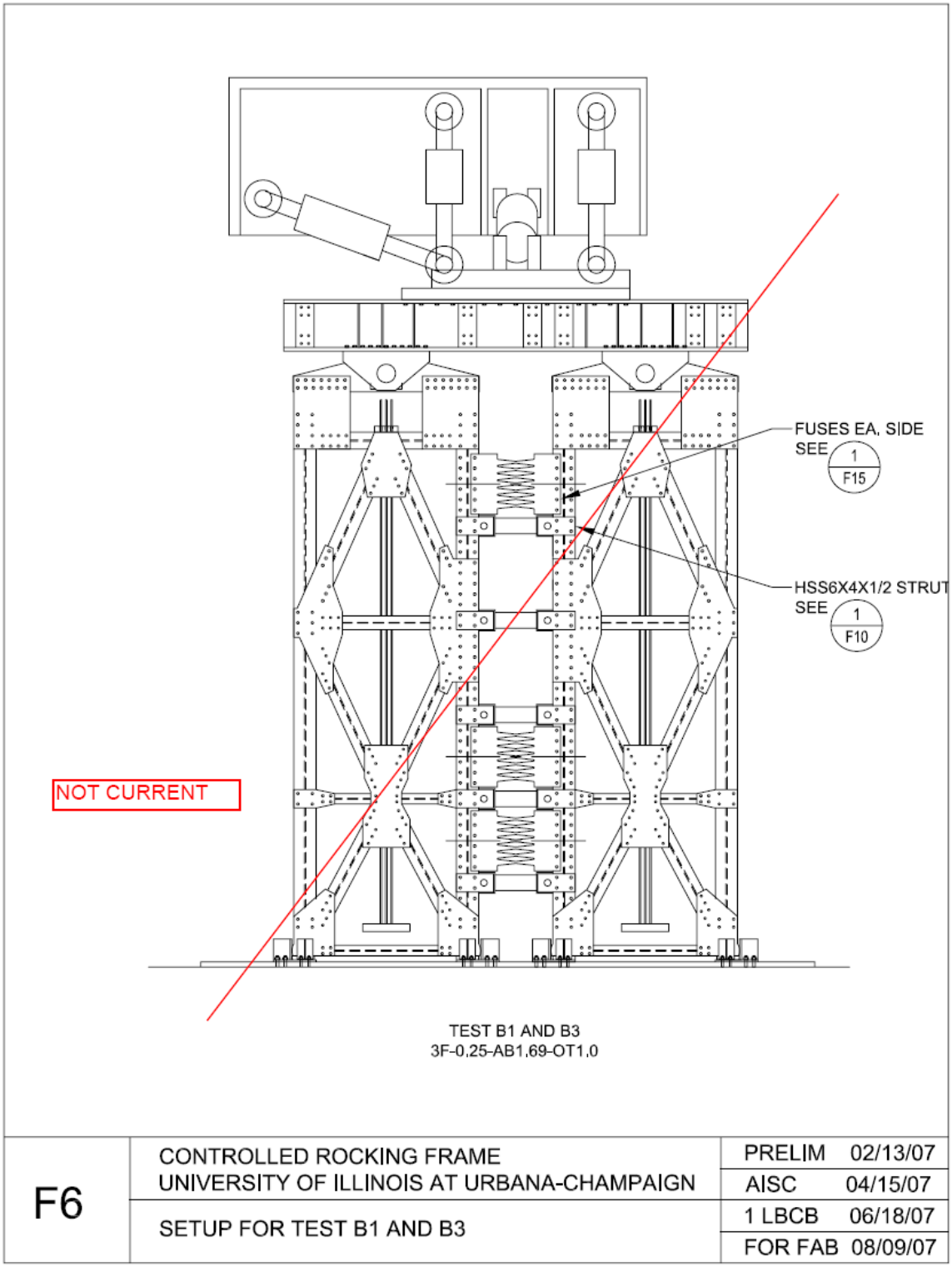

Figure A.25 Specimen Design Drawing – Setup for Test B1 and B3

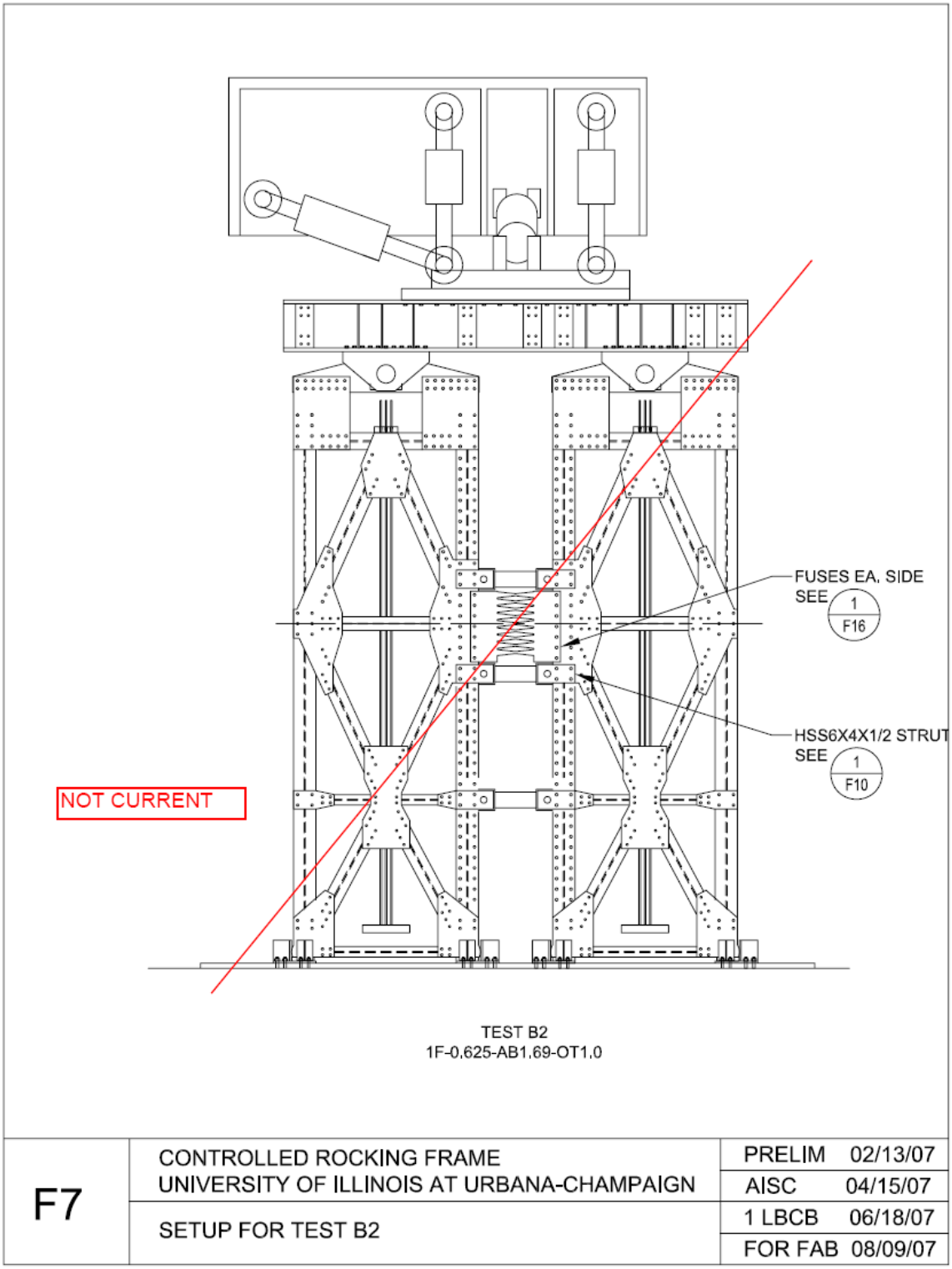

Figure A.26 Specimen Design Drawing – Setup for Test B2

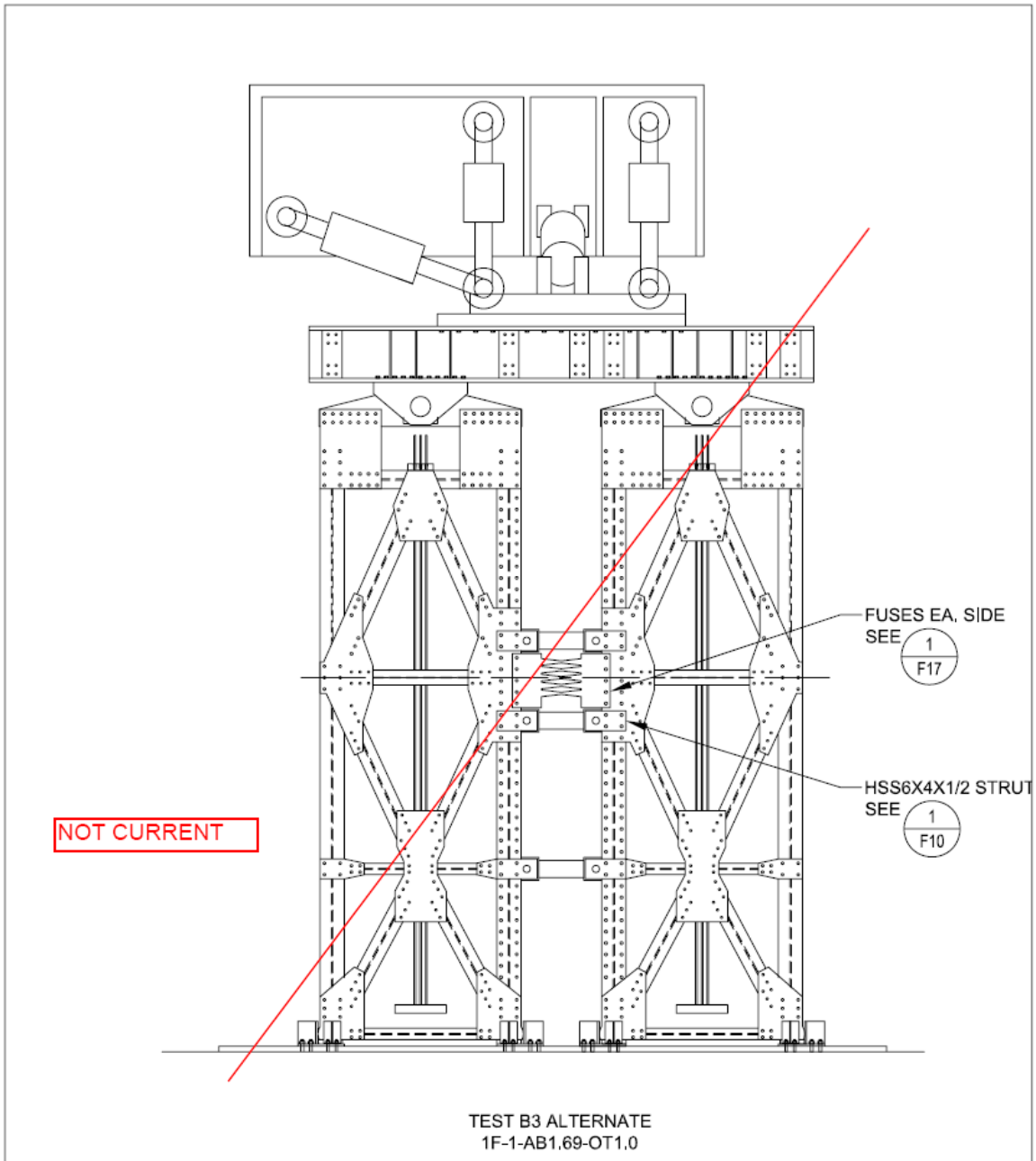

F8	CONTROLLED ROCKING FRAME UNIVERSITY OF ILLINOIS AT URBANA-CHAMPAIGN	PRELIM 02/13/07 AISC 04/15/07
	SETUP FOR TEST B3 ALTERNATE	1 LBCB 06/18/07 FOR FAB 08/09/07

Figure A.27 Specimen Design Drawing – Setup for Test B3 Alternate

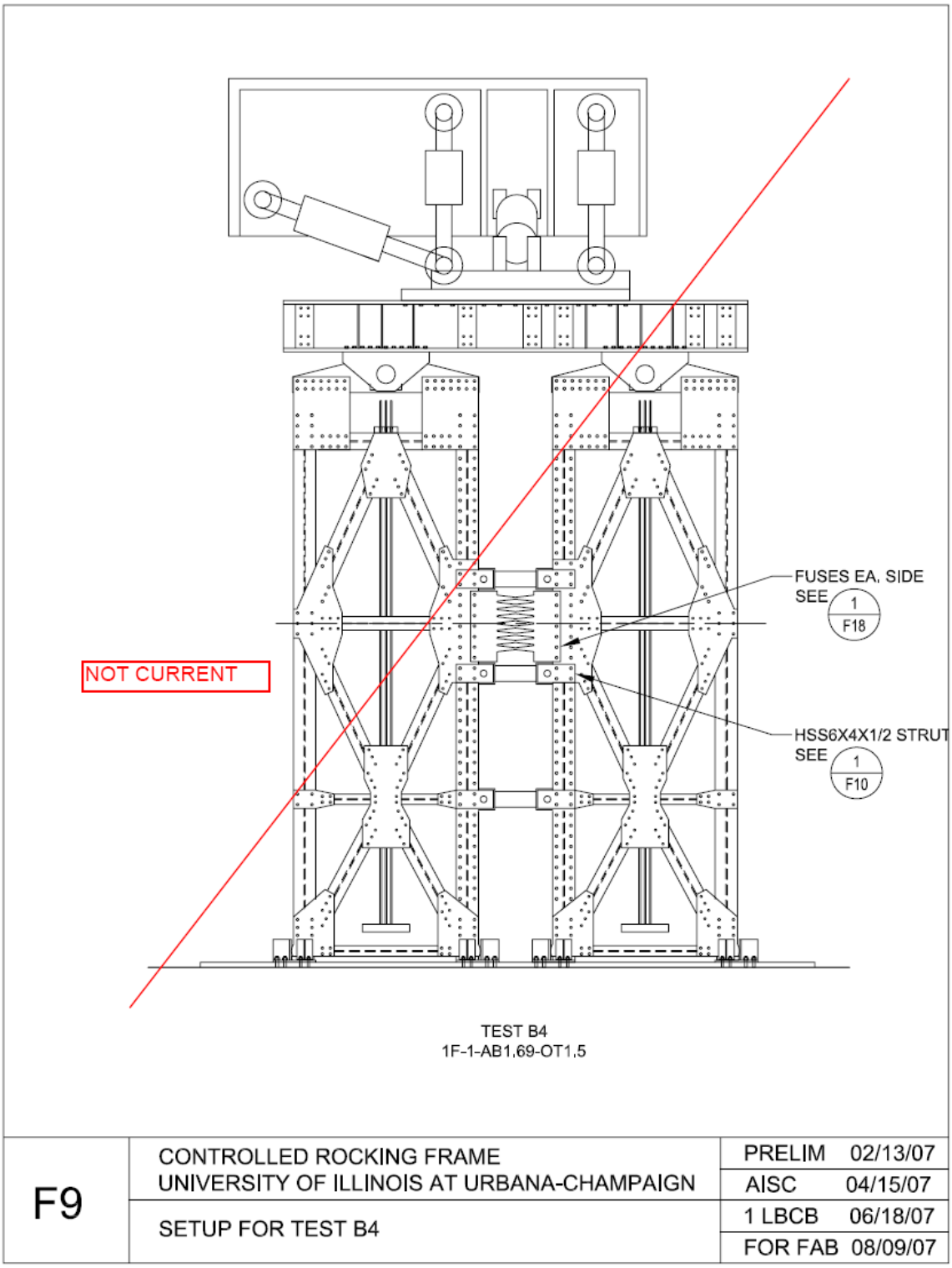

Figure A.28 Specimen Design Drawing – Setup for Test B4

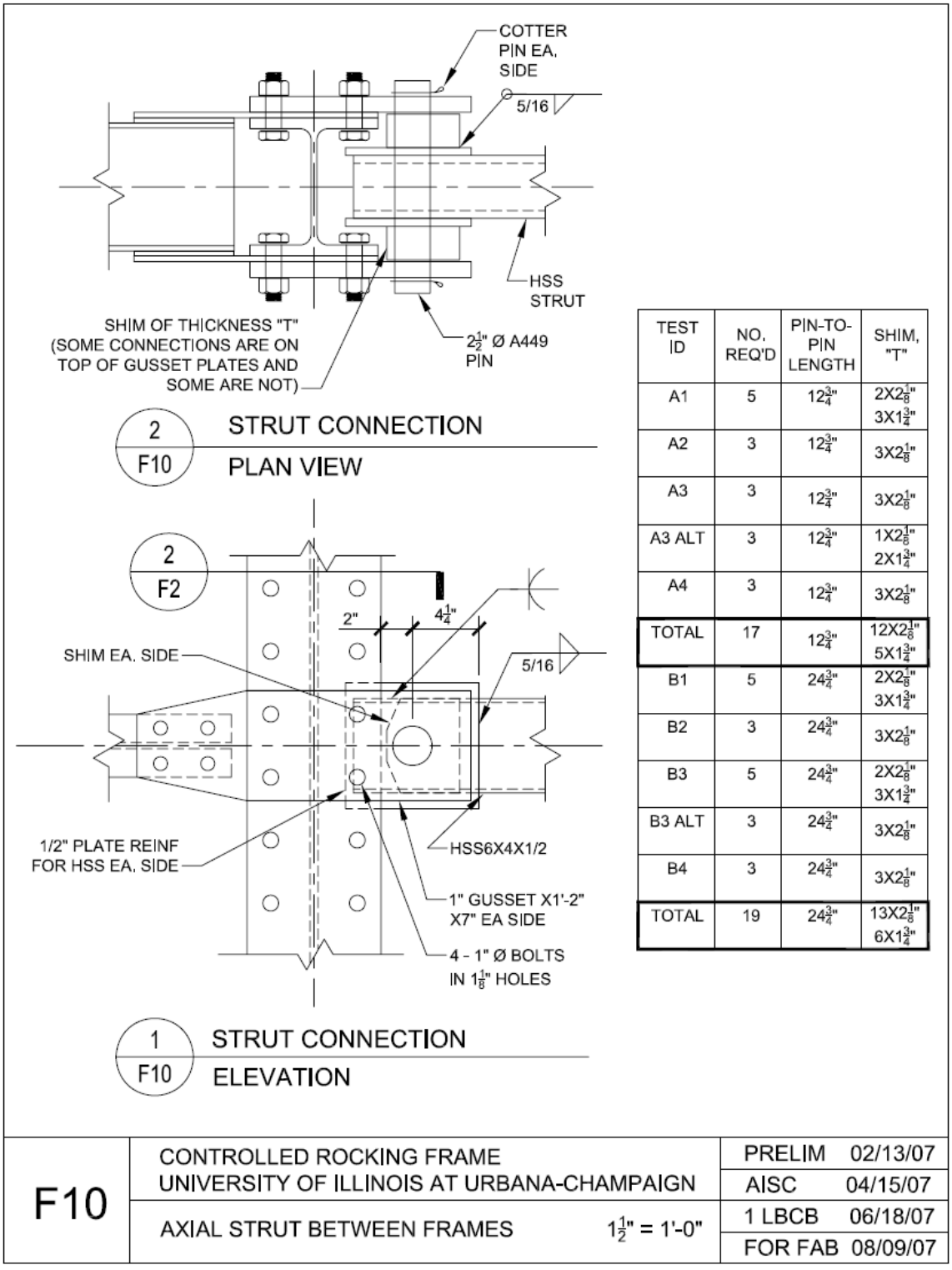

TEST ID	NO. REQ'D	PIN-TO-PIN LENGTH	SHIM, "T"
A1	5	12¾"	2X2⅛" 3X1¾"
A2	3	12¾"	3X2⅛"
A3	3	12¾"	3X2⅛"
A3 ALT	3	12¾"	1X2⅛" 2X1¾"
A4	3	12¾"	3X2⅛"
TOTAL	17	12¾"	12X2⅛" 5X1¾"
B1	5	24¾"	2X2⅛" 3X1¾"
B2	3	24¾"	3X2⅛"
B3	5	24¾"	2X2⅛" 3X1¾"
B3 ALT	3	24¾"	3X2⅛"
B4	3	24¾"	3X2⅛"
TOTAL	19	24¾"	13X2⅛" 6X1¾"

F10	CONTROLLED ROCKING FRAME UNIVERSITY OF ILLINOIS AT URBANA-CHAMPAIGN	PRELIM 02/13/07 AISC 04/15/07
	AXIAL STRUT BETWEEN FRAMES 1½" = 1'-0"	1 LBCB 06/18/07 FOR FAB 08/09/07

Figure A.29 Specimen Design Drawing – Axial Strut Between Frames

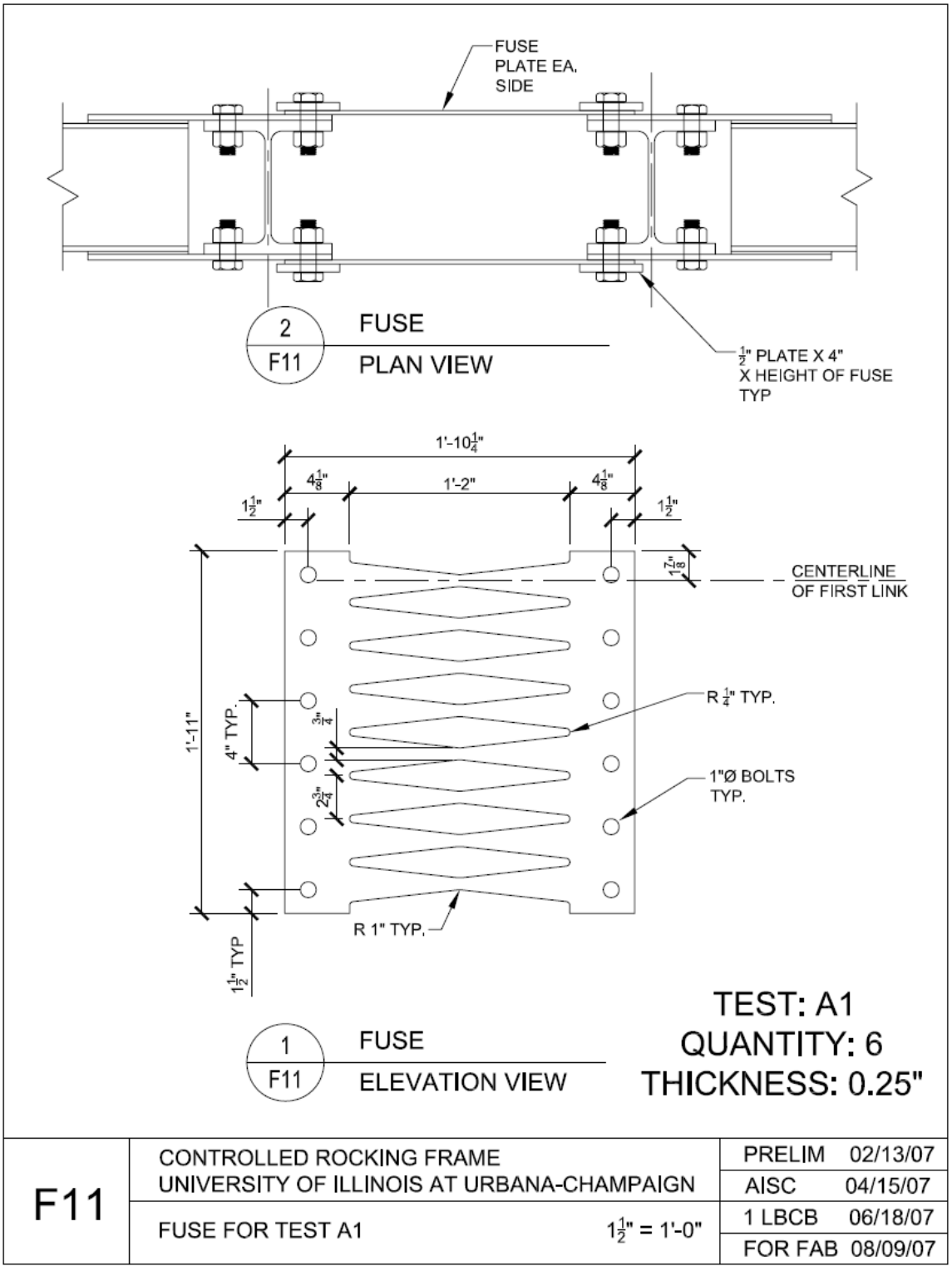

Figure A.30 Specimen Design Drawing – Fuse for Test A1

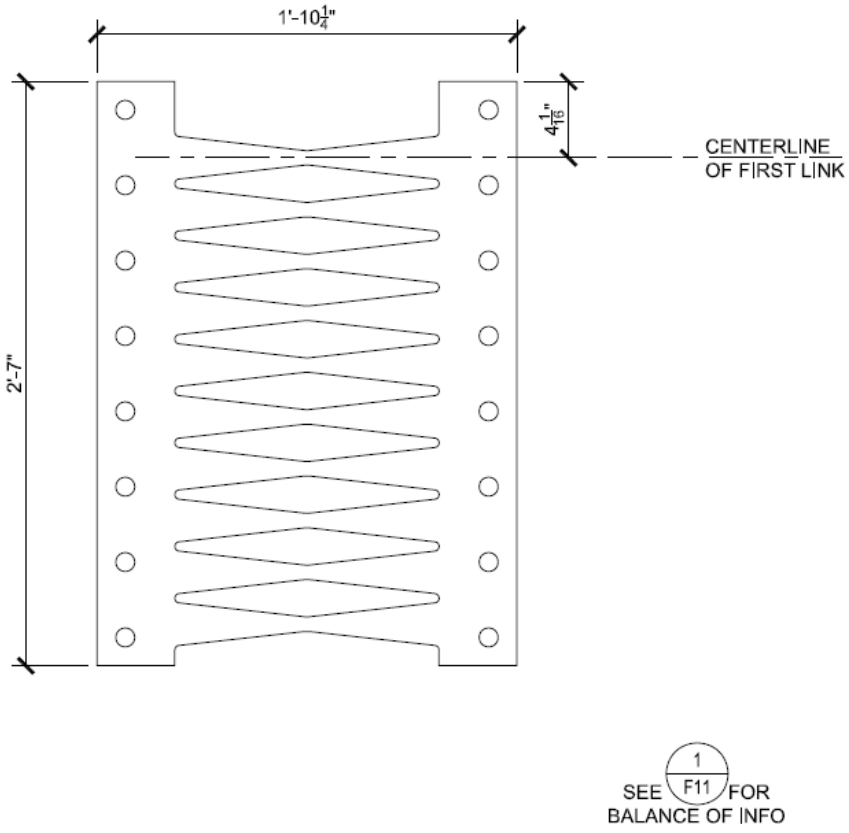

TEST: A2 AND A3
QUANTITY: 4
THICKNESS: 0.625"

F12	CONTROLLED ROCKING FRAME UNIVERSITY OF ILLINOIS AT URBANA-CHAMPAIGN	PRELIM 02/13/07 AISC 04/15/07
	FUSE FOR TEST A2 AND A3 1½" = 1'-0"	1 LBCB 06/18/07 FOR FAB 08/09/07

Figure A.31 Specimen Design Drawing – Fuse for Test A2 and A3

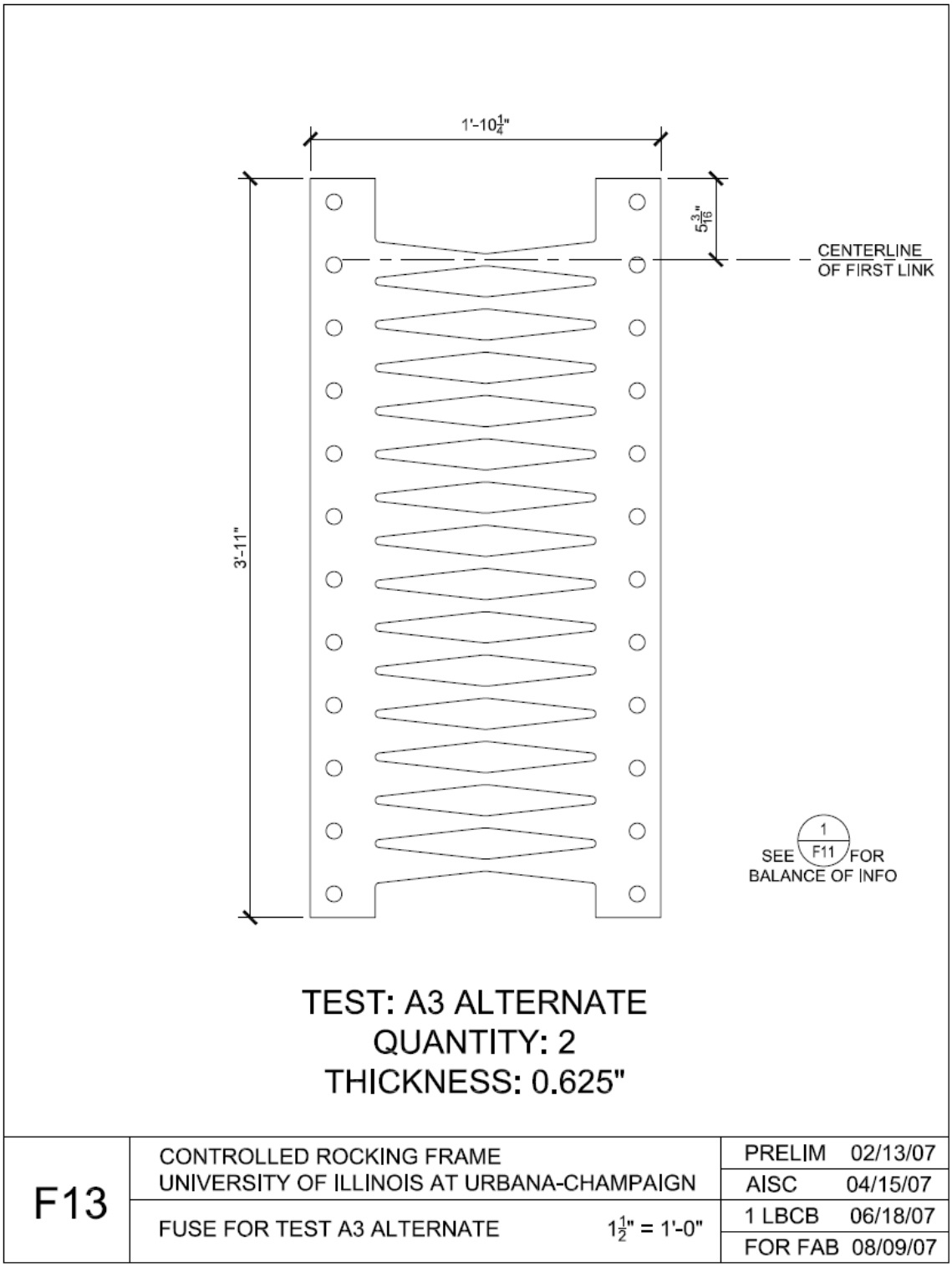

Figure A.32 Specimen Design Drawing – Fuse for Test A3 Alternate

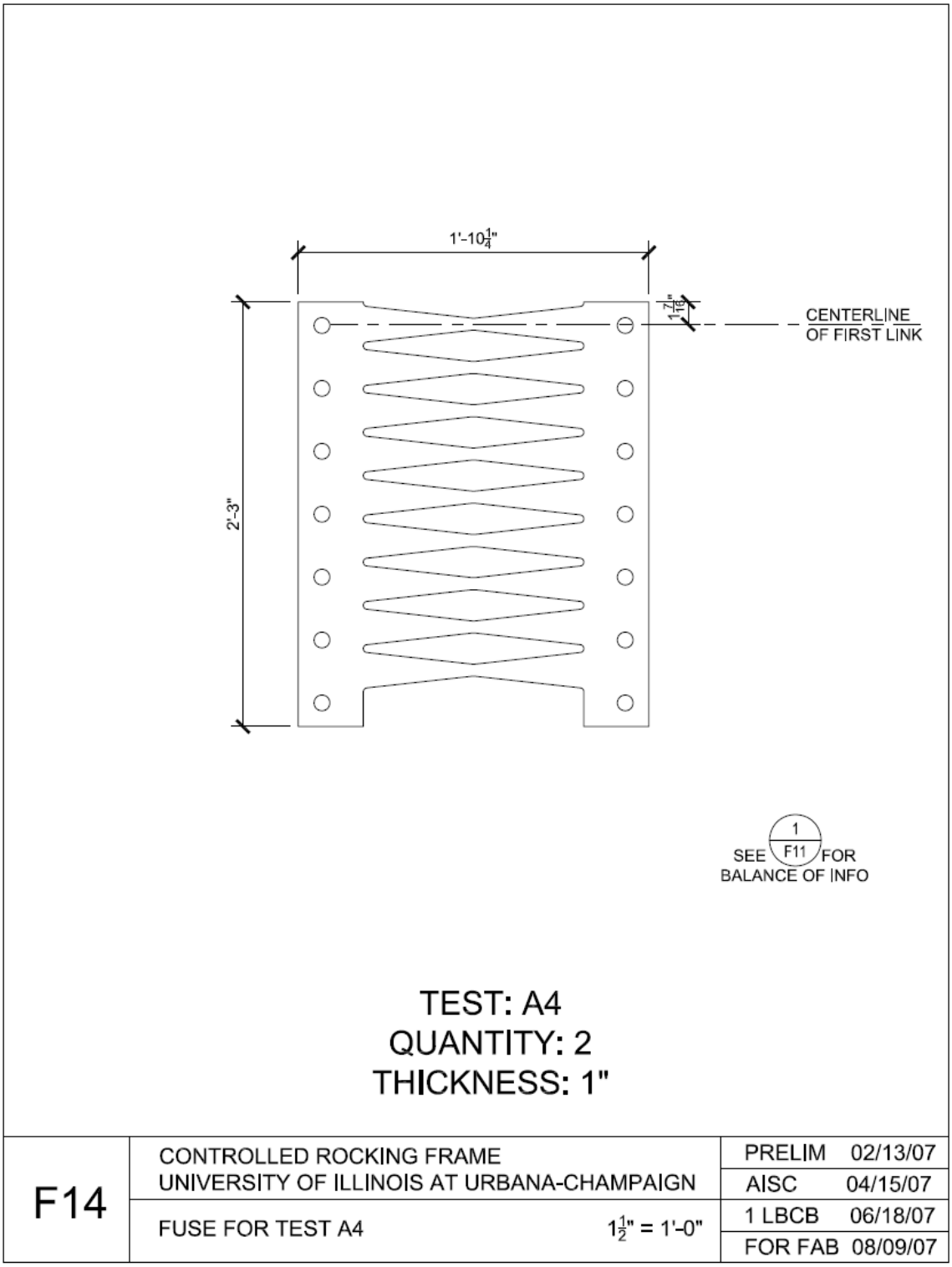

Figure A.33 Specimen Design Drawing – Fuse for Test A4

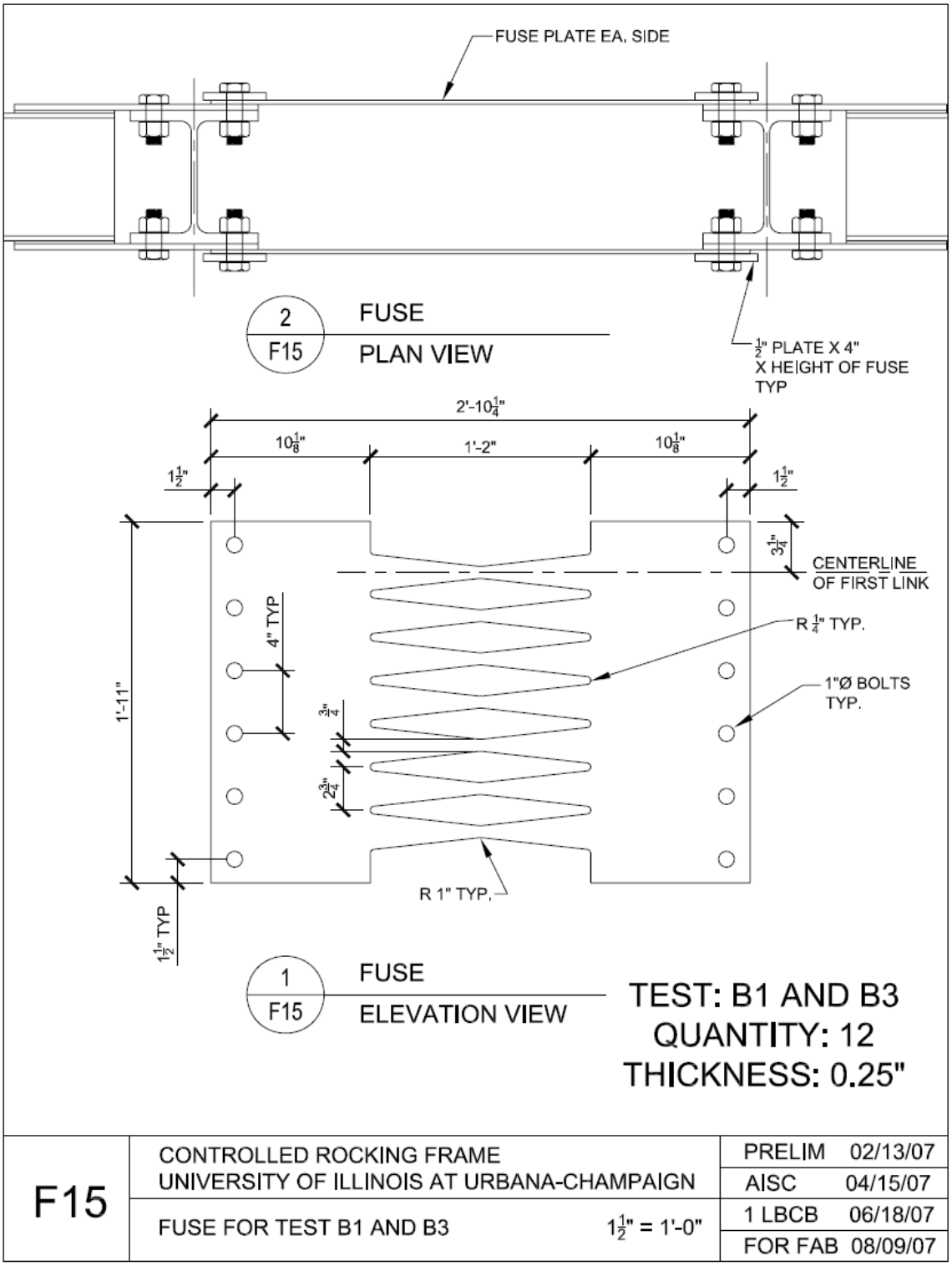

Figure A.34 Specimen Design Drawing – Fuse for Test B1 and B3

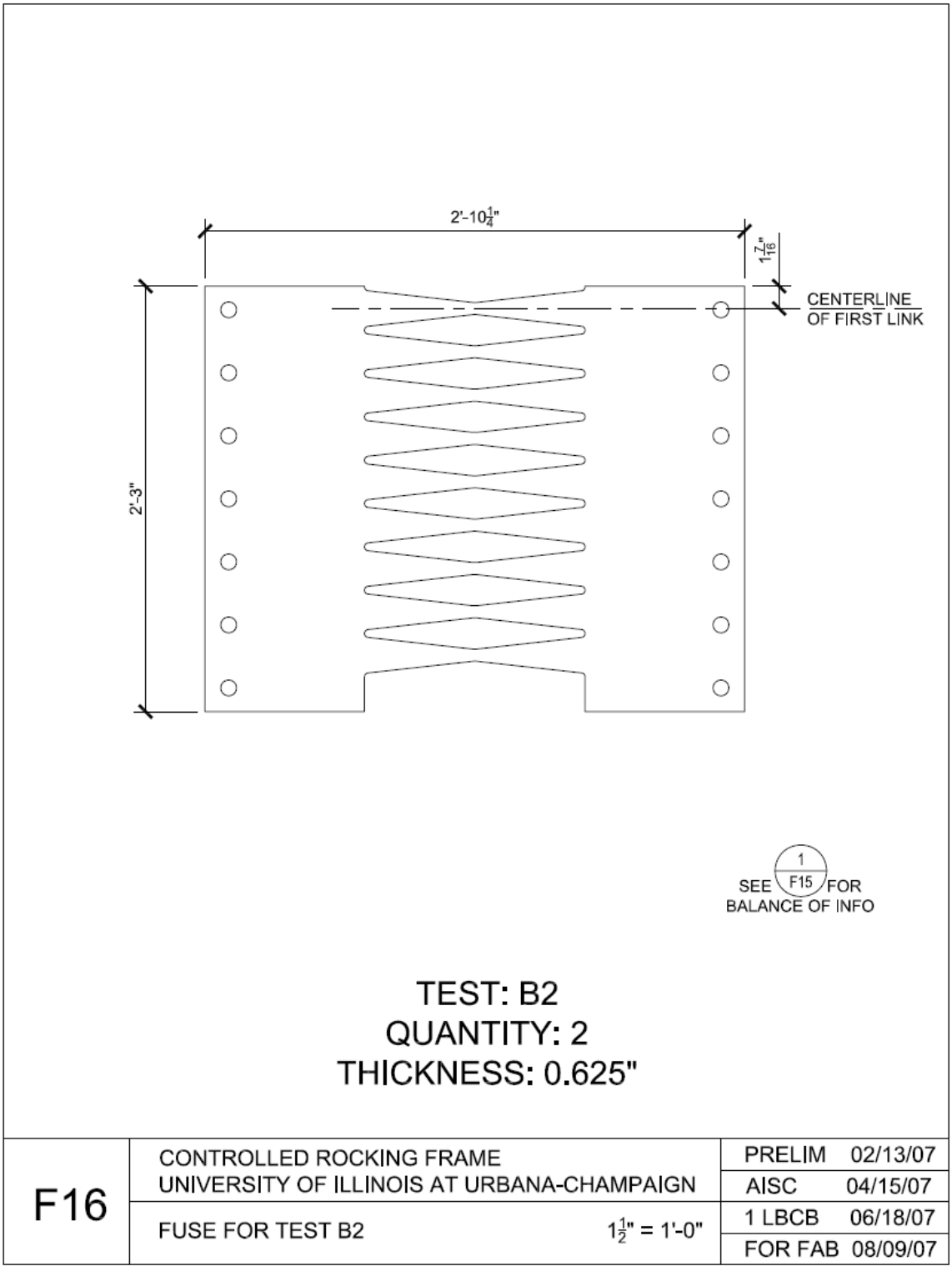

Figure A.35 Specimen Design Drawing – Fuse for Test B2

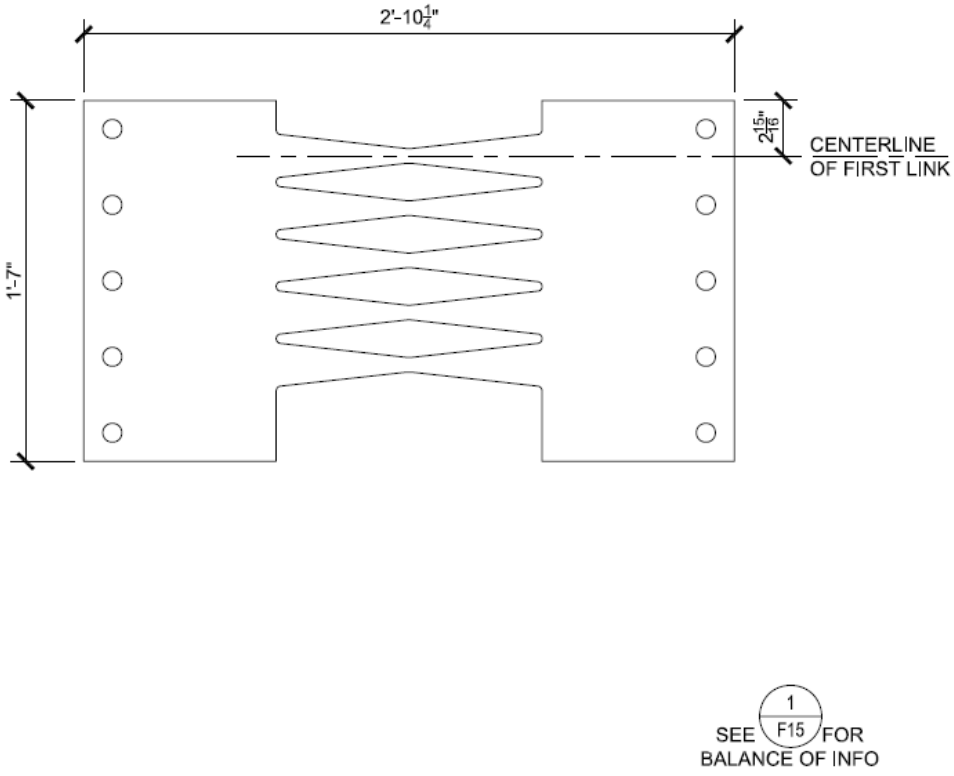

TEST: B3 ALTERNATE
QUANTITY: 2
THICKNESS: 1"

F17	CONTROLLED ROCKING FRAME UNIVERSITY OF ILLINOIS AT URBANA-CHAMPAIGN	PRELIM 02/13/07 AISC 04/15/07
	FUSE FOR TEST B3 ALTERNATE $1\frac{1}{2}$" = 1'-0"	1 LBCB 06/18/07 FOR FAB 08/09/07

Figure A.36 Specimen Design Drawing – Fuse for Test B3 Alternate

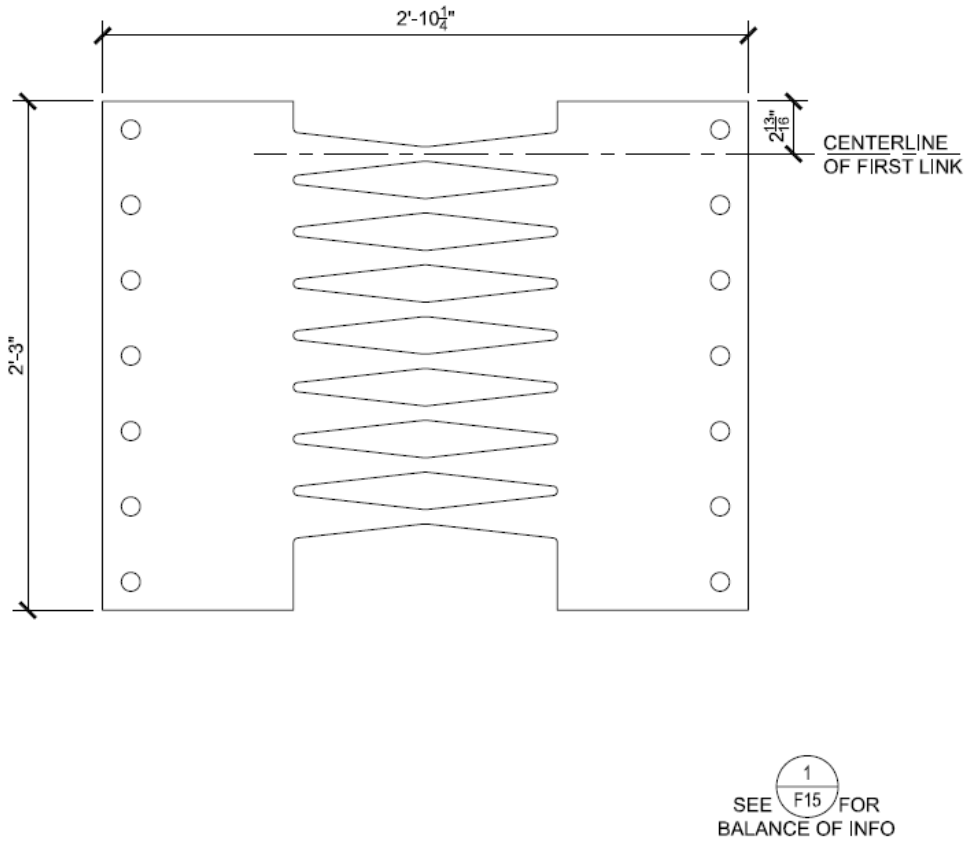

F18	CONTROLLED ROCKING FRAME UNIVERSITY OF ILLINOIS AT URBANA-CHAMPAIGN	PRELIM 02/13/07 AISC 04/15/07
	FUSE FOR TEST B4 1 1/2" = 1'-0"	1 LBCB 06/18/07 FOR FAB 08/09/07

Figure A.37 Specimen Design Drawing – Fuse for Test B4

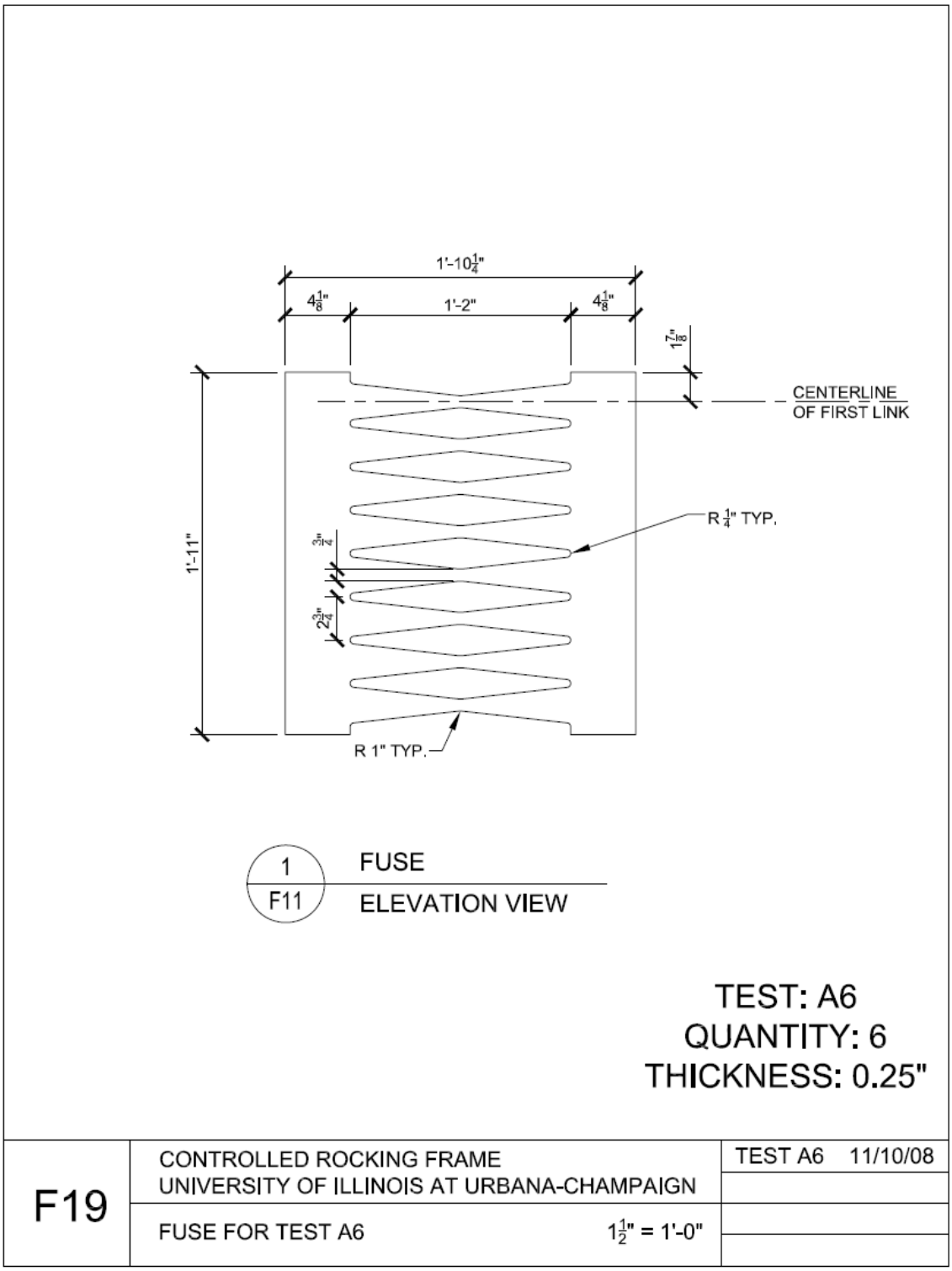

Figure A.38 Specimen Design Drawing – Fuse for Test A6

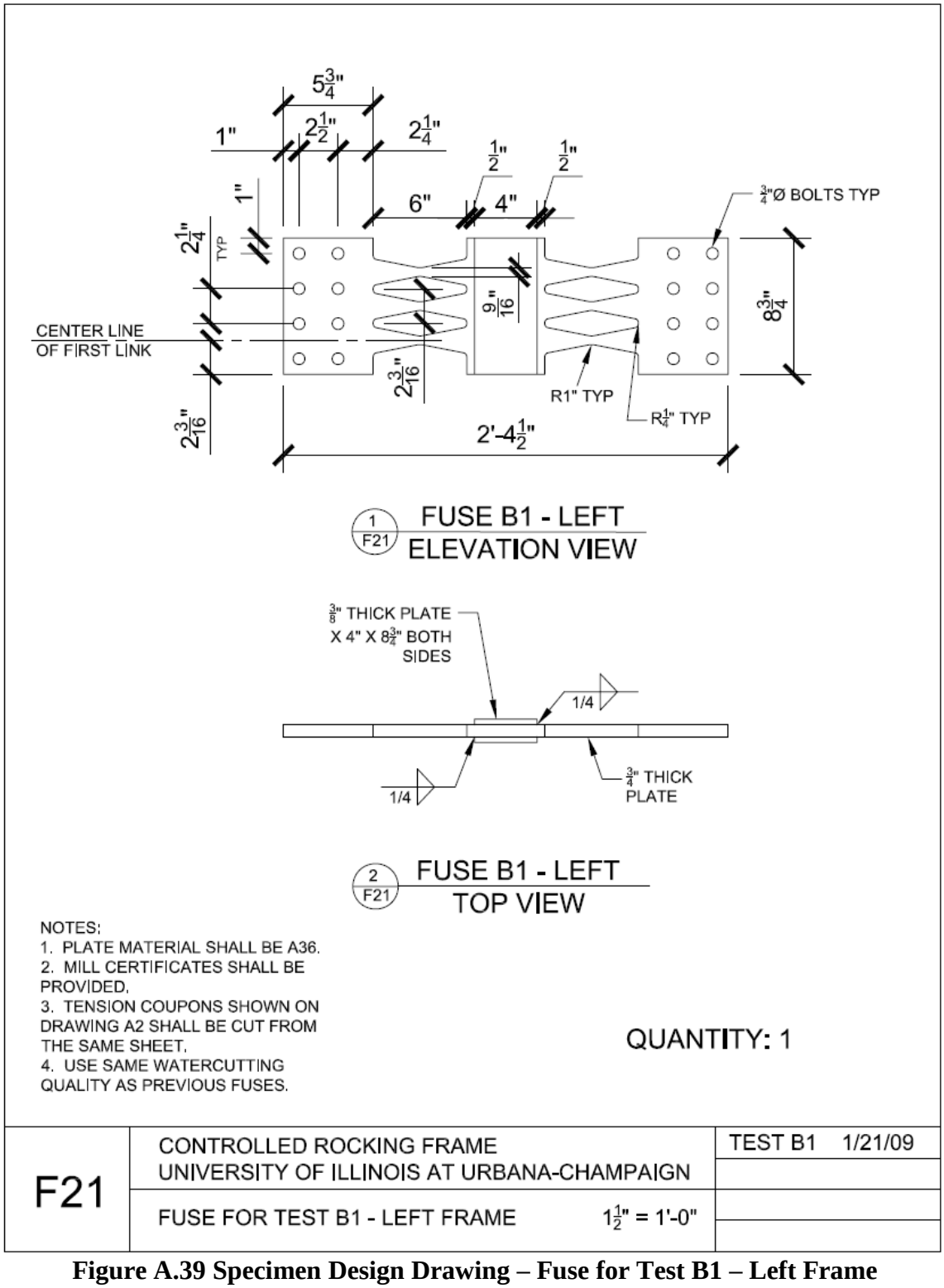

Figure A.39 Specimen Design Drawing – Fuse for Test B1 – Left Frame

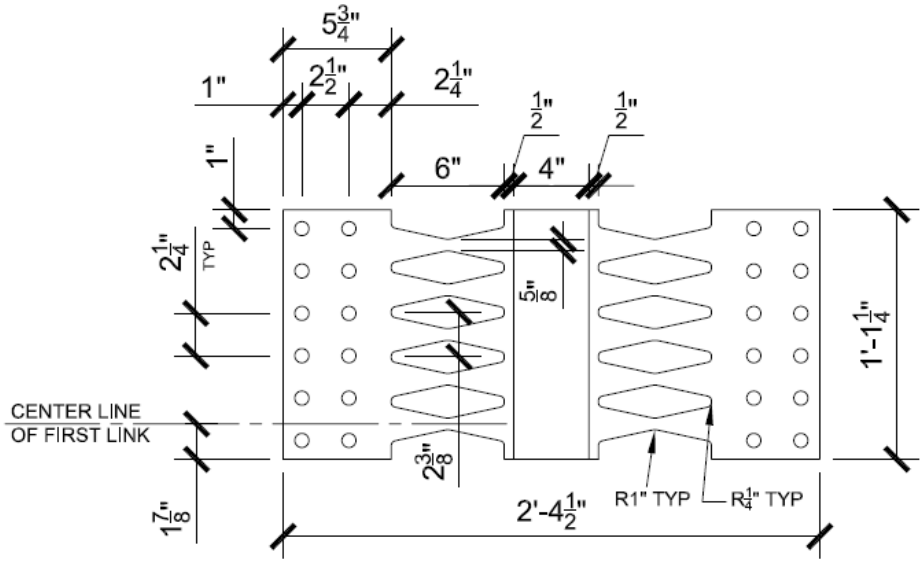

1/F22 FUSE B1 - RIGHT
ELEVATION VIEW

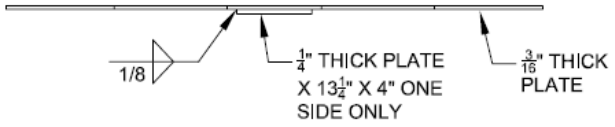

2/F22 FUSE B1 - RIGHT
PLAN VIEW

NOTES:
1. PLATE MATERIAL SHALL BE A36.
2. MILL CERTIFICATES SHALL BE PROVIDED.
3. BOTH OF THE 3/16" THICK PLATES AND THE TENSION COUPONS SHOWN ON DRAWING A2 SHALL BE CUT FROM THE SAME SHEET.
4. USE SAME WATER CUTTING QUALITY AS PREVIOUS FUSES

QUANTITY: 2

F22	CONTROLLED ROCKING FRAME UNIVERSITY OF ILLINOIS AT URBANA-CHAMPAIGN	TEST B1 1/21/09
	FUSE FOR TEST B1 - RIGHT FRAME 1 1/2" = 1'-0"	

Figure A.40 Specimen Design Drawing – Fuse for Test B1 – Right Frame

A.2 Drawings for Fabrication Conducted at UIUC

The following set of drawings was created to facilitate work done by the UIUC CEE machine shop and is designated with “WP” drawing identification to indicate they were part of the UIUC work plan.

GENERAL

1. THIS SET OF DRAWINGS (DRAWINGS STARTING WITH WP) ARE INTHE ORDER IN WHICH THEY ARE TO BE PERFORMED. HOWEVER, SOME TASKS CAN OCCUR SIMULTANEOUSLY.
2. EACH PIECE AND/OR ASSEMBLY OF STEEL PARTS SHOULD COME LABELED WITH A PIECE MARK. THE PIECE MARK IS REFERENCED ON THE FOLLOWING DRAWINGS.

ERECTION PLAN AND DEALING WITH FIT-UP

1. FABRICATION AND ASSEMBLY AT UIUC WILL START AT THE BOTTOM AND PROCEED UP THE FRAMES. ISSUES WITH FIT-UP WILL BE ADDRESSED AS EACH PIECE IS ASSEMBLED GOING UP.

TURN-OF-THE-NUT METHOD FOR BOLT TIGHTENING (FROM RCSC 2004)

ALL BOLTS SHALL BE TIGHTENED USING THE FOLLOWING STEPS:
1. WE HAVE ONE WASHER PER BOLT, AND IT SHOULD BE INSTALLED ON THE SIDE THAT IS BEING TURNED. IDEALLY THE NUT IS TURNED WHILE THE HEAD IS HELD FIXED, BUT THIS ISN'T A HARD RULE.
2. INSTALL BOLTS IN ALL HOLES, TIGHTEN UNTIL ALL PLIES ARE IN FIRM CONTACT.
3. MARK THE NUT AND PROTRUDING BOLT THREADS WITH A STRAIGHT LINE.
4. WHILE PREVENTING THE OTHER SIDE FROM ROTATING, TIGHTEN UNTIL THE MARK ON THE BOLT THREADS HAS ROTATED THE AMOUNT LISTED, RELATIVE TO THE MARK ON THE NUT.

$\frac{3}{4}$" BOLTS		1" BOLTS	
BOLT LENGTH	REQ'D ROT'N	BOLT LENGTH	REQ'D ROT'N
0" to 3"	$\frac{1}{3}$ turn	0" to 4"	$\frac{1}{3}$ turn
3" to 6"	$\frac{1}{2}$ turn	4" to 8"	$\frac{1}{2}$ turn
6" to 9"	$\frac{2}{3}$ turn	8" to 12"	$\frac{2}{3}$ turn

NOTES:
1. THE REQ'D ROTATIONS ASSUME THAT ALL PLY FACES ARE PERPENDICULAR TO THE BOLT AXIS. IF FACES ARE SLOPED, THERE ARE DIFFERENT VALUES THAT NEED TO BE USED.
2. BOLT LENGTH IS MEASURED FROM BASE OF HEAD TO THE END OF THE BOLT, REGARDLESS OF THICKNESS OF PLIES BEING CONNECTED.
3. BOLT HOLES ARE SUPPOSED TO BE $\frac{1}{16}$" LARGER THAN THE BOLT. IF THEY ARE LARGER, WASHERS SHOULD BE USED ON BOTH SIDES.

WP1	CONTROLLED ROCKING FRAME UNIVERSITY OF ILLINOIS AT URBANA-CHAMPAIGN	PRICING 01/29/08 UPDATED 02/15/08
	CONSTRUCTION SEQUENCE N.T.S.	

Figure A.41 Work Plan Drawing – Construction Sequence

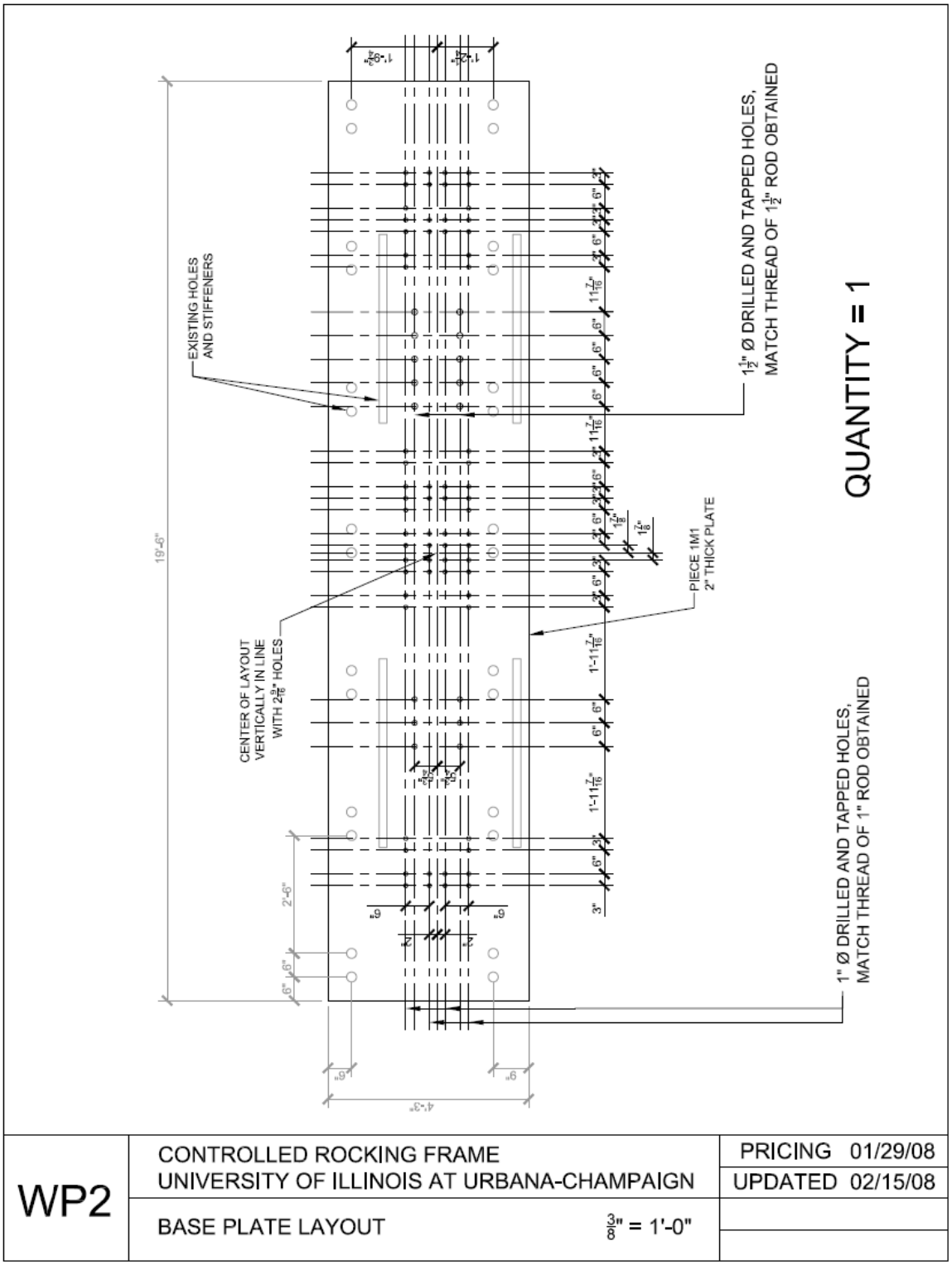

Figure A.42 Work Plan Drawing – Base Plate Layout

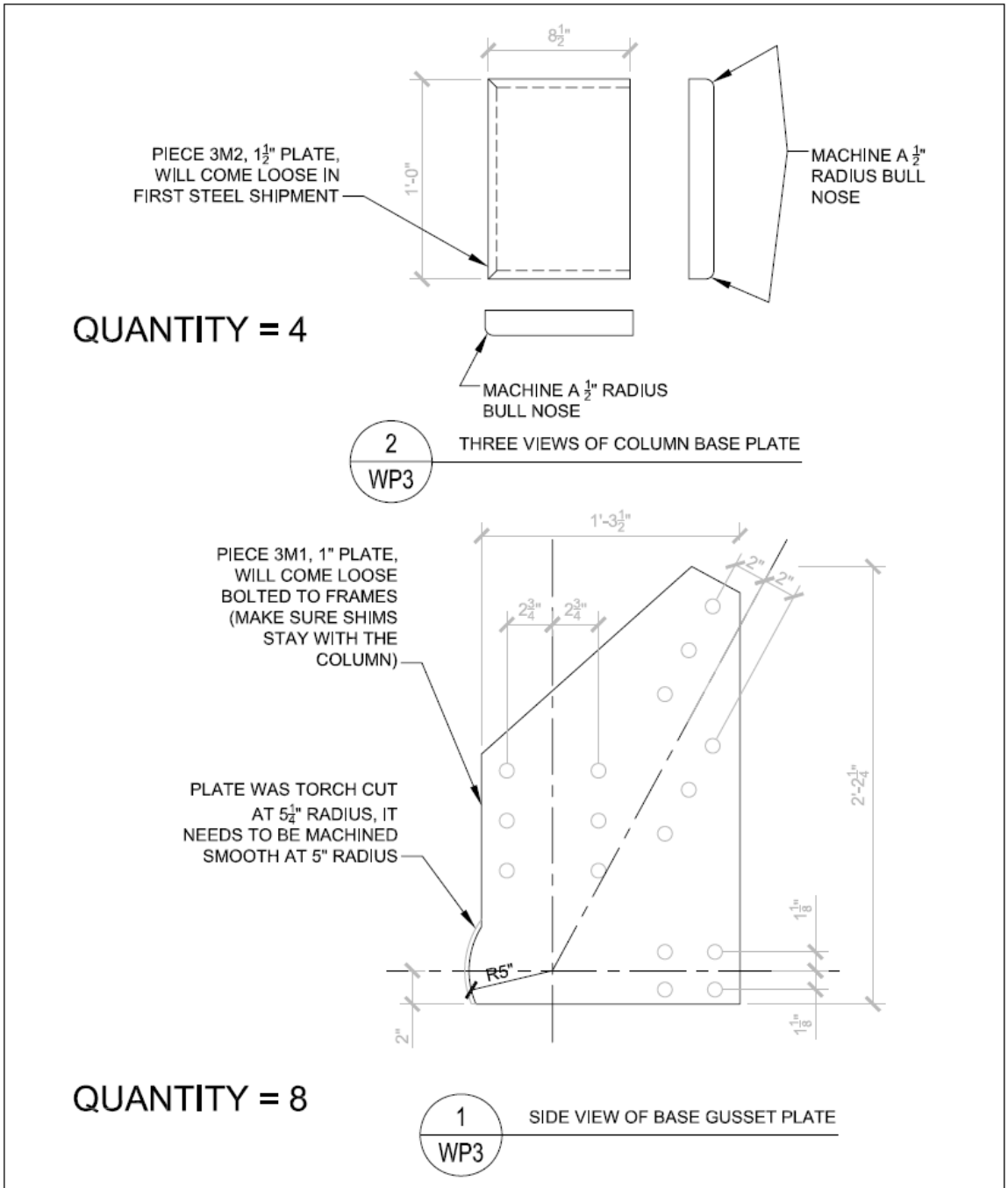

Figure A.43 Work Plan Drawing – Column Base Plate and Base Gusset Plate

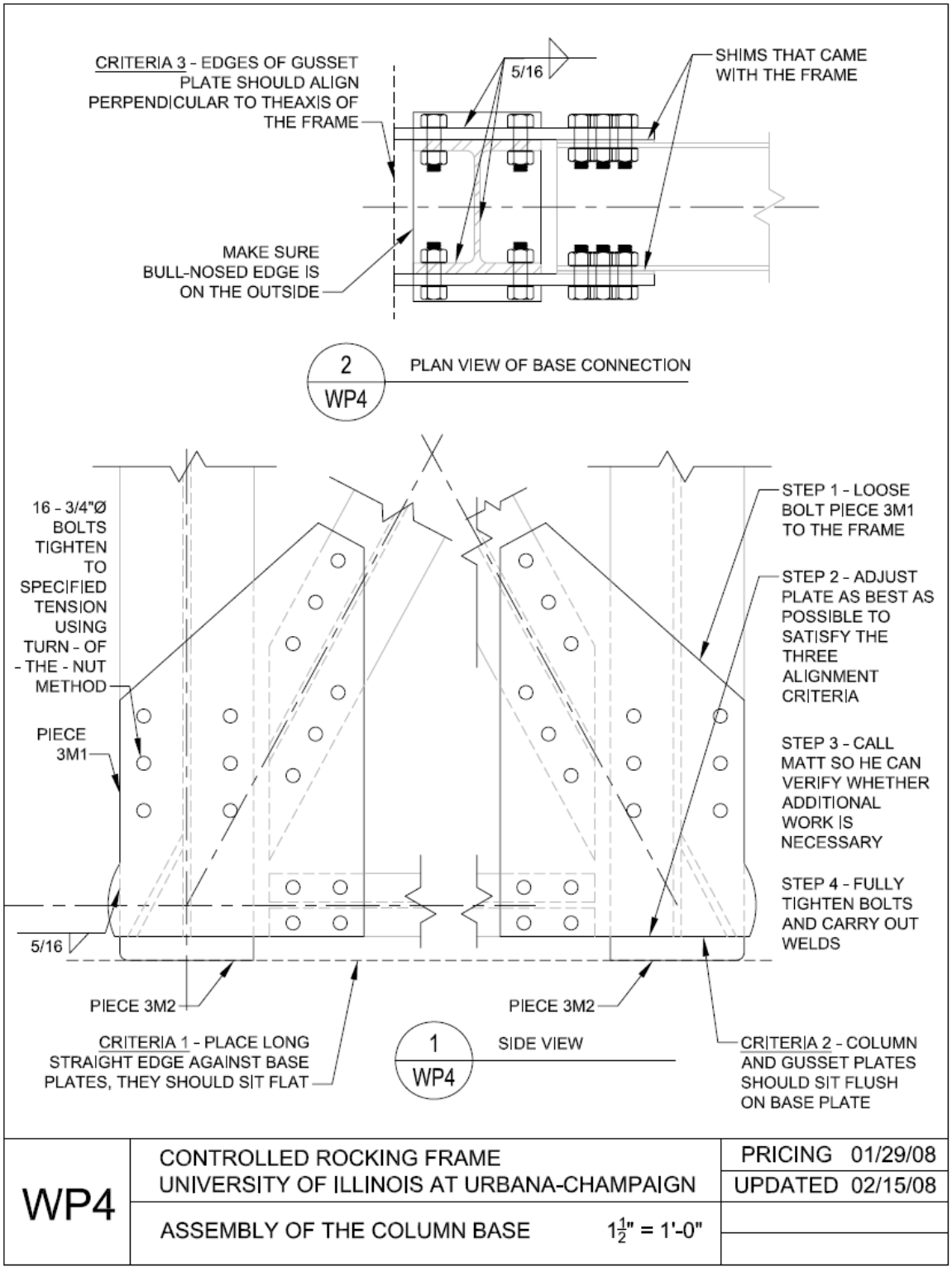

Figure A.44 Work Plan Drawing – Assembly of the Column Base

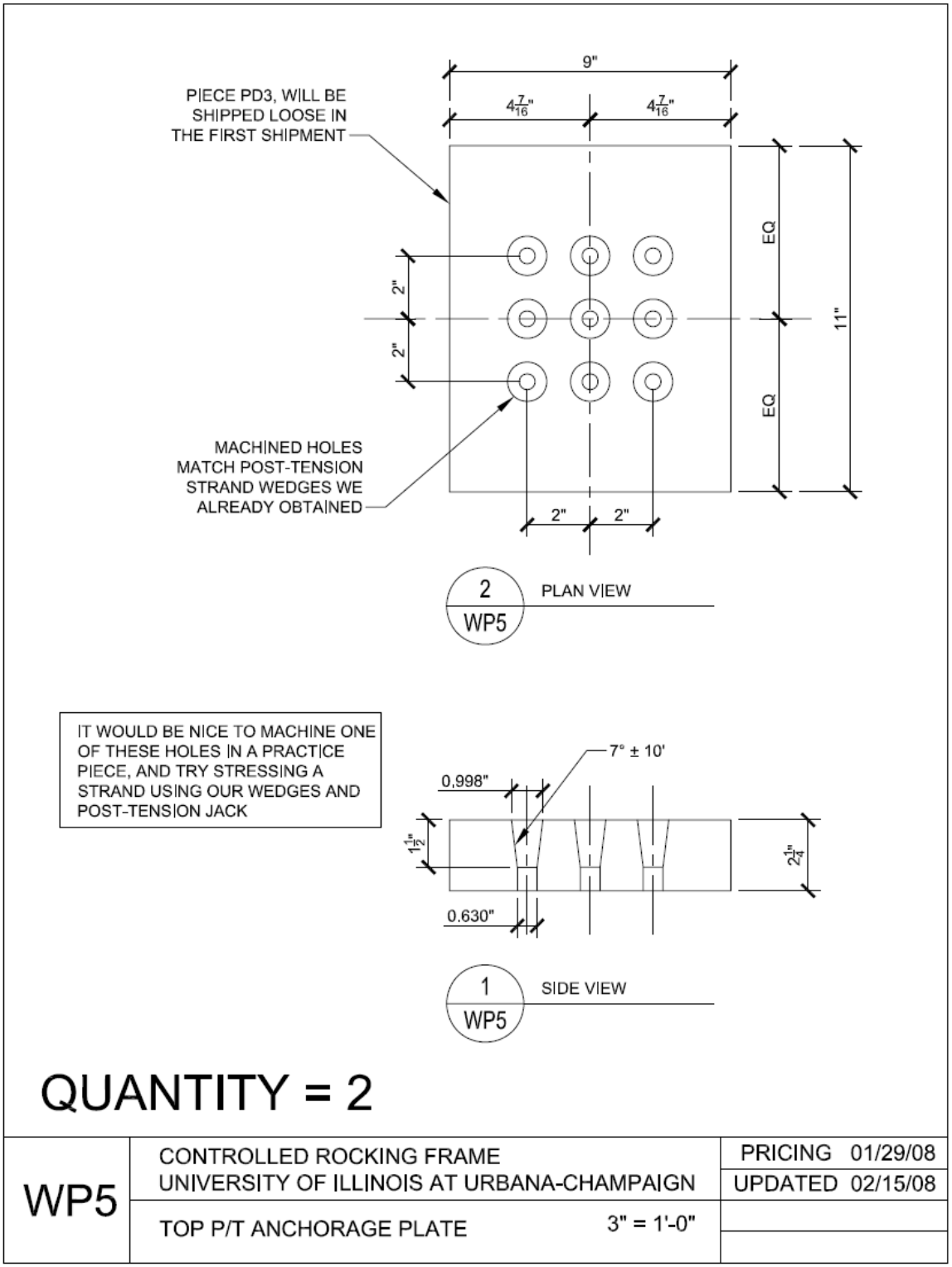

Figure A.45 Work Plan Drawing – Top Post-Tensioning Anchorage Plate

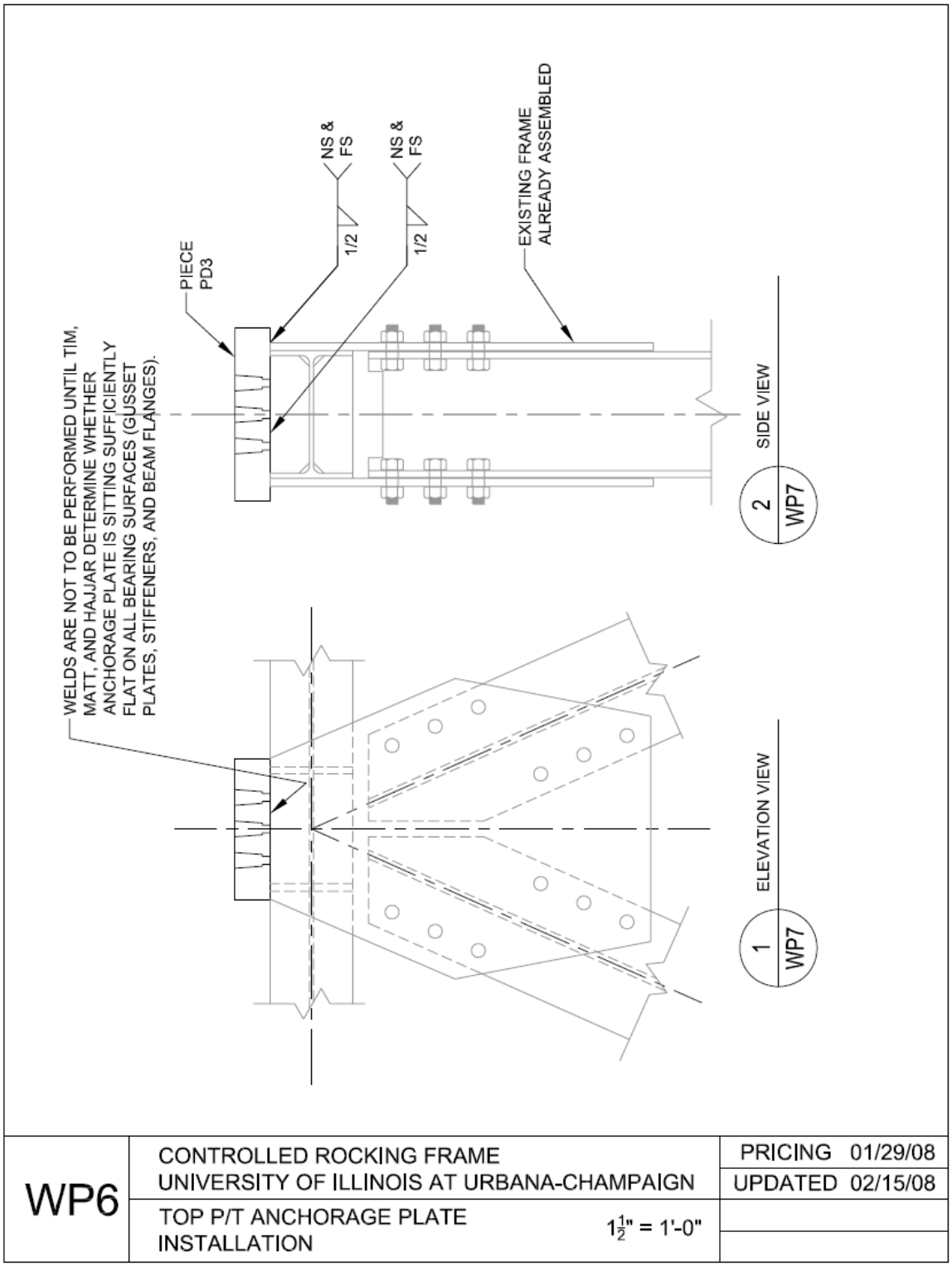

Figure A.46 Work Plan Drawing – Top Post-Tensioning Anchorage Plate Installation

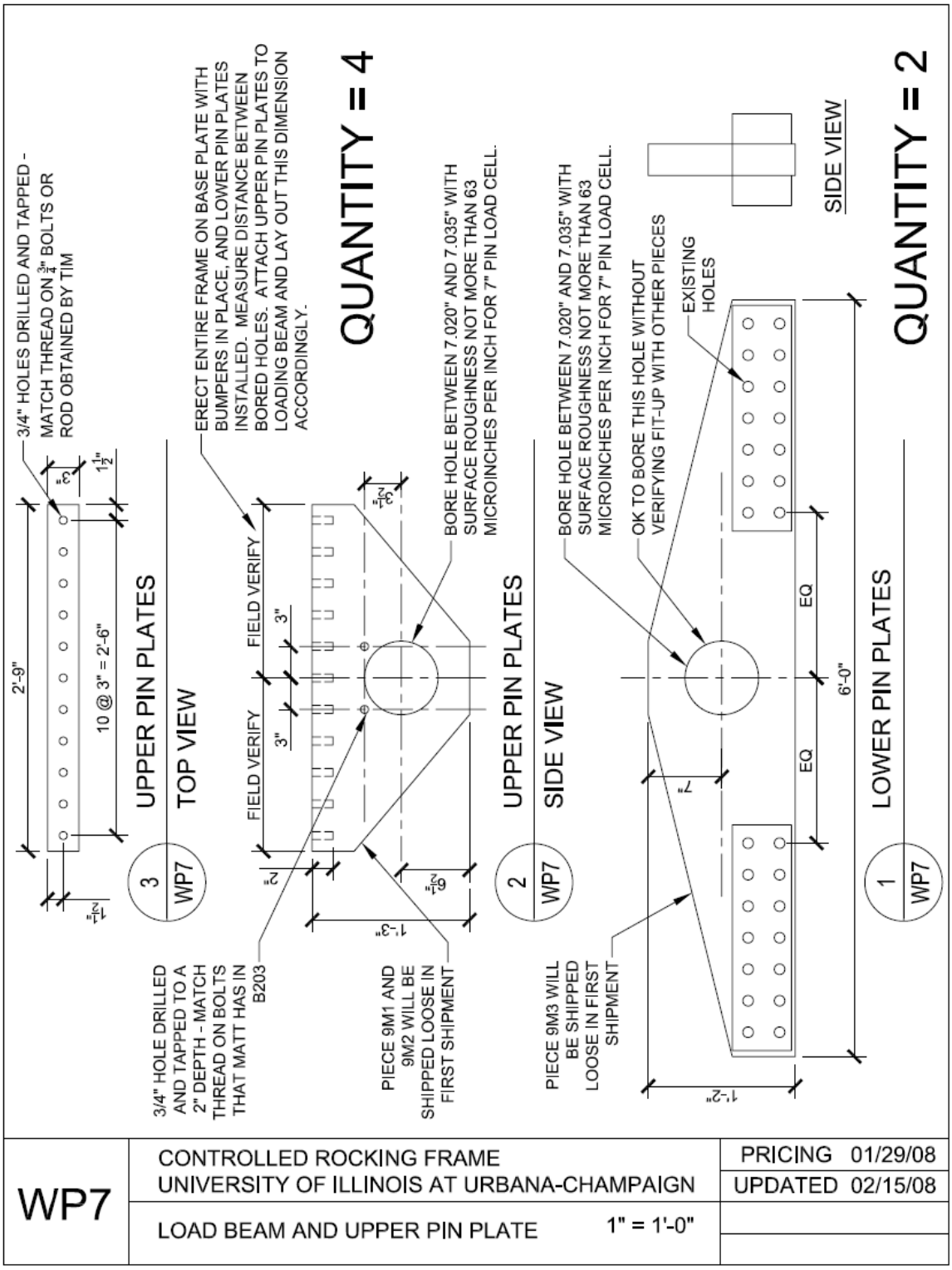

Figure A.47 Work Plan Drawing – Load Beam and Upper Pin Plate

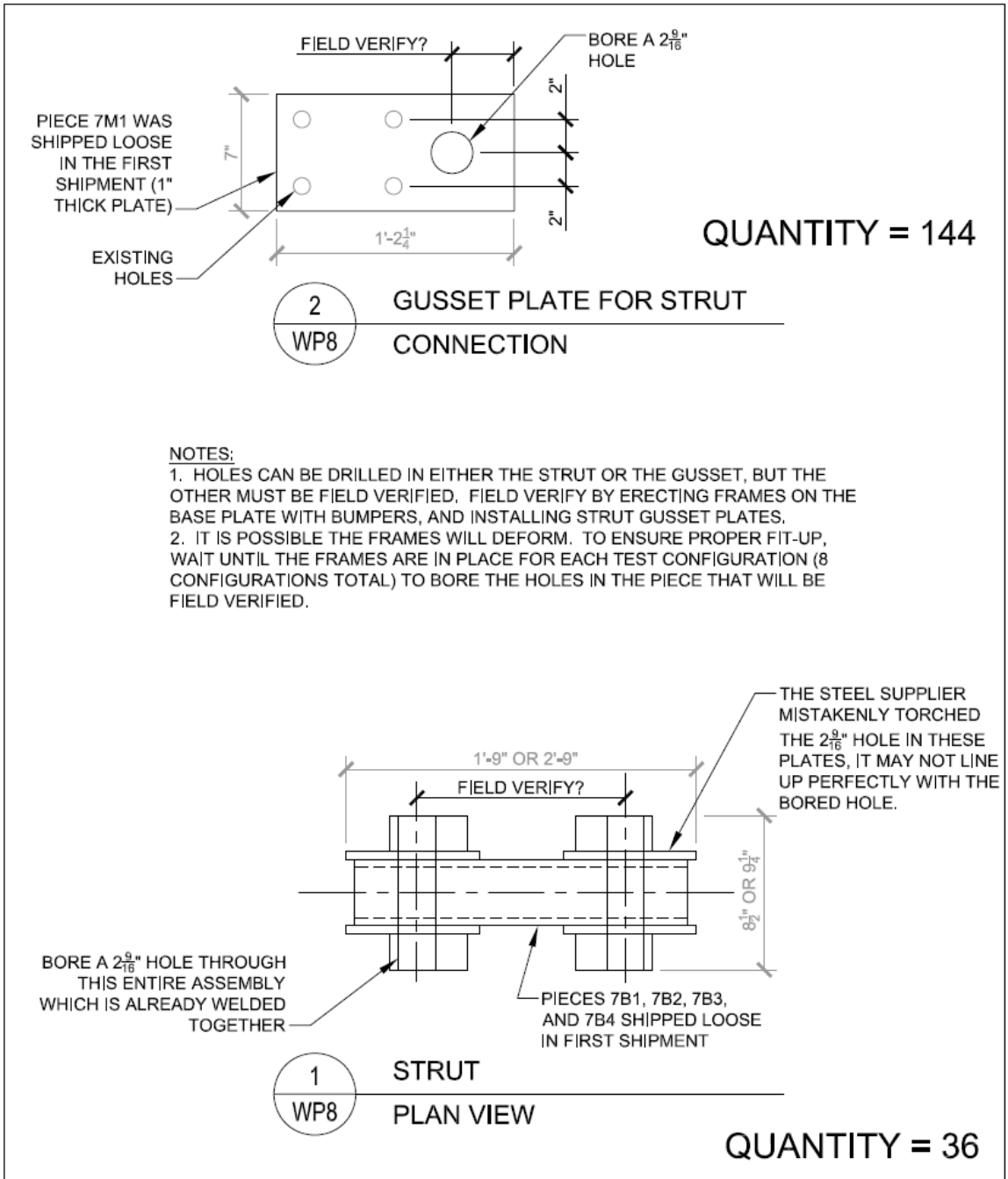

Figure A.48 Work Plan Drawing – Axial Strut Between Frames

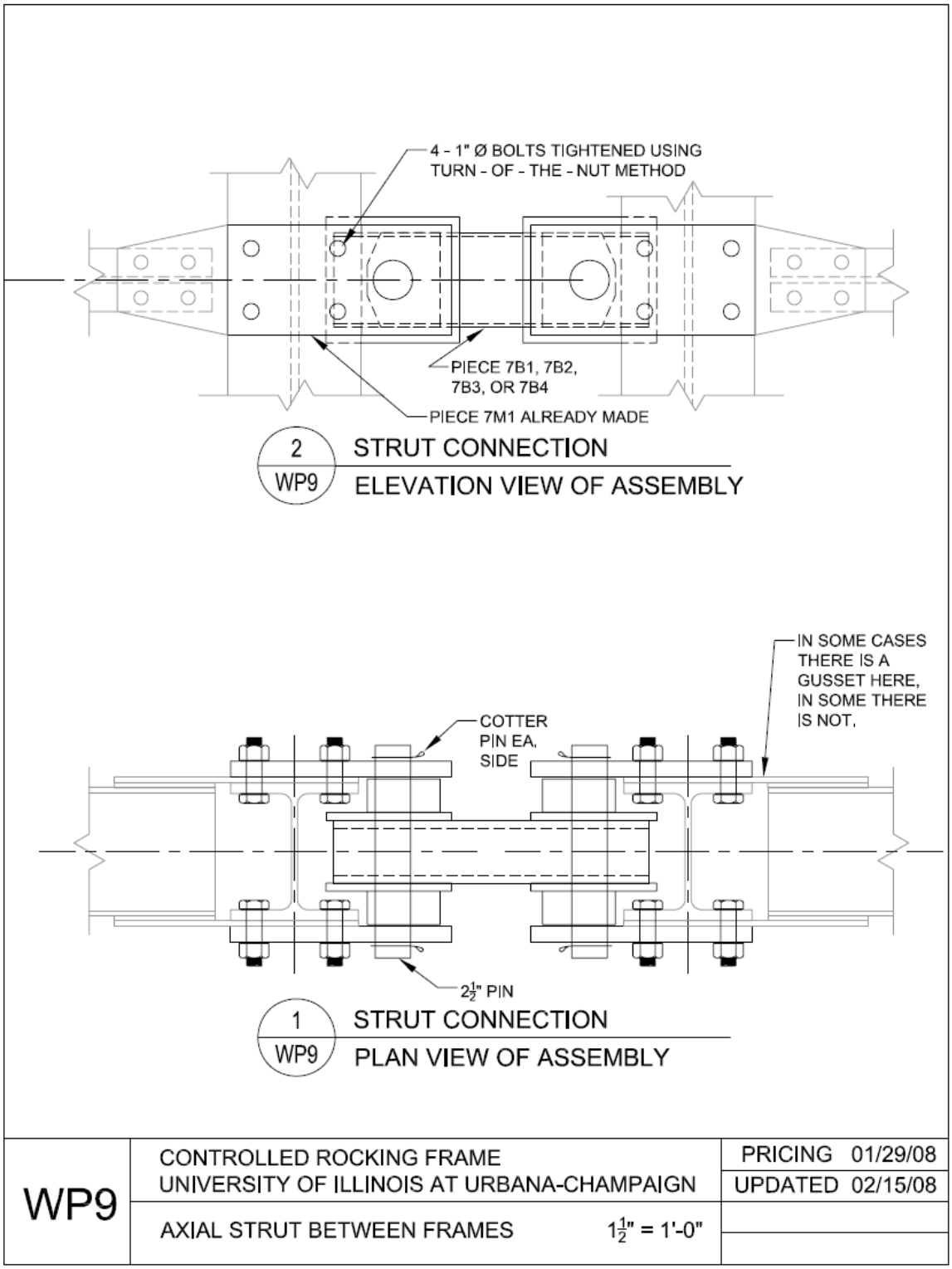

Figure A.49 Work Plan Drawing – Axial Strut Between Frames

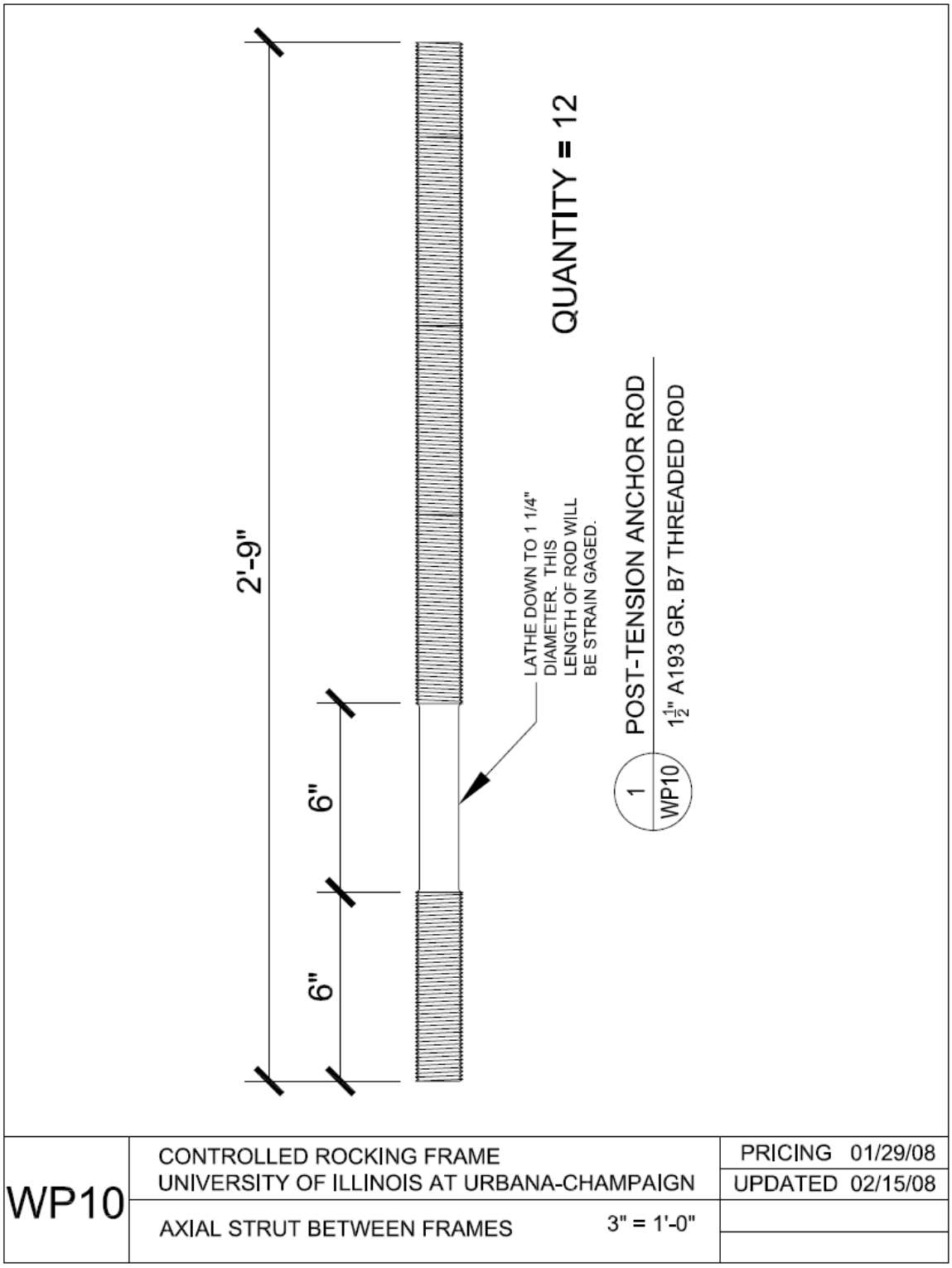

Figure A.50 Work Plan Drawing – Anchor Rods for Post-Tensioning Anchorage Plate

A.3 Drawings for Erection of the Specimens and Their Components

The following set of drawings was created to facilitate the erection of the specimens. The drawings were given the designation “EP” to indicate that they are part of the erection plan.

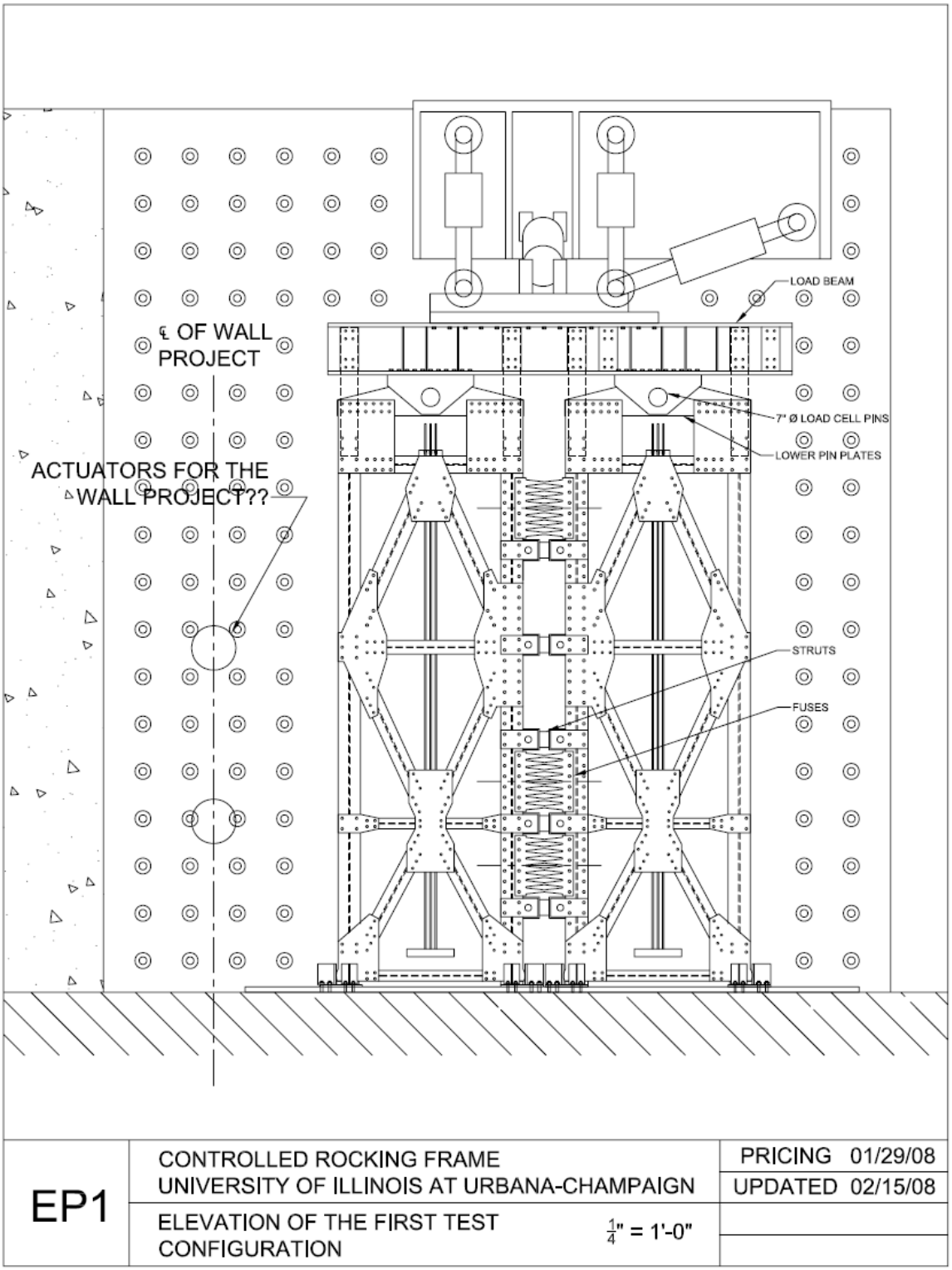

Figure A.51 Erection Plan Drawing for Specimen A1

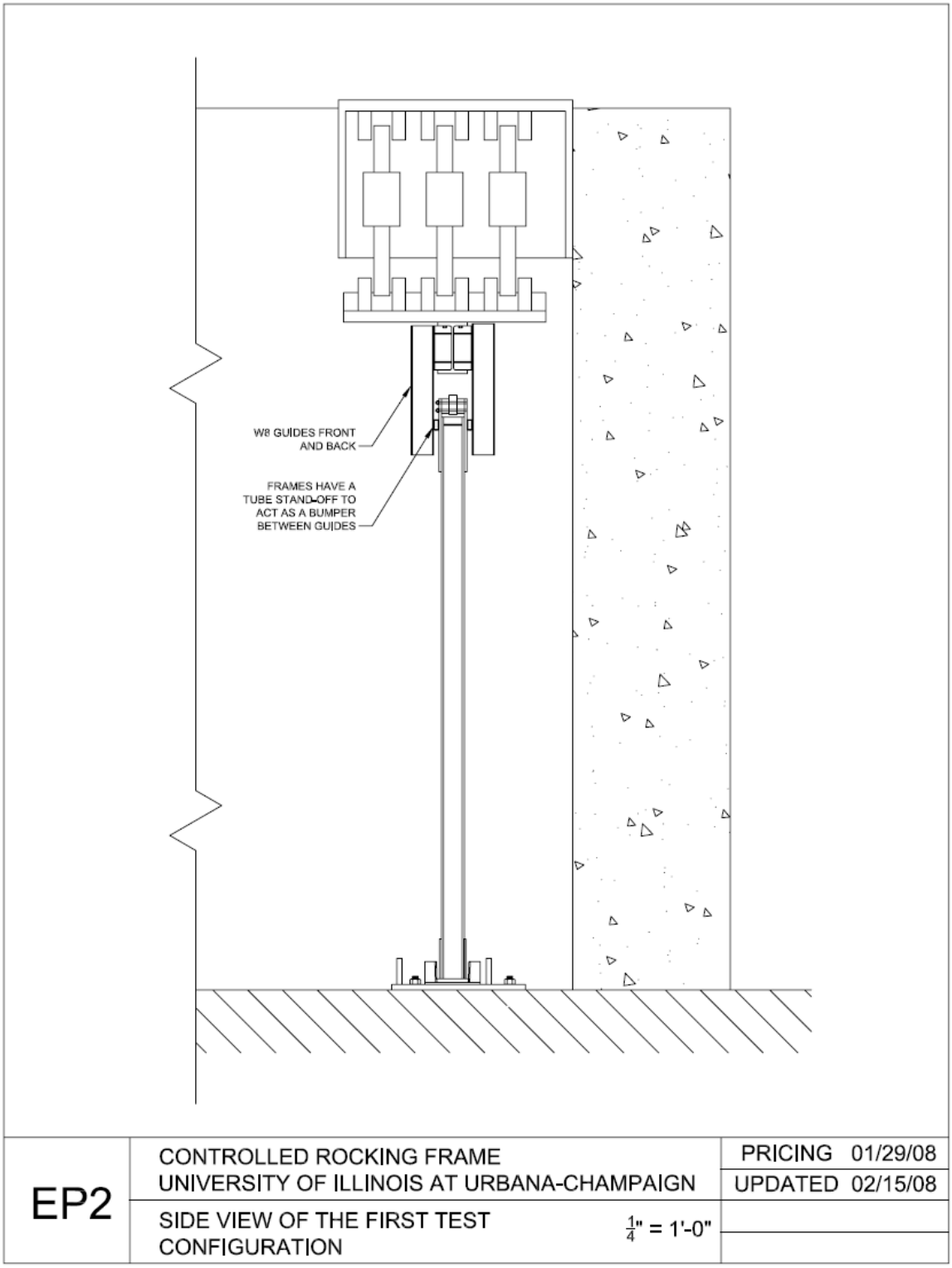

Figure A.52 Erection Plan Drawing – Side View for Specimen A1

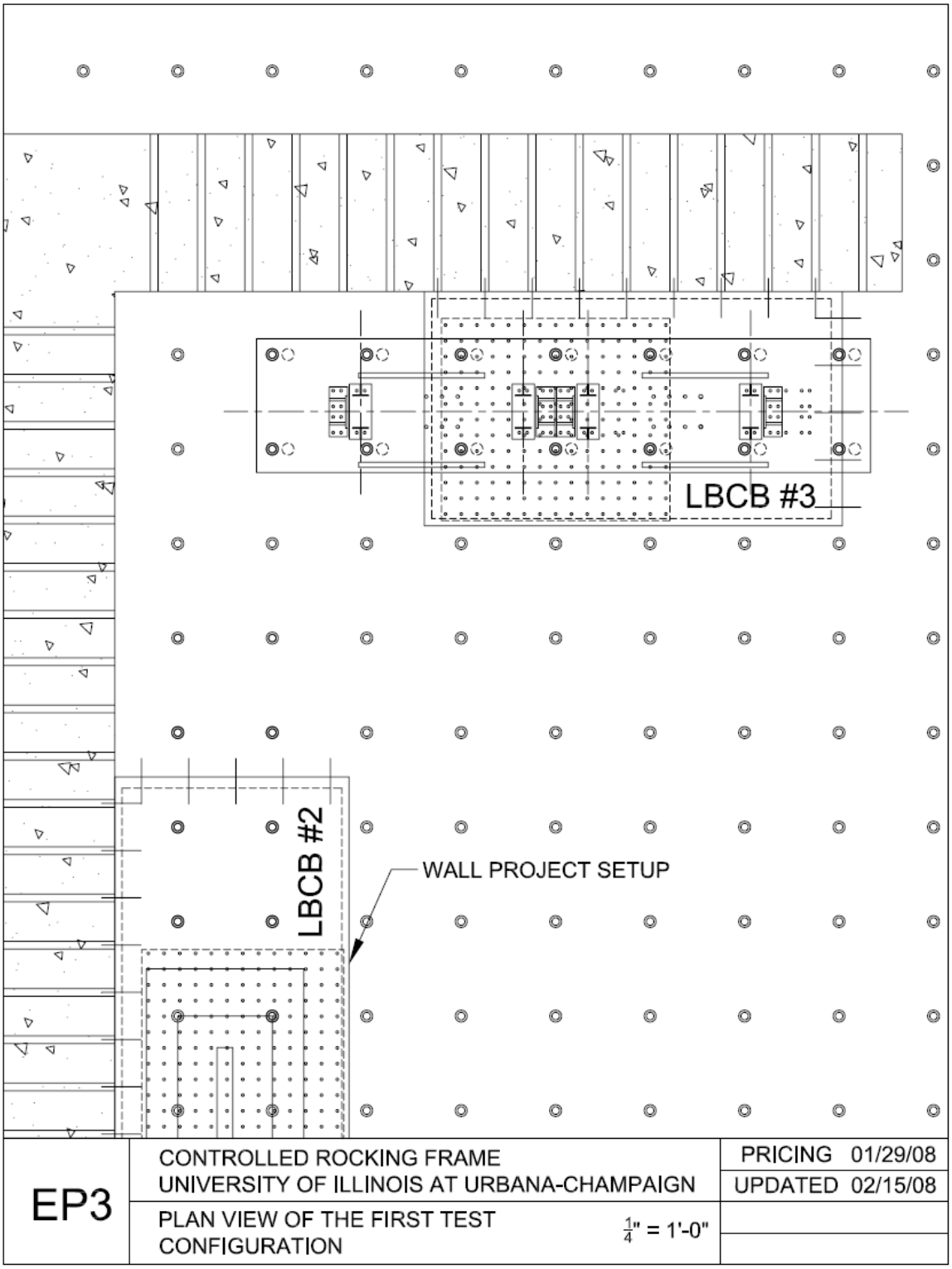

Figure A.53 Erection Plan Drawing – Plan View for Specimen A1

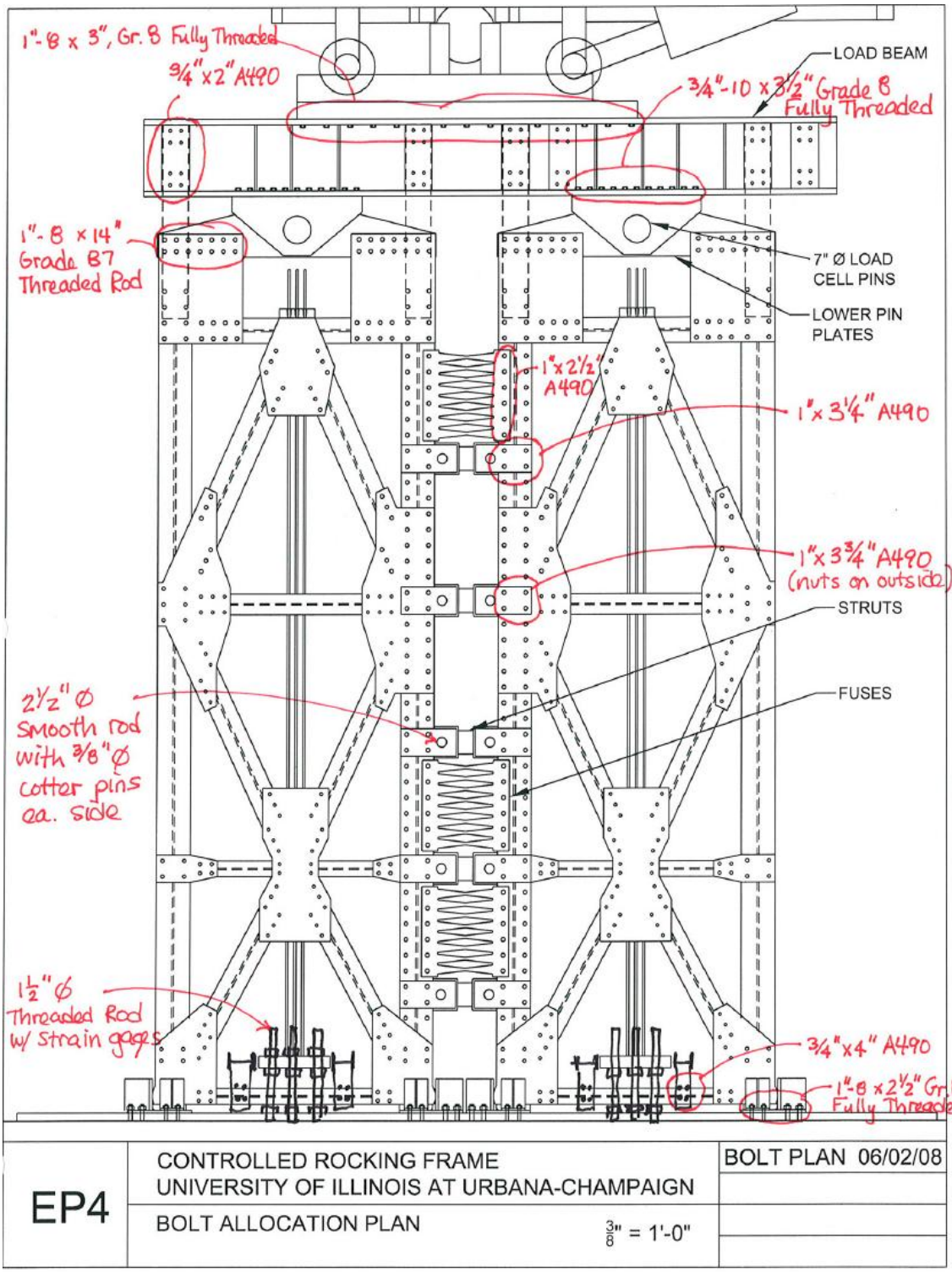

Figure A.54 Erection Plan Drawing – Bolt Allocation Plan

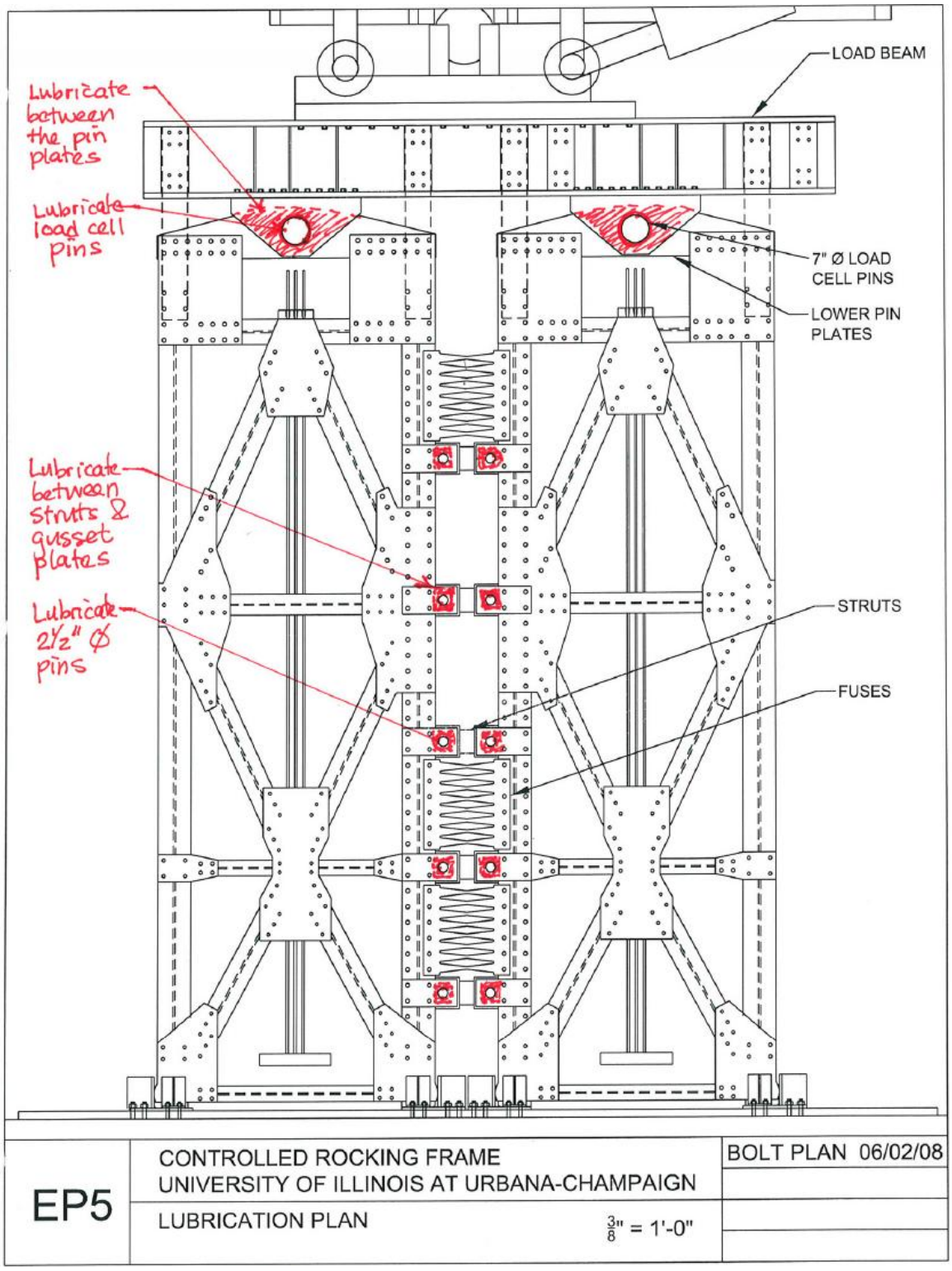

Figure A.55 Erection Plan Drawing – Lubrication Plan

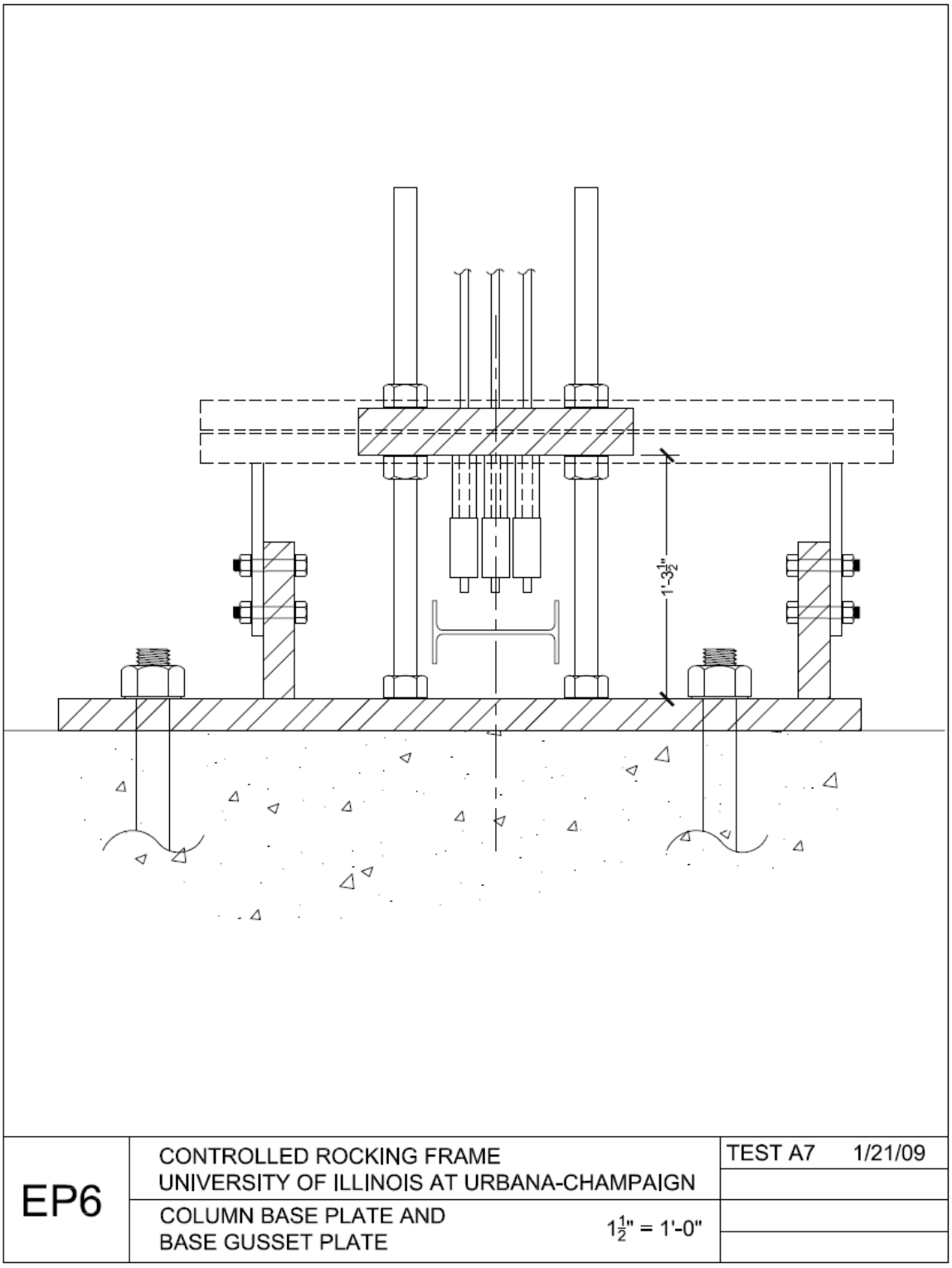

Figure A.56 Erection Plan Drawing – Lower Post-Tensioning Anchorage

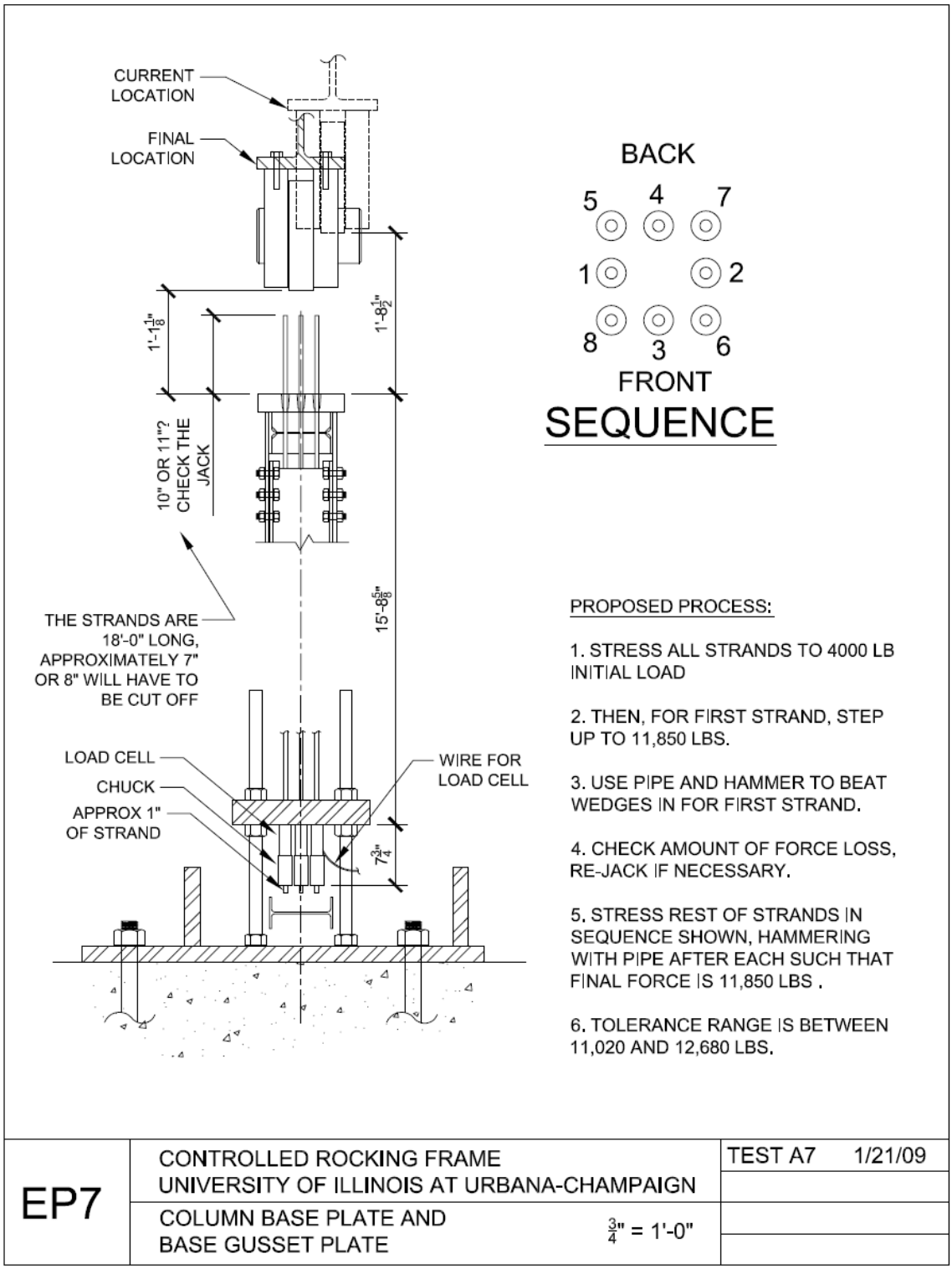

Figure A.57 Erection Plan Drawing – Post-Tensioning Installation

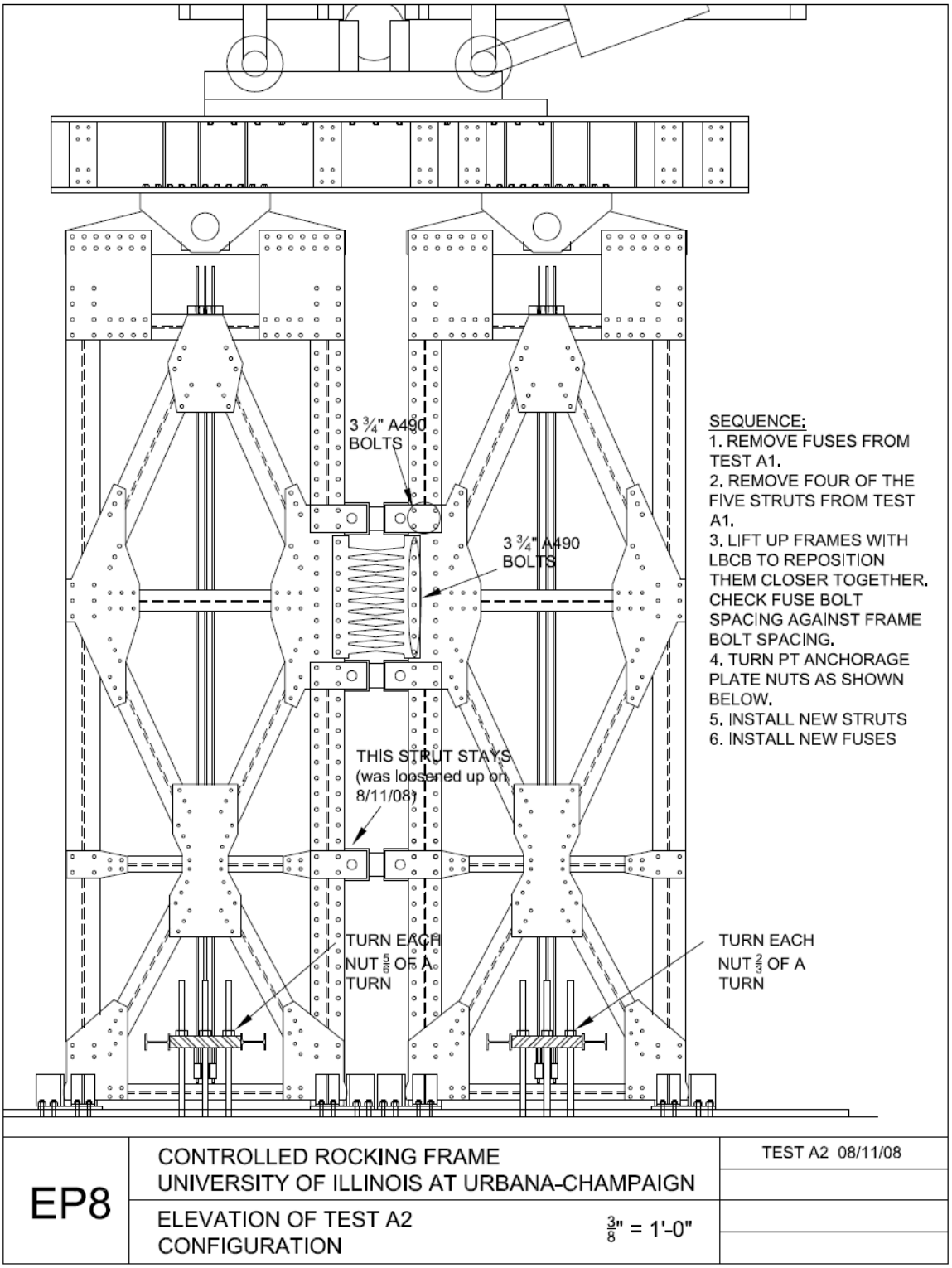

Figure A.58 Erection Plan Drawing for Specimen A2

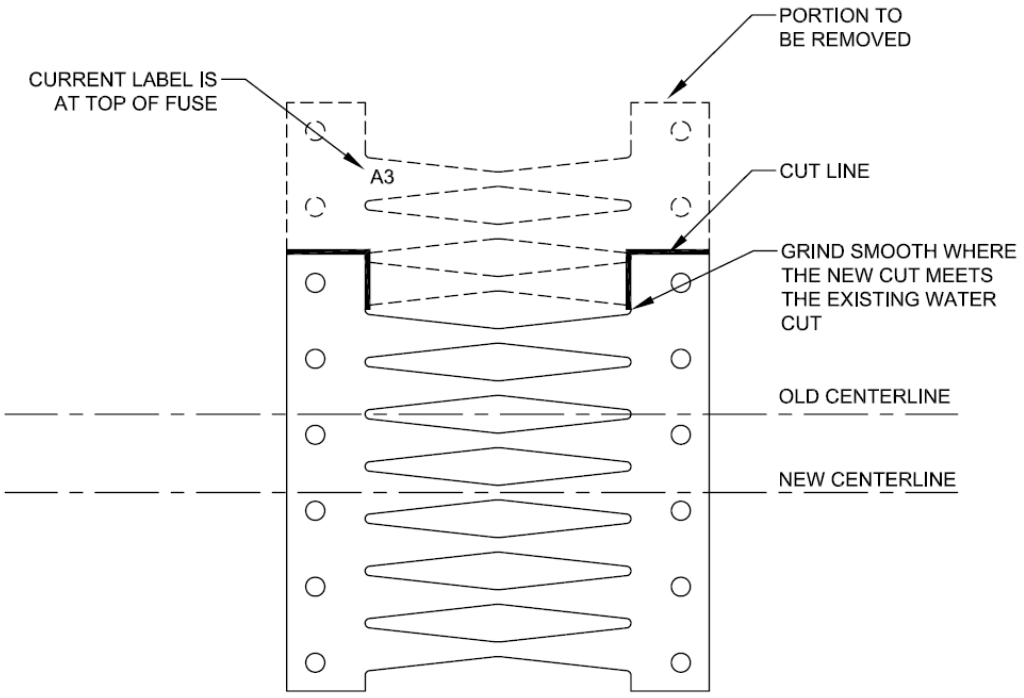

START WITH FUSES LABELED A3
CUT OUT 3 OF THE 10 LINKS AS SHOWN ABOVE

QUANTITY = 2 FUSES.

EP9	CONTROLLED ROCKING FRAME UNIVERSITY OF ILLINOIS AT URBANA-CHAMPAIGN	TEST A3 09/02/08
	MODIFICATIONS TO FUSE A3 $1\frac{1}{2}$" = 1'-0"	

Figure A.59 Erection Plan Drawing – Modifications for Specimen A3 Fuse

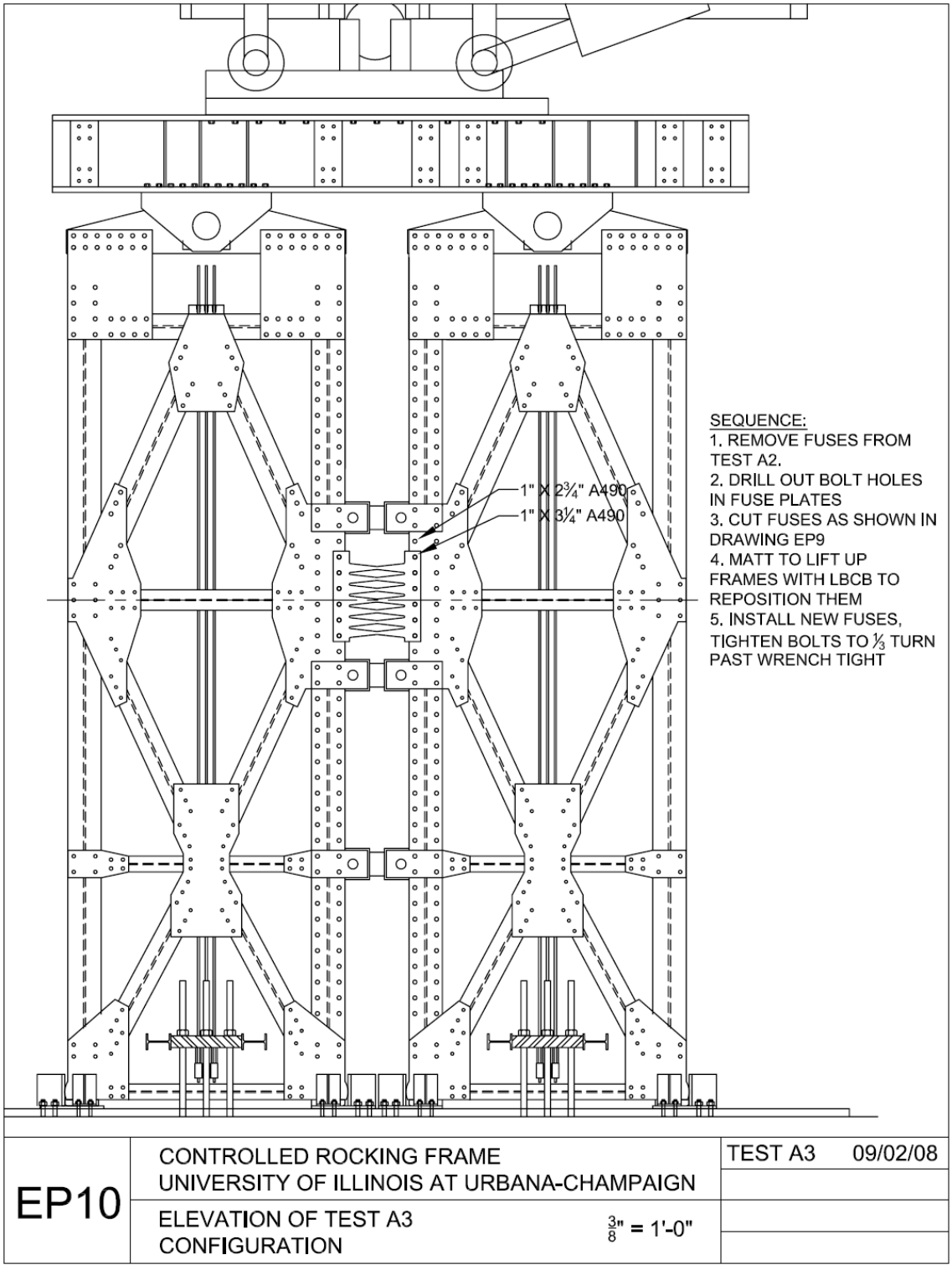

Figure A.60 Erection Plan Drawing for Specimen A3

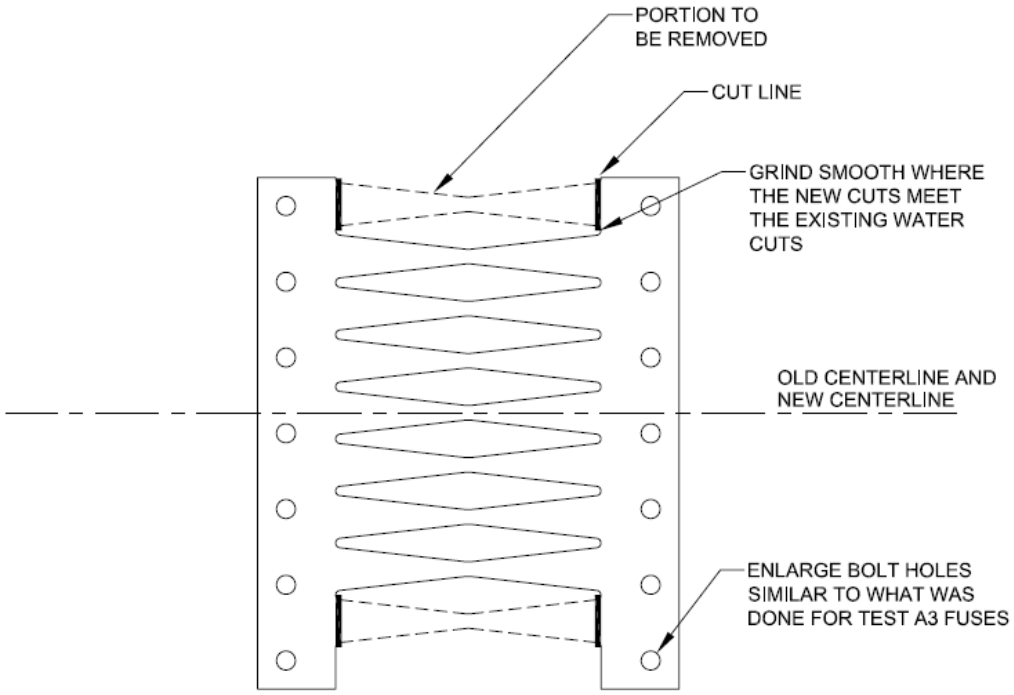

START WITH FUSES LABELED A4
CUT OUT 2 OF THE 9 LINKS AS SHOWN ABOVE

QUANTITY = 2 FUSES.

EP11	CONTROLLED ROCKING FRAME UNIVERSITY OF ILLINOIS AT URBANA-CHAMPAIGN	TEST A4 09/17/08
	MODIFICATIONS TO FUSE A3 $1\frac{1}{2}$" = 1'-0"	

Figure A.61 Erection Plan Drawing – Modifications for Specimen A4 Fuse

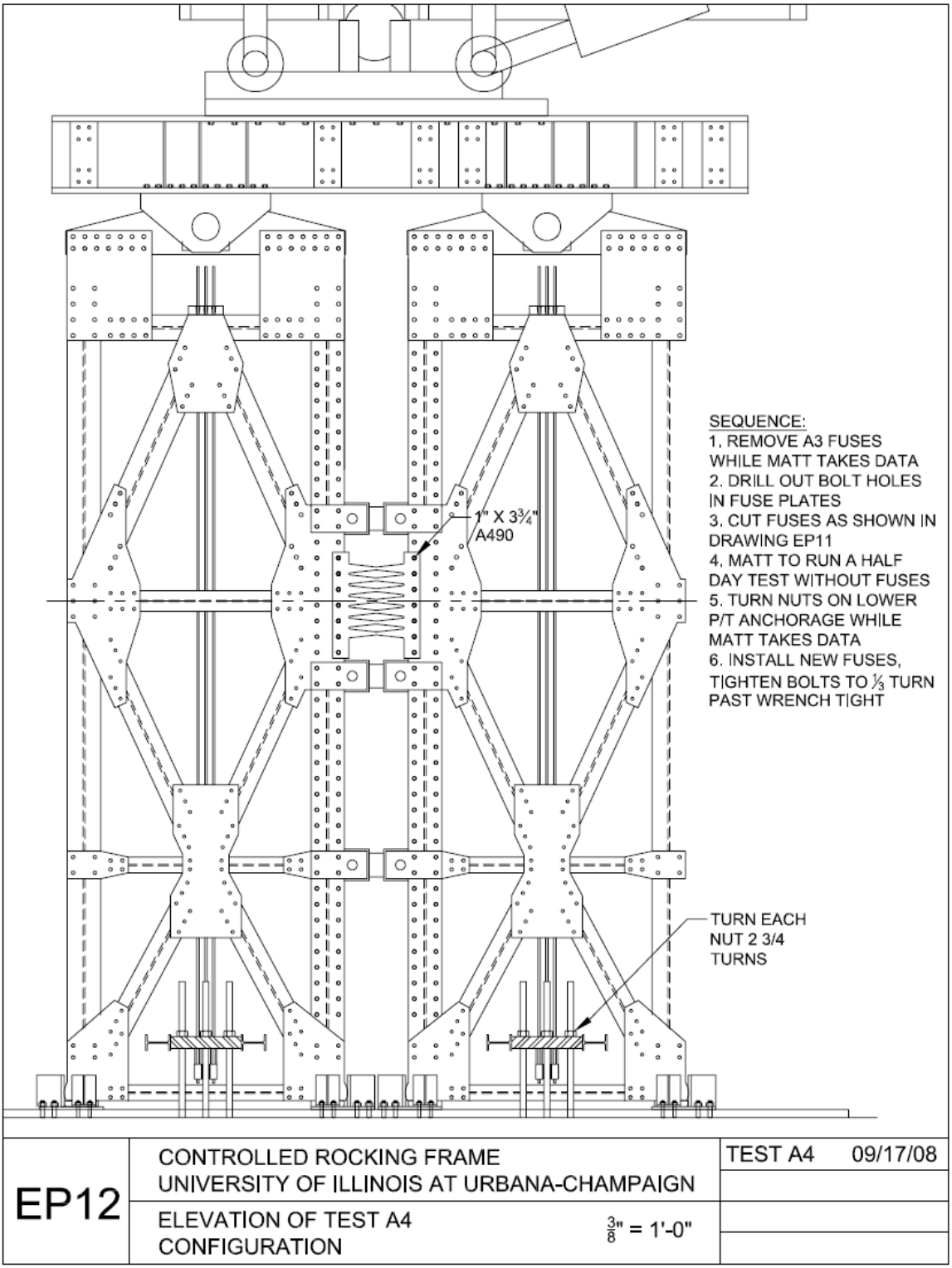

Figure A.62 Erection Plan Drawing for Specimen A4

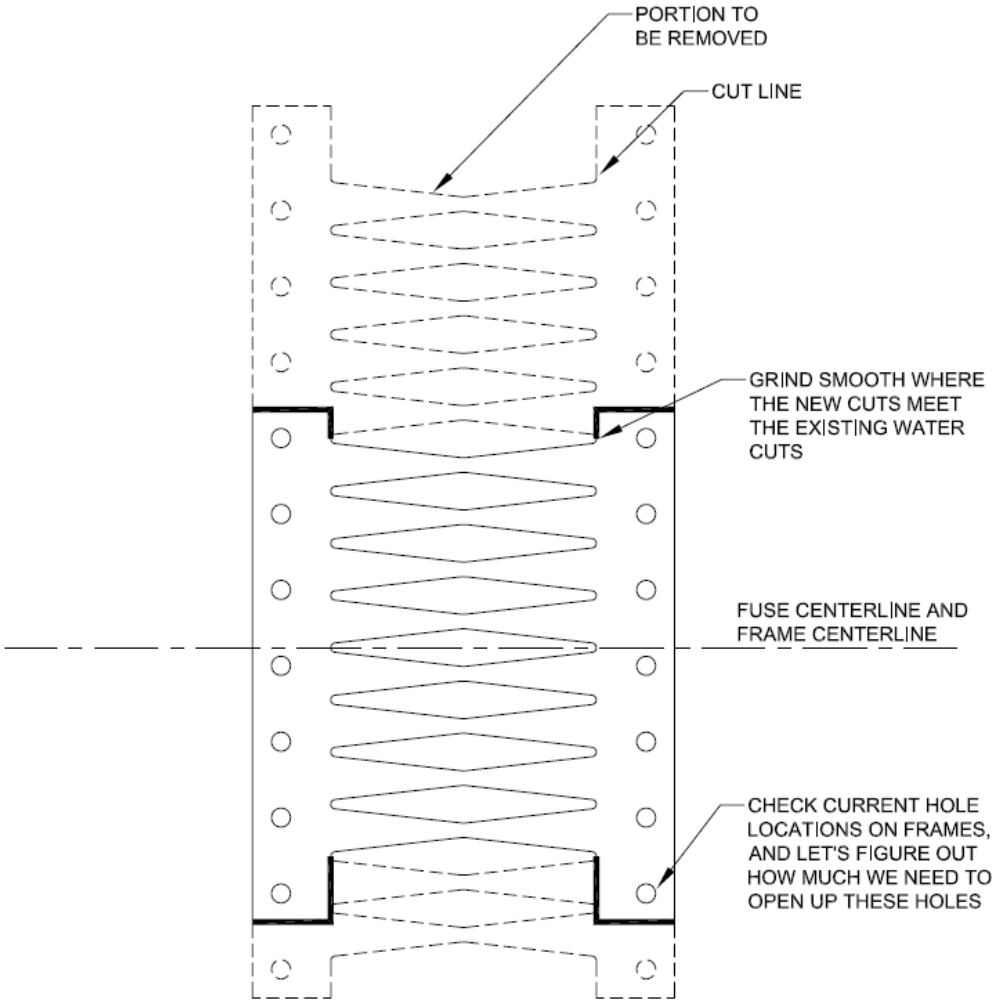

START WITH FUSES LABELED A3 ALT
CUT OUT 6 OF THE 15 LINKS AS SHOWN ABOVE

QUANTITY = 2 FUSES.

EP13	CONTROLLED ROCKING FRAME UNIVERSITY OF ILLINOIS AT URBANA-CHAMPAIGN	TEST A5 11/06/08
	MODIFICATIONS TO FUSE A3 ALT FOR TEST A5 $1\frac{1}{2}$" = 1'-0"	

Figure A.63 Erection Plan Drawing – Modifications for Specimen A5 Fuse

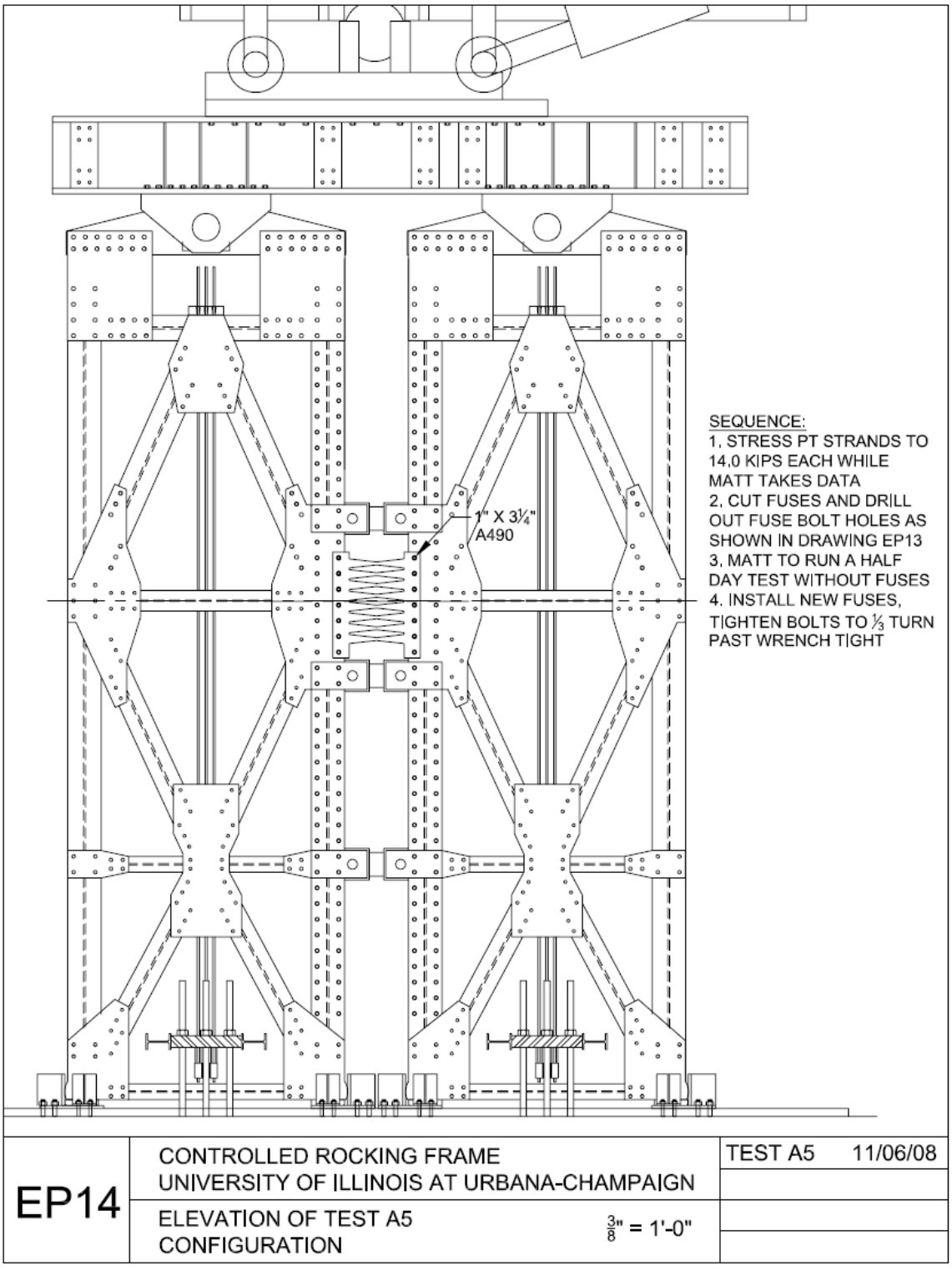

Figure A.64 Erection Plan Drawing for Specimen A5

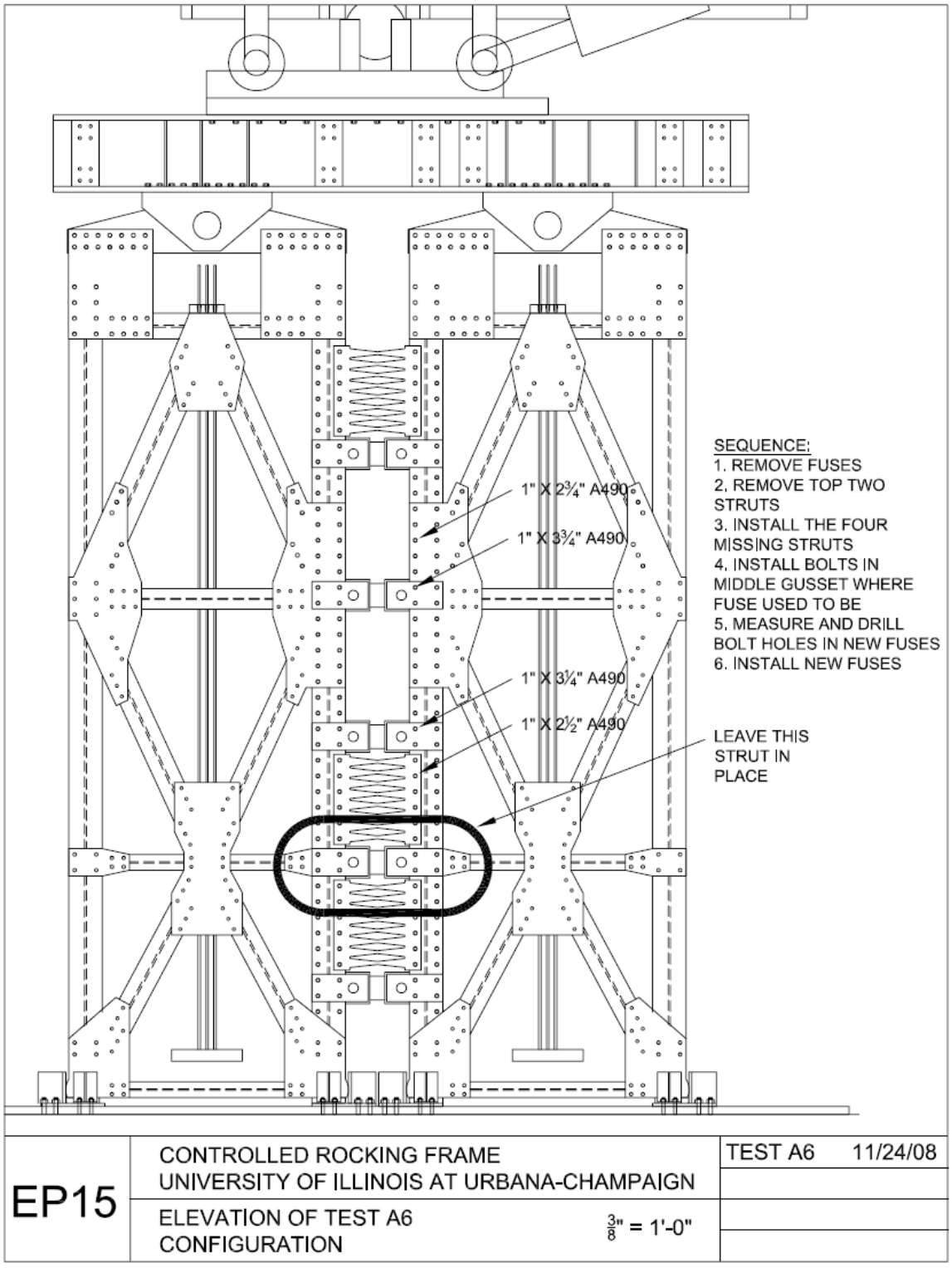

Figure A.65 Erection Plan Drawing for Specimen A6

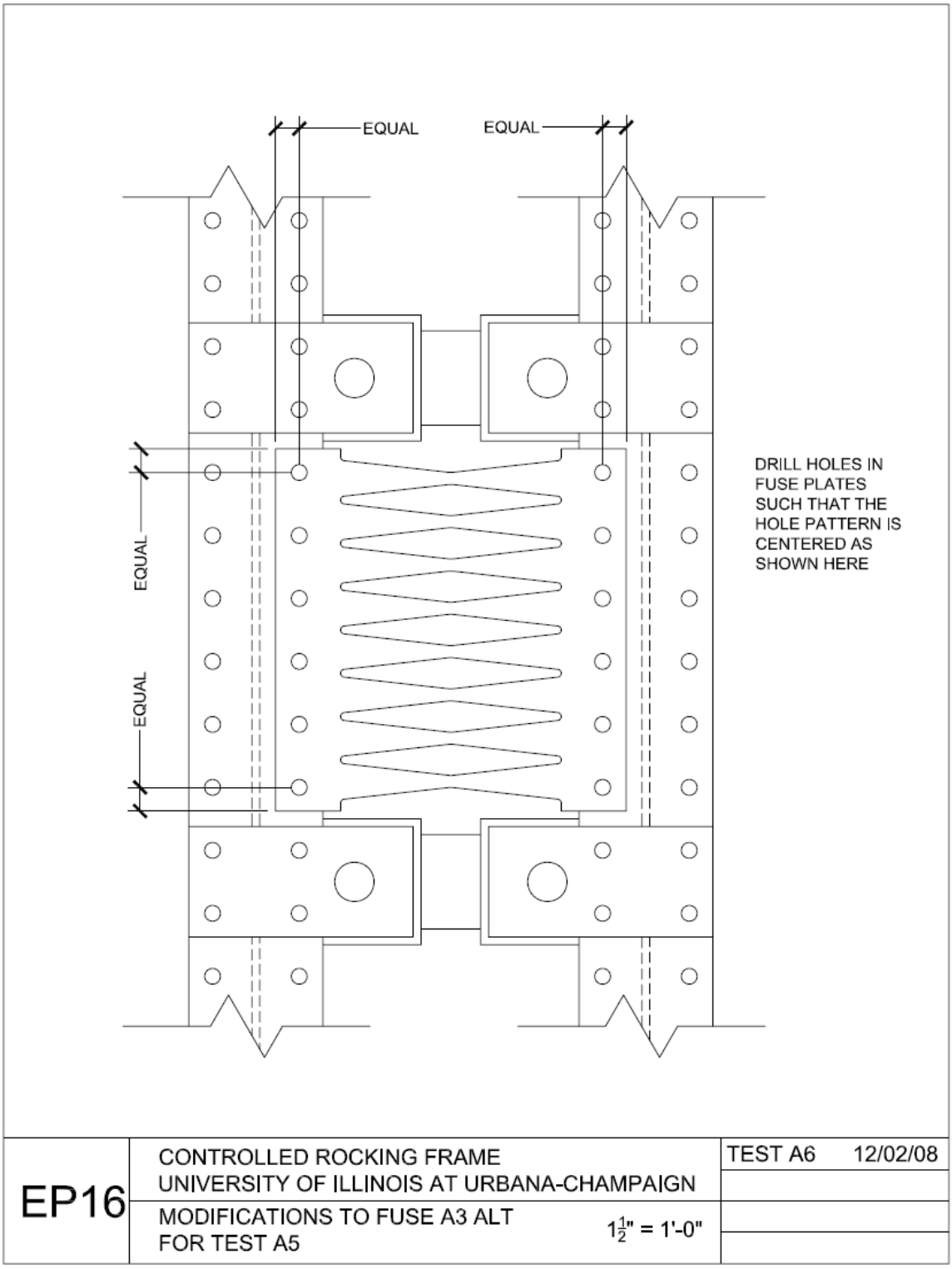

Figure A.66 Erection Plan Drawing for Specimen A6 Fuse

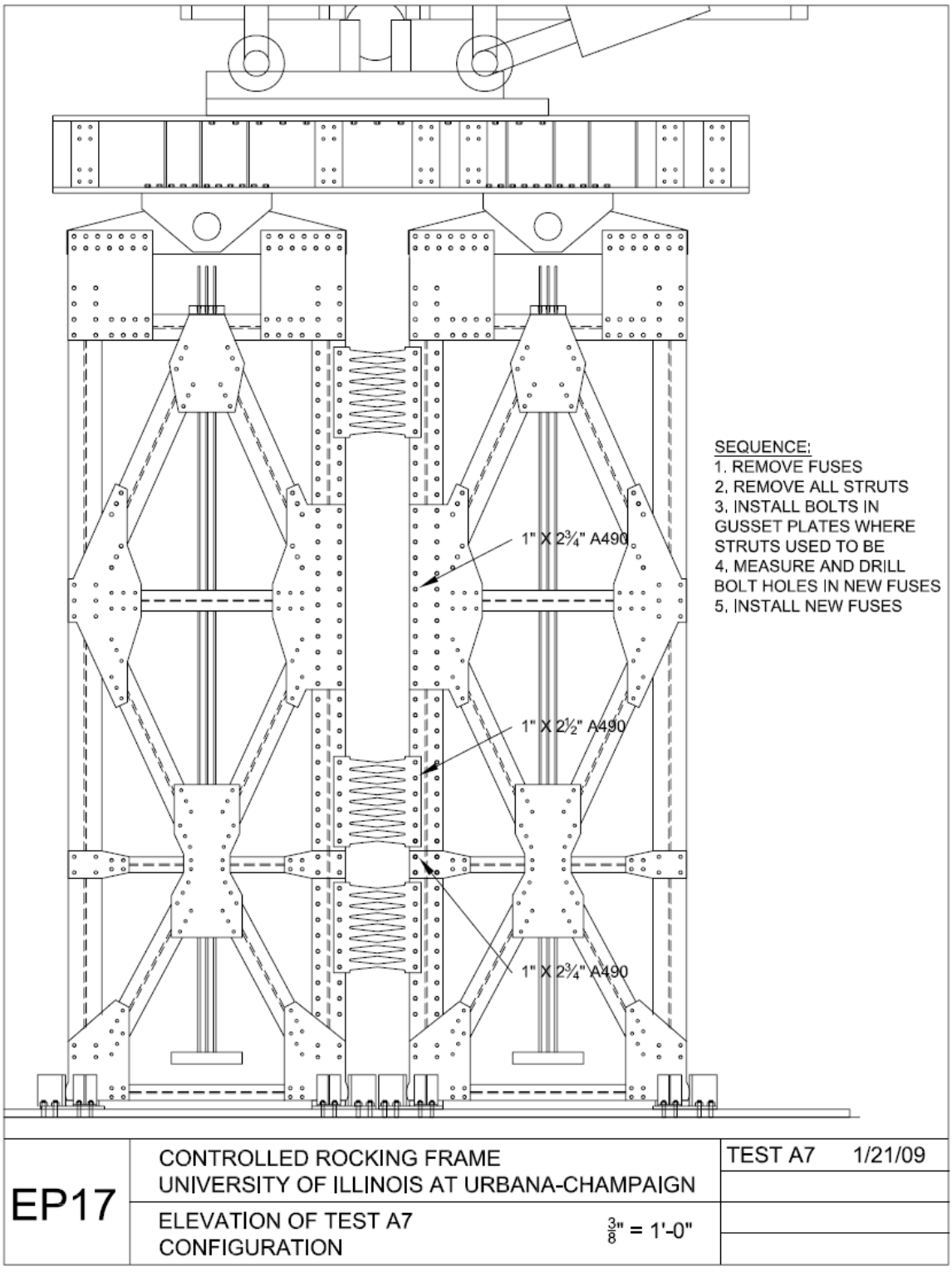

Figure A.67 Erection Plan Drawing for Specimen A7

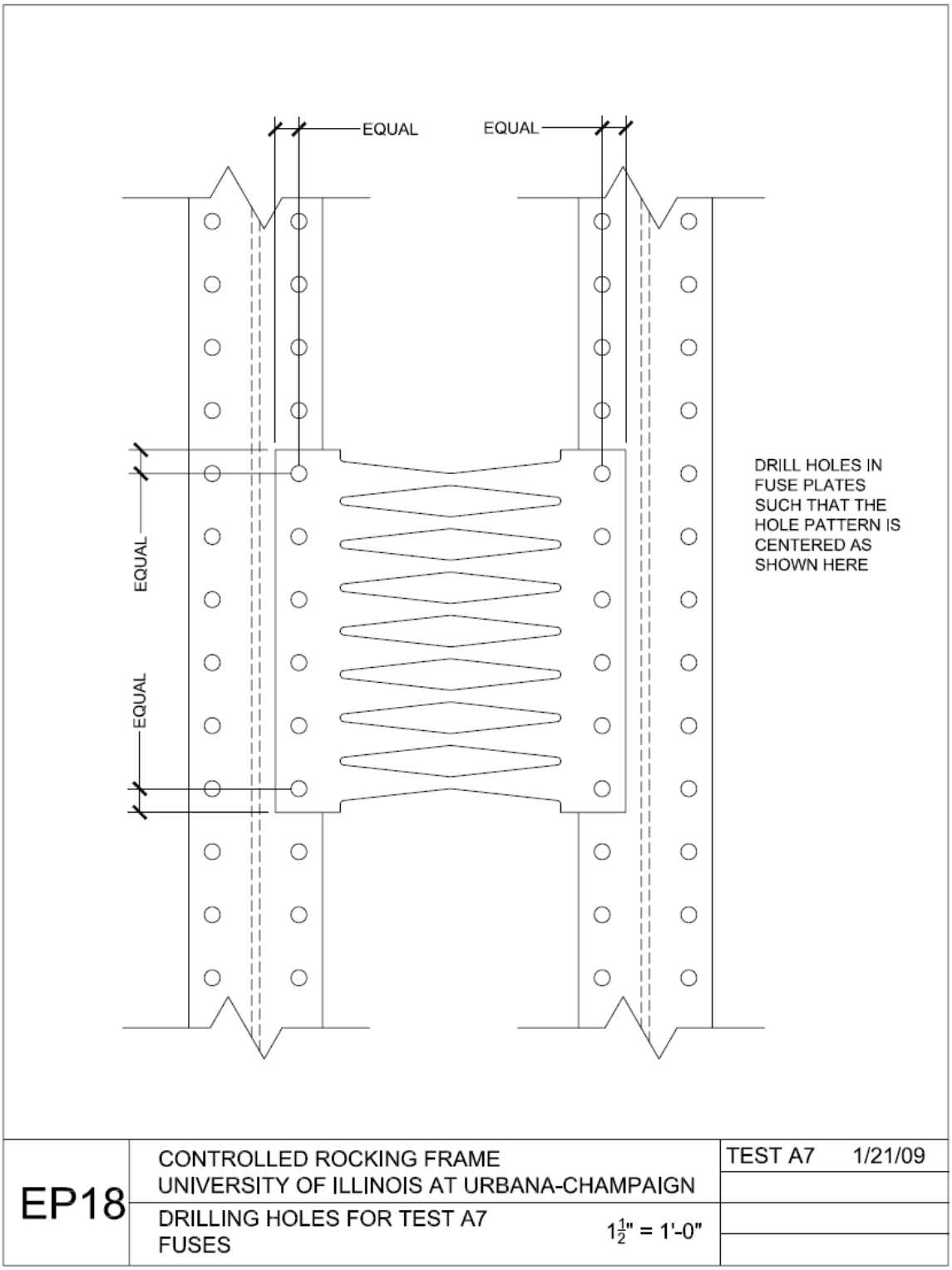

Figure A.68 Erection Plan Drawing for Specimen A7 Fuse

A.4 Design Drawings for the Single Frame Configuration

This section includes the design drawings for the single frame configuration. It should be noted that at the time these drawings were created, the single frame configurations were referred to as the C series of specimens. In the final testing program, these specimens were renamed to be the B series of specimens, which is how they are referenced in the main body of this report.

CONSTRUCTION SEQUENCE AT START OF "C" SERIES

1. LOOSEN BOLTS ON THE LOWER ANCHORAGE PLATE - RELIEVING P/T STRESS.
2. REMOVE THE STRUTS BETWEEN FRAMES. REMOVE PLEXIGLASS SHIELD. REMOVE THE FUSES.
3. REMOVE PT LOADCELLS.
4. REMOVE UNNEEDED PT STRANDS (LEAVE ONLY FOUR STRANDS).
5. REMOVE LATERAL BRACING MEMBERS FOR PT ANCHORAGE PLATE.
6. REMOVE BOTTOM BEAM.
7. LOWER PT ANCHORAGE PLATE TO AS LOW AS POSSIBLE (GROUND LEVEL?).
8. SLIDE IN THE CENTRAL COLUMN AND PUT IN THE TOP PIN.
9. SLIDE IN THE FUSE.
10. RAISE THE PT ANCHORAGE PLATE TO ITS WORKING POSITION.
11. INSTALL THE SIDE BRACING PLATES.
12. ASSEMBLE THE FUSE FRAME. KEEP ALL BOLTS LOOSE.
13. PUT IN THE BOTTOM PIN.
14. INSTALL PT LOADCELLS
15. STRESS ALL OF THE POST-TENSIONING STRANDS.
16. TIGHTEN ALL THE BOLTS.
17. CONNECT ALL INSTRUMENTATION TO DAQ, AND TEST THE INSTRUMENTATION / DAQ.
18. INSTALL PLEXIGLASS SHIELD IN FRONT OF P/T.
19. TESTING.

CONSTRUCTION SEQUENCE BETWEEN "C" SERIES AND "B" SERIES

1. LOOSEN BOLTS ON THE LOWER ANCHORAGE PLATE - RELIEVING P/T STRESS.
2. REMOVE PLEXIGLASS SHIELD. REMOVE THE FUSE ASSEMBLY FRAMES. REMOVE SIDE BRACING PLATES.
3. SLIDE OUT FUSES. REMOVE PINS. SLIDE OUT CENTRAL COLUMNS.
4. UNBOLT THE PIN PLATE AND SHEAR PLATES FROM THE SPECIMEN AND RAISE THE LBCB PLATEN AS HIGH AS POSSIBLE.
5. REMOVE THE FRONT GUIDES. REMOVE THE FRAMES USING FORKLIFT.
6. UNBOLT THE BASE PLATE, PUSH THE BASE PLATE 6" TO THE RIGHT, AND REBOLT TO THE STRONGFLOOR.
7. REMOVE BUMPERS FOR THE RIGHT FRAME, AND REAFFIX IN THE NEW LOCATION.
8. USING A FORKLIFT, POSITION FRAMES IN PLACE.
9. INSTALL INSTRUMENTATION, CONNECT ALL INSTRUMENTATION TO DAQ, AND TEST THE INSTRUMENTATION / DAQ.
10. INSTALL PLEXIGLASS SHIELD IN FRONT OF P/T.
11. STRESS ALL OF THE POST-TENSIONING STRANDS.
12. INSTALL STRUTS BETWEEN FRAMES.
13. ATTACH FUSES TO THE FRAMES. INSTALL FUSE INSTRUMENTATION.
14. LOWER THE LBCB AND BOLT PIN PLATE AND SHEAR PLATES TO SPECIMEN.
15. TESTING.

G1	SINGLE CONTROLLED ROCKING FRAME	PRELIM 11/15/08
	UNIVERSITY OF ILLINOIS AT URBANA-CHAMPAIGN	
	CONSTRUCTION SEQUENCE	

Figure A.69 Design Drawing for the Single Frame Configuration – Construction Sequence

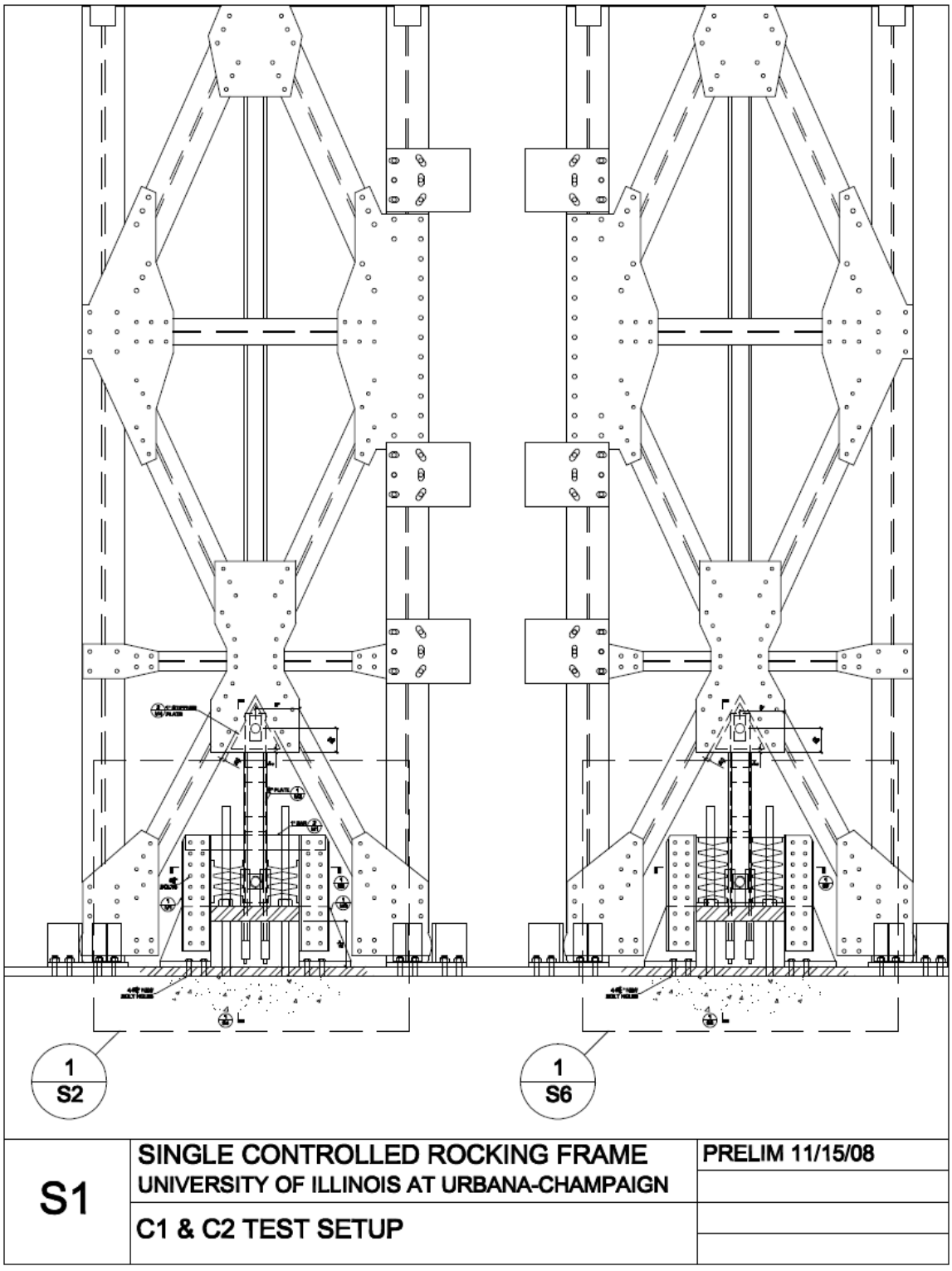

Figure A.70 Design Drawing for the Single Frame Configuration – Elevation View

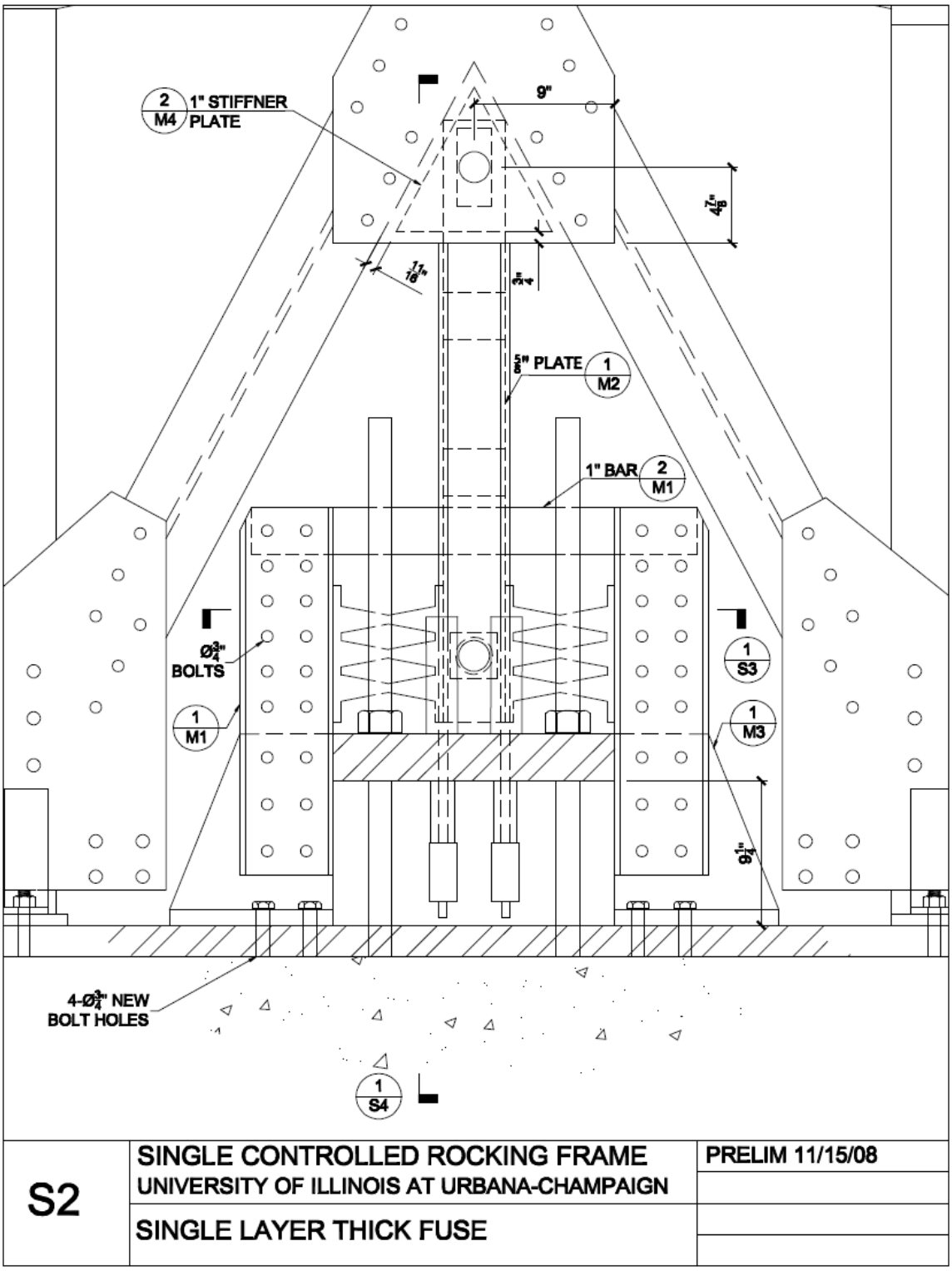

Figure A.71 Design Drawing for the Single Frame Configuration – Specimen B1 Close-Up

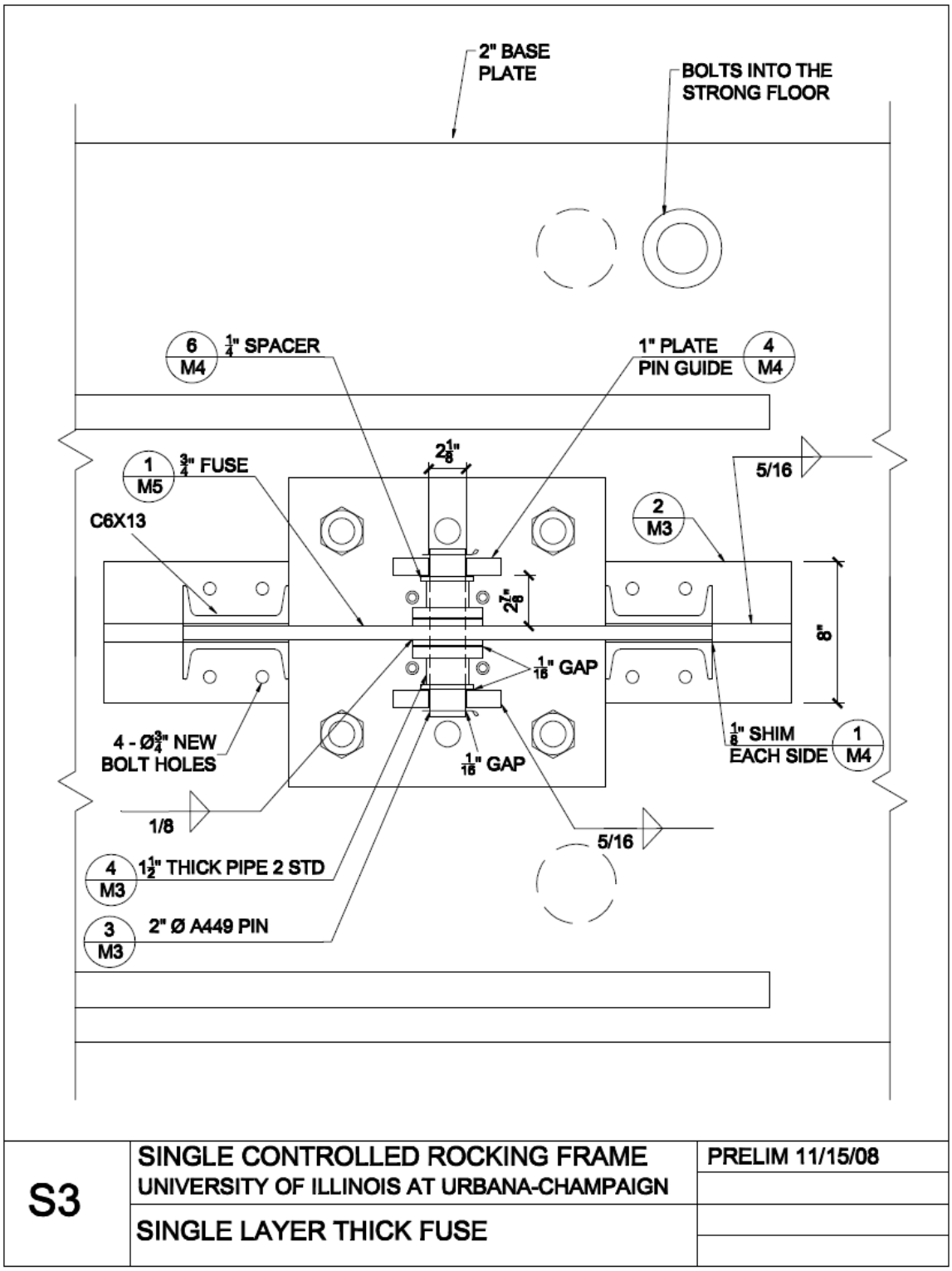

Figure A.72 Design Drawing for the Single Frame Configuration – Specimen B1 Plan

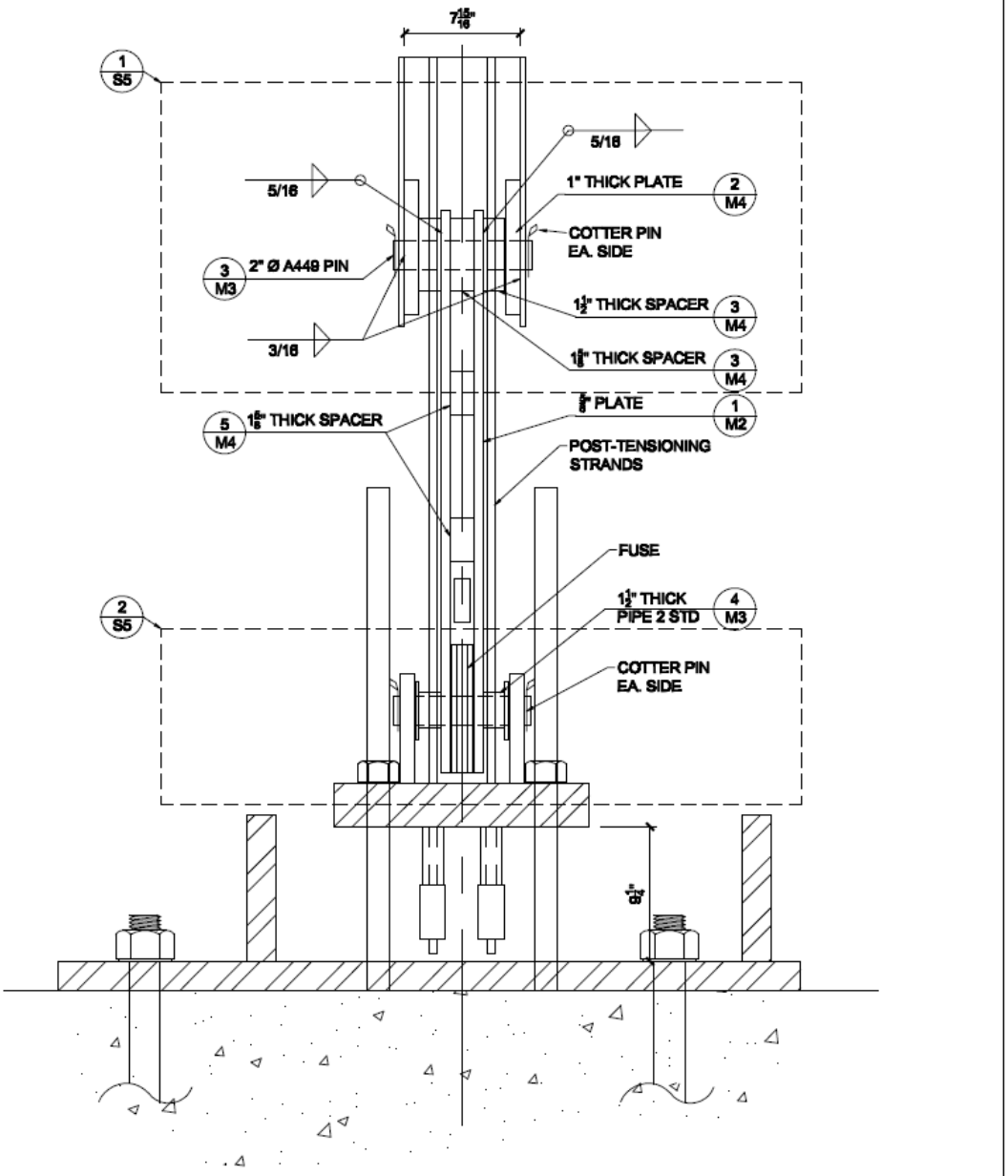

S4	SINGLE CONTROLLED ROCKING FRAME UNIVERSITY OF ILLINOIS AT URBANA-CHAMPAIGN	PRELIM 11/15/08
	SINGLE LAYER THICK FUSE	

Figure A.73 Design Drawing for the Single Frame Configuration – Specimen B1 Side View

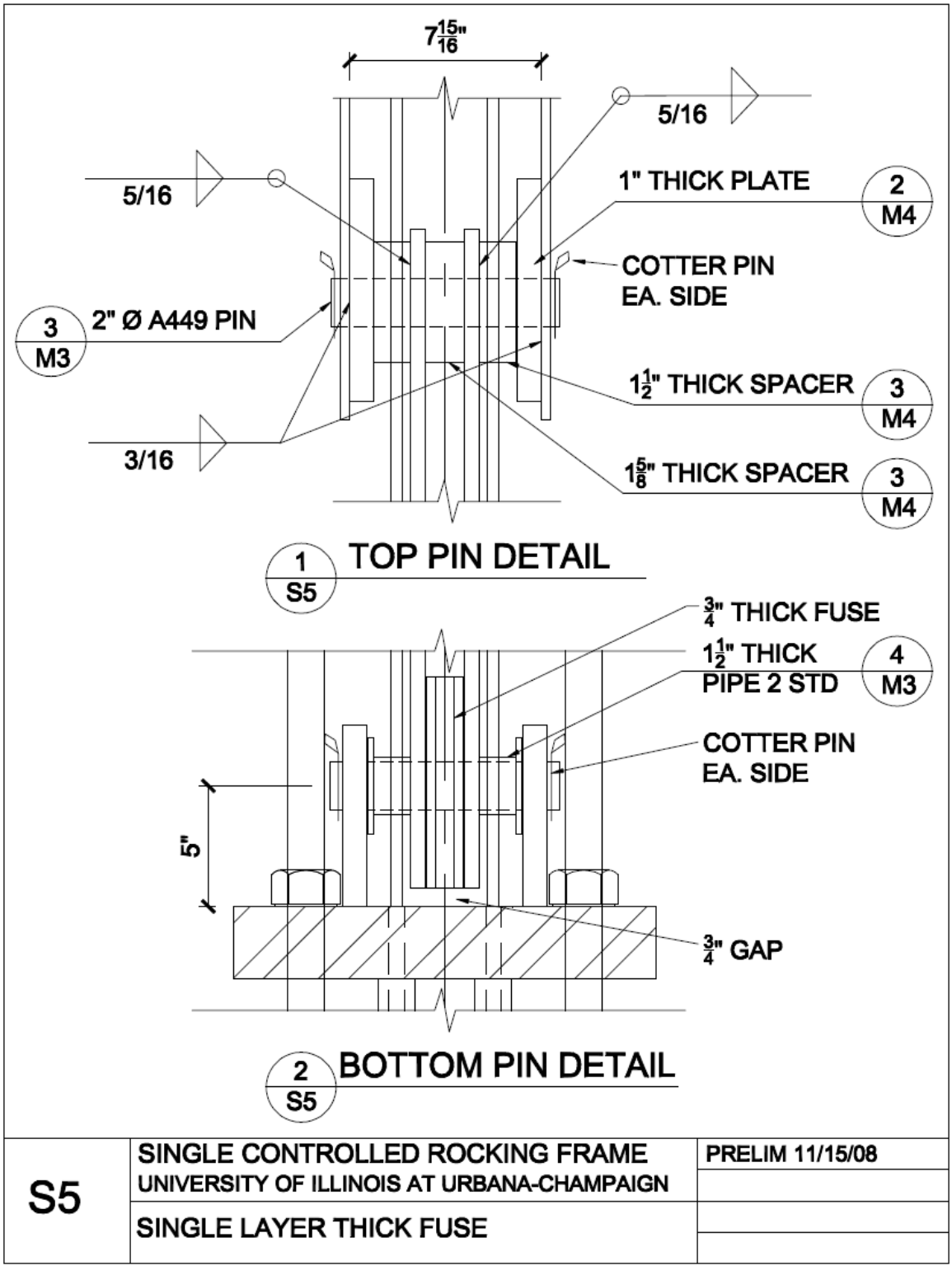

Figure A.74 Design Drawing for the Single Frame Configuration – Specimen B1 Close-Up

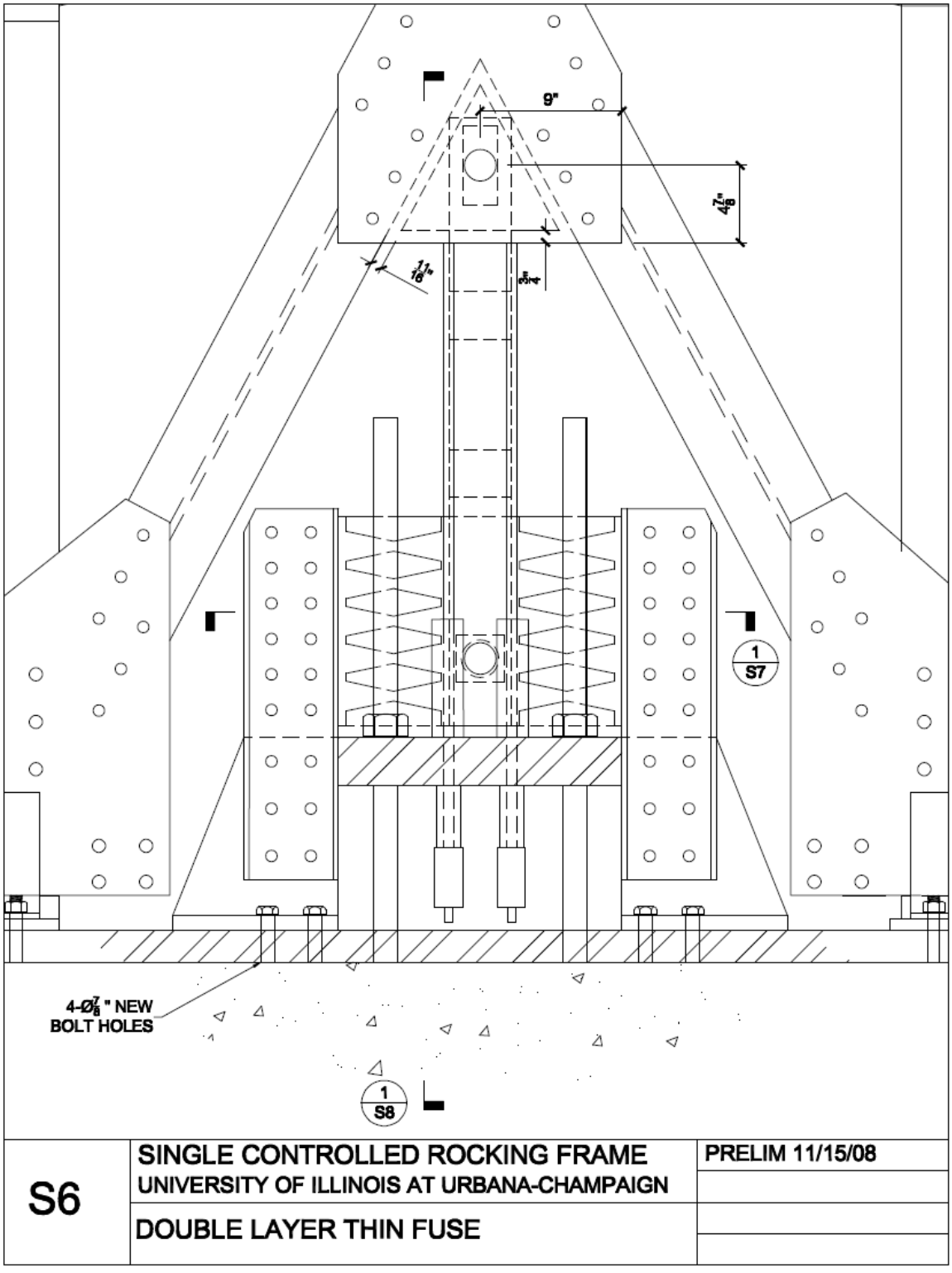

Figure A.75 Design Drawing for the Single Frame Configuration – Specimen B2 Close-Up

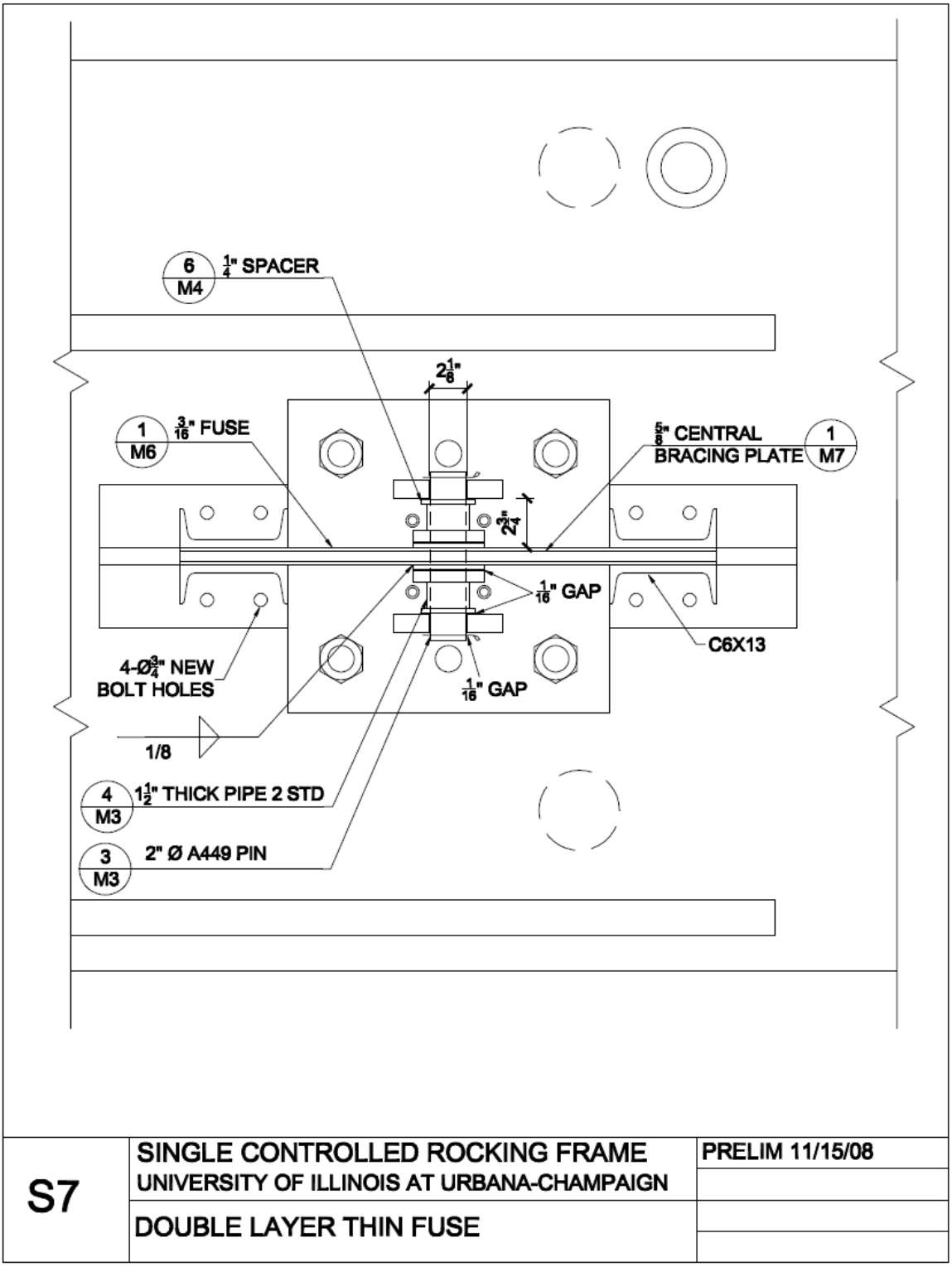

Figure A.76 Design Drawing for the Single Frame Configuration – Specimen B2 Plan

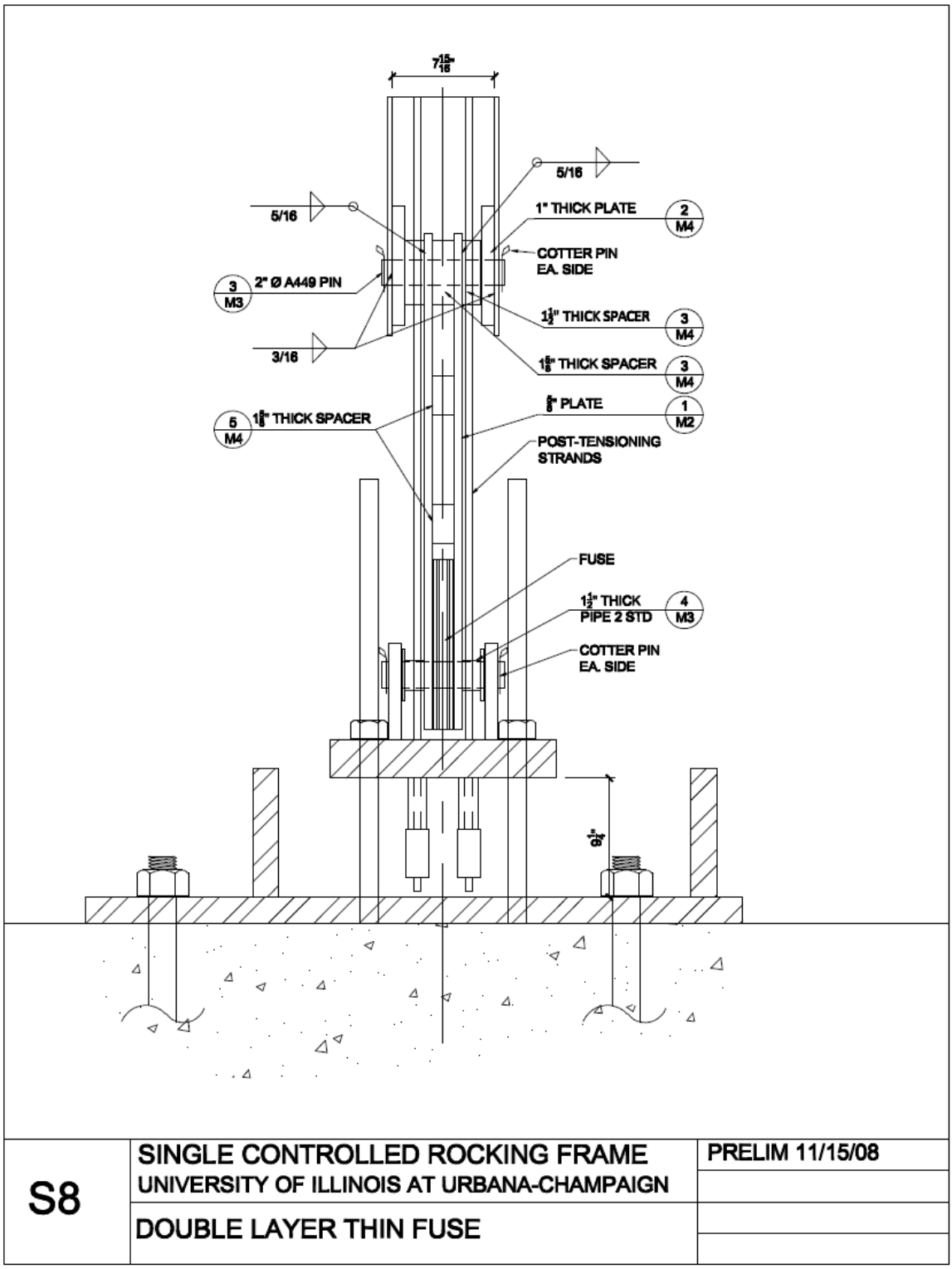

Figure A.77 Design Drawing for the Single Frame Configuration – Specimen B2 Side

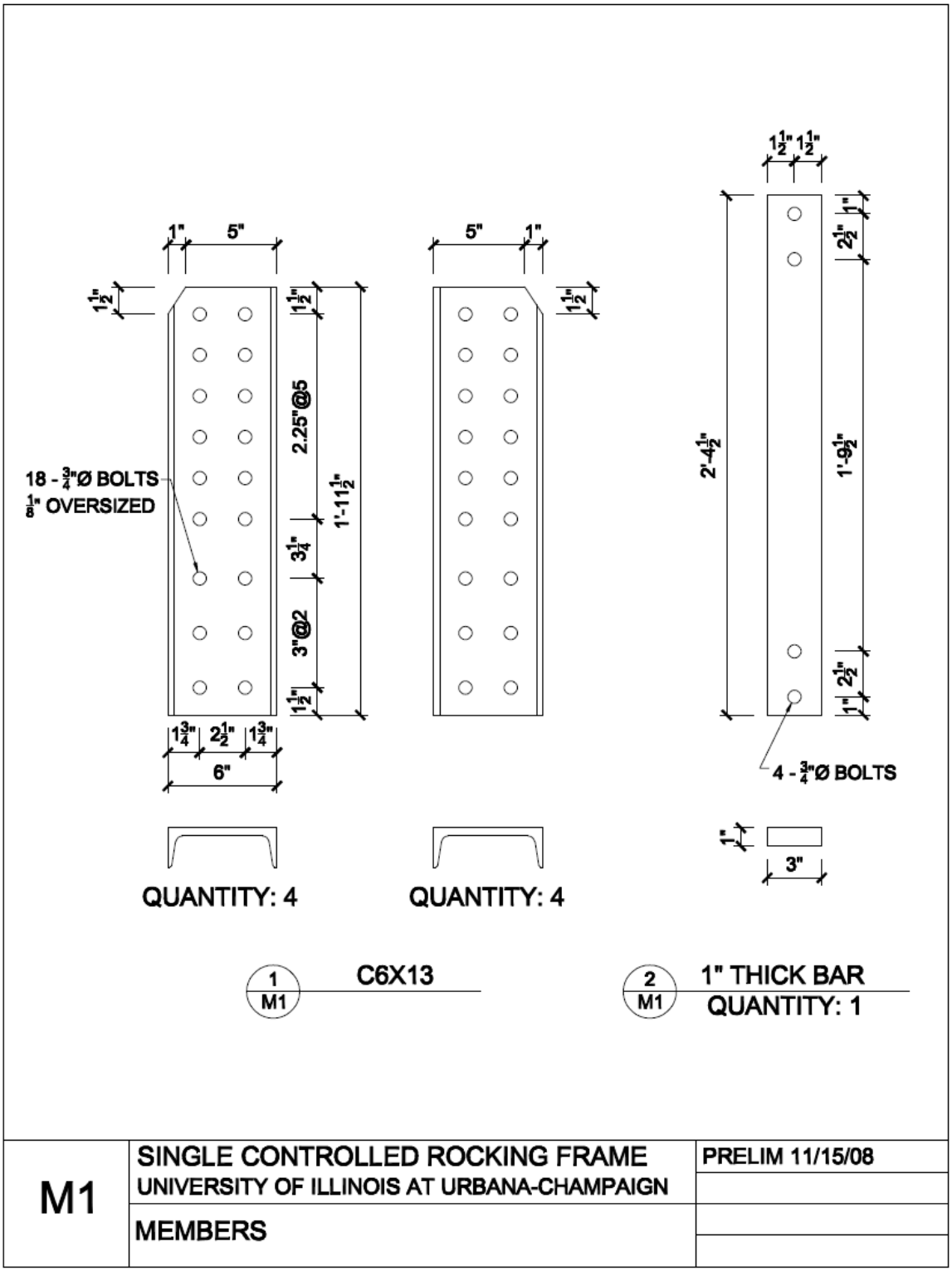

Figure A.78 Design Drawing for the Single Frame Configuration – Fabrication Pieces

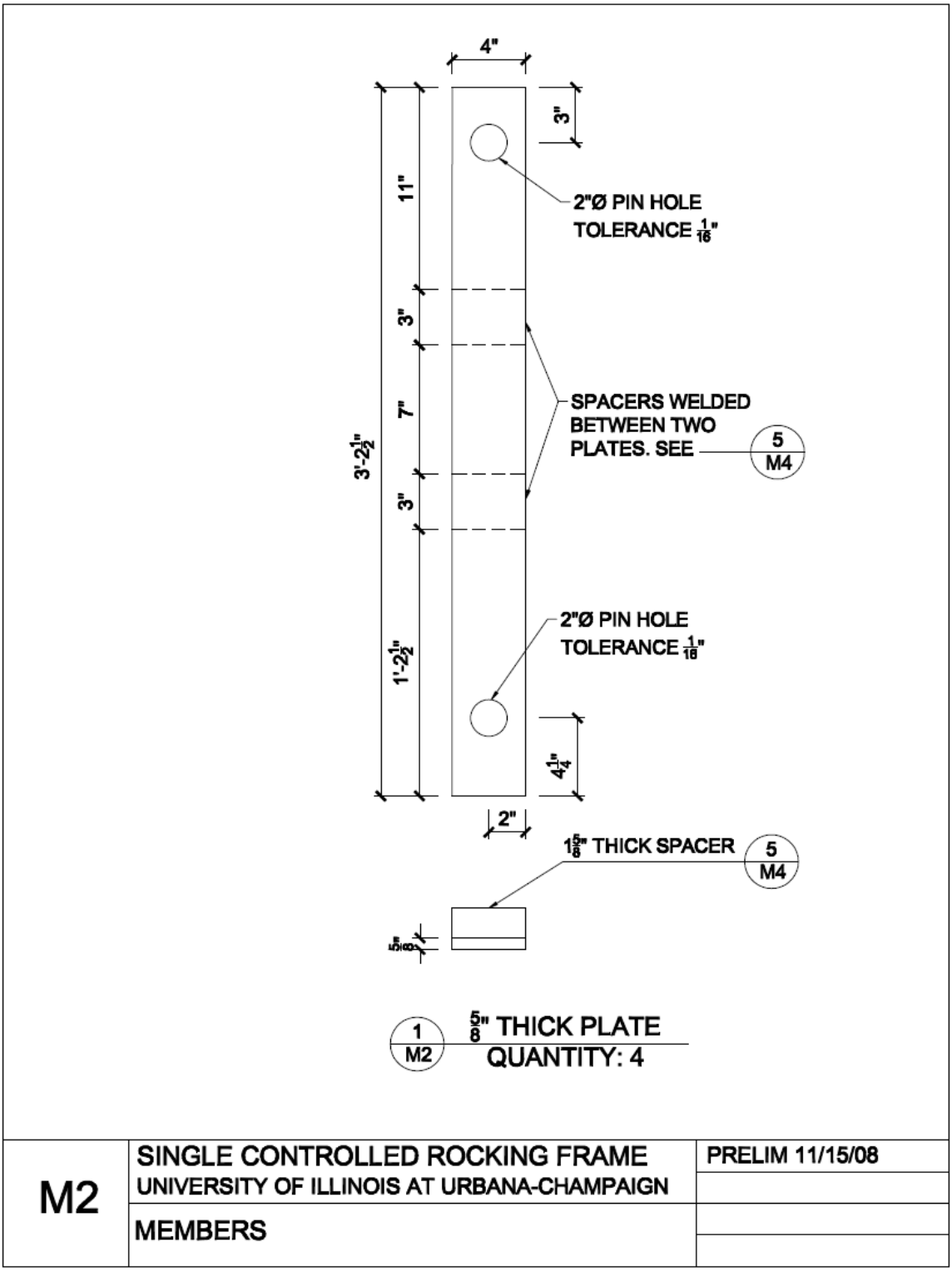

Figure A.79 Design Drawing for the Single Frame Configuration – Fabrication Pieces

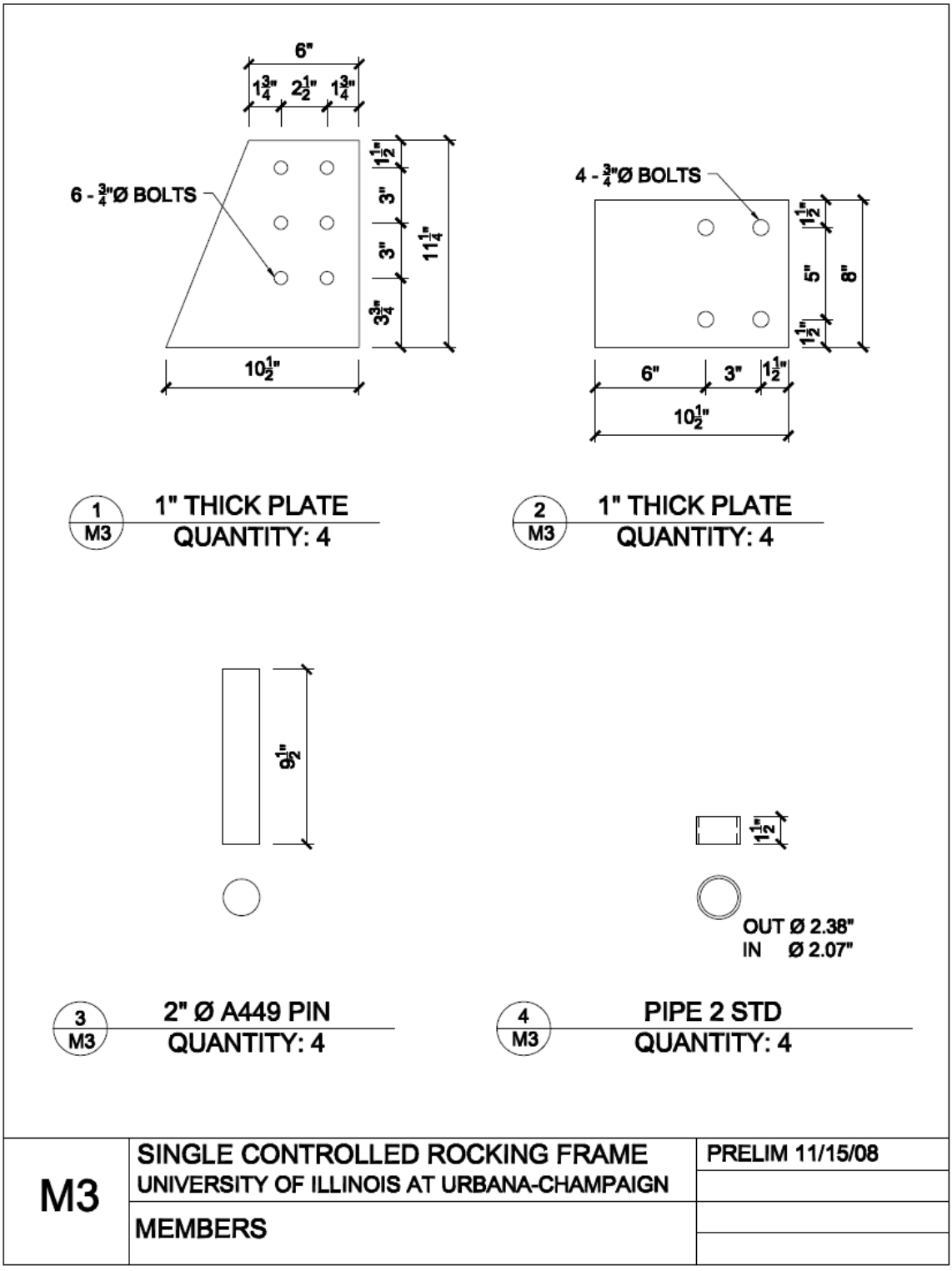

Figure A.80 Design Drawing for the Single Frame Configuration – Fabrication Pieces

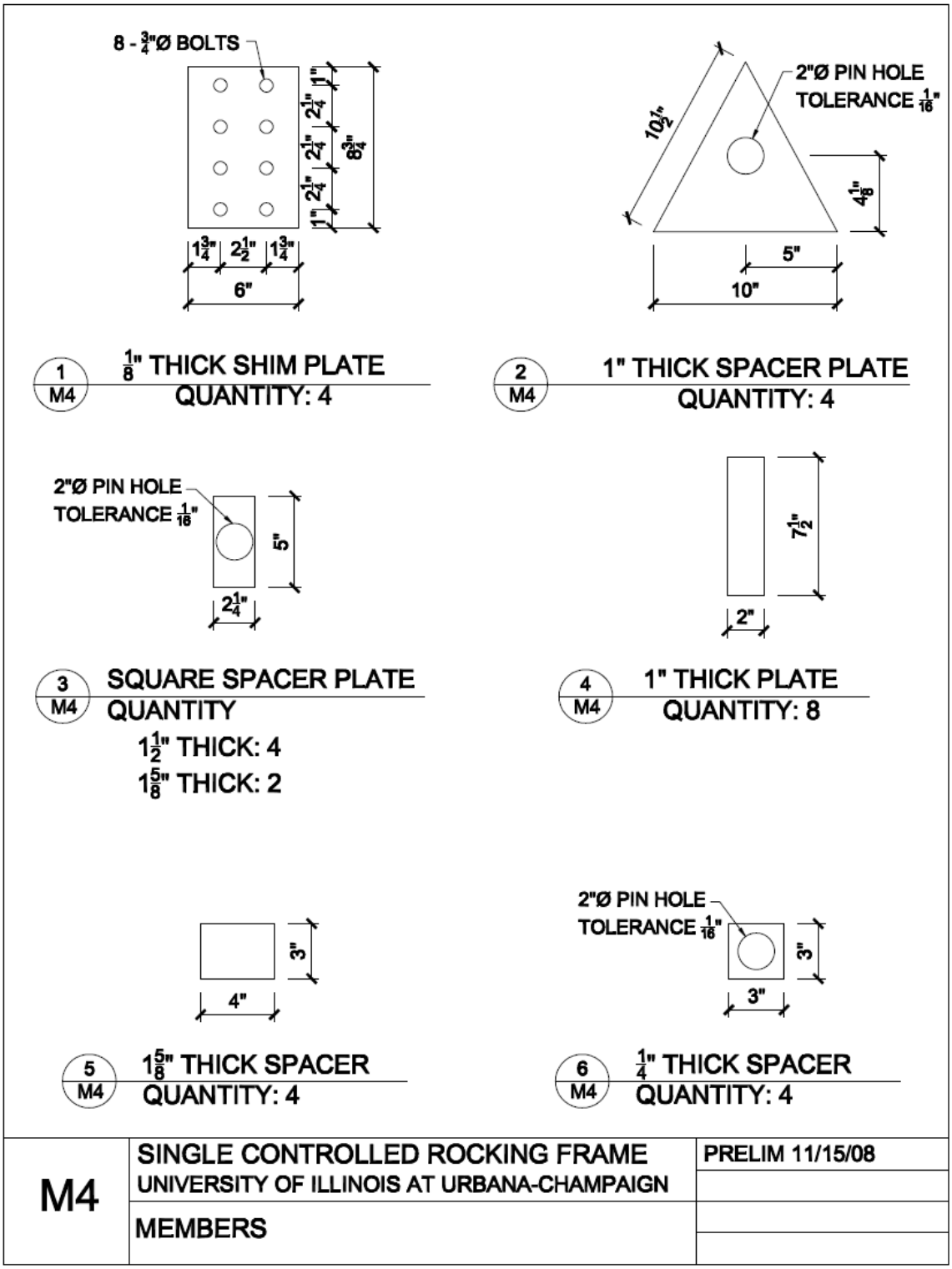

Figure A.81 Design Drawing for the Single Frame Configuration – Fabrication Pieces

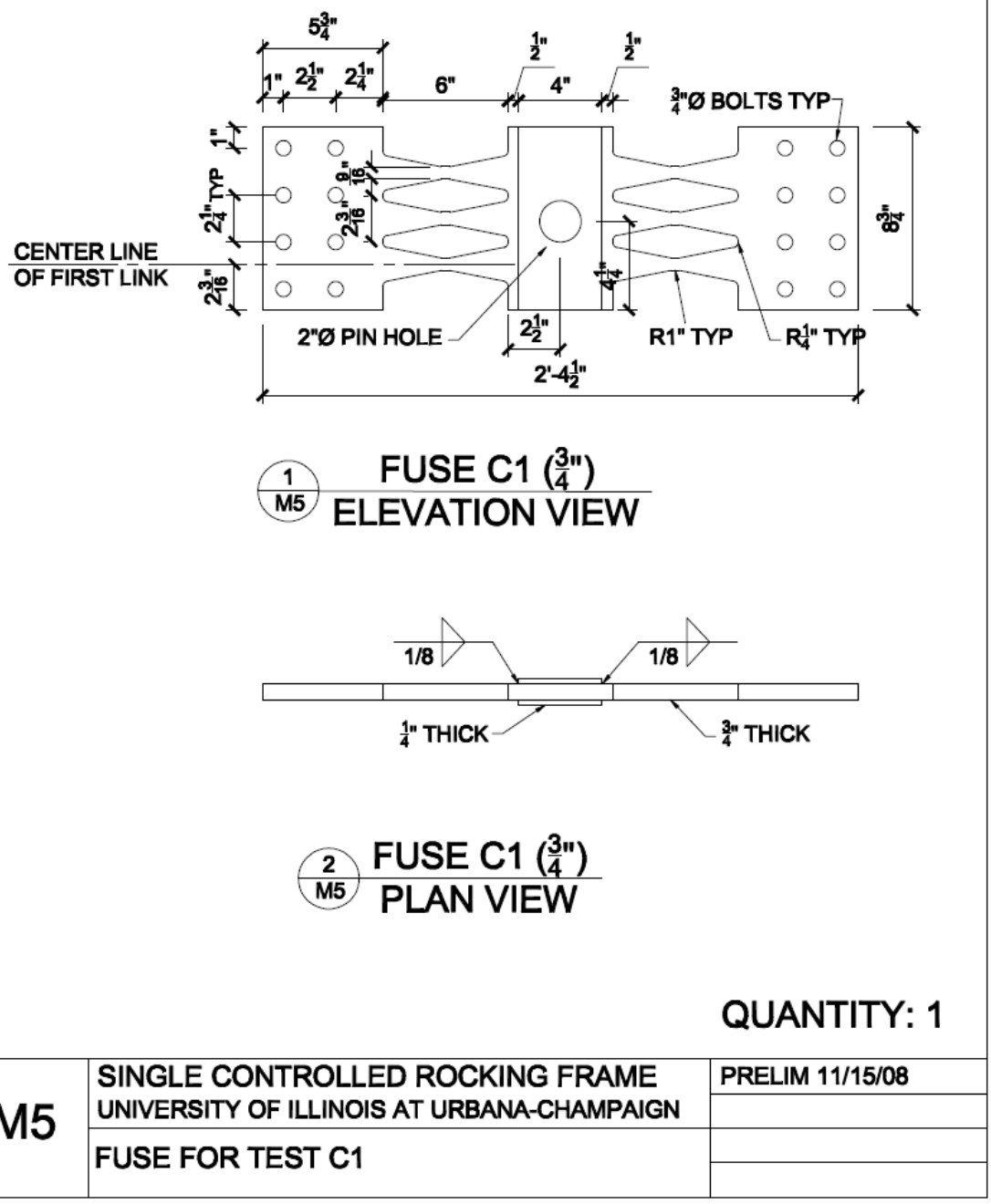

1 / M5 FUSE C1 (3/4") ELEVATION VIEW

2 / M5 FUSE C1 (3/4") PLAN VIEW

Figure A.82 Design Drawing for the Single Frame Configuration – Specimen B1 Fuse

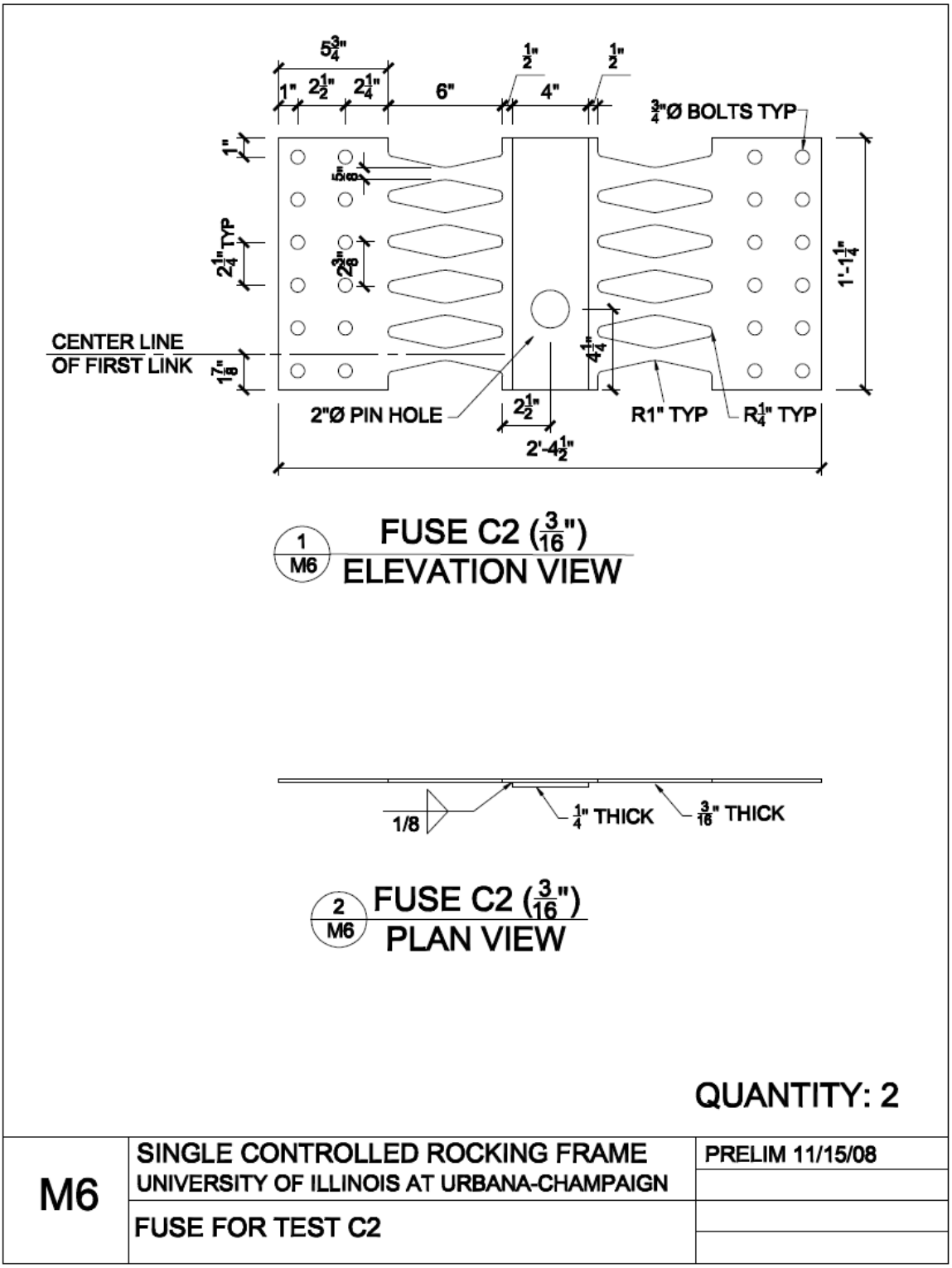

1/M6 FUSE C2 (3/16") ELEVATION VIEW

2/M6 FUSE C2 (3/16") PLAN VIEW

Figure A.83 Design Drawing for the Single Frame Configuration – Specimen B2 Fuse

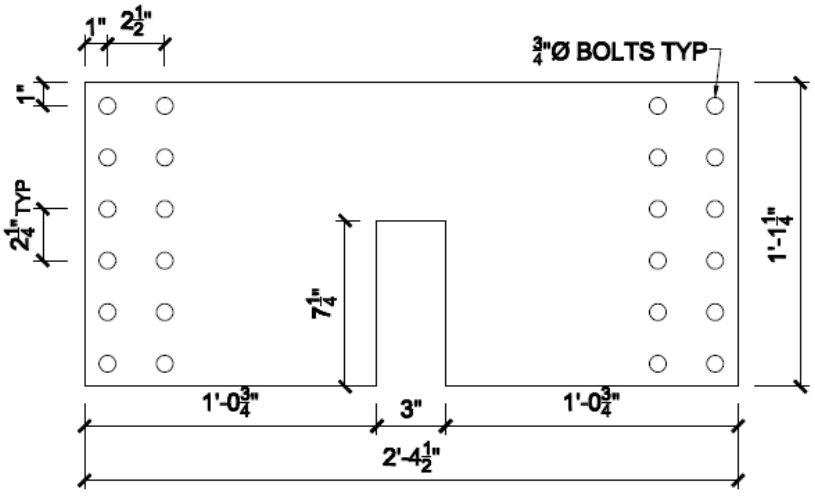

1 M7 FUSE C2 BRACING PLATE
ELEVATION VIEW

2 M7 FUSE C2 BRACING PLATE
PLAN VIEW

QUANTITY: 1

M7	SINGLE CONTROLLED ROCKING FRAME UNIVERSITY OF ILLINOIS AT URBANA-CHAMPAIGN	PRELIM 11/15/08
	BRACING PLATE FOR TEST C2	

Figure A.84 Design Drawing for the Single Frame Configuration – Specimen B2 Plate

A.5 Shop Drawings

This section includes the shop drawings created by MC detailers for the fabrication of the frames at Tefft Iron and Steel.

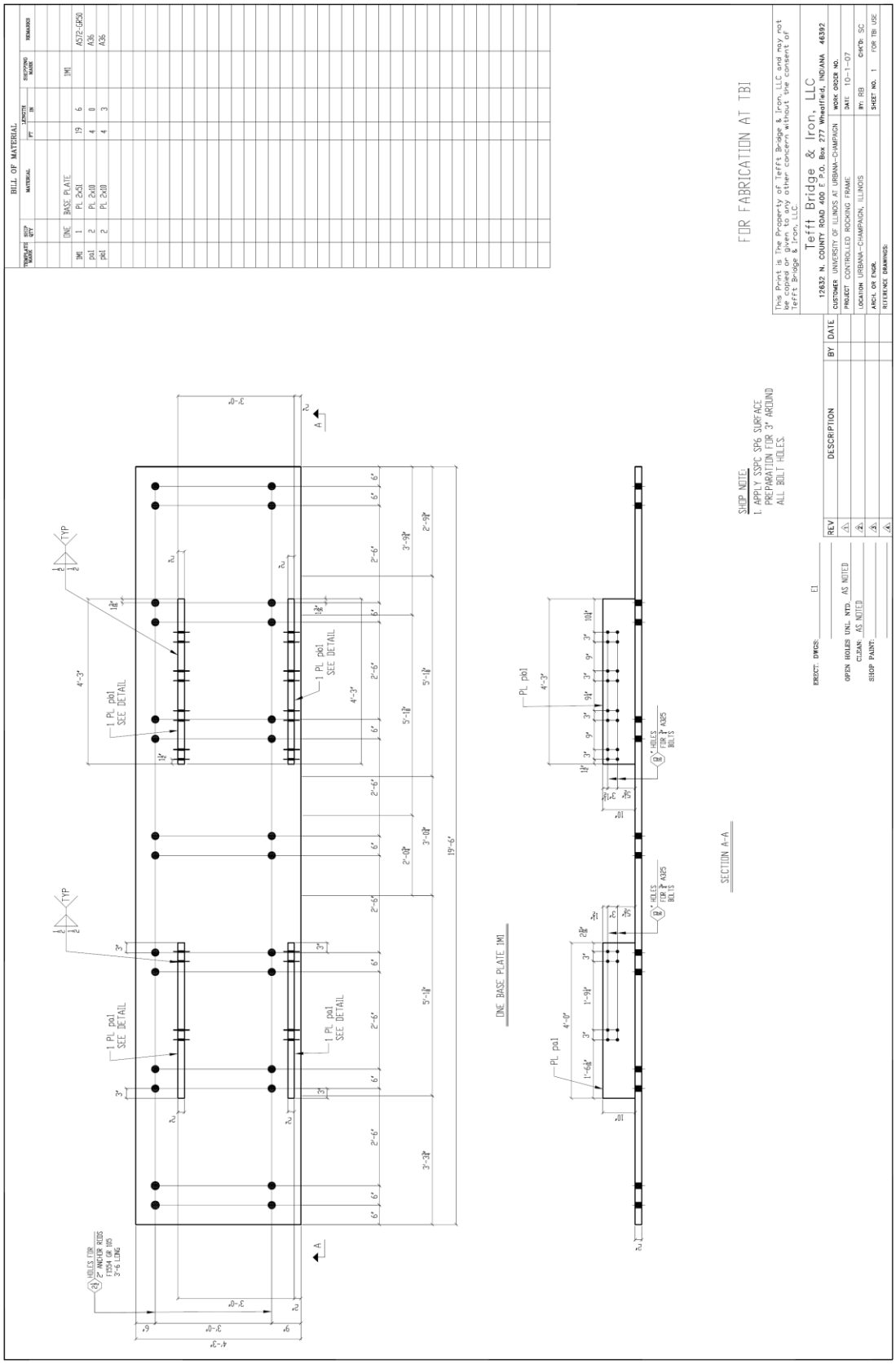

Figure A.85 Shop Drawing for Fabrication – Base Plate

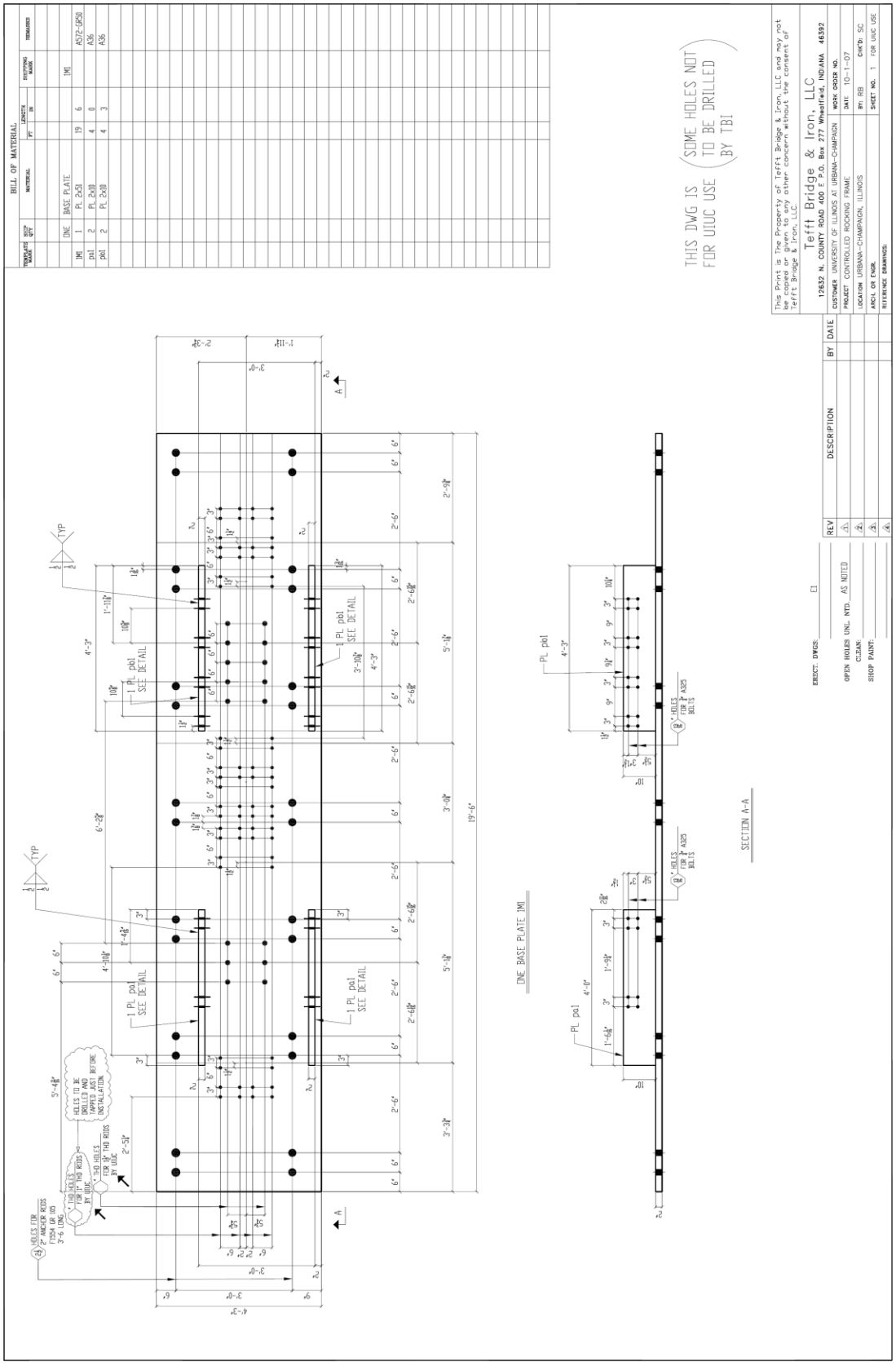

Figure A.86 Shop Drawing for Fabrication – Base Plate

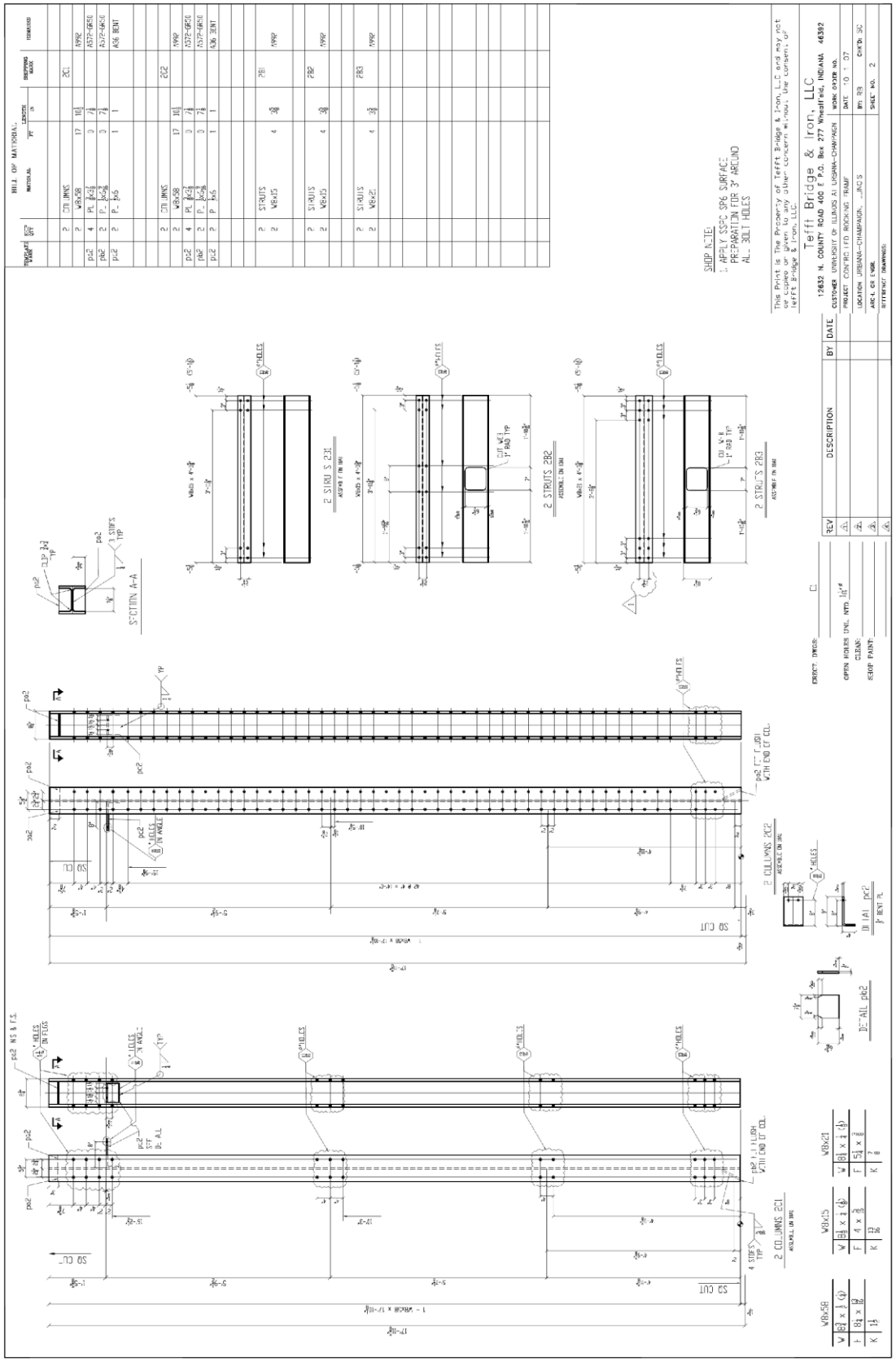

Figure A.87 Shop Drawing for Fabrication - Columns

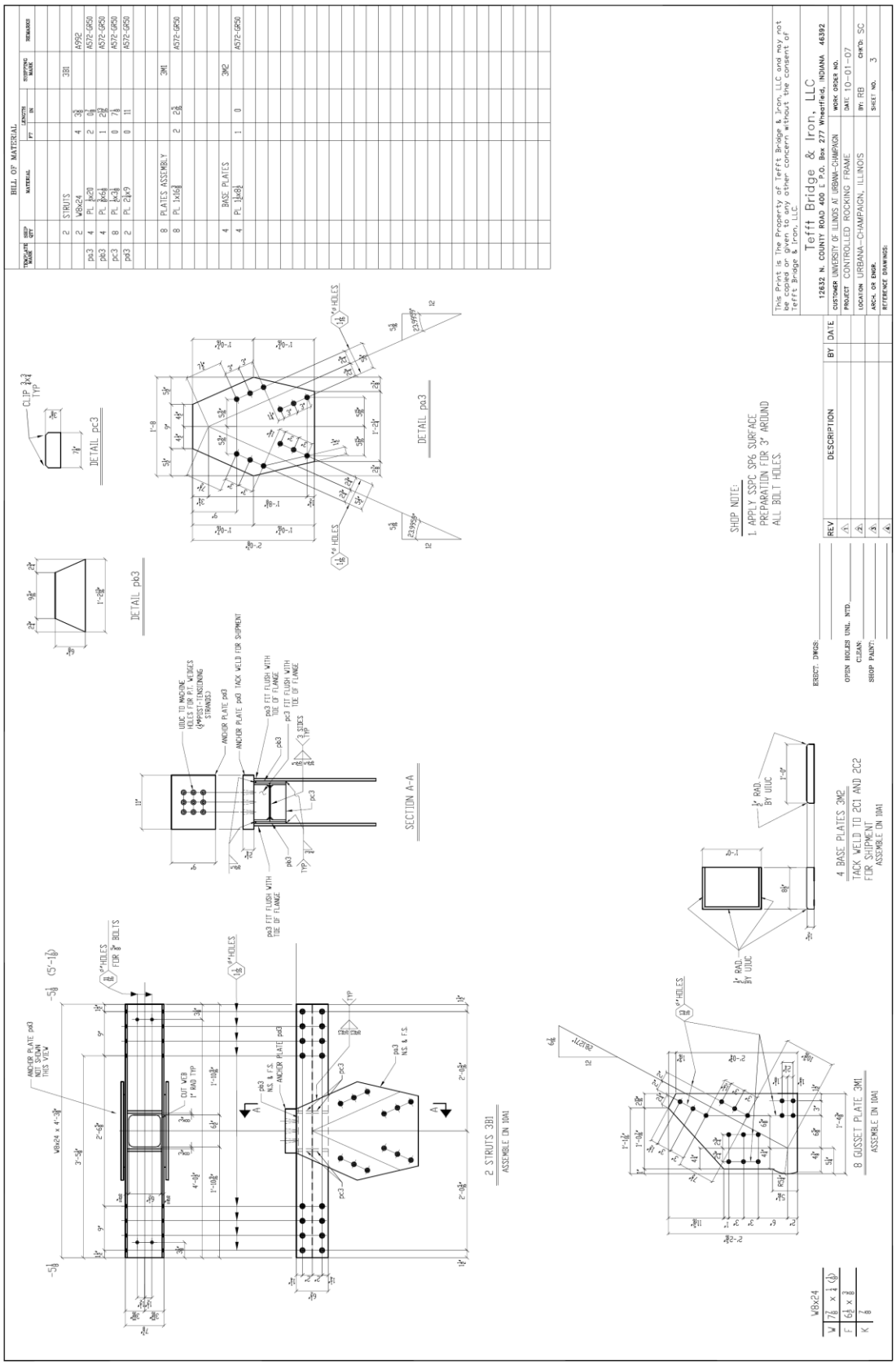

Figure A.88 Shop Drawing for Fabrication - Connections

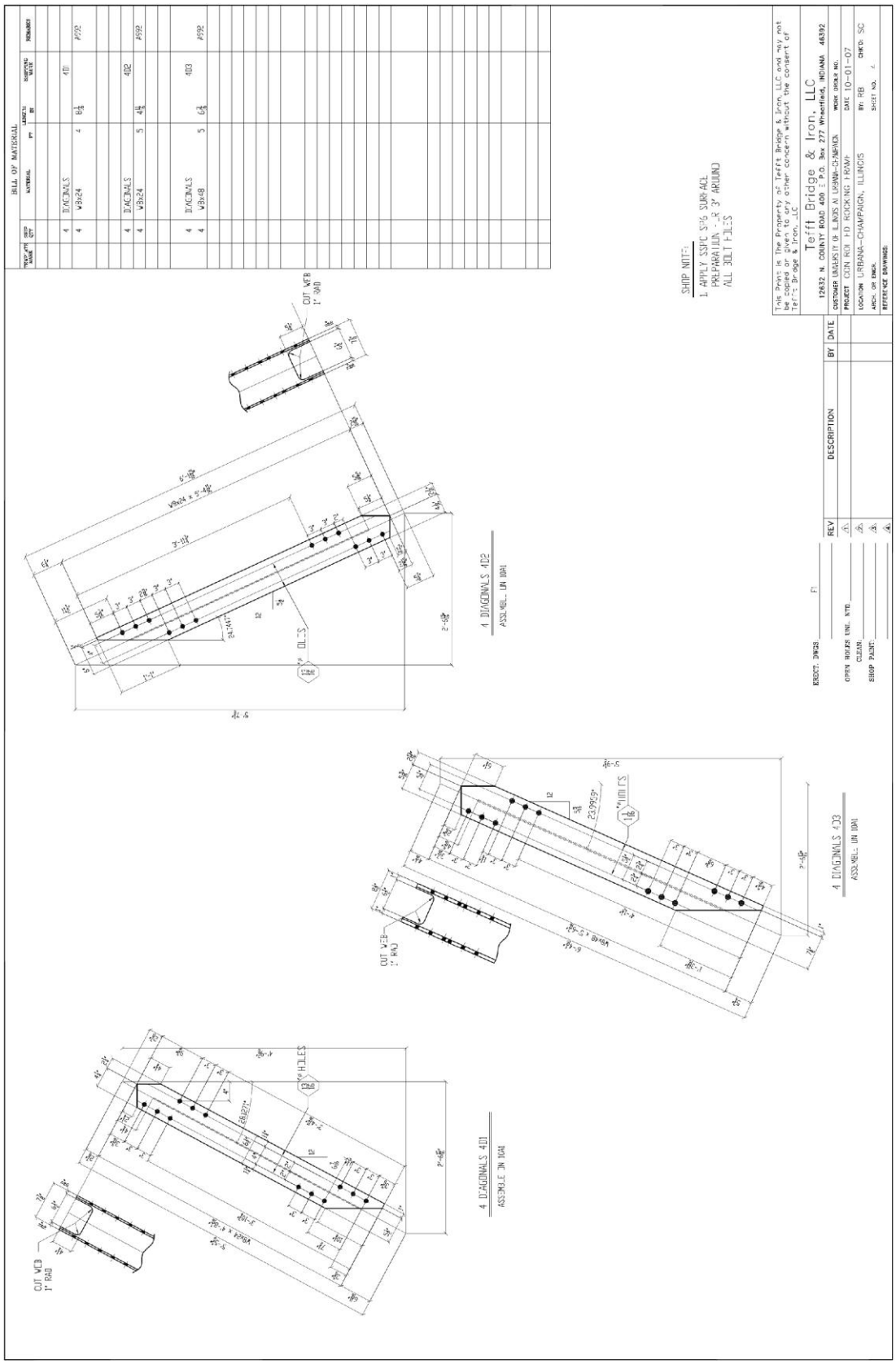

Figure A.89 Shop Drawing for Fabrication - Braces

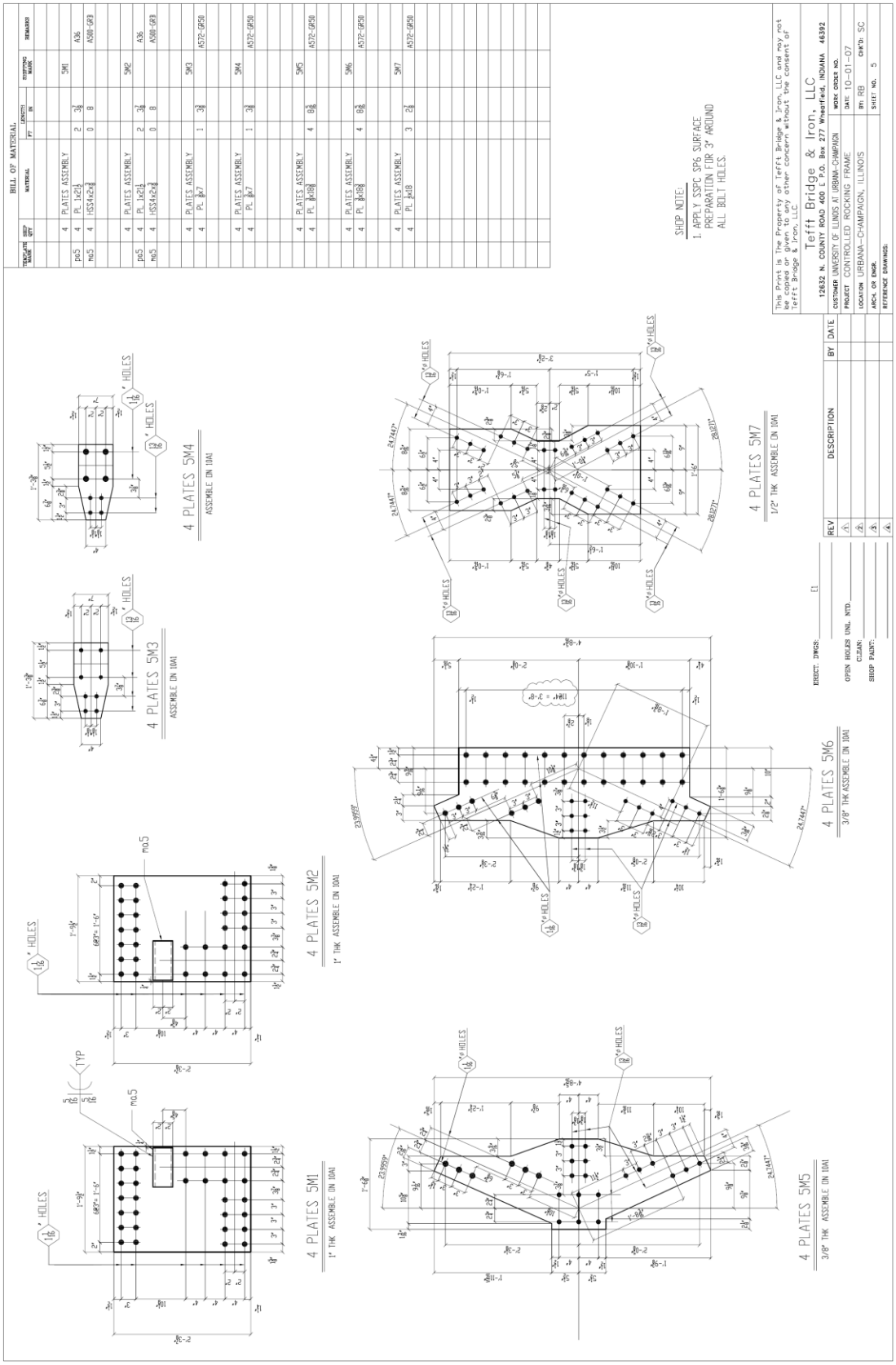

Figure A.90 Shop Drawing for Fabrication – Gusset Plates

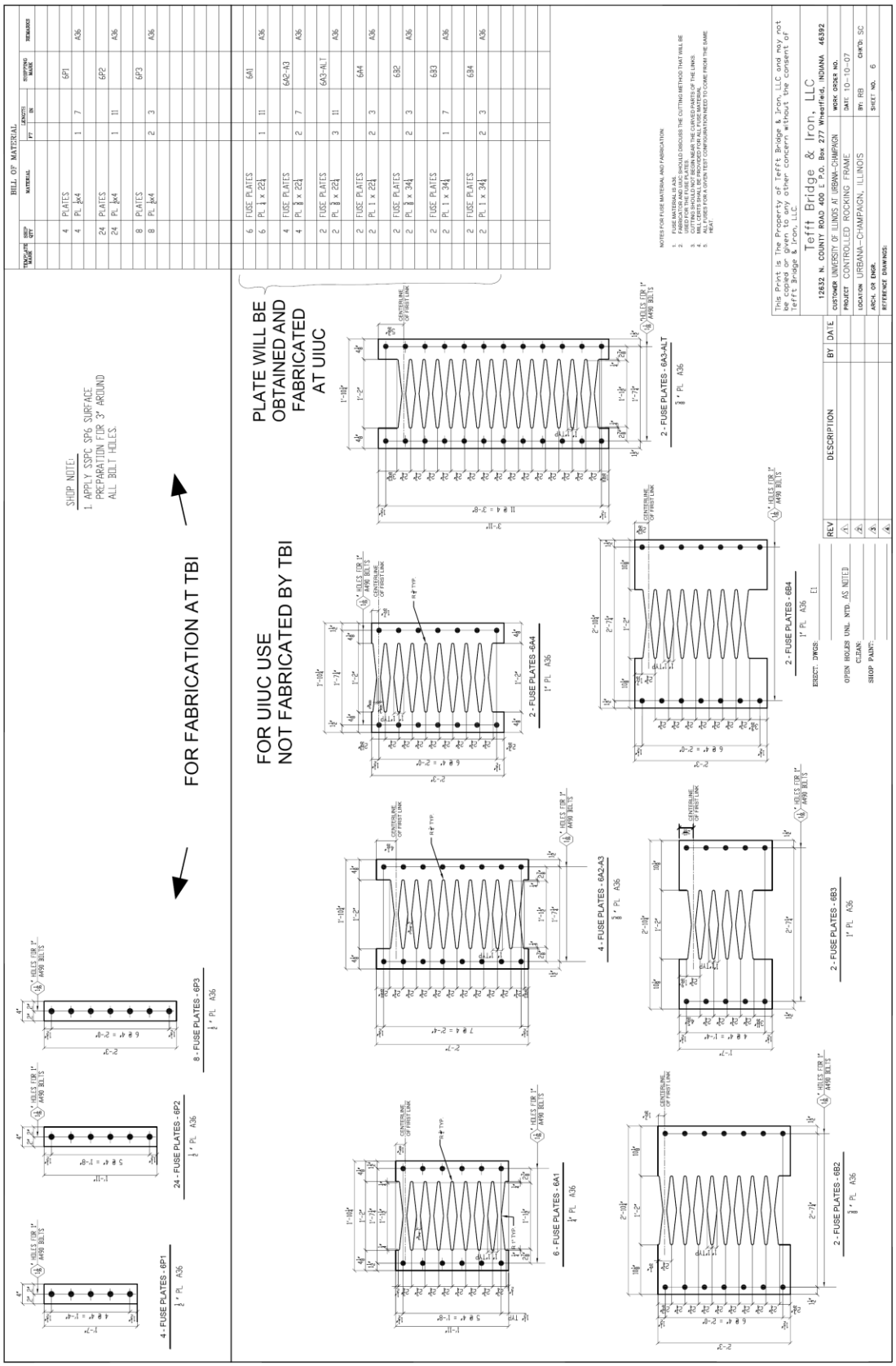

Figure A.91 Shop Drawing for Fabrication - Fuses

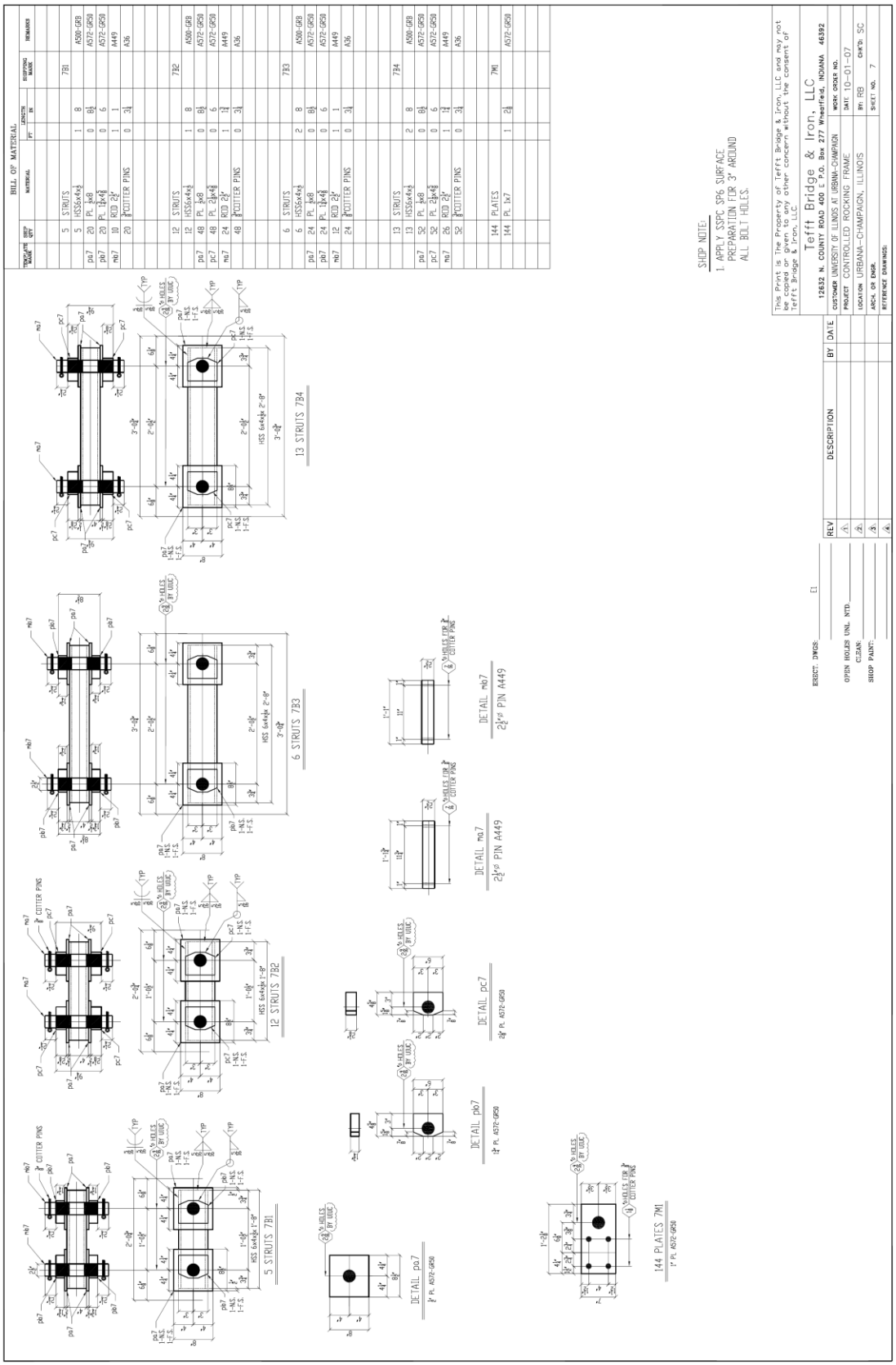

Figure A.92 Shop Drawing for Fabrication - Struts

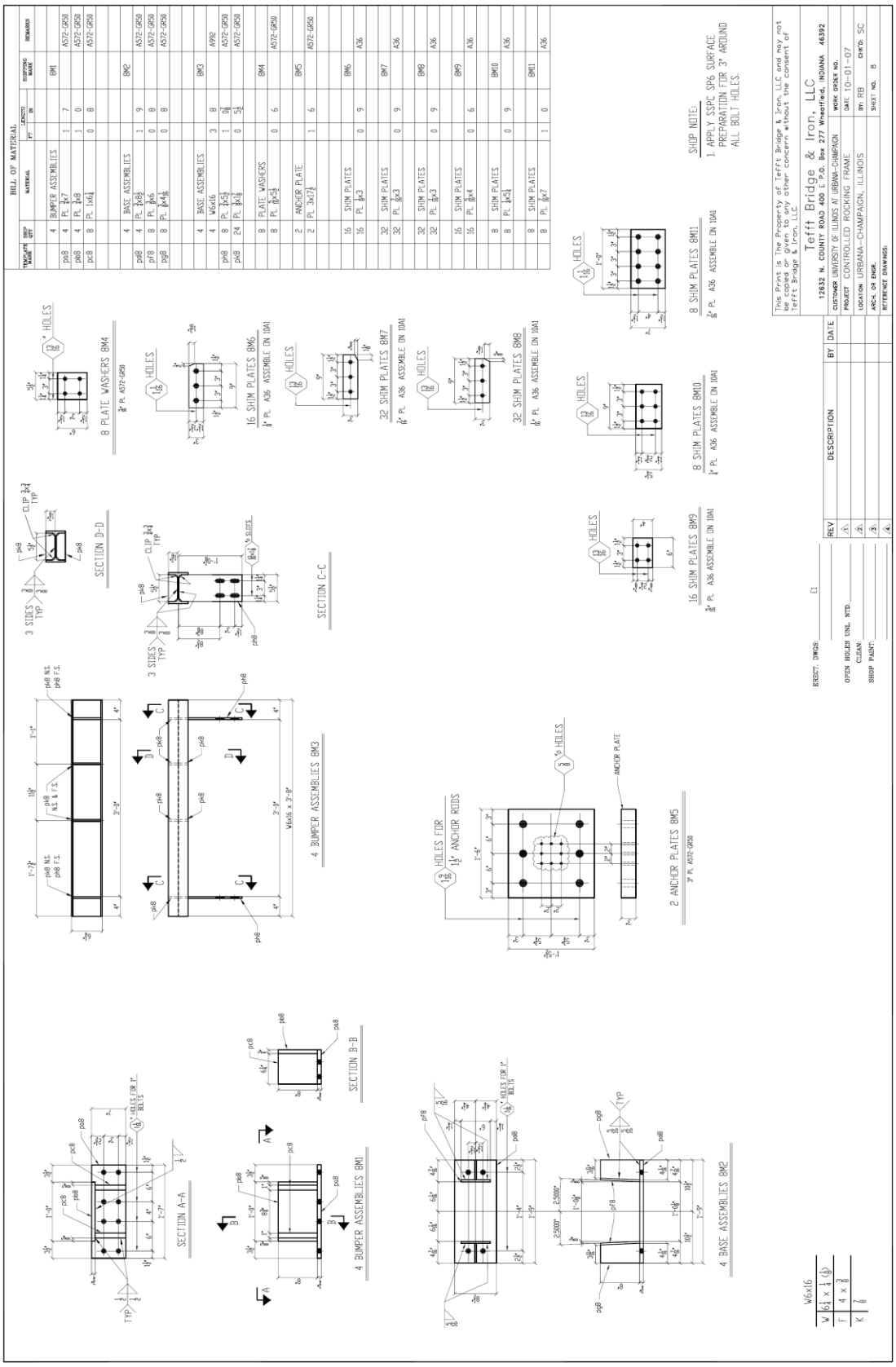

Figure A.93 Shop Drawing for Fabrication – Miscellaneous Pieces

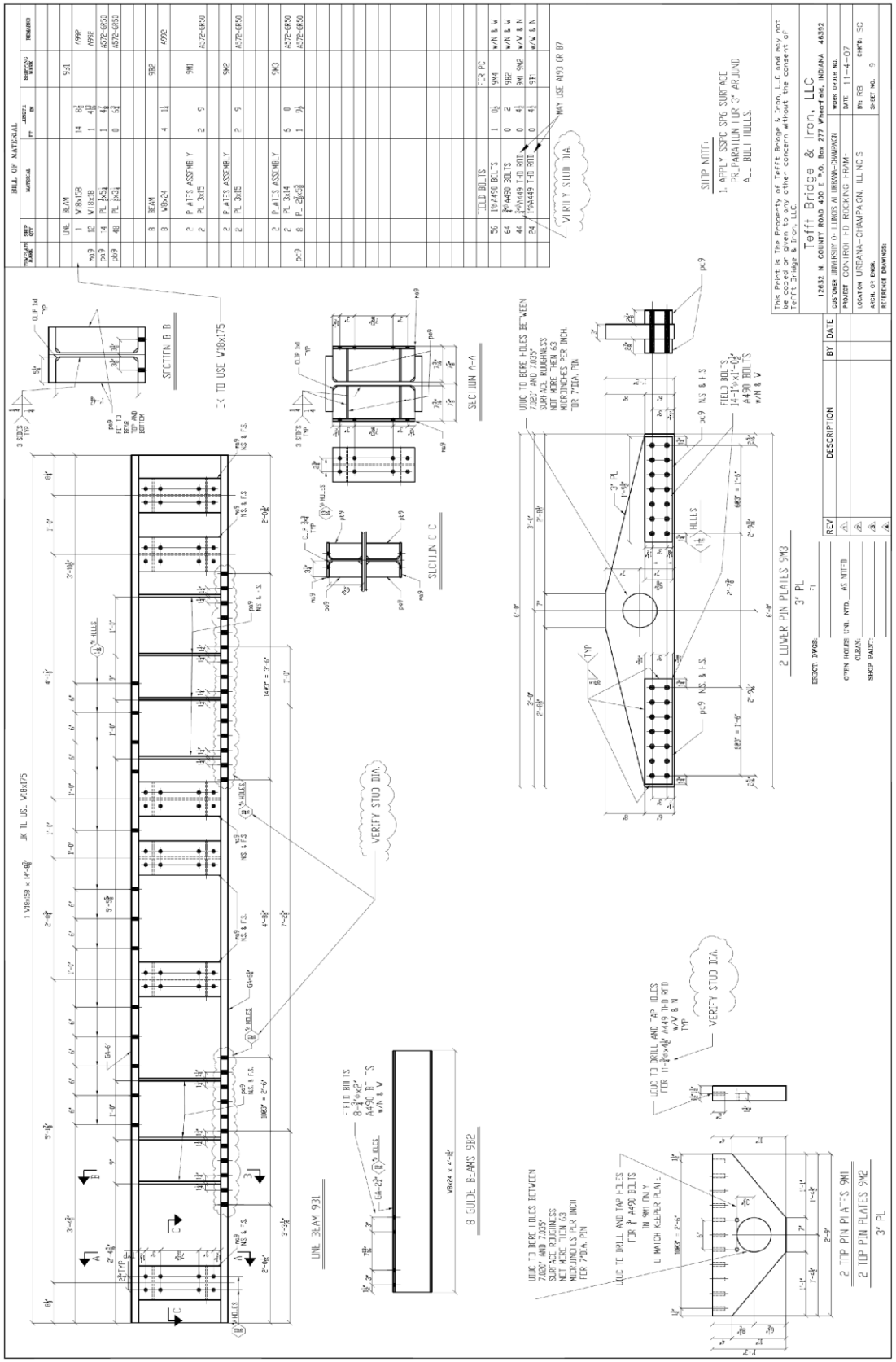

Figure A.94 Shop Drawing for Fabrication – Loading Beam and Top Connections

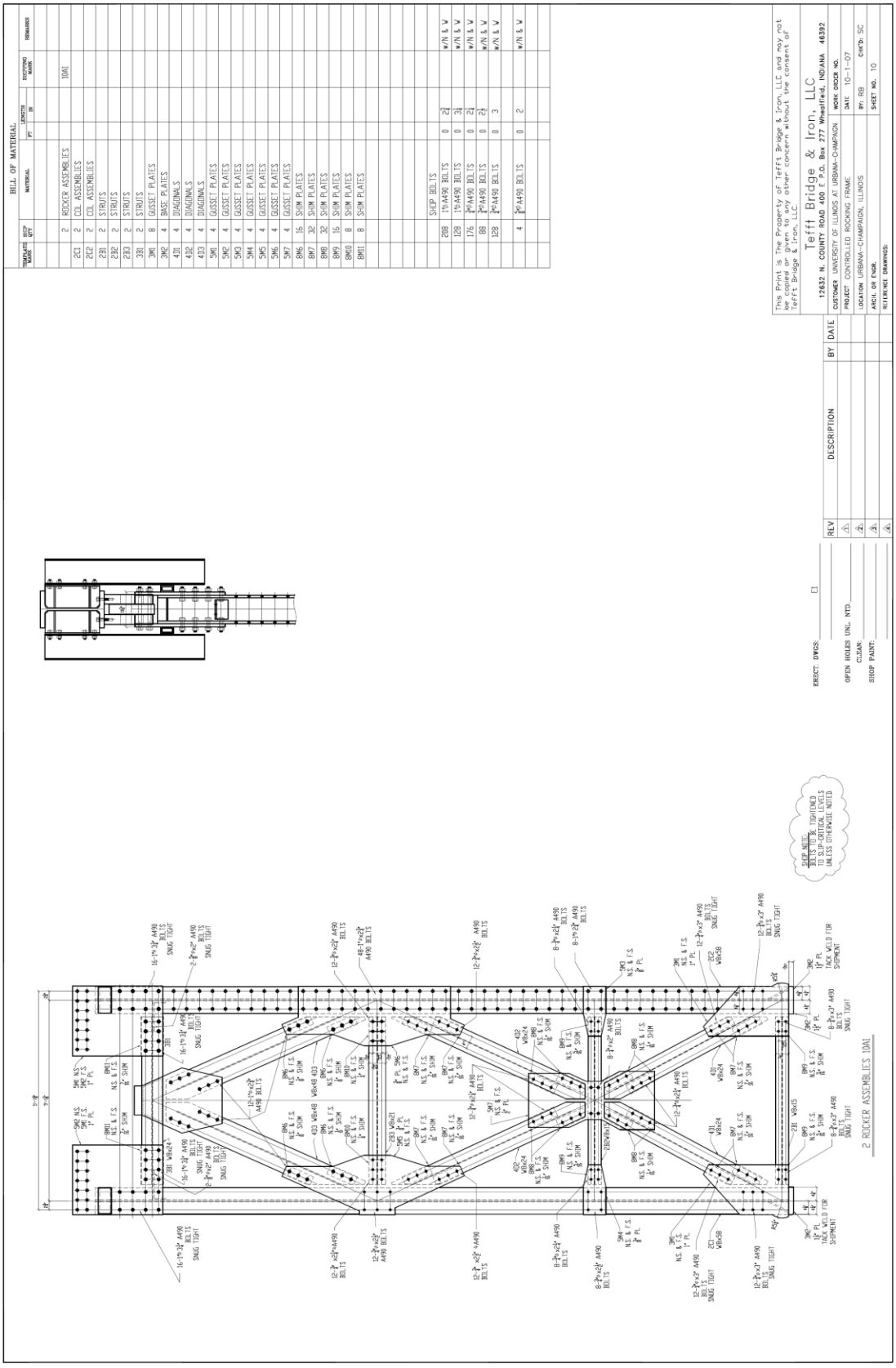

Figure A.95 Shop Drawing for Fabrication – Frame Erection Drawing

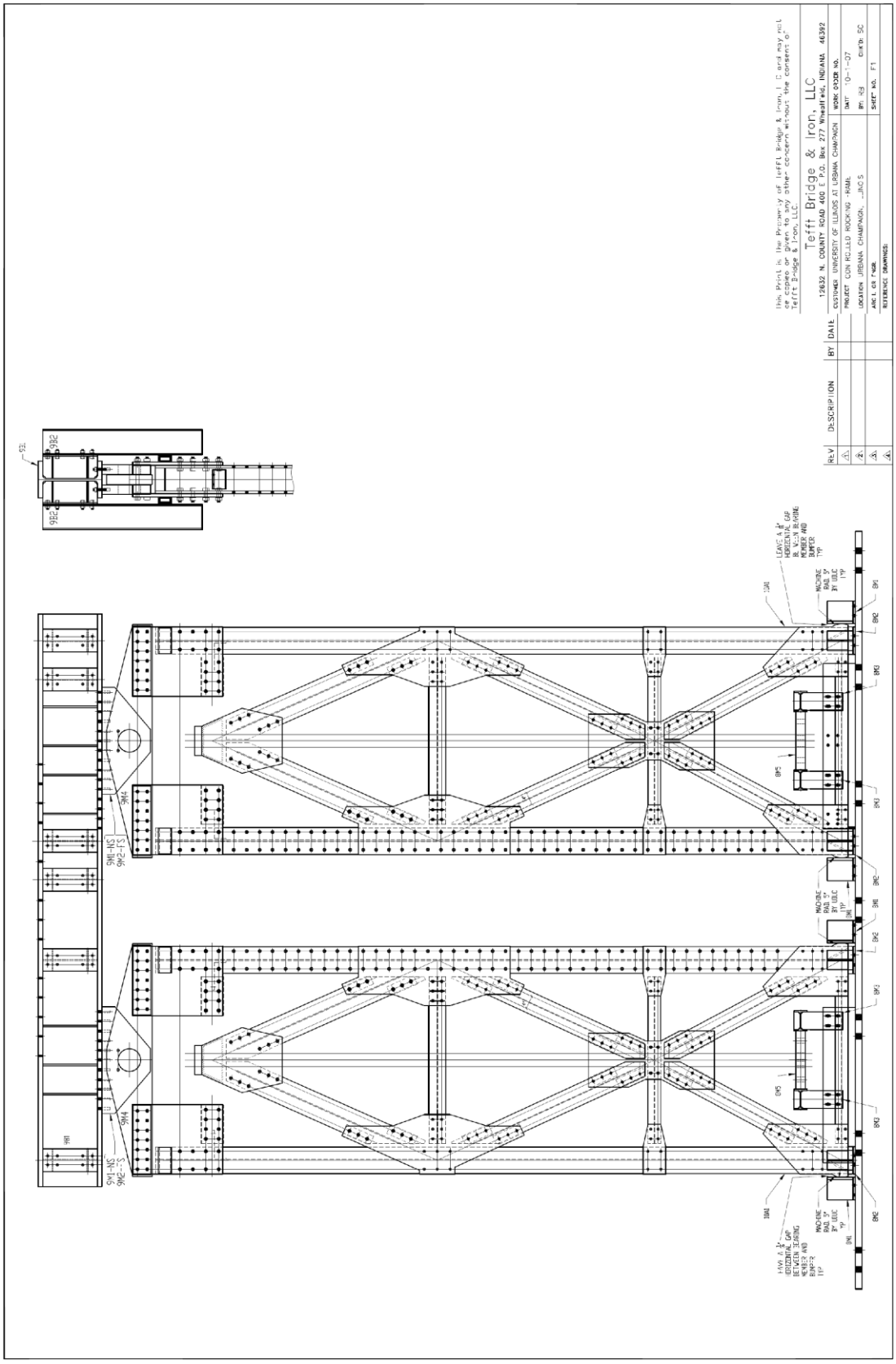

Figure A.96 Shop Drawing for Fabrication – Frames Erection Drawings

A.6 Loading Protocol

This section includes the loading protocol for each test including the displacement targets that were used as part of the control and the target fuse shear strain which was the implicit goal for each displacement step.

Table A.1 Displacement Targets for Specimen A1

Displ-acement Step	Number of Cycles	Fuse Shear Strain Target (in/in)	Expected Roof Drift Ratio (%)	Expected Roof Drift (in)	Expected LBCB Displ. (in)	Expected Post-Tension Strain (in/in)
1	6	0.00375	0.1781	0.356	0.408	0.00288
2	6	0.005	0.2125	0.425	0.488	0.00291
3	6	0.0075	0.3000	0.600	0.685	0.00304
4	6	0.01	0.3625	0.725	0.828	0.00313
5	4	0.015	0.4875	0.975	1.108	0.00333
6	2	0.02	0.6425	1.275	1.448	0.00358
7	2	0.03	0.9175	1.825	2.068	0.00398
8	1	0.04	1.1800	2.350	2.660	0.00435
9	1	0.05	1.4725	2.925	3.310	0.00483
10	1	0.07	2.0225	4.025	4.548	0.00563
11	1	0.09	2.5775	5.125	5.788	0.00651
12	1	0.11	3.1325	6.225	7.033	0.00733
13	3	0.12	3.4100	6.775	7.655	0.00774

Table A.2 Ramp Information for Specimen A1

Load Step	Substep Size (in)	Number of Substeps	Substeps Per Picture	Total Pictures per Ramp	Expected Time Per Quarter Cycle (min)	Expected Time for All Cycles (min)
1	0.018	20	4	5	1.2	28.8
2	0.018	24	4	6	1.4	34.6
3	0.025	24	4	6	1.4	34.6
4	0.025	29	4	7	1.7	41.8
5	0.025	39	4	9	2.3	37.4
6	0.025	51	5	10	3.1	24.5
7	0.025	73	6	12	4.4	35.0
8	0.025	94	7	13	5.6	22.6
9	0.025	117	8	14	7.0	28.1
10	0.025	161	11	14	9.7	38.6
11	0.025	205	13	15	12.3	49.2
12	0.025	249	16	15	14.9	59.8
13	0.025	271	18	15	16.3	195.1
					Total Ramp Times (hours) =	10.5

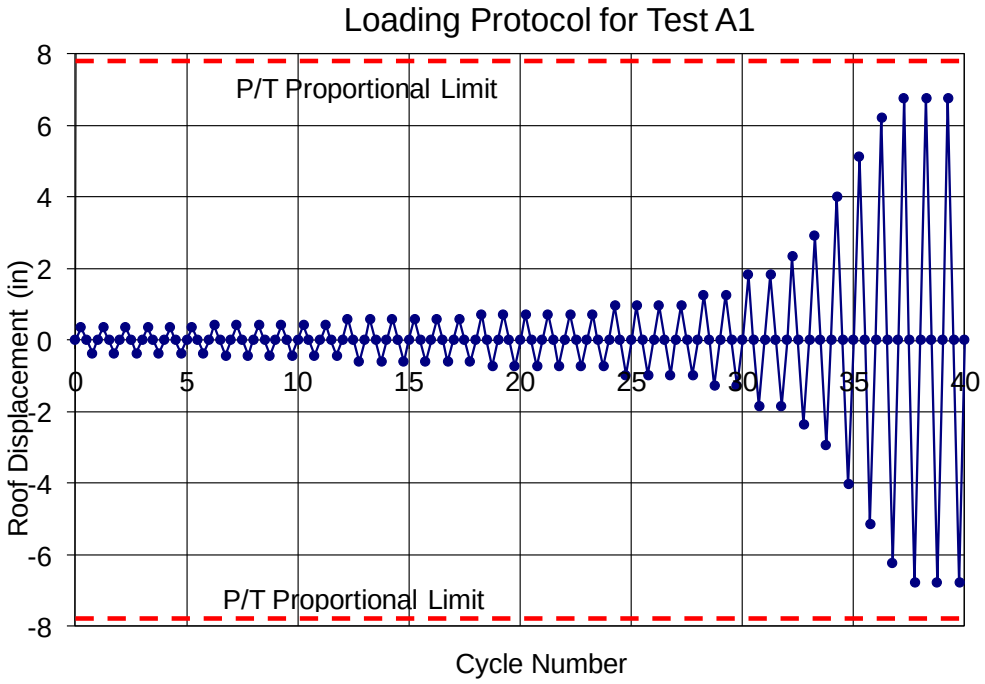

Figure A.97 Roof Displacement Targets for Specimen A1

Table A.3 Displacement Targets for Specimen A2

Displ-acement Step	Number of Cycles	Fuse Shear Strain Target (in/in)	Expected Roof Drift Ratio (%)	Expected Roof Drift (in)	Expected LBCB Displ. (in)	Expected Post-Tension Strain (in/in)
1	6	0.00375	0.1938	0.388	0.446	0.00289
2	6	0.005	0.2250	0.450	0.520	0.00295
3	6	0.0075	0.2750	0.550	0.635	0.00306
4	6	0.01	0.3250	0.650	0.745	0.00308
5	4	0.015	0.4500	0.900	1.030	0.00330
6	4	0.02	0.5667	1.133	1.290	0.00347
7	2	0.03	0.8050	1.600	1.820	0.00380
8	1	0.04	1.0300	2.050	2.355	0.00409
9	1	0.05	1.3725	2.725	3.088	0.00469
10	1	0.07	1.7400	3.450	3.905	0.00521
11	1	0.09	2.2025	4.375	4.950	0.00593
12	1	0.11	2.6783	5.317	6.015	0.00664
13	3	0.13	3.1325	6.225	7.038	0.00735

Table A.4 Ramp Information for Specimen A2

Load Step	Substep Size (in)	Number of Substeps	Substeps Per Picture	Total Pictures per Ramp	Expected Time Per Quarter Cycle (min)	Expected Time for All Cycles (min)
1	0.019	21	7	3	1.3	30.2
2	0.022	21	7	3	1.3	30.2
3	0.02	28	7	4	1.7	40.3
4	0.024	28	7	4	1.7	40.3
5	0.023	40	8	5	2.4	38.4
6	0.0252	45	9	5	2.7	43.2
7	0.0268	60	10	6	3.6	28.8
8	0.0258	80	10	8	4.8	19.2
9	0.0248	110	10	11	6.6	26.4
10	0.0266	130	10	13	7.8	31.2
11	0.0258	170	10	17	10.2	40.8
12	0.0254	210	10	21	12.6	50.4
13	0.0249	250	10	25	15.0	180.0
					Total Ramp Times (hours) =	10.0

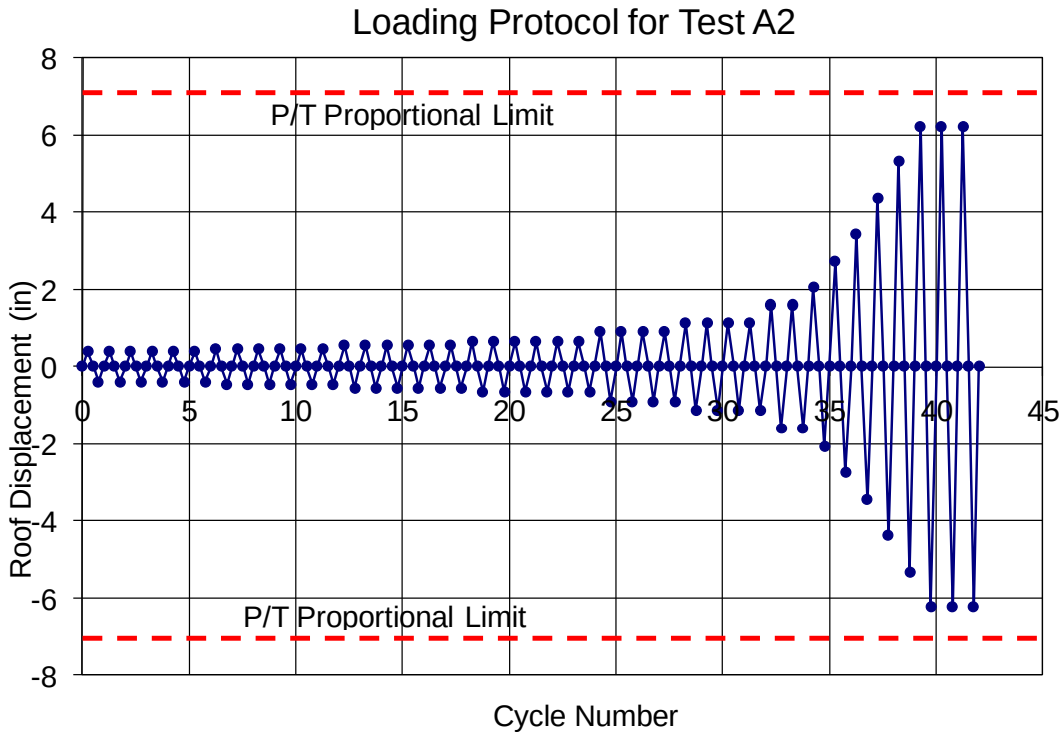

Figure A.98 Roof Displacement Targets for Specimen A2

Table A.5 Displacement Targets for Specimen A3

Displ-acement Step	Number of Cycles	Fuse Shear Strain Target (in/in)	Expected Roof Drift Ratio (%)	Expected Roof Drift (in)	Expected LBCB Displ. (in)	Expected Post-Tension Strain (in/in)
1	6	0.00375	0.18	0.356	0.412	0.0029
2	6	0.005	0.20	0.400	0.460	0.0029
3	6	0.0075	0.24	0.483	0.552	0.0030
4	6	0.01	0.30	0.600	0.680	0.0031
5	4	0.015	0.43	0.850	0.965	0.0033
6	4	0.02	0.53	1.050	1.193	0.0034
7	2	0.03	0.77	1.533	1.738	0.0038
8	1	0.04	1.01	2.000	2.265	0.0041
9	1	0.05	1.24	2.450	2.770	0.0045
10	1	0.07	1.70	3.375	3.813	0.0052
11	1	0.09	2.17	4.300	4.855	0.0059
12	1	0.11	2.63	5.225	5.903	0.0066
13	3	0.13	3.08	6.125	6.918	0.0073

Table A.6 Ramp Information for Specimen A3

Load Step	Substep Size (in)	Number of Substeps	Substeps Per Picture	Total Pictures per Ramp	Expected Time Per Quarter Cycle (min)	Expected Time for All Cycles (min)
1	0.02	18	6	3	1.1	25.9
2	0.023	18	6	3	1.1	25.9
3	0.024	21	7	3	1.3	30.2
4	0.022	28	7	4	1.7	40.3
5	0.0245	35	7	5	2.1	33.6
6	0.0252	42	7	6	2.5	40.3
7	0.024	64	8	8	3.8	30.7
8	0.0249	81	9	9	4.9	19.4
9	0.0247	100	10	10	6.0	24.0
10	0.026	130	10	13	7.8	31.2
11	0.0253	170	10	17	10.2	40.8
12	0.0262	200	10	20	12.0	48.0
13	0.0256	240	10	24	14.4	172.8
					Total Ramp Times (hours) =	9.4

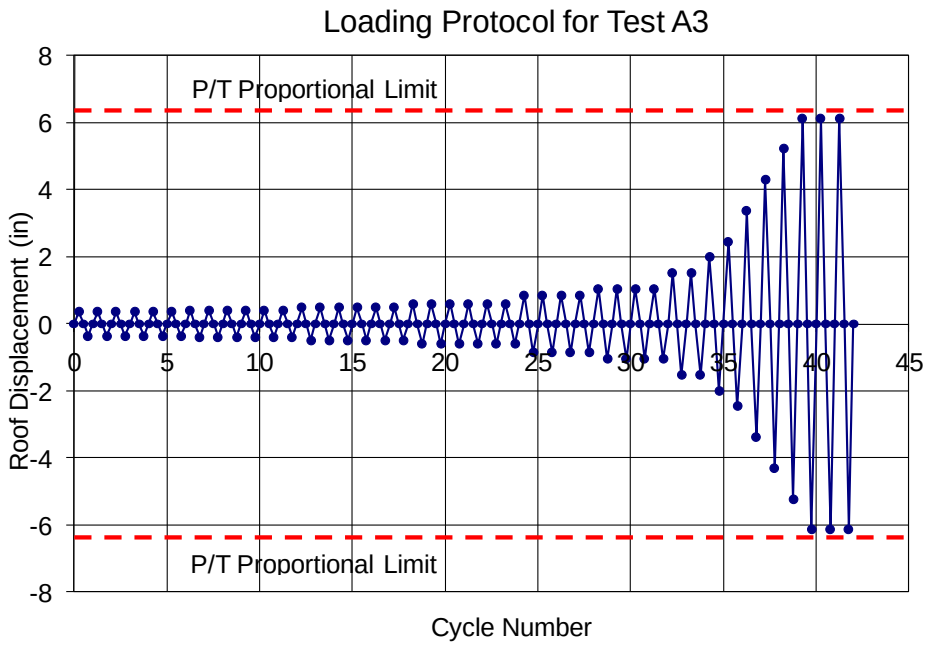

Figure A.99 Roof Displacement Targets for Specimen A3

Table A.7 Displacement Targets for Specimen A4

Displ-acement Step	Number of Cycles	Fuse Shear Strain Target (in/in)	Expected Roof Drift Ratio (%)	Expected Roof Drift (in)	Expected LBCB Displ. (in)	Expected Post-Tension Strain (in/in)
1	6	0.00375	0.22%	0.429	0.499	0.0028
2	6	0.005	0.25%	0.493	0.571	0.0028
3	6	0.0075	0.30%	0.600	0.692	0.0029
4	6	0.01	0.36%	0.707	0.813	0.0030
5	4	0.015	0.47%	0.943	1.078	0.0032
6	4	0.02	0.59%	1.173	1.338	0.0034
7	2	0.03	0.82%	1.638	1.864	0.0037
8	1	0.04	1.06%	2.109	2.396	0.0041
9	1	0.05	1.30%	2.580	2.927	0.0044
10	1	0.07	1.77%	3.510	3.977	0.0051
11	1	0.09	2.23%	4.440	5.027	0.0059
12	1	0.11	2.70%	5.371	6.078	0.0066
13	1	0.13	3.17%	6.308	7.138	0.0073
14	1	0.15	3.64%	7.238	8.188	0.0081
15	3	0.17	4.11%	8.169	9.238	0.0088

Table A.8 Ramp Information for Specimen A4

Load Step	Substep Size (in)	Number of Substeps	Substeps Per Picture	Total Pictures per Ramp	Expected Time Per Quarter Cycle (min)	Expected Time for All Cycles (min)
1	0.018	20	4	5	1.2	28.8
2	0.018	24	4	6	1.4	34.6
3	0.025	24	4	6	1.4	34.6
4	0.025	29	4	7	1.7	41.8
5	0.025	39	4	9	2.3	37.4
6	0.025	51	5	10	3.1	24.5
7	0.025	73	6	12	4.4	35.0
8	0.025	94	7	13	5.6	22.6
9	0.025	117	8	14	7.0	28.1
10	0.025	161	11	14	9.7	38.6
11	0.025	205	13	15	12.3	49.2
12	0.025	249	16	15	14.9	59.8
13	0.025	271	18	15	16.3	195.1
					Total Ramp Times (hours) =	10.5

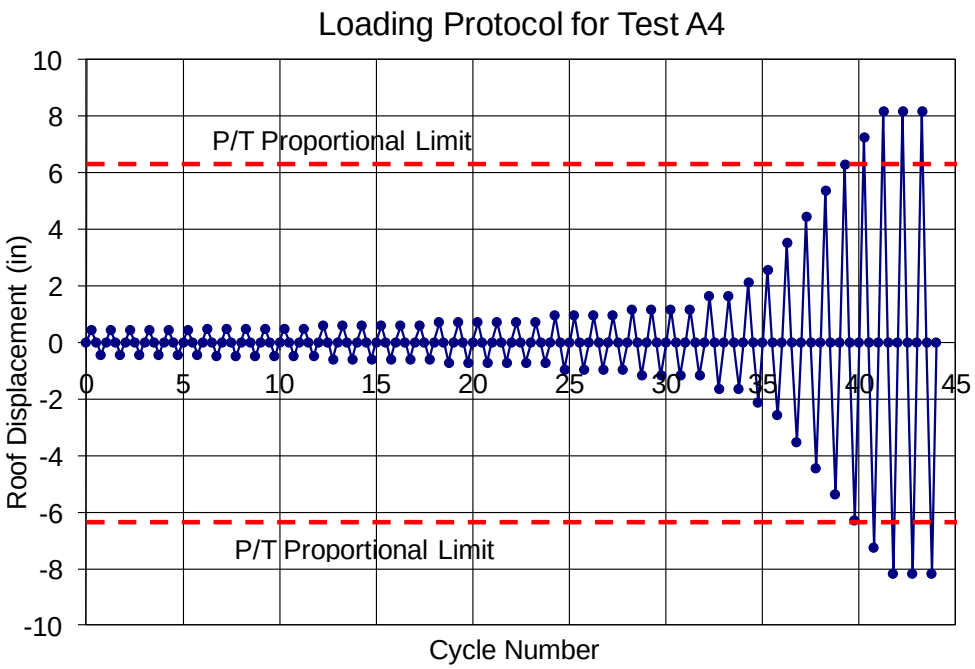

Figure A.100 Roof Displacement Targets for Specimen A4

Table A.9 Trial Runs for Specimen A5

Trial	Specimen A5 Trial Description
1	MCE 0.69 x JMA Kobe
2	1.10 x JMA Kobe
3	1.10 x JMA Kobe

Table A.10 Trial Runs for Specimen A6

Trial	Specimen A6 Trial Description
1	MCE 0.69 x JMA Kobe
2	MCE 0.69 x JMA Kobe with 30% out-of-plane motion
3	1.20 x JMA Kobe

Table A.11 Displacement Targets for Specimen A7

Displ-acement Step	Number of Cycles	Fuse Shear Strain Target (in/in)	Expected Roof Drift Ratio (%)	Expected Roof Drift (in)	Expected LBCB Displ. (in)	Expected Post-Tension Strain (in/in)
1	6	0.00375	0.18%	0.361	0.415	0.0028
2	6	0.005	0.22%	0.441	0.505	0.0029
3	6	0.0075	0.29%	0.575	0.657	0.0030
4	6	0.01	0.36%	0.709	0.808	0.0031
5	4	0.015	0.49%	0.977	1.109	0.0033
6	4	0.02	0.63%	1.245	1.412	0.0035
7	2	0.03	0.90%	1.782	2.018	0.0039
8	1	0.04	1.17%	2.322	2.626	0.0043
9	1	0.05	1.44%	2.864	3.238	0.0047
10	1	0.07	1.99%	3.955	4.470	0.0056
11	1	0.09	2.54%	5.041	5.696	0.0064
12	1	0.11	3.09%	6.135	6.933	0.0072
13	1	0.13	3.64%	7.230	8.172	0.0081
14	3	0.15	4.18%	8.315	9.401	0.0089

Table A.12 Ramp Information for Specimen A7

Load Step	Substep Size (in)	Number of Substeps	Substeps Per Picture	Total Pictures per Ramp	Expected Time Per Quarter Cycle (min)	Expected Time for All Cycles (min)
1	0.019	20	5	4	1.2	28.8
2	0.023	20	5	4	1.2	28.8
3	0.024	24	6	4	1.4	34.6
4	0.024	30	6	5	1.8	43.2
5	0.0235	42	7	6	2.5	40.3
6	0.0255	49	7	7	2.9	47.0
7	0.028	64	8	8	3.8	30.7
8	0.0288	81	9	9	4.9	19.4
9	0.0261	110	10	11	6.6	26.4
10	0.0265	150	10	15	9.0	36.0
11	0.0266	190	10	19	11.4	45.6
12	0.0267	230	10	23	13.8	55.2
13	0.0268	270	10	27	16.2	64.8
14	0.026	320	10	32	19.2	230.4
					Total Ramp Times (hours) =	12.2

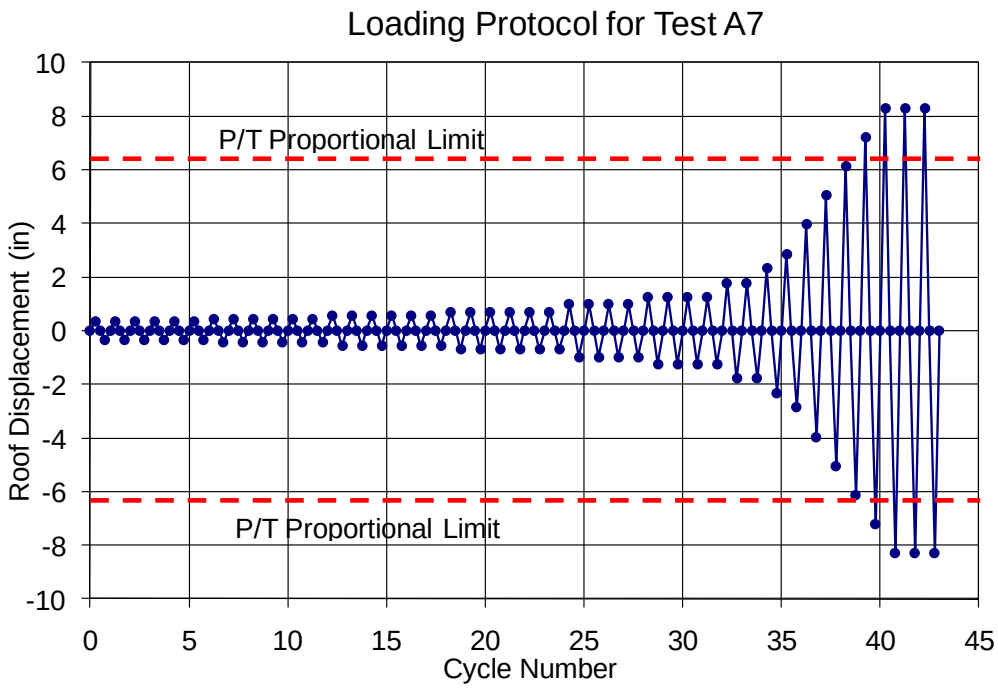

Figure A.101 Roof Displacement Targets for Specimen A7

Table A.13 Displacement Targets for Specimen B1 and B2

Displ-acement Step	Number of Cycles	Fuse Shear Strain Target (in/in)	Expected Roof Drift Ratio (%)	Expected Roof Drift (in)	Expected LBCB Displ. (in)	Expected Post-Tension Strain (in/in)
1	6	0.00375	0.29%	0.569	0.652	0.0044
2	6	0.005	0.33%	0.651	0.746	0.0045
3	6	0.0075	0.41%	0.809	0.924	0.0046
4	6	0.01	0.49%	0.960	1.096	0.0048
5	4	0.015	0.64%	1.268	1.444	0.0050
6	4	0.02	0.79%	1.572	1.789	0.0053
7	2	0.03	1.10%	2.185	2.482	0.0059
8	1	0.04	1.41%	2.800	3.178	0.0064
9	1	0.05	1.73%	3.423	3.882	0.0070
10	1	0.07	2.36%	4.668	5.289	0.0081
11	1	0.09	2.97%	5.887	6.664	0.0092
12	1	0.11	3.58%	7.083	8.011	0.0103
13	1	0.13	4.18%	8.274	9.351	0.0114

Table A.14 Ramp Information for Specimen B1 and B2

Load Step	Substep Size (in)	Number of Substeps	Substeps Per Picture	Total Pictures per Ramp	Expected Time Per Quarter Cycle (min)	Expected Time for All Cycles (min)
1	0.019	30	5	6	1.8	43.2
2	0.022	30	5	6	1.8	43.2
3	0.023	36	6	6	2.2	51.8
4	0.023	42	6	7	2.5	60.5
5	0.023	56	7	8	3.4	53.8
6	0.025	63	7	9	3.8	60.5
7	0.0275	80	8	10	4.8	38.4
8	0.0285	99	9	11	5.9	23.8
9	0.0265	130	10	13	7.8	31.2
10	0.026	180	10	18	10.8	43.2
11	0.0268	220	10	22	13.2	52.8
12	0.0263	270	10	27	16.2	64.8
13	0.0267	310	10	31	18.6	74.4
					Total Ramp Times (hours) =	10.7

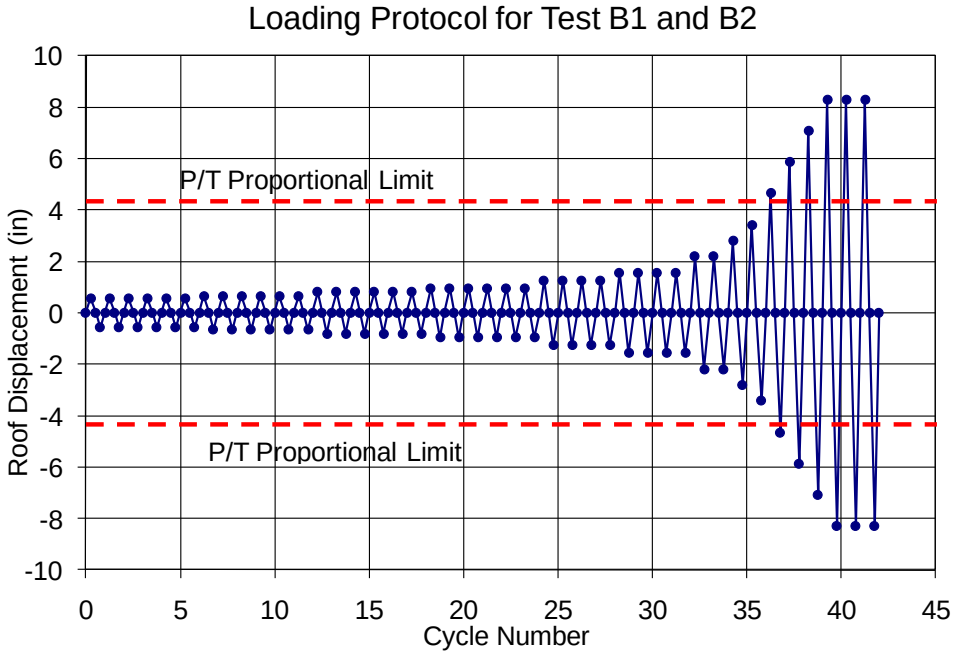

Figure A.102 Roof Displacement Targets for Specimen B1 and B2

A.7 LBCB Plugin Screen Shot and Floor Plan for the Test Setup

This section contains a screen shot of the LBCB Plugin used in the experimental program and a drawing of the experimental setup on a floor plan of the MUST-SIM facility.

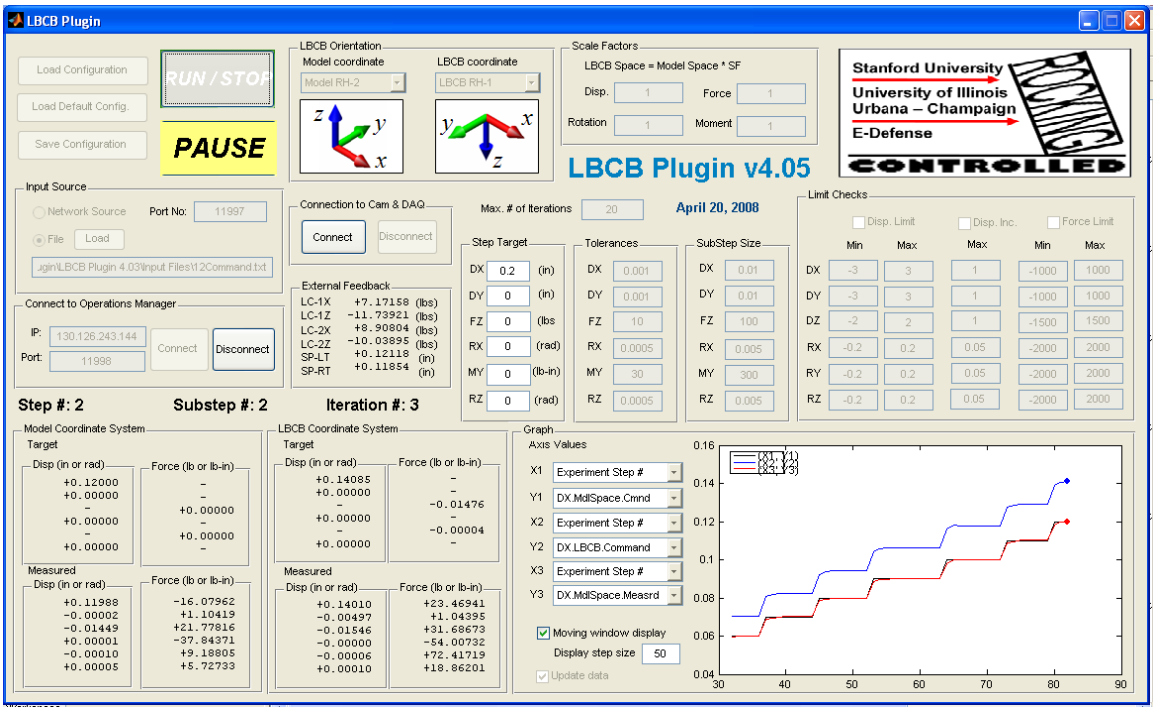

Figure A.103 Screen Shot of the Controlled Rocking LBCB Plugin

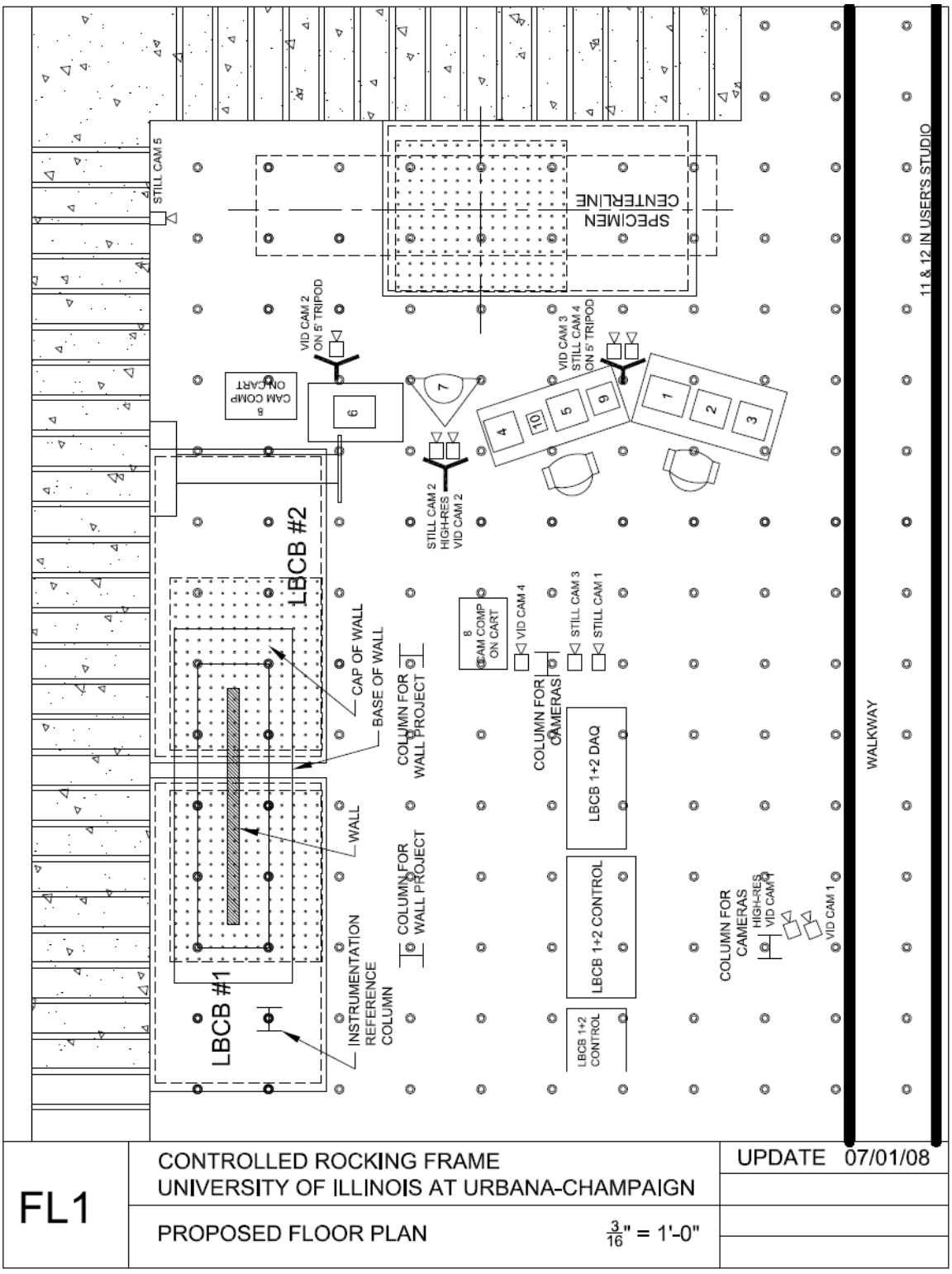

Figure A.104 Floor Plan Drawing - Layout

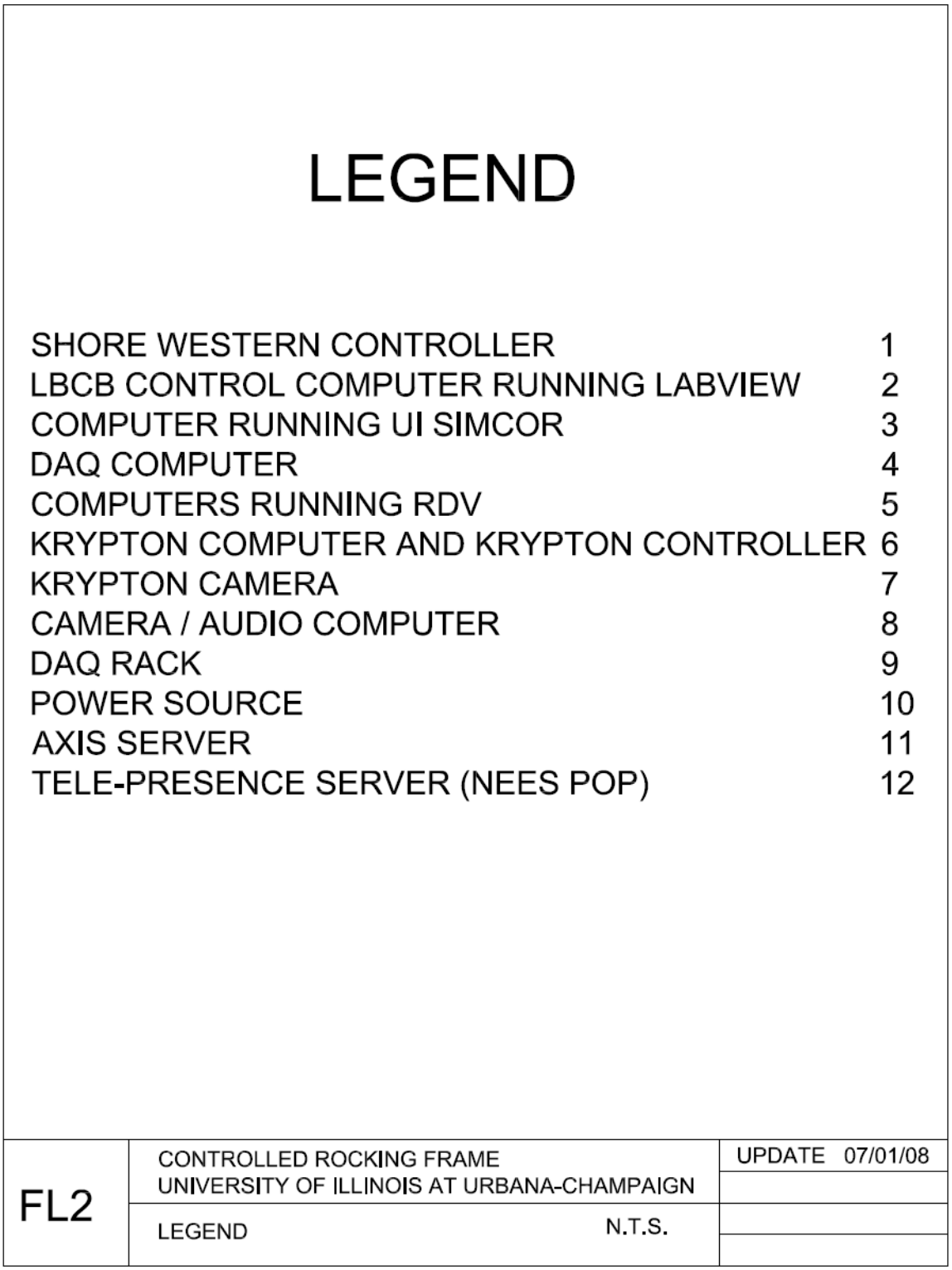

Figure A.105 Floor Plan Drawing – Key

A.8 Instrumentation Plans

This section includes instrumentation plan drawings. The first group of drawings labeled with the designation “N” either apply to all of the specimens or to specific dual frame configurations (Series A) as labeled. The second group of drawings labeled with the designation “SN” apply to the single frame configurations (Series B).

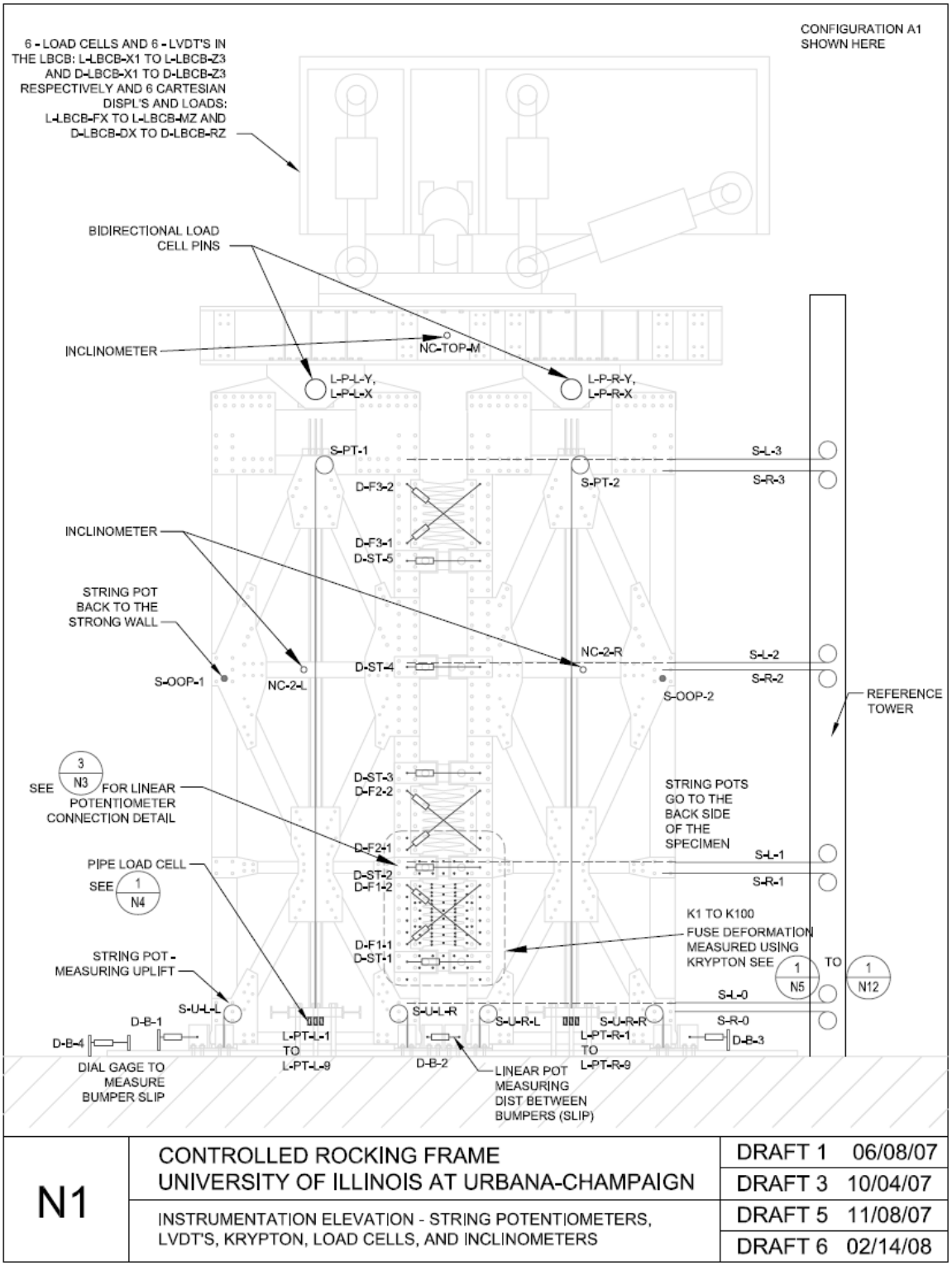

Figure A.106 Instrumentation Plan Drawing – Displacement and Inclinometers

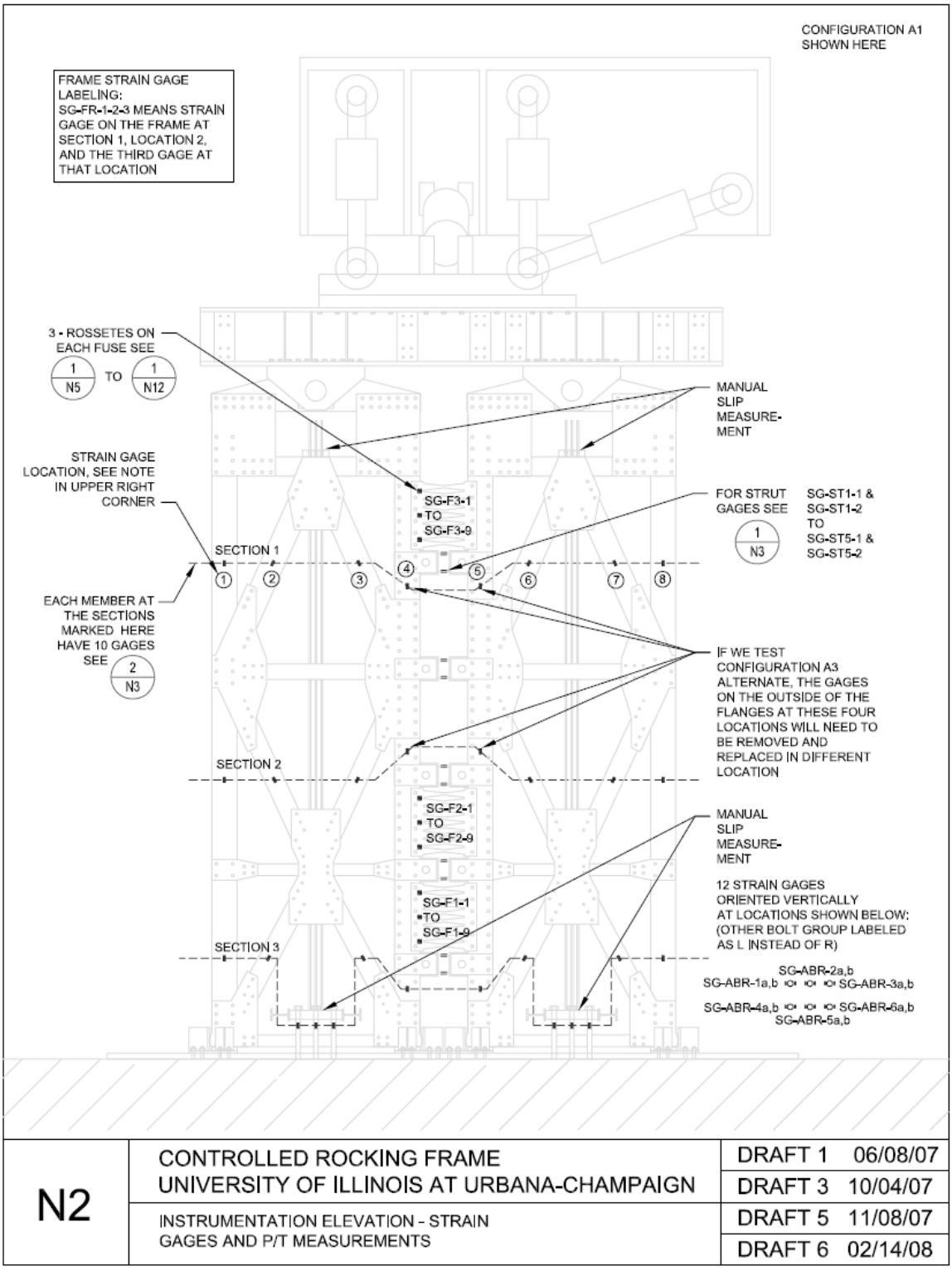

Figure A.107 Instrumentation Plan Drawing – Strain Gage Plan

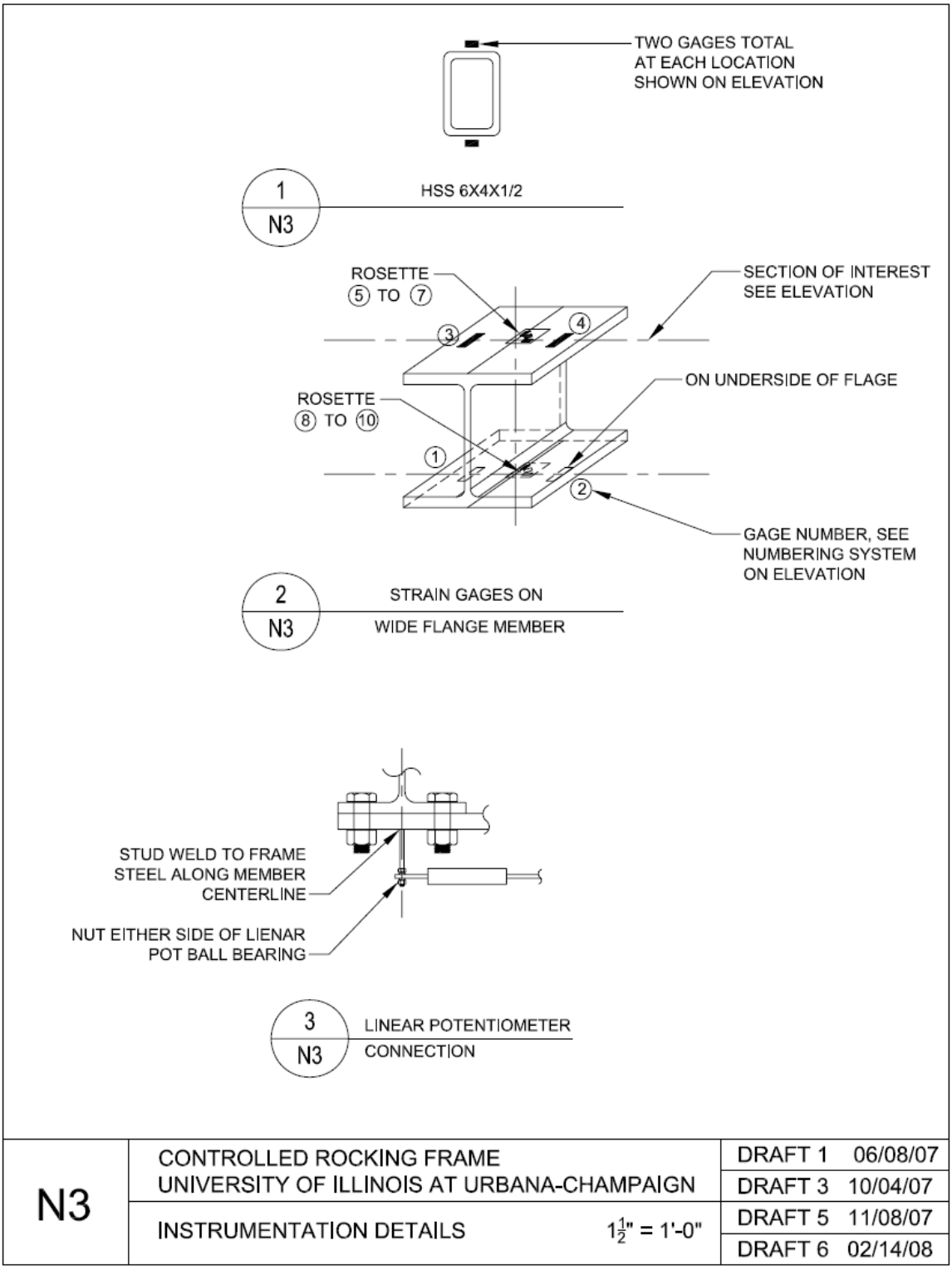

Figure A.108 Instrumentation Plan Drawing - Details

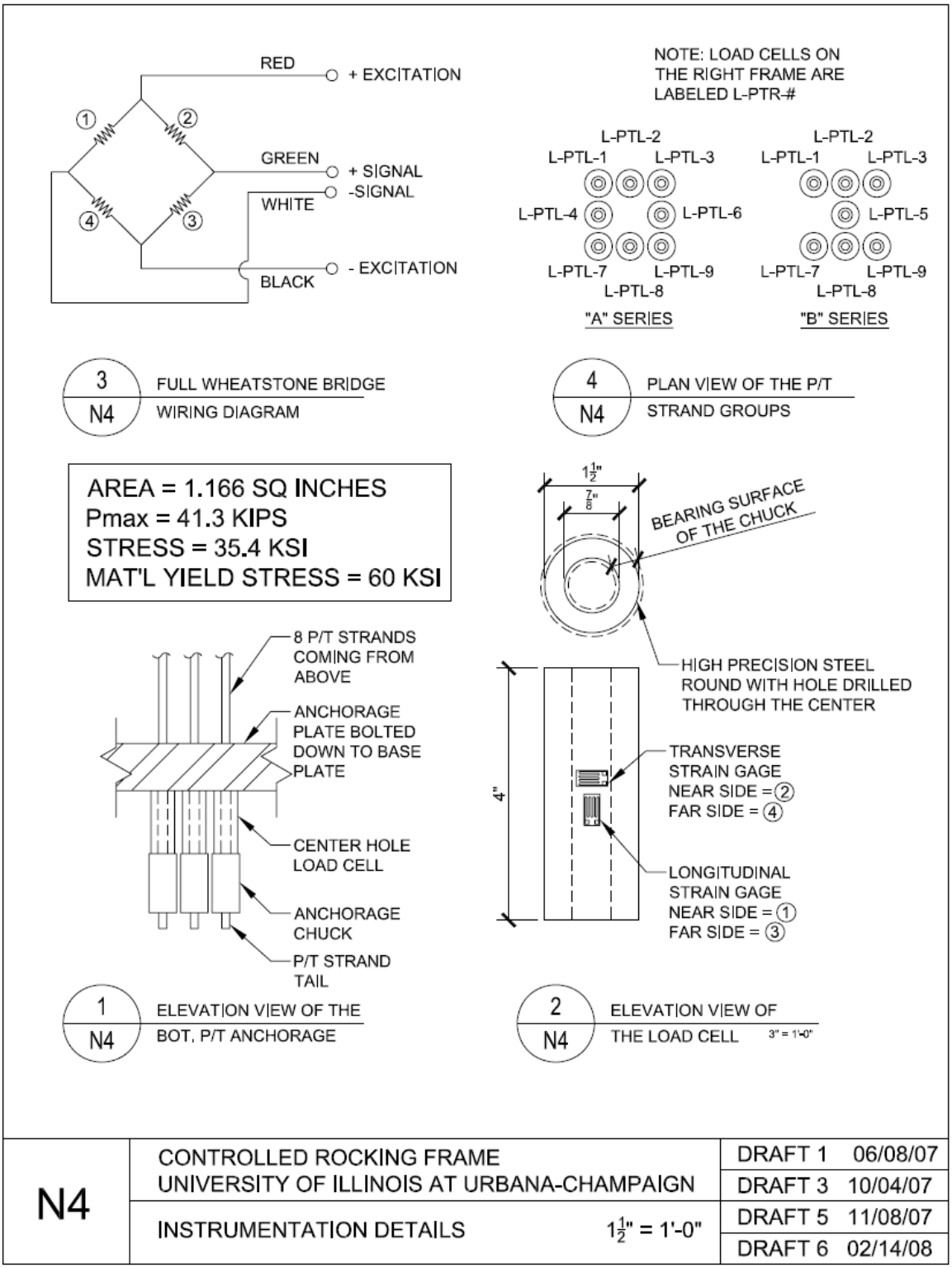

Figure A.109 Instrumentation Plan Drawing – Post-Tensioning Load Cells

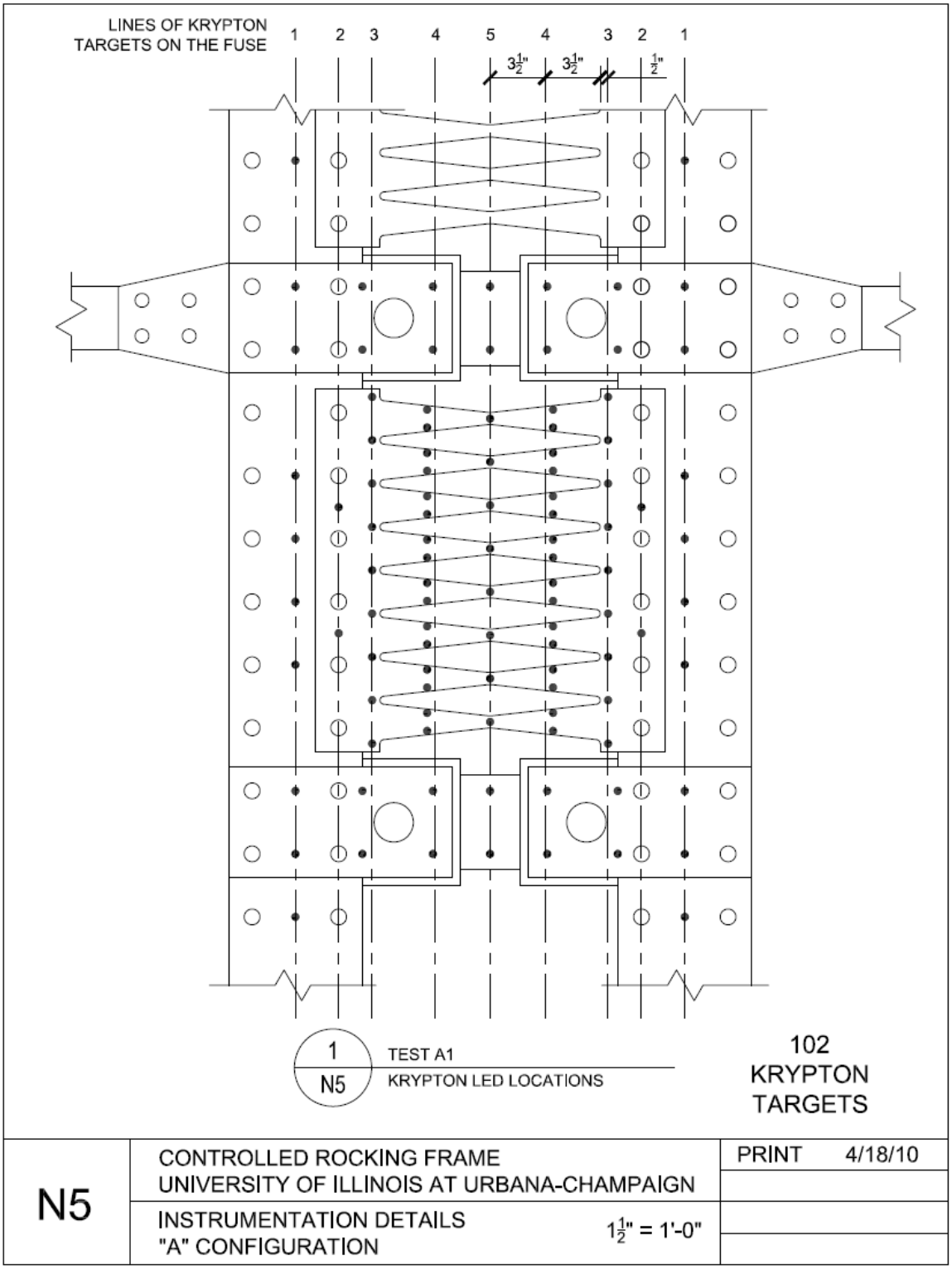

Figure A.110 Instrumentation Plan Drawing – Krypton LED's for Specimen A1

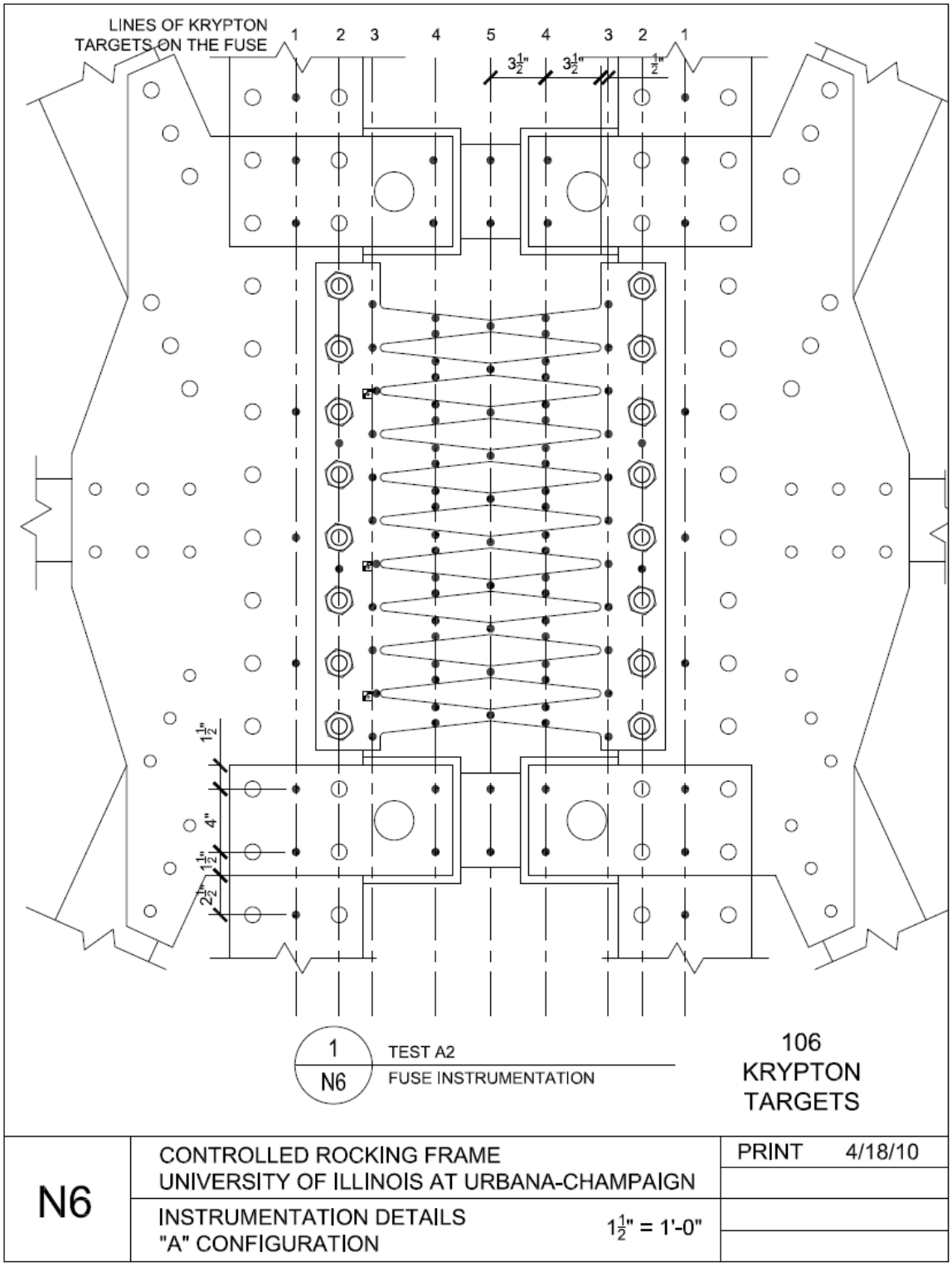

Figure A.111 Instrumentation Plan Drawing – Krypton LED's for Specimen A2

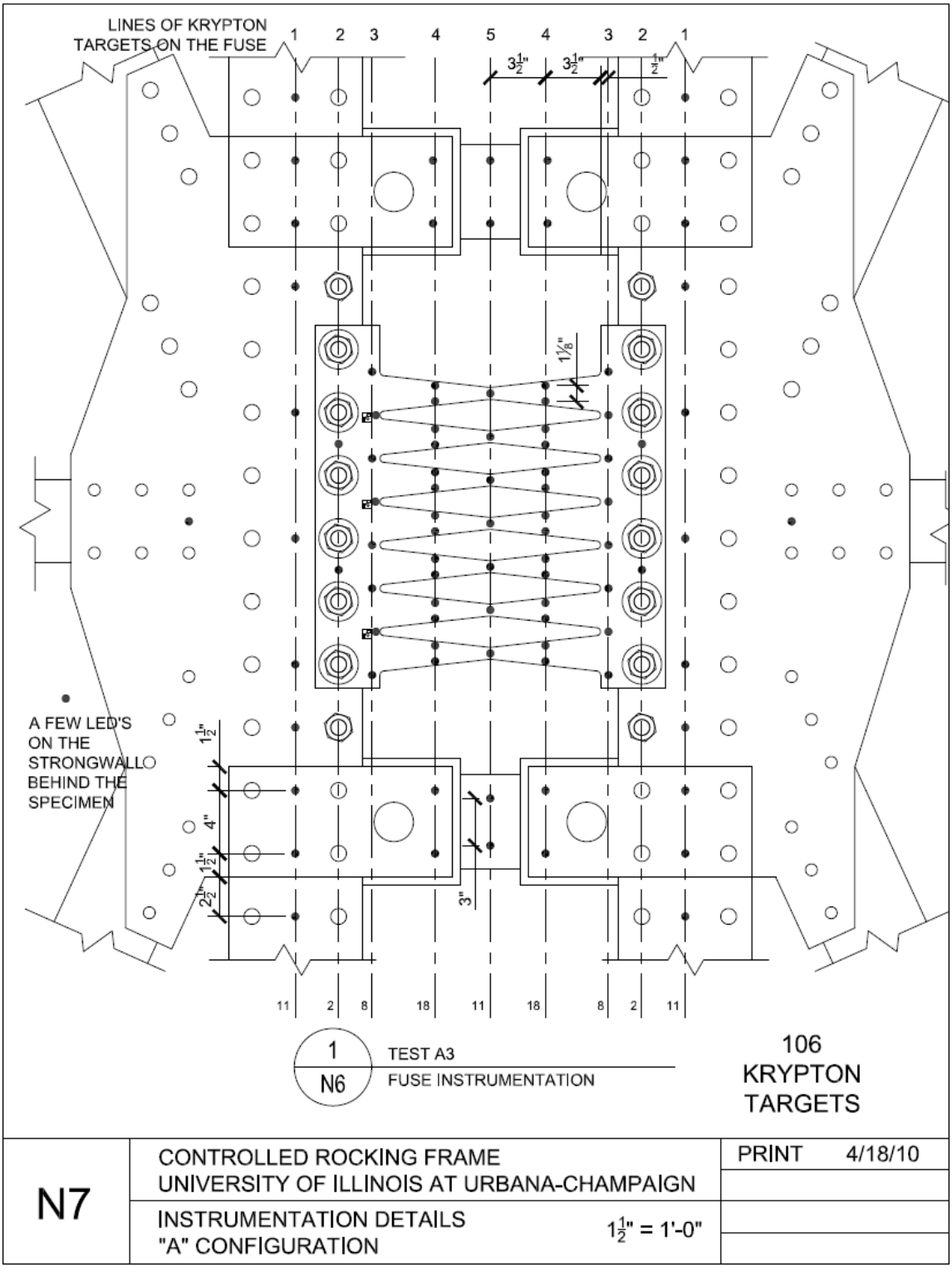

Figure A.112 Instrumentation Plan Drawing – Krypton LED's for Specimen A3

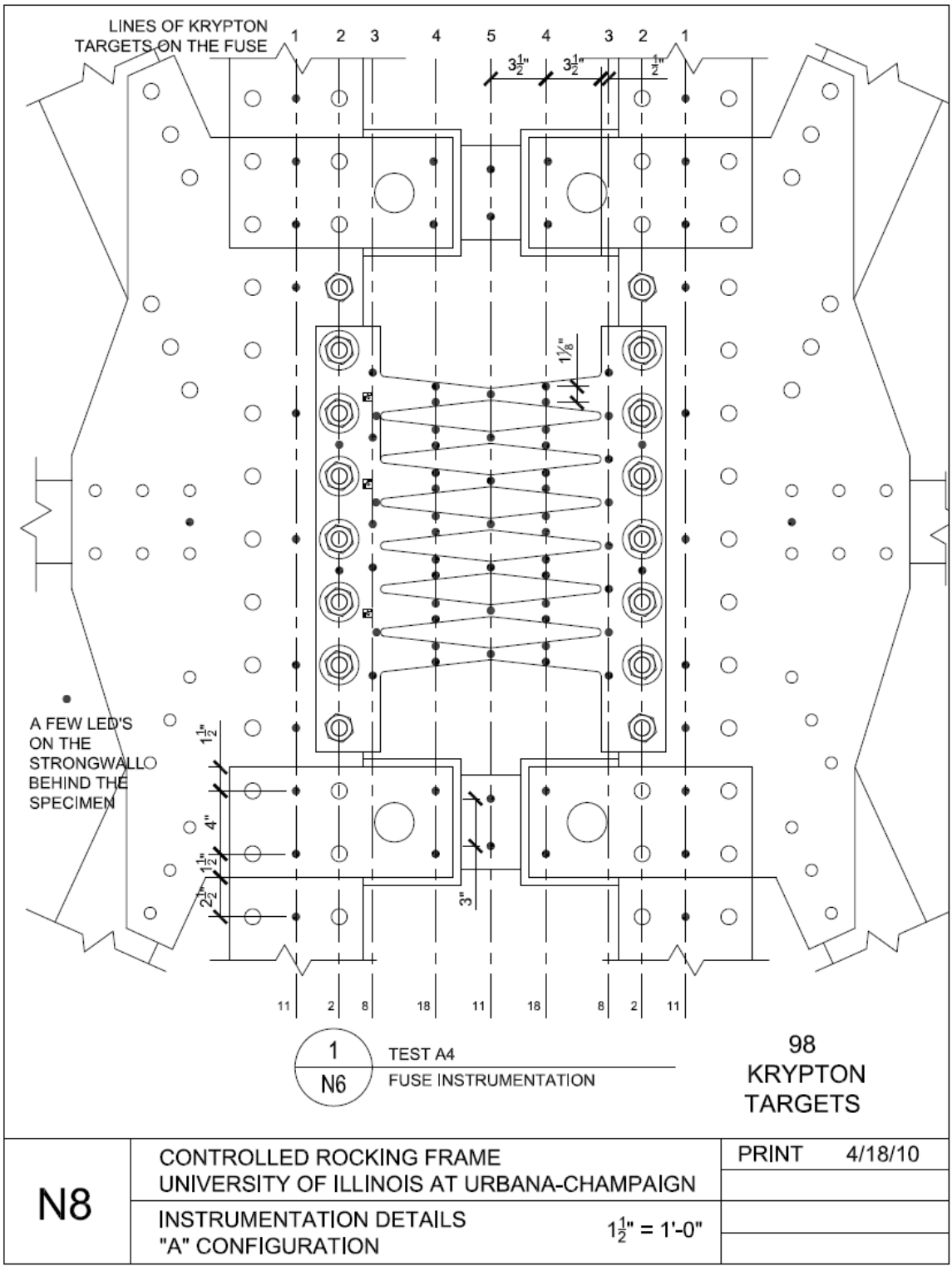

Figure A.113 Instrumentation Plan Drawing – Krypton LED's for Specimen A4

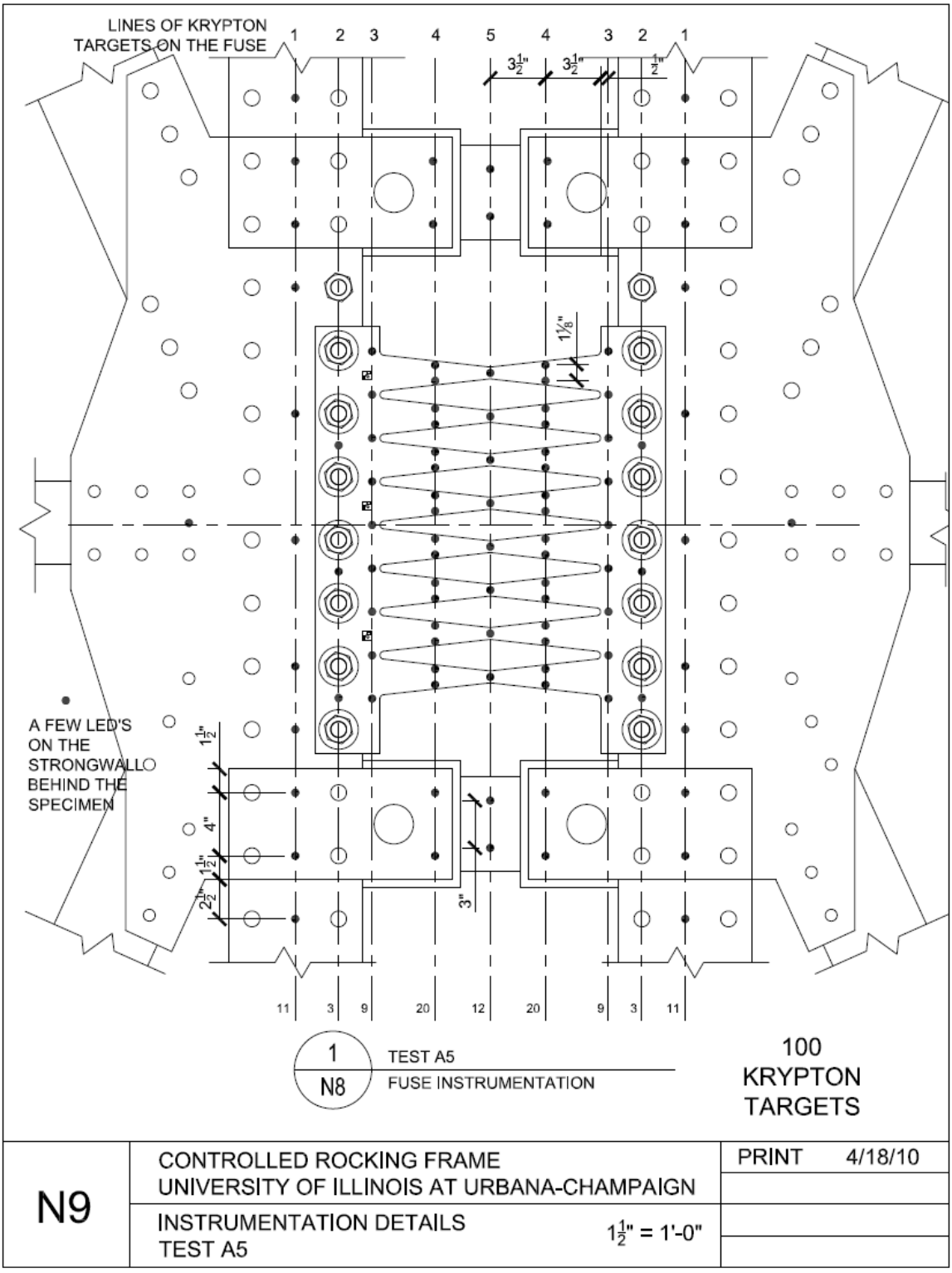

Figure A.114 Instrumentation Plan Drawing – Krypton LED's for Specimen A5

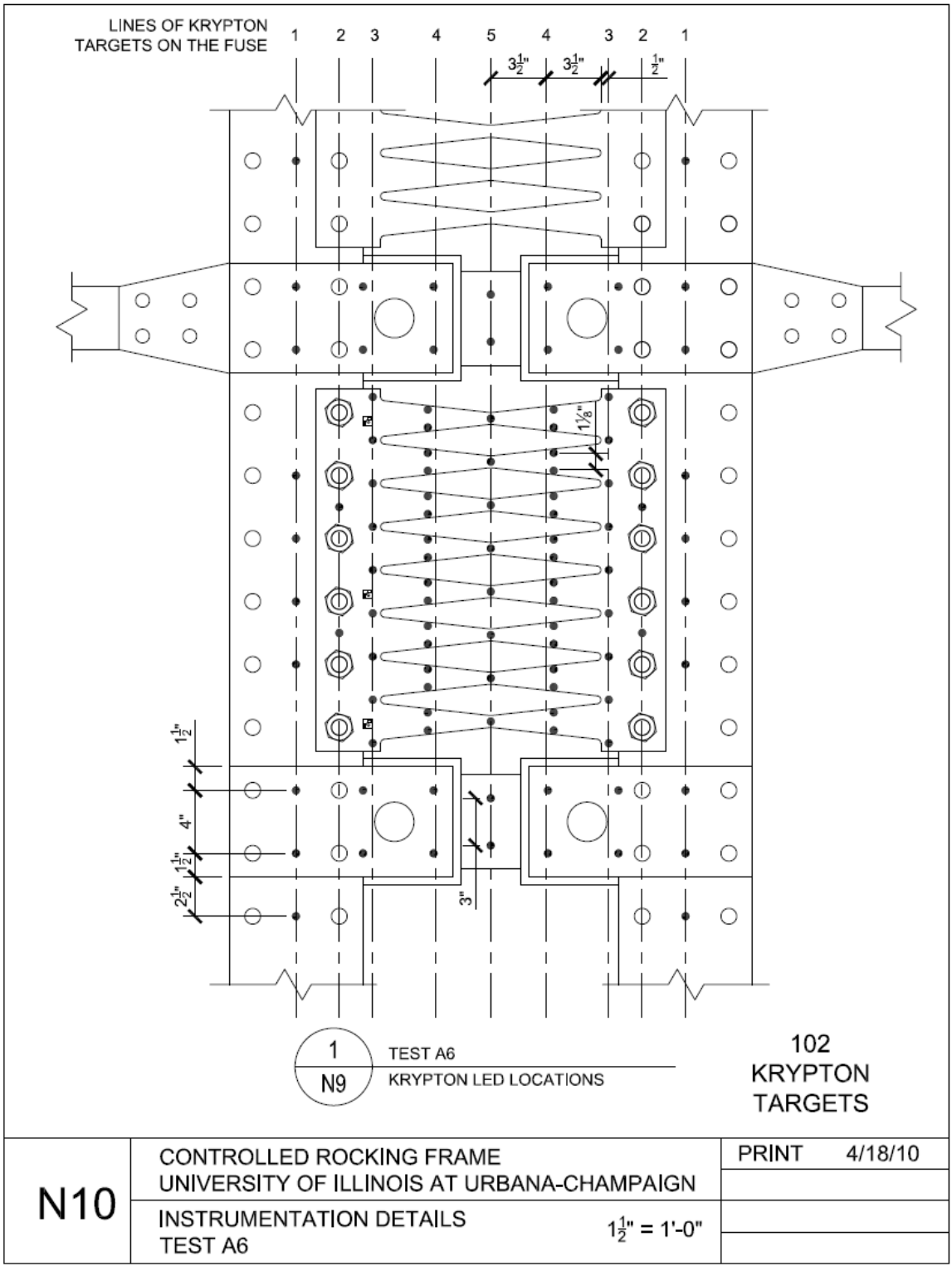

Figure A.115 Instrumentation Plan Drawing – Krypton LED's for Specimen A6

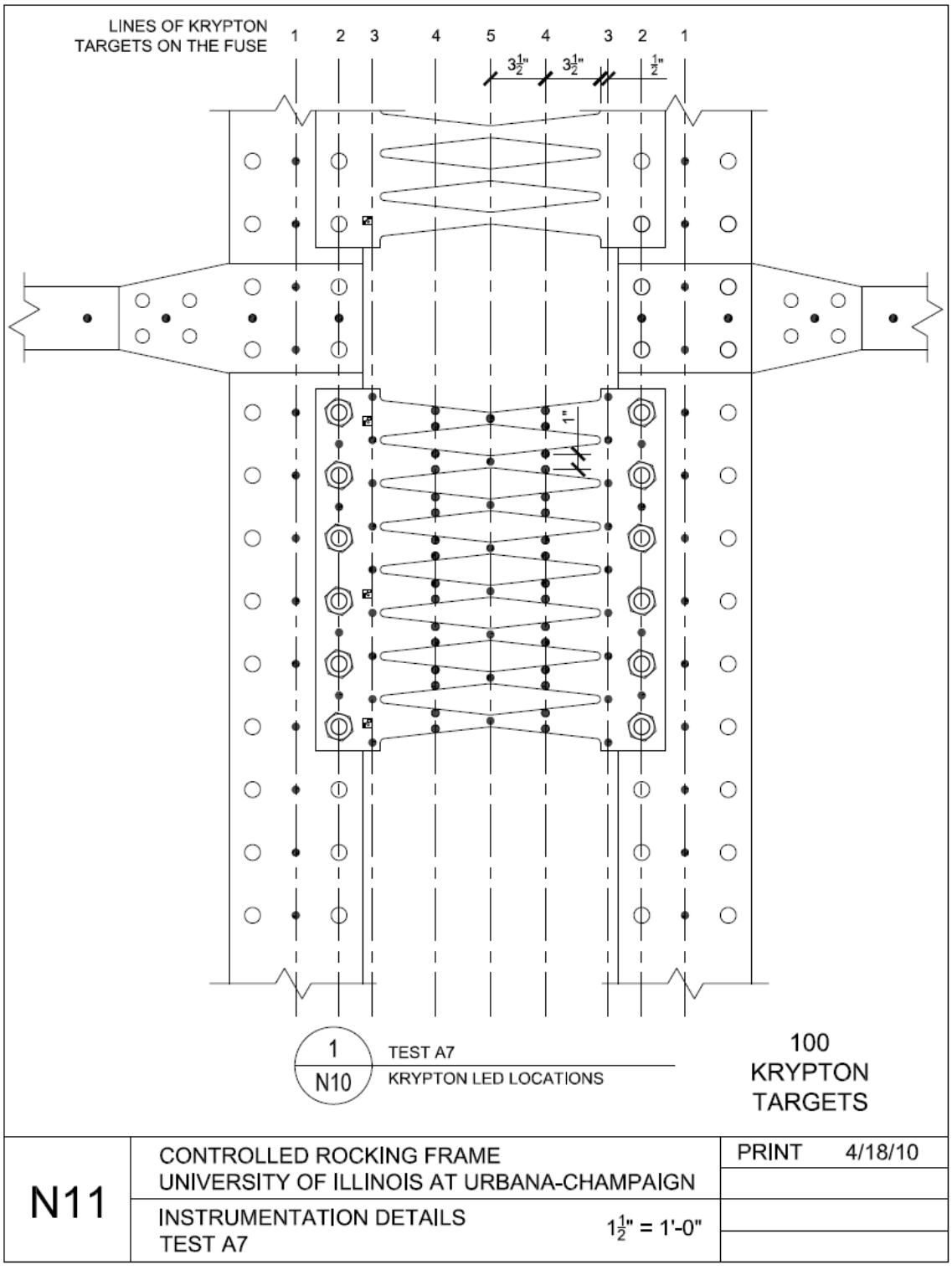

Figure A.116 Instrumentation Plan Drawing – Krypton LED's for Specimen A7

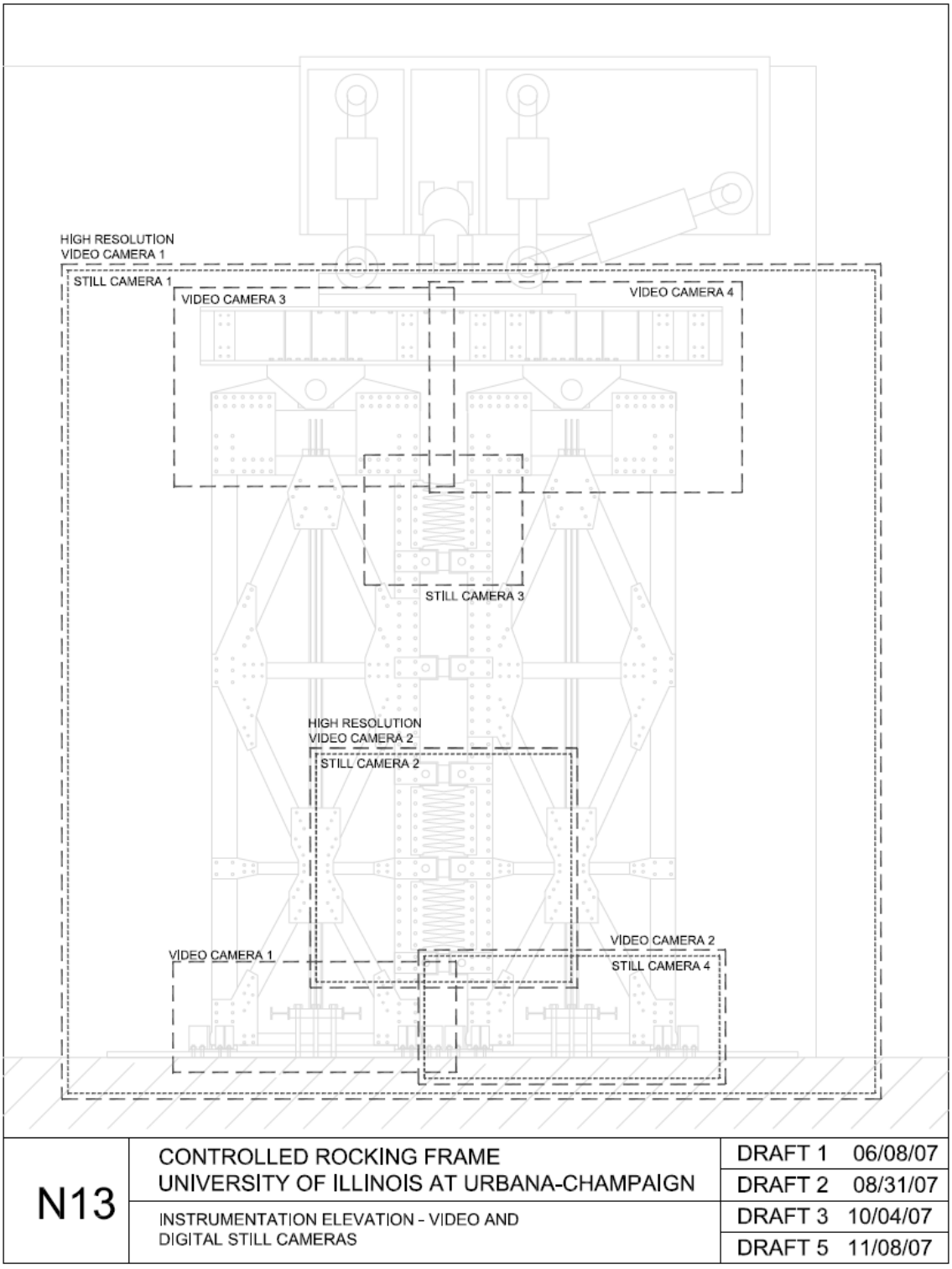

Figure A.117 Instrumentation Plan Drawing – Video and Digital Still Plan

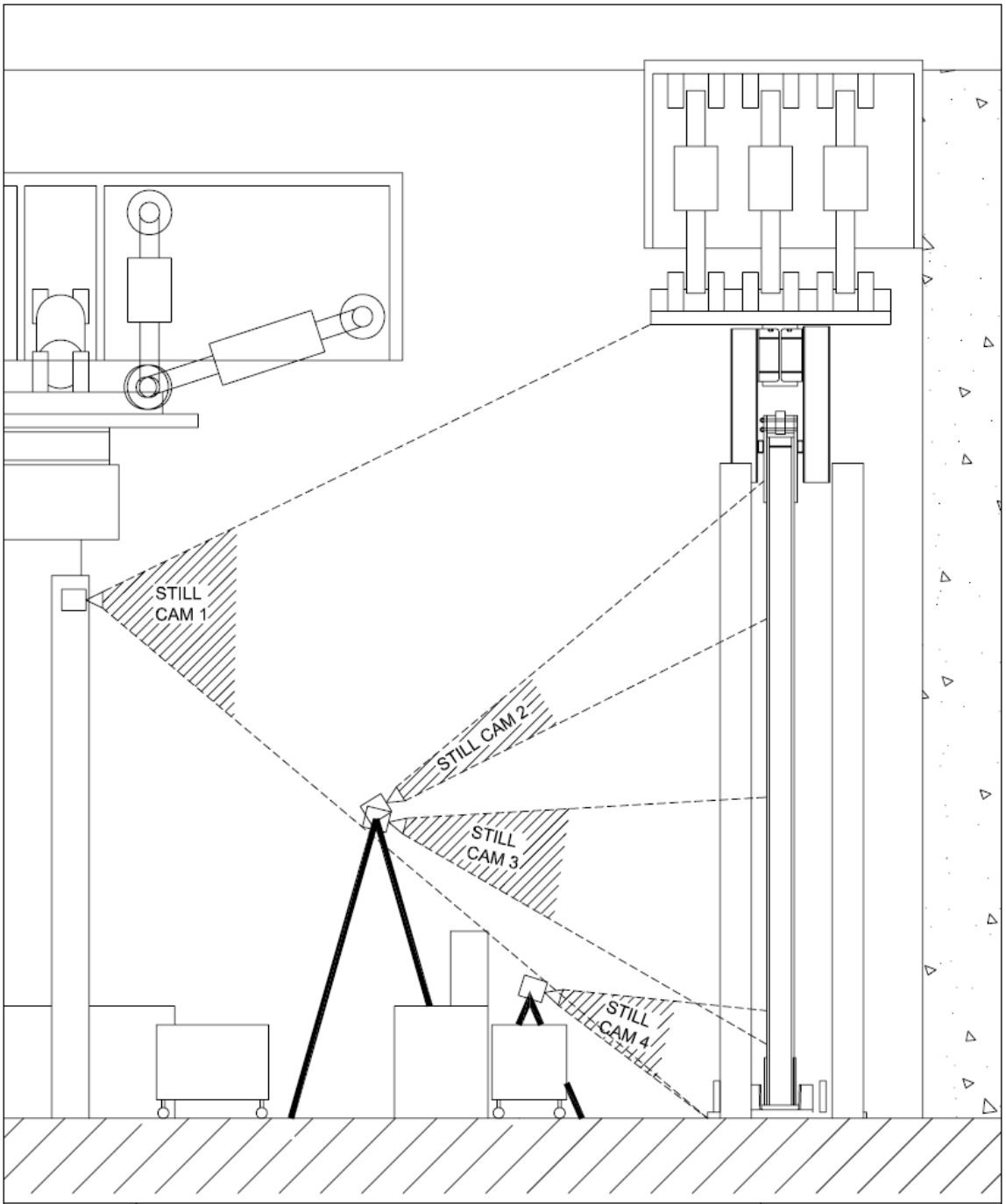

Figure A.118 Instrumentation Plan Drawing – Digital Still Camera Location Plan

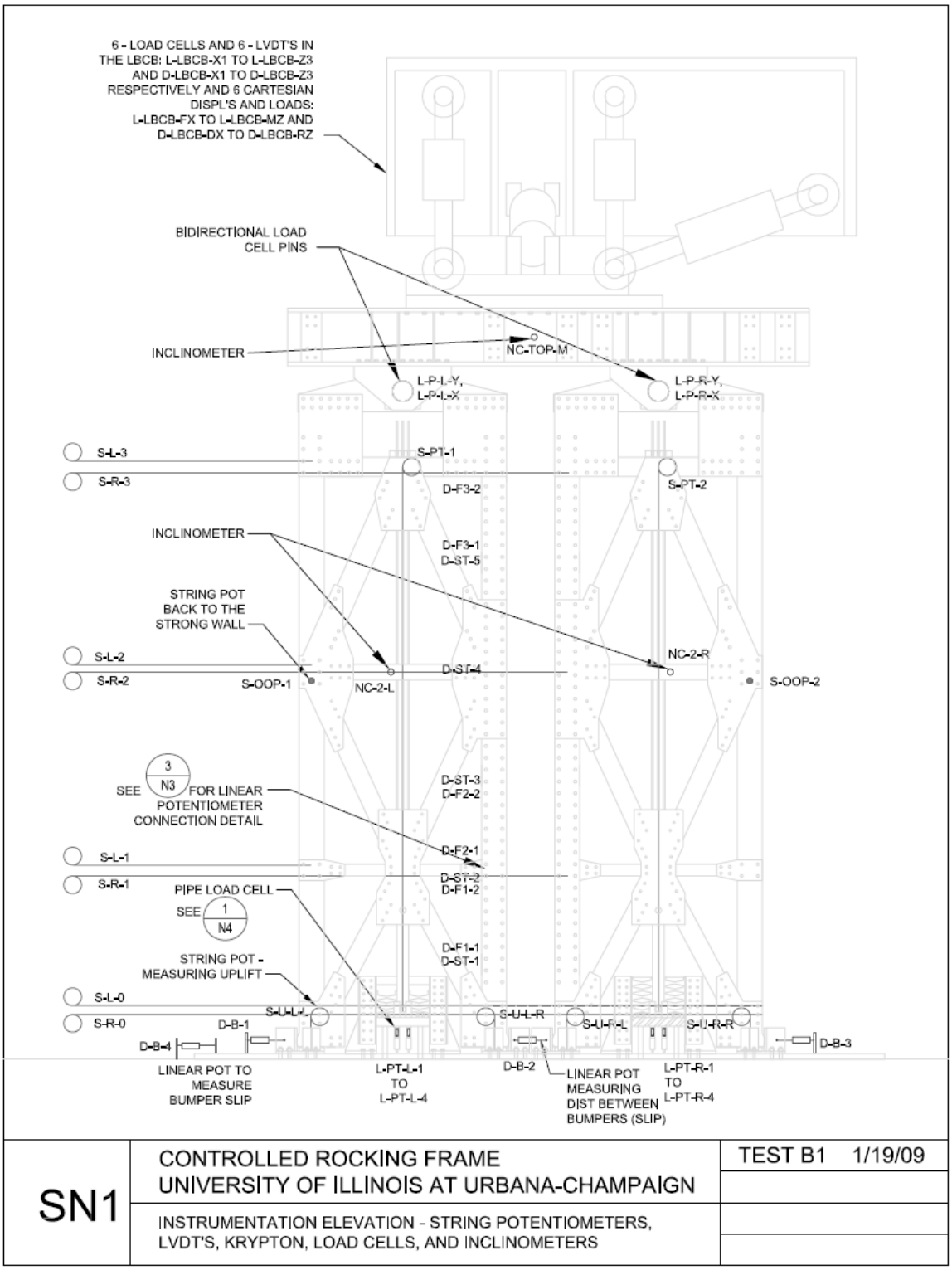

Figure A.119 Single Frame Instrumentation Plan – Displacement and Inclinometers

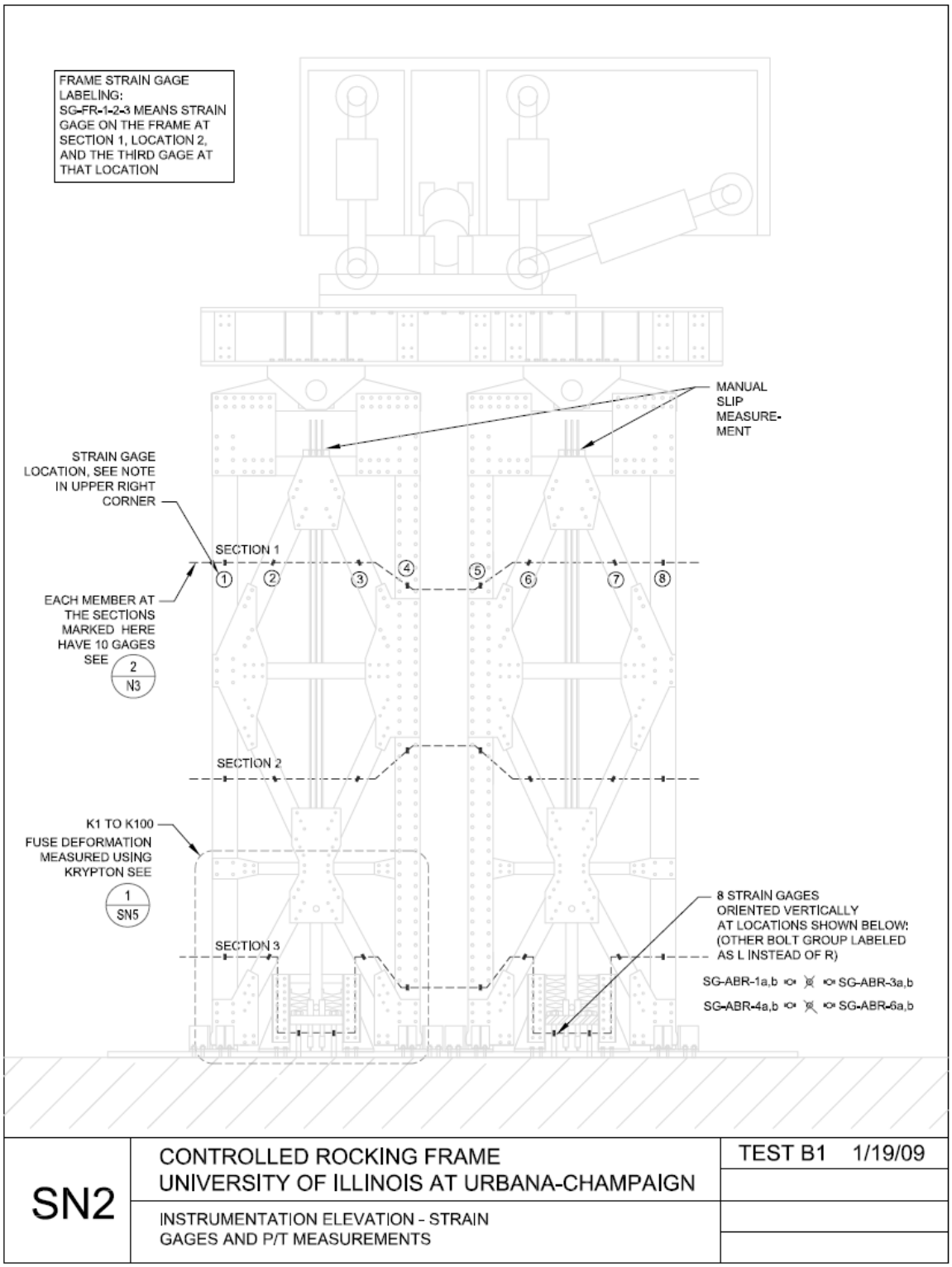

Figure A.120 Single Frame Configuration Instrumentation Plan – Strain Gages

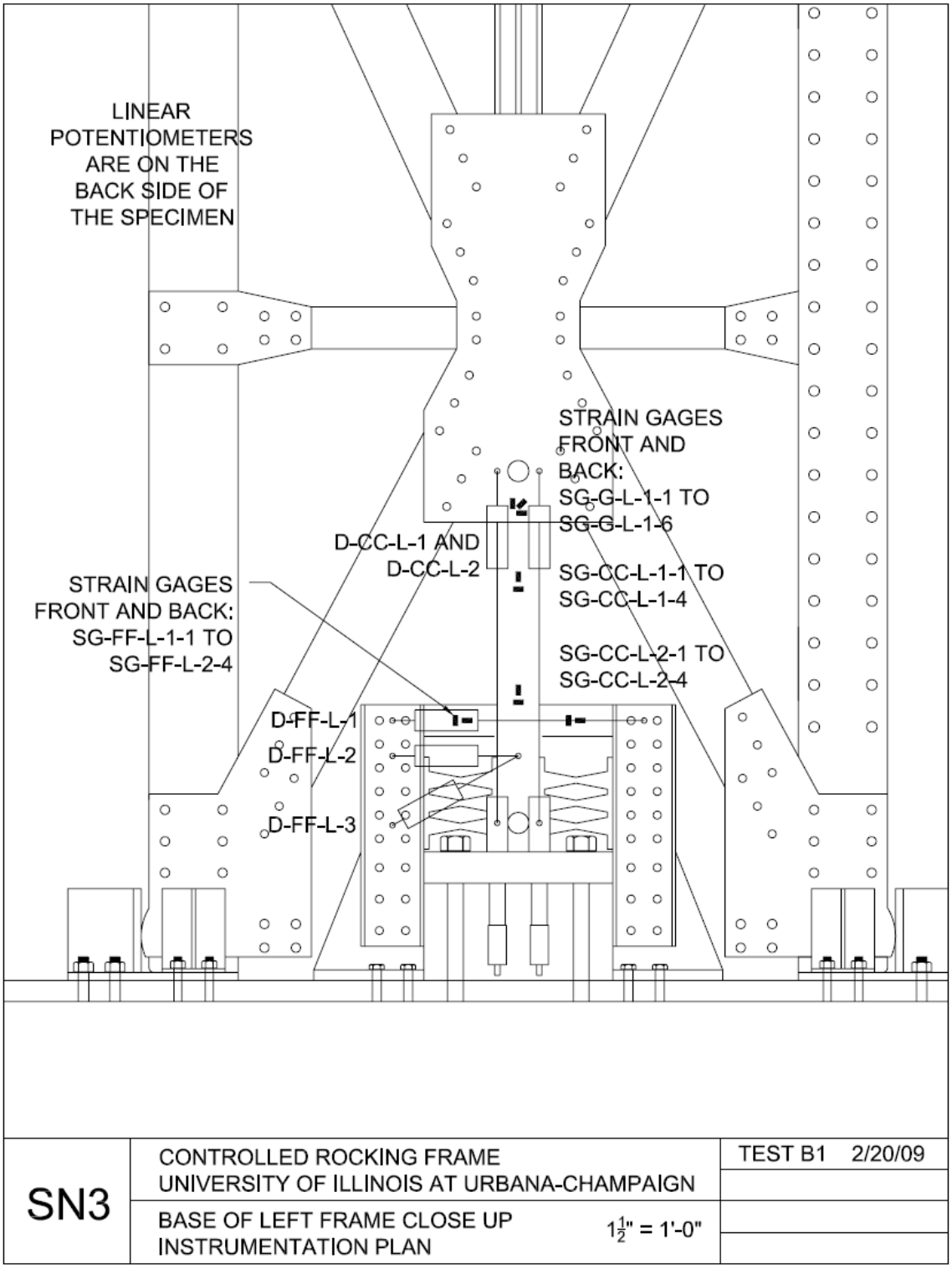

Figure A.121 Single Frame Configuration Instrumentation Plan Drawing – Specimen B1

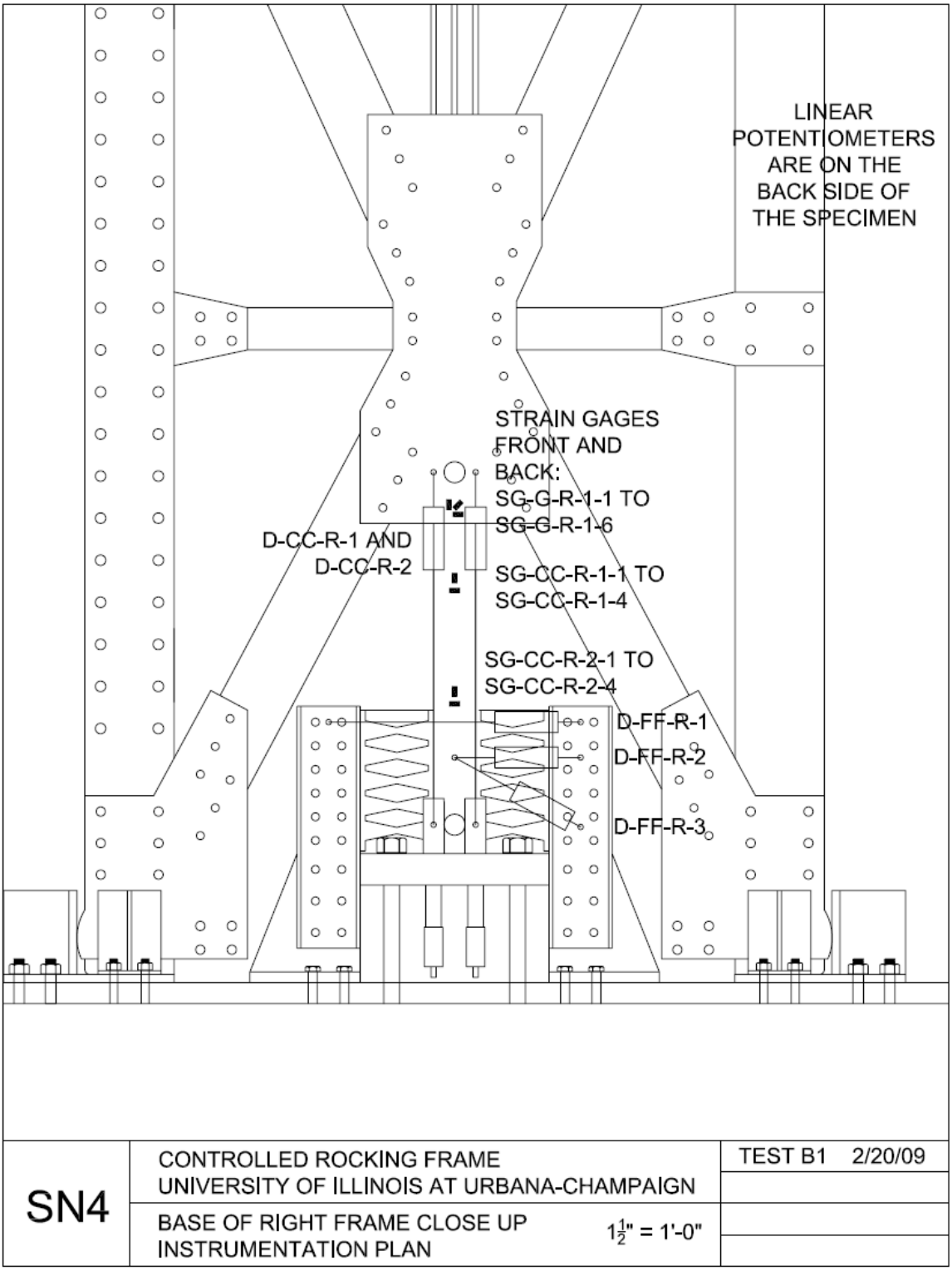

Figure A.122 Single Frame Configuration Instrumentation Plan Drawing – Specimen B2

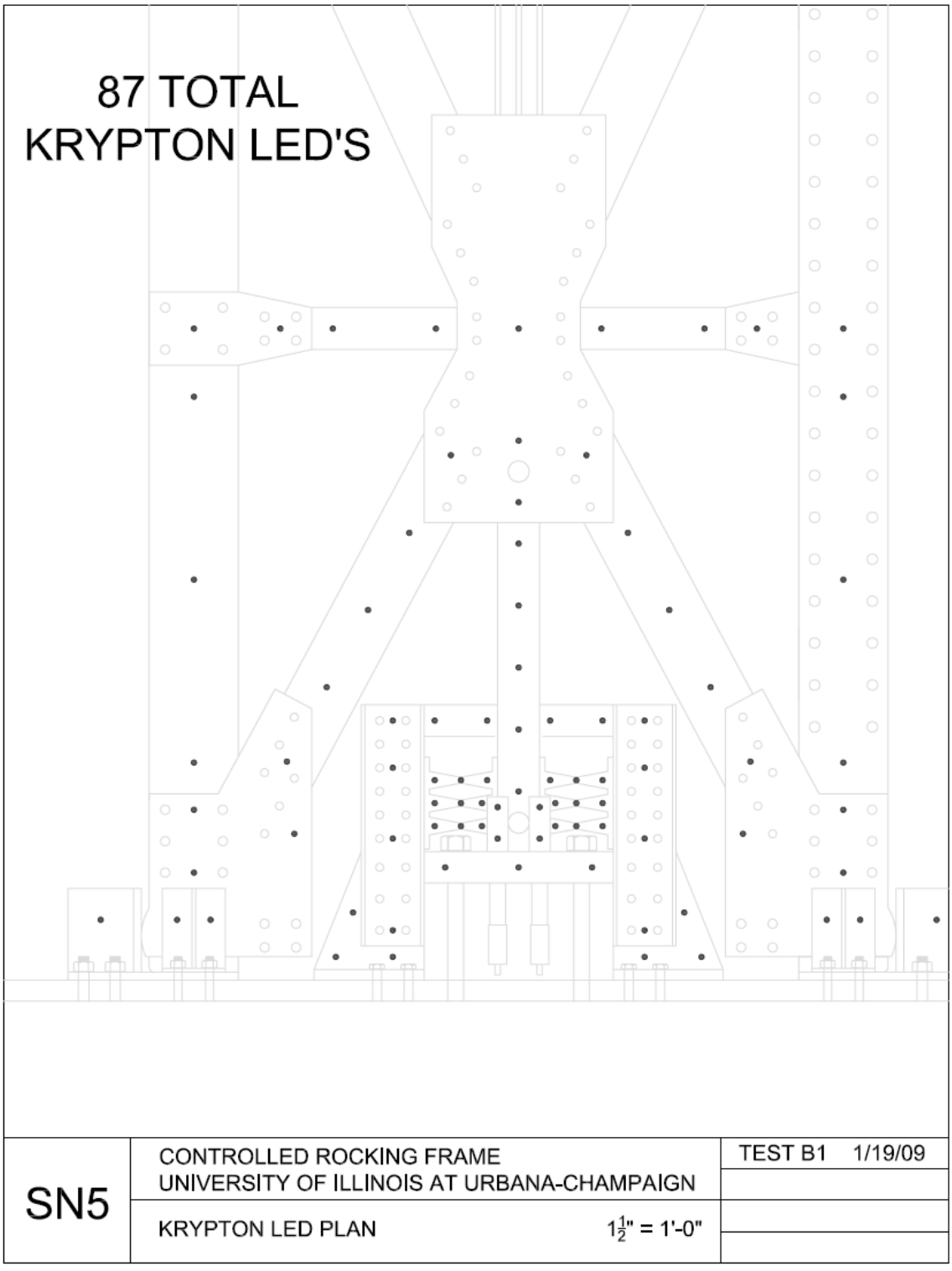

Figure A.123 Single Frame Configuration Instrumentation Plan Drawing – Krypton LED's

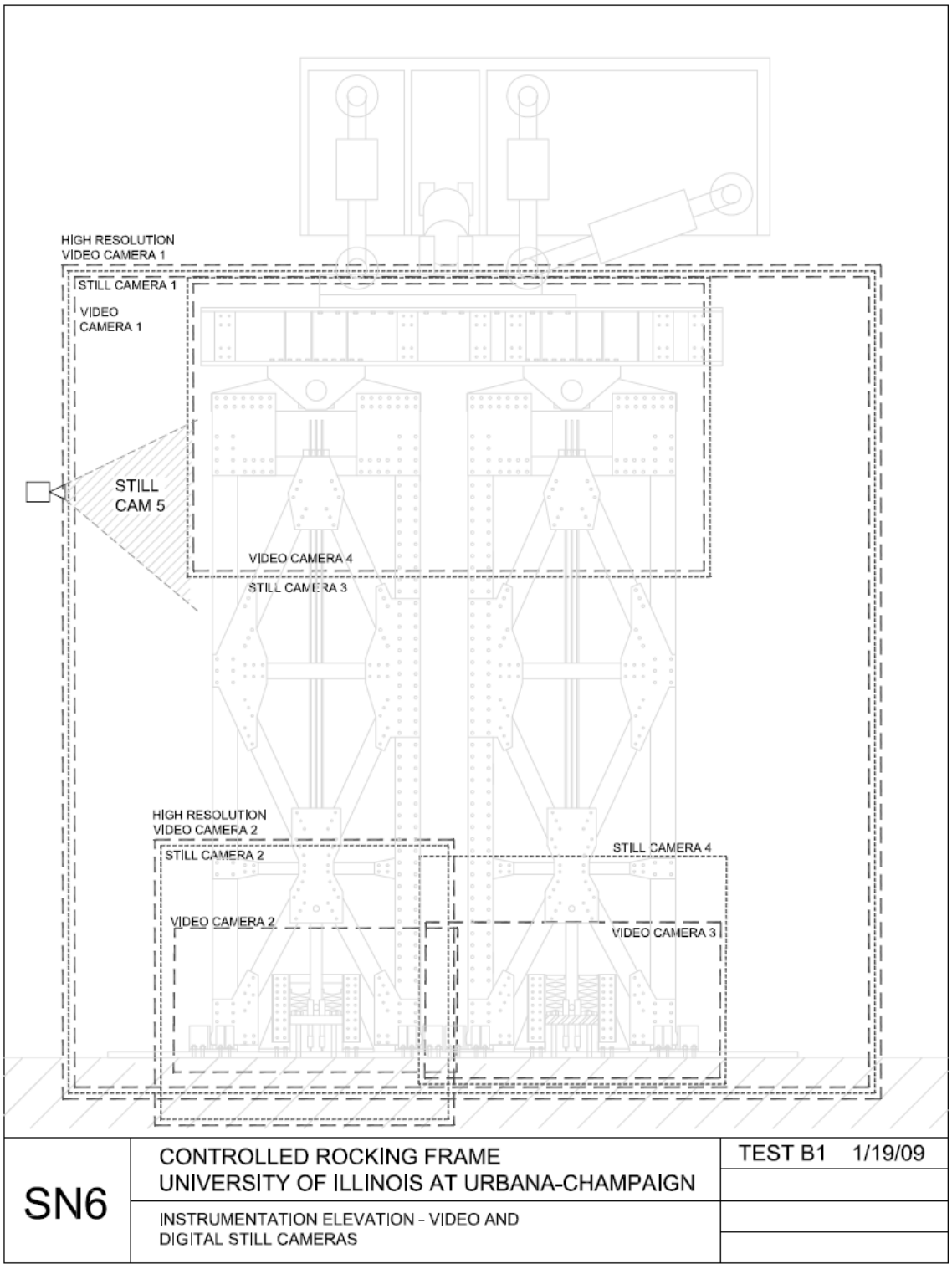

Figure A.124 Single Frame Configuration Instrumentation Plan Drawing – Camera Plan

A.9 Data Acquisition Chassis Configuration

Table A.15 Data Acquisition Chassis Number 1 SCXI-1001: SC1

Slot	Module	Terminal	Sensor Type	Max Channels	Sensors
1	NI SCXI-1521B: "SC1Mod1"	SCXI-1317 (1)	Strain	24	Section 1 - Left Frame
2	NI SCXI-1521B: "SC1Mod2"	SCXI-1317 (2)	Strain	24	Section 1 - Left Frame / Right Frame
3	NI SCXI-1521B: "SC1Mod3"	SCXI-1317 (3)	Strain	24	Section 1 - Right Frame
4	NI SCXI-1521B: "SC1Mod4"	SCXI-1317 (4)	Strain	24	Section 1 - Right Frame / Section 2 - Right Frame
5	NI SCXI-1521B: "SC1Mod5"	SCXI-1317 (5)	Strain	24	Section 2 - Right Frame
6	NI SCXI-1521B: "SC1Mod6"	SCXI-1317 (6)	Strain	24	Section 2 - Right Frame / Left Frame
7	NI SCXI-1521B: "SC1Mod7"	SCXI-1317 (7)	Strain	24	Section 2 - Left Frame / Section 3 Left Frame
8	NI SCXI-1521B: "SC1Mod8"	SCXI-1317 (8)	Strain	24	Section 3 - Left Frame
9	NI SCXI-1521B: "SC1Mod9"	SCXI-1317 (9)	Strain	24	Section 3 - Left Frame / Right Frame
10	NI SCXI-1521B: "SC1Mod10"	SCXI-1317 (10)	Strain	24	Section 3 - Right Frame
11	NI SCXI-1521B: "SC1Mod11"	SCXI-1317 (11)	Strain	24	Section 3 - Right Frame / Rt P/T anchor Rods
12	NI SCXI-1104c: "SC1Mod12"	BNC-2095 (1)	BNC Input	32	Fuse, Strut, Base Slip, Inclinometers, Excitation Voltage, Pin Load Cells

Table A.16 Data Acquisition Chassis Number 2 SCXI-1001: SC2

Slot	Module	Terminal	Sensor Type	Max Channels	Sensors
1	NI SCXI-1521B: "SC2Mod1"	SCXI-1317 (12)	Strain	24	Left P/T anchor Rods, Struts, Fuse
2	NI SCXI-1521B: "SC2Mod2"	SCXI-1317 (13)	Strain	24	Fuse, Struts
3	NI SCXI-1520: "SC2Mod3"	SCXI-1314 (1)	Strain	8	Fuse
4	NI SCXI-1520: "SC2Mod4"	SCXI-1314 (2)	Strain	8	Struts
5	NI SCXI-1520: "SC2Mod5"	SCXI-1314 (3)	Strain	8	Fuse
6	NI SCXI-1520: "SC2Mod6"	SCXI-1314 (4)	Strain	8	Fuse
7	NI SCXI-1520: "SC2Mod7"	SCXI-1314 (5)	Strain	8	Fuse
8	NI SCXI-1520: "SC2Mod8"	SCXI-1314 (6)	Strain	8	Left P/T Load Cells
9	NI SCXI-1520: "SC2Mod9"	SCXI-1314 (7)	Strain	8	Right P/T Load Cells
10	NI SCXI-1540: "SC2Mod10"	SCXI-1315 (1)	String Pot	8	Horizontal Drift
11	NI SCXI-1540: "SC2Mod11"	SCXI-1315 (2)	String Pot	8	P/T Elongation, Uplift
12	NI SCXI-1540: "SC2Mod12"	SCXI-1315 (3)	String Pot	8	Out-Of-Plane

Table A.17 Channels Obtained Through TCP/IP Connection with LBCB Operations Manager

Sensor Type	Max Channels	Sensors
LVDT	6	Actuator LVDT Displacements
Computed Displacement	6	Cartesian Displacements
Load Cell	6	Actuator Load Cells
Computed Force	6	Cartesian Forces

Table A.18 Instrumentation Channels

Location	Measurement	Instrument	Expected Range	Gage Range	Quantity
Strain Gages					
Section 1 - Left Frame	Strain	Strain Gages & Rosettes	1550 με	15,000 με	40
Section 1 - Right Frame	Strain	Strain Gages & Rosettes	1550 με	15,000 με	40
Section 2 - Left Frame	Strain	Strain Gages & Rosettes	1550 με	15,000 με	40
Section 2 - Right Frame	Strain	Strain Gages & Rosettes	1550 με	15,000 με	40
Section 3 - Left Frame	Strain	Strain Gages & Rosettes	1550 με	15,000 με	40
Section 3 - Right Frame	Strain	Strain Gages & Rosettes	1550 με	15,000 με	40
P/T Anchor Rods	Strain	Strain Gage	1000 με	15,000 με	24
Struts	Strain	Strain Gage	1550 με	15,000 με	10
Fuses	Strain	Strain Gage Rossetes	80,000 με	100,000 με	54
					328
Linear Potentiometers					
Diagonal Across Fuses	Relative Displacement	Linear Pot	± 3.25"	8"	6
Struts	Relative Displacement	Linear Pot	± 1/4"	1"	5
Base Slip	Relative Displacement	Linear Pot	± 1/8"	1"	4
					15
String Potentiometers					
Base Horizontal Drift	Absolute Displacement	String Pot	± 1/8"	2"	2
1st Floor Horizontal Drift	Absolute Displacement	String Pot	± 2.6"	10"	2
2nd Floor Horizontal Drift	Absolute Displacement	String Pot	± 5.7"	25"	2
3rd Floor Horizontal Drift	Absolute Displacement	String Pot	± 8.6"	25"	2
Frame Uplift	Absolute Displacement	String Pot	+ 3"	10"	4
P/T Elongation	Relative Displacement	String Pot	+ 2"	5"	2
Out-Of-Plane	Absolute Displacement	String Pot	± 1/4"	3"	2
					16
LBCB Data From TCP/IP Connection					
Actuator Displacement	Absolute Displacement	LVDT			6
Cartesian Displacement	Absolute Displacement	LVDT + Transformation	± 10"	± 10"	6
Actuator Force	Load Cell	Load Cell			6
Cartesian Force	Load Cell	Load Cell + Transformation	± 230 kips	± 600 kips	6
					24
Load Cells					
Pin type Load Cells Left Frame	Load	Load Cell	± 230 kips	± 600 kips	2
Pin type Load Cells Right Right	Load	Load Cell	± 230 kips	± 600 kips	2
P/T Load Cells	Load	Load Cell	42 kips	55 kips	16
					20
Inclinometers					
Inclinometers	Rotation	Inclinometer	± 2.5°	75°	**3**
Krypton					
Fuse Deformation	Displacement	Krypton LED	N/A	N/A	**100**
Video and Cameras					
Camera	Still Images	Canon		-	5
Video Camera	Video			-	4
High Resolution Video Camera	Video				1
					10

A.10 Catalog of Data that Was Obtained

Table A.19 Listing of the Data that was Collected From All Tests

				DAQ Computer				Operations
				Continuous		Step		Manager
	Description	Dates	Location in Archive	DAQ	OM	DAQ	OM	Record
1	Stiffness Tests	7/3/08	Test A1	X				X
2	Moving LBCB	7/9/08	Test A1	X				
3	Dry Run 1	7/18/08, 7/19/08	Test A1	X	X			X
4	Dry Run 2	7/22/08	Test A1	X	X	X	X	X
5	Dry Run 3	7/22/08	Test A1	X	X	X	X	Same folder as prev.
6	Post Tensioning	7/25/08, 7/28/08, 7/29/08	Test A1	X				
7	Reattach to LBCB	7/29/08	Test A1	X	X			X
8	Test A1	8/4/08, 8/5/08, 8/6/08	Test A1	X	X	X	X	X
9	Removing Fuses	8/8/08	Test A1	X	X			X
10	Increase PT Force	8/14/08	Test A2	X	X			
11	Test A2	8/25/08, 8/26/08, 8/27/08	Test A2	X	X	X	X	X
12	Negative Cycle After Test A2	8/29/08	Test A2	X	X	X	X	X
13	Removing Fuses	9/2/08	Test A2	X	X			X
14	Installing Fuses	9/4/08	Test A3	X	X			X
15	Test A3	9/8/08, 9/9/08, 9/11/08, 9/12/08	Test A3	X	X	X	X	X
16	Removing Fuses	9/18/08	Test A3	X	X			X
17	Run without Fuses	9/18/08	Test A3	X	X	X	X	X
18	Increase PT Force	9/19/08, 9/22/08	Test A4	X	X			X
19	Run without Fuses	9/24/08	Test A4	X	X	X	X	X
20	Test A4	10/1/08, 10/2/08, 10/3/08	Test A4	X	X	X	X	X
21	Removing Fuses	10/8/08	Test A4	X	X			X
22	Disconnect From Frame	10/9/08	Test A5	X	X			X
23	Post Tensioning	11/10/08, 11/11/08	Test A5	X	X			11/10 but not 11/11
24	Reattach to LBCB	11/12/08	Test A5	X	X			X
25	Run without Fuses	11/12/08	Test A5	X	X	X	X	Same folder as prev.
26	Installing Fuses	11/13/08	Test A5	X	X			X
27	Test A5 MCE	11/14/08	Test A5	X	X	X	X	X
28	Test A5 JMA Kobe x 1.10 Trial 1	11/15/08	Test A5	X	X	X	X	X
29	Test A5 JMA Kobe x 1.10 Trial 2	11/17/08	Test A5	X	X	X	X	X
30	Removing Fuses	12/2/08	Test A5	X	X			X
31	Test A6 Elastic Cycles	12/19/08	Test A6					
32	Test A6 JMA Kobe x 0.69	12/19/08	Test A6	X	X	X	X	X
33	Test A6 JMA Kobe x 0.69 with OOP	12/20/08	Test A6	X	X	X	X	X
34	Test A6 JMA Kobe x 1.20	12/20/08	Test A6	X	X	X	X	Same folder as prev.
35	Remove Fuses	1/5/09	Test A6	X	X			X
36	Test A7	1/28/09, 1/29/09, 1/30/09	Test A7	X	X	X	X	X
37	Disconnect From LBCB	2/5/09	Test B1 / B2	X	X			X
38	Post Tensioning	2/24/09	Test B1 / B2	X	X			X
39	Reconnect to LBCB	2/25/09	Test B1 / B2	X	X			X
40	Run without Fuses	2/26/09	Test B1 / B2	X	X			X
41	Increase PT Force	3/2/09	Test B1 / B2	X	X			X
42	Test B1 / B2	3/9/09, 3/10/09, 3/11/09	Test B1 / B2	X	X	X	X	X
43	Detach LBCB	3/23/09	Test B1 / B2	X	X			X

Table A.20 Listing of the Data that was Collected From All Tests

		Camera	Camera	LBCB		Krypton	Roaming		Low Res.	High Res
		Computer	Computer	Plugin	Simcor	Computer	Camera	Audio	Web Cam	Video
	Description	1	2	Computer	Computer	Data	Pictures	Recordings	Pictures	Tapes
1	Stiffness Tests									
2	Moving LBCB									
3	Dry Run 1								7/18 only	
4	Dry Run 2									
5	Dry Run 3									
6	Post Tensioning						X			
7	Reattach to LBCB						X			
8	Test A1	X	X	X		X	X	X	X	6
9	Removing Fuses									
10	Increase PT Force									
11	Test A2	X	X	X		X	X	X		3
12	Negative Cycle After Test A2									
13	Removing Fuses									
14	Installing Fuses									
15	Test A3	X	X	X		X	X	X		3
16	Removing Fuses									
17	Run without Fuses									
18	Increase PT Force									
19	Run without Fuses									
20	Test A4	X	X	X		X	X	X		3
21	Removing Fuses									
22	Disconnect From Frame									
23	Post Tensioning									
24	Reattach to LBCB									
25	Run without Fuses									
26	Installing Fuses									
27	Test A5 MCE	X	X	X	X	X				
28	Test A5 JMA Kobe x 1.10 Trial 1	X	X	X	X	X	X			2
29	Test A5 JMA Kobe x 1.10 Trial 2	X	X	X	X	With Prev.				4
30	Removing Fuses									
31	Test A6 Elastic Cycles									
32	Test A6 JMA Kobe x 0.69	X	X	X	X	X				
33	Test A6 JMA Kobe x 0.69 with OOP	X	X	X	X	With Next	With Next			2
34	Test A6 JMA Kobe x 1.20	X	X	X	X	X	X			2
35	Remove Fuses									
36	Test A7	X	X	X		X				4
37	Disconnect From LBCB									
38	Post Tensioning									
39	Reconnect to LBCB									
40	Run without Fuses									
41	Increase PT Force									
42	Test B1 / B2	X	X	X		X	X			3
43	Detach LBCB									

A.11 Lists of Channels Recorded for Each Specimen

Table A.21 Listing of the Channels that were Recorded for All Specimens

File Name	Test A1	Test A2	Test A3	Test A4	Test A5	Test A6	Test A7	Test B1 / B2
D_Base_Slip	4	4	4	4	4	4	4	4
D_Center_Column	None	None	None	None	None	None	None	4
D_Fuse_Diagonal	6	6	6	6	6	6	6	None
D_Fuse_Frame	None	None	None	None	None	None	None	6
D_Struts	5	5	5	5	5	5	5	None
EV	4 (1 is junk)	4 (1 is junk)	4 (1 is junk)	4 (1 is junk)	4 (1 is junk)	4 (1 is junk)	4 (1 is junk)	4 (1 is junk)
Inclinometers	3	3	3	3	3	3	3	3
L_Pin_Load_Cells	Junk	None	None	None	None	None	None	None
L_PT_Left	8	8	8	8	8	8	8	4
L_PT_Right	8	8	8	8	8	8	8	4
S_Fuse	None	None	None	None	None	None	None	2
S_Horizontal	8 (2 are junk)	6	6	6	6	6	6	6
S_Out_Of_Plane	2	2	2	2	2	2	2	2
S_PT_Elongation	2	2	2	2	2	2	2	2
S_Uplift	4	4	4	4	4	4	4	4
SG_Anchor_Rods_Left	12	12	12	12	12	12	12	8
SG_Anchor_Rods_Right	12	12	12	12	12	12	12	8
SG_Center_Column	None	None	None	None	None	None	None	24
SG_Fuse_Frame	None	None	None	None	None	None	None	12
SG_Fuses	54	***10 FL** + 18 F***	18	18	18	54	54	None
SG_Gusset	None	None	None	None	None	None	None	12
SG_Section_1_Beams	None	None	None	***8****	***8****	None	None	None
SG_Section_1_Left	***40****	***40****	***40****	***40****	***40****	***40****	***40****	***40****
SG_Section_1_Right	***40****	***40****	***40****	***40****	***40****	***40****	***40****	***40****
SG_Section_2_Beams	None	None	None	None	None	None	None	***16****
SG_Section_2_Left	***40****	***40****	***40****	***40****	***40****	***40****	***40****	***40****
SG_Section_2_Right	***40****	***40****	***40****	***40****	***40****	***40****	***40****	***40****
SG_Section_3_Beams	None	None	None	***8****	***8****	***8****	***8****	***8****
SG_Section_3_Left	***40****	***40****	***40****	***40****	***40****	***40****	***40****	***40****
SG_Section_3_Right	***40****	***40****	***40****	***40****	***40****	***40****	***40****	***40****
SG_Struts	10	6	6	6	6	10	None	None

** indicates the columns of raw data were out of order because the data was written in alphabetical order, not numerical order (e.g. 1, 10, 2, 3, etc. instead of 1, 2, 3, 4, etc.).

EXPERIMENTAL RAW DATA

This appendix contains all the raw data from the experimental program. The raw data was recorded in engineering units as presented in the included plots. The data is included for all nine specimens including all three trials for Specimen A5 and all three trials for Specimen A6.

B.1 Specimen A1

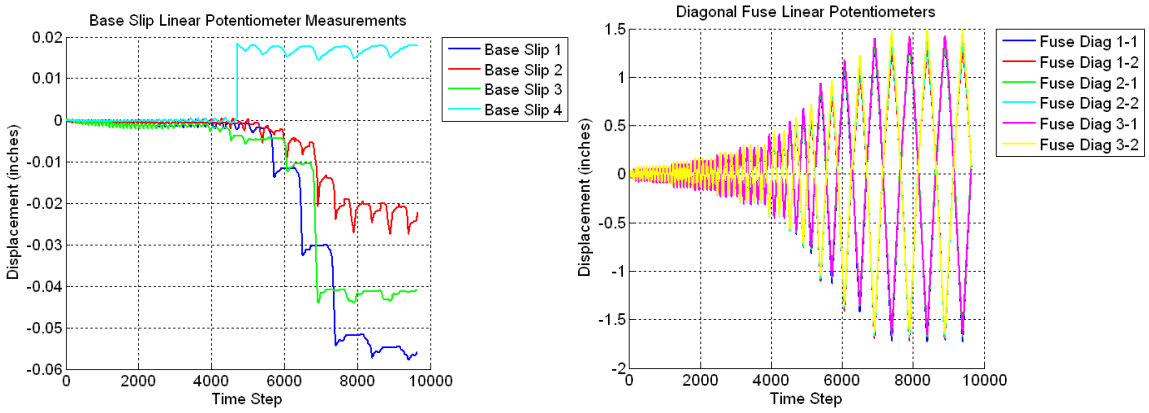

Figure B.1 Raw Data for Specimen A1 – Base Slip (Left) and Diagonal Fuse Linear Potentiometers (Right)

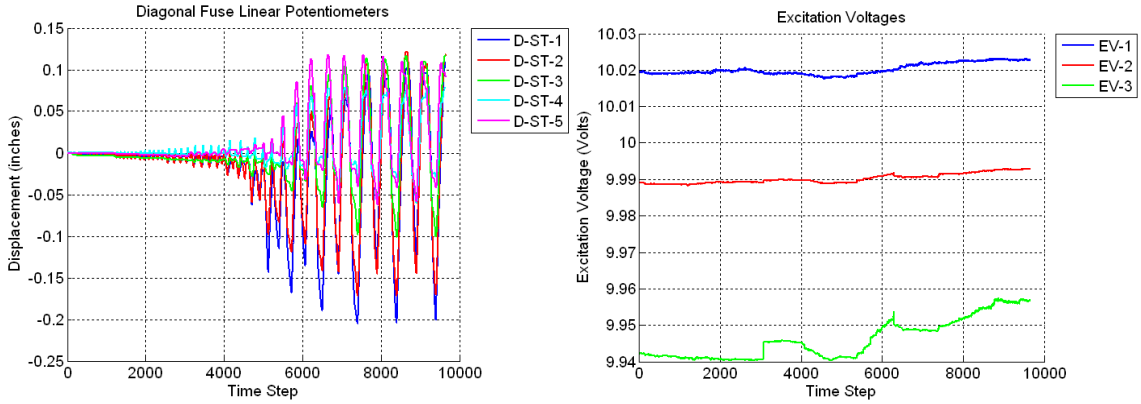

Figure B.2 Raw Data For Specimen A1 – Strut Linear Potentiometers (Left) and Excitation Voltages (Right)

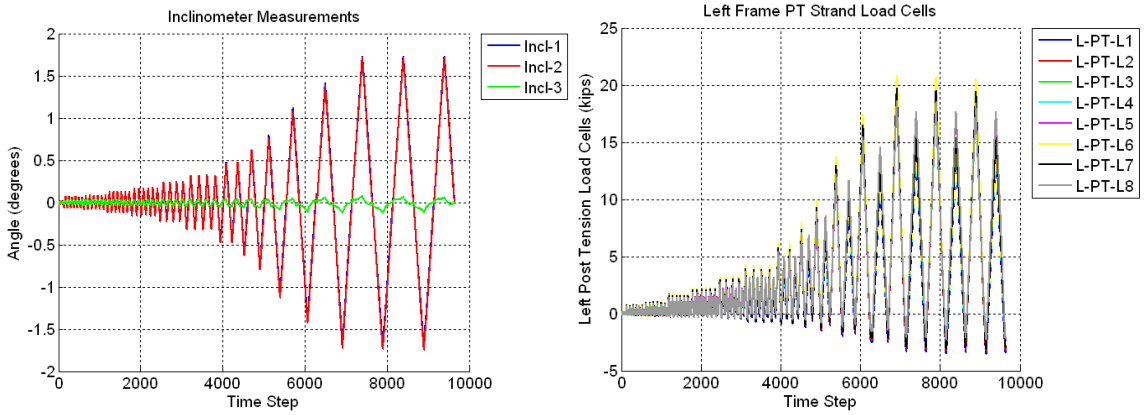

Figure B.3 Raw Data for Specimen A1 – Inclinometers (Left) and Left Frame PT Load Cells (Right)

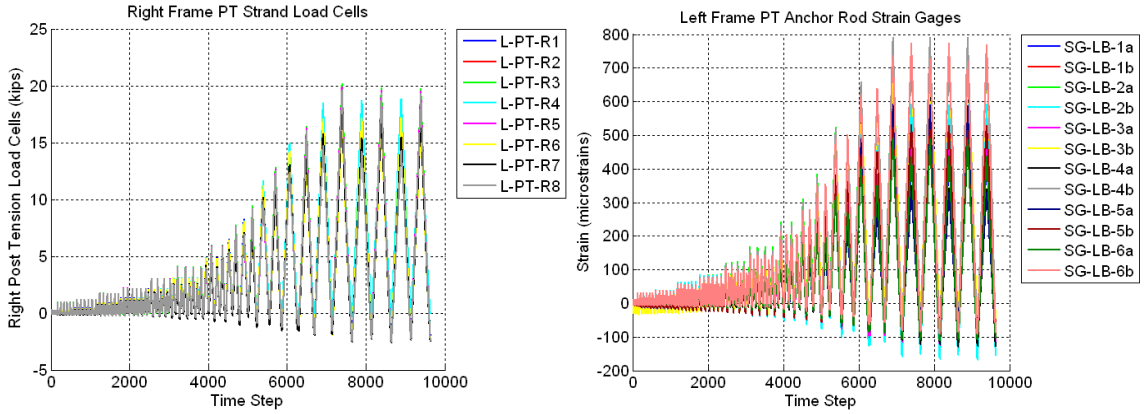

Figure B.4 Raw Data for Specimen A1 – Right Frame PT Load Cells (Left) and Left Frame PT Anchor Rod Strains (Right)

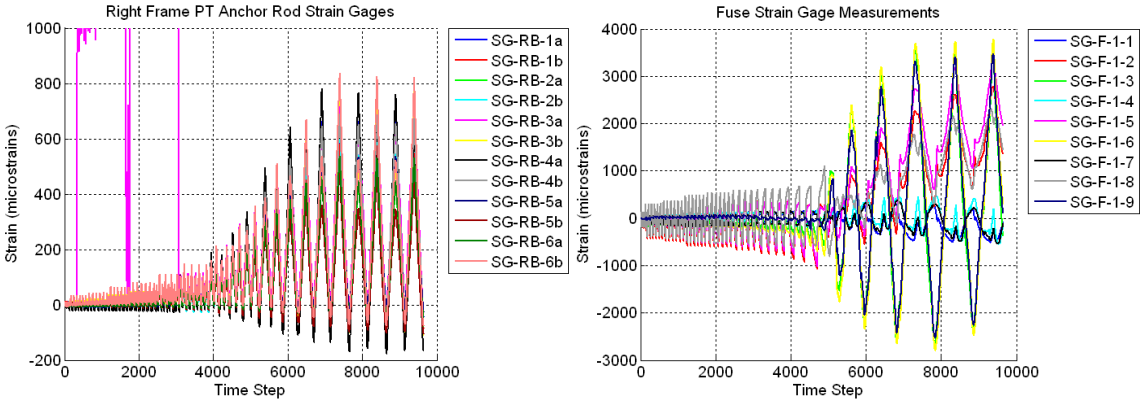

Figure B.5 Raw Data for Specimen A1 – Right Frame PT Anchor Rod Strains (Left) and Bottom Back Fuse Strains (Right)

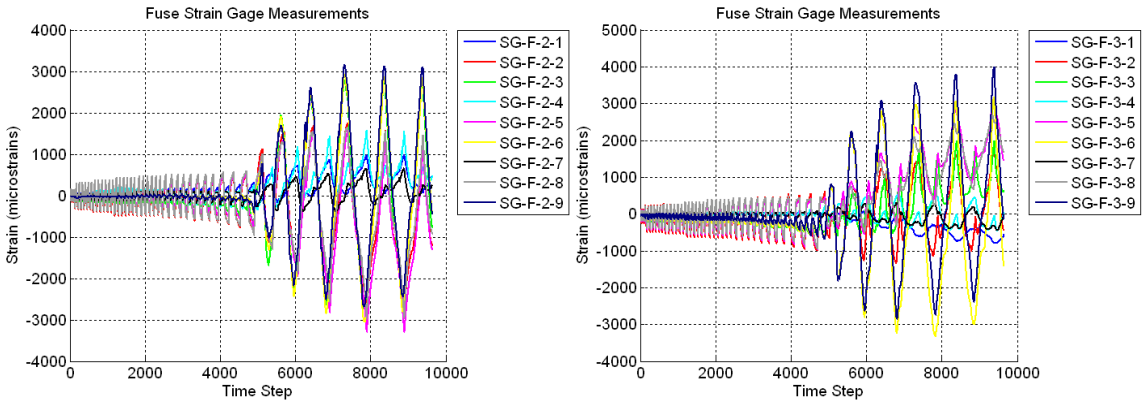

Figure B.6 Raw Data For Specimen A1 – Bottom Front Fuse Strain Gages (Left) and Mid-Height Back Fuse Strain Gages (Right)

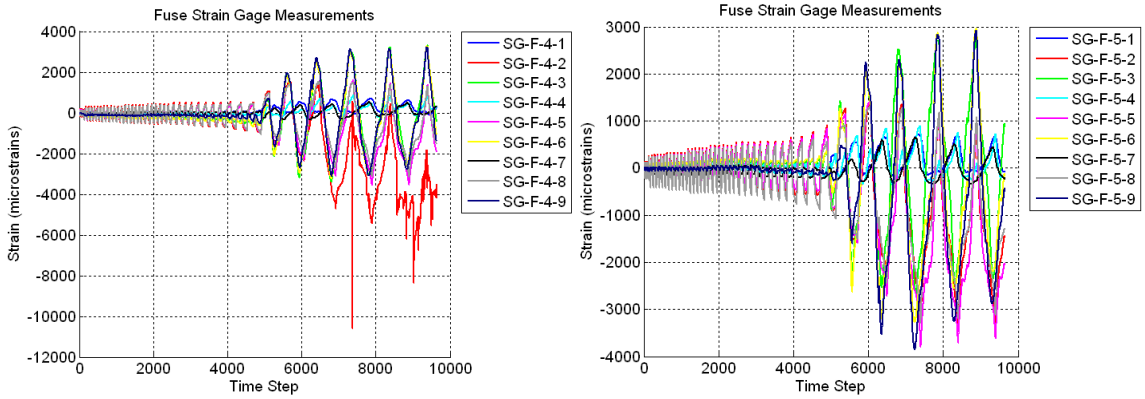

Figure B.7 Raw Data For Specimen A1 – Mid-Height Front Fuse Strain Gages (Left) and Top Back Fuse Strain Gages (Right)

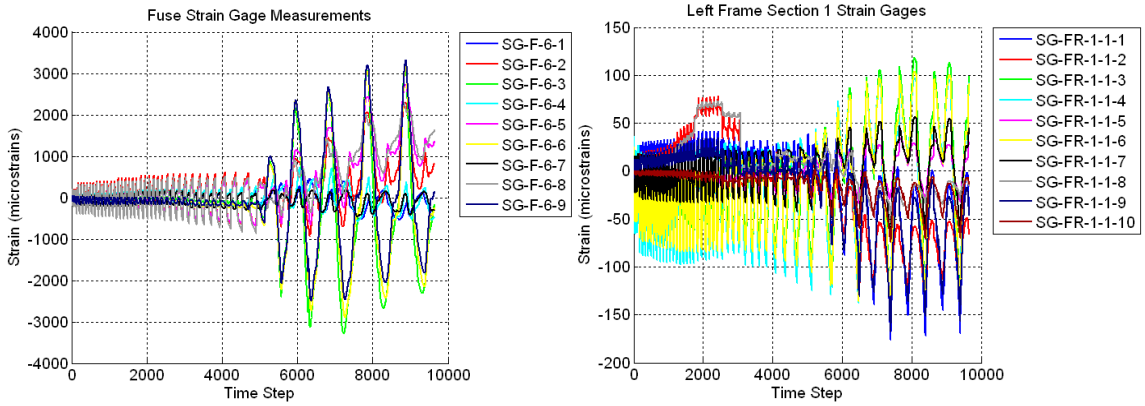

Figure B.8 Raw Data For Specimen A1 – Top Front Fuse Strain Gages (Left) and Left Frame Section 1-1 Strain Gages (Right)

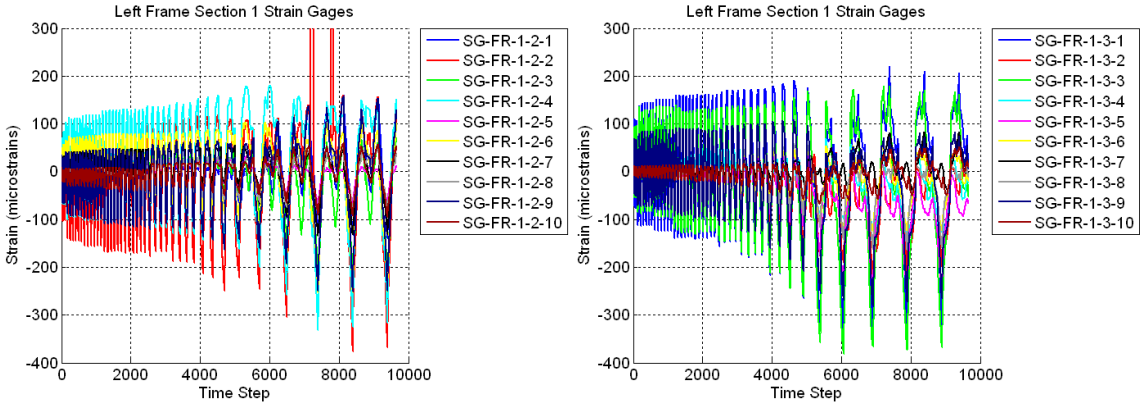

Figure B.9 Raw Data For Specimen A1 – Left Frame Section 1-2 Strain Gages (Left) and Left Frame Section 1-3 Strain Gages (Right)

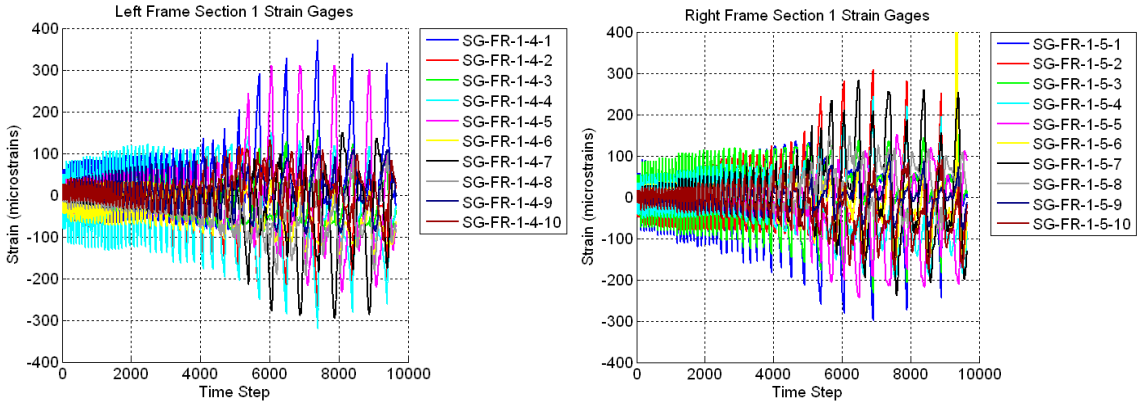

Figure B.10 Raw Data For Specimen A1 – Left Frame Section 1-4 Strain Gages (Left) and Right Frame Section 1-5 Strain Gages (Right)

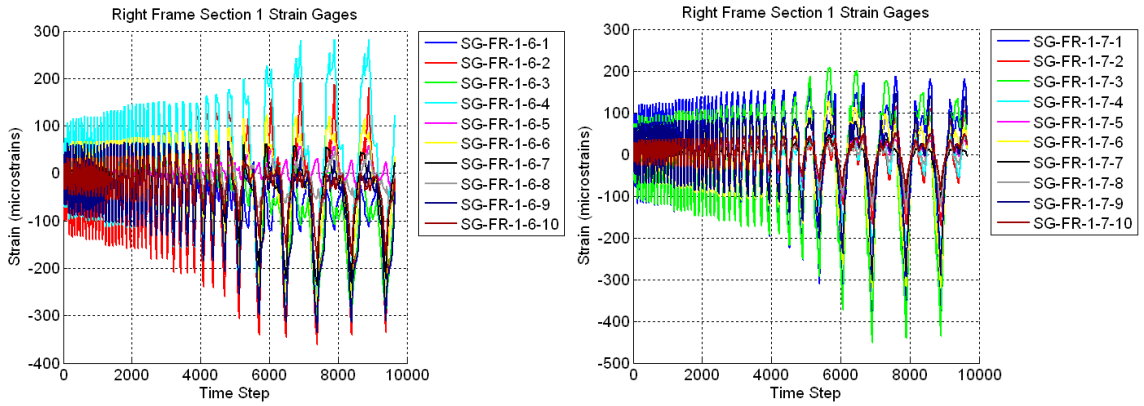

Figure B.11 Raw Data For Specimen A1 – Right Frame Section 1-6 Strain Gages (Left) and Right Frame Section 1-7 Strain Gages (Right)

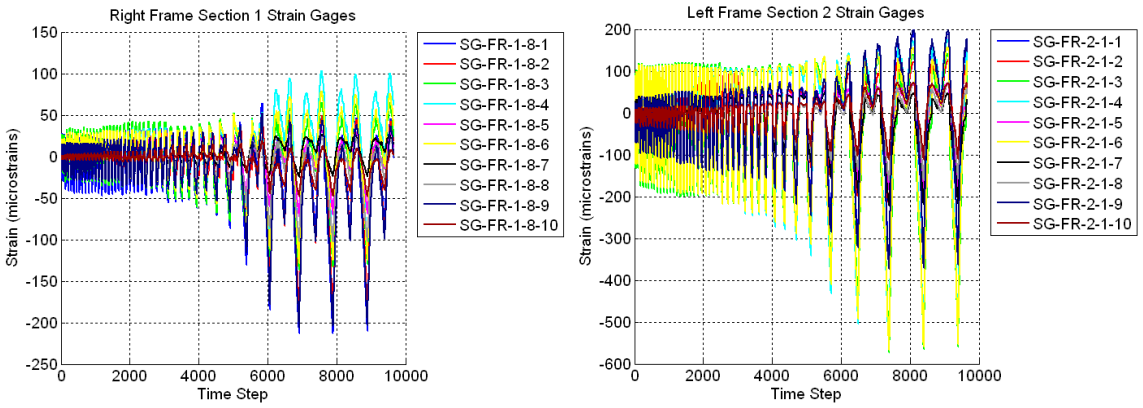

Figure B.12 Raw Data For Specimen A1 – Right Frame Section 1-8 Strain Gages (Left) and Left Frame Section 2-1 Strain Gages (Right)

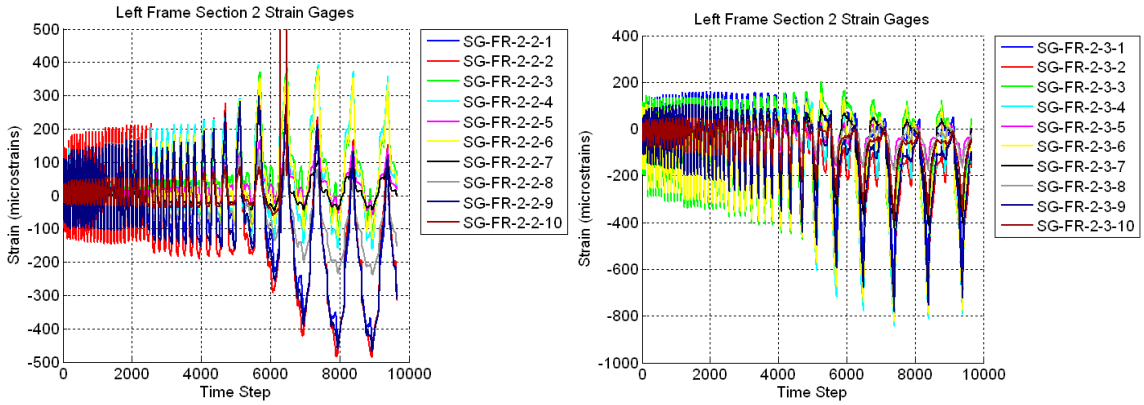

Figure B.13 Raw Data For Specimen A1 – Left Frame Section 2-2 Strain Gages (Left) and Left Frame Section 2-3 Strain Gages (Right)

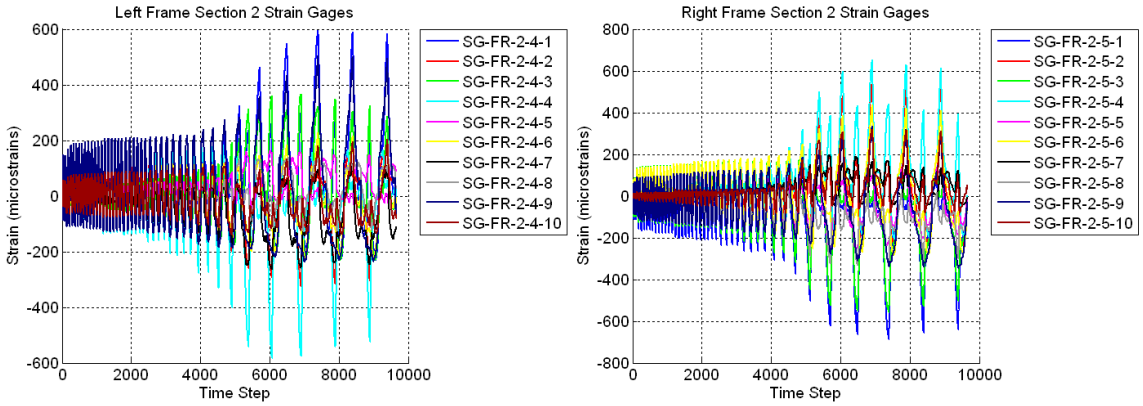

Figure B.14 Raw Data For Specimen A1 – Left Frame Section 2-4 Strain Gages (Left) and Right Frame Section 2-5 Strain Gages (Right)

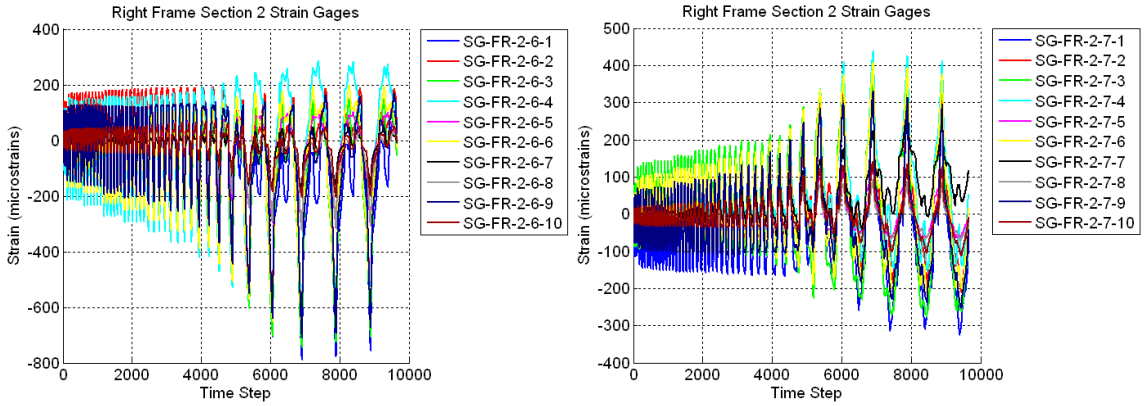

Figure B.15 Raw Data For Specimen A1 – Right Frame Section 2-6 Strain Gages (Left) and Right Frame Section 2-7 Strain Gages (Right)

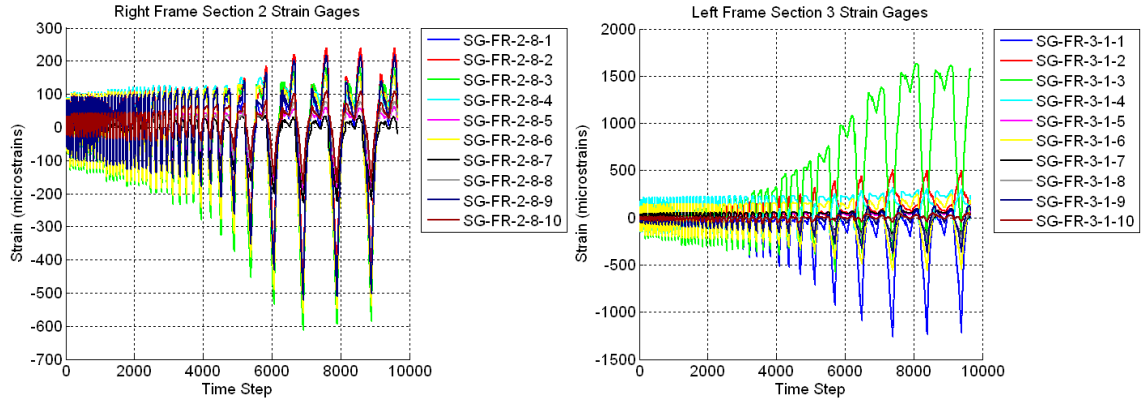

Figure B.16 Raw Data For Specimen A1 – Right Frame Section 2-8 Strain Gages (Left) and Left Frame Section 3-1 Strain Gages (Right)

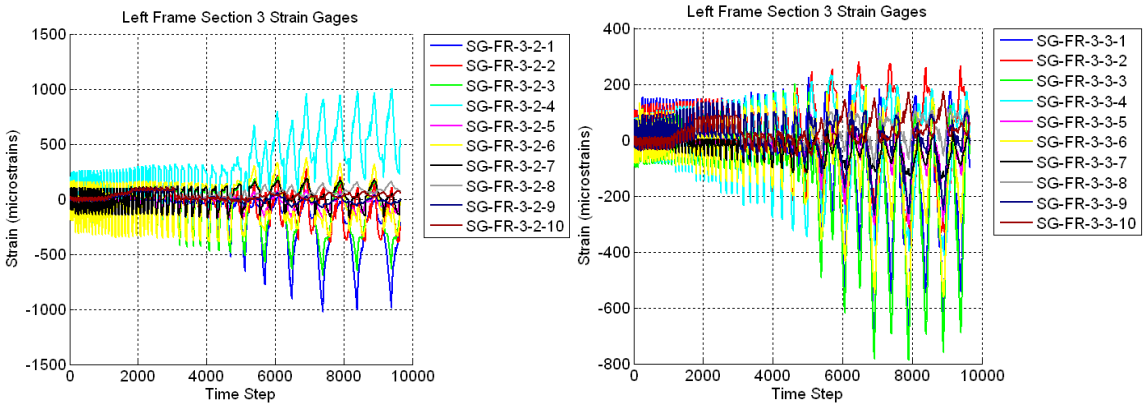

Figure B.17 Raw Data For Specimen A1 – Left Frame Section 3-2 Strain Gages (Left) and Left Frame Section 3-3 Strain Gages (Right)

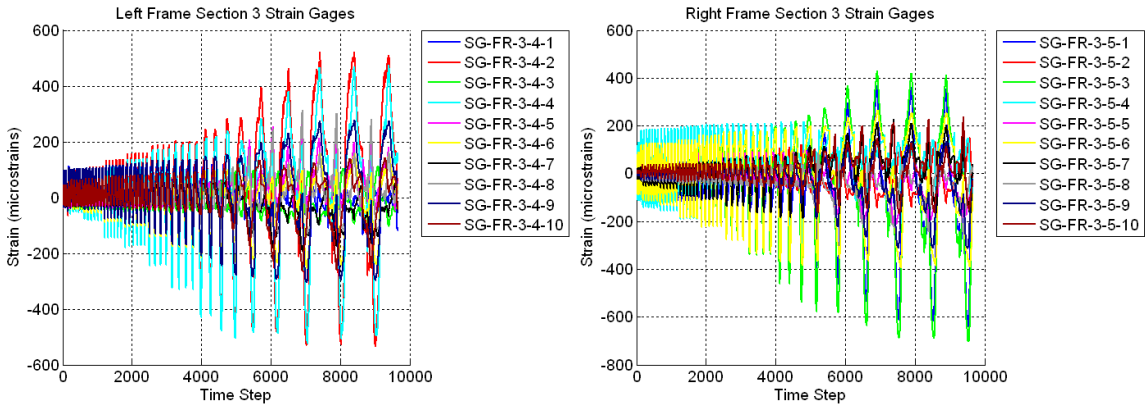

Figure B.18 Raw Data For Specimen A1 – Left Frame Section 3-4 Strain Gages (Left) and Right Frame Section 3-5 Strain Gages (Right)

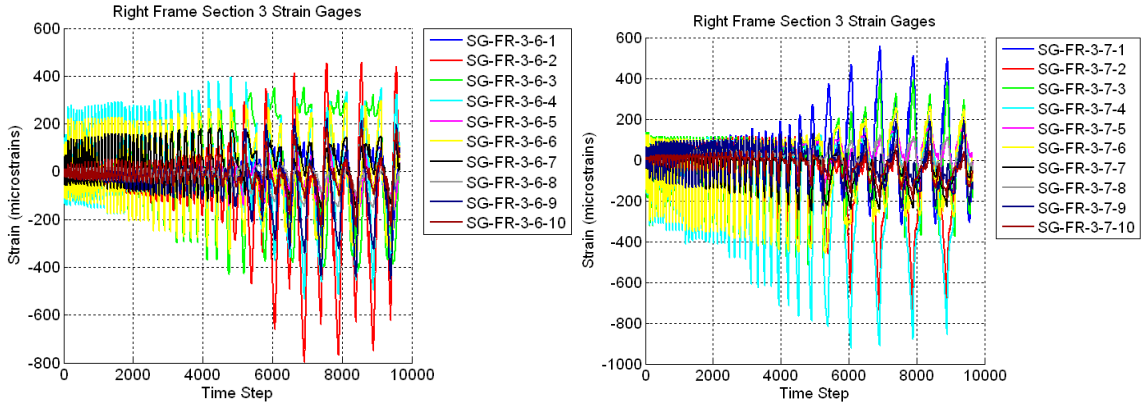

Figure B.19 Raw Data For Specimen A1 – Right Frame Section 3-6 Strain Gages (Left) and Right Frame Section 3-7 Strain Gages (Right)

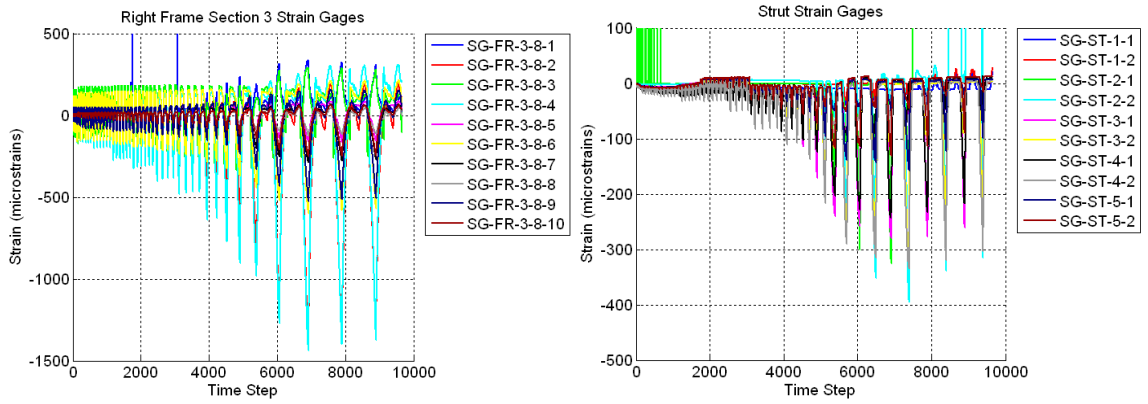

Figure B.20 Raw Data For Specimen A1 – Right Frame Section 3-8 Strain Gages (Left) and Strut Strain Gages (Right)

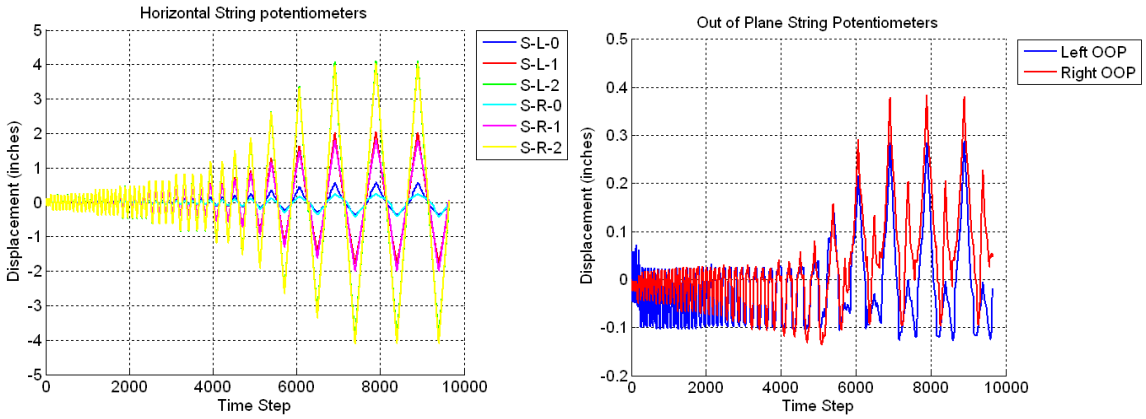

Figure B.21 Raw Data For Specimen A1 – Horizontal String Potentiometers (Left) and Out-of-Plane String Potentiometers (Right)

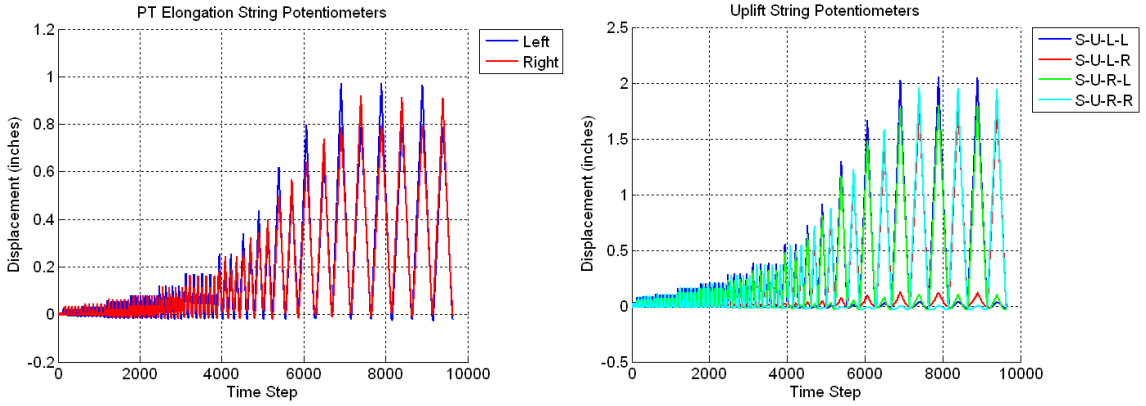

Figure B.22 Raw Data For Specimen A1 – Post-Tension Elongation String Potentiometers (Left) and Uplift String Potentiometers (Right)

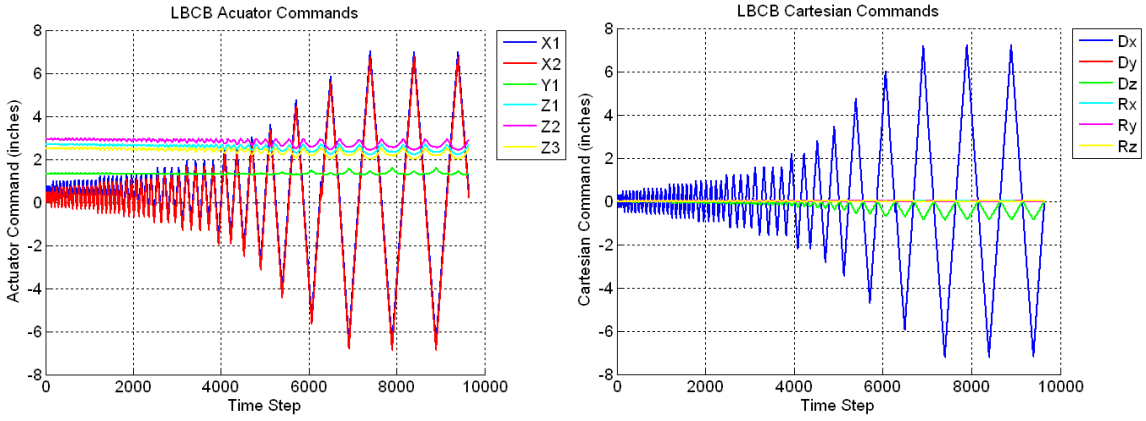

Figure B.23 Raw Data For Specimen A1 – LBCB Actuator Commands (Left) and LBCB Cartesian Commands (Right)

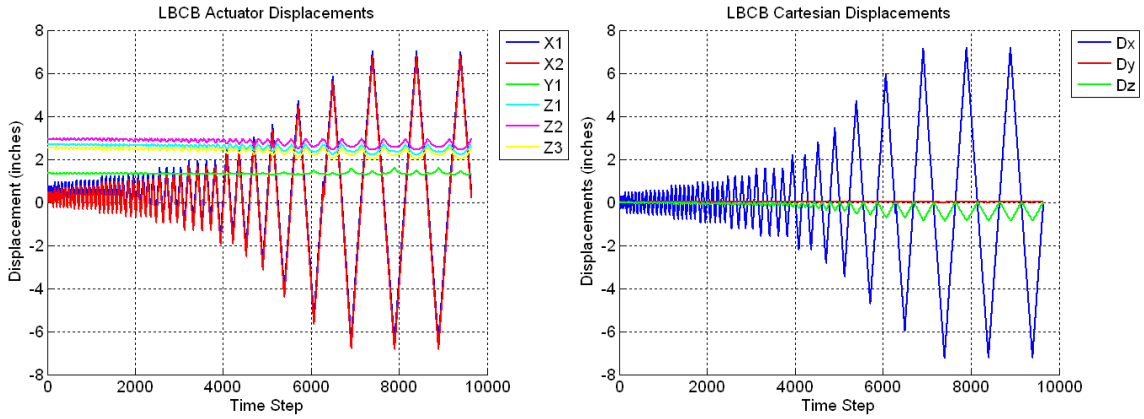

Figure B.24 Raw Data For Specimen A1 – LBCB Actuator Displacements (Left) and LBCB Cartesian Displacements (Right)

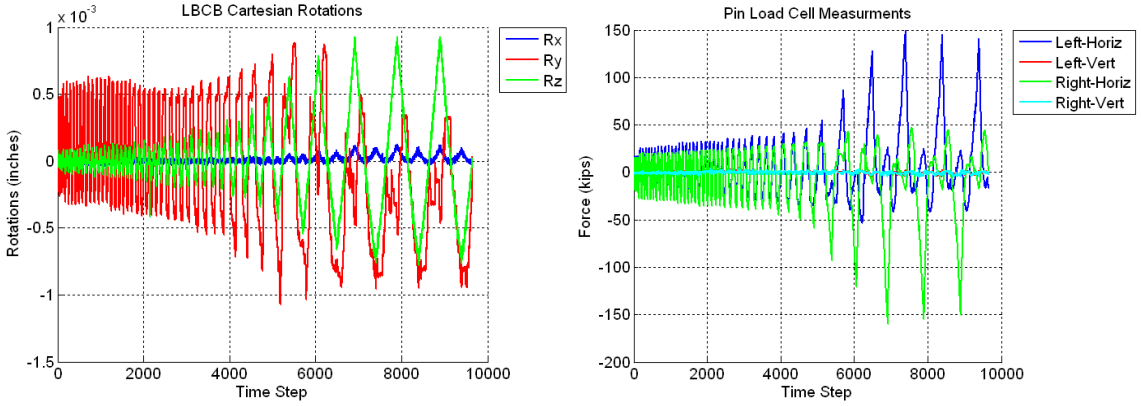

Figure B.25 Raw Data For Specimen A1 – LBCB Cartesian Rotations (Left) and Pin Load Cells (Right)

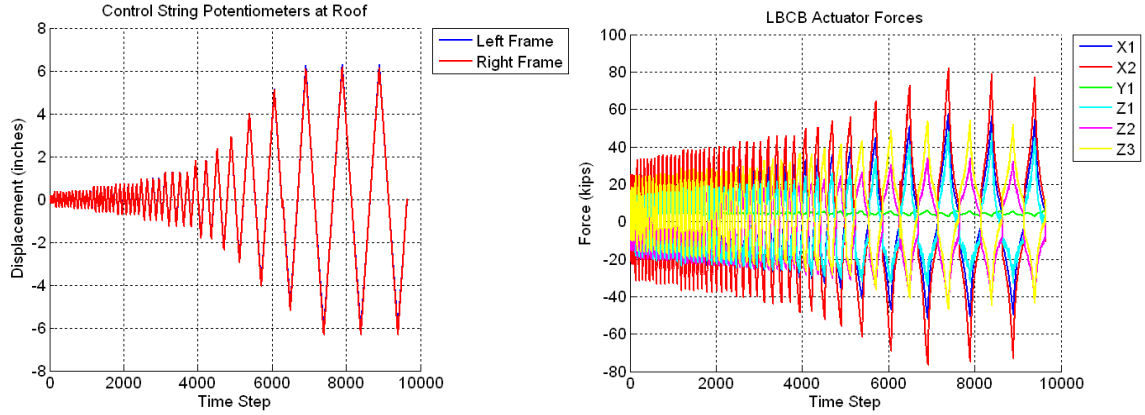

Figure B.26 Raw Data For Specimen A1 – Control Roof String Potentiometers (Left) and LBCB Actuator Forces (Right)

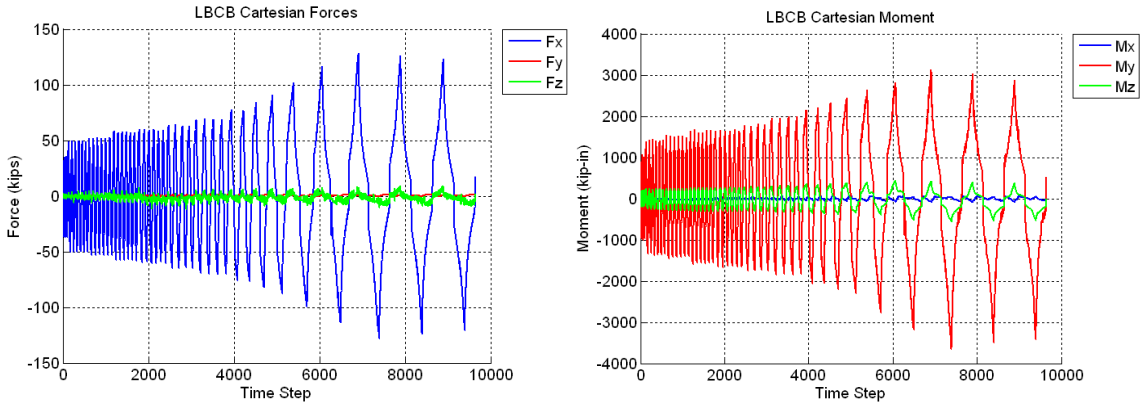

Figure B.27 Raw Data For Specimen A1 – LBCB Cartesian Forces (Left) and LBCB Cartesian Moments (Right)

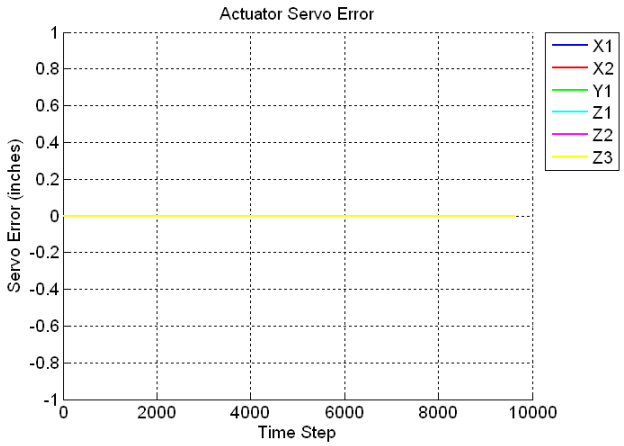

Figure B.28 Raw Data For Specimen A1 – LBCB Actuator Servo-Error

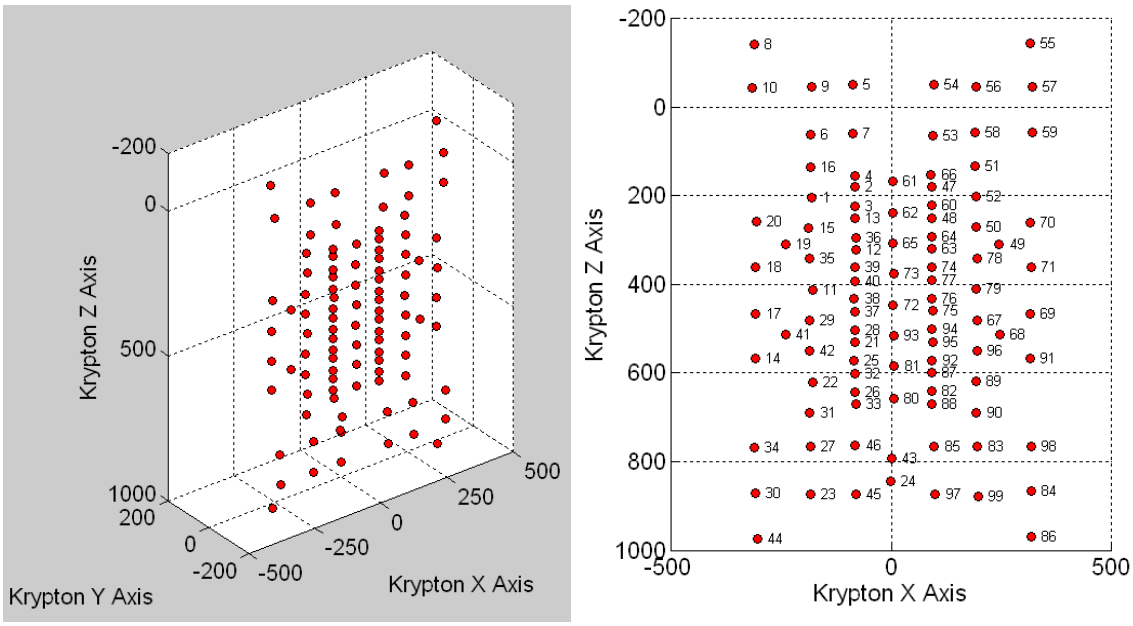

Figure B.29 Raw Data For Specimen A1 – Krypton LED Locations (Left) and Krypton LED Numbering (Right)

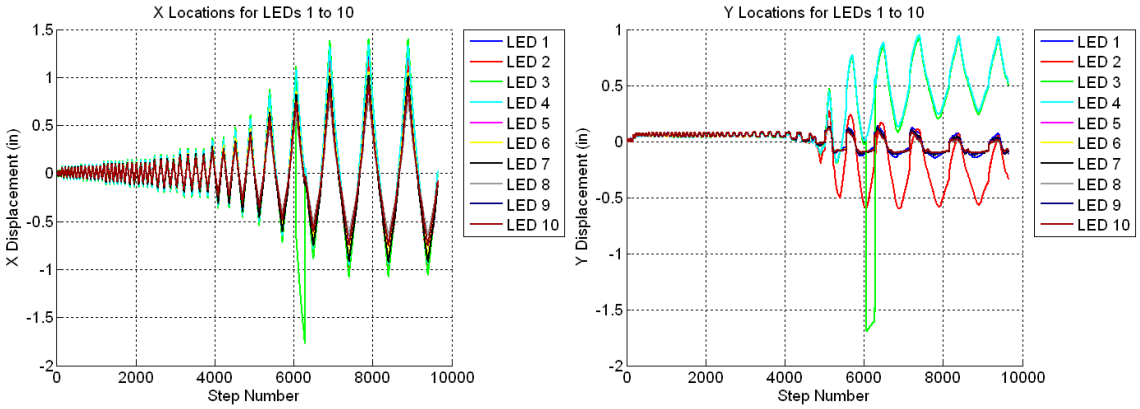

Figure B.30 Raw Data For Specimen A1 – X Displacements for LED's 1 to 10 (Left) and Y Displacements for LED's 1 to 10 (Right)

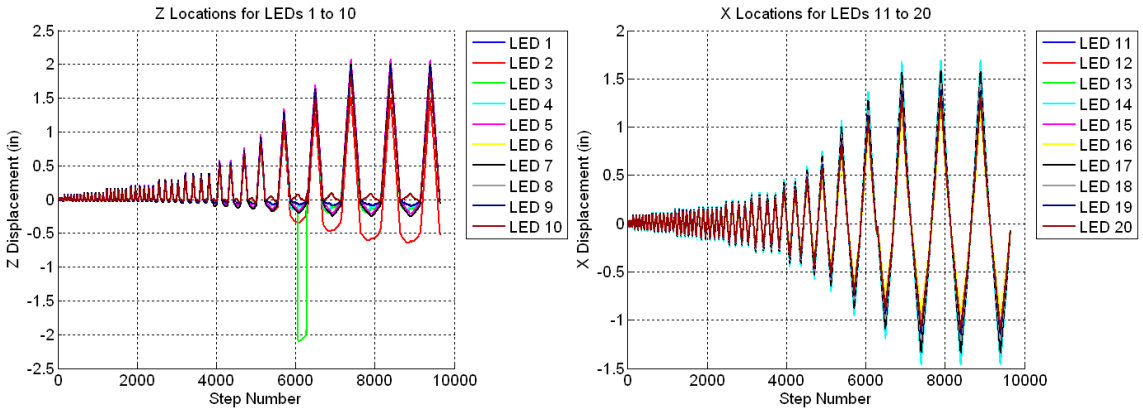

Figure B.31 Raw Data For Specimen A1 – Z Displacements for LED's 1 to 10 (Left) and X Displacements for LED's 11 to 20 (Right)

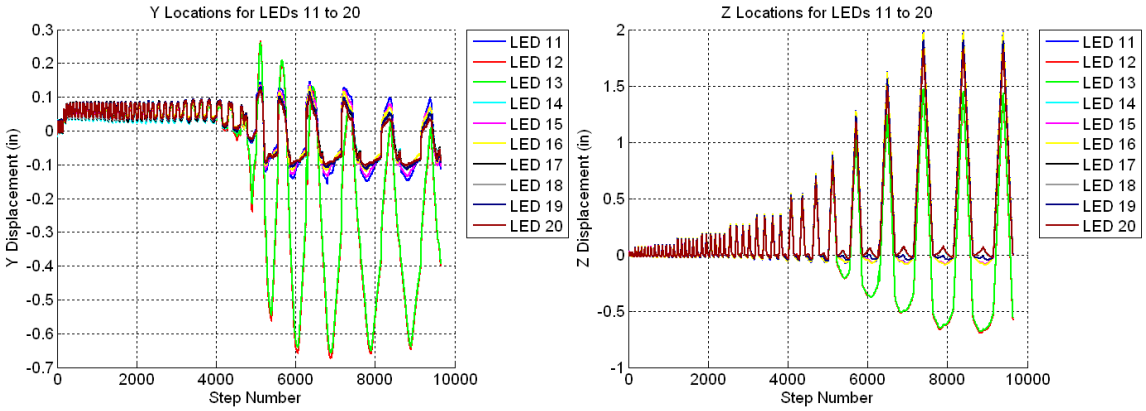

Figure B.32 Raw Data For Specimen A1 – Y Displacements for LED's 11 to 20 (Left) and Z Displacements for LED's 11 to 20 (Right)

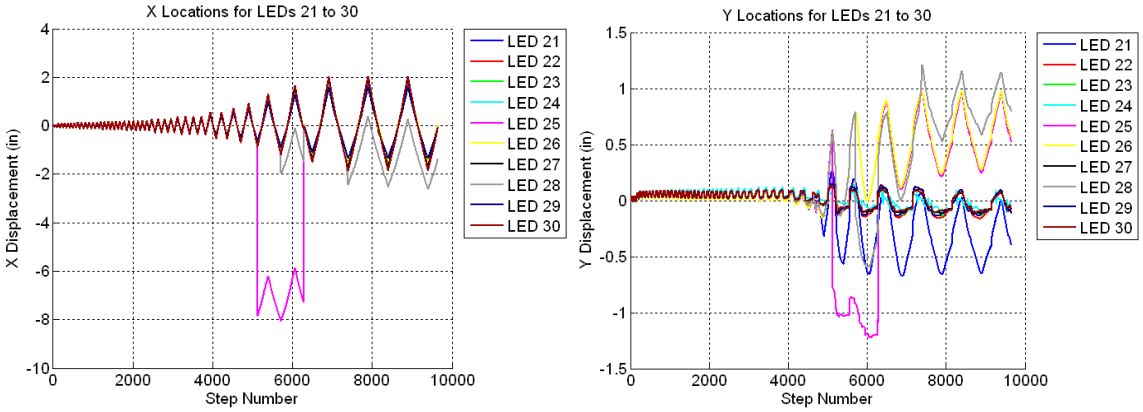

Figure B.33 Raw Data For Specimen A1 – X Displacements for LED's 21 to 30 (Left) and Y Displacements for LED's 21 to 30 (Right)

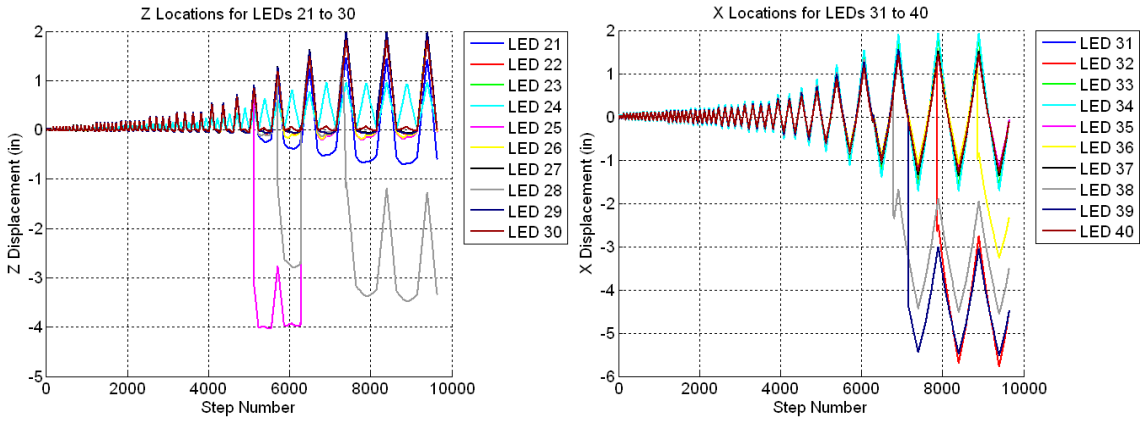

Figure B.34 Raw Data For Specimen A1 – Z Displacements for LED's 21 to 30 (Left) and X Displacements for LED's 31 to 40 (Right)

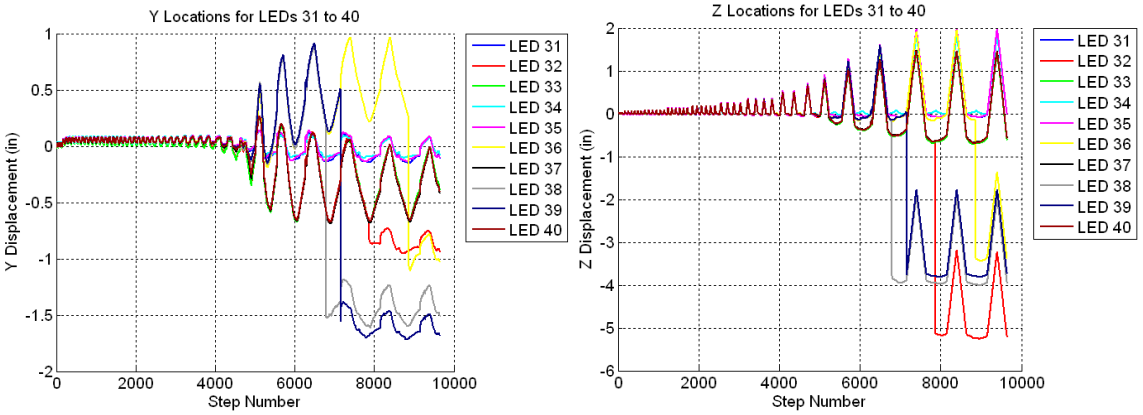

Figure B.35 Raw Data For Specimen A1 – Y Displacements for LED's 31 to 40 (Left) and Z Displacements for LED's 31 to 40 (Right)

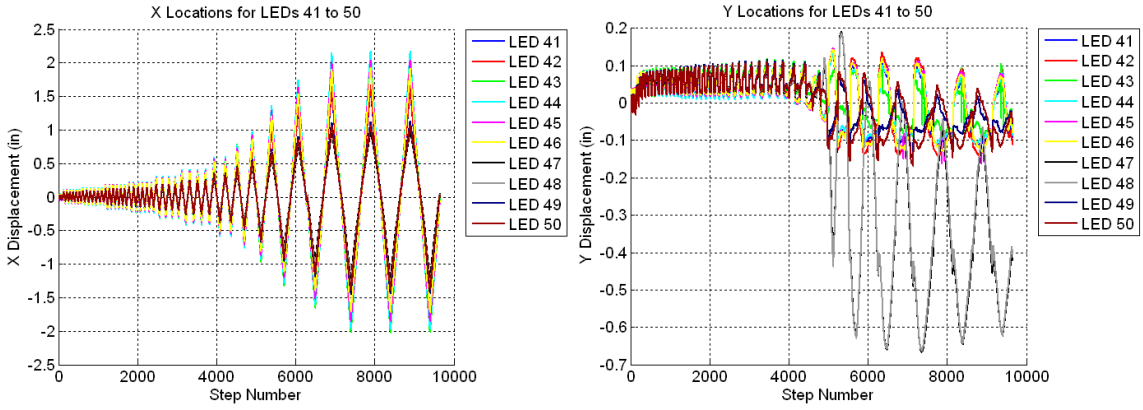

Figure B.36 Raw Data For Specimen A1 – X Displacements for LED's 41 to 50 (Left) and Y Displacements for LED's 41 to 50 (Right)

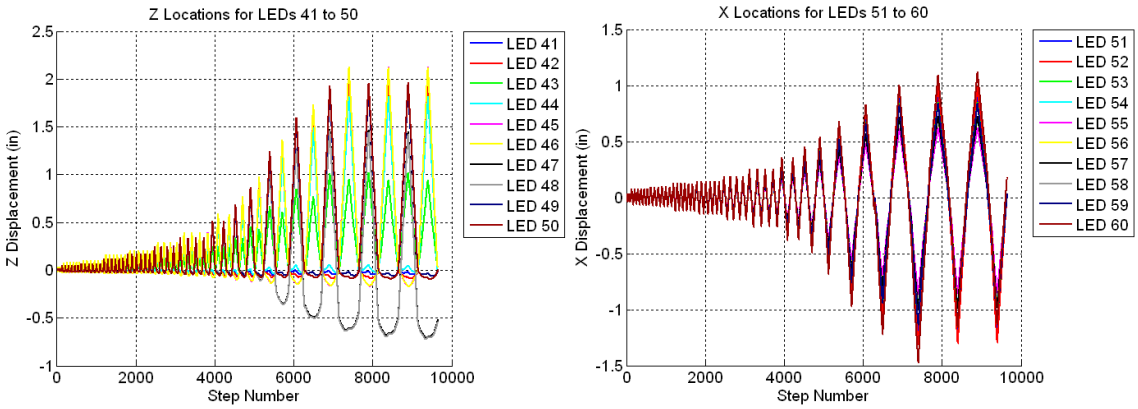

Figure B.37 Raw Data For Specimen A1 – Z Displacements for LED's 41 to 50 (Left) and X Displacements for LED's 51 to 60 (Right)

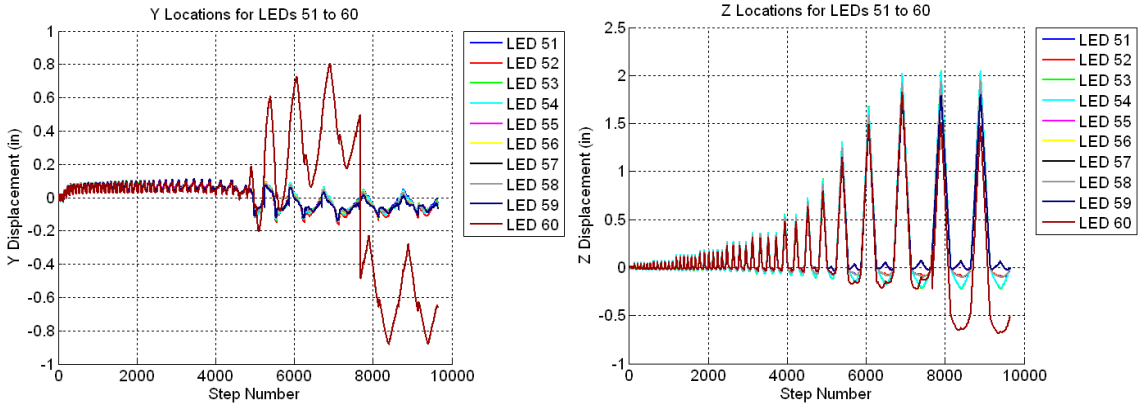

Figure B.38 Raw Data For Specimen A1 – Y Displacements for LED's 51 to 60 (Left) and Z Displacements for LED's 51 to 60 (Right)

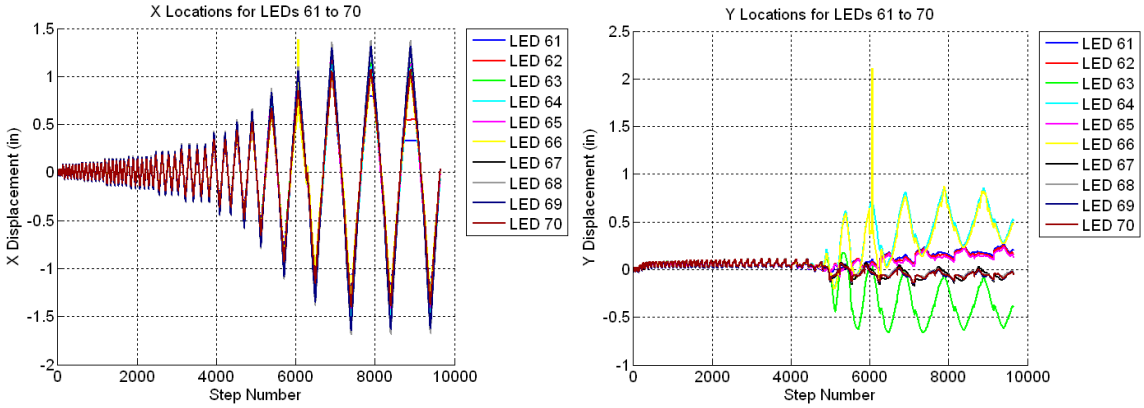

Figure B.39 Raw Data For Specimen A1 – X Displacements for LED's 61 to 70 (Left) and Y Displacements for LED's 61 to 70 (Right)

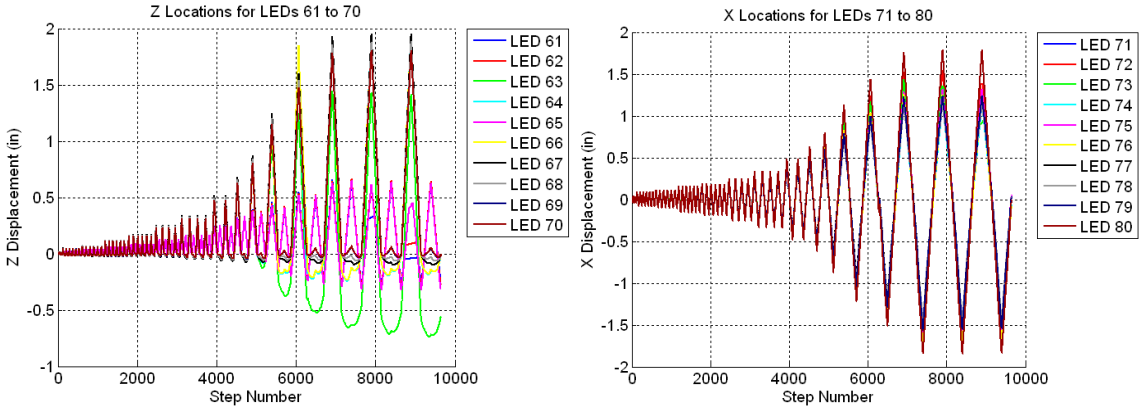

Figure B.40 Raw Data For Specimen A1 – Z Displacements for LED's 61 to 70 (Left) and X Displacements for LED's 71 to 80 (Right)

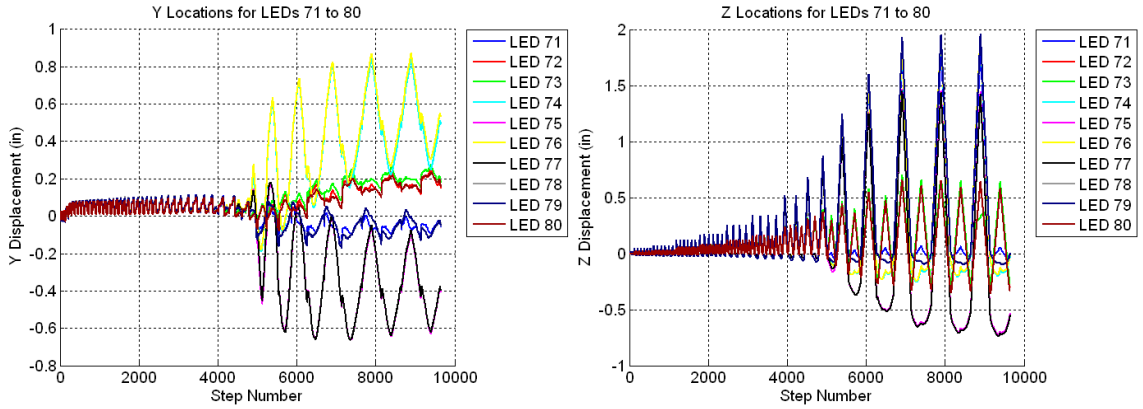

Figure B.41 Raw Data For Specimen A1 – Y Displacements for LED's 71 to 80 (Left) and Z Displacements for LED's 71 to 80 (Right)

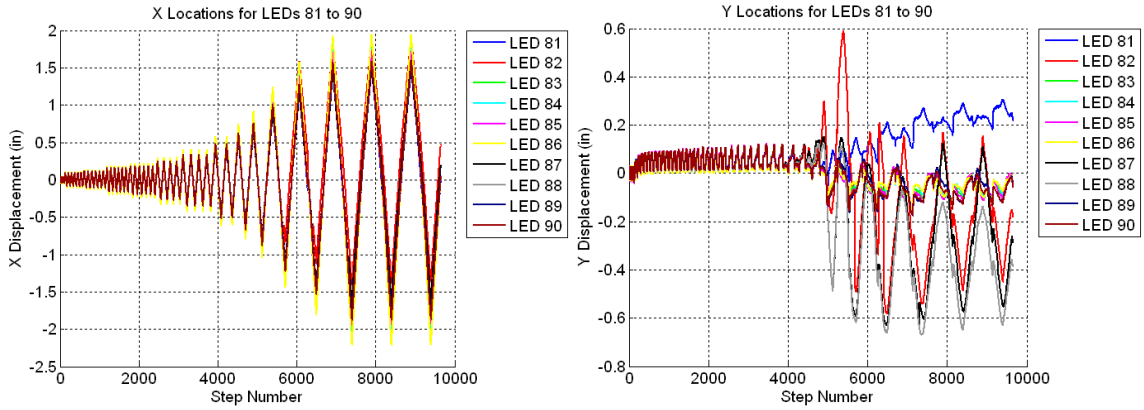

Figure B.42 Raw Data For Specimen A1 – X Displacements for LED's 81 to 90 (Left) and Y Displacements for LED's 81 to 90 (Right)

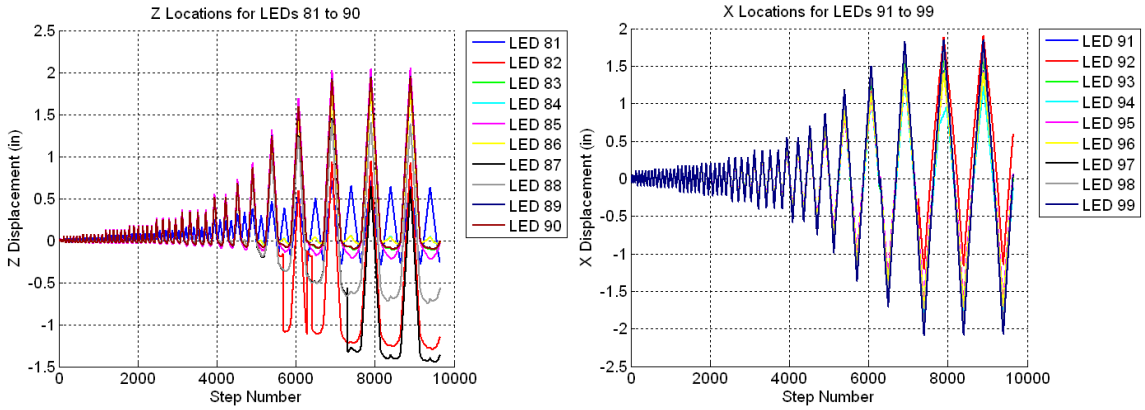

Figure B.43 Raw Data For Specimen A1 – Z Displacements for LED's 81 to 90 (Left) and X Displacements for LED's 91 to 99 (Right)

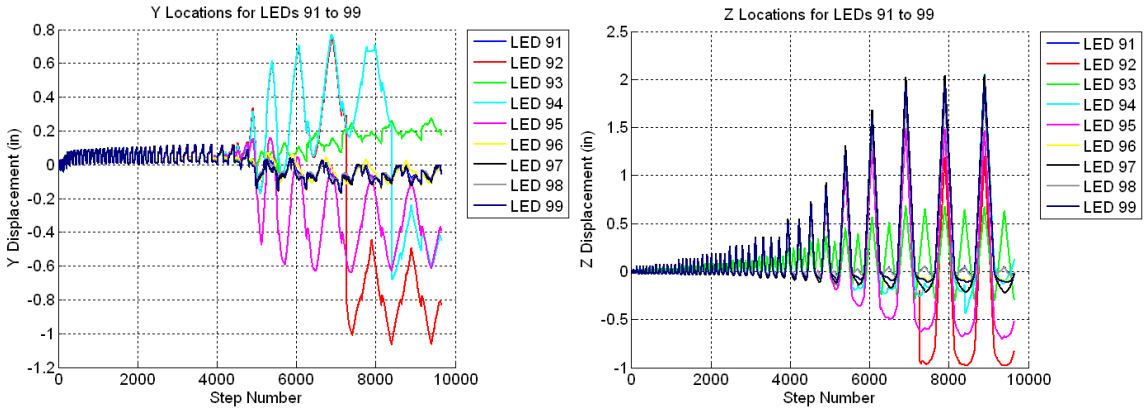

Figure B.44 Raw Data For Specimen A1 – Y Displacements for LED's 91 to 99 (Left) and Z Displacements for LED's 91 to 99 (Right)

B.2 Specimen A2

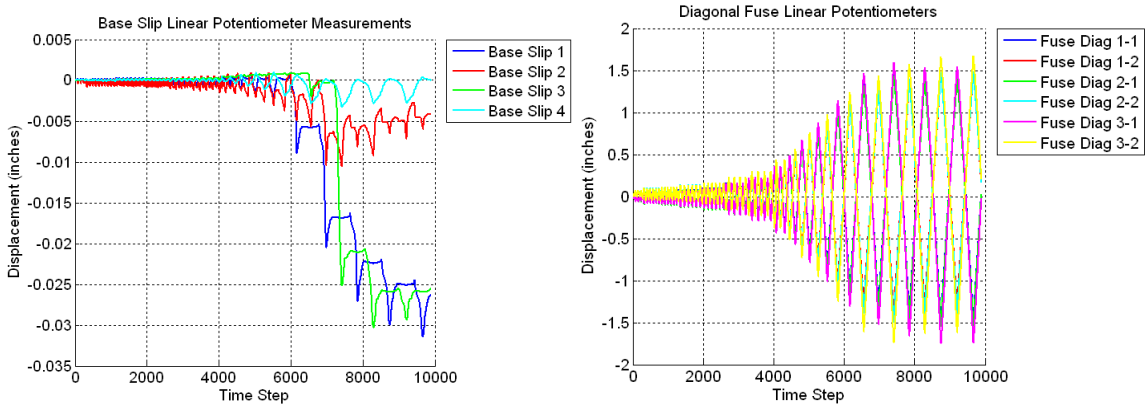

Figure B.45 Raw Data For Specimen A2 – Base Slip (Left) and Fuse Linear Pots (Right)

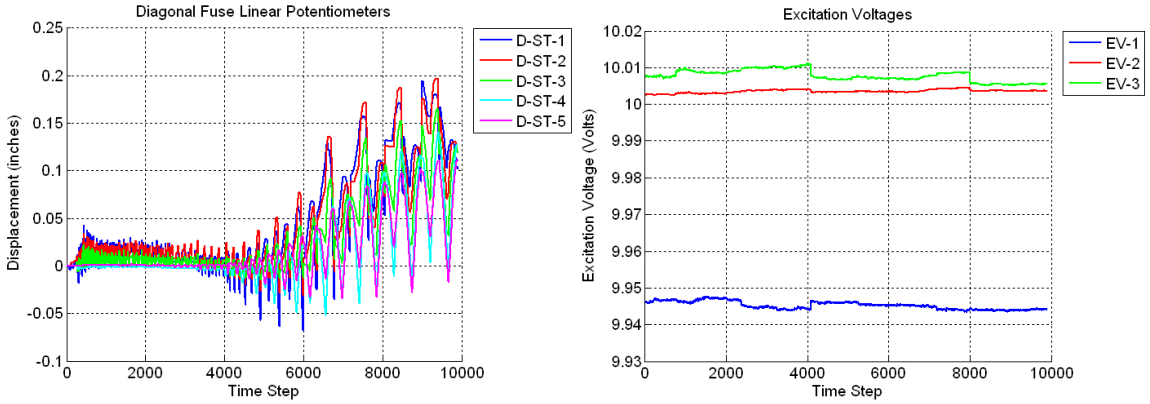

Figure B.46 Raw Data For Specimen A2 – Strut Linear Potentiometers (Left) and Excitation Voltages (Right)

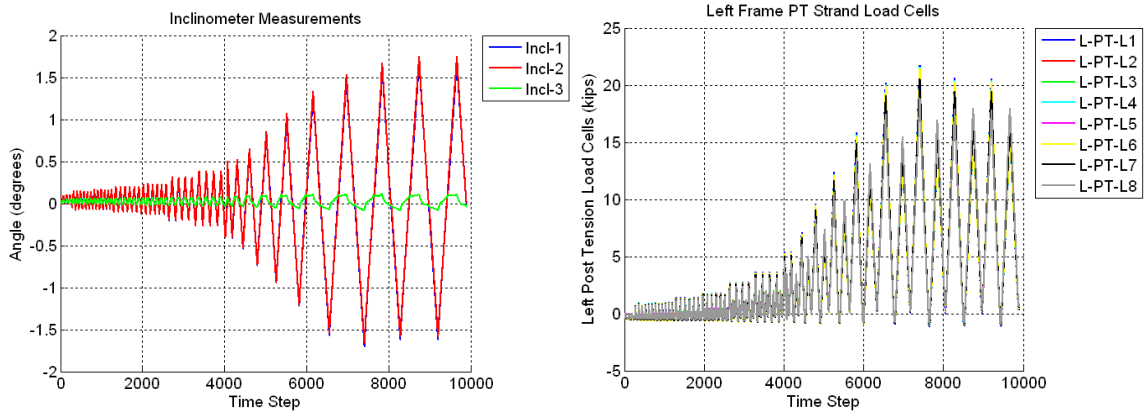

Figure B.47 Raw Data For Specimen A2 – Inclinometers (Left) and Left Frame PT Load Cells (Right)

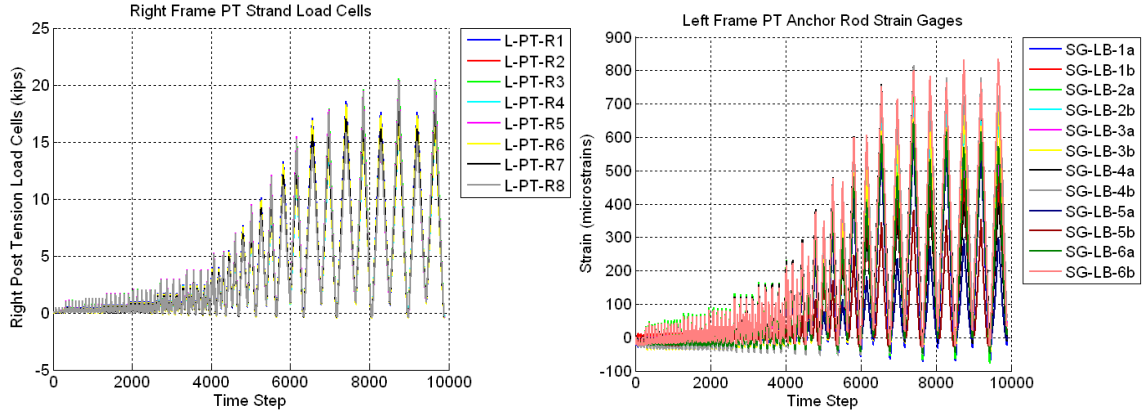

Figure B.48 Raw Data For Specimen A2 – Right Frame PT Load Cells (Left) and Left Frame Anchor Rod Strain Gages (Right)

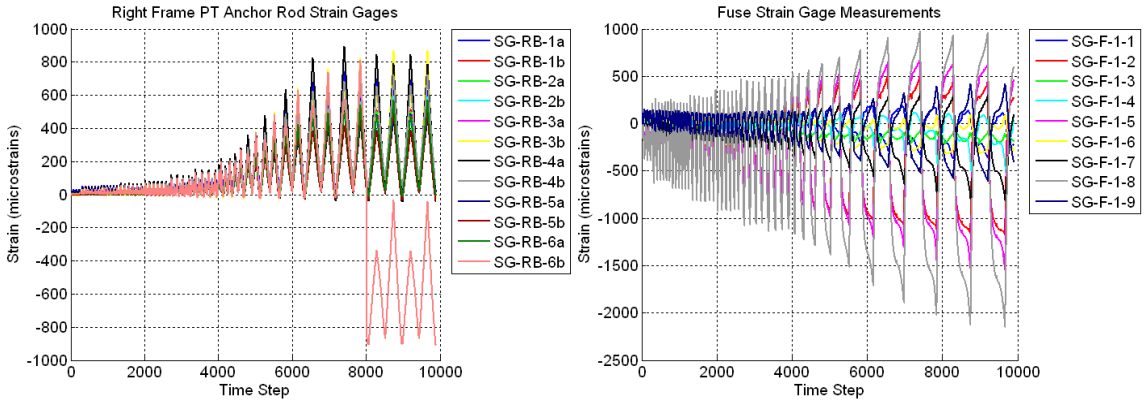

Figure B.49 Raw Data For Specimen A2 – Right Frame PT Anchor Rod Strain Gages (Left) and Back Side Fuse Strain Gages (Right)

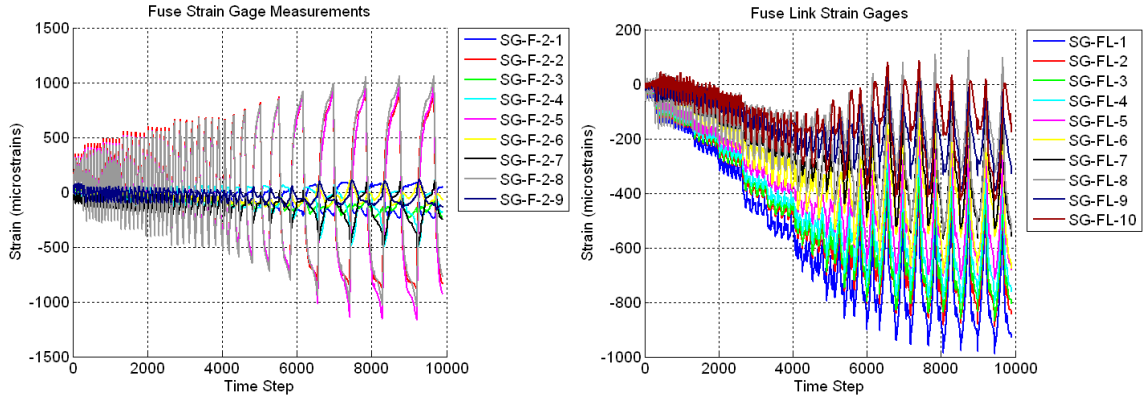

Figure B.50 Raw Data For Specimen A2 – Front Fuse Strain Gages (Left) and Fuse Link Strain Gages (Right)

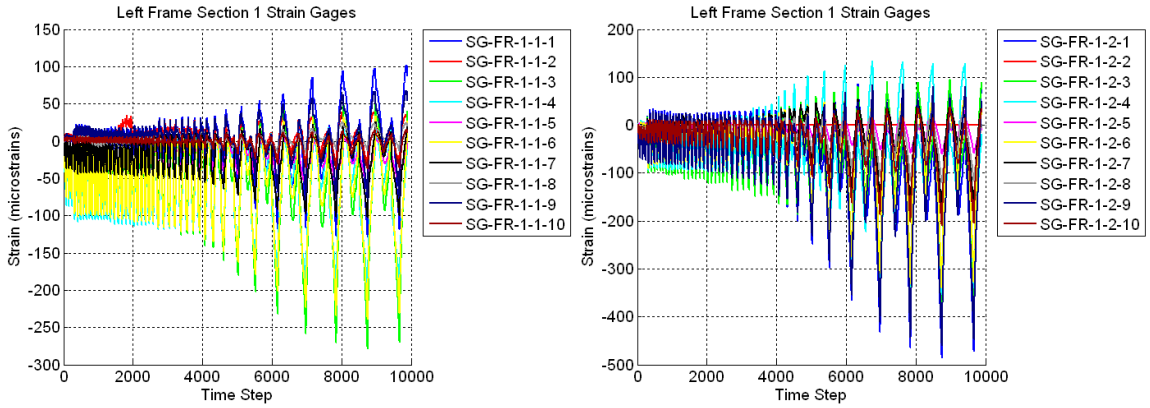

Figure B.51 Raw Data For Specimen A2 – Left Frame Section 1-1 Strain Gages (Left) and Left Frame Section 1-2 Strain Gages (Right)

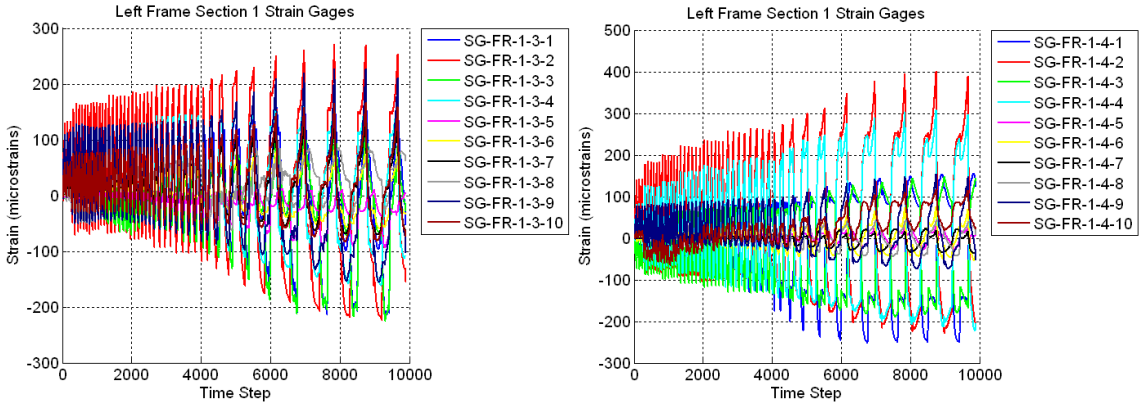

Figure B.52 Raw Data For Specimen A2 – Left Frame Section 1-3 Strain Gages (Left) and Left Frame Section 1-4 Strain Gages (Right)

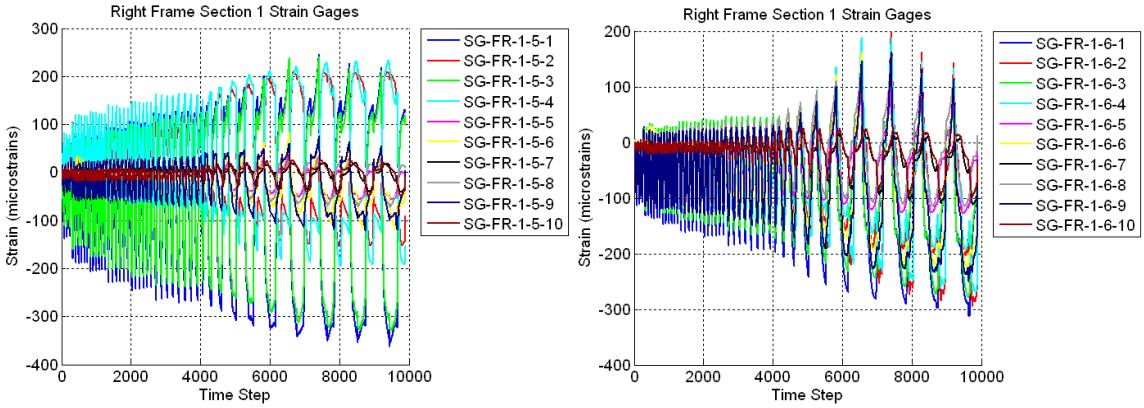

Figure B.53 Raw Data For Specimen A2 – Right Frame Section 1-5 Strain Gages (Left) and Right Frame Section 1-6 Strain Gages (Right)

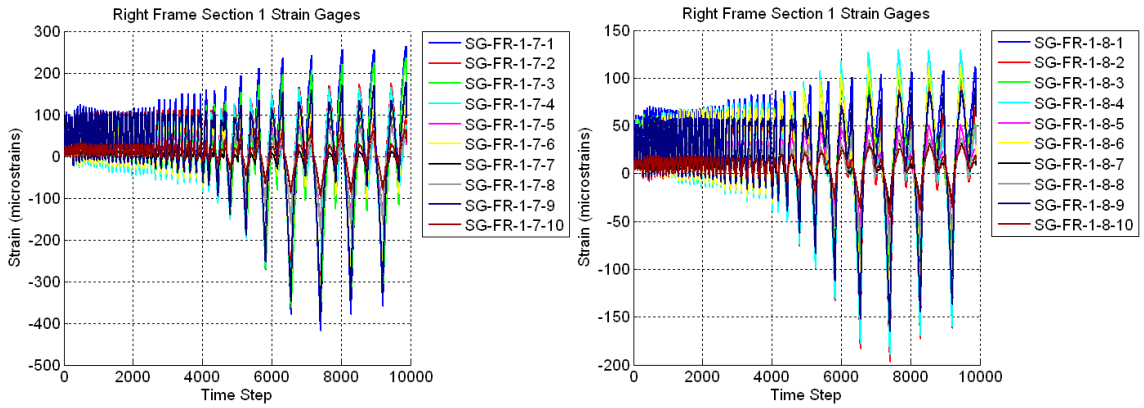

Figure B.54 Raw Data For Specimen A2 – Right Frame Section 1-7 Strain Gages (Left) and Right Frame Section 1-8 Strain Gages (Right)

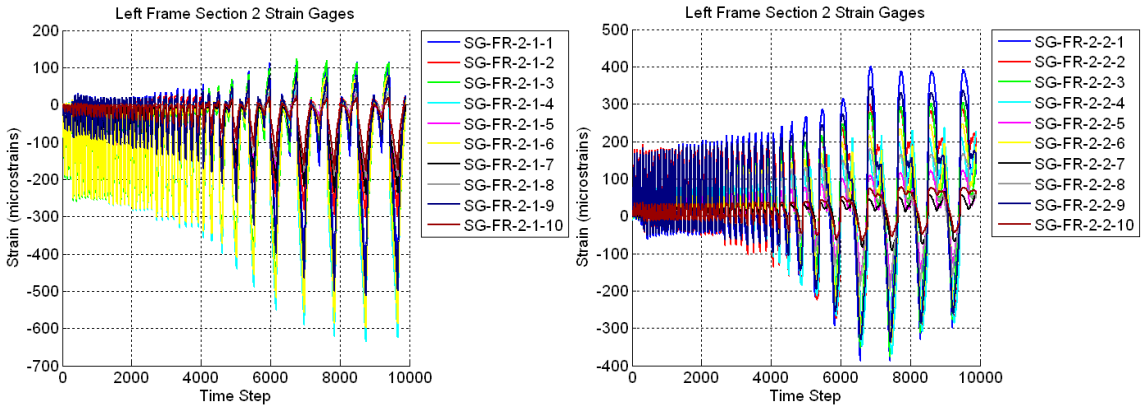

Figure B.55 Raw Data For Specimen A2 – Left Frame Section 2-1 Strain Gages (Left) and Left Frame Section 2-2 Strain Gages (Right)

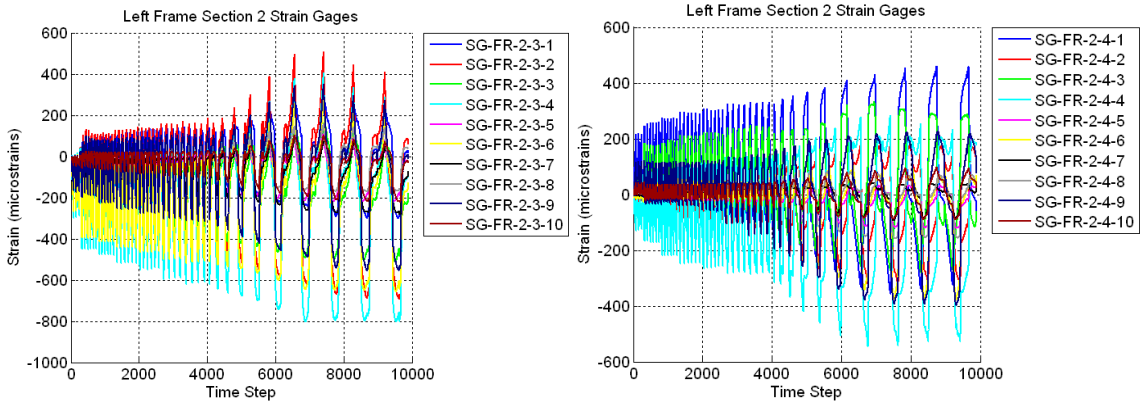

Figure B.56 Raw Data For Specimen A2 – Left Frame Section 2-3 Strain Gages (Left) and Left Frame Section 2-4 Strain Gages (Right)

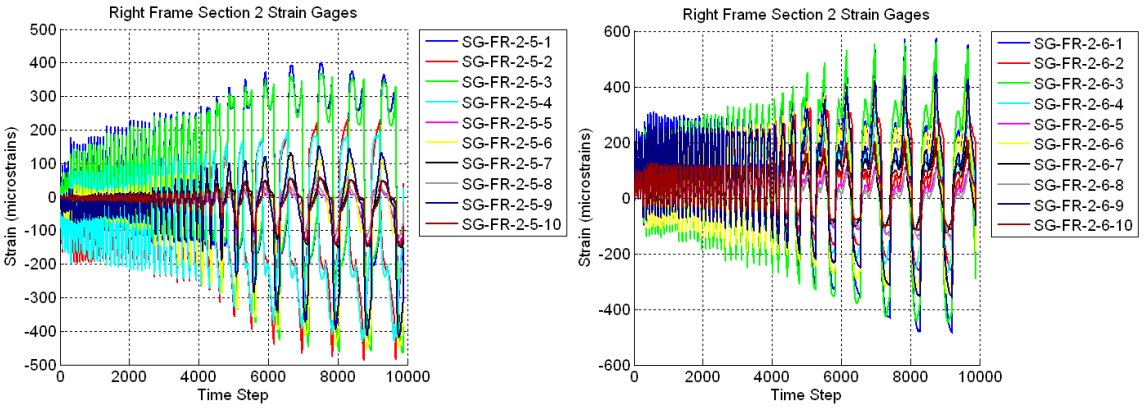

Figure B.57 Raw Data For Specimen A2 – Right Frame Section 2-5 Strain Gages (left) and Right Frame Section 2-6 Strain Gages (Right)

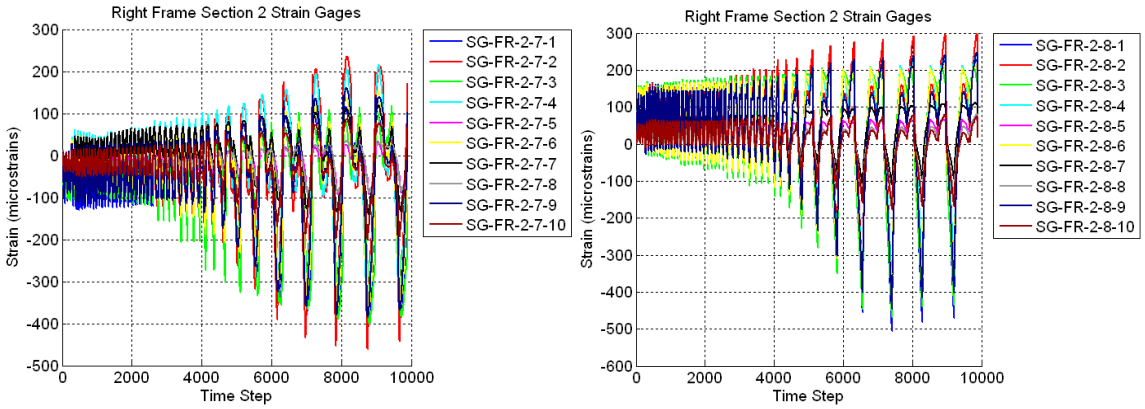

Figure B.58 Raw Data For Specimen A2 – Right Frame Section 2-7 Strain Gages (Left) and Right Frame Section 2-8 Strain Gages (Right)

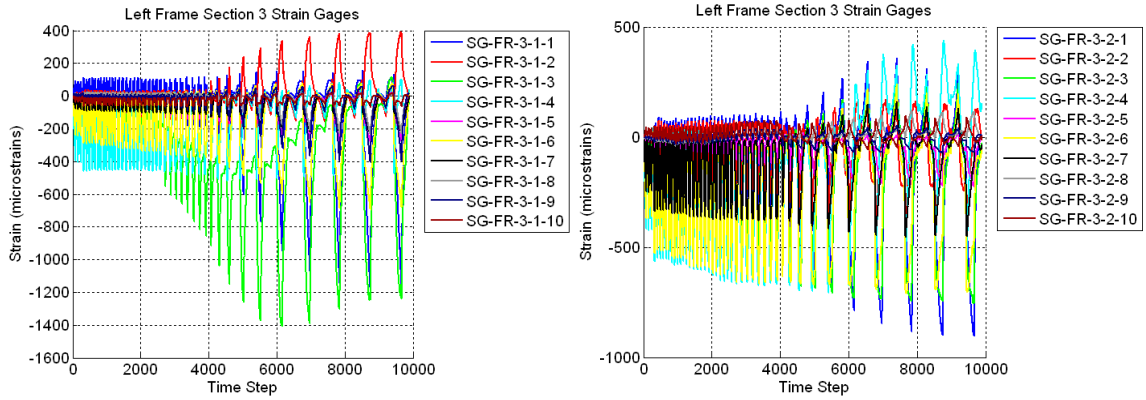

Figure B.59 Raw Data For Specimen A2 – Left Frame Section 3-1 Strain Gages (Left) and Left Frame Section 3-2 Strain Gages (Right)

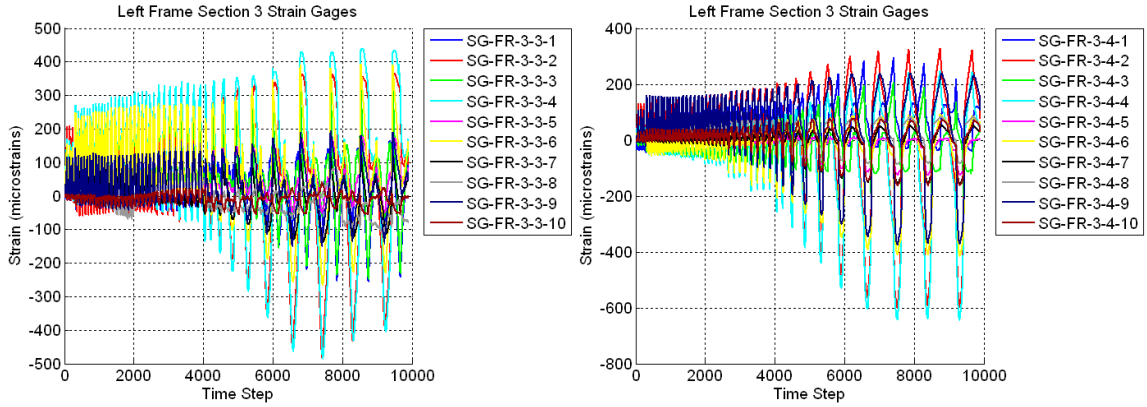

Figure B.60 Raw Data For Specimen A2 – Left Frame Section 3-3 Strain Gages (Left) and Left Frame Section 3-4 Strain Gages (Right)

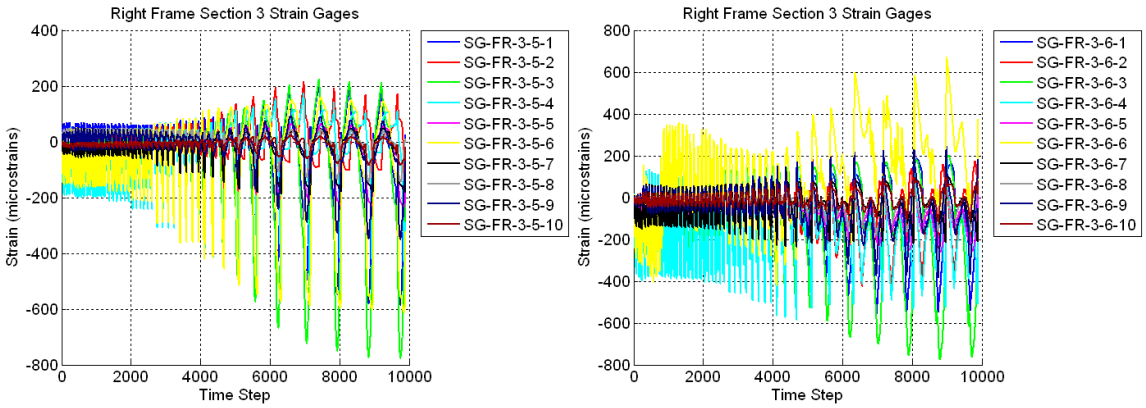

Figure B.61 Raw Data For Specimen A2 – Right Frame Section 3-5 Strain Gages (Left) and Right Frame Section 3-6 Strain Gages (Right)

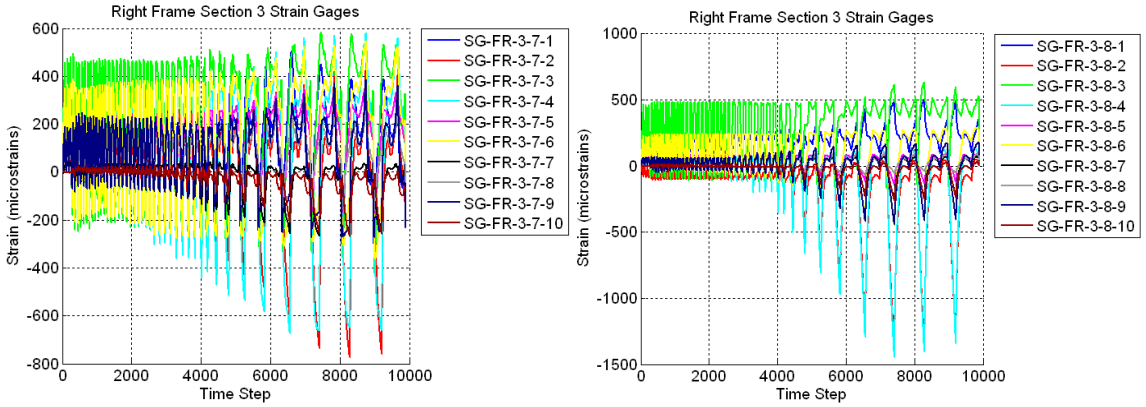

Figure B.62 Raw Data For Specimen A2 – Right Frame Section 3-7 Strain Gages (Left) and Right Frame Section 3-8 Strain Gages (Right)

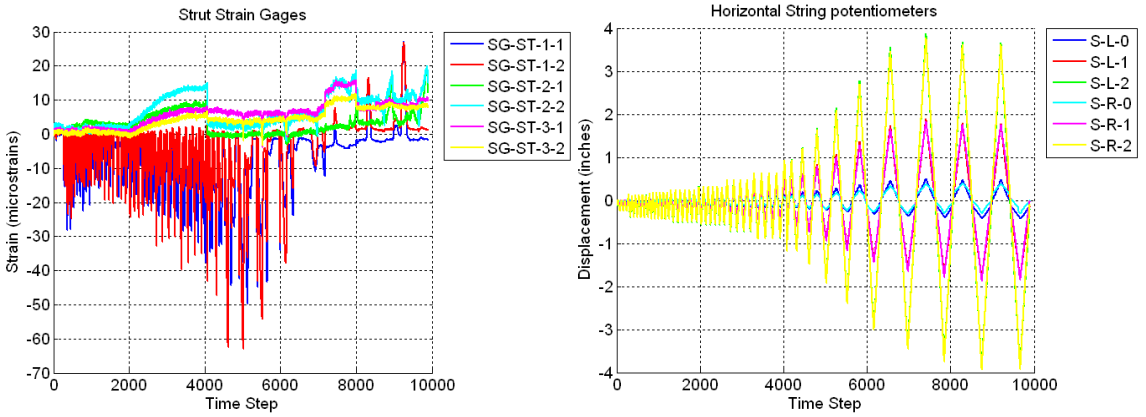

Figure B.63 Raw Data For Specimen A2 – Strut Strain Gages (Left) and Horizontal String Potentiometers (Right)

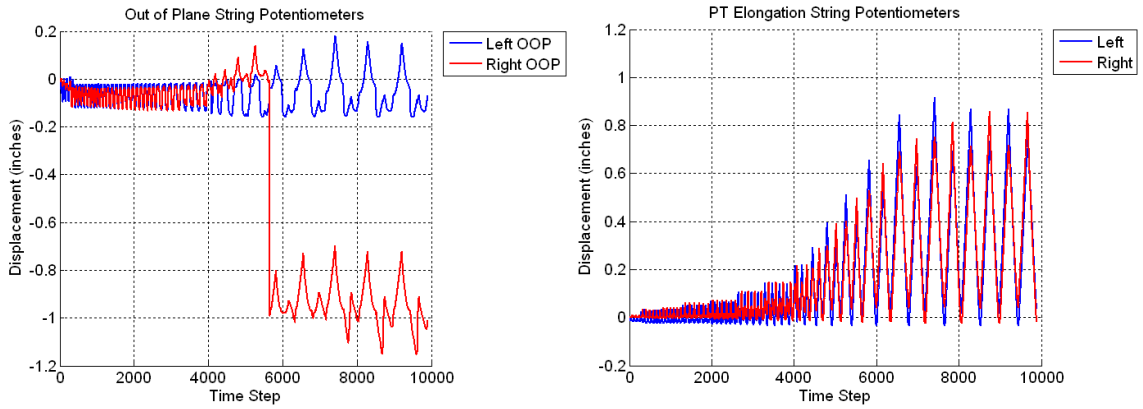

Figure B.64 Raw Data For Specimen A2 – Out-of-Plane String Potentiometers (Left) and PT Elongation String Potentiometers (Right)

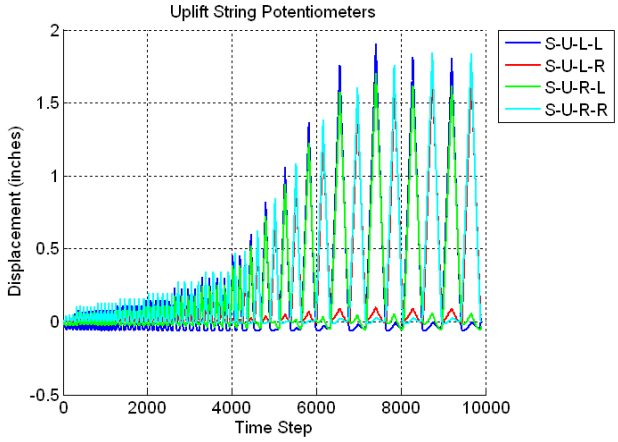

Figure B.65 Raw Data For Specimen A2 – Uplift String Potentiometers

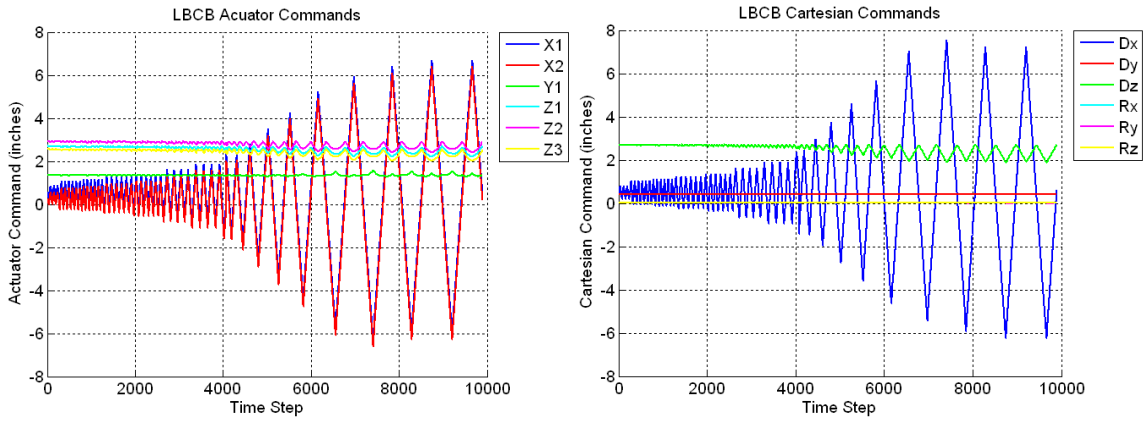

Figure B.66 Raw Data For Specimen A2 – LBCB Actuator Commands (Left) and LBCB Cartesian Commands (Right)

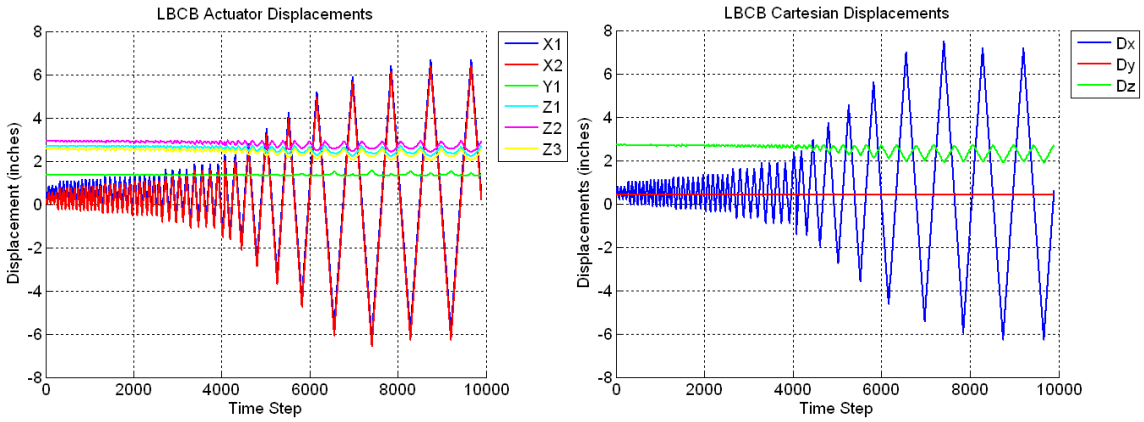

Figure B.67 Raw Data For Specimen A2 – LBCB Actuator Displacements (Left) and LBCB Cartesian Displacements (Right)

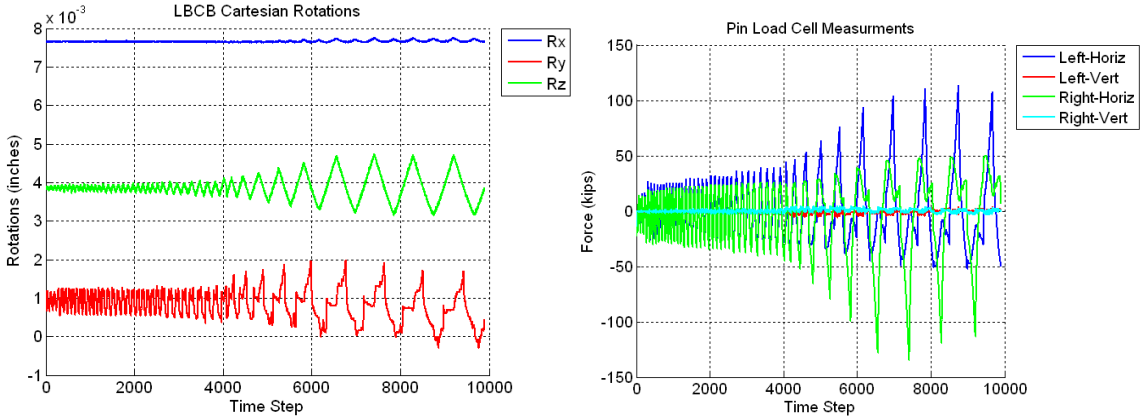

Figure B.68 Raw Data For Specimen A2 – LBCB Cartesian Rotations (Left) and Pin Load Cells (Right)

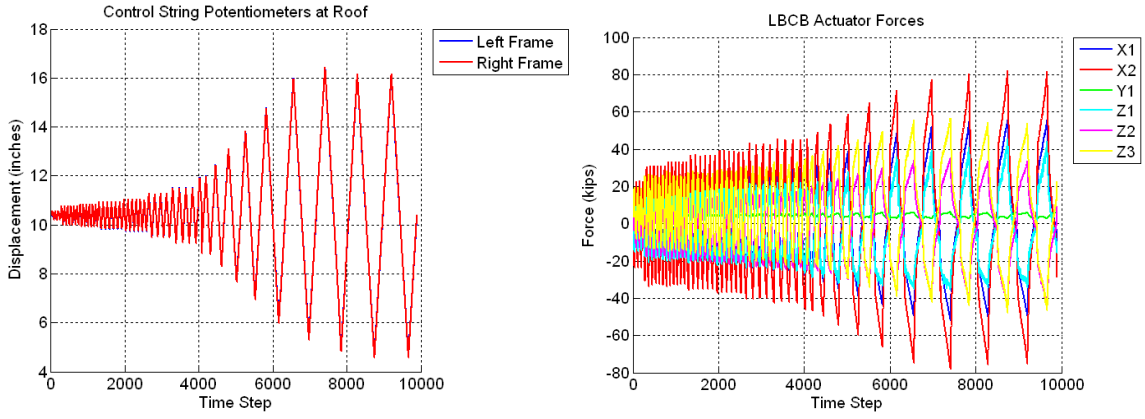

Figure B.69 Raw Data For Specimen A2 – Control Roof String Potentiometers (Left) and LBCB Actuator Forces (Right)

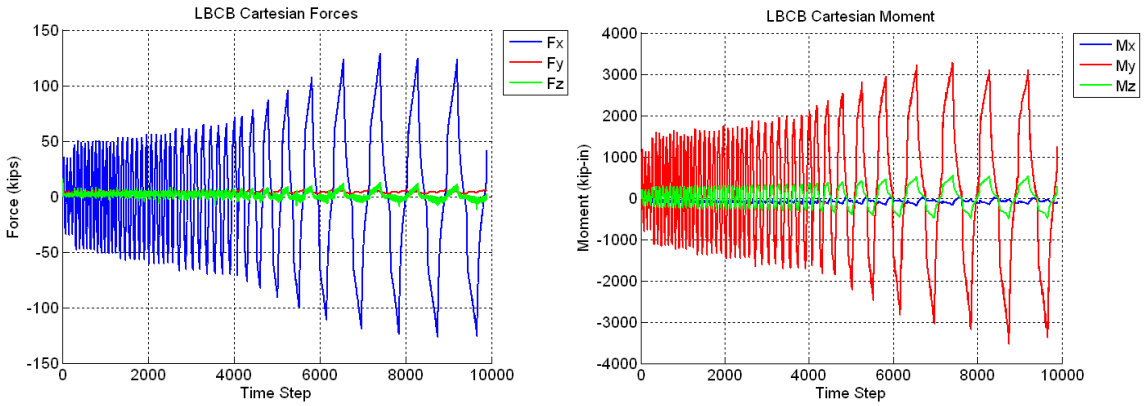

Figure B.70 Raw Data For Specimen A2 – LBCB Cartesian Forces (Left) and LBCB Cartesian Moments (Right)

Figure B.71 Raw Data For Specimen A2 – LBCB Actuator Servo-Error

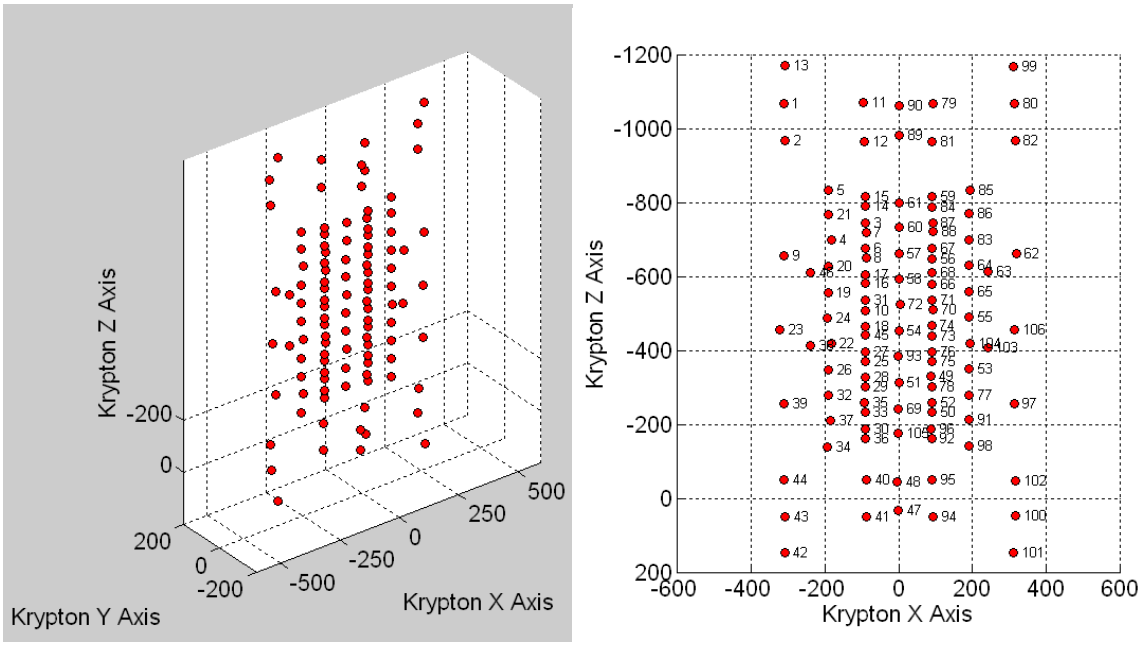

Figure B.72 Raw Data For Specimen A2 – Krypton LED Locations (Left) and Krypton LED Numbering (Right)

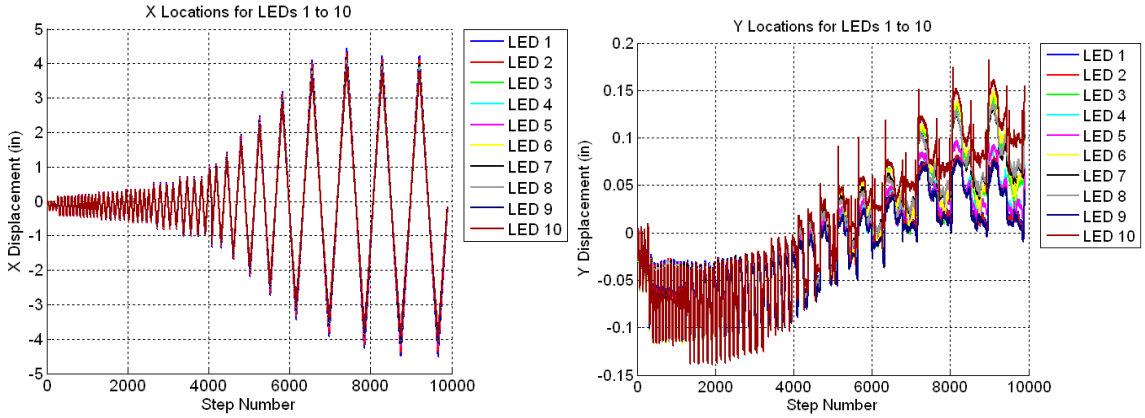

Figure B.73 Raw Data For Specimen A2 – X Displacements for LED's 1 to 10 (Left) and Y Displacements for LED's 1 to 10 (Right)

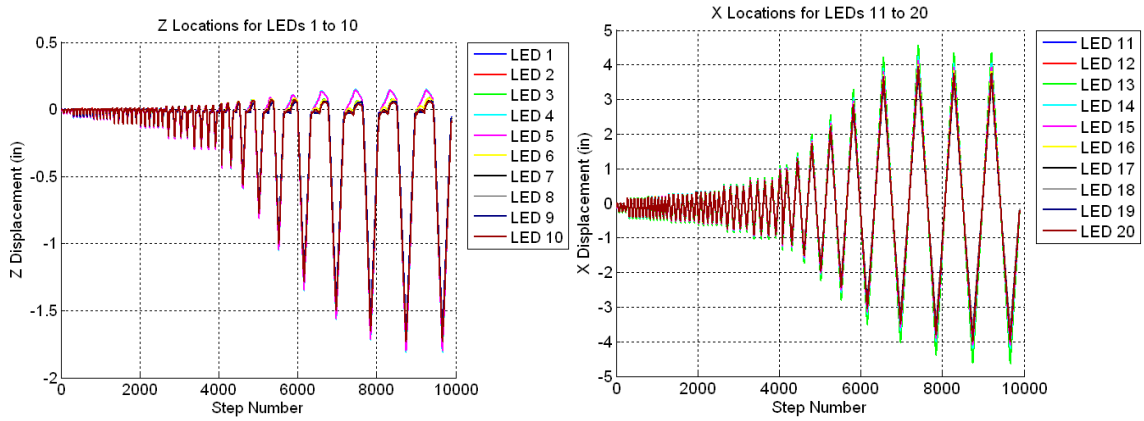

Figure B.74 Raw Data For Specimen A2 – Z Displacements for LED's 1 to 10 (Left) and X Displacements for LED's 11 to 20 (Right)

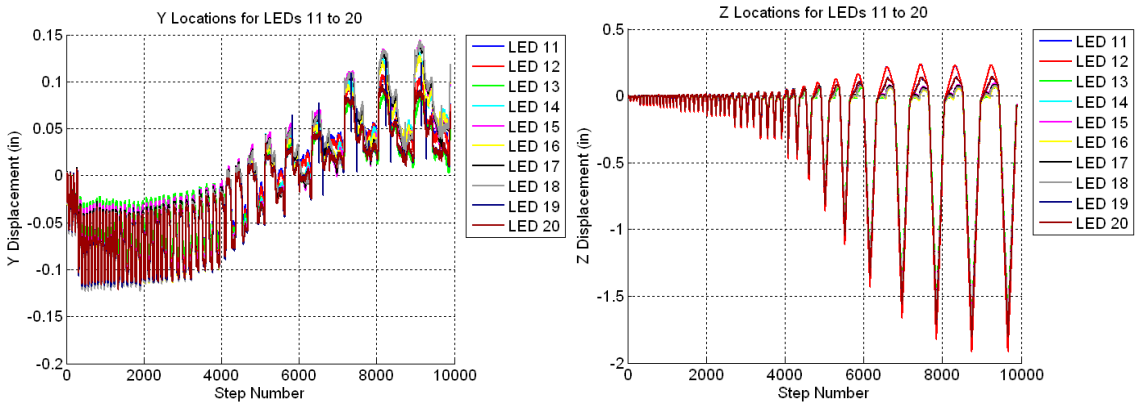

Figure B.75 Raw Data For Specimen A2 – Y Displacements for LED's 11 to 20 (Left) and Z Displacements for LED's 11 to 20 (Right)

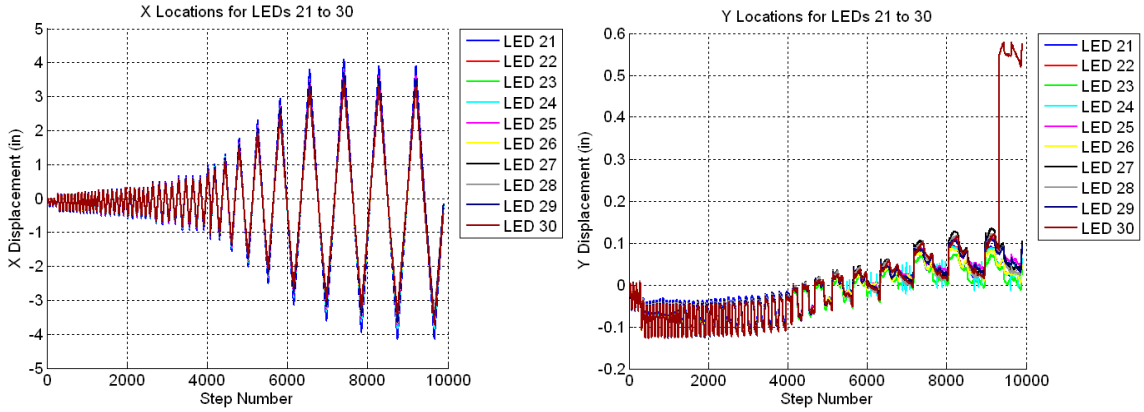

Figure B.76 Raw Data For Specimen A2 – X Displacements for LED's 21 to 30 (Left) and Y Displacements for LED's 21 to 30 (Right)

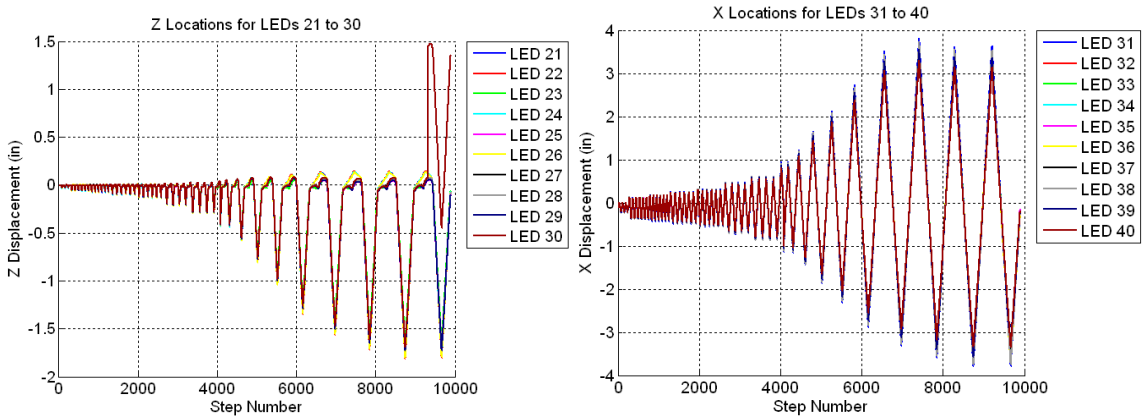

Figure B.77 Raw Data For Specimen A2 – Z Displacements for LED's 21 to 30 (Left) and X Displacements for LED's 31 to 40 (Right)

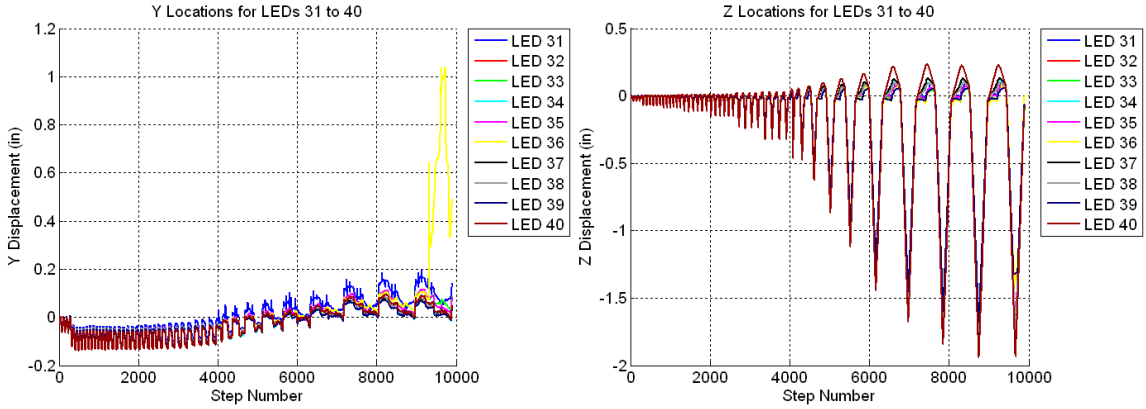

Figure B.78 Raw Data For Specimen A2 – Y Displacements for LED's 31 to 40 (Left) and Z Displacements for LED's 31 to 40 (Right)

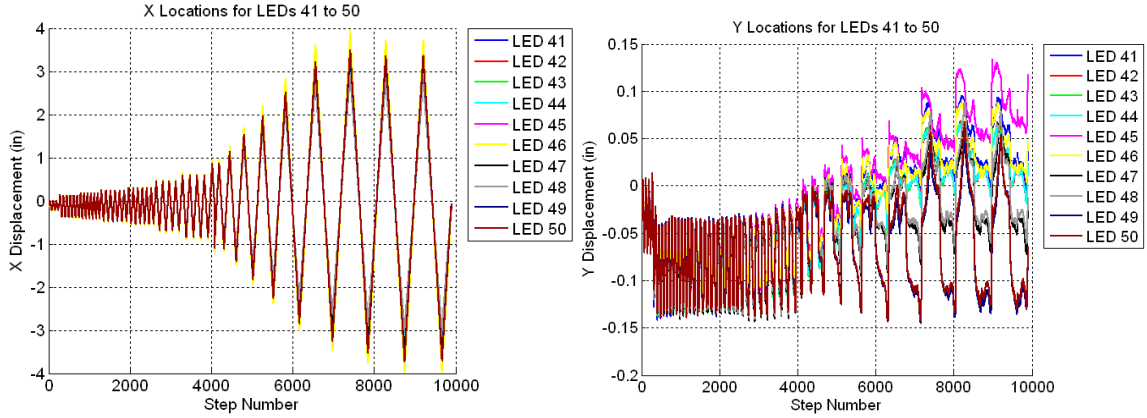

Figure B.79 Raw Data For Specimen A2 – X Displacements for LED's 41 to 50 (Left) and Y Displacements for LED's 41 to 50 (Right)

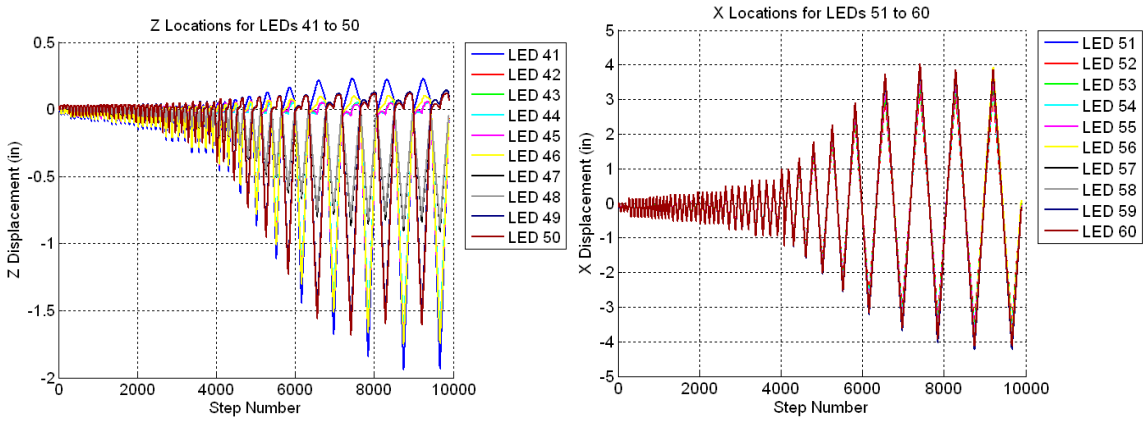

Figure B.80 Raw Data For Specimen A2 – Z Displacements for LED's 41 to 50 (Left) and X Displacements for LED's 51 to 60 (Right)

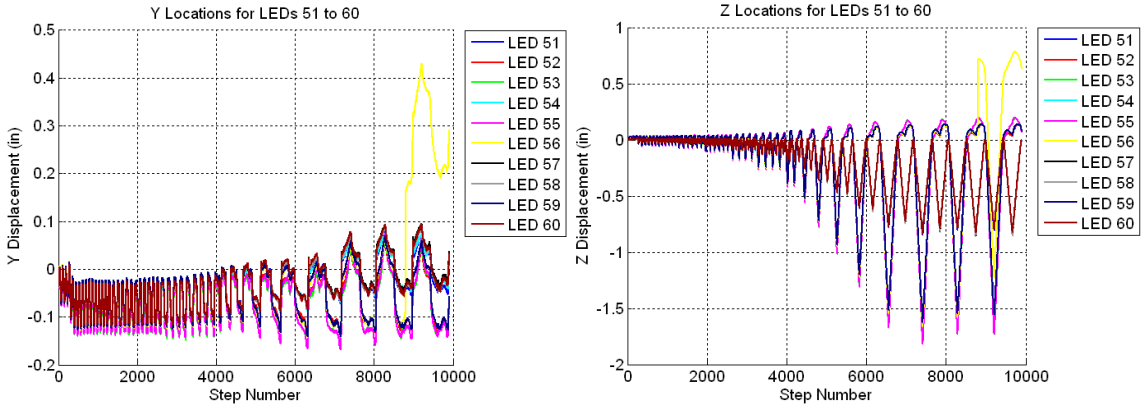

Figure B.81 Raw Data For Specimen A2 – Y Displacements for LED's 51 to 60 (Left) and Z Displacements for LED's 51 to 60 (Right)

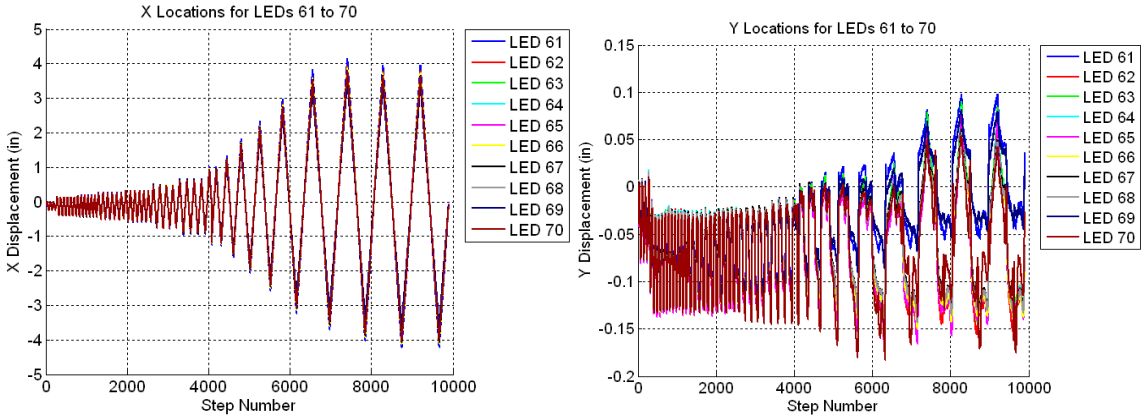

Figure B.82 Raw Data For Specimen A2 – X Displacements for LED's 61 to 70 (Left) and Y Displacements for LED's 61 to 70 (Right)

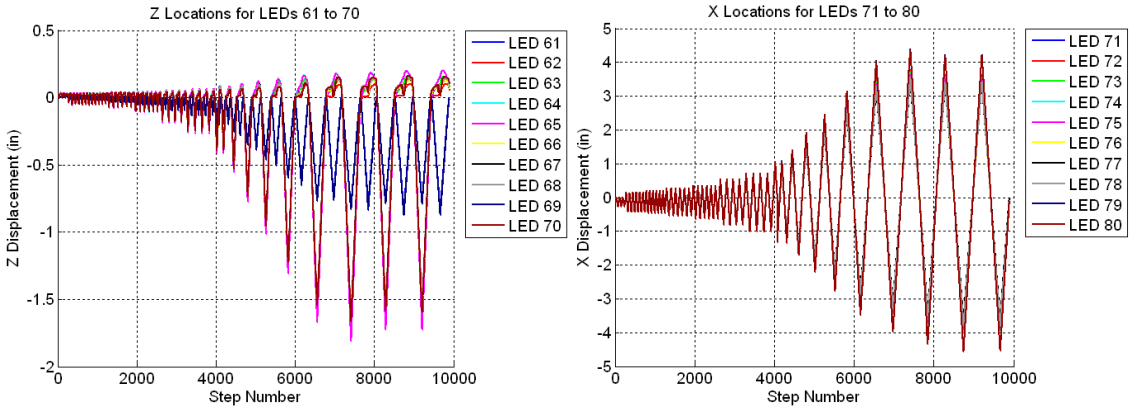

Figure B.83 Raw Data For Specimen A2 – Z Displacements for LED's 61 to 70 (Left) and X Displacements for LED's 71 to 80 (Right)

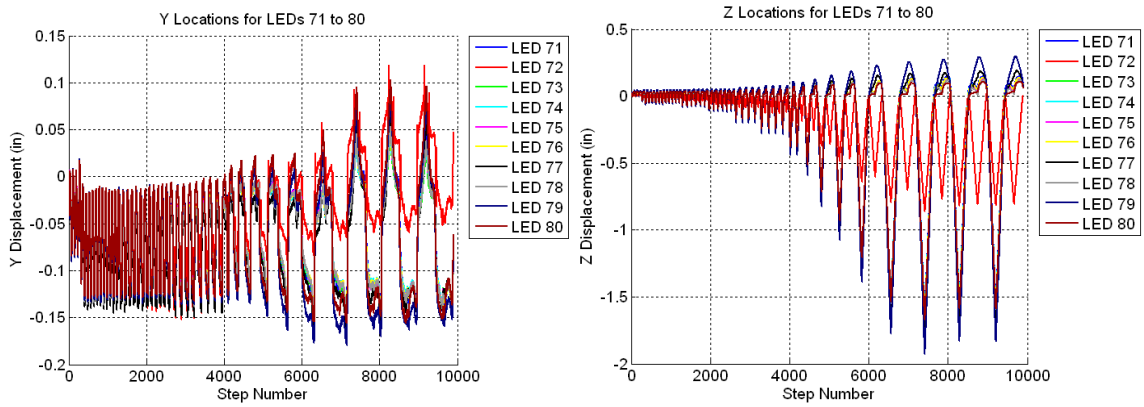

Figure B.84 Raw Data For Specimen A2 – Y Displacements for LED's 71 to 80 (Left) and Z Displacements for LED's 71 to 80 (Right)

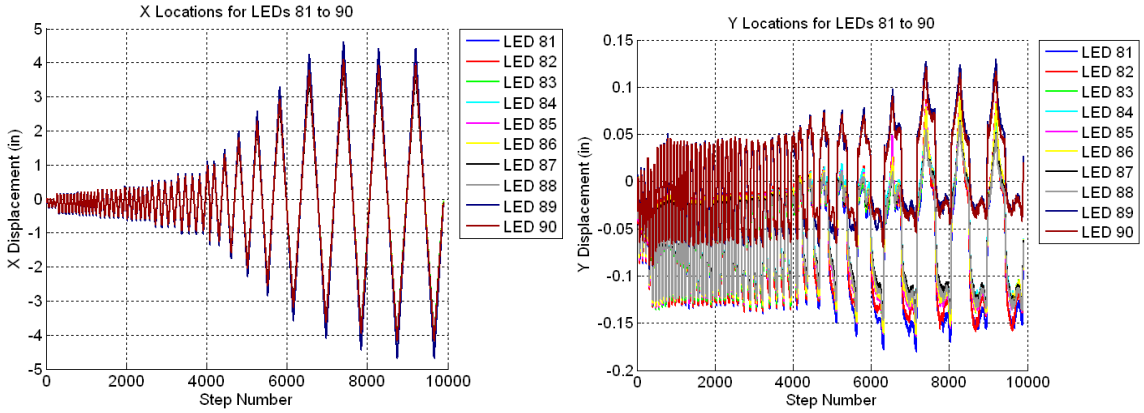

Figure B.85 Raw Data For Specimen A2 – X Displacements for LED's 81 to 90 (Left) and Y Displacements for LED's 81 to 90 (Right)

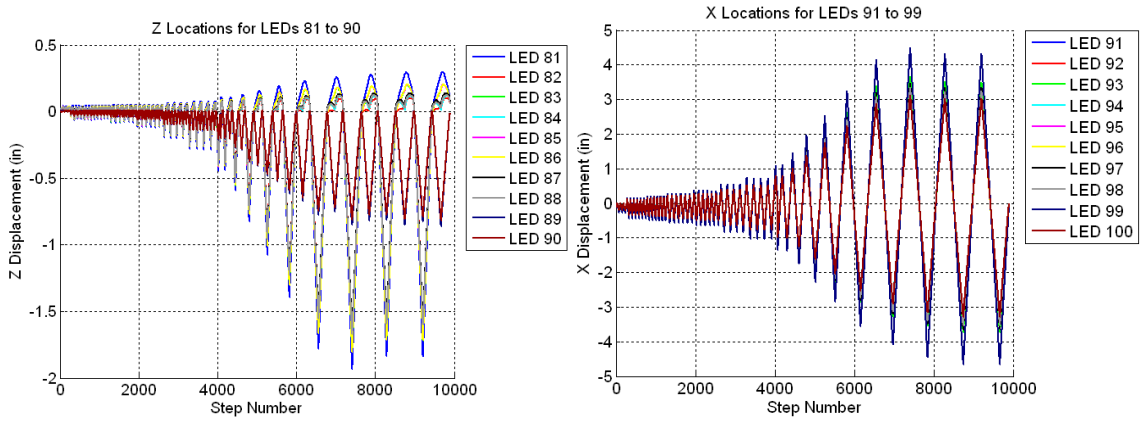

Figure B.86 Raw Data For Specimen A2 – Z Displacements for LED's 81 to 90 (Left) and X Displacements for LED's 91 to 99 (Right)

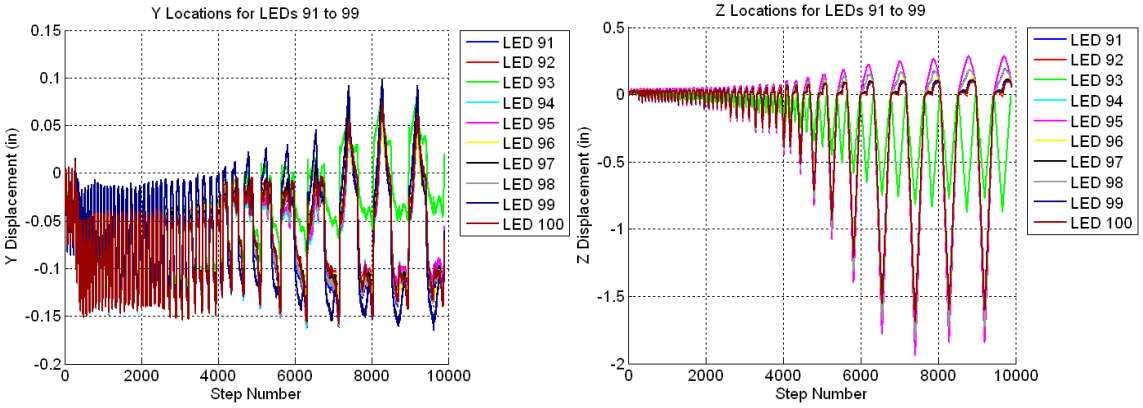

Figure B.87 Raw Data For Specimen A2 – Y Displacements for LED's 91 to 99 (Left) and Z Displacements for LED's 91 to 99 (Right)

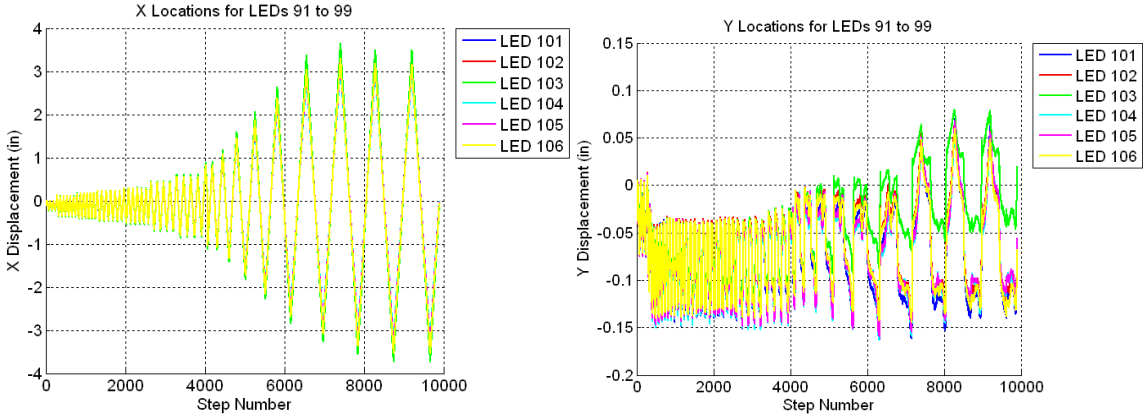

Figure B.88 Raw Data For Specimen A2 – X Displacements for LED's 91 to 99 (Left) and Y Displacements for LED's 91 to 99 (Right)

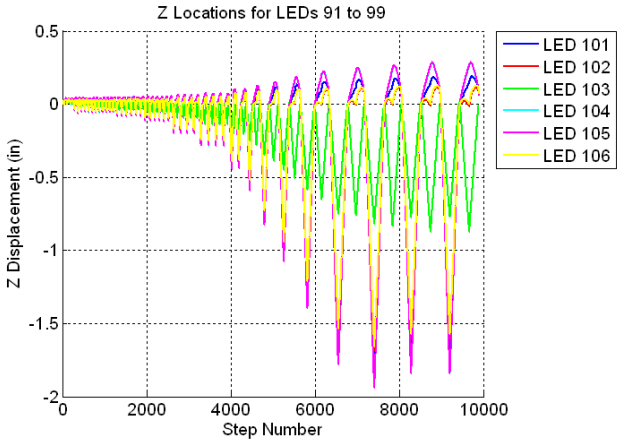

Figure B.89 Raw Data For Specimen A2 – Z Displacements for LED's 91 to 99

B.3 Specimen A3

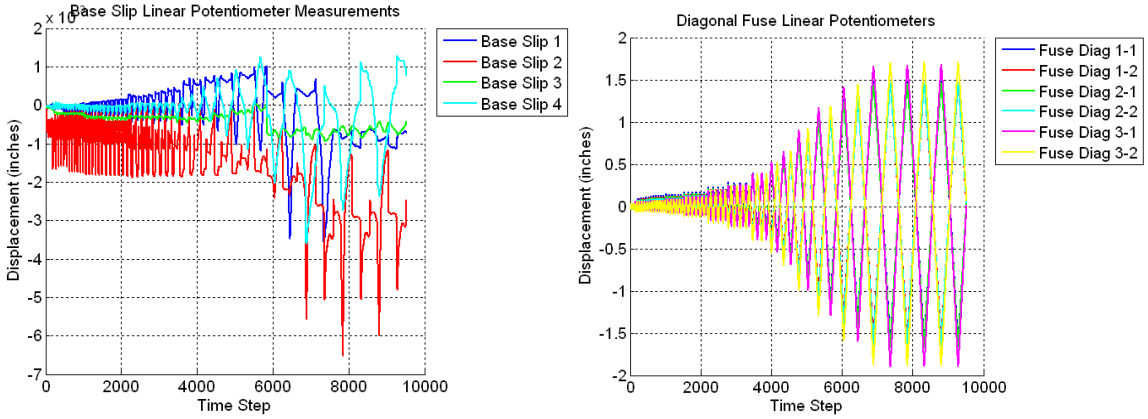

Figure B.90 Raw Data For Specimen A3 – Base Slip (Left) and Diagonal Fuse Linear Potentiometers (Right)

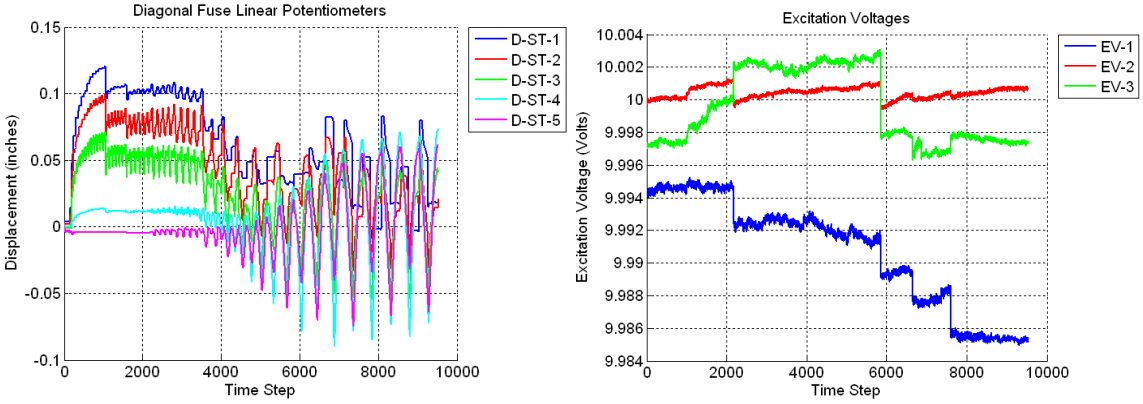

Figure B.91 Raw Data For Specimen A3 – Strut Linear Potentiometers (Left) and Excitation Voltages (Right)

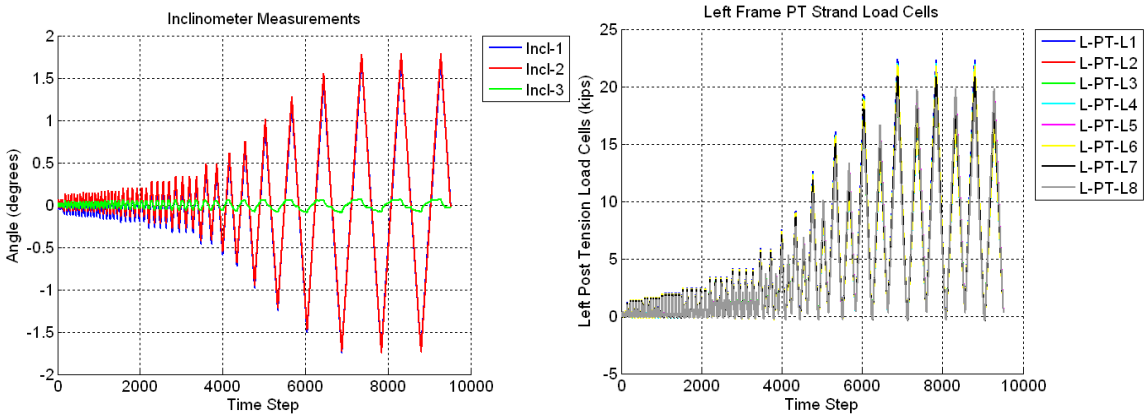

Figure B.92 Raw Data For Specimen A3 – Inclinometers (Left) and Left Frame PT Load Cells (Right)

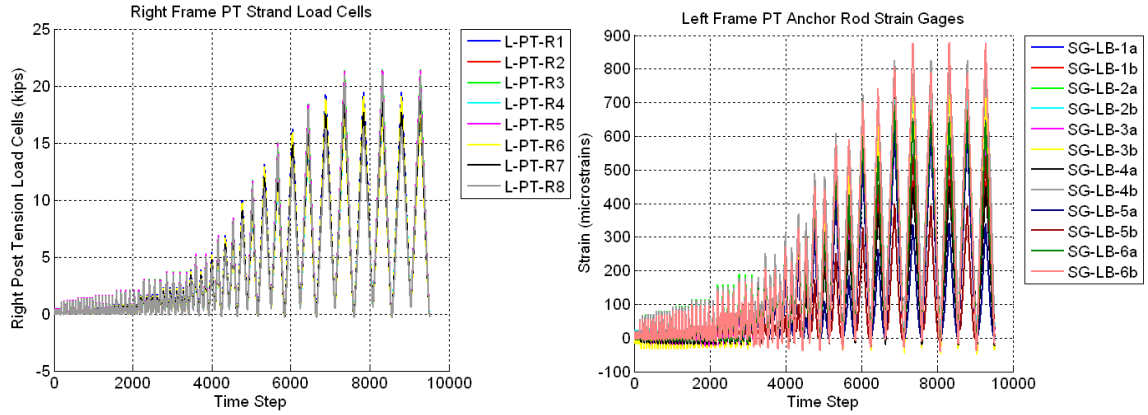

Figure B.93 Raw Data For Specimen A3 – Right Frame PT Load Cells (Left) and Left Frame PT Anchor Rods (Right)

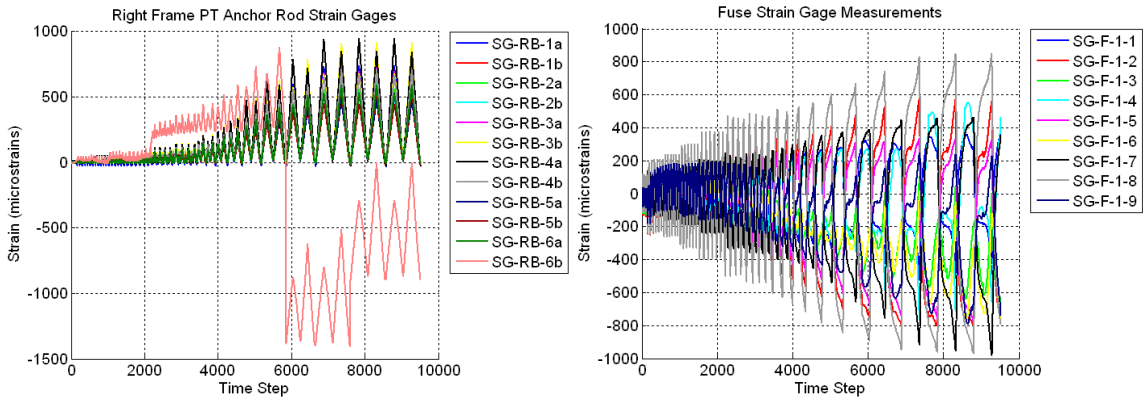

Figure B.94 Raw Data For Specimen A3 – Right Frame PT Anchor Rods (Left) and Back Fuse Strain Gages (Right)

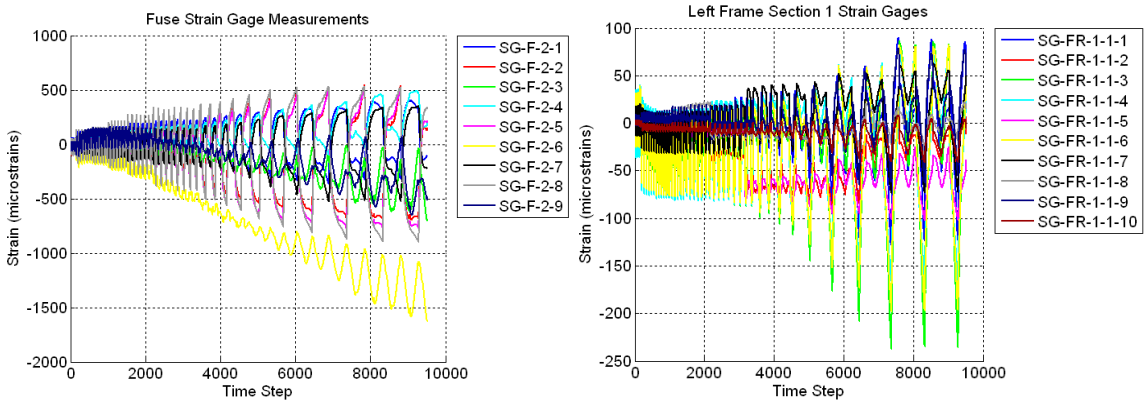

Figure B.95 Raw Data For Specimen A3 – Front Fuse Strain Gages (Left) and Left Frame Section 1-1 Strain Gages (Right)

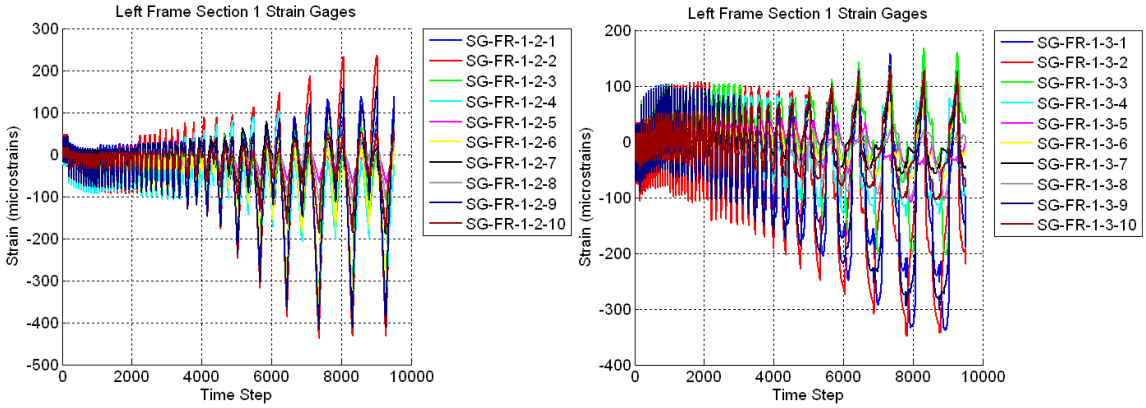

Figure B.96 Raw Data For Specimen A3 – Left Frame Section 1-2 Strain Gages (Left) and Left Frame Section 1-3 Strain Gages (Right)

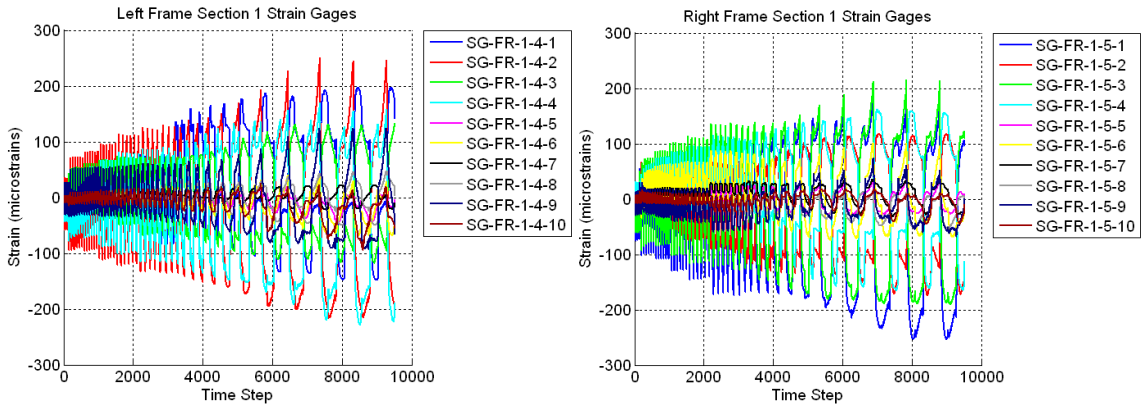

Figure B.97 Raw Data For Specimen A3 – Left Frame Section 1-4 Strain Gages (Left) and Right Frame Section 1-5 Strain Gages (Right)

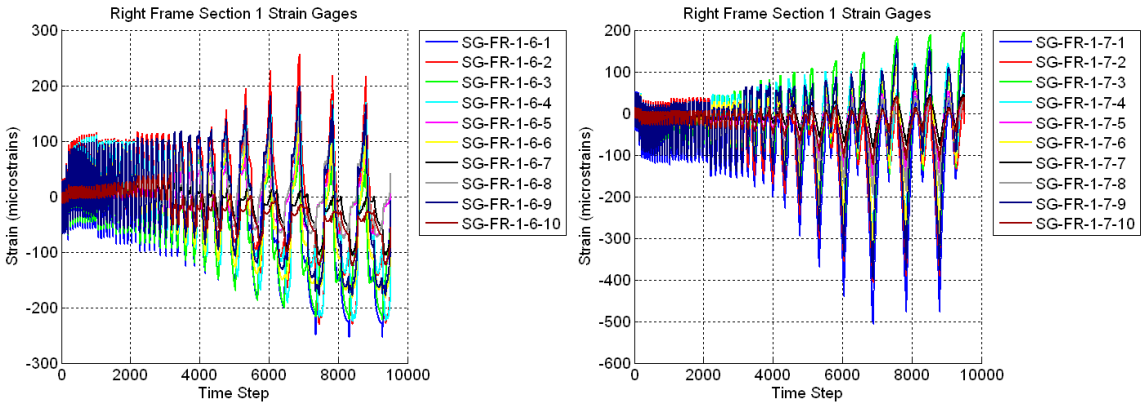

Figure B.98 Raw Data For Specimen A3 – Right Frame Section 1-6 Strain Gages (Left) and Right Frame Section 1-7 Strain Gages (Right)

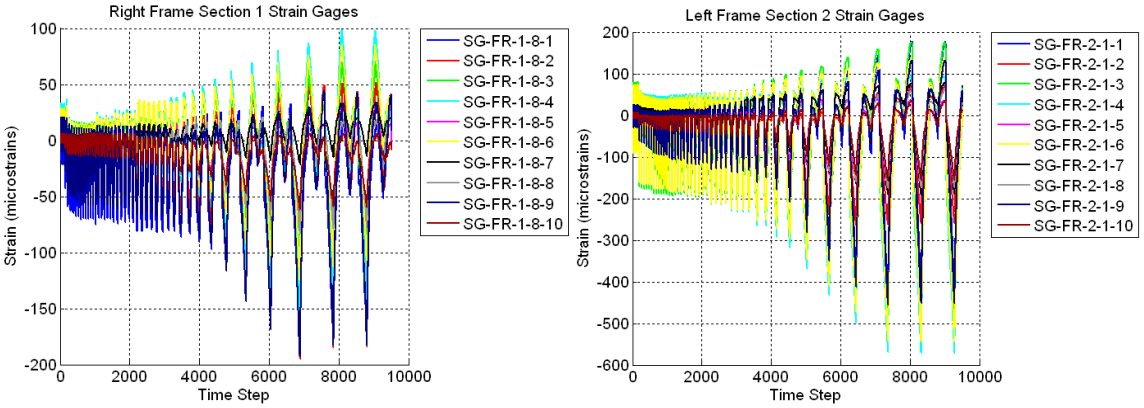

Figure B.99 Raw Data For Specimen A3 – Right Frame Section 1-8 Strain Gages (Left) and Left Frame Section 2-1 Strain Gages (Right)

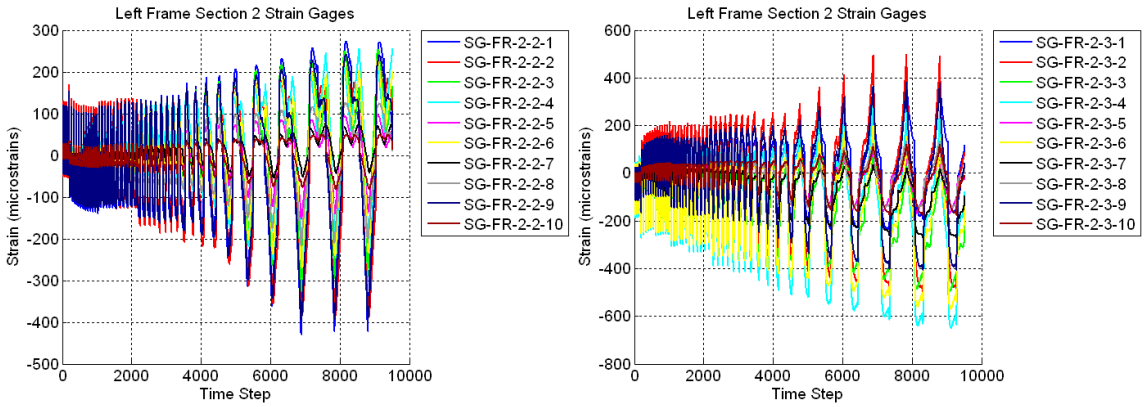

Figure B.100 Raw Data For Specimen A3 – Left Frame Section 2-2 Strain Gages (Left) and Left Frame Section 2-3 Strain Gages (Right)

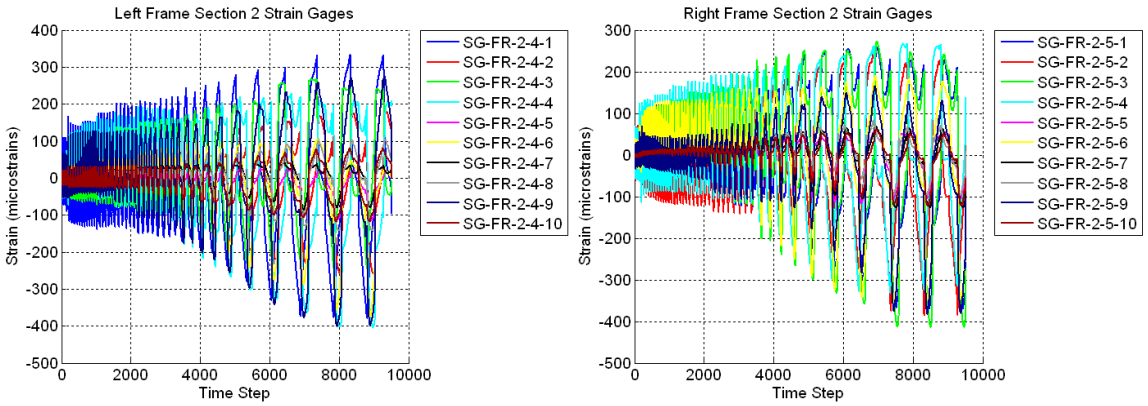

Figure B.101 Raw Data For Specimen A3 – Left Frame Section 2-4 Strain Gages (Left) and Right Frame Section 2-5 Strain Gages (Right)

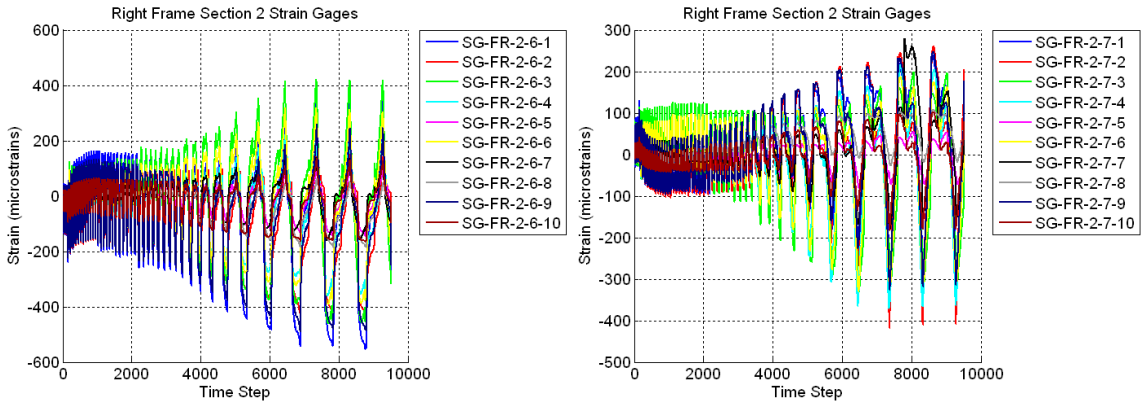

Figure B.102 Raw Data For Specimen A3 – Right Frame Section 2-6 Strain Gages (Left) and Right Frame Section 2-7 Strain Gages (Right)

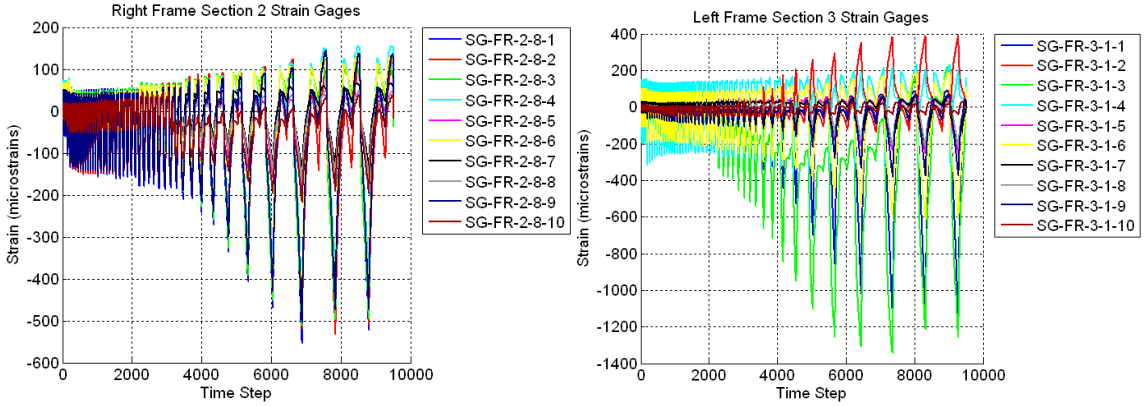

Figure B.103 Raw Data For Specimen A3 – Right Frame Section 2-8 Strain Gages (Left) and Left Frame Section 3-1 Strain Gages (Right)

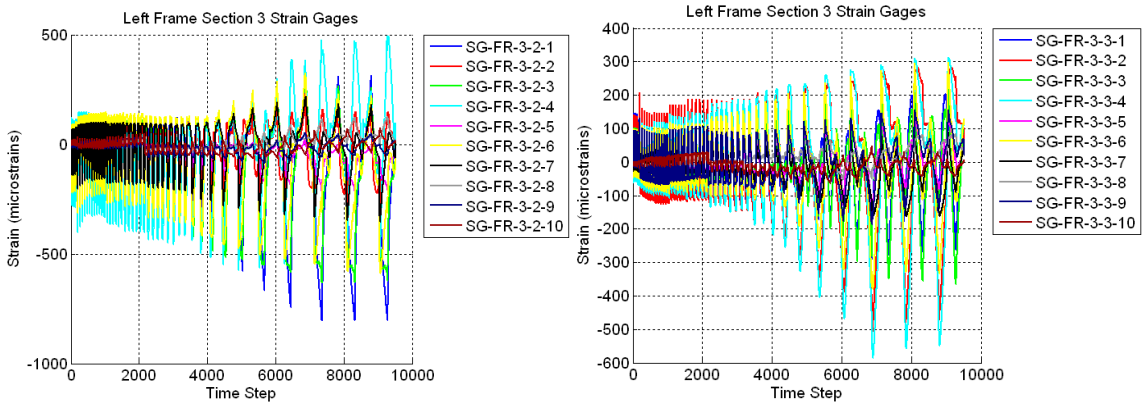

Figure B.104 Raw Data For Specimen A3 – Left Frame Section 3-2 Strain Gages (Left) and Left Frame Section 3-3 Strain Gages (Right)

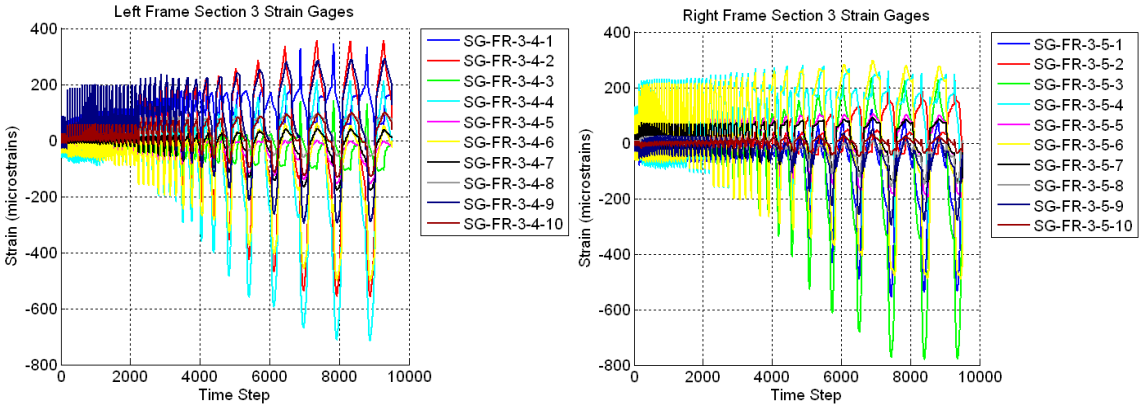

Figure B.105 Raw Data For Specimen A3 – Left Frame Section 3-4 Strain Gages (Left) and Right Frame Section 3-5 Strain Gages (Right)

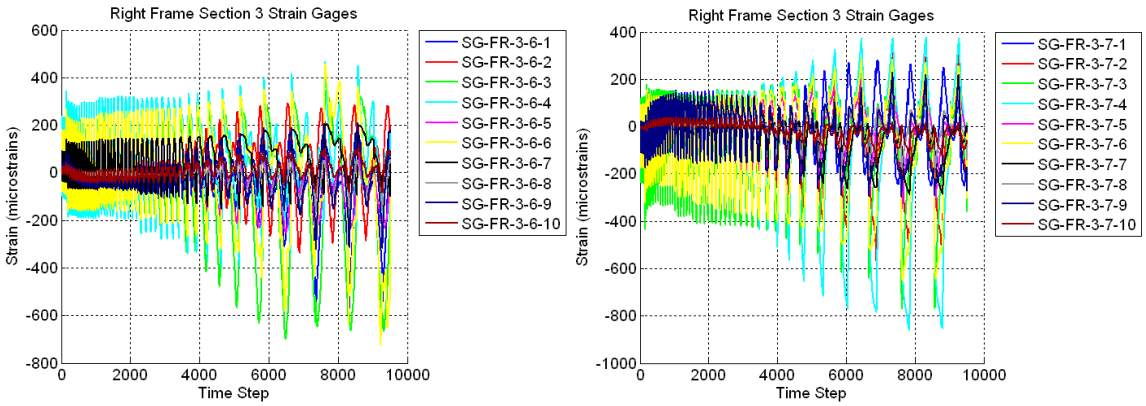

Figure B.106 Raw Data For Specimen A3 – Right Frame Section 3-6 Strain Gages (Left) and Right Frame Section 3-7 Strain Gages (Right)

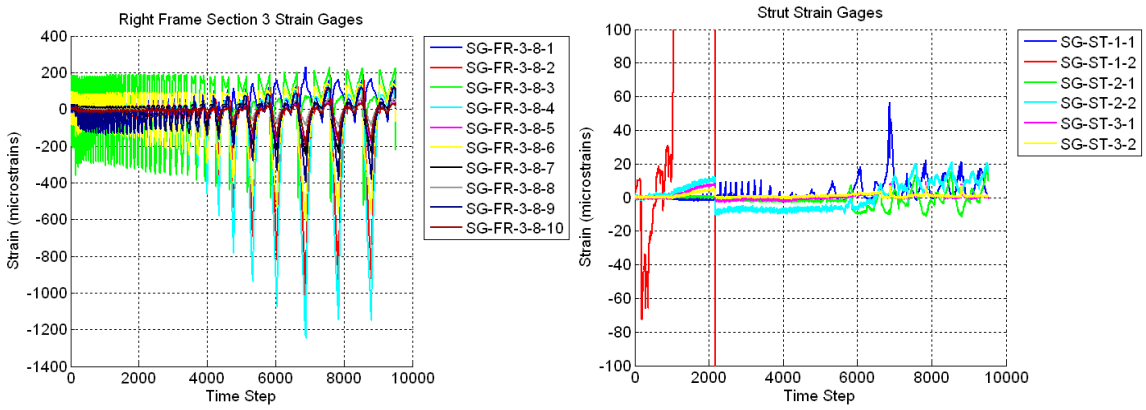

Figure B.107 Raw Data For Specimen A3 – Right Frame Section 3-8 Strain Gages (Left) and Strut Strain Gages (Right)

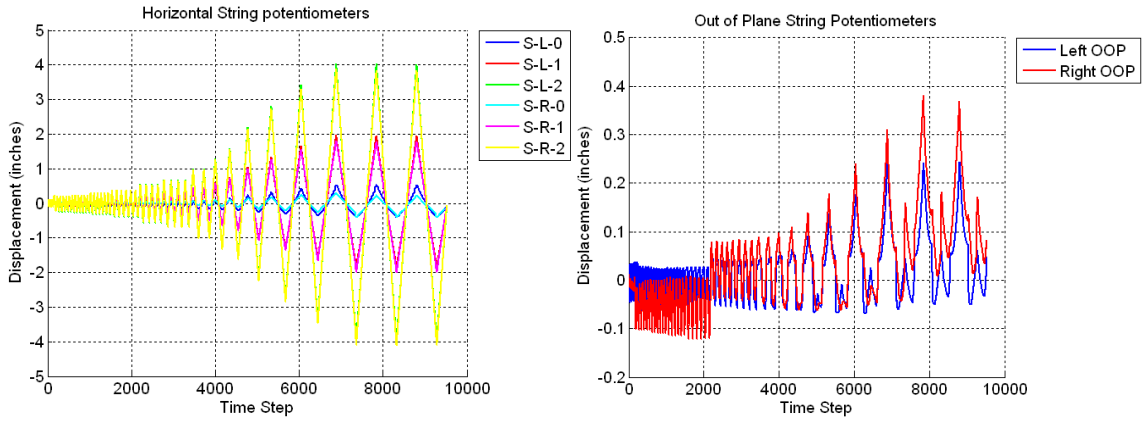

Figure B.108 Raw Data For Specimen A3 – Horizontal String Potentiometers (Left) and Out-of-Plane String Potentiometers (Right)

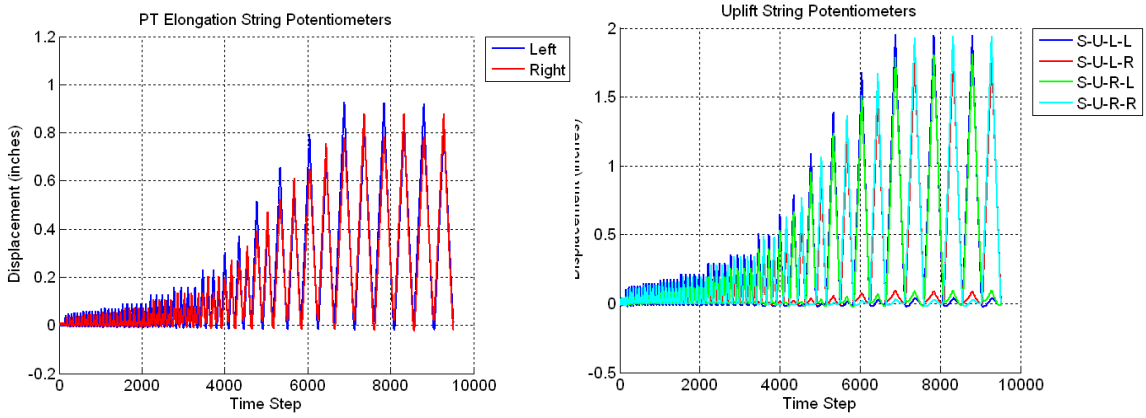

Figure B.109 Raw Data For Specimen A3 – PT Elongation String Potentiometers (Left) and Uplift String Potentiometers (Right)

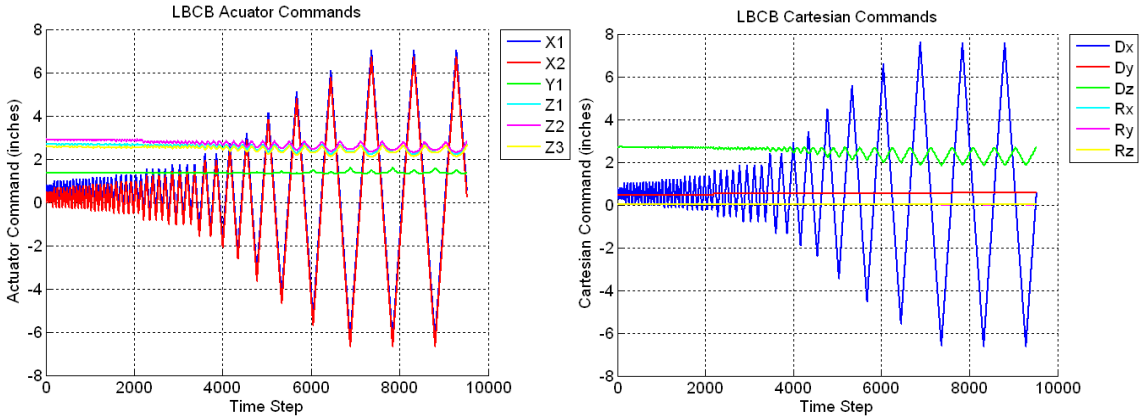

Figure B.110 Raw Data For Specimen A3 – LBCB Actuator Commands (Left) and LBCB Cartesian Commands (Right)

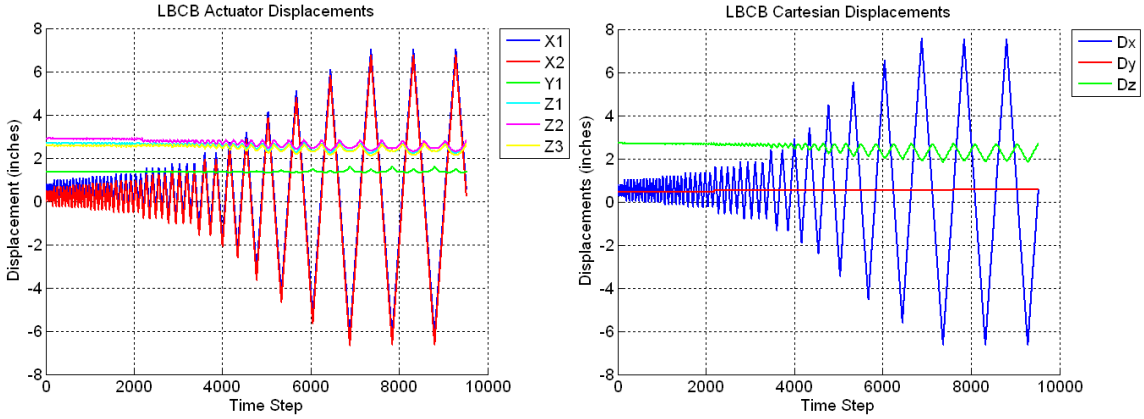

Figure B.111 Raw Data For Specimen A3 – LBCB Actuator Displacements (Left) and LBCB Cartesian Displacements (Right)

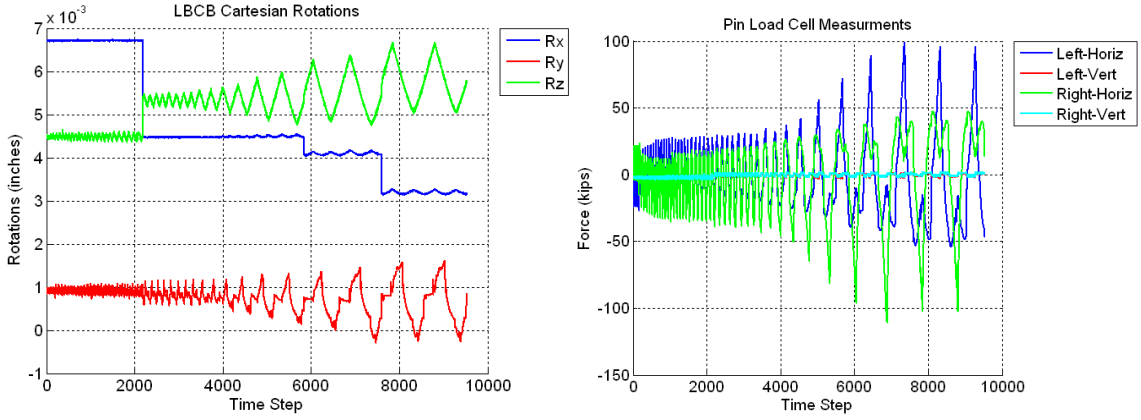

Figure B.112 Raw Data For Specimen A3 – LBCB Cartesian Rotations (Left) and Pin Load Cells (Right)

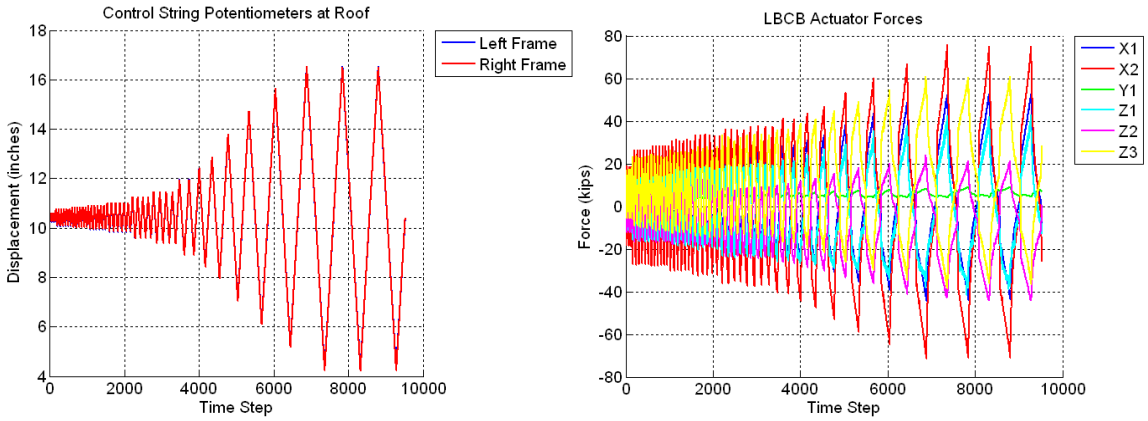

Figure B.113 Raw Data For Specimen A3 – Control Roof String Potentiometers (Left) and LBCB Actuator Forces (Right)

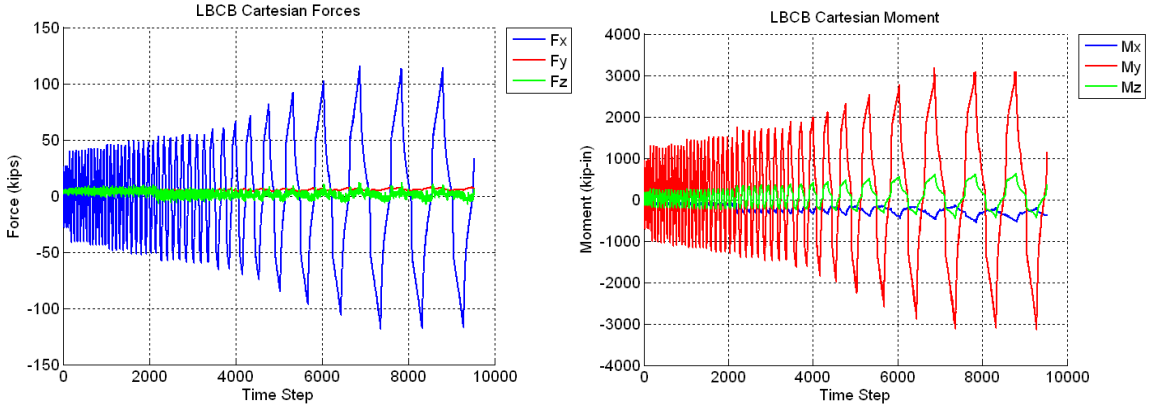

Figure B.114 Raw Data For Specimen A3 – LBCB Cartesian Forces (Left) and LBCB Cartesian Moments (Right)

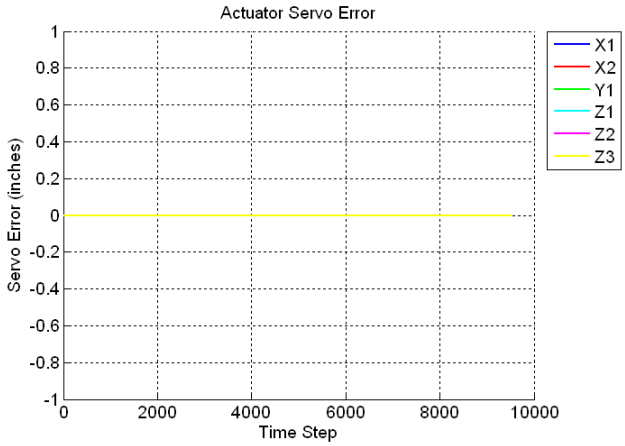

Figure B.115 Raw Data For Specimen A3 – LBCB Actuator Servo-Error

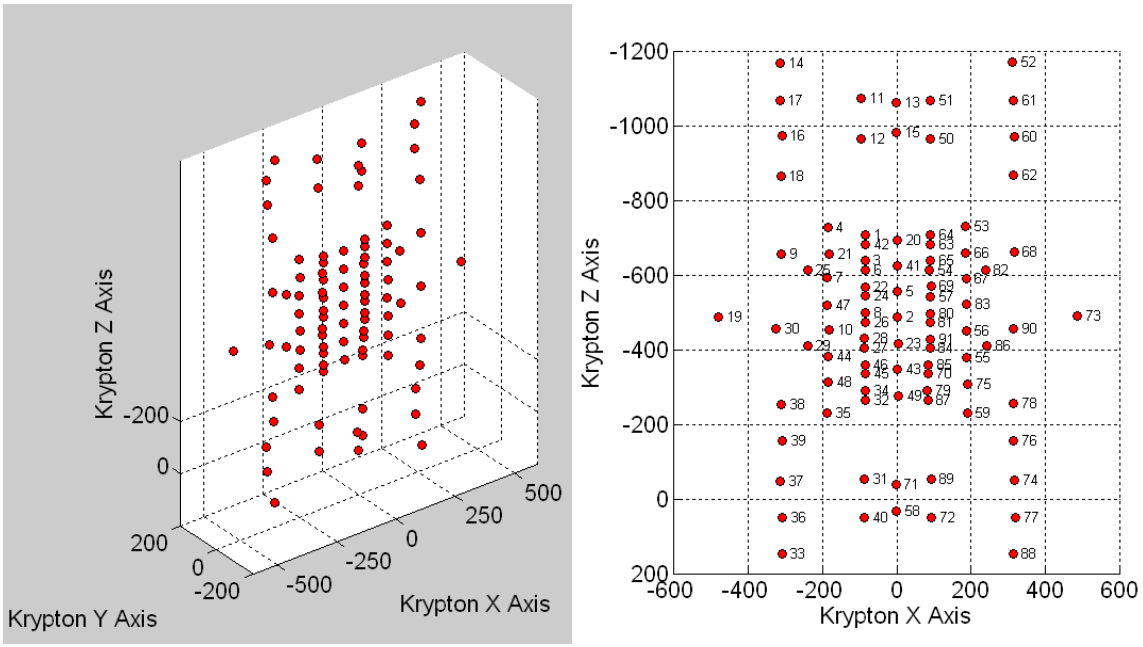

Figure B.116 Raw Data For Specimen A3 – Krypton LED Locations (Left) and Krypton LED Numbering (Right)

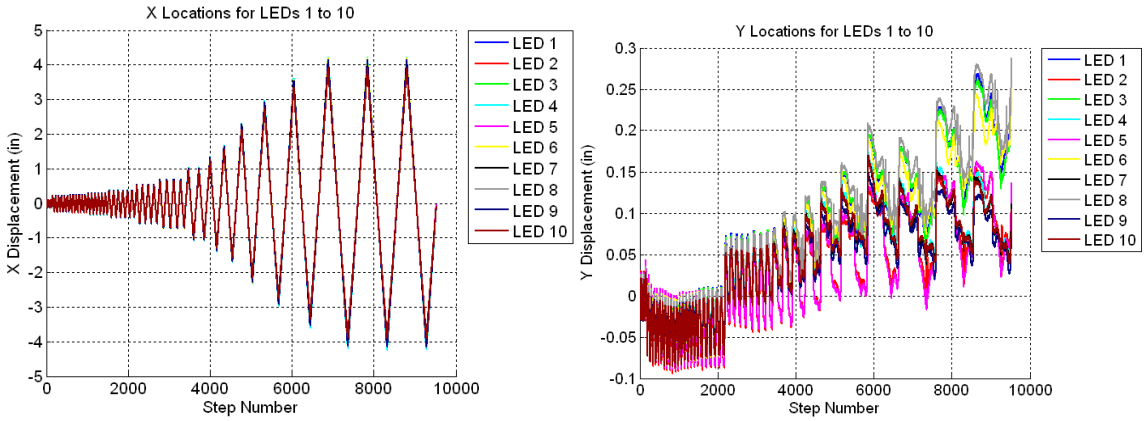

Figure B.117 Raw Data For Specimen A3 – X Displacements for LED's 1 to 10 (Left) and Y Displacements for LED's 1 to 10 (Right)

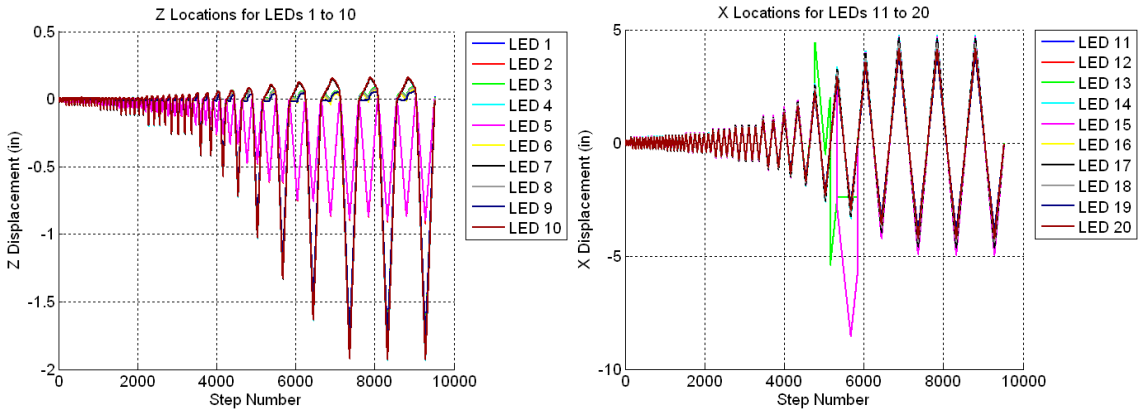

Figure B.118 Raw Data For Specimen A3 – Z Displacements for LED's 1 to 10 (Left) and X Displacements for LED's 11 to 20 (Right)

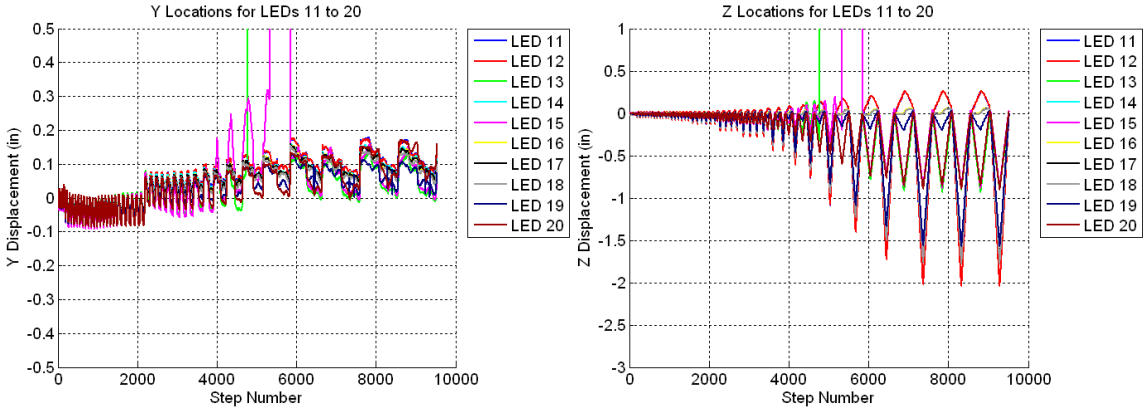

Figure B.119 Raw Data For Specimen A3 – Y Displacements for LED's 11 to 20 (Left) and Z Displacements for LED's 11 to 20 (Right)

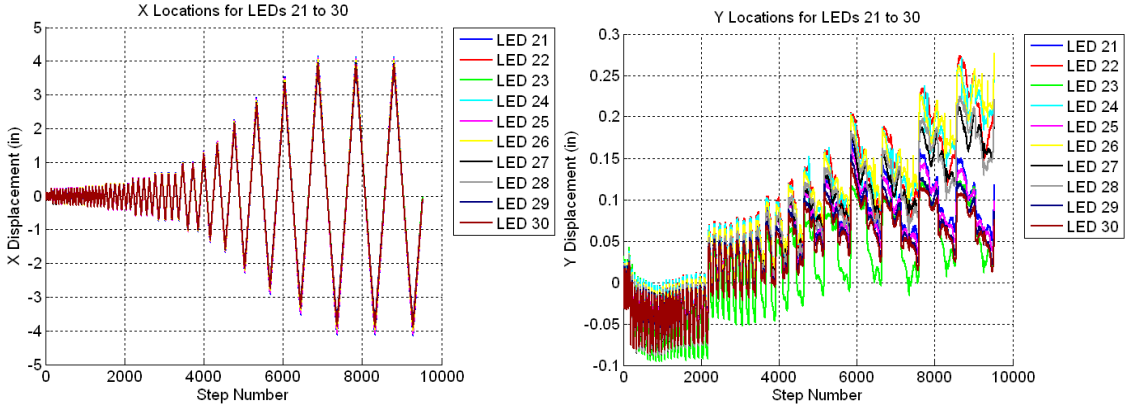

Figure B.120 Raw Data For Specimen A3 – X Displacements for LED's 21 to 30 (Left) and Y Displacements for LED's 21 to 30 (Right)

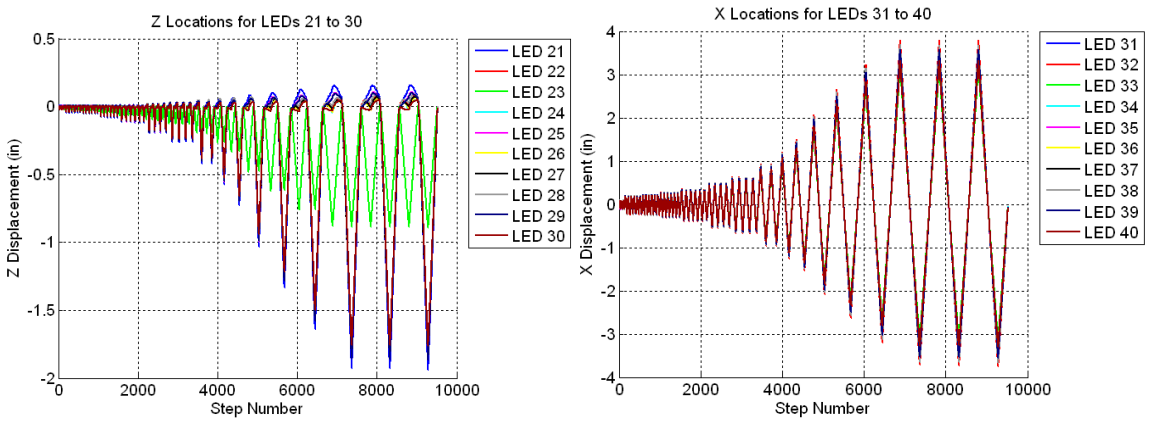

Figure B.121 Raw Data For Specimen A3 – Z Displacements for LED's 21 to 30 (Left) and X Displacements for LED's 31 to 40 (Right)

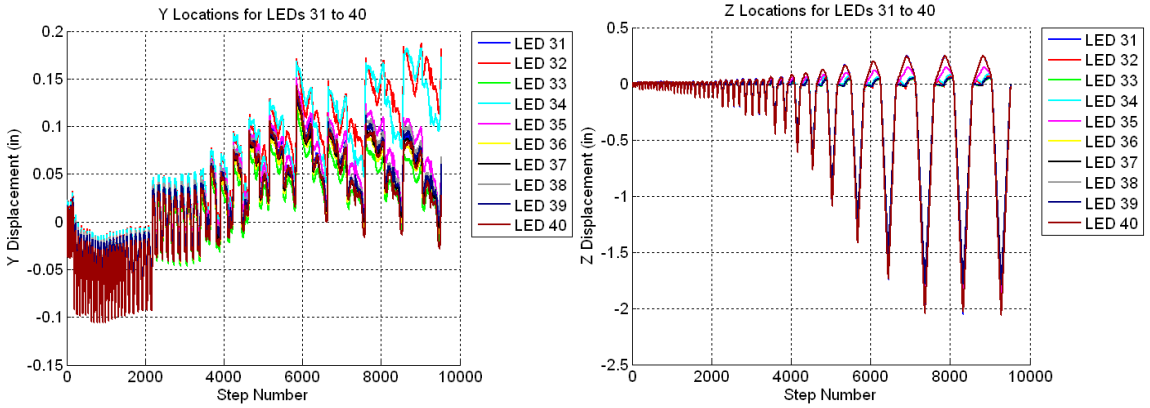

Figure B.122 Raw Data For Specimen A3 – Y Displacements for LED's 31 to 40 (Left) and Z Displacements for LED's 31 to 40 (Right)

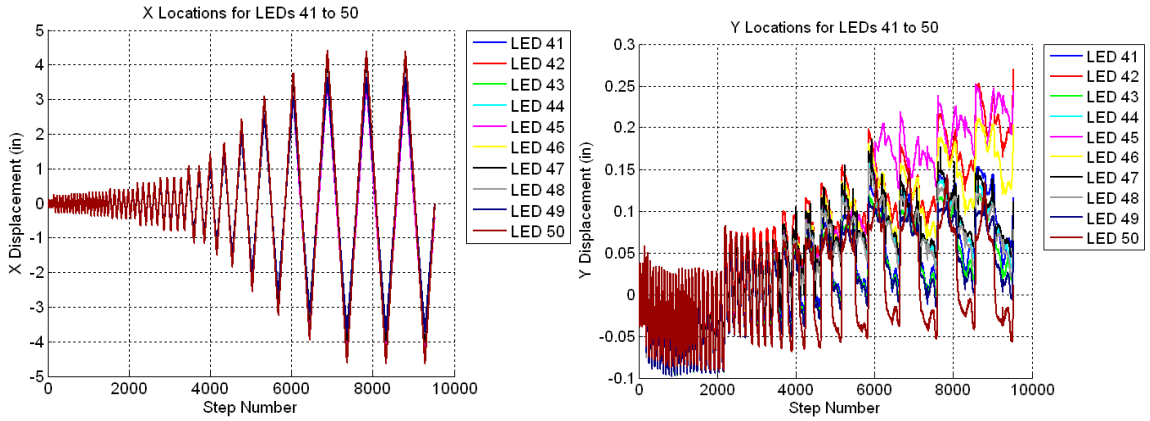

Figure B.123 Raw Data For Specimen A3 – X Displacements for LED's 41 to 50 (Left) and Y Displacements for LED's 41 to 50 (Right)

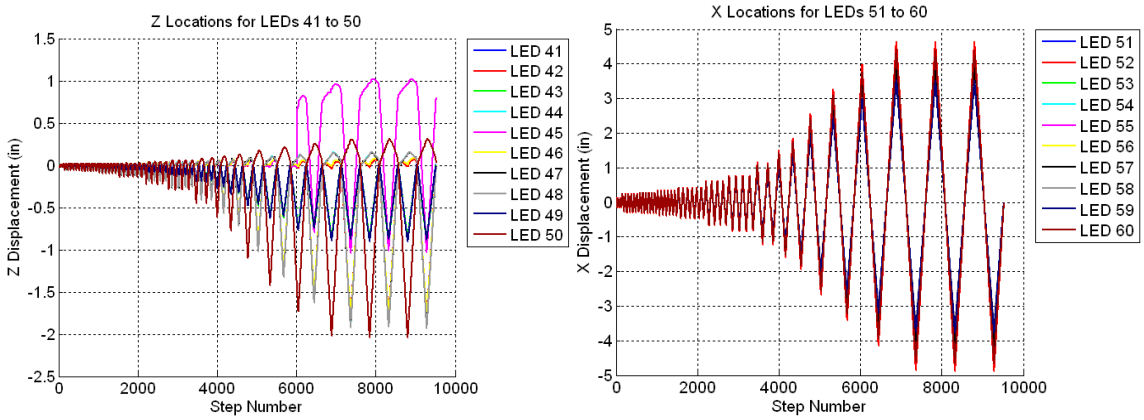

Figure B.124 Raw Data For Specimen A3 – Z Displacements for LED's 41 to 50 (Left) and X Displacements for LED's 51 to 60 (Right)

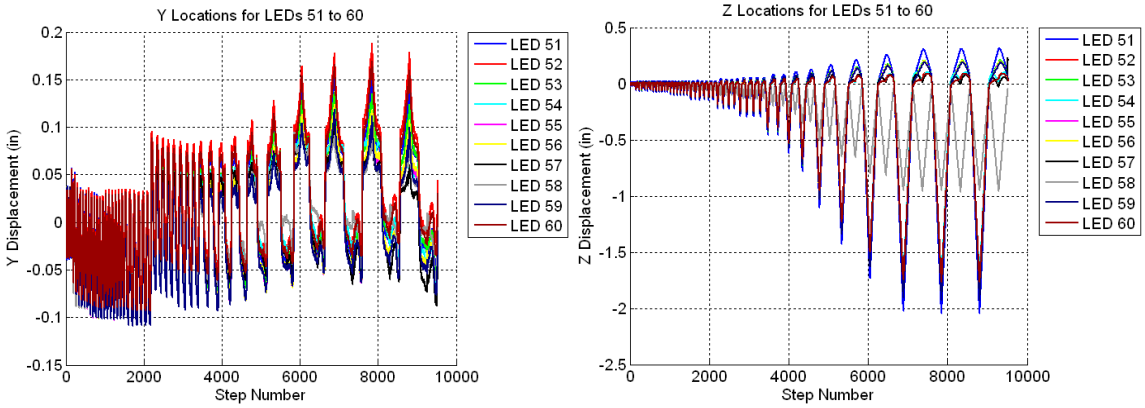

Figure B.125 Raw Data For Specimen A3 – Y Displacements for LED's 51 to 60 (Left) and Z Displacements for LED's 51 to 60 (Right)

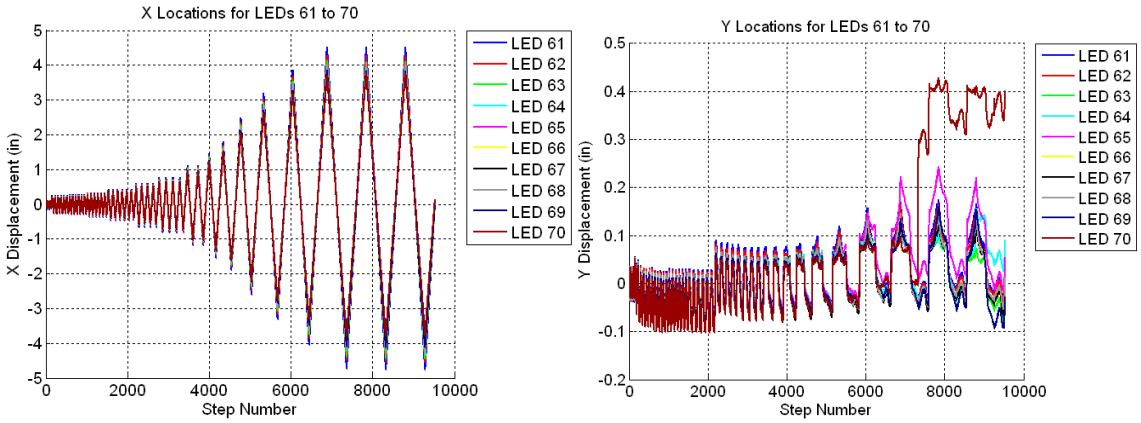

Figure B.126 Raw Data For Specimen A3 – X Displacements for LED's 61 to 70 (Left) and Y Displacements for LED's 61 to 70 (Right)

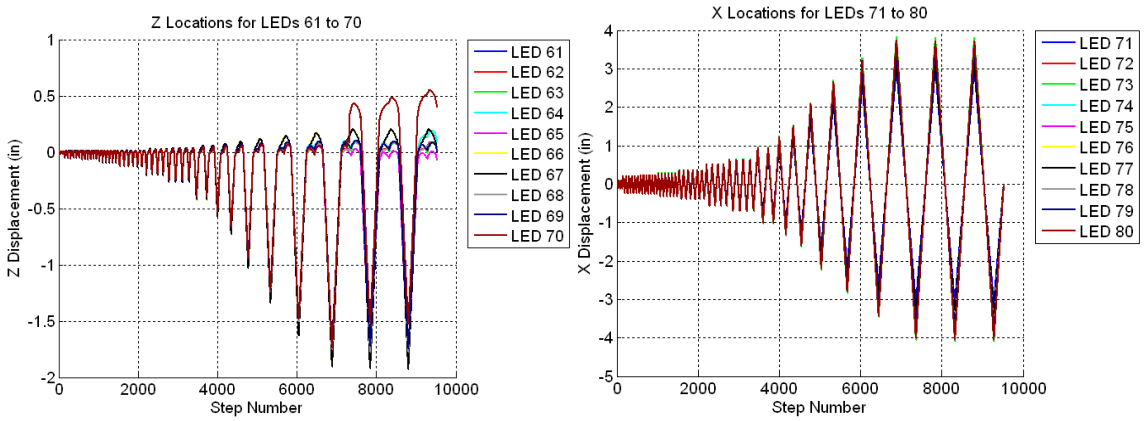

Figure B.127 Raw Data For Specimen A3 – Z Displacements for LED's 61 to 70 (Left) and X Displacements for LED's 71 to 80 (Right)

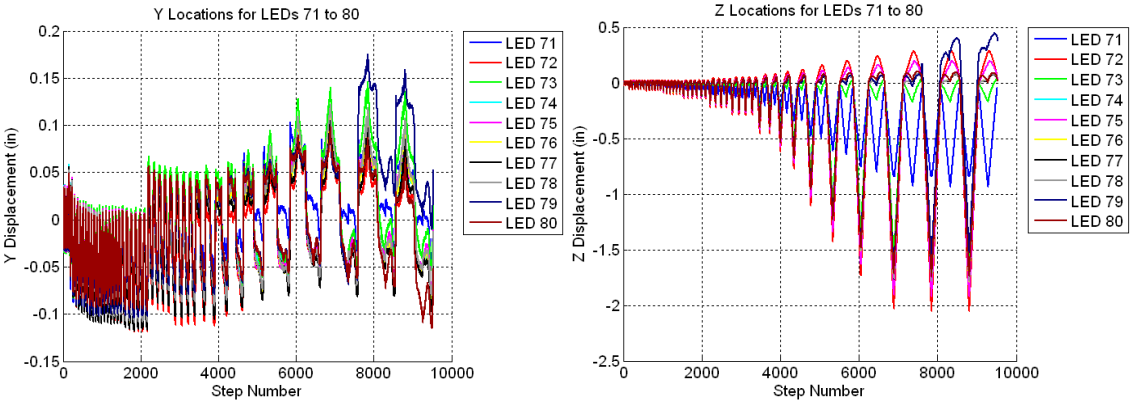

Figure B.128 Raw Data For Specimen A3 – Y Displacements for LED's 71 to 80 (Left) and Z Displacements for LED's 71 to 80 (Right)

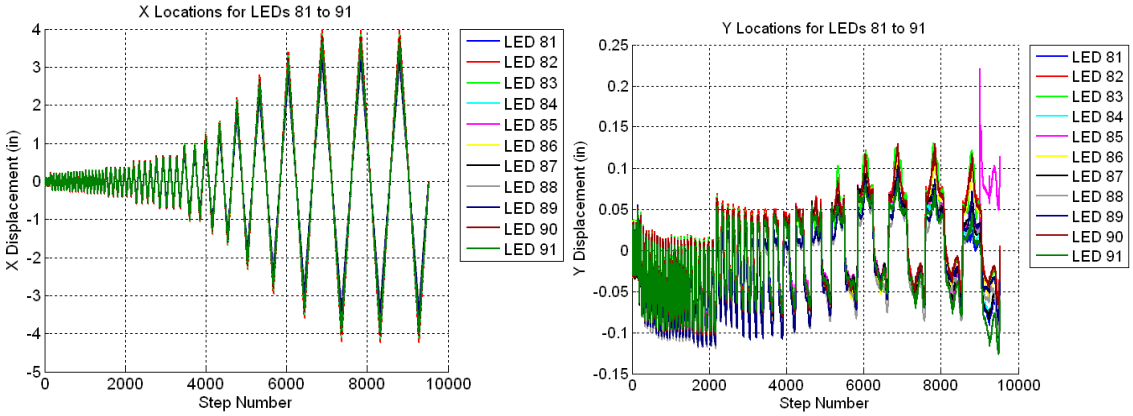

Figure B.129 Raw Data For Specimen A3 – X Displacements for LED's 81 to 91 (Left) and Y Displacements for LED's 81 to 91 (Right)

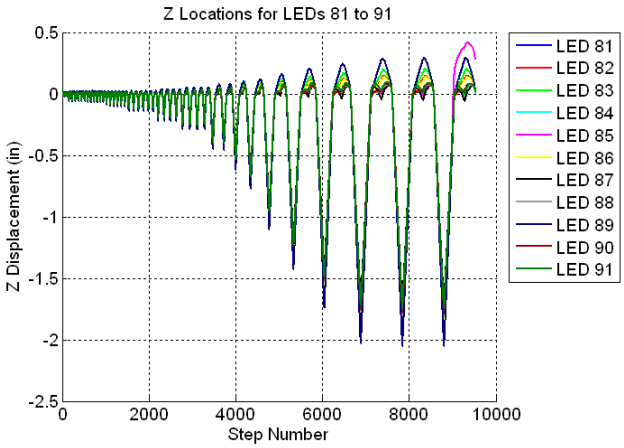

Figure B.130 Raw Data For Specimen A3 – Z Displacements for LED's 81 to 91

B.4 Specimen A4

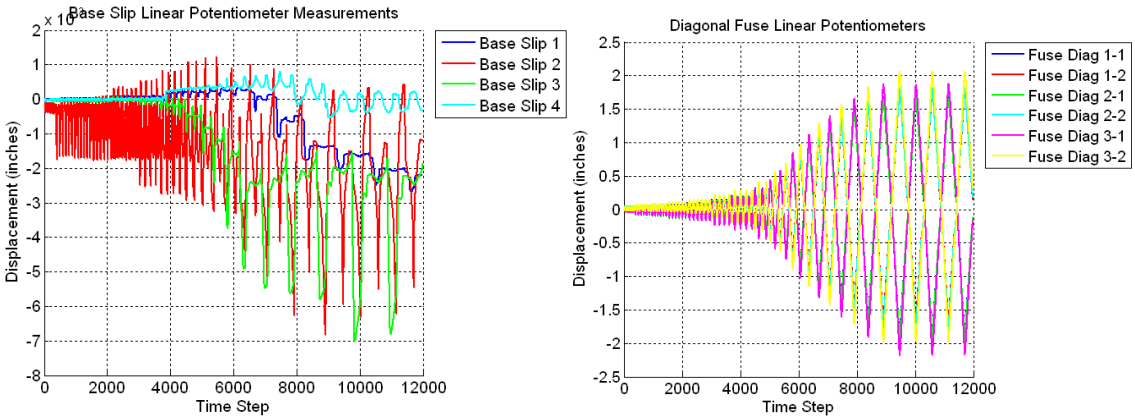

Figure B.131 Raw Data For Specimen A4 – Base Slip (Left) and Fuse Linear Pots (Right)

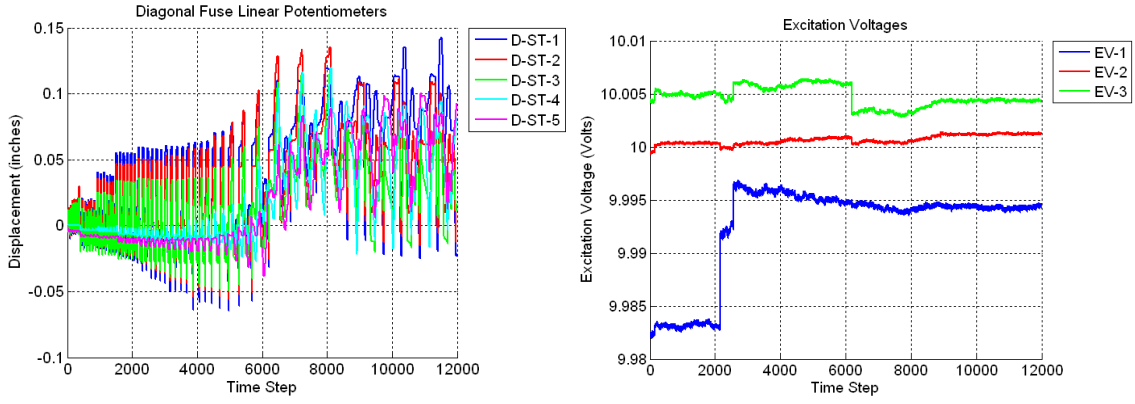

Figure B.132 Raw Data For Specimen A4 – Strut Linear Potentiometers (Left) and Excitation Voltages (Right)

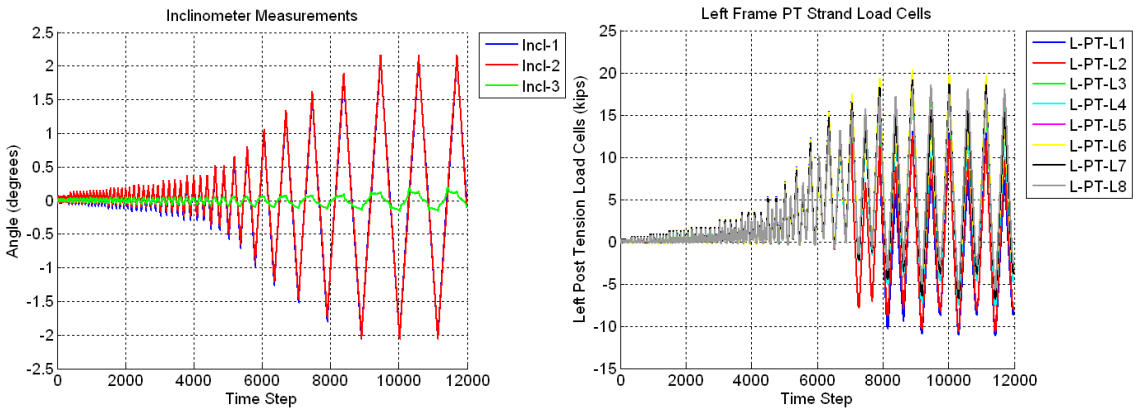

Figure B.133 Raw Data For Specimen A4 – Inclinometers (Left) and PT Load Cells (Right)

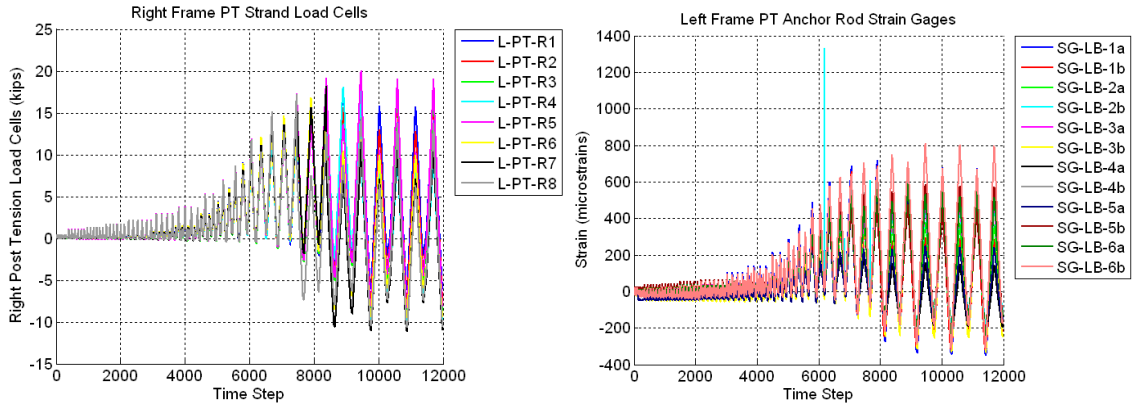

Figure B.134 Raw Data For Specimen A4 – Right Frame PT Load Cells (Left) and Left Frame PT Anchor Rods (Right)

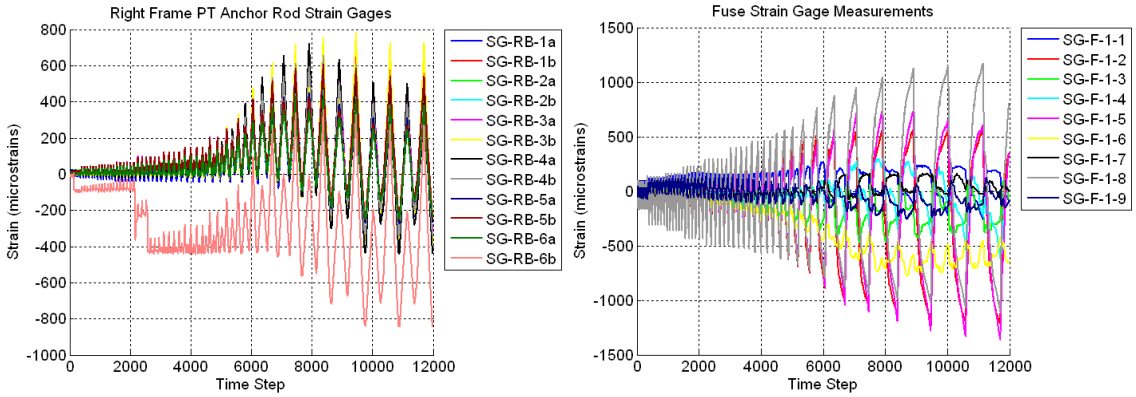

Figure B.135 Raw Data For Specimen A4 – Right Frame PT Anchor Rods (Left) and Back Fuse Strain Gages (Right)

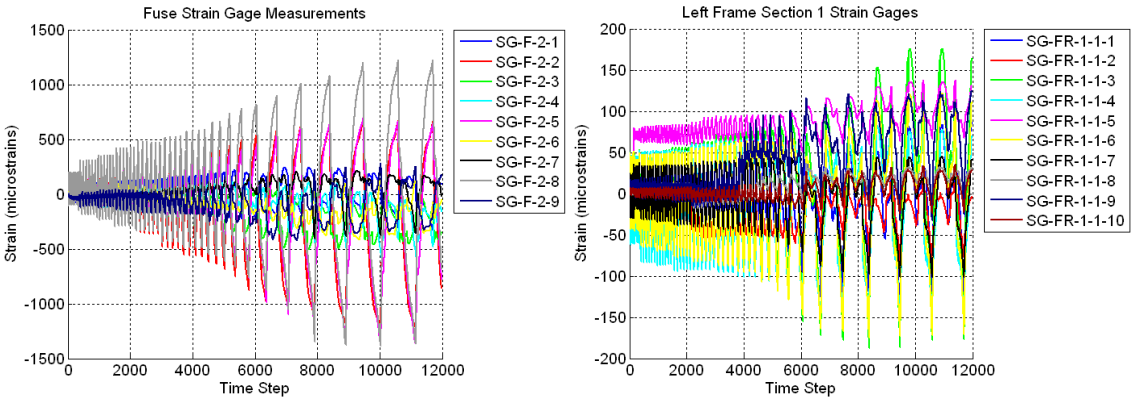

Figure B.136 Raw Data For Specimen A4 – Front Fuse Strain Gages (Left) and Left Frame Section 1-1 Strain Gages (Right)

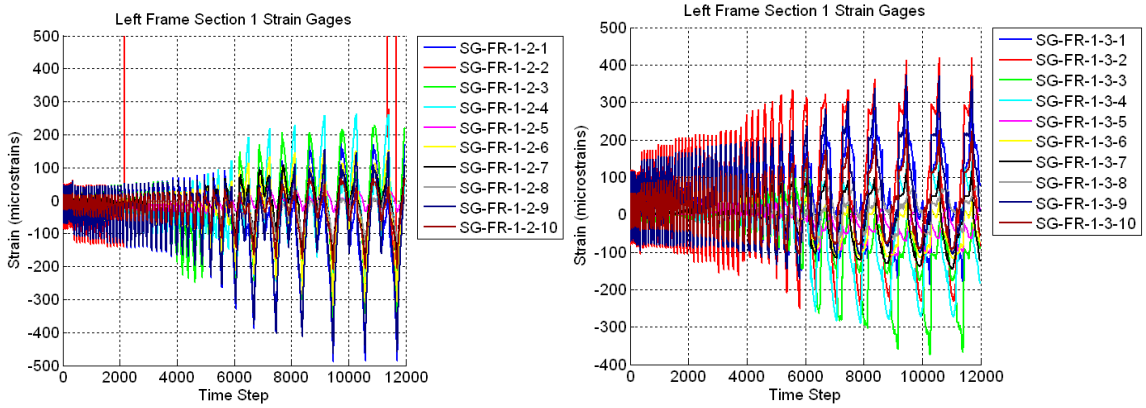

Figure B.137 Raw Data For Specimen A4 – Left Frame Section 1-2 Strain Gages (Left) and Left Frame Section 1-3 Strain Gages (Right)

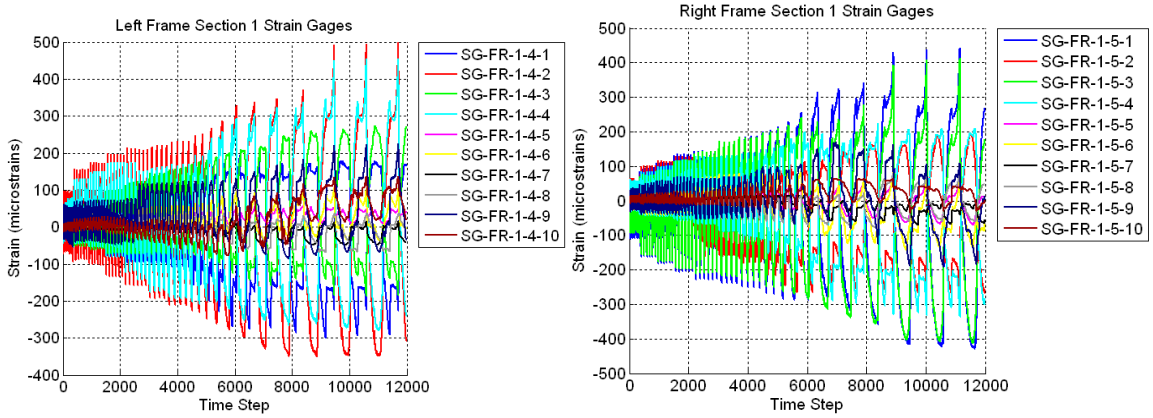

Figure B.138 Raw Data For Specimen A4 – Left Frame Section 1-4 Strain Gages (Left) and Right Frame Section 1-5 Strain Gages (Right)

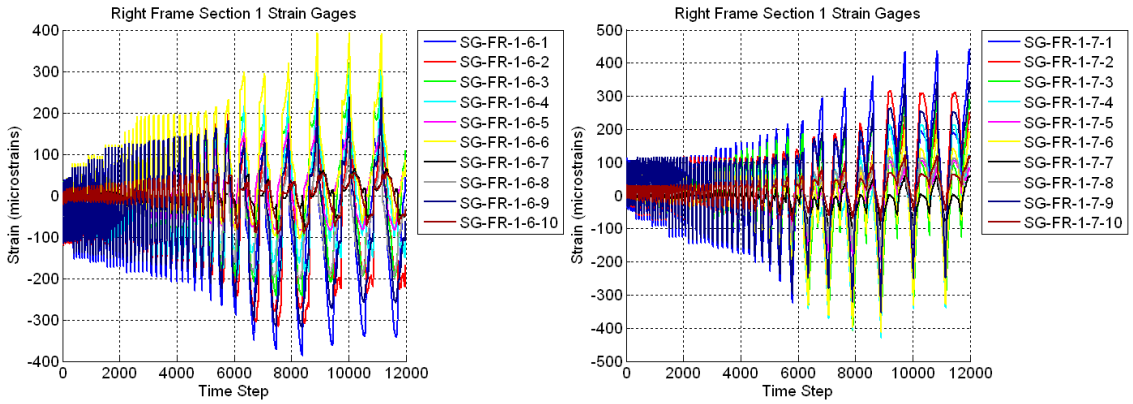

Figure B.139 Raw Data For Specimen A4 – Right Frame Section 1-6 Strain Gages (Left) and Right Frame Section 1-7 Strain Gages (Right)

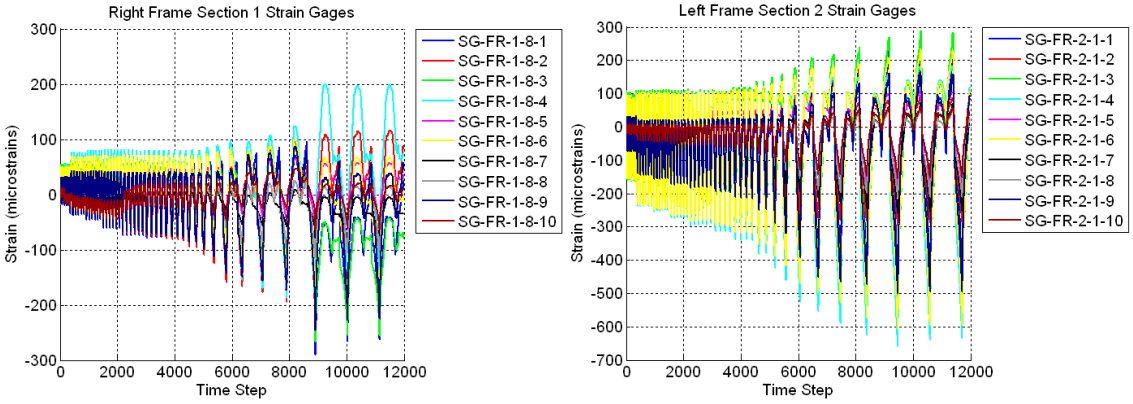

Figure B.140 Raw Data For Specimen A4 – Right Frame Section 1-8 Strain Gages (Left) and Left Frame Section 2-1 Strain Gages (Right)

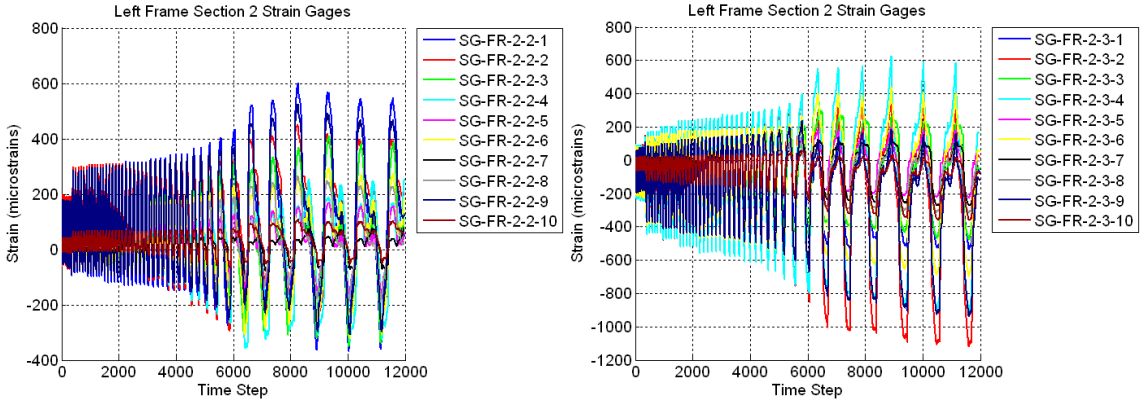

Figure B.141 Raw Data For Specimen A4 – Left Frame Section 2-2 Strain Gages (Left) and Left Frame Section 2-3 Strain Gages (Right)

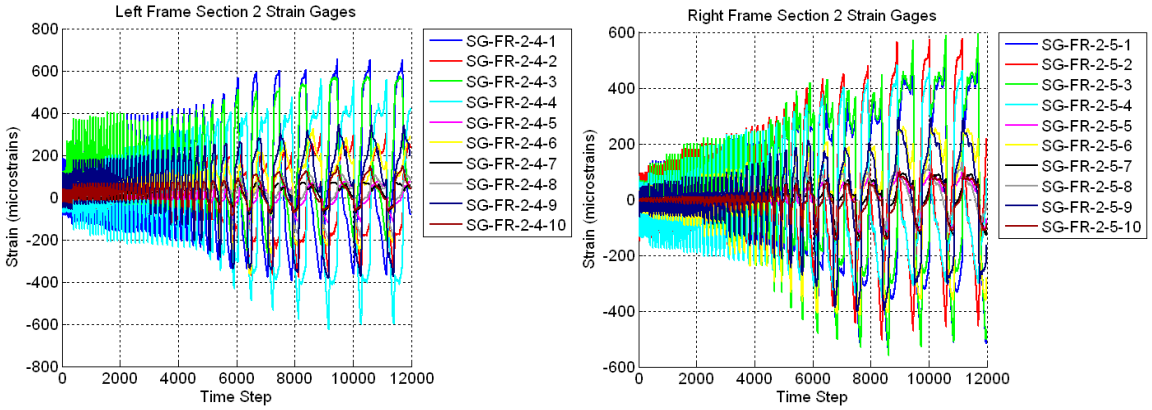

Figure B.142 Raw Data For Specimen A4 – Left Frame Section 2-4 Strain Gages (Left) and Right Frame Section 2-5 Strain Gages (Right)

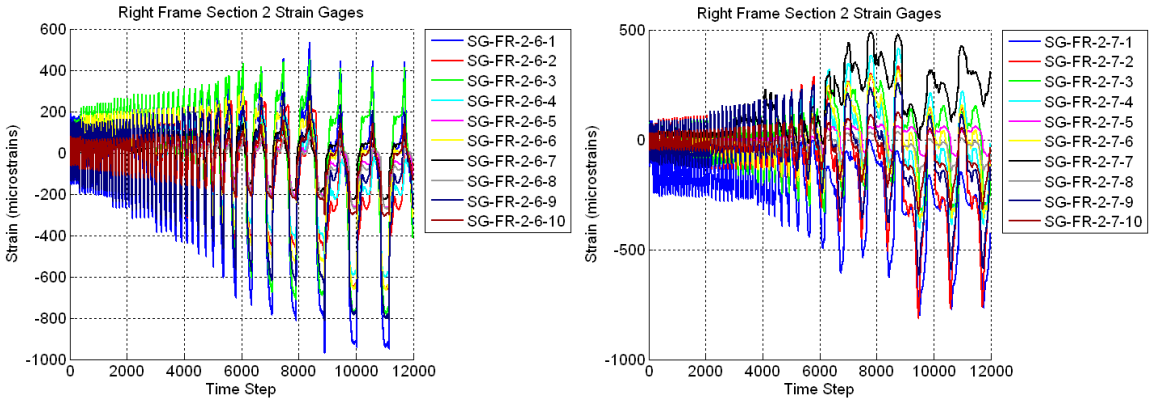

Figure B.143 Raw Data For Specimen A4 – Right Frame Section 2-6 Strain Gages (Left) and Right Frame Section 2-7 Strain Gages (Right)

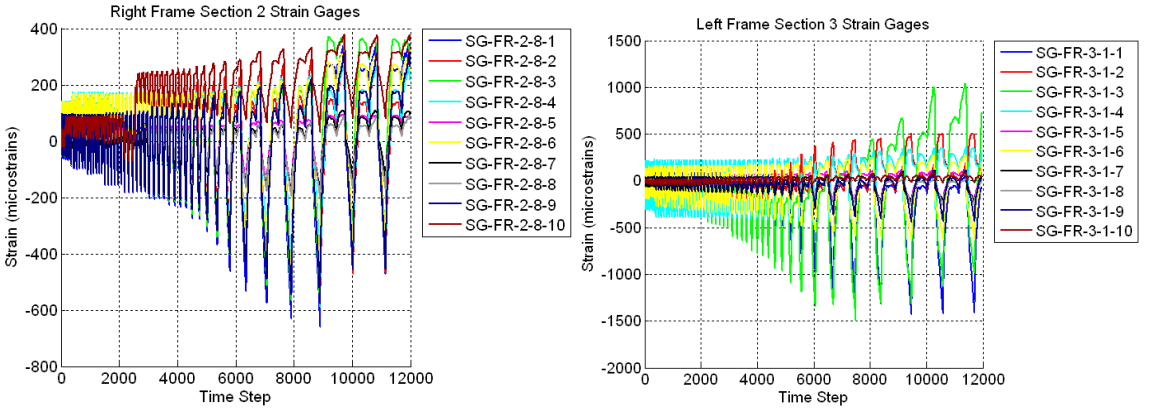

Figure B.144 Raw Data For Specimen A4 – Right Frame Section 2-8 Strain Gages (Left) and Left Frame Section 3-1 Strain Gages (Right)

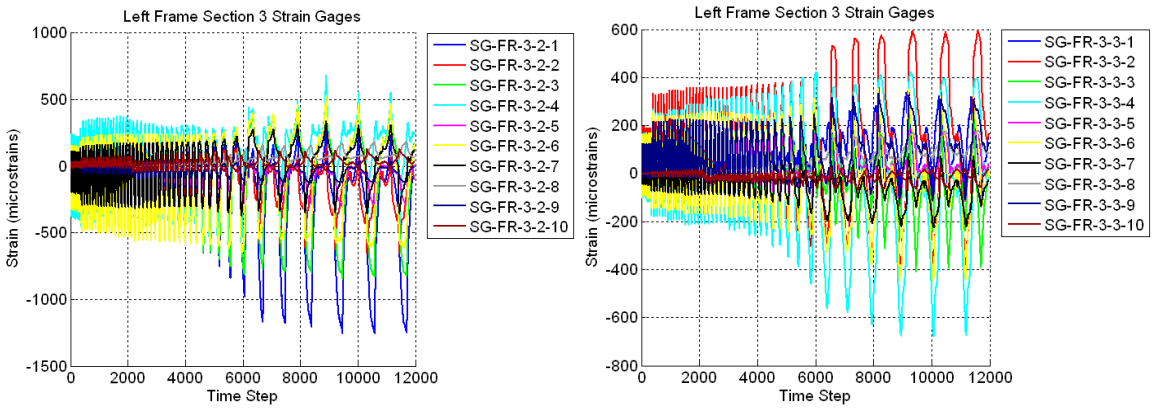

Figure B.145 Raw Data For Specimen A4 – Left Frame Section 3-2 Strain Gages (Left) and Left Frame Section 3-3 Strain Gages (Right)

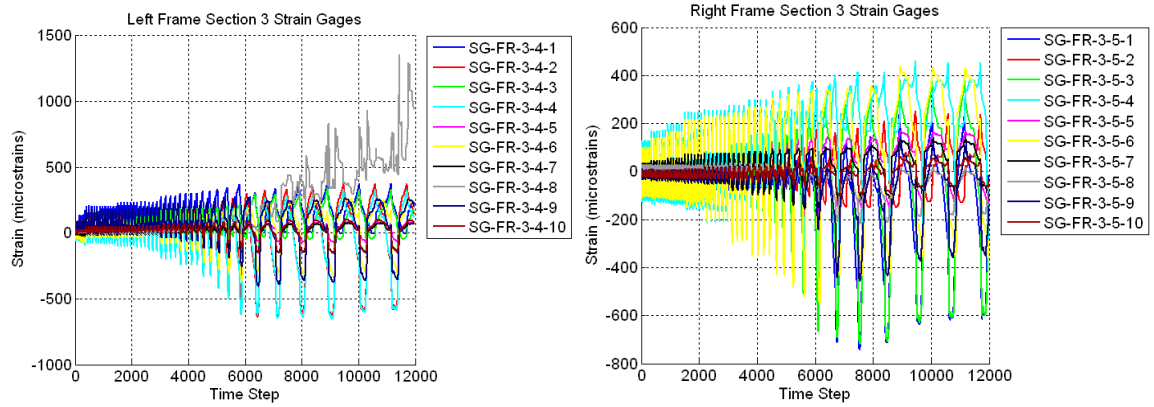

Figure B.146 Raw Data For Specimen A4 – Left Frame Section 3-4 Strain Gages (Left) and Right Frame Section 3-5 Strain Gages (Right)

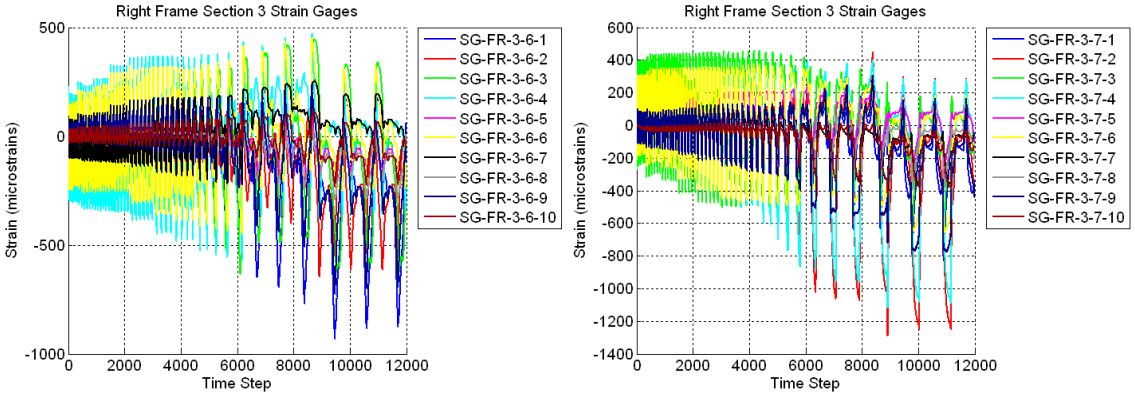

Figure B.147 Raw Data For Specimen A4 – Right Frame Section 3-6 Strain Gages (Left) and Right Frame Section 3-7 Strain Gages (Right)

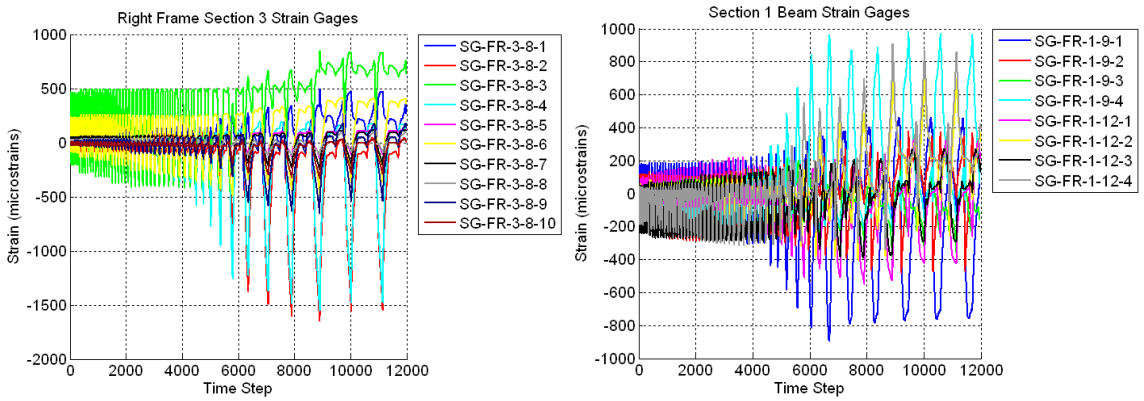

Figure B.148 Raw Data For Specimen A4 – Right Frame Section 3-8 Strain Gages (Left) and First Floor Beam Strain Gages (Right)

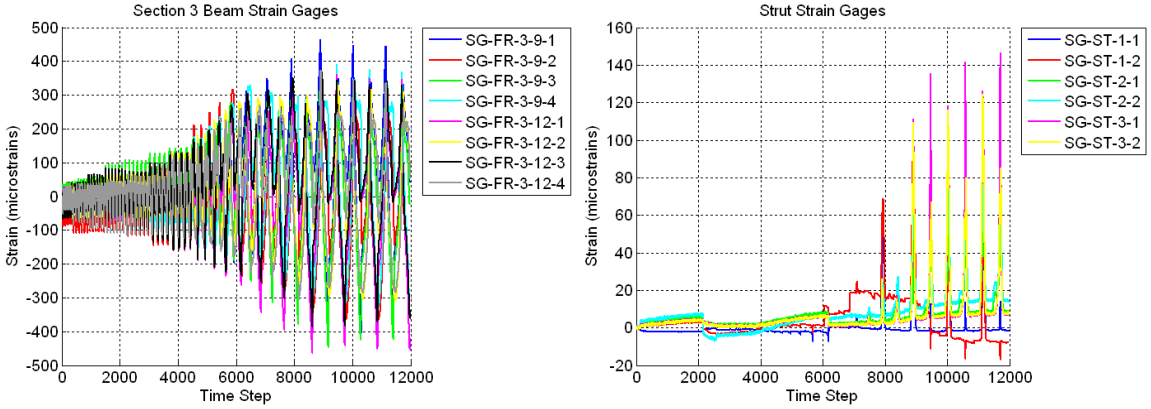

Figure B.149 Raw Data For Specimen A4 – Third Floor Beam Strain Gages (Left) and Strut Strain Gages (Right)

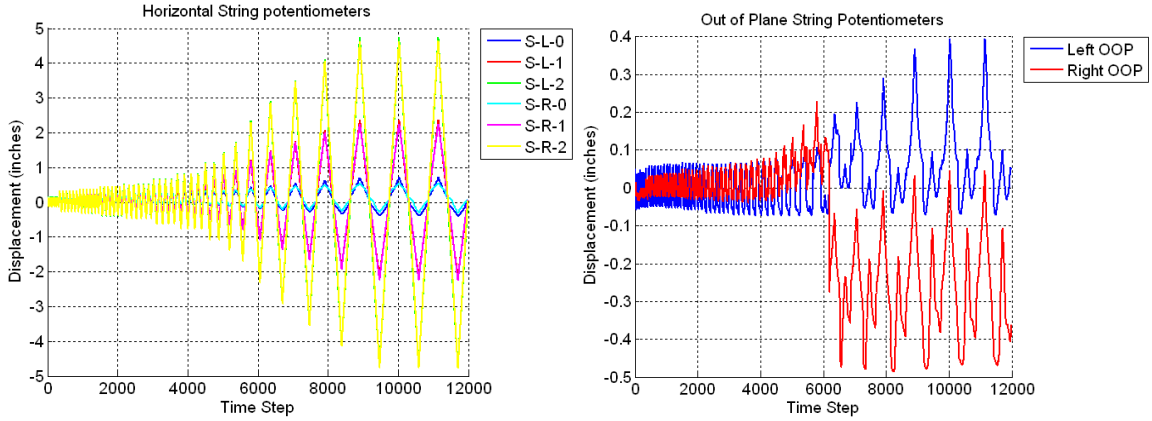

Figure B.150 Raw Data For Specimen A4 – Horizontal String Potentiometers (Left) and Out-of-Plane String Potentiometers (Right)

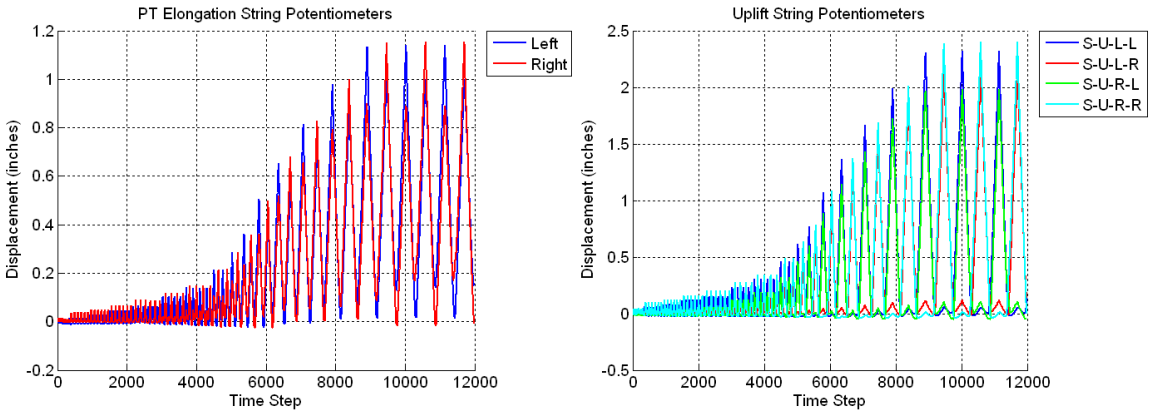

Figure B.151 Raw Data For Specimen A4 – PT Elongation String Potentiometers (Left) and Uplift String Potentiometers (Right)

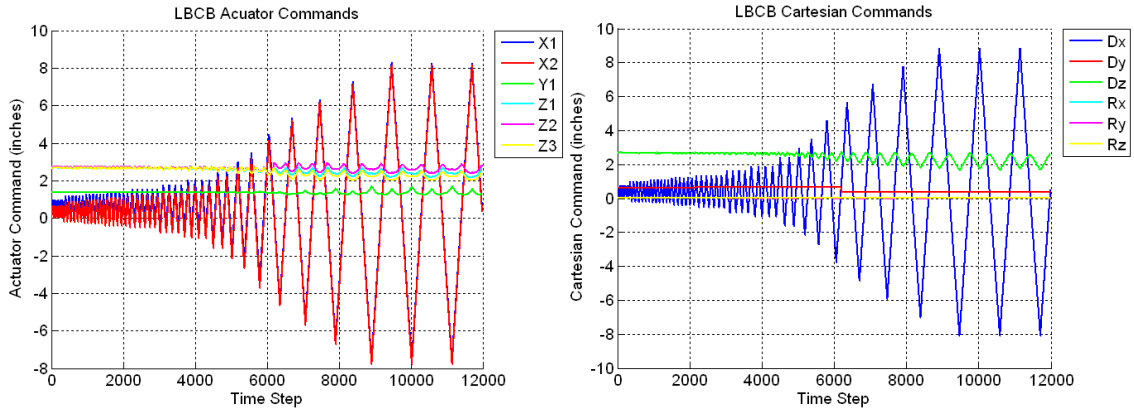

Figure B.152 Raw Data For Specimen A4 – LBCB Actuator Commands (Left) and LBCB Cartesian Commands (Right)

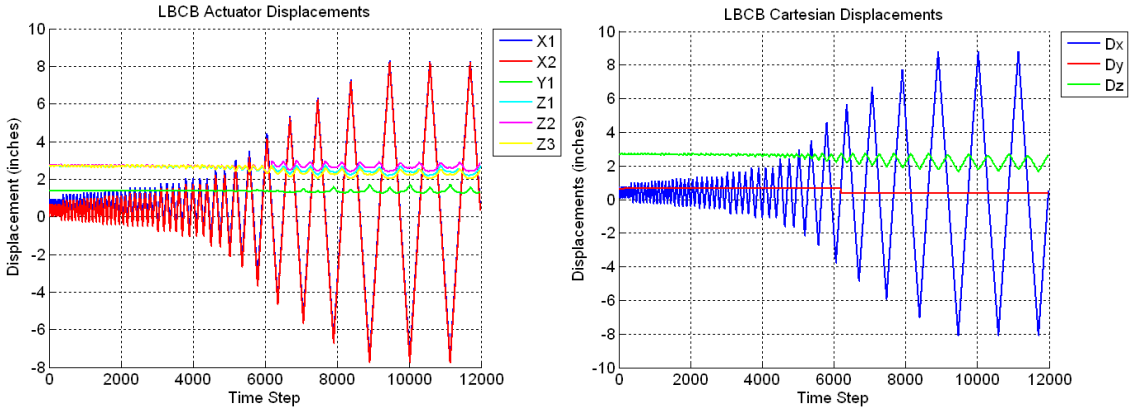

Figure B.153 Raw Data For Specimen A4 – LBCB Actuator Displacements (Left) and LBCB Cartesian Displacements (Right)

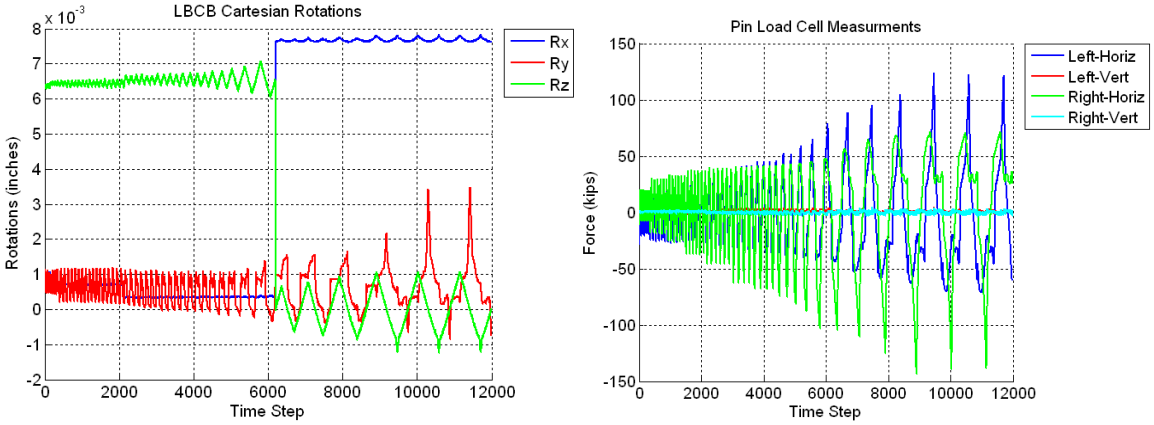

Figure B.154 Raw Data For Specimen A4 – LBCB Cartesian Rotations (Left) and Pin Load Cells (Right)

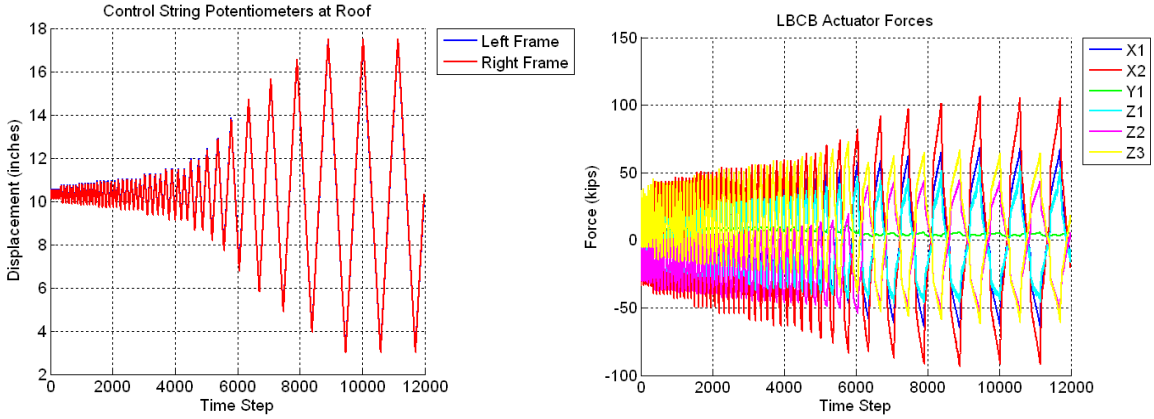

Figure B.155 Raw Data For Specimen A4 – Control String Potentiometers (Left) and LBCB Actuator Forces (Right)

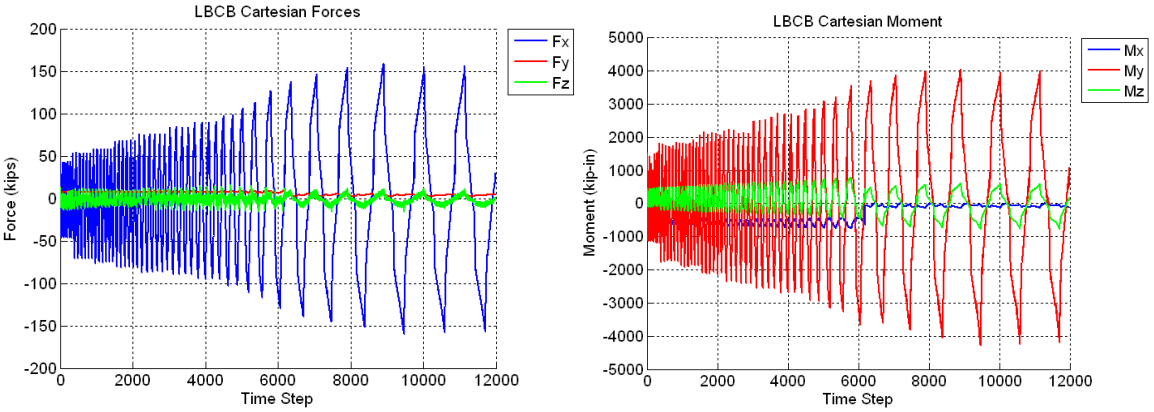

Figure B.156 Raw Data For Specimen A4 – LBCB Cartesian Forces (Left) and LBCB Cartesian Moments (Right)

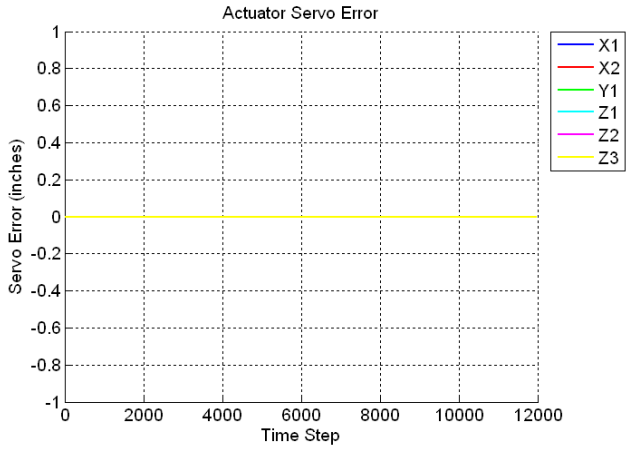

Figure B.157 Raw Data For Specimen A4 – LBCB Actuator Servo-Error

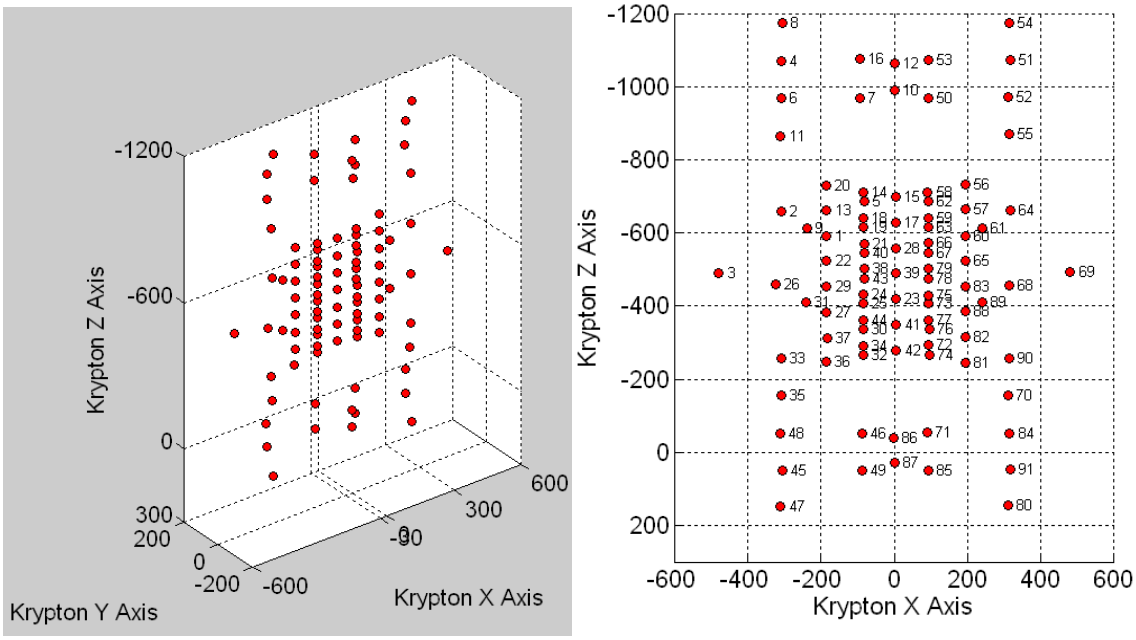

Figure B.158 Raw Data For Specimen A4 – Krypton LED Locations (Left) and Krypton LED Numbering (Right)

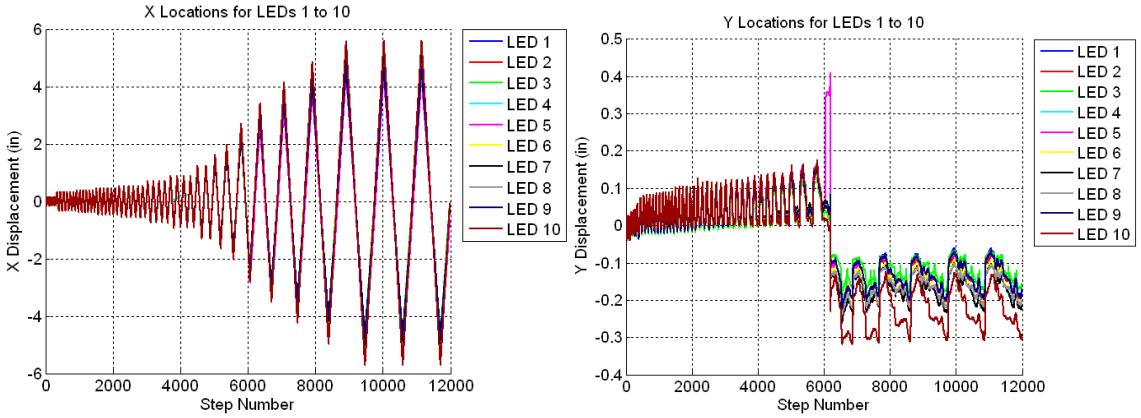

Figure B.159 Raw Data For Specimen A4 – X Displacements for LED's 1 to 10 (Left) and Y Displacements for LED's 1 to 10 (Right)

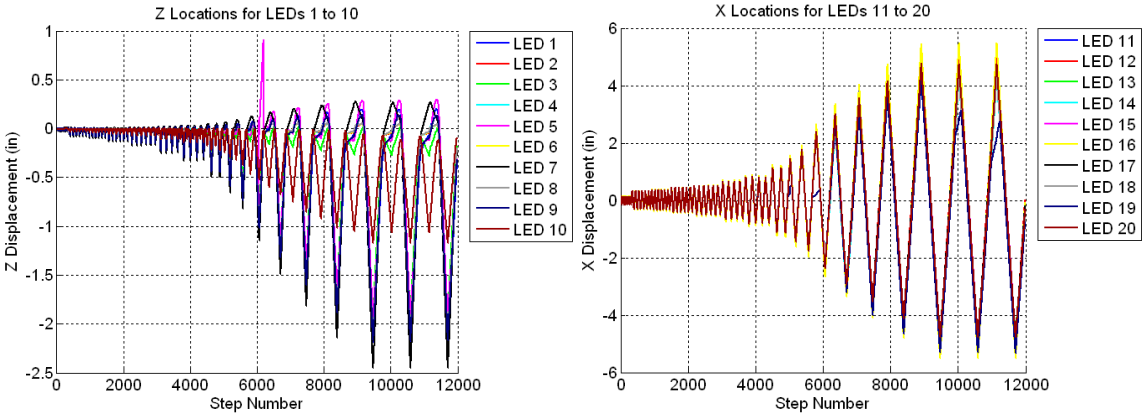

Figure B.160 Raw Data For Specimen A4 – Z Displacements for LED's 1 to 10 (Left) and X Displacements for LED's 11 to 20 (Right)

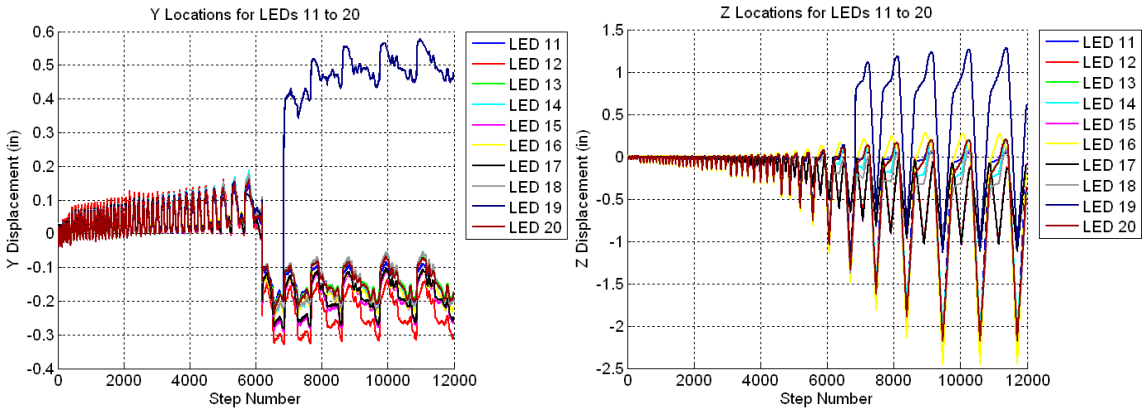

Figure B.161 Raw Data For Specimen A4 – Y Displacements for LED's 11 to 20 (Left) and Z Displacements for LED's 11 to 20 (Right)

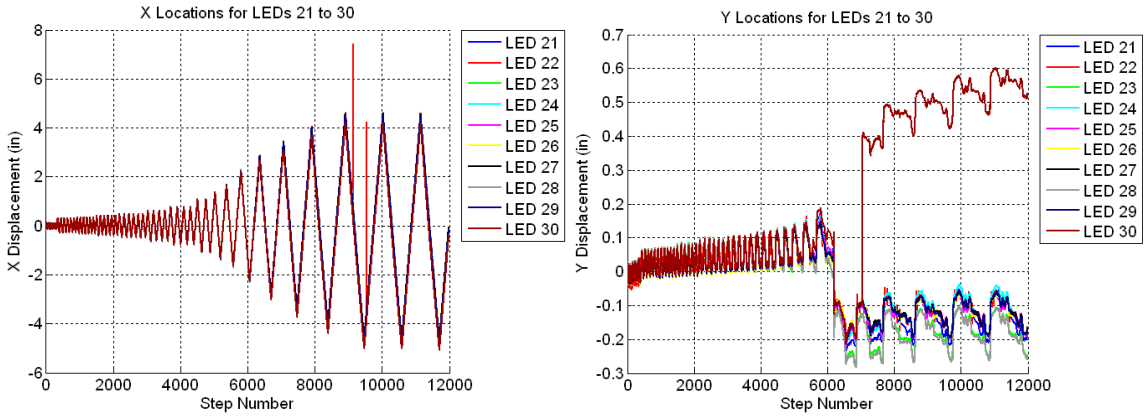

Figure B.162 Raw Data For Specimen A4 – X Displacements for LED's 21 to 30 (Left) and Y Displacements for LED's 21 to 30 (Right)

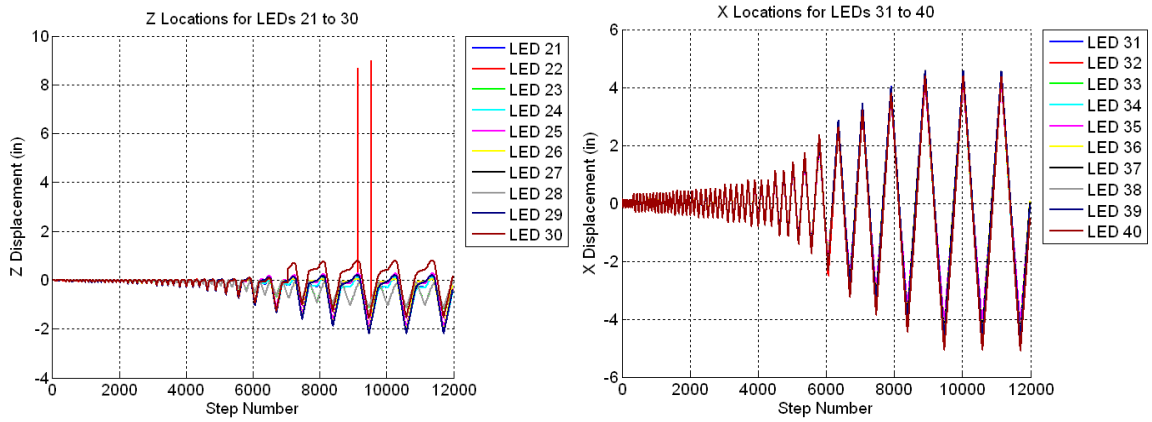

Figure B.163 Raw Data For Specimen A4 - Z Displacements for LED's 21 to 30 (Left) and X Displacements for LED's 31 to 40 (Right)

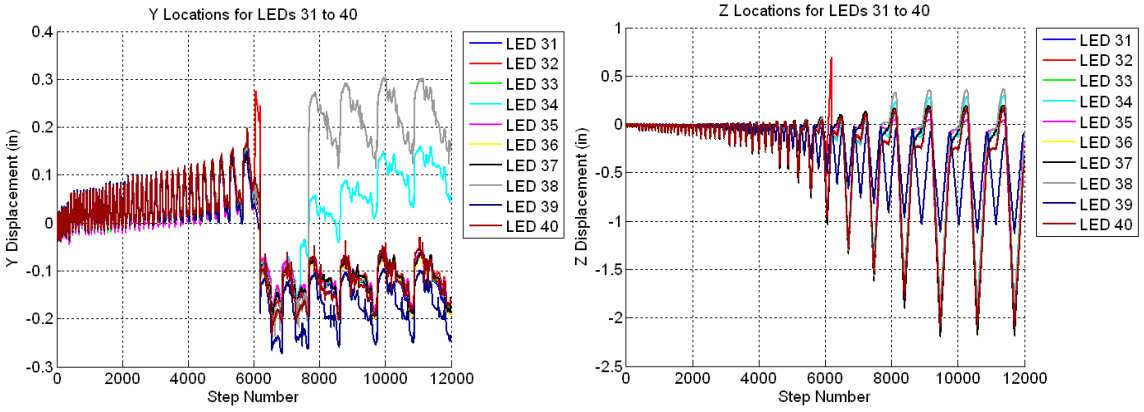

Figure B.164 Raw Data For Specimen A4 – Y Displacements for LED's 31 to 40 (Left) and Z Displacements for LED's 31 to 40 (Right)

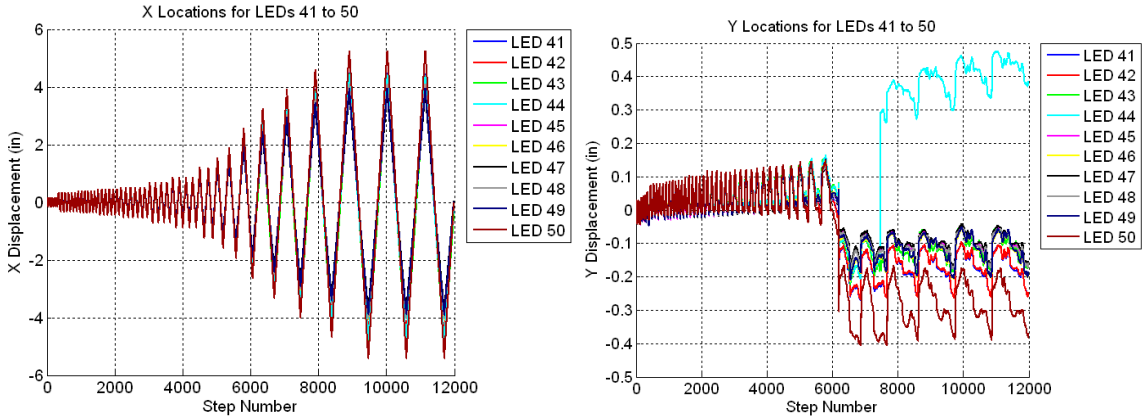

Figure B.165 Raw Data For Specimen A4 – X Displacements for LED's 41 to 50 (Left) and Y Displacements for LED's 41 to 50 (Right)

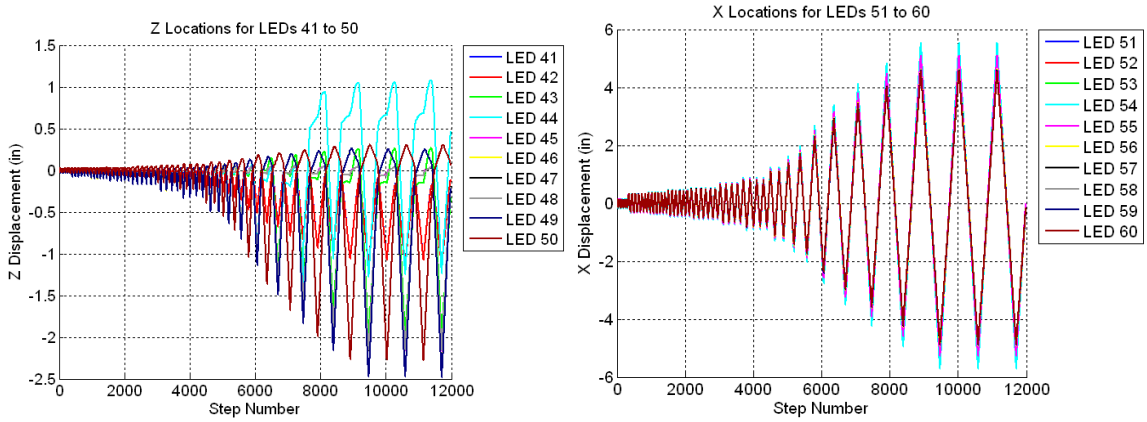

Figure B.166 Raw Data For Specimen A4 – Z Displacements for LED's 41 to 50 (Left) and X Displacements for LED's 51 to 60 (Right)

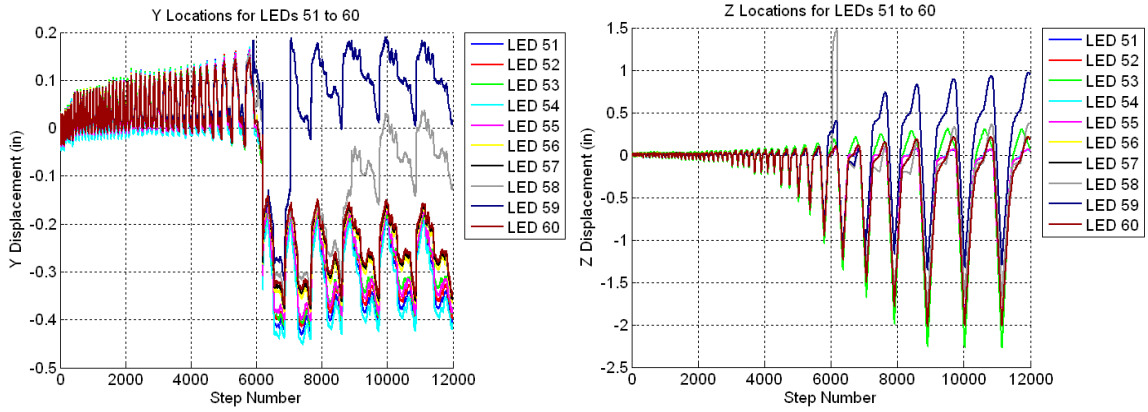

Figure B.167 Raw Data For Specimen A4 – Y Displacements for LED's 51 to 60 (Left) and Z Displacements for LED's 51 to 60 (Right)

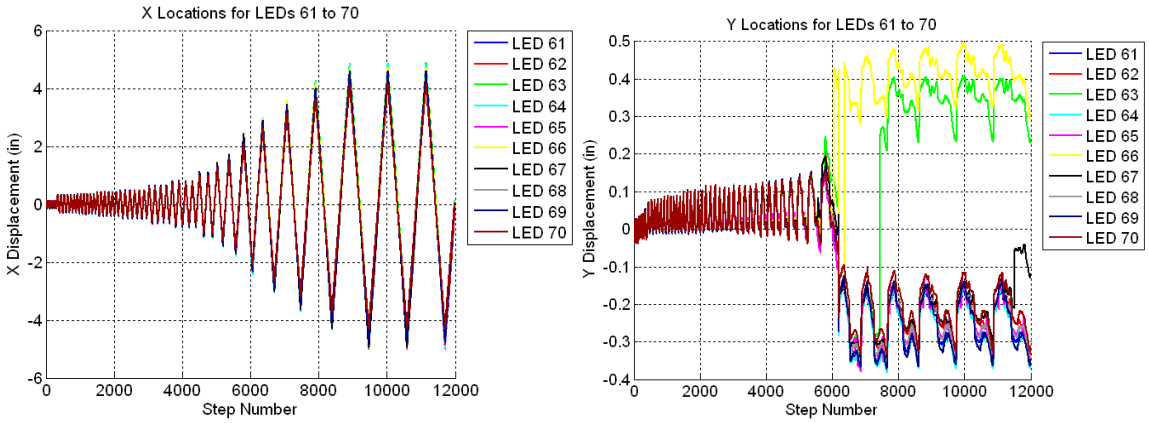

Figure B.168 Raw Data For Specimen A4 – X Displacements for LED's 61 to 70 (Left) and Y Displacements for LED's 61 to 70 (Right)

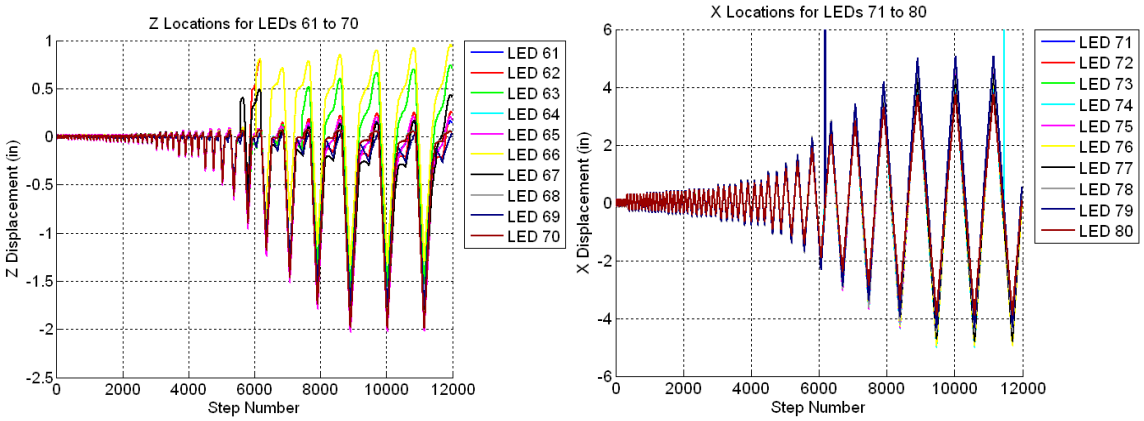

Figure B.169 Raw Data For Specimen A4 – Z Displacements for LED's 61 to 70 (Left) and X Displacements for LED's 71 to 80 (Right)

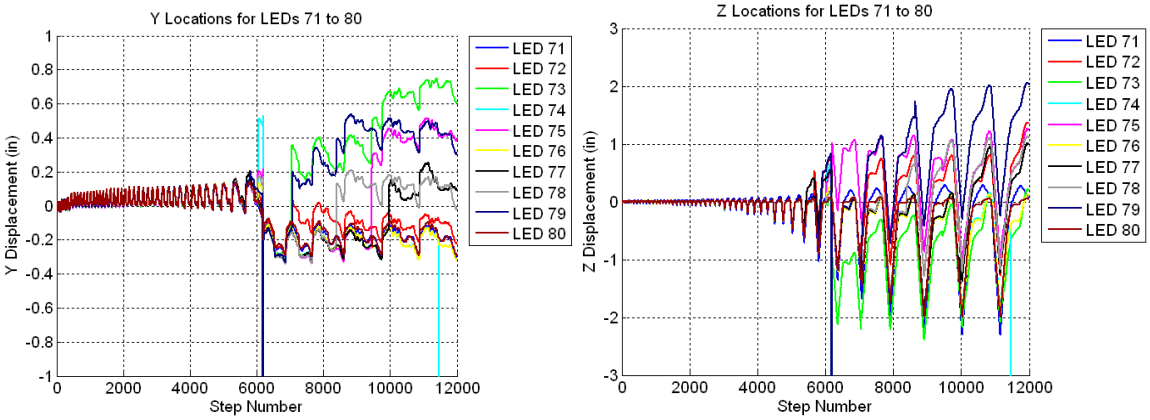

Figure B.170 Raw Data For Specimen A4 – Y Displacements for LED's 71 to 80 (Left) and Z Displacements for LED's 71 to 80 (Right)

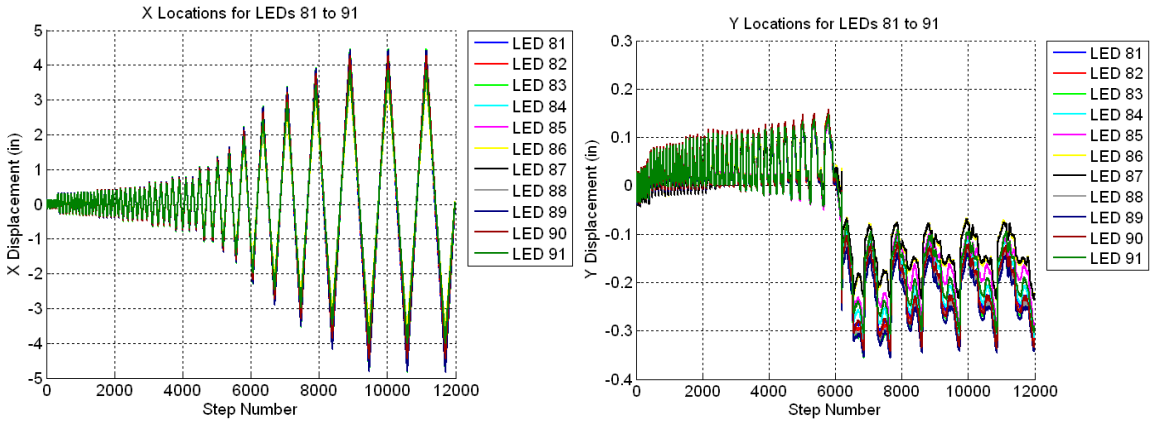

Figure B.171 Raw Data For Specimen A4 – X Displacements for LED's 81 to 91 (Left) and Y Displacements for LED's 81 to 91 (Right)

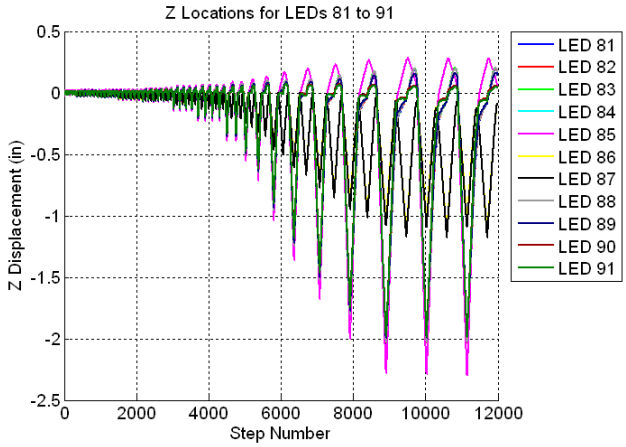

Figure B.172 Raw Data For Specimen A4 – Z Displacements for LED's 81 to 91

B.5 Specimen A5 – MCE Trial

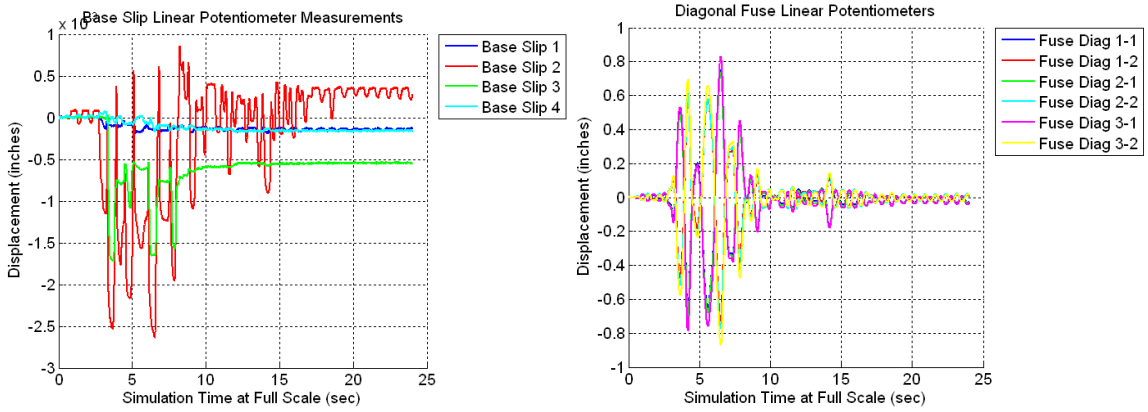

Figure B.173 Raw Data For Specimen A5 MCE Trial – Base Slip (Left) and Fuse Linear Potentiometers (Right)

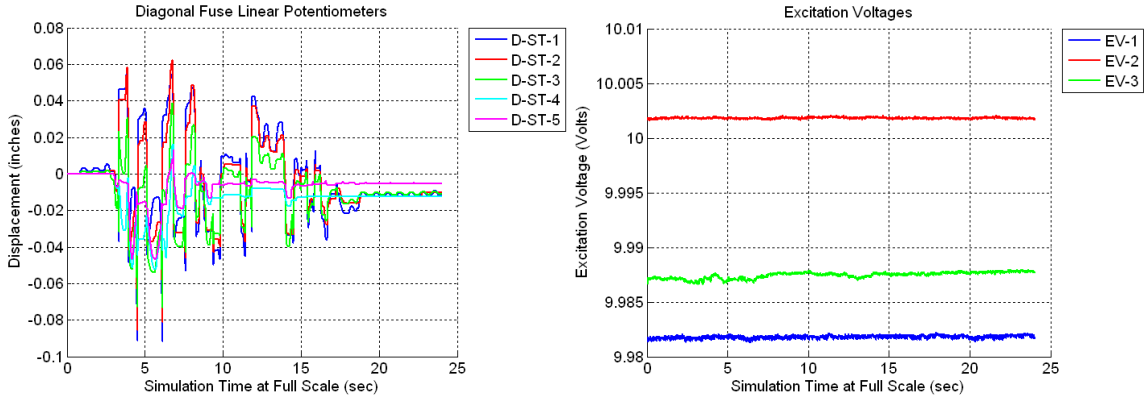

Figure B.174 Raw Data For Specimen A5 MCE Trial – Strut Linear Potentiometers (Left) and Excitation Voltages (Right)

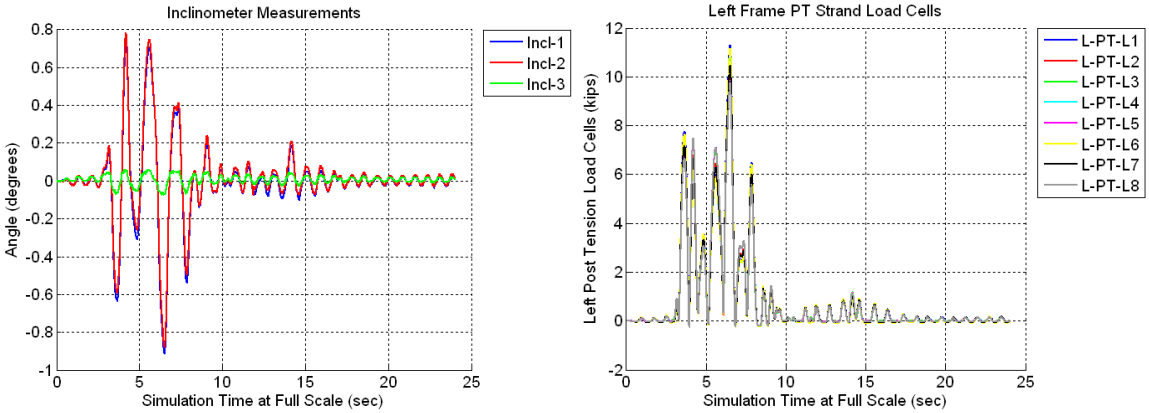

Figure B.175 Raw Data For Specimen A5 MCE Trial – Inclinometers (Left) and Left Frame PT Load Cells (Right)

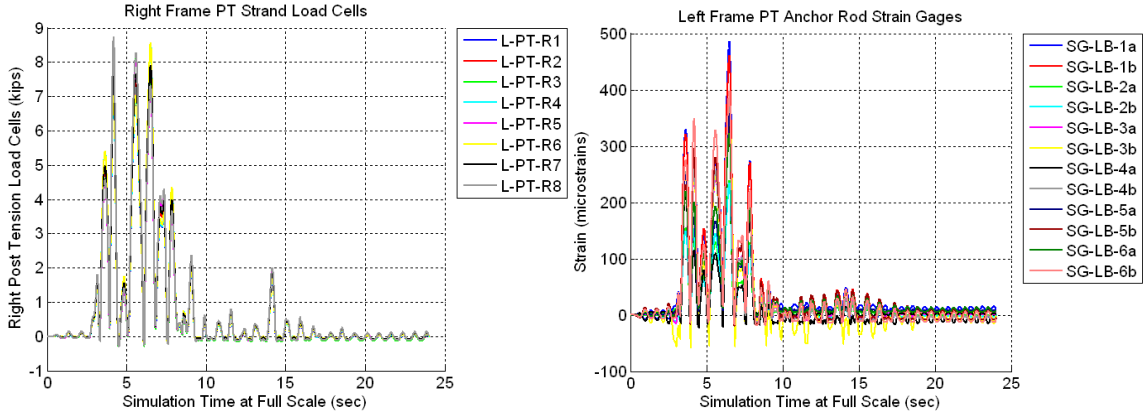

Figure B.176 Raw Data For Specimen A5 MCE Trial – Right Frame PT Load Cells (Left) and Left Frame PT Anchor Rods (Right)

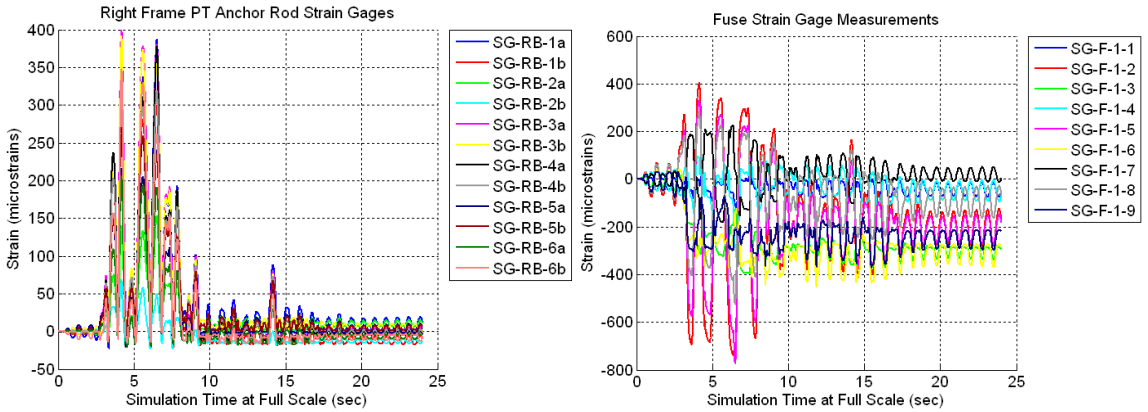

Figure B.177 Raw Data For Specimen A5 MCE Trial – Right Frame PT Anchor Rods (Left) and Back Fuse Strain Gages (Right)

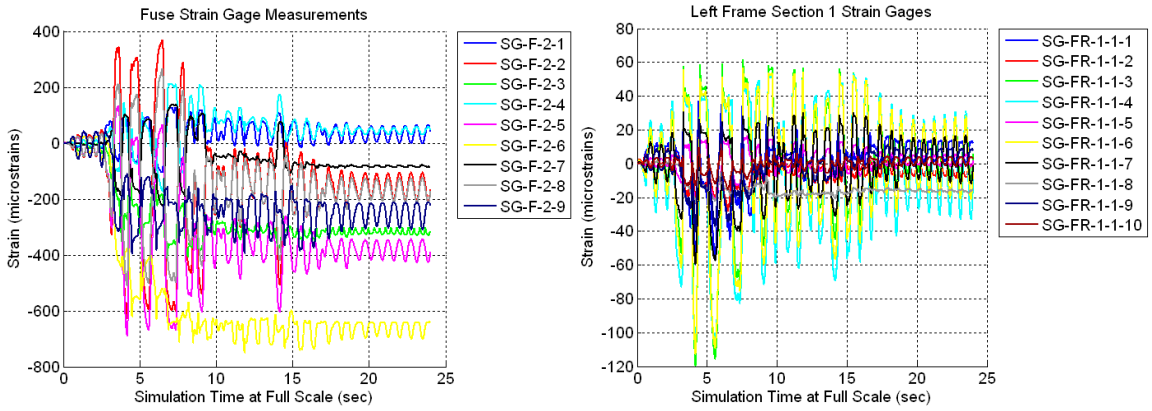

Figure B.178 Raw Data For Specimen A5 MCE Trial – Front Fuse Strain Gages (Left) and Left Frame Section 1-1 Strain Gages (Right)

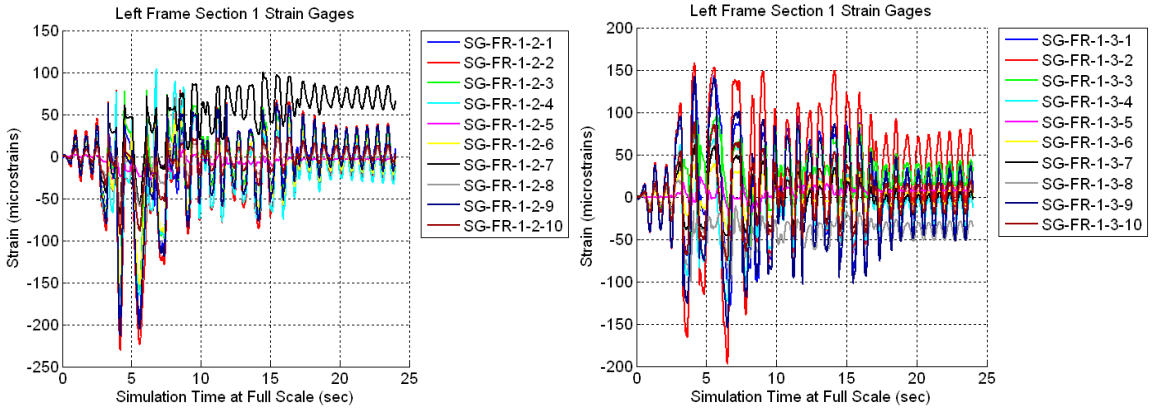

Figure B.179 Raw Data For Specimen A5 MCE Trial – Left Frame Section 1-2 Strain Gages (Left) and Left Frame Section 1-3 Strain Gages (Right)

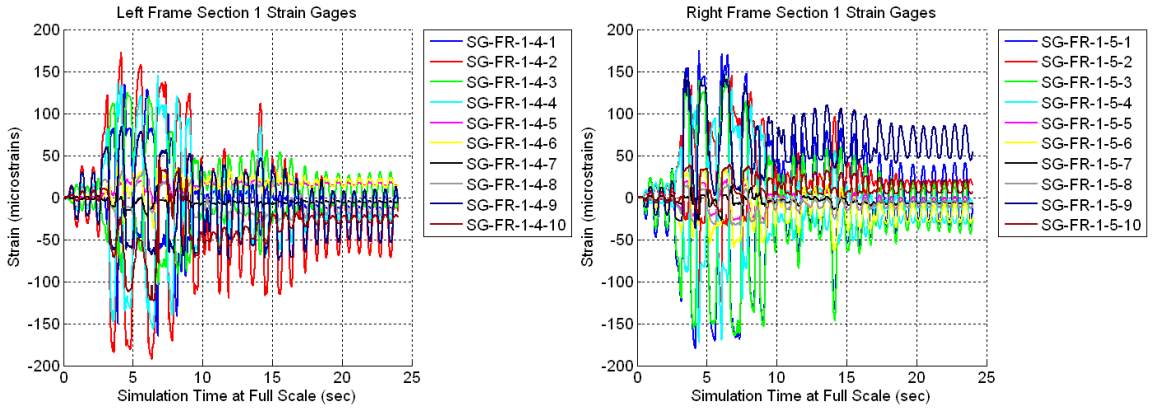

Figure B.180 Raw Data For Specimen A5 MCE Trial – Left Frame Section 1-4 Strain Gages (Left) and Right Frame Section 1-5 Strain Gages (Right)

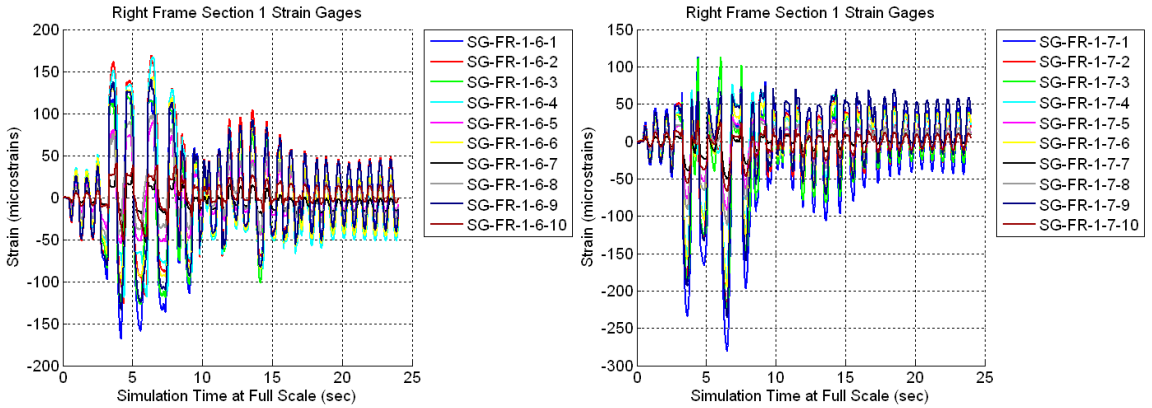

Figure B.181 Raw Data For Specimen A5 MCE Trial – Right Frame Section 1-6 Strain Gages (Left) and Right Frame Section 1-7 Strain Gages (Right)

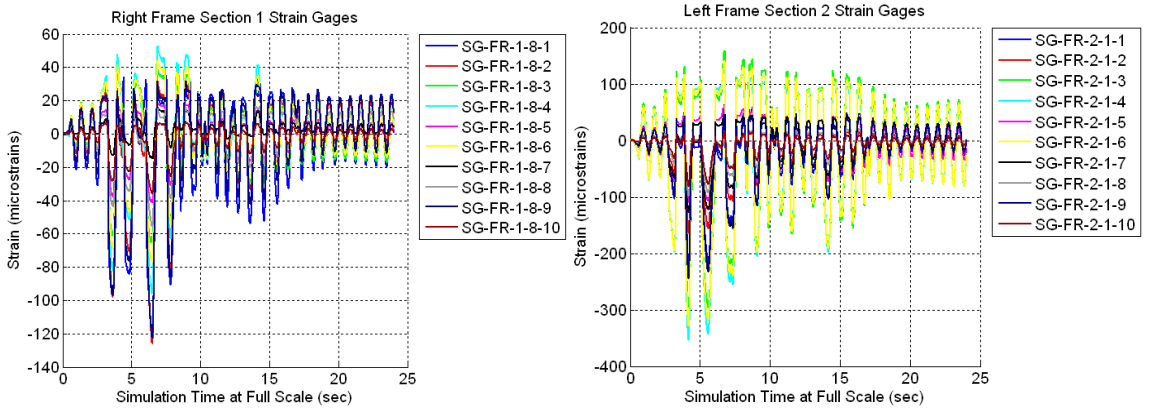

Figure B.182 Raw Data For Specimen A5 MCE Trial – Right Frame Section 1-8 Strain Gages (Left) and Left Frame Section 2-1 Strain Gages (Right)

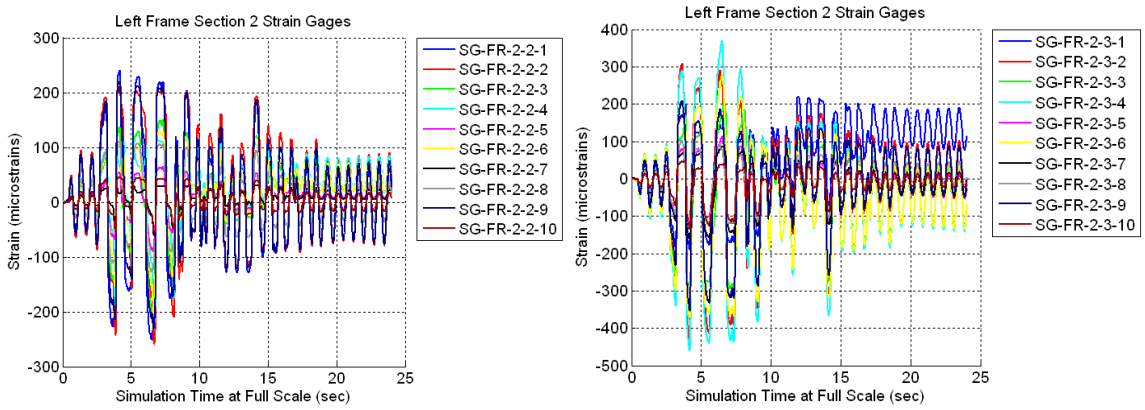

Figure B.183 Raw Data For Specimen A5 MCE Trial – Left Frame Section 2-2 Strain Gages (Left) and Left Frame Section 2-3 Strain Gages (Right)

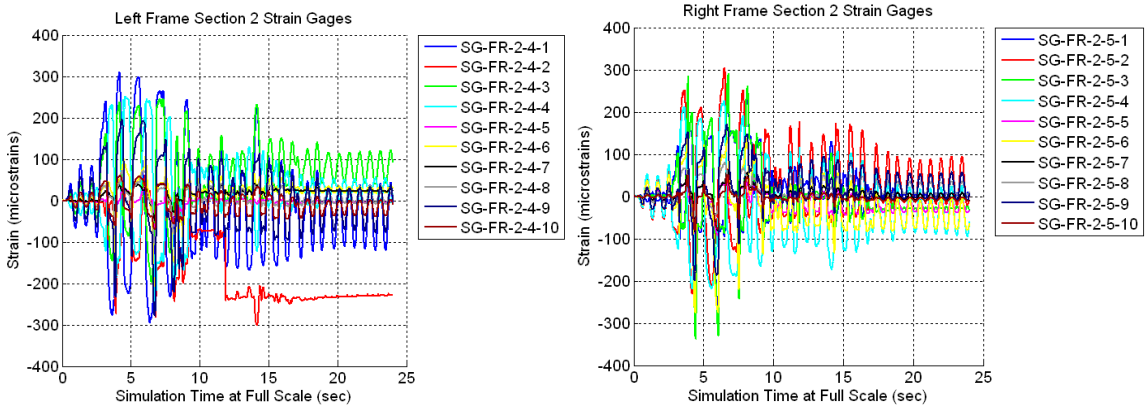

Figure B.184 Raw Data For Specimen A5 MCE Trial – Left Frame Section 2-4 Strain Gages (Left) and Right Frame Section 2-5 Strain Gages (Right)

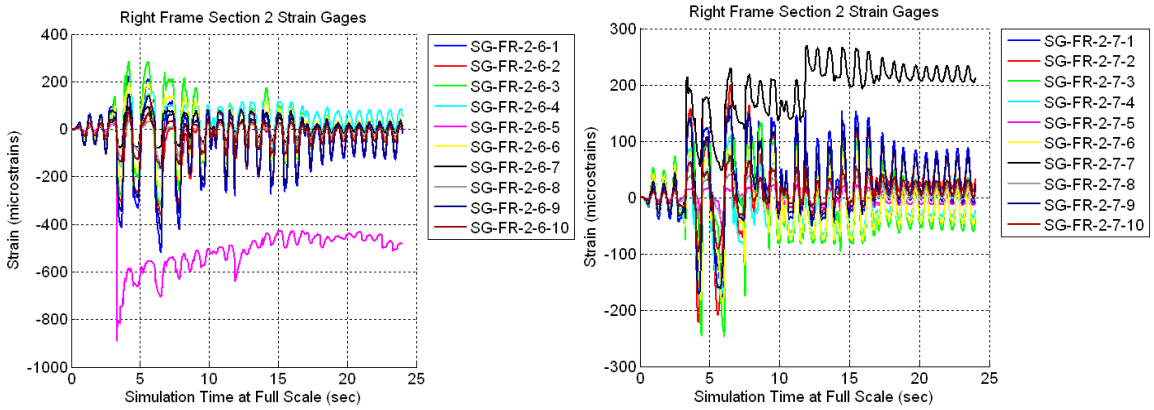

Figure B.185 Raw Data For Specimen A5 MCE Trial – Right Frame Section 2-6 Strain Gages (Left) and Right Frame Section 2-7 Strain Gages (Right)

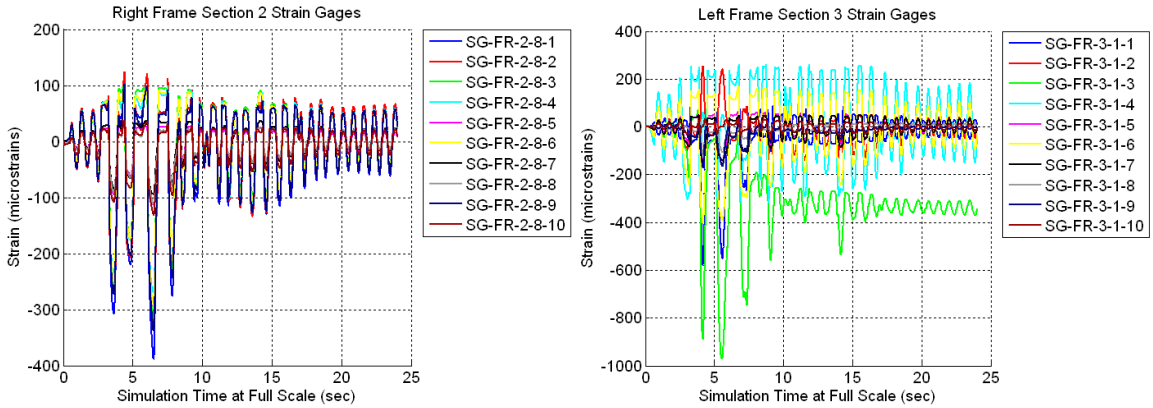

Figure B.186 Raw Data For Specimen A5 MCE Trial – Right Frame Section 2-8 Strain Gages (Left) and Left Frame Section 3-1 Strain Gages (Right)

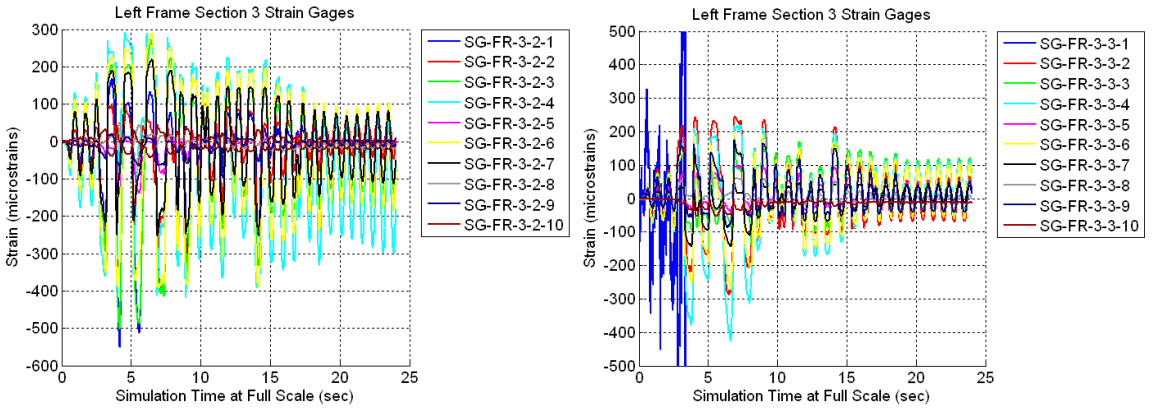

Figure B.187 Raw Data For Specimen A5 MCE Trial – Left Frame Section 3-2 Strain Gages (Left) and Left Frame Section 3-3 Strain Gages (Right)

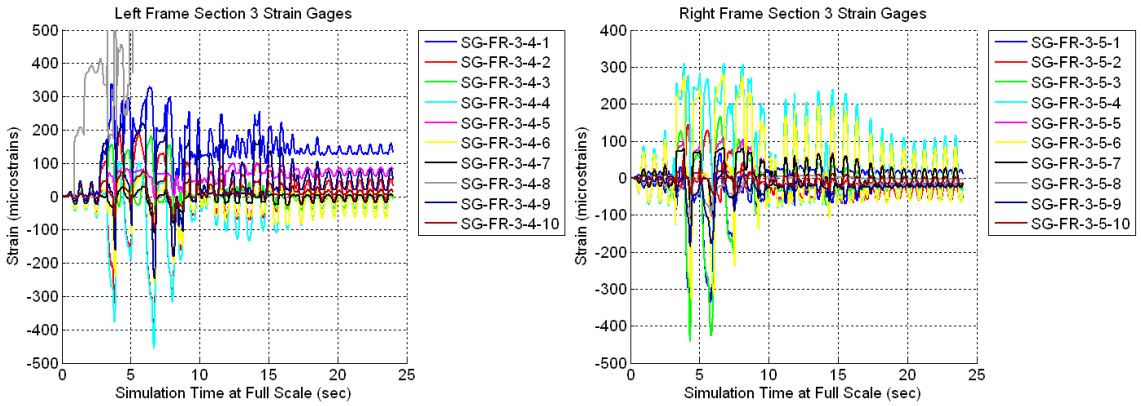

Figure B.188 Raw Data For Specimen A5 MCE Trial – Left Frame Section 3-4 Strain Gages (Left) and Right Frame Section 3-5 Strain Gages (Right)

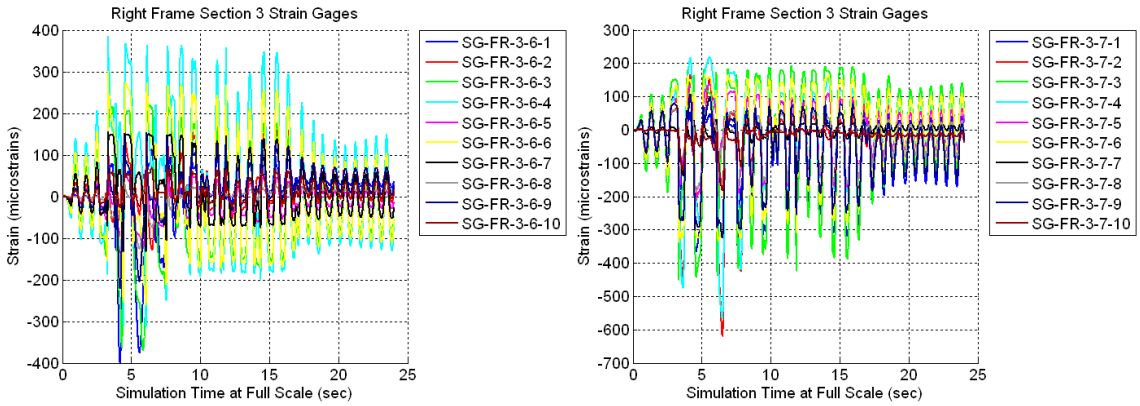

Figure B.189 Raw Data For Specimen A5 MCE Trial – Right Frame Section 3-6 Strain Gages (Left) and Right Frame Section 3-7 Strain Gages (Right)

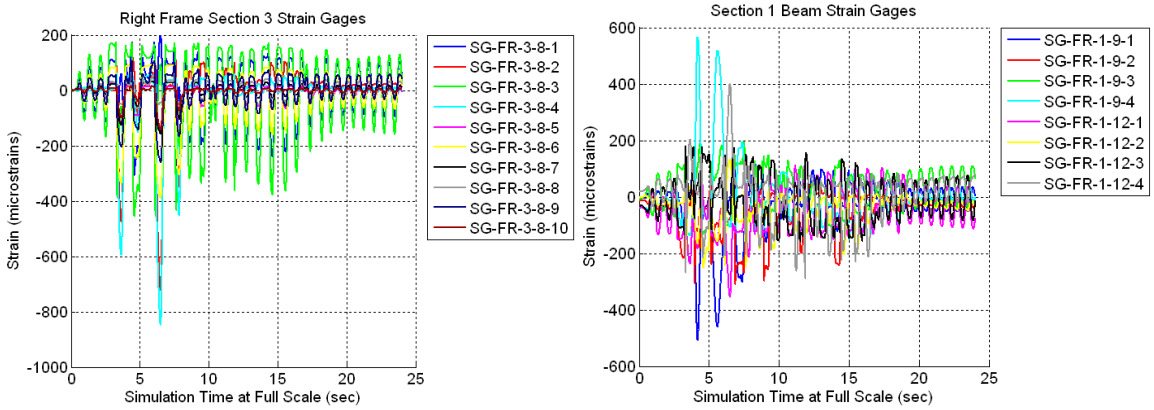

Figure B.190 Raw Data For Specimen A5 MCE Trial – Right Frame Section 3-8 Strain Gages (Left) and First Floor Beam Strain Gages (Right)

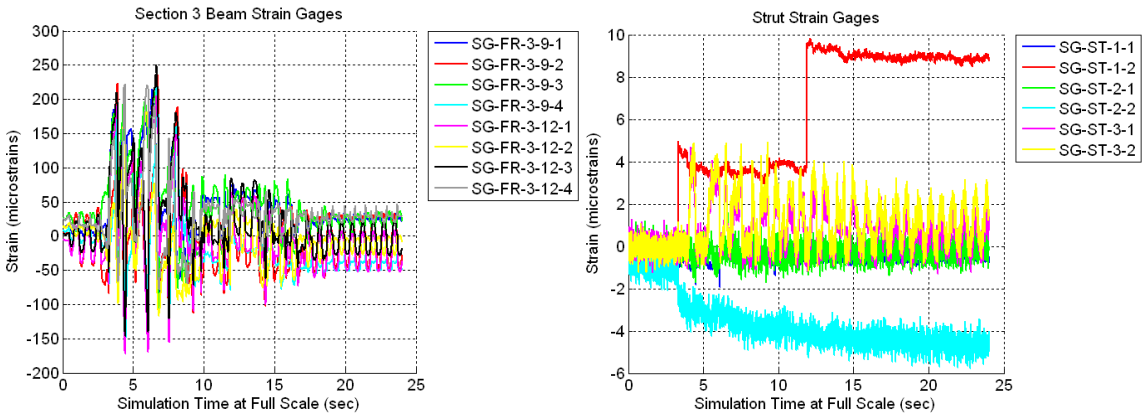

Figure B.191 Raw Data For Specimen A5 MCE Trial – Third Floor Beam Strain Gages (Left) and Strut Strain Gages (Right)

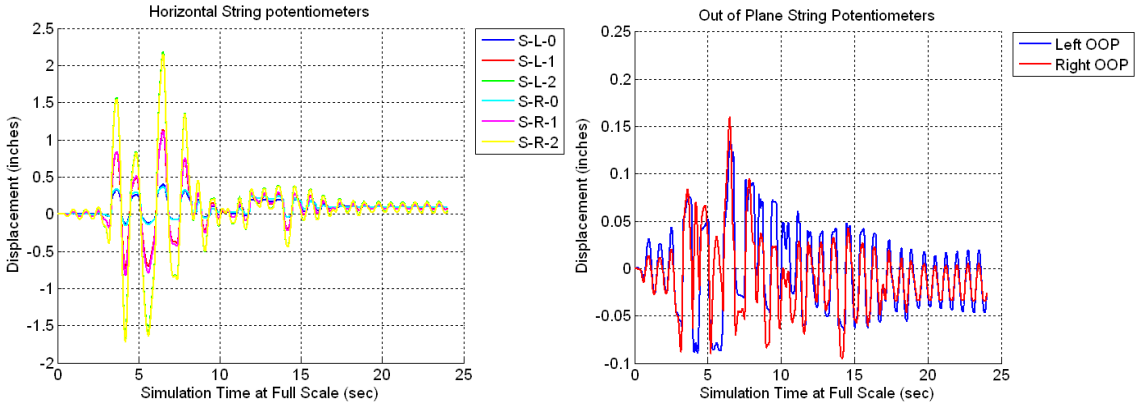

Figure B.192 Raw Data For Specimen A5 MCE Trial – Horizontal String Potentiometers (Left) and Out-of-Plane String Potentiometers (Right)

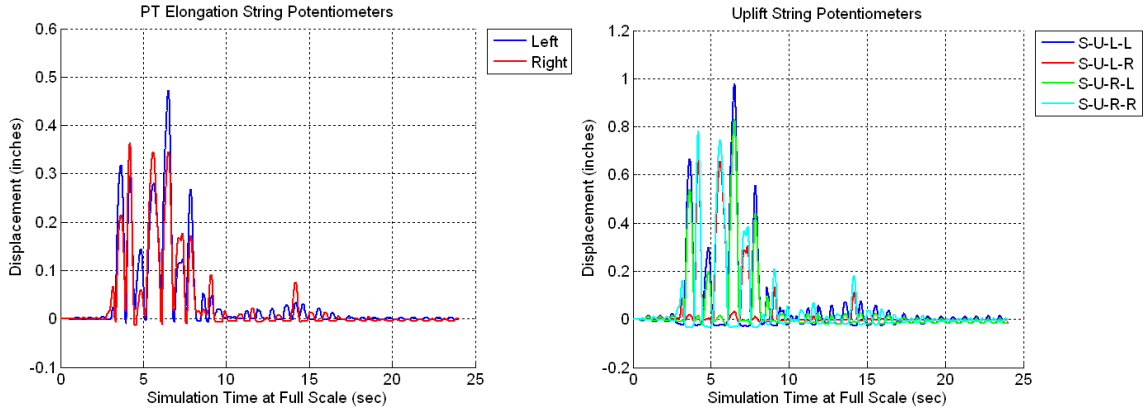

Figure B.193 Raw Data For Specimen A5 MCE Trial – PT Elongation String Potentiometers (Left) and Uplift String Potentiometers (Right)

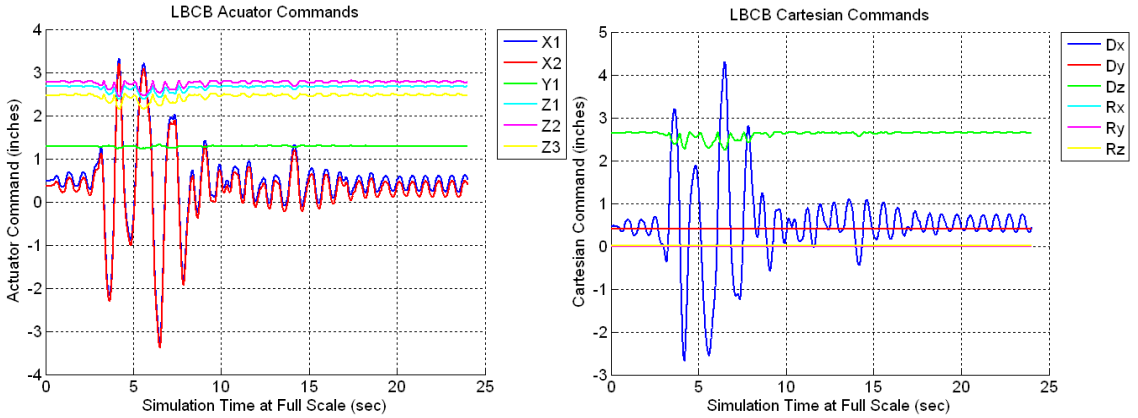

Figure B.194 Raw Data For Specimen A5 MCE Trial – LBCB Actuator Commands (Left) and LBCB Cartesian Commands (Right)

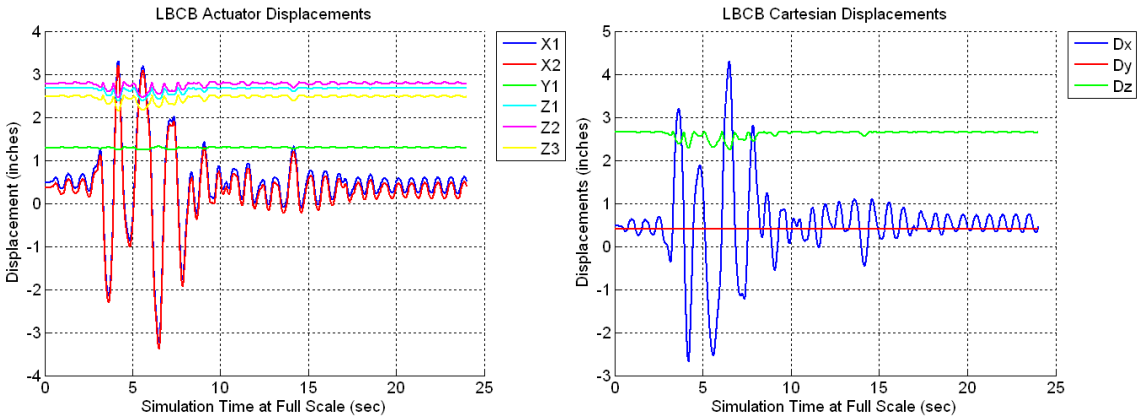

Figure B.195 Raw Data For Specimen A5 MCE Trial – LBCB Actuator Displacements (Left) and LBCB Cartesian Displacements (Right)

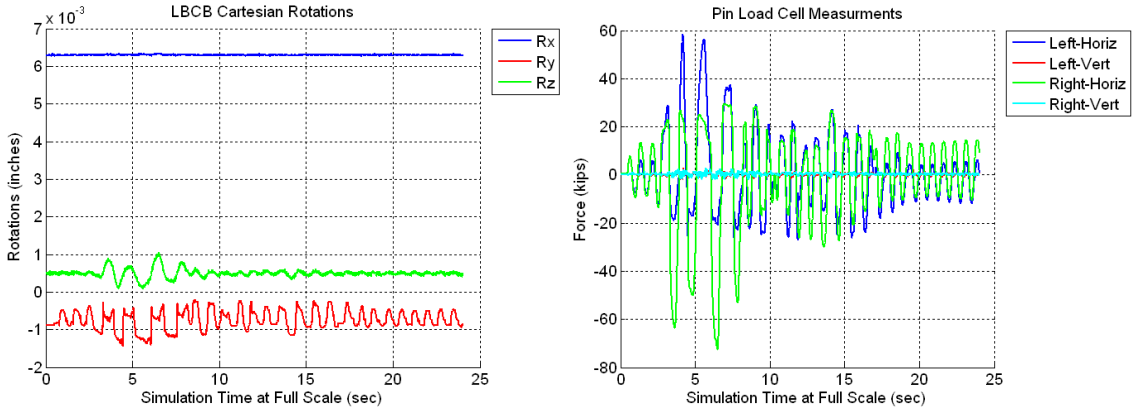

Figure B.196 Raw Data For Specimen A5 MCE Trial – LBCB Cartesian Rotations (Left) and Pin Load Cells (Right)

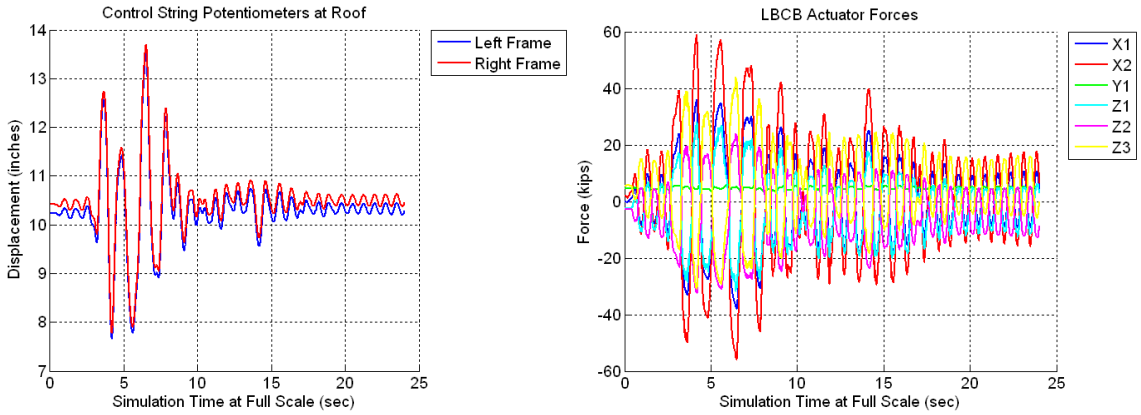

Figure B.197 Raw Data For Specimen A5 MCE Trial – Control Roof String Potentiometers (Left) and LBCB Actuator Forces (Right)

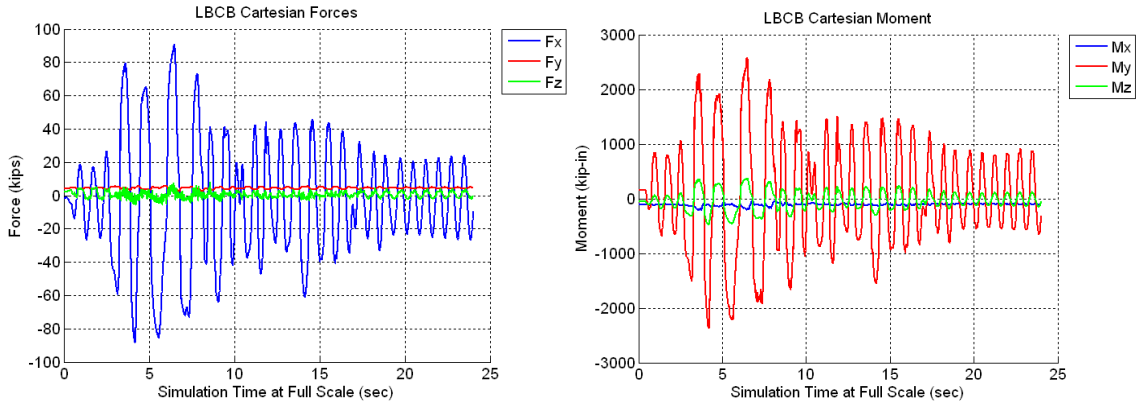

Figure B.198 Raw Data For Specimen A5 MCE Trial – LBCB Cartesian Forces (Left) and LBCB Cartesian Moments (Right)

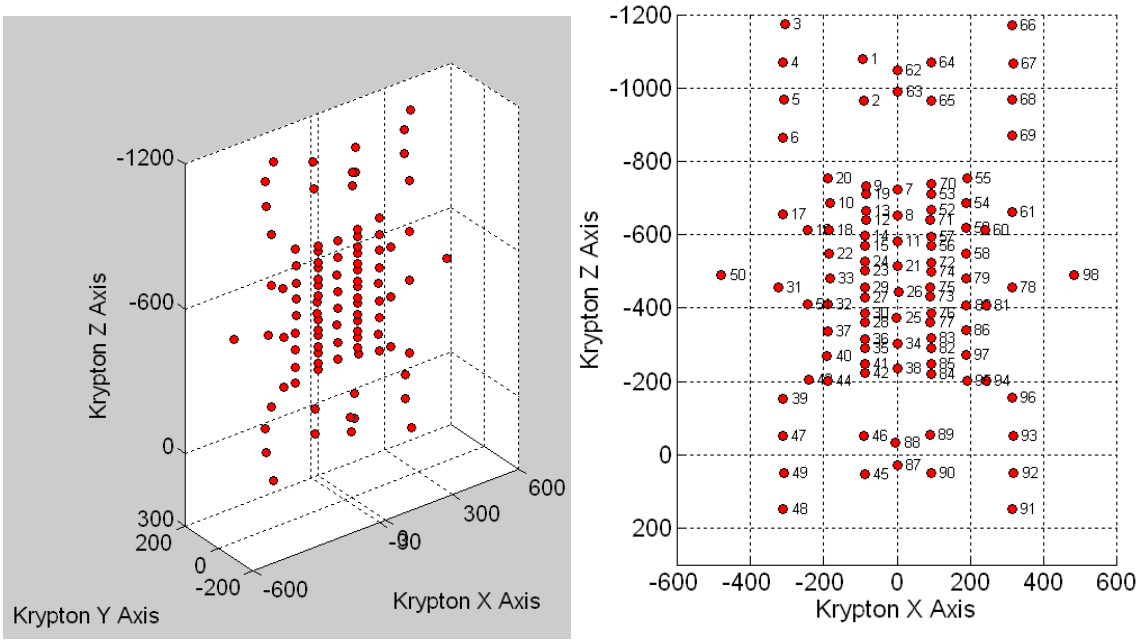

Figure B.199 Raw Data For Specimen A5 MCE Trial – Krypton LED Locations (Left) and Kyrpton LED Numbering (Right)

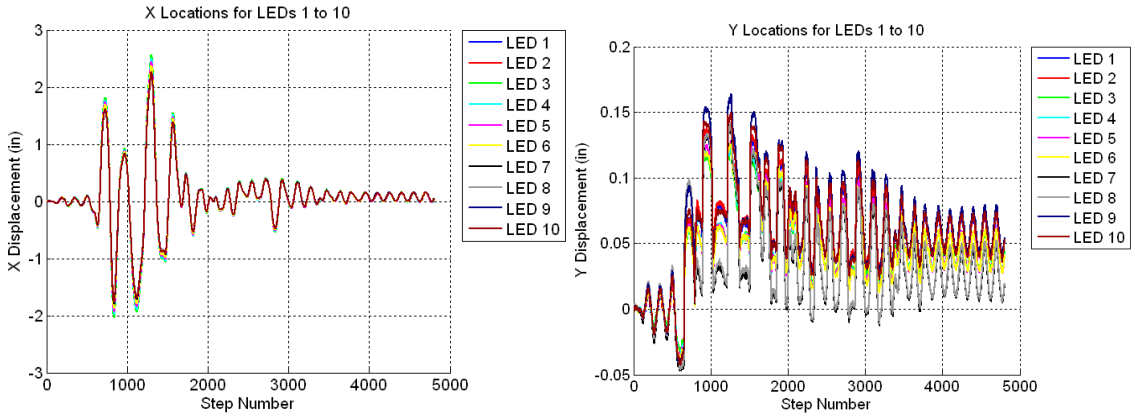

Figure B.200 Raw Data For Specimen A5 MCE Trial – X Displacements for LED's 1 to 10 (Left) and Y Displacements for LED's 1 to 10 (Right)

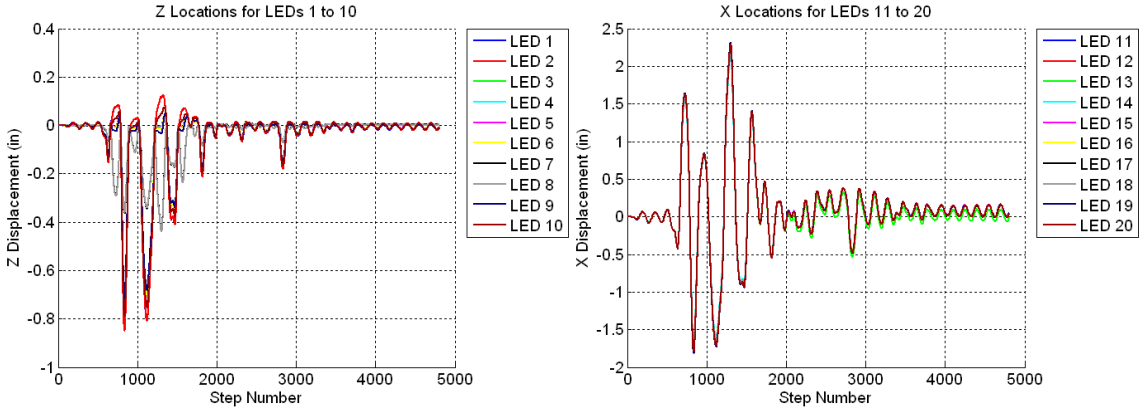

Figure B.201 Raw Data For Specimen A5 MCE Trial – Z Displacements for LED's 1 to 10 (Left) and X Displacements for LED's 11 to 20 (Right)

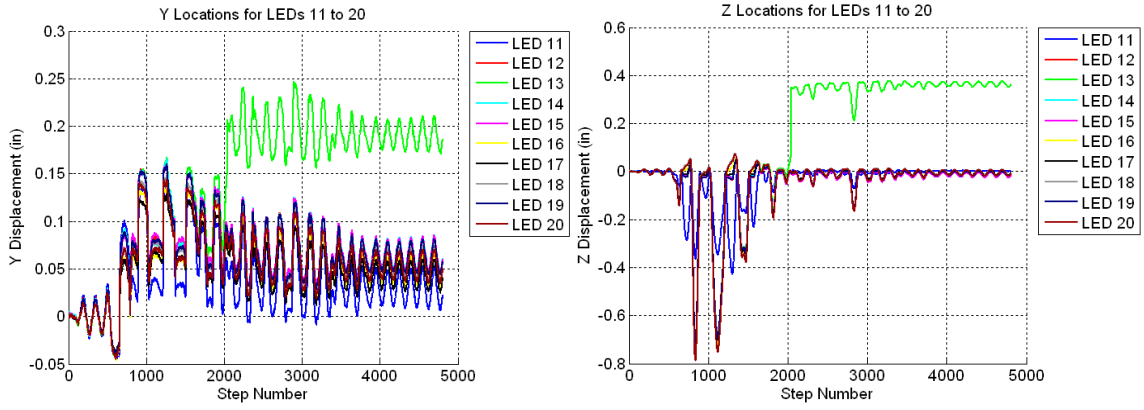

Figure B.202 Raw Data For Specimen A5 MCE Trial – Y Displacements for LED's 11 to 20 (Left) and Z Displacements for LED's 11 to 20 (Right)

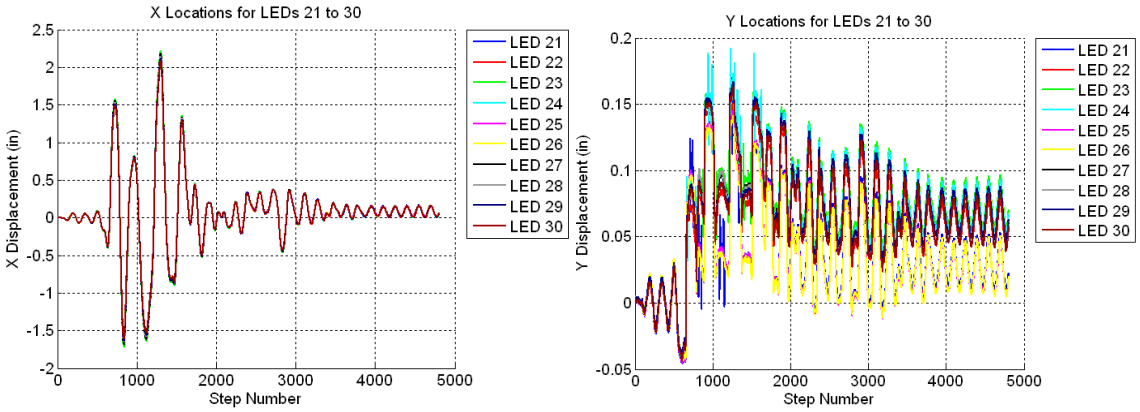

Figure B.203 Raw Data For Specimen A5 MCE Trial – X Displacements for LED's 21 to 30 (Left) and Y Displacements for LED's 21 to 30 (Right)

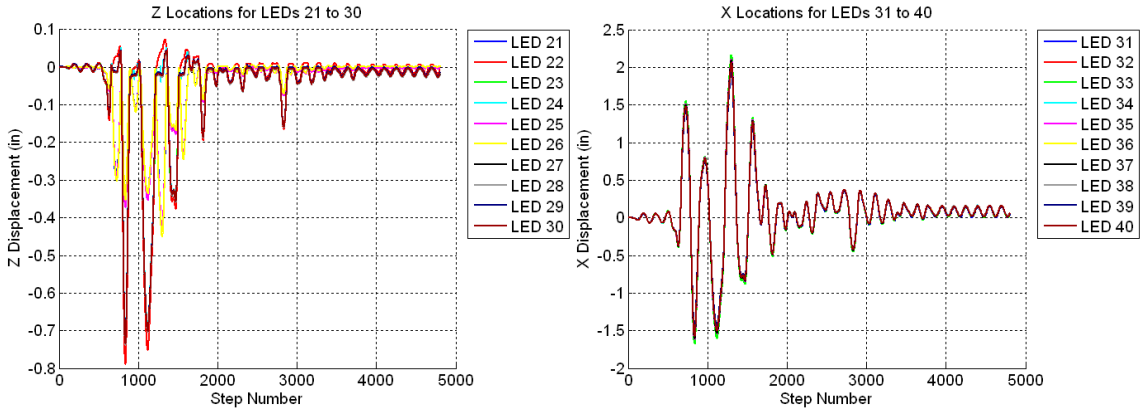

Figure B.204 Raw Data For Specimen A5 MCE Trial – Z Displacements for LED's 21 to 30 (Left) and X Displacements for LED's 31 to 40 (Right)

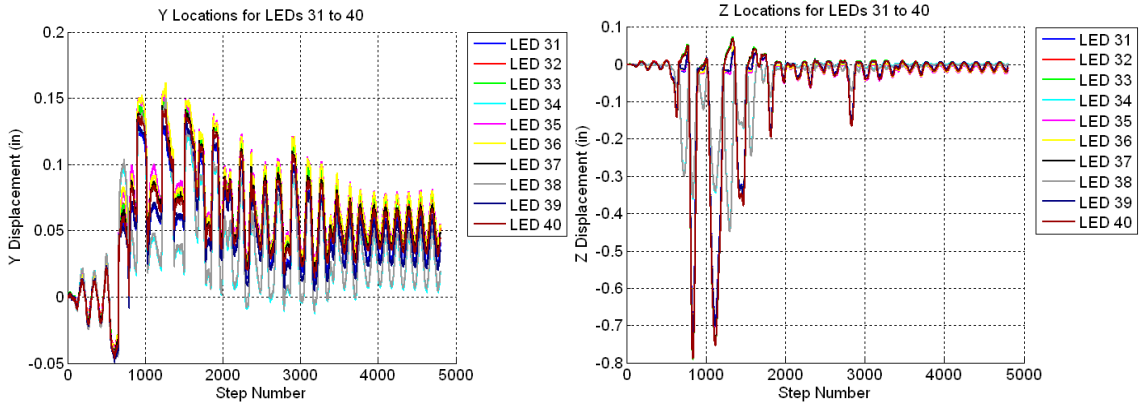

Figure B.205 Raw Data For Specimen A5 MCE Trial – Y Displacements for LED's 31 to 40 (Left) and Z Displacements for LED's 31 to 40 (Right)

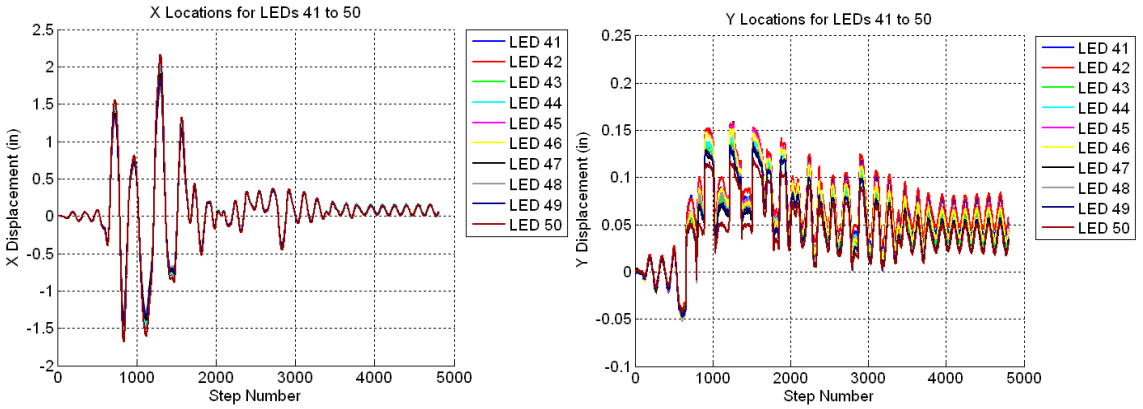

Figure B.206 Raw Data For Specimen A5 MCE Trial – X Displacements for LED's 41 to 50 (Left) and Y Displacements for LED's 41 to 50 (Right)

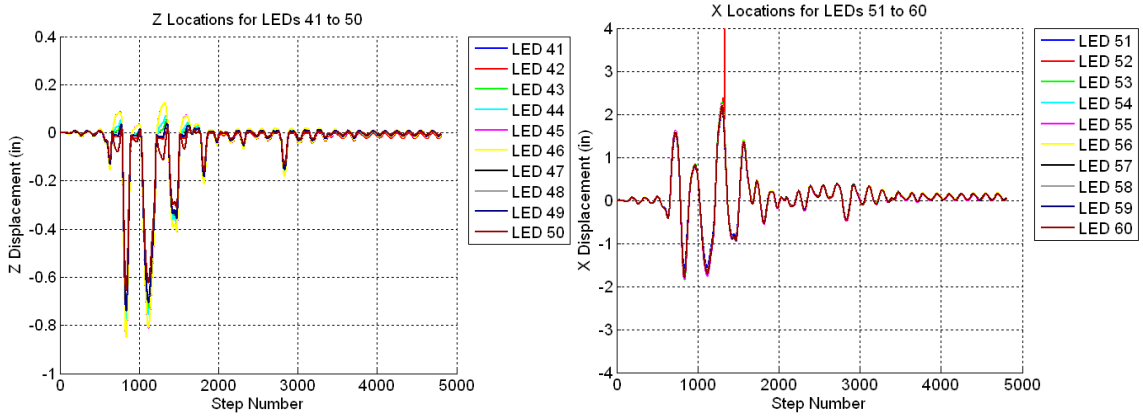

Figure B.207 Raw Data For Specimen A5 MCE Trial – Z Displacements for LED's 41 to 50 (Left) and X Displacements for LED's 51 to 60 (Right)

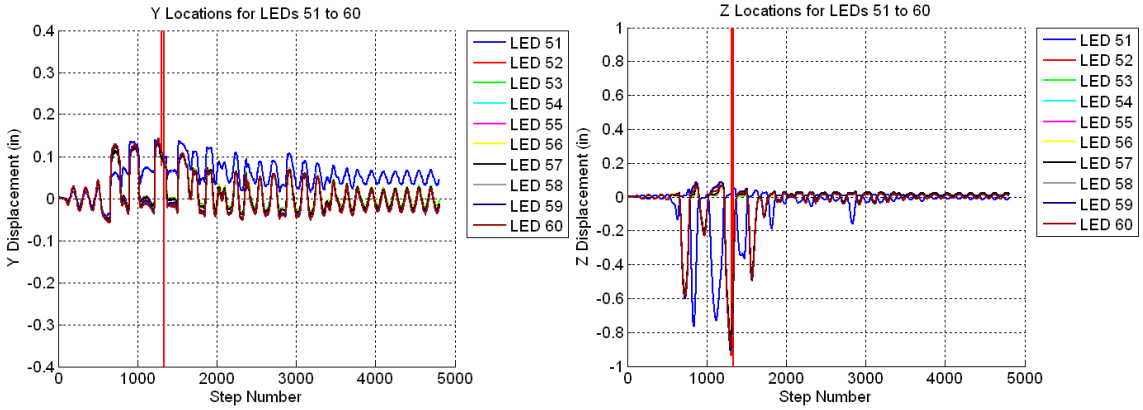

Figure B.208 Raw Data For Specimen A5 MCE Trial – Y Displacements for LED's 51 to 60 (Left) and Z Displacements for LED's 51 to 60 (Right)

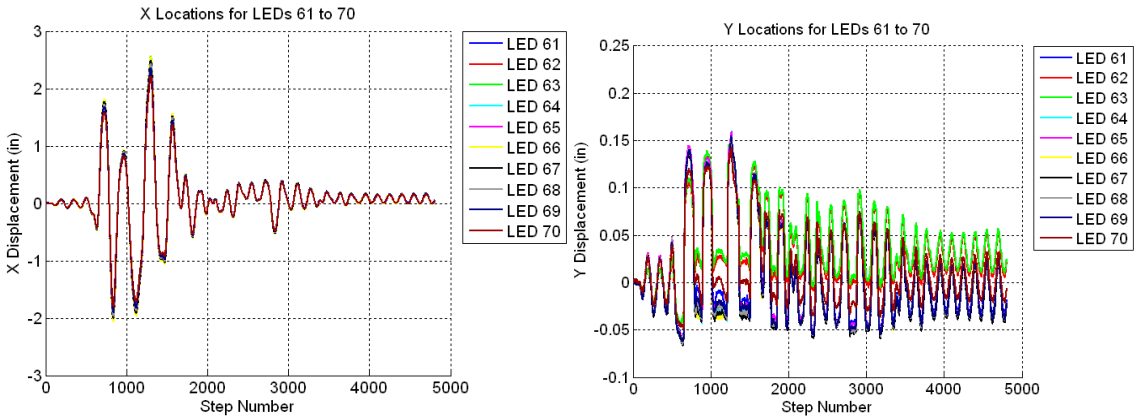

Figure B.209 Raw Data For Specimen A5 MCE Trial – X Displacements for LED's 61 to 70 (Left) and Y Displacements for LED's 61 to 70 (Right)

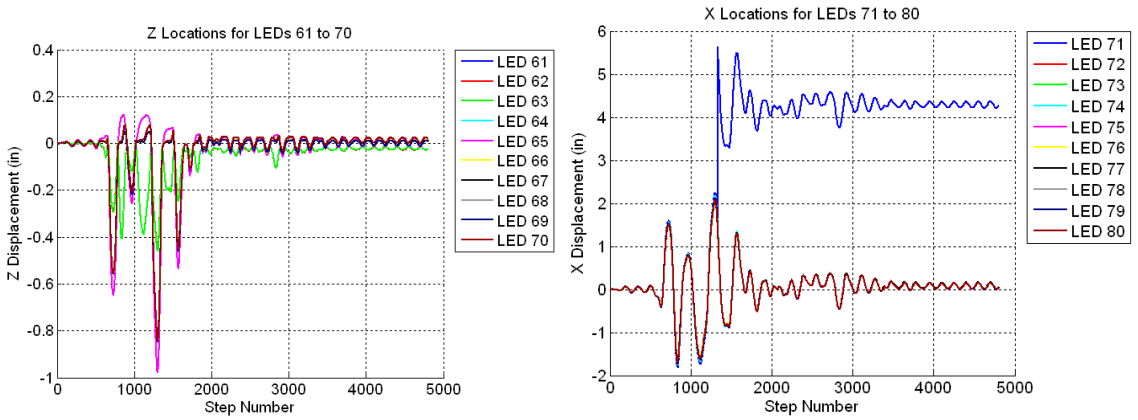

Figure B.210 Raw Data For Specimen A5 MCE Trial – Z Displacements for LEDs 61 to 70 (Left) and X Displacements for LED's 71 to 80 (Right)

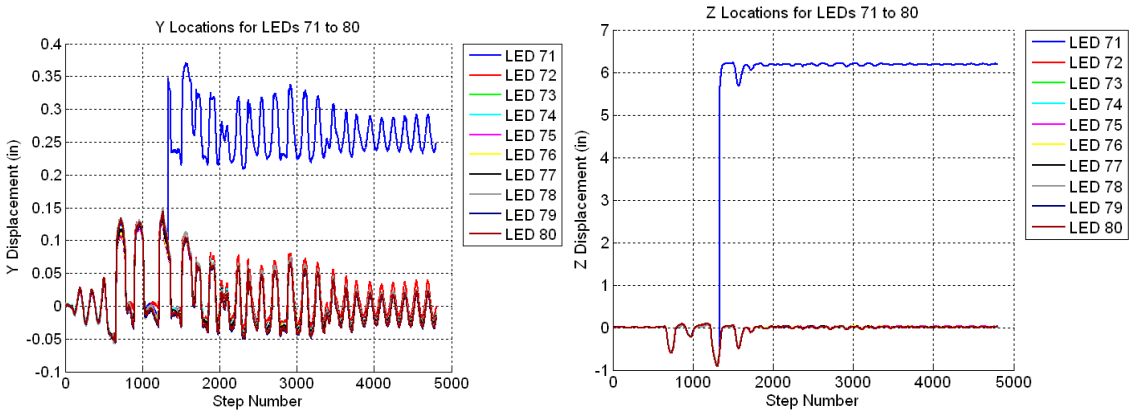

Figure B.211 Raw Data For Specimen A5 MCE Trial – Y Displacements for LED's 71 to 80 (Left) and Z Displacements for LED's 71 to 80 (Right)

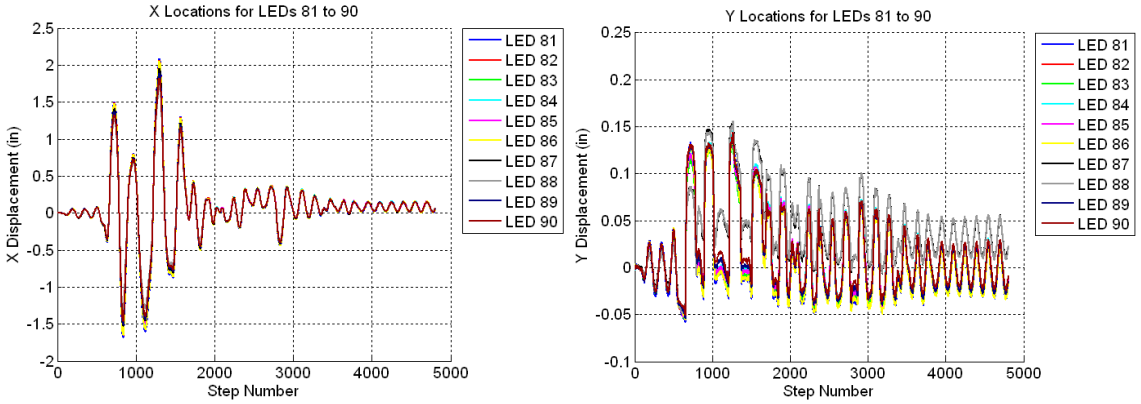

Figure B.212 Raw Data For Specimen A5 MCE Trial – X Displacements for LED's 81 to 90 (Left) and Y Displacements for LED's 81 to 90 (Right)

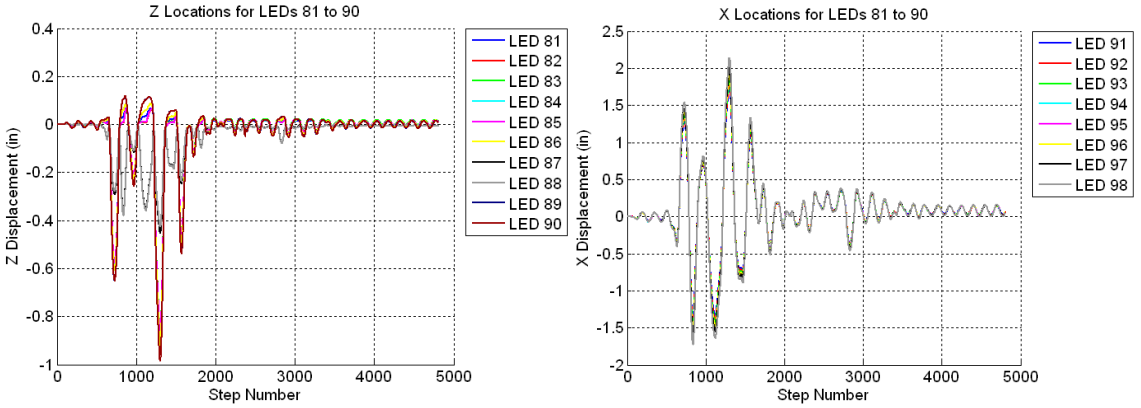

Figure B.213 Raw Data For Specimen A5 MCE Trial – Z Displacements for LED's 81 to 90 (Left) and X Displacements for LED's 91 to 98 (Right)

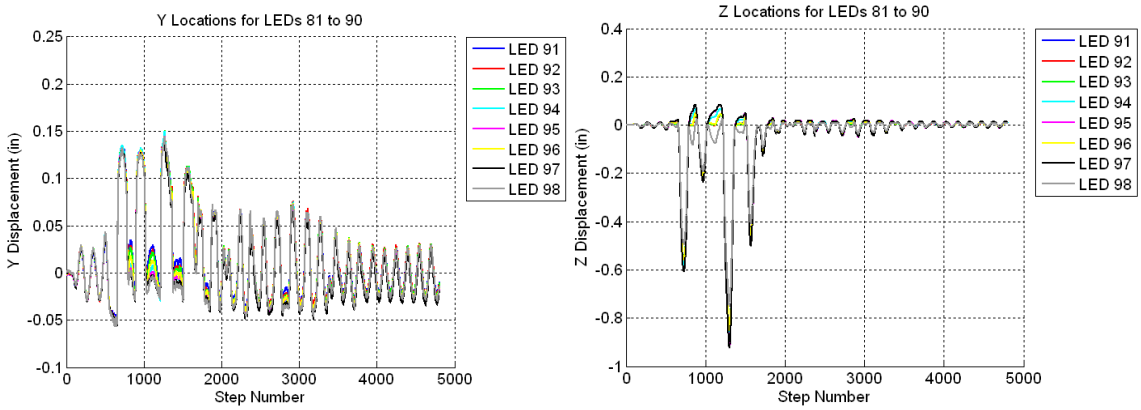

Figure B.214 Raw Data For Specimen A5 MCE Trial – Y Displacements for LED's 91 to 98 (Left) and Z Displacements for LED's 91 to 98 (Right)

B.6 Specimen A5 – 1.10xJMA Kobe Trial 1

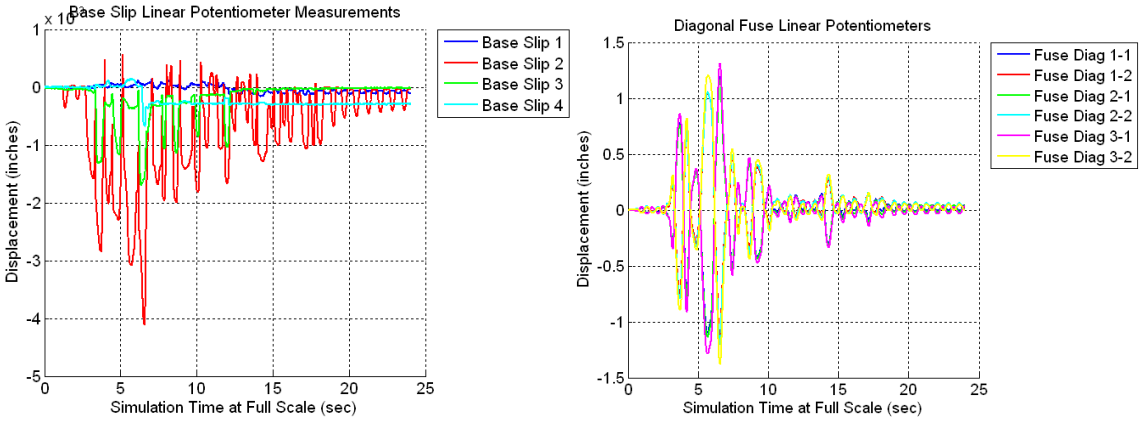

Figure B.215 Raw Data For Specimen A5 1.10xJMA Kobe Trial 1 – Base Slip (Left) and Fuse Linear Potentiometers (Right)

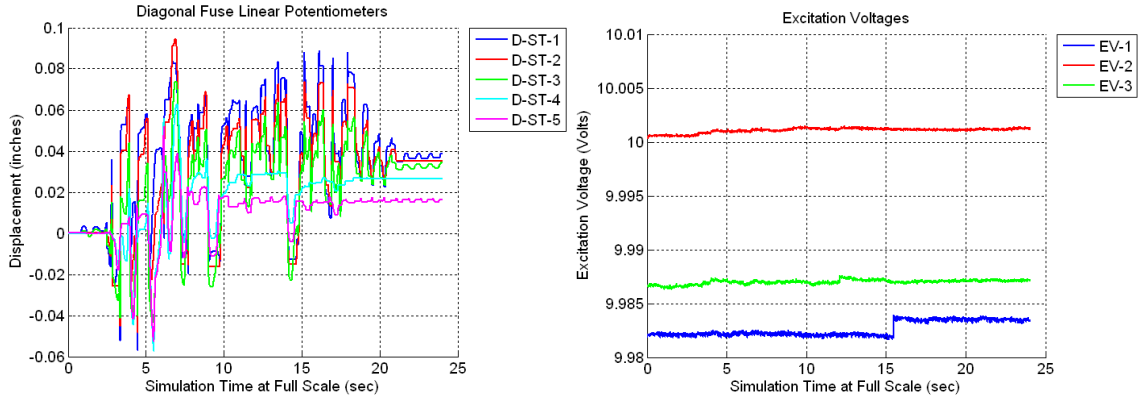

Figure B.216 Raw Data For Specimen A5 1.10xJMA Kobe Trial 1 – Strut Linear Potentiometers (Left) and Excitation Voltage (Right)

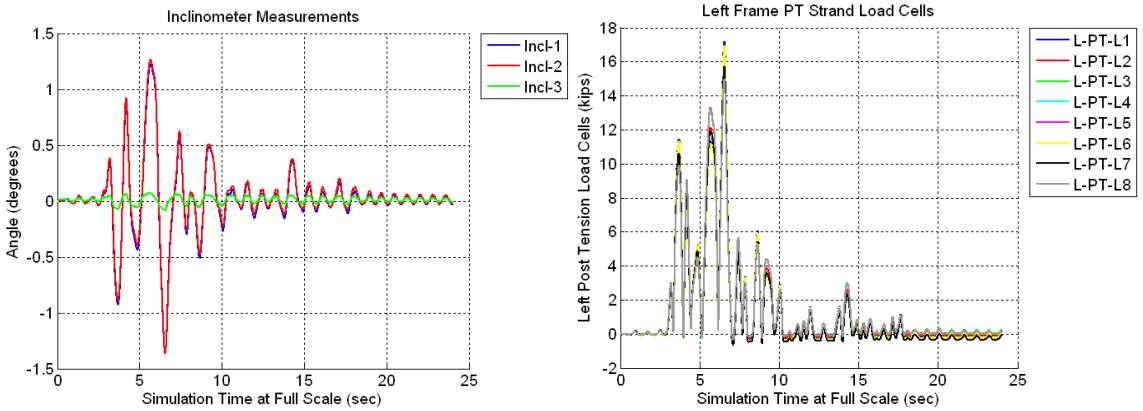

Figure B.217 Raw Data For Specimen A5 1.10xJMA Kobe Trial 1 – Inclinometers (Left) and Left Frame PT Load Cells (Right)

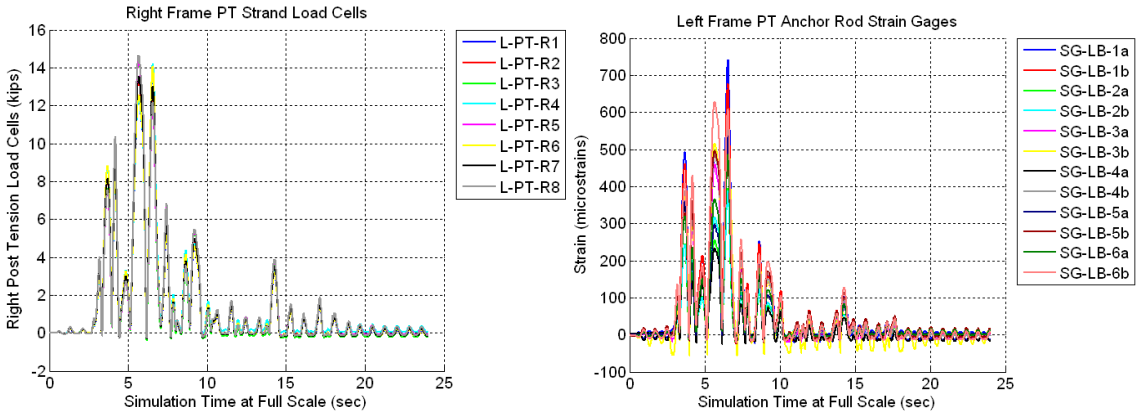

Figure B.218 Raw Data For Specimen A5 1.10xJMA Kobe Trial 1 – Right Frame PT Load Cells (Left) and Left Frame Anchor Rods (Right)

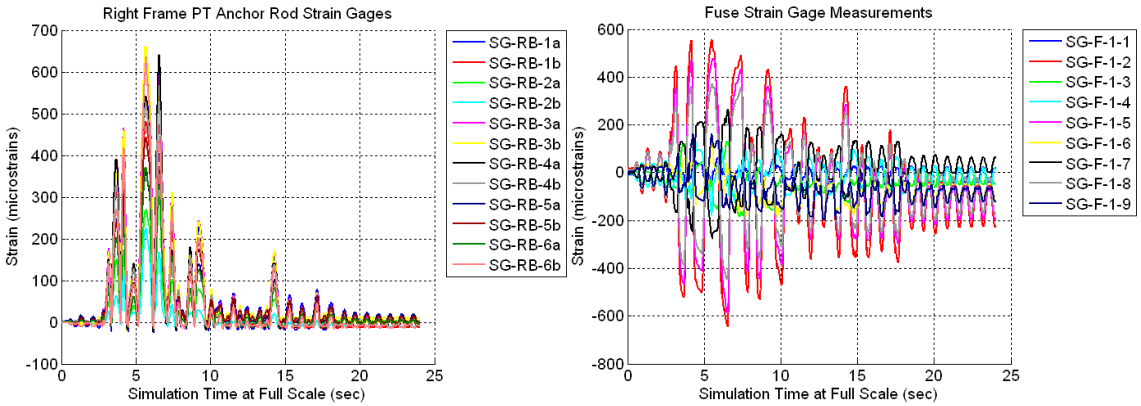

Figure B.219 Raw Data For Specimen A5 1.10xJMA Kobe Trial 1 – Right Frame Anchor Rods (Left) and Back Fuse Strain Gages (Right)

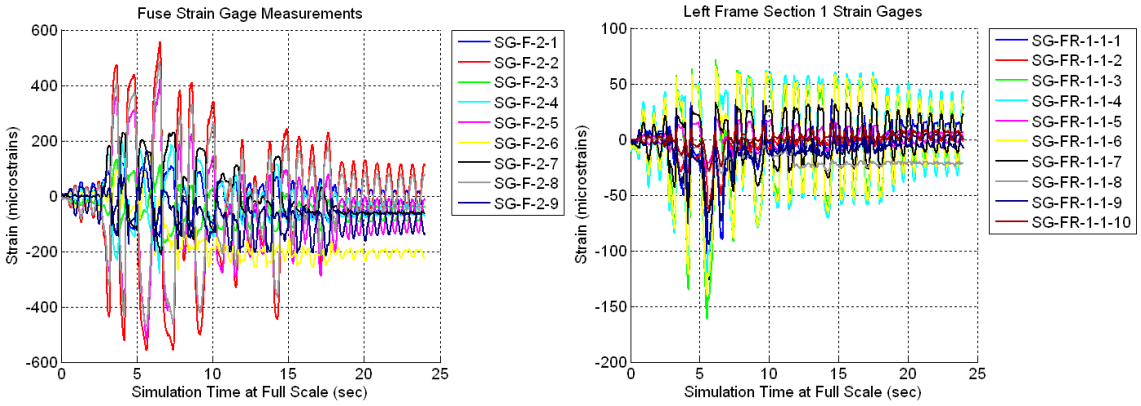

Figure B.220 Raw Data For Specimen A5 1.10xJMA Kobe Trial 1 – Front Fuse Strain Gages (Left) and Left Frame Section 1-1 Strain Gages (Right)

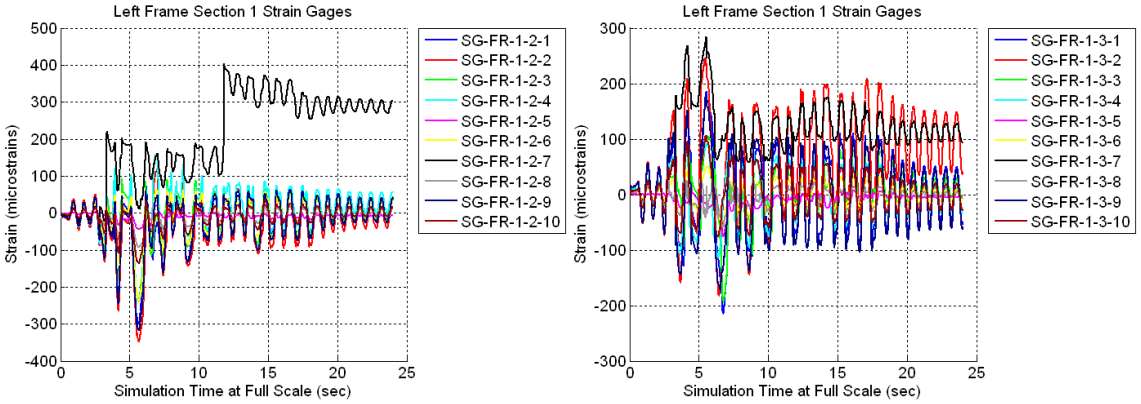

Figure B.221 Raw Data For Specimen A5 1.10xJMA Kobe Trial 1 – Left Frame Section 1-2 Strain Gages (Left) and Left Frame Section 1-3 Strain Gages (Right)

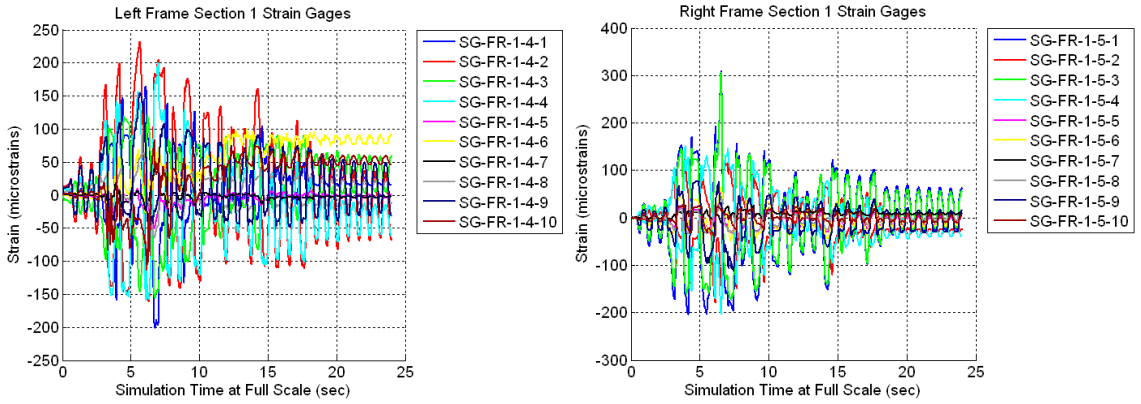

Figure B.222 Raw Data For Specimen A5 1.10xJMA Kobe Trial 1 – Left Frame Section 1-4 Strain Gages (Left) and Right Frame Section 1-5 Strain Gages (Right)

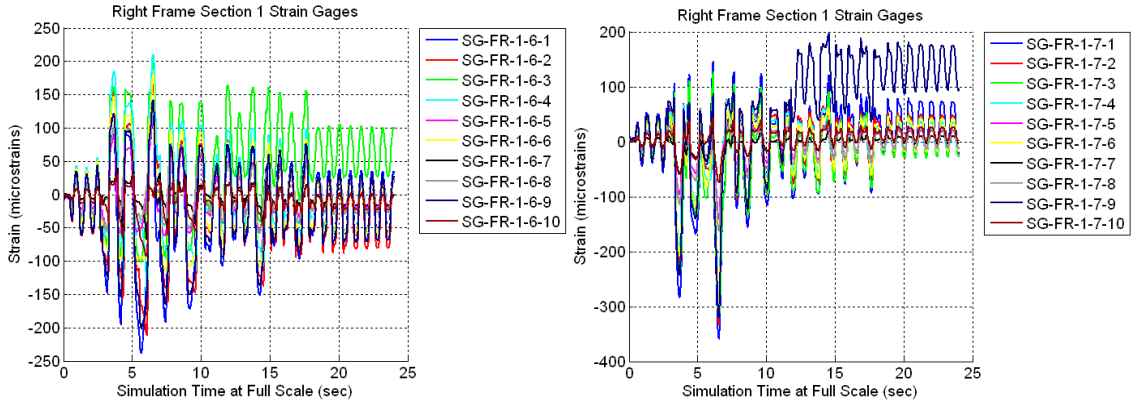

Figure B.223 Raw Data For Specimen A5 1.10xJMA Kobe Trial 1 – Right Frame Section 1-6 Strain Gages (Left) and Right Frame Section 1-7 Strain Gages (Right)

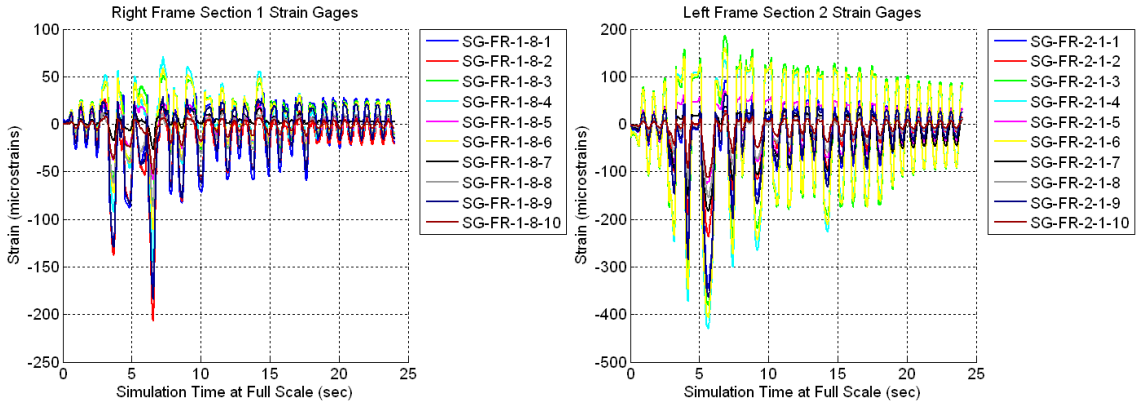

Figure B.224 Raw Data For Specimen A5 1.10xJMA Kobe Trial 1 – Right Frame Section 1-8 Strain Gages (Left) and Left Frame Section 2-1 Strain Gages (Right)

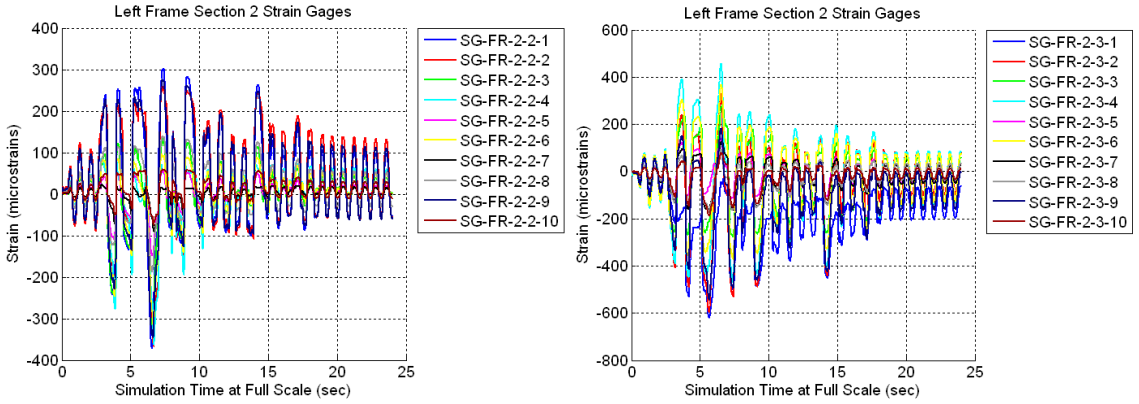

Figure B.225 Raw Data For Specimen A5 1.10xJMA Kobe Trial 1 – Left Frame Section 2-2 Strain Gages (Left) and Left Frame Section 2-3 Strain Gages (Right)

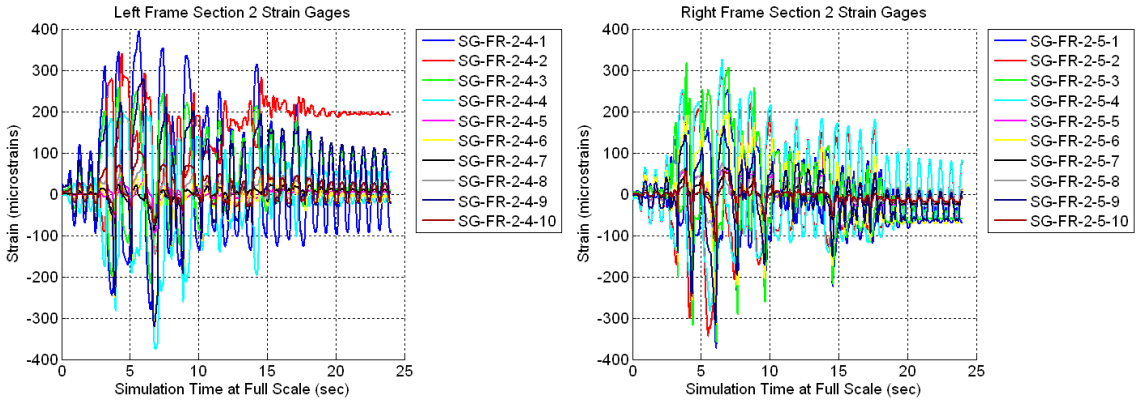

Figure B.226 Raw Data For Specimen A5 1.10xJMA Kobe Trial 1 – Left Frame Section 2-4 Strain Gages (Left) and Right Frame Section 2-5 Strain Gages (Right)

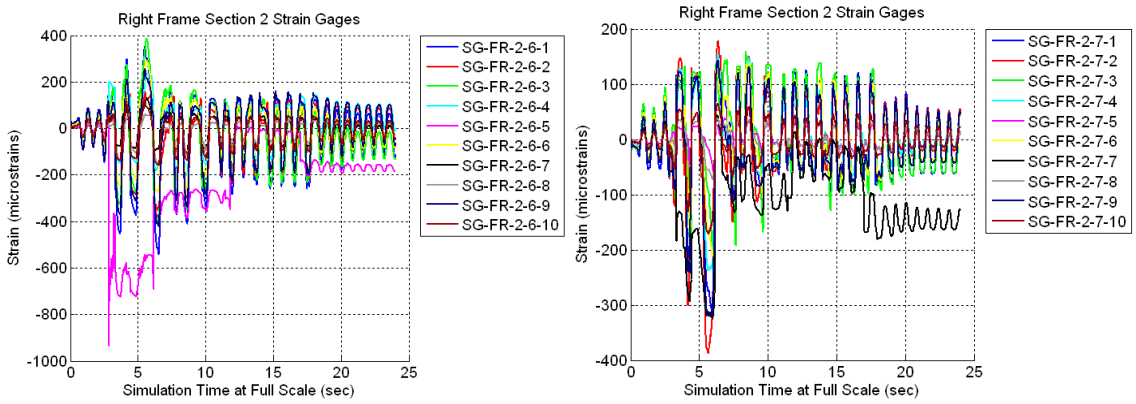

Figure B.227 Raw Data For Specimen A5 1.10xJMA Kobe Trial 1 – Right Frame Section 2-6 Strain Gages (Left) and Right Frame Section 2-7 Strain Gages (Right)

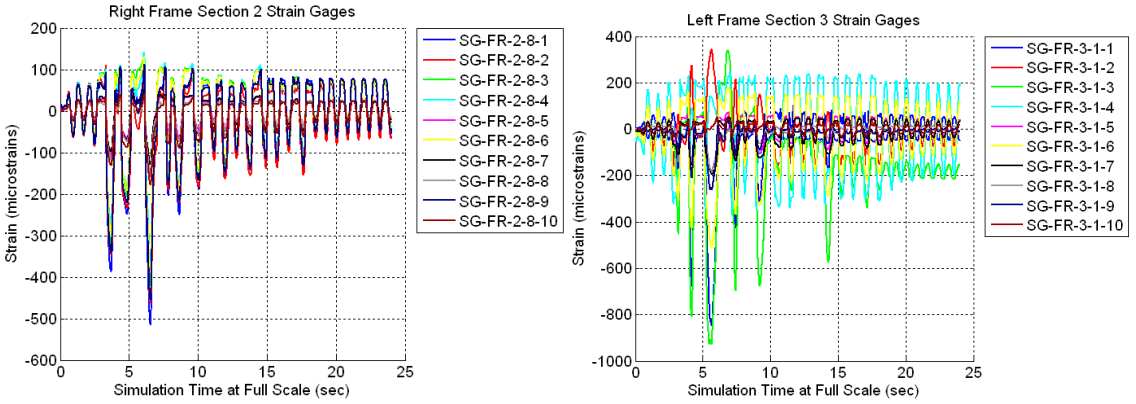

Figure B.228 Raw Data For Specimen A5 1.10xJMA Kobe Trial 1 – Right Frame Section 2-8 Strain Gages (Left) and Left Frame Section 3-1 Strain Gages (Right)

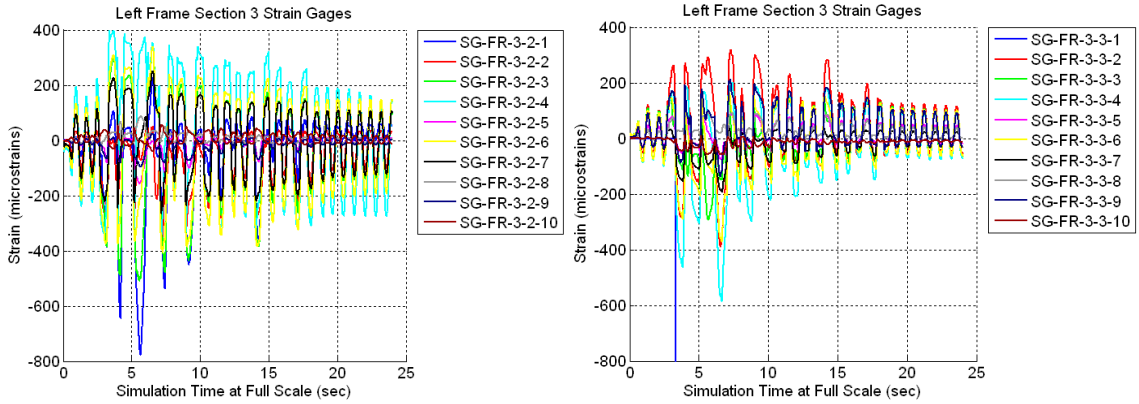

Figure B.229 Raw Data For Specimen A5 1.10xJMA Kobe Trial 1 – Left Frame Section 3-2 Strain Gages (Left) and Left Frame Section 3-3 Strain Gages (Right)

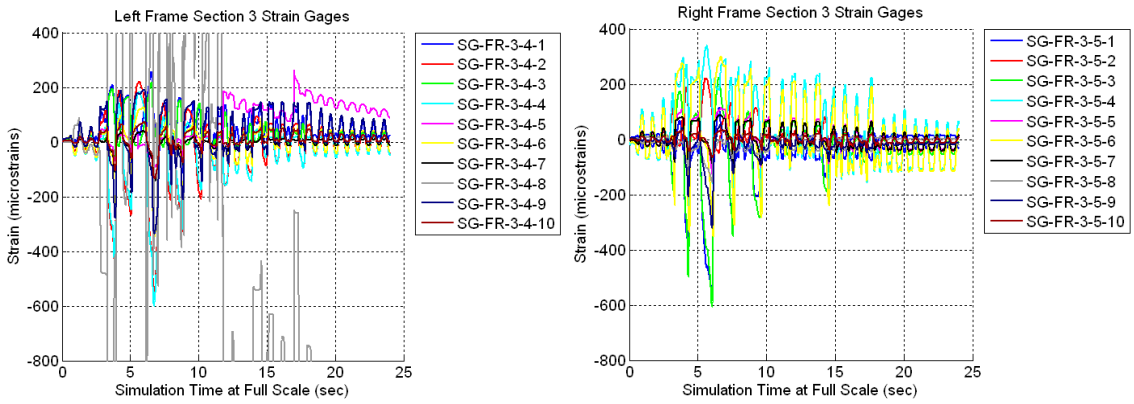

Figure B.230 Raw Data For Specimen A5 1.10xJMA Kobe Trial 1 – Left Frame Section 3-4 Strain Gages (Left) and Right Frame Section 3-5 Strain Gages (Right)

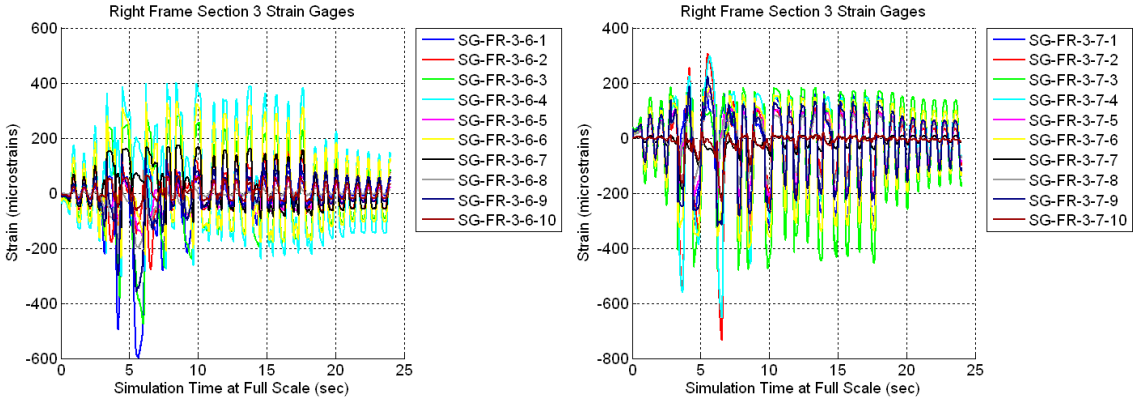

Figure B.231 Raw Data For Specimen A5 1.10xJMA Kobe Trial 1 – Right Frame Section 3-6 Strain Gages (Left) and Right Frame Section 3-7 Strain Gages (Right)

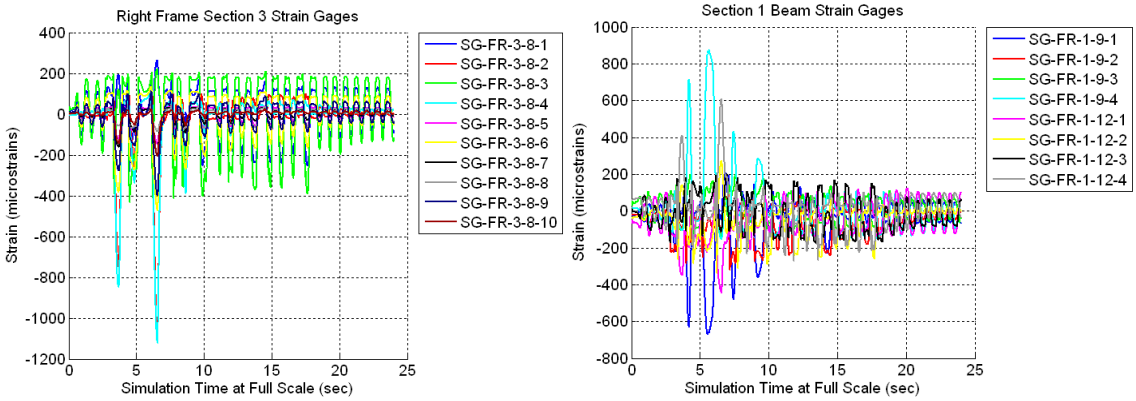

Figure B.232 Raw Data For Specimen A5 1.10xJMA Kobe Trial 1 – Right Frame Section 3-8 Strain Gages (Left) and First Floor Beam Strain Gages (Right)

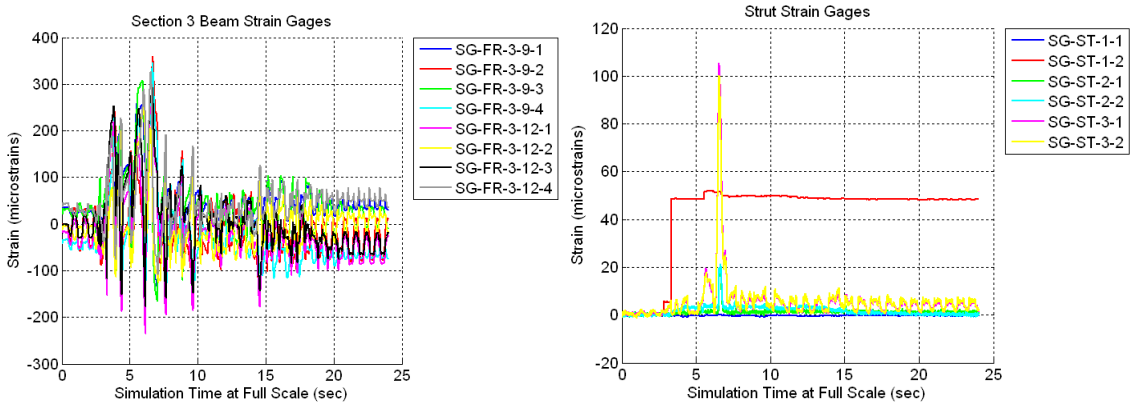

Figure B.233 Raw Data For Specimen A5 1.10xJMA Kobe Trial 1 – Third Floor Beam Strain Gages (Left) and Strut Strain Gages (Right)

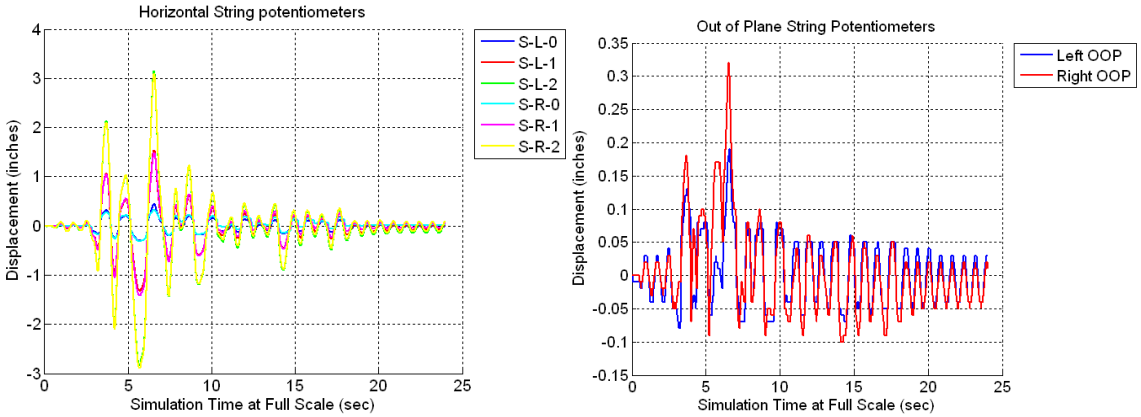

Figure B.234 Raw Data For Specimen A5 1.10xJMA Kobe Trial 1 – Horizontal String Potentiometers (Left) and Out-of-Plane String Potentiometers (Right)

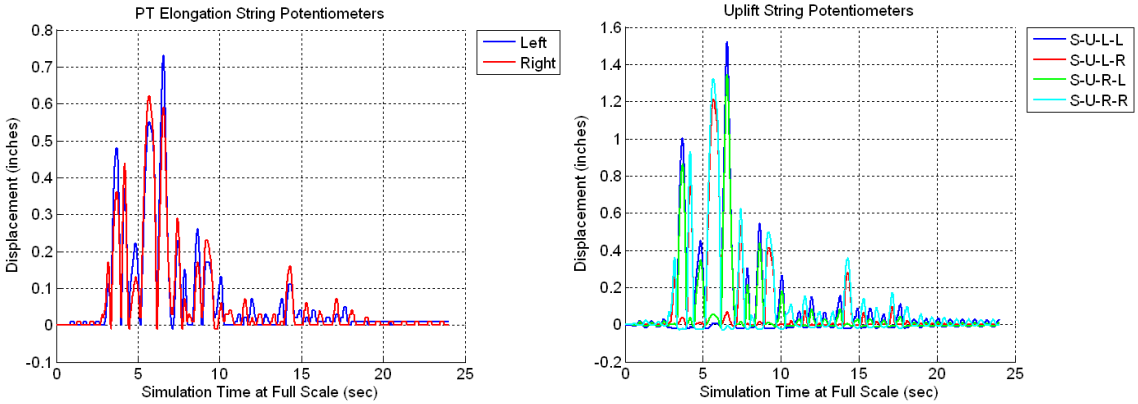

Figure B.235 Raw Data For Specimen A5 1.10xJMA Kobe Trial 1 – PT Elongation String Potentiometers (Left) and Uplift String Potentiometers (Right)

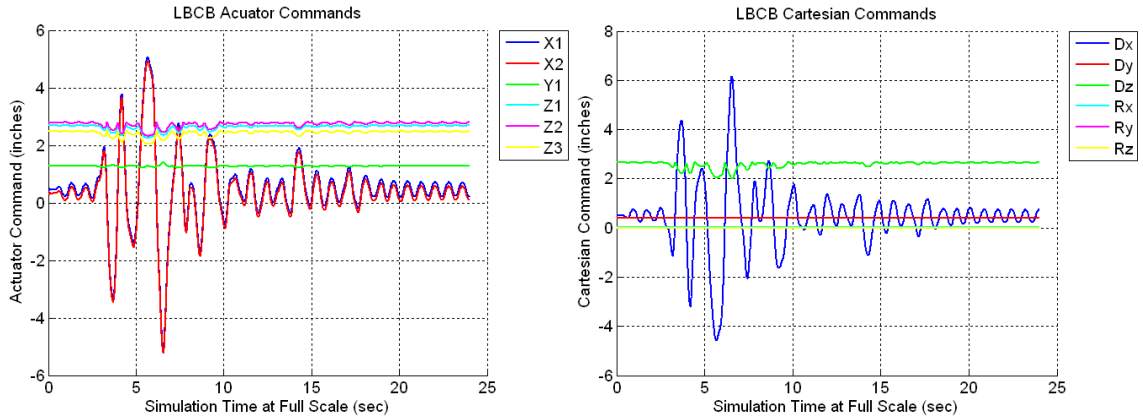

Figure B.236 Raw Data For Specimen A5 1.10xJMA Kobe Trial 1 – LBCB Actuator Commands (Left) and LBCB Cartesian Commands (Right)

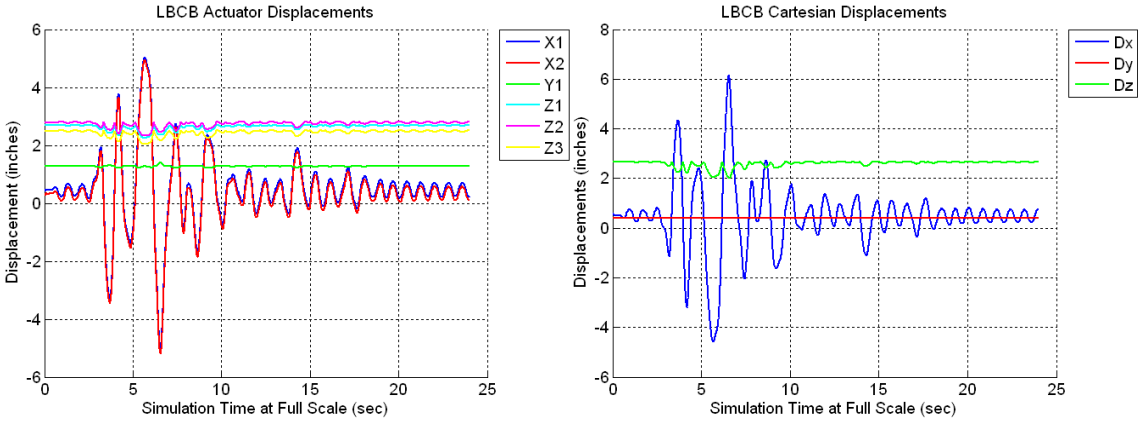

Figure B.237 Raw Data For Specimen A5 1.10xJMA Kobe Trial 1 – LBCB Actuator Displacements (Left) and LBCB Cartesian Displacements (Right)

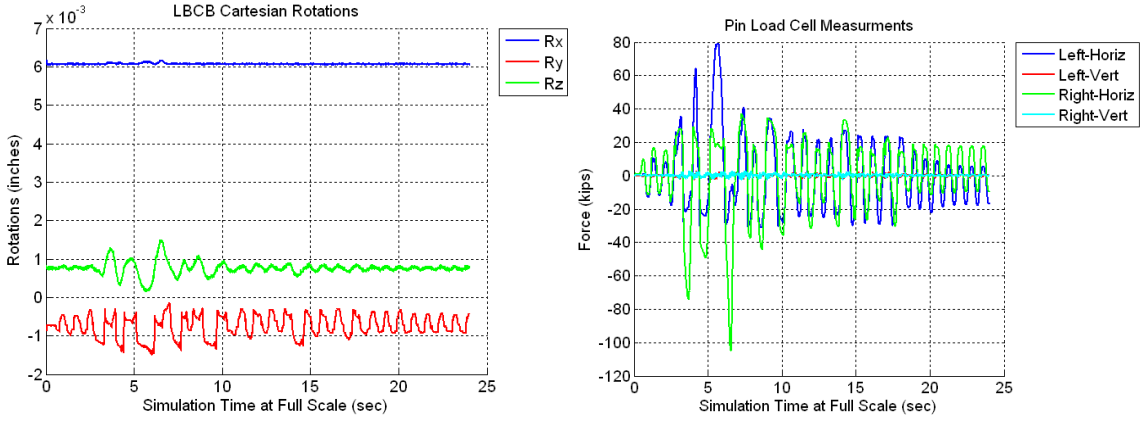

Figure B.238 Raw Data For Specimen A5 1.10xJMA Kobe Trial 1 – LBCB Cartesian Rotations (Left) and Pin Load Cells (Right)

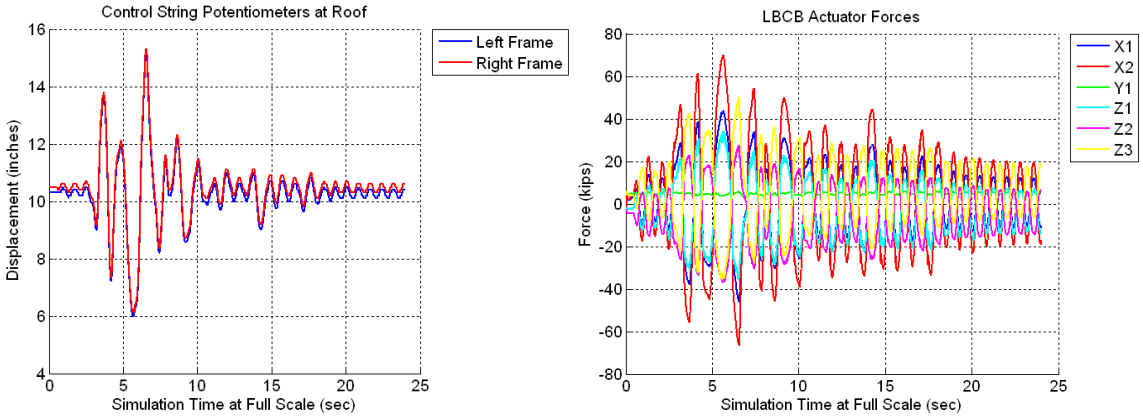

Figure B.239 Raw Data For Specimen A5 1.10xJMA Kobe Trial 1 – Control Roof String Potentiometers (Left) and LBCB Actuator Forces (Right)

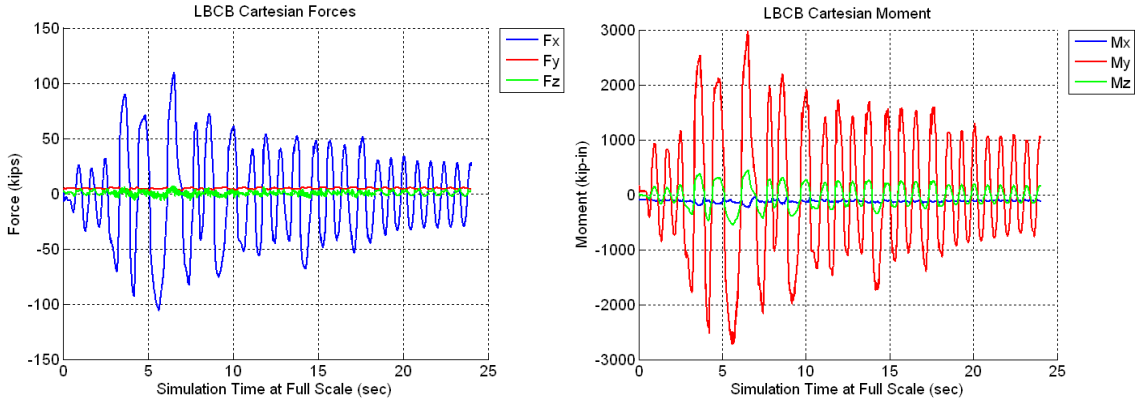

Figure B.240 Raw Data For Specimen A5 1.10xJMA Kobe Trial 1 – LBCB Cartesian Forces (Left) and LBCB Cartesian Moments (Right)

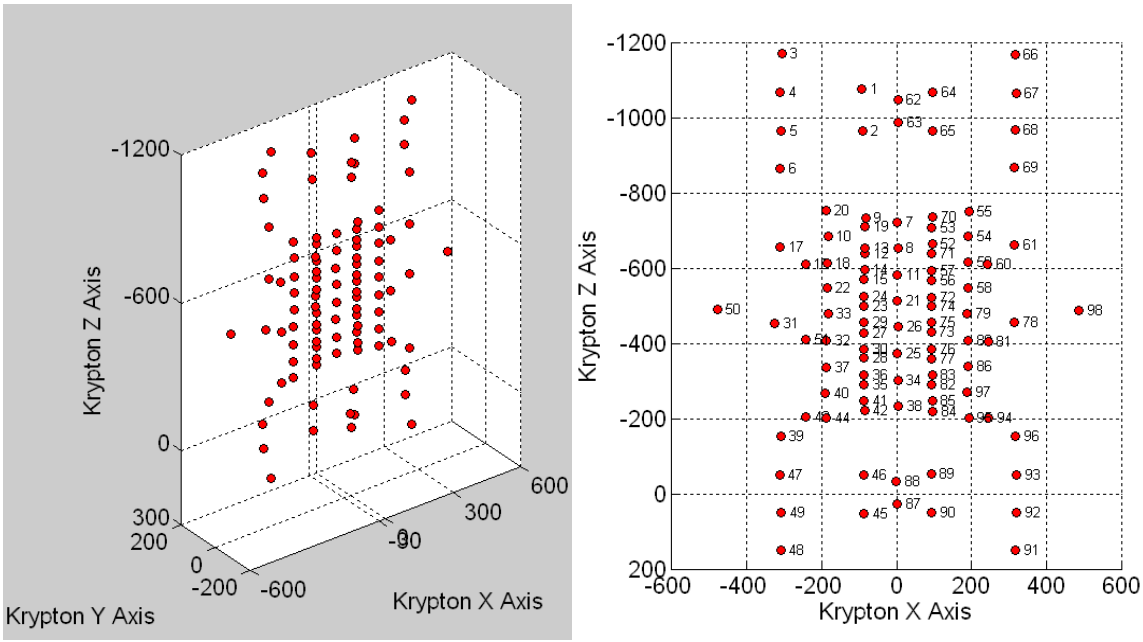

Figure B.241 Raw Data For Specimen A5 1.10xJMA Kobe Trial 1 – Krypton LED Locations (Left) and Krypton LED Numbering (Right)

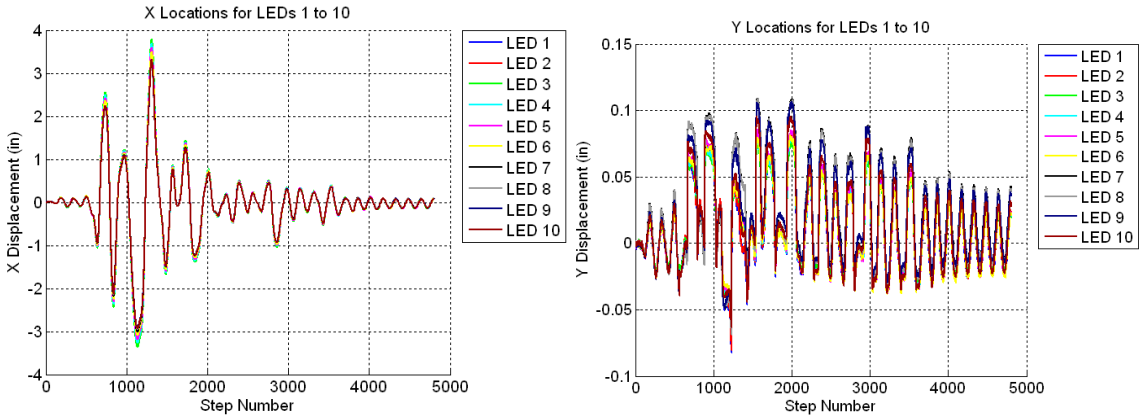

Figure B.242 Raw Data For Specimen A5 1.10xJMA Kobe Trial 1 – X Displacements for LED's 1 to 10 (Left) and Y Displacements for LED's 1 to 10 (Right)

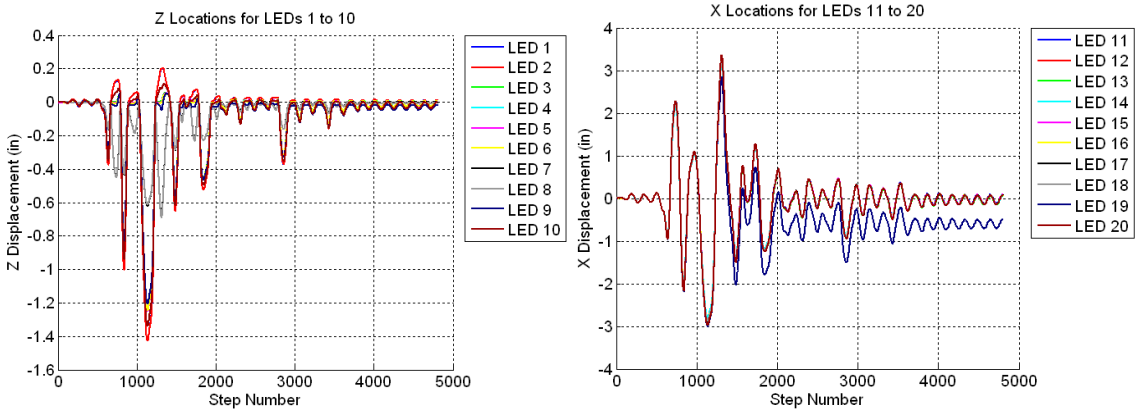

Figure B.243 Raw Data For Specimen A5 1.10xJMA Kobe Trial 1 – Z Displacements for LED's 1 to 10 (Left) and X Displacements for LED's 11 to 20 (Right)

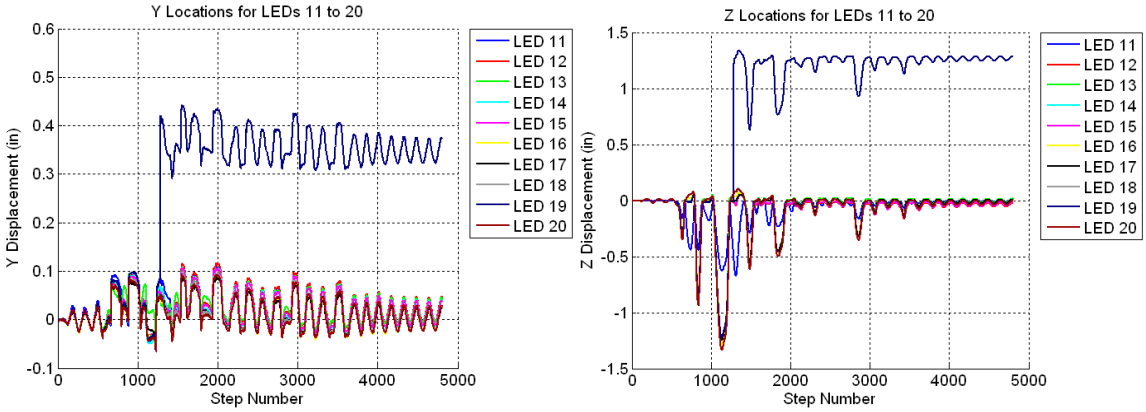

Figure B.244 Raw Data For Specimen A5 1.10xJMA Kobe Trial 1 – Y Displacements for LED's 11 to 20 (Left) and Z Displacements for LED's 11 to 20 (Right)

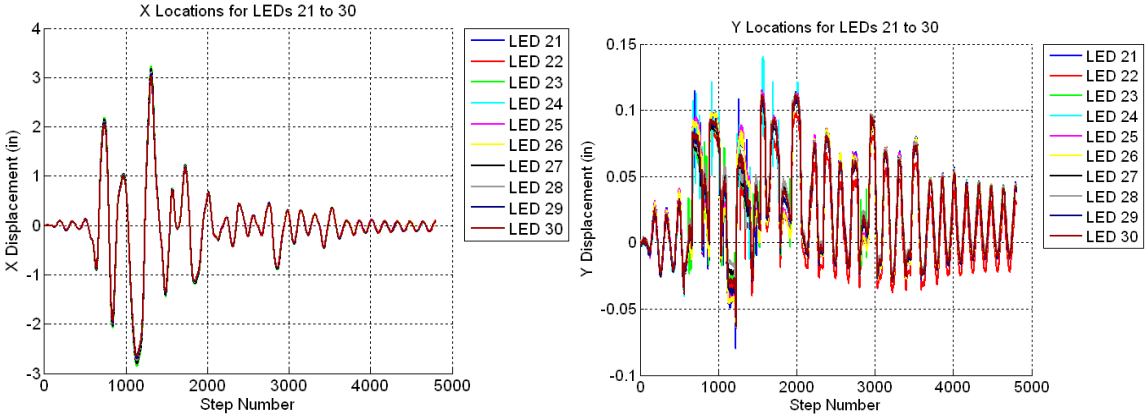

Figure B.245 Raw Data For Specimen A5 1.10xJMA Kobe Trial 1 – X Displacements for LED's 21 to 30 (Left) and Y Displacements for LED's 21 to 30 (Right)

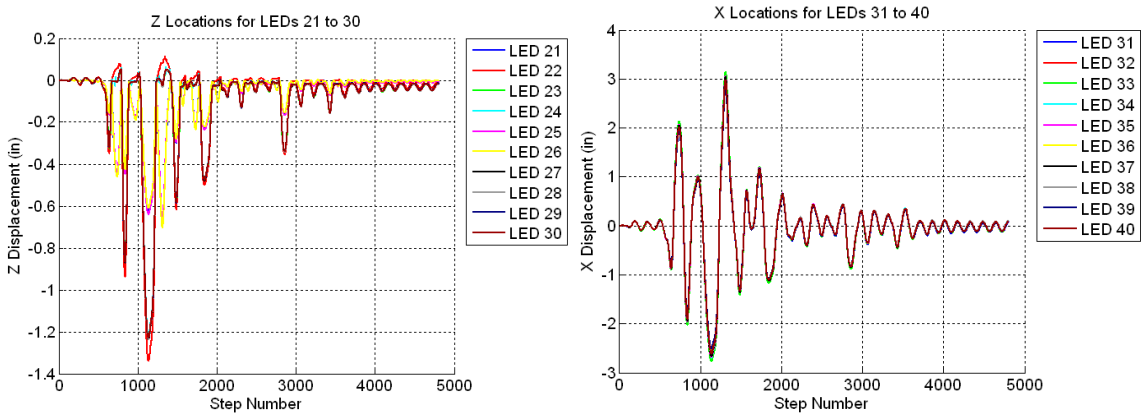

Figure B.246 Raw Data For Specimen A5 1.10xJMA Kobe Trial 1 – Z Displacements for LED's 21 to 30 (Left) and X Displacements for LED's 31 to 40 (Right)

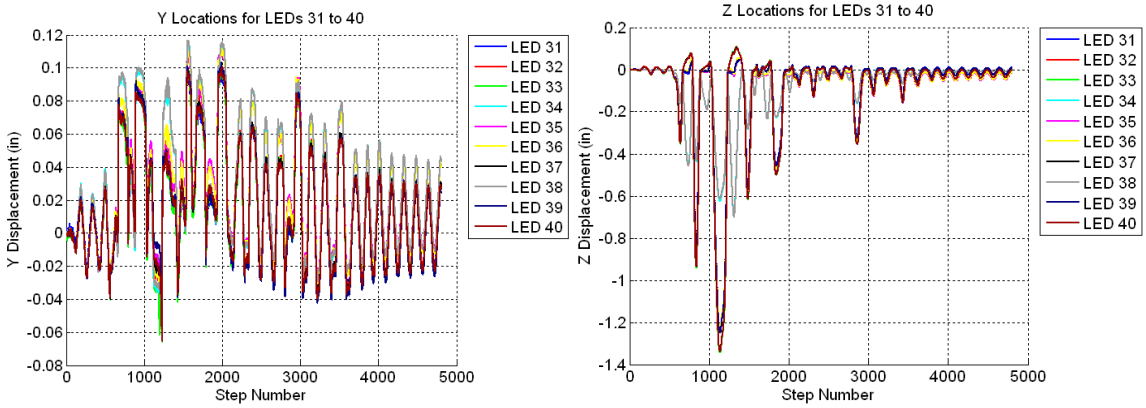

Figure B.247 Raw Data For Specimen A5 1.10xJMA Kobe Trial 1 – Y Displacements for LED's 31 to 40 (Left) and Z Displacements for LED's 31 to 40 (Right)

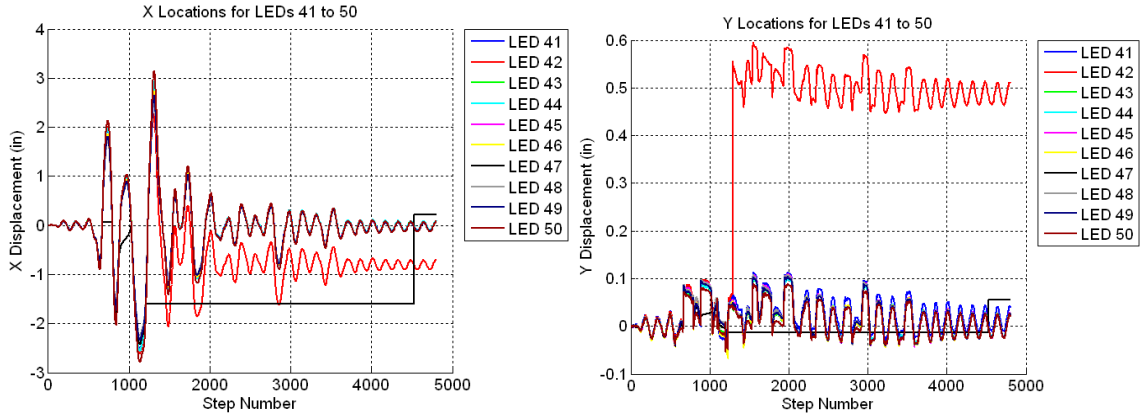

Figure B.248 Raw Data For Specimen A5 1.10xJMA Kobe Trial 1 – X Displacements for LED's 41 to 50 (Left) and Y Displacements for LED's 41 to 50 (Right)

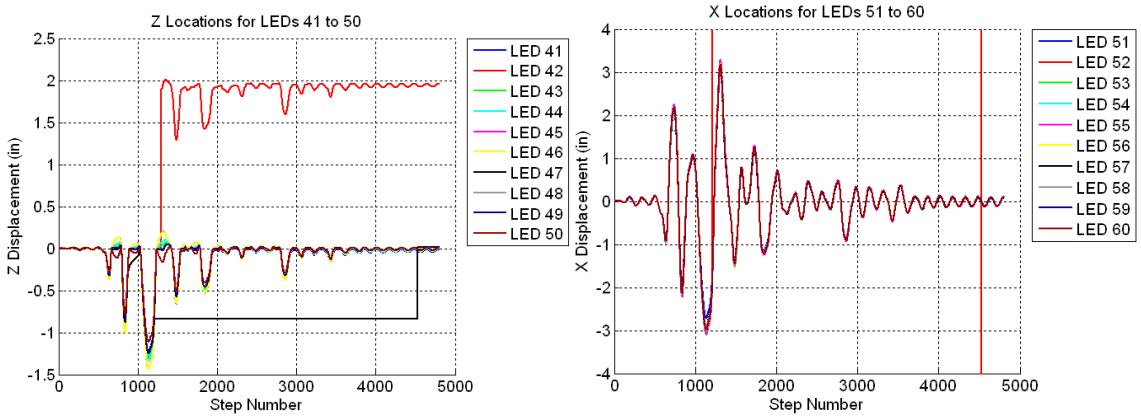

Figure B.249 Raw Data For Specimen A5 1.10xJMA Kobe Trial 1 – Z Displacements for LED's 41 to 50 (Left) and X Displacements for LED's 51 to 60 (Right)

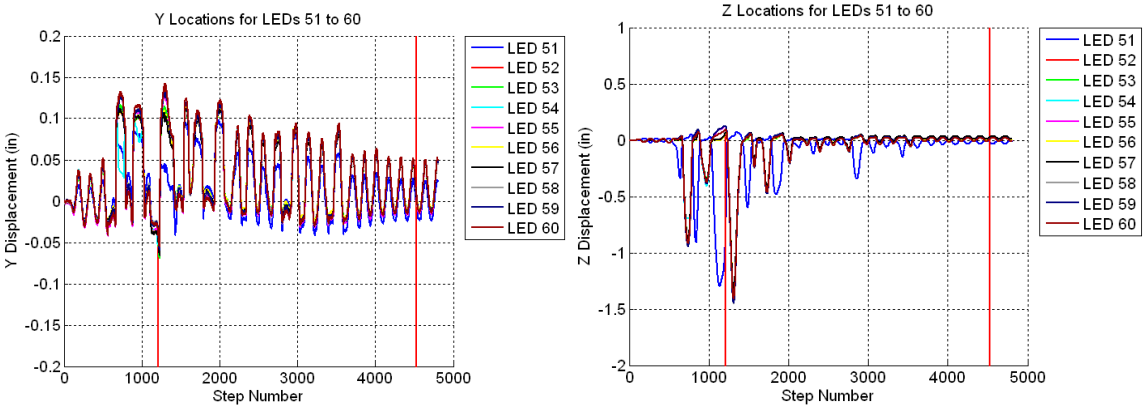

Figure B.250 Raw Data For Specimen A5 1.10xJMA Kobe Trial 1 – Y Displacements for LED's 51 to 60 (Left) and Z Displacements for LED's 51 to 60 (Right)

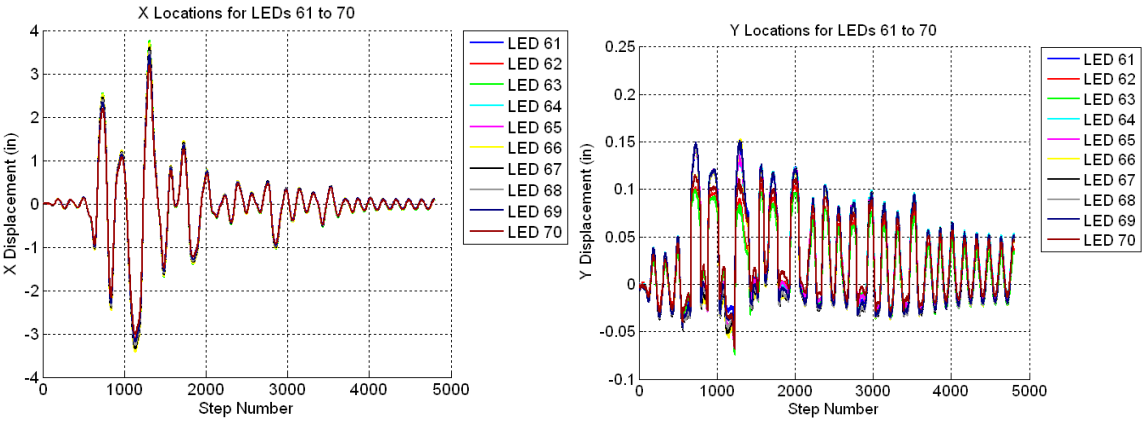

Figure B.251 Raw Data For Specimen A5 1.10xJMA Kobe Trial 1 – X Displacements for LED's 61 to 70 (Left) and Y Displacements for LED's 61 to 70 (Right)

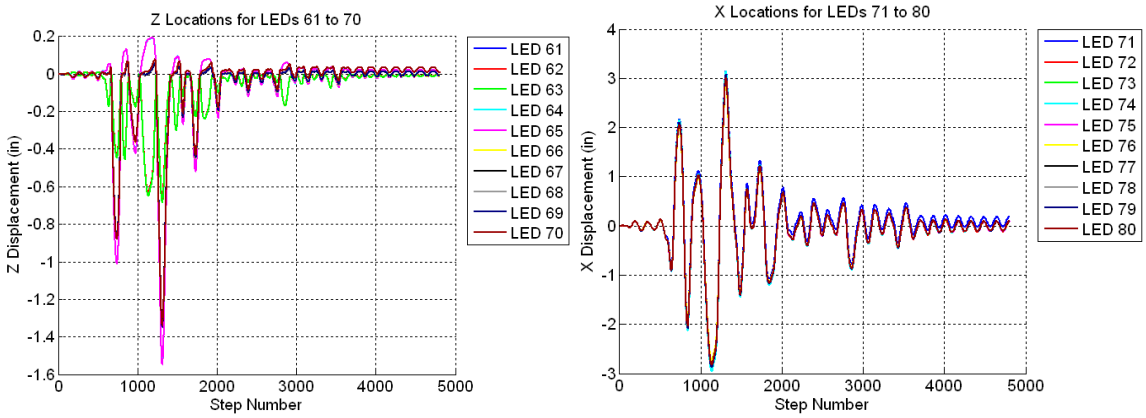

Figure B.252 Raw Data For Specimen A5 1.10xJMA Kobe Trial 1 – Z Displacements for LED's 61 to 70 (Left) and X Displacements for LED's 71 to 80 (Right)

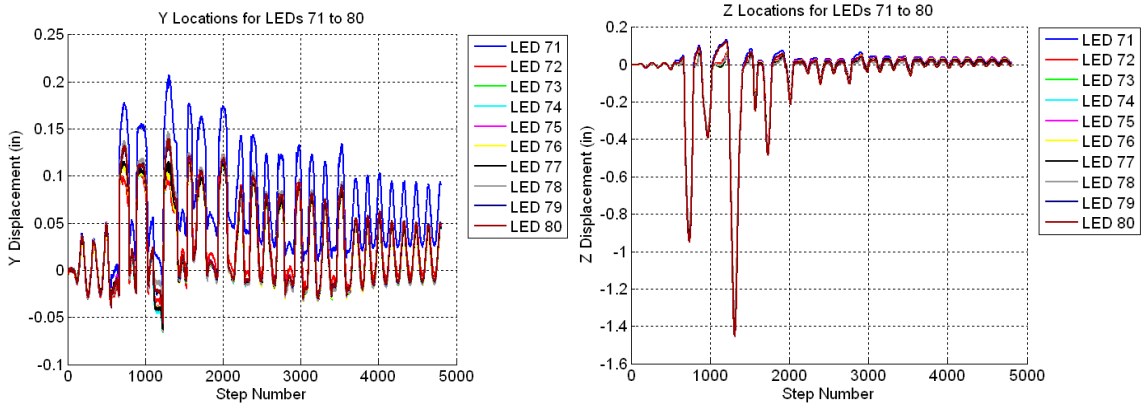

Figure B.253 Raw Data For Specimen A5 1.10xJMA Kobe Trial 1 – Y Displacements for LED's 71 to 80 (Left) and Z Displacements for LED's 71 to 80 (Right)

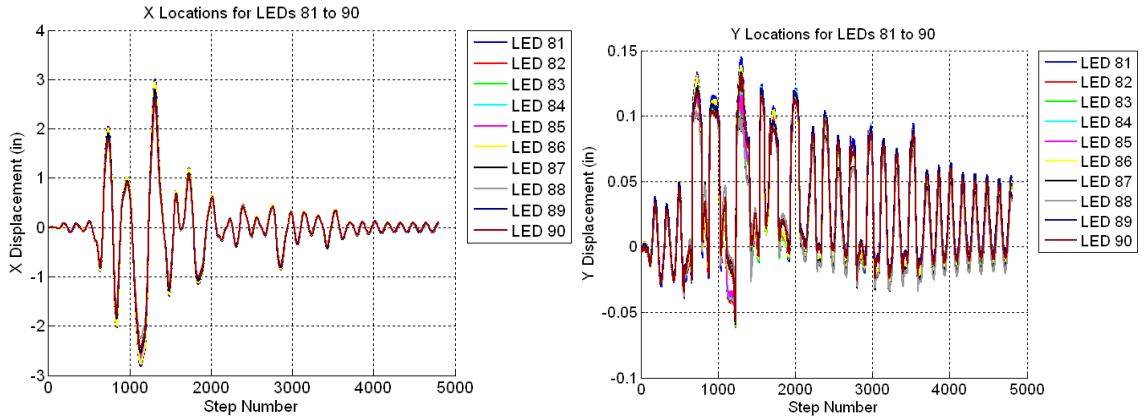

Figure B.254 Raw Data For Specimen A5 1.10xJMA Kobe Trial 1 – X Displacements for LED's 81 to 90 (Left) and Y Displacements for LED's 81 to 90 (Right)

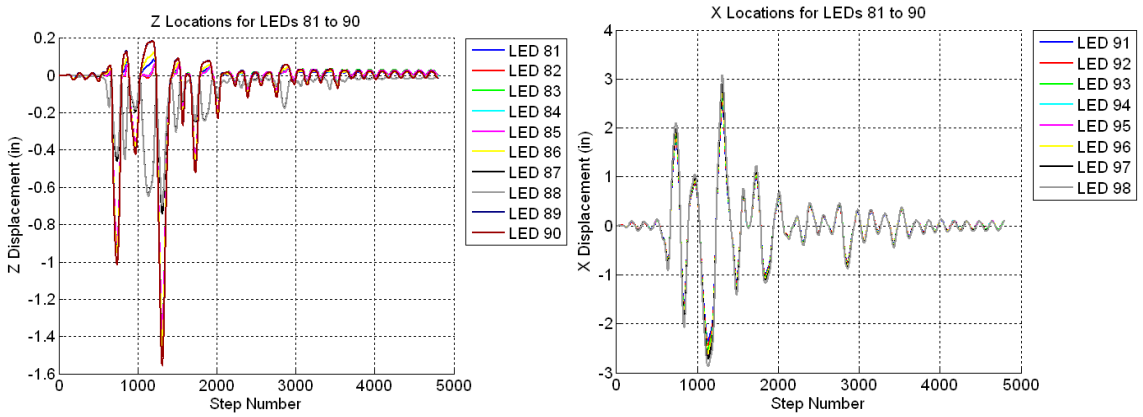

Figure B.255 Raw Data For Specimen A5 1.10xJMA Kobe Trial 1 – Z Displacements for LED's 81 to 90 (Left) and X Displacements for LED's 81 to 90 (Right)

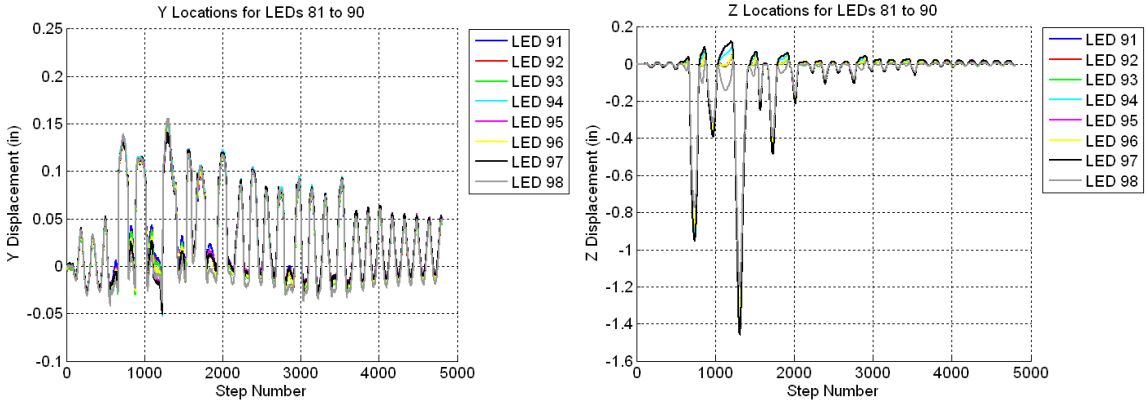

Figure B.256 Raw Data For Specimen A5 1.10xJMA Kobe Trial 1 – Y Displacements for LED's 81 to 90 (Left) and Z Displacements for LED's 81 to 90 (Right)

B.7 Specimen A5 – 1.10xJMA Kobe Trial 2

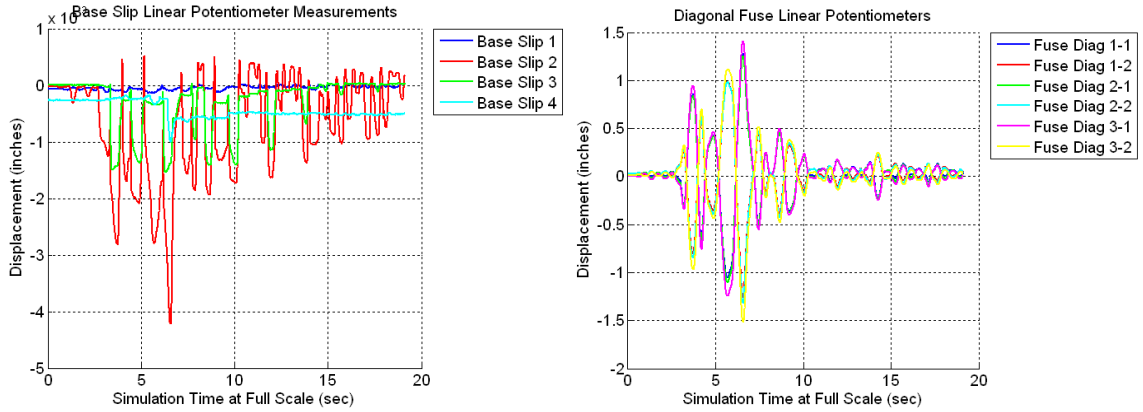

Figure B.257 Raw Data For Specimen A5 1.10xJMA Kobe Trial 2 – Base Slip (Left) and Back Fuse Linear Potentiometers (Right)

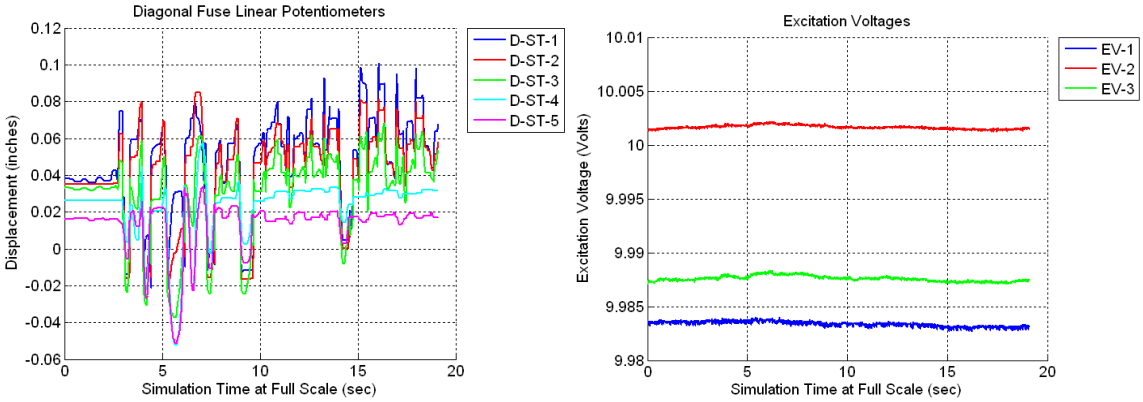

Figure B.258 Raw Data For Specimen A5 1.10xJMA Kobe Trial 2 – Strut Linear Potentiometers and Excitation Voltages (Right)

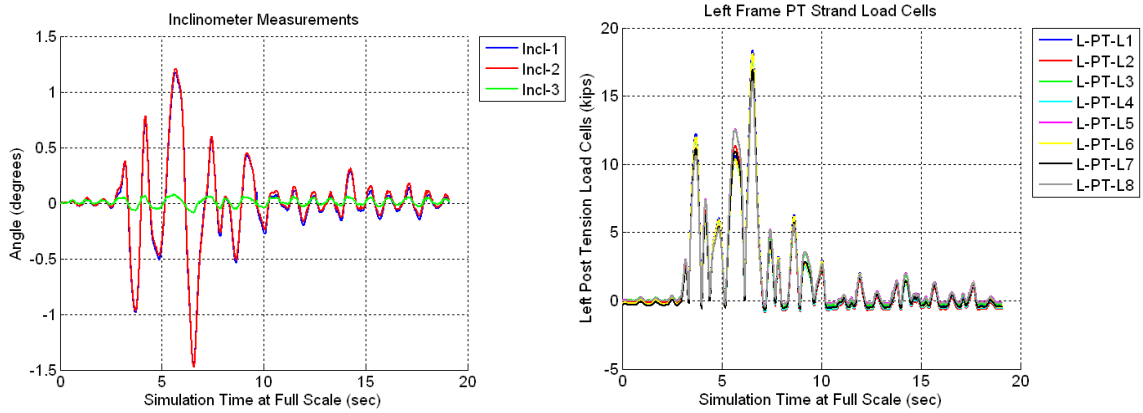

Figure B.259 Raw Data For Specimen A5 1.10xJMA Kobe Trial 2 – Inclinometers (Left) and Left Frame PT Load Cells (Right)

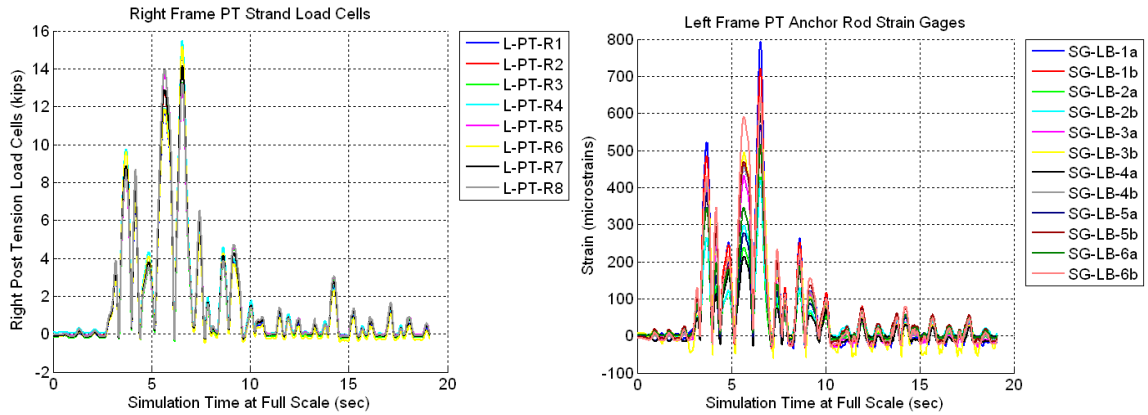

Figure B.260 Raw Data For Specimen A5 1.10xJMA Kobe Trial 2 – Right Frame PT Load Cells (Left) and Left Frame PT Anchor Rods (Right)

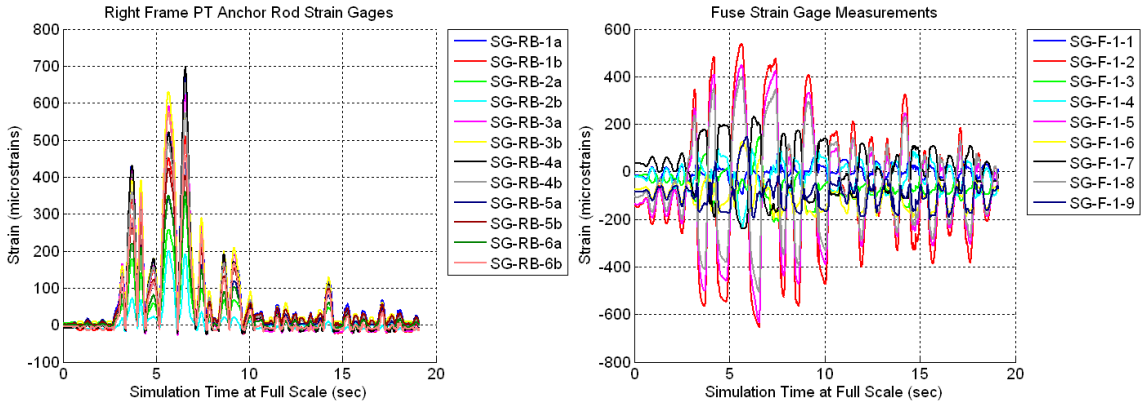

Figure B.261 Raw Data For Specimen A5 1.10xJMA Kobe Trial 2 – Right Frame PT Anchor Rods (Left) and Back Fuse Strain Gages (Right)

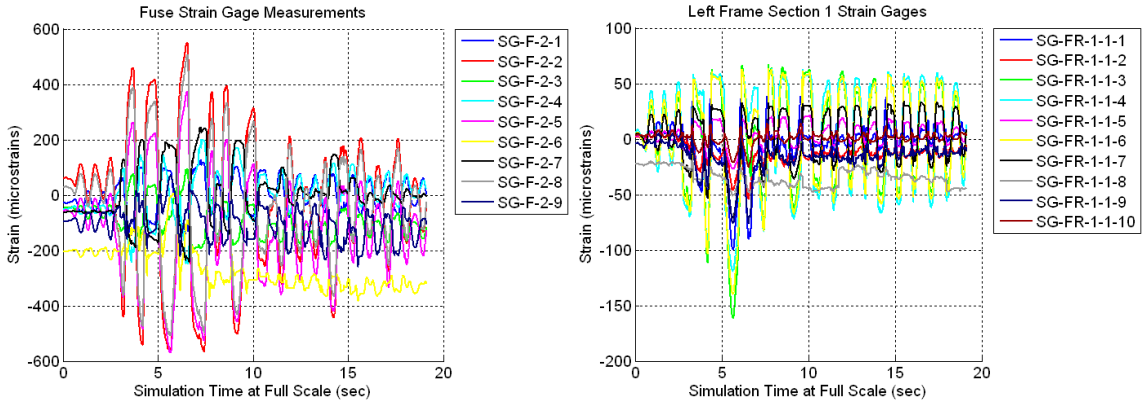

Figure B.262 Raw Data For Specimen A5 1.10xJMA Kobe Trial 2 – Front Fuse Strain Gages (Left) and Left Frame Section 1-1 Strain Gages (Right)

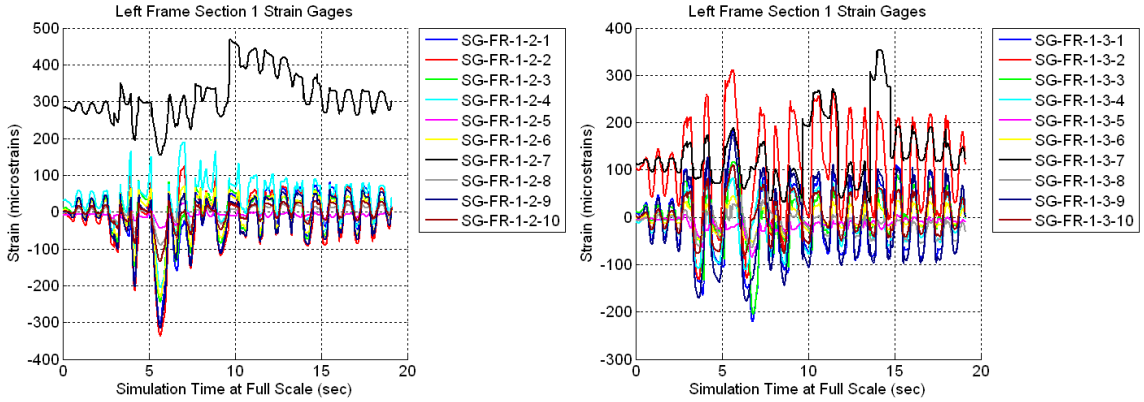

Figure B.263 Raw Data For Specimen A5 1.10xJMA Kobe Trial 2 – Left Frame Section 1-2 Strain Gages (Left) and Left Frame Section 1-3 Strain Gages (Right)

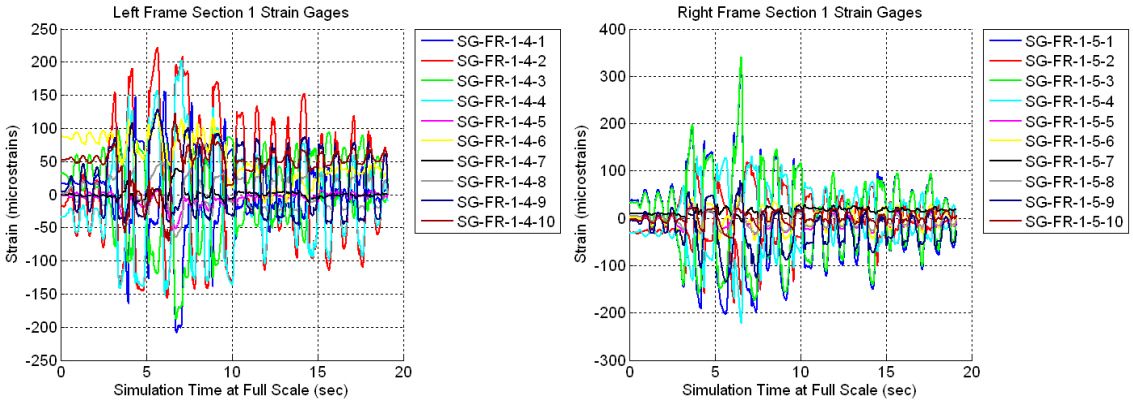

Figure B.264 Raw Data For Specimen A5 1.10xJMA Kobe Trial 2 – Left Frame Section 1-4 Strain Gages (Left) and Right Frame Section 1-5 Strain Gages (Right)

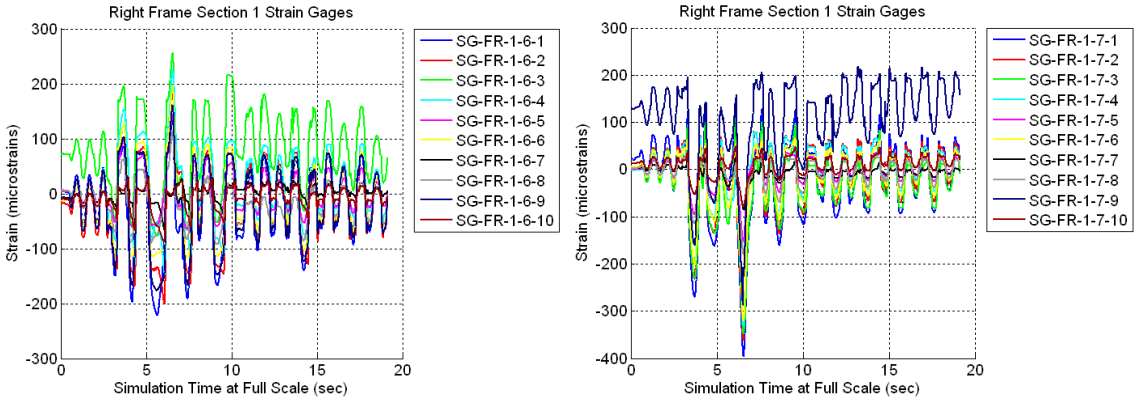

Figure B.265 Raw Data For Specimen A5 1.10xJMA Kobe Trial 2 – Right Frame Section 1-6 Strain Gages (Left) and Right Frame Section 1-7 Strain Gages (Right)

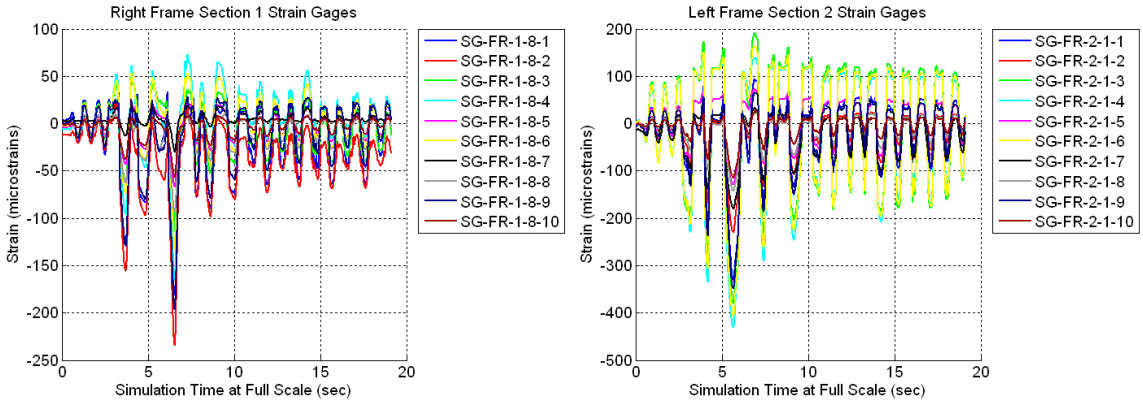

Figure B.266 Raw Data For Specimen A5 1.10xJMA Kobe Trial 2 – Right Frame Section 1-8 Strain Gages (Left) and Left Frame Section 2-1 Strain Gages (Right)

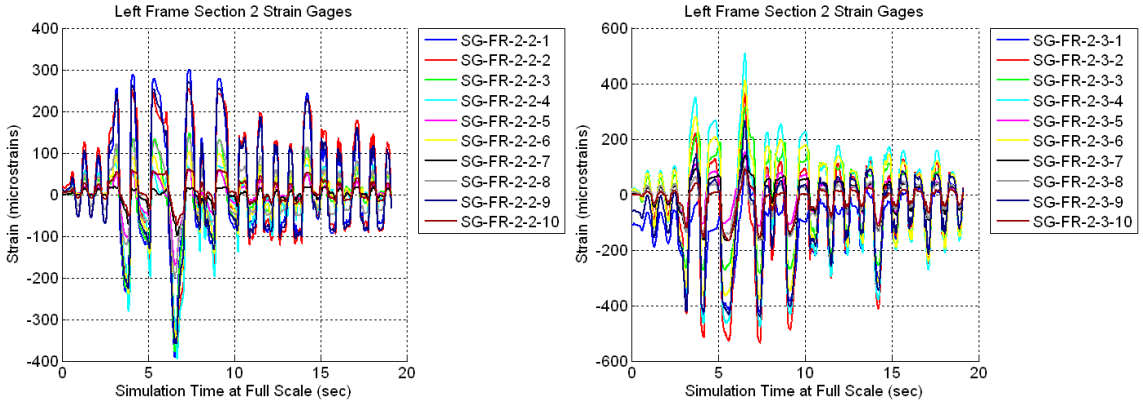

Figure B.267 Raw Data For Specimen A5 1.10xJMA Kobe Trial 2 – Left Frame Section 2-2 Strain Gages (Left) and Left Frame Section 2-3 Strain Gages (Right)

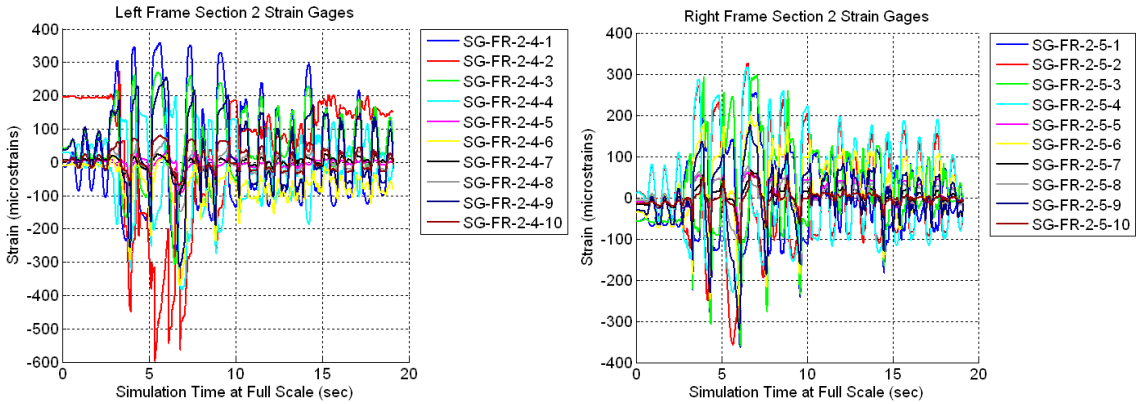

Figure B.268 Raw Data For Specimen A5 1.10xJMA Kobe Trial 2 – Left Frame Section 2-4 Strain Gages (Left) and Right Frame Section 2-5 Strain Gages (Right)

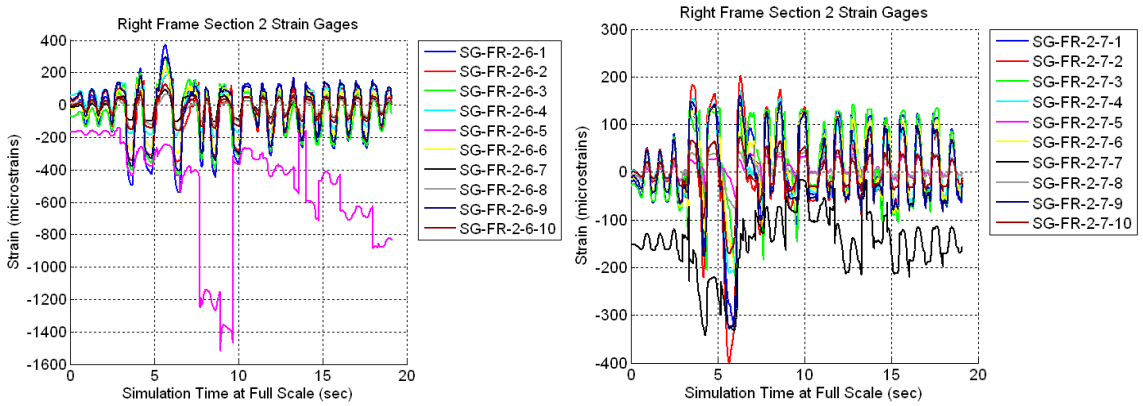

Figure B.269 Raw Data For Specimen A5 1.10xJMA Kobe Trial 2 – Right Frame Section 2-6 Strain Gages (Left) and Right Frame Section 2-7 Strain Gages (Right)

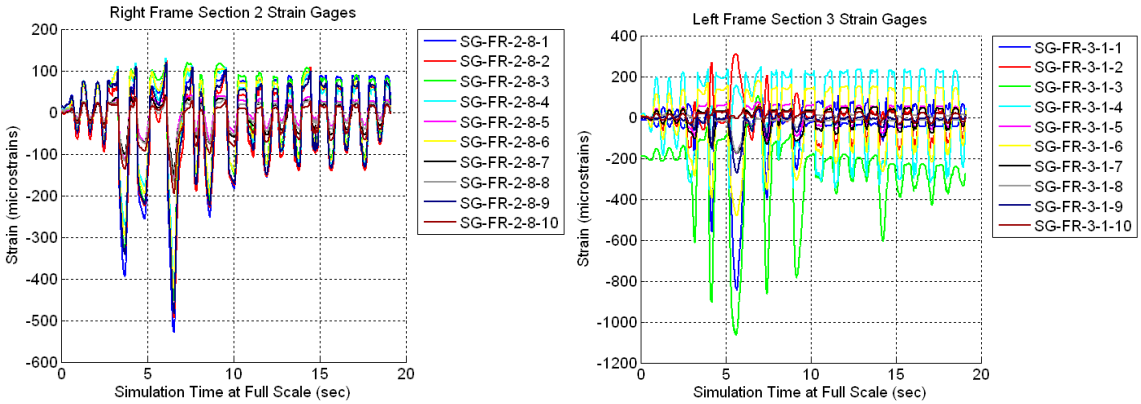

Figure B.270 Raw Data For Specimen A5 1.10xJMA Kobe Trial 2 – Right Frame Seciton 2-8 Strain Gages (Left) and Left Frame Section 3-1 Strain Gages (Right)

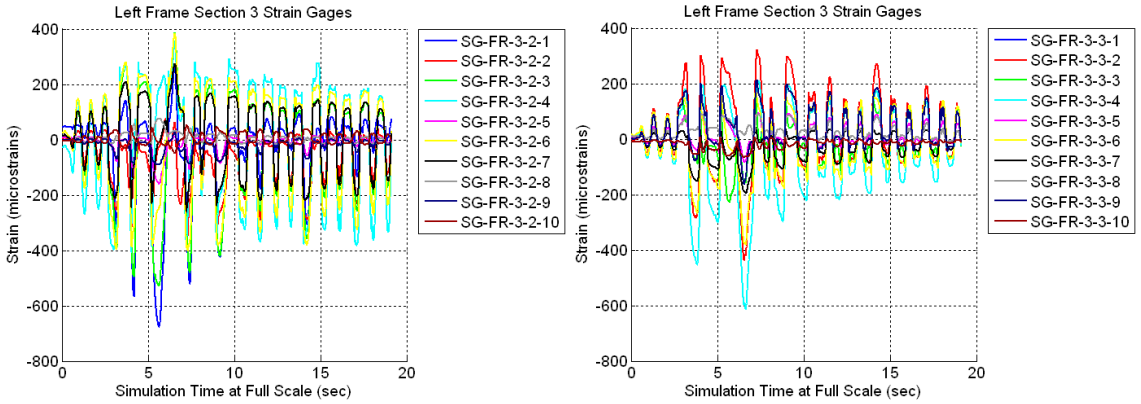

Figure B.271 Raw Data For Specimen A5 1.10xJMA Kobe Trial 2 – Left Frame Section 3-2 Strain Gages (Left) and Left Frame Section 3-3 Strain Gages (Right)

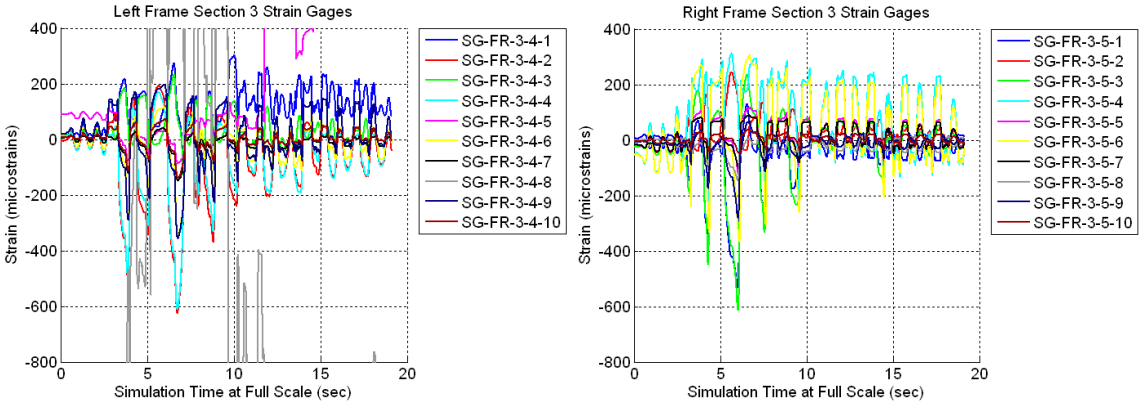

Figure B.272 Raw Data For Specimen A5 1.10xJMA Kobe Trial 2 – Left Frame Section 3-4 Strain Gages (Left) and Right Frame Section 3-5 Strain Gages (Right)

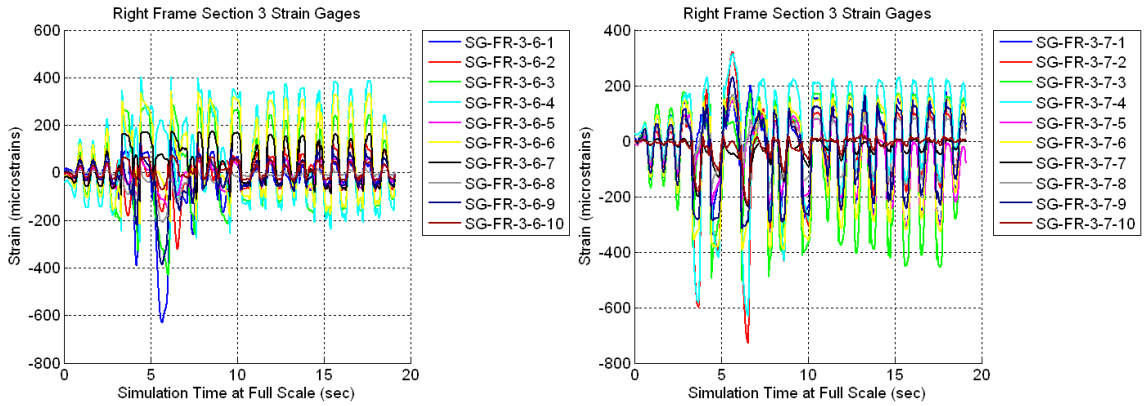

Figure B.273 Raw Data For Specimen A5 1.10xJMA Kobe Trial 2 – Right Frame Section 3-6 Strain Gages (Left) and Right Frame Section 3-7 Strain Gages (Right)

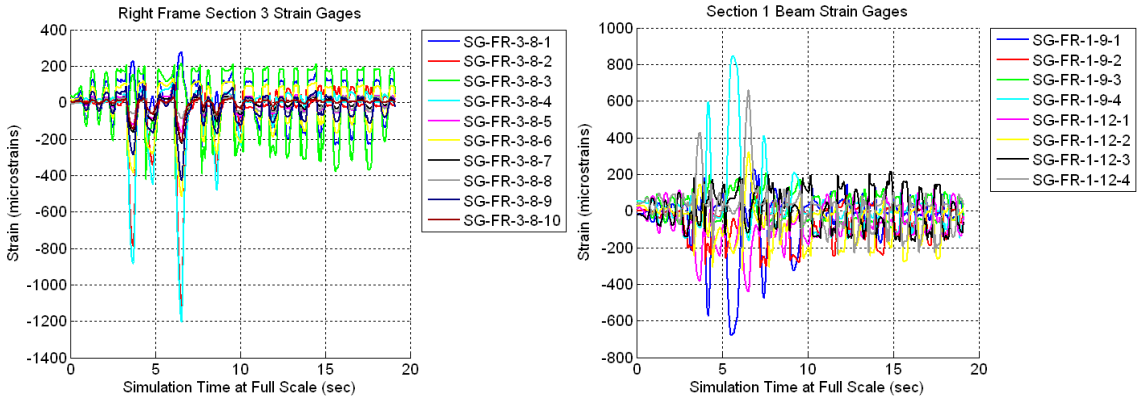

Figure B.274 Raw Data For Specimen A5 1.10xJMA Kobe Trial 2 – Right Frame Section 3-8 Strain Gages (Left) and First Floor Beam Strain Gages (Right)

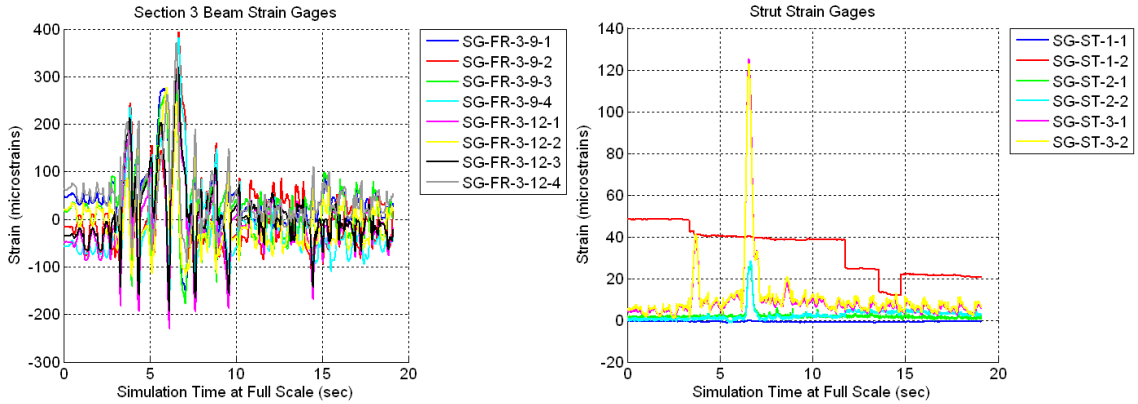

Figure B.275 Raw Data For Specimen A5 1.10xJMA Kobe Trial 2 – Third Floor Beam Strain Gages (Left) and Strut Strain Gages (Right)

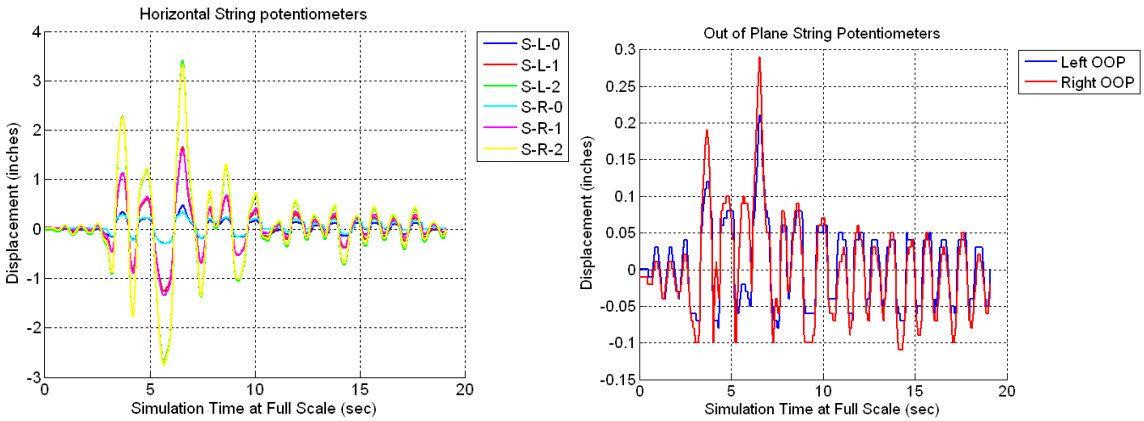

Figure B.276 Raw Data For Specimen A5 1.10xJMA Kobe Trial 2 – Horizontal String Potentiometers (Left) and Out-of-Plane String Potentiometers (Right)

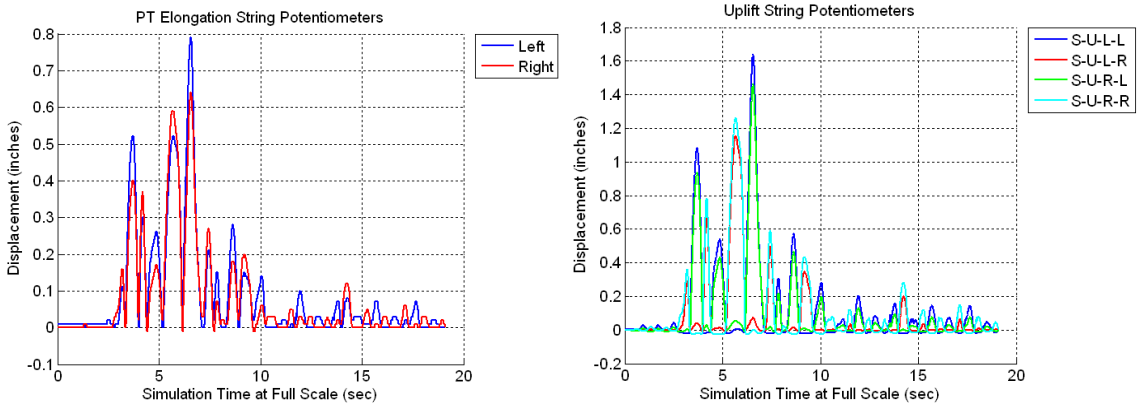

Figure B.277 Raw Data For Specimen A5 1.10xJMA Kobe Trial 2 – PT Elongation String Potentiometers (Left) and Uplift String Potentiometers (Right)

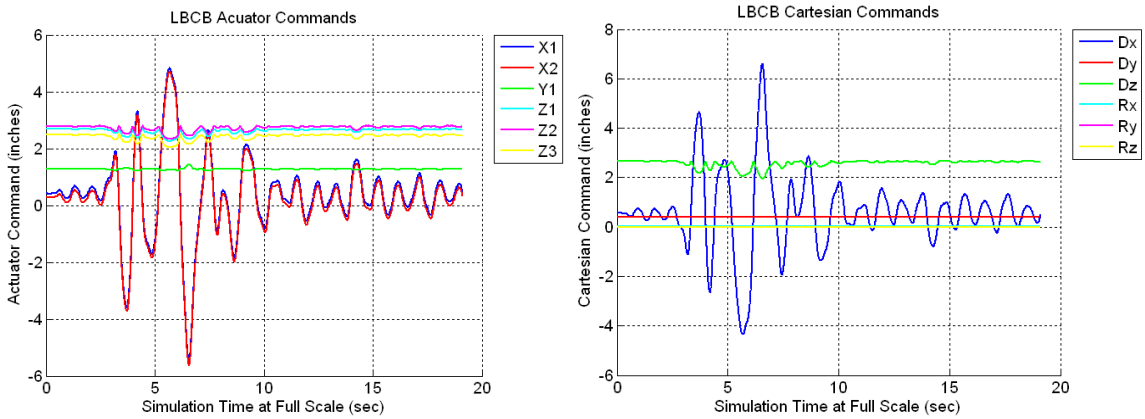

Figure B.278 Raw Data For Specimen A5 1.10xJMA Kobe Trial 2 – LBCB Actuator Commands (Left) and LBCB Cartesian Commands (Right)

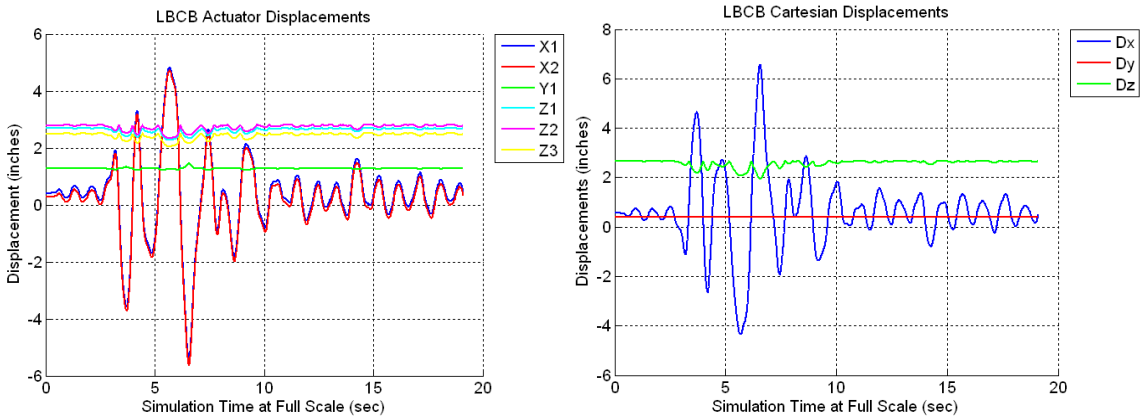

Figure B.279 Raw Data For Specimen A5 1.10xJMA Kobe Trial 2 – LBCB Actuator Displacements (Left) and LBCB Cartesian Displacements (Right)

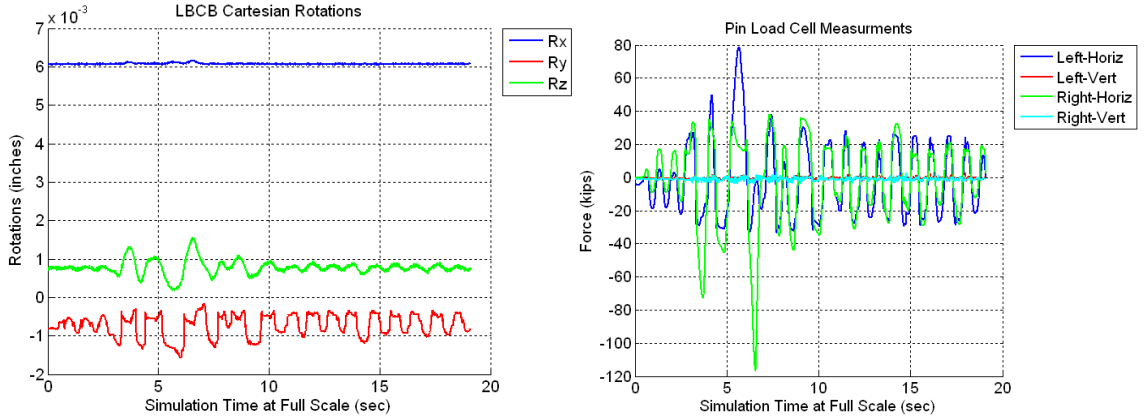

Figure B.280 Raw Data For Specimen A5 1.10xJMA Kobe Trial 2 – LBCB Cartesian Rotations (Left) and Pin Load Cells (Right)

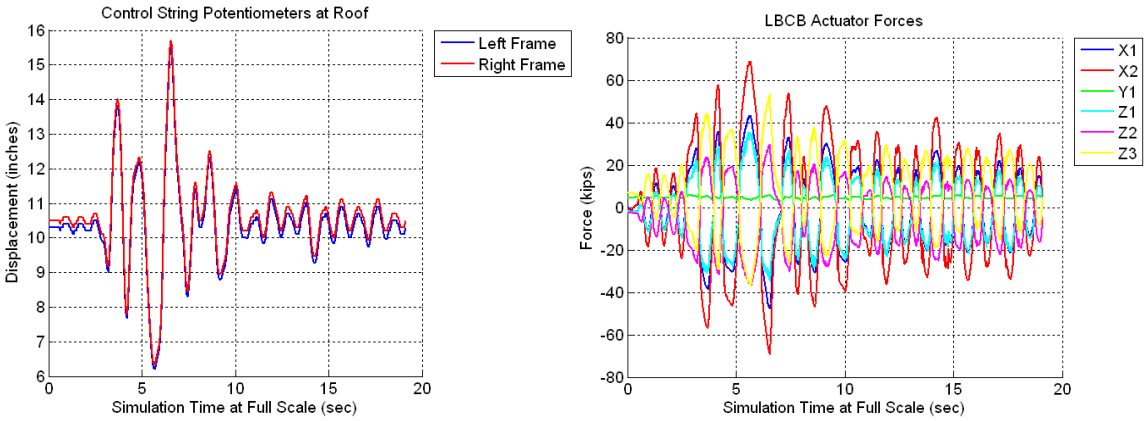

Figure B.281 Raw Data For Specimen A5 1.10xJMA Kobe Trial 2 – Control Roof String Potentiometers (Left) and LBCB Actuator Forces (Right)

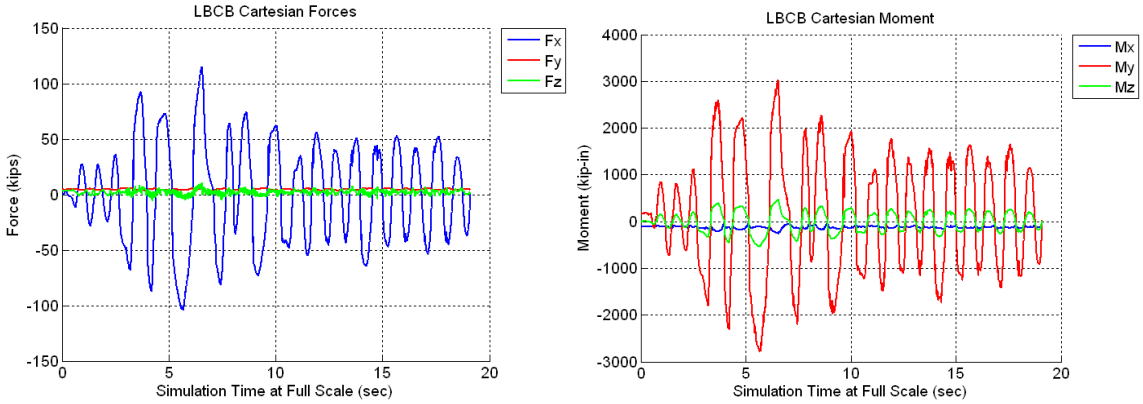

Figure B.282 Raw Data For Specimen A5 1.10xJMA Kobe Trial 2 – LBCB Cartesian Forces (Left) and LBCB Cartesian Moments (Right)

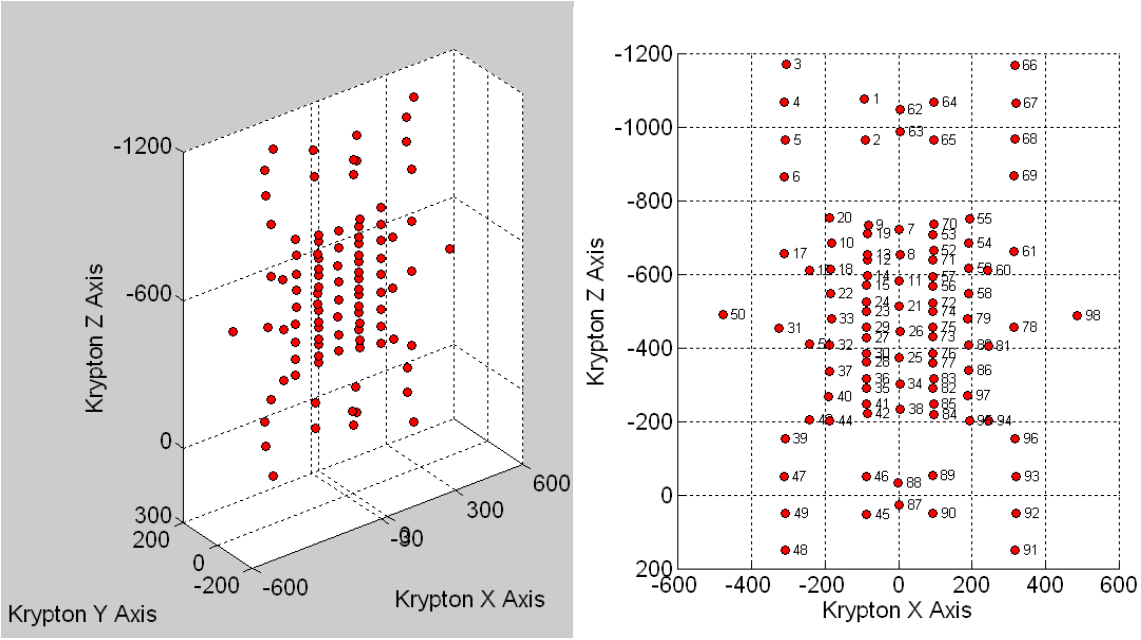

Figure B.283 Raw Data For Specimen A5 1.10xJMA Kobe Trial 2 – Krypton LED Locations (Left) and Krypton LED Numbering (Right)

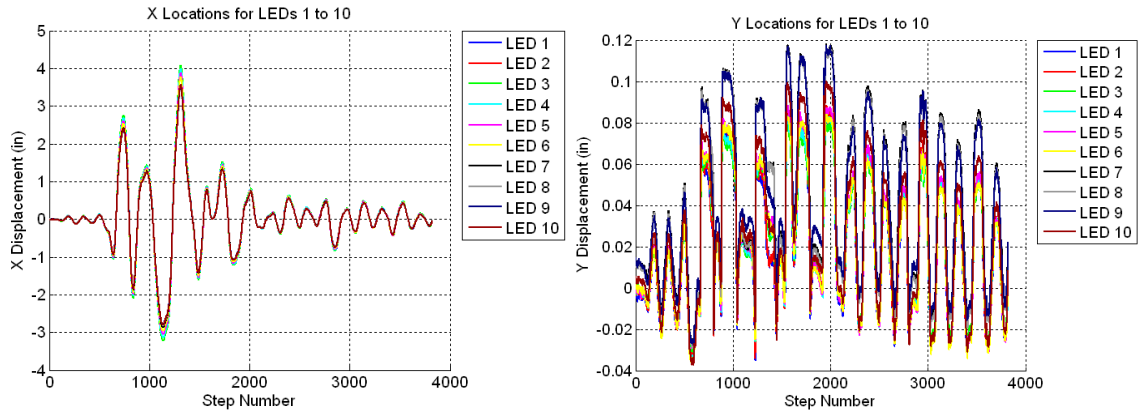

Figure B.284 Raw Data For Specimen A5 1.10xJMA Kobe Trial 2 – X Displacements for LED's 1 to 10 (Left) and Y Displacements for LED's 1 to 10 (Right)

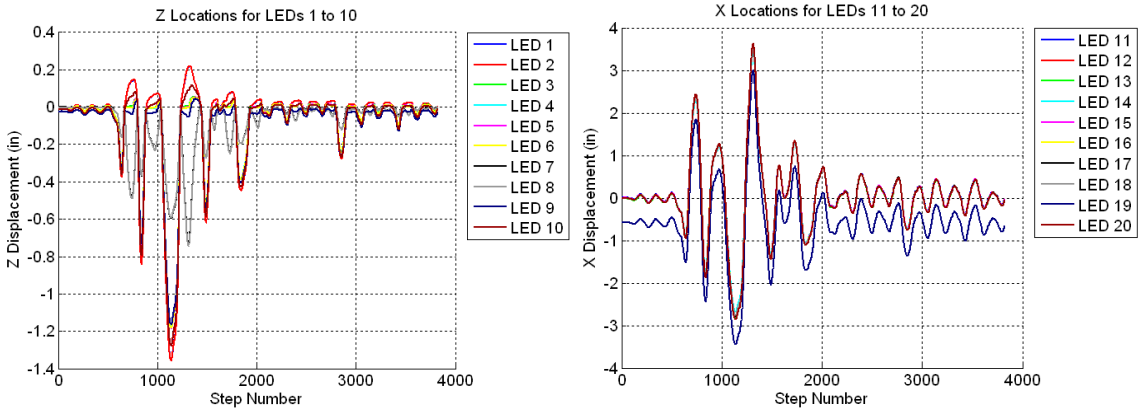

Figure B.285 Raw Data For Specimen A5 1.10xJMA Kobe Trial 2 – Z Displacements for LED's 1 to 10 (Left) and X Displacements for LED's 11 to 20 (Right)

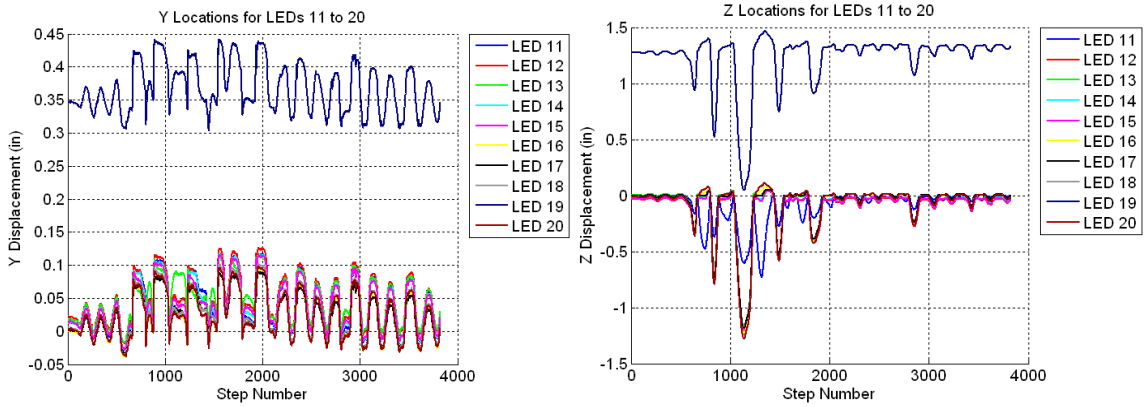

Figure B.286 Raw Data For Specimen A5 1.10xJMA Kobe Trial 2 – Y Displacements for LED's 11 to 20 (Left) and Z Displacements for LED's 11 to 20 (Right)

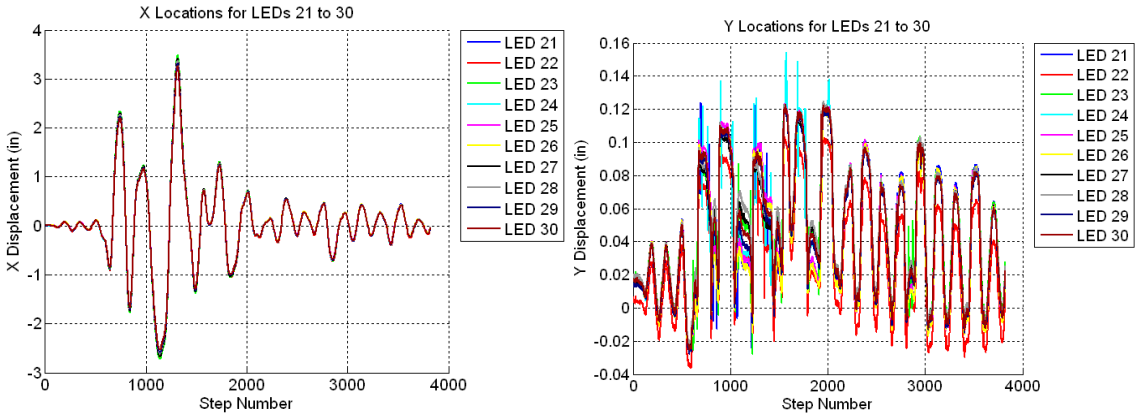

Figure B.287 Raw Data For Specimen A5 1.10xJMA Kobe Trial 2 – X Displacements for LED's 21 to 30 (Left) and Y Displacements for LED's 21 to 30 (Right)

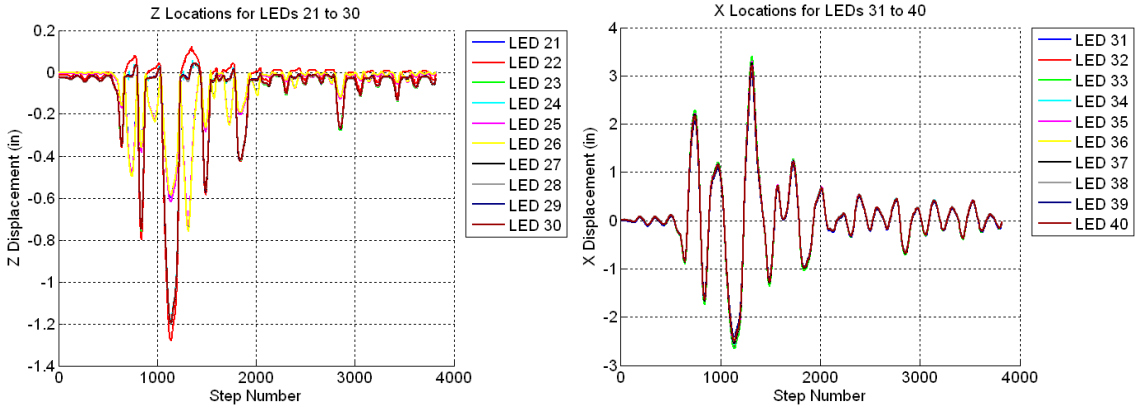

Figure B.288 Raw Data For Specimen A5 1.10xJMA Kobe Trial 2 – Z Displacements for LED's 21 to 30 (Left) and X Displacements for LED's 31 to 40 (Right)

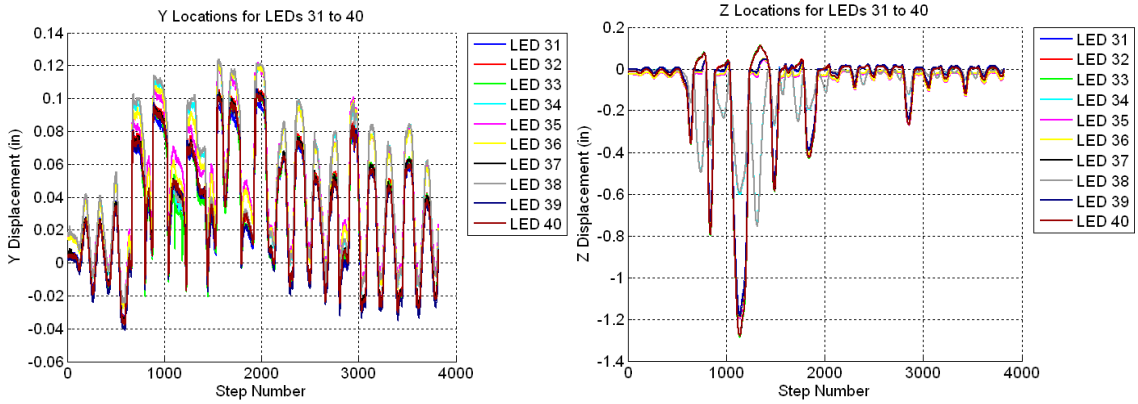

Figure B.289 Raw Data For Specimen A5 1.10xJMA Kobe Trial 2 – Y Displacements for LED's 31 to 40 (Left) and Z Displacements for LED's 31 to 40 (Right)

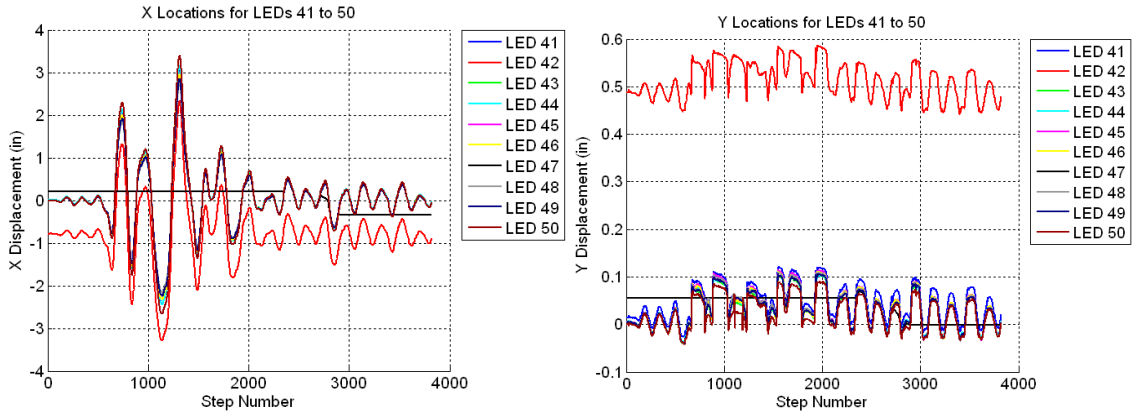

Figure B.290 Raw Data For Specimen A5 1.10xJMA Kobe Trial 2 – X Displacements for LED's 41 to 50 (Left) and Y Displacements for LED's 41 to 50 (Right)

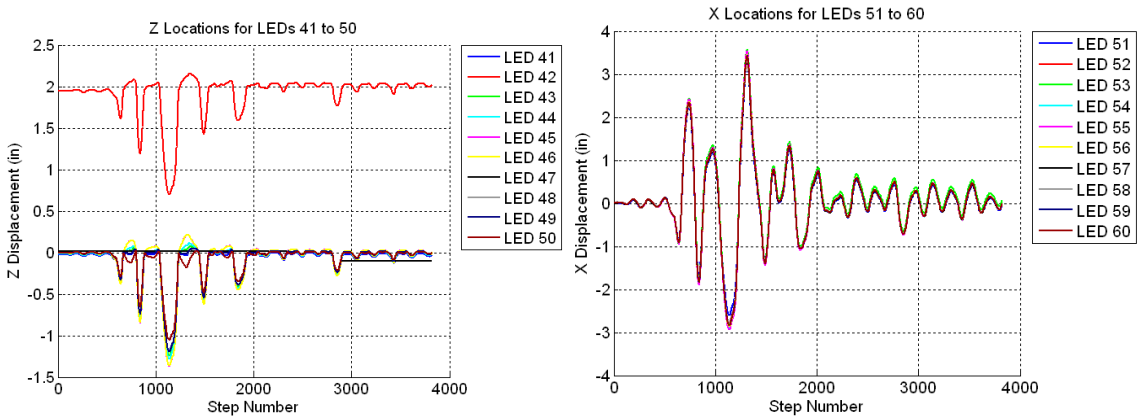

Figure B.291 Raw Data For Specimen A5 1.10xJMA Kobe Trial 2 – Z Displacements for LED's 41 to 50 (Left) and X Displacements for LED's 51 to 60 (Right)

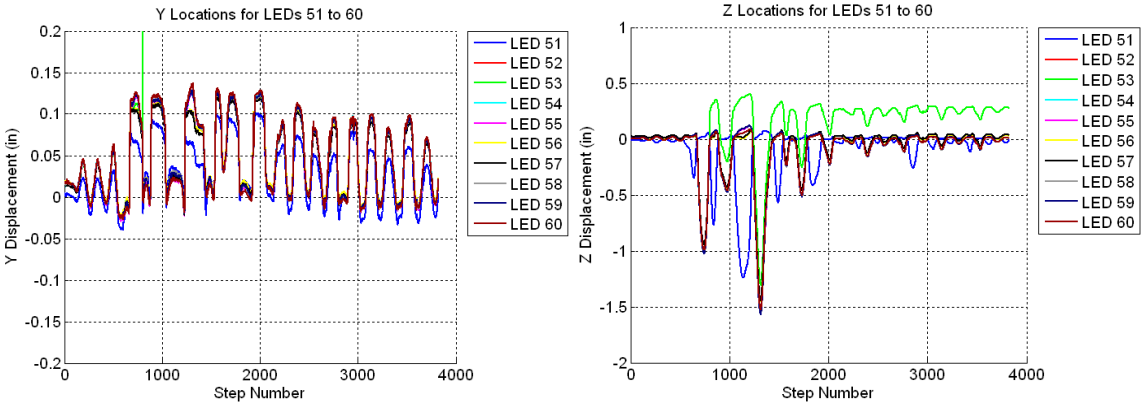

Figure B.292 Raw Data For Specimen A5 1.10xJMA Kobe Trial 2 – Y Displacements for LED's 51 to 60 (Left) and Z Displacements for LEDs 51 to 60 (Right)

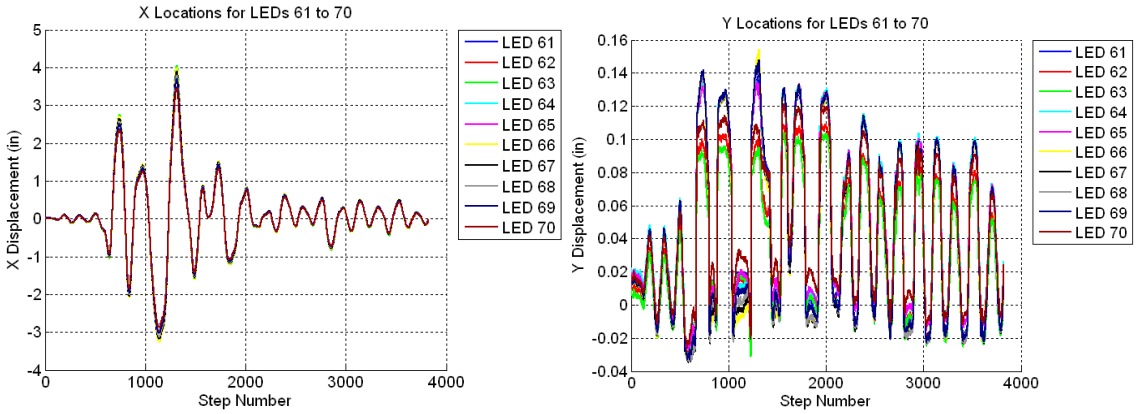

Figure B.293 Raw Data For Specimen A5 1.10xJMA Kobe Trial 2 – X Displacements for LED's 61 to 70 (Left) and Y Displacements for LED's 61 to 70 (Right)

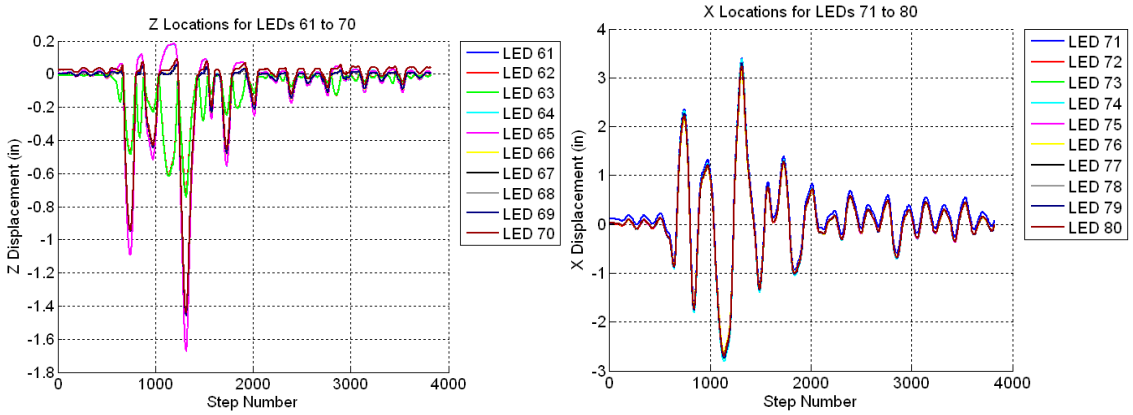

Figure B.294 Raw Data For Specimen A5 1.10xJMA Kobe Trial 2 – Z Displacements for LED's 61 to 70 (Left) X Displacements for LED's 71 to 80 (Right)

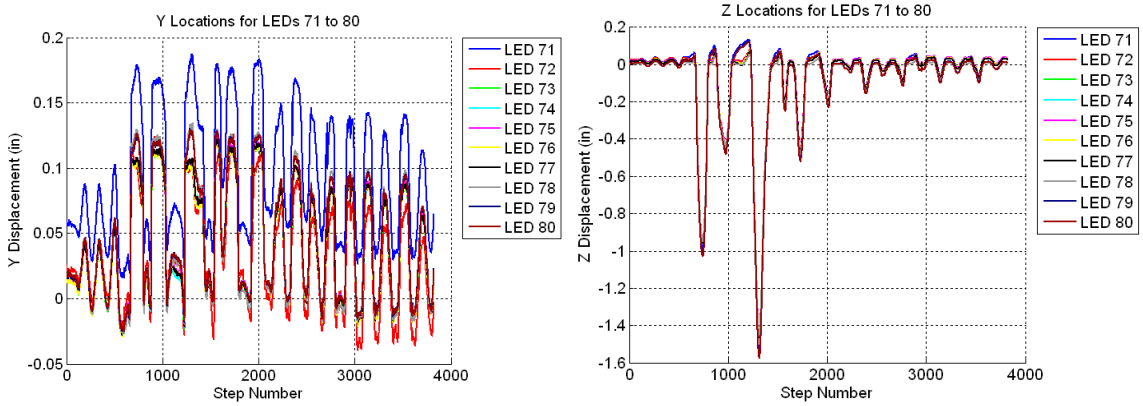

Figure B.295 Raw Data For Specimen A5 1.10xJMA Kobe Trial 2 – Y Displacements for LED's 71 to 80 (Left) and Z Displacements for LED's 71 to 80 (Right)

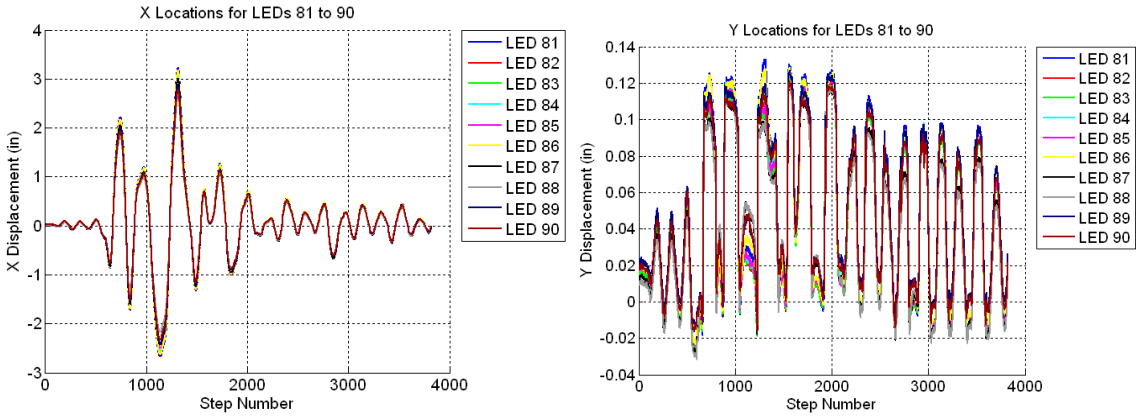

Figure B.296 Raw Data For Specimen A5 1.10xJMA Kobe Trial 2 – X Displacements for LED's 81 to 90 (Left) and Y Displacements for LED's 81 to 90 (Right)

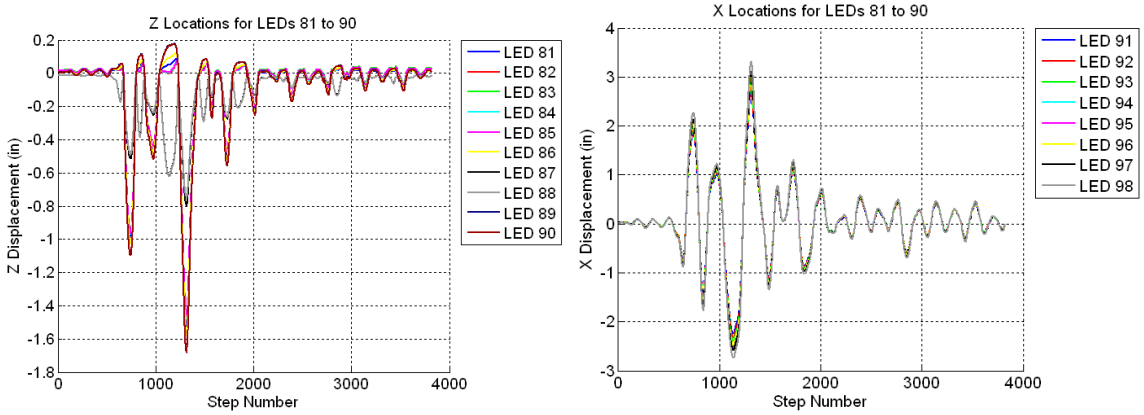

Figure B.297 Raw Data For Specimen A5 1.10xJMA Kobe Trial 2 – Z Displacements for LED's 81 to 90 (Left) and X Displacements for LED's 91 to 98 (Right)

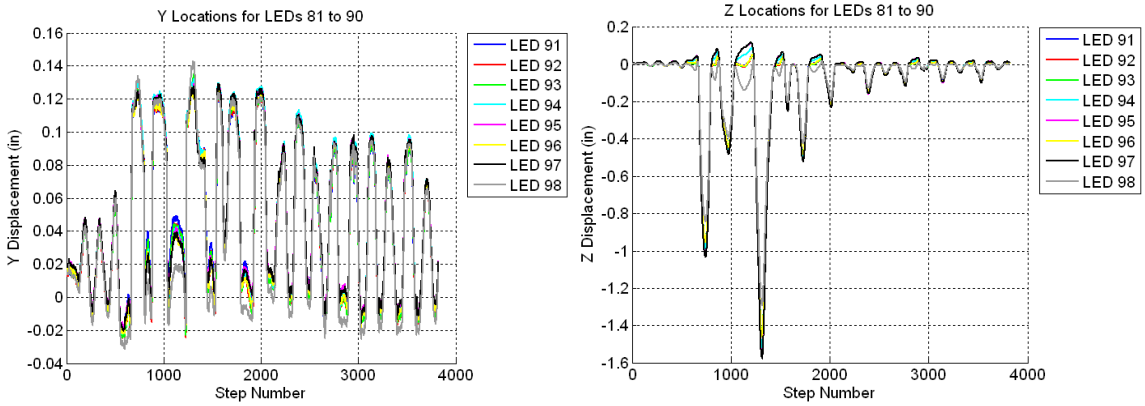

Figure B.298 Raw Data For Specimen A5 1.10xJMA Kobe Trial 2 – Y Displacements for LED's 91 to 98 (Left) and Z Displacements for LED's 91 to 98 (Right)

B.8 Specimen A6 – MCE Trial

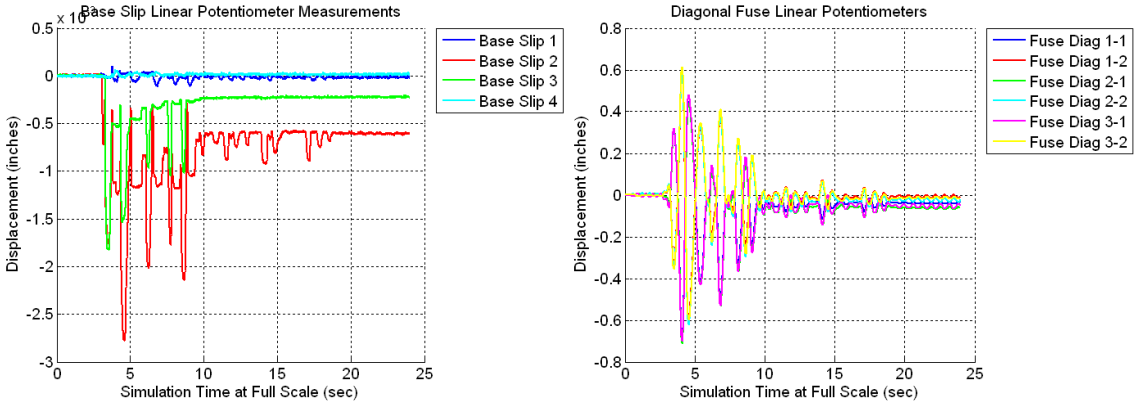

Figure B.299 Raw Data For Specimen A6 MCE Trial – Base Slip (Left) and Fuse Linear Potentiometers (Right)

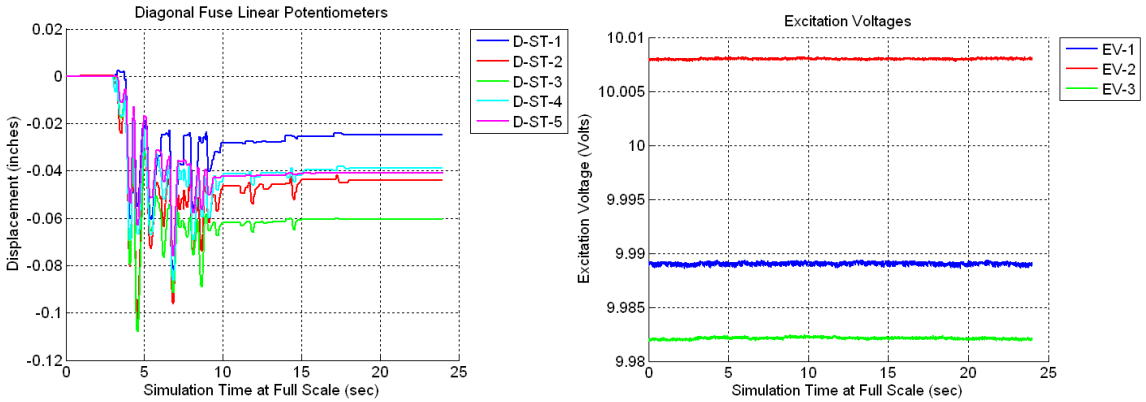

Figure B.300 Raw Data For Specimen A6 MCE Trial – Strut Linear Potentiometers (Left) and Excitation Voltage (Right)

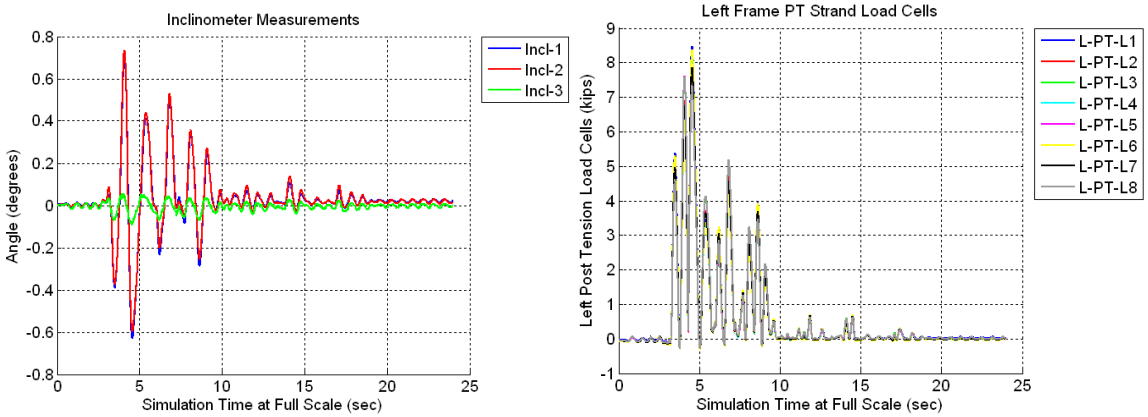

Figure B.301 Raw Data For Specimen A6 MCE Trial – Inclinometers (Left) and Left Frame PT Load Cells (Right)

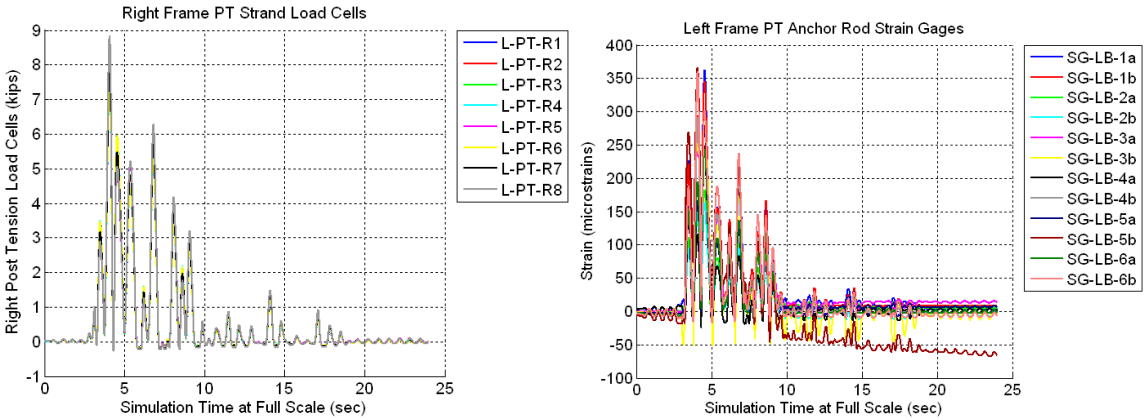

Figure B.302 Raw Data For Specimen A6 MCE Trial – Right Frame PT Load Cells (Left) and Left Frame PT Anchor Rods (Right)

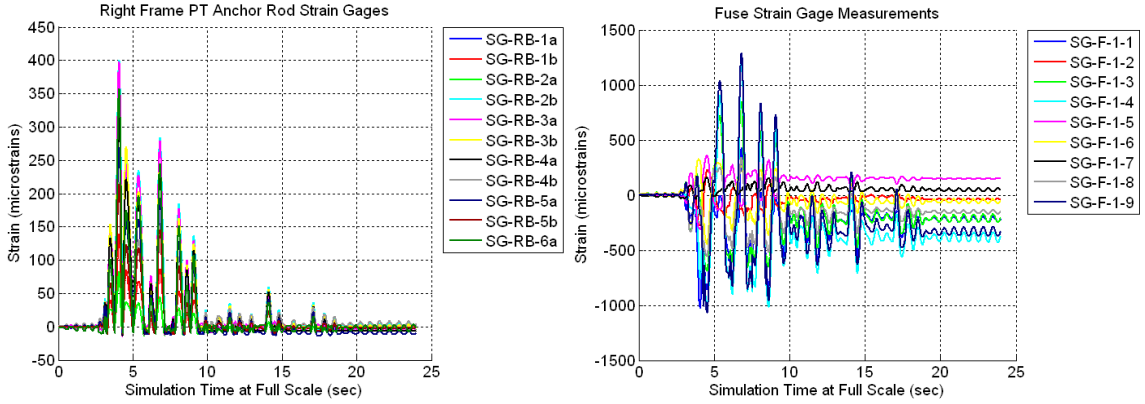

Figure B.303 Raw Data For Specimen A6 MCE Trial – Right Frame PT Anchor Rods (Left) and Bottom Back Fuse Strain Gages (Right)

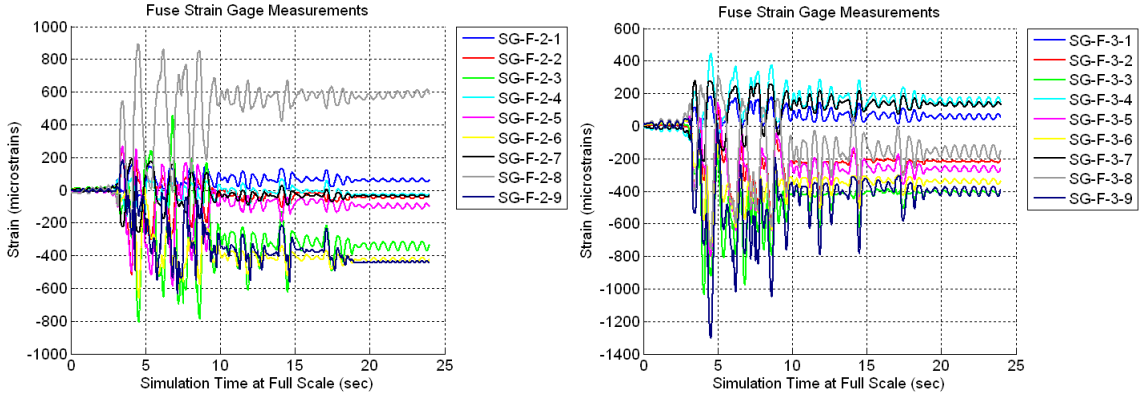

Figure B.304 Raw Data For Specimen A6 MCE Trial – Bottom Front Fuse Strain Gages (Left) and Mid-Height Back Fuse Strain Gages (Right)

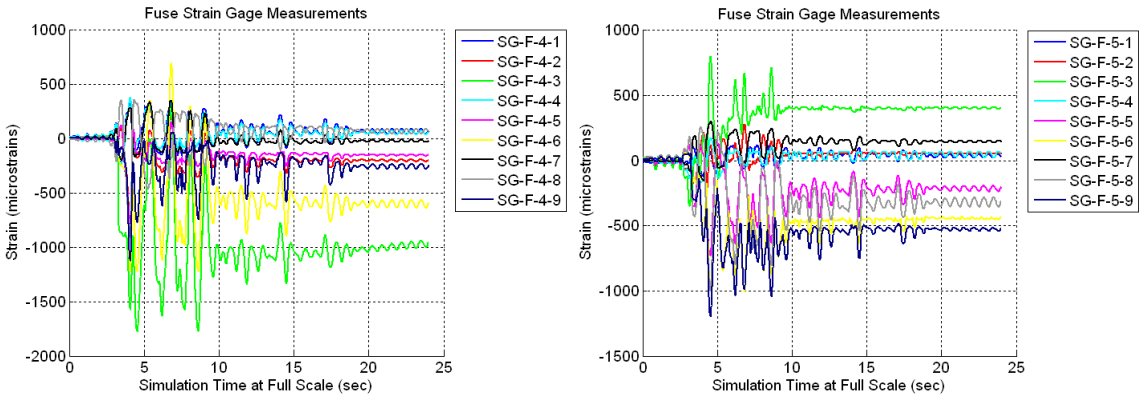

Figure B.305 Raw Data For Specimen A6 MCE Trial – Mid-Height Front Fuse Strain Gages (Left) and Top Back Fuse Strain Gages (Right)

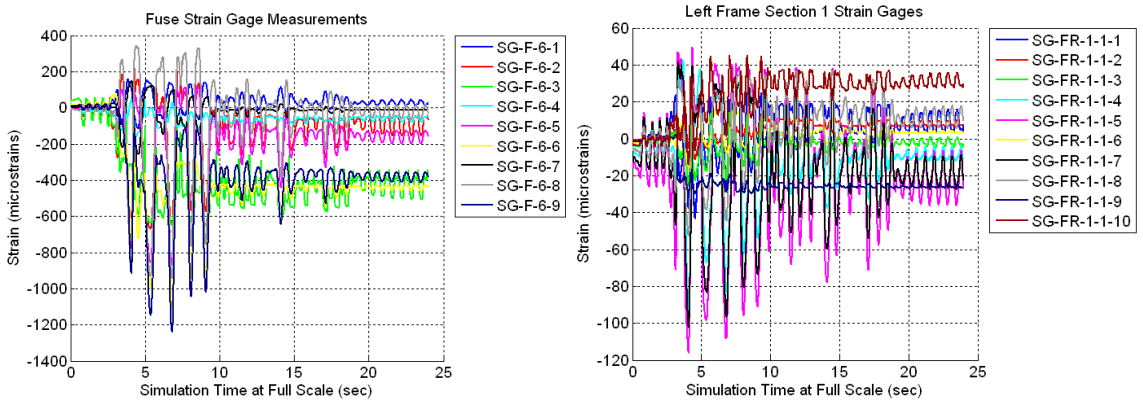

Figure B.306 Raw Data For Specimen A6 MCE Trial – Top Front Fuse Strain Gages (Left) and Left Frame Section 1-1 Strain Gages (Right)

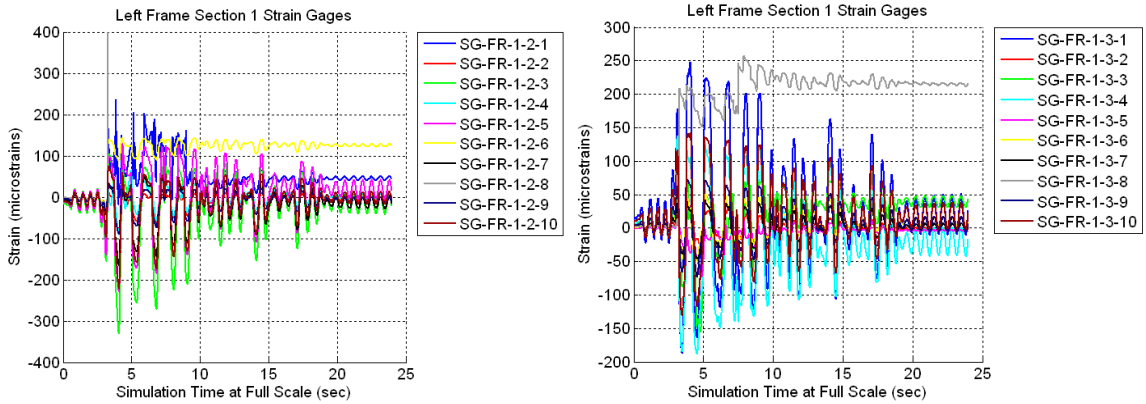

Figure B.307 Raw Data For Specimen A6 MCE Trial – Left Frame Section 1-2 Strain Gages (Left) and Left Frame Section 1-3 Strain Gages (Right)

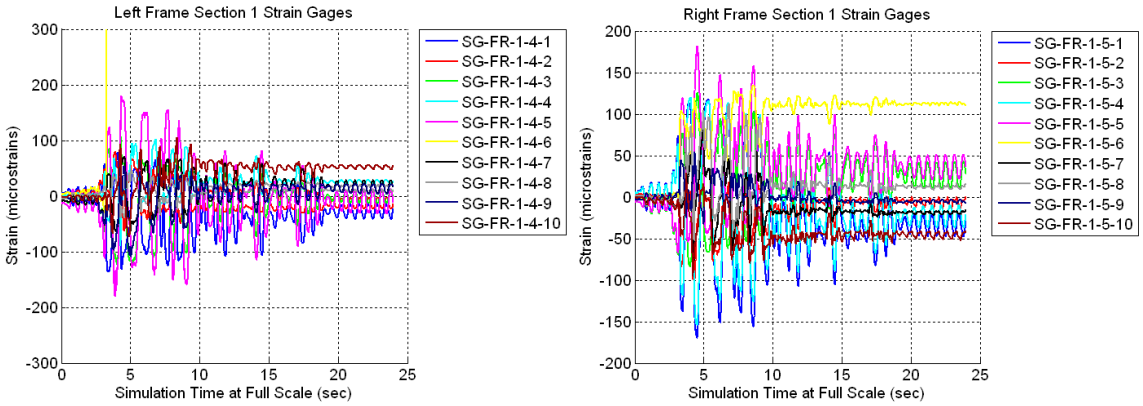

Figure B.308 Raw Data For Specimen A6 MCE Trial – Left Frame Section 1-4 Strain Gages (Left) and Right Frame Section 1-5 Strain Gages (Right)

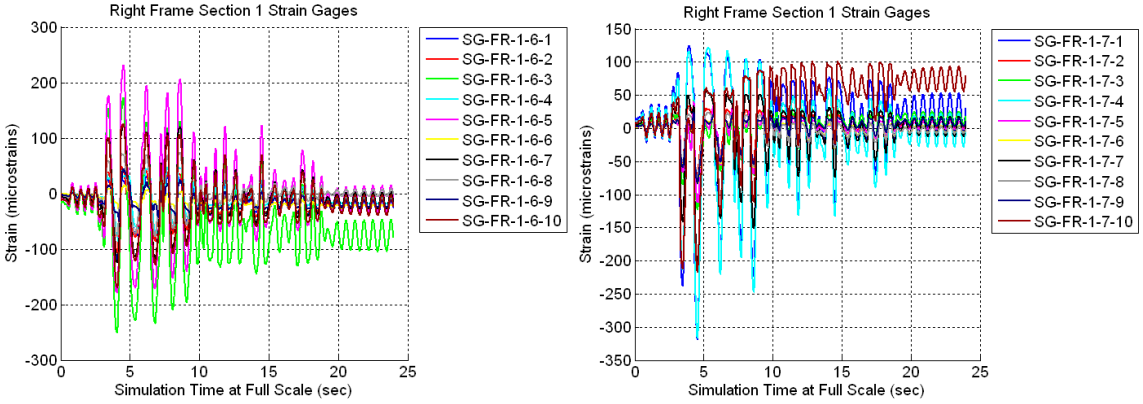

Figure B.309 Raw Data For Specimen A6 MCE Trial – Right Frame Section 1-6 Strain Gages (Left) and Right Frame Section 1-7 Strain Gages (Right)

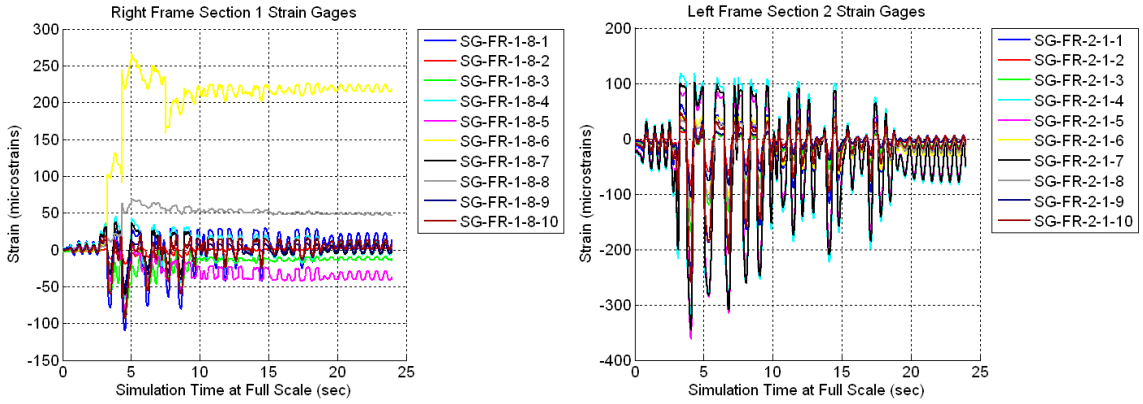

Figure B.310 Raw Data For Specimen A6 MCE Trial – Right Frame Section 1-8 Strain Gages (Left) and Left Frame Section 2-1 Strain Gages (Right)

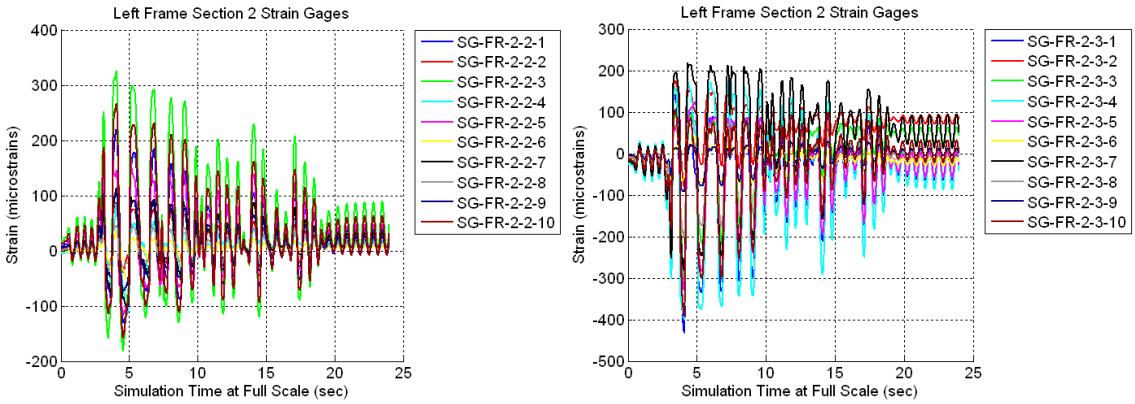

Figure B.311 Raw Data For Specimen A6 MCE Trial – Left Frame Section 2-2 Strain Gages (Left) and Left Frame Section 2-3 Strain Gages (Right)

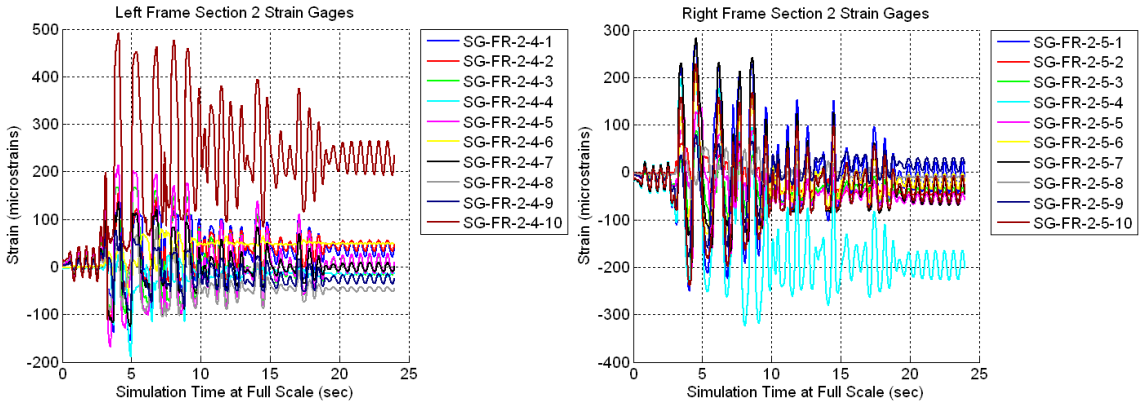

Figure B.312 Raw Data For Specimen A6 MCE Trial – Left Frame Section 2-4 Strain Gages (Left) and Right Frame Section 2- 5 Strain Gages (Right)

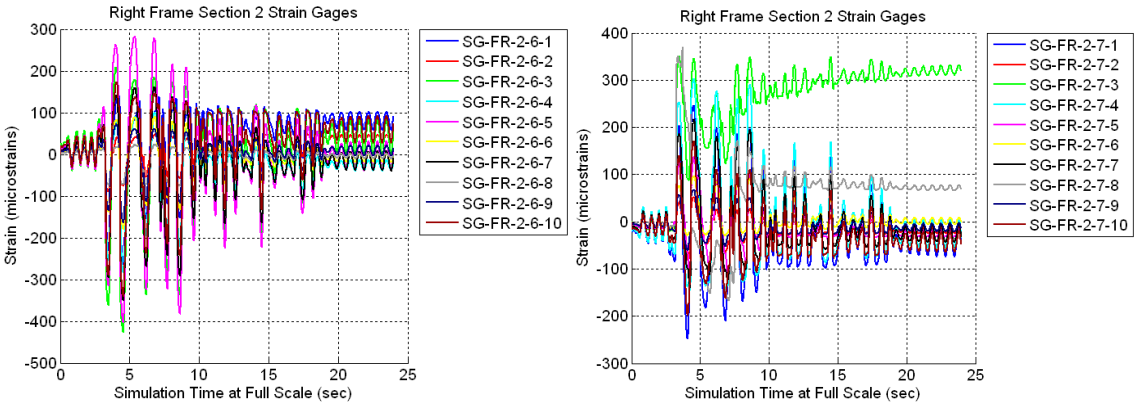

Figure B.313 Raw Data For Specimen A6 MCE Trial – Right Frame Section 2-6 Strain Gages (Left) and Right Frame Section 2-7 Strain Gages (Right)

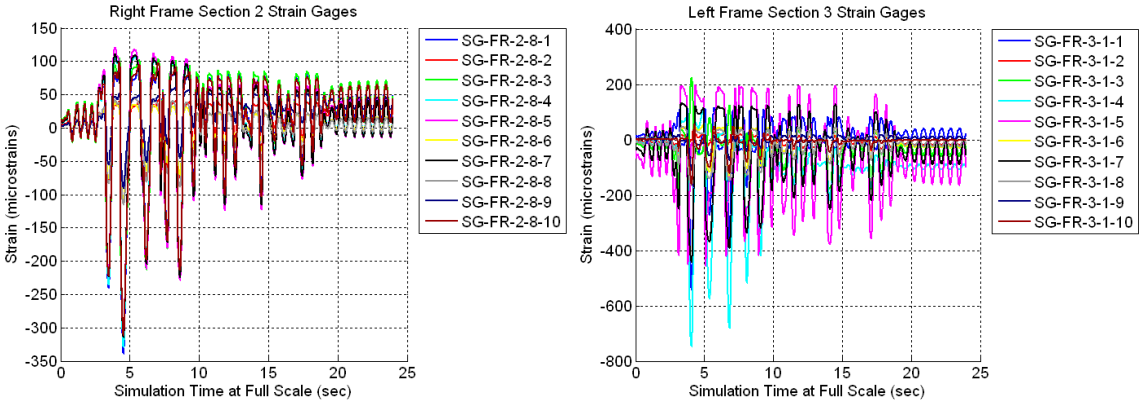

Figure B.314 Raw Data For Specimen A6 MCE Trial – Right Frame Section 2-8 Strain Gages (Left) and Left Frame Section 3-1 Strain Gages (Right)

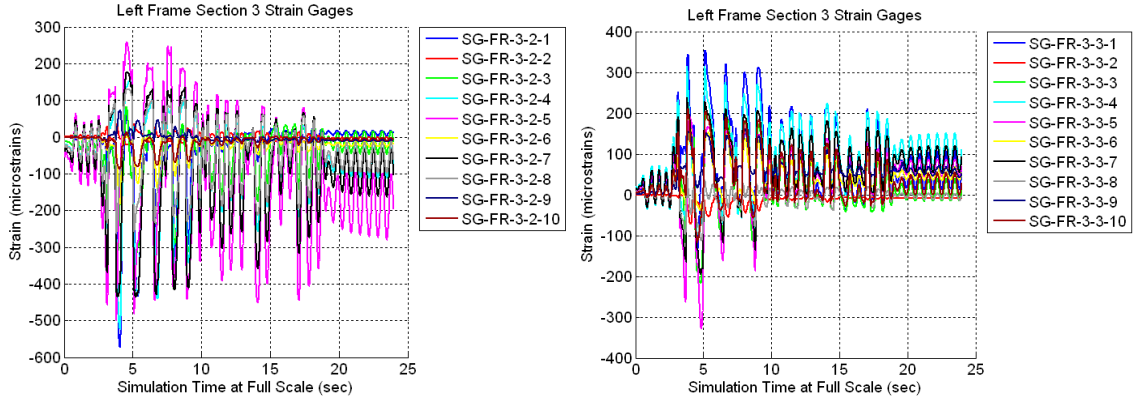

Figure B.315 Raw Data For Specimen A6 MCE Trial – Left Frame Section 3-2 Strain Gages (Left) and Left Frame Section 3-3 Strain Gages (Right)

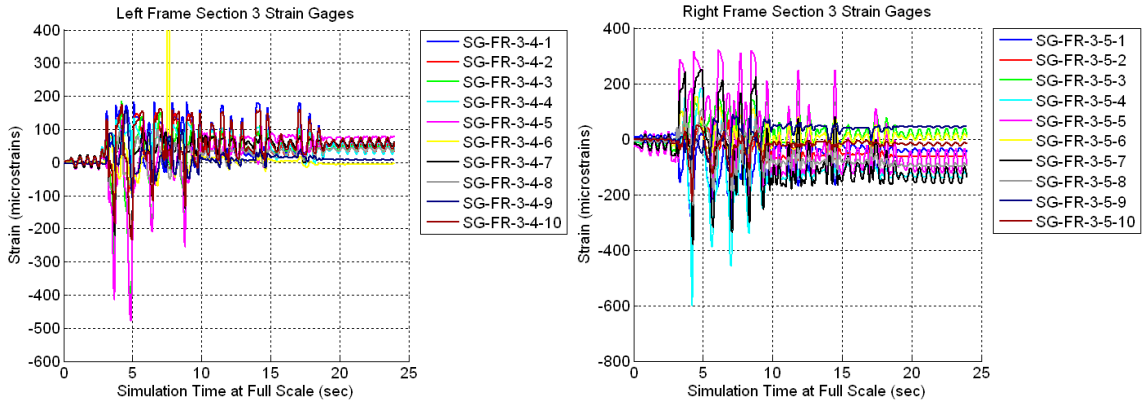

Figure B.316 Raw Data For Specimen A6 MCE Trial – Left Frame Section 3-4 Strain Gages (Left) and Right Frame Section 3-5 Strain Gages (Right)

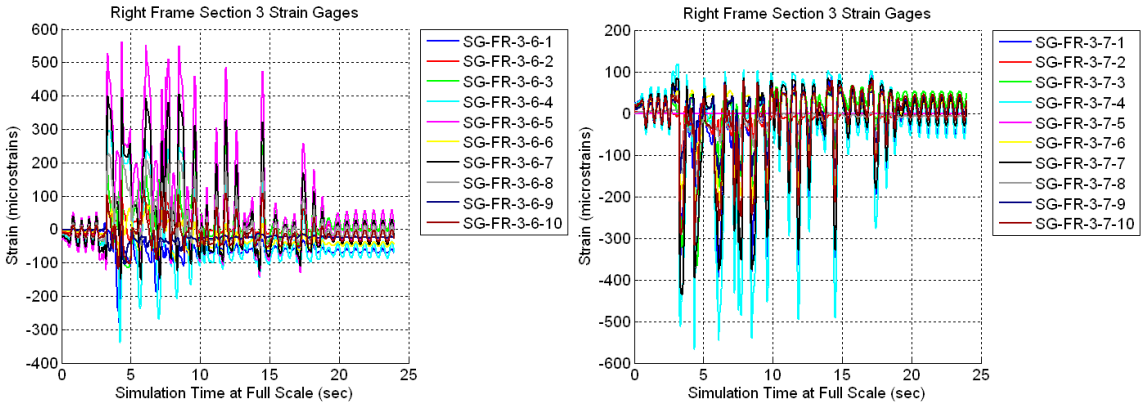

Figure B.317 Raw Data For Specimen A6 MCE Trial – Right Frame Section 3-6 Strain Gages (Left) and Right Frame Section 3-7 Strain Gages (Right)

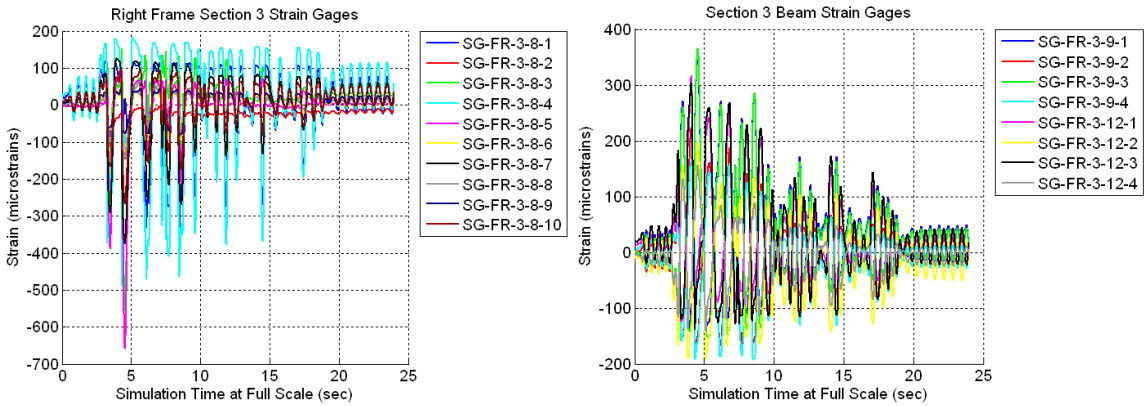

Figure B.318 Raw Data For Specimen A6 MCE Trial – Right Frame Section 3-8 Strain Gages (Left) and Third Floor Beam Strain Gages (Right)

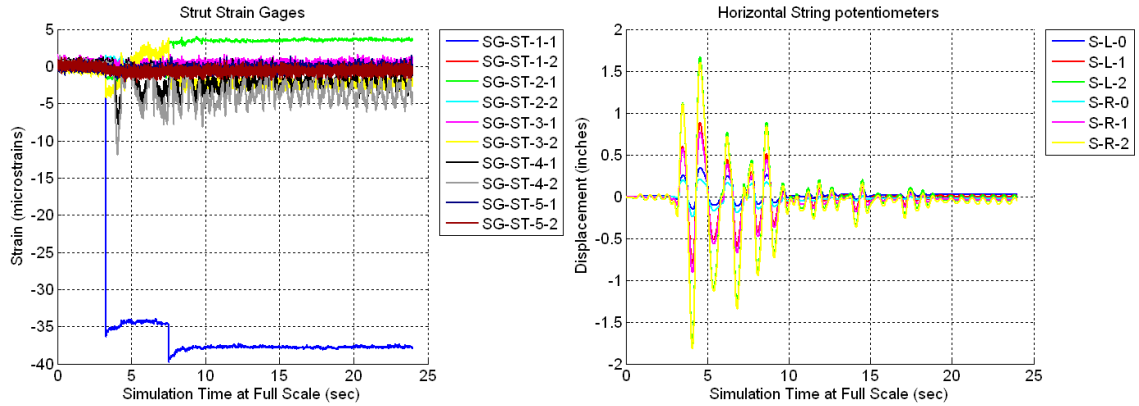

Figure B.319 Raw Data For Specimen A6 MCE Trial – Strut Strain Gages (Left) and Horizontal String Potentiometers (Right)

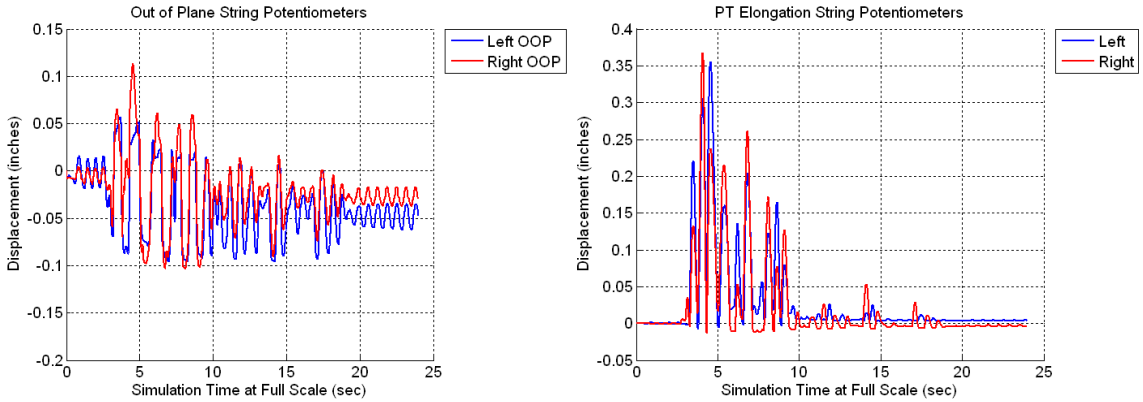

Figure B.320 Raw Data For Specimen A6 MCE Trial – Out-of-Plane String Potentiometers (Left) and PT Elongation String Potentiometers (Right)

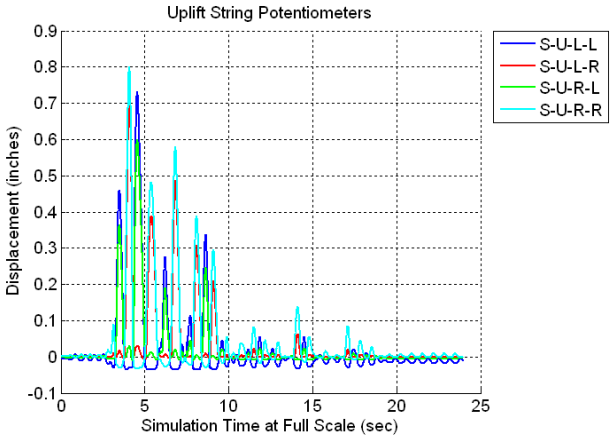

Figure B.321 Raw Data For Specimen A6 MCE Trial – Uplift String Potentiometers

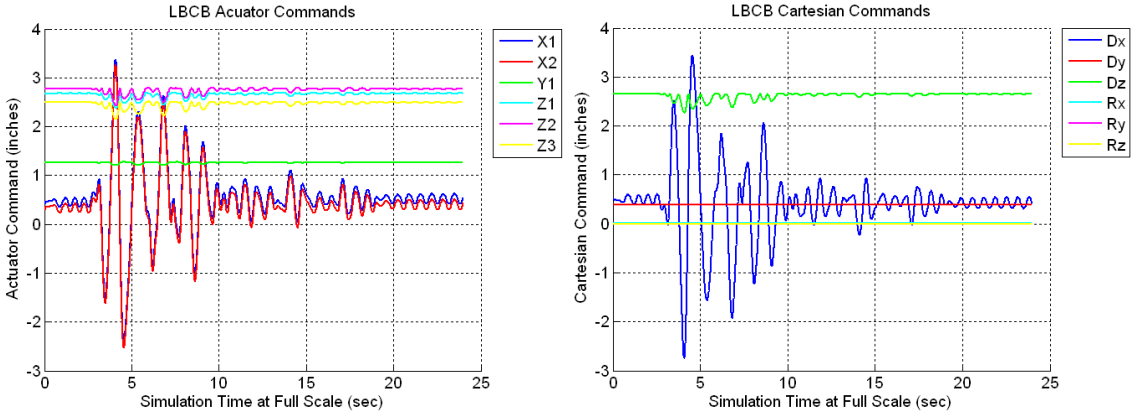

Figure B.322 Raw Data For Specimen A6 MCE Trial – LBCB Actuator Commands (Left) and LBCB Cartesian Commands (Right)

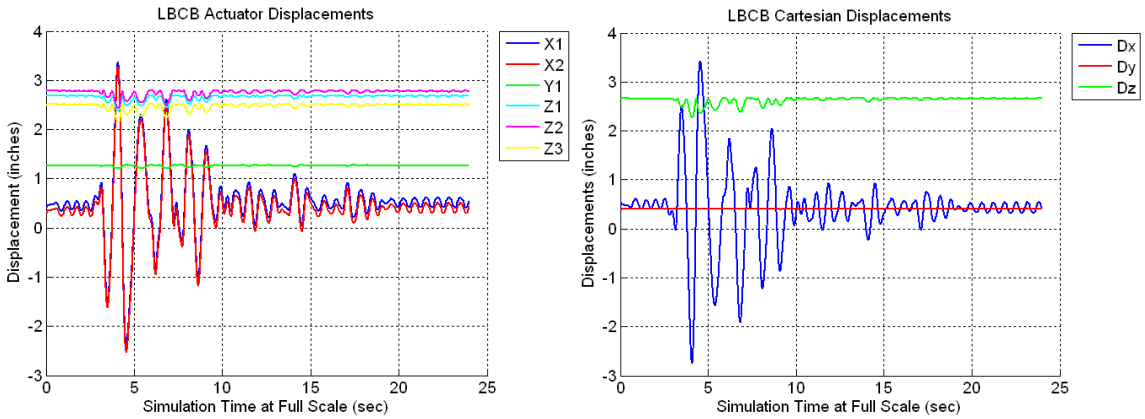

Figure B.323 Raw Data For Specimen A6 MCE Trial – LBCB Actuator Displacements (Left) LBCB Cartesian Displacements (Right)

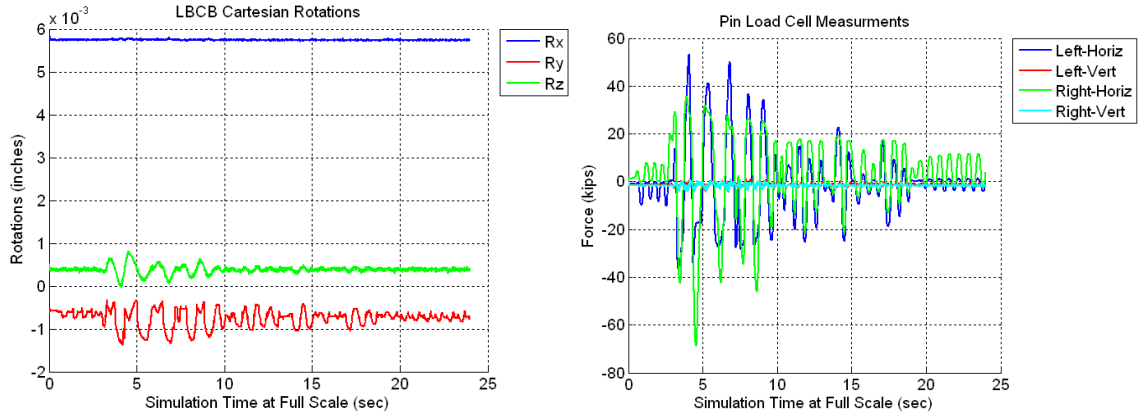

Figure B.324 Raw Data For Specimen A6 MCE Trial – LBCB Cartesian Rotations (Left) and Pin Load Cells (Right)

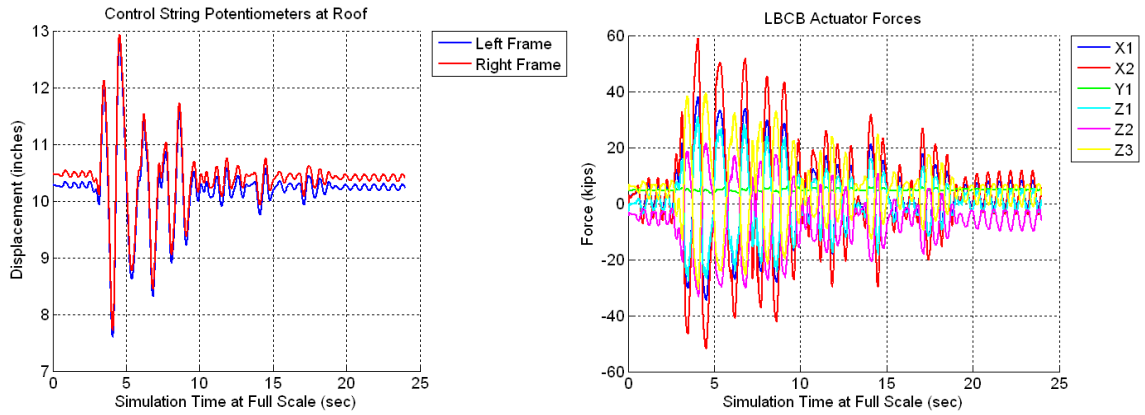

Figure B.325 Raw Data For Specimen A6 MCE Trial – Control Roof String Potentiometers (Left) and LBCB Actuator Forces (Right)

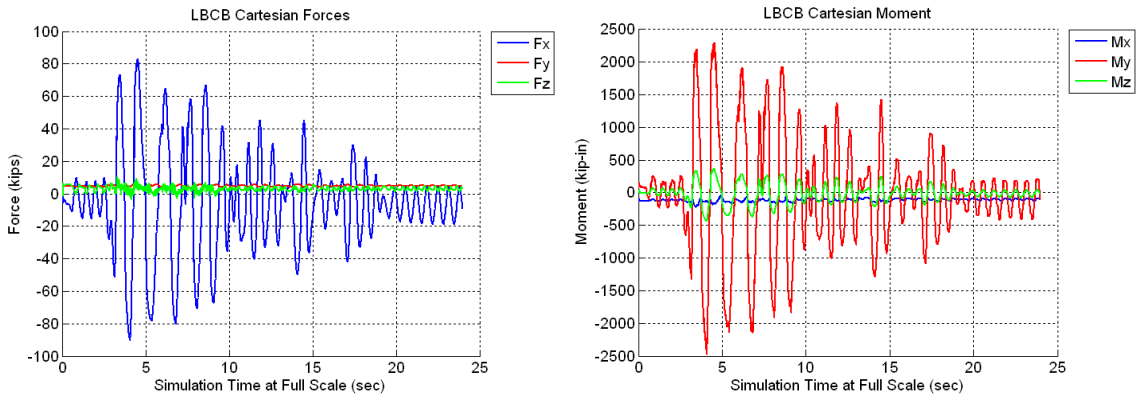

Figure B.326 Raw Data For Specimen A6 MCE Trial – LBCB Cartesian Forces (Left) and LBCB Cartesian Moments (Right)

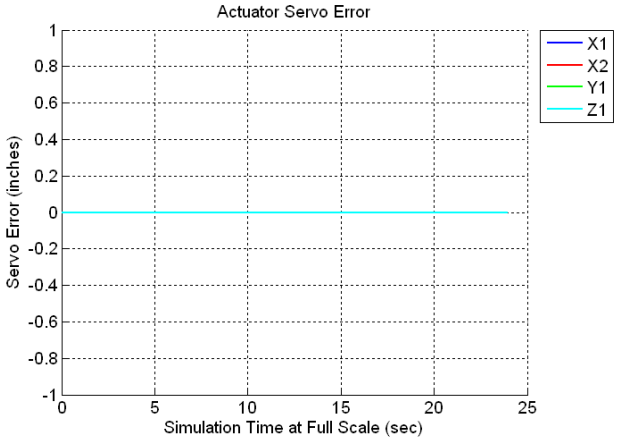

Figure B.327 Raw Data For Specimen A6 MCE Trial – LBCB Actuator Servo-Error

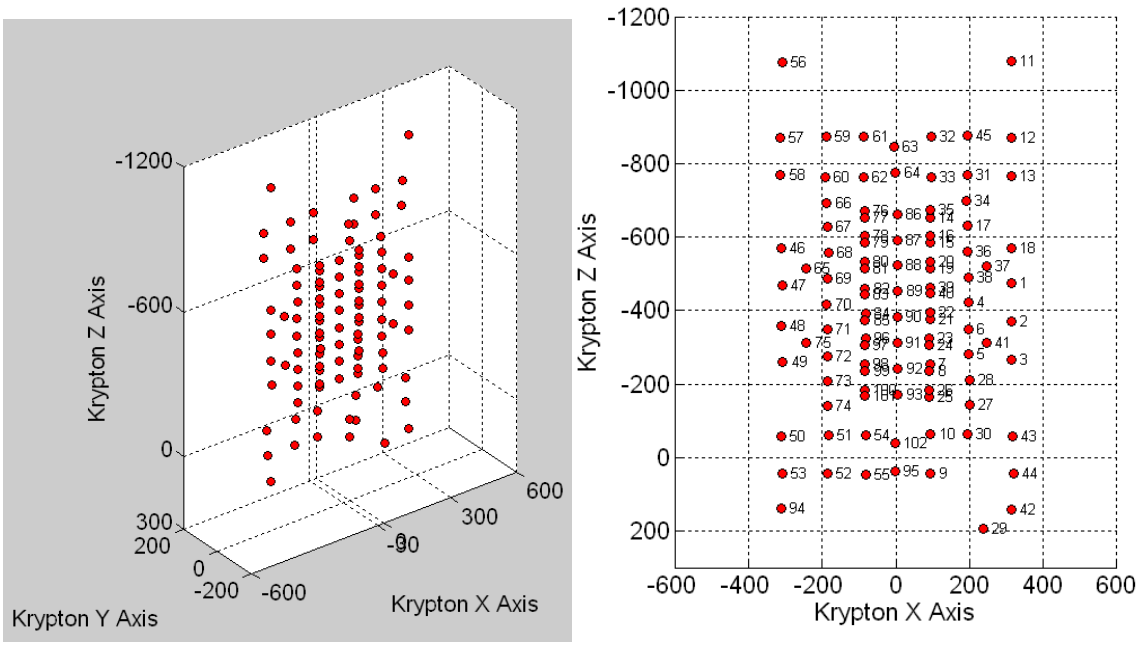

Figure B.328 Raw Data For Specimen A6 MCE Trial – Krypton LED Locations (Left) and Krytpon LED Numbering (Right)

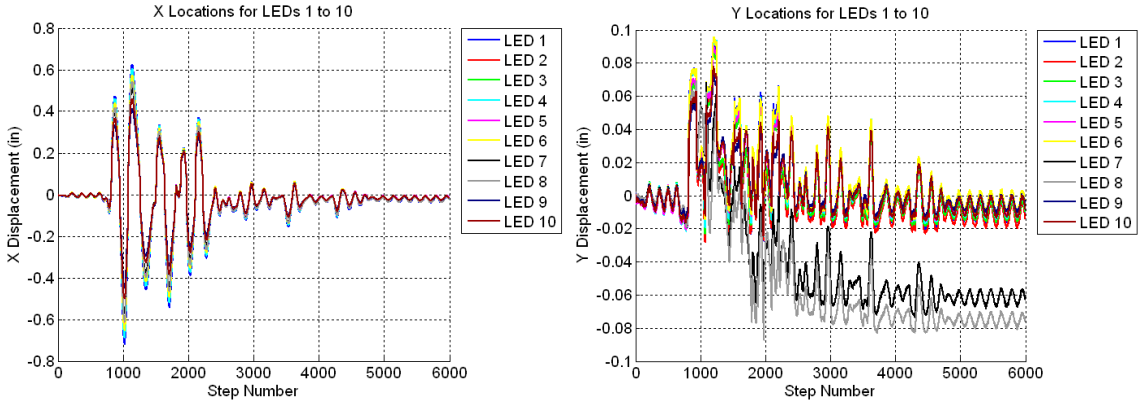

Figure B.329 Raw Data For Specimen A6 MCE Trial – X Displacements for LED's 1 to 10 (Left) and Y Displacements for LED's 1 to 10 (Right)

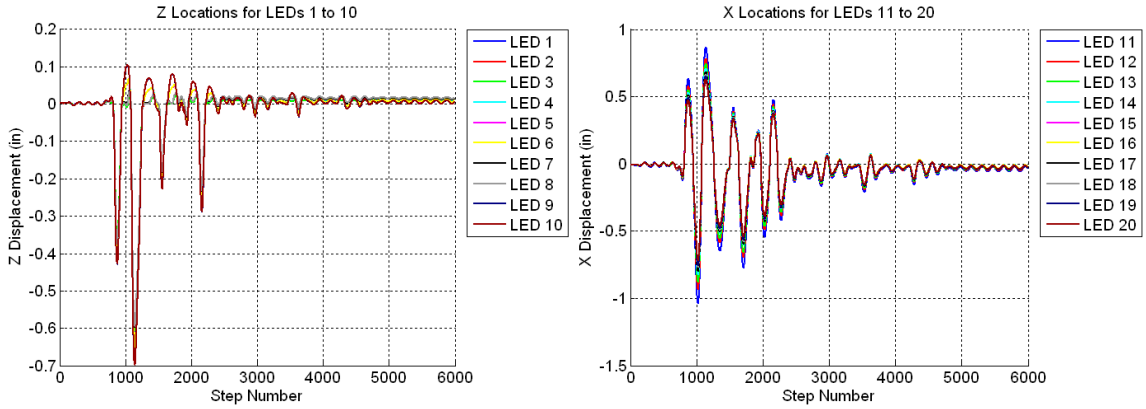

Figure B.330 Raw Data For Specimen A6 MCE Trial – Z Displacements for LED's 1 to 10 (Left) and X Displacements for LED's 11 to 20 (Right)

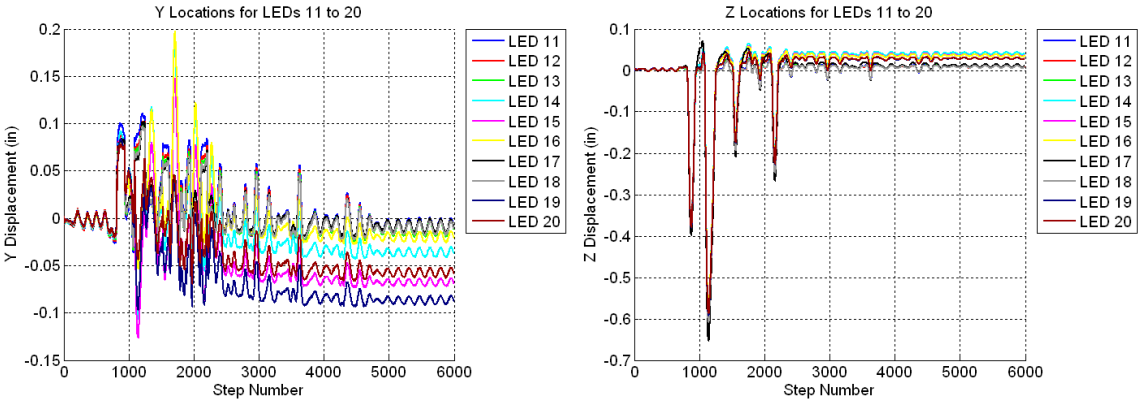

Figure B.331 Raw Data For Specimen A6 MCE Trial – Y Displacements for LED's 11 to 20 (Left) and Z Displacements for LED's 11 to 20 (Right)

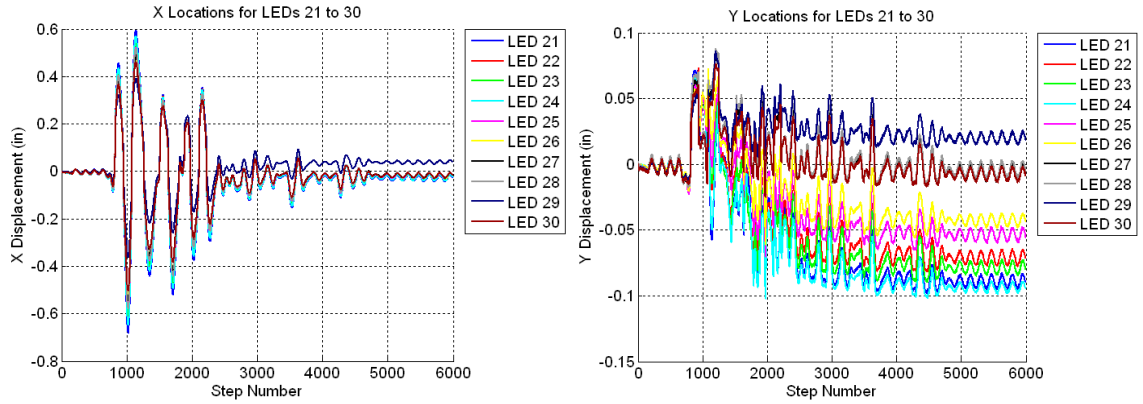

Figure B.332 Raw Data For Specimen A6 MCE Trial – X Displacements for LED's 21 to 30 (Left) and Y Displacements for LED's 21 to 30 (Right)

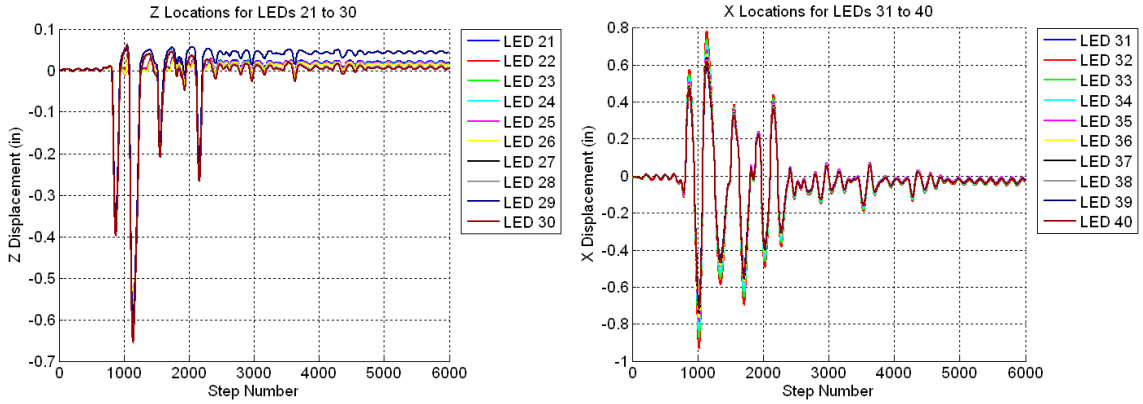

Figure B.333 Raw Data For Specimen A6 MCE Trial – Z Displacements for LED's 21 to 30 (Left) and X Displacements for LED's 31 to 40 (Right)

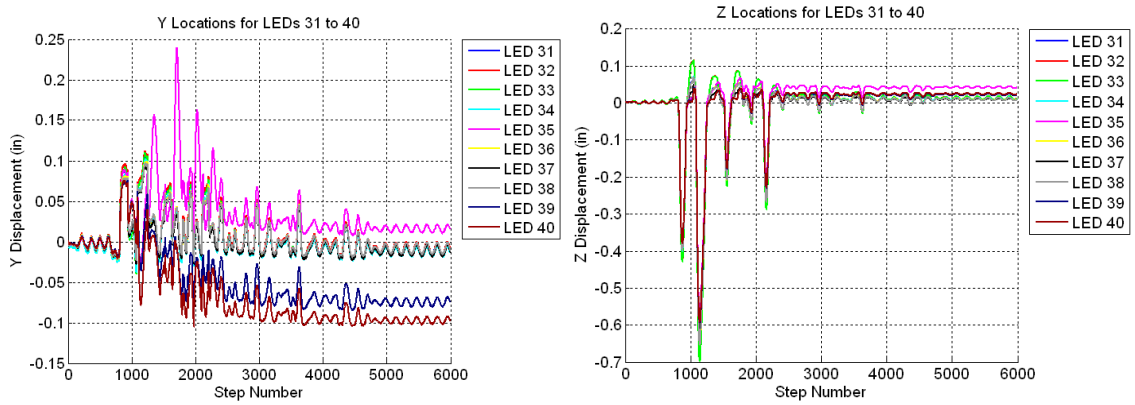

Figure B.334 Raw Data For Specimen A6 MCE Trial – Y Displacements for LED's 31 to 40 (Left) and Z Displacements for LED's 31 to 40 (Right)

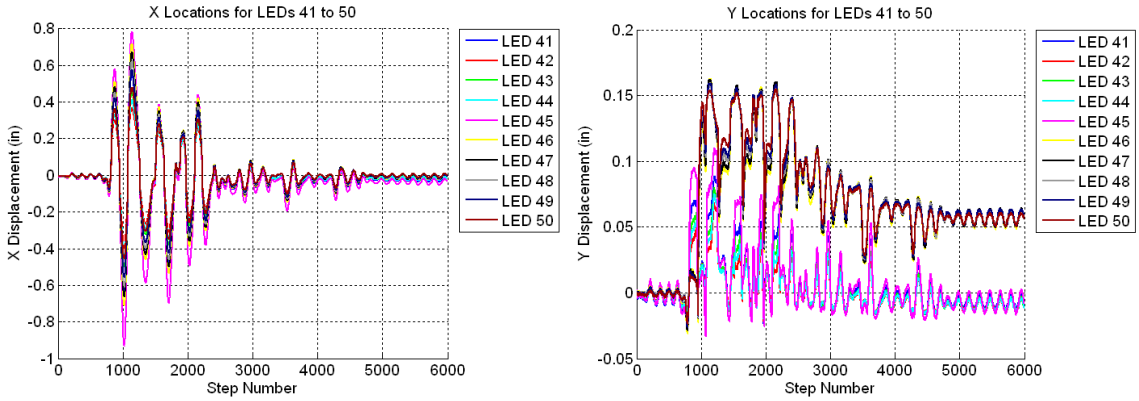

Figure B.335 Raw Data For Specimen A6 MCE Trial – X Displacements for LED's 41 to 50 (Left) and Y Displacements for LED's for 41 to 50 (Right)

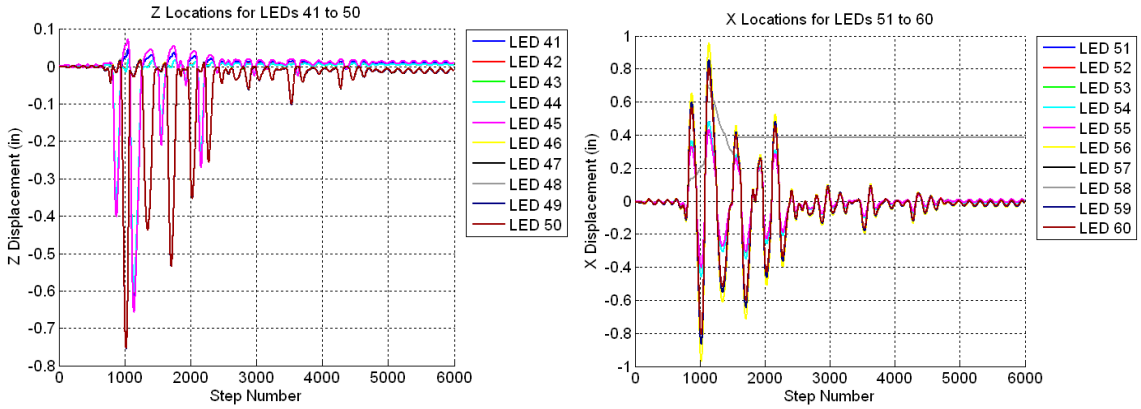

Figure B.336 Raw Data For Specimen A6 MCE Trial – Z Displacements for LED's 41 to 50 (Left) and X Displacements for LED's 51 to 60 (Right)

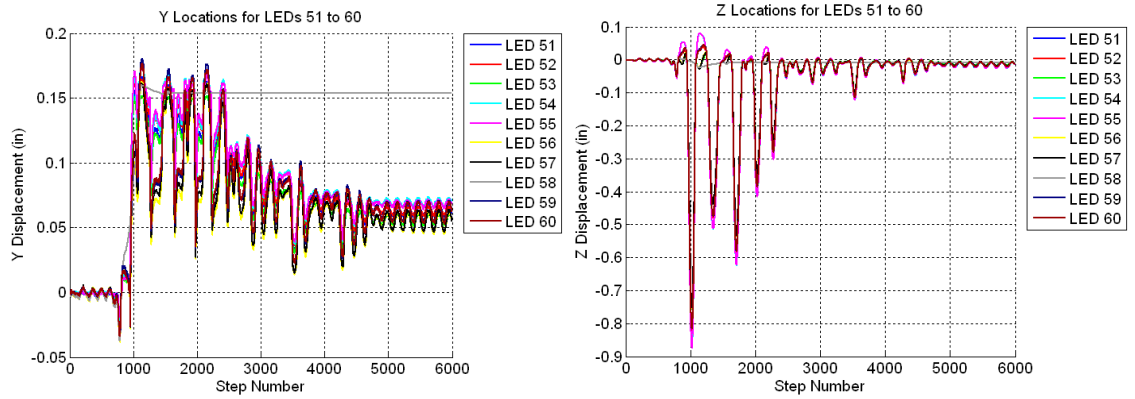

Figure B.337 Raw Data For Specimen A6 MCE Trial – Y Displacements for LED's 51 to 60 (Left) and Z Displacements for LED's 51 to 60 (Right)

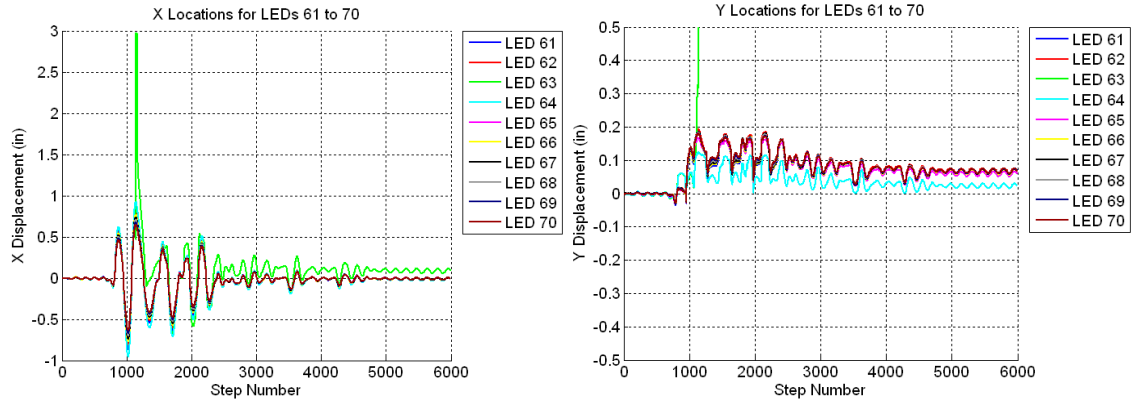

Figure B.338 Raw Data For Specimen A6 MCE Trial – X Displacements for LED's 61 to 70 (Left) and Y Displacements for LED's 61 to 70 (Right)

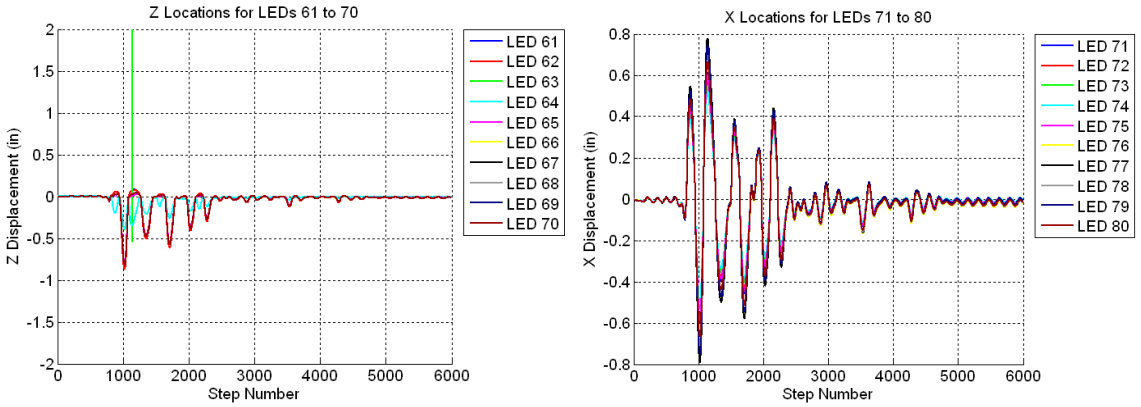

Figure B.339 Raw Data For Specimen A6 MCE Trial – Z Displacements for LED's 61 to 70 (Left) and X Displacements for LED's 71 to 80 (Right)

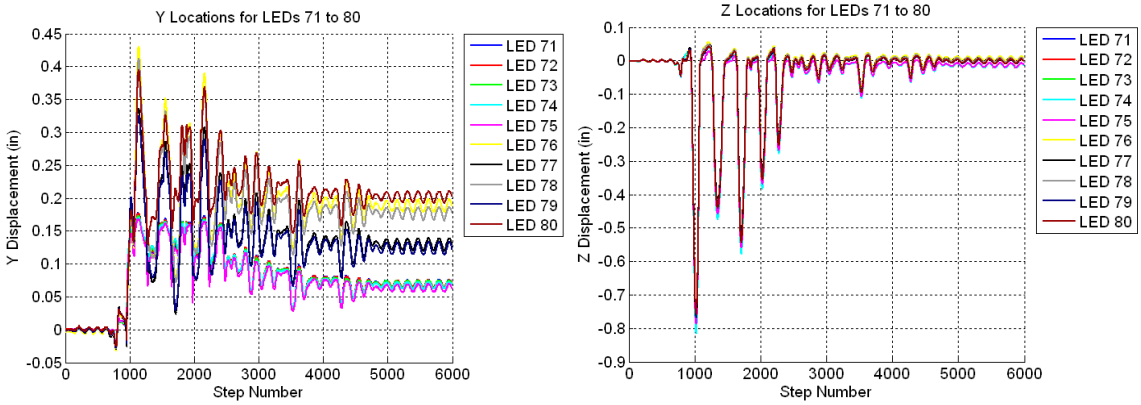

Figure B.340 Raw Data For Specimen A6 MCE Trial – Y Displacements for LED's 71 to 80 (Left) Z Displacements for LED's 71 to 80 (Right)

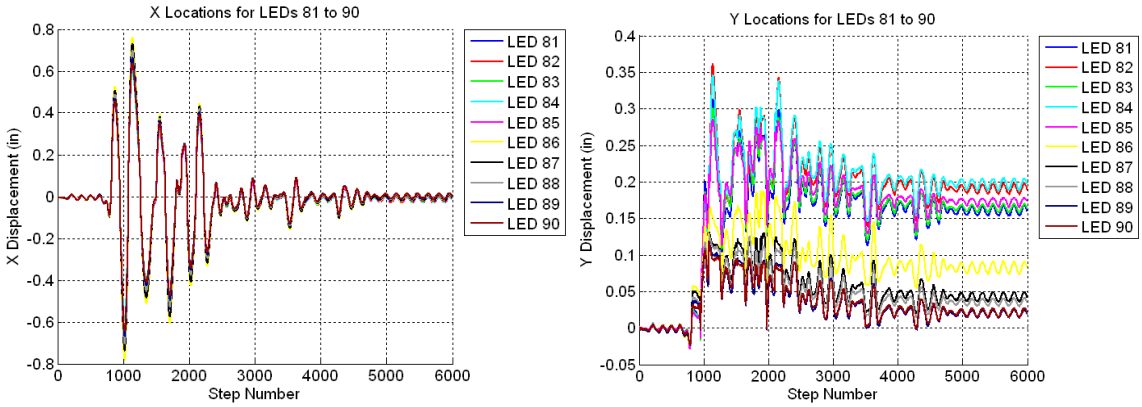

Figure B.341 Raw Data For Specimen A6 MCE Trial – X Location for LED's 81 to 90 (Left) and Y Displacements for LED's 81 to 90 (Right)

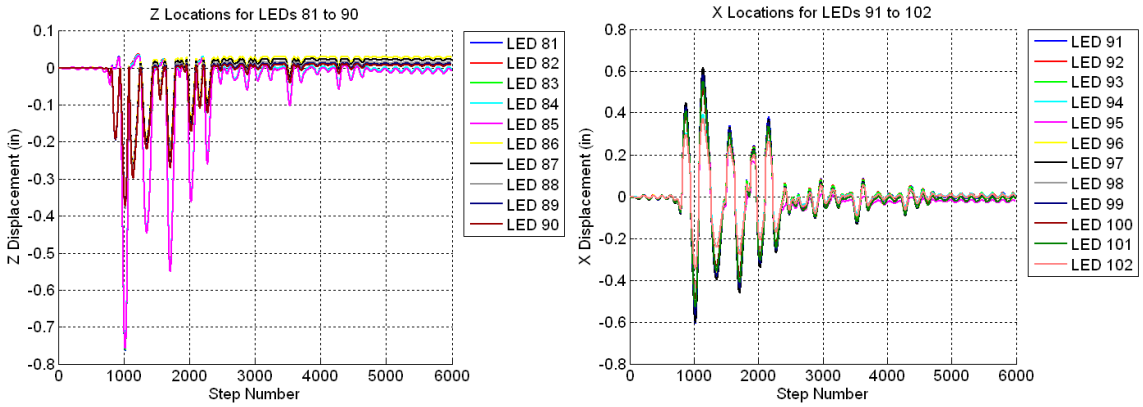

Figure B.342 Raw Data For Specimen A6 MCE Trial – Z Displacements for LED's 81 to 90 (Left) and X Displacements for LED's 91 to 102 (Right)

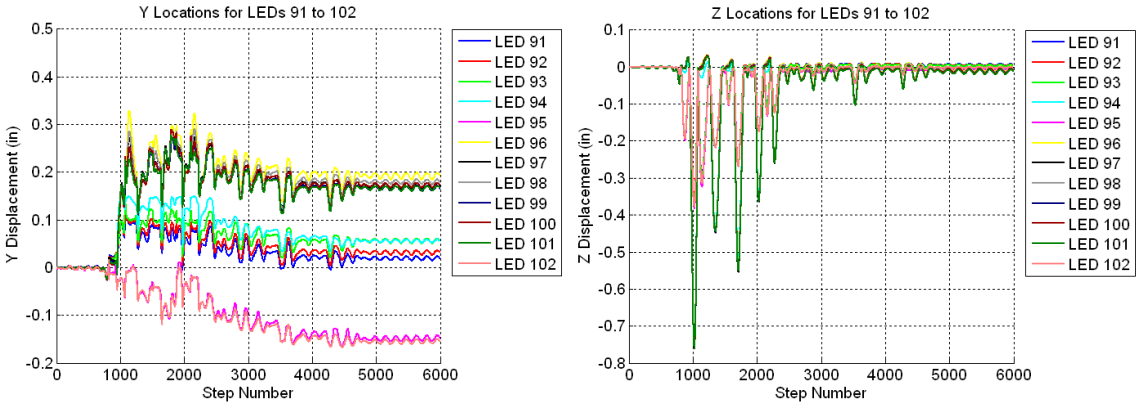

Figure B.343 Raw Data For Specimen A6 MCE Trial – Y Displacements for LED's 91 to 102 (Left) and Z Displacements for LED's 91 to 102 (Right)

B.9 Specimen A6 – MCE Trial with Out-of-Plane Motion

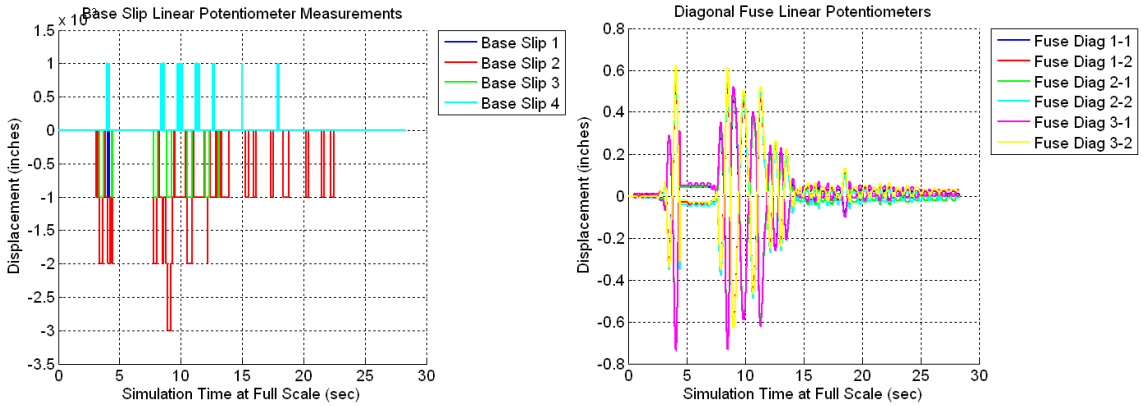

Figure B.344 Raw Data For Specimen A6 MCE Trial with Out-of-Plane Motion – Base Slip (Left) and Fuse Linear Potentiometers (Right)

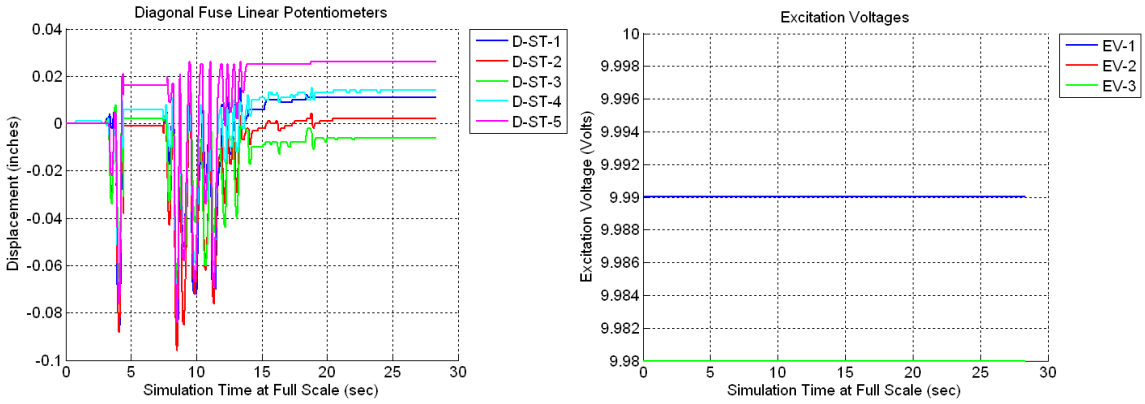

Figure B.345 Raw Data For Specimen A6 MCE Trial with Out-of-Plane Motion – Strut Strain Gages (Left) and Excitation Voltages (Right)

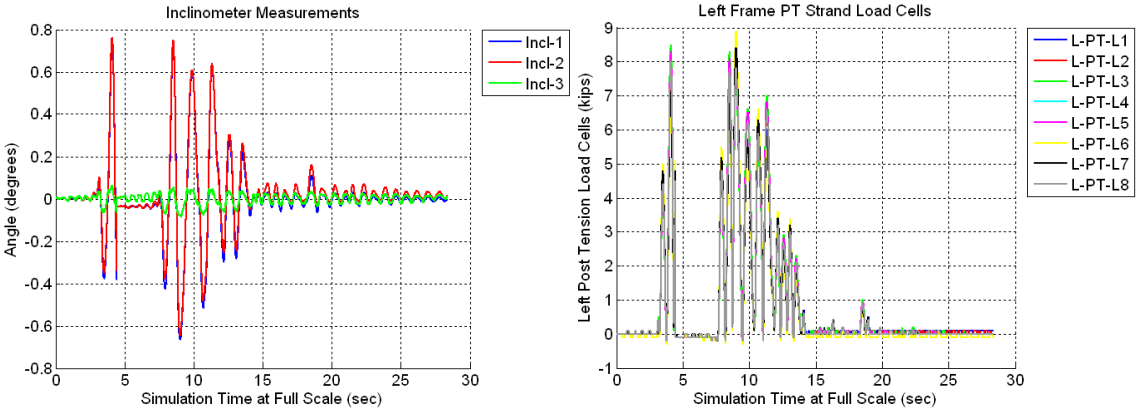

Figure B.346 Raw Data For Specimen A6 MCE Trial with Out-of-Plane Motion – Inclinometers (Left) and Left Frame PT Load Cells (Right)

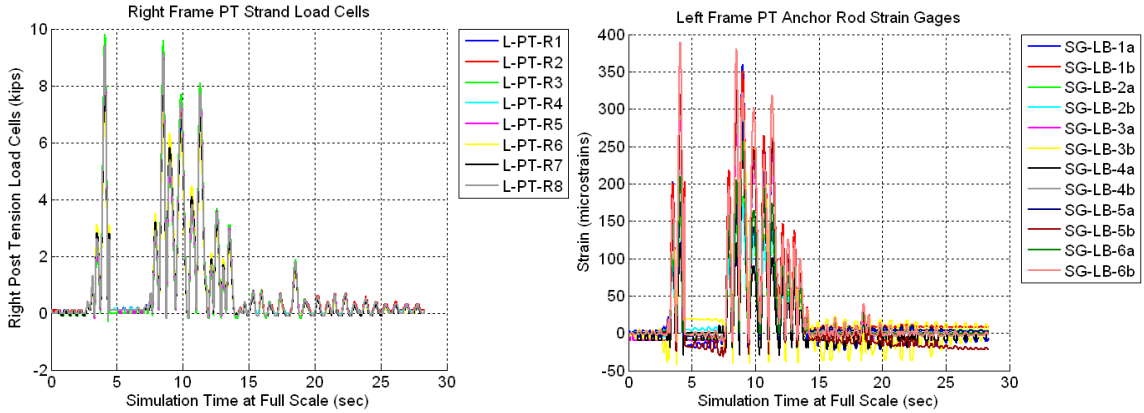

Figure B.347 Raw Data For Specimen A6 MCE Trial with Out-of-Plane Motion – Right Frame PT Load Cells (Left) and Left Frame PT Anchor Rods (Right)

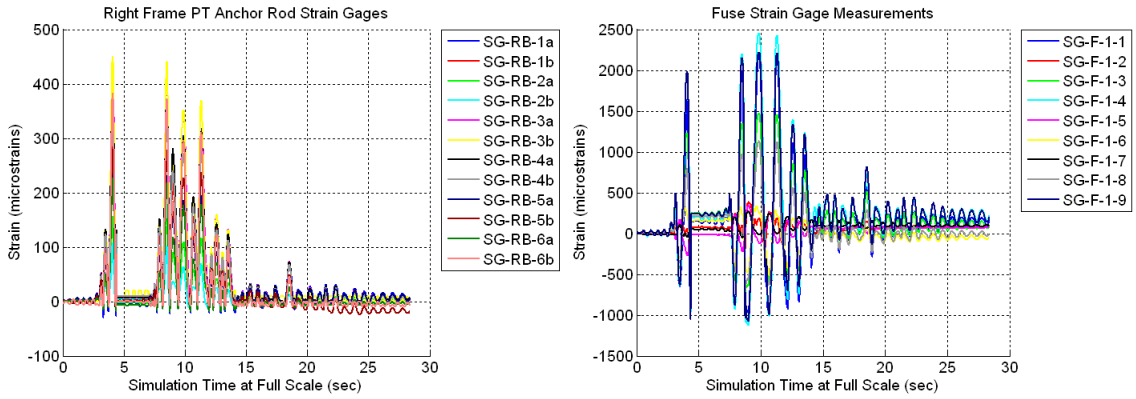

Figure B.348 Raw Data For Specimen A6 MCE Trial with Out-of-Plane Motion – Right Frame PT Anchor Rods (Left) and Bottom Back Fuse Strain Gages (Right)

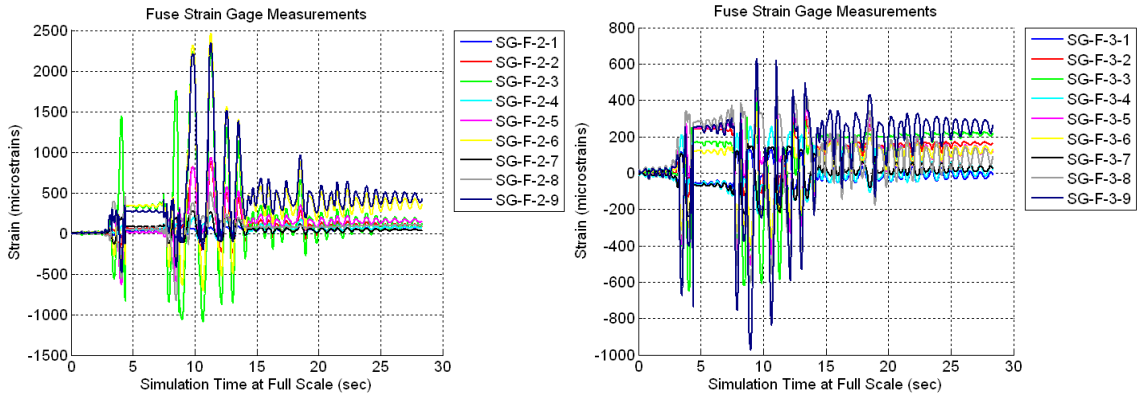

Figure B.349 Raw Data For Specimen A6 MCE Trial with Out-of-Plane Motion – Bottom Front Fuse Strain Gages (Left) and Mid-Height Back Fuse Strain Gages (Right)

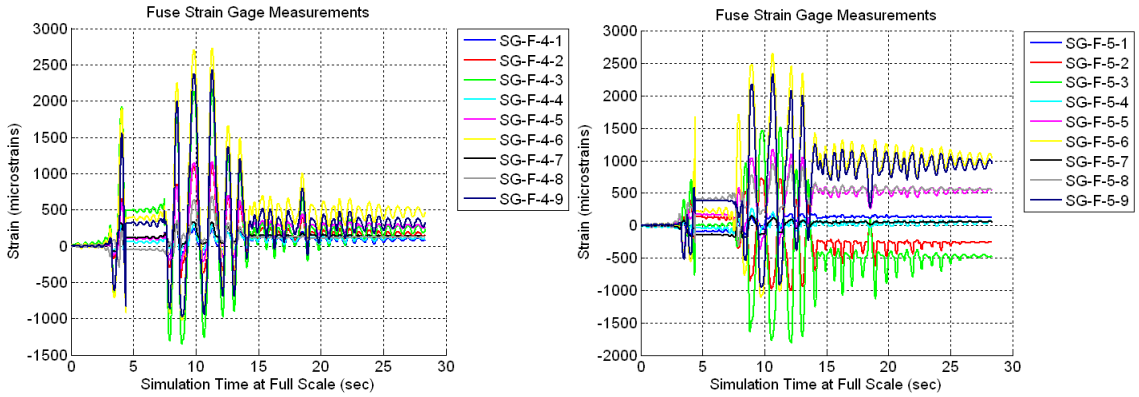

Figure B.350 Raw Data For Specimen A6 MCE Trial with Out-of-Plane Motion – Mid-Height Front Fuse Strain Gages (Left) and Top Back Fuse Strain Gages (Right)

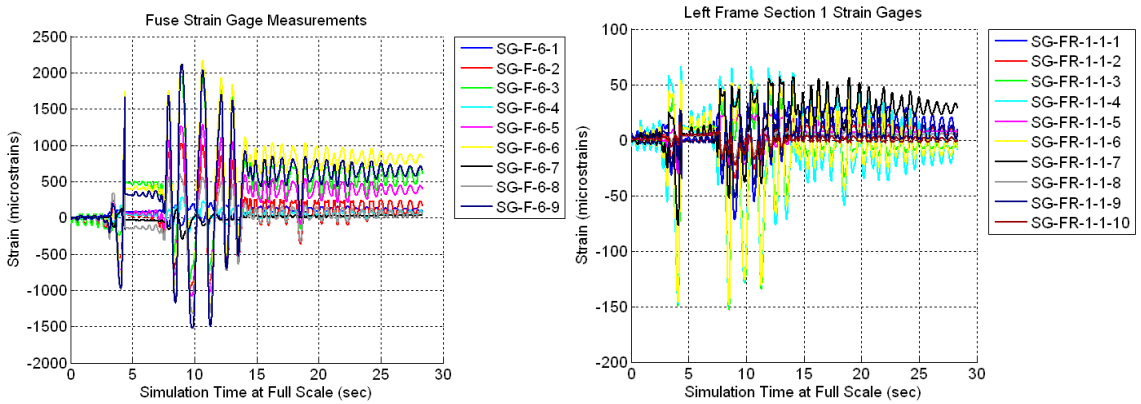

Figure B.351 Raw Data For Specimen A6 MCE Trial with Out-of-Plane Motion – Top Front Fuse Strain Gages (Left) and Left Frame Section 1-1 Strain Gages (Right)

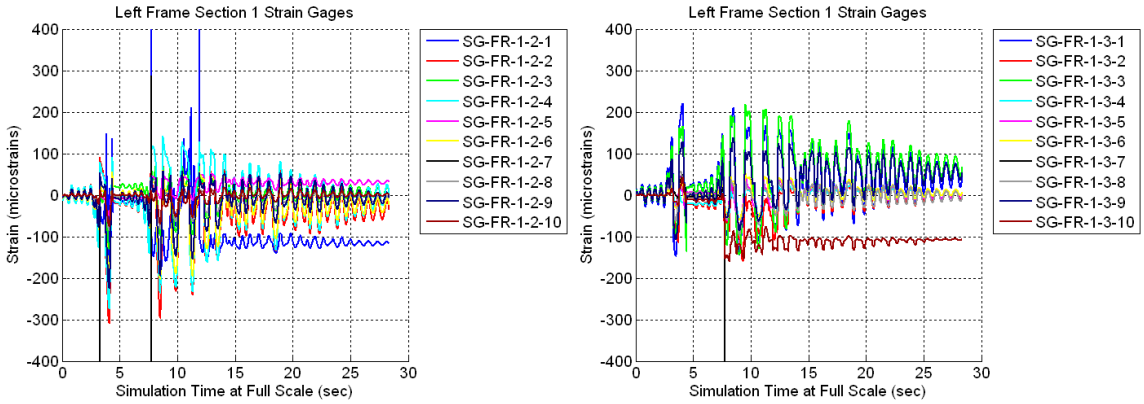

Figure B.352 Raw Data For Specimen A6 MCE Trial with Out-of-Plane Motion – Left Frame Section 1-2 Strain Gages (Left) and Left Frame Section 1-3 Strain Gages (Right)

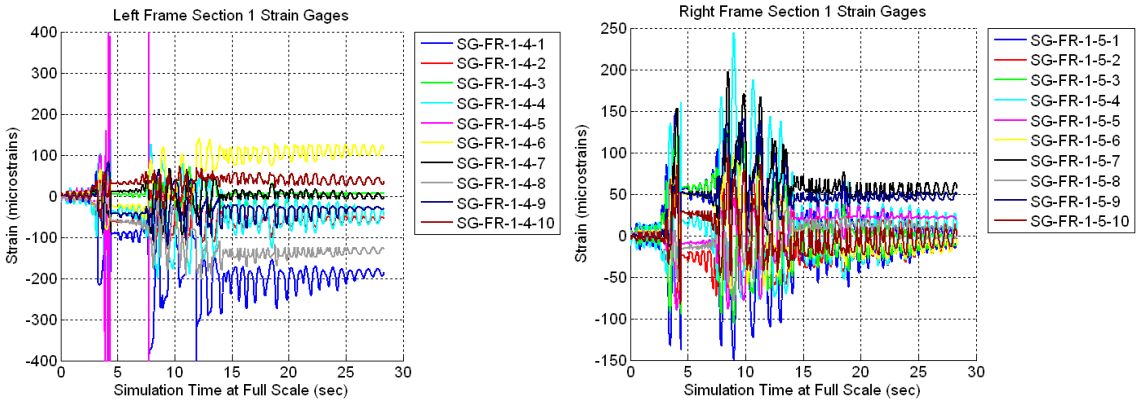

Figure B.353 Raw Data For Specimen A6 MCE Trial with Out-of-Plane Motion – Left Frame Section 1-4 Strain Gages (Left) and Right Frame Section 1-5 Strain Gages (Right)

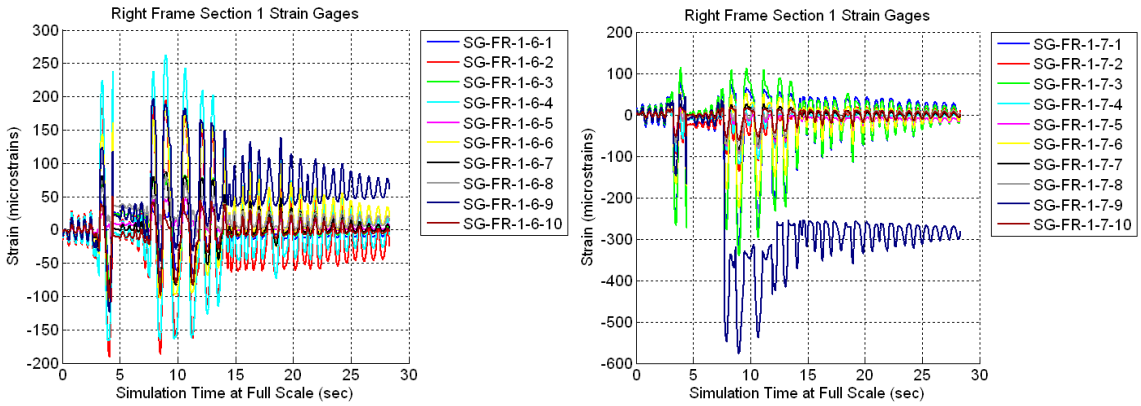

Figure B.354 Raw Data For Specimen A6 MCE Trial with Out-of-Plane Motion – Right Frame Section 1-6 Strain Gages (Left) and Right Frame Section 1-7 Strain Gages (Right)

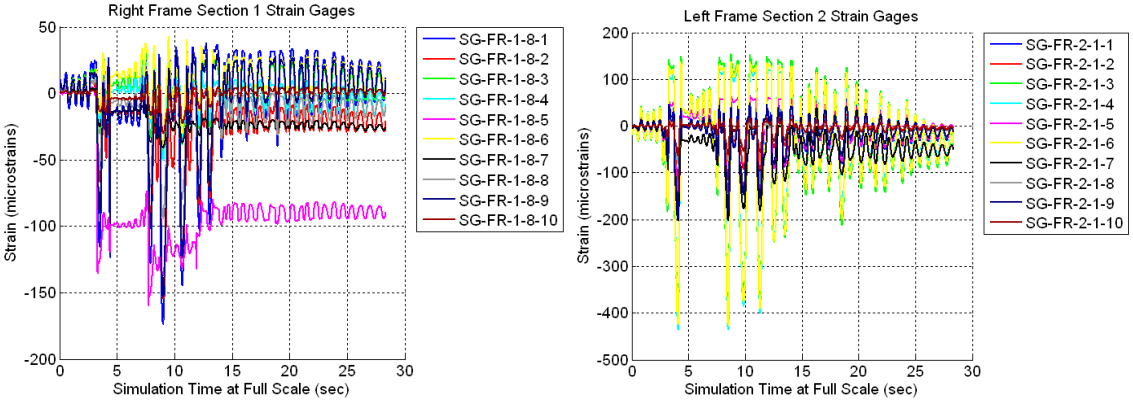

Figure B.355 Raw Data For Specimen A6 MCE Trial with Out-of-Plane Motion – Right Frame Section 1-8 Strain Gages (Left) and Left Frame Section 2-1 Strain Gages (Right)

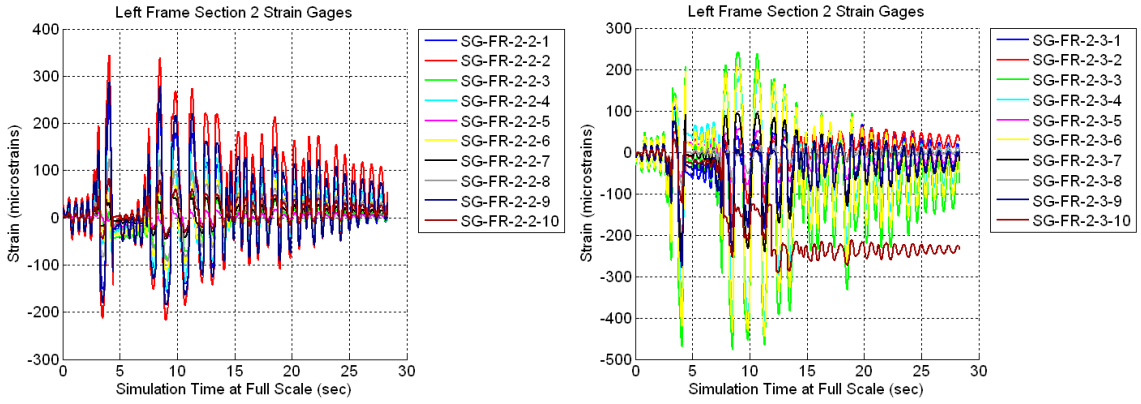

Figure B.356 Raw Data For Specimen A6 MCE Trial with Out-of-Plane Motion – Left Frame Section 2-2 Strain Gages (Left) and Left Frame Section 2-3 Strain Gages (Right)

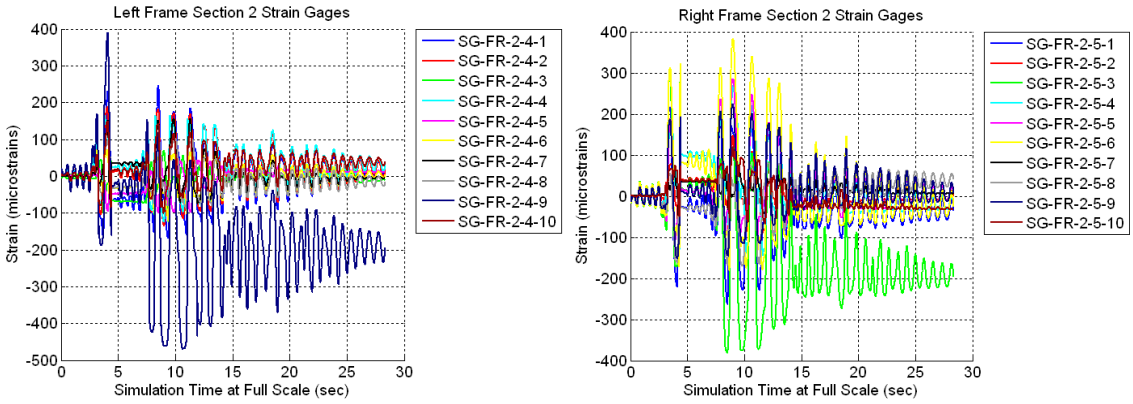

Figure B.357 Raw Data For Specimen A6 MCE Trial with Out-of-Plane Motion – Left Frame Section 2-4 Strain Gages (Left) and Right Frame Section 3-5 Strain Gages (Right)

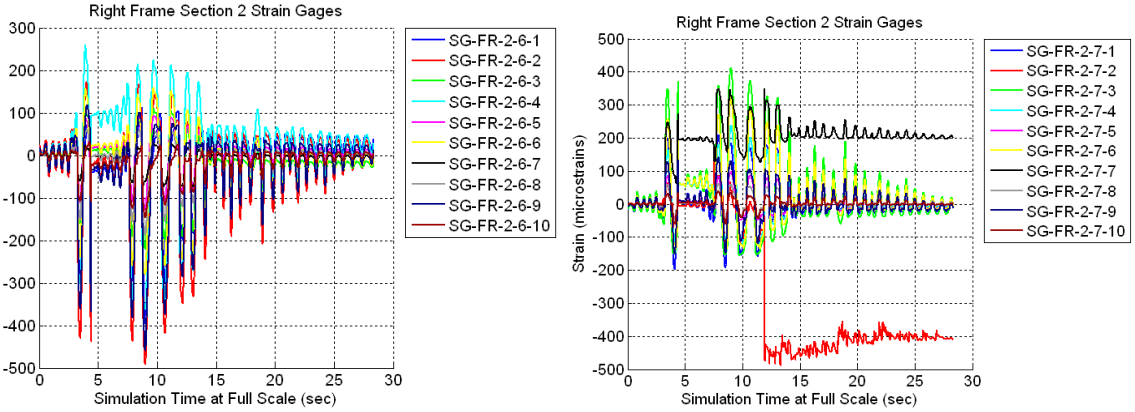

Figure B.358 Raw Data For Specimen A6 MCE Trial with Out-of-Plane Motion – Right Frame Section 2-6 Strain Gages (Left) and Right Frame Section 2-7 Strain Gages (Right)

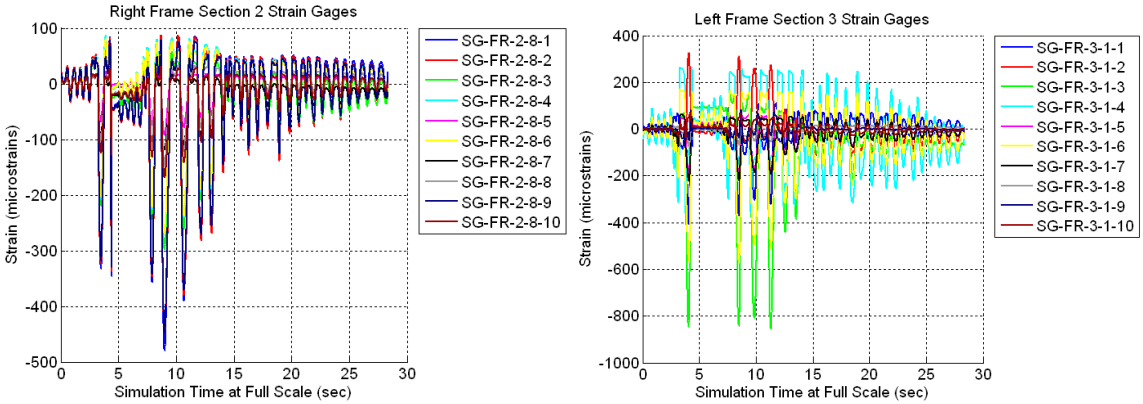

Figure B.359 Raw Data For Specimen A6 MCE Trial with Out-of-Plane Motion – Right Frame Section 2-8 Strain Gages (Left) and Left Frame Section 3-1 Strain Gages (Right)

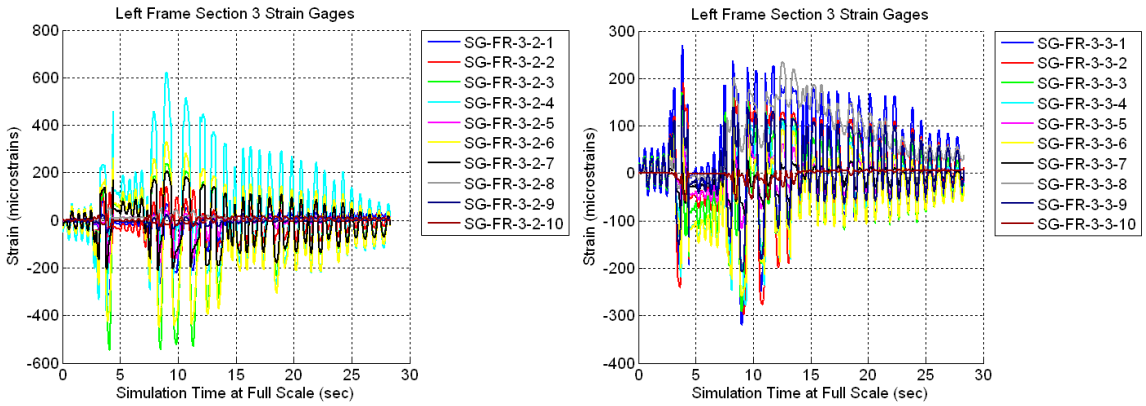

Figure B.360 Raw Data For Specimen A6 MCE Trial with Out-of-Plane Motion – Left Frame Section 3-2 Strain Gages (Left) and Left Frame Section 3-3 Strain Gages (Right)

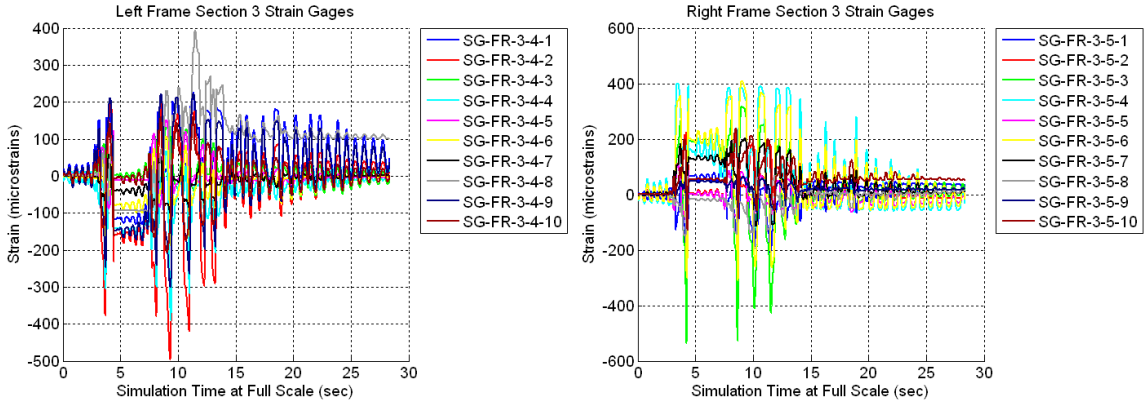

Figure B.361 Raw Data For Specimen A6 MCE Trial with Out-of-Plane Motion – Left Frame Section 3-4 Strain Gages (Left) and Right Frame Section 3-5 Strain Gages (Right)

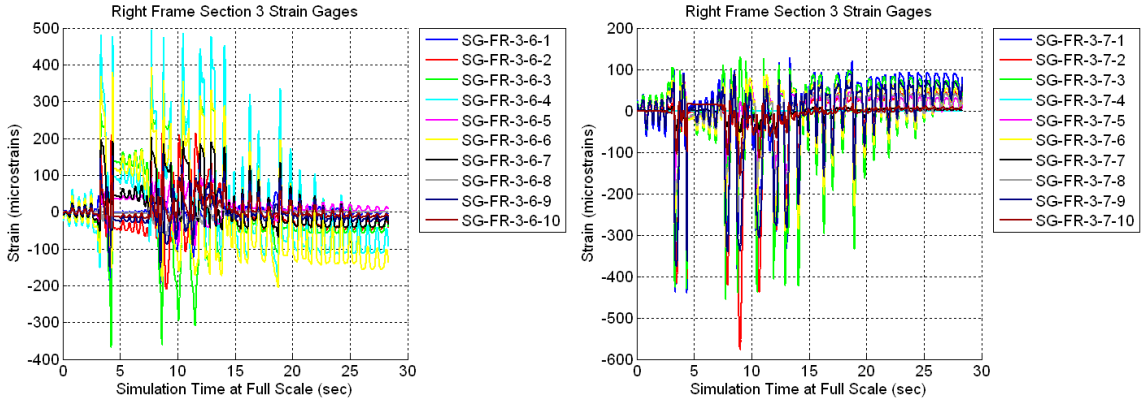

Figure B.362 Raw Data For Specimen A6 MCE Trial with Out-of-Plane Motion – Right Frame Section 3-6 Strain Gages (Left) and Right Frame Section 3-7 Strain Gages (Right)

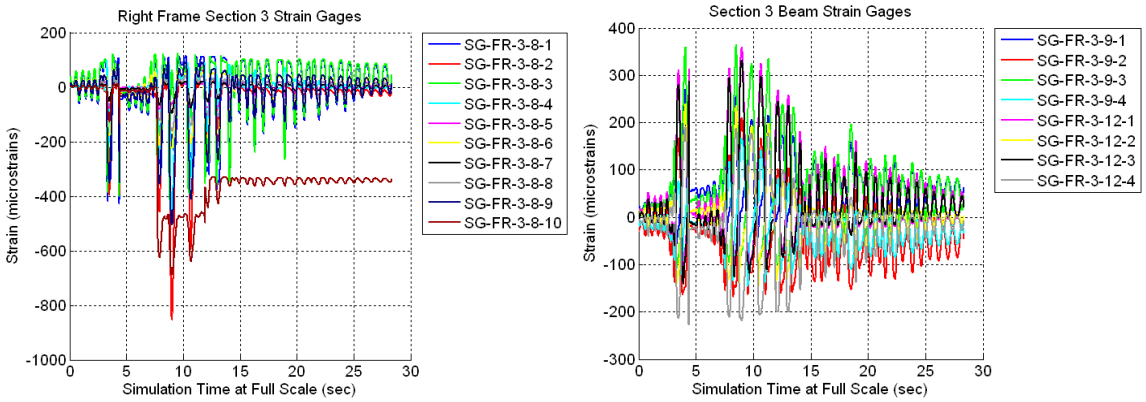

Figure B.363 Raw Data For Specimen A6 MCE Trial with Out-of-Plane Motion – Right Frame Section 3-8 Strain Gages (Left) and Third Floor Beam Strain Gages (Right)

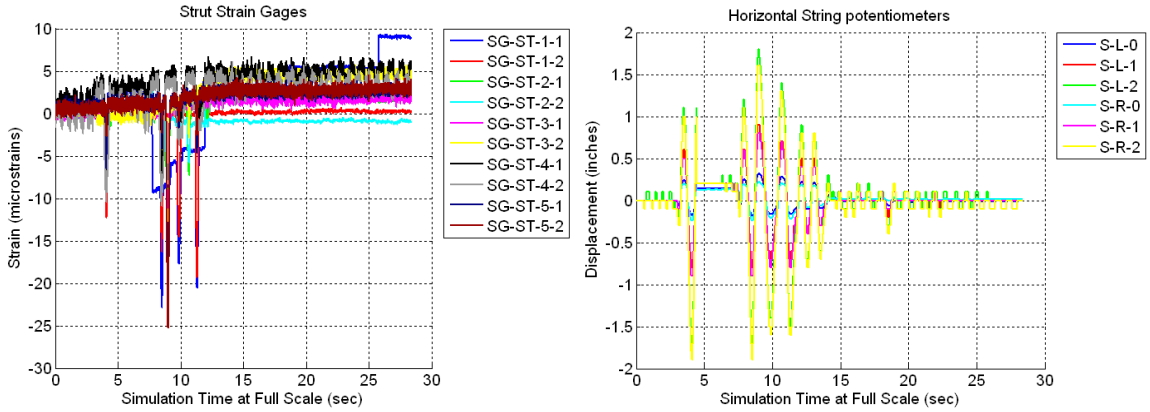

Figure B.364 Raw Data For Specimen A6 MCE Trial with Out-of-Plane Motion – Strut Strain Gages (Left) and Horizontal String Potentiometers (Right)

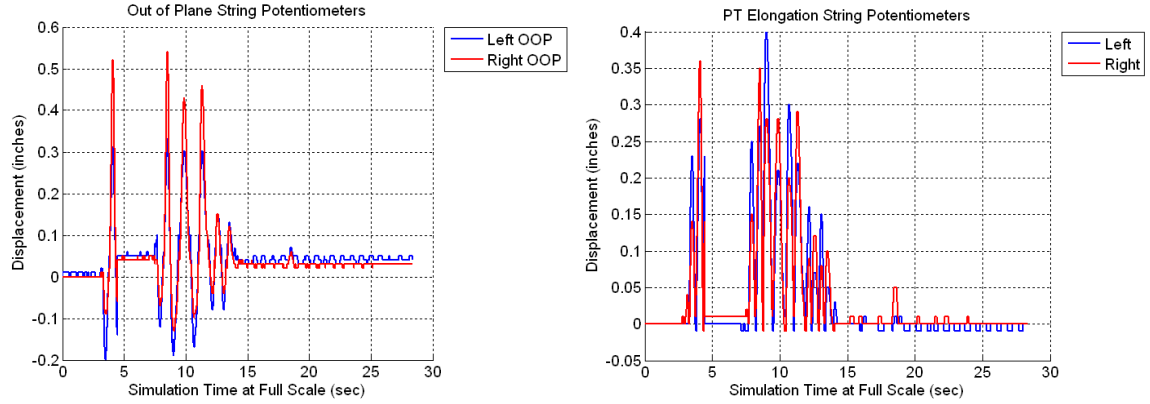

Figure B.365 Raw Data For Specimen A6 MCE Trial with Out-of-Plane Motion – Out-of-Plane String Potentiometers (Left) and PT Elongation String Potentiometers (Right)

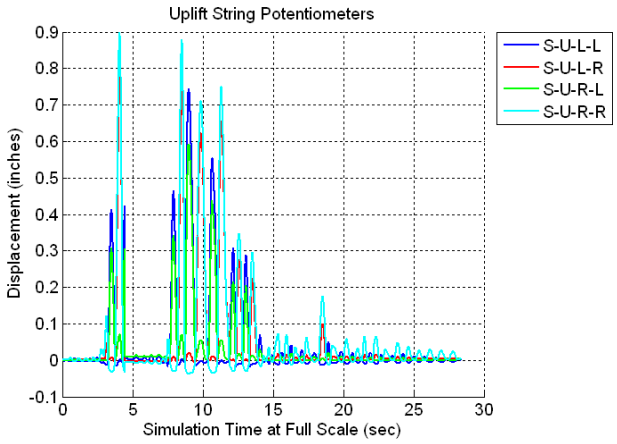

Figure B.366 Raw Data For Specimen A6 MCE Trial with Out-of-Plane Motion – Uplift String Potentiometers

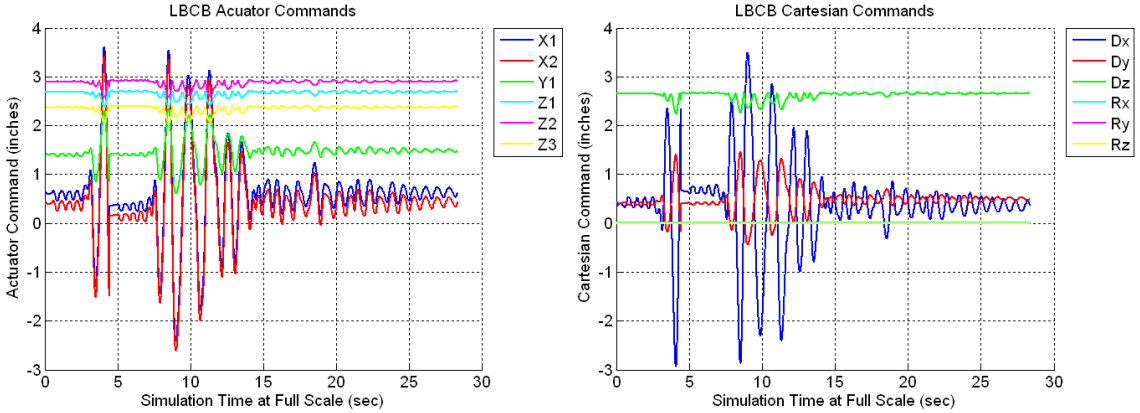

Figure B.367 Raw Data For Specimen A6 MCE Trial with Out-of-Plane Motion – LBCB Actuator Commands (Left) and LBCB Cartesian Commands (Right)

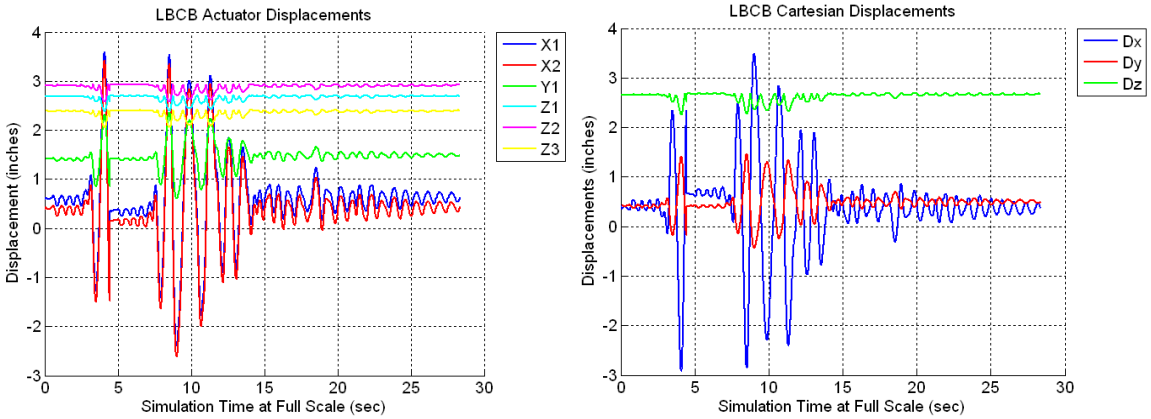

Figure B.368 Raw Data For Specimen A6 MCE Trial with Out-of-Plane Motion – LBCB Actuator Displacements (Left) and LBCB Cartesian Displacements (Right)

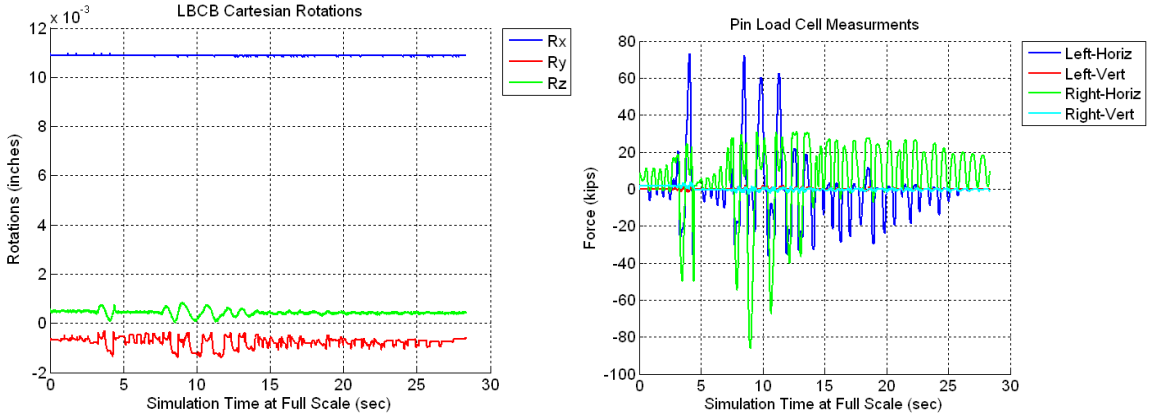

Figure B.369 Raw Data For Specimen A6 MCE Trial with Out-of-Plane Motion – LBCB Cartesian Rotations (Left) and Pin Load Cells (Right)

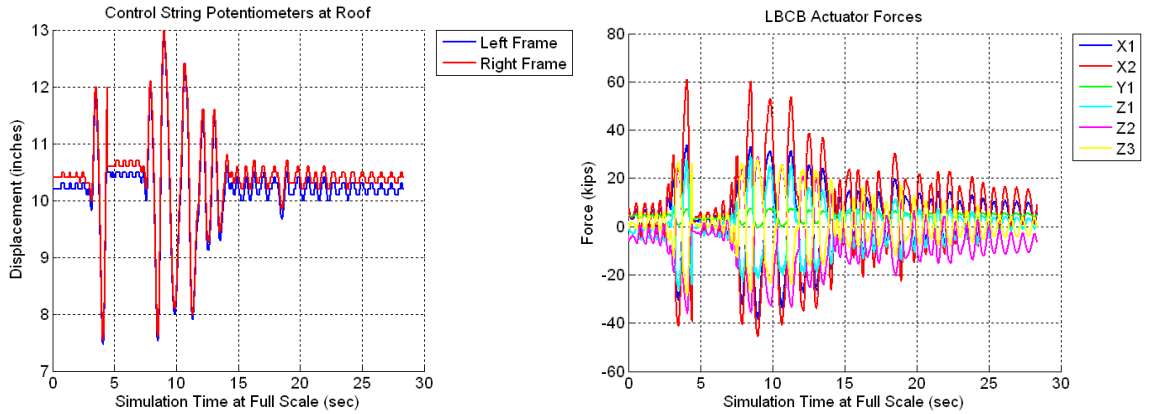

Figure B.370 Raw Data For Specimen A6 MCE Trial with Out-of-Plane Motion – Control Roof String Potentiometers (Left) and LBCB Actuator Forces (Right)

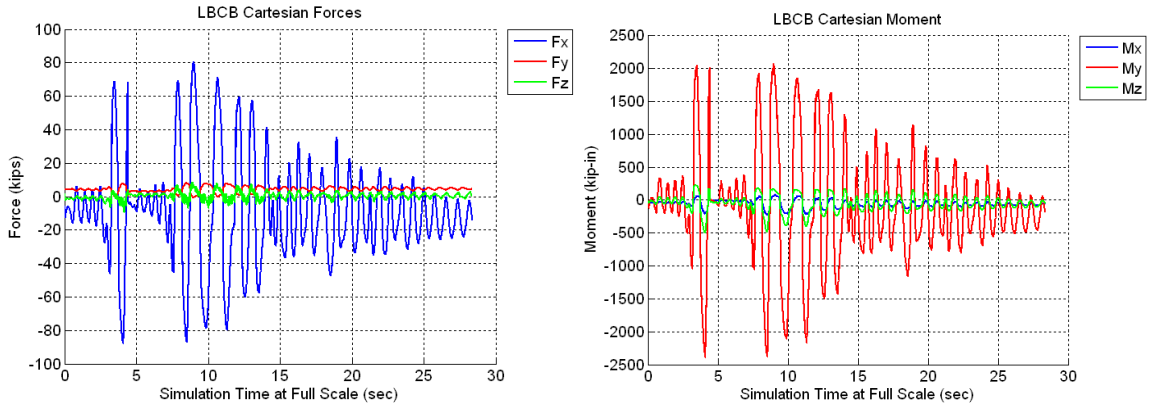

Figure B.371 Raw Data For Specimen A6 MCE Trial with Out-of-Plane Motion – LBCB Cartesian Forces (Left) and LBCB Cartesian Moments (Right)

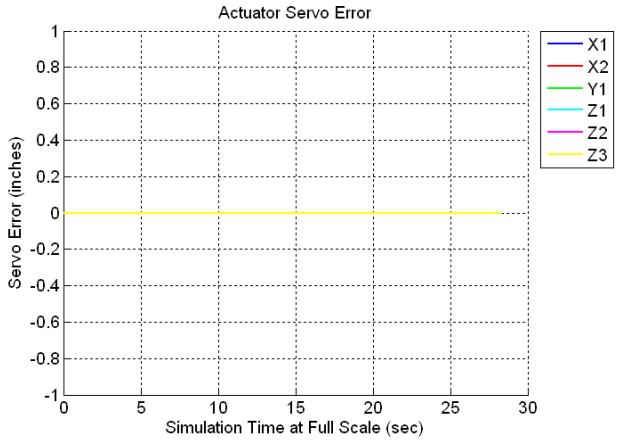

Figure B.372 Raw Data For Specimen A6 MCE Trial with Out-of-Plane Motion – LBCB Actuator Servo-Errors

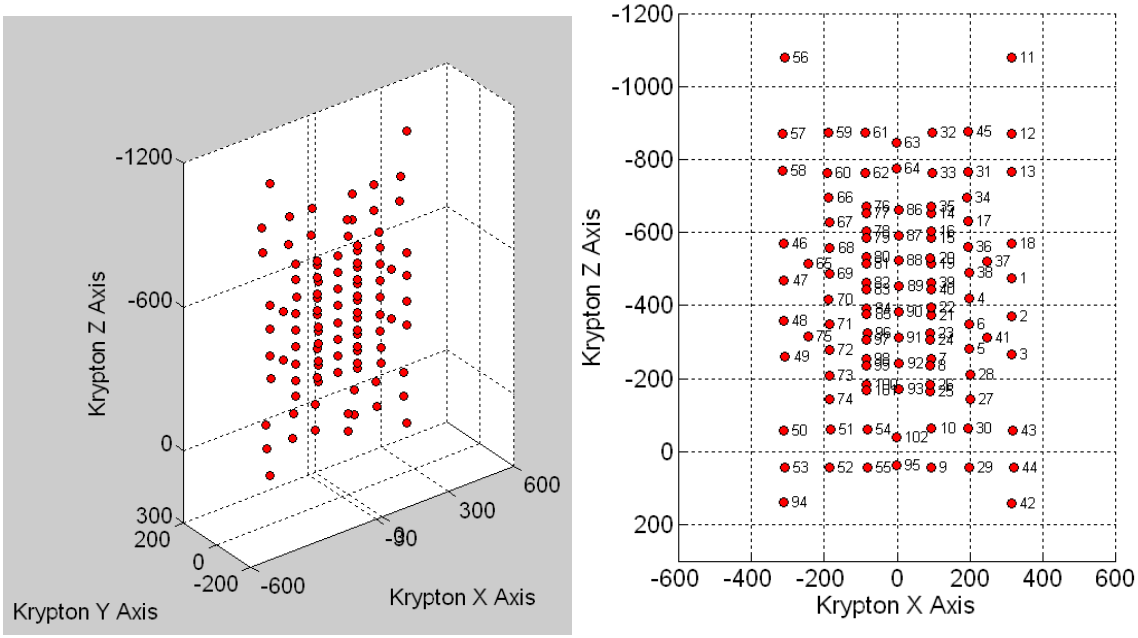

Figure B.373 Raw Data For Specimen A6 MCE Trial with Out-of-Plane Motion – Krypton LED Locations (Left) and Krypton LED Numbering (Right)

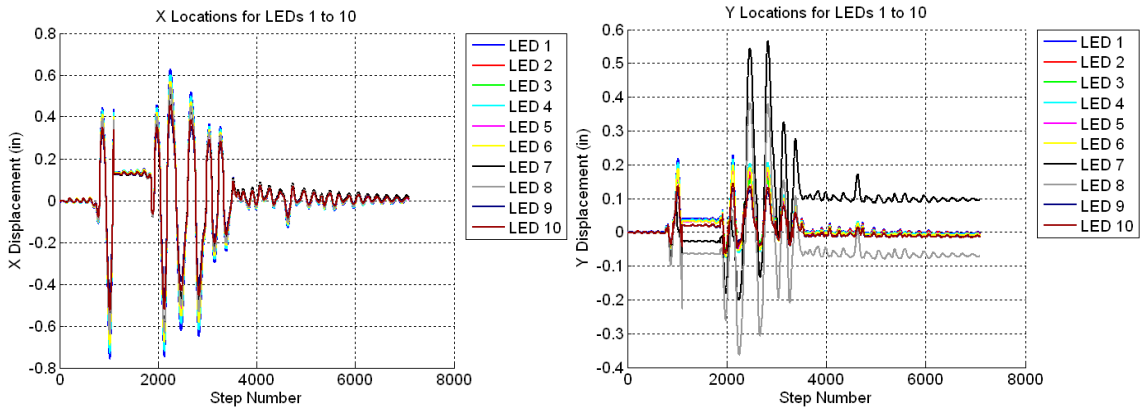

Figure B.374 Raw Data For Specimen A6 MCE Trial with Out-of-Plane Motion – X Displacements for LED's 1 to 10 (Left) and Y Displacements for LED's 1 to 10 (Right)

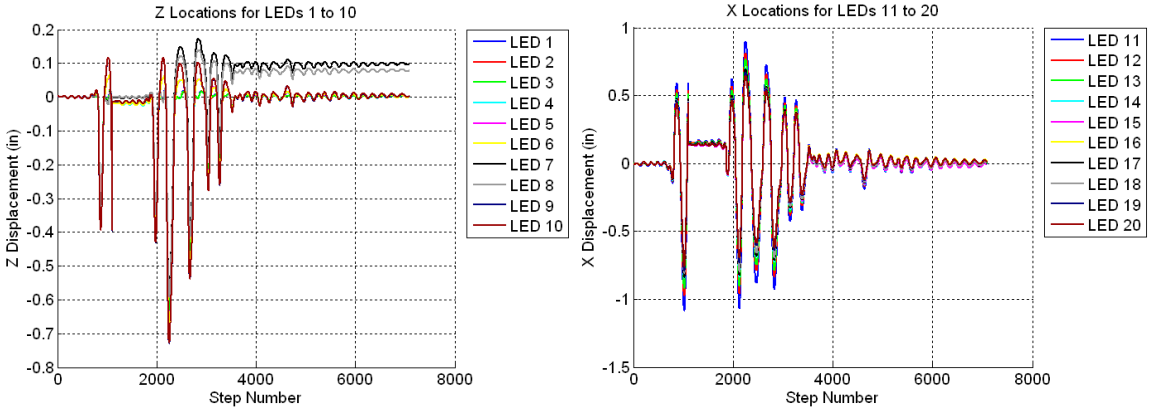

Figure B.375 Raw Data For Specimen A6 MCE Trial with Out-of-Plane Motion – Z Displacements for LED's 1 to 10 (Left) and X Displacements for LED's 11 to 20 (Right)

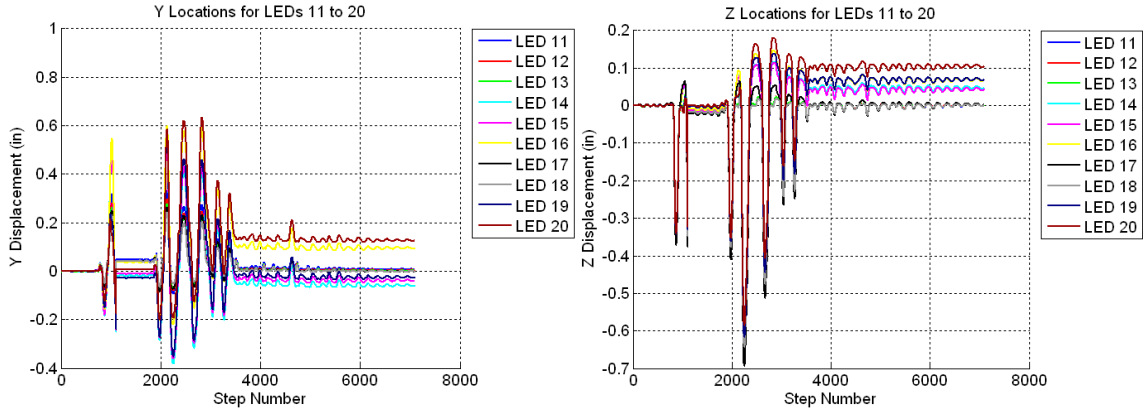

Figure B.376 Raw Data For Specimen A6 MCE Trial with Out-of-Plane Motion – Y Displacements for LED's 11 to 20 (Left) and Z Displacements for LED's 11 to 20 (Right)

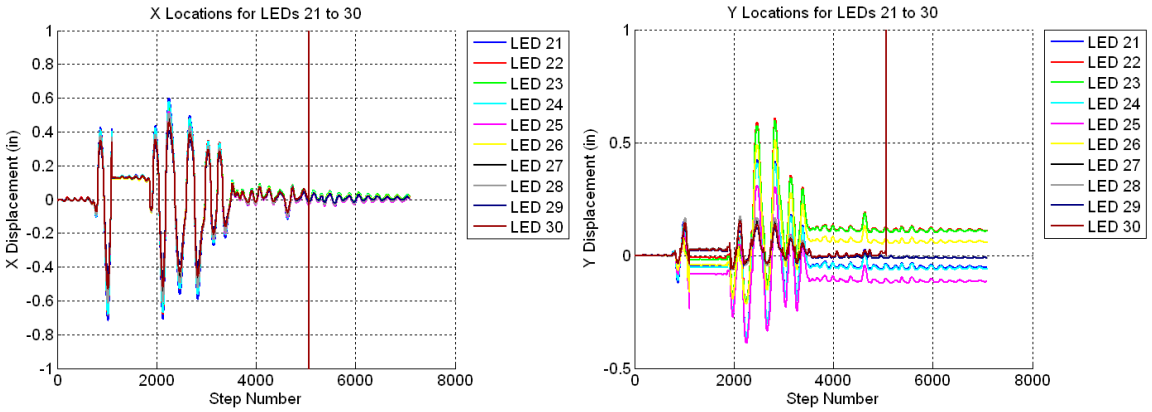

Figure B.377 Raw Data For Specimen A6 MCE Trial with Out-of-Plane Motion – X Displacements for LED's 21 to 30 (Left) and Y Displacements for LED's 21 to 30 (Right)

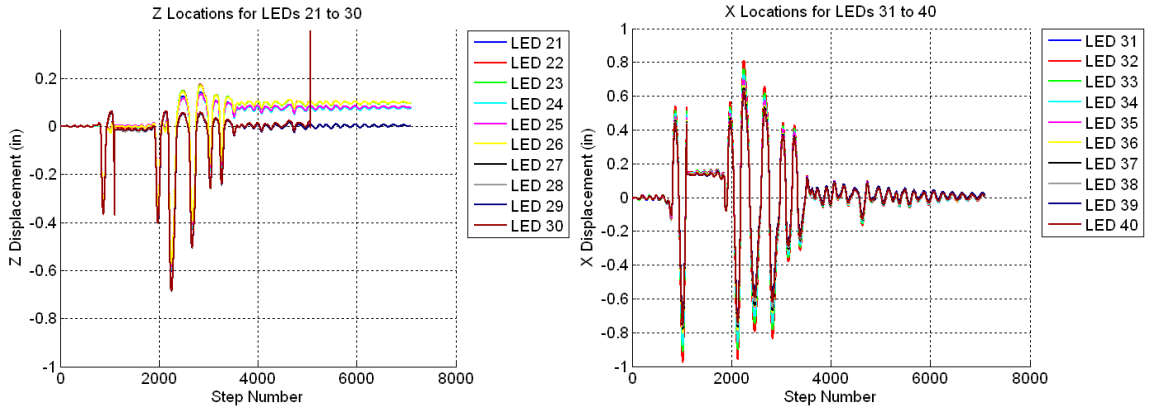

Figure B.378 Raw Data For Specimen A6 MCE Trial with Out-of-Plane Motion – Z Displacements for LED's 21 to 30 (Left) and X Displacements for LED's 31 to 40 (Right)

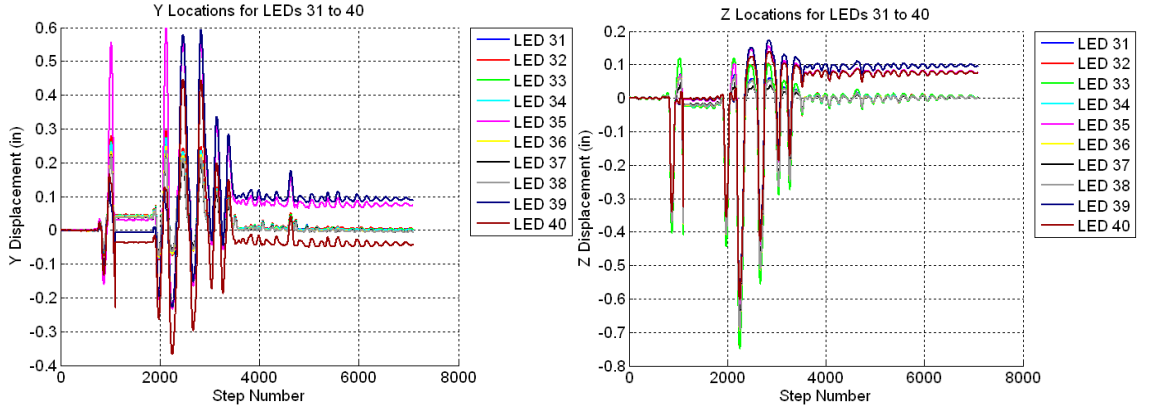

Figure B.379 Raw Data For Specimen A6 MCE Trial with Out-of-Plane Motion – Y Displacements for LED's 31 to 40 (Left) and Z Displacements for LED's 31 to 40 (Right)

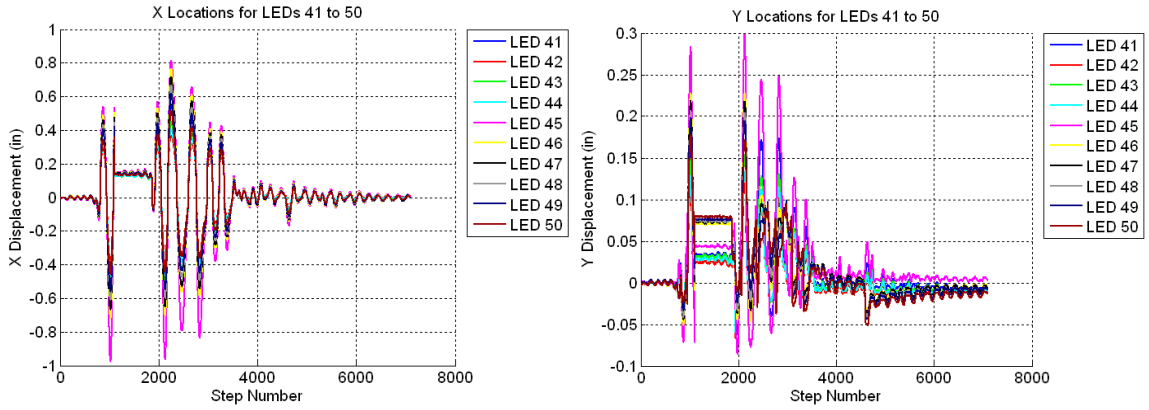

Figure B.380 Raw Data For Specimen A6 MCE Trial with Out-of-Plane Motion – X Displacements for LED's 41 to 50 (Left) and Y Displacements for LED's 41 to 50 (Right)

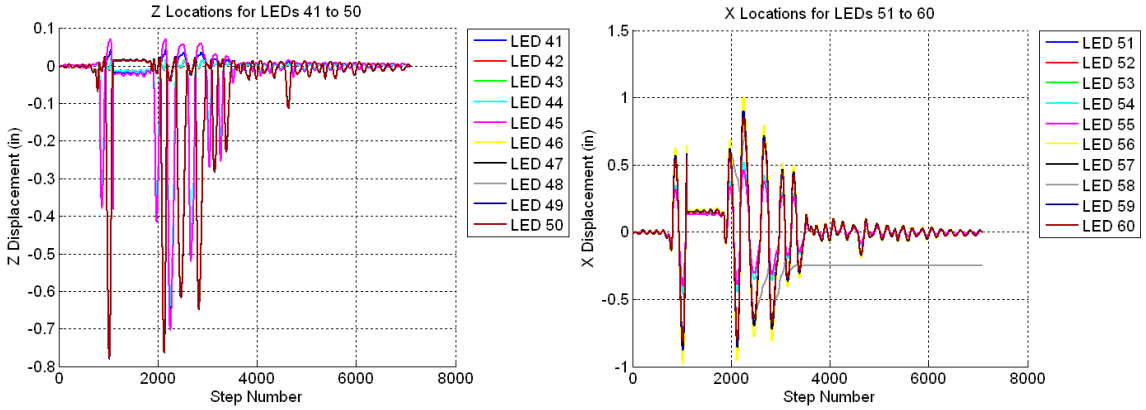

Figure B.381 Raw Data For Specimen A6 MCE Trial with Out-of-Plane Motion – Z Displacements for LED's 41 to 50 (Left) and X Displacements for LED's 51 to 60 (Right)

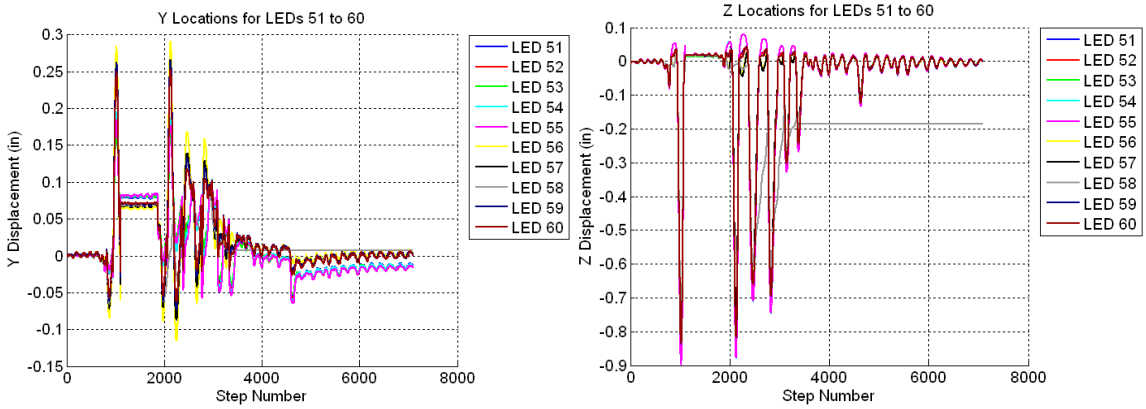

Figure B.382 Raw Data For Specimen A6 MCE Trial with Out-of-Plane Motion – Y Displacements of LED's 51 to 60 (Left) and Z Displacements for LED's 51 to 60 (Right)

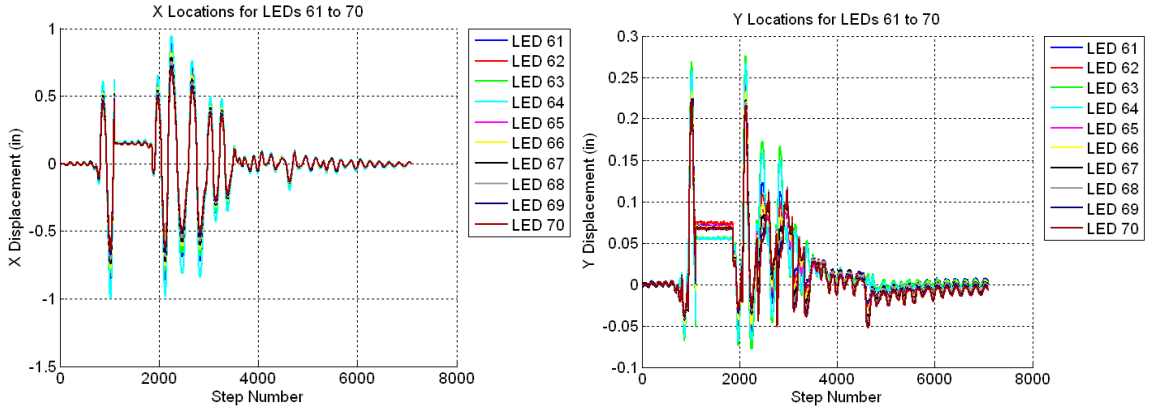

Figure B.383 Raw Data For Specimen A6 MCE Trial with Out-of-Plane Motion – X Displacements for LED's 61 to 70 (Left) and Y Displacements for LED's 61 to 70 (Right)

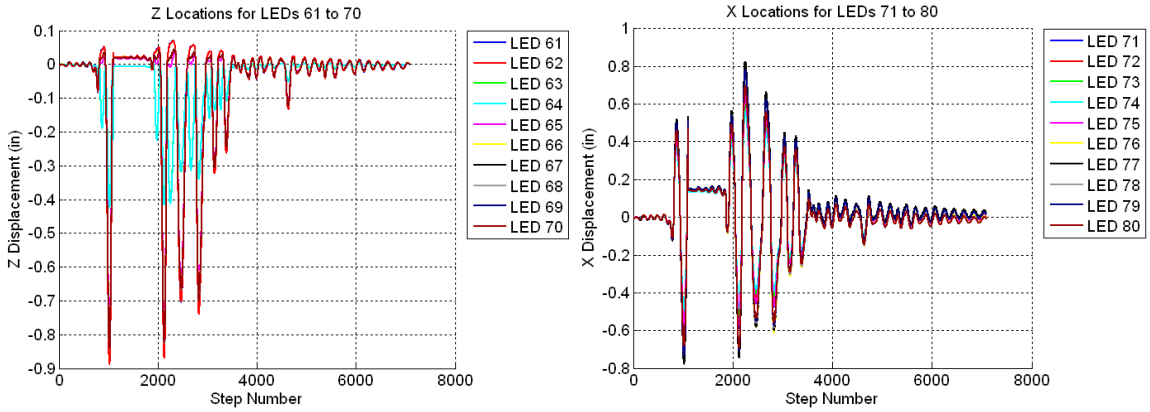

Figure B.384 Raw Data For Specimen A6 MCE Trial with Out-of-Plane Motion – Z Displacements for LED's 61 to 70 (Left) and X Displacements for LED's 71 to 80 (Right)

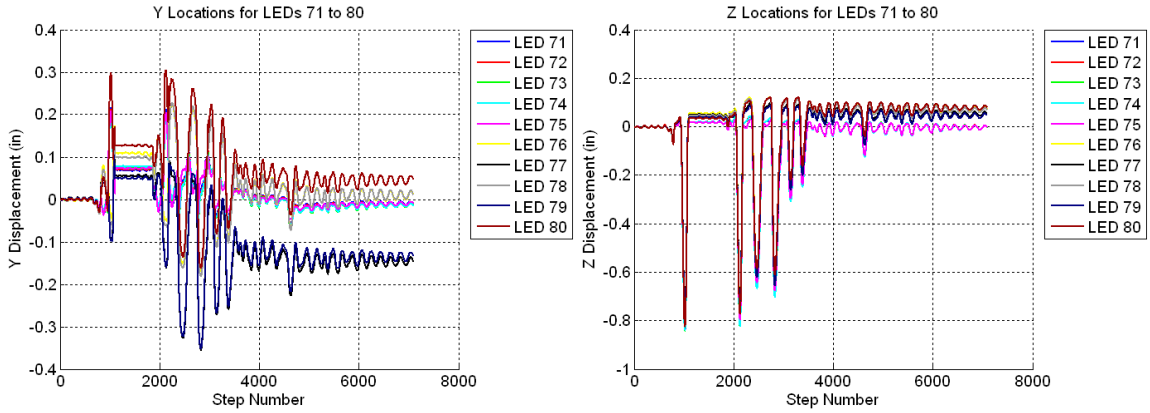

Figure B.385 Raw Data For Specimen A6 MCE Trial with Out-of-Plane Motion – Y Displacements for LED's 71 to 80 (Left) Z Displacements for LED's 71 to 80 (Right)

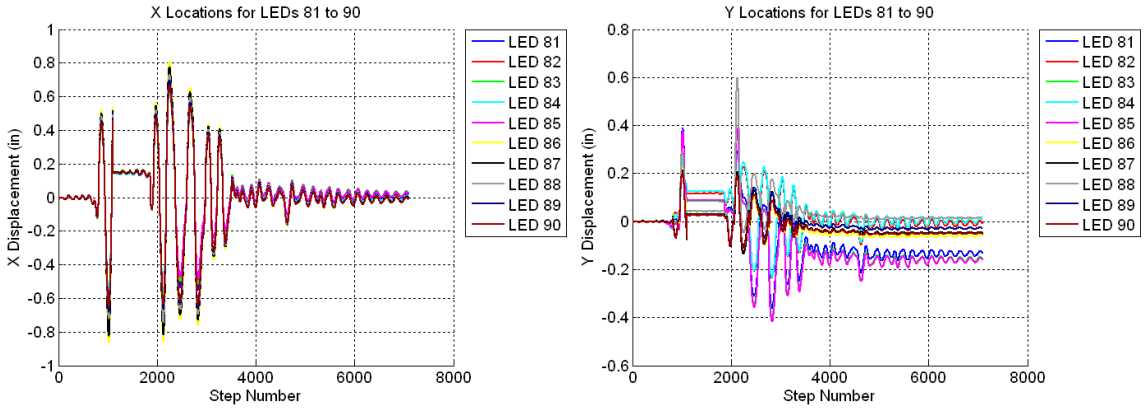

Figure B.386 Raw Data For Specimen A6 MCE Trial with Out-of-Plane Motion – X Displacements for LED's 81 to 90 (Left) and Y Displacements for LED's 81 to 90 (Right)

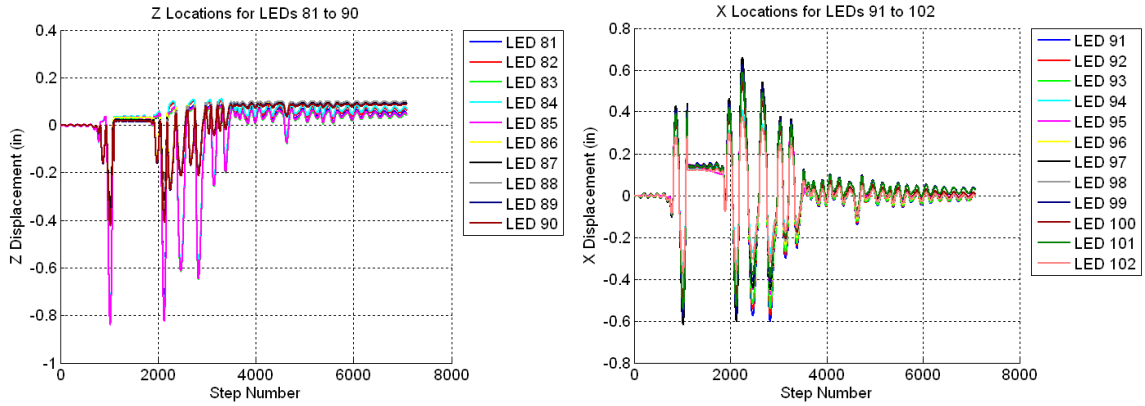

Figure B.387 Raw Data For Specimen A6 MCE Trial with Out-of-Plane Motion – Z Displacements for LED's 81 to 90 (Left) and X Displacements for LED's 91 to 102 (Right)

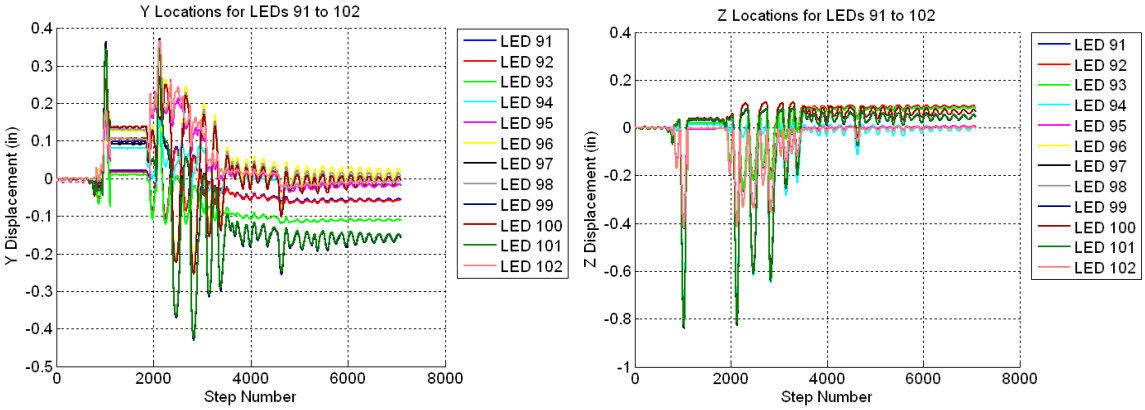

Figure B.388 Raw Data For Specimen A6 MCE Trial with Out-of-Plane Motion – Y Displacements for LED's 91 to 102 (Left) and Z Displacements for LED's 91 to 102 (Right)

B.10 Specimen A6 – 1.20xJMA Kobe Trial

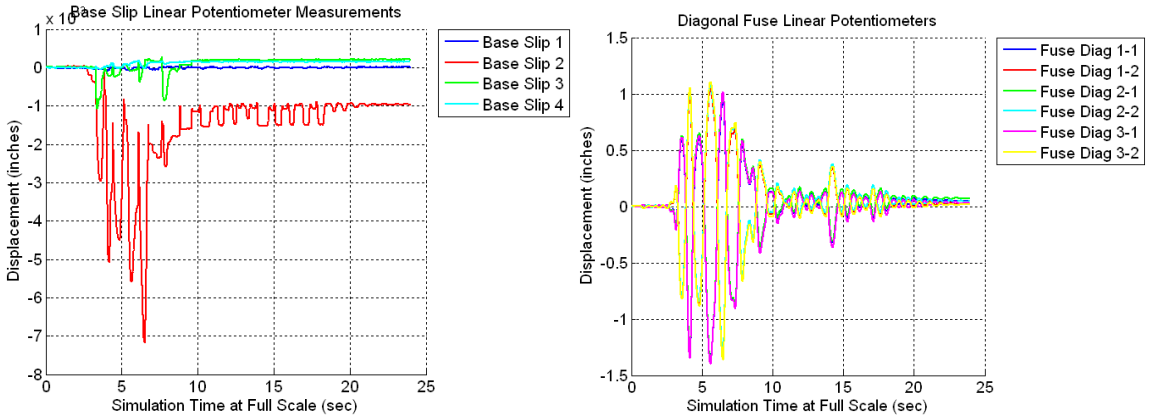

Figure B.389 Raw Data For Specimen A6 1.20xJMA Kobe Trial – Base Slip (Left) and Fuse Linear Potentiometers (Right)

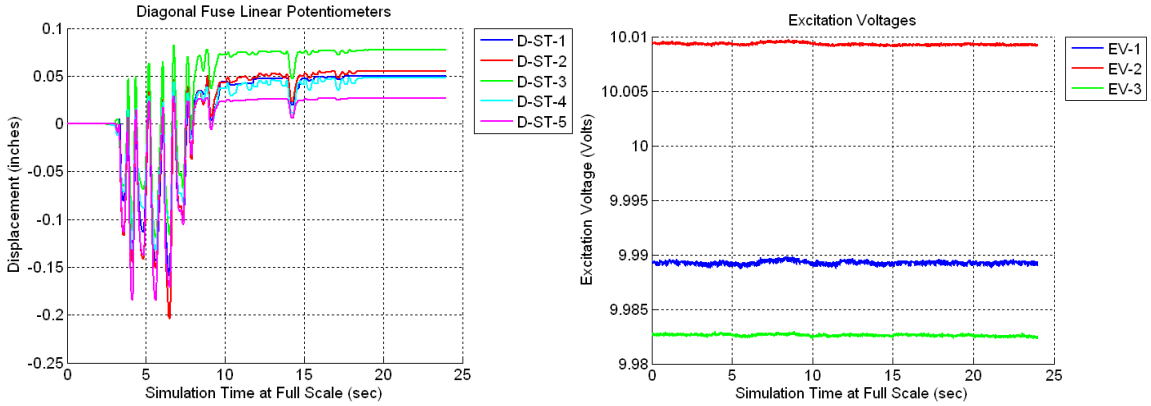

Figure B.390 Raw Data For Specimen A6 1.20xJMA Kobe Trial – Strut Linear Potentiometers (Left) and Excitation Voltage (Right)

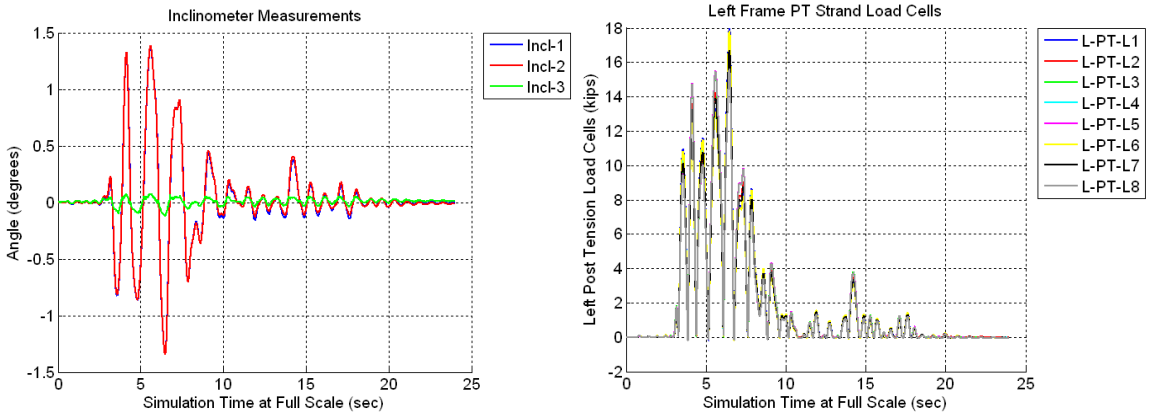

Figure B.391 Raw Data For Specimen A6 1.20xJMA Kobe Trial – Inclinometers (Left) and Left Frame PT Load Cells (Right)

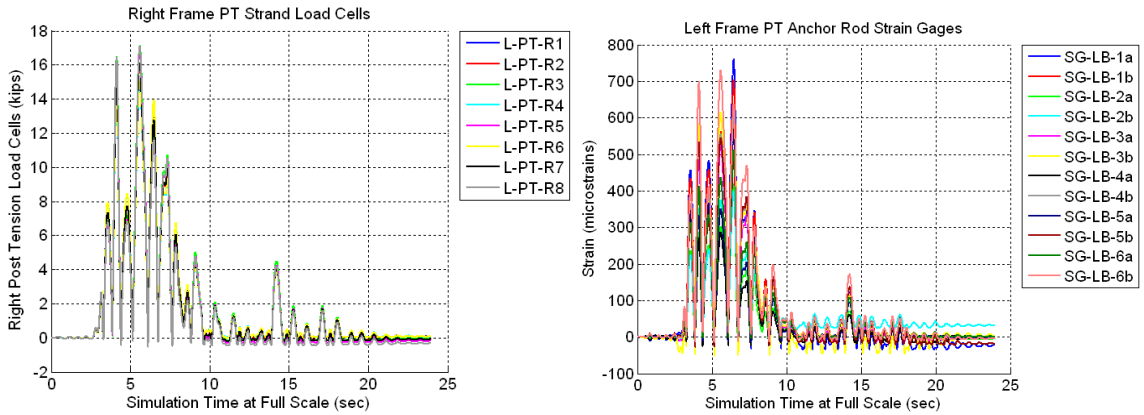

Figure B.392 Raw Data For Specimen A6 1.20xJMA Kobe Trial – Right Frame PT Load Cells (Left) and Left Frame PT Anchor Rods (Right)

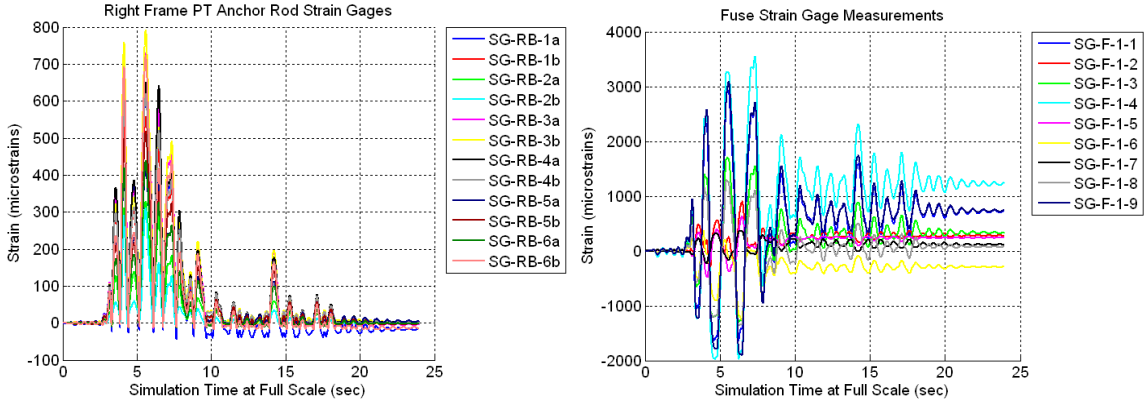

Figure B.393 Raw Data For Specimen A6 1.20xJMA Kobe Trial – Right Frame PT Anchor Rods (Left) and Back Bottom Fuse Strain Gages (Right)

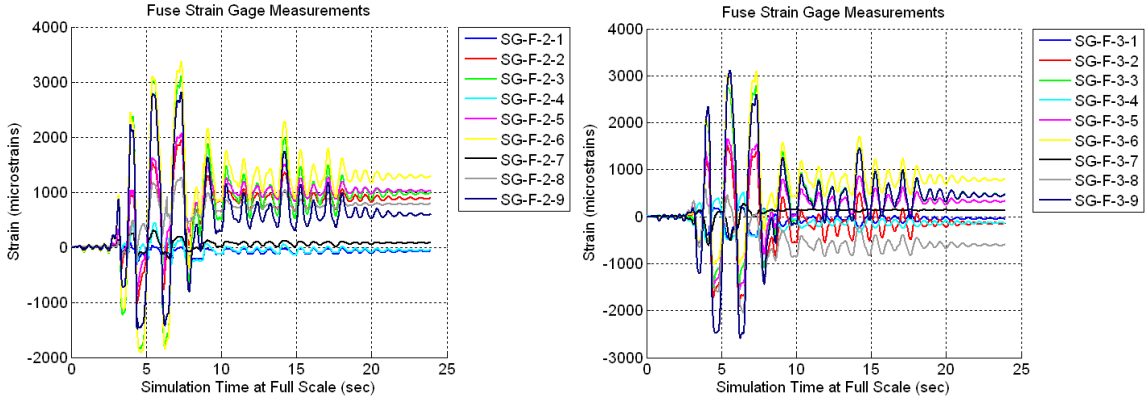

Figure B.394 Raw Data For Specimen A6 1.20xJMA Kobe Trial – Bottom Front Fuse Strain Gages (Left) and Mid-Height Back Fuse Strain Gages (Right)

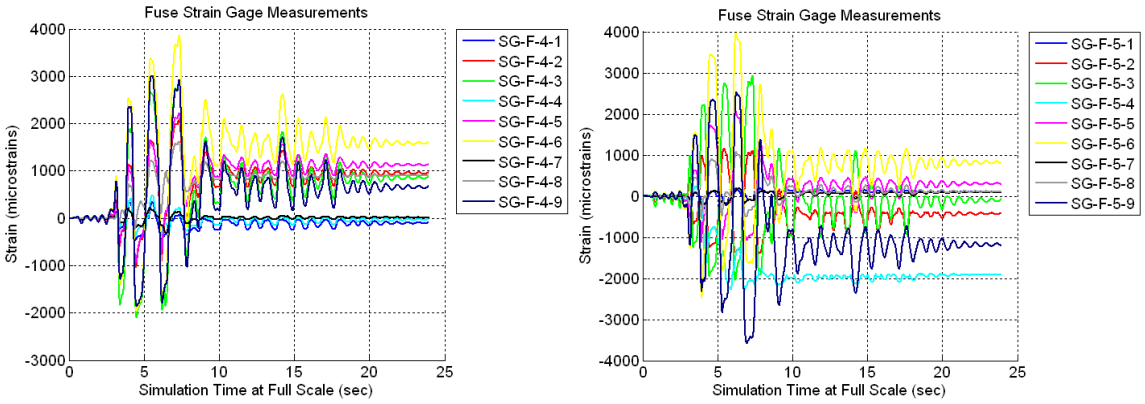

Figure B.395 Raw Data For Specimen A6 1.20xJMA Kobe Trial – Mid-Height Front Fuse Strain Gages (Left) and Top Back Fuse Strain Gages (Right)

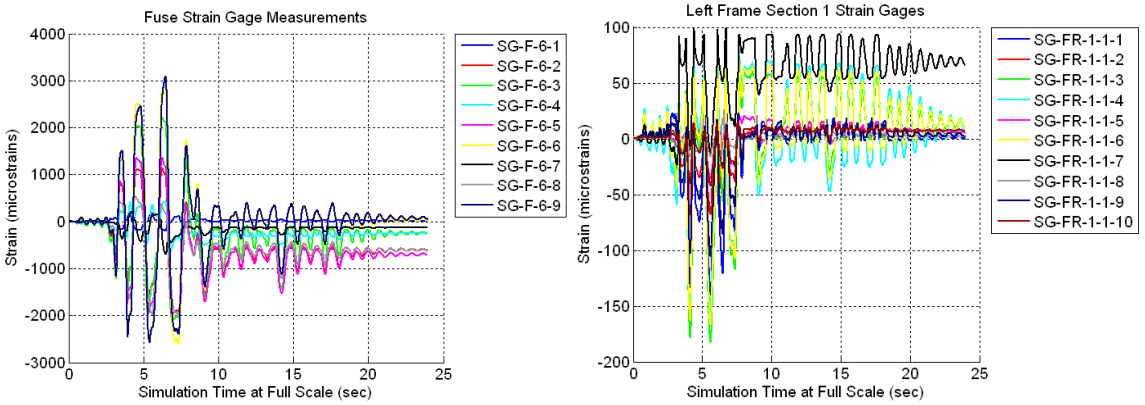

Figure B.396 Raw Data For Specimen A6 1.20xJMA Kobe Trial – Top Front Fuse Strain Gages (Left) and Left Frame Section 1-1 Strain Gages (Right)

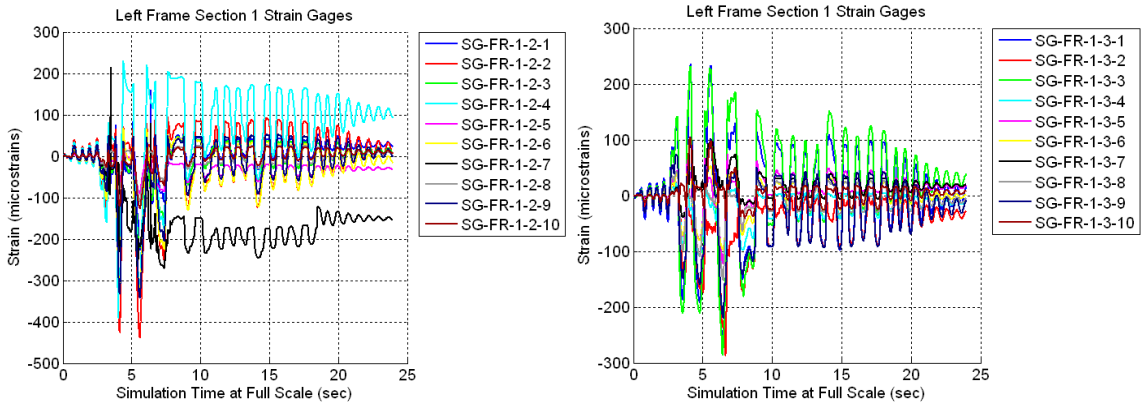

Figure B.397 Raw Data For Specimen A6 1.20xJMA Kobe Trial – Left Frame Section 1-2 Strain Gages (Left) and Left Frame Section 1-3 Strain Gages (Right)

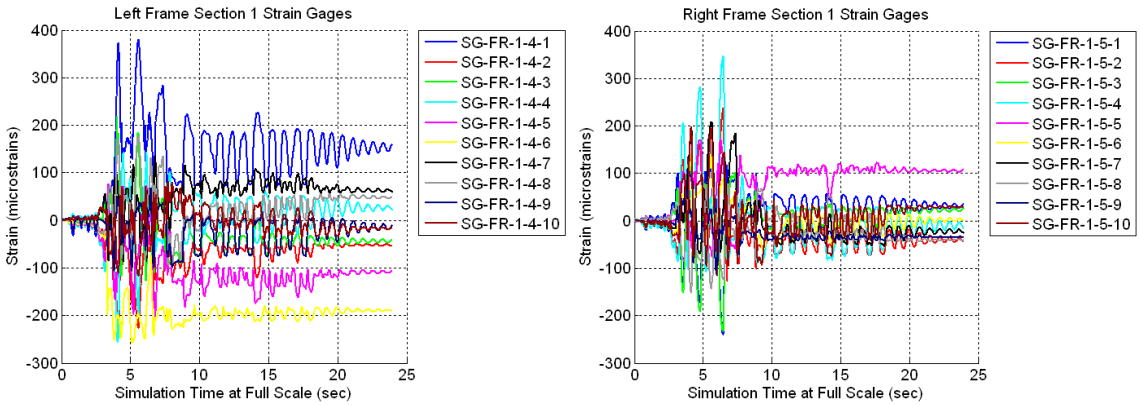

Figure B.398 Raw Data For Specimen A6 1.20xJMA Kobe Trial – Left Frame Section 1-4 Strain Gages (Left) and Right Frame Section 1-5 Strain Gages (Right)

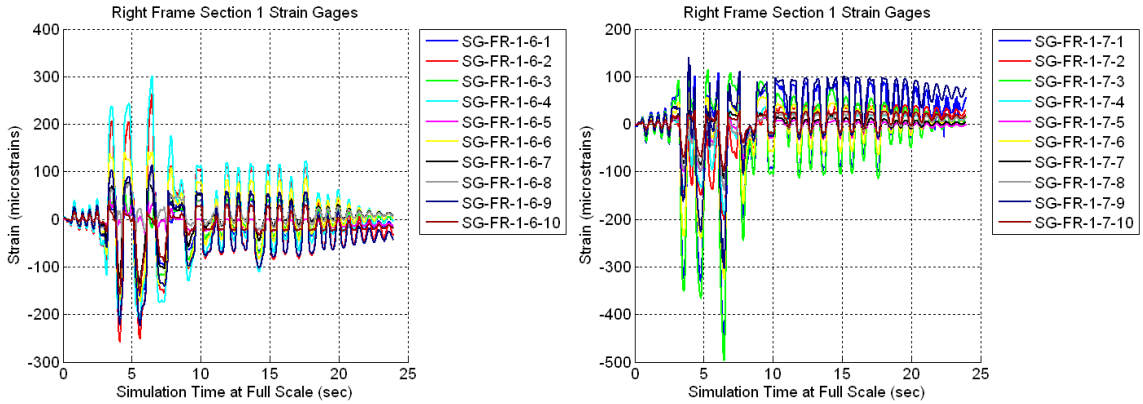

Figure B.399 Raw Data For Specimen A6 1.20xJMA Kobe Trial – Right Frame Section 1-6 Strain Gages (Left) and Right Frame Section 1-7 Strain Gages (Right)

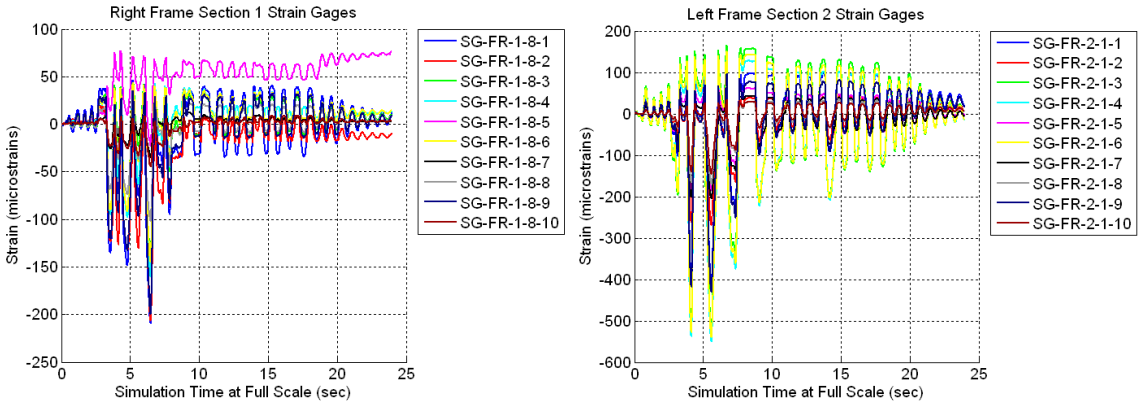

Figure B.400 Raw Data For Specimen A6 1.20xJMA Kobe Trial – Right Frame Section 1-8 Strain Gages (Left) and Left Frame Section 2-1 Strain Gages (Right)

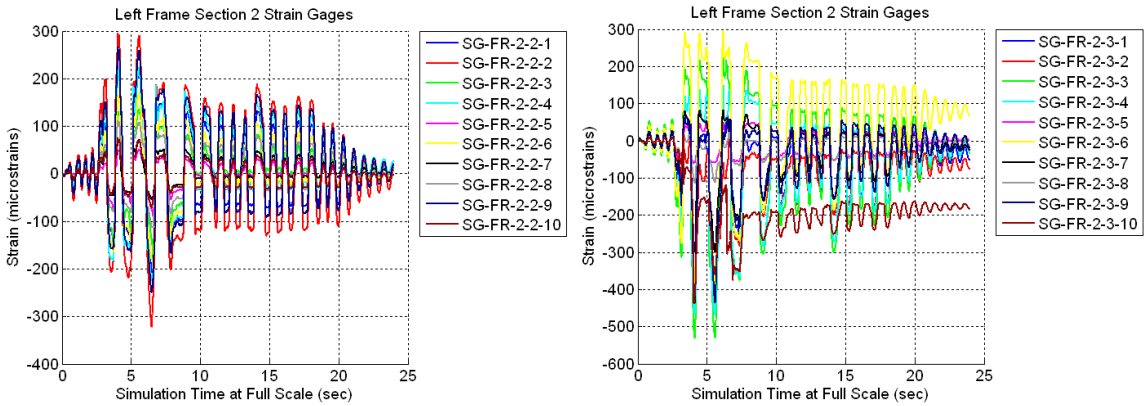

Figure B.401 Raw Data For Specimen A6 1.20xJMA Kobe Trial – Left Frame Section 2-2 Strain Gages (Left) and Left Frame Section 2-3 Strain Gages (Right)

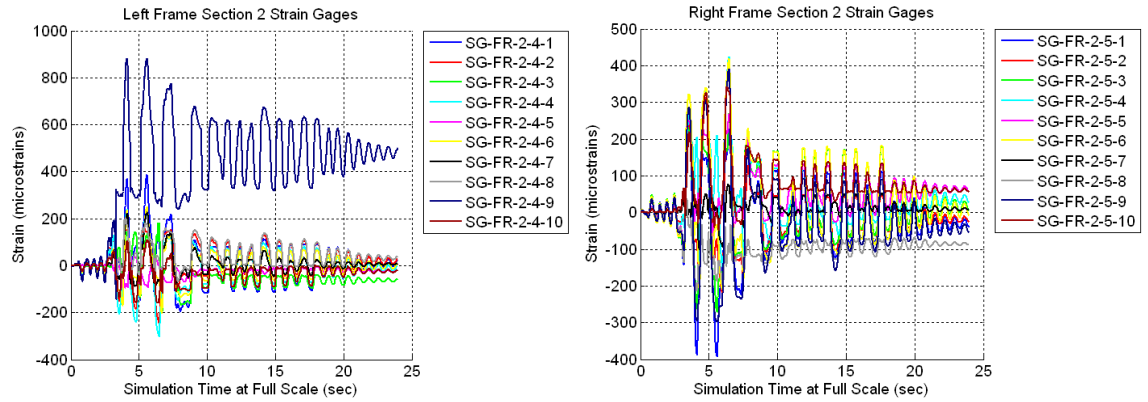

Figure B.402 Raw Data For Specimen A6 1.20xJMA Kobe Trial – Left Frame Section 2-4 Strain Gages (Left) and Right Frame Section 2-5 Strain Gages (Right)

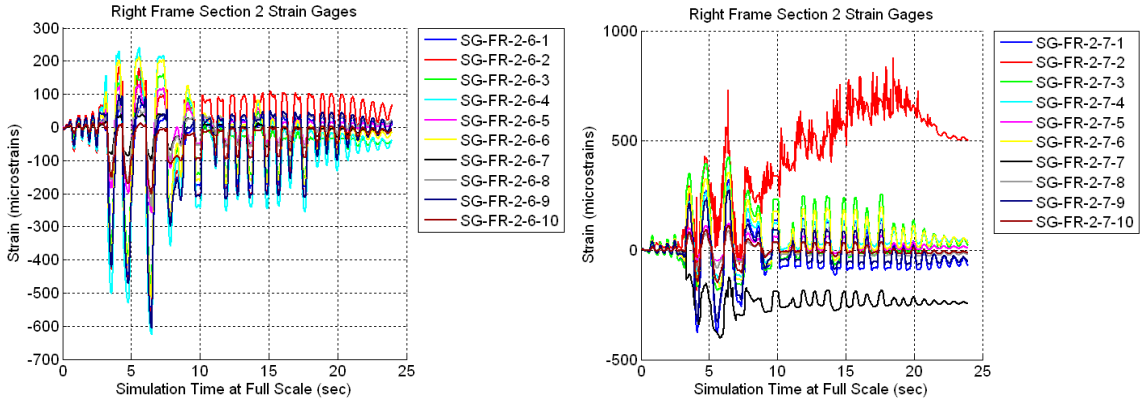

Figure B.403 Raw Data For Specimen A6 1.20xJMA Kobe Trial – Right Frame Section 2-6 Strain Gages (Left) and Right Frame Section 2-7 Strain Gages (Right)

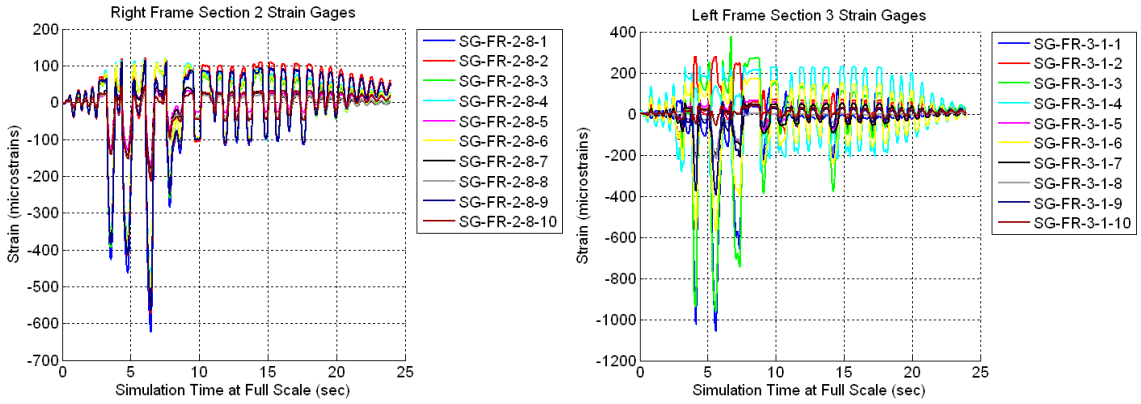

Figure B.404 Raw Data For Specimen A6 1.20xJMA Kobe Trial – Right Frame Section 2-8 Strain Gages (Left) and Left Frame Section 3-1 Strain Gages (Right)

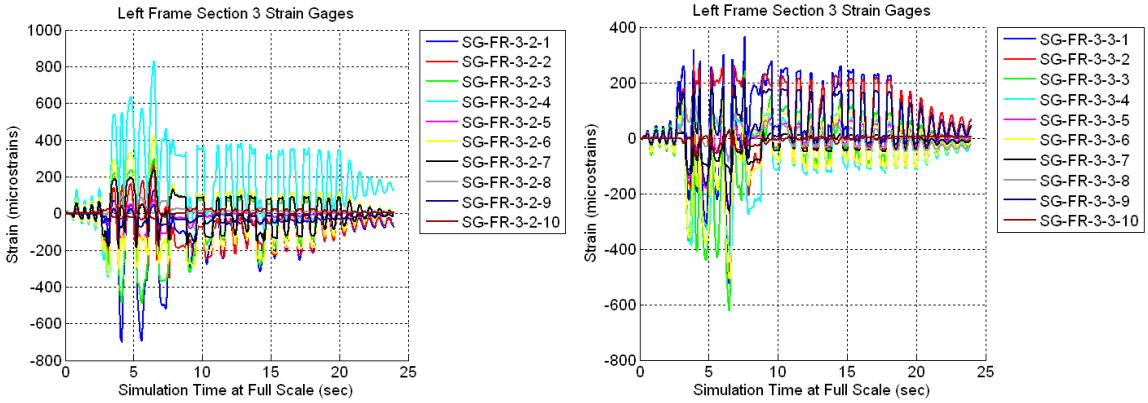

Figure B.405 Raw Data For Specimen A6 1.20xJMA Kobe Trial – Left Frame Section 3-2 Strain Gages (Left) and Left Frame Section 3-3 Strain Gages (Right)

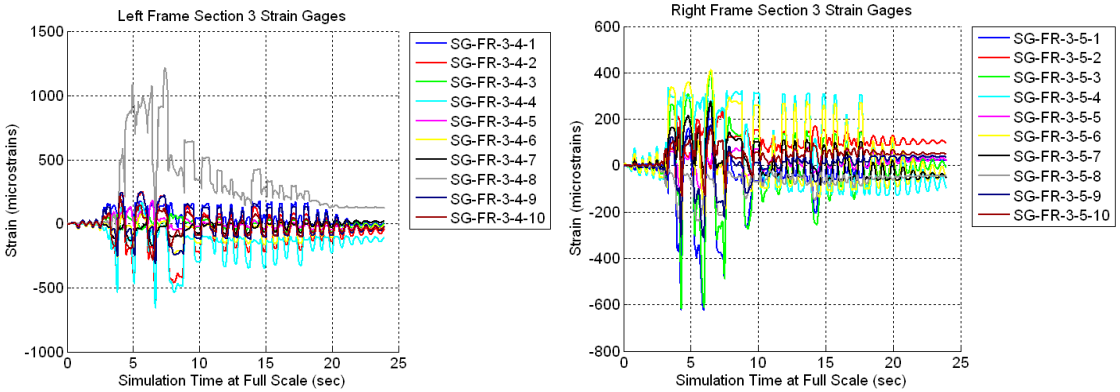

Figure B.406 Raw Data For Specimen A6 1.20xJMA Kobe Trial – Left Frame Section 3-4 Strain Gages (Left) and Right Frame Section 3-5 Strain Gages (Right)

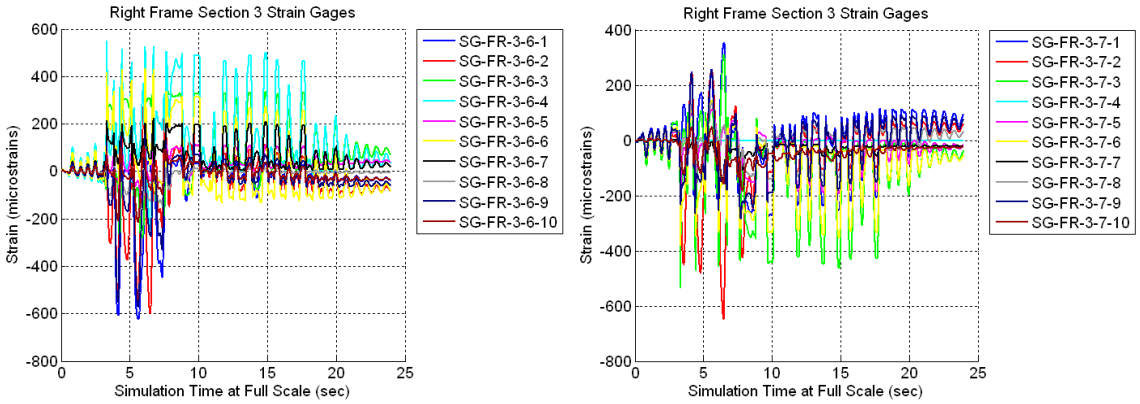

Figure B.407 Raw Data For Specimen A6 1.20xJMA Kobe Trial – Right Frame Section 3-6 Strain Gages (Left) and Right Frame Section 3-7 Strain Gages (Right)

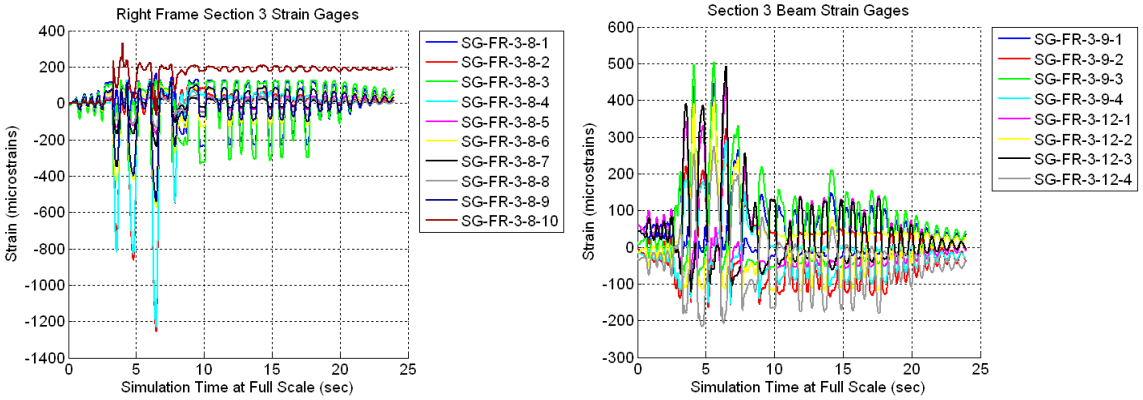

Figure B.408 Raw Data For Specimen A6 1.20xJMA Kobe Trial – Right Frame Section 3-8 Strain Gages (Left) and Third Floor Beam Strain Gages (Right)

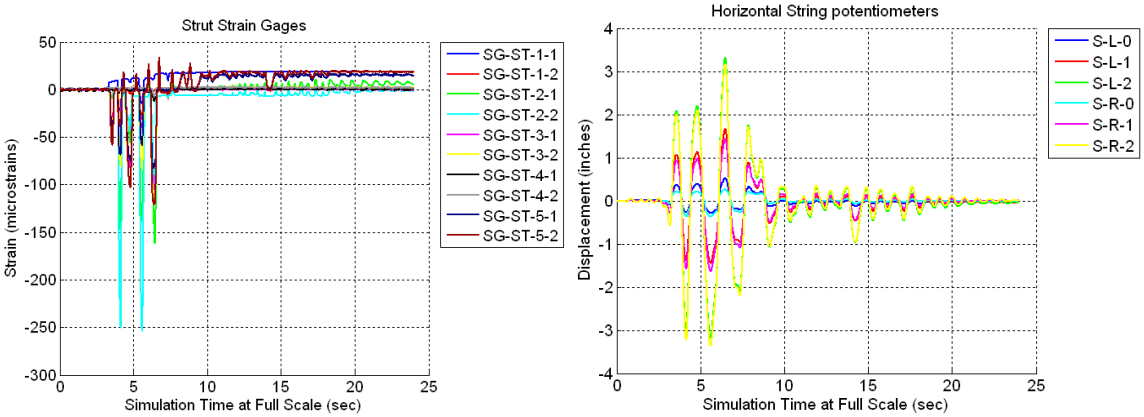

Figure B.409 Raw Data For Specimen A6 1.20xJMA Kobe Trial – Strut Strain Gages (Left) and Horizontal String Potentiometers (Right)

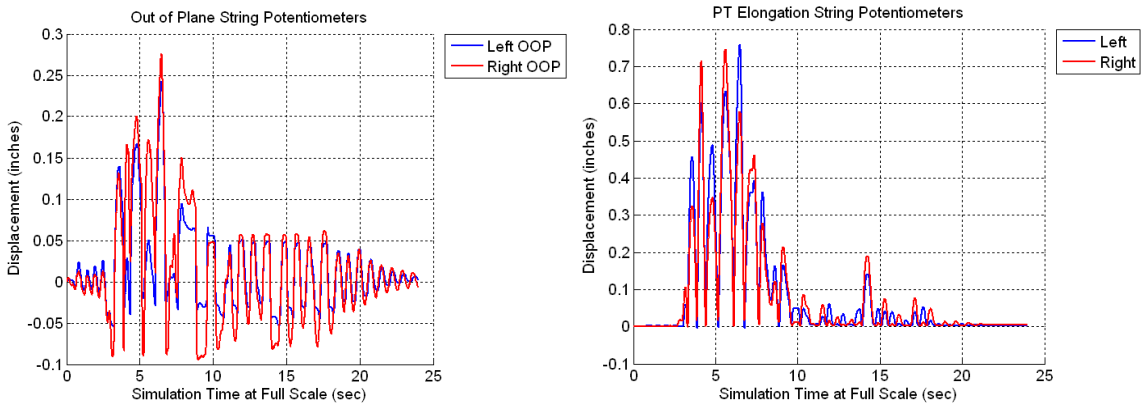

Figure B.410 Raw Data For Specimen A6 1.20xJMA Kobe Trial – Out-of-Plane String Potentiometers (Left) and PT Elongations String Potentiometers (Right)

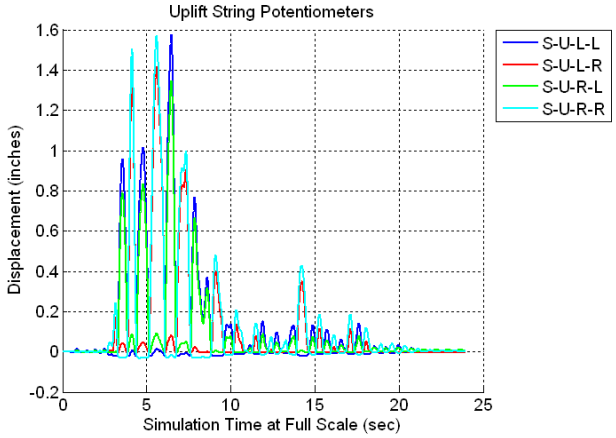

Figure B.411 Raw Data For Specimen A6 1.20xJMA Kobe Trial – Uplift String Potentiomters

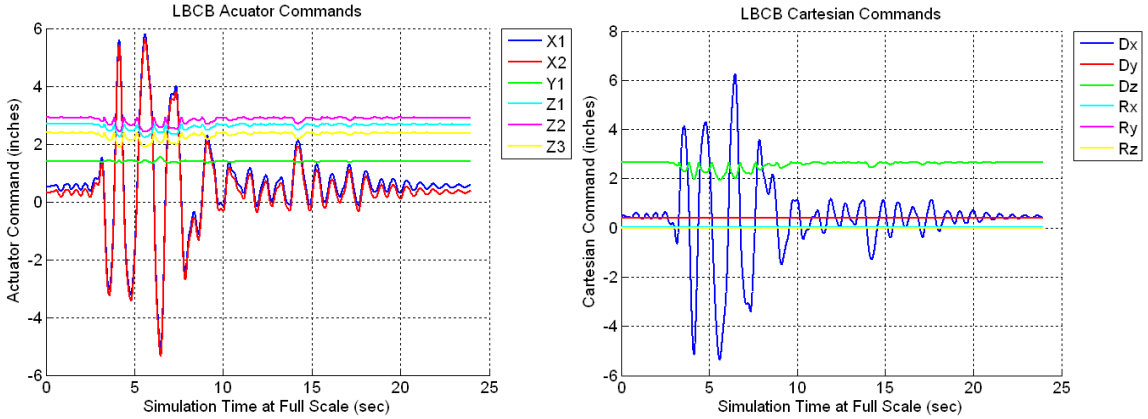

Figure B.412 Raw Data For Specimen A6 1.20xJMA Kobe Trial – LBCB Actuator Commands (Left) and LBCB Cartesian Commands (Right)

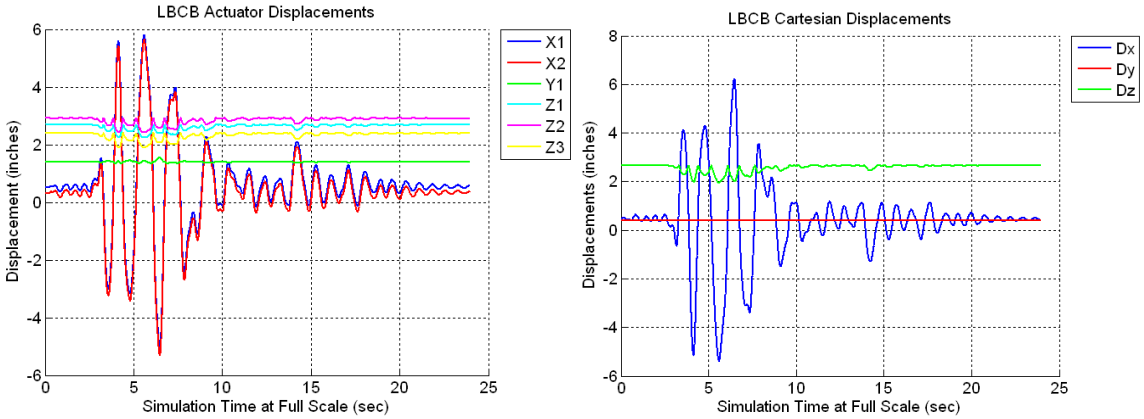

Figure B.413 Raw Data For Specimen A6 1.20xJMA Kobe Trial – LBCB Actuator Displacements (Left) and LBCB Cartesian Displacements (Right)

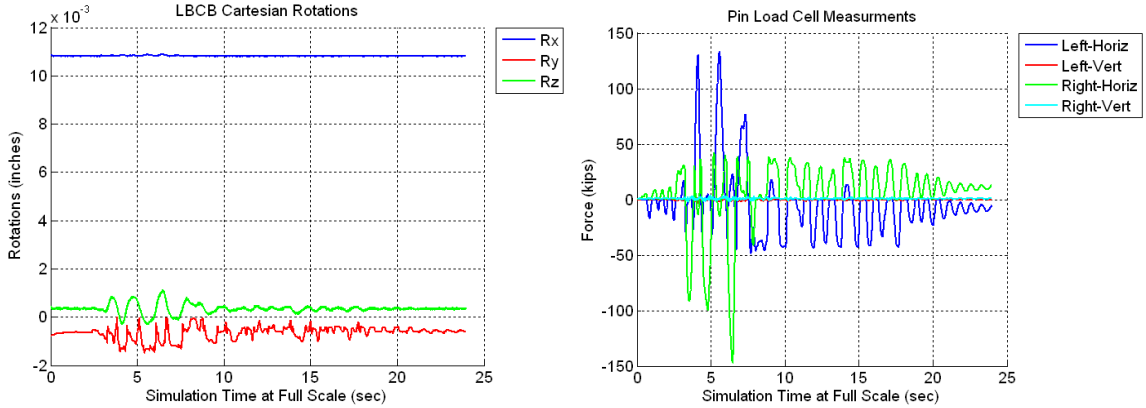

Figure B.414 Raw Data For Specimen A6 1.20xJMA Kobe Trial – LBCB Cartesian Rotations (Left) and Pin Load Cells (Right)

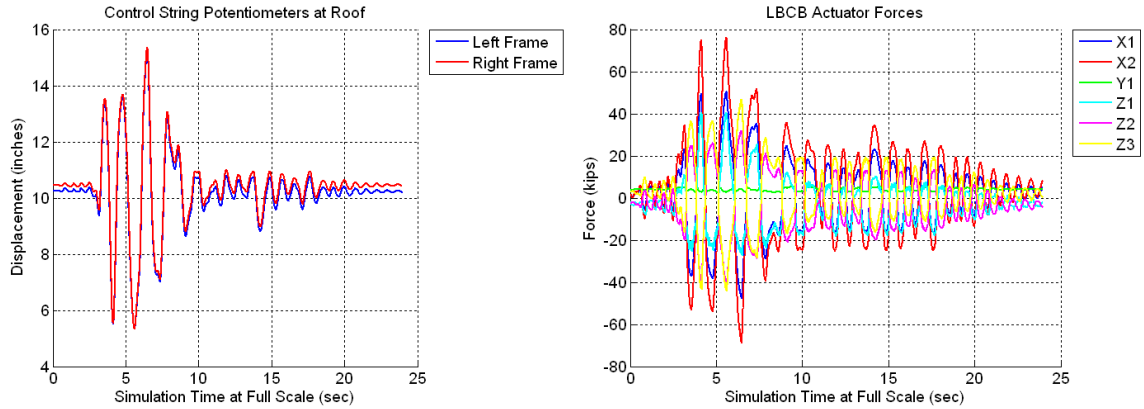

Figure B.415 Raw Data For Specimen A6 1.20xJMA Kobe Trial – Control Roof String Potentiometers (Left) and LBCB Actuator Forces (Right)

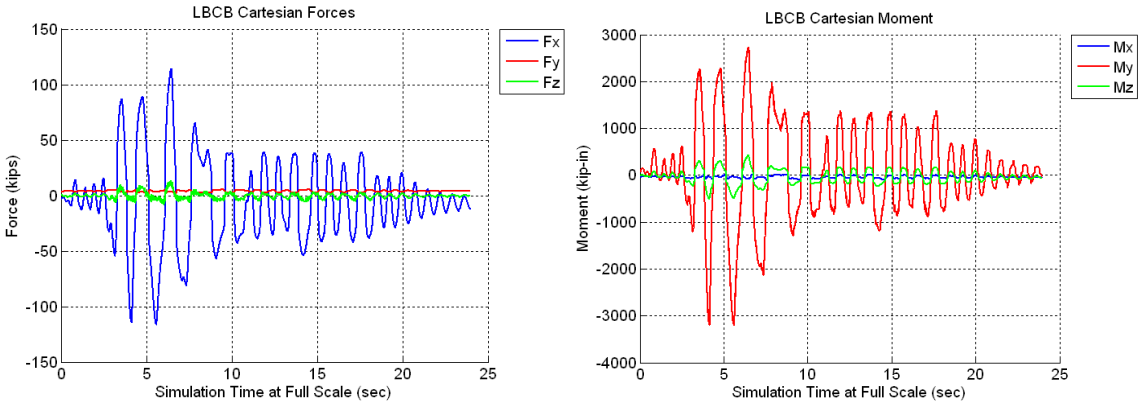

Figure B.416 Raw Data For Specimen A6 1.20xJMA Kobe Trial – LBCB Cartesian Forces (Left) and LBCB Cartesian Moments (Right)

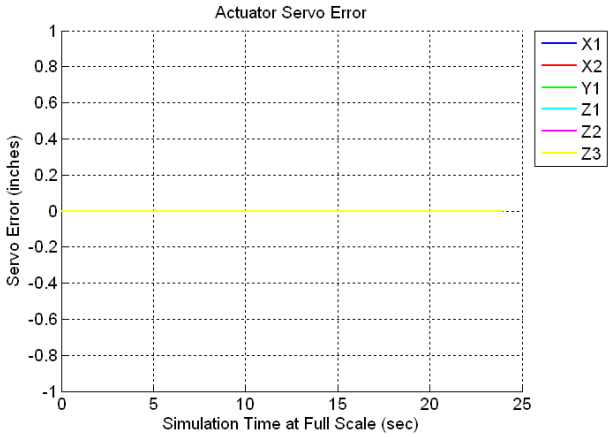

Figure B.417 Raw Data For Specimen A6 1.20xJMA Kobe Trial – LBCB Actuator Servo-Errors

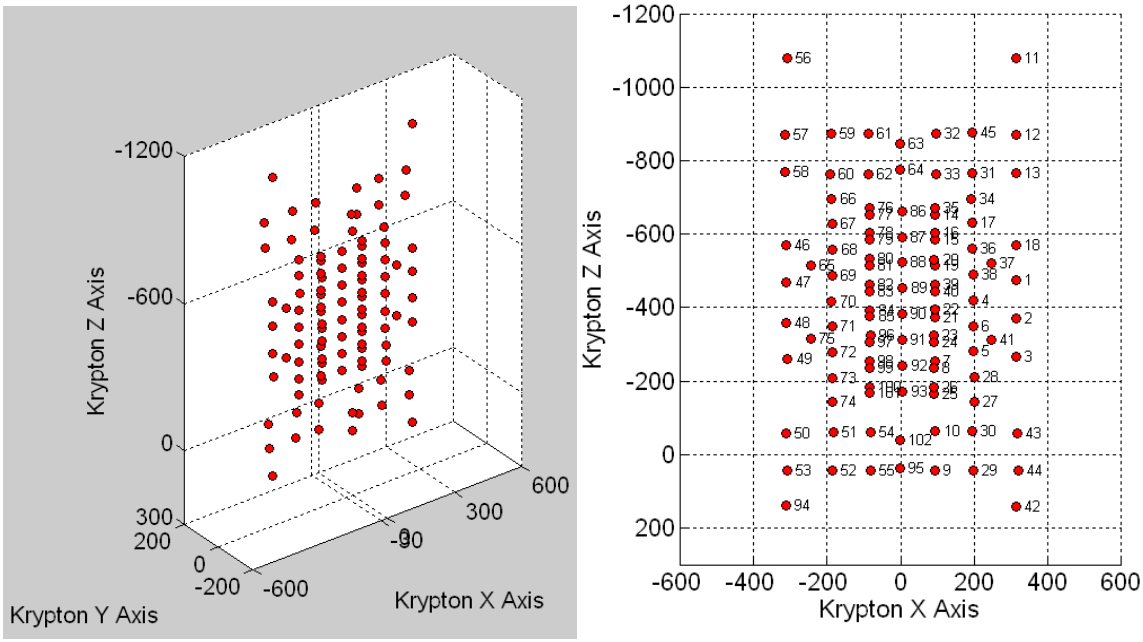

Figure B.418 Raw Data For Specimen A6 1.20xJMA Kobe Trial – Krypton LED Locations (Left) and Krypton LED Numbering (Right)

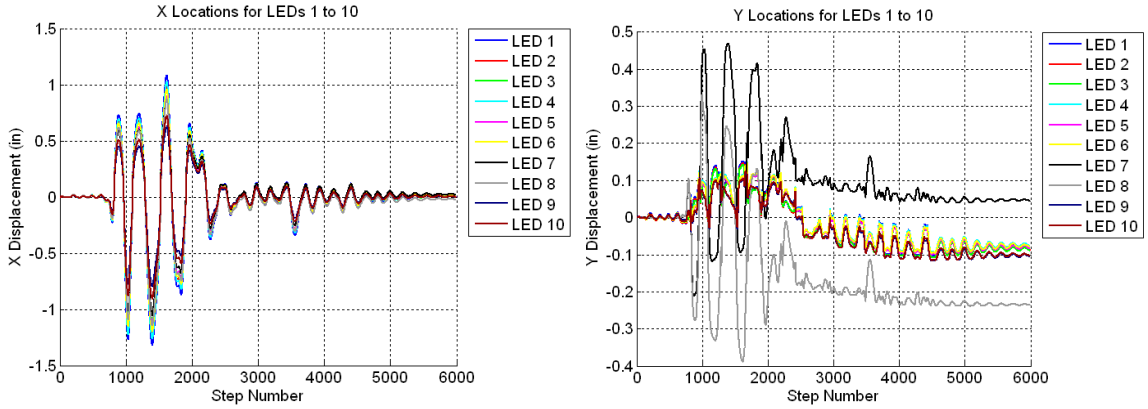

Figure B.419 Raw Data For Specimen A6 1.20xJMA Kobe Trial – X Displacements for LED's 1 to 10 (Left) and Y Displacements for LED's 1 to 10 (Right)

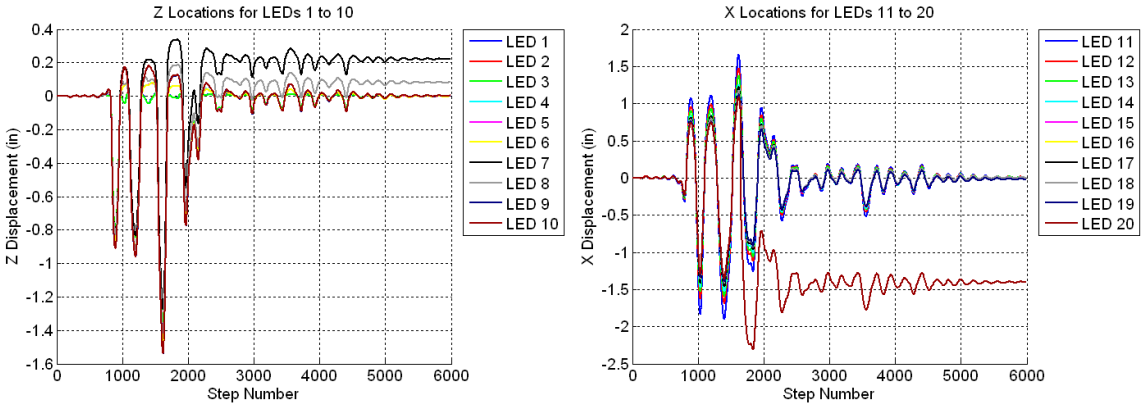

Figure B.420 Raw Data For Specimen A6 1.20xJMA Kobe Trial – Z Displacements for LED's 1 to 10 (Left) and X Displacements for LED's 11 to 20 (Right)

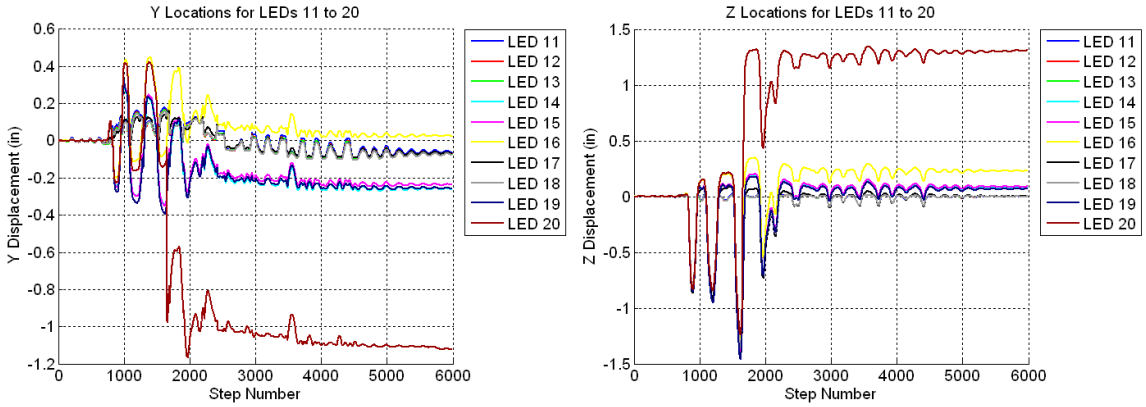

Figure B.421 Raw Data For Specimen A6 1.20xJMA Kobe Trial – Y Displacements for LED's 11 to 20 (Left) and Z Displacements for LED's 11 to 20 (Right)

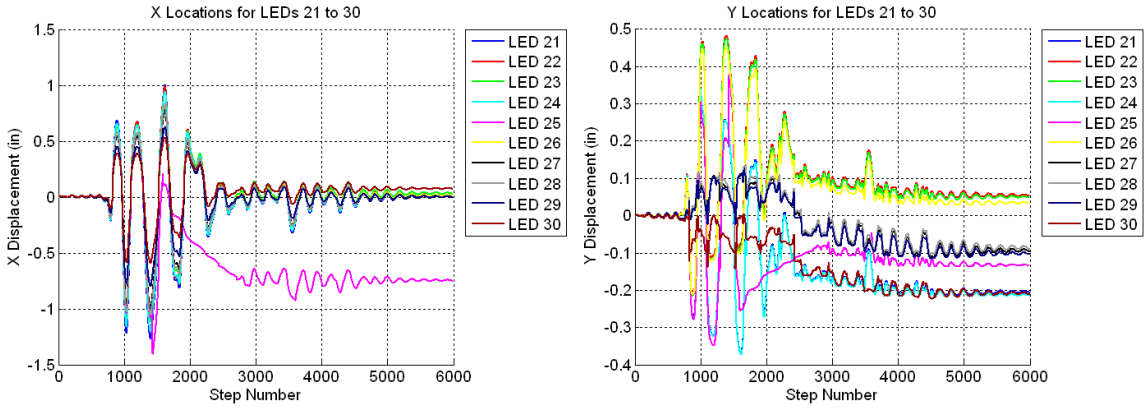

Figure B.422 Raw Data For Specimen A6 1.20xJMA Kobe Trial – X Displacements for LED's 21 to 30 (Left) and Y Displacements for LED's 21 to 30 (Right)

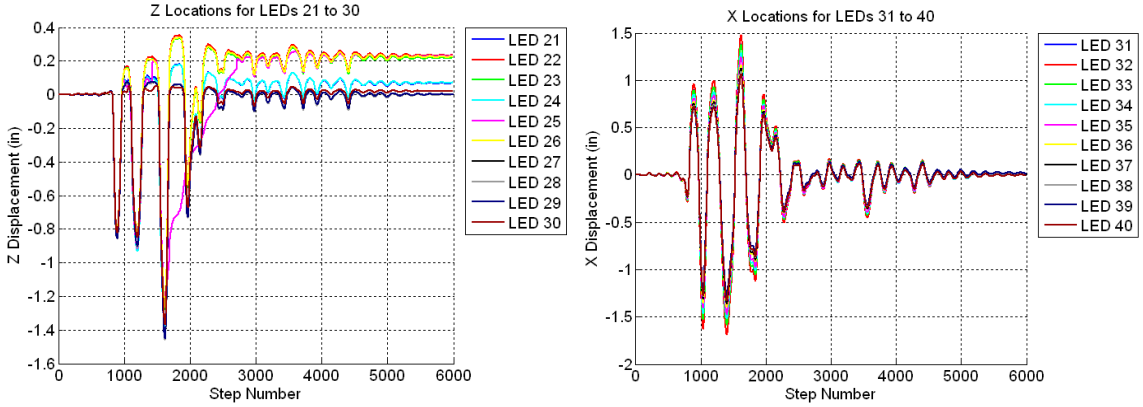

Figure B.423 Raw Data For Specimen A6 1.20xJMA Kobe Trial – Z Displacements for LED's 21 to 30 (Left) and X Displacements for LED's 31 to 40 (Right)

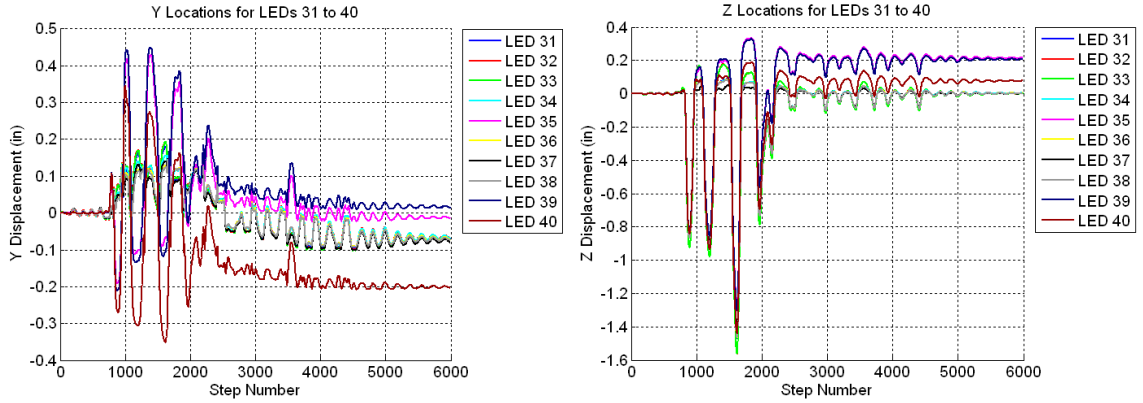

Figure B.424 Raw Data For Specimen A6 1.20xJMA Kobe Trial – Y Displacements for LED's 31 to 40 (Left) and Z Displacements for LED's 31 to 40 (Right)

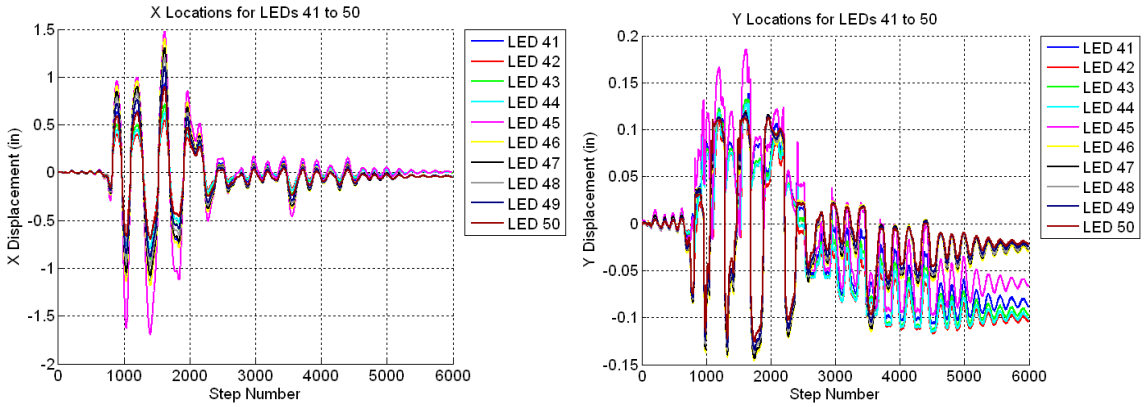

Figure B.425 Raw Data For Specimen A6 1.20xJMA Kobe Trial – X Displacements for LED's 41 to 50 (Left) and Y Displacements for LED's 41 to 50 (Right)

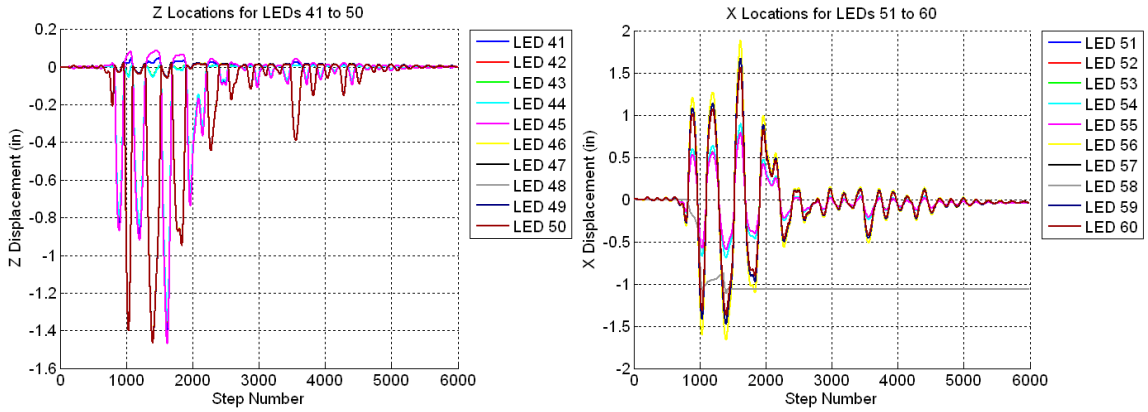

Figure B.426 Raw Data For Specimen A6 1.20xJMA Kobe Trial – Z Displacements for LED's 41 to 50 (Left) and X Displacements for LED's 51 to 60 (Right)

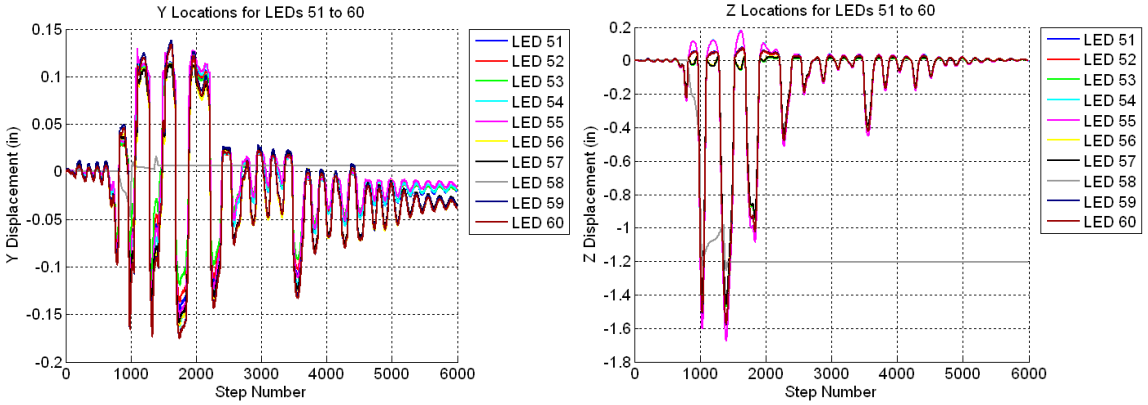

Figure B.427 Raw Data For Specimen A6 1.20xJMA Kobe Trial – Y Displacements for LED's 51 to 60 (Left) and Z Displacements for LED's 51 to 60 (Right)

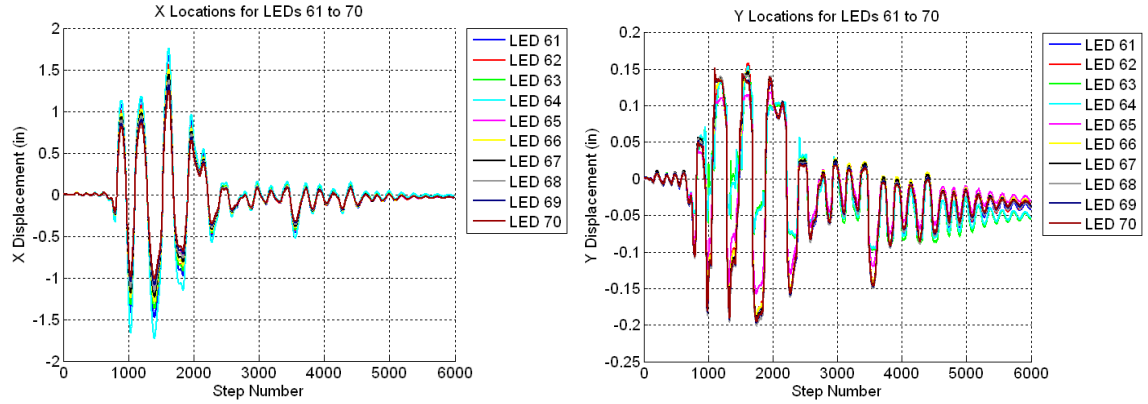

Figure B.428 Raw Data For Specimen A6 1.20xJMA Kobe Trial – X Displacements for LED's 61 to 70 (Left) and Y Displacements for LED's 61 to 70 (Right)

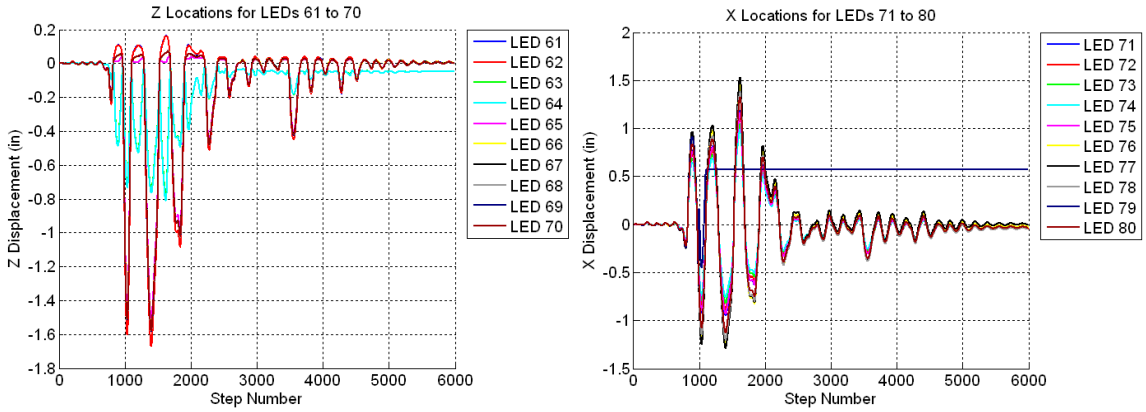

Figure B.429 Raw Data For Specimen A6 1.20xJMA Kobe Trial – Z Displacements for LED's 61 to 70 (Left) and X Displacements for LED's 71 to 80 (Right)

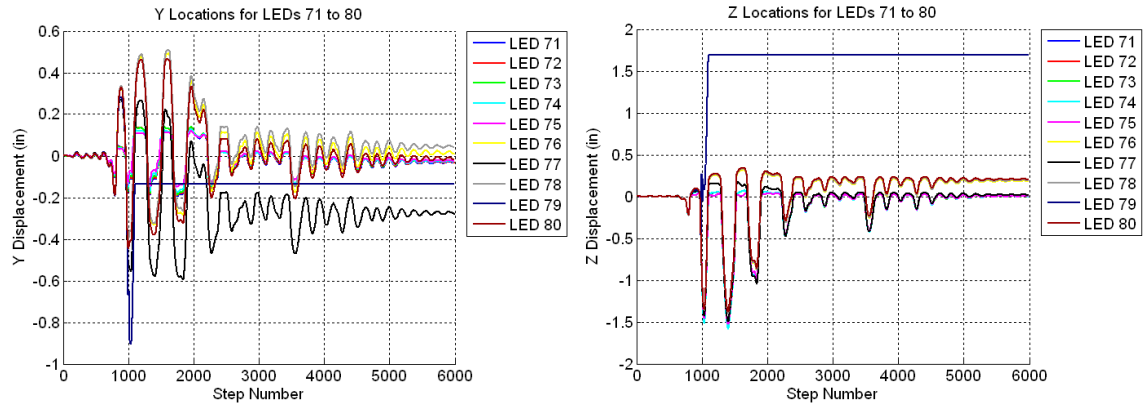

Figure B.430 Raw Data For Specimen A6 1.20xJMA Kobe Trial – Y Displacements for LED's 71 to 80 (Left) and Z Displacements for LED's 71 to 80 (Right)

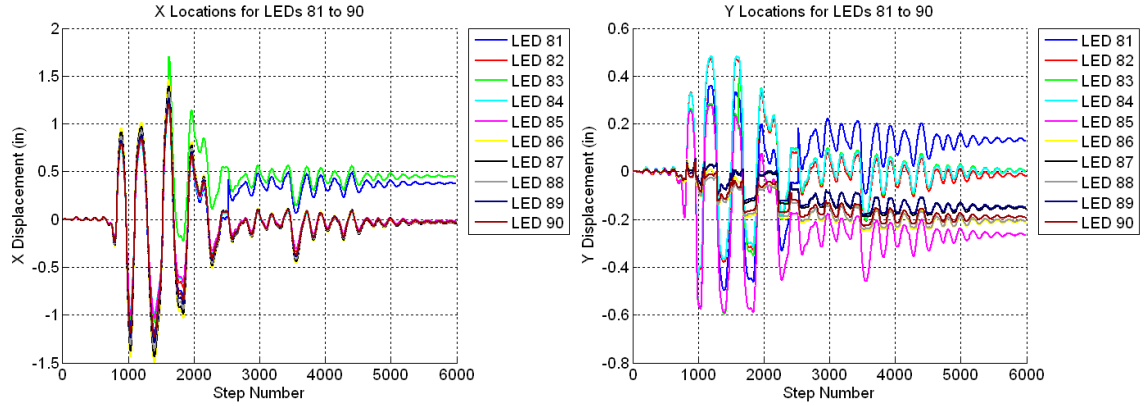

Figure B.431 Raw Data For Specimen A6 1.20xJMA Kobe Trial – X Displacements for LED's 81 to 90 (Left) and Y Displacements for LED's 81 to 90 (Right)

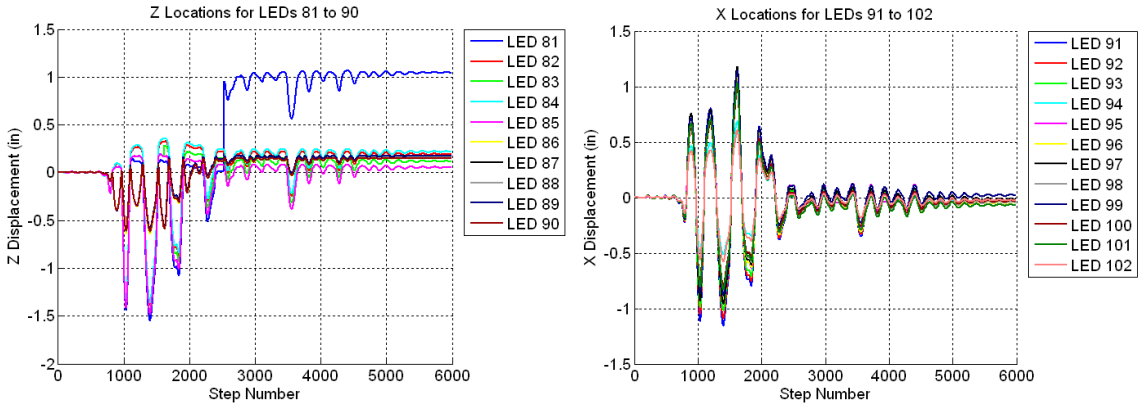

Figure B.432 Raw Data For Specimen A6 1.20xJMA Kobe Trial – Z Displacements for LED's 81 to 90 (Left) and X Displacements for LED's 91 to 102 (Right)

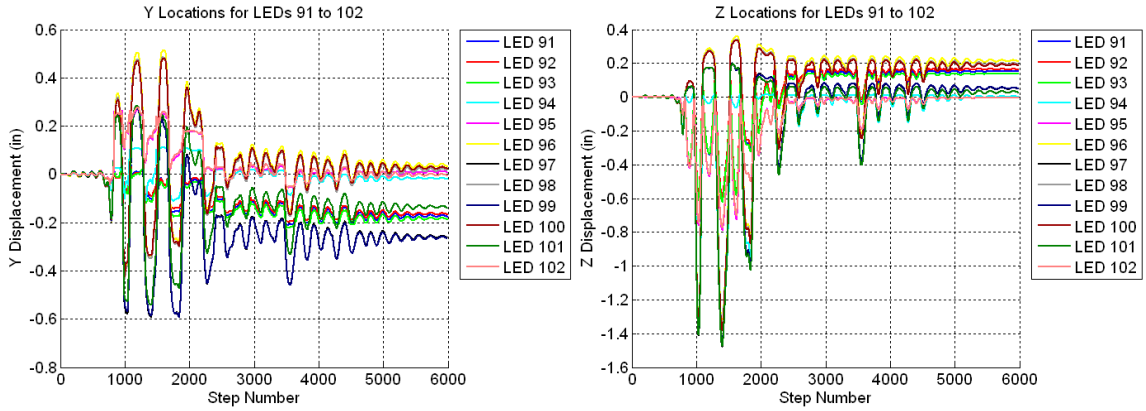

Figure B.433 Raw Data For Specimen A6 1.20xJMA Kobe Trial – Y Displacements for LED's 91 to 102 (Left) and Z Displacements for LED's 91 to 102 (Right)

B.11 Specimen A7

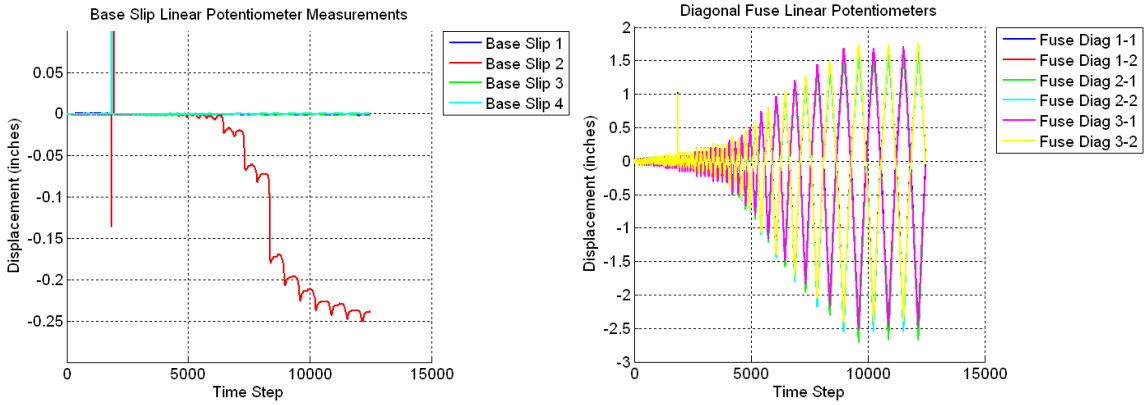

Figure B.434 Raw Data For Specimen A7 – Base Slip (Left) and Fuse Linear Potentiometers (Right)

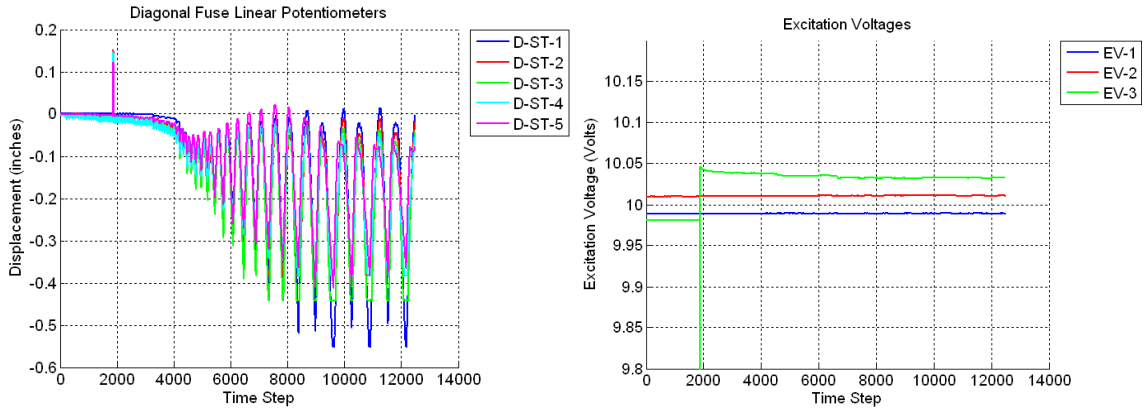

Figure B.435 Raw Data For Specimen A7 – Strut Linear Potentiometers (Left) and Excitation Voltage (Right)

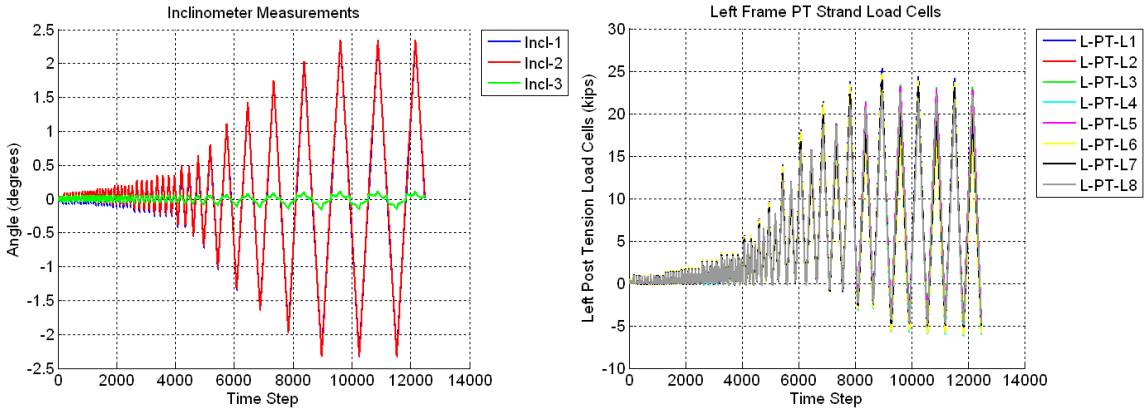

Figure B.436 Raw Data For Specimen A7 – Inclinometers and Left Frame PT Load Cells (Right)

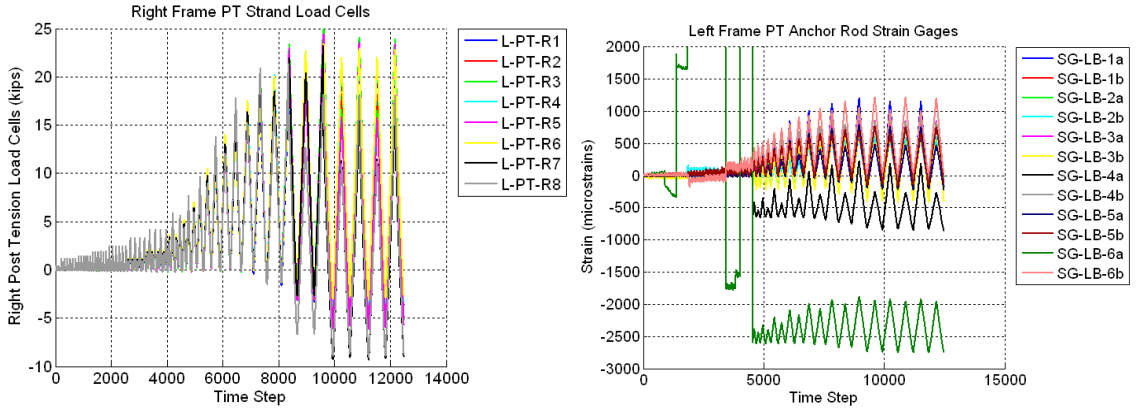

Figure B.437 Raw Data For Specimen A7 – Right Frame PT Load Cells (Left) and Left Frame PT Anchor Rods (Right)

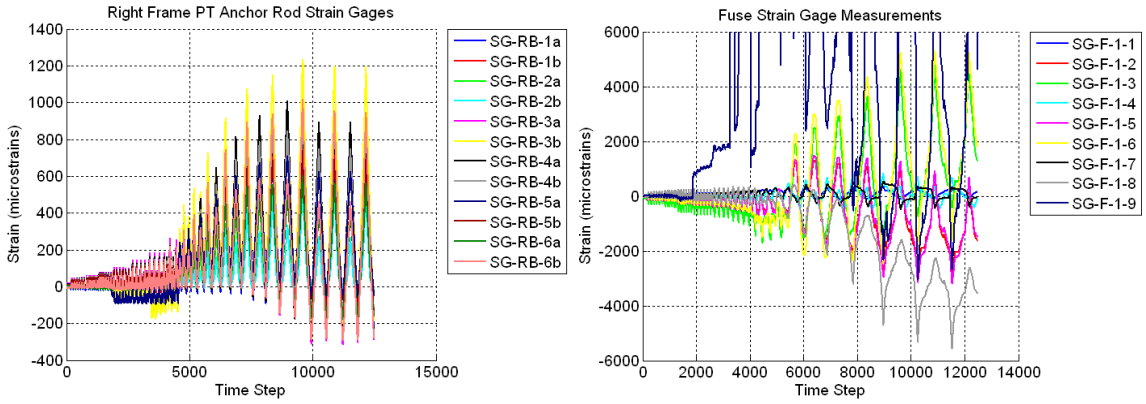

Figure B.438 Raw Data For Specimen A7 – Right Frame PT Anchor Rods (Left) and Bottom Back Fuse Strain Gages (Right)

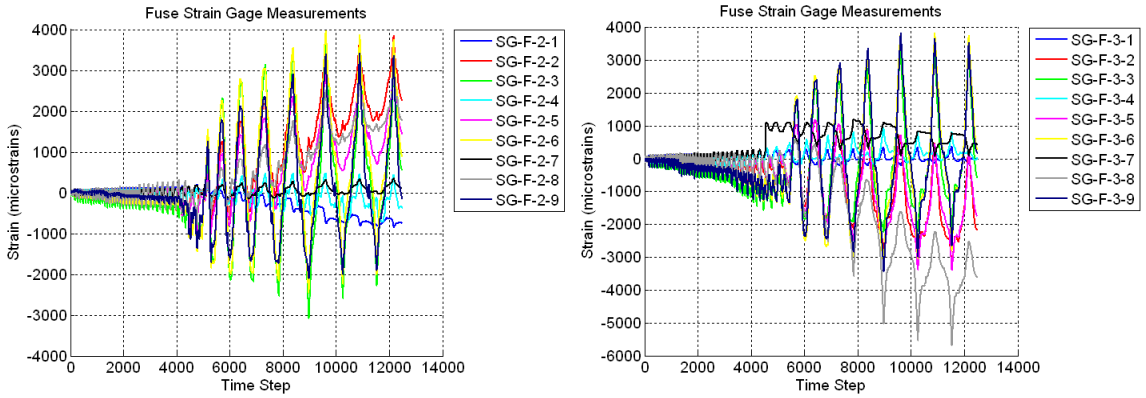

Figure B.439 Raw Data For Specimen A7 – Bottom Front Strain Gages (Left) and Mid-Height Back Fuse Strain Gages (Right)

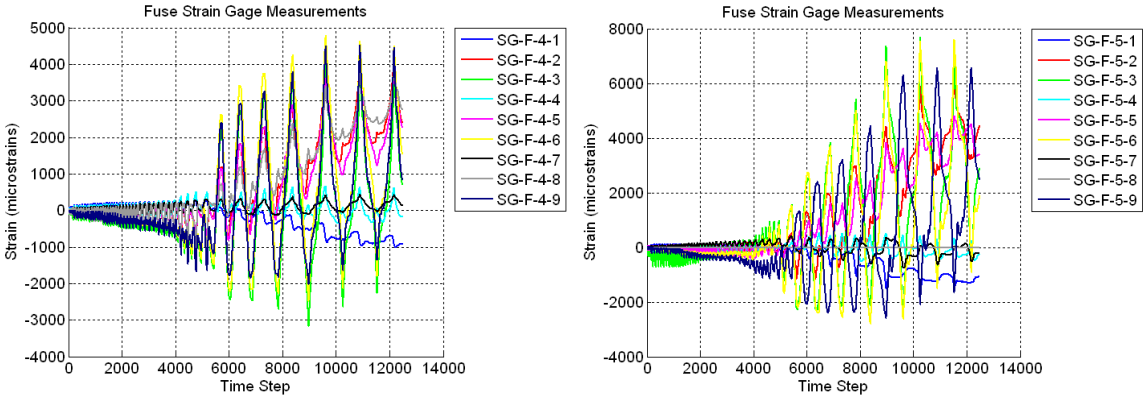

Figure B.440 Raw Data For Specimen A7 – Mid-Height Front Fuse Strain Gages (Left) and Top Back Fuse Strain Gages (Right)

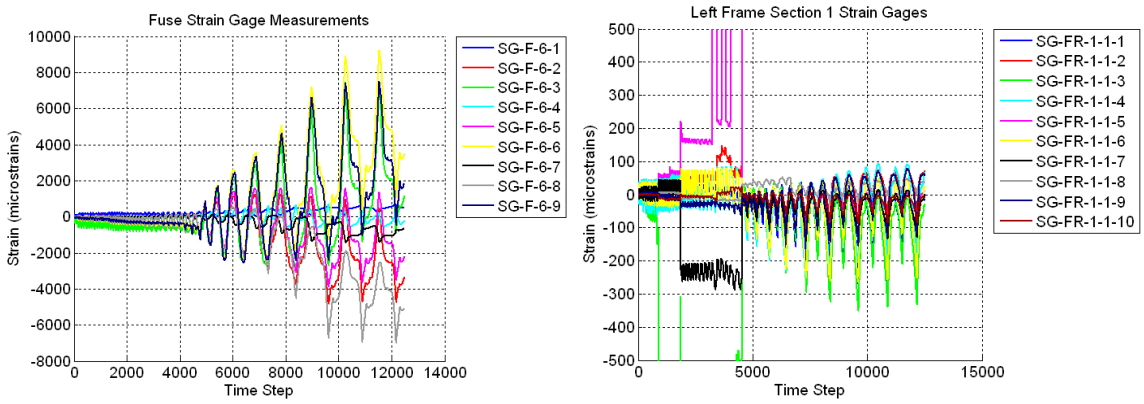

Figure B.441 Raw Data For Specimen A7 – Top Front Fuse Strain Gages (Left) and Left Frame Section 1-1 Strain Gages (Right)

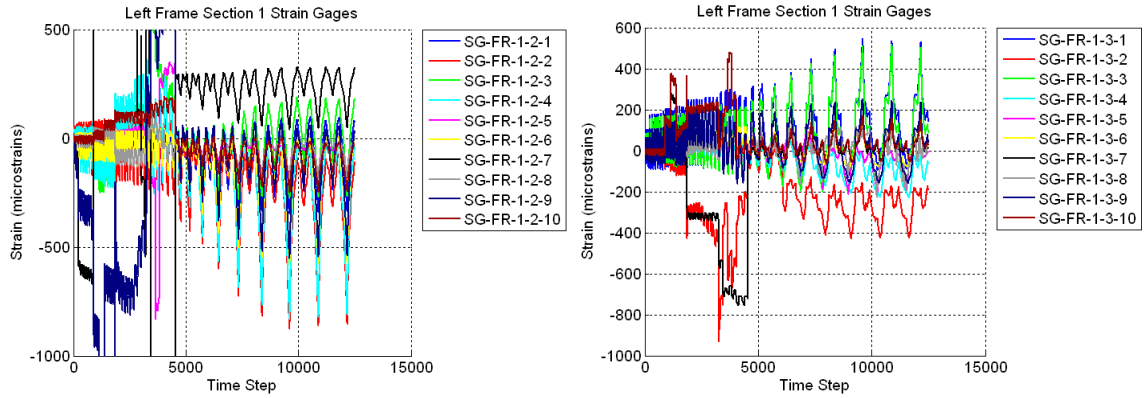

Figure B.442 Raw Data For Specimen A7 – Left Frame Section 1-2 Strain Gages (Left) and Left Frame Section 1-3 Strain Gages (Right)

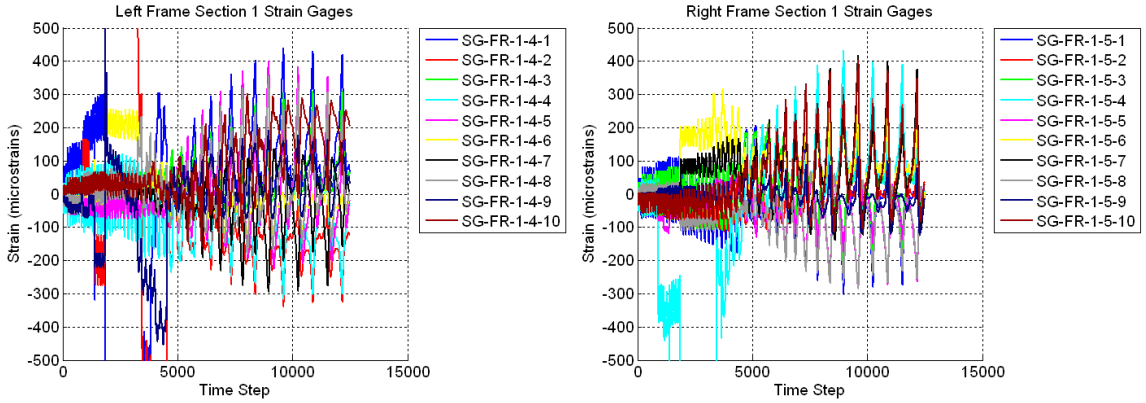

Figure B.443 Raw Data For Specimen A7 – Left Frame Section 1-4 Strain Gages (Left) and Right Frame Section 1-5 Strain Gages (Right)

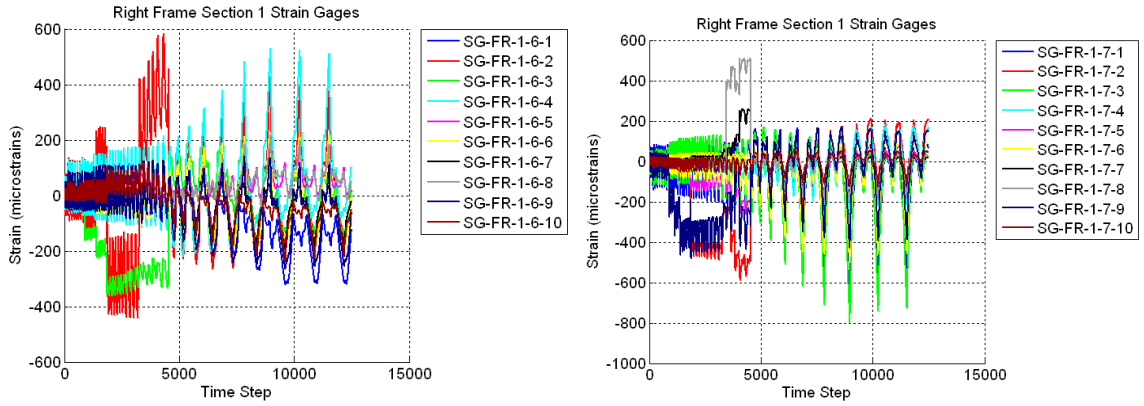

Figure B.444 Raw Data For Specimen A7 – Right Frame Section 1-6 Strain Gages (Left) and Right Frame Section 1-7 Strain Gages (Right)

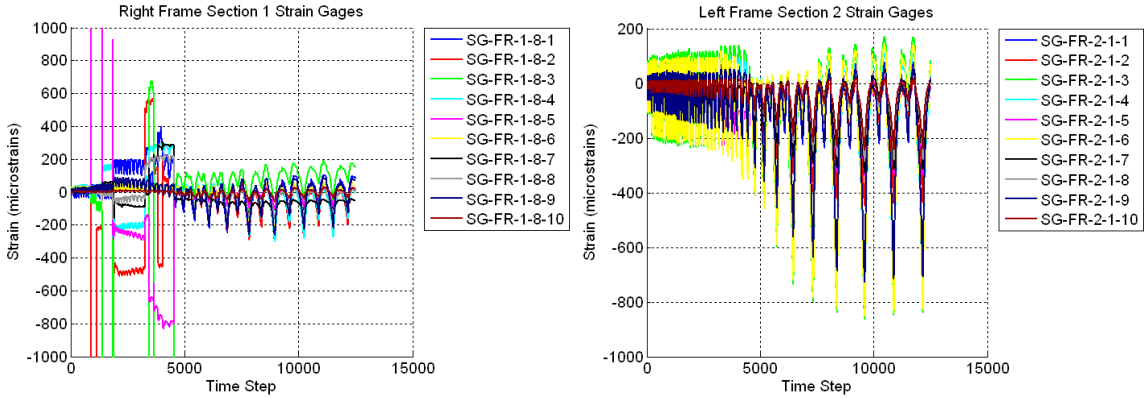

Figure B.445 Raw Data For Specimen A7 – Right Frame Section 1-8 Strain Gages (Left) and Left Frame Section 2-1 Strain Gages (Right)

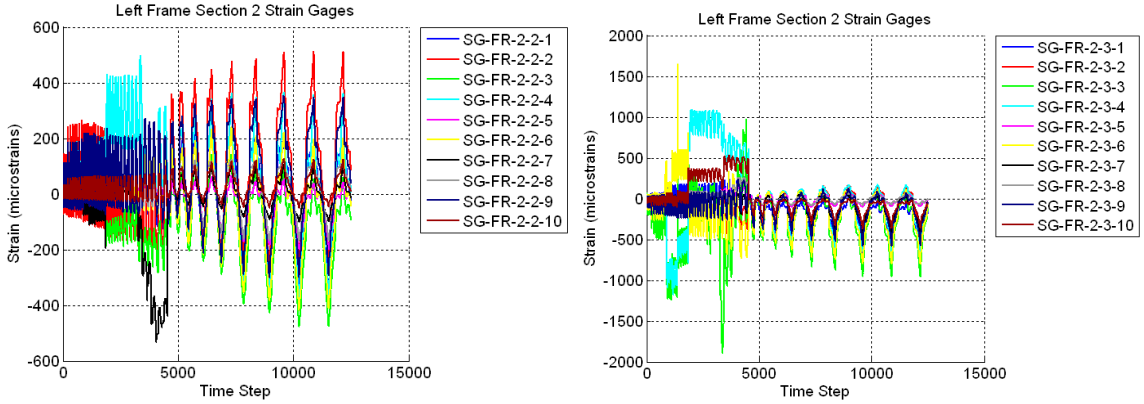

Figure B.446 Raw Data For Specimen A7 – Left Frame Section 2-2 Strain Gages (Left) and Left Frame Section 2-3 Strain Gages (Right)

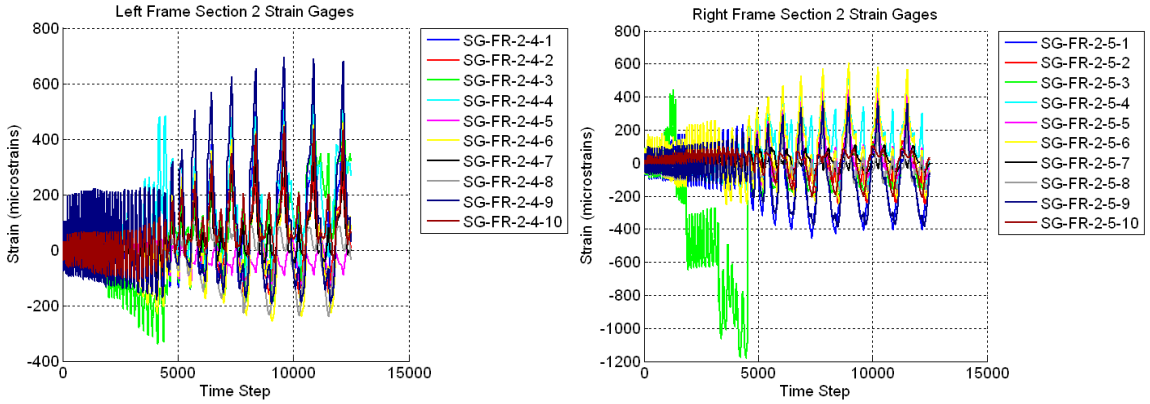

Figure B.447 Raw Data For Specimen A7 – Left Frame Section 2-4 Strain Gages (Left) and Right Frame Section 2-5 Strain Gages (Right)

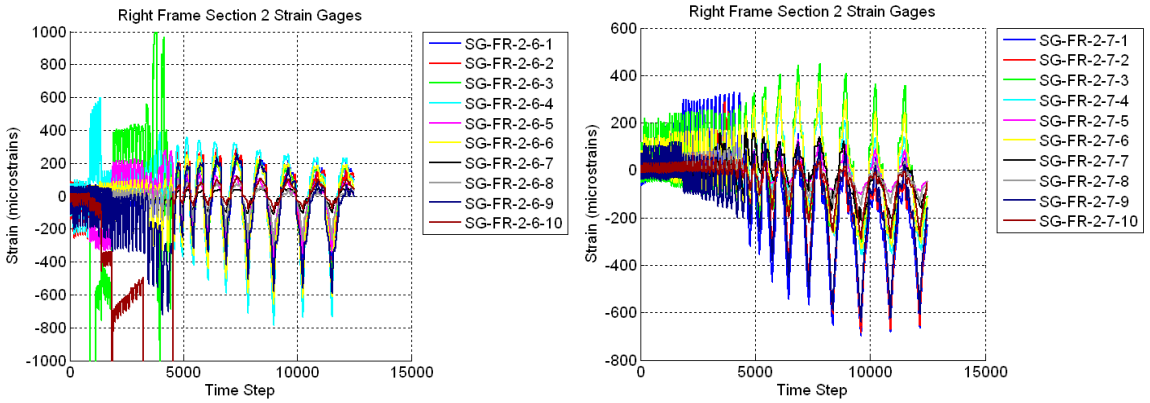

Figure B.448 Raw Data For Specimen A7 – Right Frame Section 2-6 Strain Gages (Left) and Right Frame Section 2-7 Strain Gages (Right)

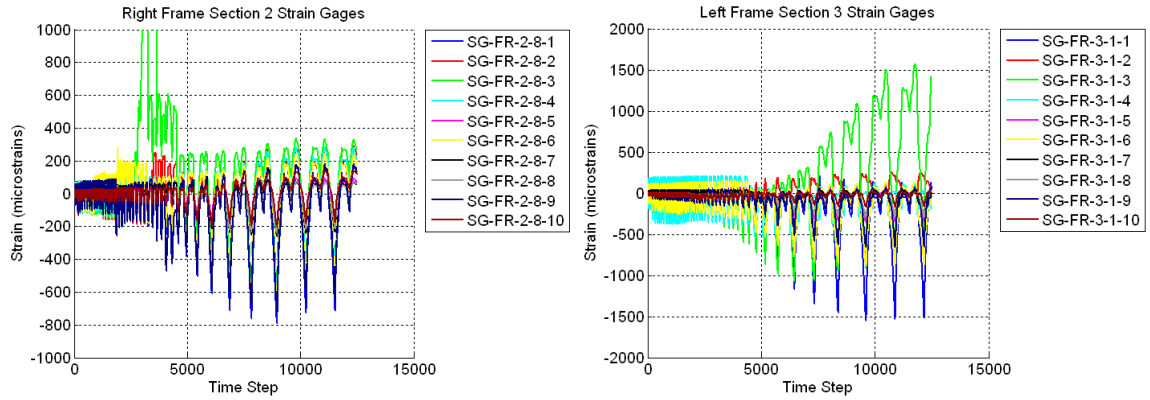

Figure B.449 Raw Data For Specimen A7 – Right Frame Section 2-8 Strain Gages (Left) and Left Frame Section 3-1 Strain Gages (Right)

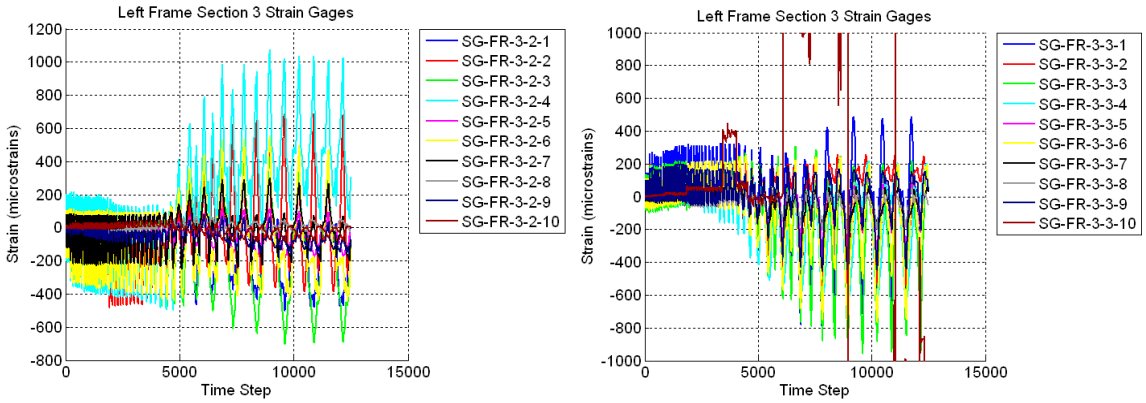

Figure B.450 Raw Data For Specimen A7 – Left Frame Section 3-2 Strain Gages (Left) and Left Frame Section 3-3 Strain Gages (Right)

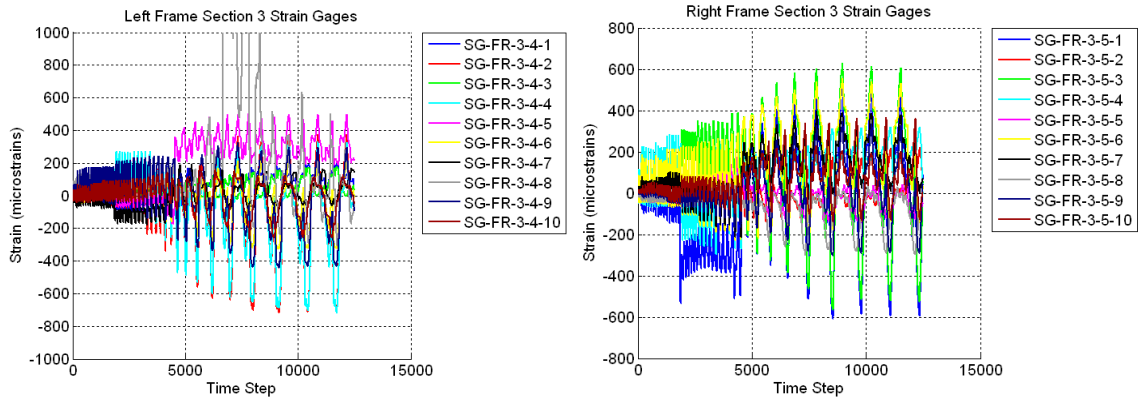

Figure B.451 Raw Data For Specimen A7 – Left Frame Section 3-4 Strain Gages (Left) and Right Frame Section 3-5 Strain Gages (Right)

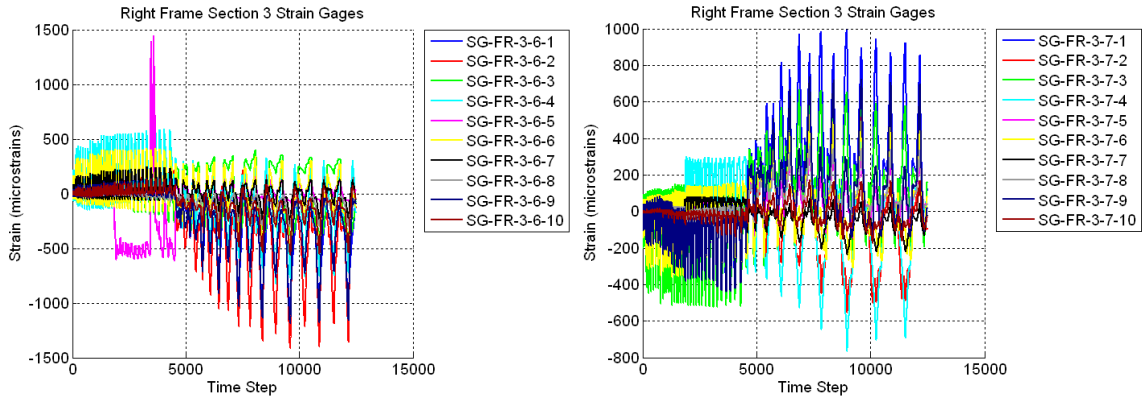

Figure B.452 Raw Data For Specimen A7 – Right Frame Section 3-6 Strain Gages (Left) and Right Frame Section 3-7 Strain Gages (Right)

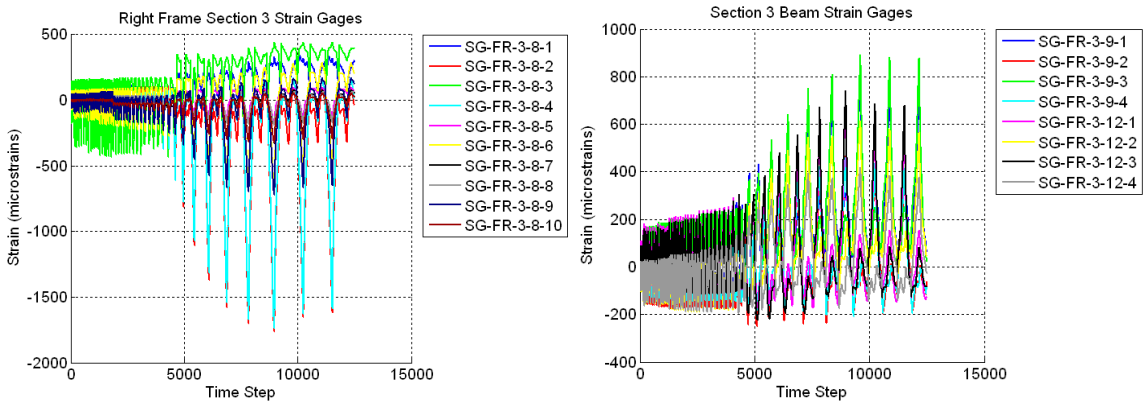

Figure B.453 Raw Data For Specimen A7 – Right Frame Section 3-8 Strain Gages (Left) and Third Floor Beam Strain Gages (Right)

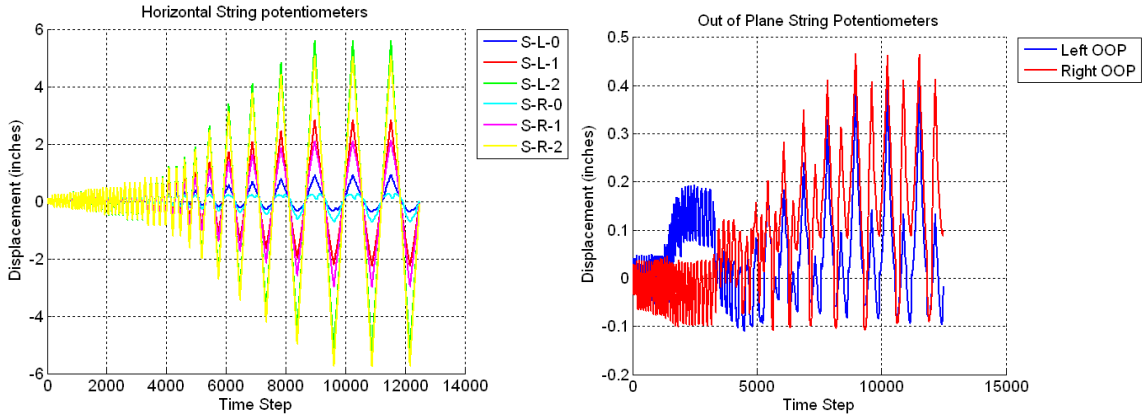

Figure B.454 Raw Data For Specimen A7 – Horizontal String Potentiometers (Left) and Out-of-Plane String Potentiometers (Right)

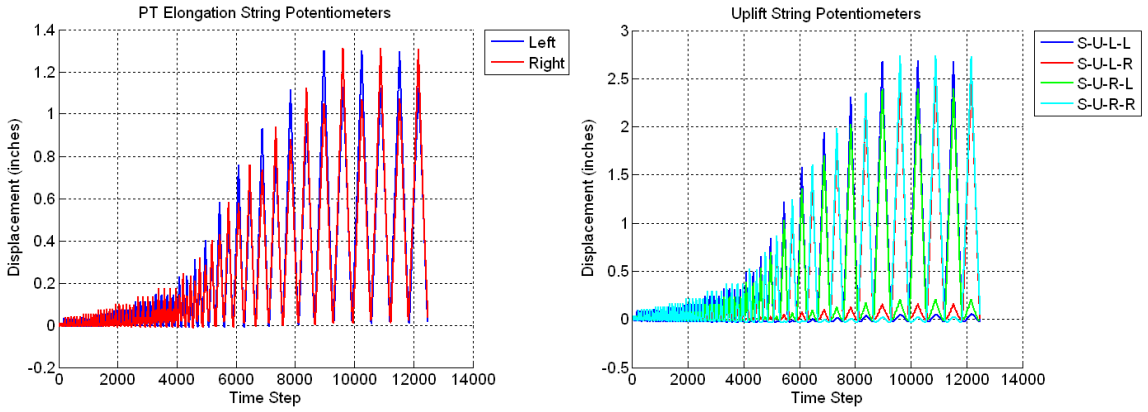

Figure B.455 Raw Data For Specimen A7 – PT Elongation String Potentiometers (Left) and Uplift String Potentiometers (Right)

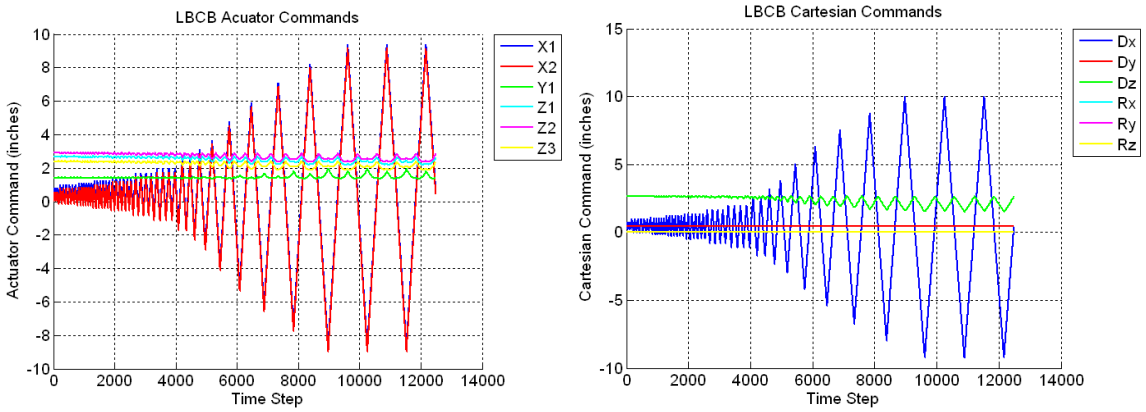

Figure B.456 Raw Data For Specimen A7 – LBCB Actuator Commands (Left) and LBCB Cartesian Commands (Right)

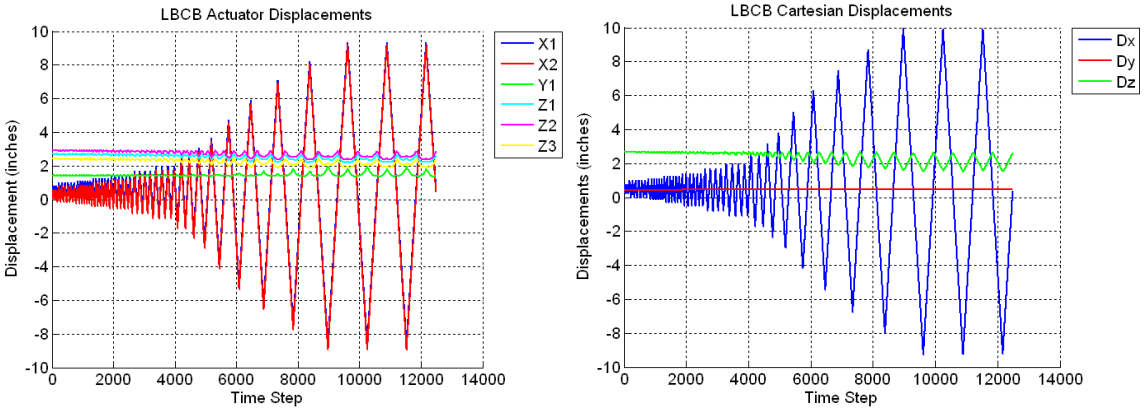

Figure B.457 Raw Data For Specimen A7 – LBCB Actuator Displacements (Left) and LBCB Cartesian Displacements (Right)

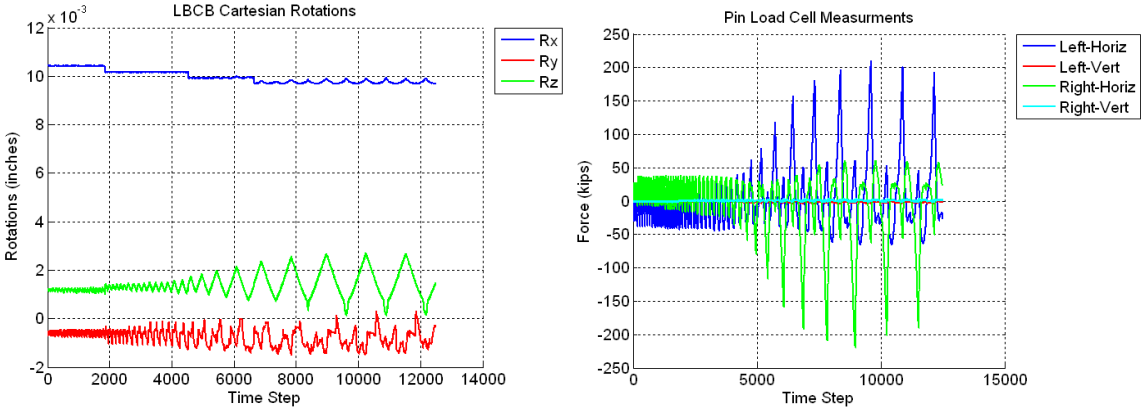

Figure B.458 Raw Data For Specimen A7 – LBCB Cartesian Rotations (Left) and Pin Load Cells (Right)

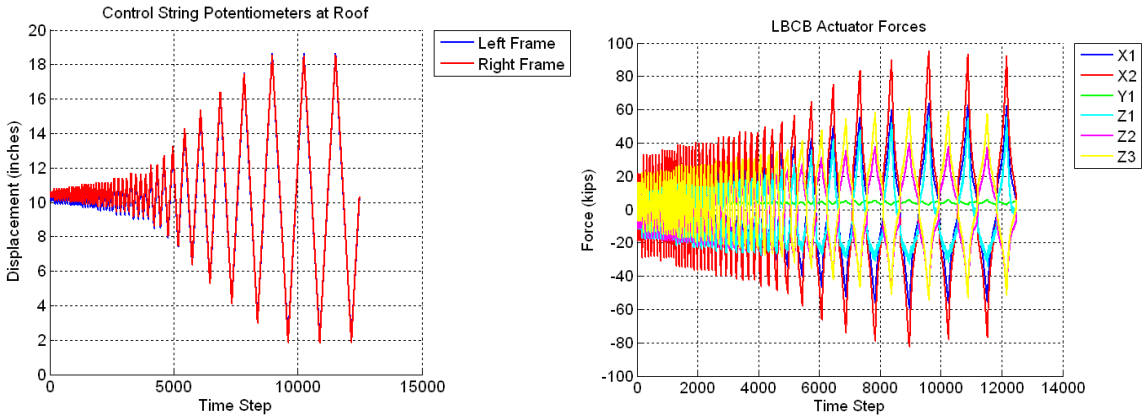

Figure B.459 Raw Data For Specimen A7 – Control Roof String Potentiometers (Left) and LBCB Actuator Forces (Right)

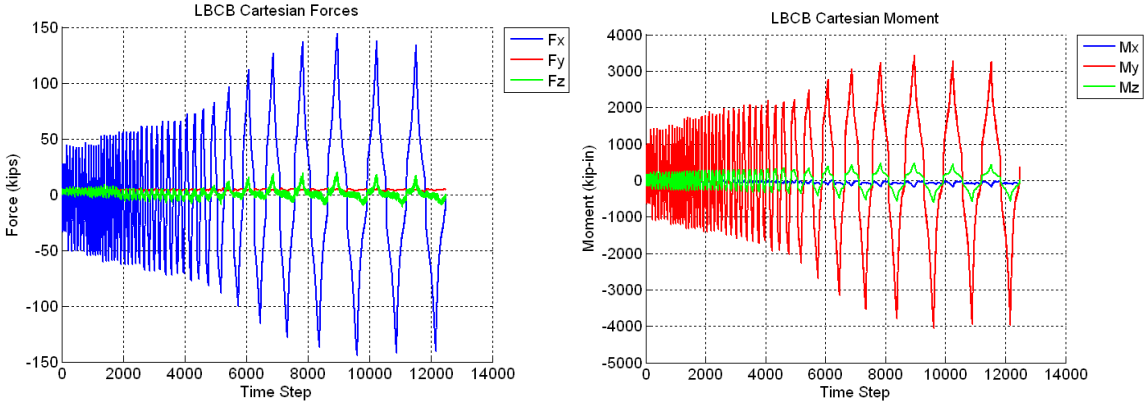

Figure B.460 Raw Data For Specimen A7 – LBCB Cartesian Forces (Left) LBCB Cartesian Moments (Right)

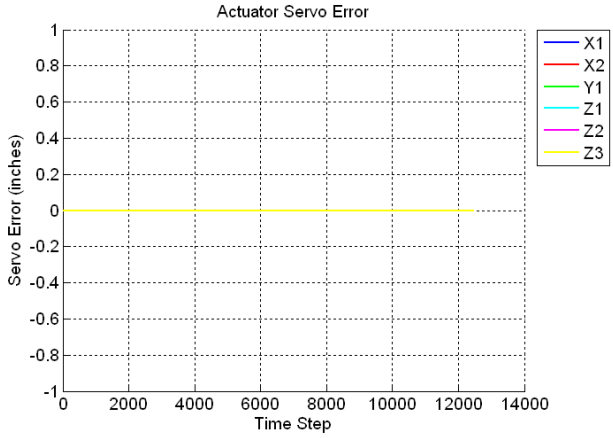

Figure B.461 Raw Data For Specimen A7 – LBCB Actuator Servo-Error

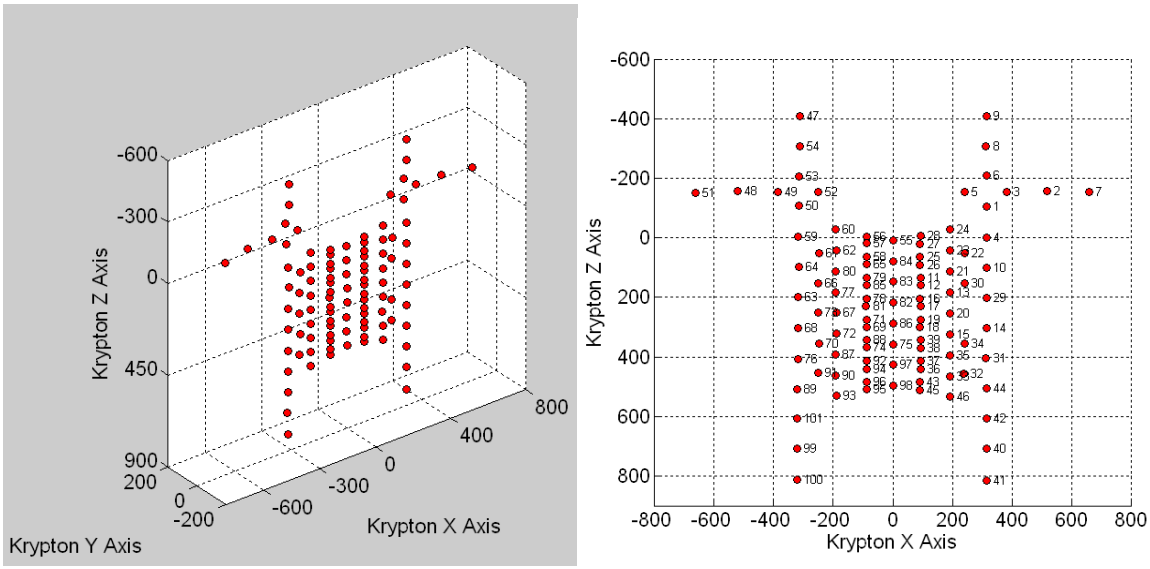

Figure B.462 Raw Data For Specimen A7 – Krypton LED Locations (Left) and Krypton LED Numbering (Right)

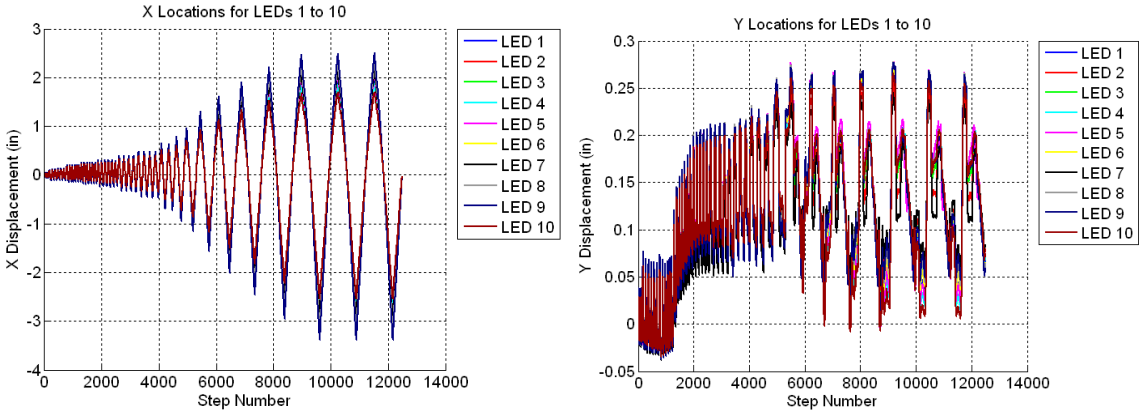

Figure B.463 Raw Data For Specimen A7 – X Displacements for LED's 1 to 10 (Left) and Y Displacements for LED's 1 to 10 (Right)

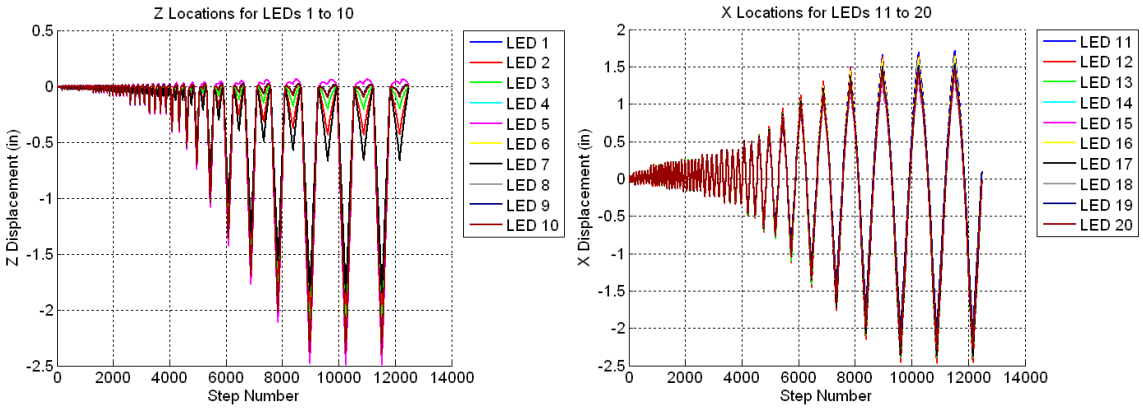

Figure B.464 Raw Data For Specimen A7 – Z Displacements for LED's 1 to 10 (Left) and X Displacements for LED's 11 to 20 (Right)

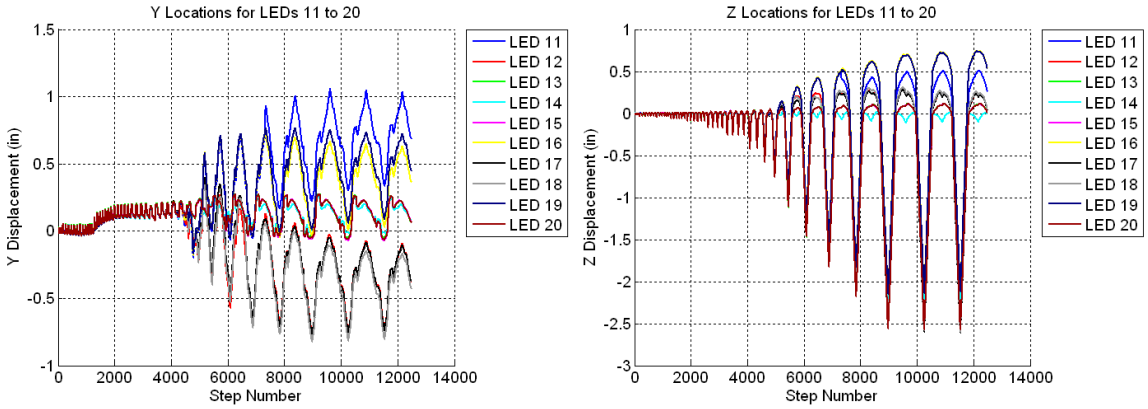

Figure B.465 Raw Data For Specimen A7 – Y Displacements for LED's 11 to 20 (Left) and Z Displacements for LED's 11 to 20 (Right)

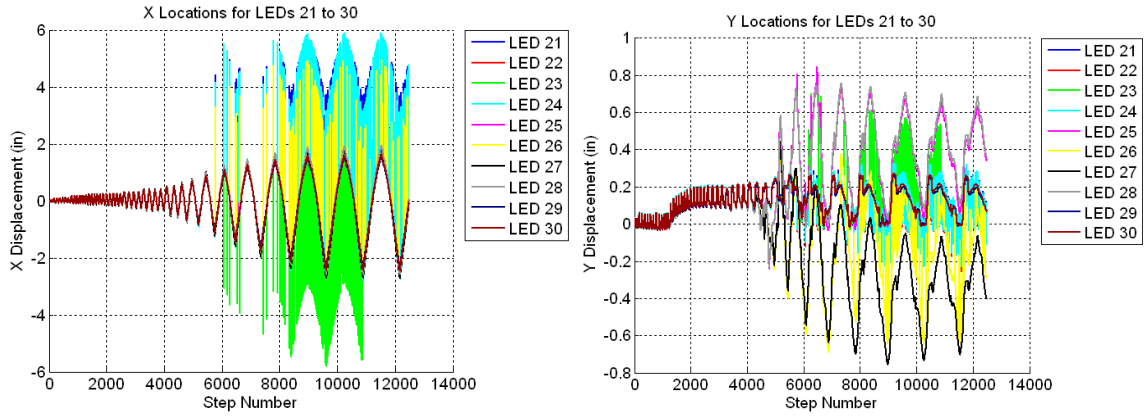

Figure B.466 Raw Data For Specimen A7 – X Displacements for LED's 21 to 30 (Left) and Y Displacements for LED's 21 to 30 (Right)

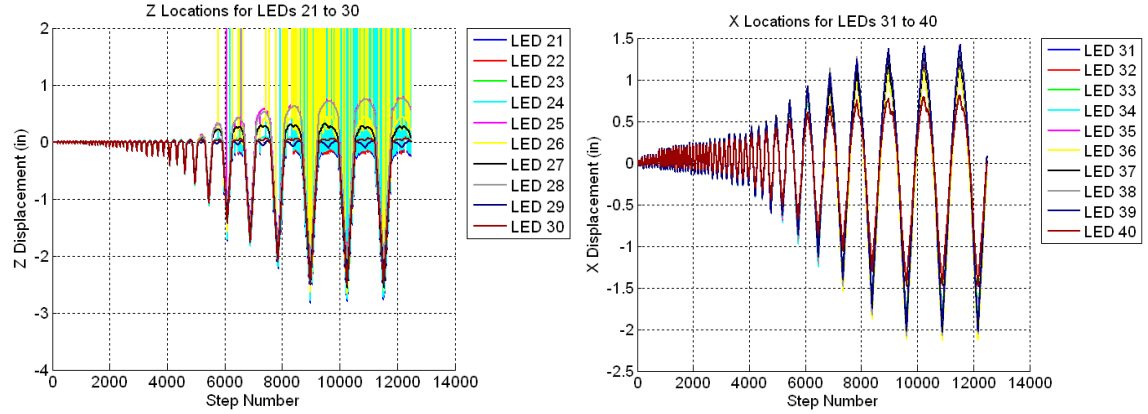

Figure B.467 Raw Data For Specimen A7 – Z Displacements for LED's 21 to 30 (Left) and X Displacements for LED's 31 to 40 (Right)

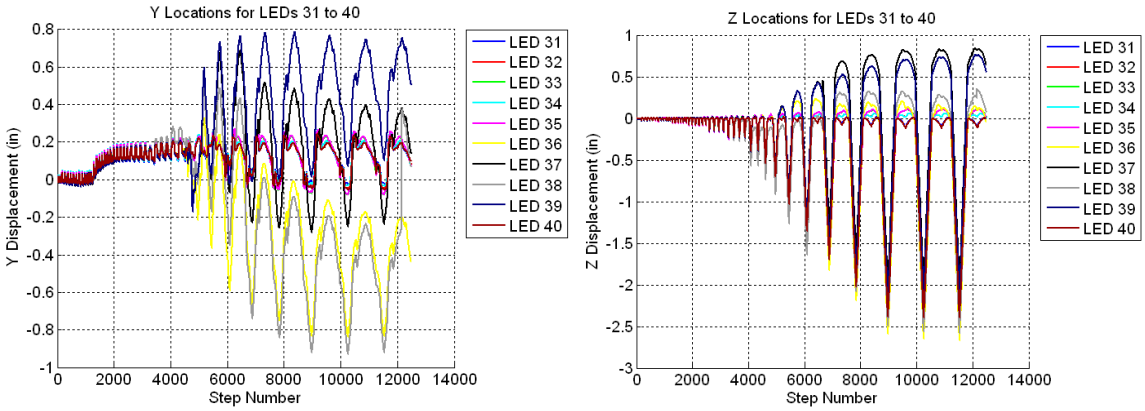

Figure B.468 Raw Data For Specimen A7 – Y Displacements for LED's 31 to 40 (Left) and Z Displacements for LED's 31 to 40 (Right)

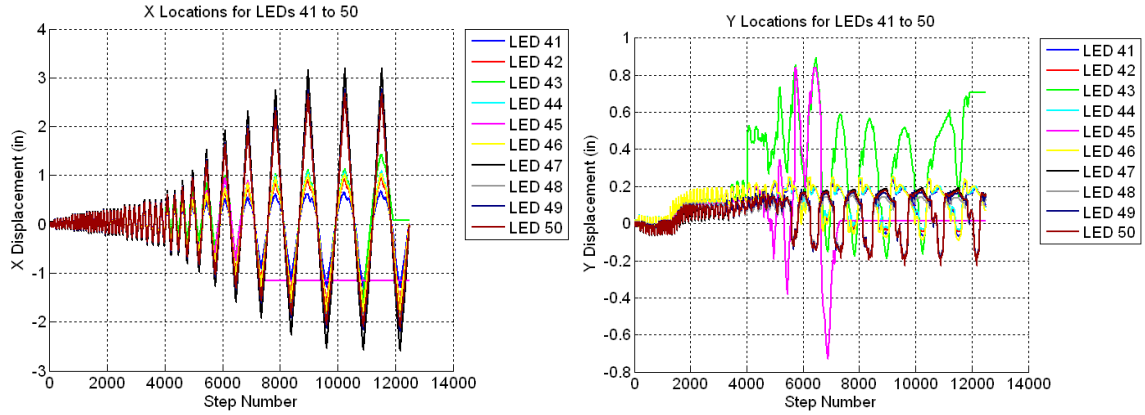

Figure B.469 Raw Data For Specimen A7 – X Displacements for LED's 41 to 50 (Left) and Y Displacements for LED's 41 to 50 (Right)

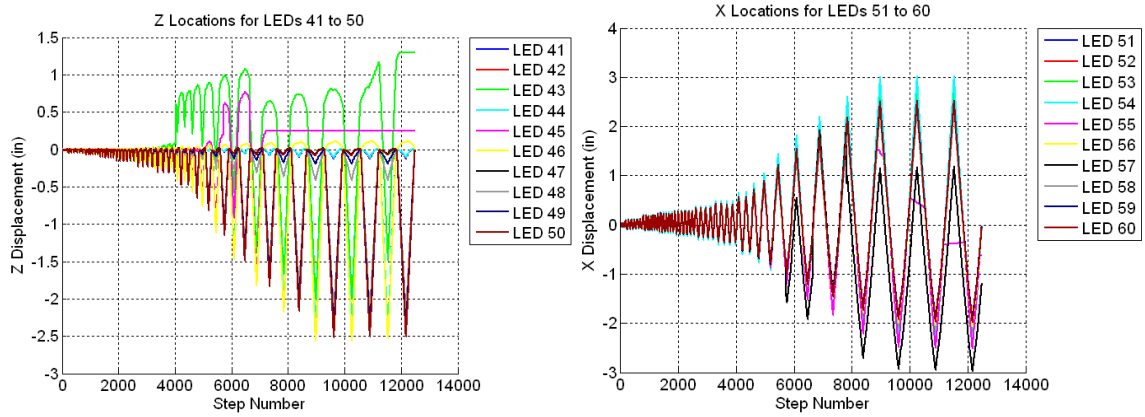

Figure B.470 Raw Data For Specimen A7 – Z Displacements for LED's 41 to 50 (Left) and X Displacements for LED's 51 to 60 (Right)

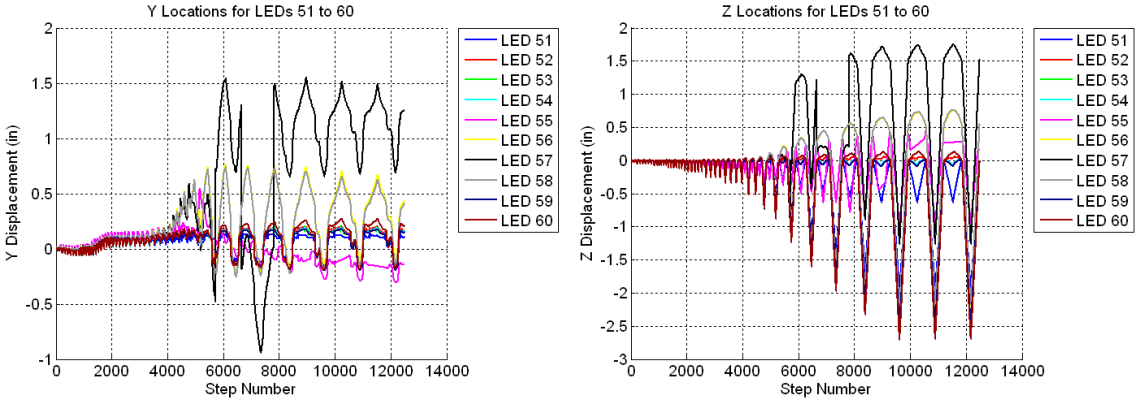

Figure B.471 Raw Data For Specimen A7 – Y Displacements for LED's 51 to 60 (Left) and Z Displacements for LED's 51 to 60 (Right)

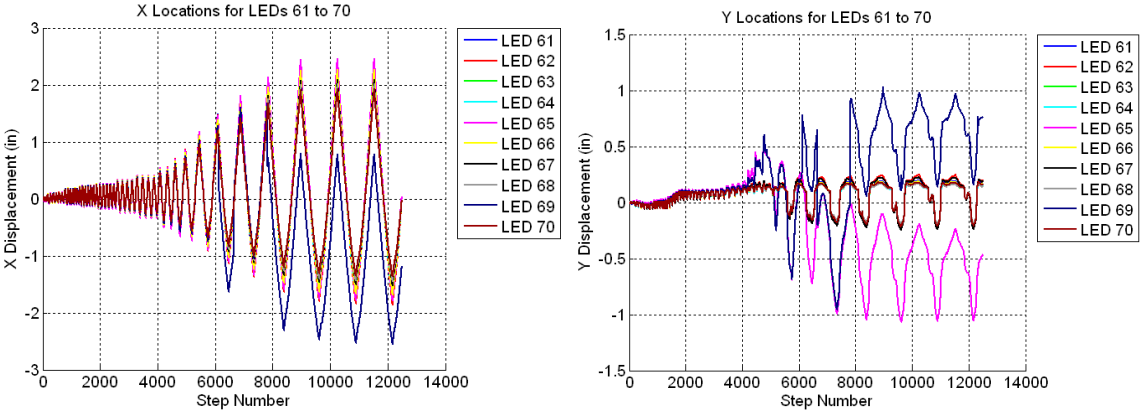

Figure B.472 Raw Data For Specimen A7 – X Displacements for LED's 61 to 70 (Left) and Y Displacements for LED's 61 to 70 (Right)

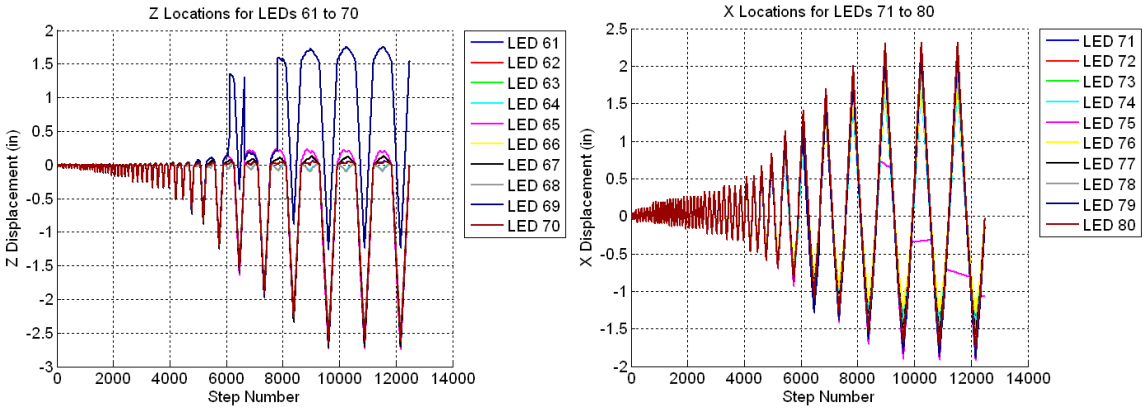

Figure B.473 Raw Data For Specimen A7 – Z Displacements for LED's 61 to 70 (Left) and X Displacements for LED's 71 to 80 (Right)

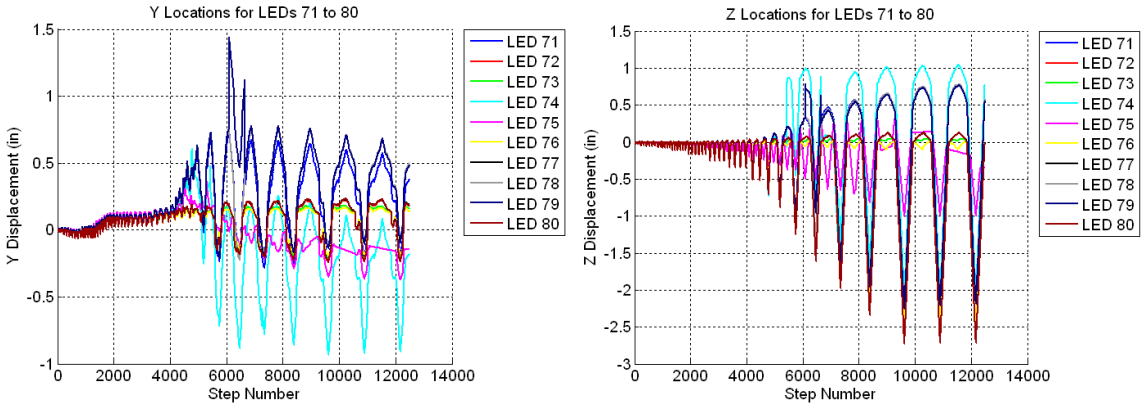

Figure B.474 Raw Data For Specimen A7 – Y Displacements for LED's 71 to 80 (Left) and Z Displacements for LED's 71 to 80 (Right)

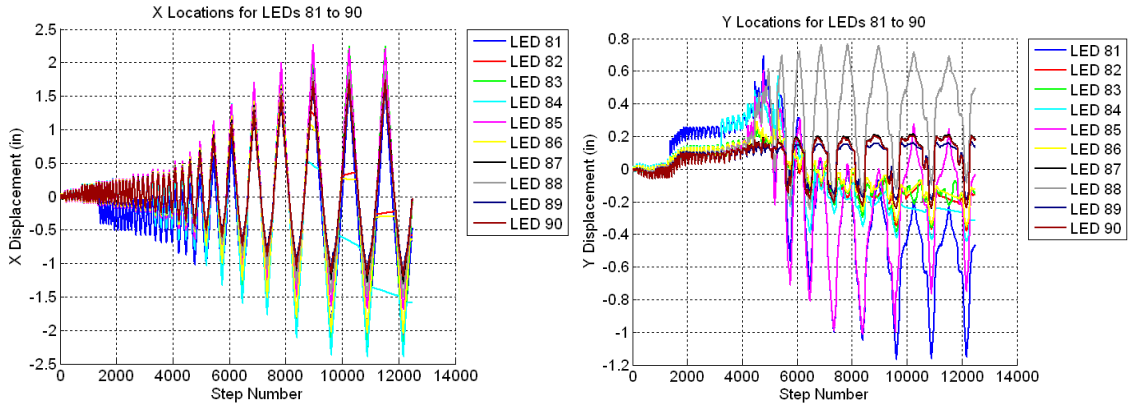

Figure B.475 Raw Data For Specimen A7 – X Displacements for LED's 81 to 90 (Left) and Y Displacements for LED's 81 to 90 (Right)

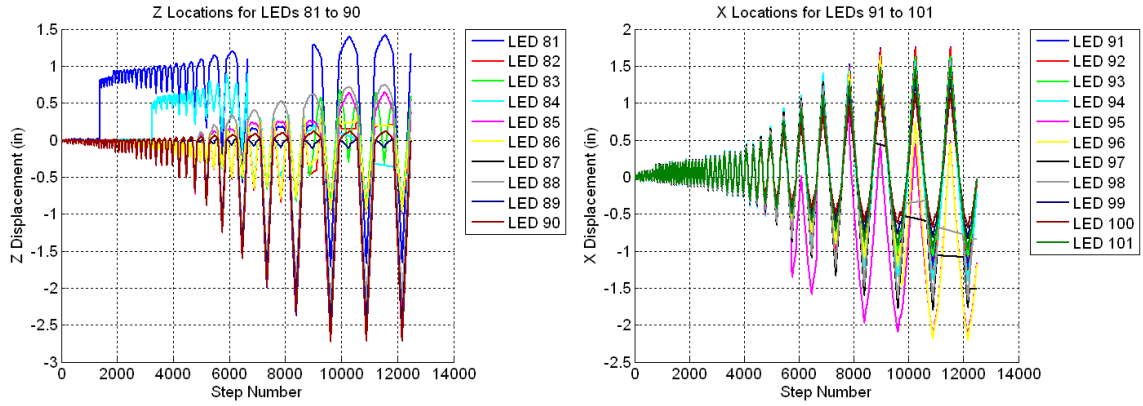

Figure B.476 Raw Data For Specimen A7 – Z Displacements for LED's 81 to 90 (Left) and X Displacements for LED's 91 to 101 (Right)

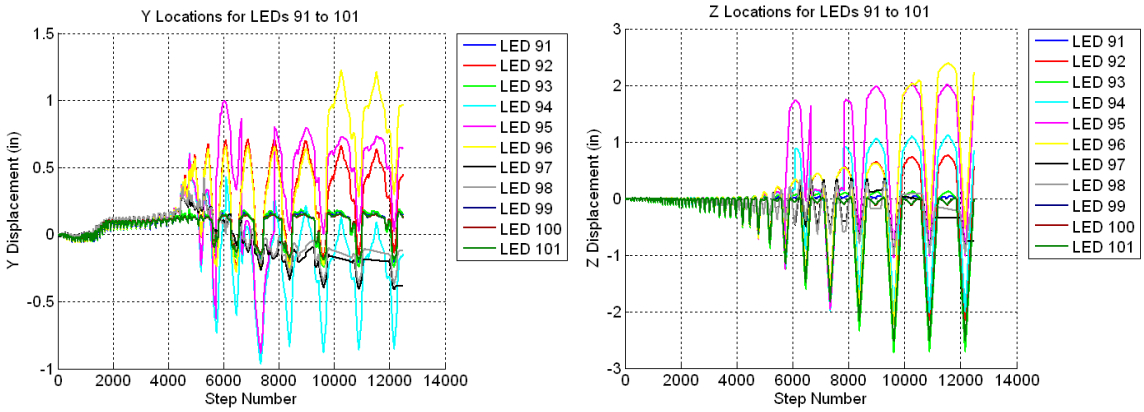

Figure B.477 Raw Data For Specimen A7 – Y Displacements for LED's 91 to 101 (Left) and Z Displacements for LED's 91 to 101 (Right)

B.12 Specimen B1 and Specimen B2

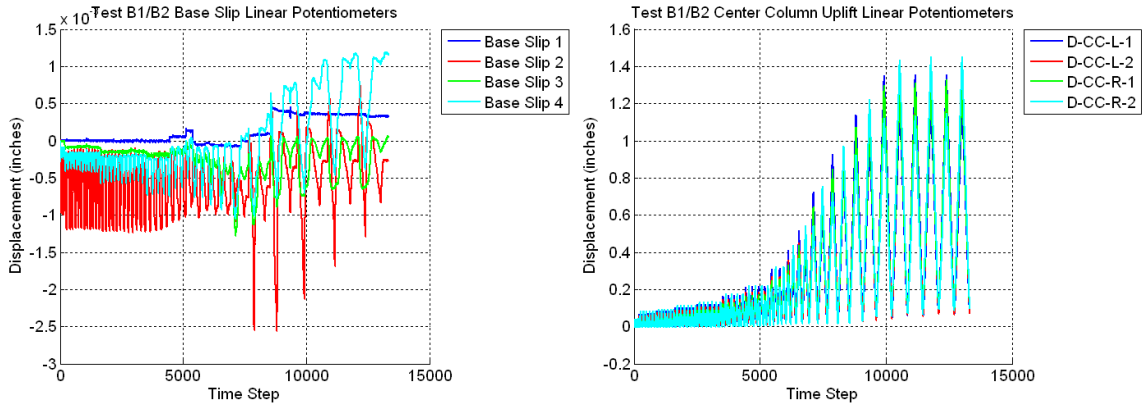

Figure B.478 Raw Data For Specimen B1 and Specimen B2 – Base Slip (Left) and Center Column Uplift Linear Potentiometers (Right)

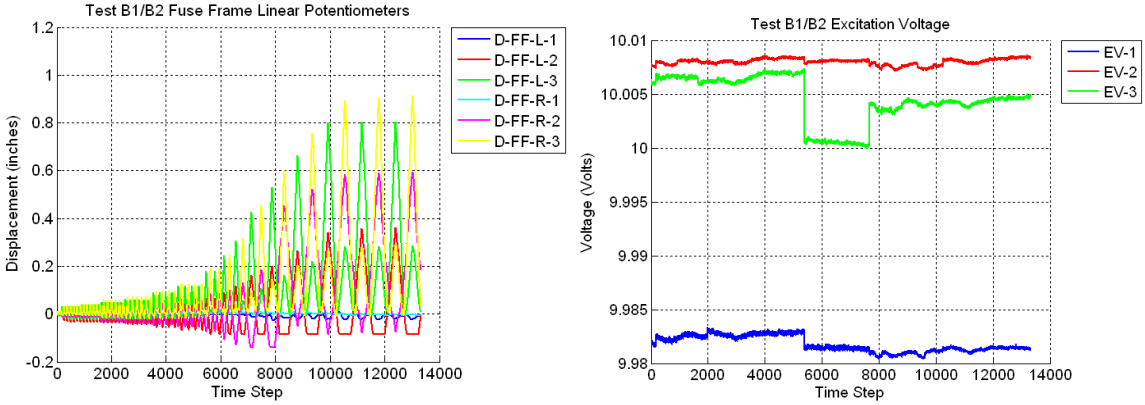

Figure B.479 Raw Data For Specimen B1 and Specimen B2 – Fuse Frame Linear Potentiometers (Left) and Excitation Voltage (Right)

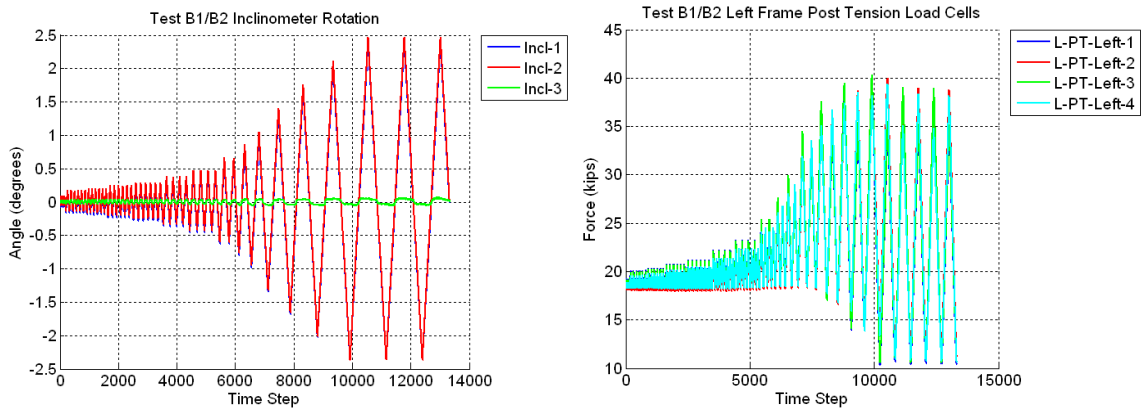

Figure B.480 Raw Data For Specimen B1 and Specimen B2 – Inclinometers (Left) and Left Frame Post-Tension Load Cells (Right)

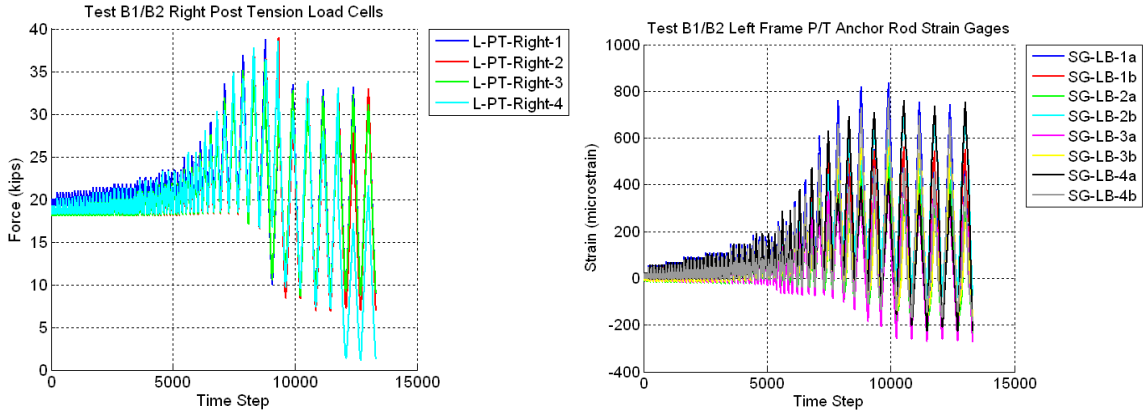

Figure B.481 Raw Data For Specimen B1 and Specimen B2 – Right Post-Tension Load Cells (Left) and Left Frame PT Anchor Rods (Right)

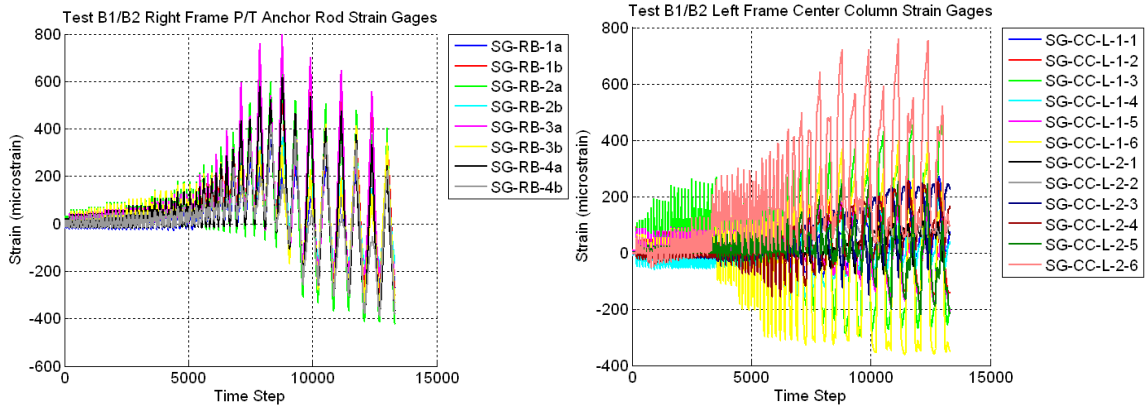

Figure B.482 Raw Data For Specimen B1 and Specimen B2 – Right Frame PT Anchor Rods (Left) and Left Frame Center Column Strain Gages (Right)

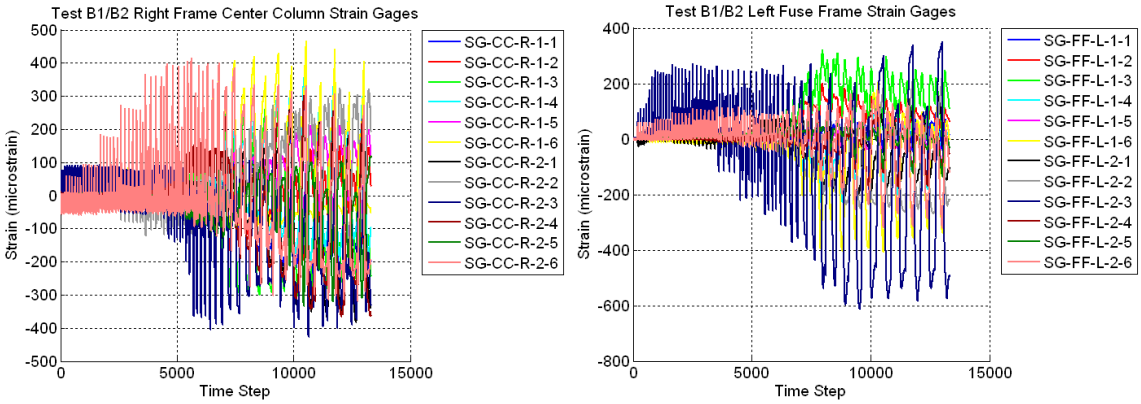

Figure B.483 Raw Data For Specimen B1 and Specimen B2 – Right Frame Center Column Strain Gages (Left) and Left Fuse Frame Strain Gages (Right)

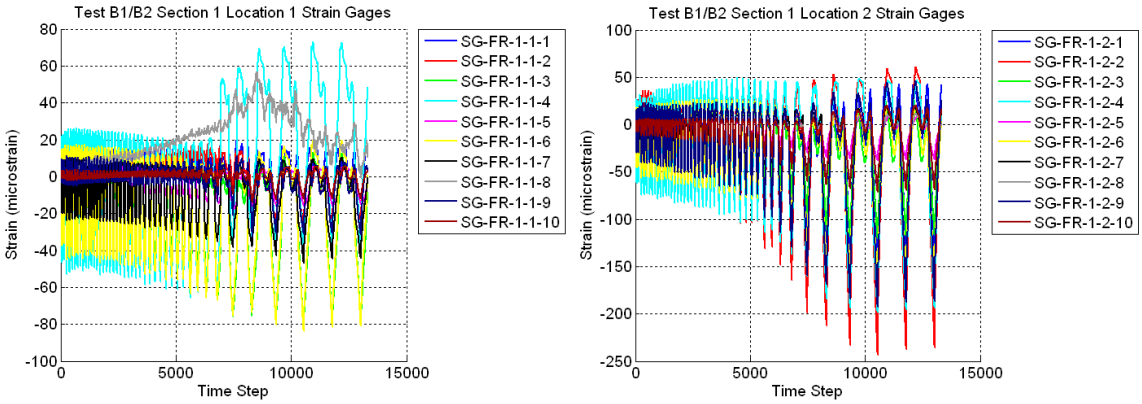

Figure B.484 Raw Data For Specimen B1 and Specimen B2 – Left Frame Section 1-1 Strain Gages (Left) and Left Frame Section 1-2 Strain Gages (Right)

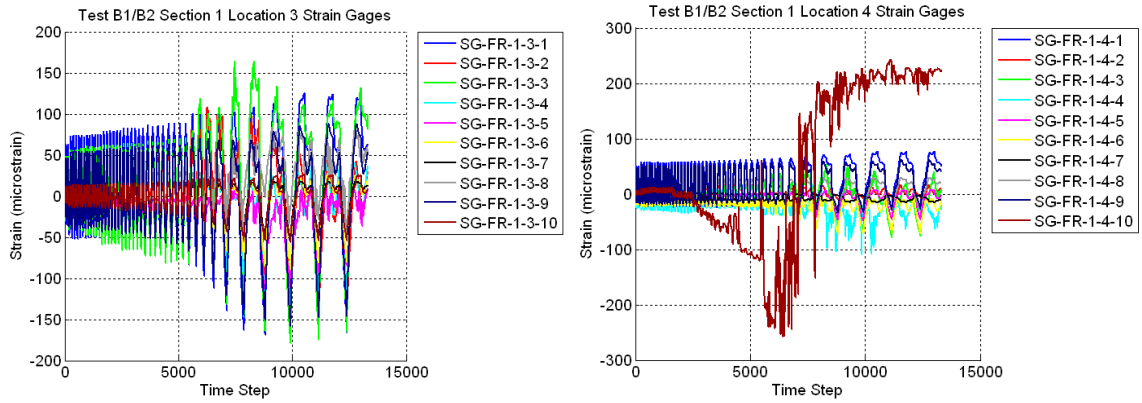

Figure B.485 Raw Data For Specimen B1 and Specimen B2 – Left Frame Section 1-3 Strain Gages (Left) and Left Frame Section 1-4 Strain Gages (Right)

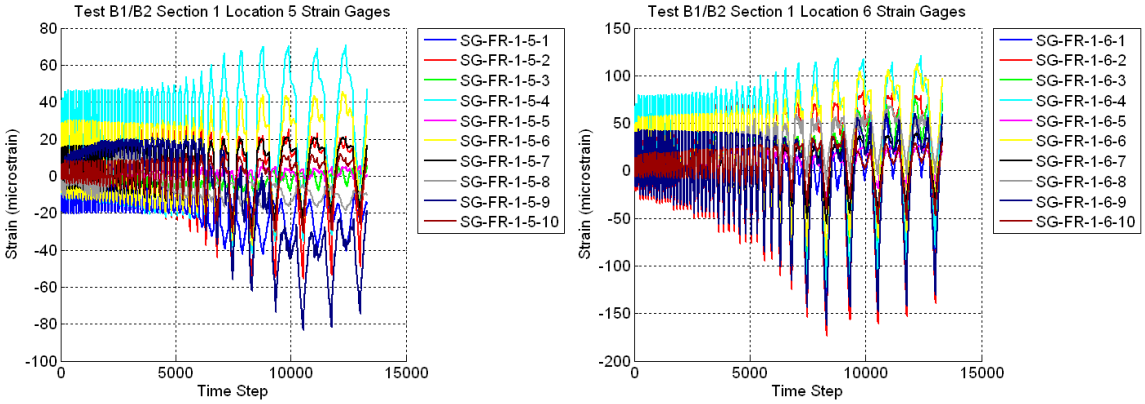

Figure B.486 Raw Data For Specimen B1 and Specimen B2 – Right Frame Section 1-5 Strain Gages (Left) and Right Frame Section 1-6 Strain Gages (Right)

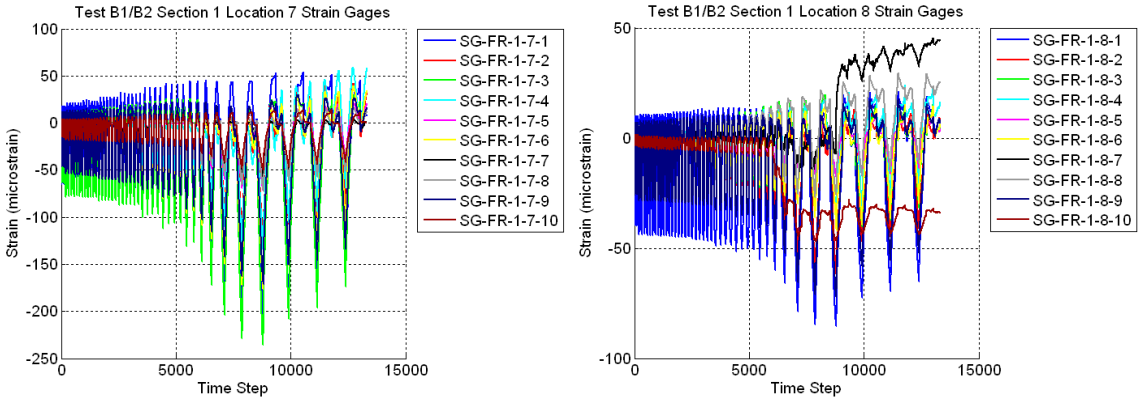

Figure B.487 Raw Data For Specimen B1 and Specimen B2 – Right Frame Section 1-7 Strain Gages (Left) and Right Frame Section 1-8 Strain Gages (Right)

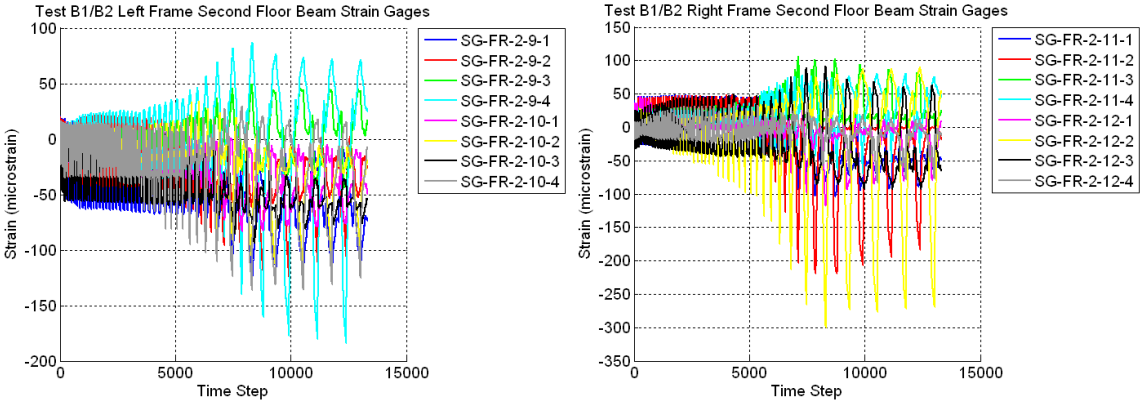

Figure B.488 Raw Data For Specimen B1 and Specimen B2 – Second Floor Beam Strain Gages (Left) and Second Floor Beam Strains (Right)

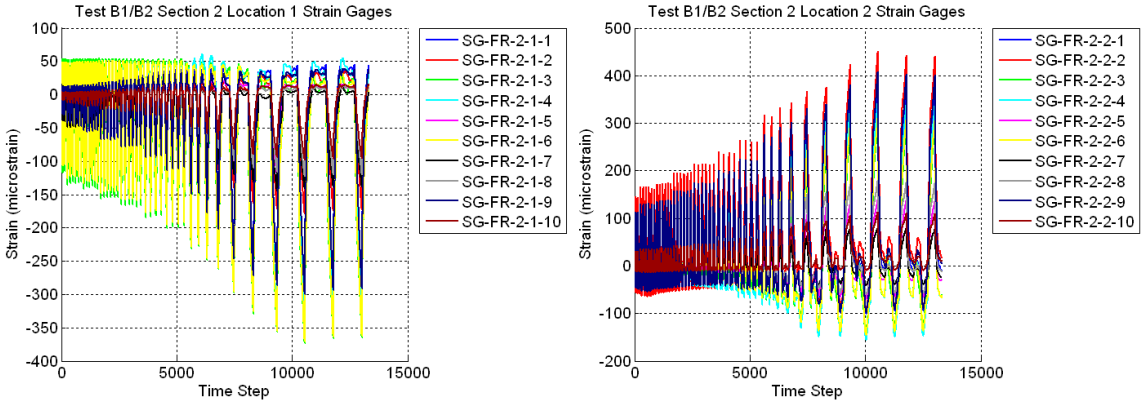

Figure B.489 Raw Data For Specimen B1 and Specimen B2 – Left Frame Section 2-1 Strain Gages (Left) and Left Frame Section 2-2 Strain Gages (Right)

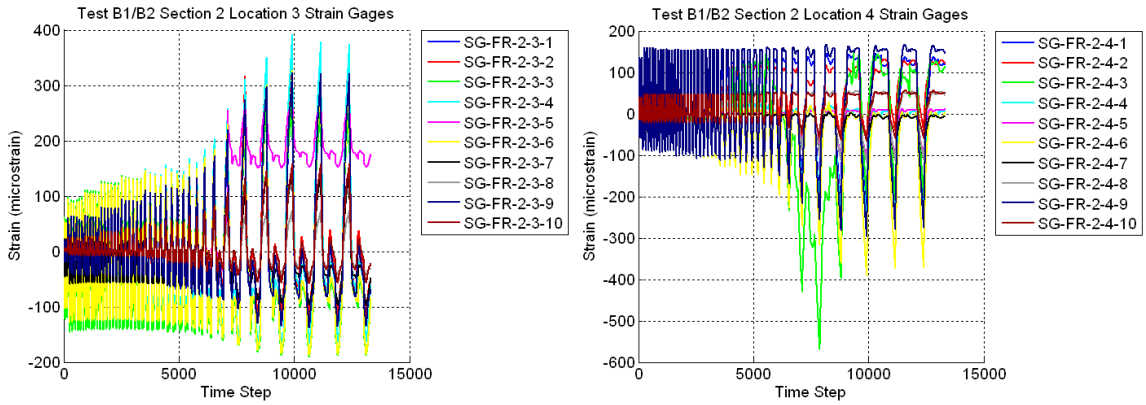

Figure B.490 Raw Data For Specimen B1 and Specimen B2 – Left Frame Section 2-3 Strain Gages (Left) and Left Frame Section 2-4 Strain Gages (Right)

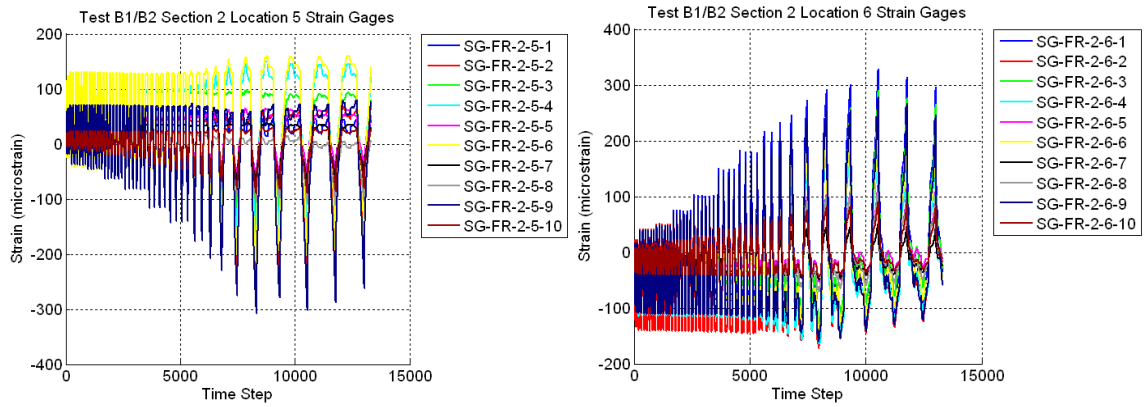

Figure B.491 Raw Data For Specimen B1 and Specimen B2 – Right Frame Section 2-5 Strain Gages (Left) and Right Frame Section 2-6 Strain Gages (Right)

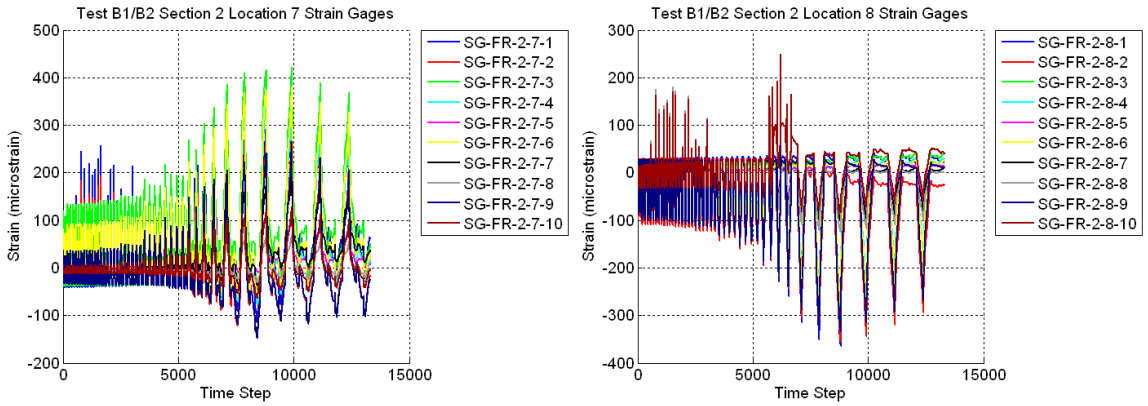

Figure B.492 Raw Data For Specimen B1 and Specimen B2 – Right Frame Section 2-7 Strain Gages (Left) and Right Frame Section 2-8 Strain Gages (Right)

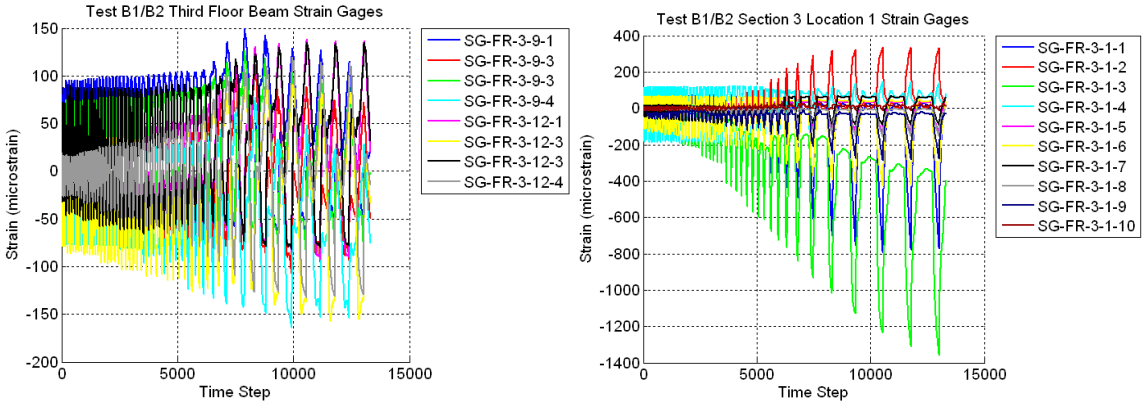

Figure B.493 Raw Data For Specimen B1 and Specimen B2 – Third Floor Beam Strain Gages (Left) and Left Frame Section 3-1 Strain Gages (Right)

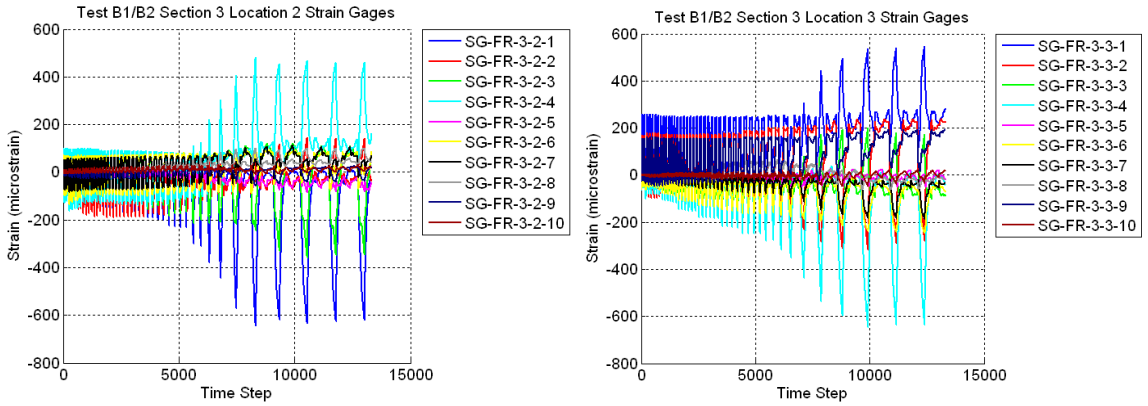

Figure B.494 Raw Data For Specimen B1 and Specimen B2 – Left Frame Section 3-2 Strain Gages (Left) and Left Frame Section 3-3 Strain Gages (Right)

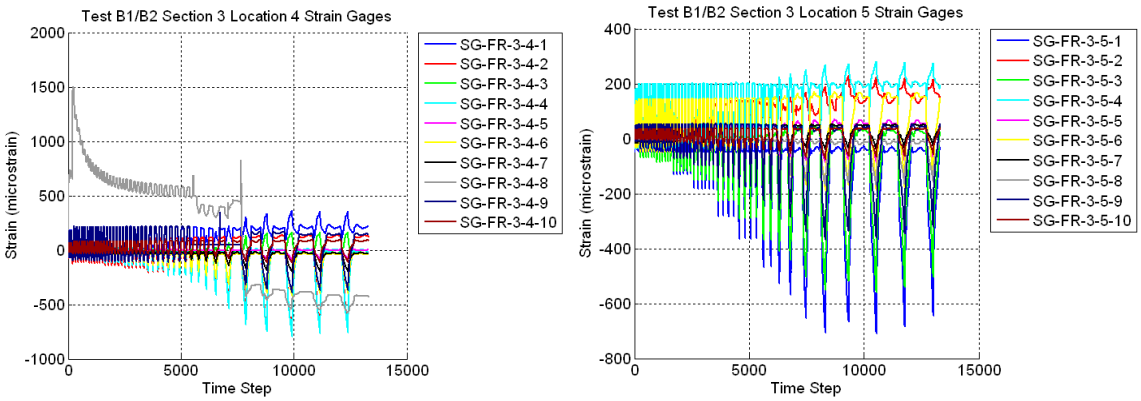

Figure B.495 Raw Data For Specimen B1 and Specimen B2 – Left Frame Section 3-4 Strain Gages (Left) and Right Frame Section 3-5 Strain Gages (Right)

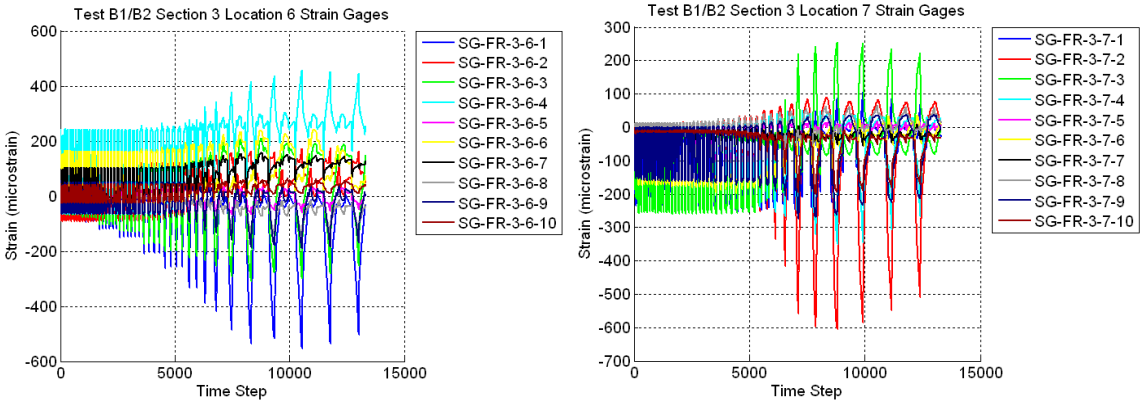

Figure B.496 Raw Data For Specimen B1 and Specimen B2 – Right Frame Section 3-6 Strain Gages (Left) and Right Frame Section 3-7 Strain Gages (Right)

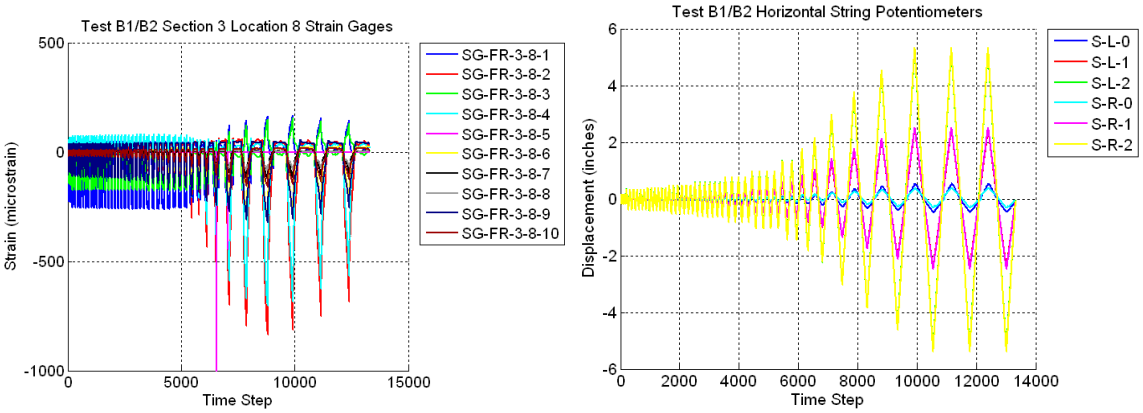

Figure B.497 Raw Data For Specimen B1 and Specimen B2 – Right Frame Section 3-8 Strain Gages (Left) and Horizontal String Potentiometers (Right)

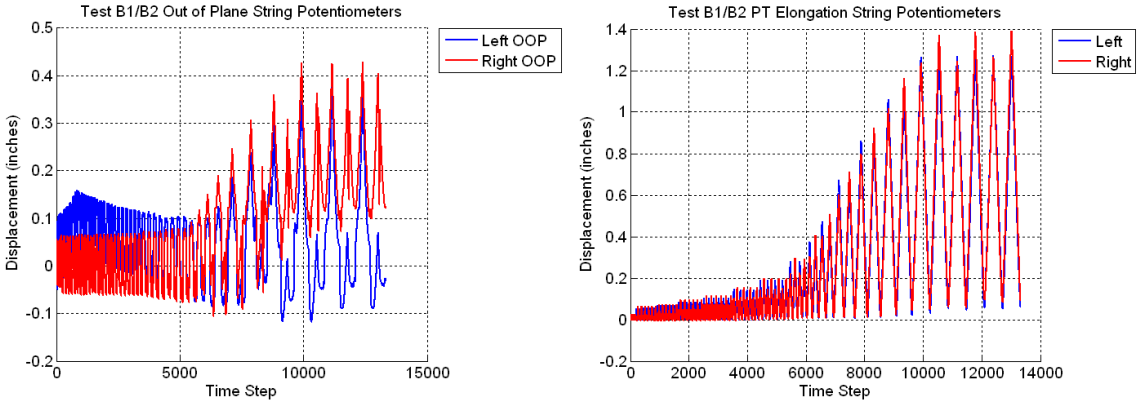

Figure B.498 Raw Data For Specimen B1 and Specimen B2 – Out-of-Plane String Potentiometers (Left) and PT Elongation String Potentiometers (Right)

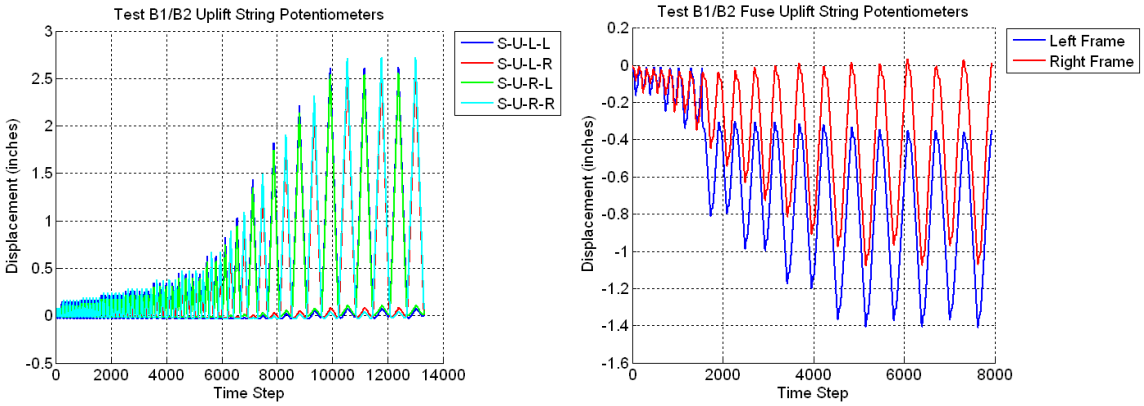

Figure B.499 Raw Data For Specimen B1 and Specimen B2 – Uplift String Potentiometers (Left) and Fuse Uplift String Potentiometers (Right)

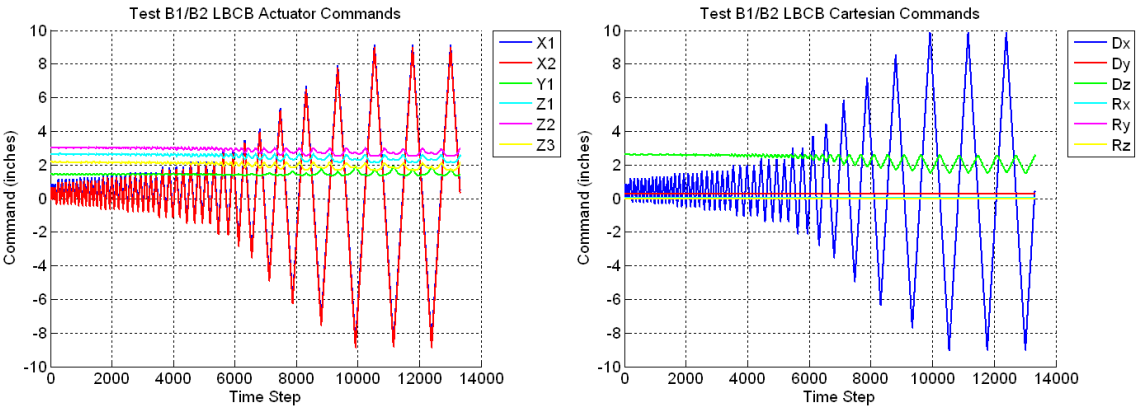

Figure B.500 Raw Data For Specimen B1 and Specimen B2 – LBCB Actuator Commands (Left) and LBCB Cartesian Commands (Right)

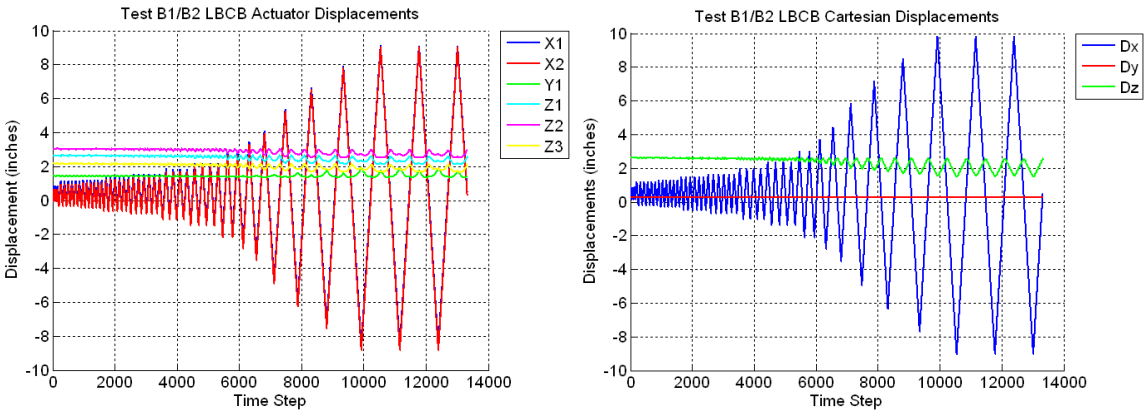

Figure B.501 Raw Data For Specimen B1 and Specimen B2 – LBCB Actuator Displacements (Left) and LBCB Cartesian Displacements (Right)

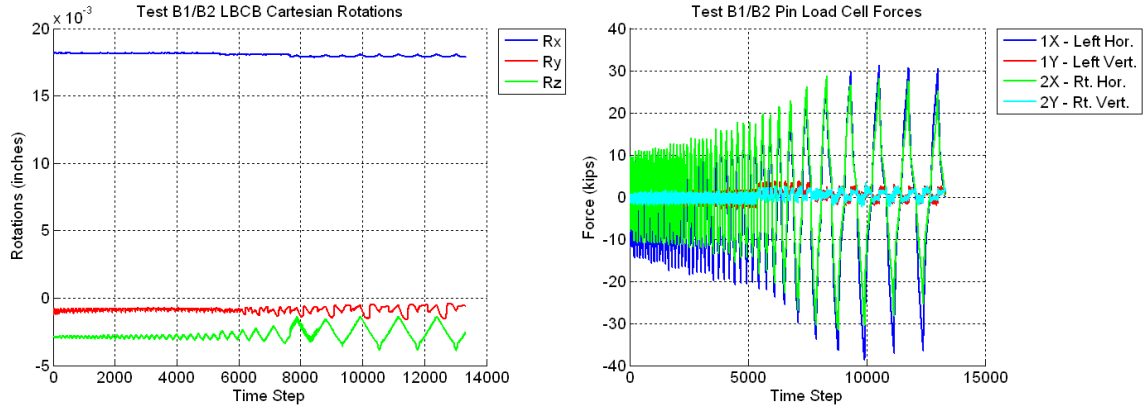

Figure B.502 Raw Data For Specimen B1 and Specimen B2 – LBCB Cartesian Rotations (Left) and Pin Load Cells (Right)

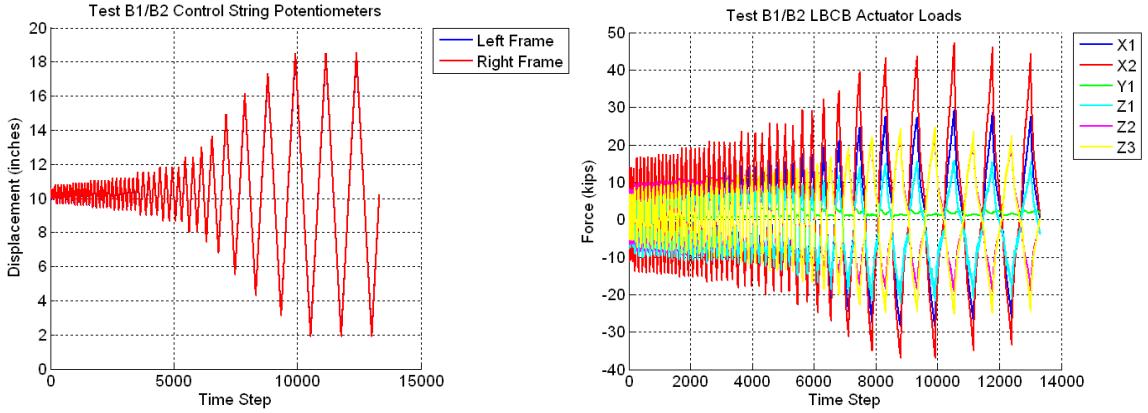

Figure B.503 Raw Data For Specimen B1 and Specimen B2 – Control Roof String Potentiometers (Left) and LBCB Actuator Loads (Right)

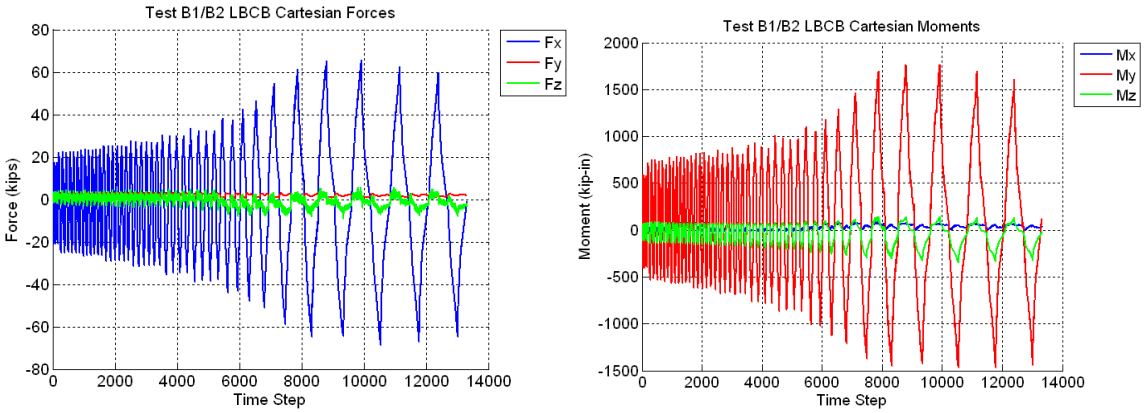

Figure B.504 Raw Data For Specimen B1 and Specimen B2 – LBCB Cartesian Forces (Left) and LBCB Cartesian Moments (Right)

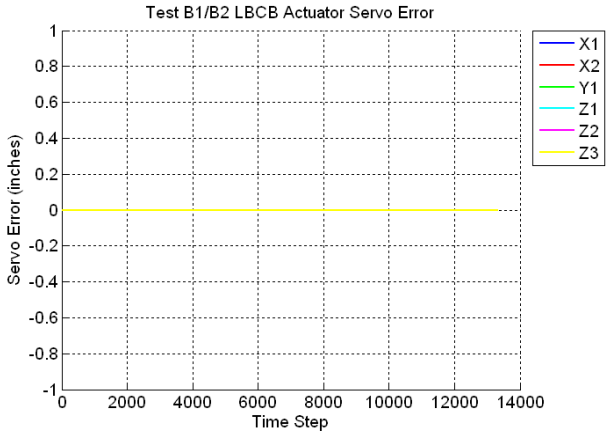

Figure B.505 Raw Data For Specimen B1 and Specimen B2 – LBCB Actuator Servo-Error

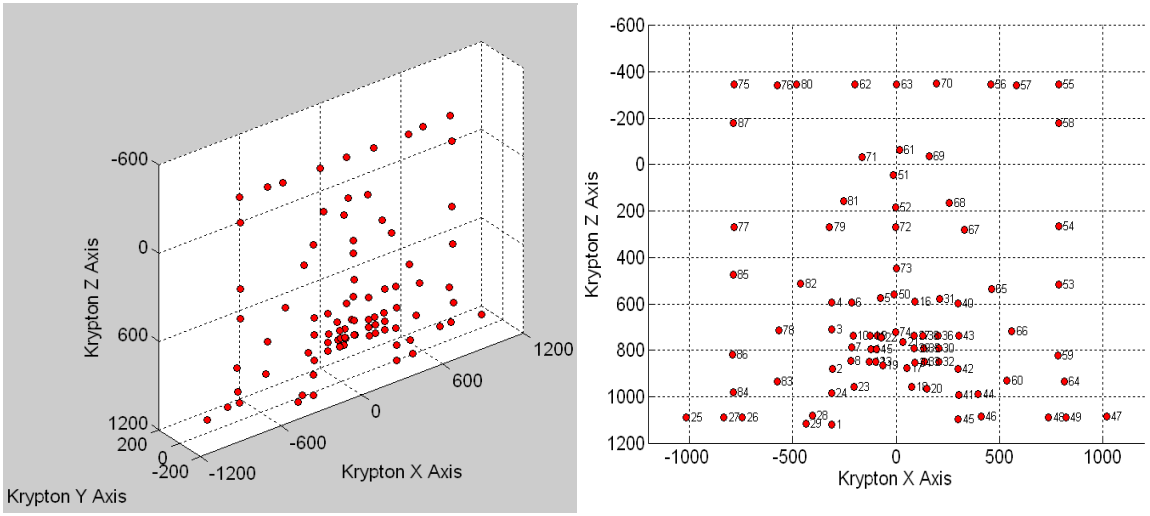

Figure B.506 Raw Data For Specimen B1 and Specimen B2 – Krypton LED Locations (Left) and Krypton LED Numbering (Right)

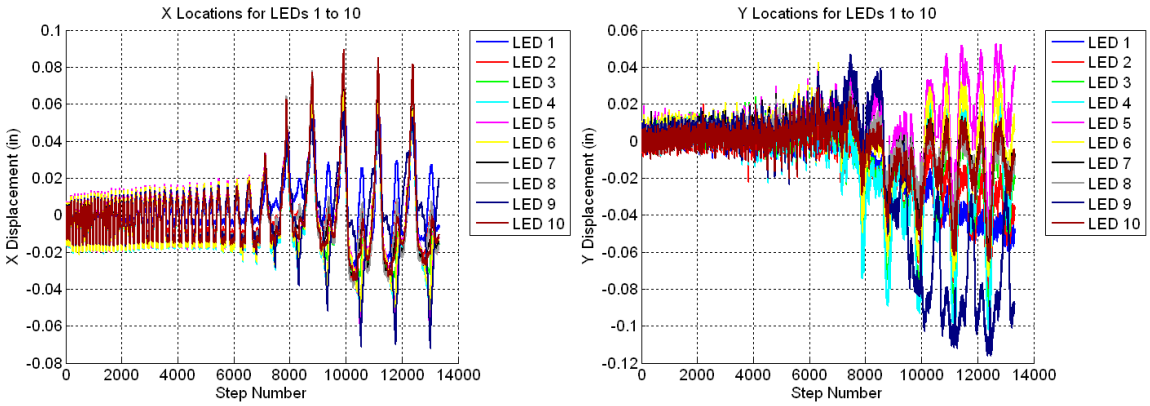

Figure B.507 Raw Data For Specimen B1 and Specimen B2 – X Displacements for LED's 1 to 10 (Left) and Y Displacements for LED's 1 to 10 (Right)

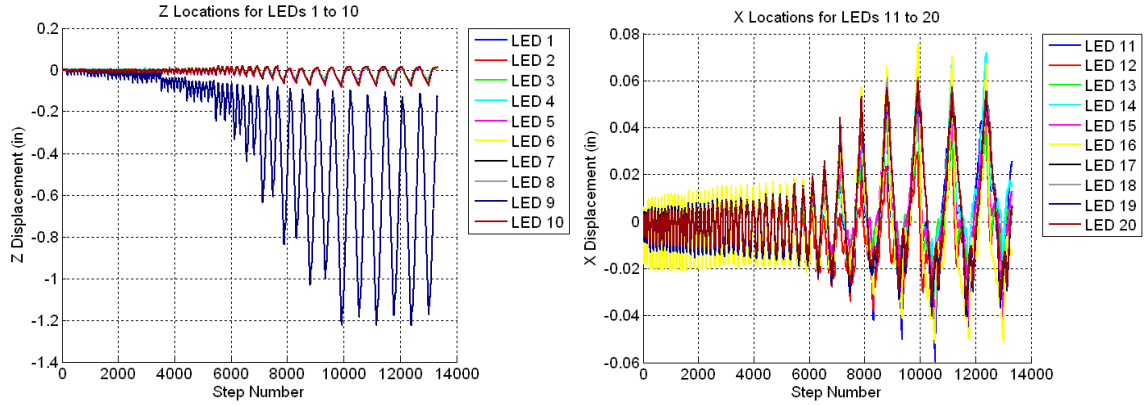

Figure B.508 Raw Data For Specimen B1 and Specimen B2 – Z Displacements for LED's 1 to 10 (Left) and X Displacements for LED's 11 to 20 (Right)

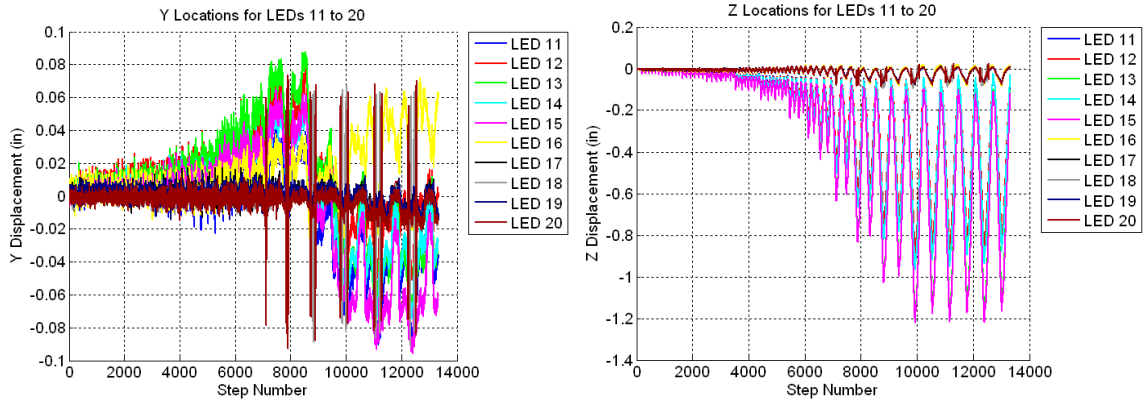

Figure B.509 Raw Data For Specimen B1 and Specimen B2 – Y Displacements for LED's 11 to 20 (Left) and Z Displacements for LED's 11 to 20 (Right)

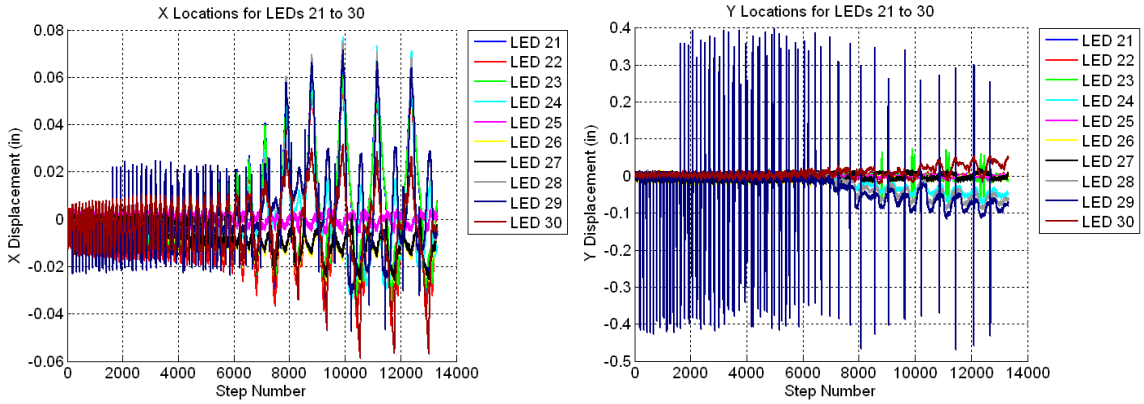

Figure B.510 Raw Data For Specimen B1 and Specimen B2 – X Displacements for LED's 21 to 30 (Left) and Y Displacements for LED's 21 to 30 (Right)

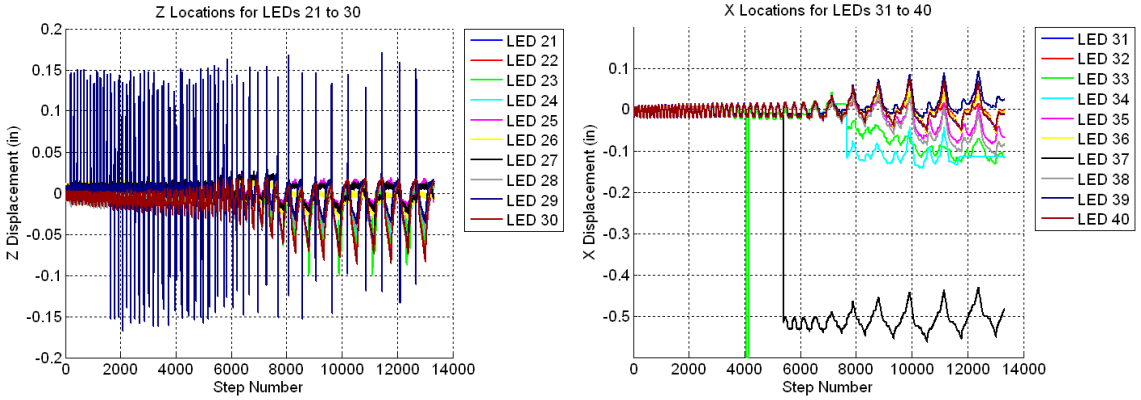

Figure B.511 Raw Data For Specimen B1 and Specimen B2 – Z Displacements for LED's 21 to 30 (Left) and X Displacements for LED's 31 to 40 (Right)

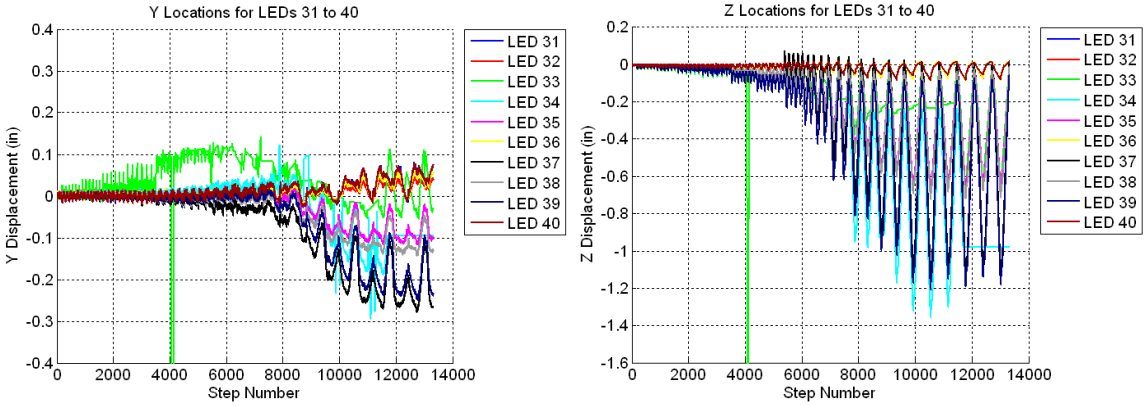

Figure B.512 Raw Data For Specimen B1 and Specimen B2 – Y Displacements for LED's 31 to 40 (Left) and Z Displacements for LED's 31 to 40 (Right)

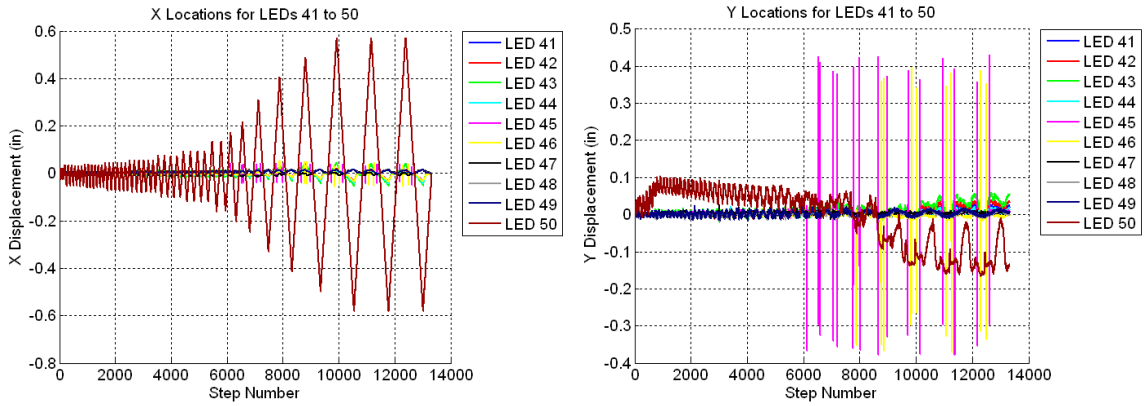

Figure B.513 Raw Data For Specimen B1 and Specimen B2 – X Displacements for LED's 41 to 50 (Left) and Y Displacements for LED's 41 to 50 (Right)

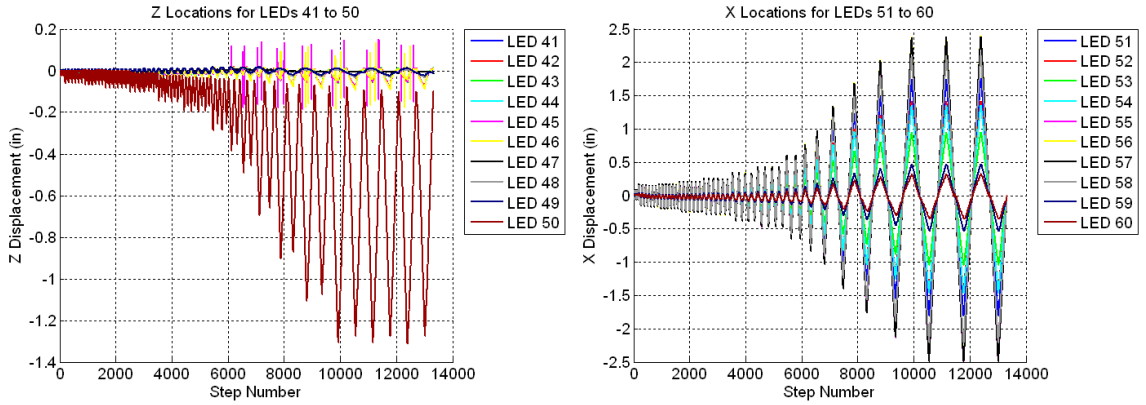

Figure B.514 Raw Data For Specimen B1 and Specimen B2 – Z Displacements for LED's 41 to 50 (Left) and X Displacements for LED's 51 to 60 (Right)

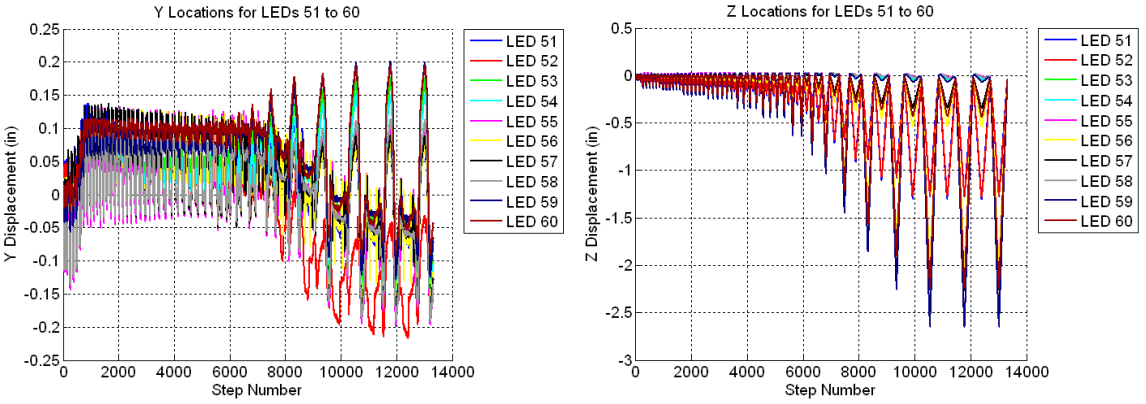

Figure B.515 Raw Data For Specimen B1 and Specimen B2 – Y Displacements for LED's 51 to 60 (Left) and Z Displacements for LED's 51 to 60 (Right)

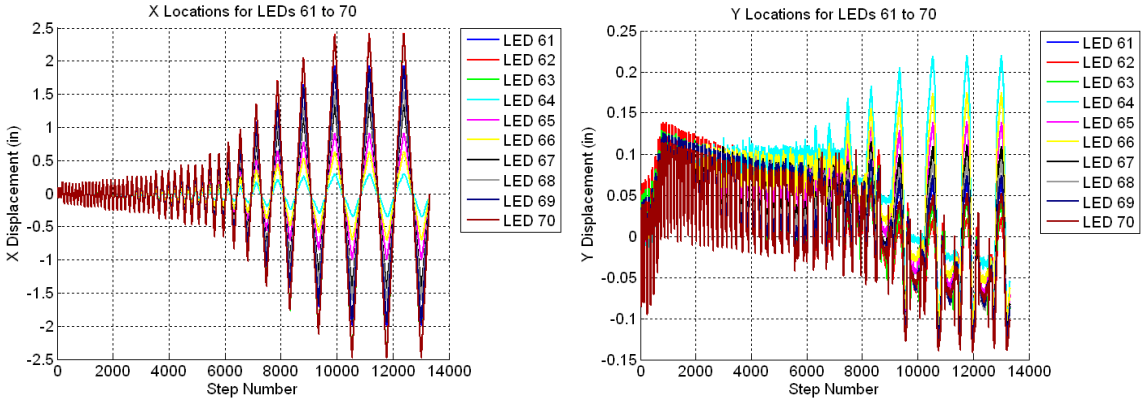

Figure B.516 Raw Data For Specimen B1 and Specimen B2 – X Displacements for LED's 61 to 70 (Left) and Y Displacements for LED's 61 to 70 (Right)

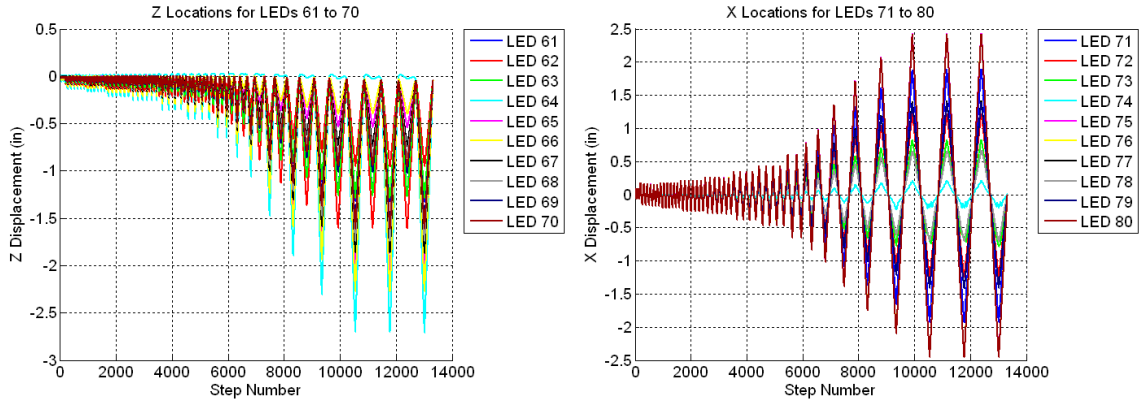

Figure B.517 Raw Data For Specimen B1 and Specimen B2 – Z Displacements for LED's 61 to 70 (Left) and X Displacements for LED's 71 to 80 (Right)

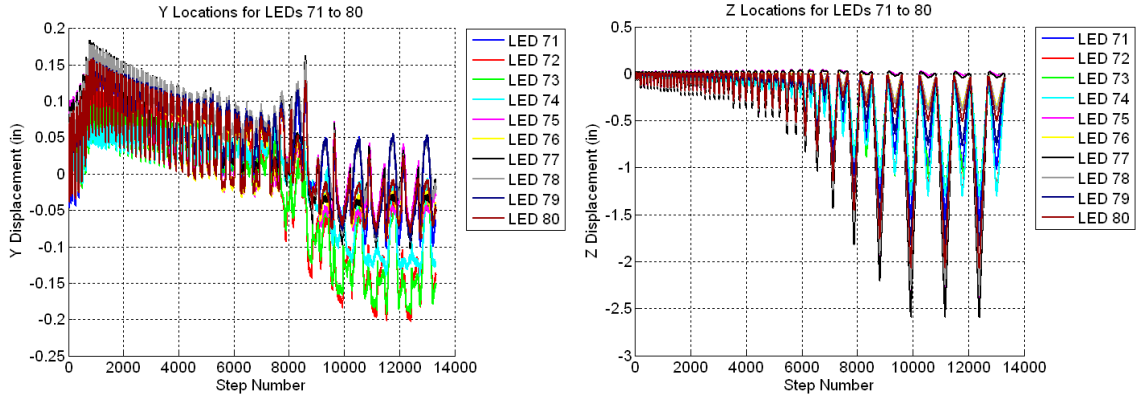

Figure B.518 Raw Data For Specimen B1 and Specimen B2 – Y Displacements for LED's 71 to 80 (Left) and Z Displacements for LED's 71 to 80 (Right)

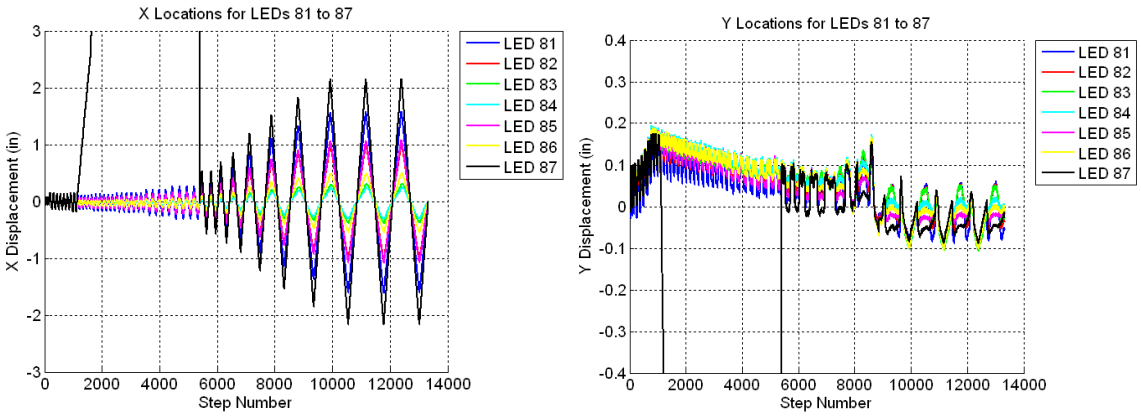

Figure B.519 Raw Data For Specimen B1 and Specimen B2 – X Displacements for LED's 81 to 87 (Left) and Y Displacements for LED's 81 to 87 (Right)

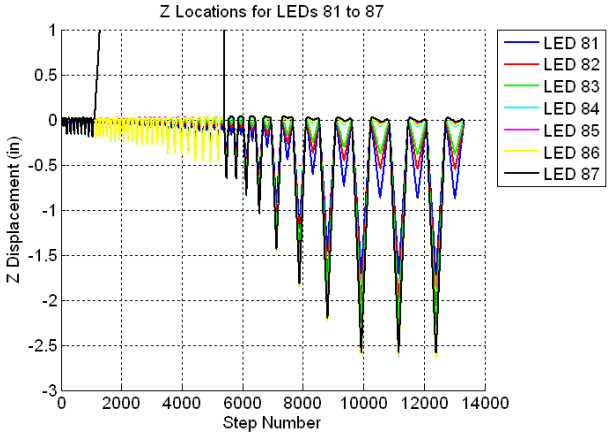

Figure B.520 Raw Data For Specimen B1 and Specimen B2 – Z Displacements for LED's 81 to 87

EXPERIMENTAL DATA REDUCTION CALCULATIONS

C.1 Calculation of System Response Values

Figure C.1 shows the dimensions used for the following calculations along with the definition of some of the variables.

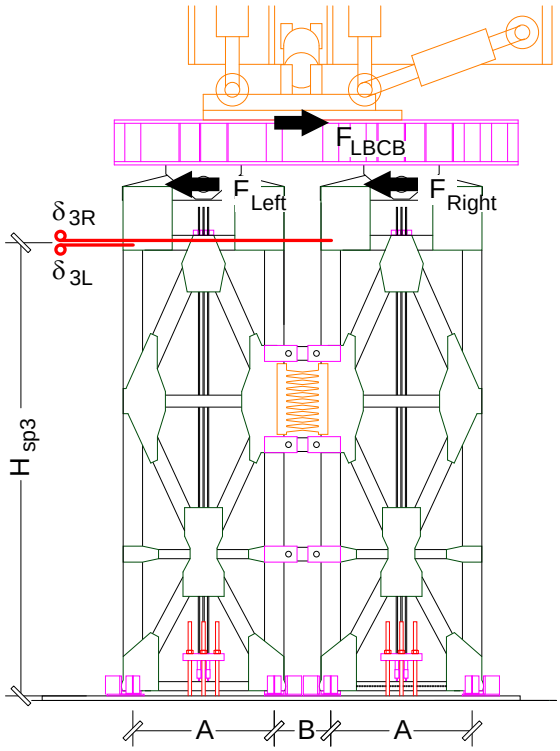

Figure C.1 Dimensions and Definitions for Calculation of System Response Values

The measurements for the dimensions given in Figure C.1 are:

H_{sp3} = 198.05” (Height from bearing point to roof string potentiometers)
A = 5.16’
B = 2.06’
H_{pin} = 223.6” (Height from bearing point to pin load cells)

The roof drift ratio is calculated as the average displacement at the roof level divided by the height from the bearing point to the roof level as given in Equation (C.1) and Equation (C.2).

$$RDR = \frac{\delta_{3L} + \delta_{3R}}{2H_{sp3}} \qquad \text{(DUAL FRAME)} \qquad \text{(C.1)}$$

$$RDR = \frac{\delta_{3L} \text{ or } \delta_{3R}}{H_{sp3}} \qquad \text{(SINGLE FRAME)} \qquad \text{(C.2)}$$

The overturning moment applied to the specimen is calculated as the sum of the forces transferred through the pin load cells multiplied by the height of the pins above the point of bearing as given in Equation (C.3) and Equation (C.4). The overturning moment is normalized to the yield overturning moment, My, for many of the graphs presented in this report. The yield overturning moment is calculated as the initial post-tensioning force and fuse shear yield capacity acting at their respective moment arms as given in Equation (C.5) and Equation (C.6).

$$M_{ovt} = \left(F_{Left} + F_{Right}\right) H_{pin} \qquad \text{(DUAL FRAME)} \qquad \text{(C.3)}$$

$$M_{ovt} = \left(F_{Left} \text{ or } F_{Right}\right) H_{pin} \qquad \text{(SINGLE FRAME)} \qquad \text{(C.4)}$$

$$M_y = F_{pti} A + V_{fp}\left(A + B\right) \qquad \text{(DUAL FRAME)} \qquad \text{(C.5)}$$

$$M_y = \left(F_{pti} + V_{fp}\right)\frac{A}{2} \qquad \text{(SINGLE FRAME)} \qquad \text{(C.6)}$$

Where F_{pti} = Initial Post Tension Force

$V_{fp} = \frac{4}{9} N_{fuses} N_{links} \frac{b^2 t}{L} F_y$ (Fuse Shear Capacity)

N_{fuses} = Number of fuses

N_{links} = Number of links per fuse

b = Height of fuse link at end of the link

t = thickness of the fuse plate

L = length of the fuse link

F_y = Yield strength of the fuse plate

C.2 Calculation of Section Resultants Based on a Strain-Gaged Section

The numbering for the strain gages in a strain-gaged section are included in Figure C.2. The beams had only longitudinal gages applied as shown in Figure C.3 and Figure C.4. The sign convention for force and moment resultants is shown in Figure C.5.

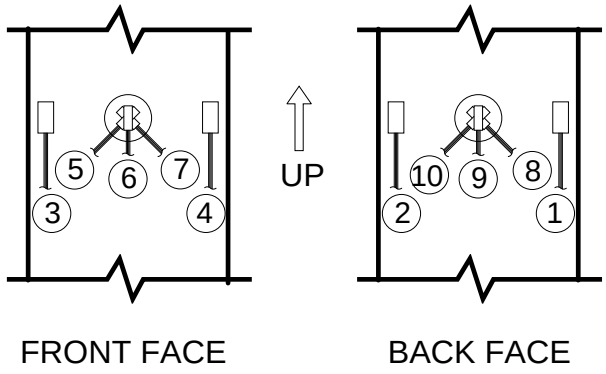

Figure C.2 Strain Gage Locations and Numbering for Brace and Column Strain-Gaged Sections

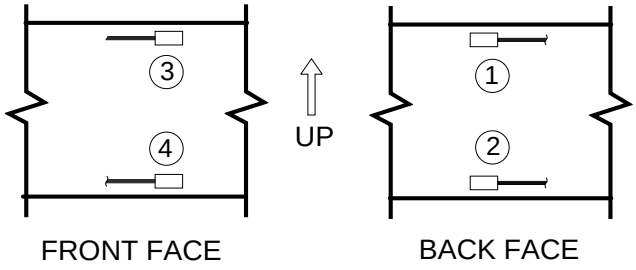

Figure C.3 Strain Gage Locations and Numbering for Beam Strain-Gaged Sections at 1st Floor and 3rd Floor Beams

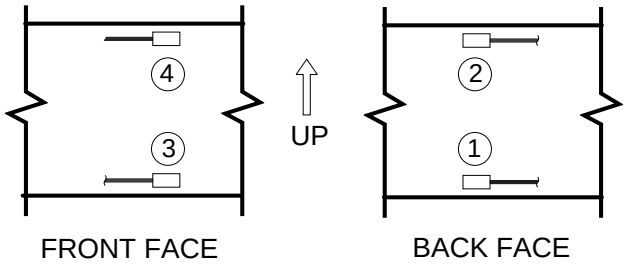

Figure C.4 Strain Gage Locations and Numbering for Beam Strain-Gaged Sections at 2nd Floor Beams

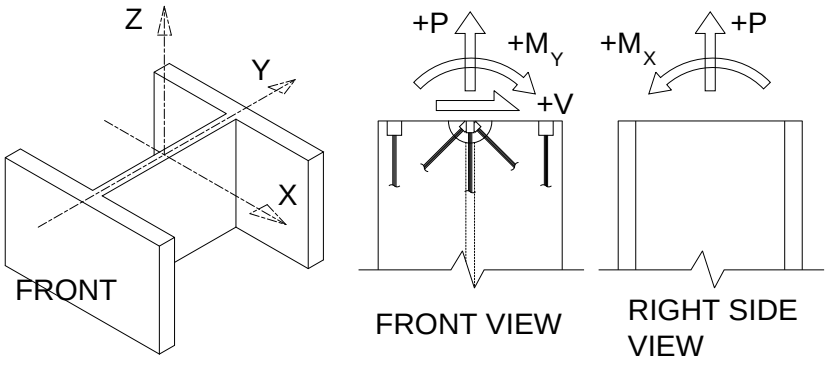

Figure C.5 Sign Convention for Resultant Forces and Moments

C.2.1 Axial Force:

The axial force was calculated as the average of the longitudinal strains multiplied by the modulus of elasticity and the nominal area of the wide flange section. The calculation is given in Equation (C.7)

$$P_{ij} = \frac{\varepsilon_{ij1} + \varepsilon_{ij2} + \varepsilon_{ij3} + \varepsilon_{ij4} + \varepsilon_{ij6} + \varepsilon_{ij9}}{6} EA \qquad \text{(C.7)}$$

Where E=29000 ksi

C.2.2 Major Axis Moment

The curvature was calculated as the difference between the average extreme fiber strain on the front face and the average extreme fiber strain on the back face divided by the nominal depth of the section as given in Equation (C.8), Equation (C.9), and Equation (C.10). The major axis moment was calculated as given in Equation (C.11).

$$\varepsilon_{Fnt-ij} = \frac{\varepsilon_{ij3} + \varepsilon_{ij6} + \varepsilon_{ij4}}{3} \qquad \text{Average Strain on Front Face} \qquad \text{(C.8)}$$

$$\varepsilon_{Bck-ij} = \frac{\varepsilon_{ij1} + \varepsilon_{ij9} + \varepsilon_{ij2}}{3} \qquad \text{Average Strain on Back Face} \qquad \text{(C.9)}$$

$$\phi_{Maj-ij} = \frac{\varepsilon_{Bck-ij} - \varepsilon_{Fnt-ij}}{d} \qquad \text{Major Axis Curvature} \qquad \text{(C.10)}$$

Where d = nominal depth of the section

$$M_{Xij} = \phi_{Maj-ij} EI_x \qquad \text{Major Axis Moment} \qquad \text{(C.11)}$$

C.2.3 Minor Axis Moment

The minor axis moment was calculated in a similar way as the major axis moment. The calculations are given in Equation (C.12), Equation (C.13), Equation (C.14), and Equation (C.15).

$$\varepsilon_{Left-ij} = \frac{\varepsilon_{ij3} + \varepsilon_{ij1}}{2} \qquad \text{Average Strain on Front Face} \qquad (C.12)$$

$$\varepsilon_{Right-ij} = \frac{\varepsilon_{ij4} + \varepsilon_{ij2}}{2} \qquad \text{Average Strain on Back Face} \qquad (C.13)$$

$$\phi_{Minor-ij} = \frac{\varepsilon_{Left-ij} - \varepsilon_{Right-ij}}{2c_y} \qquad \text{Major Axis Curvature} \qquad (C.14)$$

$$\text{Where } c_y = \frac{b_f}{2} - \frac{3}{4}$$

$$M_{Yij} = \phi_{Minor-ij} EI_y \qquad \text{Major Axis Moment} \qquad (C.15)$$

C.2.4 Shear Force

The shear strains were calculated using the strain gage rosettes. Figure C.6 shows the Mohr's circle for the strain gage rosette strains.

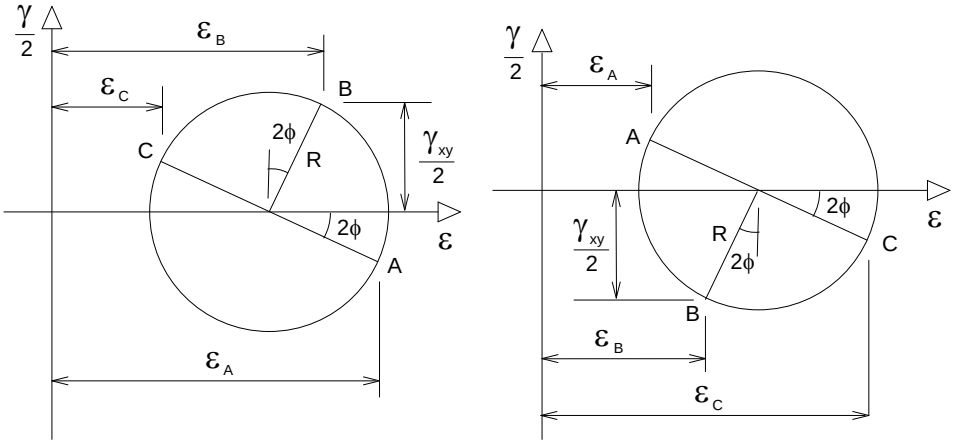

Figure C.6 Mohr's Circle for Calculation of Shear Strain For $\varepsilon_A > \varepsilon_C$ (left) and $\varepsilon_C > \varepsilon_A$ (right)

The strain directions A, B, and C are related to the strain gage channels shown in Figure C.2 as given in Equation (C.16). The angle from strain A to the principal strain axis is calculated in Equation (C.17). The radius of the Mohr's circle for the rosette on the front flange is given in Equation (C.18). The resulting shear strains are calculated using Equation (C.19) and Equation (C.20).

$$\varepsilon_A = \varepsilon_5 \qquad \varepsilon_B = \varepsilon_6 \qquad \varepsilon_C = \varepsilon_7 \tag{C.16}$$

$$2\phi_{frnt} = \tan^{-1}\left(\frac{2\varepsilon_6 - \varepsilon_5 - \varepsilon_7}{\varepsilon_5 - \varepsilon_7}\right) \tag{C.17}$$

$$R_{frnt} = \frac{1}{2}\sqrt{\left(\varepsilon_5 - \varepsilon_7\right)^2 + \left(2\varepsilon_6 - \varepsilon_5 - \varepsilon_7\right)^2} \tag{C.18}$$

$$\gamma_{xy-frnt} = 2R_{frnt}\cos\left(2\phi_{frnt}\right) \text{ For } \varepsilon_A > \varepsilon_C \tag{C.19}$$

$$\gamma_{xy-frnt} = -2R_{frnt}\cos\left(2\phi_{frnt}\right) \text{ For } \varepsilon_C > \varepsilon_A \tag{C.20}$$

Similar calculations were conducted for the strain gage rosette applied to the back flange as given in Equation (C.21), Equation (C.22), Equation (C.23), Equation (C.24), and Equation (C.25).

$$\varepsilon_A = \varepsilon_8 \qquad \varepsilon_B = \varepsilon_9 \qquad \varepsilon_C = \varepsilon_{10} \tag{C.21}$$

$$2\phi_{back} = \tan^{-1}\left(\frac{2\varepsilon_9 - \varepsilon_{10} - \varepsilon_8}{\varepsilon_{10} - \varepsilon_8}\right) \tag{C.22}$$

$$R_{back} = \frac{1}{2}\sqrt{\left(\varepsilon_{10} - \varepsilon_8\right)^2 + \left(2\varepsilon_9 - \varepsilon_{10} - \varepsilon_8\right)^2} \tag{C.23}$$

$$\gamma_{xy-back} = 2R_{back}\cos\left(2\phi_{back}\right) \text{ For } \varepsilon_A > \varepsilon_C \tag{C.24}$$

$$\gamma_{xy-back} = -2R_{back}\cos\left(2\phi_{back}\right) \text{ For } \varepsilon_C > \varepsilon_A \tag{C.25}$$

The shear stress at the middle of the flange was calculated using the average of the shear strain on the front and back flanges as given in Equation (C.26). The resultant shear force in the section is calculated by assuming shear stress distribution associated with a rectangular section as given in Equation (C.27). Since the section is used in minor axis bending in the frame, the flanges resist the majority of the shear and are approximated as a single rectangular section.

$$\tau = G\frac{\left(\gamma_{xy-frnt} - \gamma_{xy-back}\right)}{2} \tag{C.26}$$

$$V = \tau A_v \frac{2}{3} \tag{C.27}$$

C.2.5 Strategy for Handling Erratic Gages and Data Offsets

Through the course of the experimental program, some strain gages gave erratic or no readings during a particular test. The strategy for performing the above calculations in the presence of bad strain measurements are discussed below:

1. All gages experienced some amount of offset between days of testing. The shift was as large as 150 microstrains. For gages where this was

significant, the change in the readings as measured in the continuous data from the end of the test one day to just before the test resumed the next day was subtracted from the subsequent data.

2. Channels that experienced continued drift, or stop reading at some point during the test were identified. These channels were neglected in the preceding calculations as described in the following:
    a. For bad longitudinal gages, the missing strain data was replaced by values calculated by fitting a plane to the other longitudinal strain values. It is assumed that plane sections remain plane, so a plane is fit to the other strain values using least squares. The strain coordinate of the plane where it intersects the gage location is used in place of the missing strain value. This is demonstrated in Figure C.7 and Figure C.8.
    b. For a bad diagonal gage, the shear strain calculation for that face will be neglected. Shear force was based on the other rosette only.
    c. For multiple bad strain gages in one strain-gaged section, the resultants were evaluated on a case by case basis.

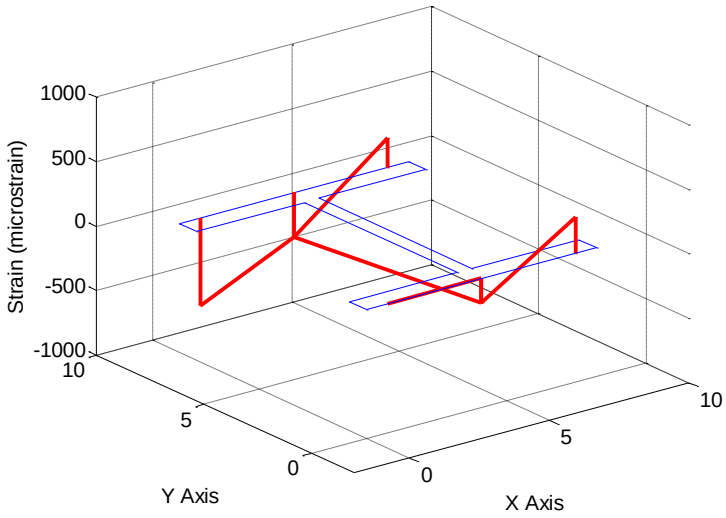

Figure C.7 Example of a Strain Distribution With a Missing Strain Value at Coordinates (0,0)

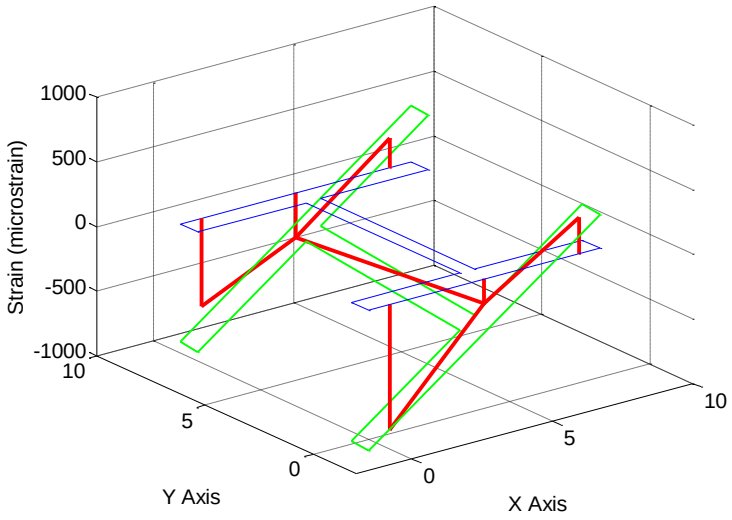

Figure C.8 Example of Replacing the Missing Strain Data with a Value Calculated Using a Least Squares Fit Plane

C.2.6 Possible Sources of Error

The primary possible sources of error in calculating the resultant forces and moments were identified and are listed below:

1. Strain gages were not attached exactly in line with member axes
2. Calculation of axial and moment resultants assume that the axial strain distribution is planar. The actual axial strain distribution is not always planar.
3. Calculation of shear force assumes that shear is only carried in the flanges and conforms to the shear distribution in a rectangular section. The rosette is attached on the face of the flange opposite the web. Shear flow at this location may not conform to that of a rectangular section.
4. Strain gages that stopped reading correctly during a test are discarded. The resultants are calculated without that gage which is an approximation.
5. Strains were measured as the frame was moving. Movement consisted of quick jerky steps which could have caused dynamic spikes in forces or slight differences in the time when the strain gage measurements were taken.

C.3 Calculation of Resultant Forces and Moments for the Entire Frame

The strain-gaged sections and associated gage location numbers are included in Figure C.9. Resultant forces and moments were calculated for the entire frame to allow comparison of the data across the three strain gaged section and comparison to the pin load cell forces and LBCB forces.

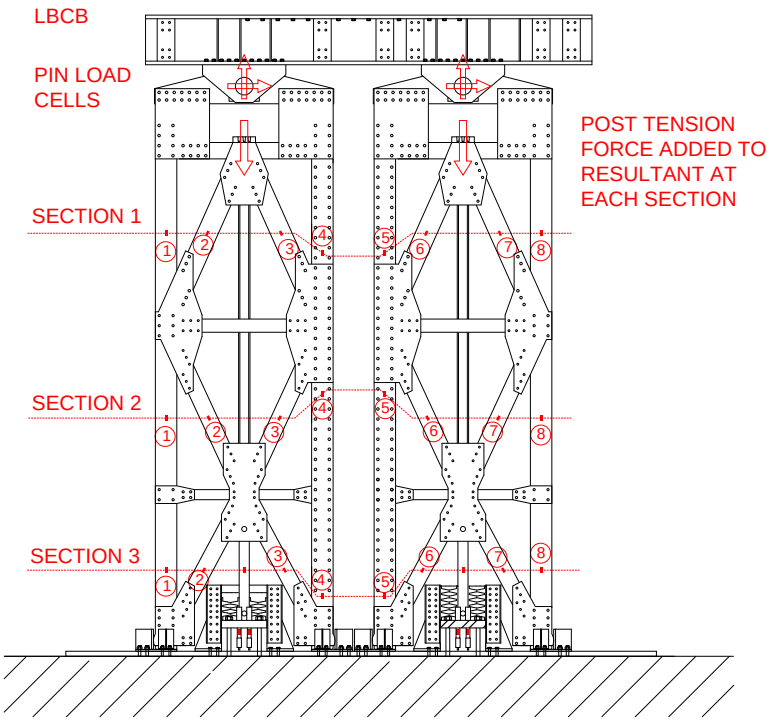

Figure C.9 Strain-Gage Section Locations

Sample calculations are presented here for the left frame, but similar calculations were applied to the right frame. The frame resultants at the third floor were calculated using Equation (C.28). The resultants for the second floor were calculated using Equation (C.29). The resultants for the first floor were calculated using Equation (C.30).

Resultants at the third floor:

$$
\begin{aligned}
P_{Left} &= P_1 + P_2\cos\theta_3 - V_2\sin\theta_3 + P_3\cos\theta_3 + V_3\sin\theta_3 + P_4 - F_{PT} \\
P_{Left-Rotated} &= P_{Left}Cos(\alpha_{Left}) \\
V_{Left} &= V_1 + P_2\sin\theta_3 + V_2\cos\theta_3 - P_3\sin\theta_3 + V_3\cos\theta_3 + V_4 \\
V_{Left-Rotated} &= V_{Left}Cos(\alpha_{Left}) + F_{PT}Sin(\alpha_{Left}) \\
M_{X-Left} &= M_{X1} + M_{X2} + M_{X3} + M_{X4} \\
M_{Y-Left} &= M_{Y1} + M_{Y2} + M_{Y3} + M_{Y4}
\end{aligned}
\qquad \text{(C.28)}
$$

Resultants at the second floor:

$$\begin{aligned} P_{Left} &= P_1 + P_2\cos\theta_2 + V_2\sin\theta_2 + P_3\cos\theta_2 - V_3\sin\theta_2 + P_4 - F_{PT} \\ P_{Left-Rotated} &= P_{Left}Cos(\alpha_{Left}) \\ V_{Left} &= V_1 - P_2\sin\theta_2 + V_2\cos\theta_2 + P_3\sin\theta_2 + V_3\cos\theta_2 + V_4 \\ V_{Left-Rotated} &= V_{Left}Cos(\alpha_{Left}) + F_{PT}Sin(\alpha_{Left}) \end{aligned} \quad \text{(C.29)}$$

Resultants at the first floor:

$$\begin{aligned} P_{Left} &= P_1 + P_2\cos\theta_1 - V_2\sin\theta_1 + P_3\cos\theta_1 + V_3\sin\theta_1 + P_4 - F_{PT} \\ P_{Left-Rotated} &= P_{Left}Cos(\alpha_{Left}) \quad \text{(Dual Frame)} \\ P_{Left-Rotated} &= P_{Left}Cos(\alpha_{Left}) - F_{CC} \quad \text{(Single Frame)} \\ V_{Left} &= V_1 + P_2\sin\theta_1 + V_2\cos\theta_1 - P_3\sin\theta_1 + V_3\cos\theta_1 + V_4 \\ V_{Left-Rotated} &= V_{Left}Cos(\alpha_{Left}) + F_{PT}Sin(\alpha_{Left}) \end{aligned} \quad \text{(C.30)}$$

Where:

- θ is the angle the brace makes relative to vertical and is θ_1=28.14°, θ_2=24.03°, and θ_3=24.78° for the first floor, second floor and third floor respectively.
- α is tilt of the frame and was measured using the inclinometer attached to the beam at the second floor.
- F_{PT} is the total post tension force in that frame relative to the beginning of the test (the initial PT force is zeroed out to allow comparison to pin load cell forces and LBCB forces).
- F_{CC} is the force in the center column attached to the fuse (single frame configuration only)

Possible sources of error were identified as:

1. See calculation of strain gage resultants for possible error related to the calculation of resultant forces at a strain-gaged section.
2. Columns may not be perfectly vertical. Braces may not be exactly at the angle prescribed in the design drawings. Beams may not be exactly horizontal.
3. The tilt of the frame at any time is measured using the inclinometers. Elastic deformation of the frame may cause different tilt angle at each section.
4. The pin load cells have a retainer bar holding them rotationally fixed relative to the loading beam. The loading beam stays relatively horizontal during the test. An inclinometer measures the rotation of the loading beam, but this is currently not being used in the comparison of section forces relative to pin load cell readings.
5. The post-tensioning strands are assumed to be at the same angle relative to vertical as the inclinometer reading. This is not exactly accurate as the bottom anchorage of the post-tensioning is at a fixed location.

C.4 Fuse Response

This section contains the calculation of fuse shear strains, fuse shear forces, and the development of a consistent method for calculating fuse yield.

C.4.1 Fuse Shear Strain for A Series

The configuration for linear potentiometers that were measuring deformations across the fuse and struts in the dual frame configuration is given in Figure C.10.

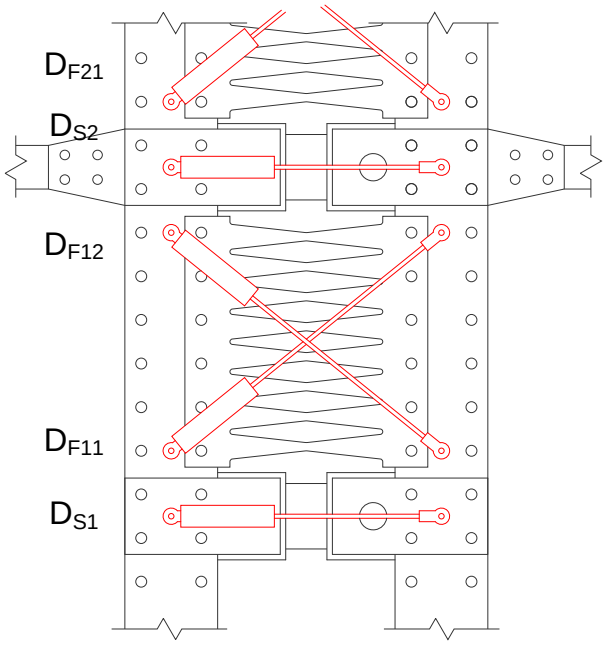

Figure C.10 Linear Potentiometer Configuration for the A Series

The calculation for the fuse shear strain is given in Equation (C.31), Equation (C.32), and Equation (C.33).

$$Cos(\alpha) = \frac{W_{LinPot}^{\ 2} + H_{LinPot}^{\ 2} - L_{final}^{\ 2}}{2L_{final} \bullet W_{LinPot} \bullet H_{LinPot}} \tag{C.31}$$

$$\gamma_{CL} = \alpha - \frac{\pi}{2} \tag{C.32}$$

$$\gamma = \frac{\left(\gamma_{DF11} - \gamma_{DF12}\right)}{2} \frac{W_{linPot}}{L_{link}} \tag{C.33}$$

Where W_{linPot} = Width between linear pot fixture to the frame measured at beginning of test and included at end of this appendix

H_{LinPot} = Height between linear pot fixture to the frame measured

at beginning of test and included at end of this appendix

L_{final} = L_{init} + Measured Change in Length

L_{init} = Initial length of linear potentiometer measured at the beginning of test and included at end of this appendix

γ_{CL} = Shear Strain Between Column Center Lines

γ = Shear Strain Across the Fuse Link

C.4.2 Fuse Shear Strain for B Series

The fuse shear strain for the single frame configuration was calculated three different ways and compared in Appendix D. Fuse shear strain was calculated using the diagonal linear potentiometer connected to the center column, the vertical linear potentiometers spanning from the frame down to the post-tensioning anchorage plate, and string potentiometers between the anchorage plate and the fuse.

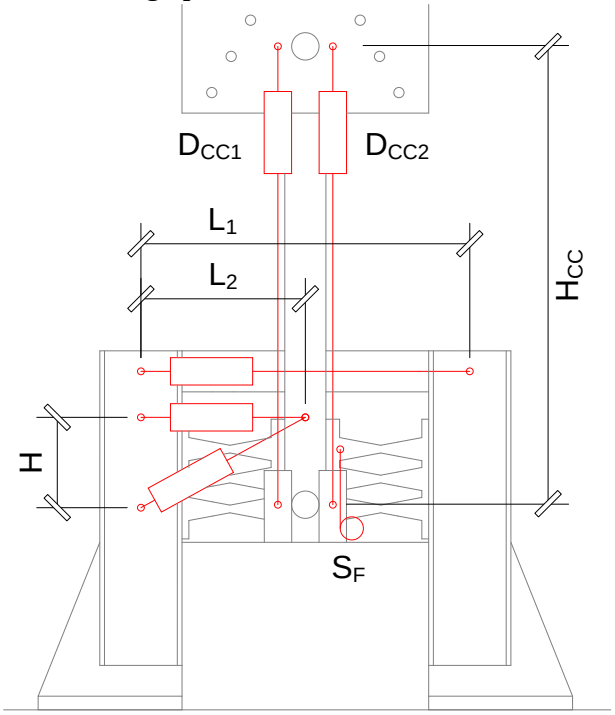

Figure C.11 Linear Potentiometer Arrangement for the Single Frame Configuration

Table C.1 Measured Distances for Test B1 and B2

	Test B1 Left Frame	Test B2 Right Frame
$L_{1\text{-initial}}$	12.125”	12.06”
$L_{2\text{-initial}}$	13.58”	13.42”
$H_{initial}$	6.125”	5.875”

A. Calculating fuse shear strain using diagonal linear potentiometer:

A triangle can be formed using the two linear potentiometers, D_{FF2} and D_{FF3}. The lengths of the sides of the triangle are calculated using Equation (C.34) and Equation (C.35). The law of cosines is used to find the angle, α, as given in Equation (C.36). The shear strain between linear pot attachments is calculated in Equation (C.37), and the shear strain across the fuse link is calculated in Equation (C.38) and Equation (C.39).

$$L_{2-current} = L_{2-initial} + D_{FF2} \tag{C.34}$$

$$L_{3-current} = \sqrt{H_{initial}{}^2 + L_{2-initial}{}^2} + D_{FF3} \tag{C.35}$$

$$\cos(\alpha) = \frac{L_{2-current}{}^2 + H_{initial}{}^2 - L_{3-current}{}^2}{2\, L_{2-current}\, H_{initial}} \tag{C.36}$$

$$\gamma' = \alpha - \pi/2 \tag{C.37}$$

$$\Delta_A = L_{2-current} \sin(\gamma') \tag{C.38}$$

$$\gamma_A = \frac{\Delta_A}{L_{Link}} \tag{C.39}$$

B. Calculating fuse shear strain using vertical linear potentiometers:

The shear strain was also calculated using the vertical linear potentiometers shown in Figure C.11. The calculation is given in Equation (C.40) and Equation (C.41).

$$\Delta_B = \frac{D_{CC1} + D_{CC2}}{2} \tag{C.40}$$

$$\gamma_B = \frac{\Delta_B}{L_{Link}} \tag{C.41}$$

C. Calculating fuse shear strain using vertical string potentiometers:

The third method for calculating fuse shear strain used the vertical string potentiometers. The calculation is given in Equation (C.42) and Equation (C.43).

$$\Delta_C = S_F \tag{C.42}$$

$$\gamma_C = \frac{\Delta_C}{L_{Link}} \tag{C.43}$$

The main difference between the three measurements for fuse shear strain in the single frame configuration was the amount of motion due to pins moving in pin holes. The pin hole tolerances allowed motion of the frame and center column that did not cause an increase in fuse deformation. The amount of pin hole tolerances can be calculated based on the quantities given above. Measurement C does not include any motion due to pin hole tolerances. Measurement A includes the bottom pin hole tolerance only. Measurement B includes both the top and bottom pin hole tolerances. The amount of pin hole tolerances were calculated using Equation (C.44), Equation (C.45), and Equation (C.46).

$$\Delta_{slop-bot} = \Delta_A - \Delta_C \tag{C.44}$$

$$\Delta_{slop-top} = \Delta_B - \Delta_A \tag{C.45}$$

$$\Delta_{Tot-slop} = \Delta_B - \Delta_C \tag{C.46}$$

C.4.3 Fuse Shear Force for the Dual Frame Configuration

The fuse shear forces were calculated as the difference between the resultant forces above and below the fuses. Figure C.12 shows an example for the dual frame configuration that has six fuses. Total section resultants consisting of all forces crossing the section line were resolved to vertical components for each frame as described earlier in this Appendix. The difference in the vertical resultant for the left frame was averaged with the difference in the vertical resultants for the right frame and taken to be the fuse shear force. This difference was divided by four to represent average fuse shear force in the four fuses. Similar calculations were conducted for the dual frame configurations that used only two fuses. In that case, it was the difference between section 1 and section 2 resultants that were calculated and they were divided by two to represent the average for the two fuses.

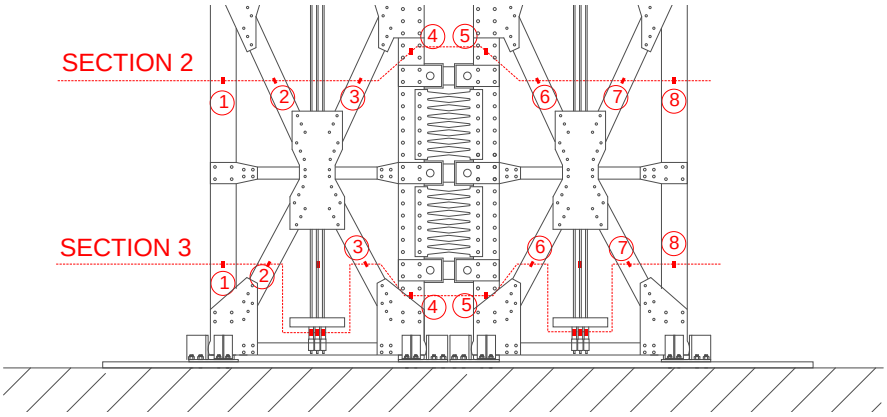

Figure C.12 Strain Gaged Sections Used to Calculate Shear Forces For Specimen A1, A6, and A7

The fuse shear forces were also approximated by the difference in column axial forces above and below the fuses. The differences in column axial forces were divided by the number of fuses and averaged for the left and right interior columns. These values

are compared to the fuse shear forces calculated using the entire frame section in Appendix D.

C.4.4 Fuse Shear Force for B Series

The fuse shear force for the single frame configuration was calculated based on the strain gage measurements on the center columns. The calculation is given in Equation (C.47).

$$F_{fuse} = \frac{(\varepsilon_3 + \varepsilon_6)}{2} EA \tag{C.47}$$

Where ε_3 is the vertical strain gage at the top rosette and ε_6 is the vertical strain at the bottom rosette. E is assumed to be 29,000 ksi, and A is assumed equal to the nominal cross-sectional area of the center column equal to 5 in^2.

C.4.5 Consistent Calculation of Fuse Yield Force

It was desired to quantify the fuse shear yield force and associated displacements. The yield force is assumed to be the intersection of the post-yield stiffness and the initial stiffness. Computing the yield force this way is subjective though especially when the post-yield stiffness is unclear. Furthermore, this method for calculating yield force does not produce a meaningful fuse yield displacement. A more consistent approach was adopted using an offset strain. An offset strain approach can be applied more consistently. A 1.5% offset fuse link shear strain was used to determine fuse shear yield force. The average fuse shear yield force was computed to be 27.8 kips compared to the average intersection of the initial slope with the post-yield slope which was 26.9 kips. Therefore, the 1.5% offset approach produces yield forces that are similar to those obtained as the intersection of the initial stiffness and post-yield stiffness. The calculation of the offset fuse yield force is demonstrated in Figure C.13, Figure C.14, Figure C.15, Figure C.16, and Figure C.17.

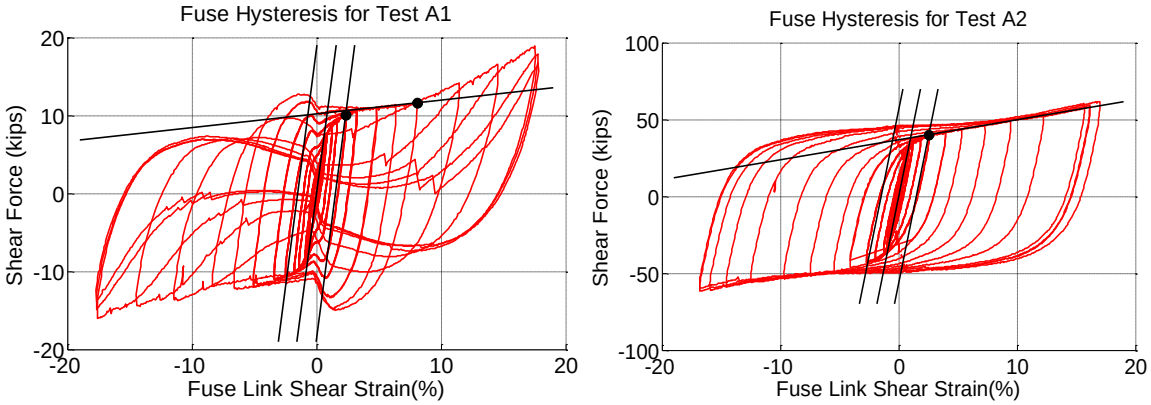

Figure C.13 Calculation of the 1.5% Offset Fuse Yield Force

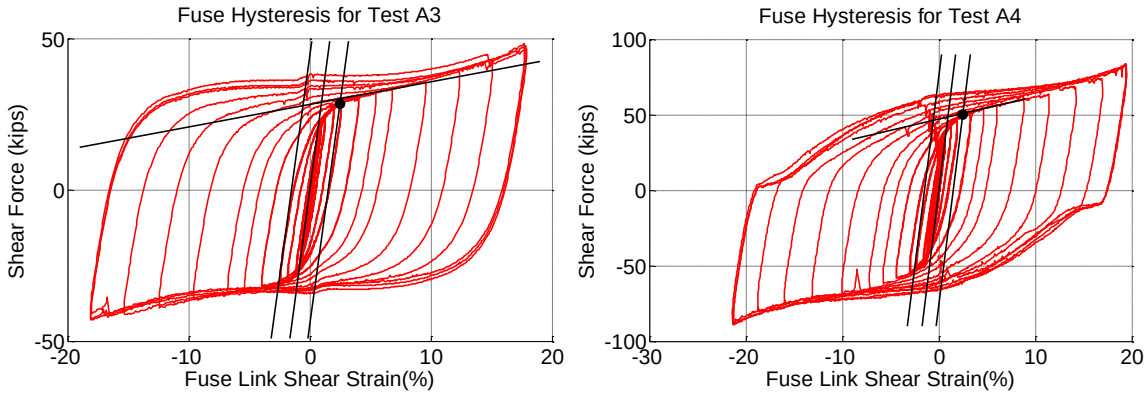

Figure C.14 Calculation of the 1.5% Offset Fuse Yield Force

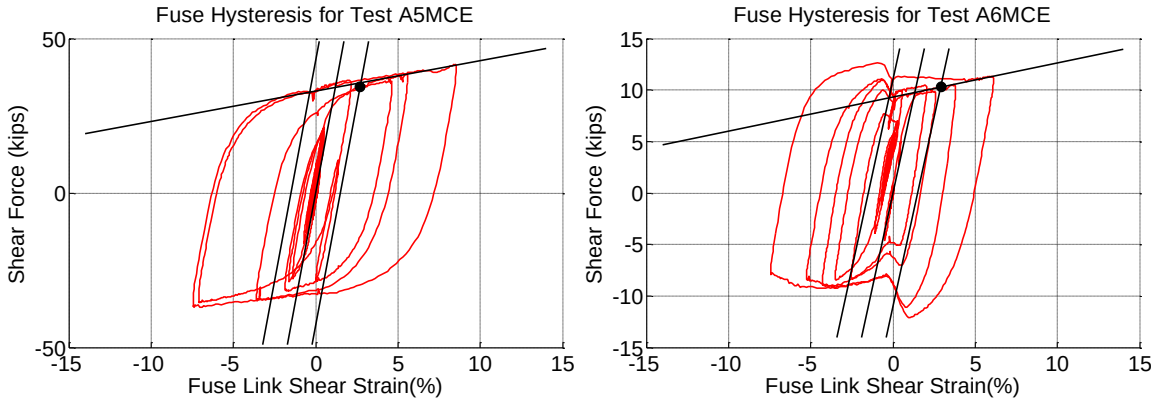

Figure C.15 Calculation of the 1.5% Offset Fuse Yield Force

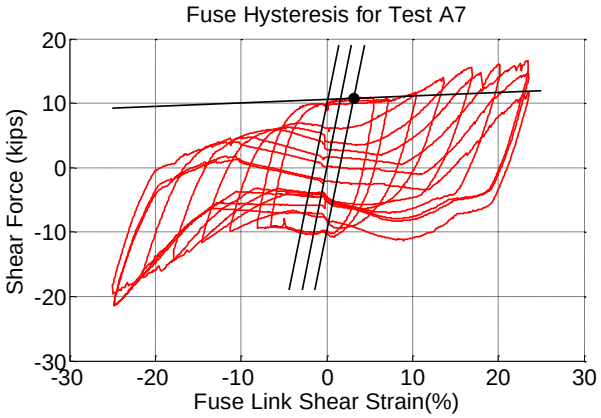

Figure C.16 Calculation of the 1.5% Offset Fuse Yield Force

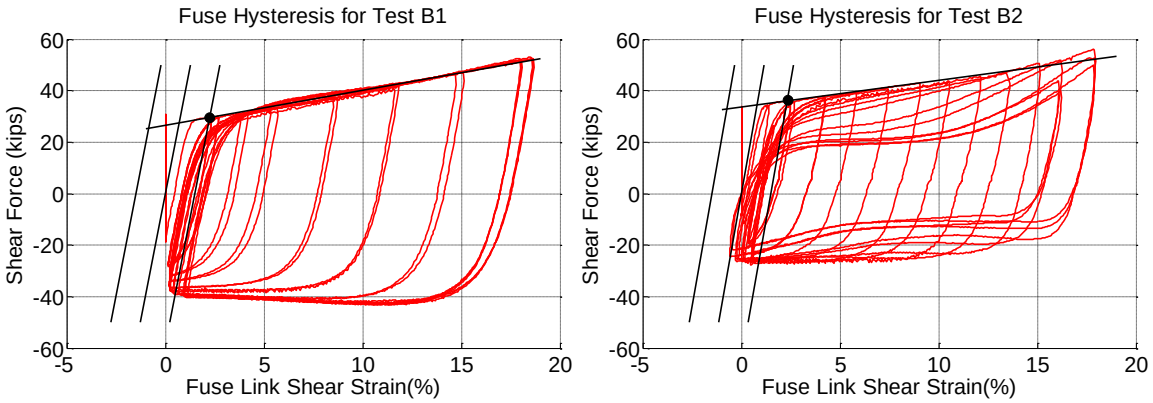

Figure C.17 Calculation of the 1.5% Offset Fuse Yield Force

C.5 Post-Tensioning Response

C.5.1 Calculate Stress and Strain in the PT Strand

The post-tensioning instrumentation, dimensions, and variable definitions are shown in Figure C.18. The post-tensioning stress was calculated using

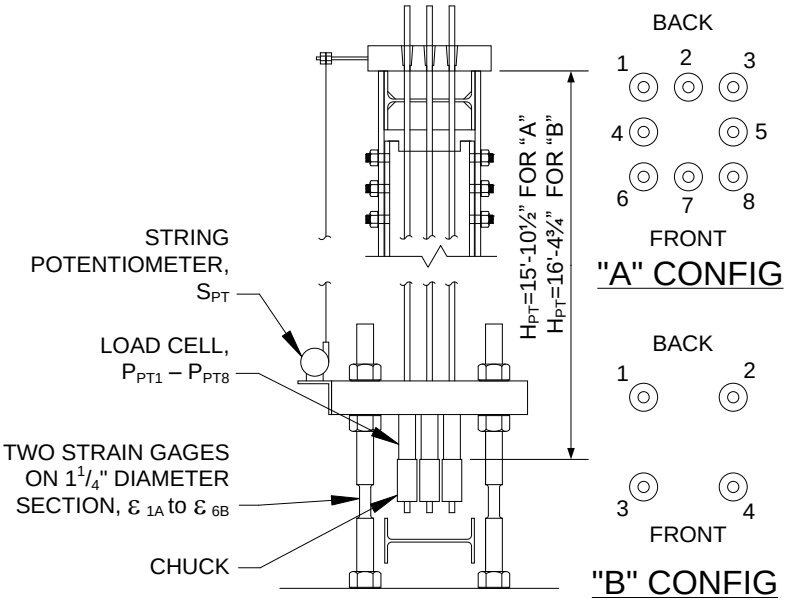

Figure C.18 Post-Tensioning Configuration and Instrumentation

$$\sigma_{PT} = \frac{P_{PT-i}}{A_{PT}} \tag{C.48}$$

$$\varepsilon_{PT} = \frac{P_{PT-i-initial}}{A_{PT}E_{PT}} + \frac{\Delta S_{PT}}{H_{PT}} + ULR \bullet e_{strand} \quad \text{(C.49)}$$

Where $P_{PT\text{-}i}$ is the force in the load cell i
A_{PT} = 0.153 in^2 nominal
E_{PT} = 29,300 ksi from material test
ΔS_{PT} = Change in String Potentiometer Reading Relative to the Beginning of the Test

$$ULR = \frac{\left(\delta_{up-left} - \delta_{up-right}\right)}{A} \text{ = uplift ratio}$$

$\delta_{up\text{-}left}$ = Uplift String Potentiometer Reading on Left Side of Frame
$\delta_{up\text{-}right}$ = Uplift String Pot. Reading on Right Side of Frame
e_{strand} = eccentricity of the strand relative to the center

The total post-tensioning force was calculated by two methods:

$$F_{PT-A} = \sum_i P_{PT-i} \quad \text{(C.50)}$$

$$F_{PT-B} = \sum_{i=1}^{6} \left(\frac{\varepsilon_{iA} + \varepsilon_{iB}}{2} \right) E_{rod} A_{rod} \quad \text{(C.51)}$$

Where E_{rod} = 29,000 ksi nominal
A_{rod} is based on 1-1/4" diameter

C.5.2 Calculating PT Force Offsets for Test A1 through A4

The post-tensioning load cells were not zeroed properly before post-tensioning the frames prior to the Specimen A1 test. As a result, there were offsets in the post-tensioning load cell data for all tests until the post-tensioning strands were replaced after the Specimen A4 test. The offsets listed in Table C.2 were subtracted from the post-tensioning load cell data for Specimens A1 through A4.

Table C.2 Offsets for the Post-Tensioning Strands Used for Tests A1 Through A4

	Left Frame	Right Frame
L-PT- 1	12.21	2.99
L-PT- 2	10.19	-1.43
L-PT- 3	5.47	-16.80
L-PT- 4	-9.75	34.78
L-PT- 5	9.35	-21.64
L-PT- 6	-12.78	2.72
L-PT- 7	-13.10	16.43
L-PT- 8	1.07	2.40

C.6 Decomposing Response into Post-Tensioned Frame and Fuse

It was desired to examine the behavior of the two main components of the controlled rocking system. The restoring moment due to the post-tensioning, M_{PT}, and fuse, M_{fuse}, were calculated and summed together to equal the total restoring moment, $M_{restore}$. The restoring moment is compared to the applied overturning moment in Appendix D.

C.6.1 Calculation of Restoring Moments for the Dual Frame Configuration

The calculation of the restoring moment due to post-tensioning force is given in Equation (C.52). For small values of the uplift ratio, both legs of the frame may be bearing on the support. If both legs are in bearing, then the freebody diagram of the frame changes. Equation (C.52), takes this into account using the vertical reactions at the base of the frame (measured using the strain gage sections and converted to resultant forces as described above).

$$\begin{aligned} M_{PT} &= -F_{PT}W_{rock} && \text{For } ULR < -0.1\% \\ M_{PT} &= F_{PT}W_{rock}R_{rock} && \text{For } -0.1\% < ULR < 0.1\% \\ M_{PT} &= F_{PT}W_{rock} && \text{For } ULR > 0.1\% \end{aligned} \tag{C.52}$$

Where:

$$R_{rock} = \frac{R_{react}}{\left|R_{react}\right|} \qquad \text{For } \left|R_{react}\right| > 1.0$$

$$R_{rock} = R_{react} \qquad \text{For } \left|R_{react}\right| < 1.0$$

$$R_{react} = \frac{\left(R_{lefts} - R_{rights}\right)}{F_{PTi}}$$

R_{lefts} = Total vertical reaction on left side of both frames
R_{rights} = Total vertical reaction on right side of both frames
F_{PTi} = Total initial post tension force
W_{rock} = 34.7”

The restoring moment due to the fuse were calculate using Equation (C.53), and the total restoring force for the frame was calculated as the sum of the restoring force due to the post-tensioning and fuse as given in Equation (C.54).

$$M_{fuse} = F_F\left(A + B\right) \tag{C.53}$$

$$M_{restore} = M_{PT} + M_{fuse} \tag{C.54}$$

C.6.2 Calculation of the Restoring Moments for the Single Frame Configuration

The forces due to the post-tensioning, fuse, and base reaction after uplift are shown in Figure C.19 for the single frame configuration.

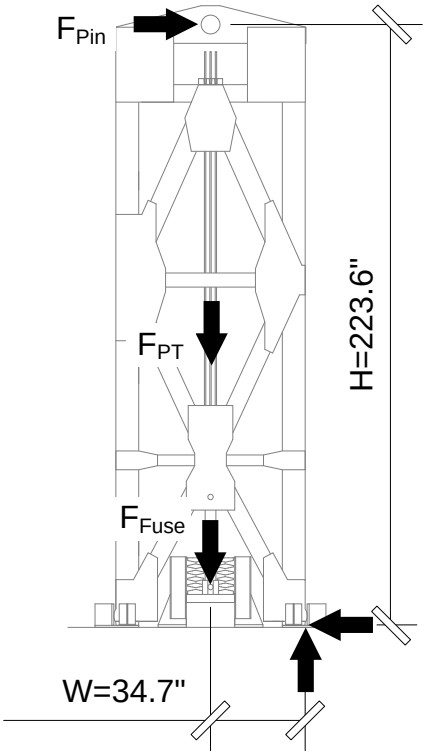

Figure C.19 Freebody Diagram for a Single Frame for the Single Frame Configuration

The restoring moment due to post-tensioning was calculated the same as for the dual frame configuration. The restoring moment due to the fuse was calculated as given in Equation (C.55).

$$M_{fuse} = -F_{fuse} W_{rock} \quad \text{For } ULR < 0\% \qquad (C.55)$$
$$M_{fuse} = F_{fuse} W_{rock} \quad \text{For } ULR \geq 0\%$$

C.7 Motion of the System

Several values were computed based on the motion of the controlled rocking frames. Figure C.20 shows the schematic locations for the string potentiometers that measured the displacement of the frames.

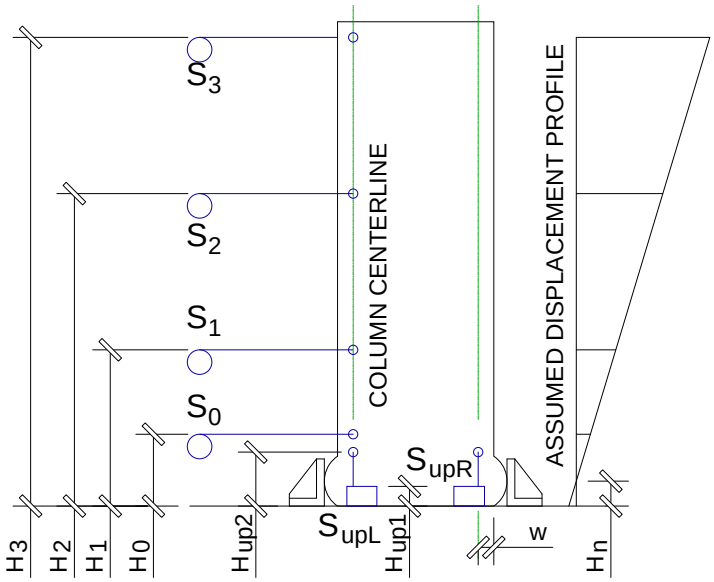

Figure C.20 Schematic Locations for String Potentiometers

The interstory drift ratios were calculated as given in Equation (C.56), Equation (C.57), and Equation (C.58).

$$ISD_1 = \frac{(S_1 - S_0)}{(H_1 - H_0)} \tag{C.56}$$

$$ISD_2 = \frac{(S_2 - S_1)}{(H_2 - H_1)} \tag{C.57}$$

$$ISD_3 = \frac{(S_3 - S_2)}{(H_3 - H_2)} \tag{C.58}$$

The amount of sliding at the base of the frames was calculated using similar triangles as given in Equation (C.59).

$$\Delta_{slide} = S_1 - \frac{S_1 - S_0}{H_1 - H_0} H_1 \tag{C.59}$$

Although the figures showing column uplift throughout this report show uncorrected data, a correction was conducted and investigated in Appendix D. The uplift reading, Δup, was corrected to eliminate horizontal movement of the dead end using similar triangles and trigonometry. This correction is given in Equation (C.60), Equation (C.61), Equation (C.62), Equation (C.63), and Equation (C.64).

$$\Delta_{hor} = S_1 - \frac{S_1 - S_0}{H_1 - H_0}(H_1 - H_{up2}) \tag{C.60}$$

$$H_{string} = H_{up2} - H_{up1} \tag{C.61}$$

$$L_{string} = H_{string} + S_{up} \tag{C.62}$$

$$\alpha = \sin^{-1}\left(\frac{\Delta_{hor}}{L_{string}}\right) \tag{C.63}$$

$$\Delta_{up} = L_{string}\cos(\alpha) - H_{string} \tag{C.64}$$

The uplift reported in prior chapters of this report was measured at the centerline of the column. Since there was an eccentricity between the centerline of the column and the pivot point at the base of the column, the measured uplift was found to change for the pivoting columns as the frame rotated. An uplift at the pivot point was calculated and is examined in Appendix D. The calculation is given in Equation (C.65) based on an eccentricity, w=3.75" from the centerline of the column.

$$\Delta_{up-pivot} = \Delta_{up} + RDR * 3.75" \tag{C.65}$$

It was also found in the examination of the frame motion that the center of rotation was not at the pivot point. The height at which the horizontal displacement was zero, H_n was calculated using Equation (C.66) and is discussed in Appendix D.

$$H_n = H_0 - \frac{H_1 - H_0}{S_1 - S_0} S_0 \tag{C.66}$$

The amount of pin hole tolerances in the load cell pin connections was calculated. As given in (C.67), the frame displacement at the height of the pins was extrapolated based on ground floor and 3rd floor displacements. The amount of pin hole tolerance was calculated as the difference between frame displacement at the height of the pin and the LBCB displacement as given in Equation (C.68). The amount of pin hole tolerance at the pin load cell connection is discussed in Appendix D.

$$\Delta_{calc-pin} = S_3 + \frac{S_3 - S_0}{H_3 - H_0}\left(H_{Pin} - H_0\right) \tag{C.67}$$

$$\Delta_{slop} = \Delta_{LBCB} - \Delta_{calc-pin} \tag{C.68}$$

C.8 Measured String Potentiometer Locations

The measured locations of the ends of the string potentiometer are included in this section. The coordinates are given in reference to the corner of the strong wall as shown in Figure C.21. The coordinate of the gage end is measured to the location where the string comes out of the gage. The coordinate of the frame end is measured to the attachment on the stud which is welded to the frame. The measurements given in this section were executed using a tape measure. The measurements are given in Table C.3, Table C.4, Table C.5, Table C.6, and Table C.7.

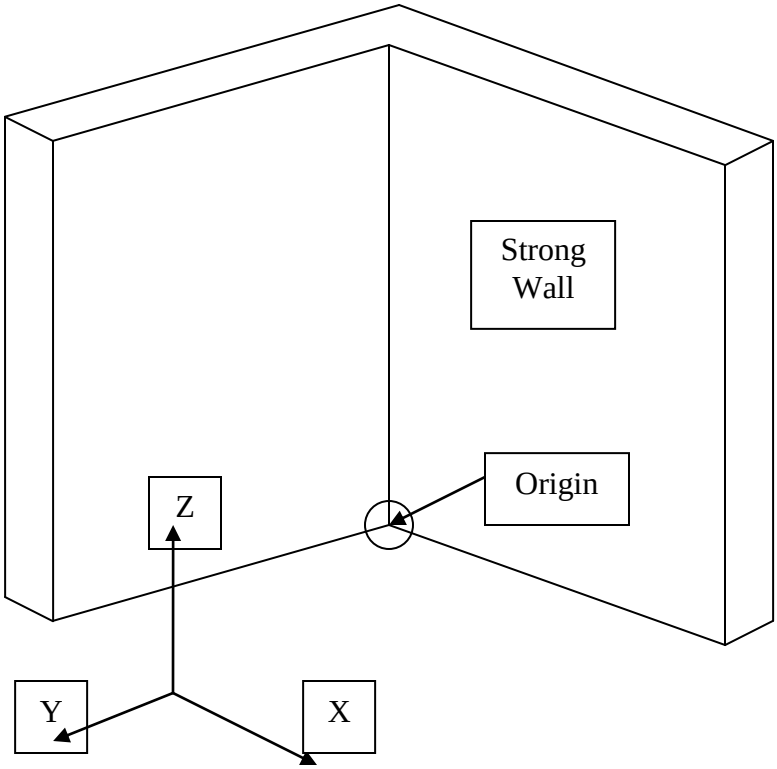

Figure C.21 Coordinate System for Measured String Potentiometer Locations

Table C.3 Measured String Potentiometer Locations on 7/7/08 for Specimen A1 (inches)

Gage End		Frame End	
S-L-3	X: 4.13	S-L-3	X: 93.50
	Y: 39.50		Y: 39.13
	Z: 200.94		Z: 200.94
S-R-3	X: 3.31	S-R-3	X: 180.38
	Y: 53.13		Y: 53.44
	Z: 200.75		Z: 200.81
S-L-2	X: 3.31	S-L-2	X: 93.69
	Y: 38.63		Y: 38.63
	Z: 131.31		Z: 131.38
S-R-2	X: 3.31	S-R-2	X: 180.13
	Y: 53.38		Y: 53.38
	Z: 131.81		Z: 132.31
S-L-1	X: 3.31	S-L-1	X: 93.75
	Y: 38.56		Y: 38.56
	Z: 64.19		Z: 64.25
S-R-1	X: 3.31	S-R-1	X: 180.25
	Y: 54.25		Y: 54.25
	Z: 64.19		Z: 64.25
S-L-0	X: 3.31	S-L-0	X: 180.50
	Y: 38.25		Y: 38.25
	Z: 17.56		Z: 17.69
S-R-0	X: 3.31	S-R-0	X: 180.50
	Y: 3.31		Y: 54.25
	Z: 17.63		Z: 17.56
DOOP-1	X: 87.31	DOOP-1	X: 87.31
	Y: 3.44		Y: 41.88
	Z: 109.63		Z: 109.63
DOOP-2	X: 248.00	DOOP-2	X: 248.00
	Y: 3.44		Y: 41.69
	Z: 109.81		Z: 109.50
S-PT-1	X: 124.50	S-PT-1	X: 124.61
	Y: 54.69		Y: 54.38
	Z: 22.50		Z: 205.25
S-PT-2	X: 211.13	S-PT-2	X: 211.19
	Y: 54.69		Y: 54.63
	Z: 22.50		Z: 205.19

Table C.4 Measured String Potentiometer Locations on 8/20/08 for Specimen A2 (inches)

Gage End			Frame End		
S-L-3	X:	4.13	S-L-3	X:	93.50
	Y:	39.50		Y:	39.13
	Z:	200.94		Z:	200.88
S-R-3	X:	3.31	S-R-3	X:	180.25
	Y:	53.13		Y:	53.25
	Z:	200.75		Z:	200.88
S-L-2	X:	3.31	S-L-2	X:	93.75
	Y:	38.63		Y:	38.50
	Z:	131.31		Z:	131.25
S-R-2	X:	3.31	S-R-2	X:	179.81
	Y:	53.38		Y:	53.38
	Z:	131.81		Z:	131.50
S-L-1	X:	3.31	S-L-1	X:	93.75
	Y:	38.56		Y:	38.56
	Z:	64.19		Z:	64.00
S-R-1	X:	3.31	S-R-1	X:	180.19
	Y:	54.25		Y:	54.25
	Z:	64.19		Z:	64.00
S-L-0	X:	3.31	S-L-0	X:	93.44
	Y:	38.25		Y:	38.25
	Z:	17.56		Z:	18.13
S-R-0	X:	3.50	S-R-0	X:	180.25
	Y:	54.63		Y:	54.14
	Z:	11.63		Z:	12.38
DOOP-1	X:	87.31	DOOP-1	X:	88.06
	Y:	3.44		Y:	42.00
	Z:	109.63		Z:	109.88
DOOP-2	X:	248.00	DOOP-2	X:	249.13
	Y:	3.44		Y:	42.00
	Z:	109.81		Z:	109.63
S-PT-1	X:	124.50	S-PT-1	X:	124.63
	Y:	54.69		Y:	54.75
	Z:	22.50		Z:	205.13
S-PT-2	X:	211.13	S-PT-2	X:	211.38
	Y:	54.69		Y:	54.75
	Z:	22.50		Z:	205.38

Table C.5 Measured String Potentiometer Locations on 9/5/08 for Specimen A3 (inches)

Gage End			Frame End		
S-L-3	X:	see previous	S-L-3	X:	93.69
	Y:	see previous		Y:	39.06
	Z:	see previous		Z:	200.81
S-R-3	X:	see previous	S-R-3	X:	180.14
	Y:	see previous		Y:	53.56
	Z:	see previous		Z:	200.88
S-L-2	X:	see previous	S-L-2	X:	93.75
	Y:	see previous		Y:	38.25
	Z:	see previous		Z:	131.13
S-R-2	X:	see previous	S-R-2	X:	179.94
	Y:	see previous		Y:	131.50
	Z:	see previous		Z:	53.31
S-L-1	X:	see previous	S-L-1	X:	93.75
	Y:	see previous		Y:	38.25
	Z:	see previous		Z:	64.13
S-R-1	X:	3.25	S-R-1	X:	178.19
	Y:	52.25		Y:	54.19
	Z:	64.25		Z:	64.19
S-L-0	X:	5.00	S-L-0	X:	93.38
	Y:	38.25		Y:	38.25
	Z:	17.88		Z:	18.06
S-R-0	X:	see previous	S-R-0	X:	180.44
	Y:	see previous		Y:	54.31
	Z:	see previous		Z:	12.38
DOOP-1	X:	see previous	DOOP-1	X:	88.25
	Y:	see previous		Y:	41.06
	Z:	see previous		Z:	109.75
DOOP-2	X:	248.19	DOOP-2	X:	249.25
	Y:	3.44		Y:	41.75
	Z:	109.69		Z:	109.75
S-PT-1	X:	see previous	S-PT-1	X:	124.69
	Y:	see previous		Y:	53.88
	Z:	see previous		Z:	205.13
S-PT-2	X:	see previous	S-PT-2	X:	211.19
	Y:	see previous		Y:	54.56
	Z:	see previous		Z:	205.19

Table C.6 Measured String Potentiometer Locations on 9/29/08 for Specimen A4 and Specimen A5 (inches)

Gage End			Frame End		
S-L-3	X:	see previous	S-L-3	X:	93.25
	Y:	see previous		Y:	39.13
	Z:	see previous		Z:	200.88
S-R-3	X:	see previous	S-R-3	X:	180.25
	Y:	see previous		Y:	54.44
	Z:	see previous		Z:	200.88
S-L-2	X:	see previous	S-L-2	X:	93.75
	Y:	see previous		Y:	58.50
	Z:	see previous		Z:	131.13
S-R-2	X:	see previous	S-R-2	X:	180.63
	Y:	see previous		Y:	53.50
	Z:	see previous		Z:	131.50
S-L-1	X:	see previous	S-L-1	X:	93.75
	Y:	see previous		Y:	38.38
	Z:	see previous		Z:	64.00
S-R-1	X:	see previous	S-R-1	X:	180.00
	Y:	see previous		Y:	54.25
	Z:	see previous		Z:	64.00
S-L-0	X:	see previous	S-L-0	X:	93.25
	Y:	see previous		Y:	38.25
	Z:	see previous		Z:	18.00
S-R-0	X:	see previous	S-R-0	X:	180.13
	Y:	see previous		Y:	54.44
	Z:	see previous		Z:	12.50
DOOP-1	X:	see previous	DOOP-1	X:	88.25
	Y:	see previous		Y:	41.69
	Z:	see previous		Z:	109.75
DOOP-2	X:	see previous	DOOP-2	X:	248.50
	Y:	see previous		Y:	41.94
	Z:	see previous		Z:	109.50
S-PT-1	X:	see previous	S-PT-1	X:	124.38
	Y:	see previous		Y:	54.75
	Z:	see previous		Z:	205.00
S-PT-2	X:	see previous	S-PT-2	X:	211.13
	Y:	see previous		Y:	55.19
	Z:	see previous		Z:	205.00

Table C.7 Measured String Potentiometer Locations on 12/18/08 for Specimen A6, Specimen A7, Specimen B1, and Specimen B2 (inches)

Gage End			Frame End		
S-L-3	X:	93.38	S-L-3	X:	4.9375
	Y:	39.25		Y:	39.69
	Z:	201.00		Z:	200.25
S-R-3	X:	180.13	S-R-3	X:	3.25
	Y:	54.13		Y:	35.38
	Z:	200.88		Z:	192.75
S-L-2	X:	93.50	S-L-2	X:	3.5
	Y:	38.25		Y:	39
	Z:	131.00		Z:	131.19
S-R-2	X:	179.88	S-R-2	X:	3.4375
	Y:	54.13		Y:	53.4375
	Z:	132.13		Z:	131.8125
S-L-1	X:	93.63	S-L-1	X:	3.375
	Y:	38.38		Y:	38.75
	Z:	64.00		Z:	64.19
S-R-1	X:	180.13	S-R-1	X:	3.375
	Y:	54.00		Y:	52.4375
	Z:	63.88		Z:	64.25
S-L-0	X:	93.25	S-L-0	X:	4.9375
	Y:	38.38		Y:	38.3125
	Z:	18.00		Z:	17.6875
S-R-0	X:	179.94	S-R-0	X:	3.4375
	Y:	54.50		Y:	54.625
	Z:	12.38		Z:	11.5625
DOOP-1	X:	88.00	DOOP-1	X:	87.5
	Y:	41.63		Y:	see previous
	Z:	109.75		Z:	see previous
DOOP-2	X:	248.50	DOOP-2	X:	24.5
	Y:	41.50		Y:	3.375
	Z:	109.50		Z:	109.75
S-PT-1	X:	124.63	S-PT-1	X:	124.25
	Y:	54.50		Y:	54.63
	Z:	205.00		Z:	24.5
S-PT-2	X:	211.25	S-PT-2	X:	211
	Y:	54.50		Y:	54.89
	Z:	205.25		Z:	24.5

C.9 Measured Linear Potentiometer Locations

The measured locations of the linear potentiometers are included in this section. The height (or Z coordinate) above the 2" thick steel base plate was measured for each end of each linear potentiometer. The width between the studs that were used for linear potentiometer attachment was measured at each height. For diagonal linear potentiometers, there is a measurement of the width between the studs at the bottom and top attachment. Figure C.22 shows an example of these measurements. The measurements are given in Table C.8, Table C.9, Table C.10, Table C.11, Table C.12, and Table C.13.

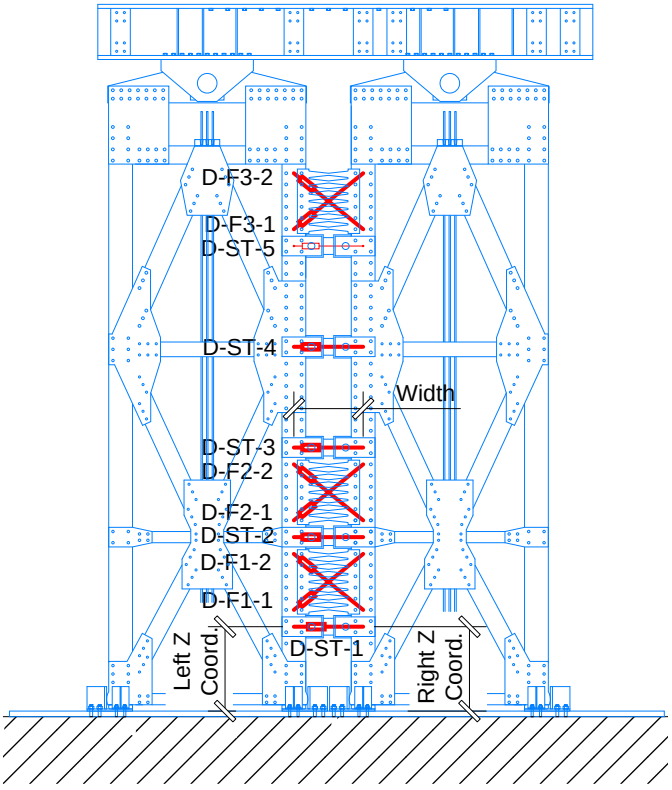

Figure C.22 Key to the Measured Linear Potentiometer Locations

Table C.8 Measured Linear Potentiometer Locations on 7/8/08 for Specimen A1

	Left Z Coordinate (in)	Right Z Coordinate (in)	Bottom Width (in)	Top Width (in)
D-ST-1	30.75	30.44	25.94	--
D-ST-2	62.50	62.38	24.69	--
D-ST-3	94.31	94.19	24.56	--
D-ST-4	130.25	130.38	24.44	--
D-ST-5	166.38	166.31	24.44	--
D-F-1-1	56.19	36.69	25.06	24.81
D-F-1-2	37.06	56.06	25.06	24.81
D-F-2-1	87.69	68.63	24.63	24.69
D-F-2-2	68.88	87.88	24.63	24.69
D-F-3-1	191.75	172.69	24.50	24.38
D-F-3-2	172.63	191.94	24.50	24.38

Table C.9 Measured Linear Potentiometer Locations on 8/20/08 for Specimen A2

	Left Z Coordinate (in)	Right Z Coordinate (in)	Bottom Width (in)	Top Width (in)
D-ST-1	16.13	16.25	24.94	--
D-ST-2	36.75	36.63	24.75	--
D-ST-3	62.25	62.25	24.63	--
D-ST-4	110.13	110.19	24.50	--
D-ST-5	150.31	150.06	24.50	--
D-F-1-1	56.06	36.63	24.75	24.63
D-F-1-2	36.75	56.06	24.75	24.63
D-F-2-1	87.94	68.56	24.63	24.50
D-F-2-2	68.75	87.75	24.63	24.50
D-F-3-1	141.50	116.88	24.31	24.56
D-F-3-2	116.69	141.69	24.31	24.56

Table C.10 Measured Linear Potentiometer Locations on 9/5/08 for Specimen A3

	Left Z Coordinate (in)	Right Z Coordinate (in)	Bottom Width (in)	Top Width (in)
D-ST-1	16.19	16.19	25.13	--
D-ST-2	36.63	36.63	24.94	--
D-ST-3	62.25	62.31	24.69	--
D-ST-4	109.88	110.13	24.56	--
D-ST-5	150.19	150.06	24.50	--
D-F-1-1	56.00	36.63	24.94	24.75
D-F-1-2	36.63	55.81	24.94	24.75
D-F-2-1	87.75	68.50	24.63	24.63
D-F-2-2	68.75	87.50	24.63	24.63
D-F-3-1	141.44	116.81	24.50	24.63
D-F-3-2	116.56	141.56	24.50	24.63

Table C.11 Measured Linear Potentiometer Locations on 9/30/08 for Specimen A4 and Specimen A5

	Left Z Coordinate (in)	Right Z Coordinate (in)	Bottom Width (in)	Top Width (in)
D-ST-1	16.19	16.25	25.00	--
D-ST-2	36.56	36.63	24.94	--
D-ST-3	62.25	62.25	24.69	--
D-ST-4	110.06	110.06	24.50	--
D-ST-5	150.19	150.00	24.44	--
D-F-1-1	56.06	36.63	24.94	24.75
D-F-1-2	36.56	55.88	24.94	24.75
D-F-2-1	87.94	68.56	24.63	24.50
D-F-2-2	68.81	87.88	24.63	24.50
D-F-3-1	141.63	116.88	24.50	24.50
D-F-3-2	116.75	141.50	24.50	24.50

Table C.12 Measured Linear Potentiometer Locations on 12/18/08 for Specimen A6

	Left Z Coordinate (in)	Right Z Coordinate (in)	Bottom Width (in)	Top Width (in)
D-ST-1	30.25	30.00	24.88	--
D-ST-2	62.25	62.25	24.75	--
D-ST-3	94.00	94.00	24.63	--
D-ST-4	130.13	130.00	24.63	--
D-ST-5	166.13	166.00	24.63	--
D-F-1-1	56.00	36.88	25.00	24.75
D-F-1-2	36.75	56.00	25.00	24.75
D-F-2-1	87.88	68.50	24.75	24.63
D-F-2-2	68.75	87.75	24.75	24.63
D-F-3-1	191.63	172.50	24.75	24.63
D-F-3-2	172.25	191.63	24.75	24.63

Table C.13 Measured Linear Potentiometer Locations on 1/28/09 for Specimen A7

	Left Z Coordinate (in)	Right Z Coordinate (in)	Bottom Width (in)	Top Width (in)
D-ST-1	36.63	36.75	25.00	--
D-ST-2	56.00	55.88	24.88	--
D-ST-3	87.88	87.63	24.63	--
D-ST-4	116.75	116.69	24.63	--
D-ST-5	168.19	168.25	24.75	--
D-F-1-1	56.00	36.75	25.00	24.88
D-F-1-2	36.63	55.88	25.00	24.88
D-F-2-1	87.88	68.50	24.75	24.63
D-F-2-2	68.75	87.63	24.75	24.63
D-F-3-1	191.63	172.56	24.75	24.63
D-F-3-2	172.63	191.63	24.75	24.63

Table C.14 Measured Linear Potentiometer Locations on 3/6/09 for Specimen B1 and Specimen B2 (See Figure C.11 for Dimension Locations)

	Specimen B1 Dimension (in)	Specimen B2 Dimension (in)
L1	24.00	24.13
L2	12.06	12.13
H	5.88	6.13
HCC	31.38	31.40

C.10 Measured Strain Gage Locations

The measured locations of the strain-gaged sections are given in Figure C.23.

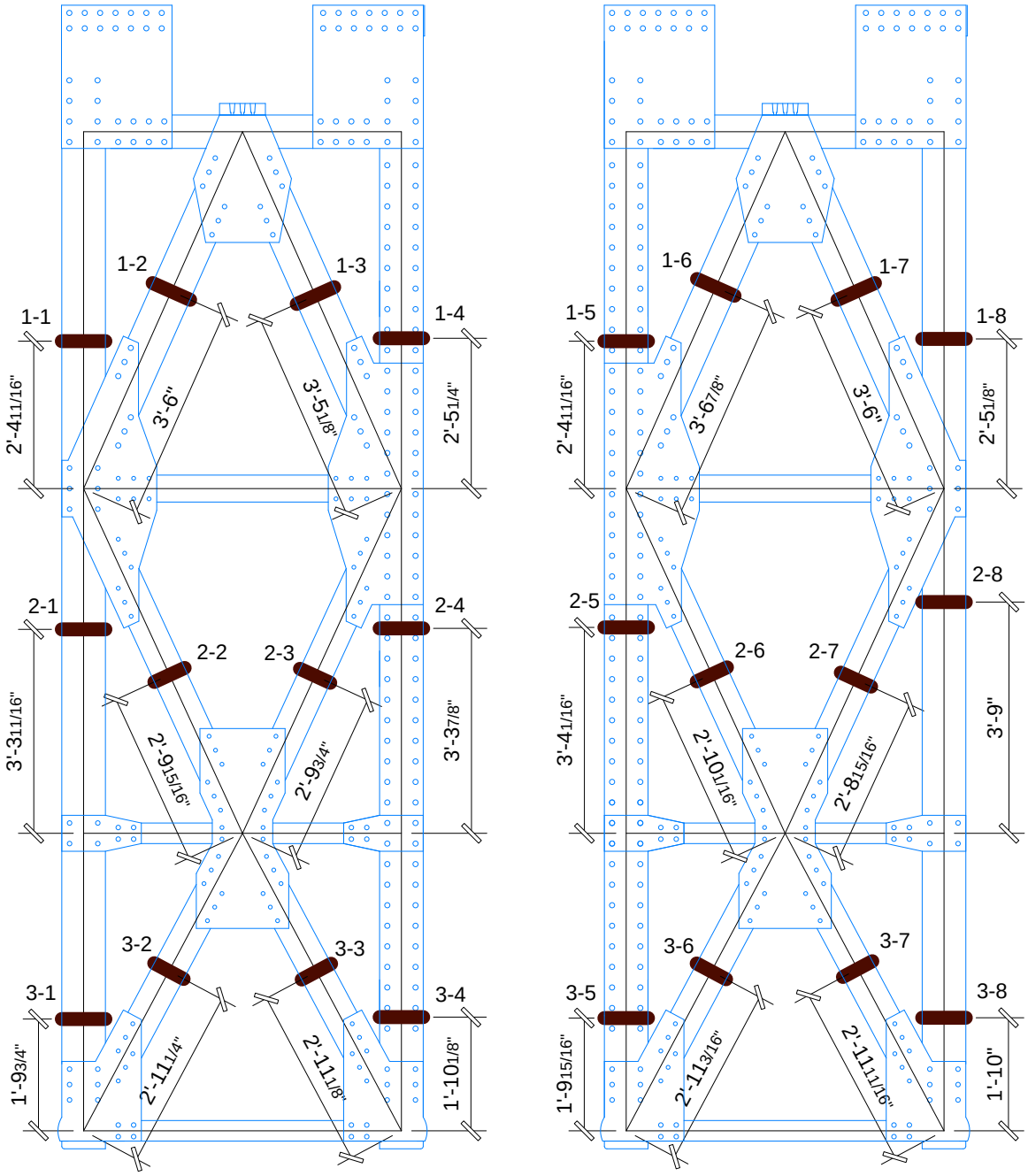

Figure C.23 Measured Strain Gage Section Locations

REDUCED DATA AND DATA VALIDATION

The experimental data was converted into useful quantities using the calculations given in Appendix C. The experimental data was also validated by comparing quantities that were measured in more than one way. This section is organized by specimen. All of the plots are discussed for Specimen A1, but only the unique trends are discussed for the other specimens. The plots are included for all specimens.

D.1 Specimen A1

Notes on data reduction for Specimen A1:

- The first 133 lines of data from the step data correspond to a test of the DAQ system before the test began. These lines of data do not have a step number or substep number and were deleted from the data prior to plotting. Similarly, there were two other lines of data without corresponding step numbers that were deleted.
- Offsets for the post-tension load cells were calculated using data points just before the stressing process began. These same offsets were used to compute post-tension forces for Test A1.

D.1.1 System Response

The system response was decomposed into the components due to the post-tensioned frame and fuse as shown on the left of Figure D.1. The plot is given in the moment domain for the reasons given at the beginning of Chapter 5. Since these two components are meant to be the primary means for resisting lateral loads, the sum of the two components should approximately equal the applied moments. The right side of Figure D.1 shows that the sum of the post-tensioning and fuse resistance components, referred to as restoring moment, is similar to the applied overturning moment. Figure D.2 shows that the restoring moment is nearly equal to the overturning moment for small drifts, but is less than the overturning moment at larger drifts. As the drifts increased, the struts and other constraint between the two frames created small additional resistance to lateral loads. For specimens with fewer struts between the frames and thicker fuses, the effect of forces between the frames was not as great and the restoring moment more closely matched the overturning moment.

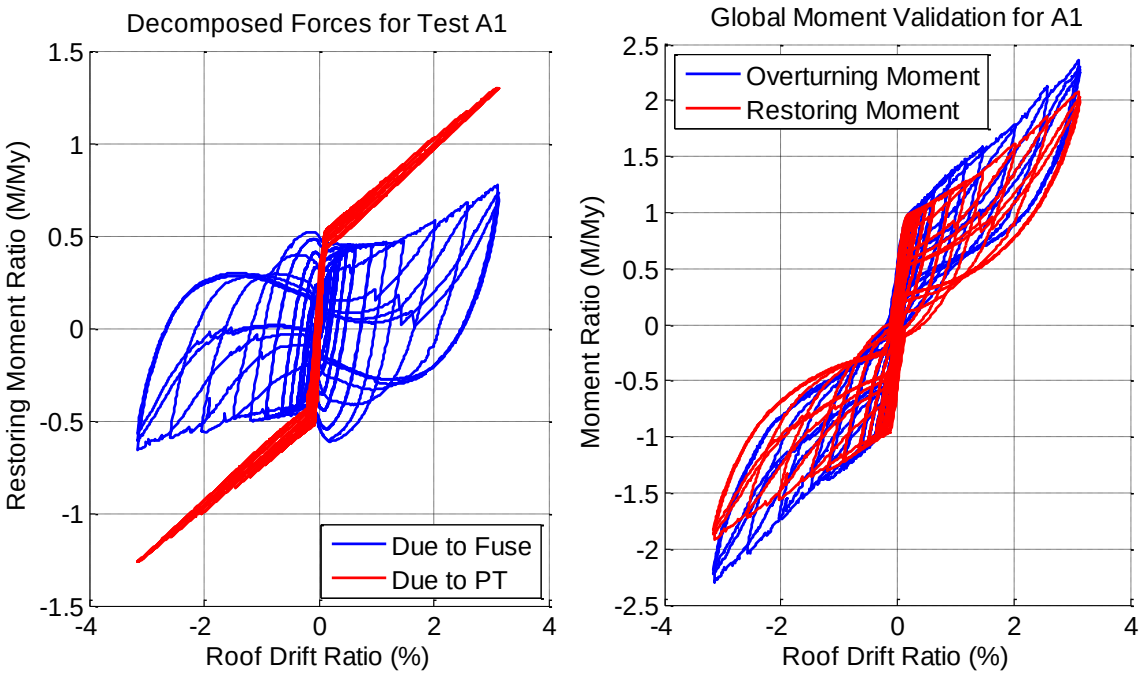

Figure D.1 Specimen A1 - Decomposing System Response into Fuse and Post-Tensioning Components

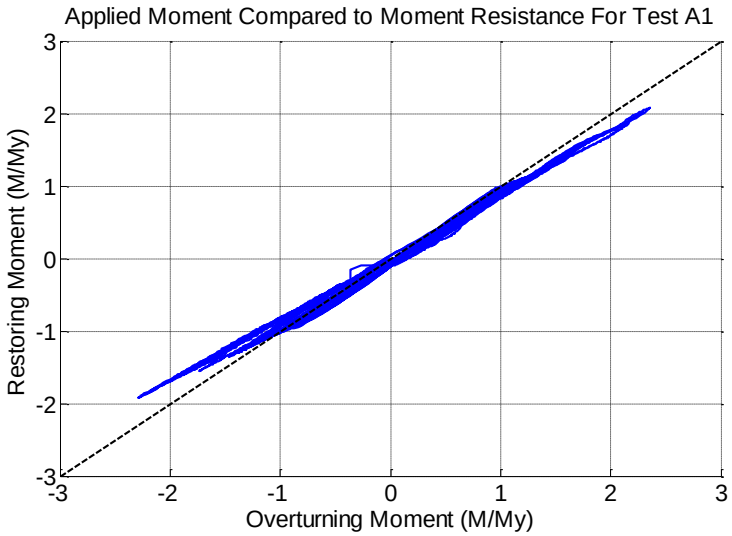

Figure D.2 Specimen A1 - Comparing Restoring Moment and Overturning Moment

The horizontal forces measured by the pin load cells was compared to the horizontal force measured with the LBCB. Figure D.3 shows that the two methods for measuring horizontal force produced very similar results.

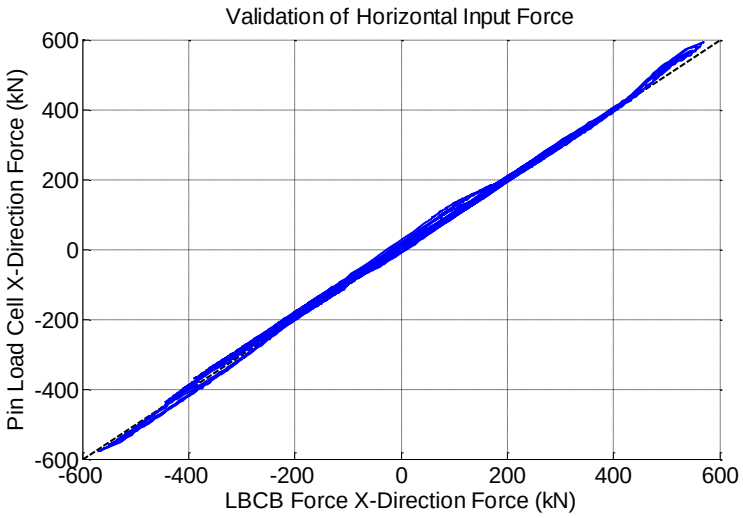

Figure D.3 Specimen A1 - Validation of Horizontal Forces Applied to the Frames

D.1.2 Post Tension Force Validation

The stress-strain response of every post-tensioning strand is included in Figure D.4 and Figure D.5. The total post-tensioning force was calculated as the sum of the post-tensioning load cell readings and separately using the strain gaged anchor rods that held down the post-tensioning anchorage plate. The six anchor rods were lathed down at the area of the gage and the average diameter was found to be 1.274". Using this area and a modulus of elasticity of E=29,000 ksi, the axial load was calculated. Figure D.6 shows the comparison of these two measurements.

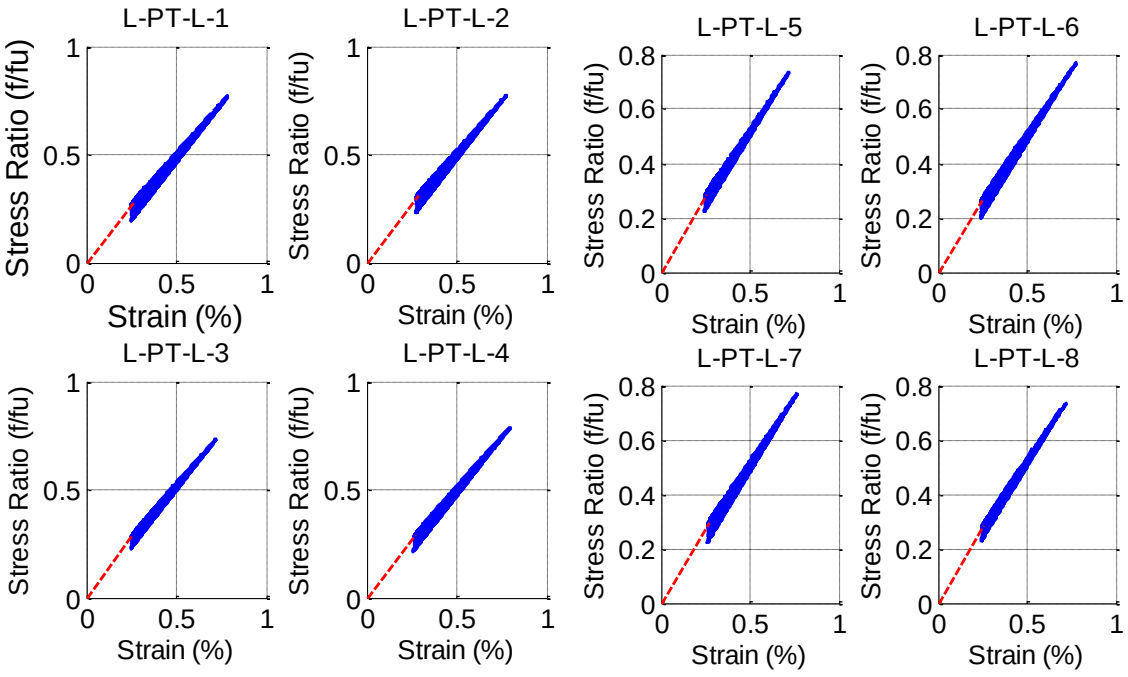

Figure D.4 Specimen A1 - Post-Tensioning Stress-Strain Response

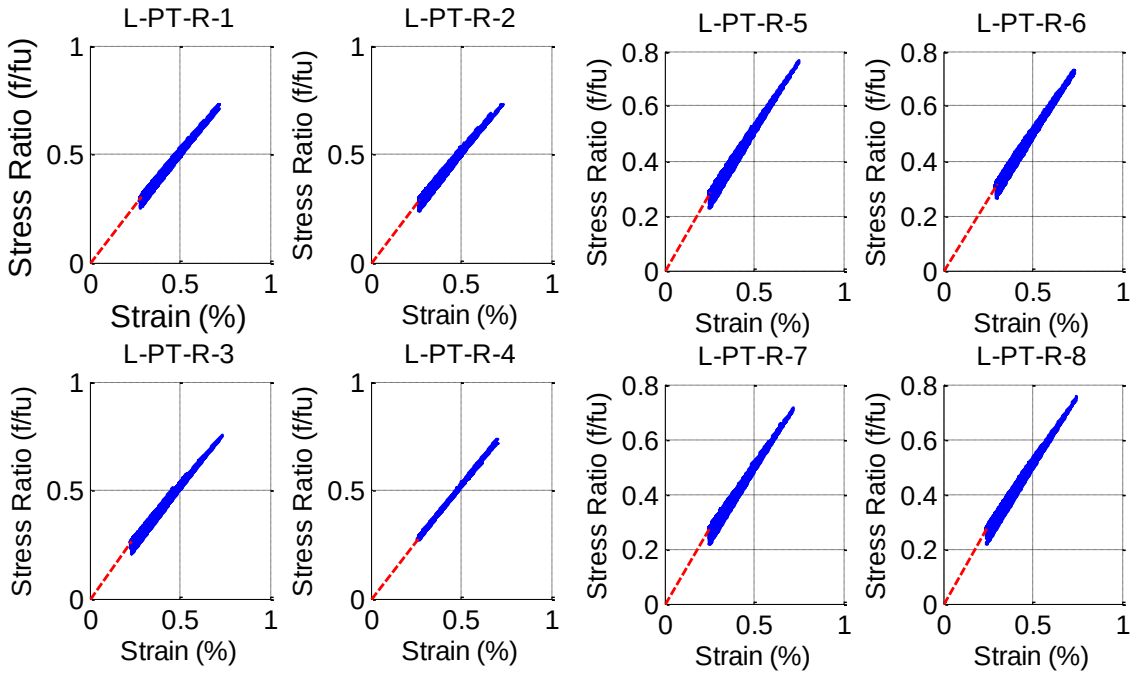

Figure D.5 Specimen A1 - Post-Tensioning Stress-Strain Response

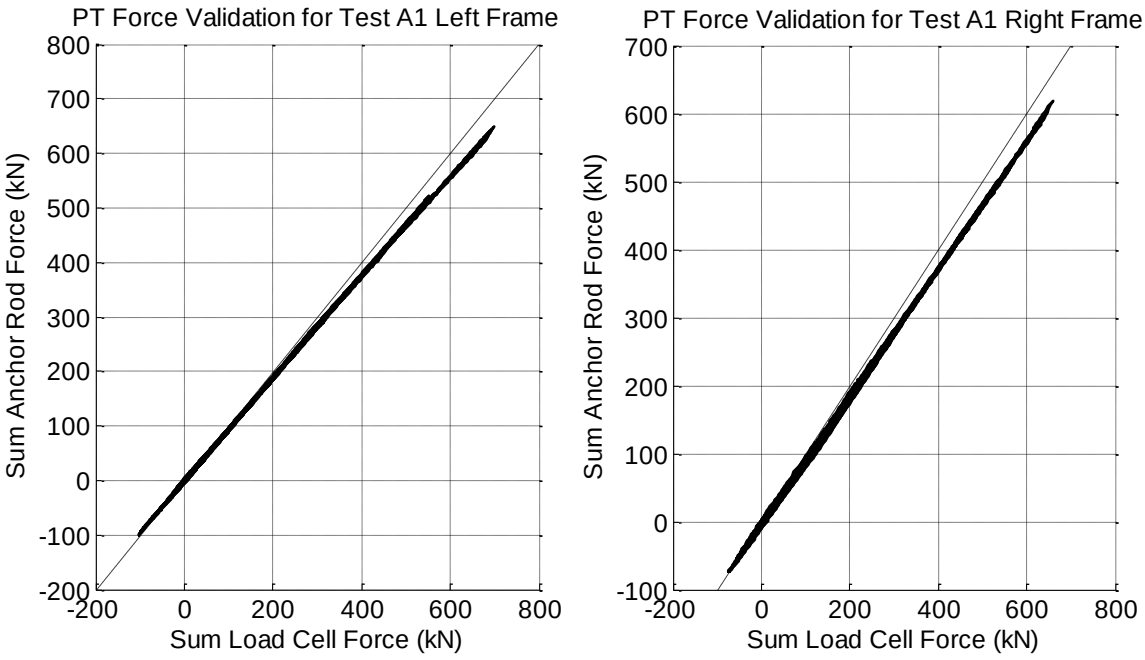

Figure D.6 Specimen A1 - Validation of Post-Tensioning Forces

D.1.3 Data Validation for Fuse Response

As described in Appendix C, the fuse shear force was typically calculated using the difference in resultant frame forces above and below the fuses. Figure D.7 shows a comparison of the fuse load-deformation behavior as plotted with the difference in frame forces and the difference in interior column forces. For specimen A1, it was determined that errors in some of the strain-gaged sections caused errors in the frame resultant forces. Figure D.7 shows that the fuse shear forces calculated using frame section forces were less antisymmetric, exhibited positive shear force when loading into the negative shear strain regime late in the displacement history, and when used to calculate restoring moment had worse correlation with overturning moment. For these reasons, the fuse shear force calculated using the difference in column forces above and below the fuse was used for the plots shown in this report. For all other specimens, the difference in frame resultants was used for calculation of fuse shear force.

The right side of Figure D.7 shows the fuse shear strain for all three floors. The fuse shear strain is shown to be within 6% for each of the three floors. For plots in the report, the average of the three values was used.

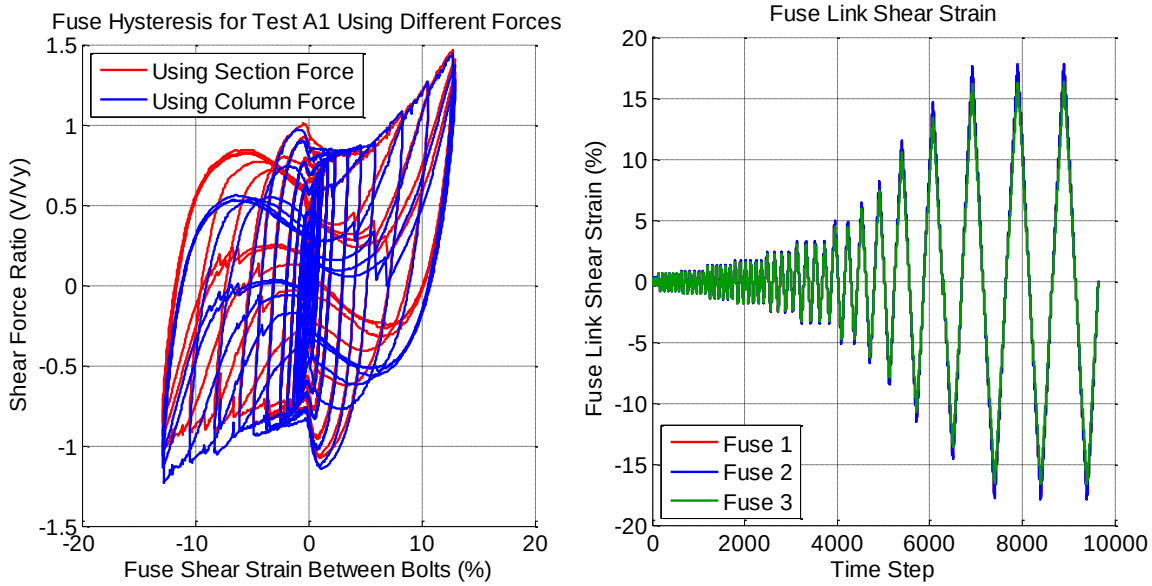

Figure D.7 Specimen A1 - Fuse Shear Force Calculated Two Ways (Left), Fuse Link Shear Strain For All Three Floors (Right)

The out-of-plane motion of the top fuse link in the fuse that was instrumented with Krypton LEDs is shown in Figure D.8. The fuse link is shown to be virtually planar up to step number 4800. The behavior of the fuse link changes at this point, which is evidenced in the axial strains shown on the right of Figure D.8.

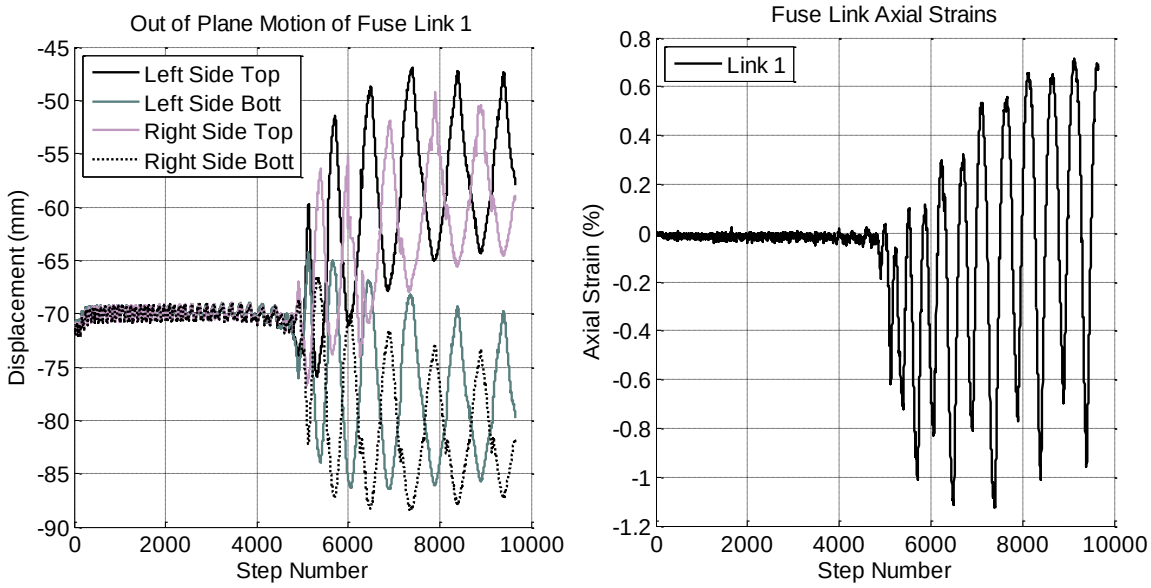

Figure D.8 Specimen A1 - Out-of-Plane Motion of Fuse Link Using Krypton (Left) and Axial Strain in the Top Fuse Link of the Lowermost Fuse (Right)

D.1.4 Motion of the System

The interstory drift ratios for all three floors are shown in Figure D.9. The interstory drifts are shown to be nearly equal to each other and to the roof drift ratio. The displacement of the controlled rocking frame is close to rigid body rotation and deformations in the frame are small in comparison. This point is further supported by the uplift ratio which is shown in Figure D.10 to closely match the roof drift ratio.

The drift ratio for each floor relative to the bearing point is shown in Figure D.9. Although the 2nd floor and LBCB exhibit drift ratios that are almost equal to the 3rd floor (roof drift) ratio, the first floor and ground floor show some deviation. The deviation in drift at the ground floor and 1st floor is due to sliding at the base of the frames.

The measured amount of pin hole tolerance at the pin load cells is shown in Figure D.10. The calculation for this quantity is given in Appendix C and consists of extrapolating the horizontal drift of the frame up to the height of the pin load cells and subtracting the amount of LBCB horizontal drift. The movement at zero roof drift is approximately 6mm which corresponds to 3mm of hole tolerance in each ply.

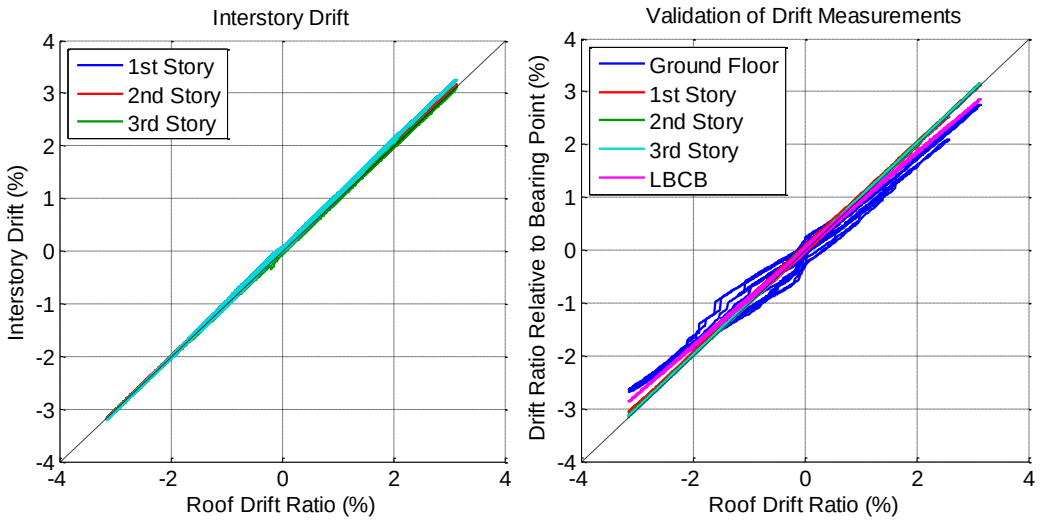

Figure D.9 Specimen A1 - Interstory Drifts (Left) and Drift Ratios Relative to Base (Right)

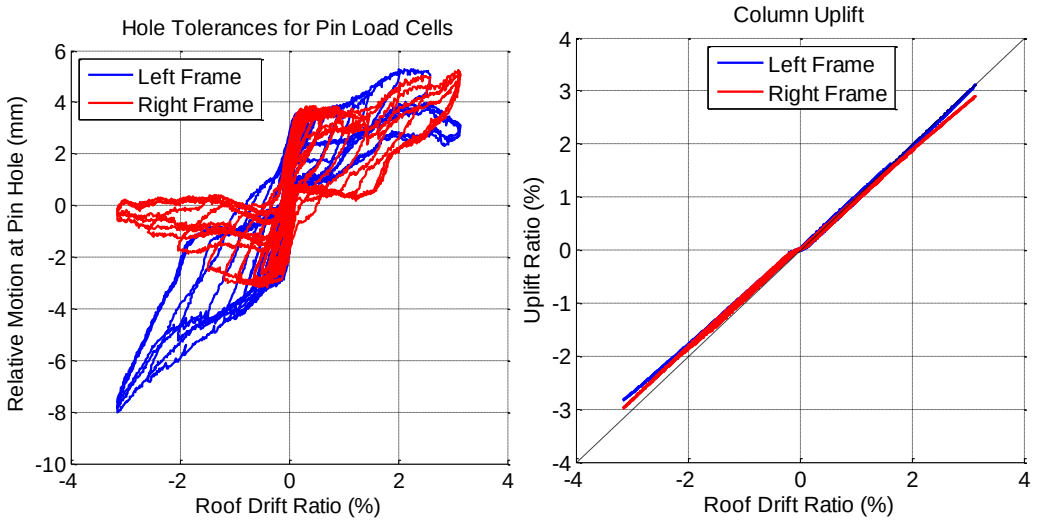

Figure D.10 Specimen A1 - Pin Hole Tolerances for the Pin Load Cells (Left), and Uplift Ratio (Right)

D.1.5 Member Resultants

The resultant axial force, shear force, minor axis moment, and major axis moment were calculated for each strain-gaged member using the calculations described in Appendix C. The resulting member forces are given in Figure D.11, Figure D.12, Figure D.13, Figure D.14, Figure D.15, Figure D.16, Figure D.17, and Figure D.18.

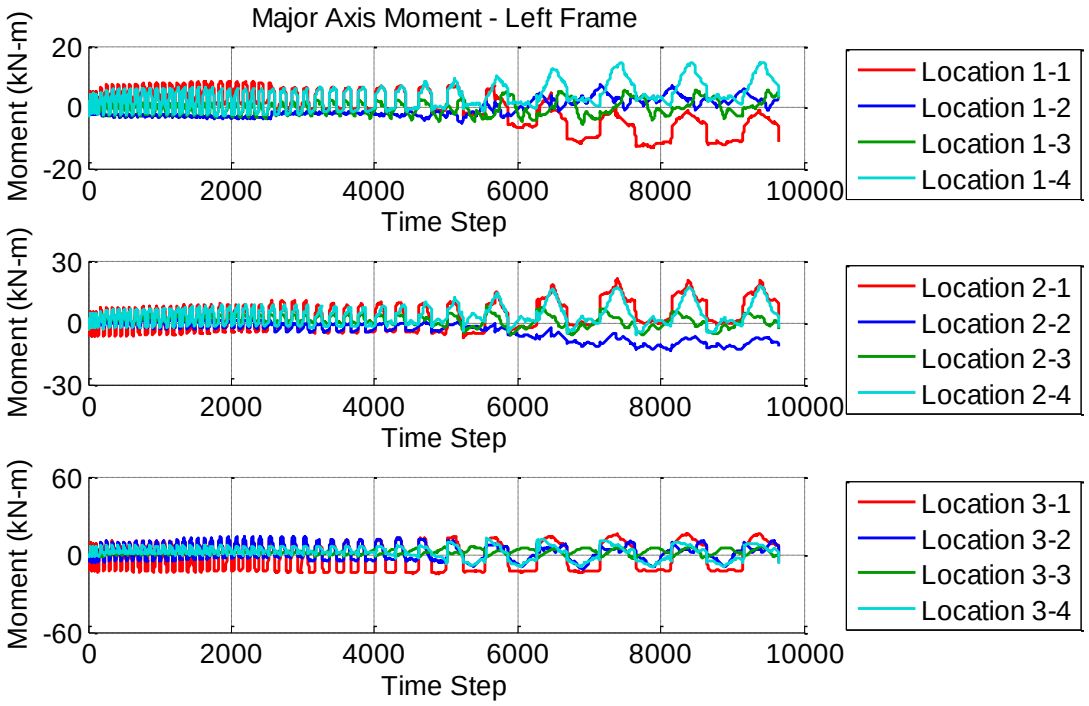

Figure D.11 Specimen A1 - Calculated Member Resultant Forces

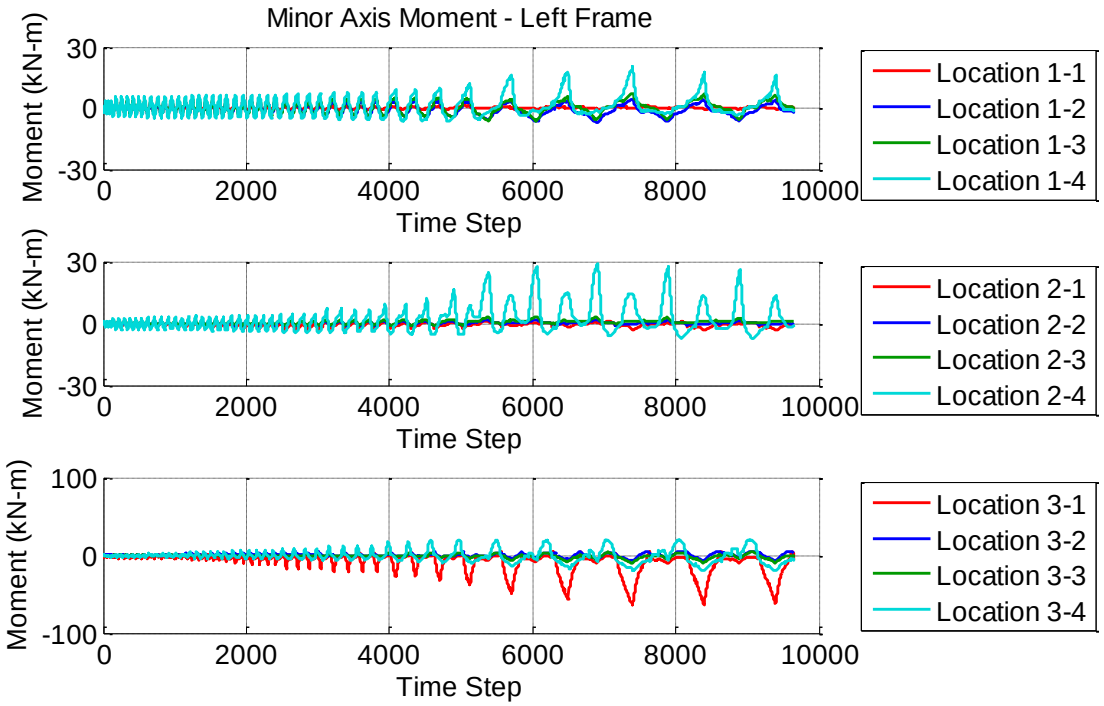

Figure D.12 Specimen A1 - Calculated Member Resultant Forces

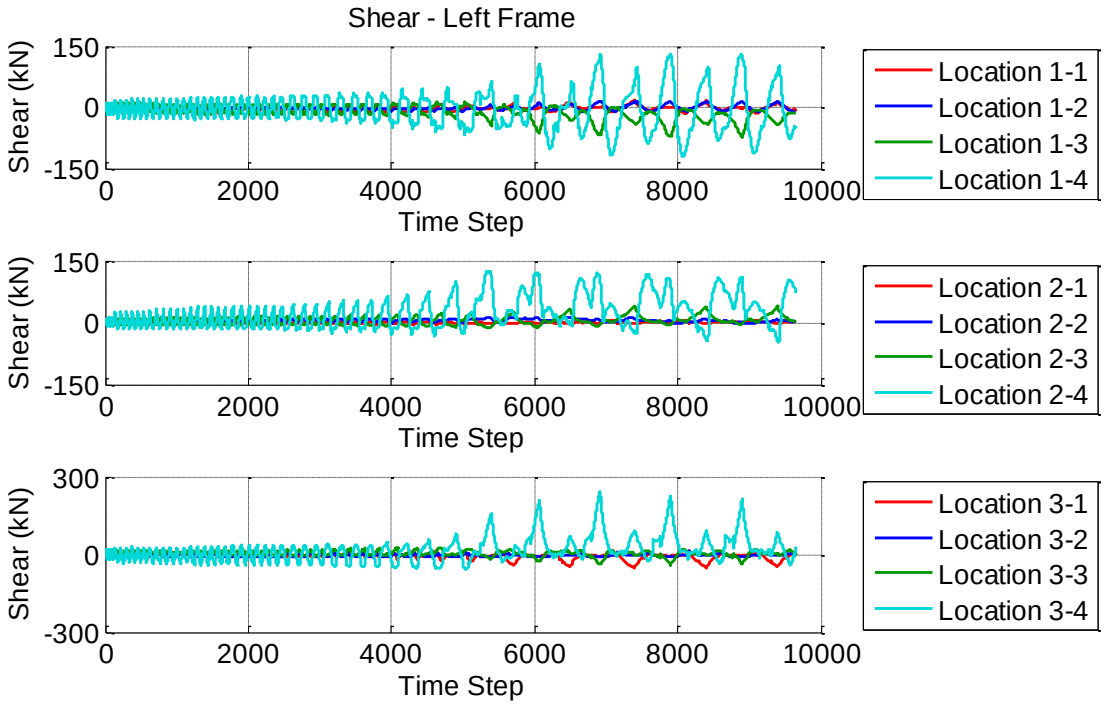

Figure D.13 Specimen A1 - Calculated Member Resultant Forces

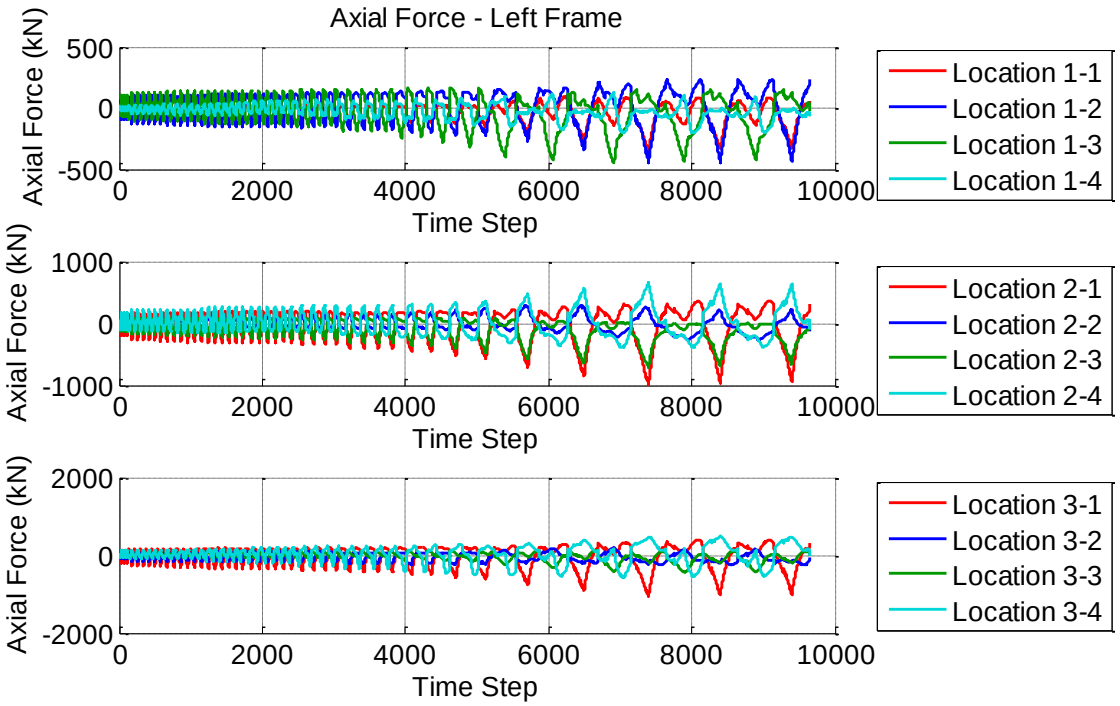

Figure D.14 Specimen A1 - Calculated Member Resultant Forces

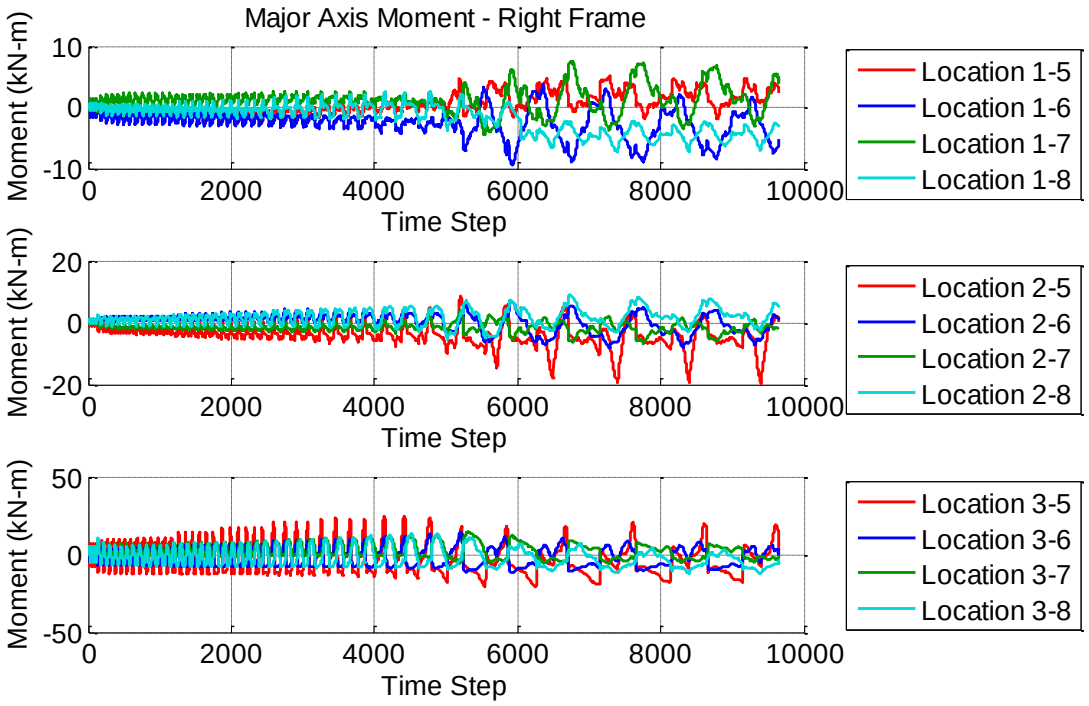

Figure D.15 Specimen A1 - Calculated Member Resultant Forces

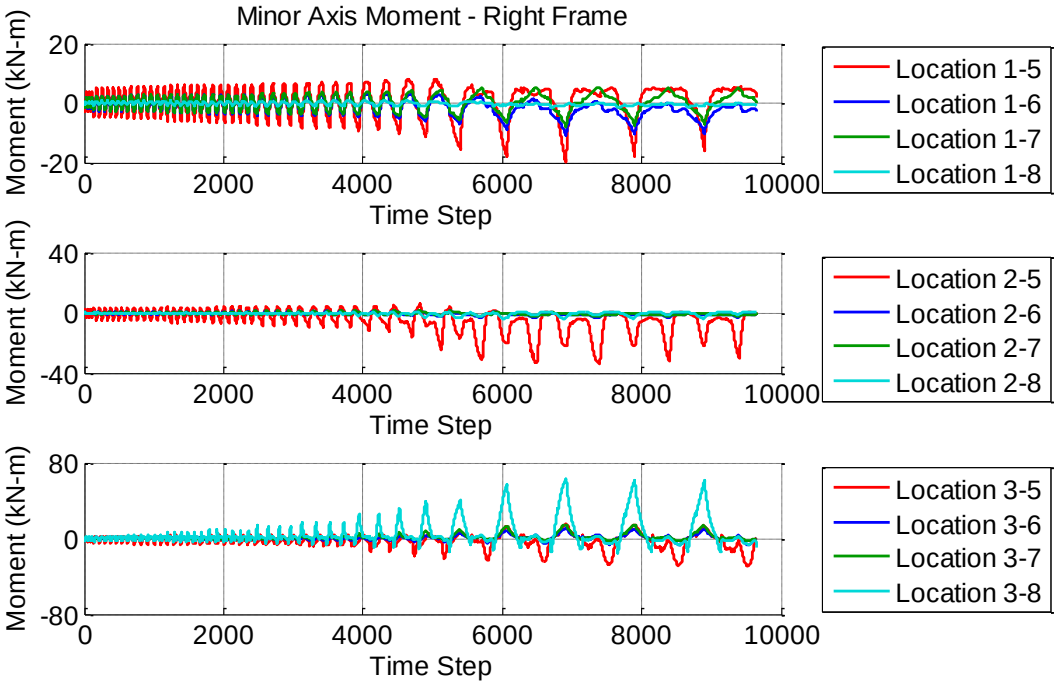

Figure D.16 Specimen A1 - Calculated Member Resultant Forces

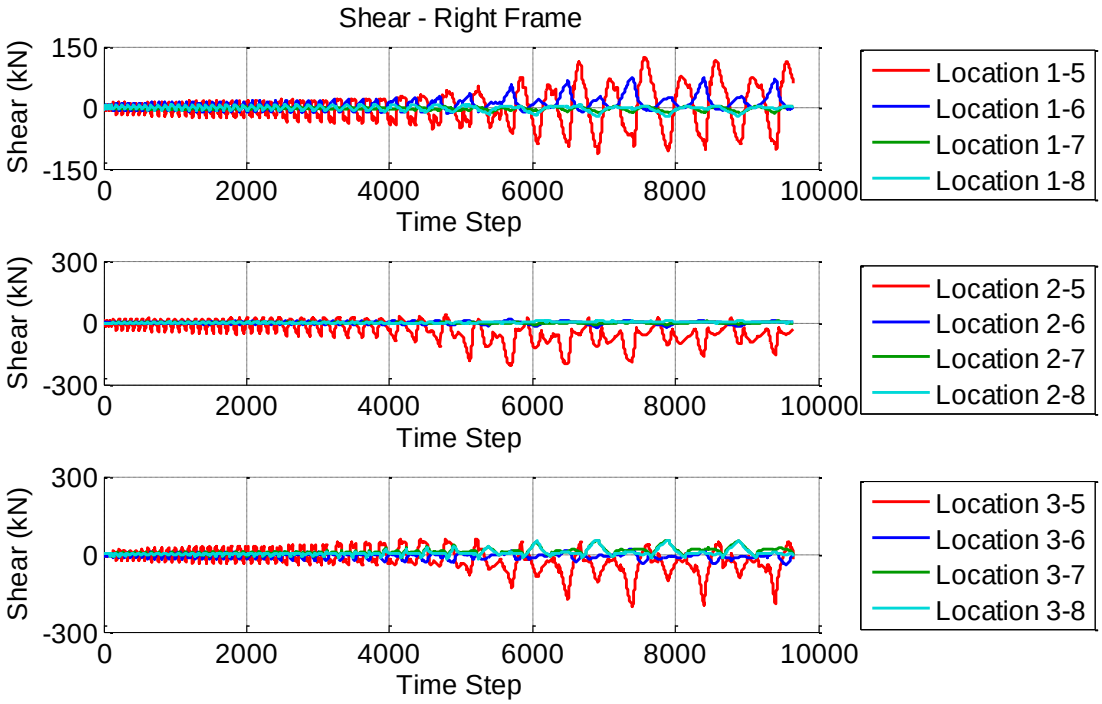

Figure D.17 Specimen A1 - Calculated Member Resultant Forces

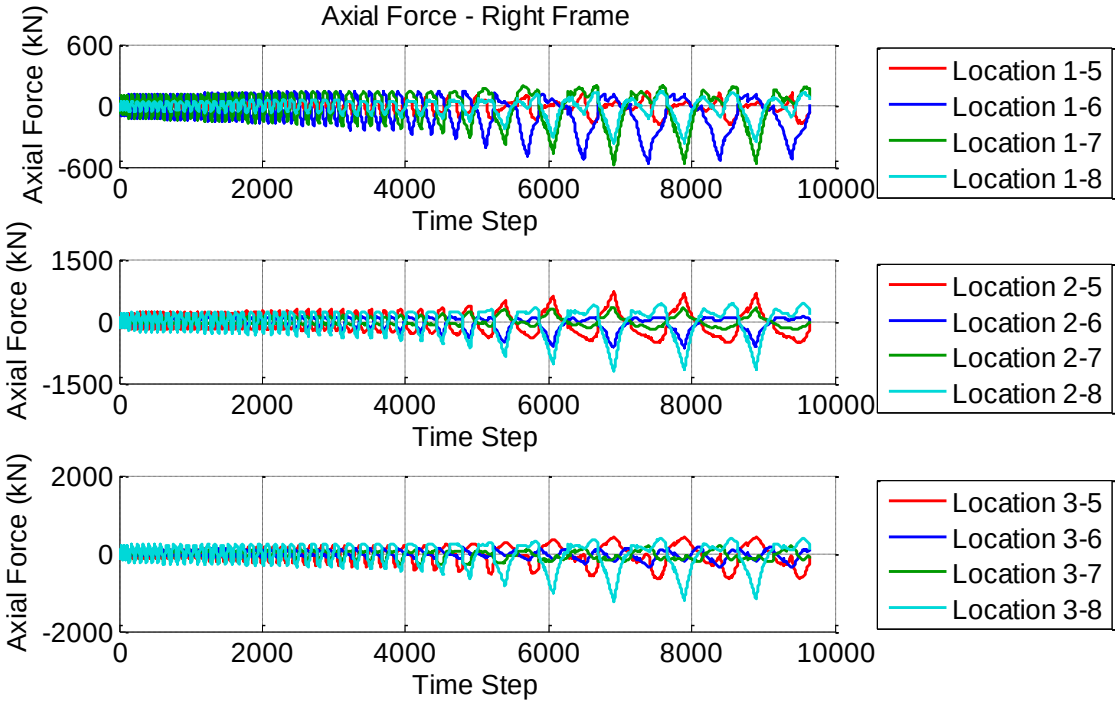

Figure D.18 Specimen A1 - Calculated Member Resultant Forces

D.1.6 Sum of the Forces at Each Section

The resultant forces for the entire frame were calculated using the member forces reported in the previous section. The calculations are given in Appendix C. Figure D.19 shows the total shear force across both frames. It is shown that the total shear forces for all three strain-gaged sections match each other and the horizontal pin load cell force and the horizontal LBCB force. This point is further demonstrated in Figure D.20. Figure D.21 shows the total vertical force resultant for both frames compared for all three strain-gaged sections along with the pin load cells and LBCB.

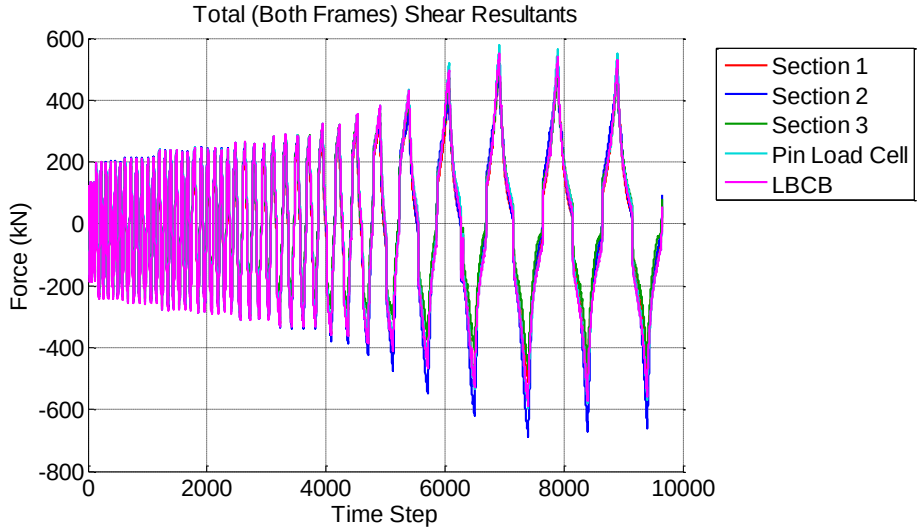

Figure D.19 Specimen A1 - Sum of the Shear Forces

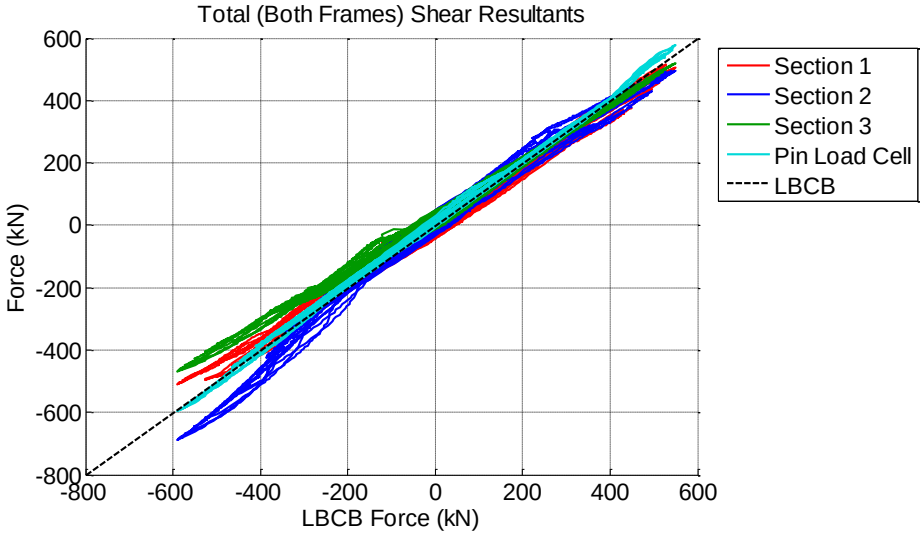

Figure D.20 Specimen A1 - Validation of Shear Forces Calculated From Strain-Gaged Sections

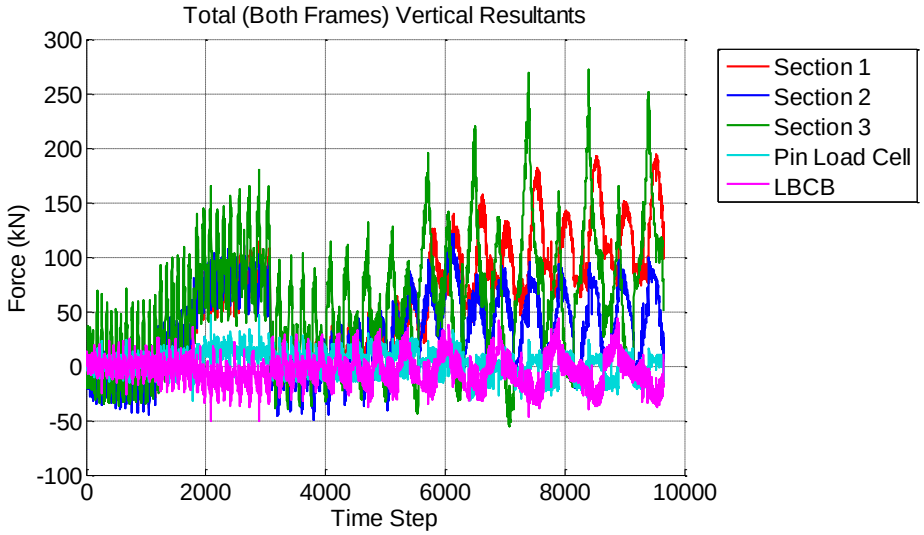

Figure D.21 Specimen A1 - Vertical Forces Calculated From Strain-Gaged Sections

D.2 Specimen A2

Note on Data Reduction:

- The same offsets for post-tension load cell forces from Specimen A1 were used for this specimen.

D.2.1 System Response

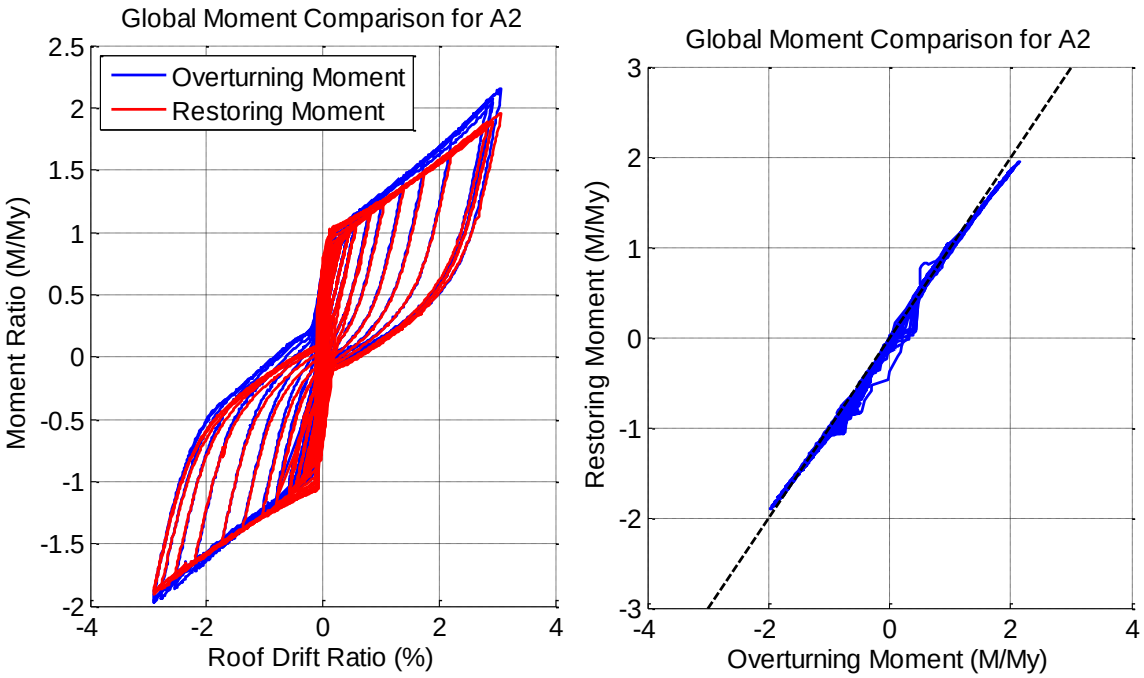

Figure D.22 Specimen A2 - Comparing Restoring Moment to Applied Overturning Moment

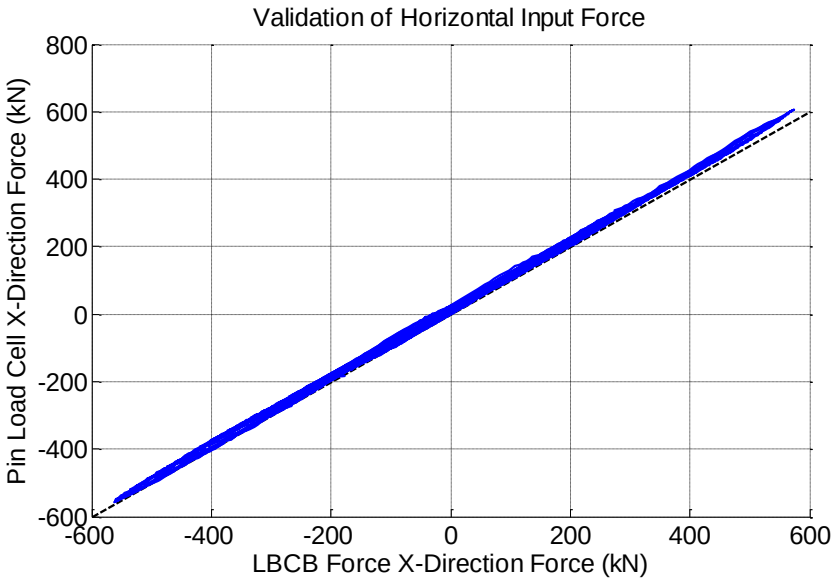

Figure D.23 Specimen A2 - Validation of Horizontal Forces Applied to the Frames

D.2.2 Post-Tensioning Force Validation

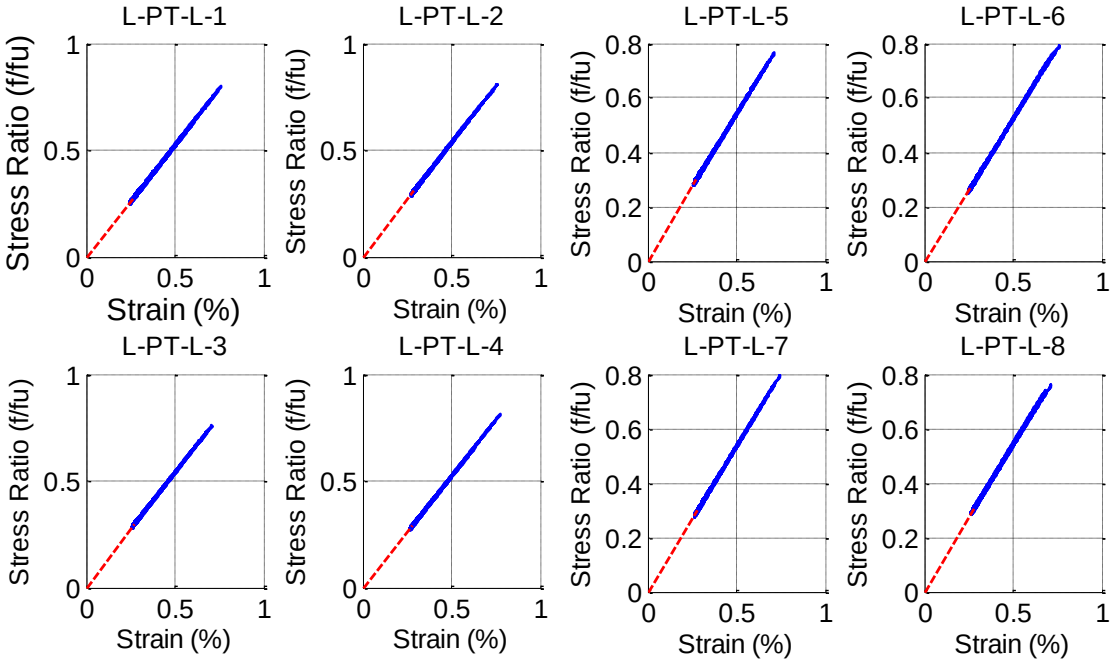

Figure D.24 Specimen A2 - Post-Tensioning Stress-Strain Response

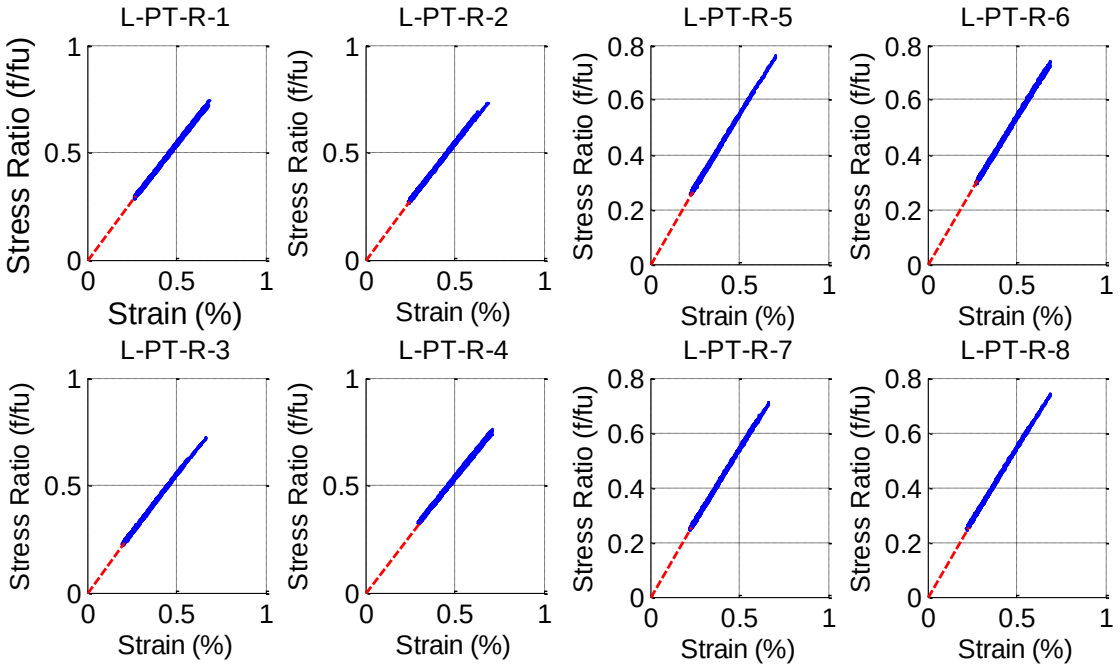

Figure D.25 Specimen A2 - Post-Tensioning Stress-Strain Response

Anchor rod forces for the right frame were calculated without gage 6b which may cause the forked response in the sum of the right frame anchor rods shown in Figure D.26.

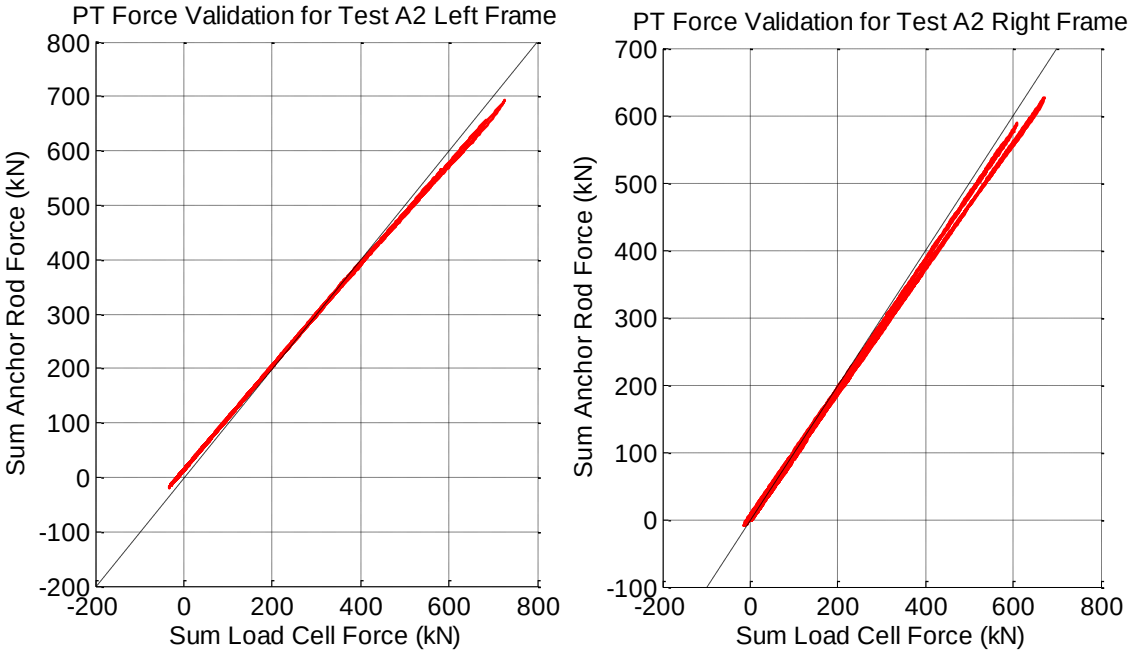

Figure D.26 Specimen A2 - Validation of Post-Tensioning Forces

D.2.3 Motion of the System

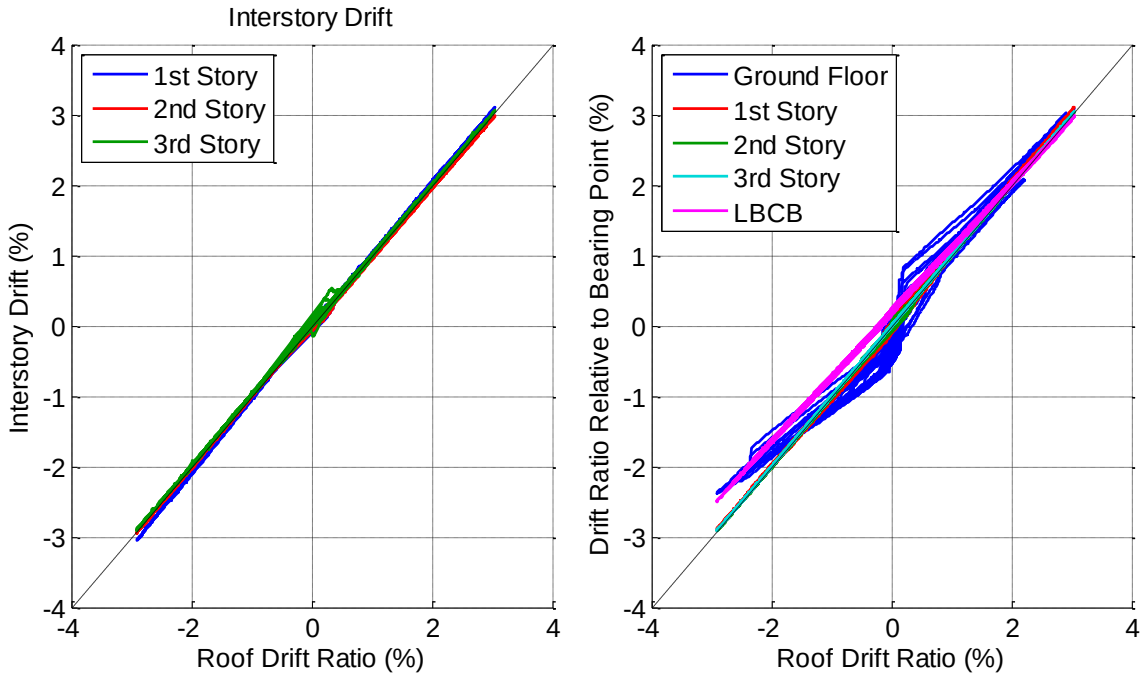

Figure D.27 Specimen A2 - Interstory Drifts (Left) and Drift Ratios Relative to Base (Right)

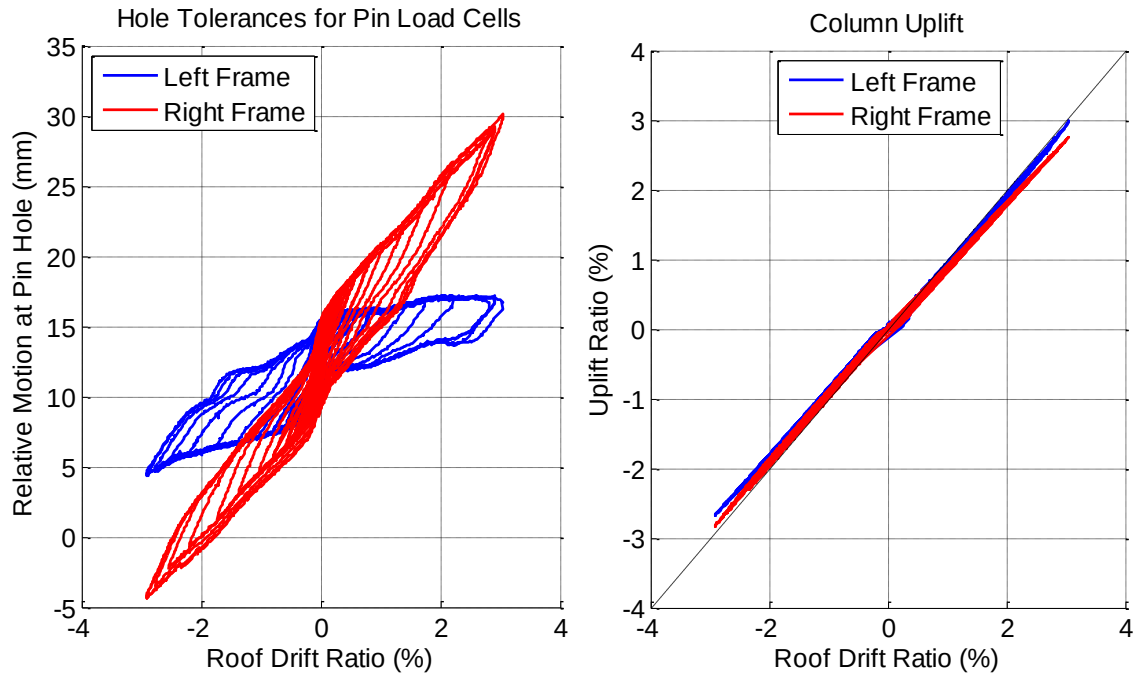

Figure D.28 Specimen A2 - Pin Hole Tolerances for the Pin Load Cells (Left), and Uplift Ratio (Right)

D.2.4 Member Resultants

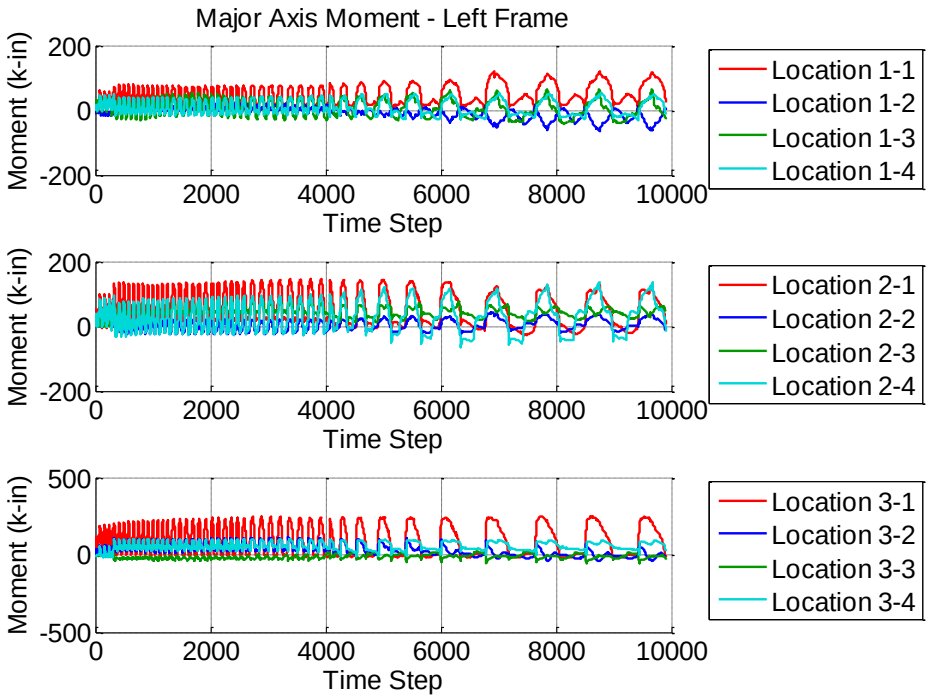

Figure D.29 Specimen A2 - Calculated Member Resultant Forces

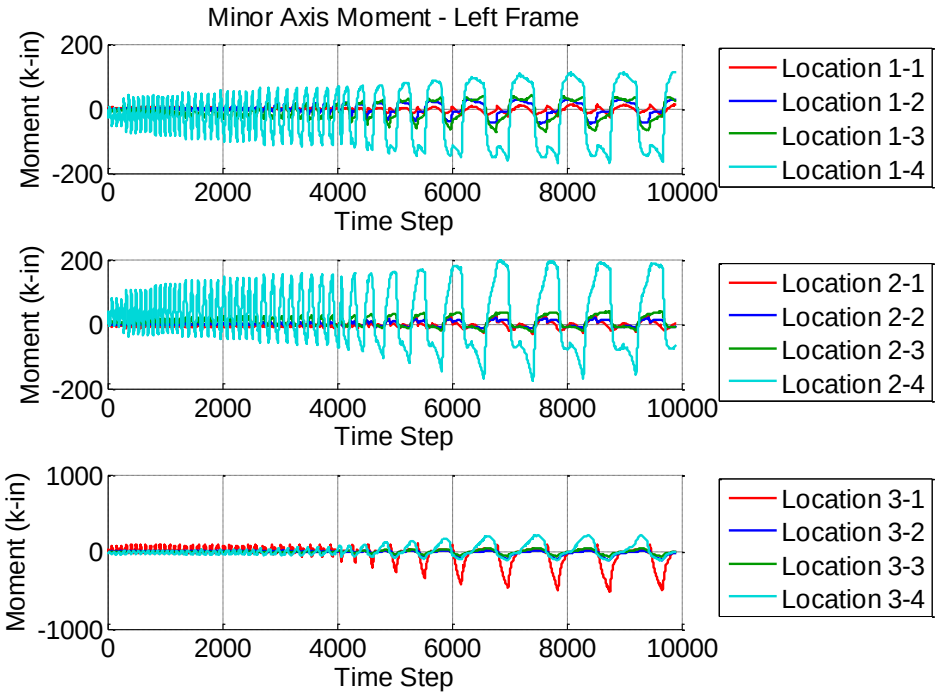

Figure D.30 Specimen A2 - Calculated Member Resultant Forces

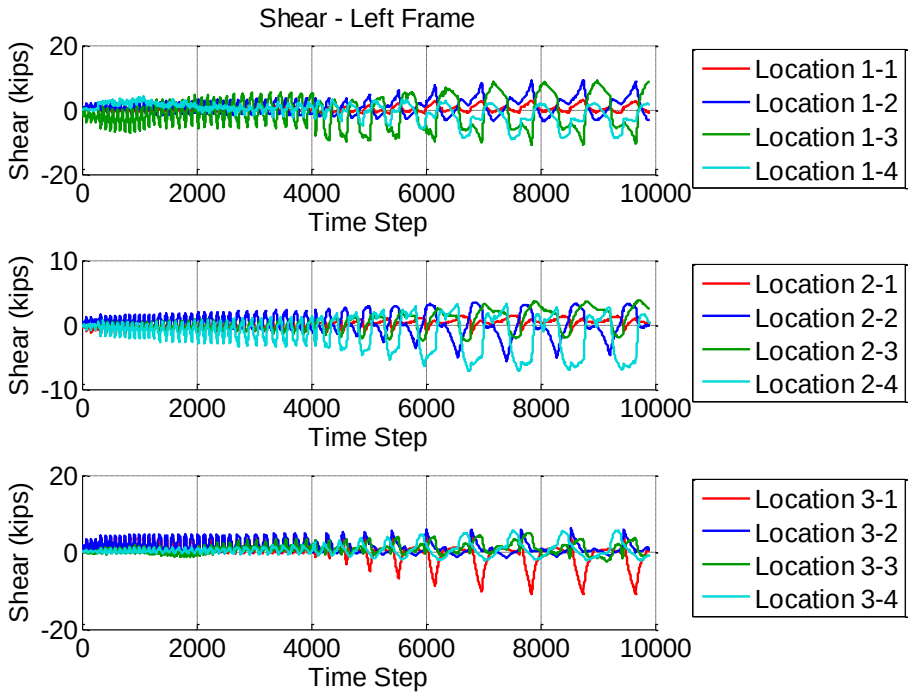

Figure D.31 Specimen A2 - Calculated Member Resultant Forces

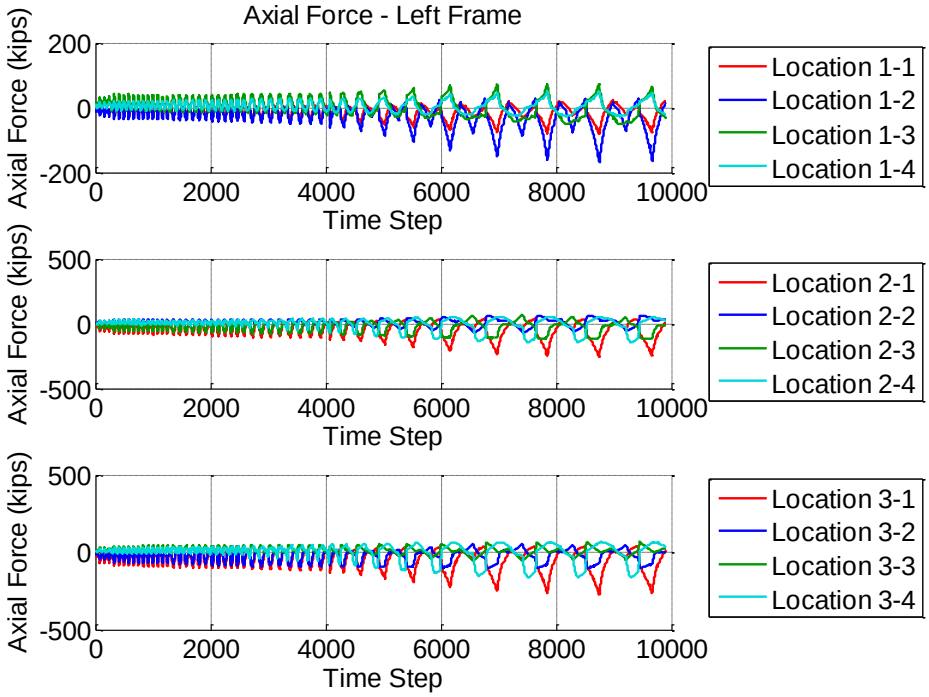

Figure D.32 Specimen A2 - Calculated Member Resultant Forces

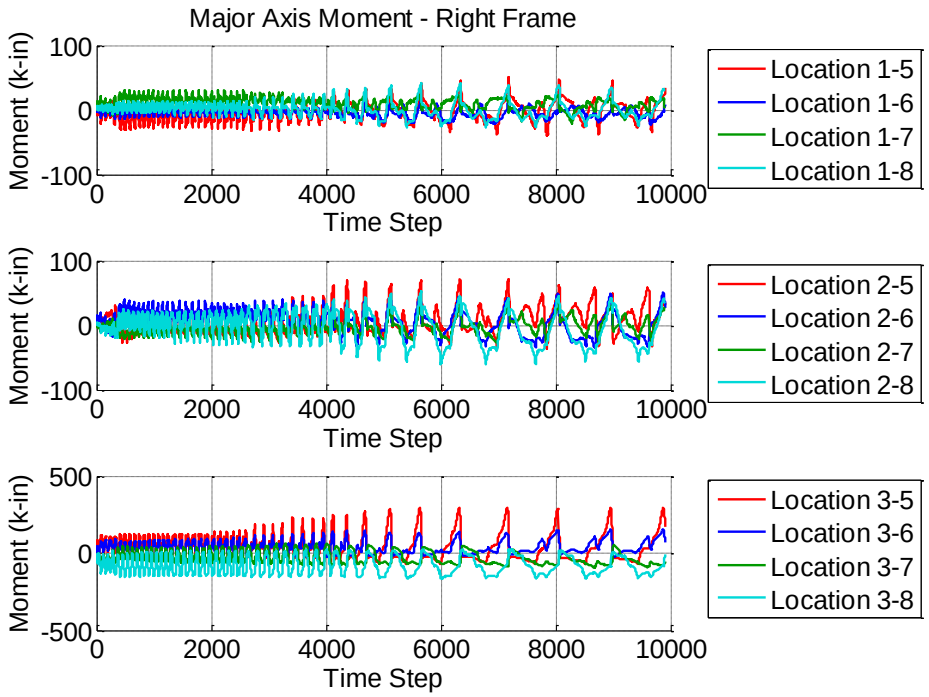

Figure D.33 Specimen A2 - Calculated Member Resultant Forces

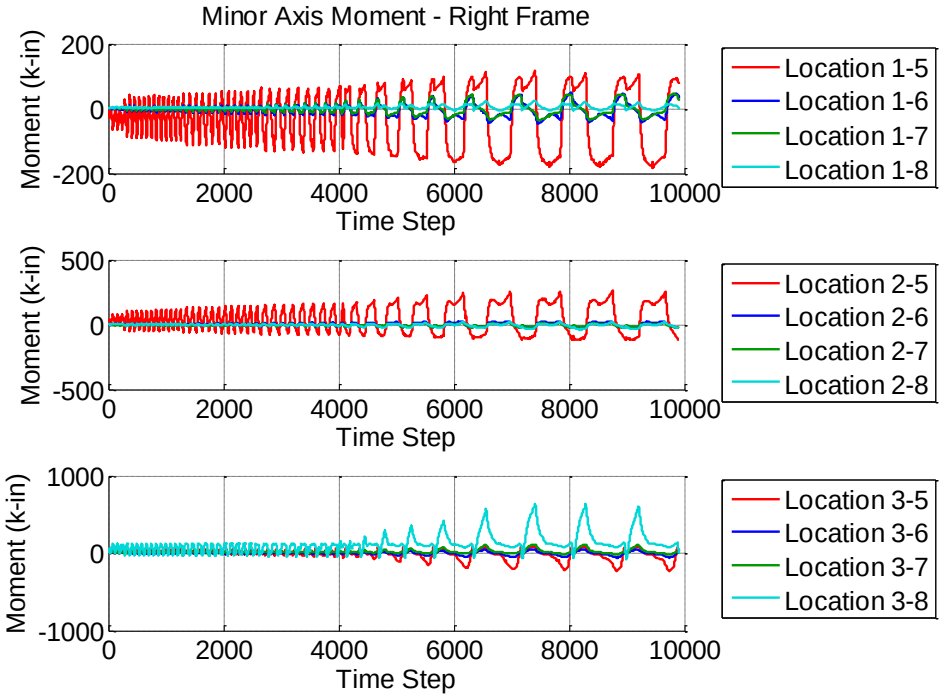

Figure D.34 Specimen A2 - Calculated Member Resultant Forces

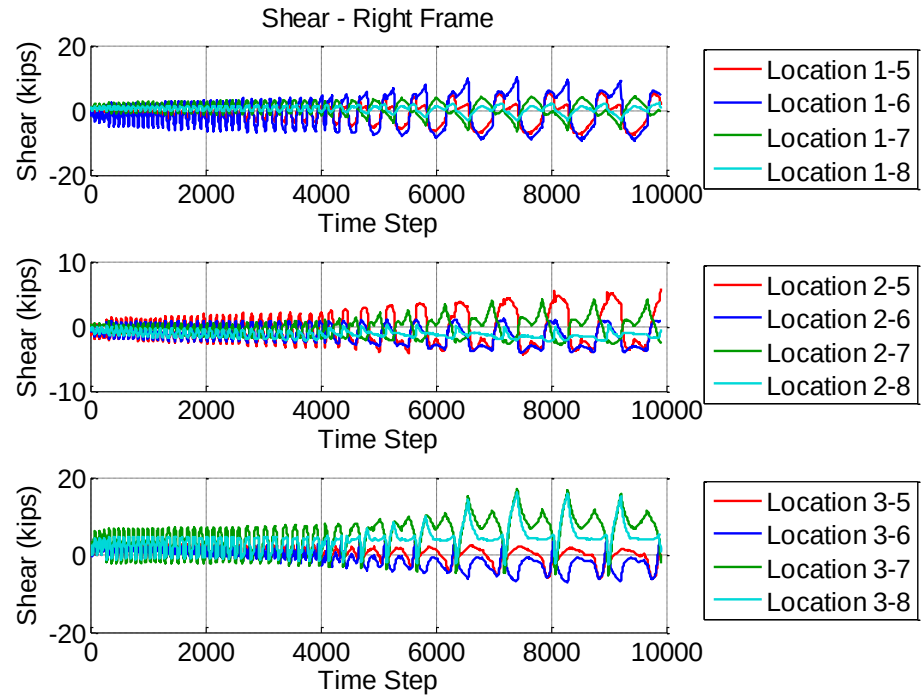

Figure D.35 Specimen A2 - Calculated Member Resultant Forces

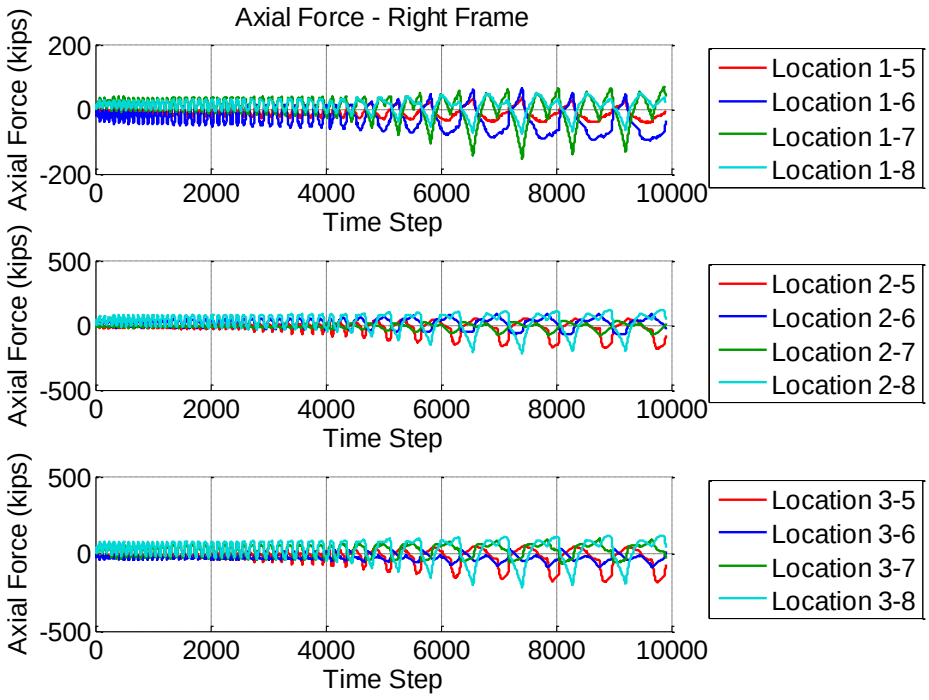

Figure D.36 Specimen A2 - Calculated Member Resultant Forces

D.2.5 Sum Forces at Each Section

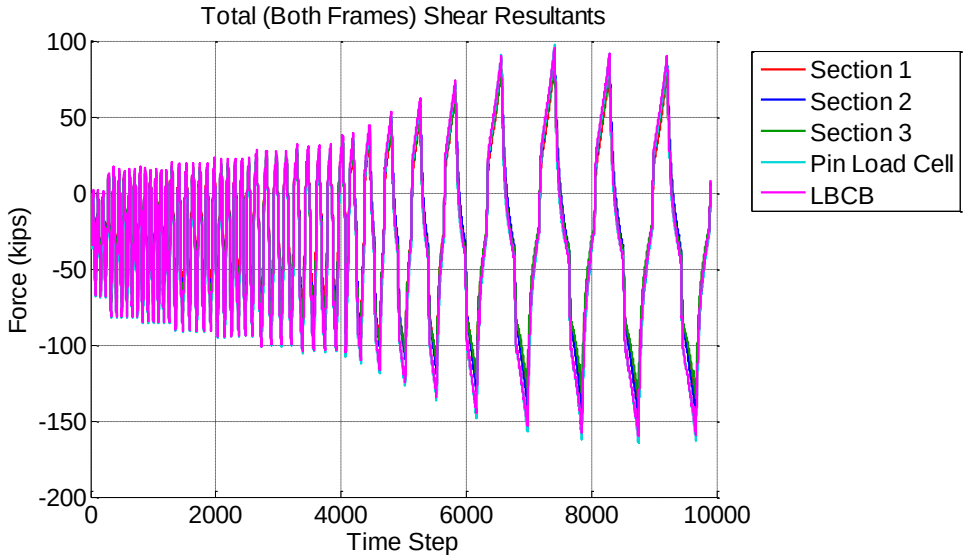

Figure D.37 Specimen A2 - Sum of the Shear Forces

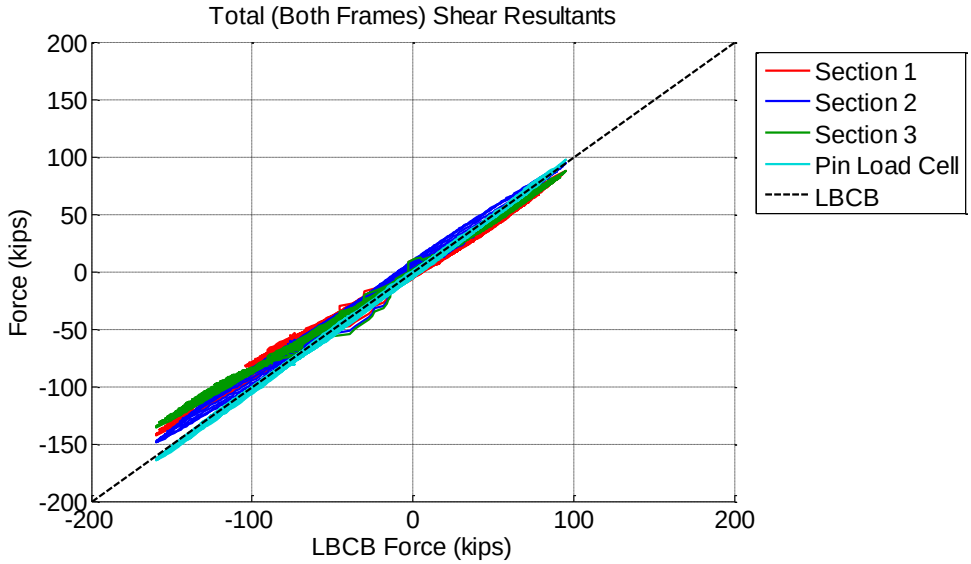

Figure D.38 Specimen A2 - Validation of Shear Forces Calculated From Strain-Gaged Sections

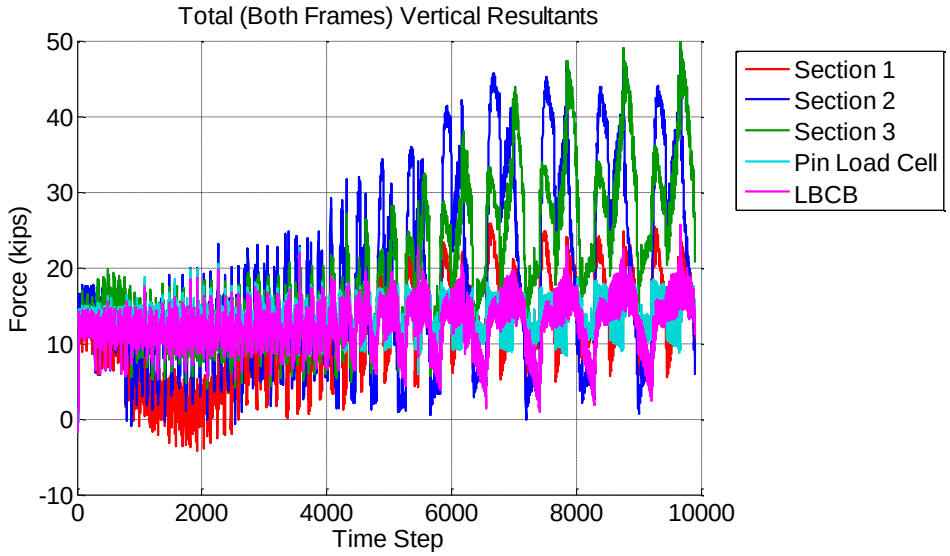

Figure D.39 Specimen A2 - Vertical Forces Calculated From Strain-Gaged Sections

D.3 Specimen A3

Notes on Data Reduction:

- The same offsets for post-tension load cell forces from Specimen A1 were used for this specimen.

D.3.1 System Response

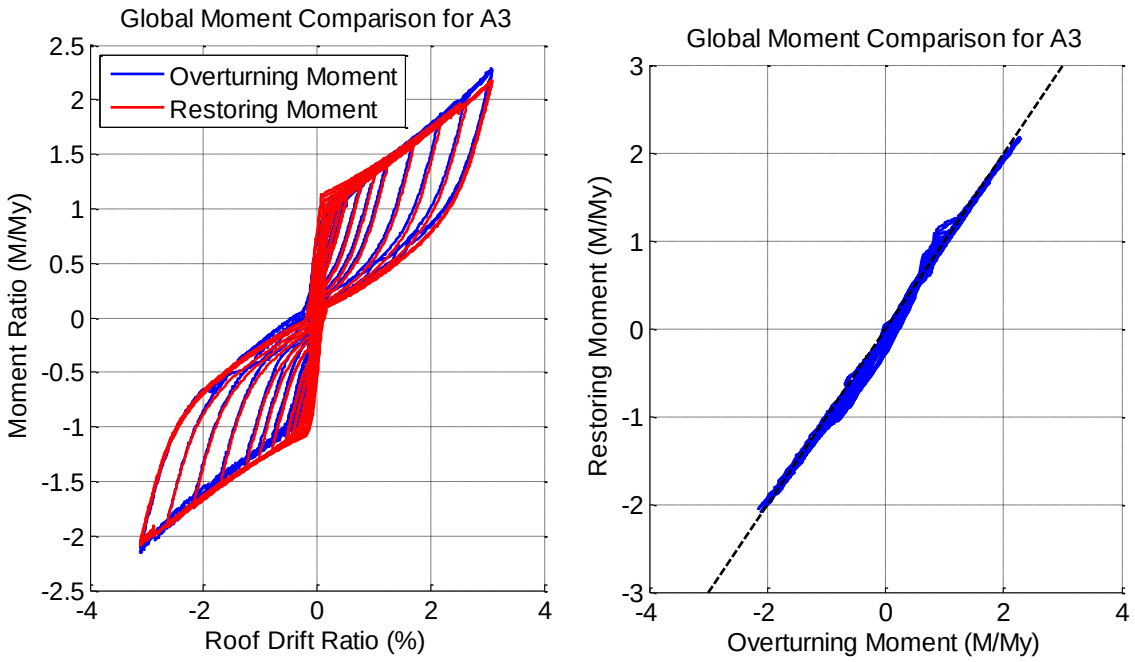

Figure D.40 Specimen A3 - Comparing Restoring Moment to Applied Overturning Moment

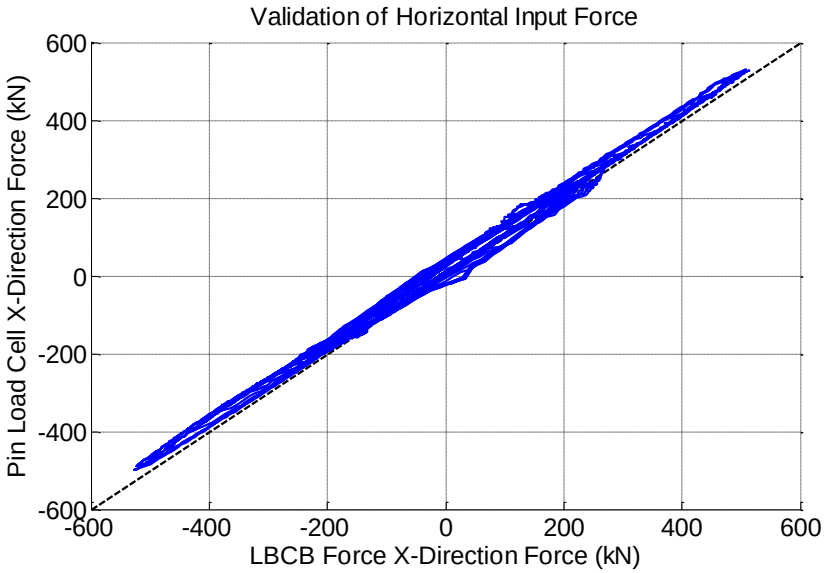

Figure D.41 Specimen A3 - Validation of Horizontal Forces Applied to the Frames

D.3.2 Post-Tensioning Force Validation

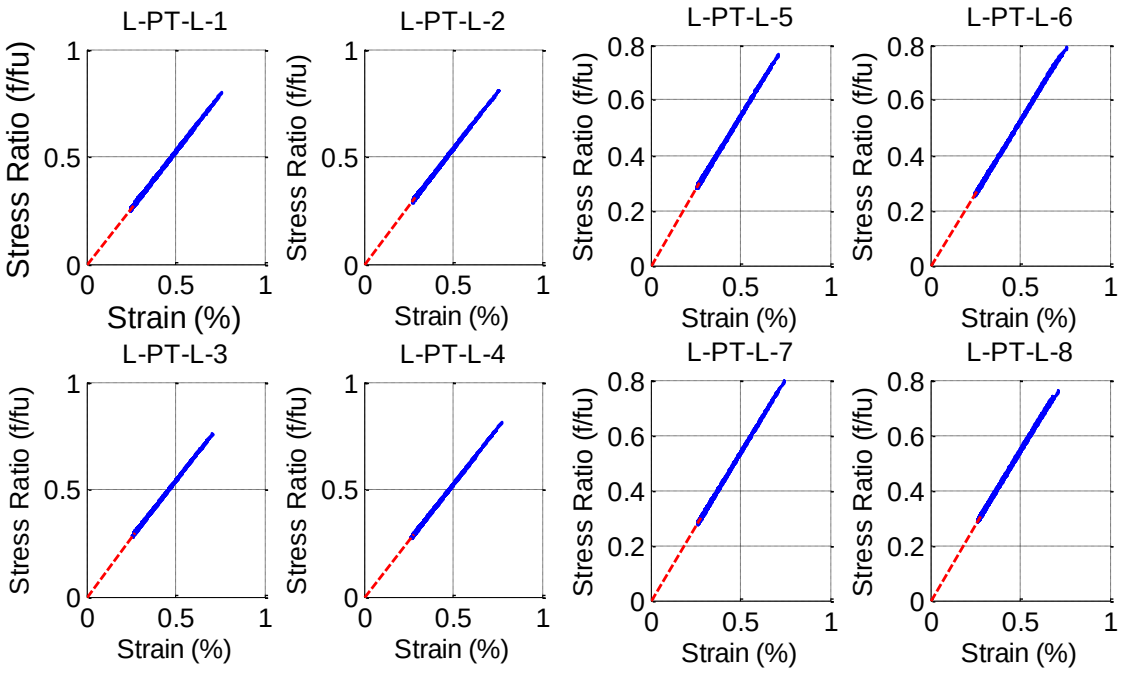

Figure D.42 Specimen A3 - Post-Tensioning Stress-Strain Response

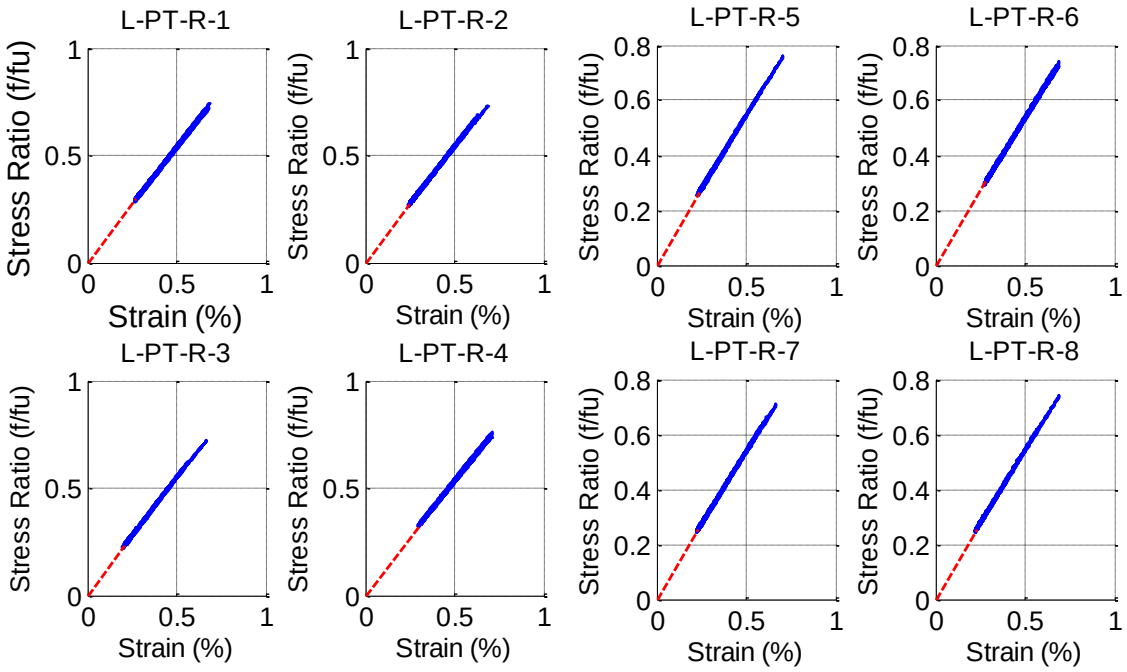

Figure D.43 Specimen A3 - Post-Tensioning Stress-Strain Response

Anchor rod force for the right frame was calculated without gage 6b which may cause the forked response in the sum of the right frame anchor rods shown in Figure D.44.

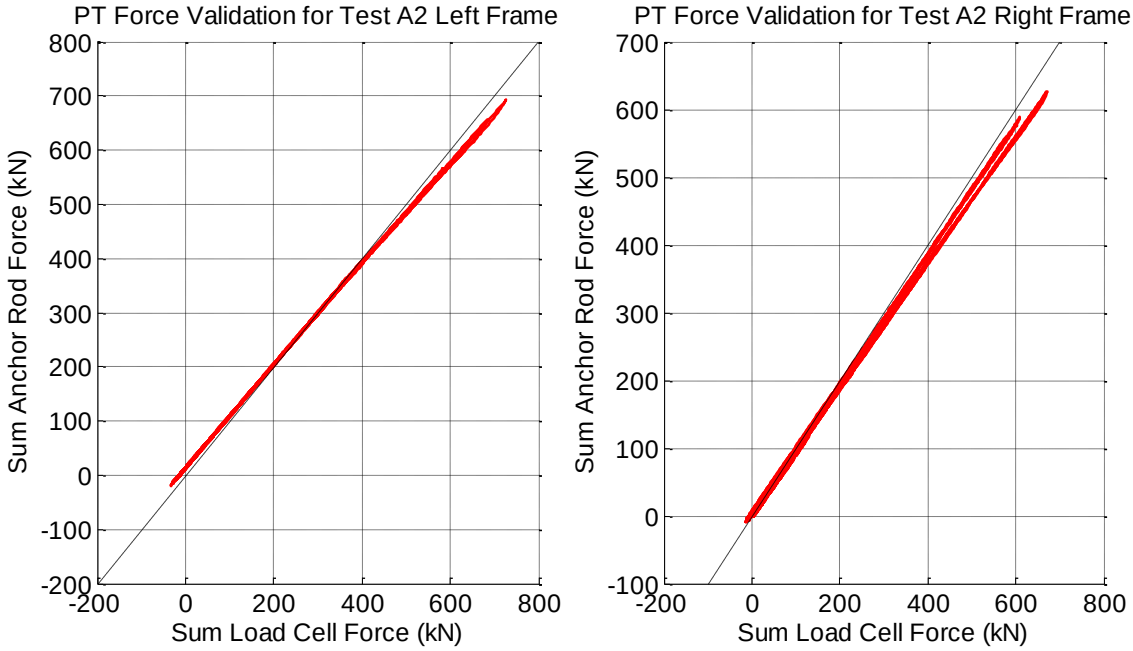

Figure D.44 Specimen A3 - Validation of Post-Tensioning Forces

D.3.3 Motion of the System

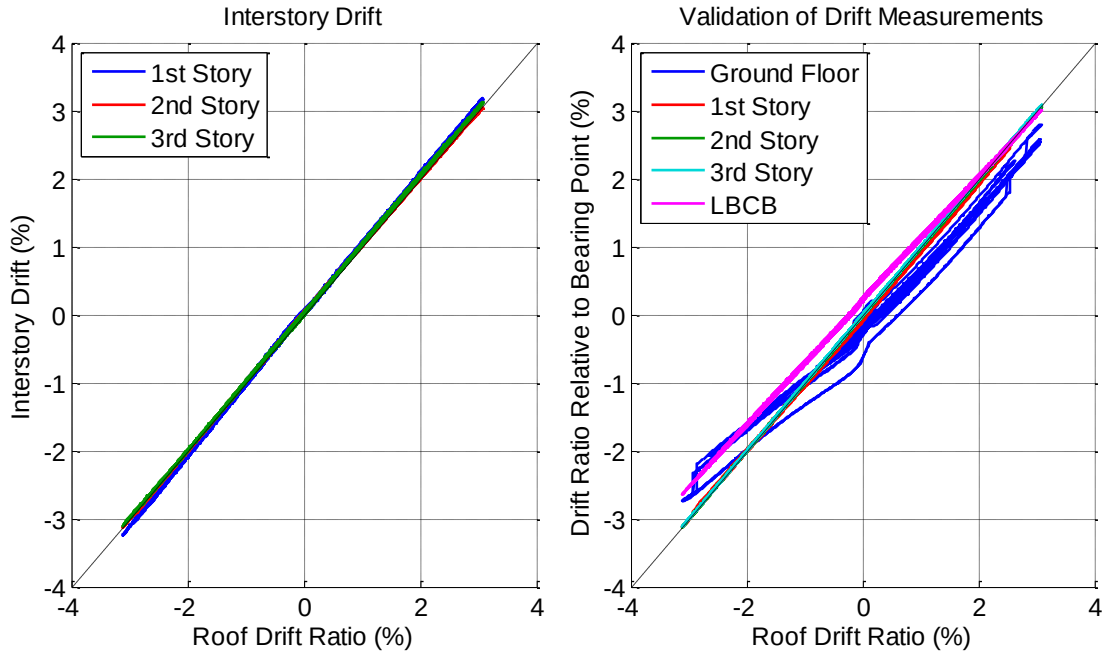

Figure D.45 Specimen A3 - Interstory Drifts (Left) and Drift Ratios Relative to Base (Right)

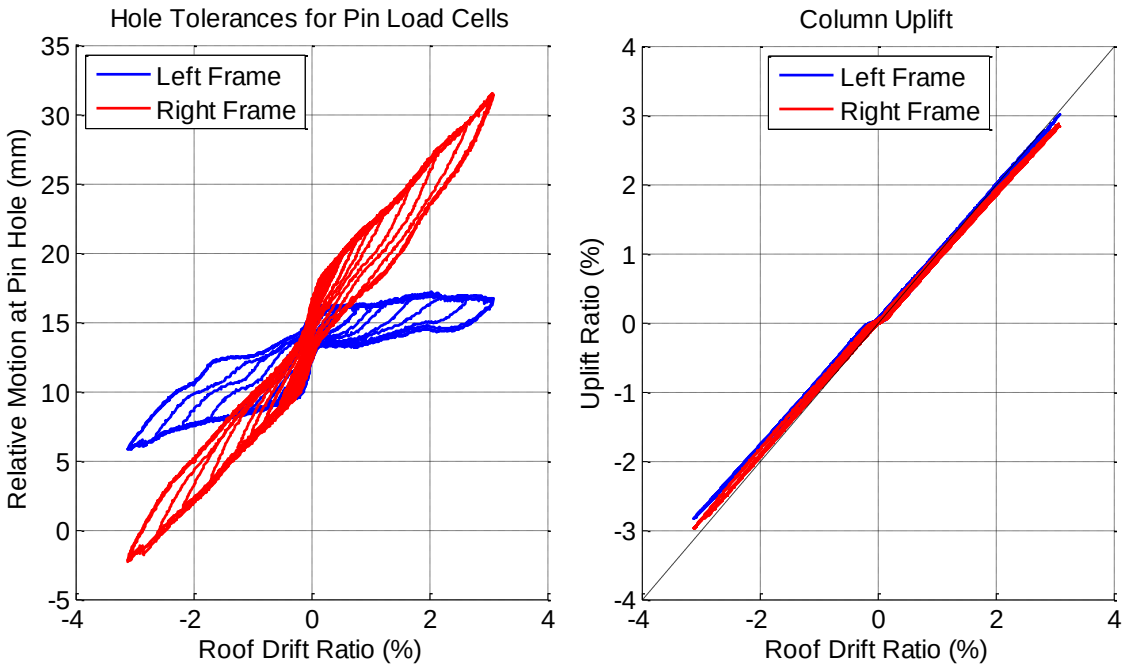

Figure D.46 Specimen A3 - Pin Hole Tolerances for the Pin Load Cells (Left), and Uplift Ratio (Right)

D.3.4 Member Resultants

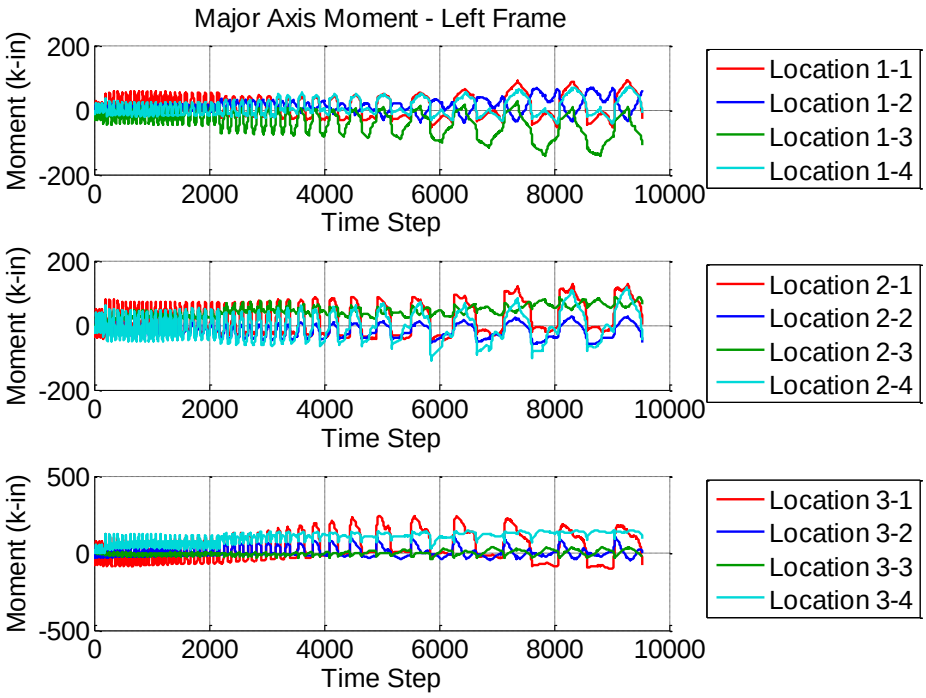

Figure D.47 Specimen A3 - Calculated Member Resultant Forces

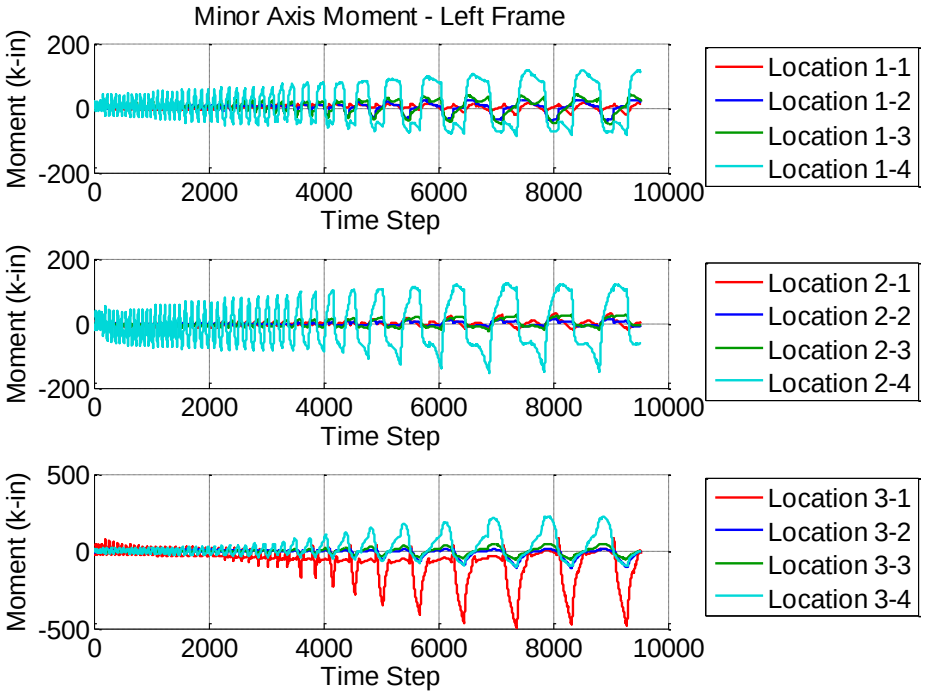

Figure D.48 Specimen A3 - Calculated Member Resultant Forces

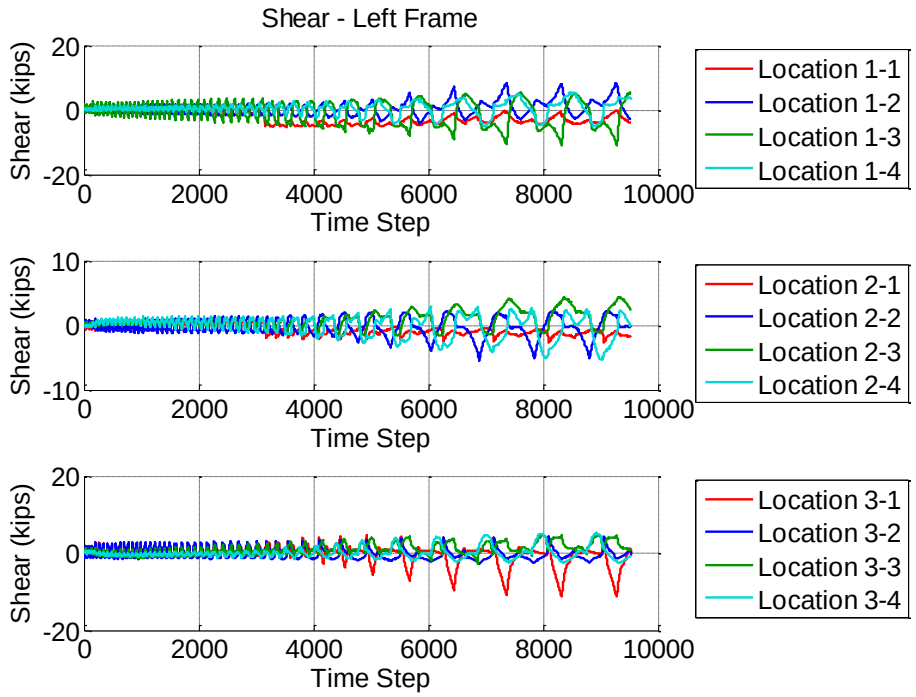

Figure D.49 Specimen A3 - Calculated Member Resultant Forces

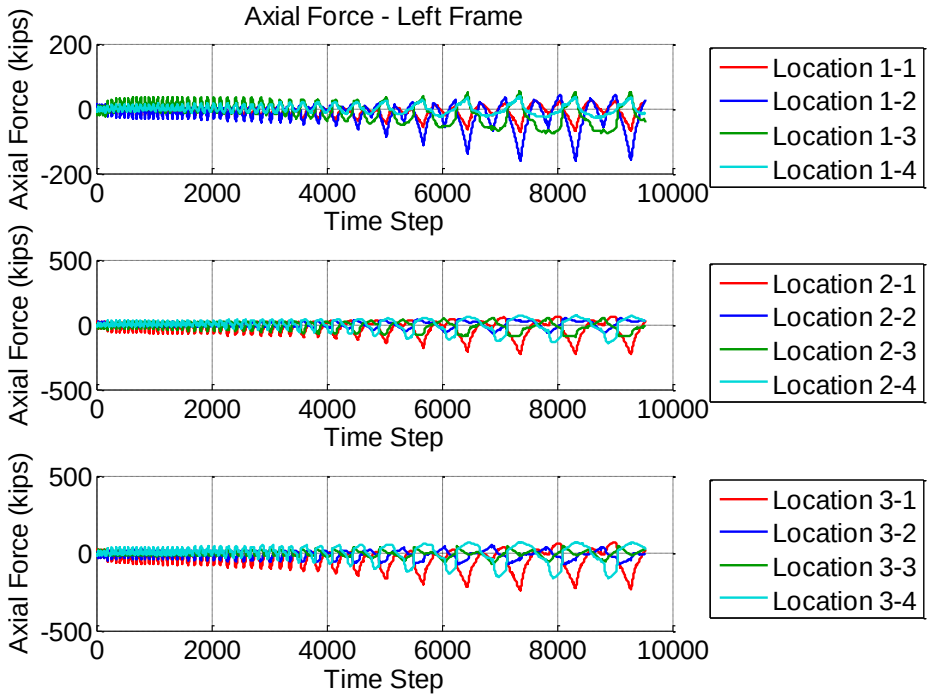

Figure D.50 Specimen A3 - Calculated Member Resultant Forces

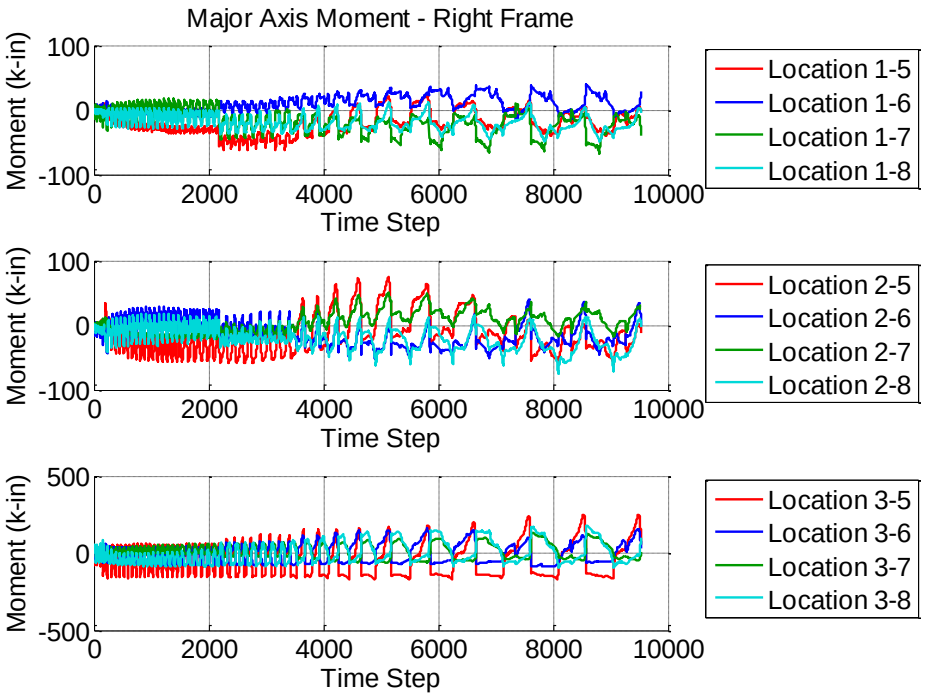

Figure D.51 Specimen A3 - Calculated Member Resultant Forces

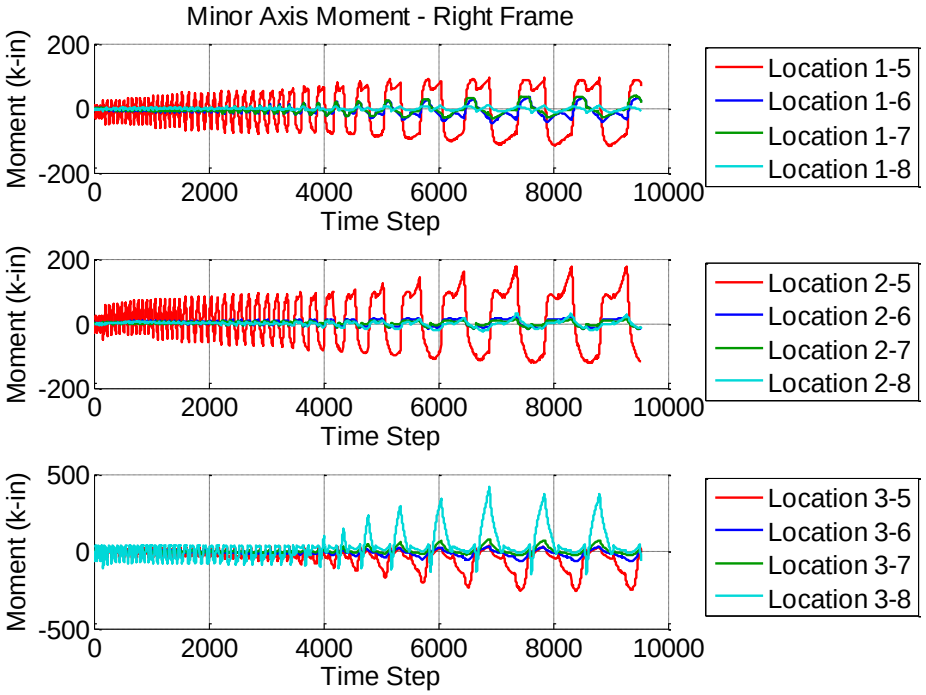

Figure D.52 Specimen A3 - Calculated Member Resultant Forces

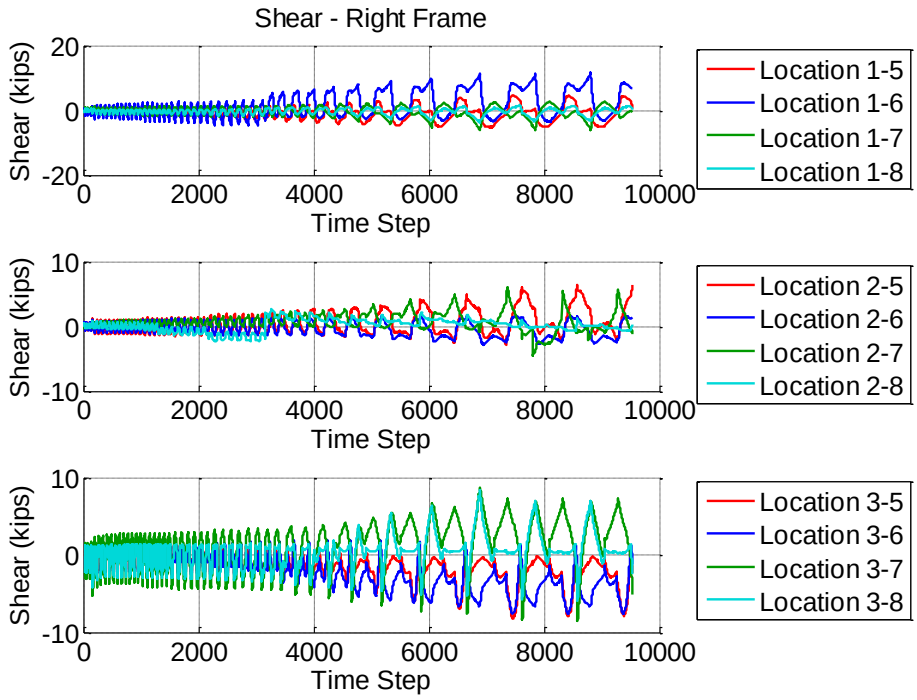

Figure D.53 Specimen A3 - Calculated Member Resultant Forces

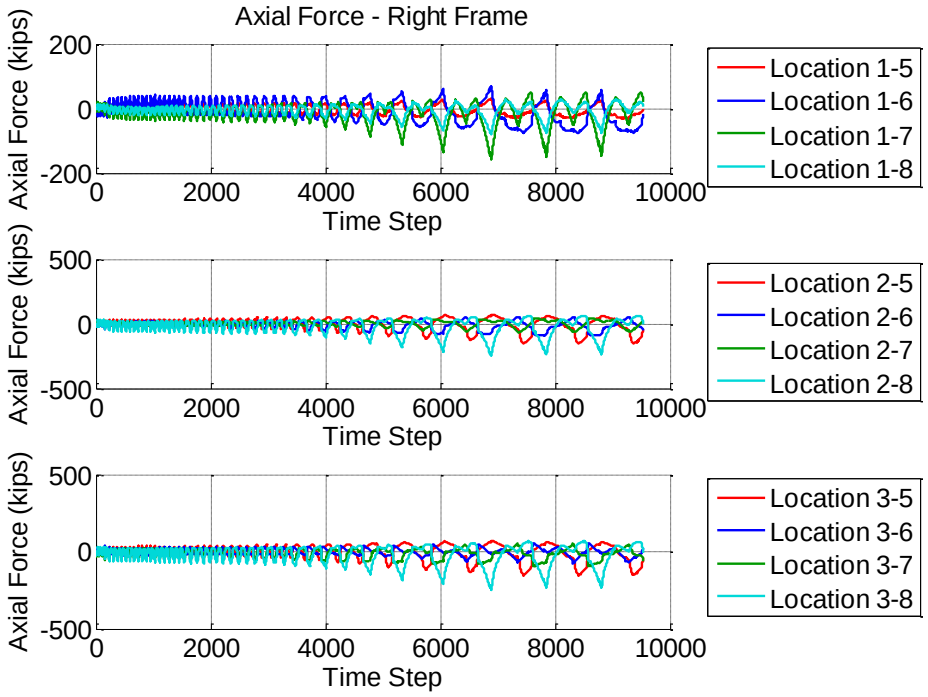

Figure D.54 Specimen A3 - Calculated Member Resultant Forces

D.3.5 Sum Forces at Each Section

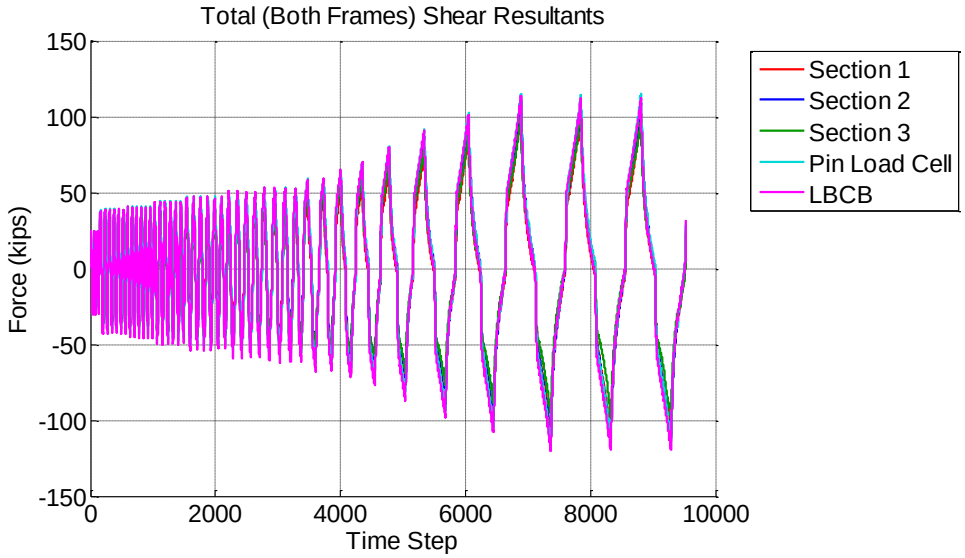

Figure D.55 Specimen A3 - Sum of the Shear Forces

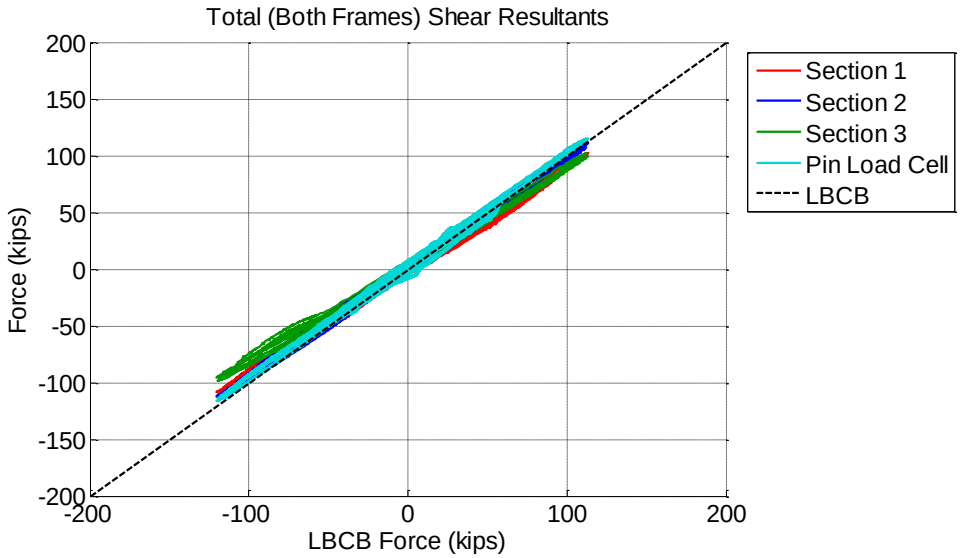

Figure D.56 Specimen A3 - Validation of Shear Forces Calculated From Strain-Gaged Sections

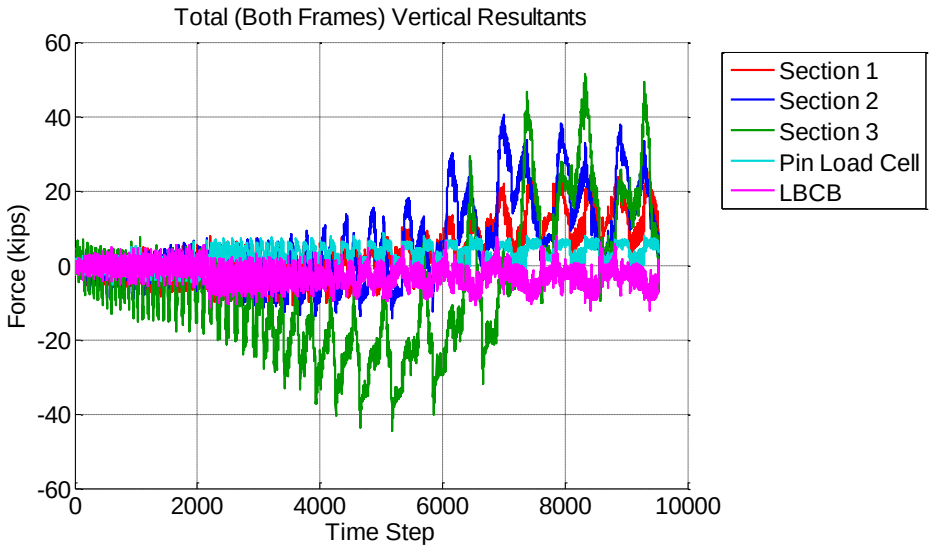

Figure D.57 Specimen A3 - Vertical Forces Calculated From Strain-Gaged Sections

D.4 Specimen A4

Notes on Data Reduction

- The same offsets for post-tension load cell forces from Specimen A1 were used for this specimen.

D.4.1 System Response

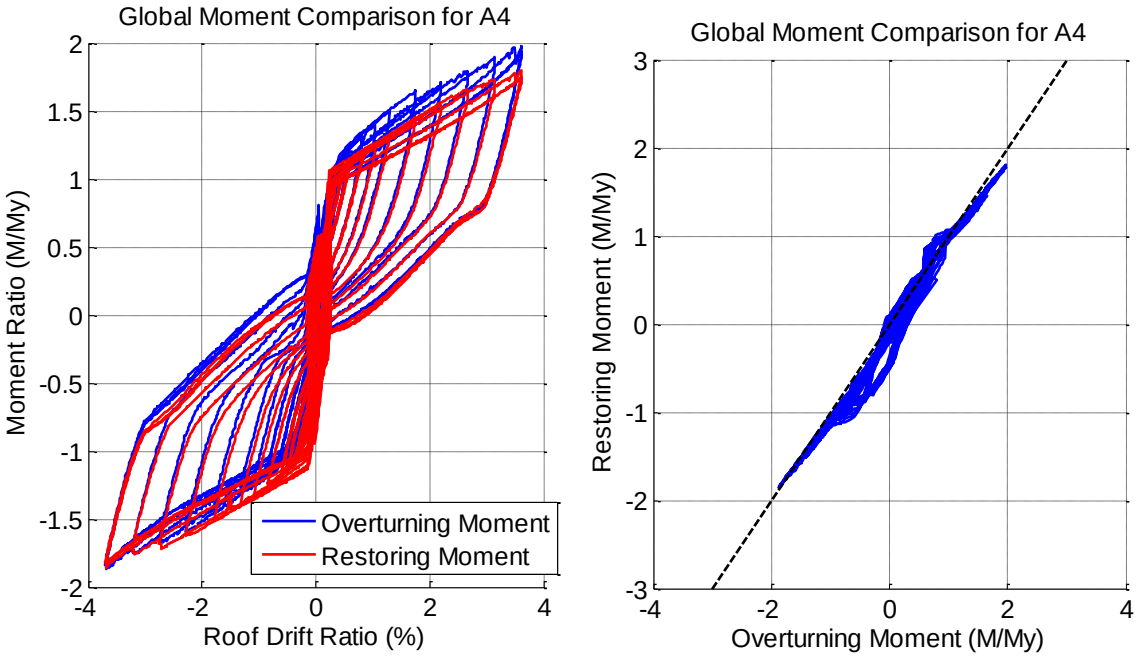

Figure D.58 Specimen A4 - Comparing Restoring Moment to Applied Overturning Moment

In the middle of the testing of Specimen A4 it was found that load was being transferred through friction between the pin plates. This was fixed by adjusting the LBCB in the out of plane direction so that the frame was more vertical and then adjusting the out of plane rotation so that there was no moment being applied through the pin plates. As shown in Figure 1.7, after the fix was implemented, almost all of the load was then transferred through the pin load cells.

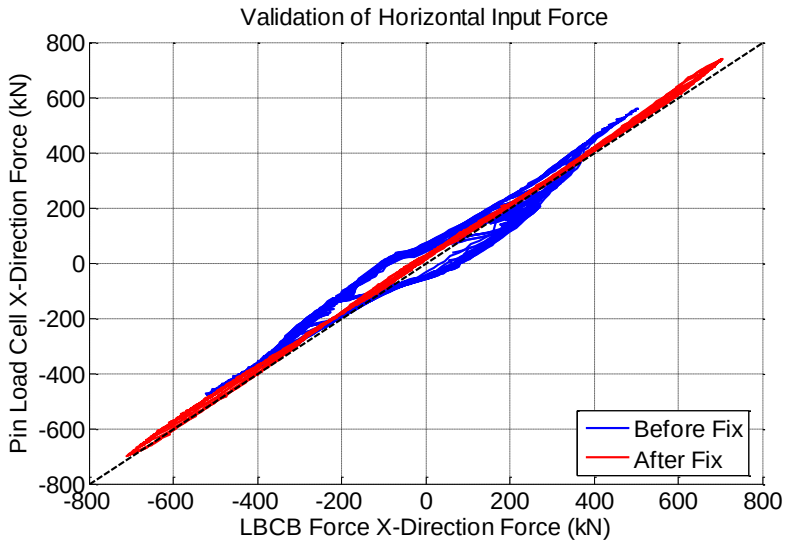

Figure D.59 Specimen A4 - Validation of Horizontal Forces Applied to the Frames

D.4.2 Post-Tensioning Force Validation

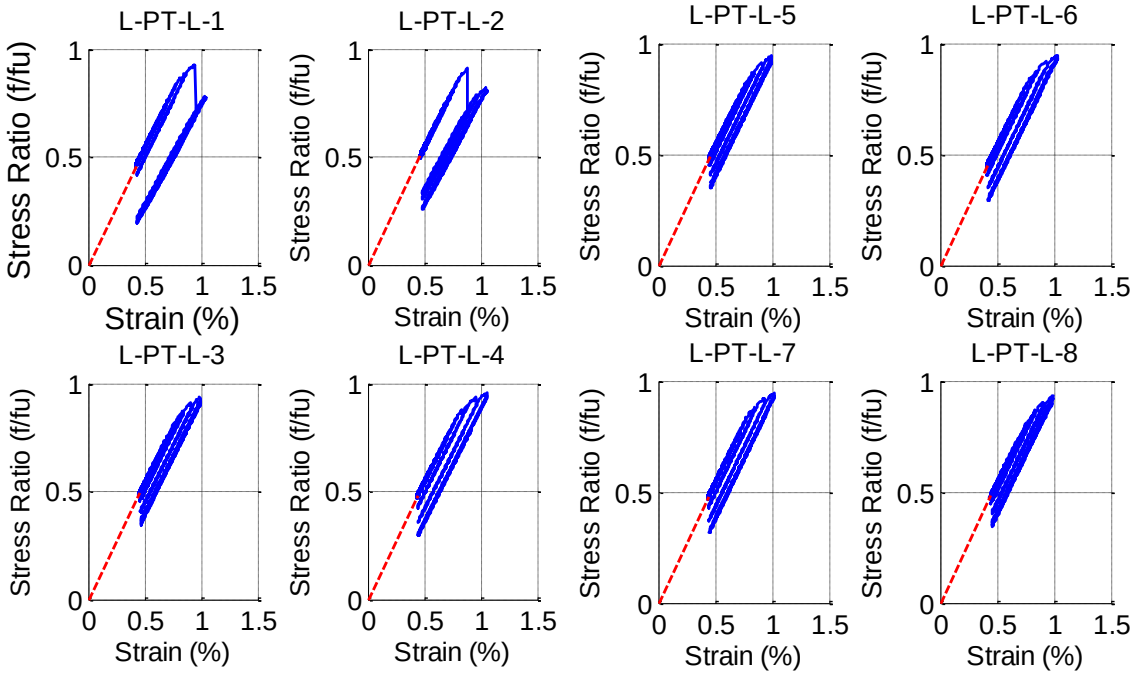

Figure D.60 Specimen A4 - Post-Tensioning Stress-Strain Response

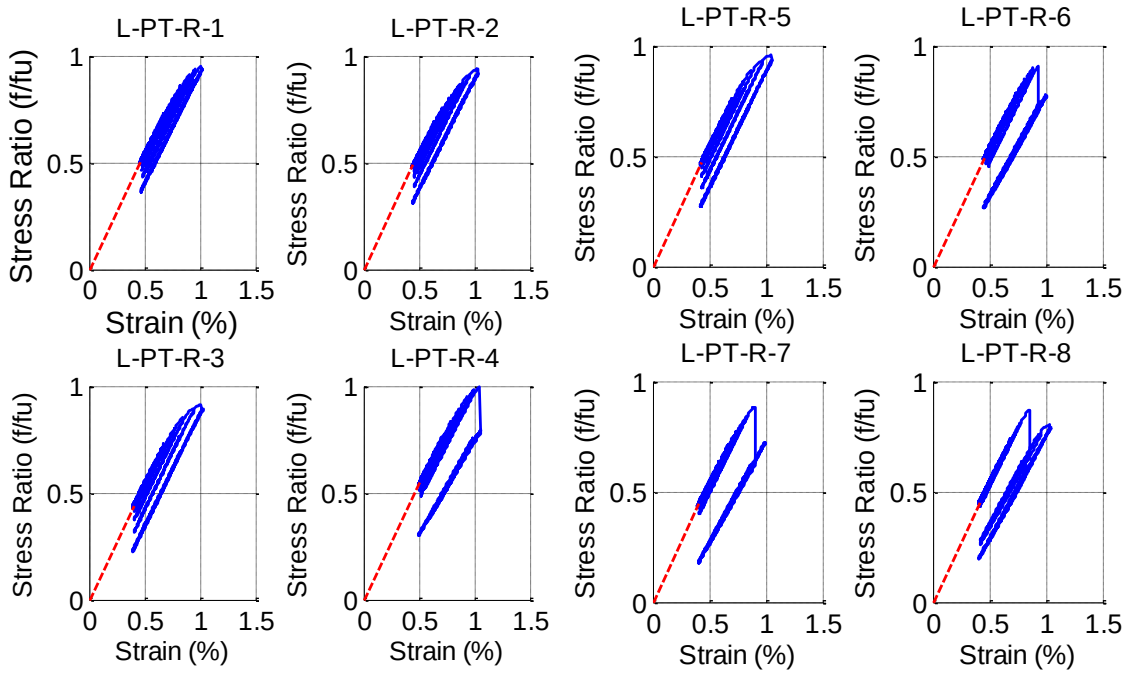

Figure D.61 Specimen A4 - Post-Tensioning Stress-Strain Response

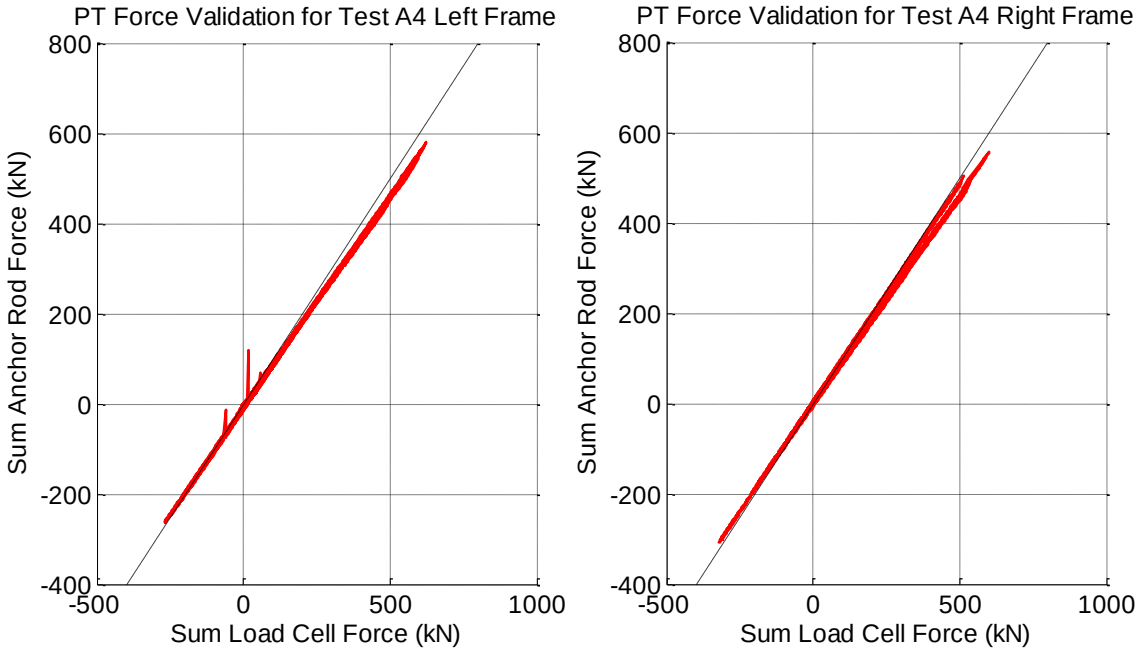

Figure D.62 Specimen A4 - Validation of Post-Tensioning Forces

D.4.3 Motion of the System

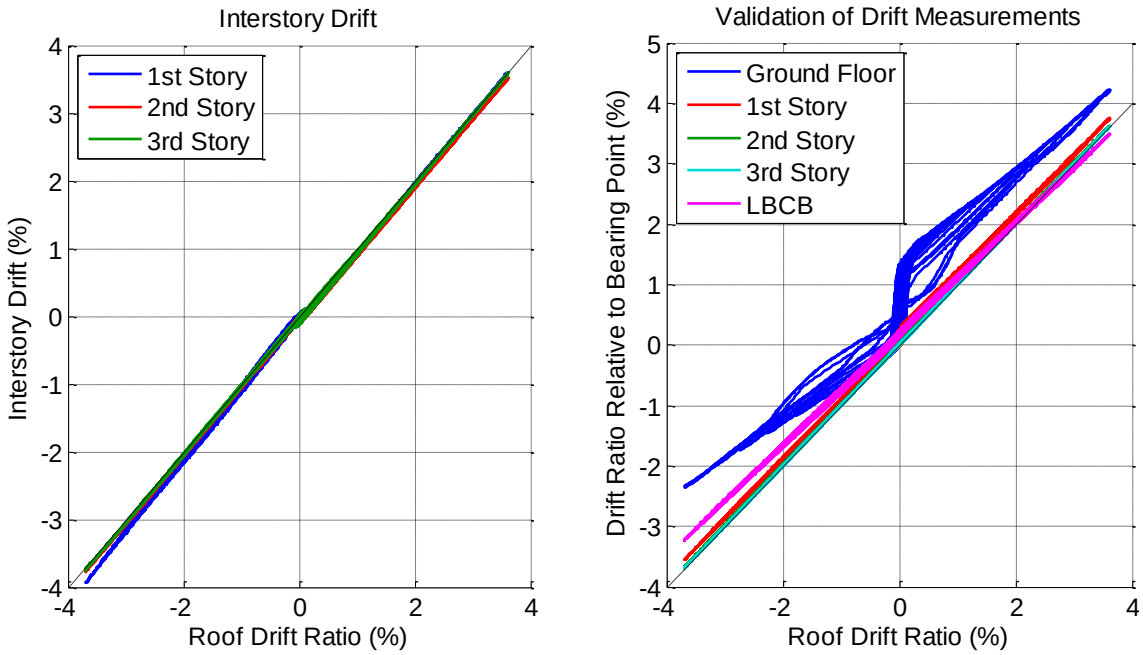

Figure D.63 Specimen A4 - Interstory Drifts (Left) and Drift Ratios Relative to Base (Right)

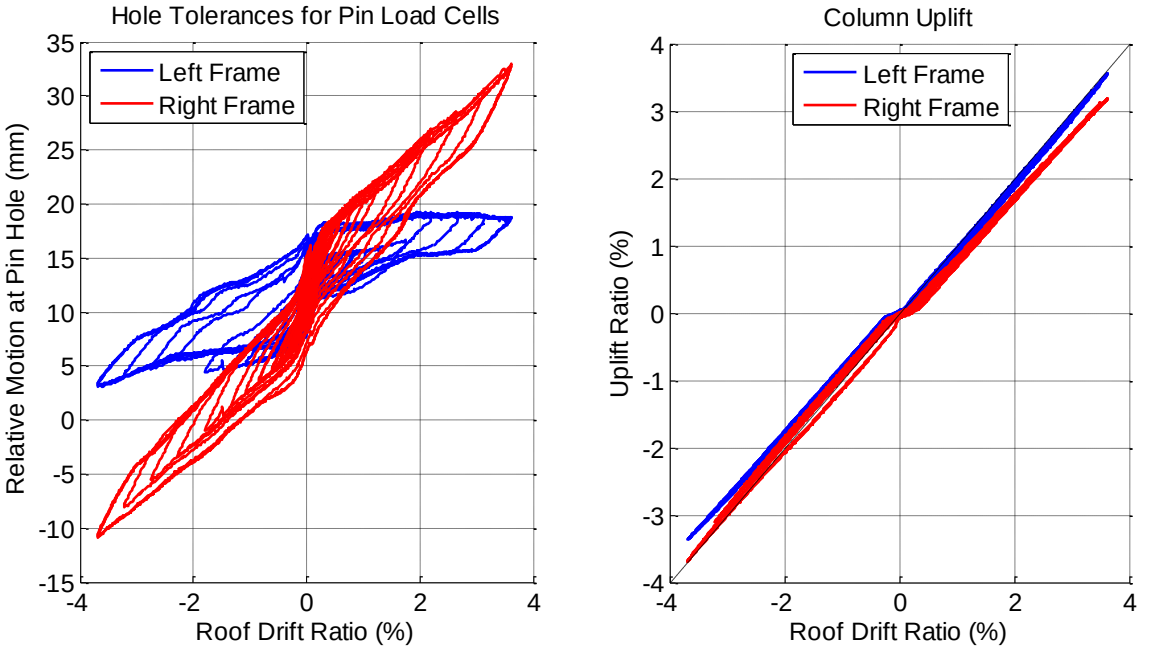

Figure D.64 Specimen A4 - Pin Hole Tolerances for the Pin Load Cells (Left), and Uplift Ratio (Right)

D.4.4 Member Resultants

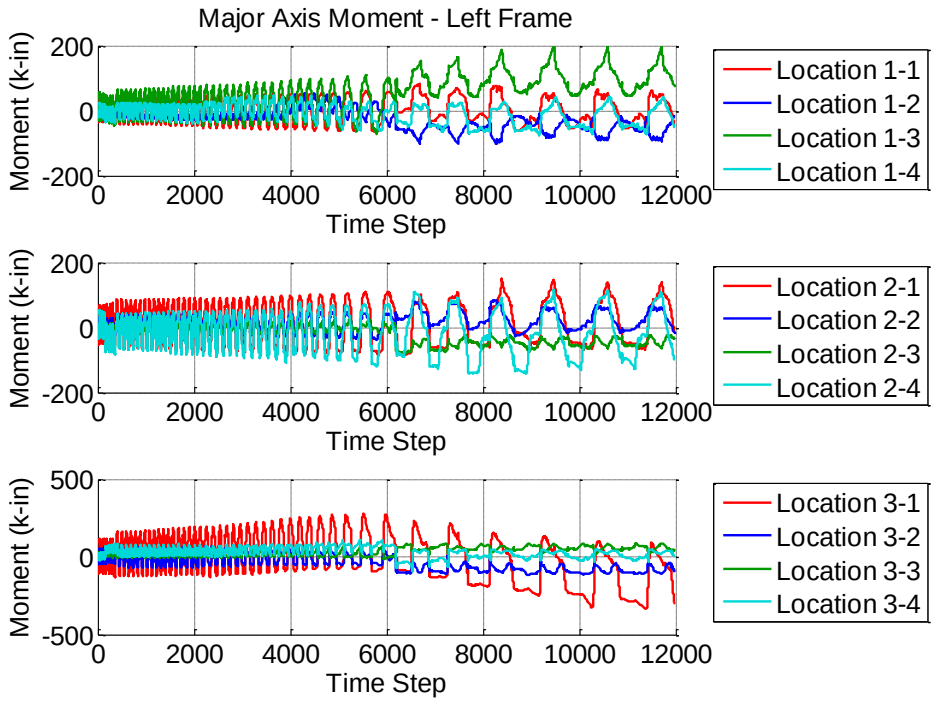

Figure D.65 Specimen A4 - Calculated Member Resultant Forces

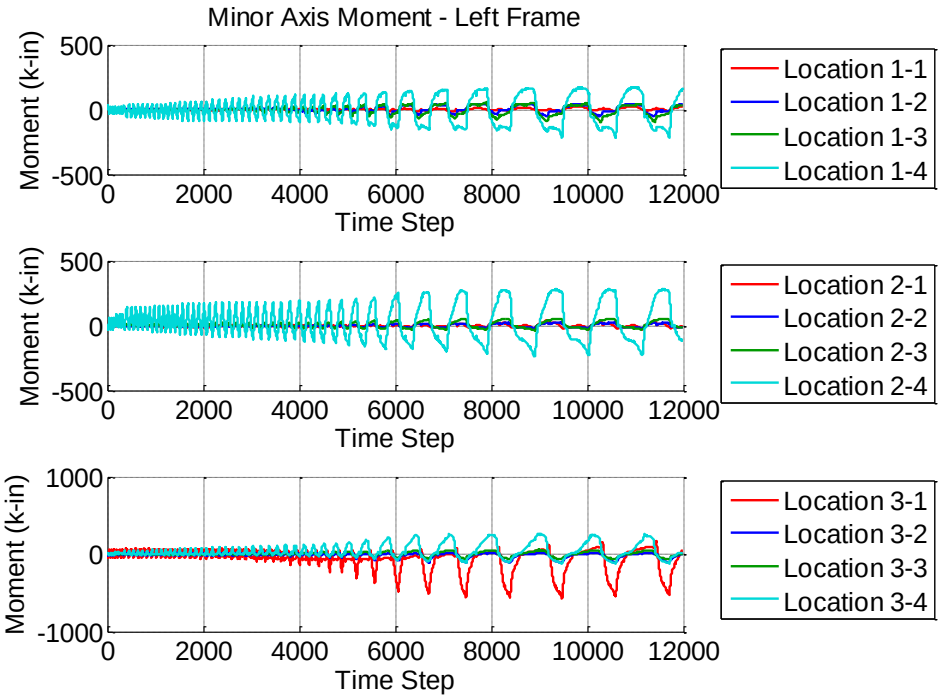

Figure D.66 Specimen A4 - Calculated Member Resultant Forces

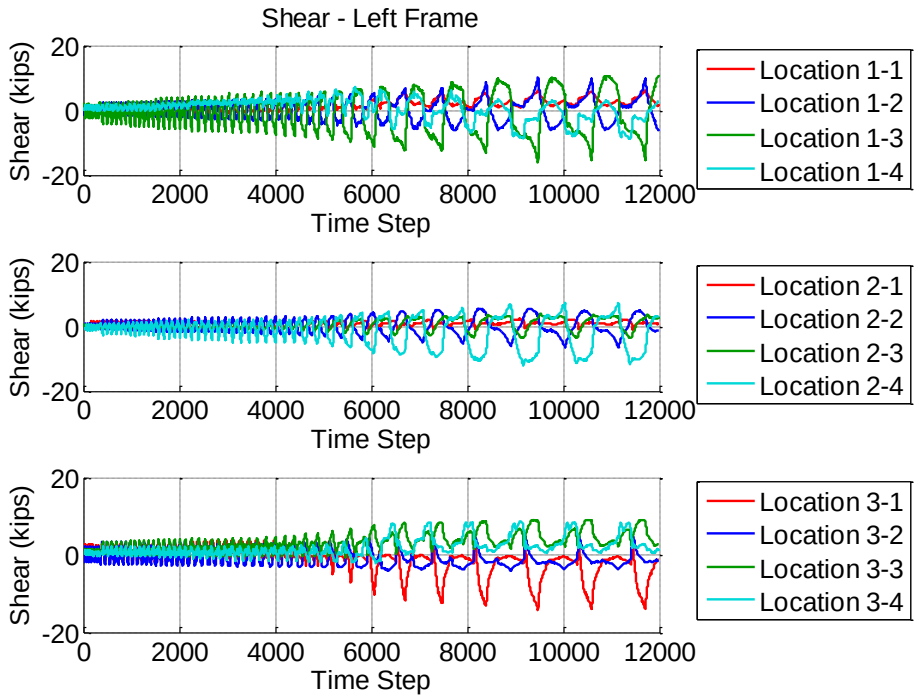

Figure D.67 Specimen A4 - Calculated Member Resultant Forces

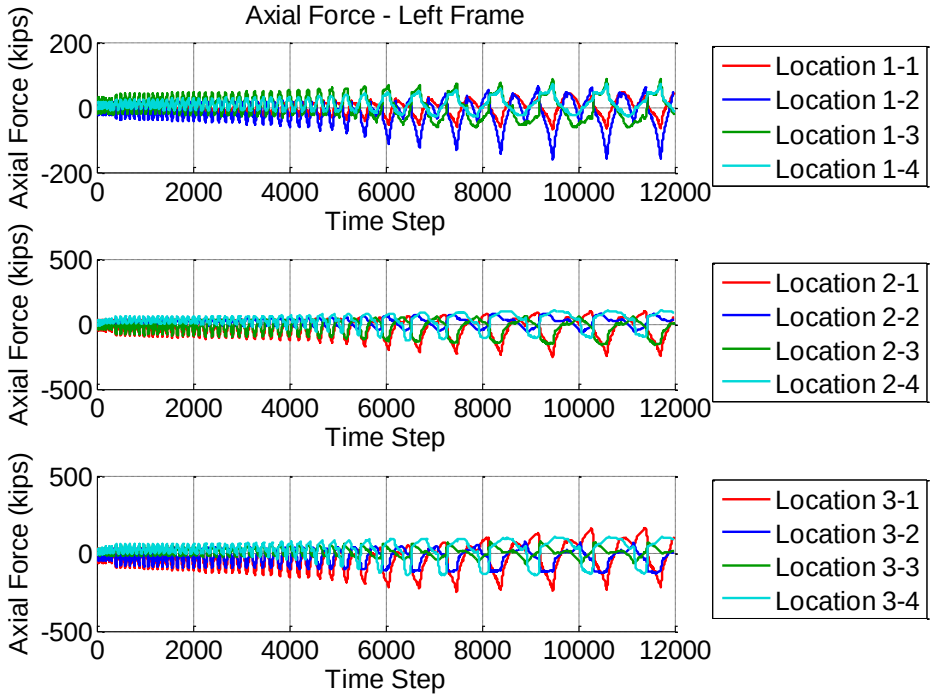

Figure D.68 Specimen A4 - Calculated Member Resultant Forces

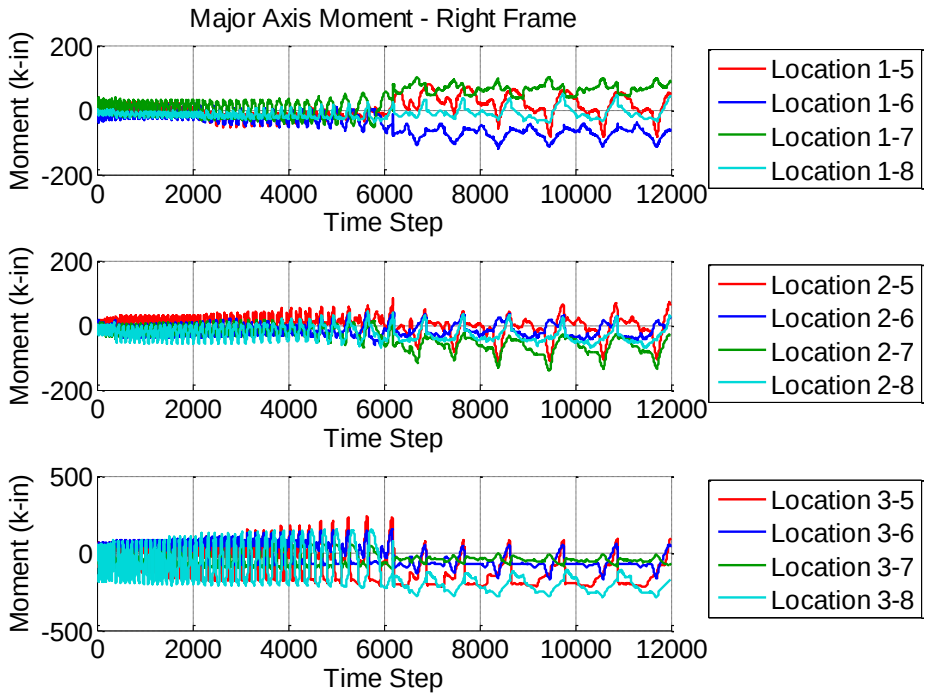

Figure D.69 Specimen A4 - Calculated Member Resultant Forces

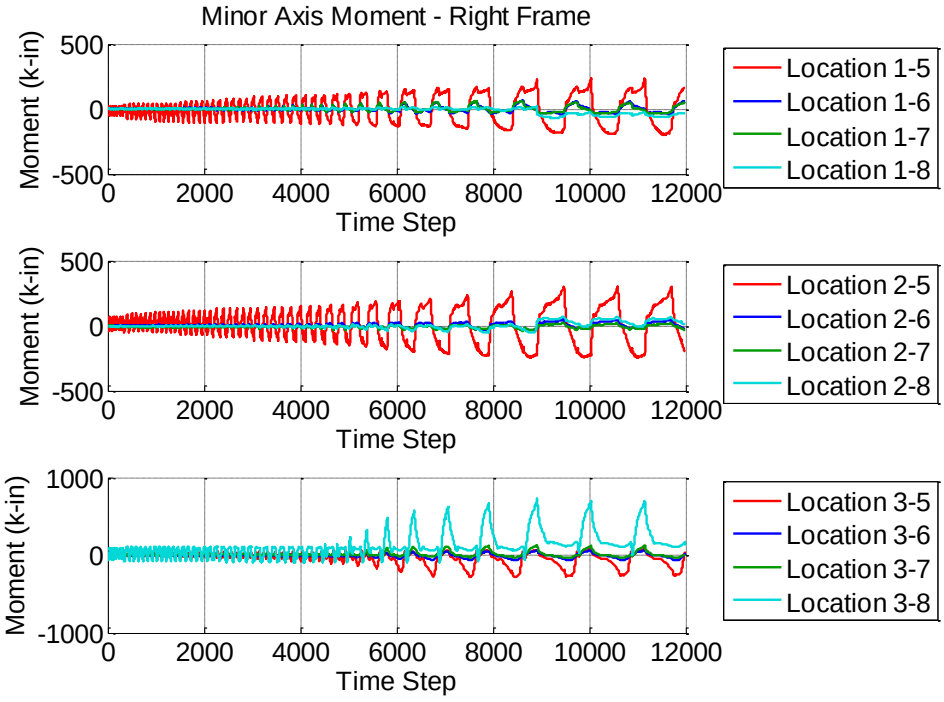

Figure D.70 Specimen A4 - Calculated Member Resultant Forces

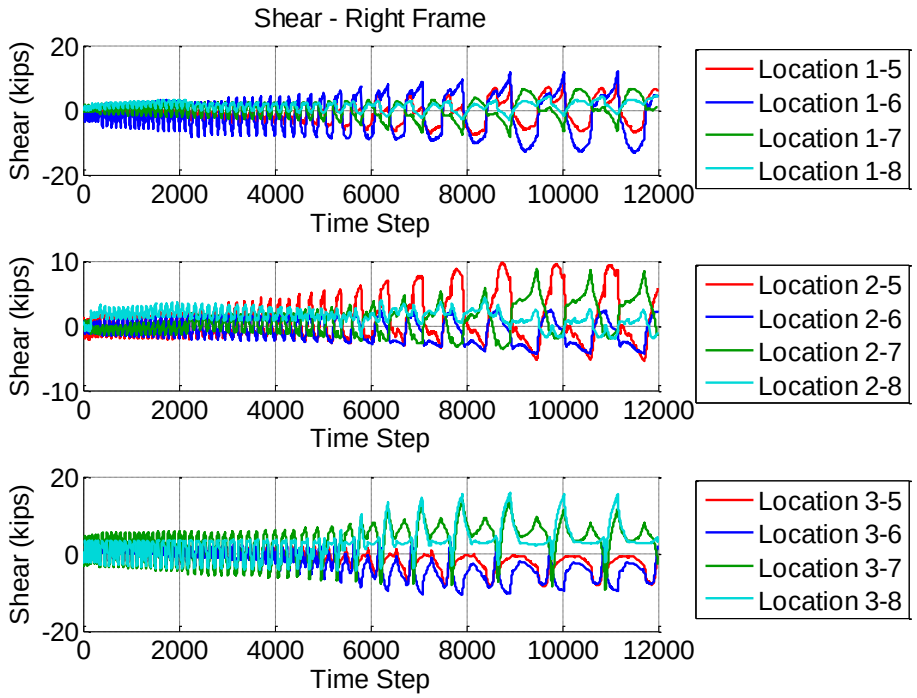

Figure D.71 Specimen A4 - Calculated Member Resultant Forces

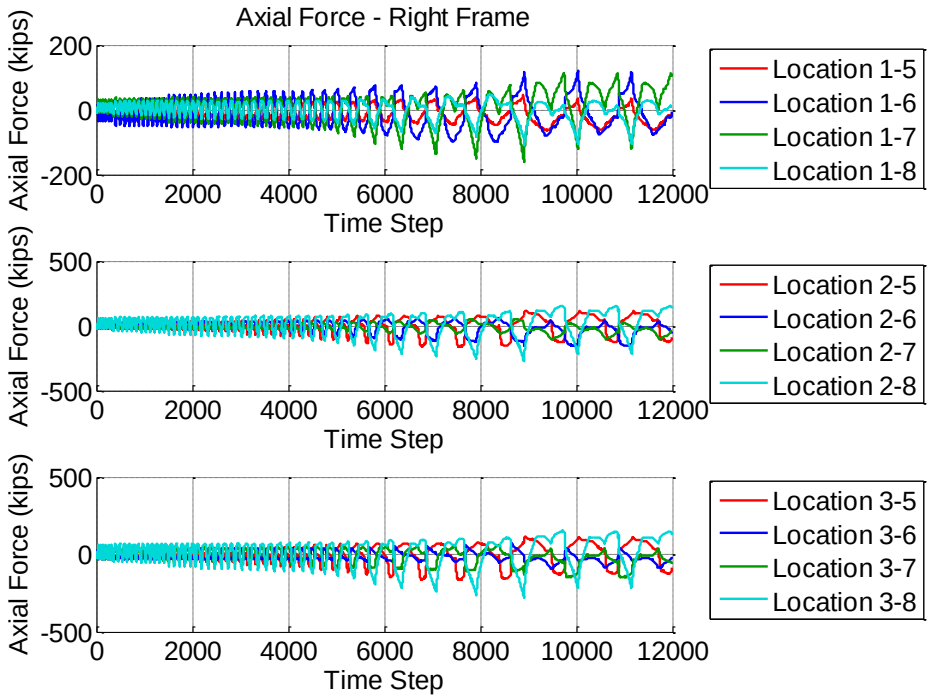

Figure D.72 Specimen A4 - Calculated Member Resultant Forces

D.4.5 Sum Forces at Each Section

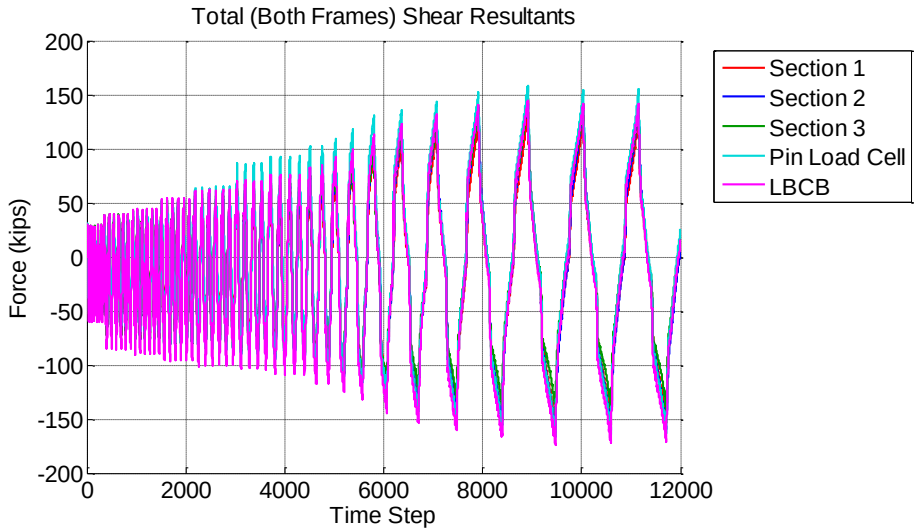

Figure D.73 Specimen A4 - Sum of the Shear Forces

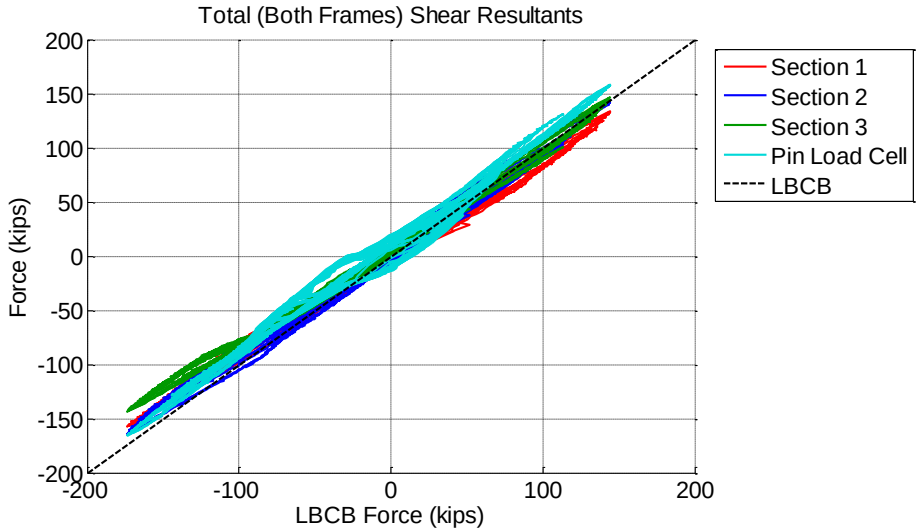

Figure D.74 Specimen A4 - Validation of Shear Forces Calculated From Strain-Gaged Sections

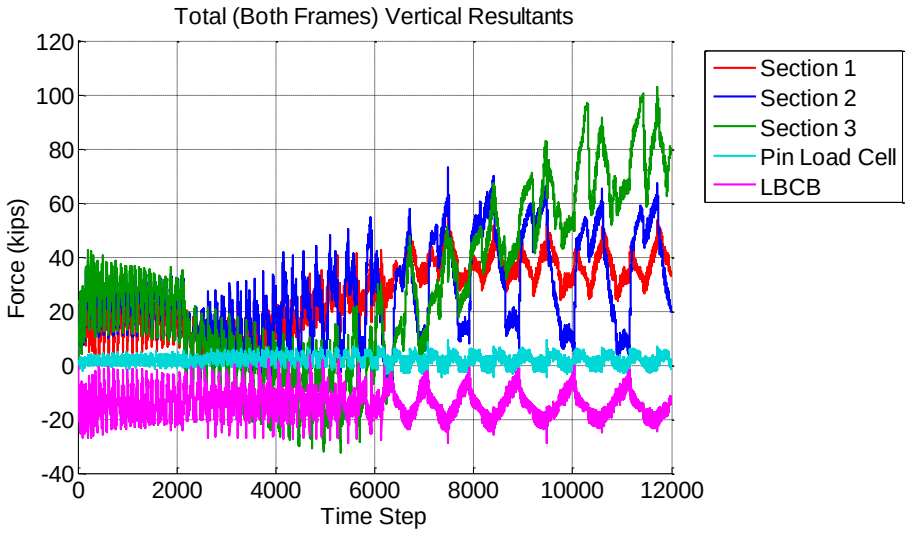

Figure D.75 Specimen A4 - Vertical Forces Calculated From Strain-Gaged Sections

D.5 Specimen A5 – MCE Trial

D.5.1 System Response

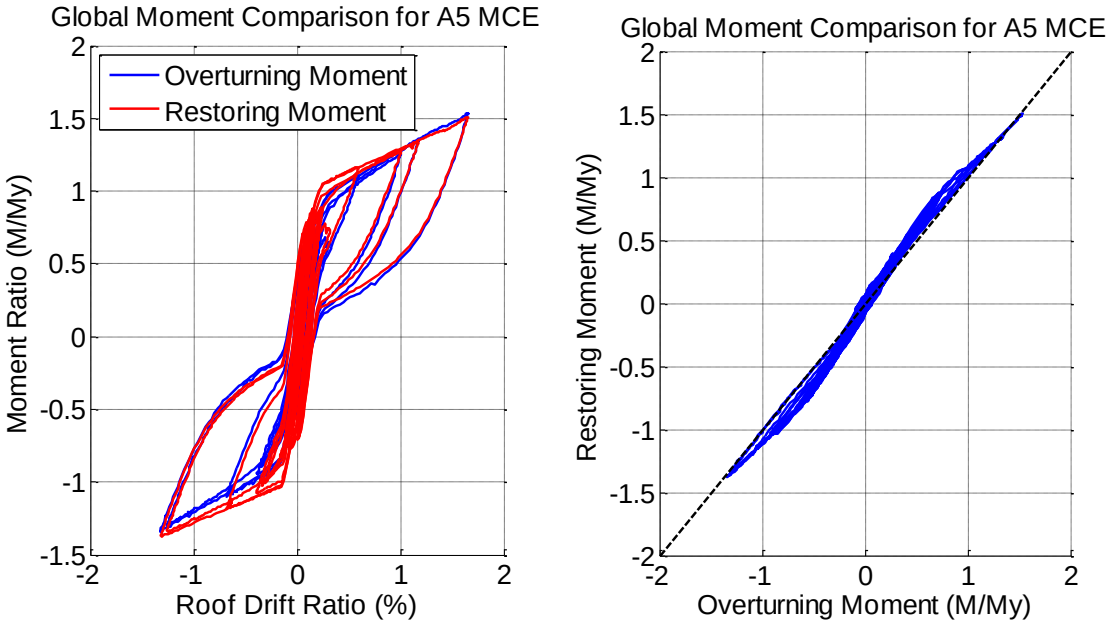

Figure D.76 Specimen A5 MCE Trial - Comparing Restoring Moment to Applied Overturning Moment

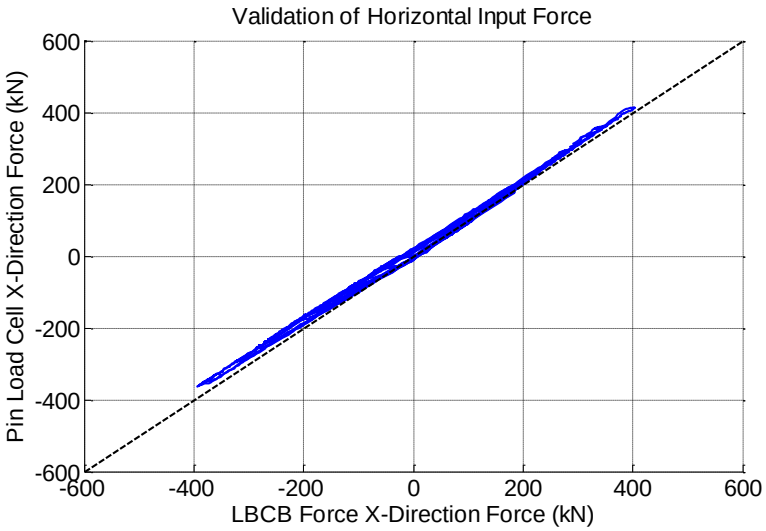

Figure D.77 Specimen A5 MCE Trial - Validation of Horizontal Forces Applied to the Frames

D.5.2 Post-Tensioning Force Validation

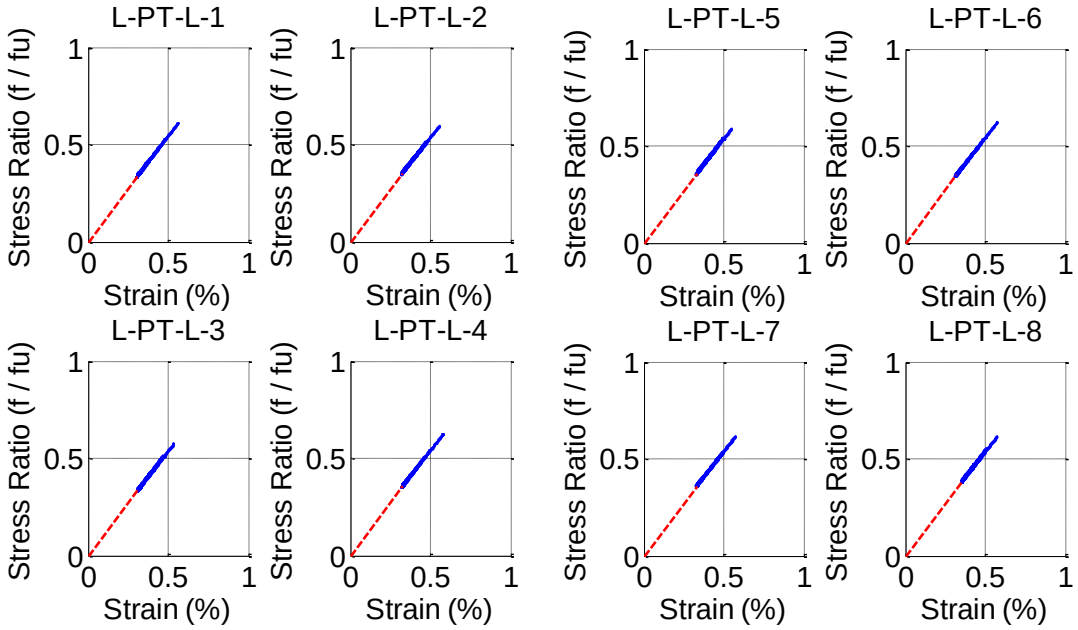

Figure D.78 Specimen A5 MCE Trial - Post-Tensioning Stress-Strain Response

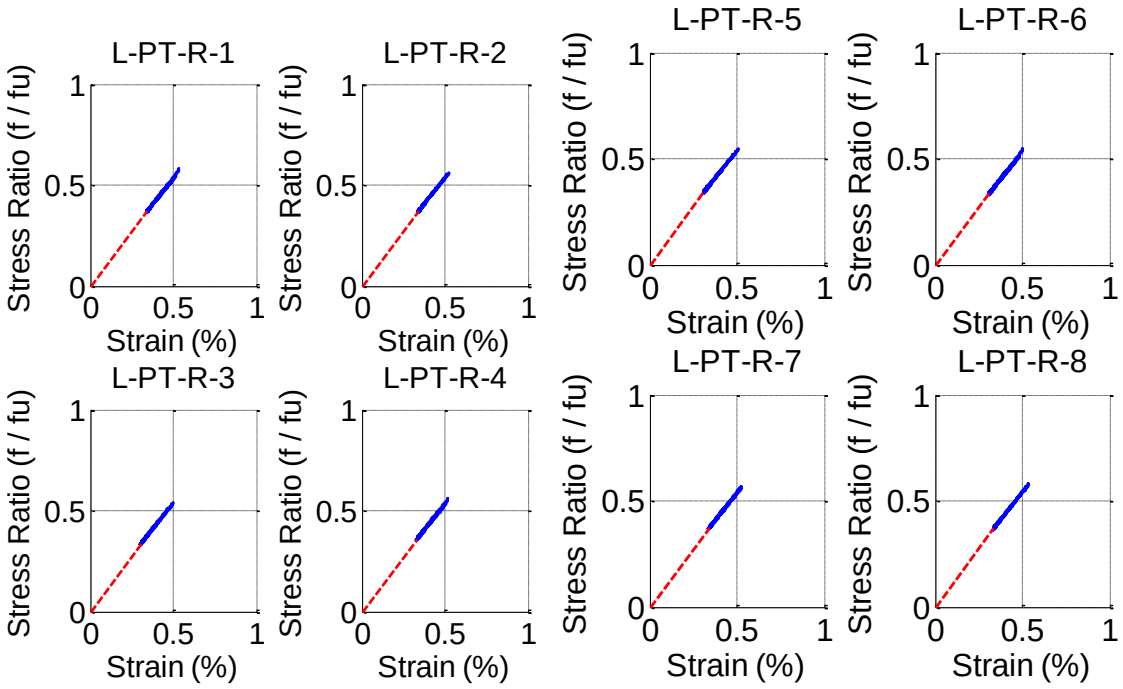

Figure D.79 Specimen A5 MCE Trial - Post-Tensioning Stress-Strain Response

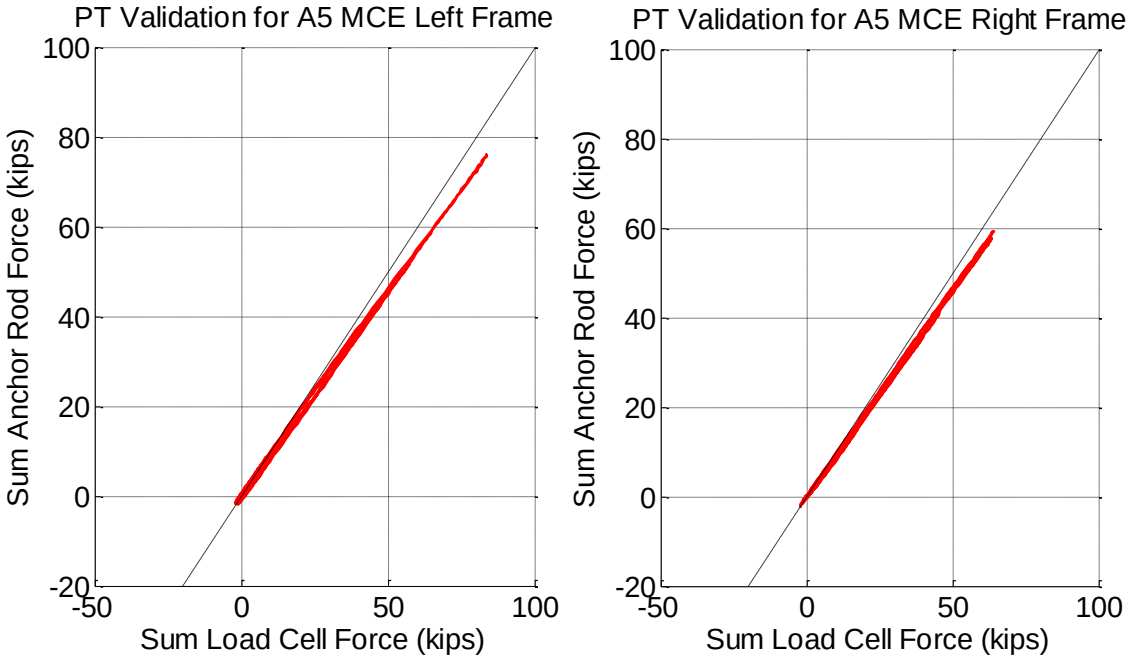

Figure D.80 Specimen A5 MCE Trial - Validation of Post-Tensioning Forces

D.5.3 Motion of the System

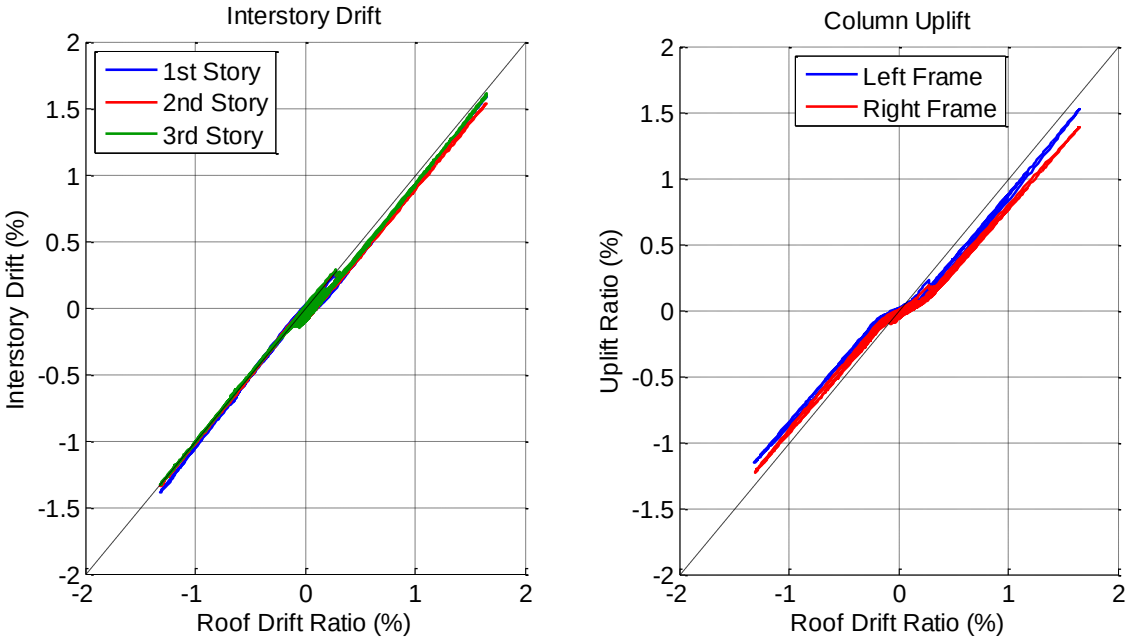

Figure D.81 Specimen A5 MCE Trial - Interstory Drifts (Left) and Drift Ratios Relative to Base (Right)

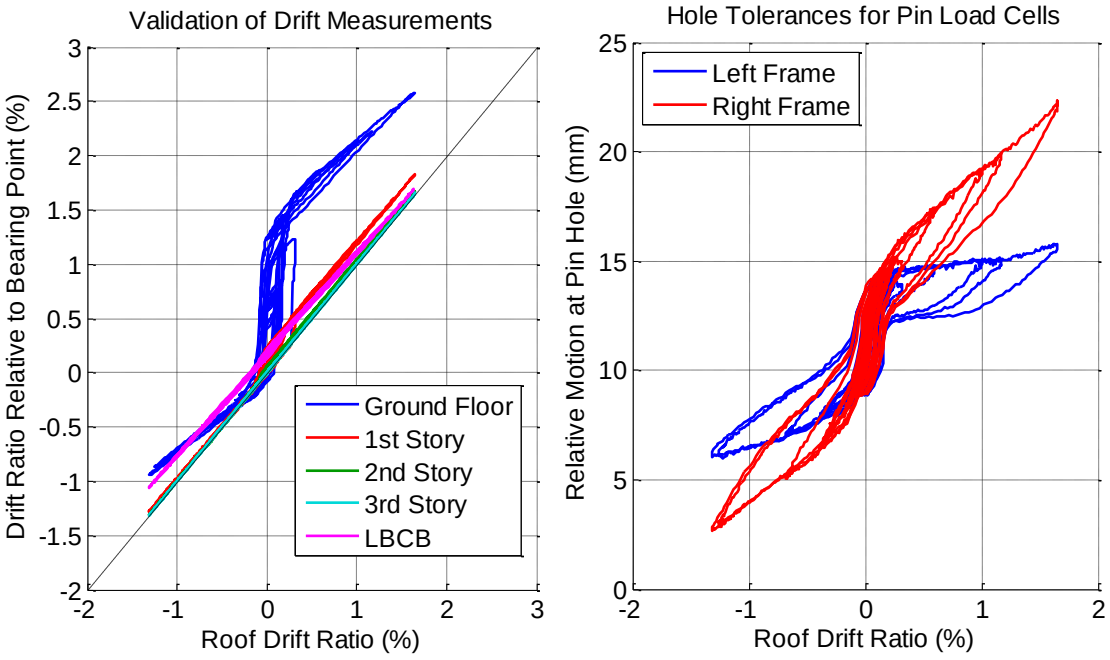

Figure D.82 Specimen A5 MCE Trial - Pin Hole Tolerances for the Pin Load Cells (Left), and Uplift Ratio (Right)

D.5.4 Member Resultants

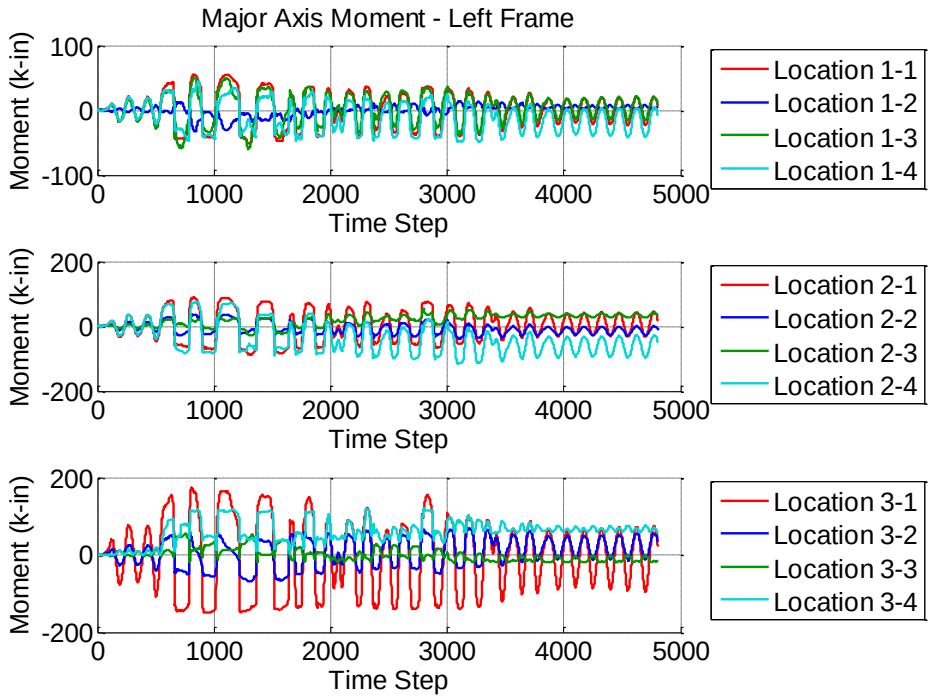

Figure D.83 Specimen A5 MCE Trial - Calculated Member Resultant Forces

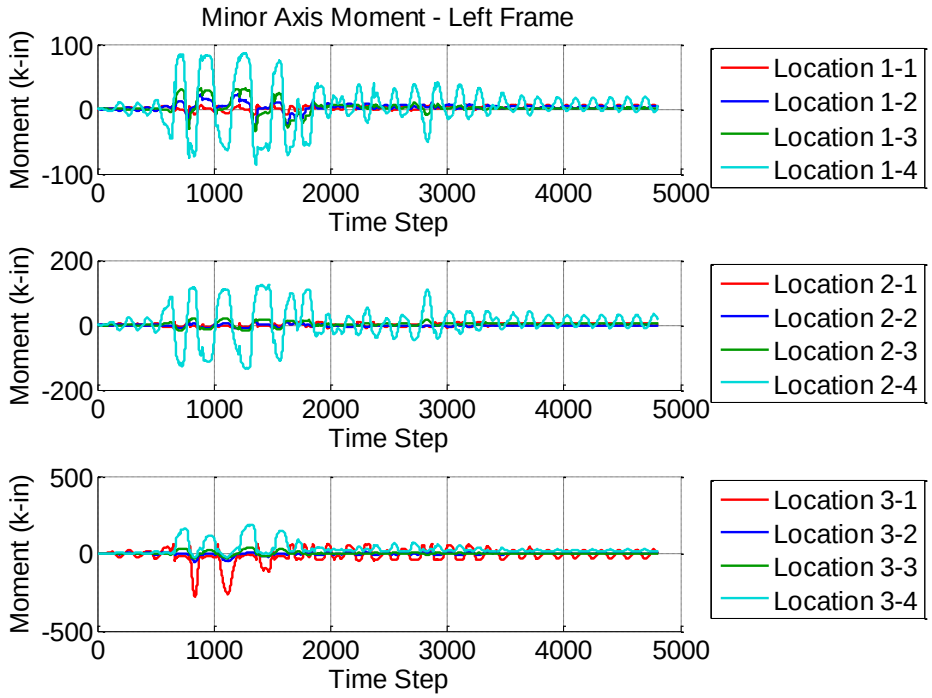

Figure D.84 Specimen A5 MCE Trial - Calculated Member Resultant Forces

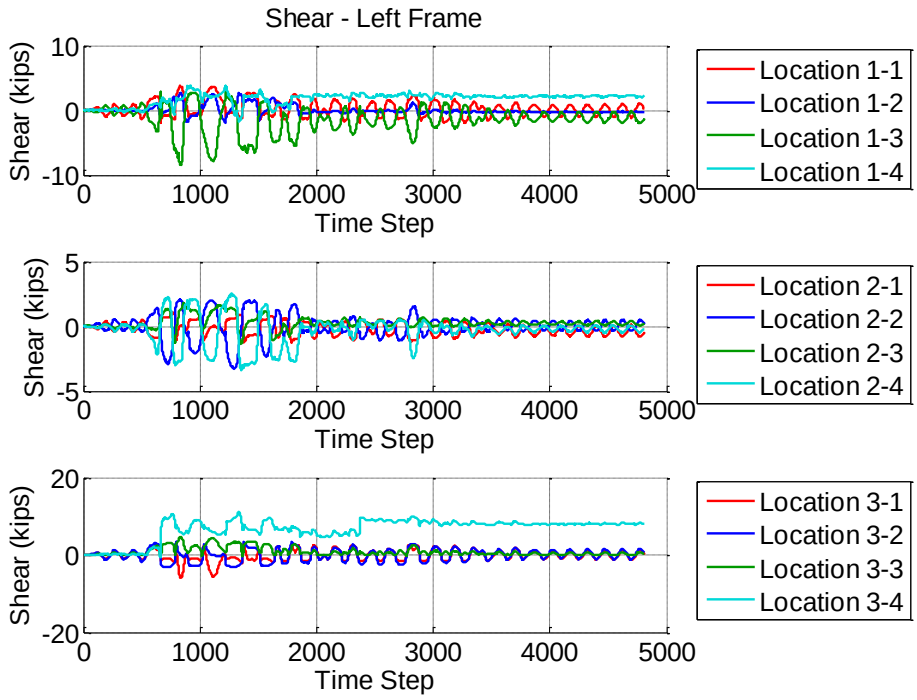

Figure D.85 Specimen A5 MCE Trial - Calculated Member Resultant Forces

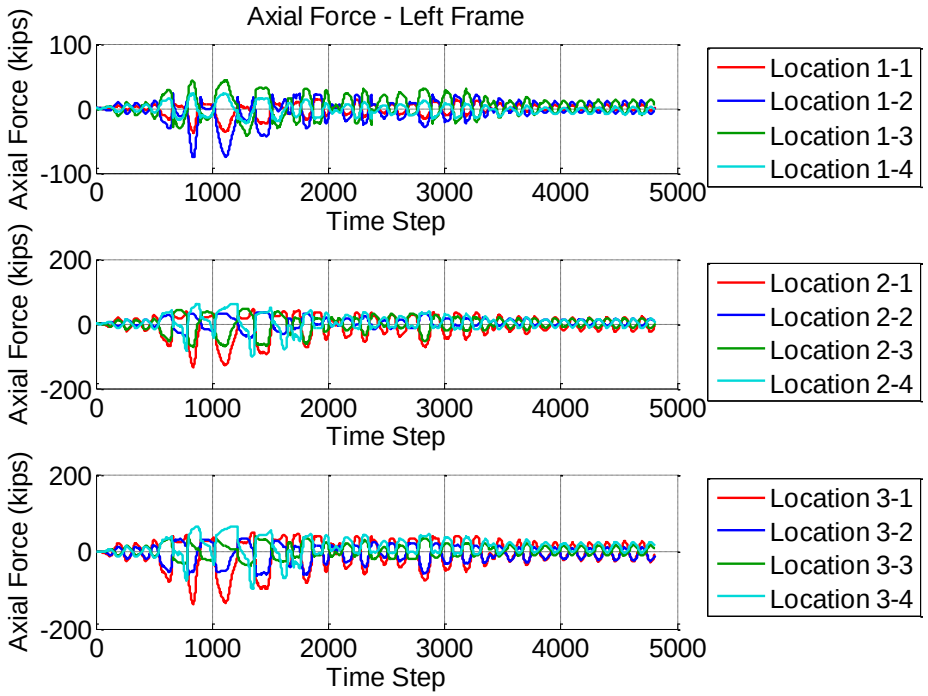

Figure D.86 Specimen A5 MCE Trial - Calculated Member Resultant Forces

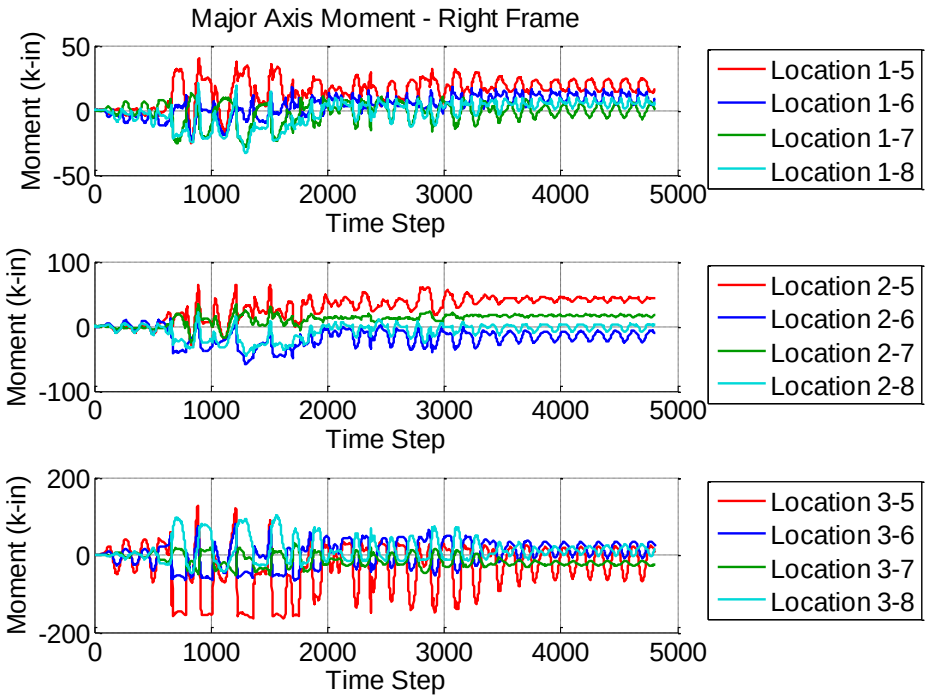

Figure D.87 Specimen A5 MCE Trial - Calculated Member Resultant Forces

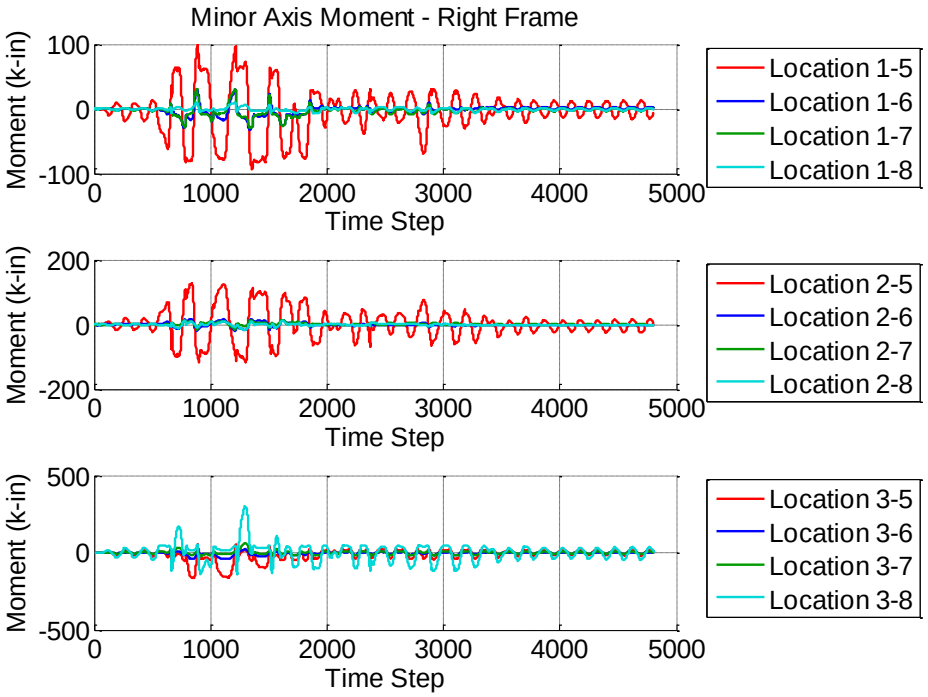

Figure D.88 Specimen A5 MCE Trial - Calculated Member Resultant Forces

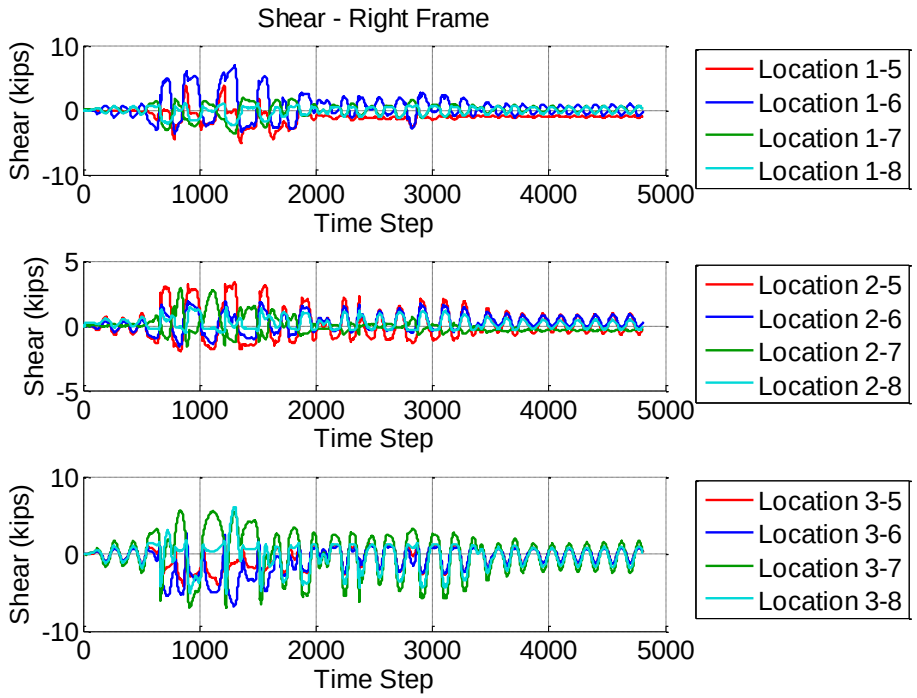

Figure D.89 Specimen A5 MCE Trial - Calculated Member Resultant Forces

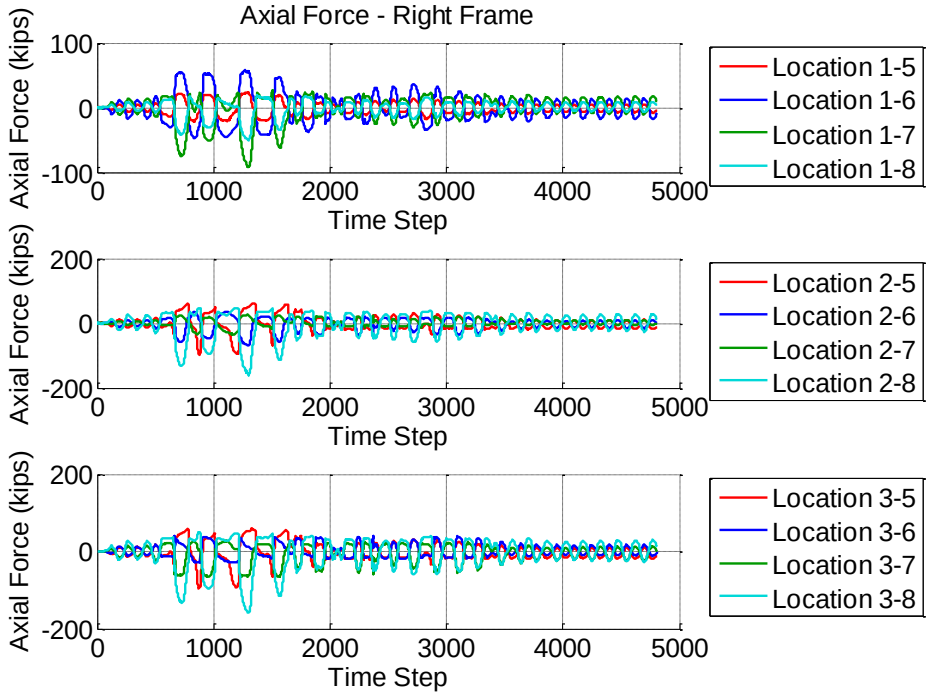

Figure D.90 Specimen A5 MCE Trial - Calculated Member Resultant Forces

D.5.5 Sum Forces at Each Section

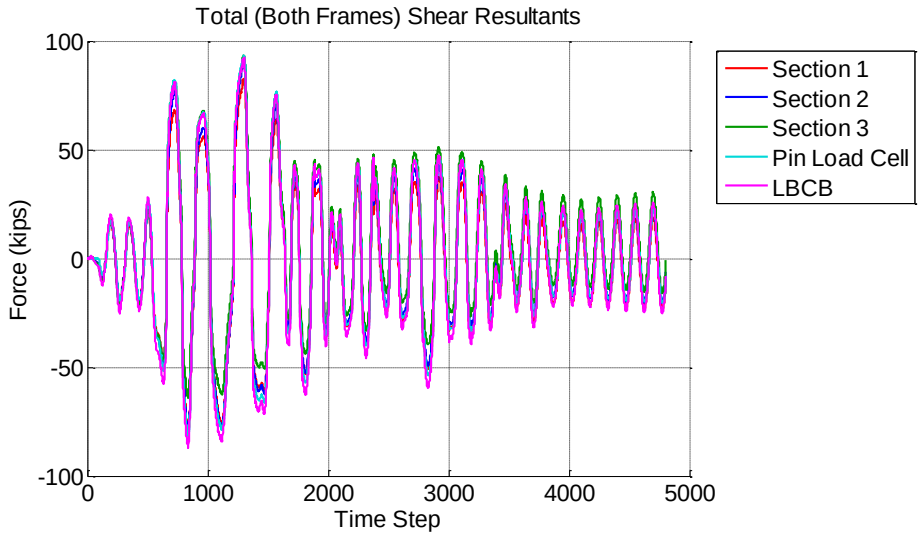

Figure D.91 Specimen A5 MCE Trial - Sum of the Shear Forces

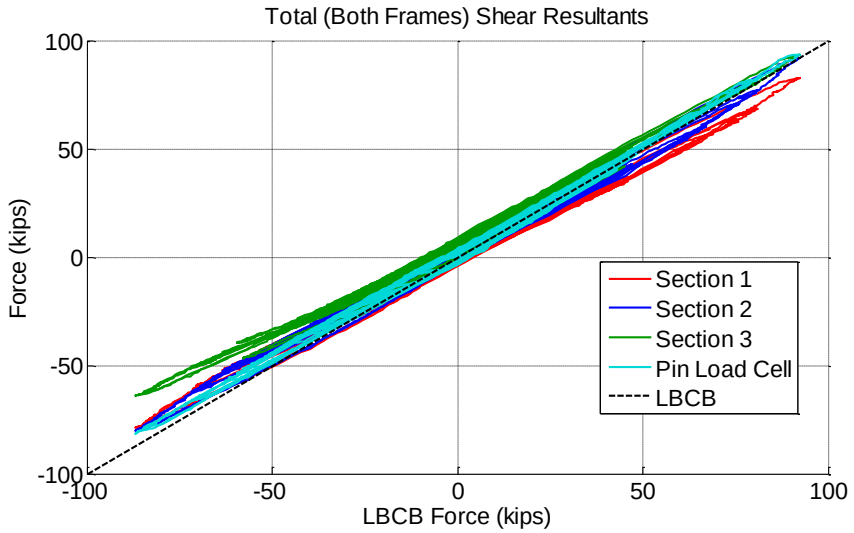

Figure D.92 Specimen A5 MCE Trial - Validation of Shear Forces Calculated From Strain-Gaged Sections

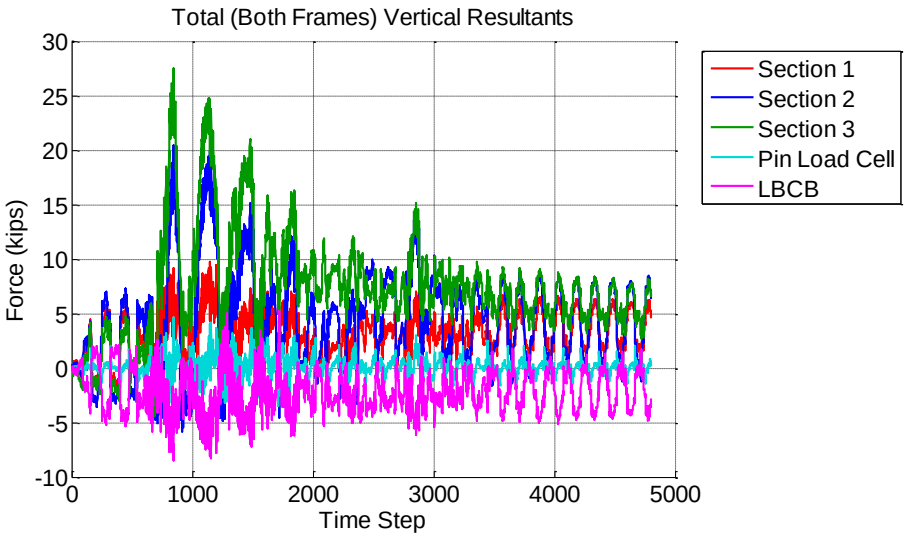

Figure D.93 Specimen A5 MCE Trial - Vertical Forces Calculated From Strain-Gaged Sections

D.6 Specimen A5 – Both Trials at 1.10 x JMA Kobe

The restoring moment due to fuse force for the 1.10 JMA Kobe run was found to be not centered around zero because although all the channels were zeroed out at the beginning of this trial, there were initial forces in the fuse. The fuse restoring moment was adjusted by adding 0.0694My. This number was determined to make the total restoring moment best fit the overturning moment.

D.6.1 System Response

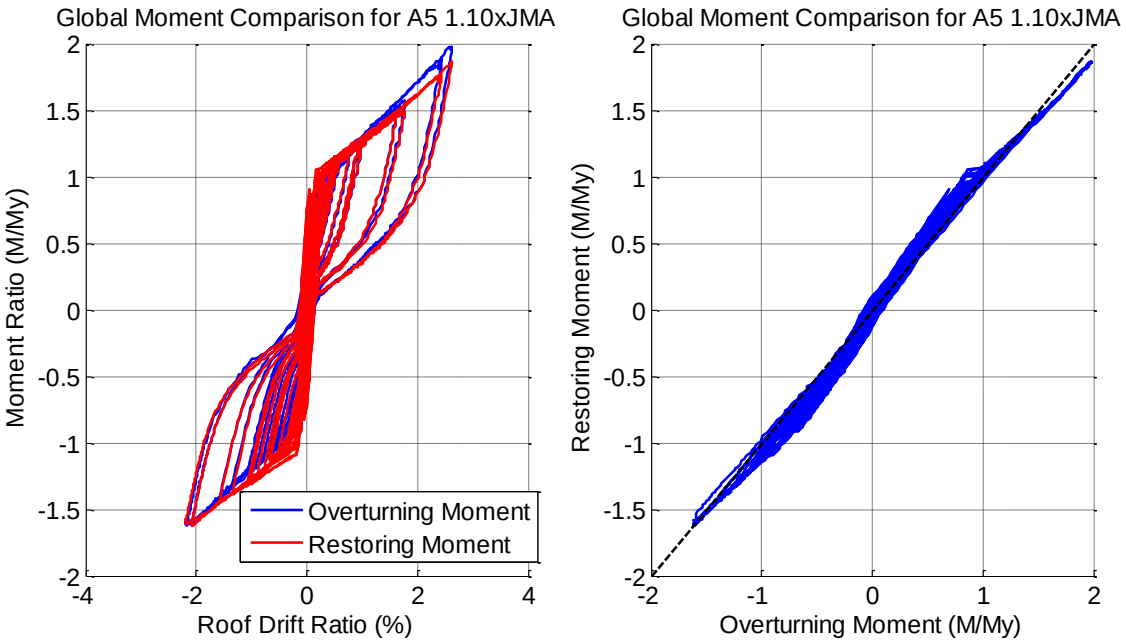

Figure D.94 Specimen A5 1.10xJMA Kobe Trials - Comparing Restoring Moment to Applied Overturning Moment

D.6.2 Post-Tensioning Force Validation

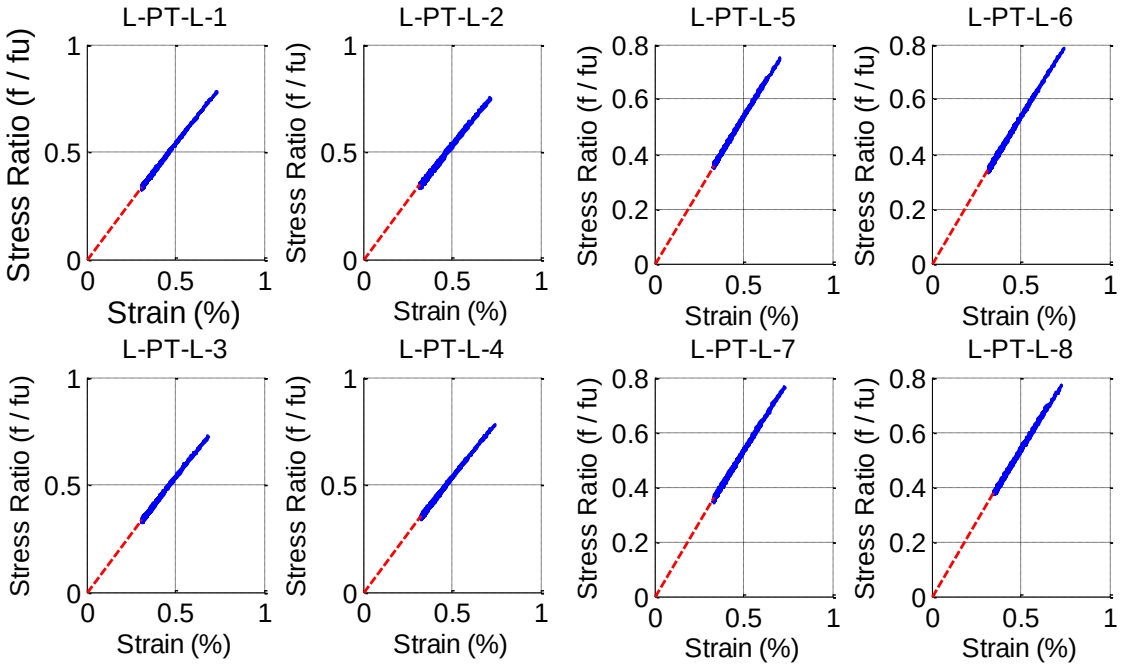

Figure D.95 Specimen A5 1.10xJMA Kobe Trials - Post-Tensioning Stress-Strain Response

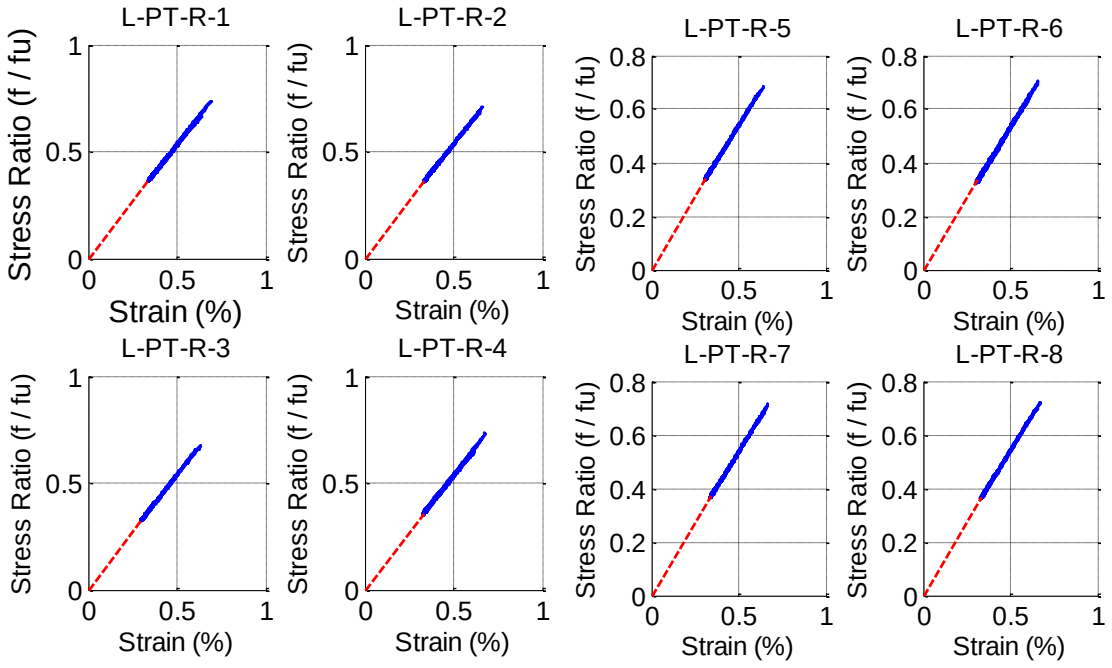

Figure D.96 Specimen A5 1.10xJMA Kobe Trials - Post-Tensioning Stress-Strain Response

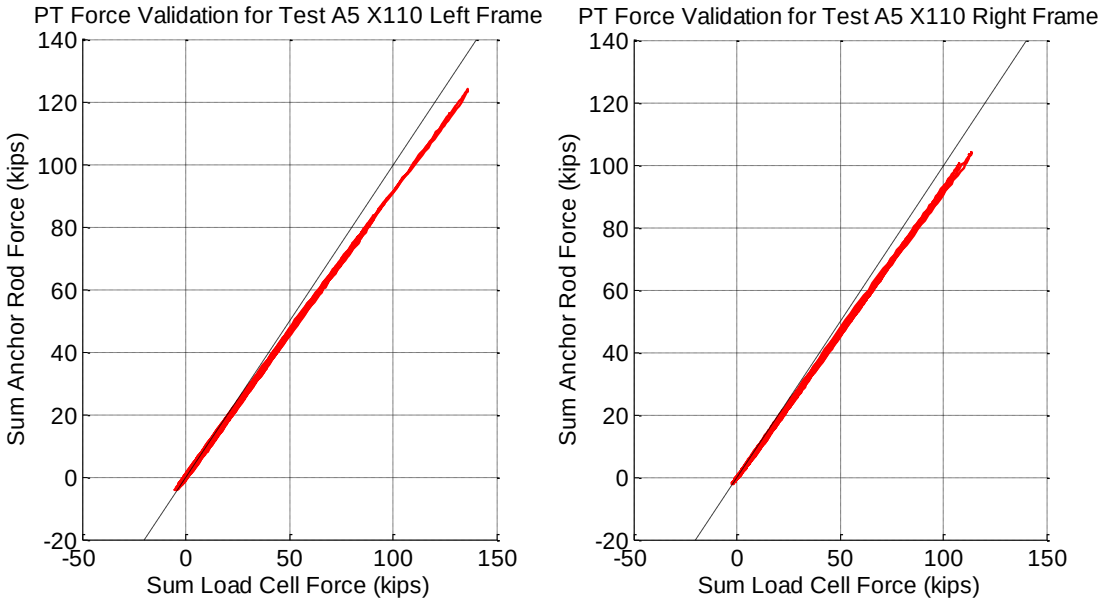

Figure D.97 Specimen A5 1.10xJMA Kobe Trials - Validation of Post-Tensioning Forces

D.6.3 Motion of the System

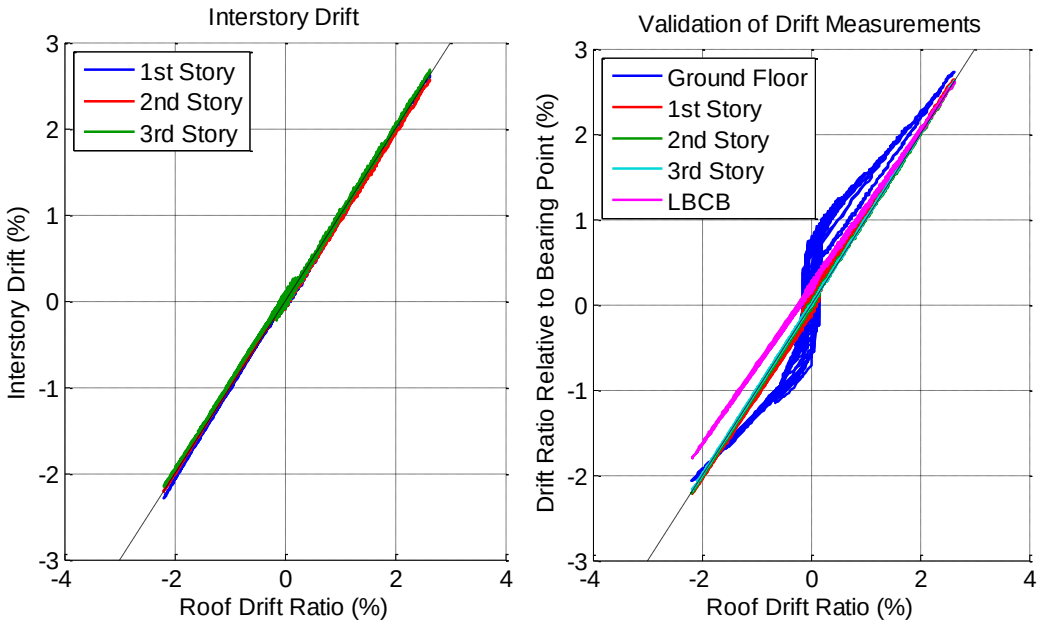

Figure D.98 Specimen A5 1.10xJMA Kobe Trials - Interstory Drifts (Left) and Drift Ratios Relative to Base (Right)

D.6.4 Member Resultants

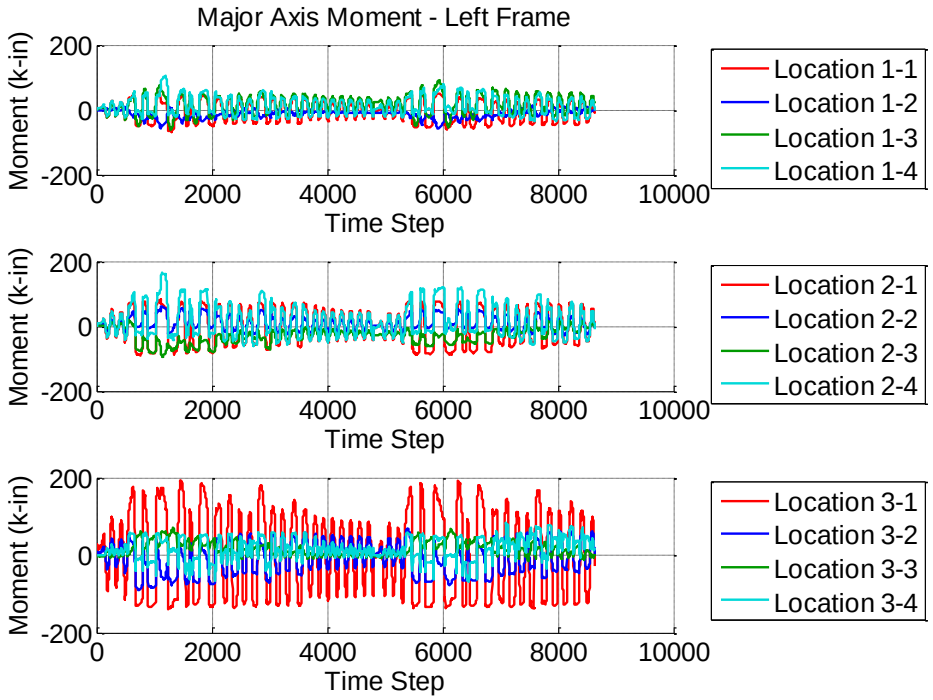

Figure D.99 Specimen A5 1.10xJMA Kobe Trials - Calculated Member Resultant Forces

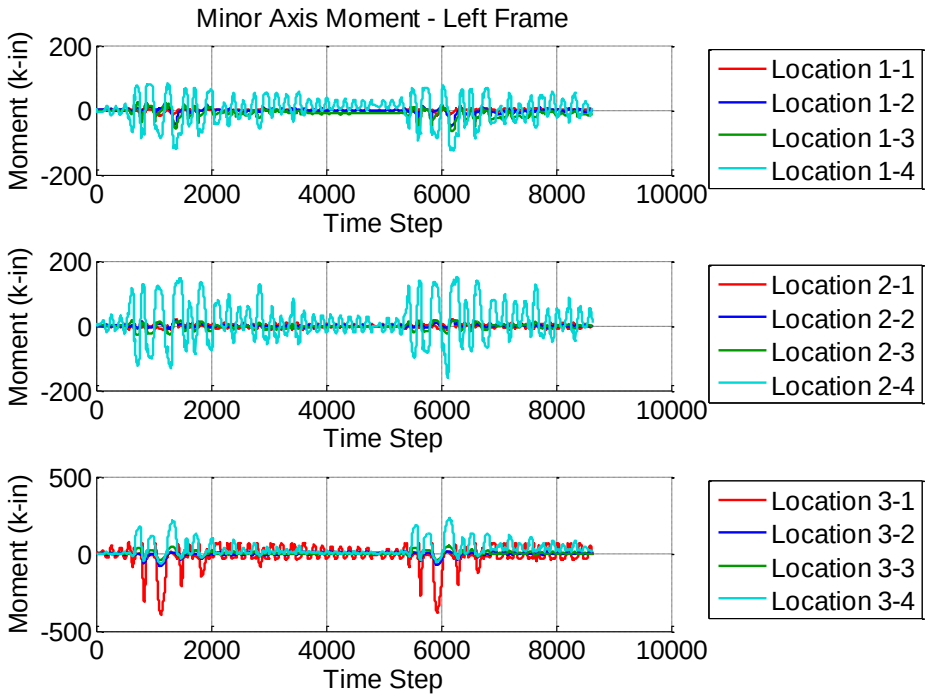

Figure D.100 Specimen A5 1.10xJMA Kobe Trials - Calculated Member Resultant Forces

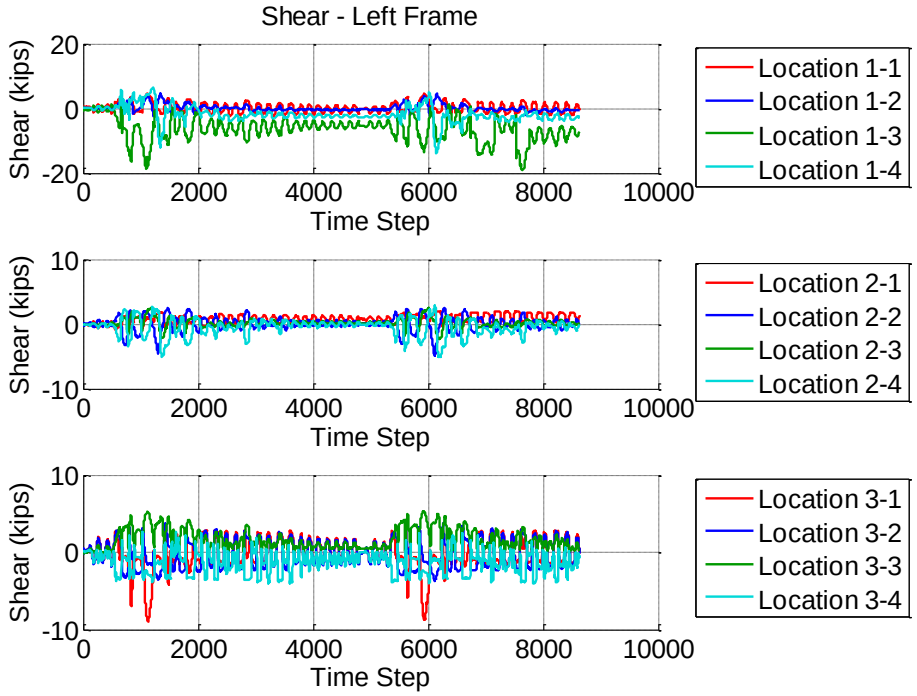

Figure D.101 Specimen A5 1.10xJMA Kobe Trials - Calculated Member Resultant Forces

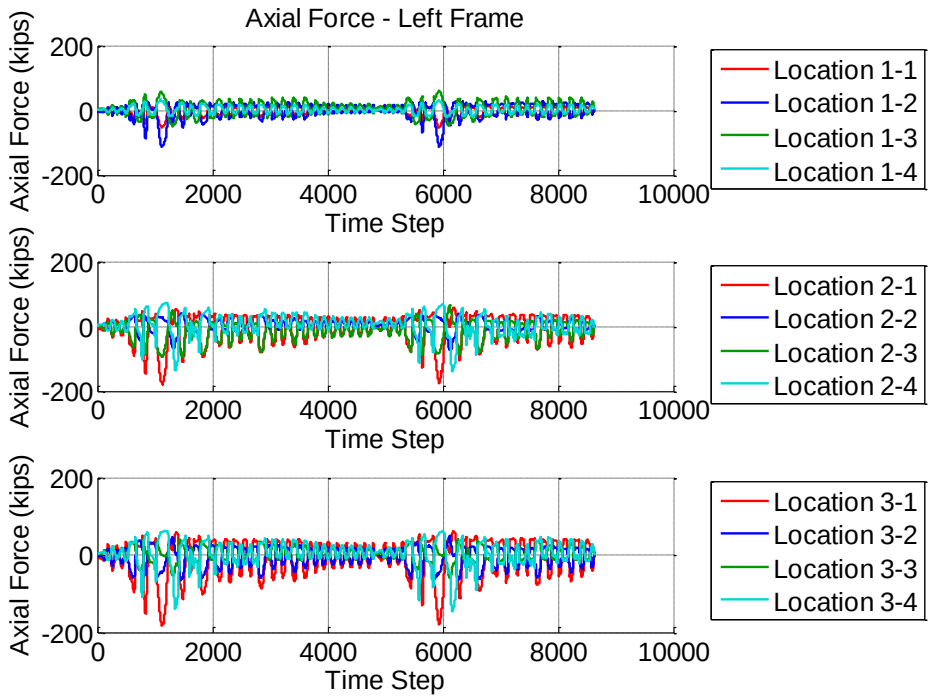

Figure D.102 Specimen A5 1.10xJMA Kobe Trials - Calculated Member Resultant Forces

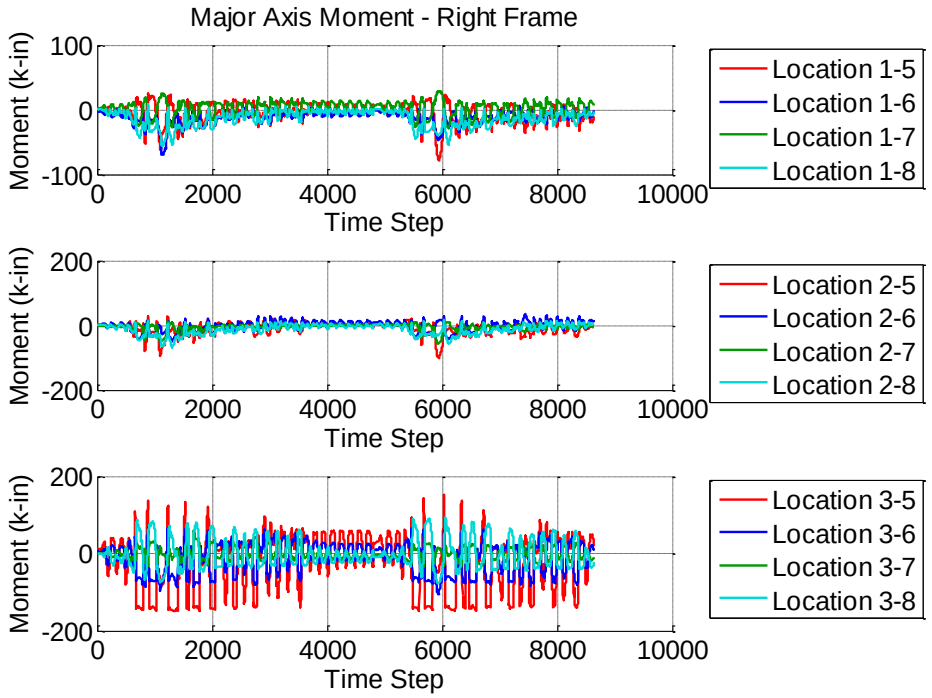

Figure D.103 Specimen A5 1.10xJMA Kobe Trials - Calculated Member Resultant Forces

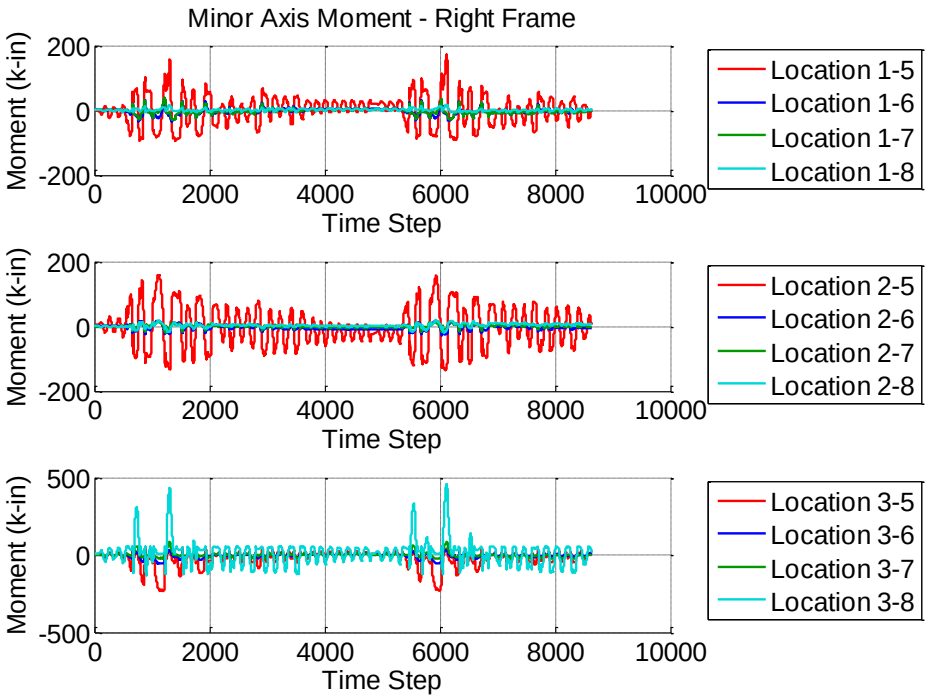

Figure D.104 Specimen A5 1.10xJMA Kobe Trials - Calculated Member Resultant Forces

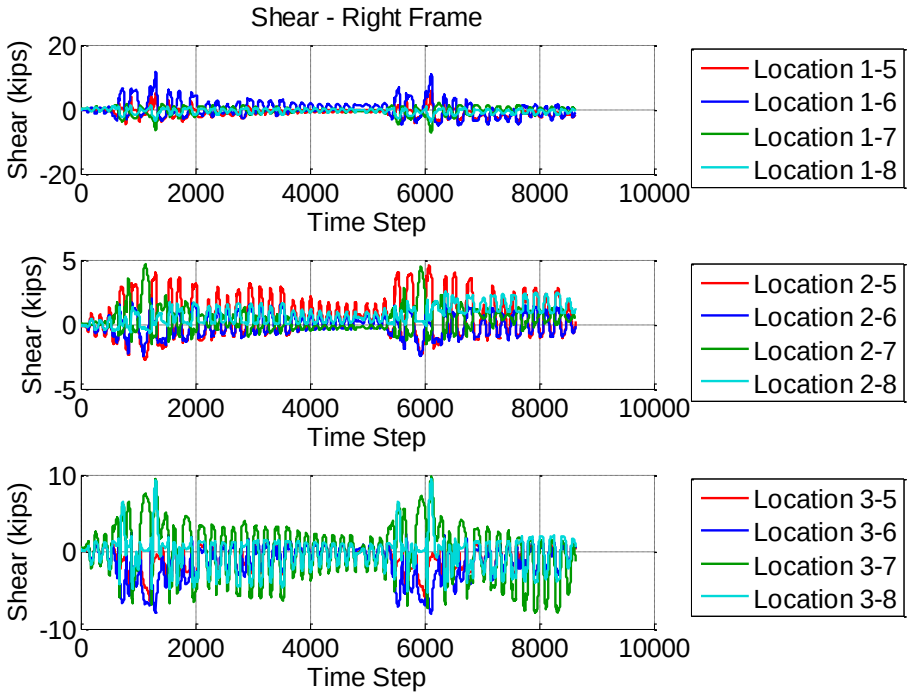

Figure D.105 Specimen A5 1.10xJMA Kobe Trials - Calculated Member Resultant Forces

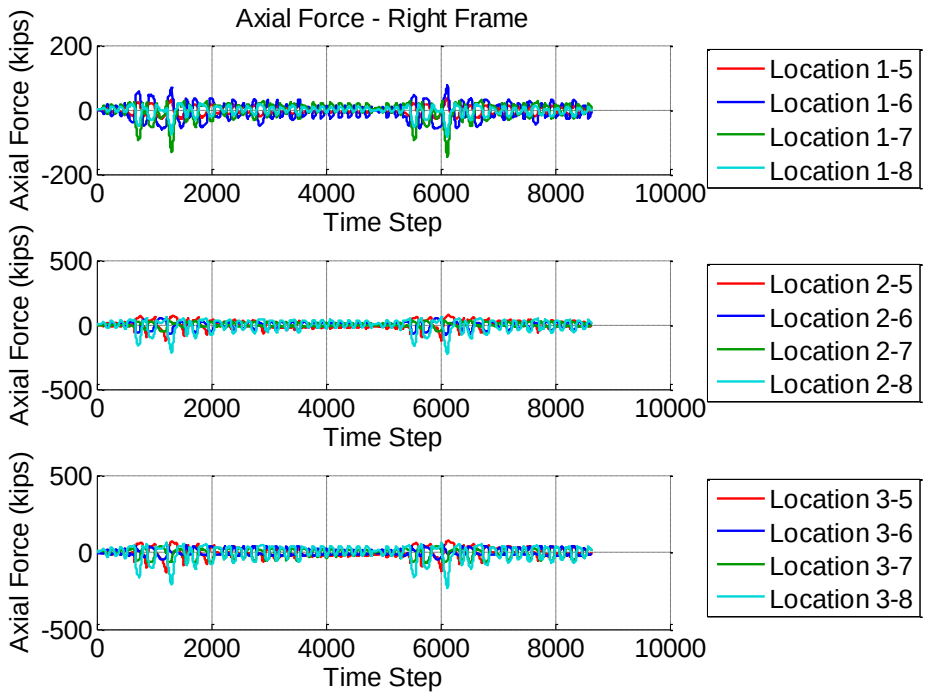

Figure D.106 Specimen A5 1.10xJMA Kobe Trials - Calculated Member Resultant Forces

D.6.5 Sum Forces at Each Section

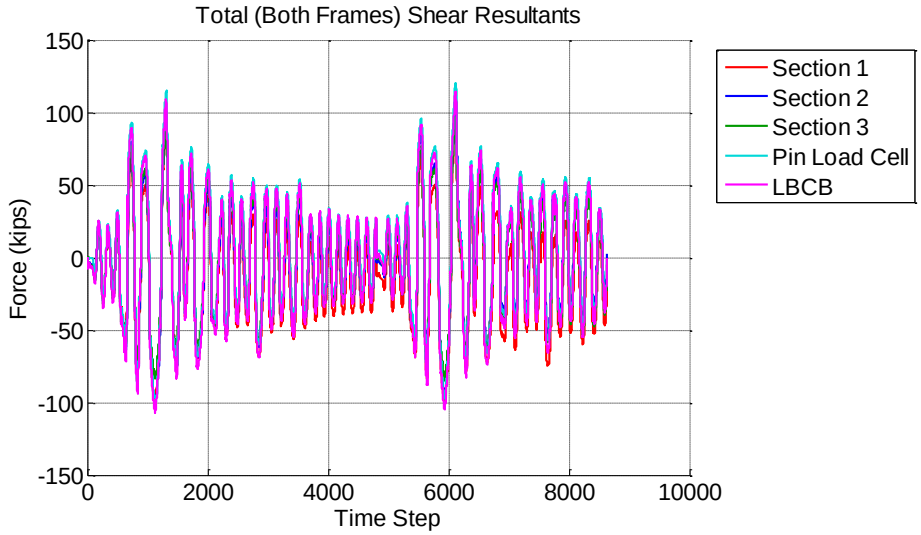

Figure D.107 Specimen A5 1.10xJMA Kobe Trials - Sum of the Shear Forces

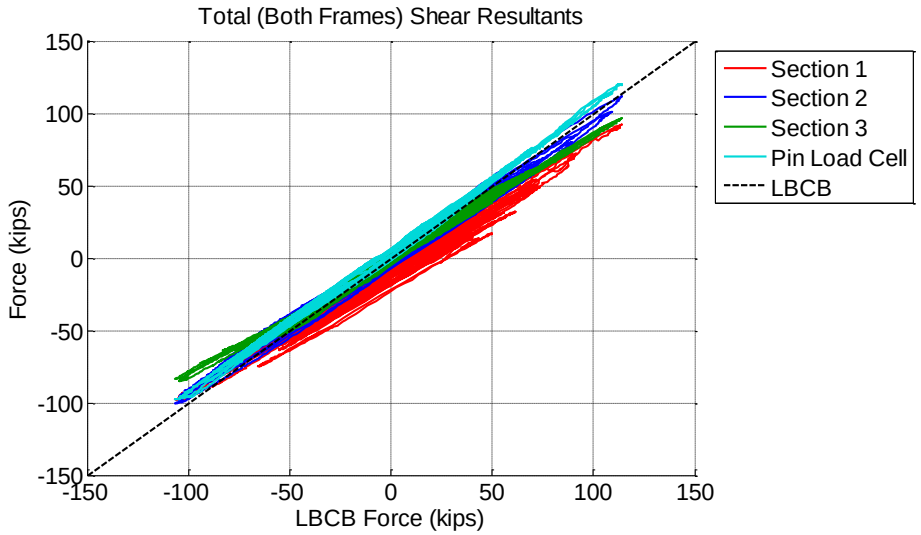

Figure D.108 Specimen A5 1.10xJMA Kobe Trials - Validation of Shear Forces Calculated From Strain-Gaged Sections

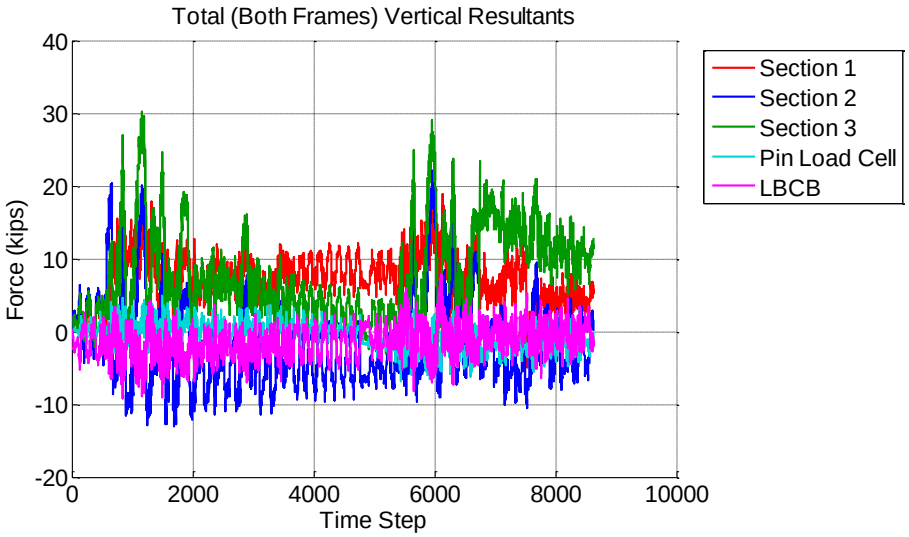

Figure D.109 Specimen A5 1.10xJMA Kobe Trials - Vertical Forces Calculated From Strain-Gaged Sections

D.7 Specimen A6 – MCE Trial

Notes on Data Reduction:

- All of the data for Specimen A6 was recorded with only 3 significant digits of precision as opposed to 7 significant digits which was used for all other tests. However, the data recorded by the NEES Data Turbine still had all seven significant digits. The Data Turbine data files were continuous data recorded at 1 Hz. The step data files were rebuilt from the Data Turbine files by selecting the appropriate records using the time stamps.

D.7.1 System Response

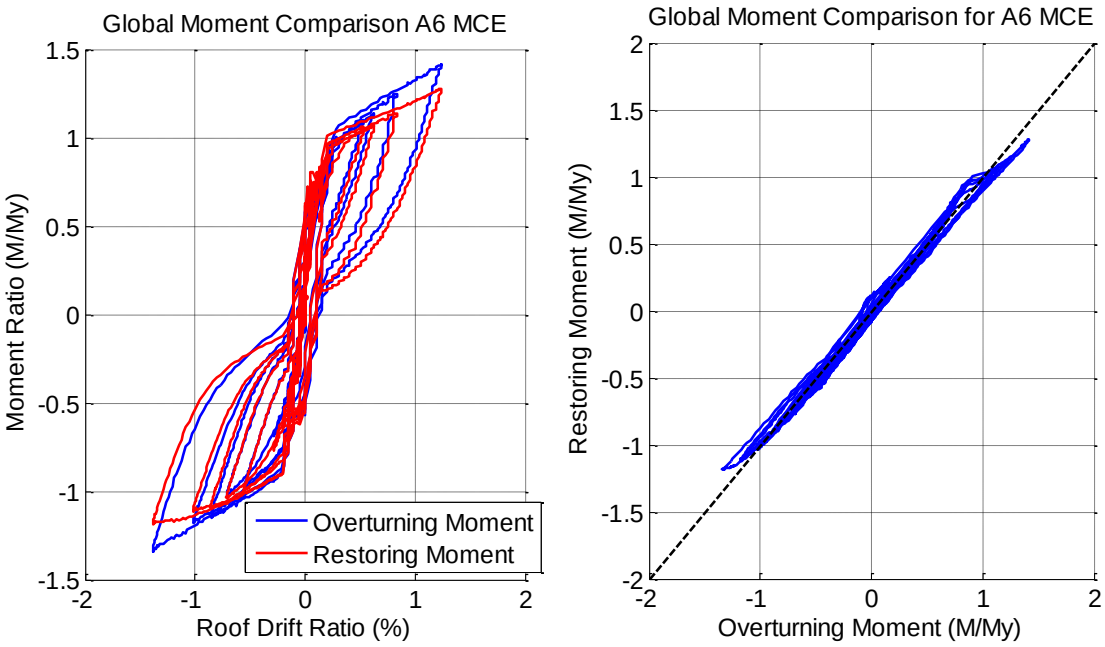

Figure D.110 Specimen A6 MCE - Comparing Restoring Moment to Applied Overturning Moment

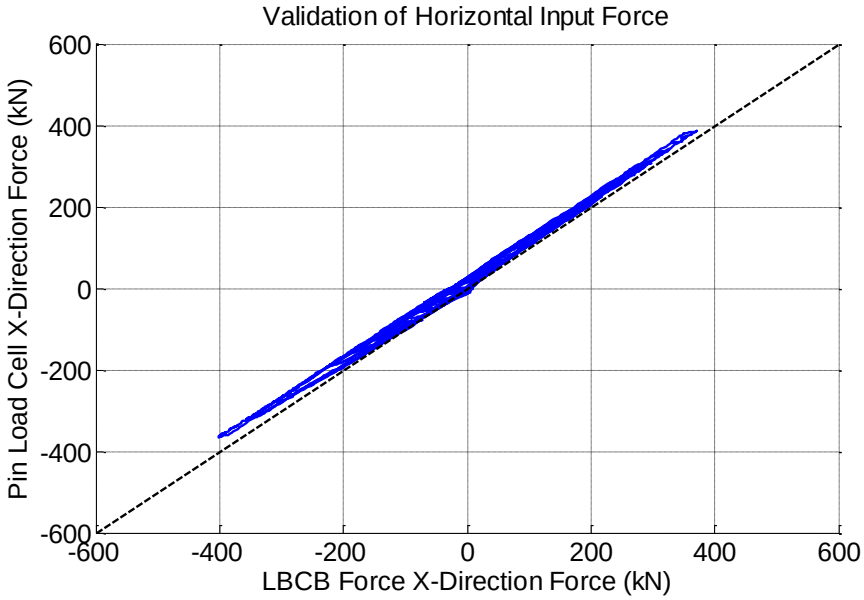

Figure D.111 Specimen A6 MCE - Validation of Horizontal Forces Applied to the Frames

D.7.2 Post-Tensioning Force Validation

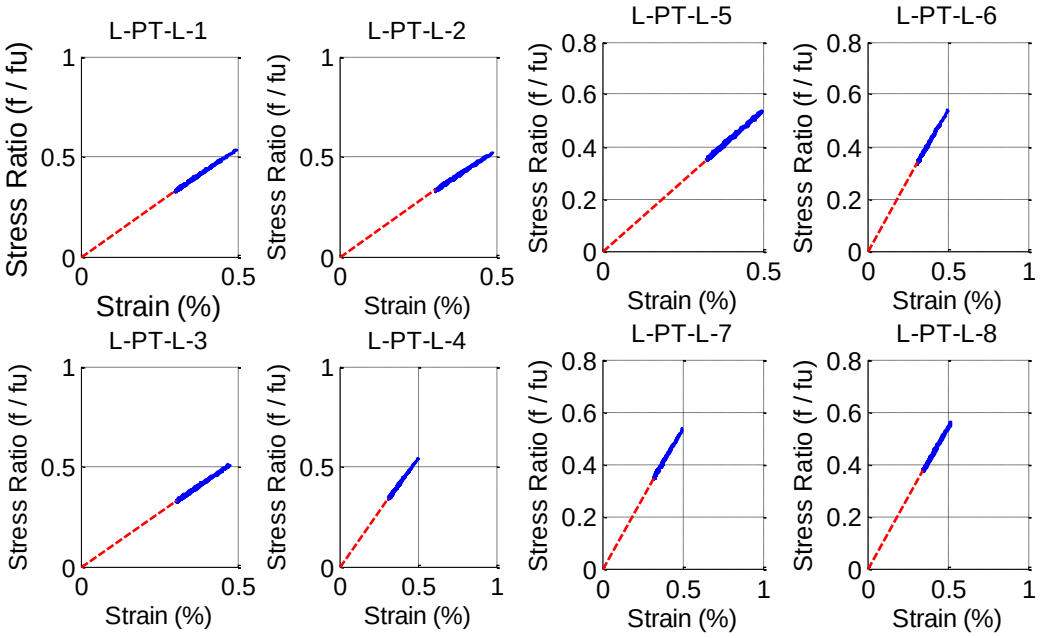

Figure D.112 Specimen A6 MCE - Post-Tensioning Stress-Strain Response

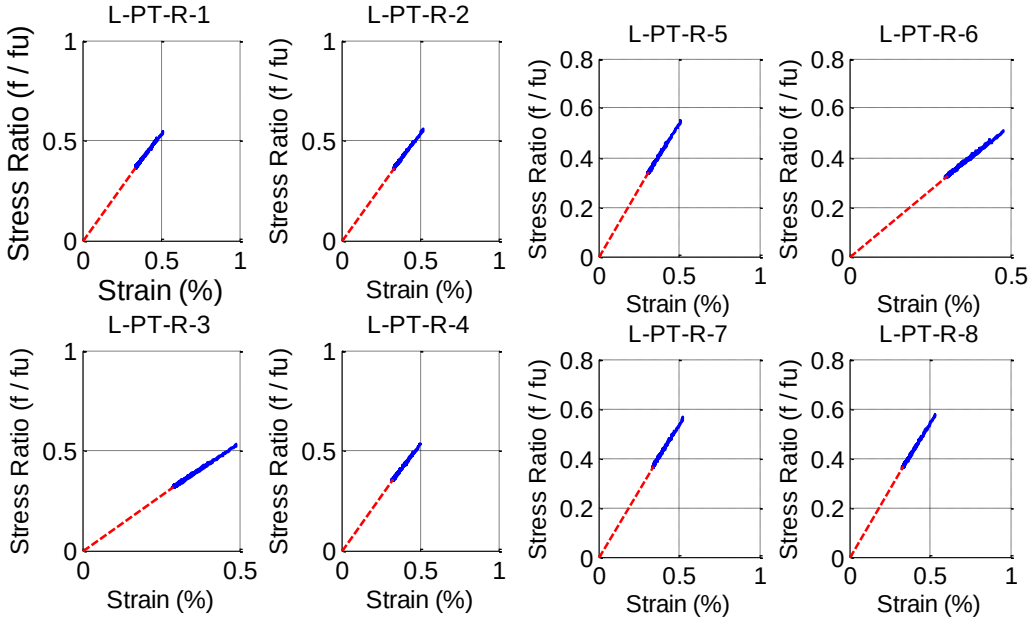

Figure D.113 Specimen A6 MCE - Post-Tensioning Stress-Strain Response

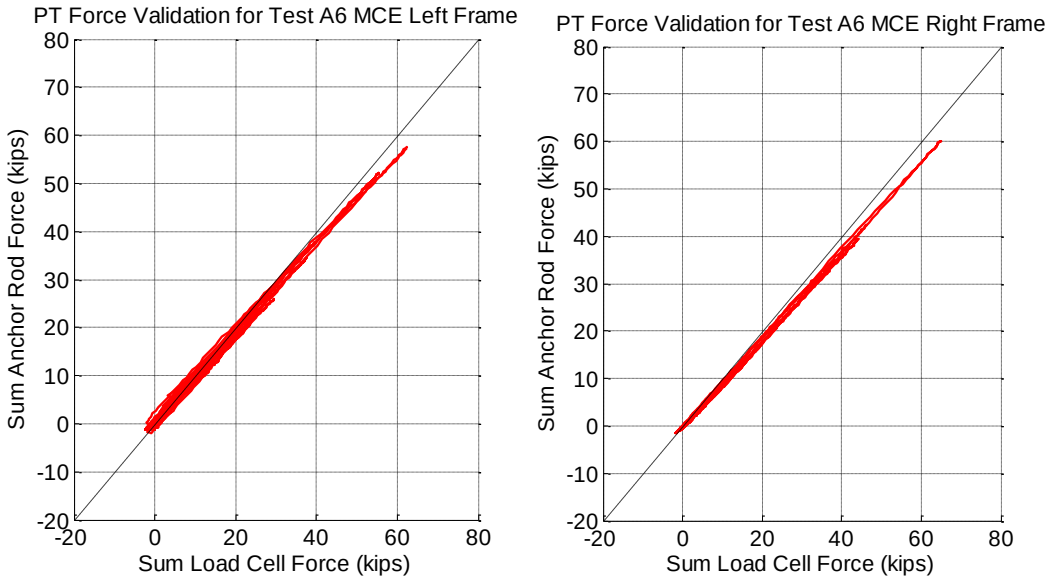

Figure D.114 Specimen A6 MCE - Validation of Post-Tensioning Forces

D.7.3 Data Validation for Fuse Response

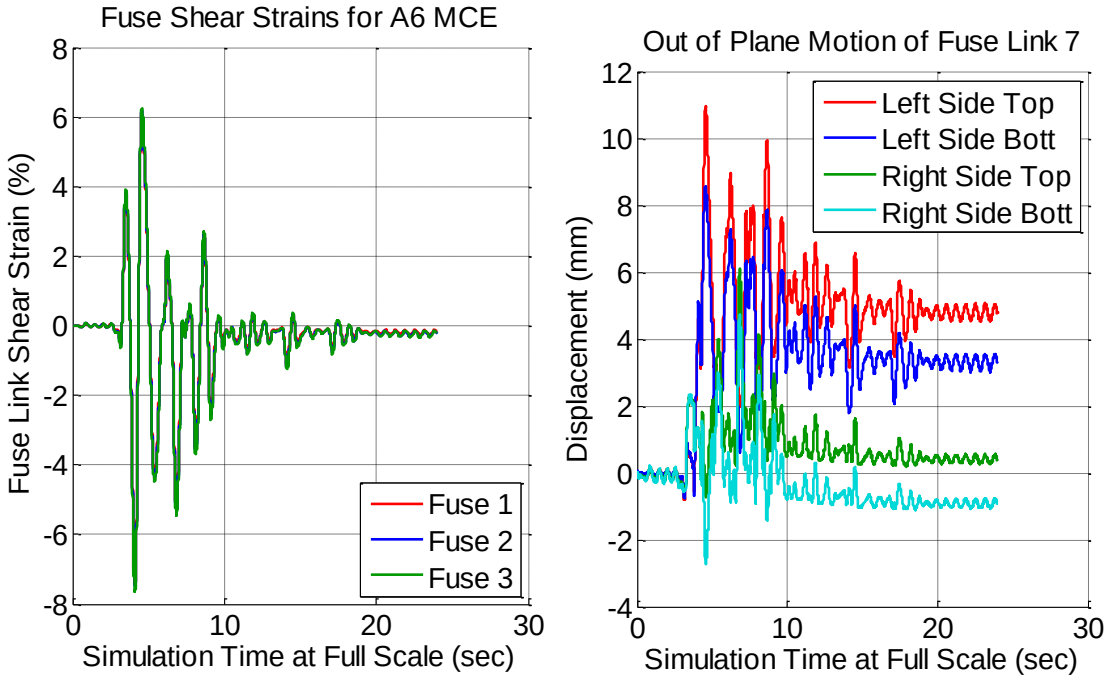

Figure D.115 Specimen A6 MCE - Fuse Link Shear Strain For All Three Floors (Left) Out-of-Plane Motion of Fuse Link Using Krypton (Right)

D.7.4 Motion of the System

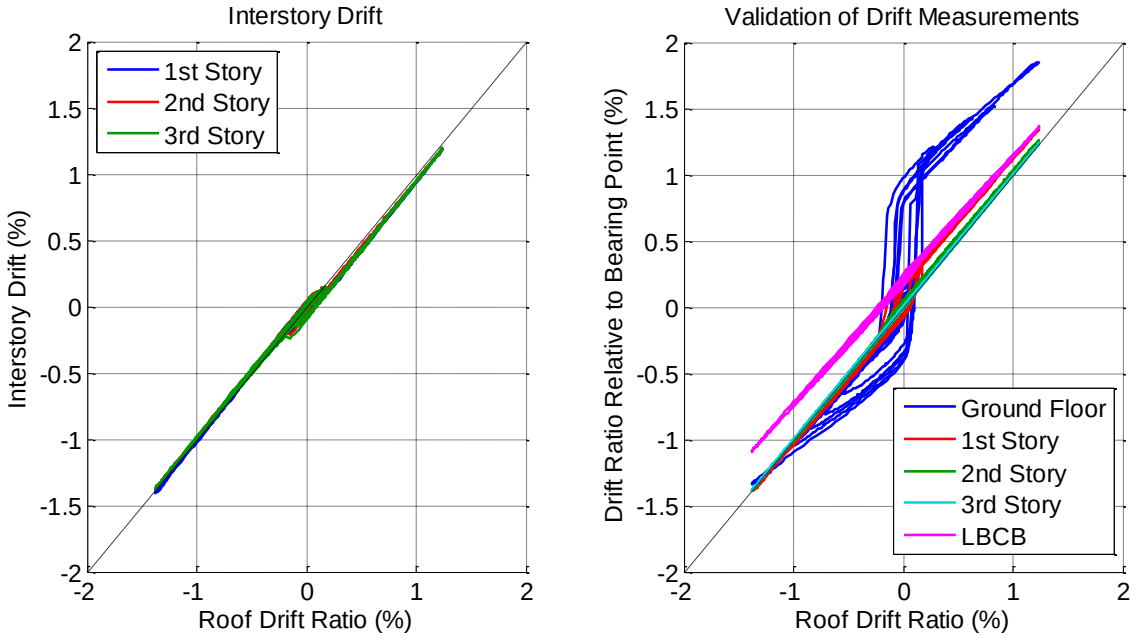

Figure D.116 Specimen A6 MCE - Interstory Drifts (Left) and Drift Ratios Relative to Base (Right)

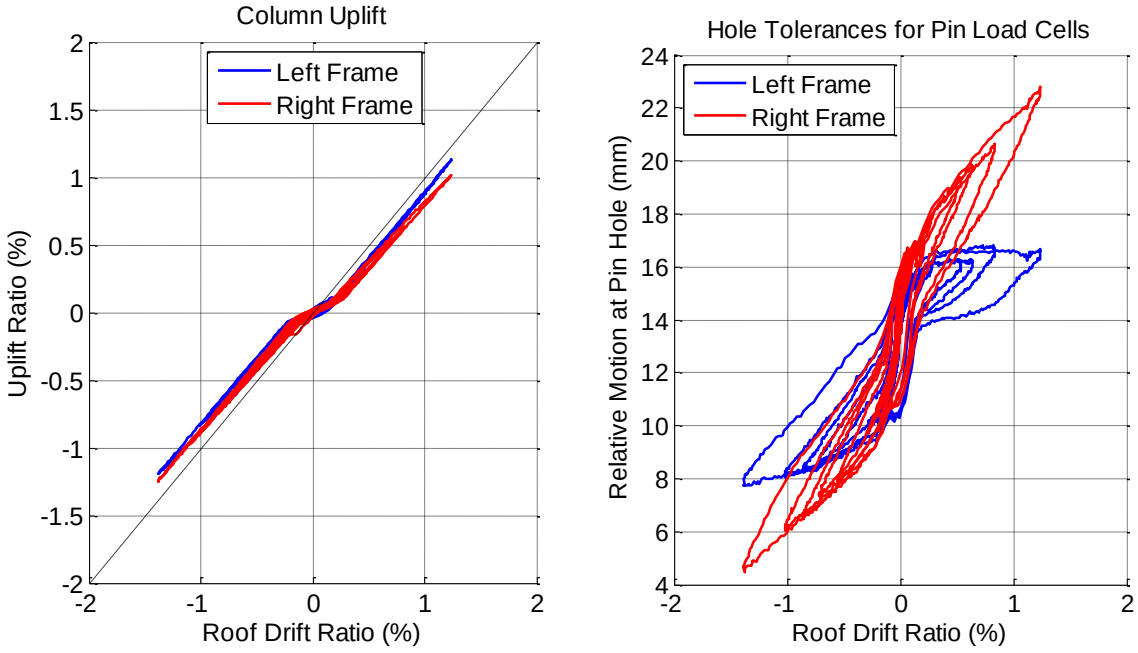

Figure D.117 Specimen A6 MCE - Pin Hole Tolerances for the Pin Load Cells (Left), and Uplift Ratio (Right)

D.7.5 Member Resultants

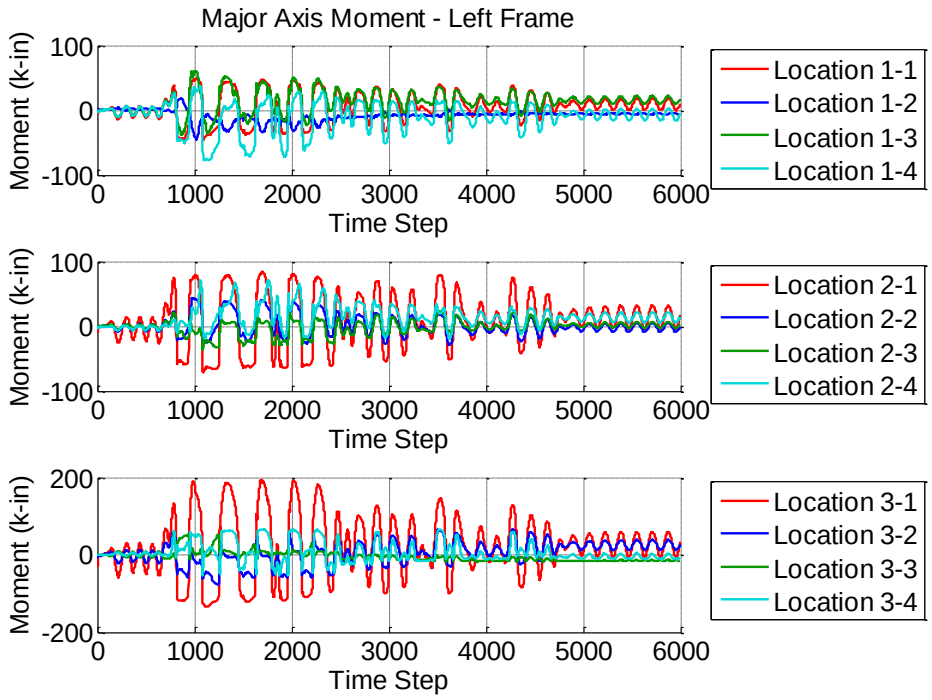

Figure D.118 Specimen A6 MCE - Calculated Member Resultant Forces

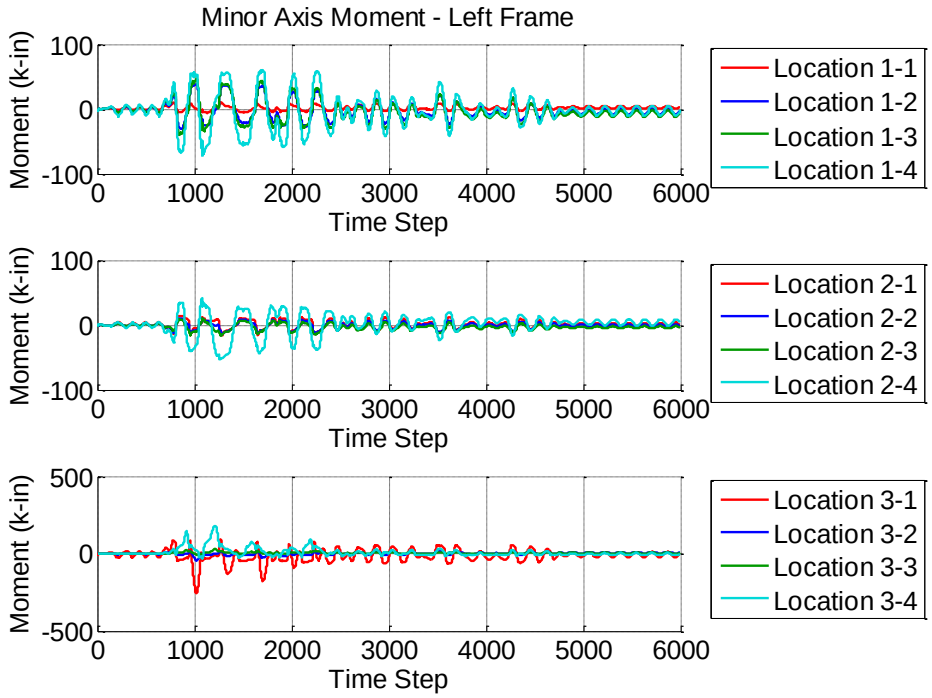

Figure D.119 Specimen A6 MCE - Calculated Member Resultant Forces

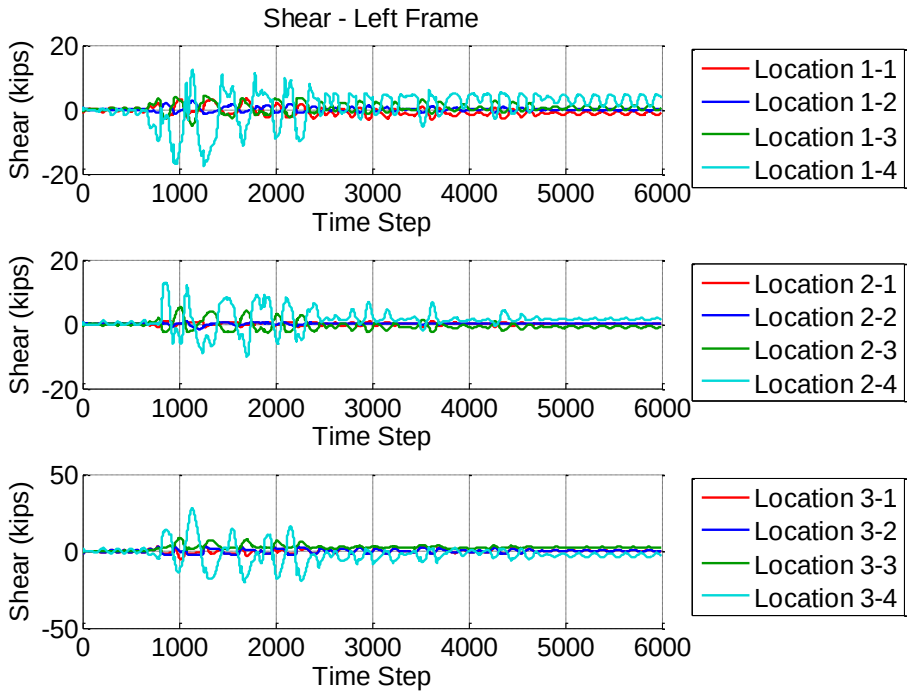

Figure D.120 Specimen A6 MCE - Calculated Member Resultant Forces

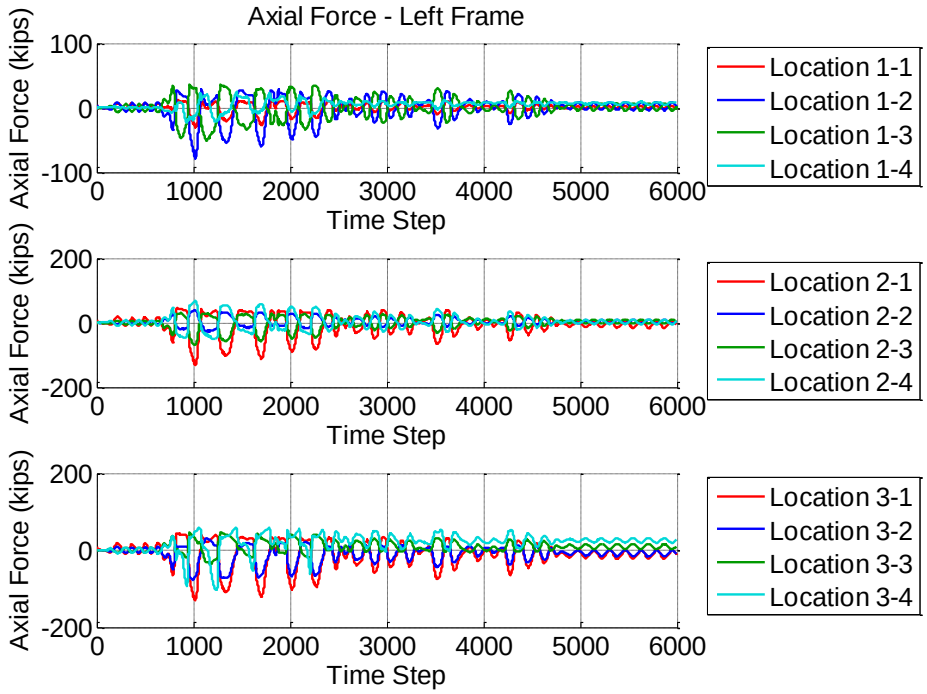

Figure D.121 Specimen A6 MCE - Calculated Member Resultant Forces

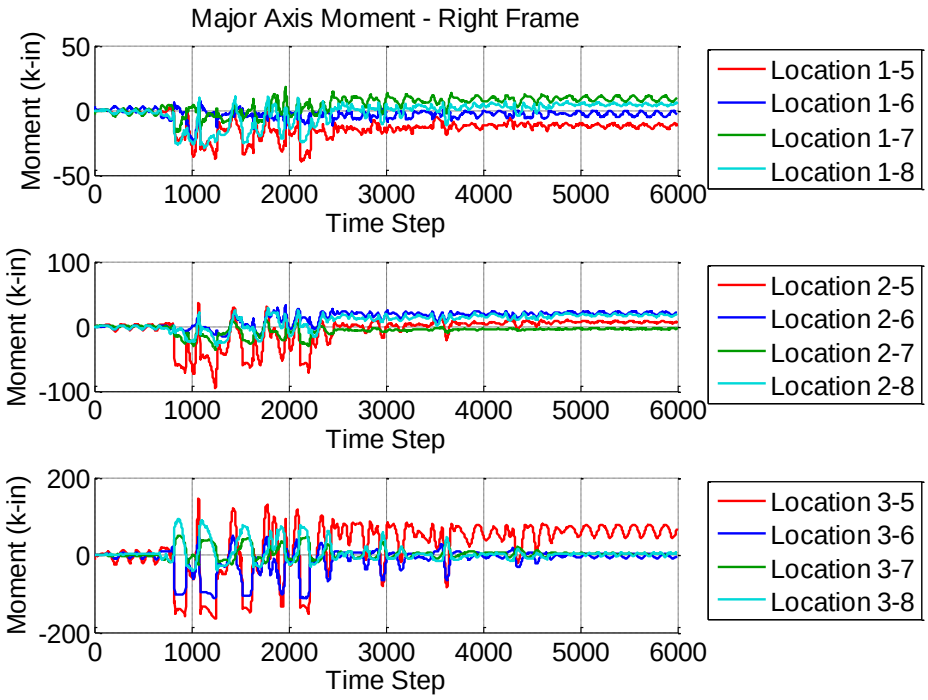

Figure D.122 Specimen A6 MCE - Calculated Member Resultant Forces

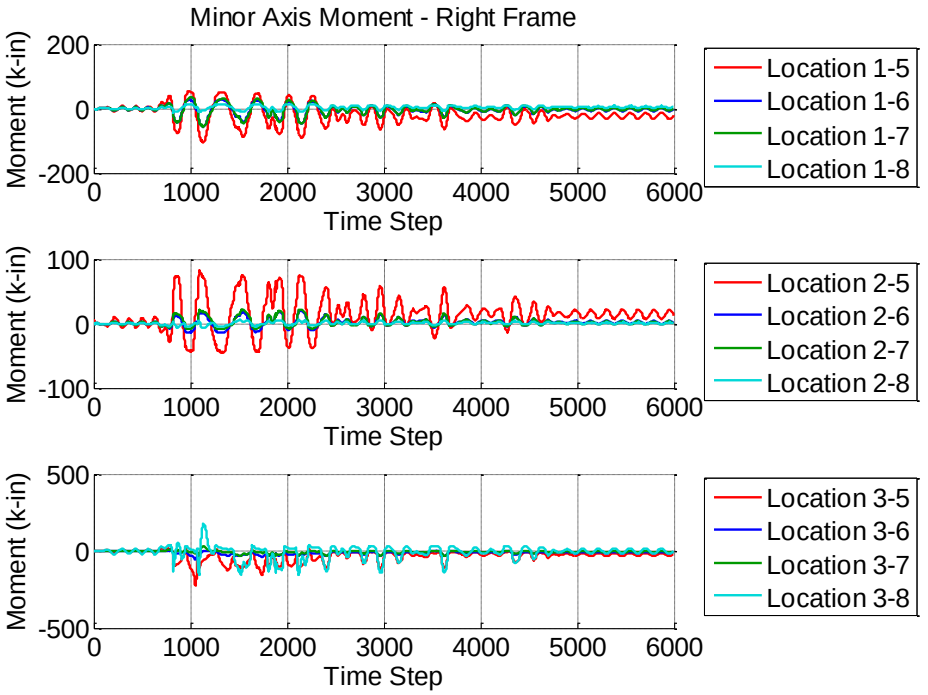

Figure D.123 Specimen A6 MCE - Calculated Member Resultant Forces

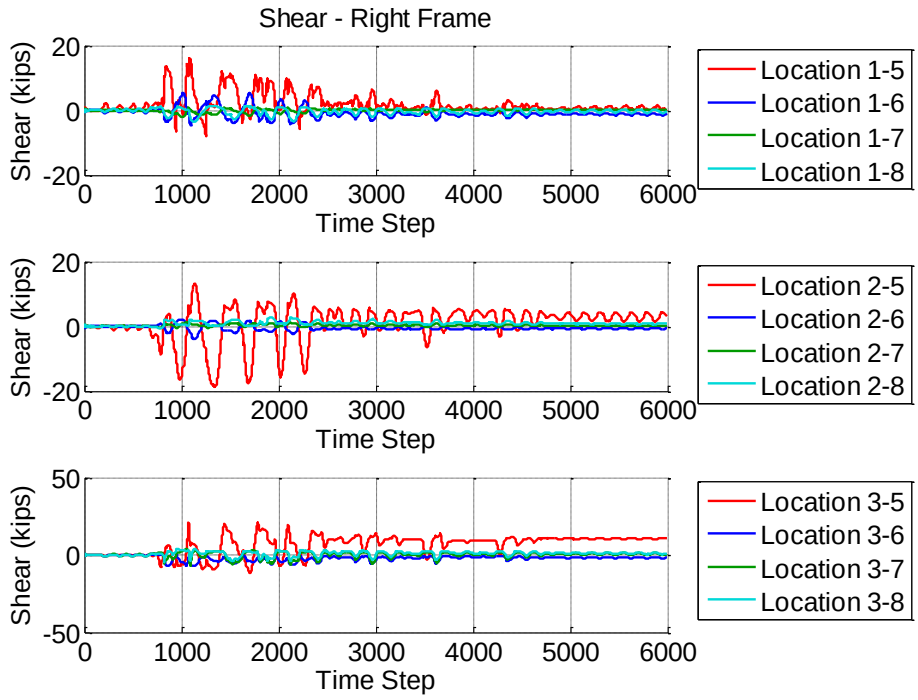

Figure D.124 Specimen A6 MCE - Calculated Member Resultant Forces

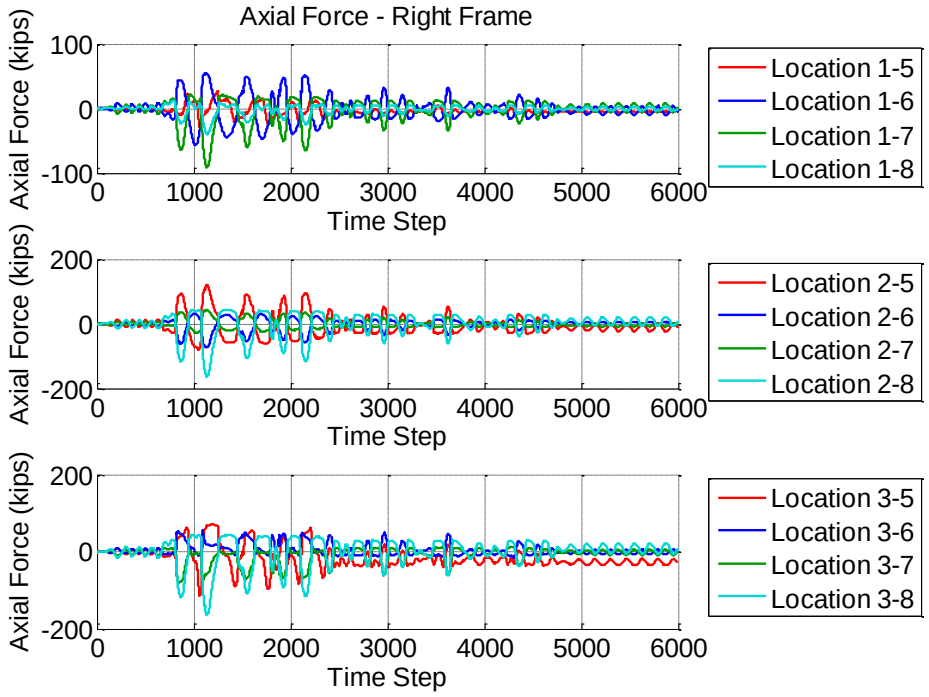

Figure D.125 Specimen A6 MCE - Calculated Member Resultant Forces

D.7.6 Sum Forces at Each Section

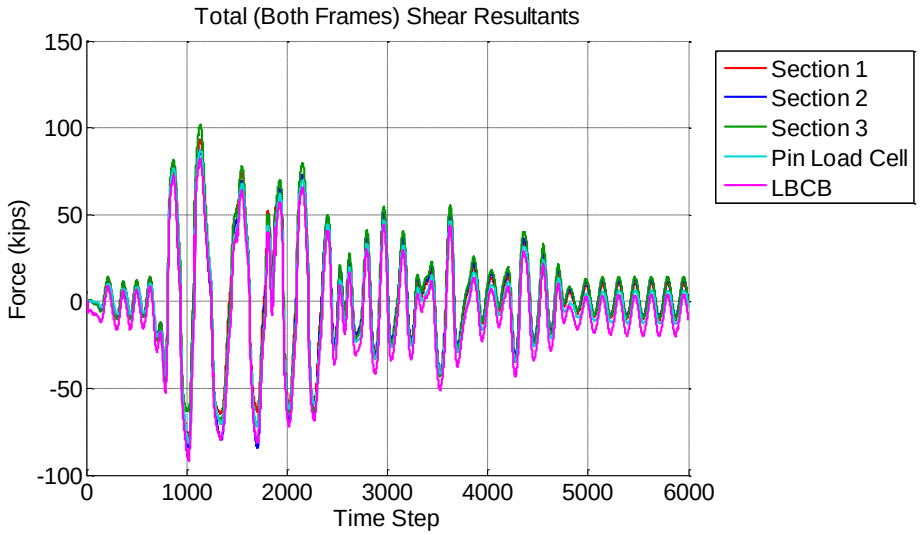

Figure D.126 Specimen A6 MCE - Sum of the Shear Forces

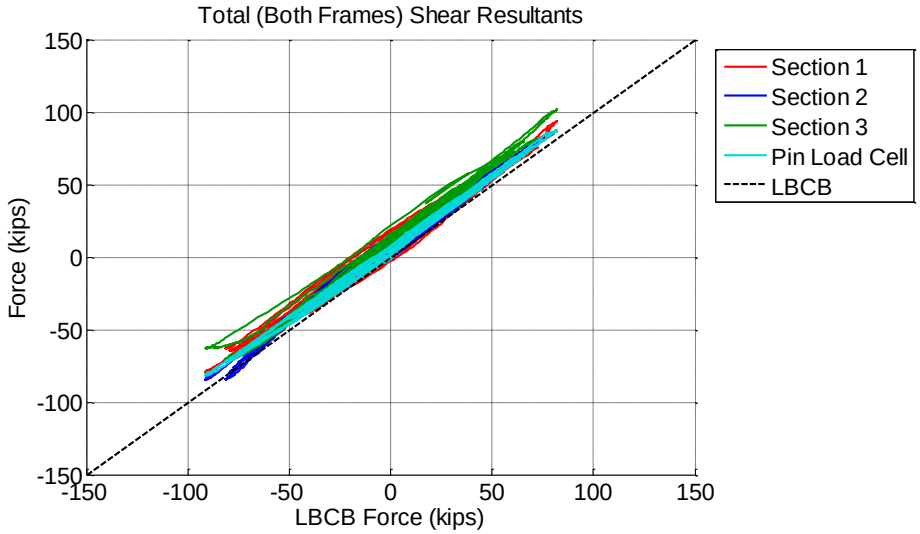

Figure D.127 Specimen A6 MCE - Validation of Shear Forces Calculated From Strain-Gaged Sections

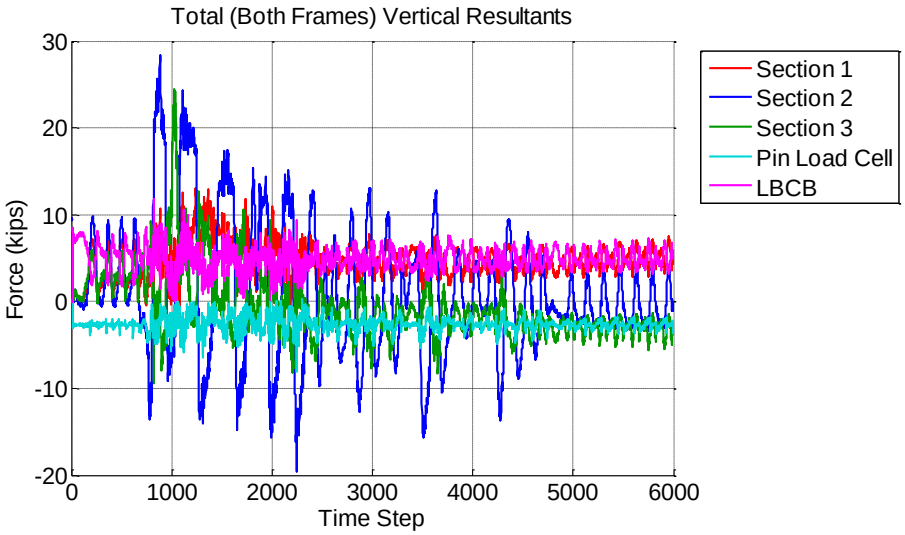

Figure D.128 Specimen A6 MCE - Vertical Forces Calculated From Strain-Gaged Sections

D.8 Specimen A6 – MCE Trial with Out-of-Plane Motion

Notes on Data Reduction:

- All of the data for Specimen A6 MCE trial with out-of-plane motion was recorded with only 3 significant digits of precision as opposed to 7 significant digits which was used for all other tests. The plots for this trial appear jagged as a result.
- The MCE with out of plane motion trial was started, stopped, and restarted. The first 1110 data points in the MCE with OOP set are discarded, but are left in for the member resultant plots.

D.8.1 System Response

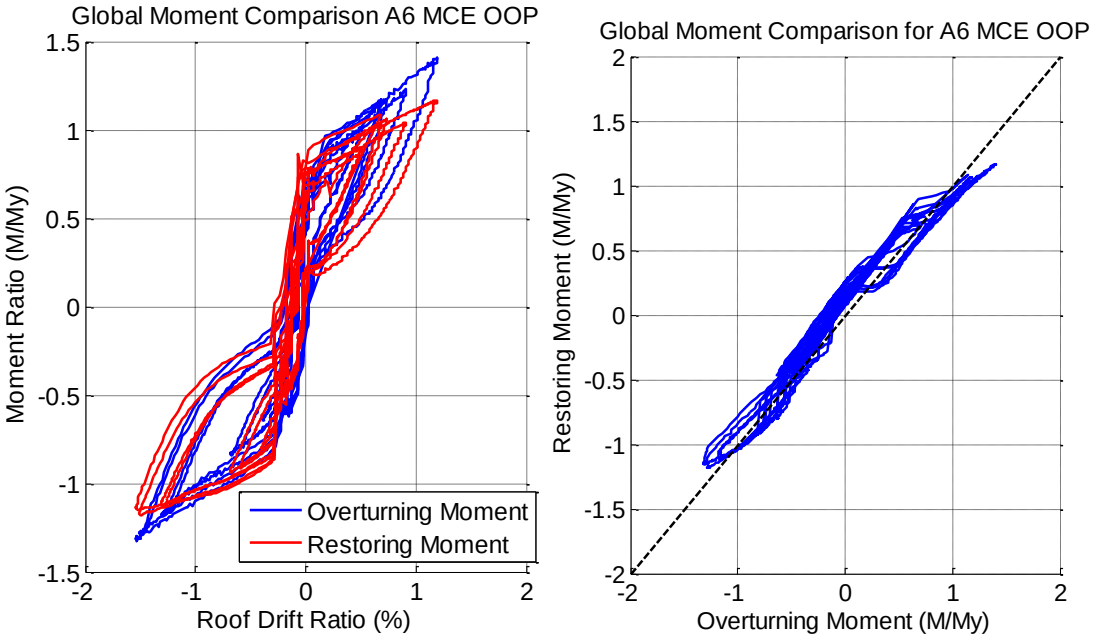

Figure D.129 Specimen A6 MCE with OOP Trial - Comparing Restoring Moment to Applied Overturning Moment

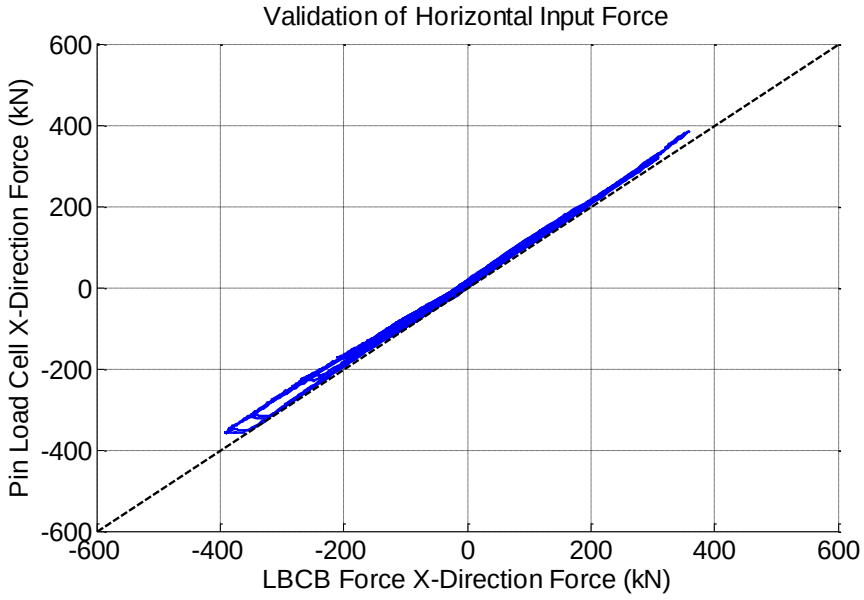

Figure D.130 Specimen A6 MCE with OOP Trial - Validation of Horizontal Forces Applied to the Frames

D.8.2 Post-Tensioning Force Validation

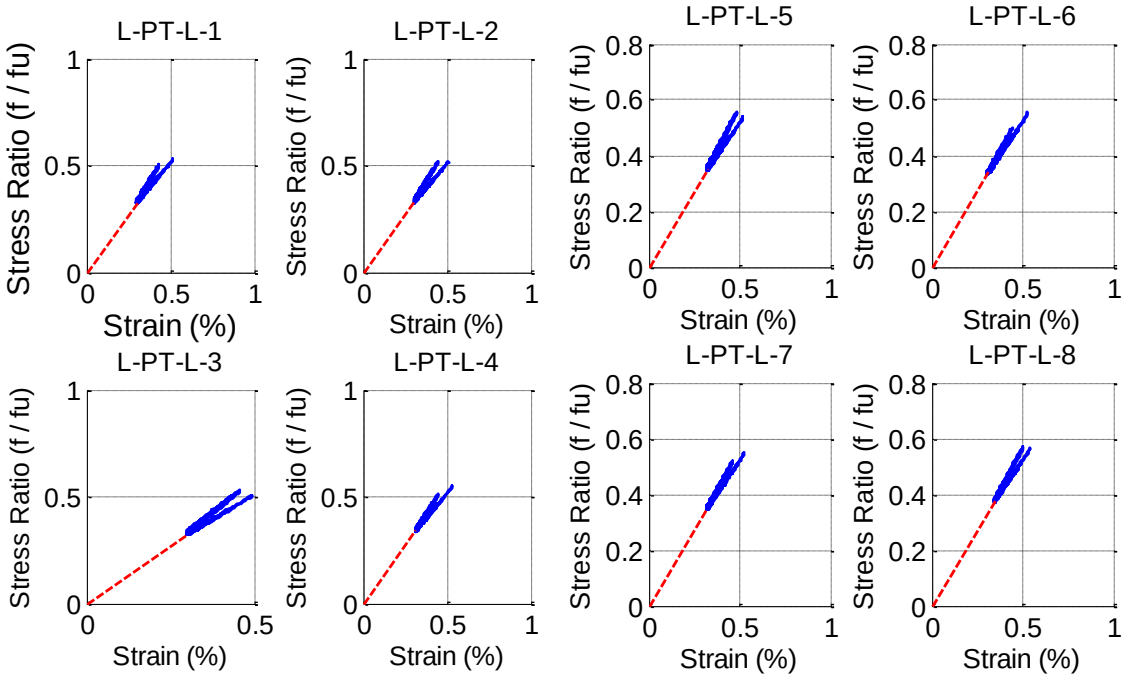

Figure D.131 Specimen A6 MCE with OOP Trial - Post-Tensioning Stress-Strain Response

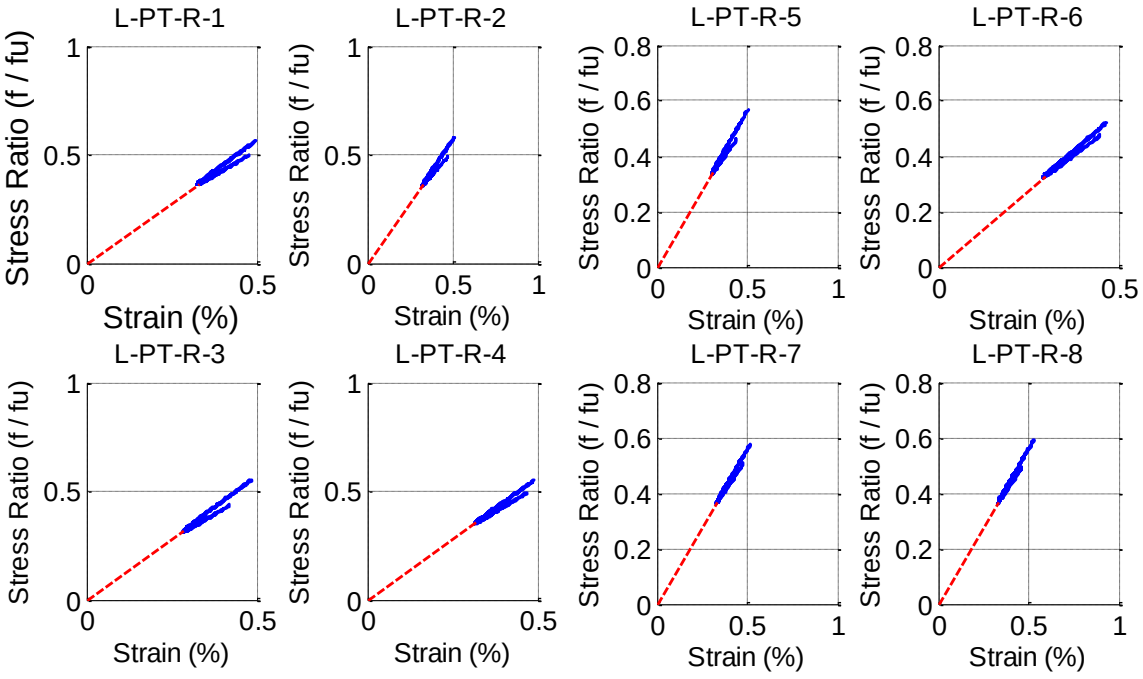

Figure D.132 Specimen A6 MCE with OOP Trial - Post-Tensioning Stress-Strain Response

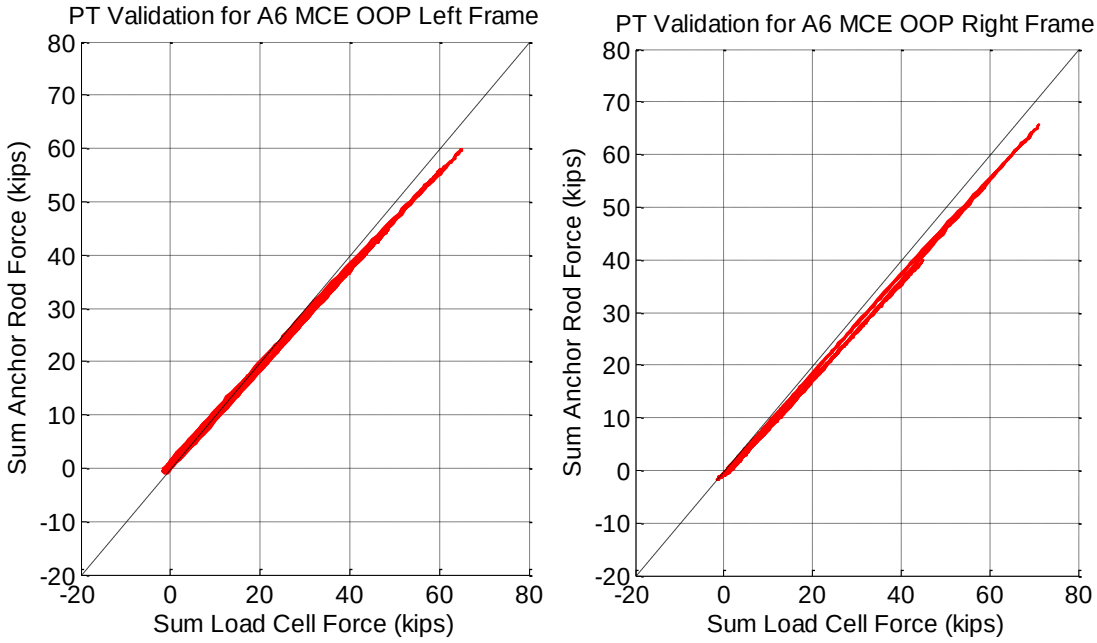

Figure D.133 Specimen A6 MCE with OOP Trial - Validation of Post-Tensioning Forces

D.8.3 Data Validation for Fuse Response

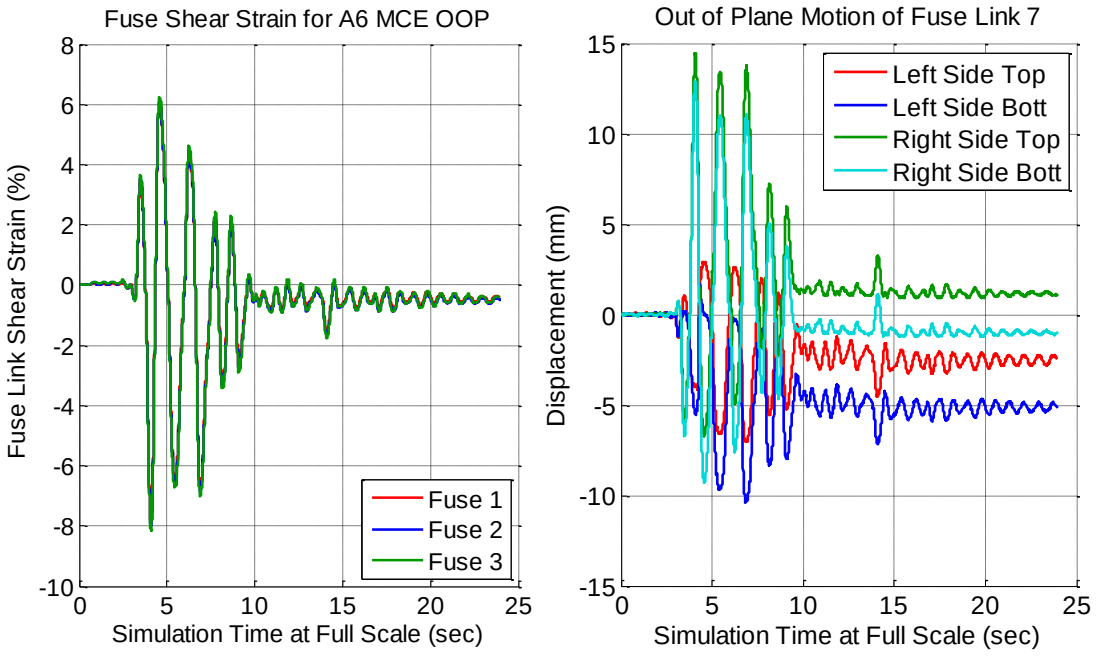

Figure D.134 Specimen A6 MCE with OOP Trial - Fuse Link Shear Strain For All Three Floors (Left) Out-of-Plane Motion of Fuse Link Using Krypton (Right)

D.8.4 Motion of the System

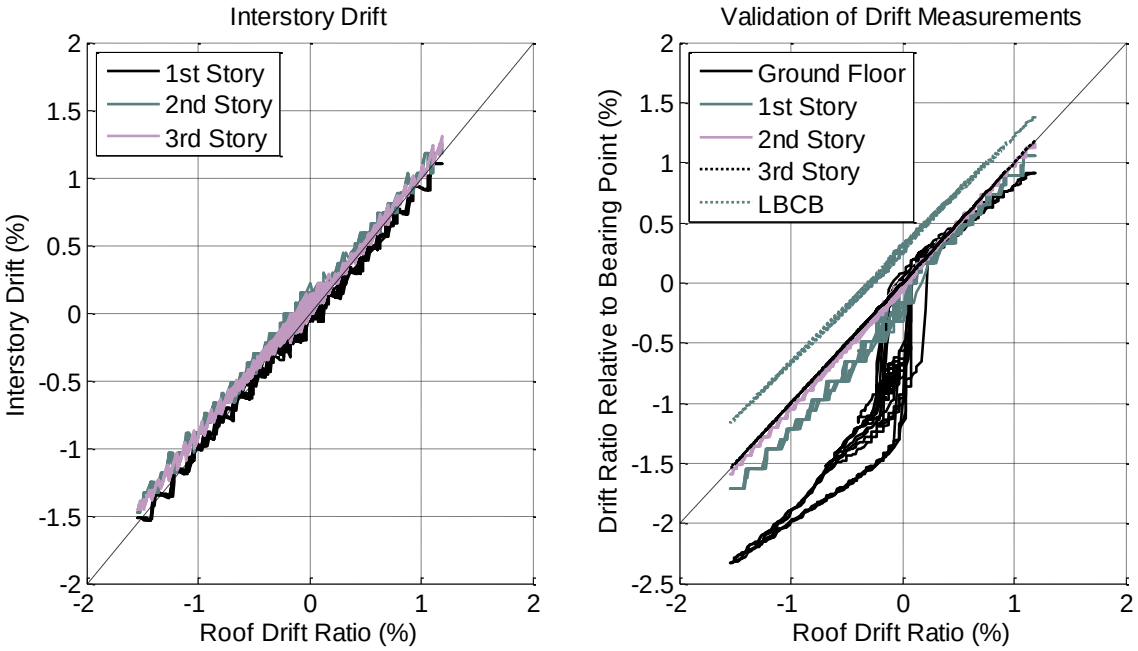

Figure D.135 Specimen A6 MCE with OOP Trial - Interstory Drifts (Left) and Drift Ratios Relative to Base (Right)

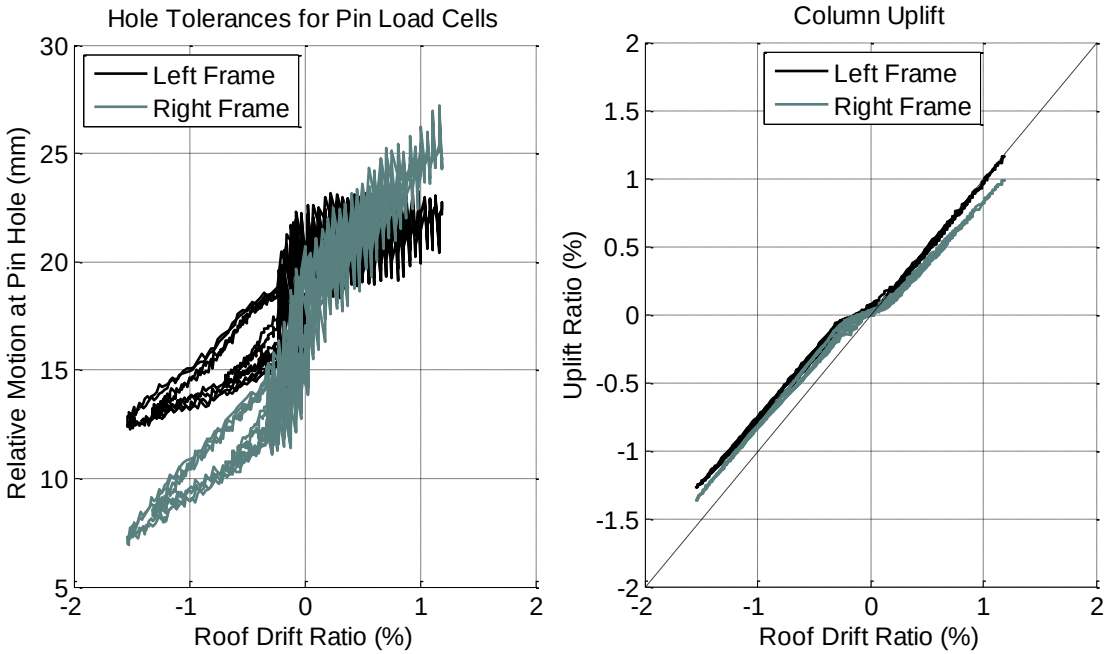

Figure D.136 Specimen A6 MCE with OOP Trial - Pin Hole Tolerances for the Pin Load Cells (Left), and Uplift Ratio (Right)

D.8.5 Member Resultants

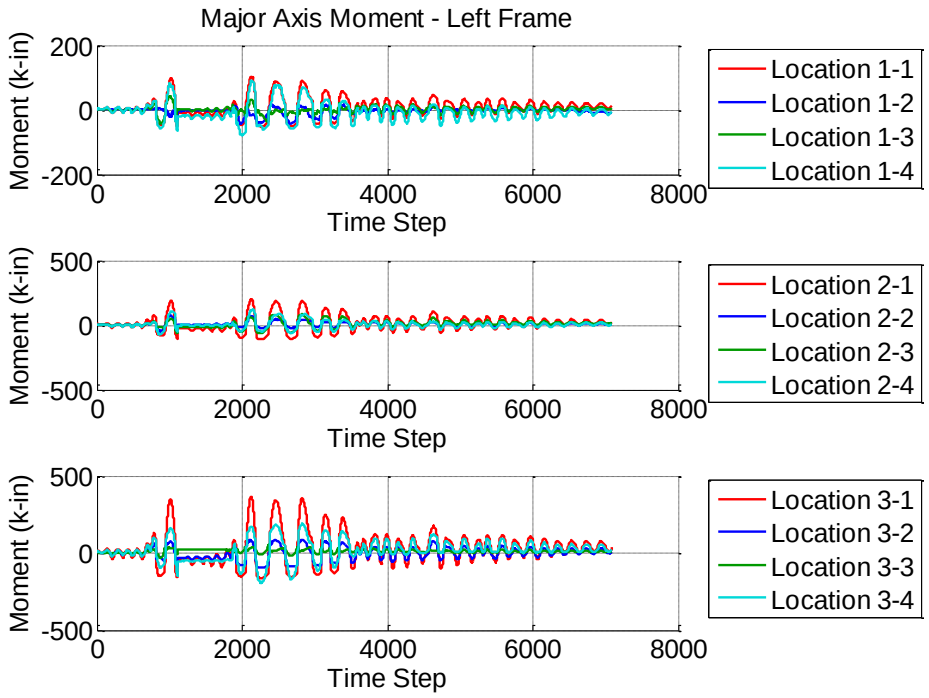

Figure D.137 Specimen A6 MCE with OOP Trial - Calculated Member Resultant Forces

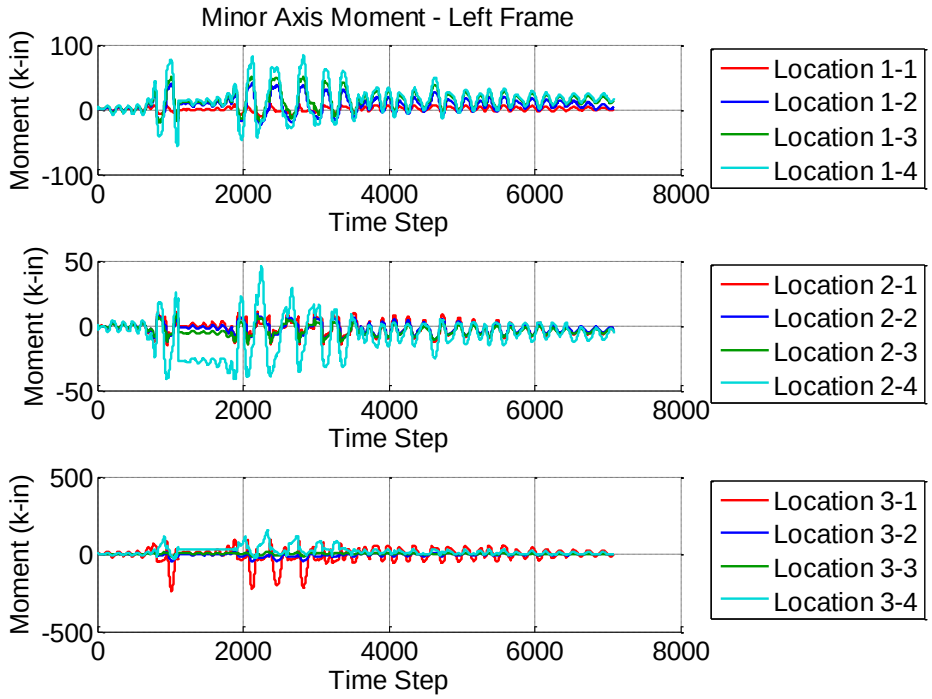

Figure D.138 Specimen A6 MCE with OOP Trial - Calculated Member Resultant Forces

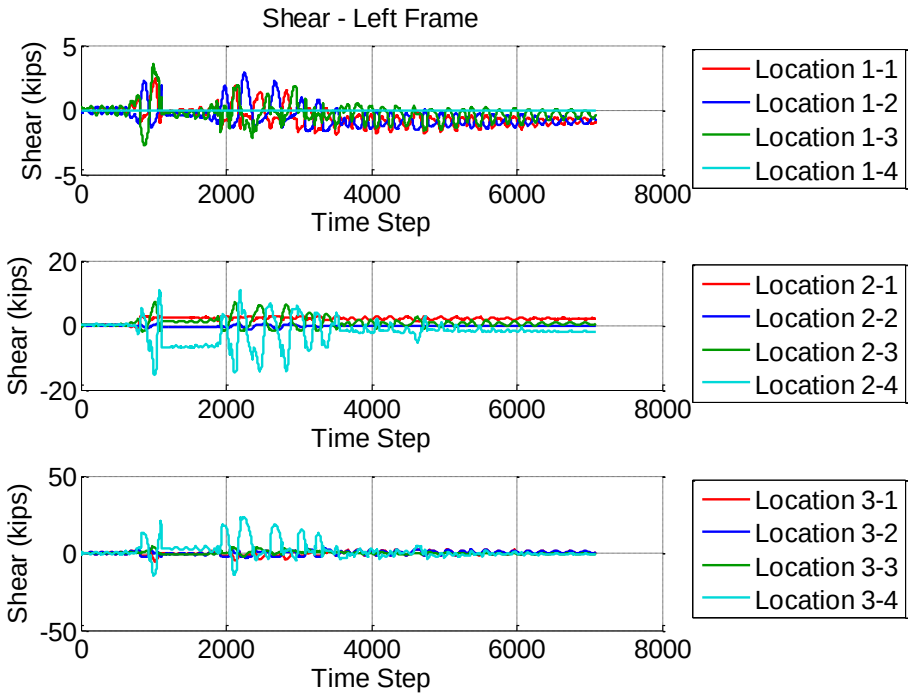

Figure D.139 Specimen A6 MCE with OOP Trial - Calculated Member Resultant Forces

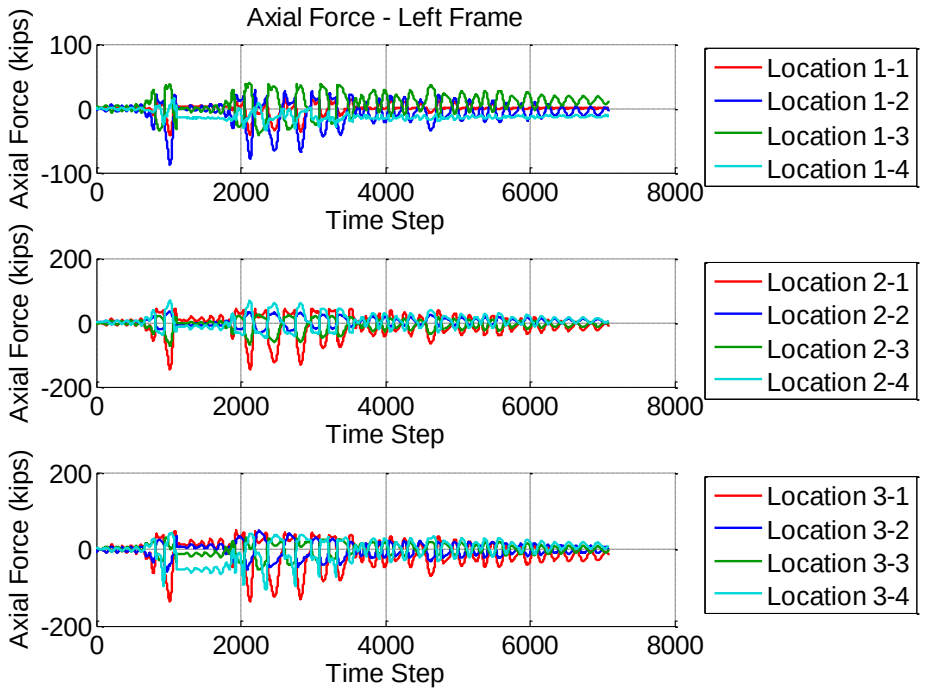

Figure D.140 Specimen A6 MCE with OOP Trial - Calculated Member Resultant Forces

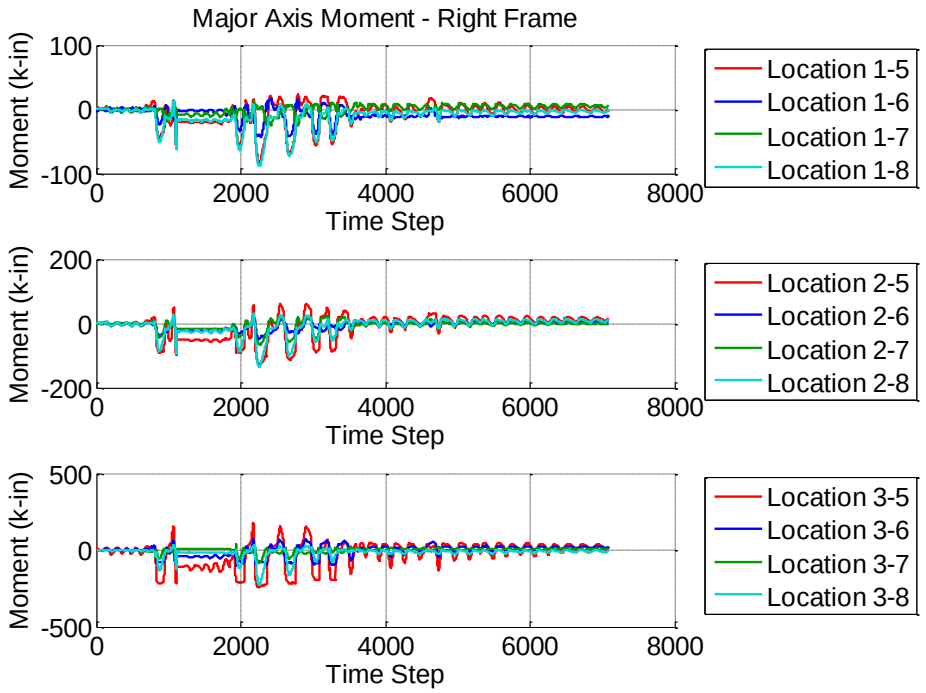

Figure D.141 Specimen A6 MCE with OOP Trial - Calculated Member Resultant Forces

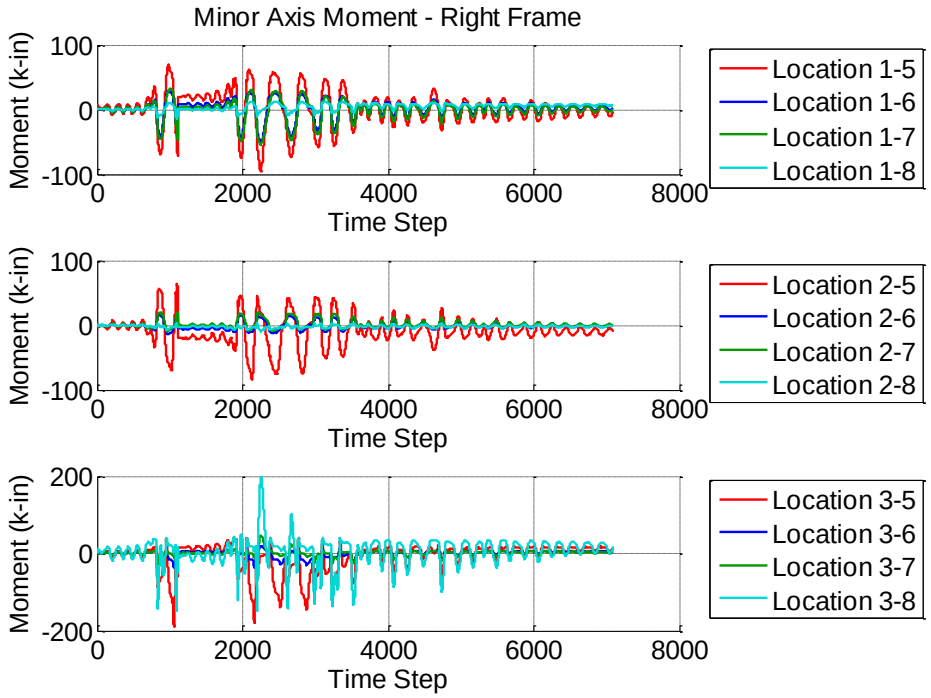

Figure D.142 Specimen A6 MCE with OOP Trial - Calculated Member Resultant Forces

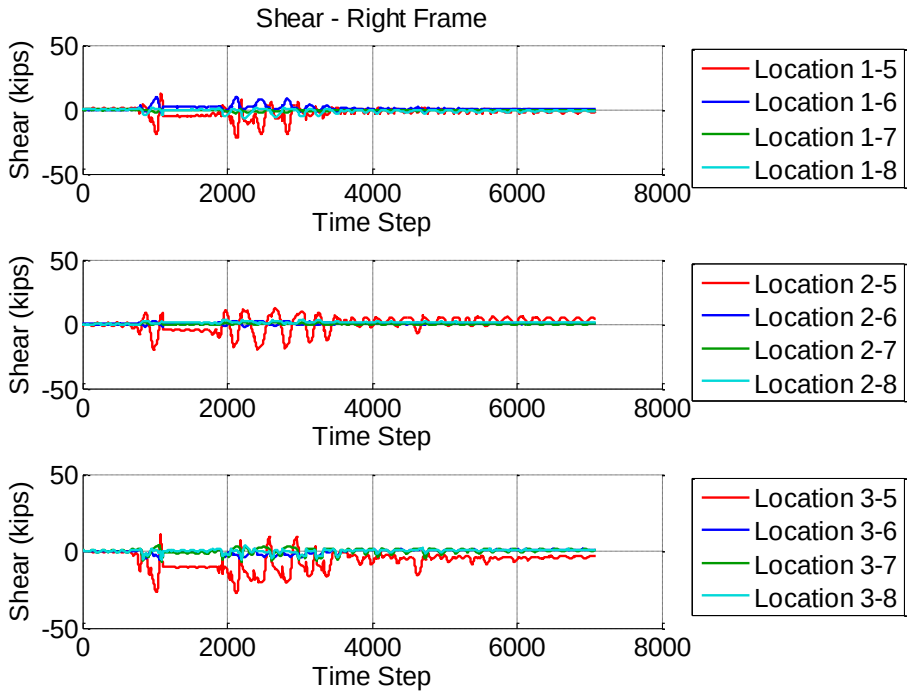

Figure D.143 Specimen A6 MCE with OOP Trial - Calculated Member Resultant Forces

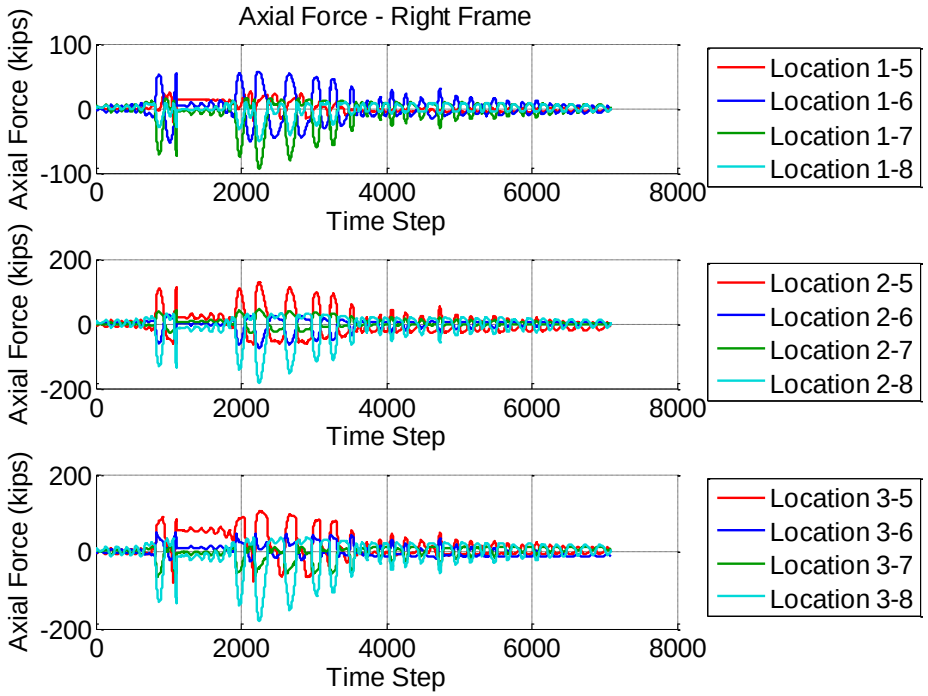

Figure D.144 Specimen A6 MCE with OOP Trial - Calculated Member Resultant Forces

D.8.6 Sum Forces at Each Section

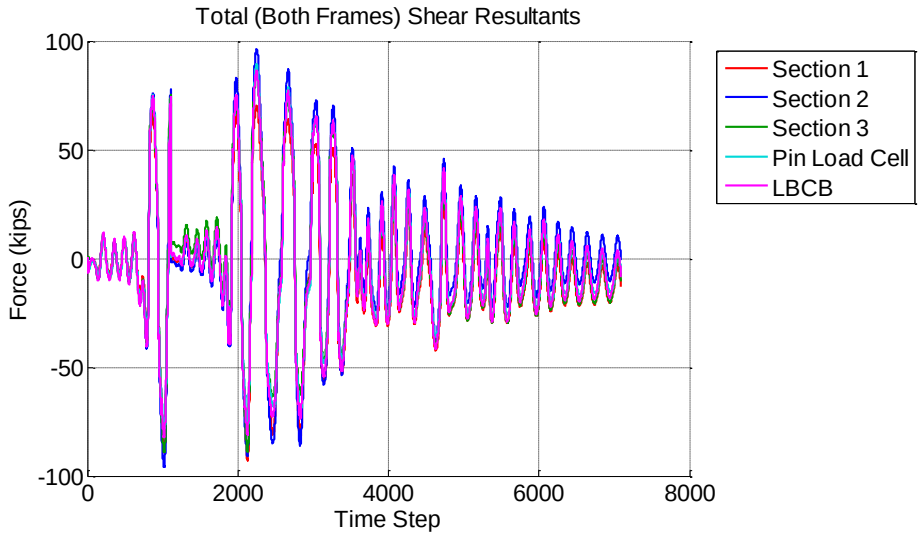

Figure D.145 Specimen A6 MCE with OOP Trial - Sum of the Shear Forces

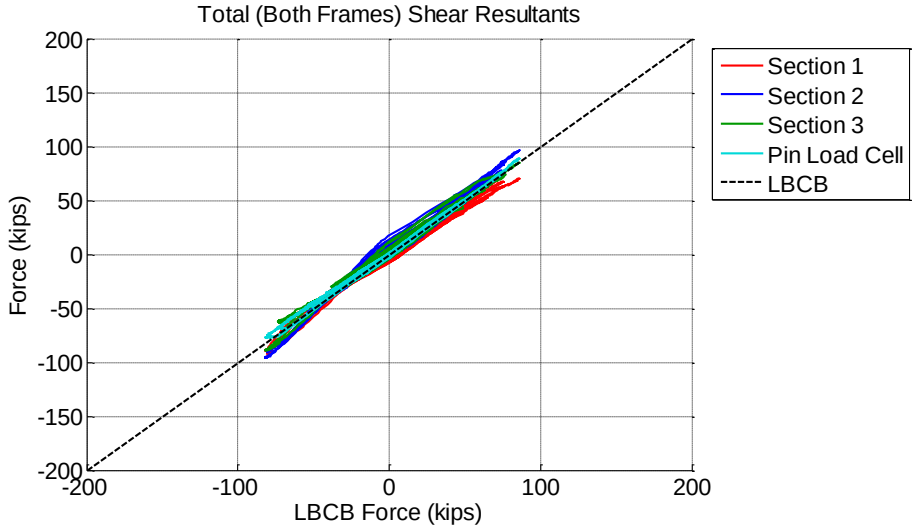

Figure D.146 Specimen A6 MCE with OOP Trial - Validation of Shear Forces Calculated From Strain-Gaged Sections

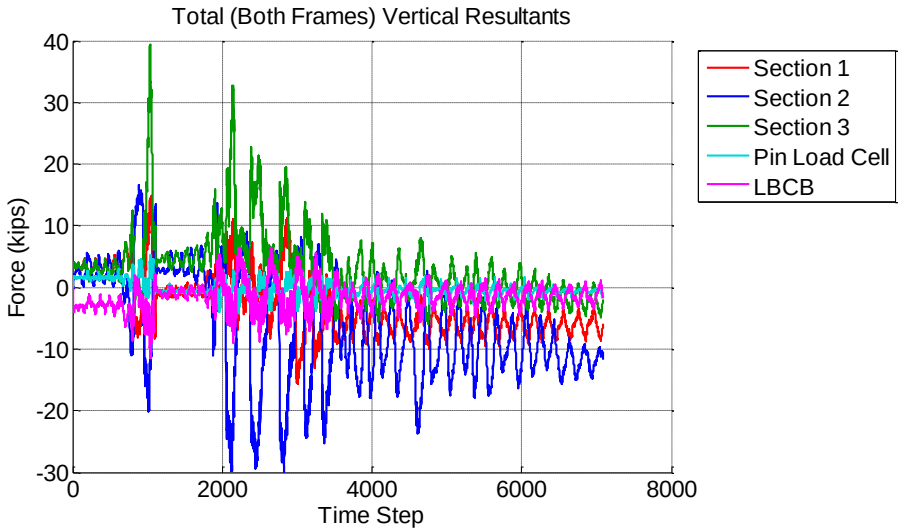

Figure D.147 Specimen A6 MCE with OOP Trial - Vertical Forces Calculated From Strain-Gaged Sections

D.9 Specimen A6 – 1.20 x JMA Kobe Trial

D.9.1 System Response

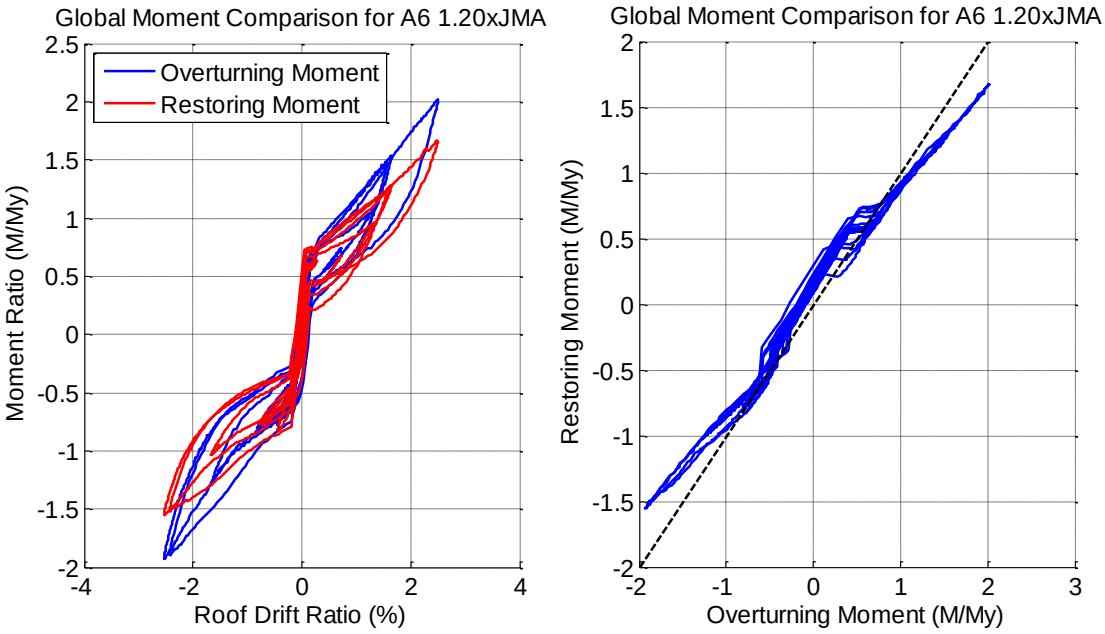

Figure D.148 Specimen A6 1.20xJMA Kobe Trial - Comparing Restoring Moment to Applied Overturning Moment

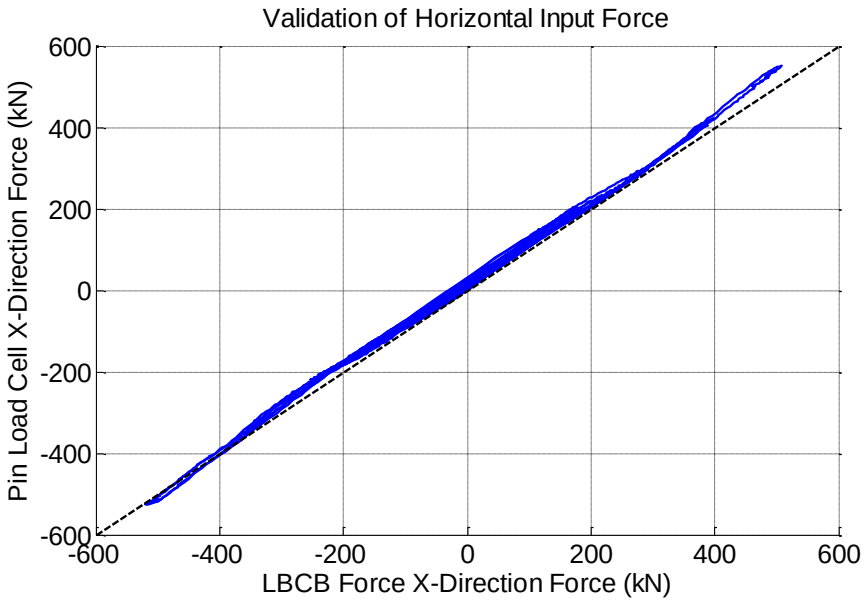

Figure D.149 Specimen A6 1.20xJMA Kobe Trial - Validation of Horizontal Forces Applied to the Frames

D.9.2 Post-Tensioning Force Validation

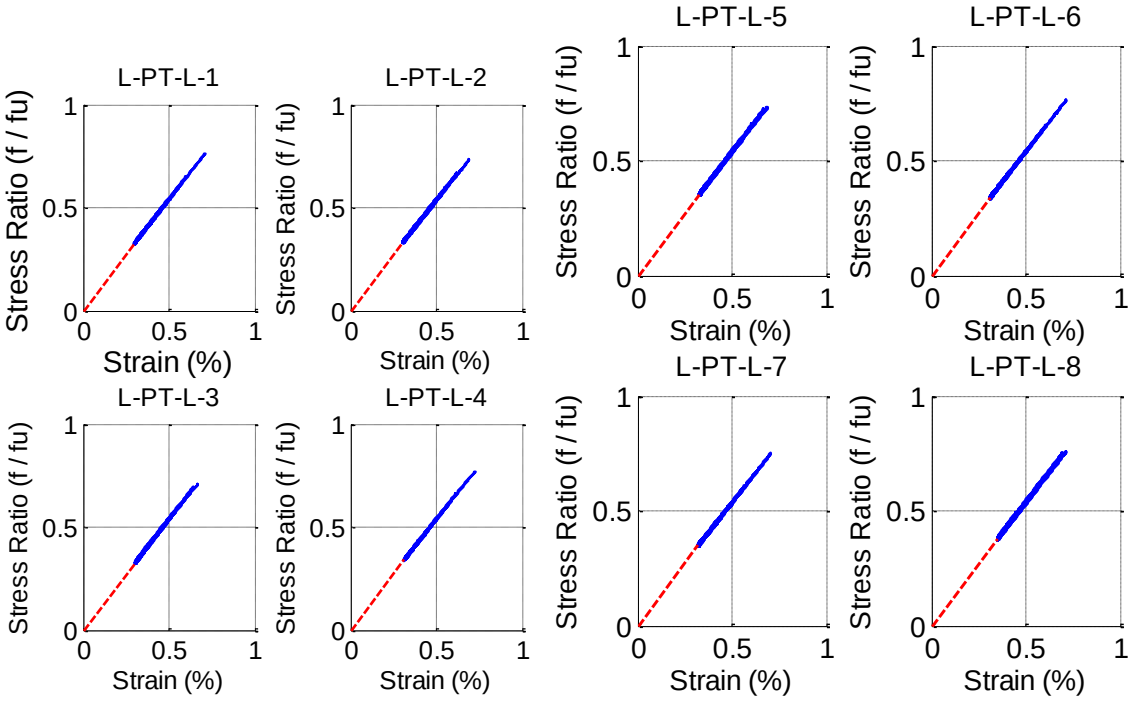

Figure D.150 Specimen A6 1.20xJMA Kobe Trial - Post-Tensioning Stress-Strain Response

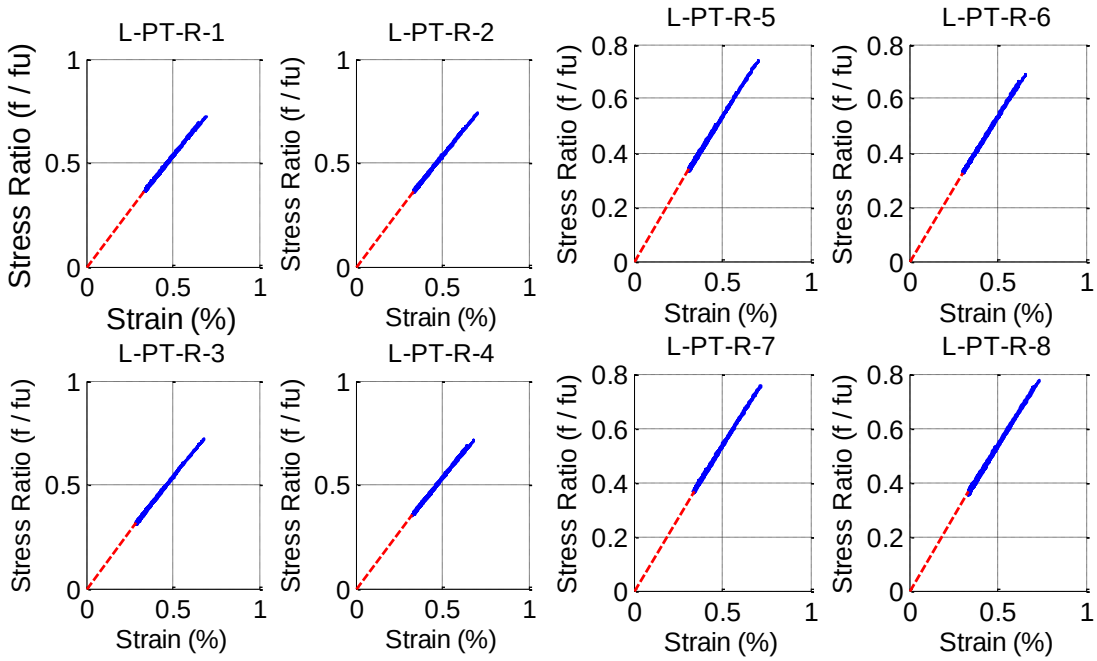

Figure D.151 Specimen A6 1.20xJMA Kobe Trial - Post-Tensioning Stress-Strain Response

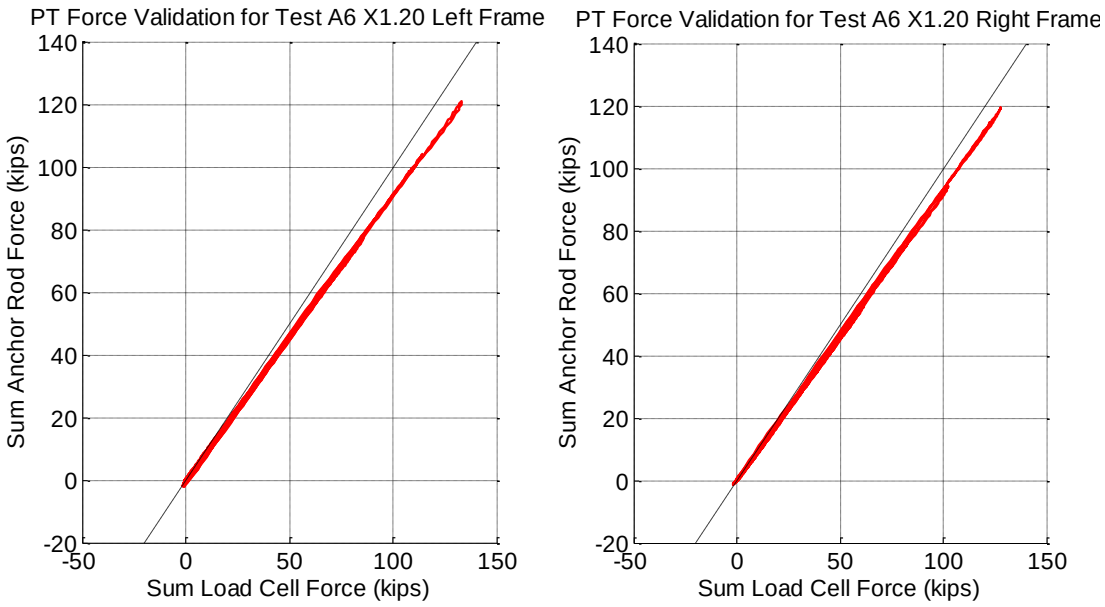

Figure D.152 Specimen A6 1.20xJMA Kobe Trial - Validation of Post-Tensioning Forces

D.9.3 Data Validation for Fuse Response

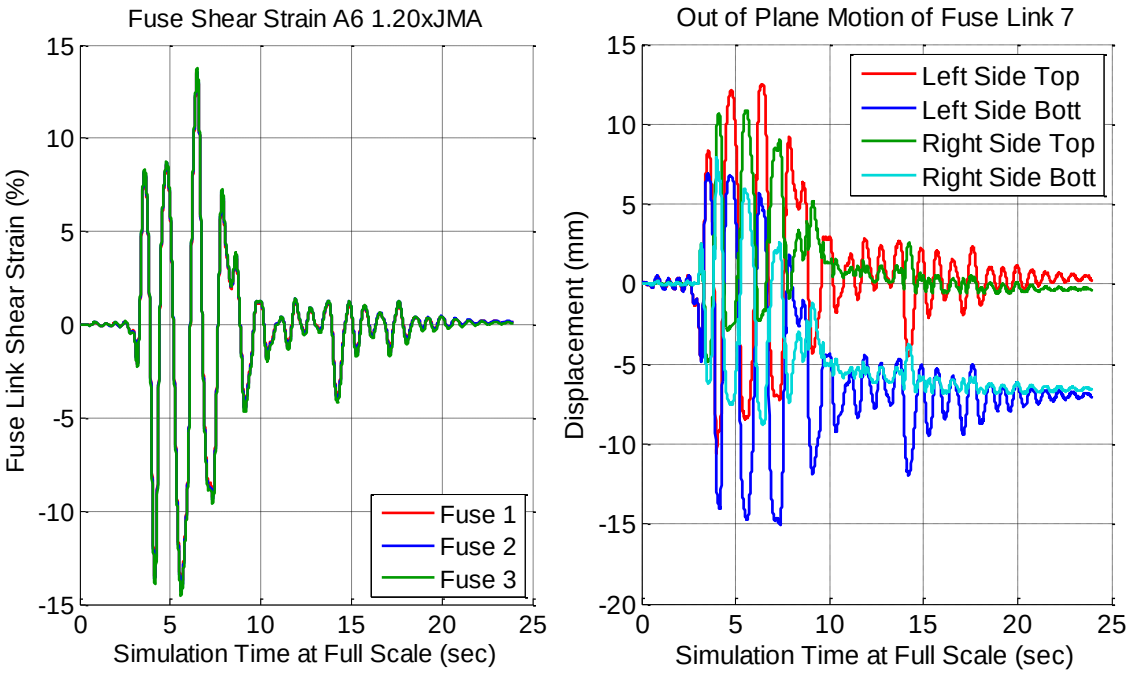

Figure D.153 Specimen A6 1.20xJMA Kobe Trial - Fuse Link Shear Strain For All Three Floors (Left) Out-of-Plane Motion of Fuse Link Using Krypton (Right)

D.9.4 Motion of the System

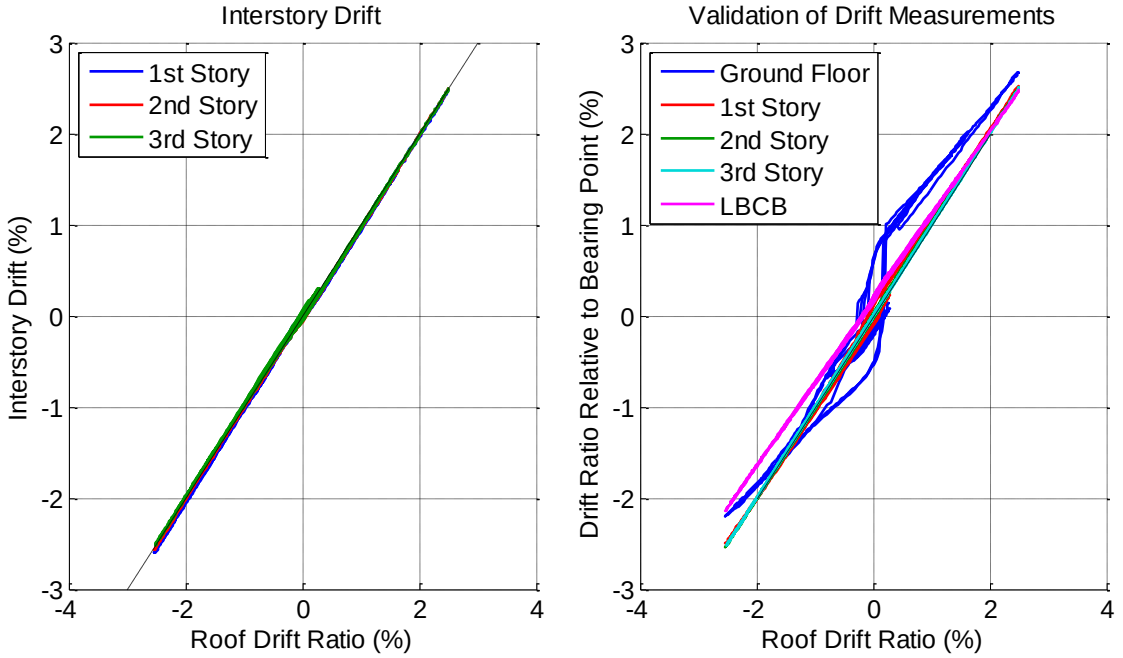

Figure D.154 Specimen A6 1.20xJMA Kobe Trial - Interstory Drifts (Left) and Drift Ratios Relative to Base (Right)

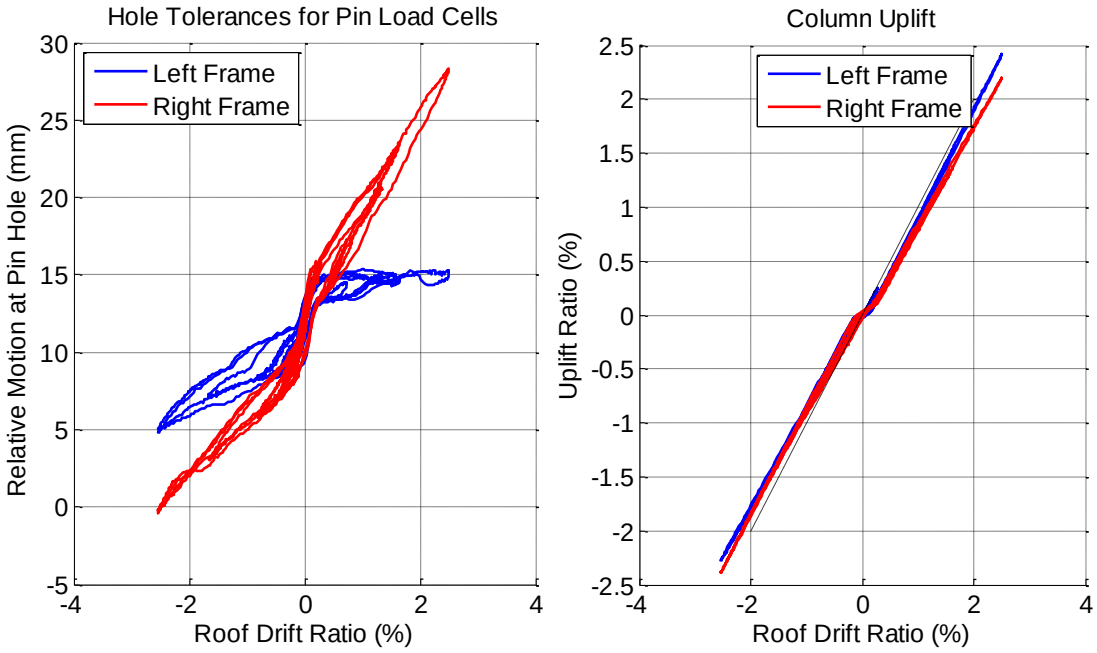

Figure D.155 Specimen A6 1.20xJMA Kobe Trial - Pin Hole Tolerances for the Pin Load Cells (Left), and Uplift Ratio (Right)

D.9.5 Member Resultants

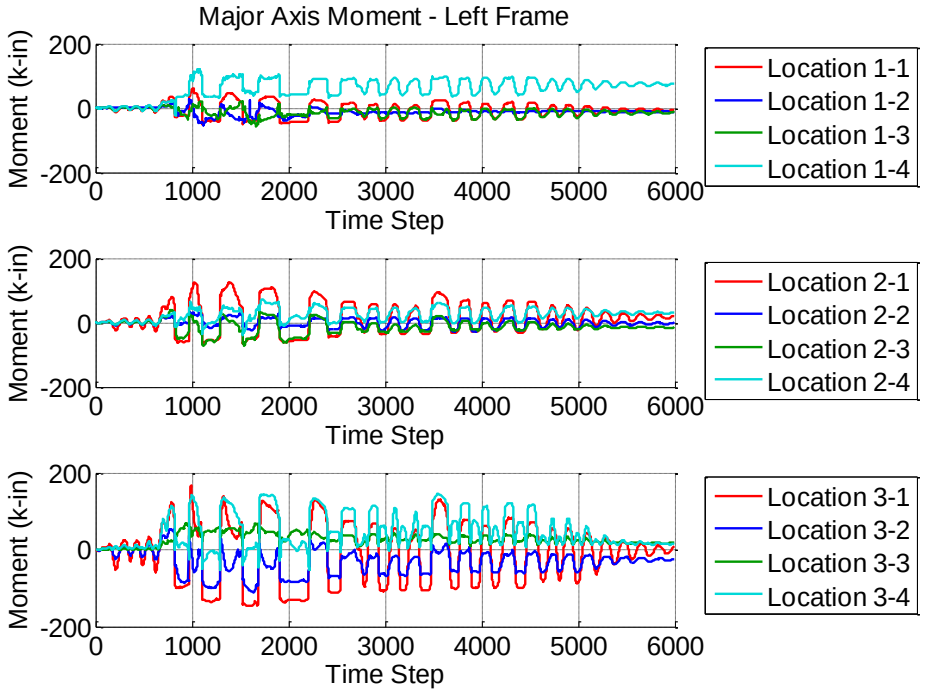

Figure D.156 Specimen A6 1.20xJMA Kobe Trial - Calculated Member Resultant Forces

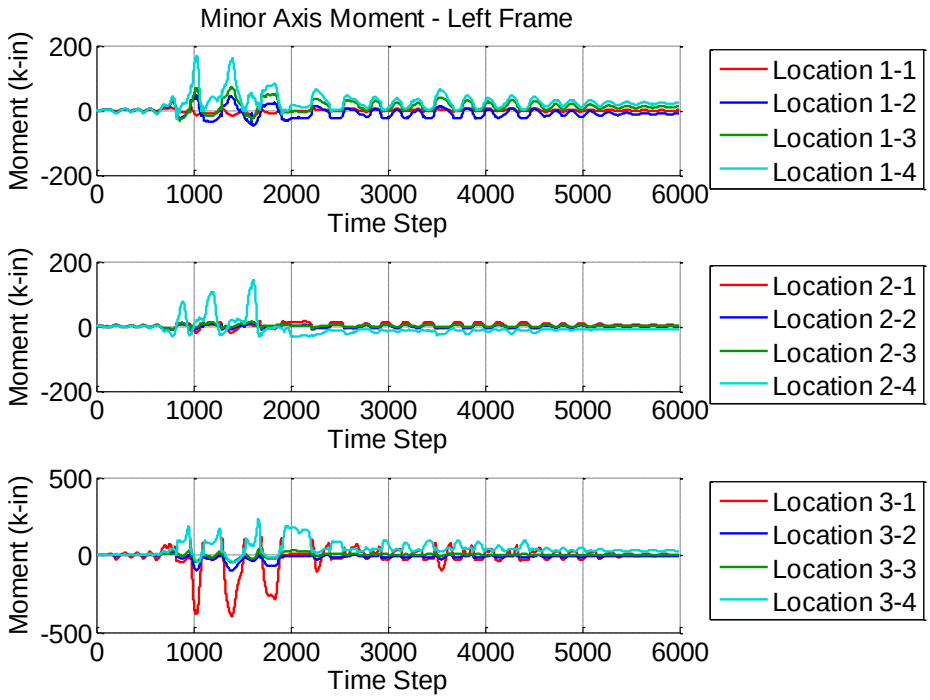

Figure D.157 Specimen A6 1.20xJMA Kobe Trial - Calculated Member Resultant Forces

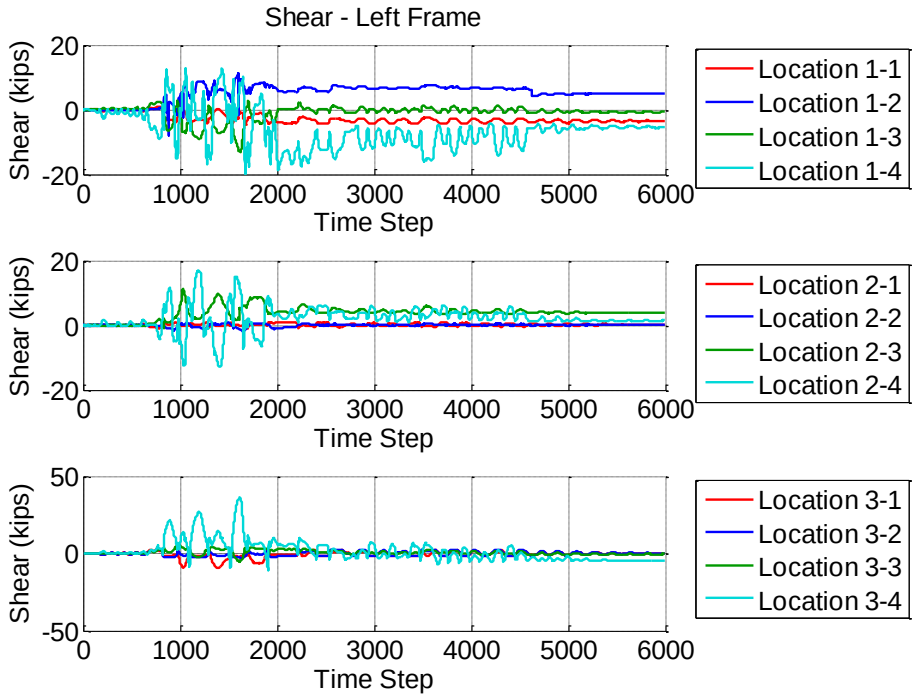

Figure D.158 Specimen A6 1.20xJMA Kobe Trial - Calculated Member Resultant Forces

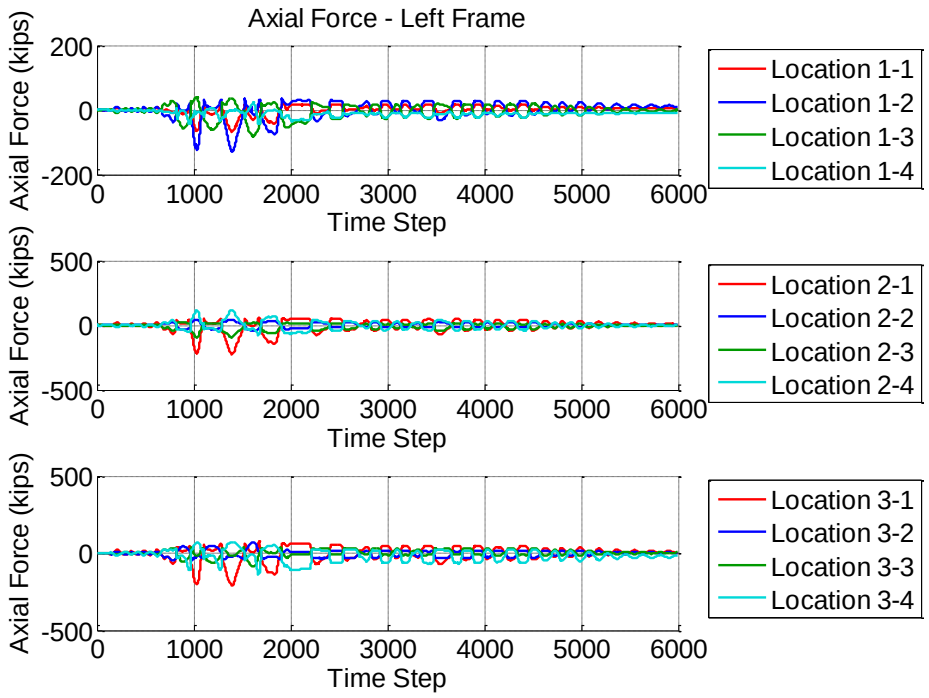

Figure D.159 Specimen A6 1.20xJMA Kobe Trial - Calculated Member Resultant Forces

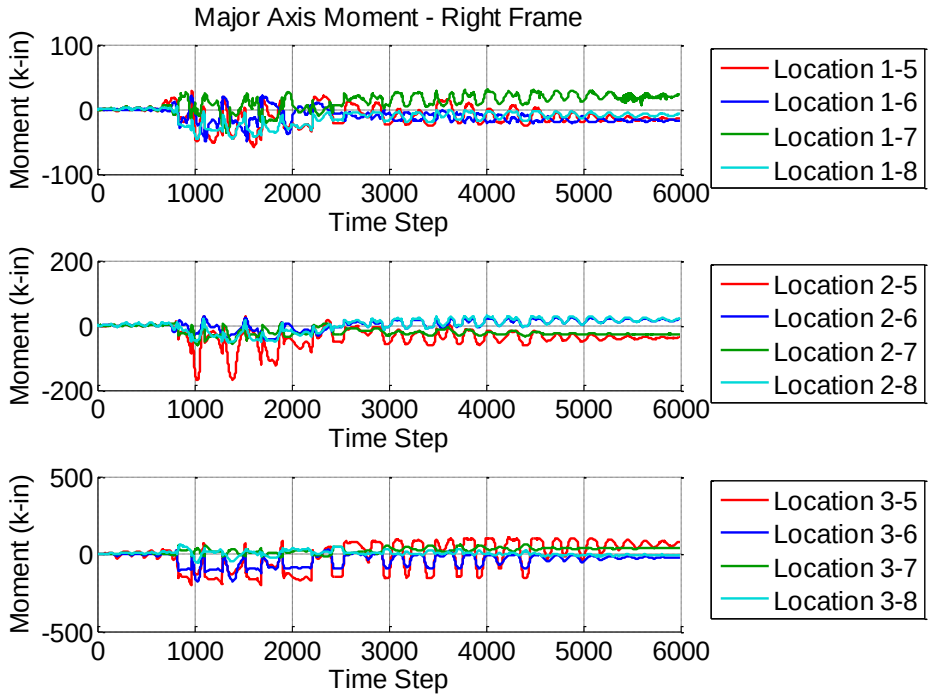

Figure D.160 Specimen A6 1.20xJMA Kobe Trial - Calculated Member Resultant Forces

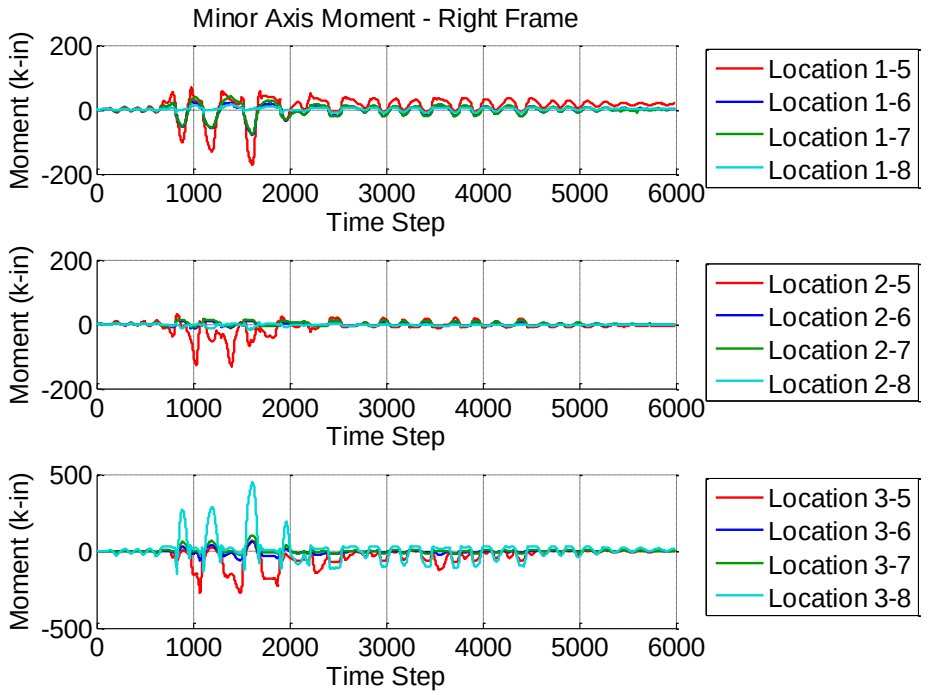

Figure D.161 Specimen A6 1.20xJMA Kobe Trial - Calculated Member Resultant Forces

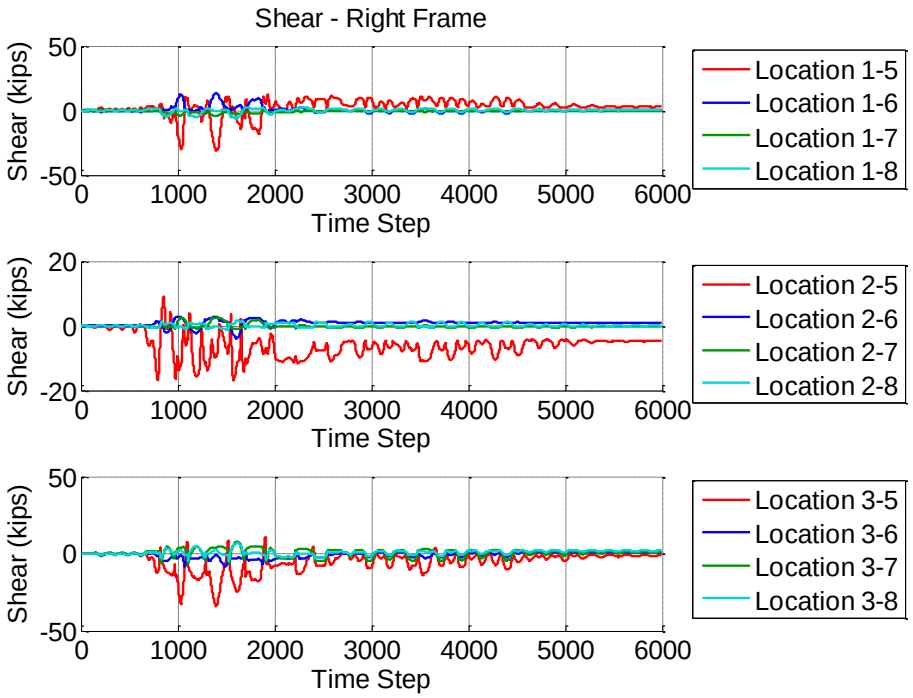

Figure D.162 Specimen A6 1.20xJMA Kobe Trial - Calculated Member Resultant Forces

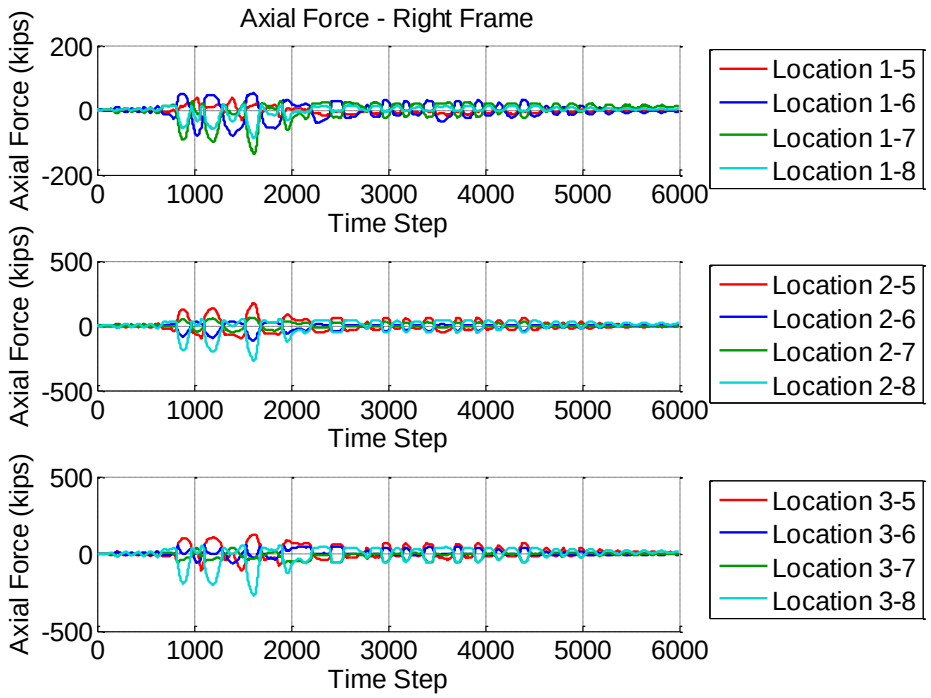

Figure D.163 Specimen A6 1.20xJMA Kobe Trial - Calculated Member Resultant Forces

D.9.6 Sum Forces at Each Section

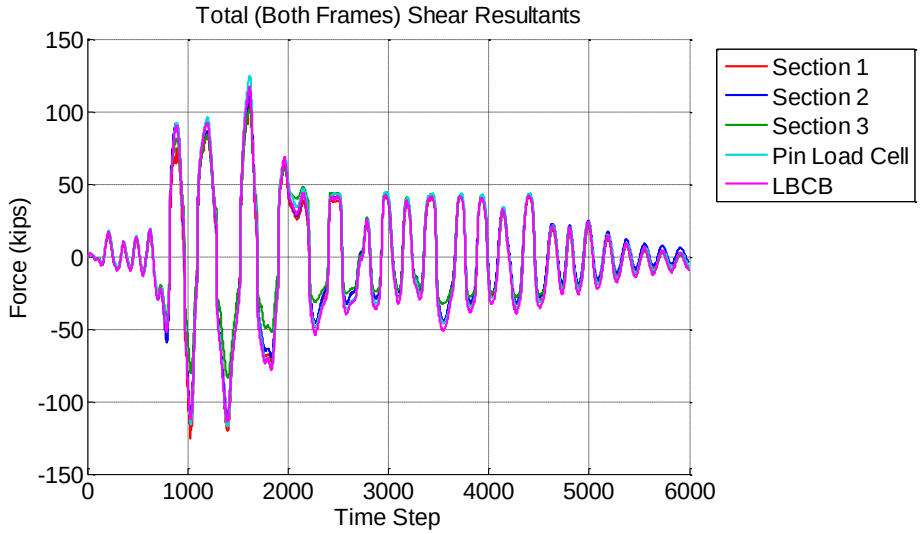

Figure D.164 Specimen A6 1.20xJMA Kobe Trial - Sum of the Shear Forces

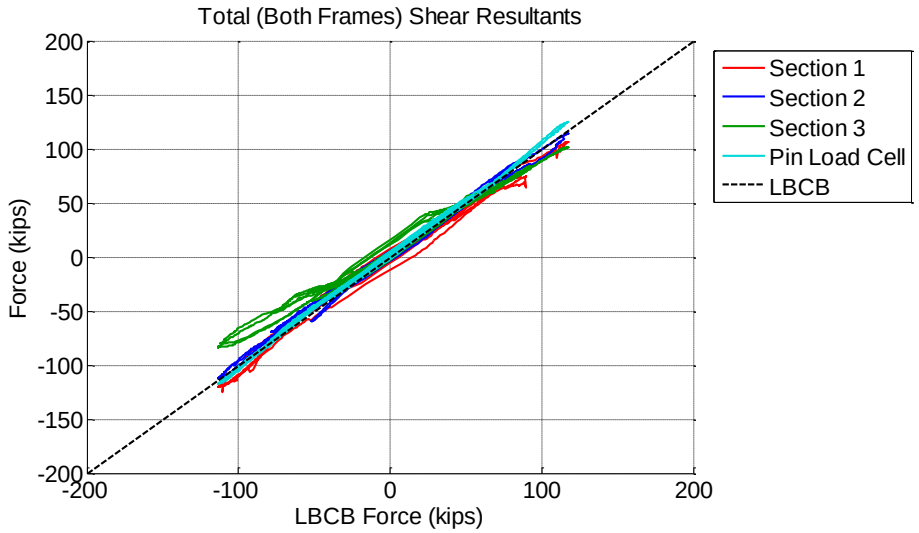

Figure D.165 Specimen A6 1.20xJMA Kobe Trial - Validation of Shear Forces Calculated From Strain-Gaged Sections

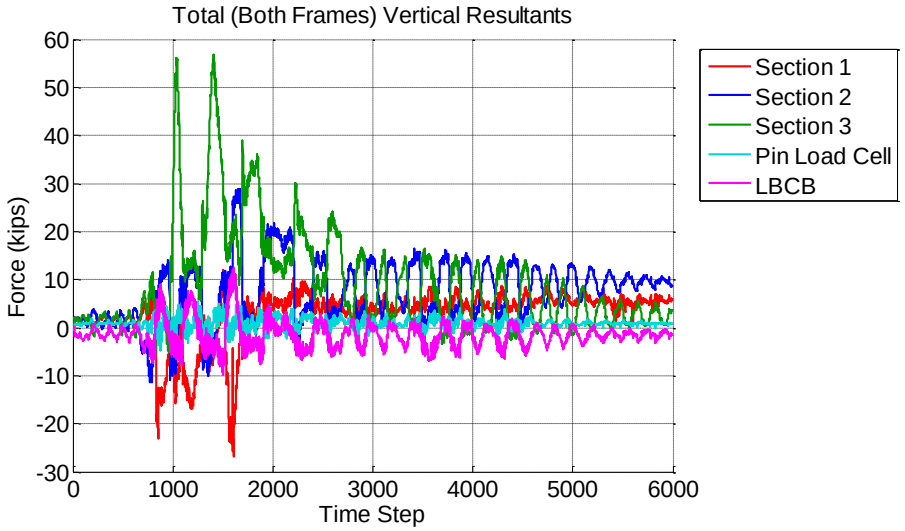

Figure D.166 Specimen A6 1.20xJMA Kobe Trial - Vertical Forces Calculated From Strain-Gaged Sections

D.10 Specimen A7

Notes on Data Reduction:

- Midway through the test it was found that many of the strain gage terminals had become loose. This caused significant problems in the strain gage data with drifting of signals and cutting out of signals. After the problem was identified, all strain gage terminals were tightened and all strain gages were zeroed out. The data was zeroed out for step 3539 and the offsets at this time step as determined using the continuous data are added into the data before 3539.

D.10.1 System Response

As with test A1, there is force going somewhere other than the PT and fuse as shown in the differences between the restoring moment and overturning moment demonstrated in Figure D.167. This force is likely due to the forces between the frames due to constraint and exacerbated by axial forces in thinner buckling fuses.

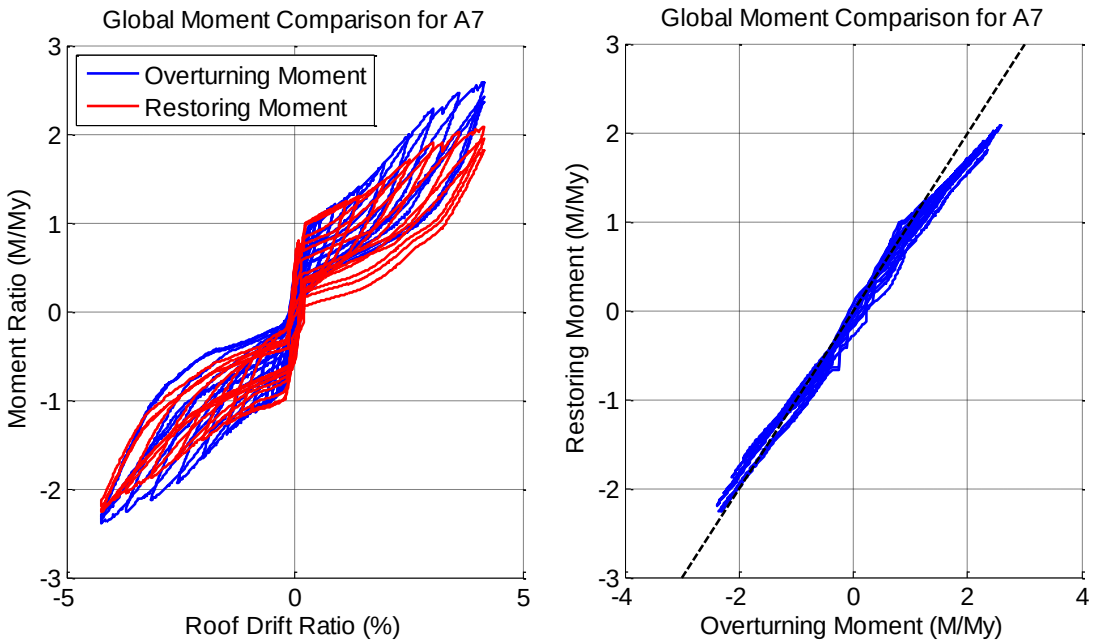

Figure D.167 Specimen A7 - Comparing Restoring Moment to Applied Overturning Moment

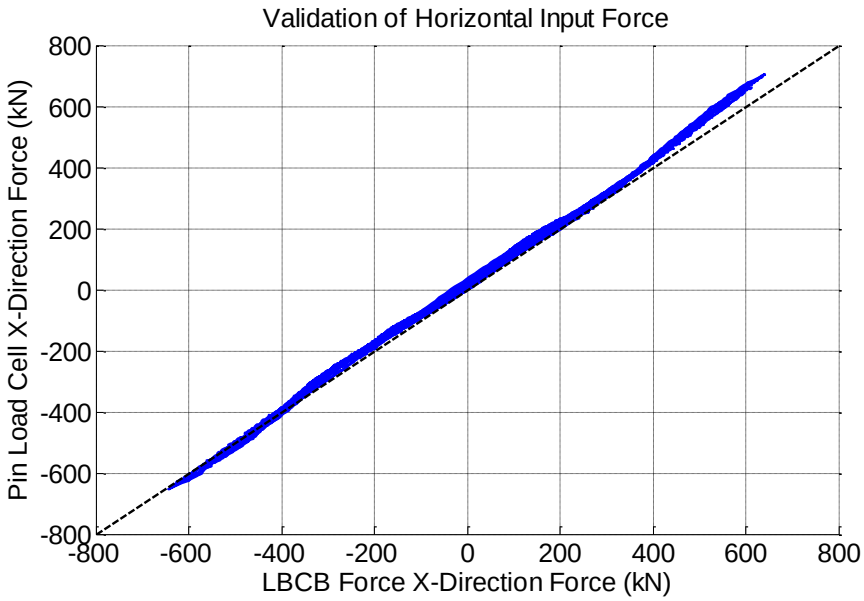

Figure D.168 Specimen A7 - Validation of Horizontal Forces Applied to the Frames

D.10.2 Post-Tensioning Force Validation

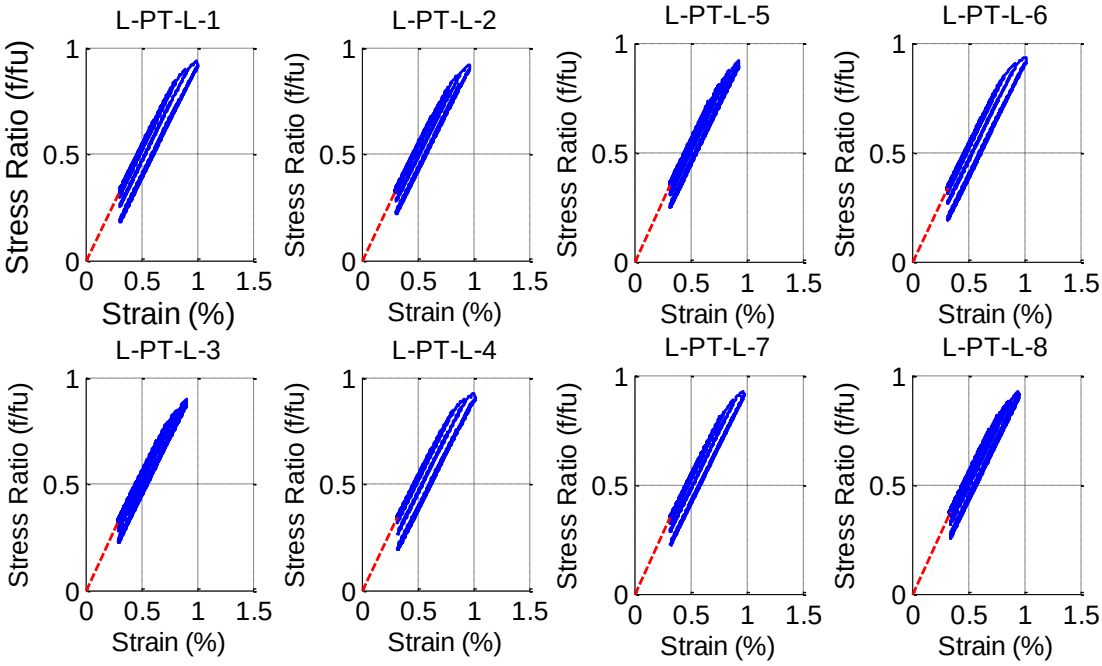

Figure D.169 Specimen A7 - Post-Tensioning Stress-Strain Response

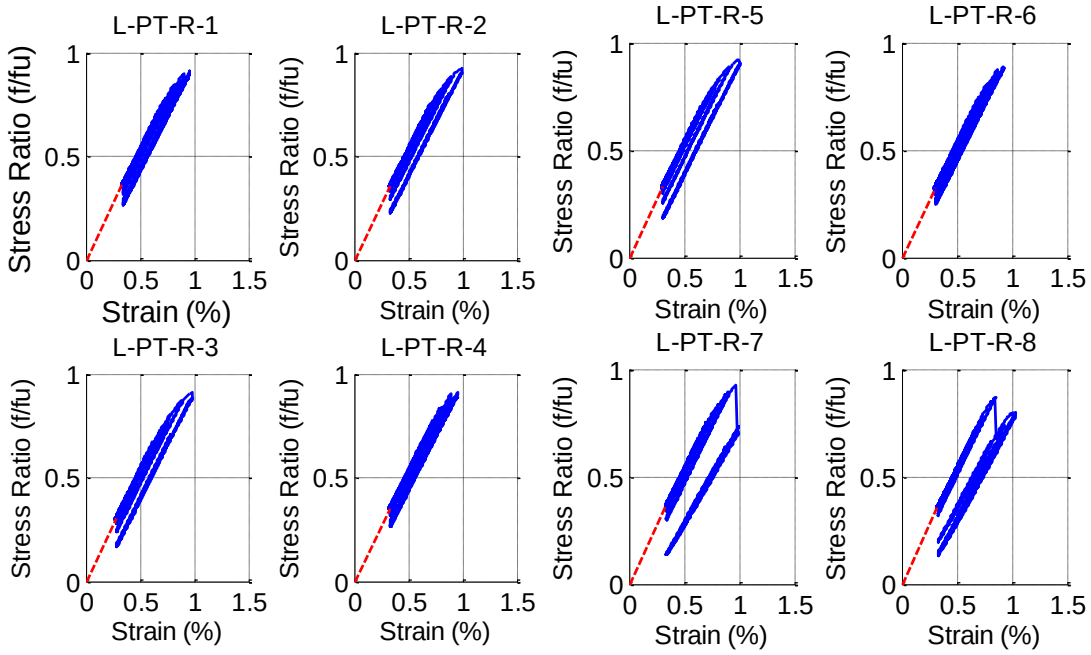

Figure D.170 Specimen A7 - Post-Tensioning Stress-Strain Response

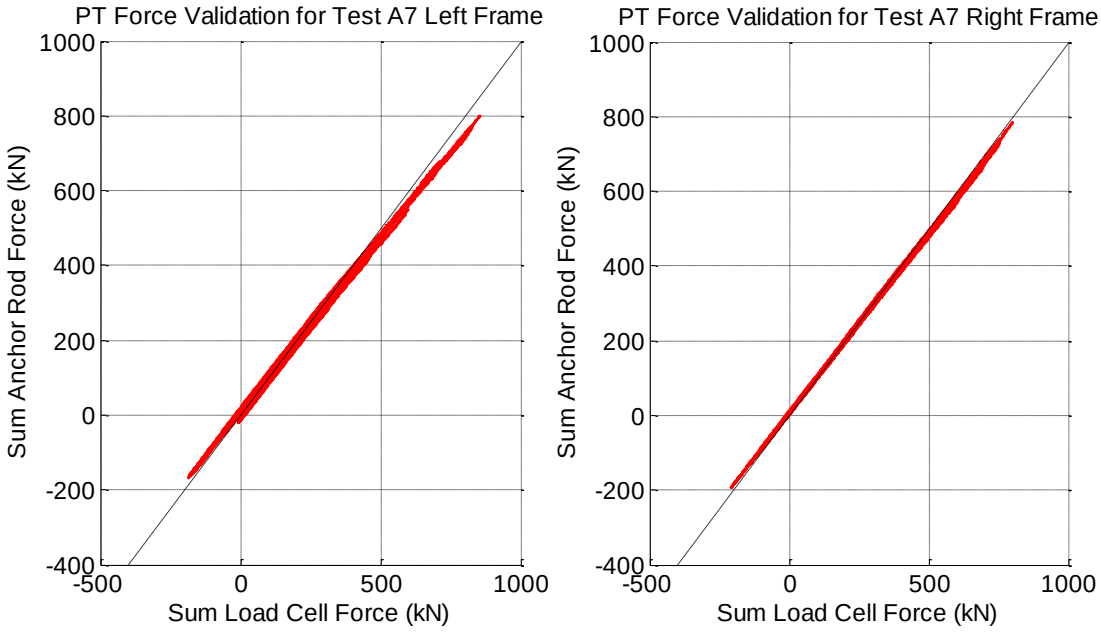

Figure D.171 Specimen A7 - Validation of Post-Tensioning Forces

D.10.3 Data Validation for Fuse Response

The right side of Figure D.172 shows that lateral-torsional buckling followed by cycles of compression buckling occured around step number 4000. This is demonstrated by the left side moving in the positive Y direction as the right side of the fuse link moves in the negative Y direction. The buckling appears to continue in a predominately compression mode instead of a lateral-torsional buckling.

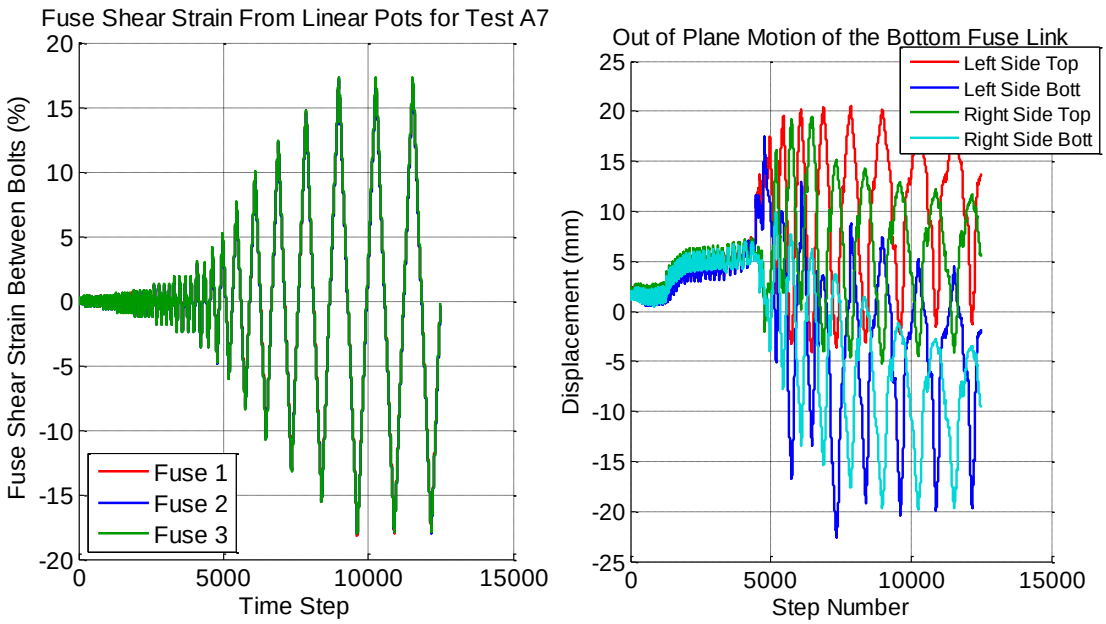

Figure D.172 Specimen A7 - Fuse Link Shear Strain For All Three Floors (Left) Out-of-Plane Motion of Fuse Link Using Krypton (Right)

D.10.4 Motion of the System

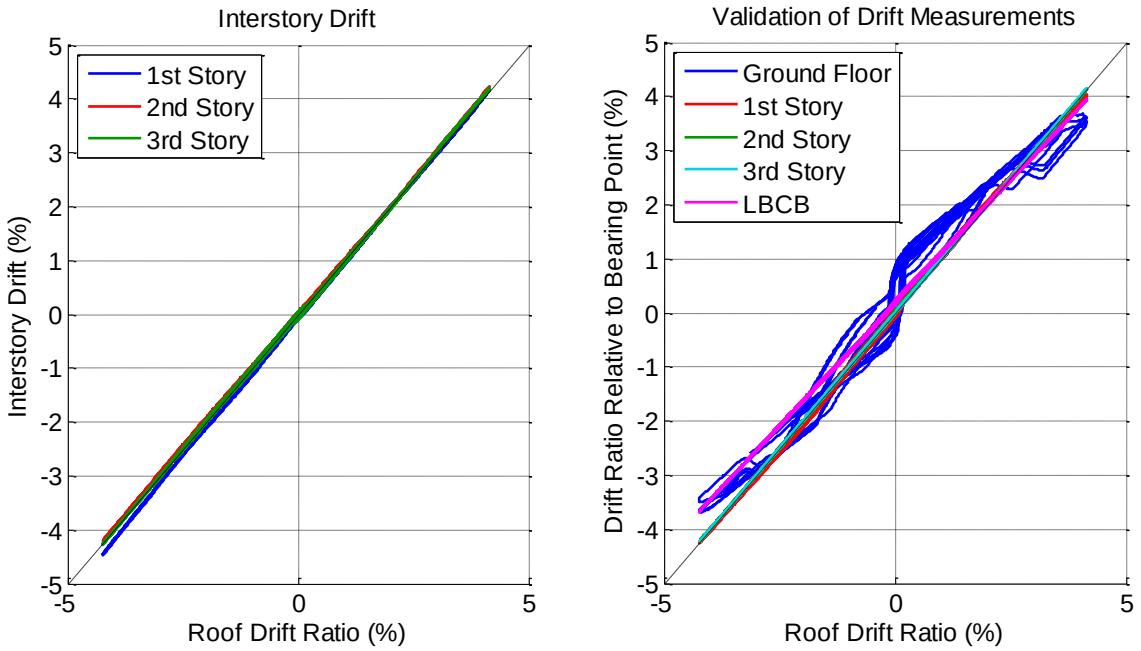

Figure D.173 Specimen A7 - Interstory Drifts (Left) and Drift Ratios Relative to Base (Right)

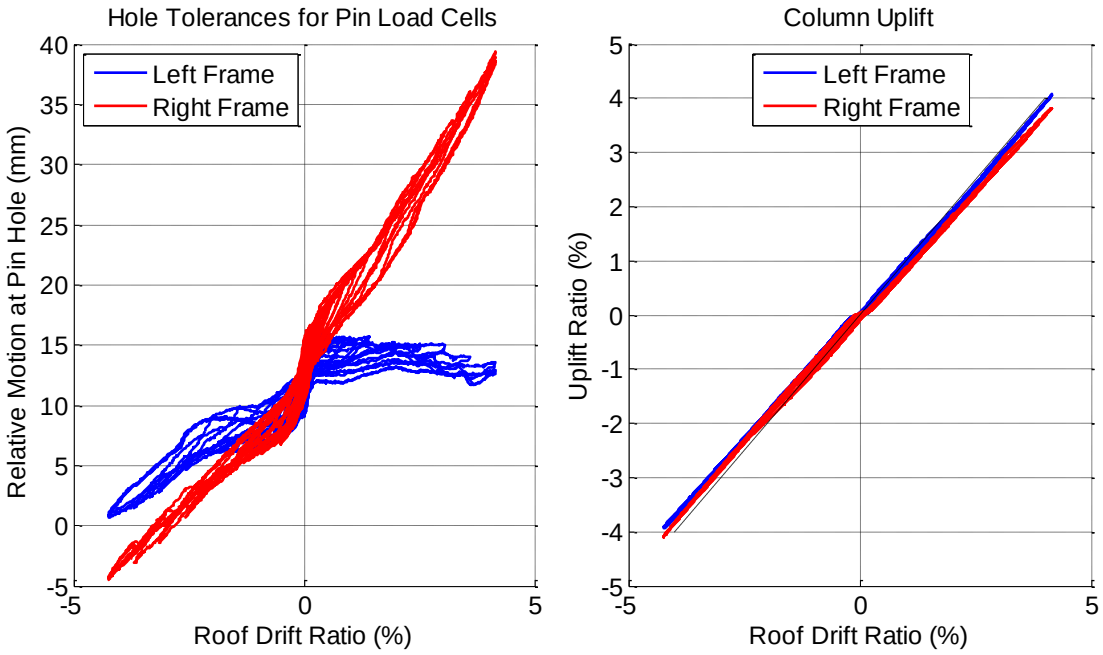

Figure D.174 Specimen A7 - Pin Hole Tolerances for the Pin Load Cells (Left), and Uplift Ratio (Right)

D.10.5 Member Resultants

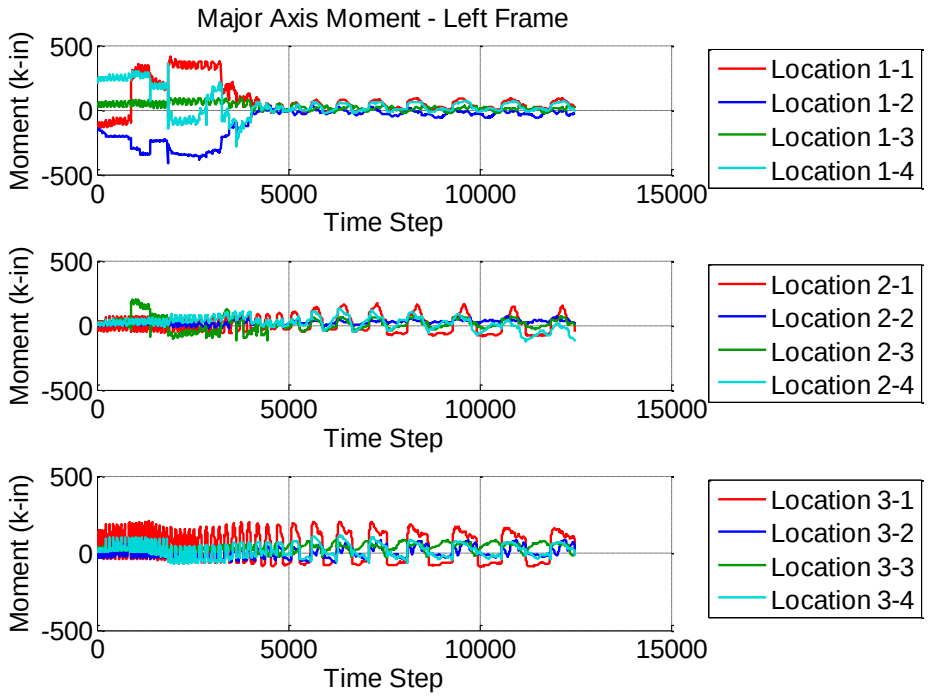

Figure D.175 Specimen A7 - Calculated Member Resultant Forces

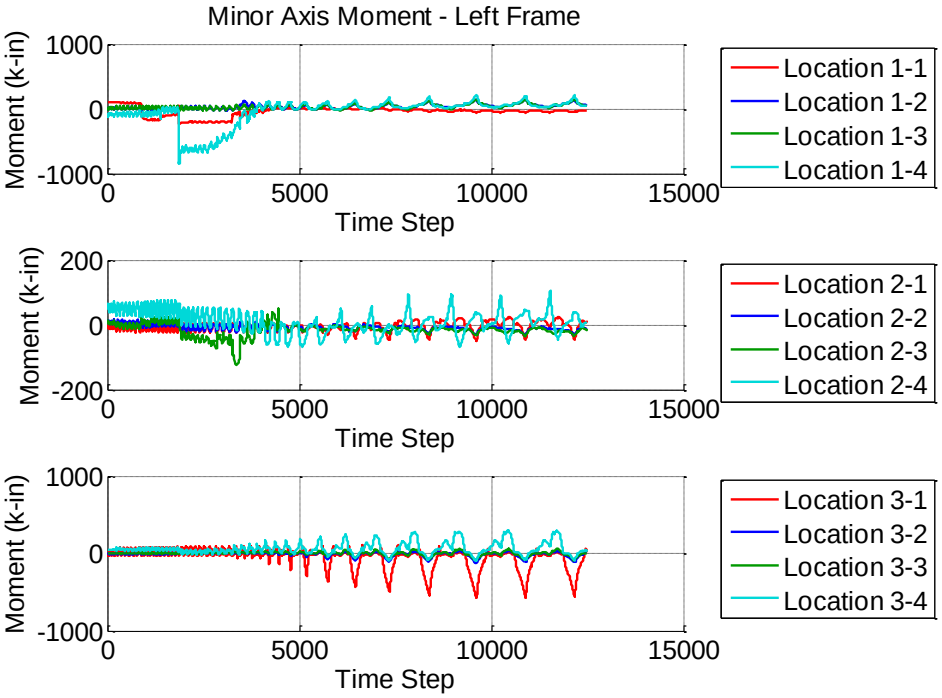

Figure D.176 Specimen A7 - Calculated Member Resultant Forces

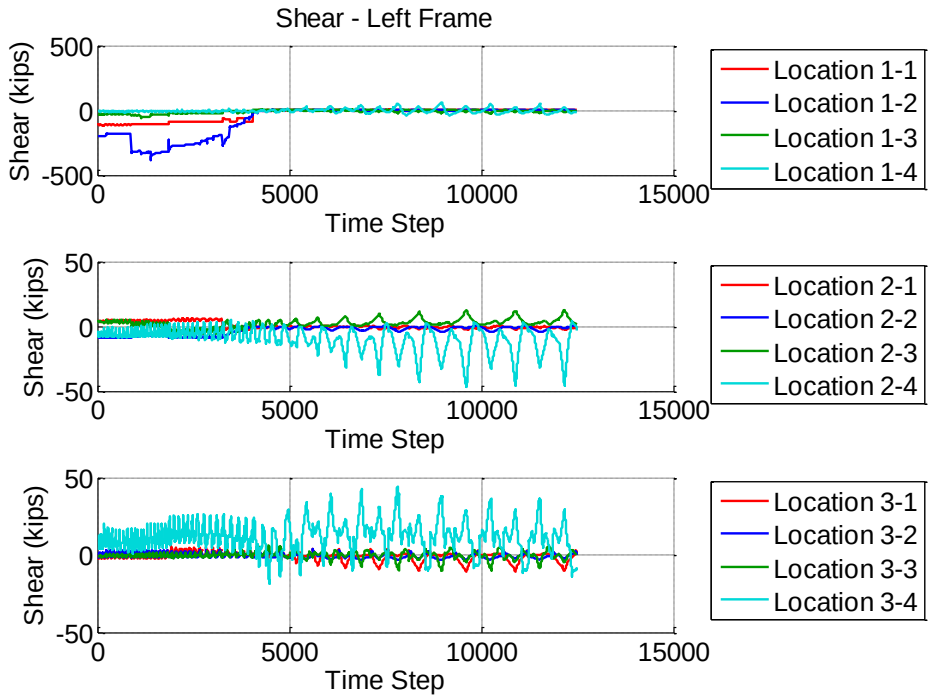

Figure D.177 Specimen A7 - Calculated Member Resultant Forces

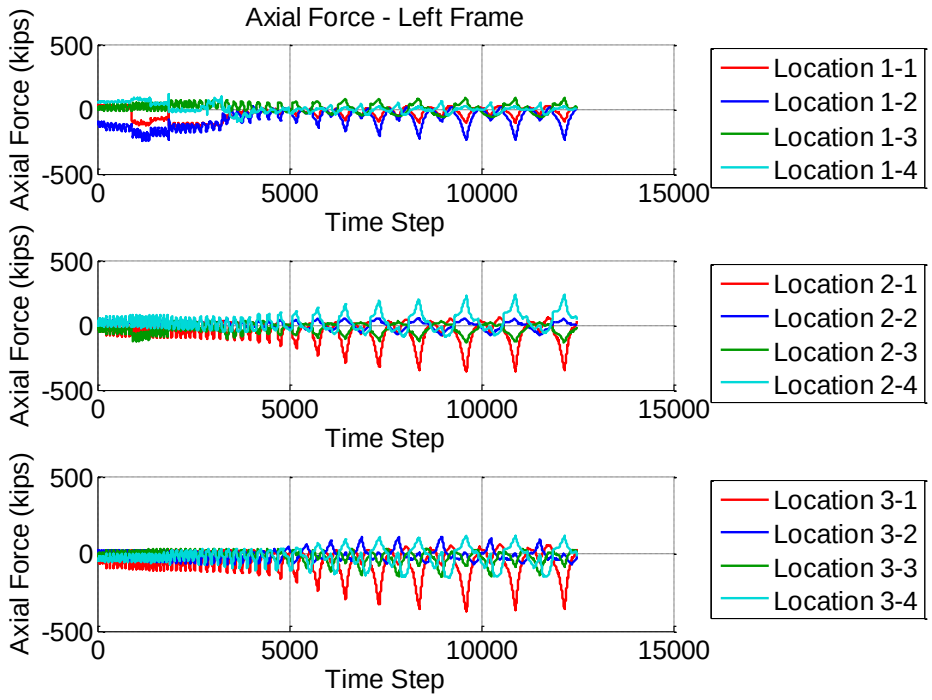

Figure D.178 Specimen A7 - Calculated Member Resultant Forces

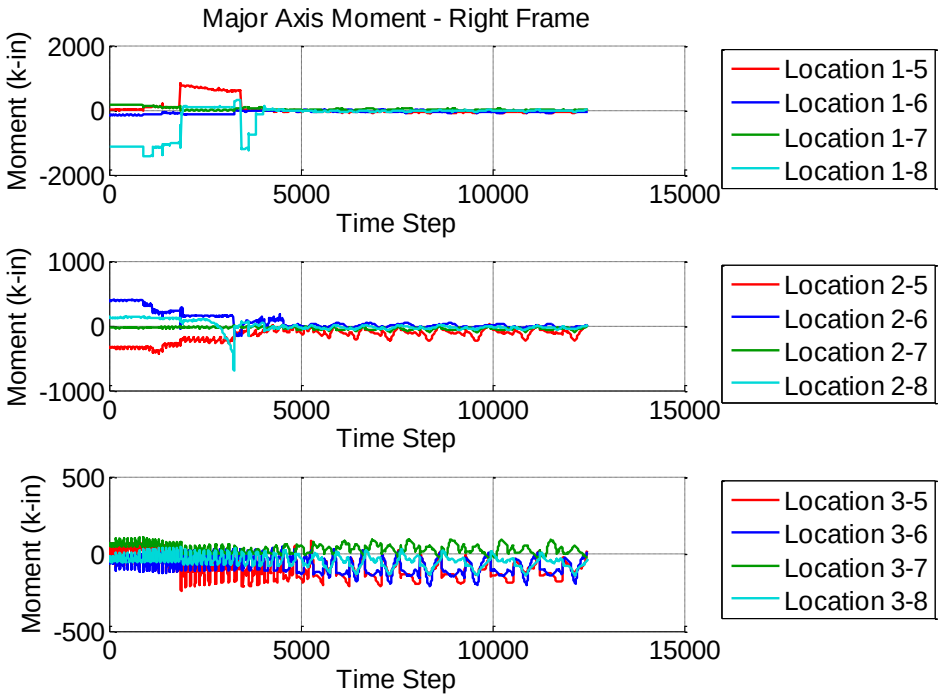

Figure D.179 Specimen A7 - Calculated Member Resultant Forces

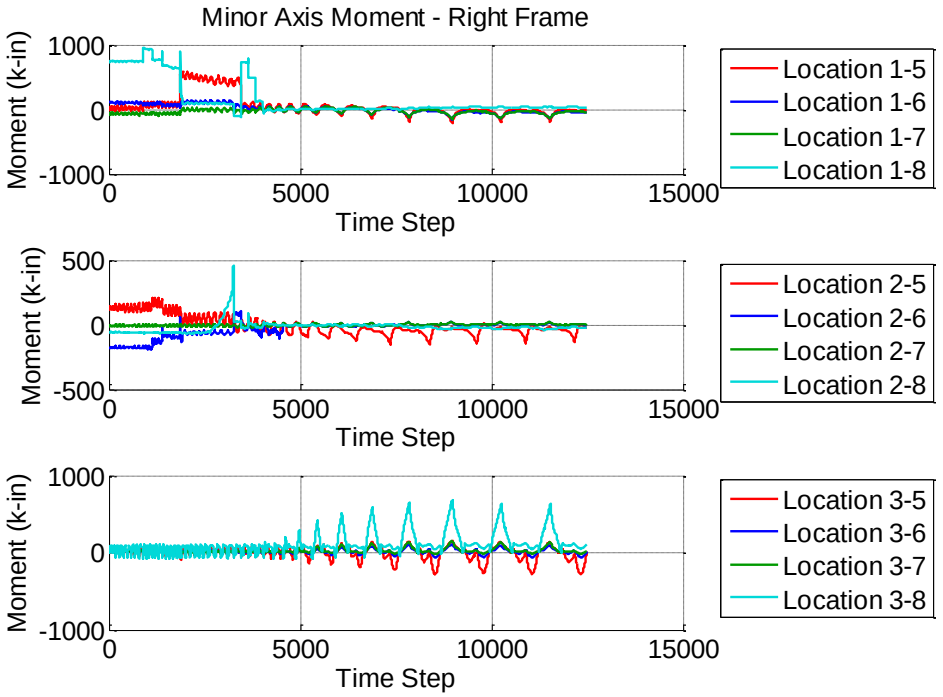

Figure D.180 Specimen A7 - Calculated Member Resultant Forces

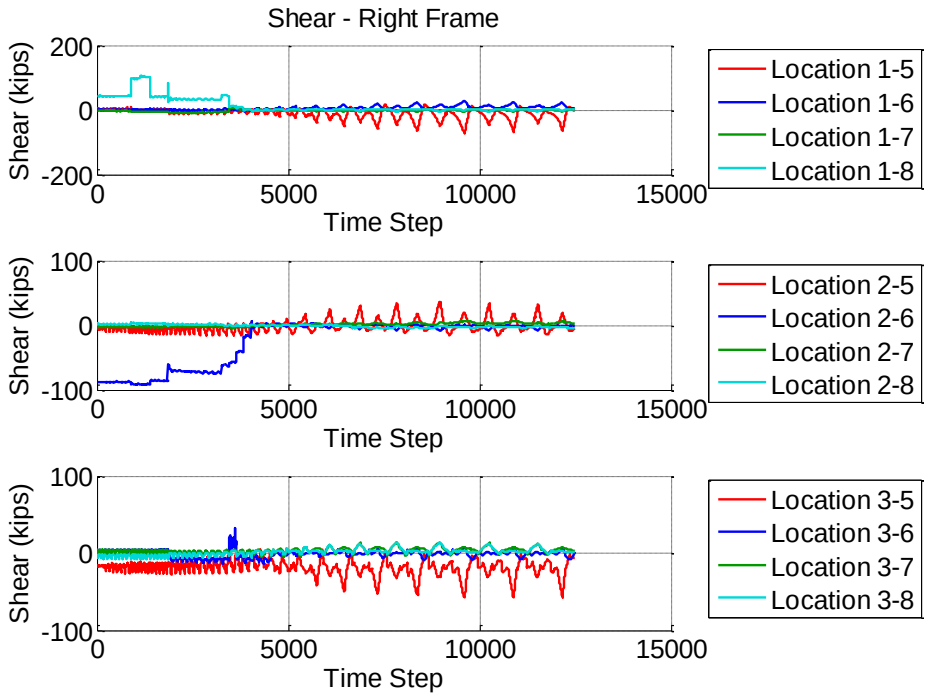

Figure D.181 Specimen A7 - Calculated Member Resultant Forces

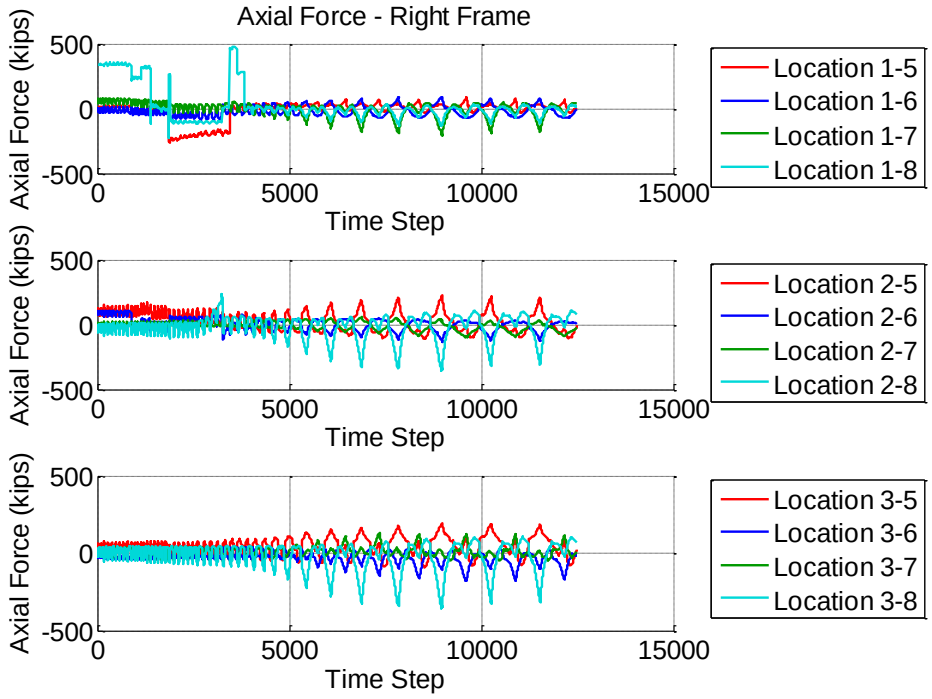

Figure D.182 Specimen A7 - Calculated Member Resultant Forces

D.10.6 Sum Forces at Each Section

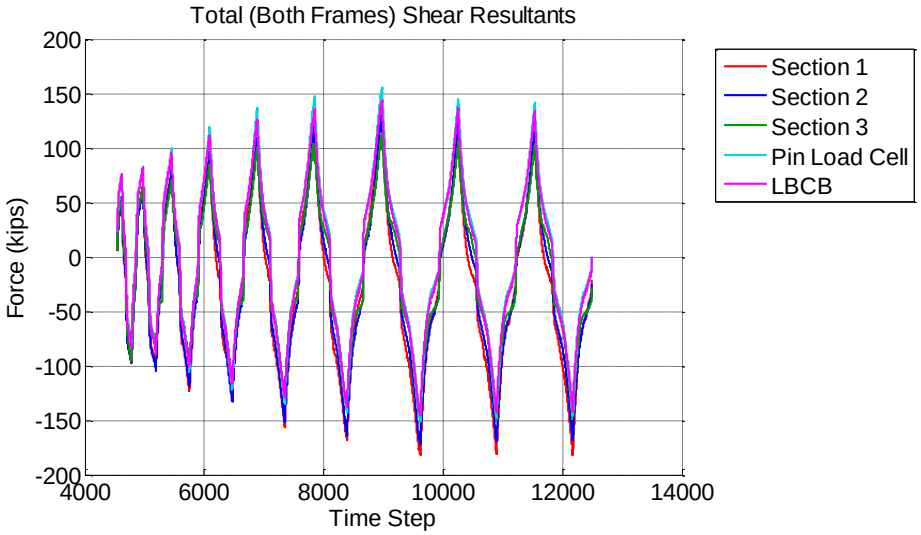

Figure D.183 Specimen A7 - Sum of the Shear Forces

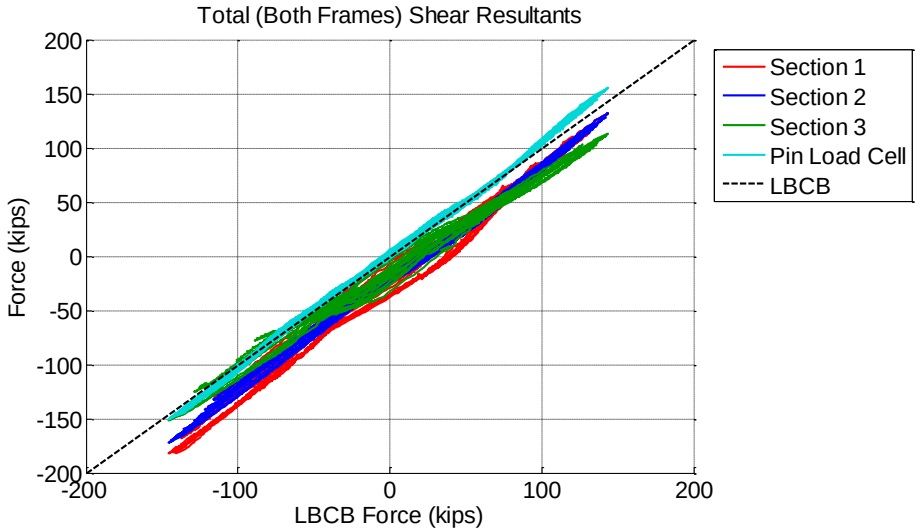

Figure D.184 Specimen A7 - Validation of Shear Forces Calculated From Strain-Gaged Sections

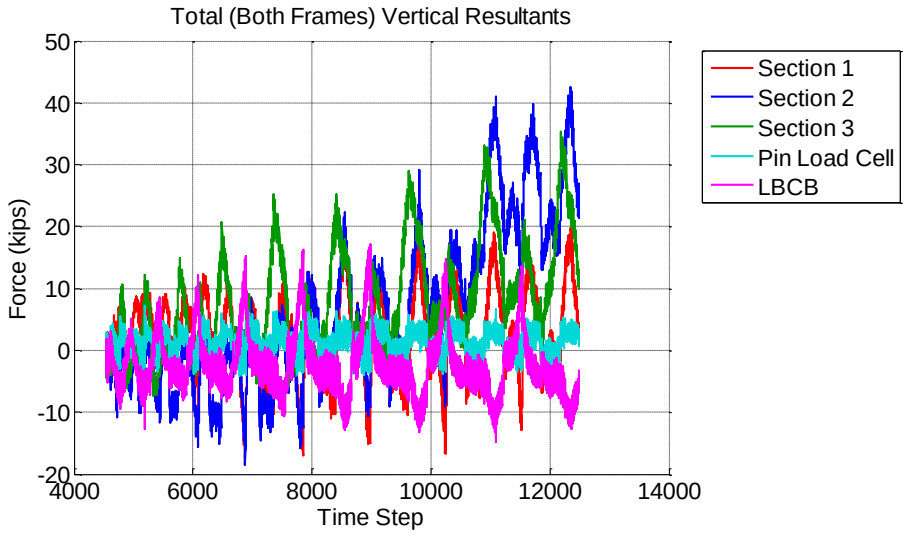

Figure D.185 Specimen A7 - Vertical Forces Calculated From Strain-Gaged Sections

D.11 Specimen B1

D.11.1 System Response

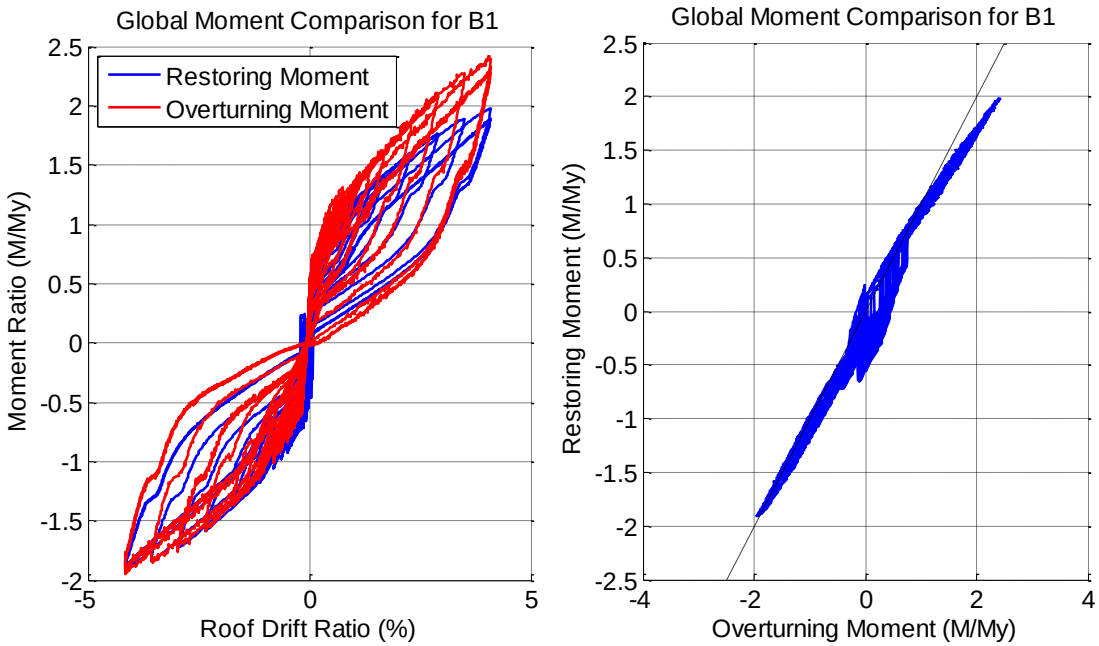

Figure D.186 Specimen B1 - Comparing Restoring Moment to Applied Overturning Moment

D.11.2 Post-Tensioning Force Validation

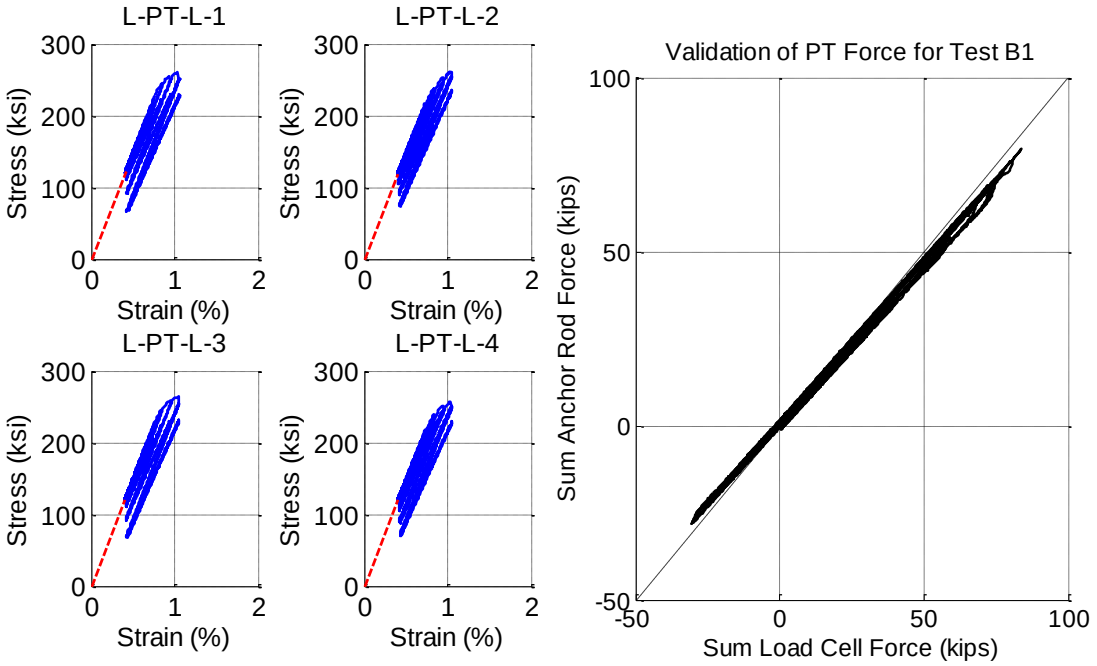

Figure D.187 Specimen B1 - Post-Tensioning Stress-Strain Response (Left) and Validation of Post-Tensioning Force (Right)

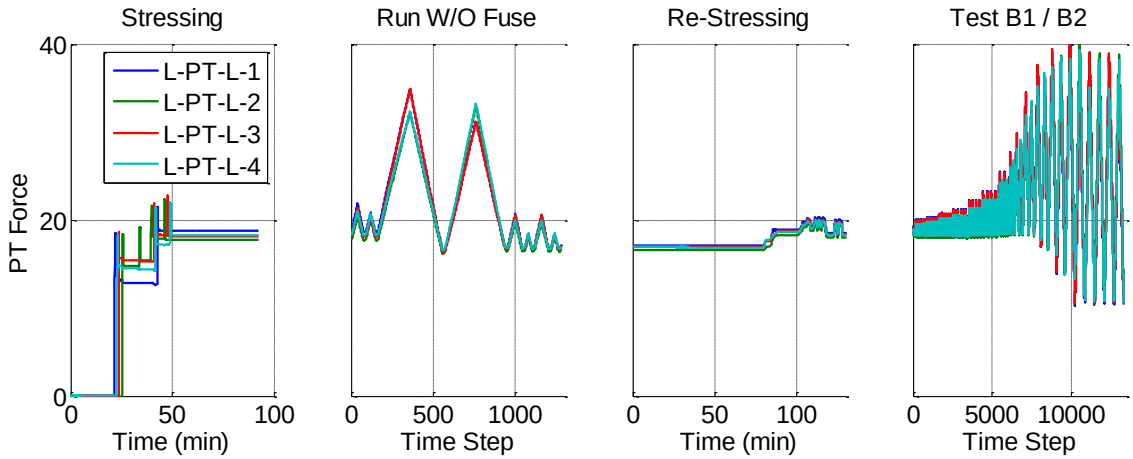

Figure D.188 Specimen B1 - PT Strand Forces Throughout the Stressing and Testing Process

D.11.3 Motion of the System

The bearing point for horizontal loads occurs at the height where the rounded gusset touches the bumper which is 3.5" above the bearing point. The calculation of the point that doesn't displace horizontally is given in Appendix C and is shown in Figure D.189. Although the calculation becomes prone to error at small roof drift, the trend at

large roof drift levels approximately confirms the height of 3.5" as the point on the frames that does not displace horizontally.

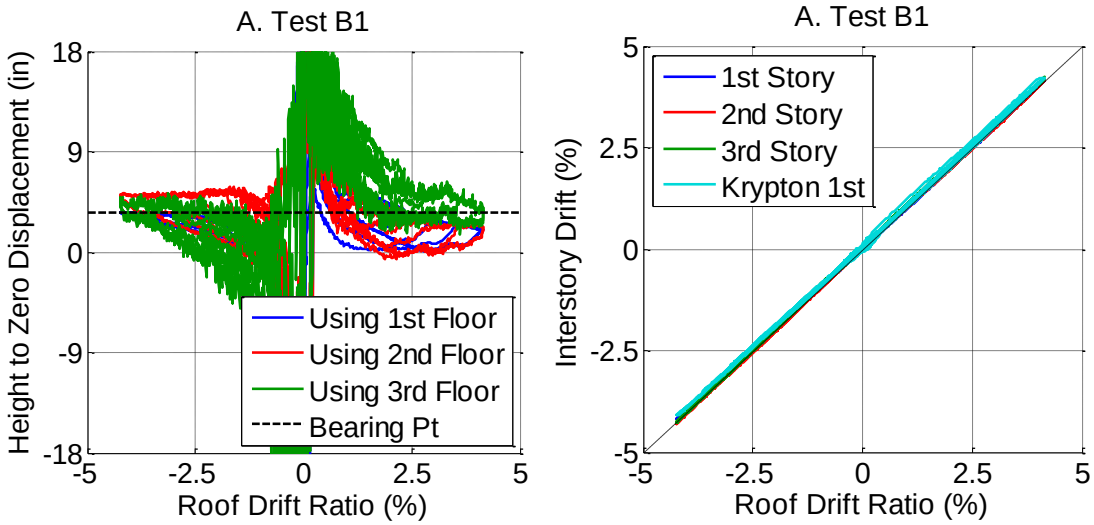

Figure D.189 Specimen B1 - Height to Zero Horizontal Displacement (Left) and Interstory Drifts (Right)

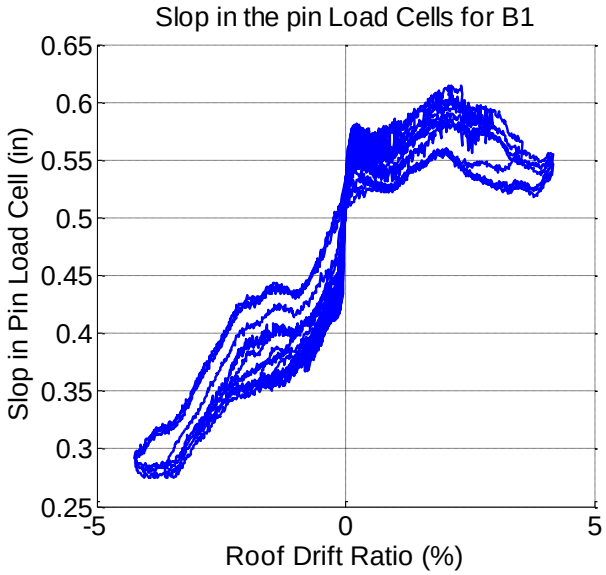

Figure D.190 Specimen B1 - Pin Hole Tolerances for the Pin Load Cells

D.11.4 Member Resultants

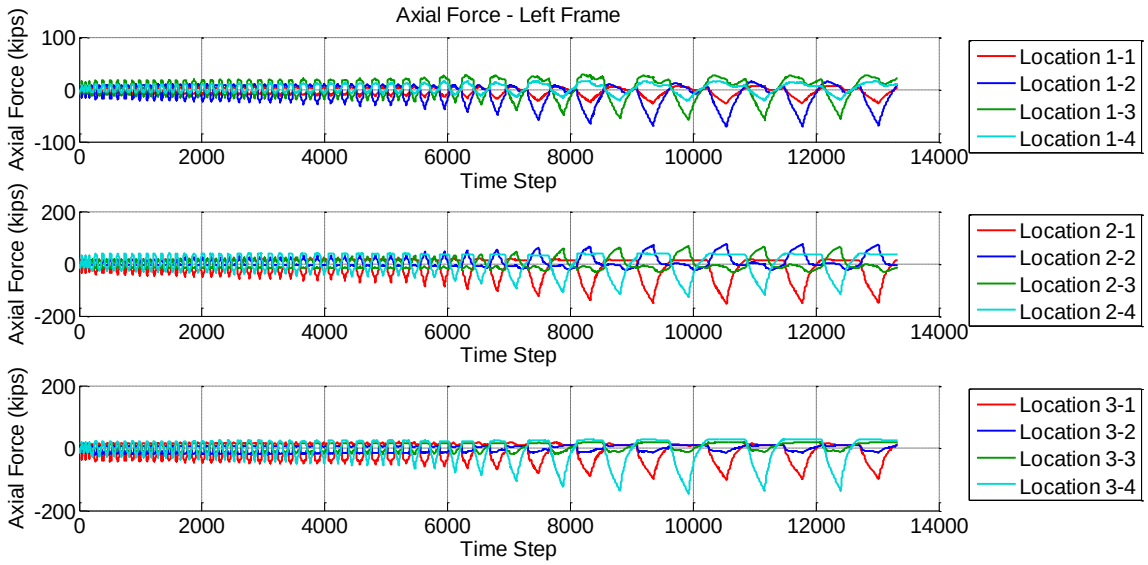

Figure D.191 Specimen B1 - Calculated Member Resultant Forces

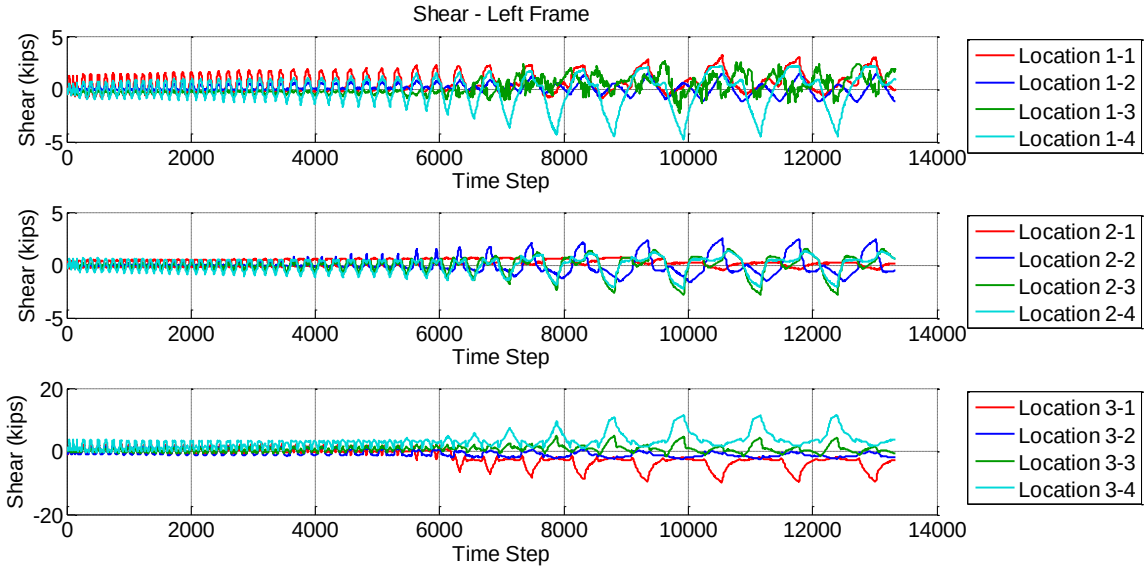

Figure D.192 Specimen B1 - Calculated Member Resultant Forces

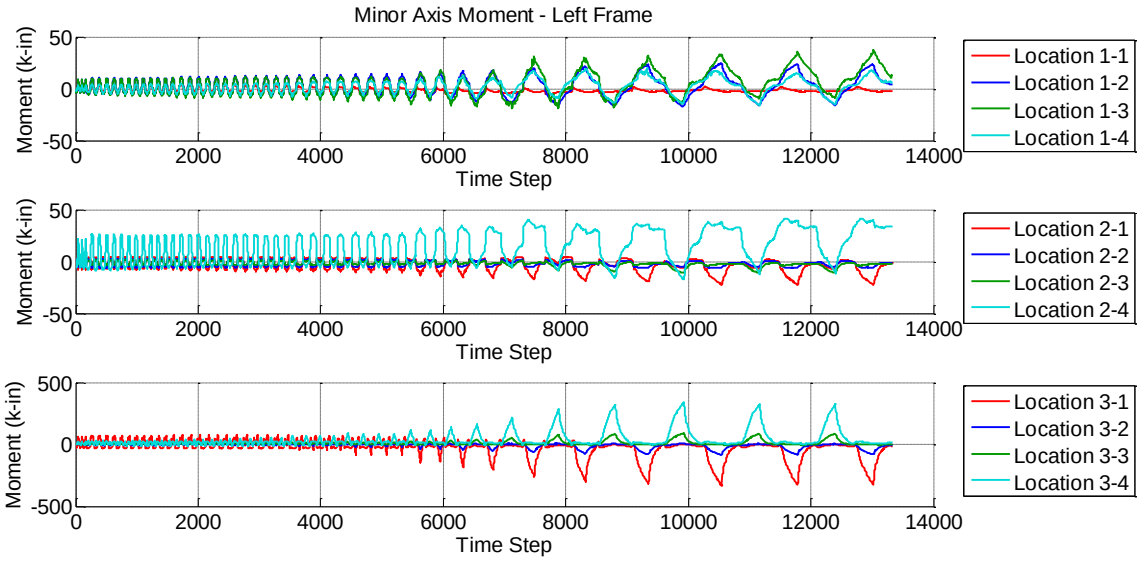

Figure D.193 Specimen B1 - Calculated Member Resultant Forces

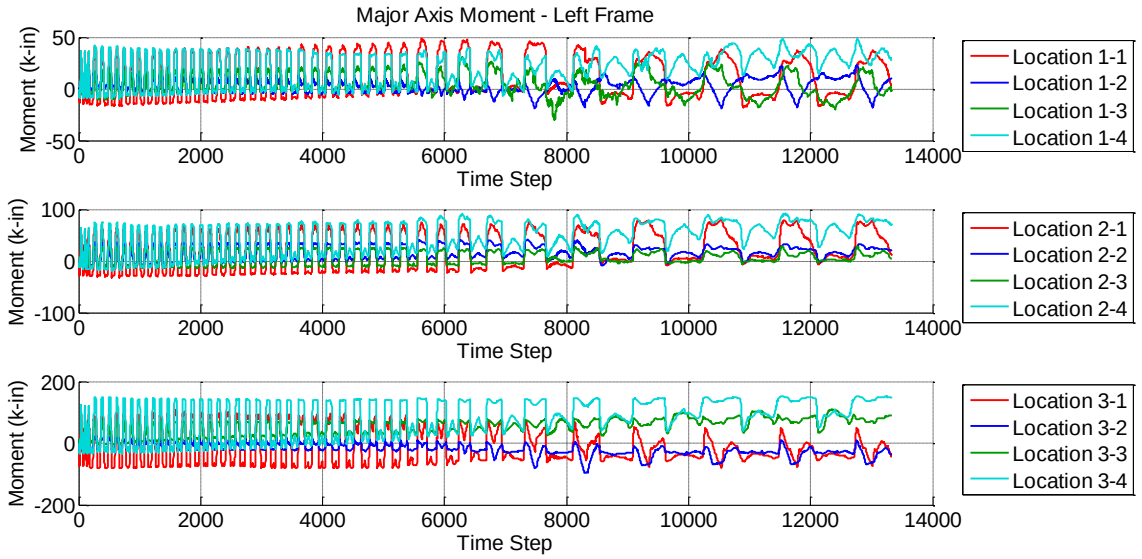

Figure D.194 Specimen B1 - Calculated Member Resultant Forces

D.11.5 Sum Forces at Each Section

The horizontal resultants for all three sections are similar as shown in Figure D.195, Figure D.196, and Figure D.197. Overall, the accuracy of the strain-gaged section resultants validate the measurements and calculations performed to obtain resultants**.** Table D.1 shows that the strain gage section resultants at the last positive and negative peaks are within 30% of the pin load cell reading.

The resultant vertical forces in the system are part of the test control. The vertical pin load cell force is controlled to be within a few kips of zero. The left frame resultant vertical forces were as high as 60 kips in section 3, but 25 kips in section 1 and 2. Since the vertical resultant force in the left frame strain-gaged sections is not zero and do not match each other, there is likely some error in either the strain gage data.

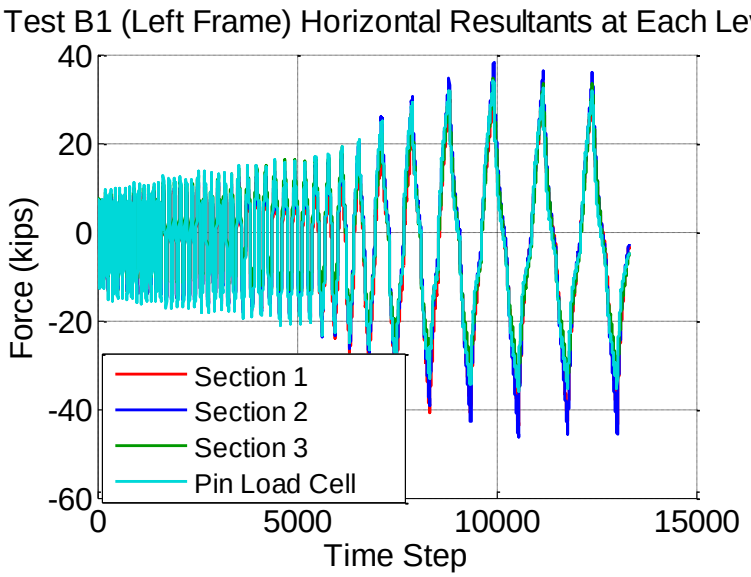

Figure D.195 Specimen B1 - Sum of the Shear Forces

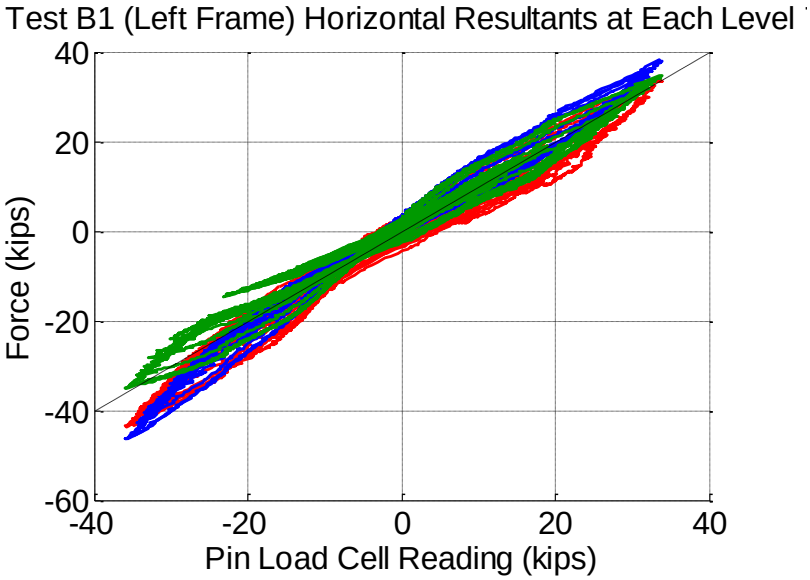

Figure D.196 Specimen B1 - Validation of Shear Forces Calculated From Strain-Gaged Sections

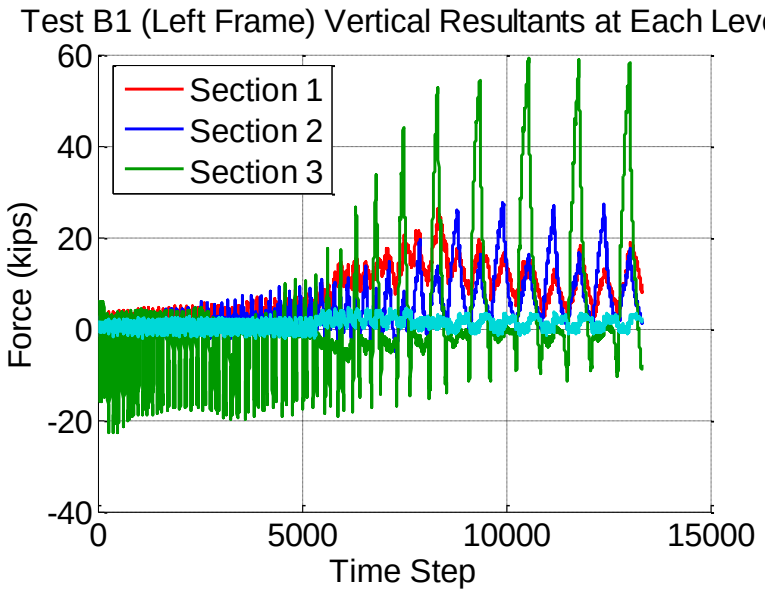

Figure D.197 Specimen B1 - Vertical Forces Calculated From Strain-Gaged Sections

Table D.1 Specimen B1 - Left Frame Horizontal Resultants at the End of the Test

	Last Positive Peak (kips)	Difference From Pin Load Cell	Last Negative Peak (kips)	Difference From Pin Load Cell
Section 1	32.08	0.6%	-43.23	23.8%
Section 2	35.9	12.6%	-45.51	30.3%
Section 3	33.34	4.6%	-34.11	2.3%
Pin Load Cell	31.88	0.0%	-34.92	0.0%

D.12 Specimen B2

D.12.1 System Response

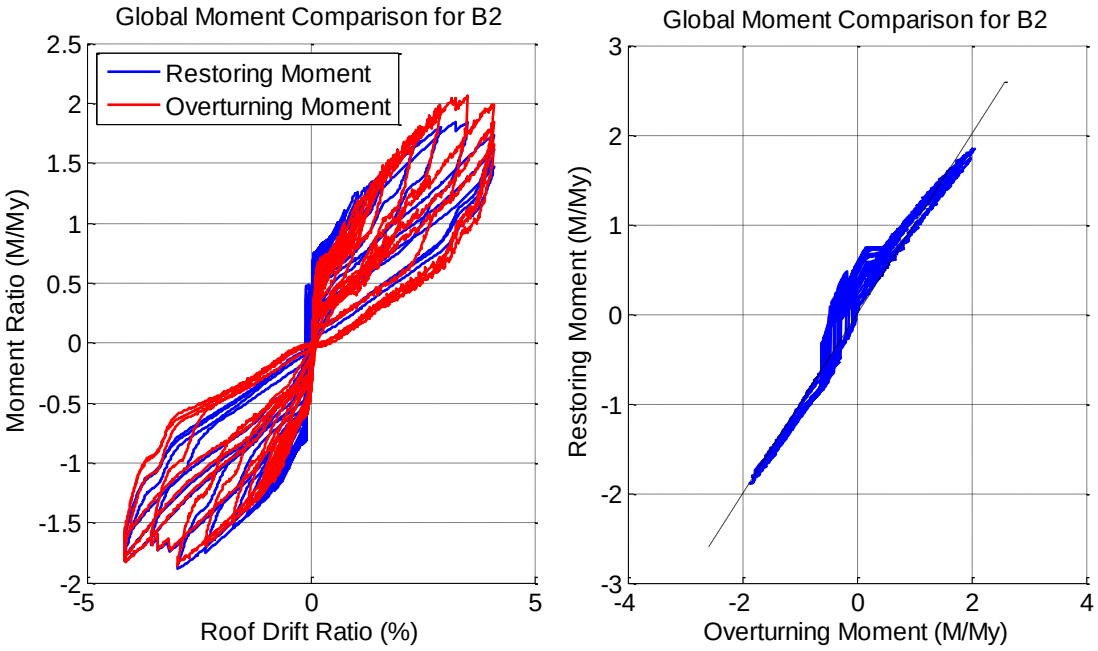

Figure D.198 Specimen B2 - Comparing Restoring Moment to Applied Overturning Moment

D.12.2 Post-Tensioning Force Validation

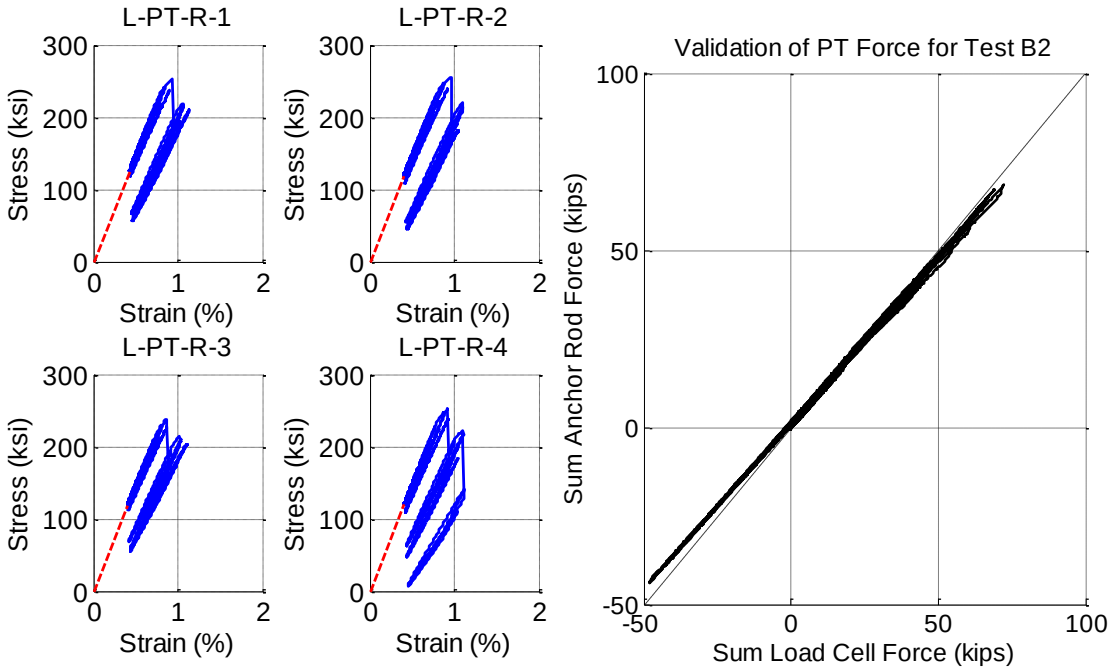

Figure D.199 Specimen B2 - Post-Tensioning Stress-Strain Response (Left) and Validation of Post-Tensioning Force (Right)

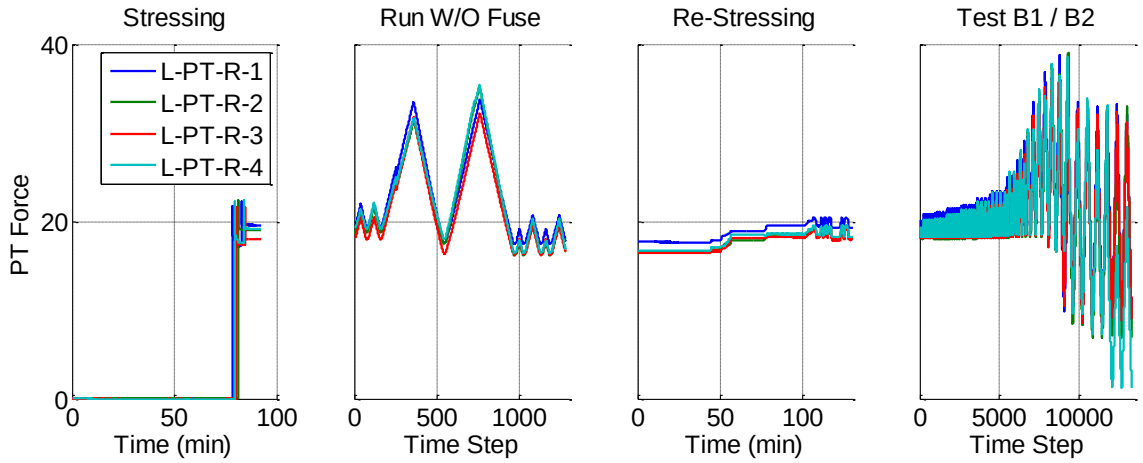

Figure D.200 Specimen B2 - PT Strand Forces Throughout the Stressing and Testing Process

D.12.3 Motion of the System

The bearing point for horizontal loads occurs at the height where the rounded gusset touches the bumper which is 3.5" above the bearing point. The calculation of the point that doesn't displace horizontally is given in Appendix C and is shown in Figure D.201. Although the calculation becomes prone to error at small roof drift, the trend at large roof drift levels approximately confirms the height of 3.5" as the point on the frames that does not displace horizontally.

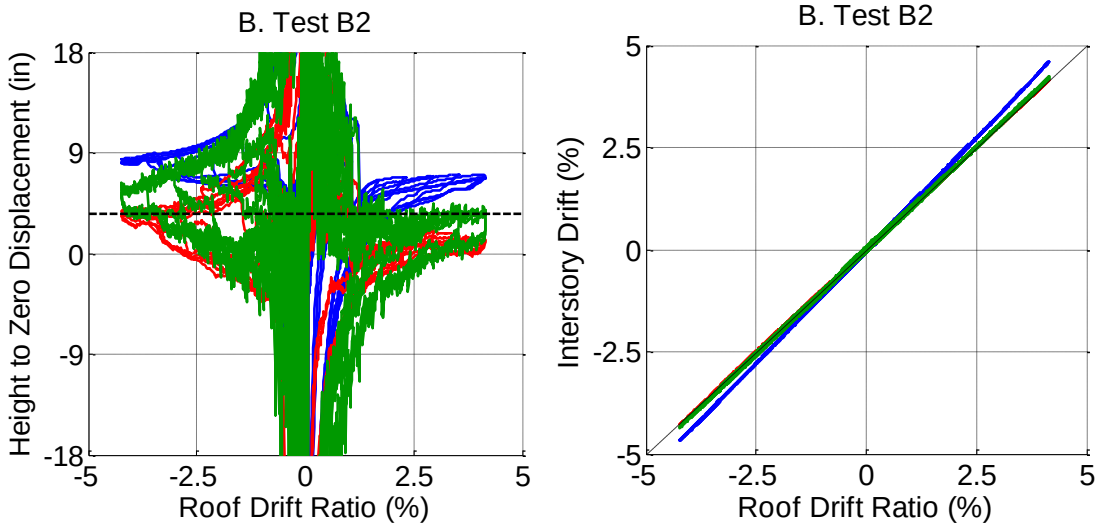

Figure D.201 Specimen B2 - Height to Zero Horizontal Displacement (Left) and Interstory Drifts (Right)

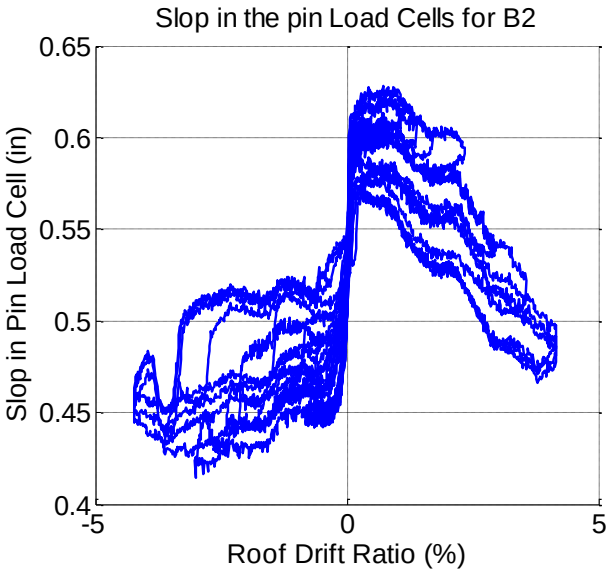

Figure D.202 Specimen B2 - Pin Hole Tolerances for the Pin Load Cells

D.12.4 Member Resultants

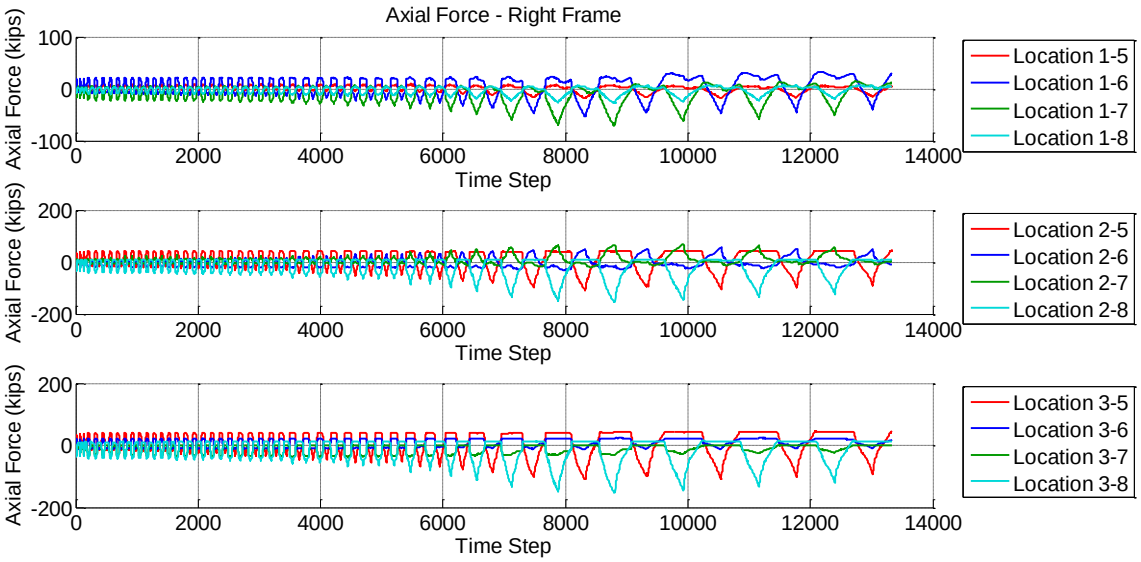

Figure D.203 Specimen B2 - Calculated Member Resultant Forces

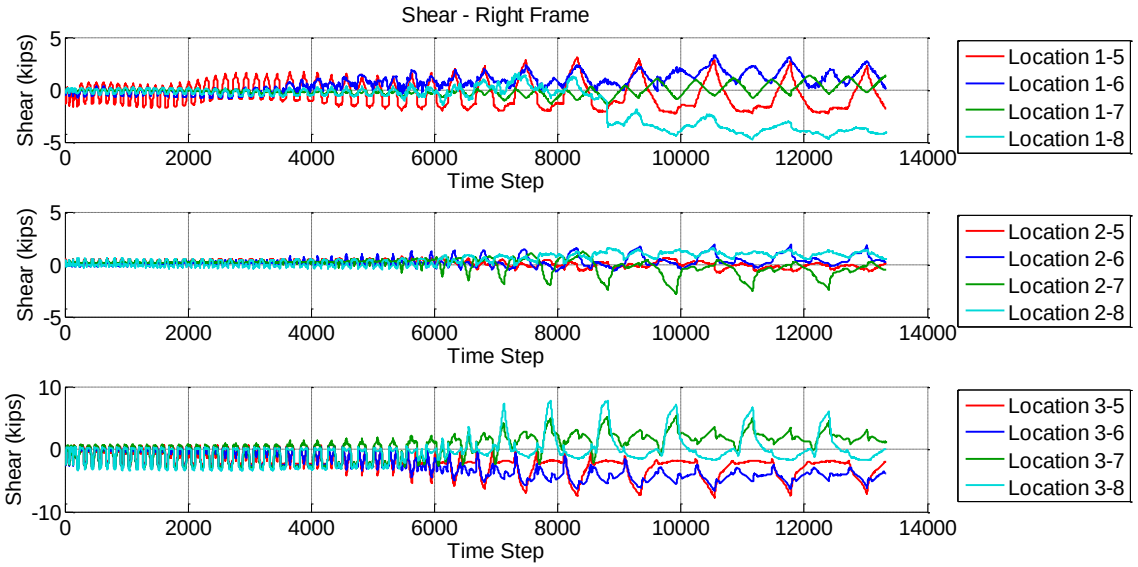

Figure D.204 Specimen B2 - Calculated Member Resultant Forces

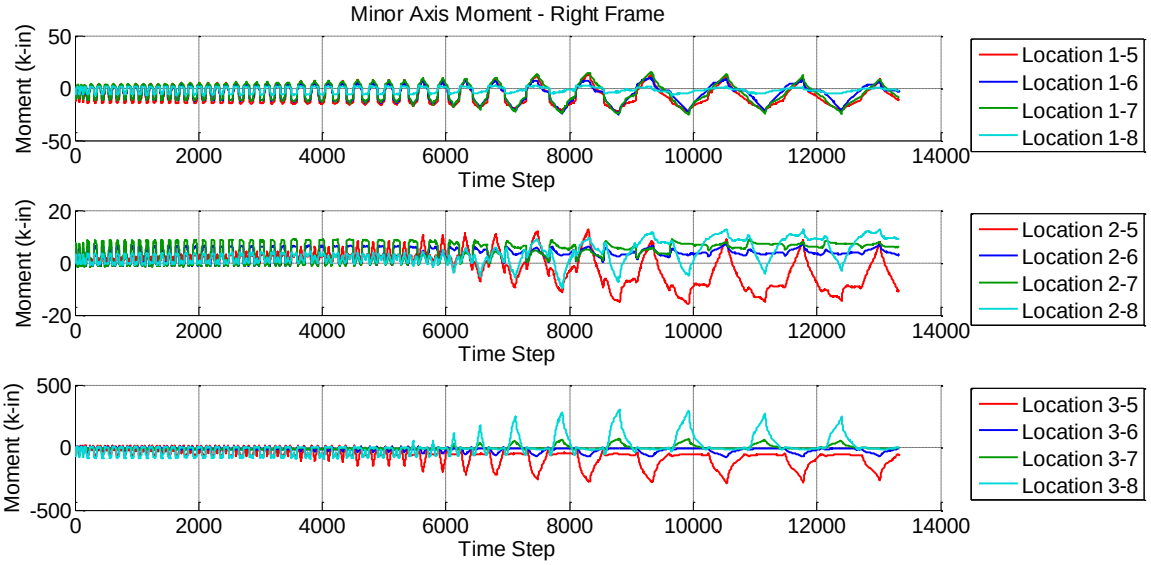

Figure D.205 Specimen B2 - Calculated Member Resultant Forces

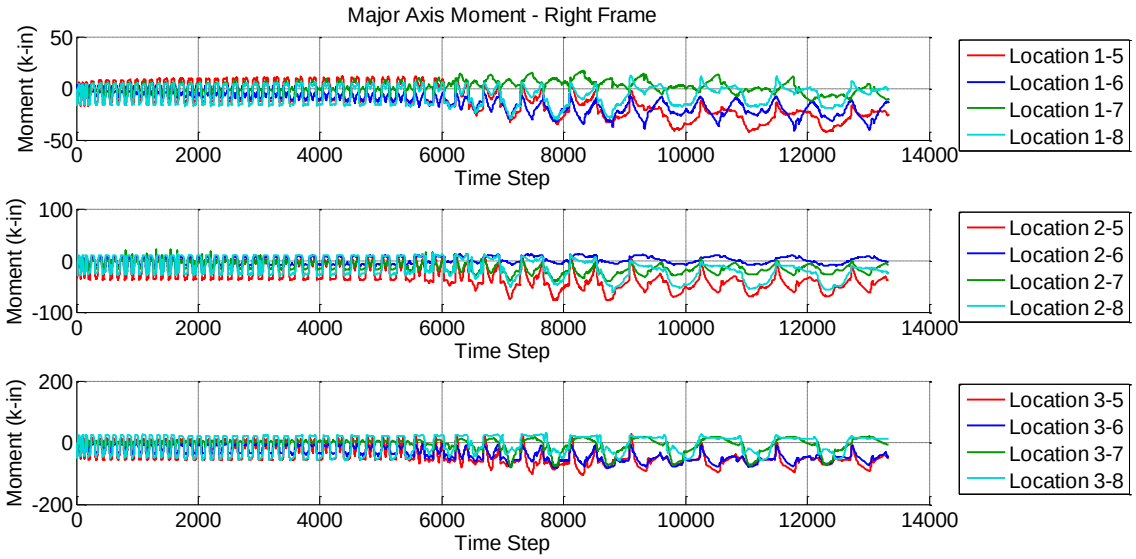

Figure D.206 Specimen B2 - Calculated Member Resultant Forces

D.12.5 Sum Forces at Each Section

The horizontal resultants for all three sections are similar as shown in Figure D.207, Figure D.208, and Figure D.209. Overall, the accuracy of the strain-gaged section resultants validate the measurements and calculations performed to obtain resultants**.** Table D.2 shows that the strain gage section resultants at the last positive and negative peaks are within 43% of the pin load cell reading.

The resultant vertical forces in the system are part of the test control. The vertical pin load cell force is controlled to be within a few kips of zero. The left frame resultant vertical forces were as high as 20 kips in section 2, but 12 kips in section 1 and 3. The data and calculations for the right frame are validated by near zero vertical resultants.

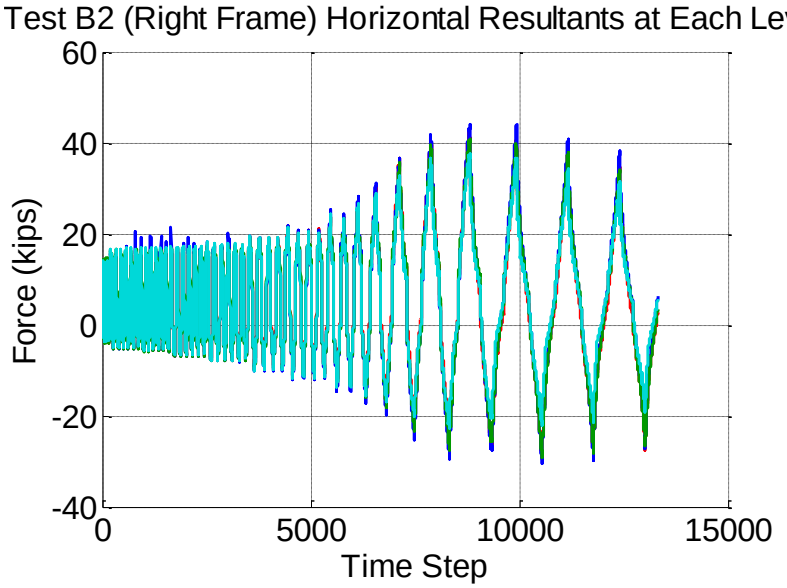

Figure D.207 Specimen B2 - Sum of the Shear Forces

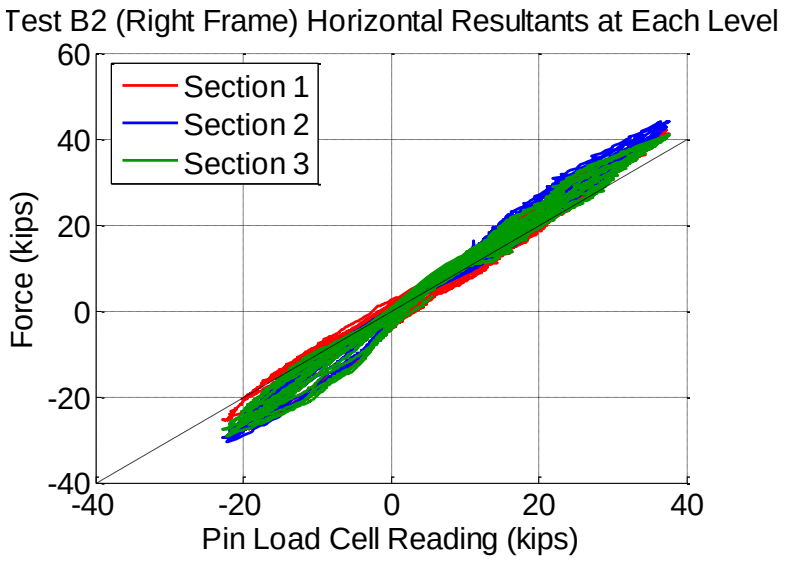

Figure D.208 Specimen B2 - Validation of Shear Forces Calculated From Strain-Gaged Sections

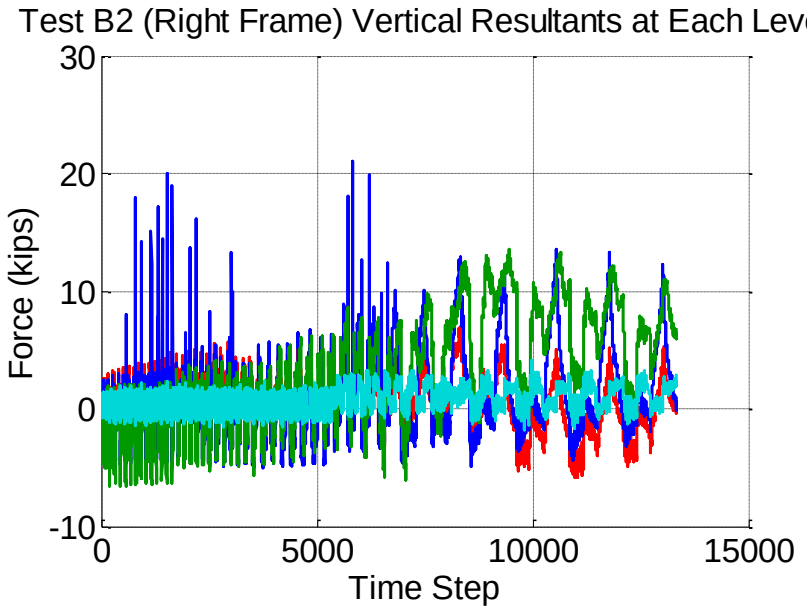

Figure D.209 Specimen B2 - Vertical Forces Calculated From Strain-Gaged Sections

Table D.2 Specimen B2 - Right Frame Horizontal Resultants at the End of the Test

	Last Postive Peak (kips)	Difference From Pin Load Cell	Last Negative Peak (kips)	Difference From Pin Load Cell
Section 1	34.71	10.5%	-27.59	43.2%
Section 2	38.08	21.2%	-27.35	41.9%
Section 3	34.09	8.5%	-26.75	38.8%
Pin Load Cell	31.41	0.0%	-19.27	0.0%

List of Recent NSEL Reports

No.	*Authors*	*Title*	*Date*
010	Zhu, J. and Popovics, J.S.	Non-contact NDT of Concrete Structures Using Air Coupled Sensors	May 2008
011	Gao, Y. and Spencer, B.F.	Structural Health Monitoring Strategies for Smart Sensor Networks	May 2008
012	Andrews, B., Fahnestock, L.A. and Song, J.	Performance-based Engineering Framework and Ductility Capacity Models for Buckling-Restrained Braces	July 2008
013	Pallarés, L. and Hajjar, J.F.	Headed Steel Stud Anchors in Composite Structures: Part I – Shear	April 2009
014	Pallarés, L. and Hajjar, J.F.	Headed Steel Stud Anchors in Composite Structures: Part II – Tension and Interaction	April 2009
015	Walsh, S. and Hajjar, J.F.	Data Processing of Laser Scans Towards Applications in Structural Engineering	June 2009
016	Reneckis, D. and LaFave, J.M.	Seismic Performance of Anchored Brick Veneer	Aug. 2009
017	Borello, D.J., Denavit, M.D., and Hajjar, J.F.	Behavior of Bolted Steel Slip-critical Connections with Fillers	Aug. 2009
018	Rice, J.A. and Spencer, B.F.	Flexible Smart Sensor Framework for Autonomous Full-scale Structural Health Monitoring	Aug. 2009
019	Sim, S.-H. and Spencer, B.F.	Decentralized Strategies for Monitoring Structures using Wireless Smart Sensor Networks	Nov. 2009
020	Kim, J. and LaFave, J.M.	Joint Shear Behavior of Reinforced Concrete Beam-Column Connections subjected to Seismic Lateral Loading	Nov. 2009
021	Linderman, L.E., Rice, J.A., Barot, S., Spencer, B.F., and Bernhard, J.T.	Characterization of Wireless Smart Sensor Performance	Feb. 2010
.			
022	Miller, T.I. and Spencer, B.F.	Solar Energy Harvesting and Software Enhancements for Autonomous Wireless Smart Sensor Networks	March 2010
023	Denavit, M.D. and Hajjar, J.F.	Nonlinear Seismic Analysis of Circular Concrete-Filled Steel Tube Members and Frames	March 2010
024	Spencer, B.F. and Yun, C.-B. (Eds.)	Wireless Sensor Advances and Applications for Civil Infrastructure Monitoring	June 2010
025	Eatherton, M.R.. and Hajjar, J.F.	Large-Scale Cyclic and Hybrid Simulation Testing and Development of a Controlled-Rocking Steel Building System with Replaceable Fuses	Sept. 2010